CODEN: JASMAN 4966

THE JOURNAL of the Acoustical Society of America

Vol. 105, No. 5 May 1999

SOUNDINGS SECTION

(Continued)

CONTENTS—*Continued from preceding page*

(Continued)

CONTENTS—*Continued from preceding page*

(Continued)

CONTENTS—*Continued from preceding page*

ACOUSTICS RESEARCH LETTERS ONLINE

NOTES CONCERNING ARTICLE ABSTRACTS

1. The number following the abstract copyright notice is a Publisher Item Identifier (PII) code that provides a unique and concise identification of each individual published document. This PII number should be included in all document delivery requests for copies of the article.
2. PACS numbers are for subject classification and indexing. See June and December issues for detailed listing of acoustical classes and subclasses.
3. The initials in brackets following the PACS numbers are the initials of the JASA Associate Editor who accepted the paper for publication.

Studies of acousto-electrically levitated drop and particle clusters and arrays

Robert E. Apfel, Yibing Zheng, Yuren Tian

Department of Mechanical Engineering, Yale University, New Haven, Connecticut 06511, USA
robert.apfel@yale.edu yibing.zheng@yale.edu yuren.tian@yale.edu

Abstract: Research into the behavior of clusters and arrays of fluid or solid particles is made possible by acousto-electric levitation in air and charging of "seed" droplets (10-30μm in diameter) which come together in 2-D clusters (with up to 300 droplets). Such clusters condense into larger drops (e.g. 50-300μm) which form uniformly spaced 2-D arrays of monodispersed drops. Similar behavior has been observed for charged solid particles. This research has applications to studies of drop evaporation, combustion, nucleation, and materials synthesis.

Pacs numbers: 43.25.Ts, 43.80.Sh

Context of present work

The generation, control, and applications of sprays and aerosols cover a vast subject of relevance to the energy, environmental, and materials sciences. Fuels, soot and other environmental by-products, coatings, and intermediaries in particle synthesis all begin as sprays and aerosols. Understanding the behavior of multi-drop and particle systems and controlling the processes that created them require a good correspondence between theoretical modeling and benchmark experiments. Single drop evaporation and/or combustion has been studied with a wide variety of techniques. Models of evaporation have been validated, for example, by levitating a drop either electrodynamically[1] or using an acoustical technique described by Tian and Apfel.[2] These techniques are also appropriate for multicomponent drops.[3] High temperature liquid structure has been investigated using aeroacoustic levitation techniques which permit the handling of heavy particles or drops.[4] Yet for many processes involving dense sprays, evaporation, ignition, and combustion processes are controlled by the interaction of droplets[5]; therefore, single drop evaporation models are entirely inadequate.

The study of the combustion of drops and sprays has advanced both experimentally and theoretically, as reviewed recently in the volume edited by Chiu and Chigier.[6] Some of the important advances illustrate how the evaporation, ignition and combustion of sprays are controlled by different parameters for dense vs. dilute clusters because of droplet interactions. "The allure of small controlled groups of droplets," according to Dunn-Rankin et al. "is that they provide an opportunity to isolate the effects of neighboring droplets on drop aerodynamics, drop vaporization, and drop combustion" which is not possible in spatially and temporally unsteady fields characteristic of a full spray or flame.[7] In his review, Chiu reviews the research accomplishments in droplet and spray combustion over a 40-year period. He concludes: "Needless to say, extensive experimental studies must be initiated to validate theoretical and numerical results."[8] In his report, Tambour considers the influence of multisize sprays on flame properties, spanning the range from small drops (20-25 μm), which are comparable to the "seed drops" we discuss below, to large drops (80-100 μm) which are of the same order as the array drops we produced with our apparatus.[9] Control of arrays of drops and/or particles has recently improved with further development of the original work on multi-particle levitation using an electrodynamic balance by Wuerker et al.[10] The group of E. J. Davis, for example, used a double-ring electrodynamic balance apparatus to levitate $NaNO_3$

particles with particle size nominally of 3.5 μm. They were able to achieve improved control of particle size and charge, as well as to manipulate the relative spacing of the particles.[11]

Need for a new benchmark system for multi-drop/particle systems

These studies barely begin to scratch the surface of the broad amount of theoretical, experimental, and numerical work being done to understand drop and particle clusters and arrays, and their many applications. Just as the study of the evaporation of a single drop became the central focus of very dilute evaporating or combusting systems, we need equivalent controllable benchmark multi-drop systems to validate dense spray evaporation and combustion models.

An apparatus for levitating multiple small drops and/or particles is shown in Figure 1. It is an acoustic levitation cell driven by a composite transducer consisting of back-to-back piezoelectric discs, an aluminum horn, and a suitable reflector required for establishing an acoustic standing wave at approximately 26.8 kHz. The spacing between reflectors is about 1.3 cm. If several drops of liquid are simultaneously levitated in this apparatus, acoustic radiation forces will normally drive them to a position just below a pressure node along the axis of the system. There they will aggregate and coalesce.

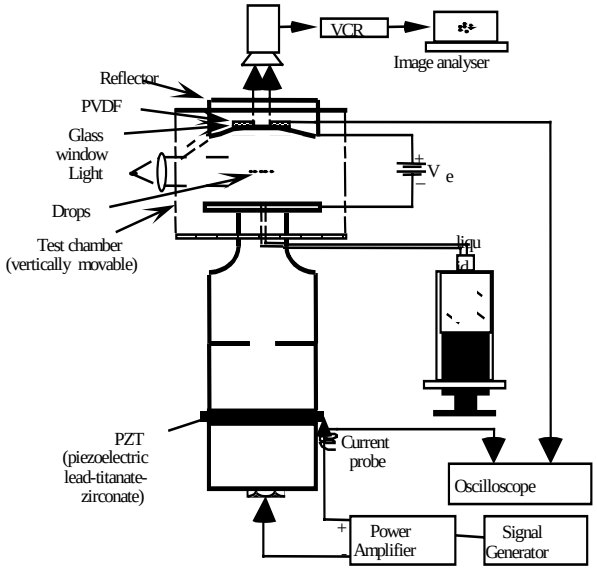

Fig. 1. Schematic of acousto-electric levitator

By holding the top and bottom reflectors in the acoustic standing wave at an electric potential varying from a few hundred to three thousand volts, a new range of capabilities is realized.[12] (See, also, the work of Trinh, et al.[13] First, a liquid placed on the lower plate can be atomized into "seed" droplets and charged by the vibrations of the electrodes. Second, as these "seed" droplets are drawn toward the levitation plane, we note that they aggregate into two-dimensional clusters (which we define to be a number of drops that are virtually touching in one plane). Third, as seed drops are added to the cluster, there comes a point when the drops suddenly coalesce into a single drop (with perhaps a few “petals” of seed drops on the exterior of the drop). This coalesced drop becomes part of a two-dimensional array of drops, as the process is repeated with new seed drops and clusters. An array, for the purposes of this discussion, is characterized by drops spaced by more than one drop diameter.

We are left with a number of important questions: What defines the size of a seed drop? What defines the size of the cluster of seed drops? What triggers the cluster to coalesce? How uniform in size are the array drops arising from cluster coalescence? What

determines the spacing of the array drops and how uniform is this spacing? What determines the degree of stability of the array? If cluster size, array drop size, and array drop spacing could be controlled, as well as drop material and host gas, what applications would suggest themselves, both in terms of validating theoretical models and in terms of technological significance? Can solid particles be similarly clustered and arrayed, and if so, what are the controlling parameters and potential applications? Some of these questions are addressed in what follows. Some are the subject of ongoing research.

Initial observations and interpretation with the new apparatus

The fluid dynamical processes by which seed drops become clusters, and clusters become arrays have transient phases which are difficult to capture in still figures. Two video clips of the cluster and array formation processes are found in multimedia files Mm. 1 and Mm 2. Other examples are on the world wide web.[14]

Mm. 1 Cluster formation (384 KB)

Mm. 2 Drop array formation (299KB)

It is observed that if a few drops of ethanol are placed on the bottom plate of the 26.8 kHz resonator, then at a threshold level of vibration, atomization, clustering, and arraying processes commence. This process leads to two or more planes of collected drops near the pressure nodes of the sound field: Fig. 2, photo (1). These collected clusters and arrays have originated from a mist of fine droplets rising from the bottom plate of the cell: Fig. 2, photo (2). These drops, which we call "seed" drops, are approximately 25-40 μm in diameter and fairly uniform in size. The mechanism of generation is quite clear. The capillary wavelength of the ethanol surface is given by $\lambda_c = (2\pi\gamma/\rho f^2)^{1/3}$; here, γ is the surface tension, ρ is ethanol's density, and f is the acoustic frequency. According to Lang et al.[15], the drop diameter from the surface instability ~ 0.67 λ_c. In the present case, the observed size is somewhat smaller than the predictions. The discrepancy may be attributed to the state of agitation of the surface or to the small electric charge on each seed drop.

Each seed drop is attracted toward the center of the cell by acoustic radiation forces. They aggregate together into a two-dimensional cluster, as shown in the two-figure sequence of Fig. 2, photo (3), but because of the small electrical charge on each drop, they do not immediately coalesce. The size of these clusters is determined by the balance of acoustic attraction and electric repulsion. The acoustic attraction comes from two sources, as described in our lab's earlier work[16]: 1) the primary acoustic radiation force draws all drops to the same position in the sound field, and 2) a secondary, attractive interparticle force draws the drops toward each other. The repulsive force is simply coulombic in nature. The maximum size is determined when a new seed drop feels sufficient repulsion as to be expelled from the periphery of the flat cluster. By increasing the acoustic field or decreasing the charge on the seeds, the cluster size can grow. In one instance, for example, we counted a 2-D cluster of 242 seed drops! Clusters of this size have been observed to fission under appropriate acoustic conditions. The interparticle forces between drops plus the gentle agitation of the acoustic field increase the probability that two of the seed drops in the cluster will touch and coalesce. Seed drops form dimers and trimers as a precursor to the rapid (10-50 msec) formation of a cluster, which then coalesces to an array drop, as shown in “before-after” sequence of Fig. 2-(3a and b). The initial coalescence starts a chain reaction, because the secondary interparticle force goes as the diameter of the drop to the sixth power.[16] As soon as two drops coalesce, increasing their effective diameter, the forces of attraction become stronger, and the process promotes more and more coalescence, until almost all of the drops have formed into a single drop, which we call an "array" drop for reasons to be made clear shortly. Here 85 seed drops of about 45 μm diameter have coalesced into a single drop of approximately 200 μm.

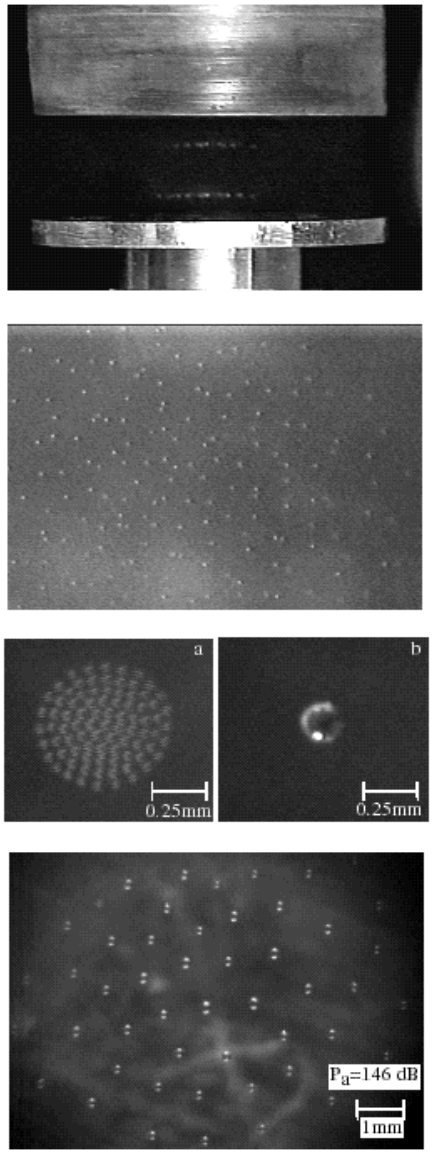

Fig. 2. (1) (top photo) Side view of levitation region in 2-D levitator. The two drop arrays are spaced by 6.4 mm; (2) (second photo) top view of "seed" droplets created by atomization of liquid sample placed on bottom plate of acoustic system; (3) (pair of photos) charged seed drops form 2-dimensional clusters (top view) in acoustic field, labeled (a), and subsequently coalesce into a single "array" drop (labeled b); (4) (bottom photo) top view of several array drops forming 2-dimensional array of nearly uniformly spaced drops.

Occasionally an array drop appears with a few "petals," which are seed drops that haven't coalesced, perhaps because the smaller total drop area of the array drop (compared to the sum of the areas of the seed drops) increases the surface charge density, and thus produces greater coulombic repulsion.

As each array drop forms, it is repelled from the center of the levitation cell by the newly generated seed drops which are aggregating and then coalescing. Each array drop remains in the potential well of the acoustic field but finds a new position with a minimum total energy of the system. This is a dynamic equilibrium, with the array of drops moving, and sometimes rotating around the central position. Fig. 2-photo (4) shows a 2-D array of drops formed in the combined acoustical and electrical fields.

One can control the motion of the drop array by altering the acoustic and electric fields. For example, by lowering the acoustic field and raising the electric field, the primary force for levitation against gravity becomes electrical. In fact, this is precisely how the charge of the array drops can be measured. If the electric field is reduced too much, the drops will fall out. This is just the "Millikan oil drop experiment." In this way, we have observed that the drop charge density is approximately 1/1000 of the critical charge density — $q^* = 8\pi(\varepsilon\gamma a^3)^{1/2}$, which is referred to as the Rayleigh limit.

By varying acoustic and electric field parameters, we observe that as the electric field increases for a constant acoustic field, the charge per seed drop goes up, and therefore the cluster size at which coalescence occurs decreases. Increased acoustic field strength for a constant electric field tends to reduce drop spacing without having a major effect on drop size. From these figures we note a few remarkable features: 1) The drop spacing appears uniform and controllable with electric and acoustic field adjustments. 2) The array drop size seems reasonably uniform.[12]

The initial investigations reported above suggest that this new "Cluster and Array Generation," or CAG apparatus, can provide benchmark conditions for testing a significant set of questions related to evaporation and combustion studies. Initial studies on evaporation of one, two, three, and four drop systems have been reported.[12] Moreover, the proper engineering of this capability may provide opportunities for new technologies in energy, pollution, and materials processing studies.

Two video sequences are linked in this article, the first showing how a cluster forms from the coalescence of dimers and trimers, and the second showing how array drops are born from coalescing clusters.

Acknowledgments

This work was supported in part by NASA, through grant NAG3-2147.

References and links:

[1] W. Li and E. James Davis, Aerosol Sci. and Tech. **25**, 11 (1996).

[2] Y. Tian and R. E. Apfel, J. Acoust. Soc. Am. **93**, 3096 (1993).

[3] See, for example, C. L. Aardahl, W. R. Foss and E. J. Davis, Ind. Eng. Chem. Res. **35**, 2834 (1996).

[4] See, for example, S. Ansell, S. Krishnan, J. K. Richard Weber, J. J. Felten, P.C. Nordine, M. A. Beno, D. L. Price and M. L. Saboungi, Phys. Rev. Lett., **78**, 464 (1997).

[5] G. Chen and A. Gomez, Combustion and Flame, **110**, 392 (1997).

[6] H.H. Chiu and N. Chigier, **(1995)**. *Mechanics and Combustion of Droplets and Sprays*, Eds. (Begell House, New York).

[7] D. Dunn-Rankin, W. A. Sirignano, R. H. Rangel and M. E. Orme, "Drop Arrays and Streams," Ref. 4, p.76.

[8] H. H. Chiu, "Modern developments in mechanics and combustion of many droplet systems," Ref. 4, p. 183.

[9] Y. Tambour, "Structure of multisize sprays and its effect on spray flame properties," Ref. 4, pp. 210 ff.

[10] R. F. Wuerker, H. Shelton and R. V., Langmuir, J. Appl. Phys. **30,** 342 (1959).

[11] See, for example., R. Vehring, C. L. Aardahl, E. J. Davis, G. Schweiger and D.S. Covert, Rev. Sci. Instrum. **68**, 70 (1997).

[12] Y. Tian and R. E. Apfel, J. Aerosol Sci. **27**, 721 (1996).

[13] E.H. Trinh, R. G. Holt, and D. B. Thiessen, Phys. Fluids **8**,43 (1996).

[14] Sequences supplementing Mm1. and Mm2. are at: http://www.yale.edu/bubble/array

[15] J. Lang, J. Acoust. Soc. Am. **34**, 6 (1962).

[16] M. A. H. Weiser, R. E. Apfel, and E. A. Neppiras, Acustica, **56**, 114 (1984).

FDTD simulation of finite-amplitude pressure and temperature fields for biomedical ultrasound

Ibrahim M. Hallaj[a]

Applied Physics Laboratory, University of Washington, Seattle, WA 98105
ibrahim@bwh.harvard.edu

Robin O. Cleveland

Department of Aerospace and Mechanical Engineering, Boston University, Boston, MA 02215
robinc@bu.edu

Abstract: Full wave simulations provide a valuable tool for studying the spatial and temporal nature of an acoustic field. One method for producing such simulations is the finite-difference time-domain (FDTD) method. This method uses discrete differences to approximate derivatives in the governing partial differential equations. We used the FDTD method to model the propagation of finite-amplitude sound in a homogeneous thermoviscous fluid. The calculated acoustic pressure field was then used to compute the transient temperature rise in the fluid; the heating results from absorption of acoustic energy by the fluid. As an example, the transient temperature field was calculated in biological tissue in response to a pulse of focused ultrasound. Enhanced heating of the tissue from finite-amplitude effects was observed. The excess heating was attributed to the nonlinear generation of higher-frequency harmonics which are absorbed more readily than the fundamental. The effect of nonlinear distortion on temperature rise in tissue was observed to range from negligible at 1 MPa source pressure to an 80% increase in temperature elevation at 10 MPa source pressure.

PACS numbers: 43.25.Cb, 43.20.Fn, 43.80.Sh

1. Introduction

There has been increasing interest in the use of high intensity ultrasound in tissue. At high intensities finite-amplitude effects can lead to the production of nonlinearly generated harmonics. These harmonics have been exploited in recent years to improve imaging capabilites in diagnostic ultrasound machines - a technique commonly referred to as harmonic imaging. In addition, focused ultrasound surgery (FUS) is a promising technique that uses high-intensity ultrasound to destroy tissue in a confined region which will avoid the necessity of traditional invasive methods.

One aspect of finite-amplitude propagation that is relevant to biomedical applications is the issue of heat deposition. Although heating occurs for all acoustic propagation in lossy media, the generation of higher harmonics due to nonlinear distortion enhances the heating effects.[1,2,3] This phenomenon is particularly important for FUS where ther-

[a]Current affiliation: *Brigham and Women's Hospital, Harvard Medical School, 221 Longwood Ave., Boston, MA 02115.*

mal dose typically determines the therapeutic effects. Modeling of finite-amplitude ultrasound effects in tissue heating is a two-tiered process: first, the sound propagation through tissue is solved using a nonlinear wave equation; second, the diffusion of heat in the tissue is calculated using the previously calculated acoustic field as the source term. In this work we describe a numerical method for solving both the propagation and heating problems.

The solution of the propagation problem is complicated by the nonlinear distortion. There are few analytical solutions available and numerical simulations are currently the best means of making predictions for nonlinear propagation. One numerical technique which provides full-wave solutions to the propagation problem is the finite-difference time-domain (FDTD) method. Simulations of linear[4] and nonlinear[5] propagation in inhomogeneous tissue-like media have been recently presented. In this work we solve both the propagation and heating problems for finite-amplitude sound propagation in a homogeneous medium using the FDTD method.

2. The nonlinear absorbing wave equation

We used the Westervelt equation as a model equation for the propagation of finite-amplitude sound in a thermoviscous fluid. The equation can be derived from the equations of fluid motion by keeping terms up to quadratic order (see, for example, Hamilton and Morfey[6]). The Westervelt equation can be written in the following form

$$\nabla^2 p - \frac{1}{c_0^2}\frac{\partial^2 p}{\partial t^2} + \frac{\delta}{c_0^4}\frac{\partial^3 p}{\partial t^3} + \frac{\beta}{\rho_0 c_0^4}\frac{\partial^2 p^2}{\partial t^2} = 0, \tag{1}$$

where p is the acoustic pressure, ρ_0 and c_0 are the ambient density and sound speed, δ is the diffusivity of sound, $\beta = 1 + \frac{B}{2A}$ is the coefficient of nonlinearity and B/A is the parameter of nonlinearity of the fluid.

The first two terms in Eq.(1) are the D'Alembertian operator acting on the acoustic pressure. This term describes linear lossless wave propagation at the small-signal sound speed. The third term in Eq.(1) is the loss term, which is due to the thermal conduction and the viscosity of the fluid. We model soft tissue as a thermoviscous fluid. The fourth term describes nonlinear distortion of the wave due to finite-amplitude effects.

3. Solving the wave equation using the FDTD method

The numerical solution of Eq.(1) was calculated on a polar cylindrical grid. The source was modeled as a spherical cap (bowl) having azimuthal symmetry about the axis of the source. The acoustic and temperature fields need only be computed using a two dimensional spatial grid, x, in the axial direction and r in the radial direction. We used the explicit finite-difference time-domain (FDTD) method, which was introduced in its contemporary form by Yee.[7] The FDTD method approximates the spatial and temporal partial derivatives with discrete differences which are obtained from Taylor series expansions about each node on the computational grid. The grid consisted of two spatial dimensions with uniform spacing Δx and Δr, indexed by (i, j) and a temporal dimension with uniform spacing Δt, indexed by n. Absorbing boundary conditions were applied at the edge of the grid to prevent numerical reflections from affecting the results.

Temporal derivatives were calculated to second order accuracy, $\mathcal{O}(\Delta t^2)$, as follows

$$\begin{aligned}\frac{\partial^2 p}{\partial t^2} &\approx \frac{1}{(\Delta t)^2}(p_{i,j}^{n+1} - 2p_{i,j}^{n} + p_{i,j}^{n-1}),\\ \frac{\partial^3 p}{\partial t^3} &\approx \frac{1}{(2\Delta t)^3}(6p_{i,j}^{n} - 23p_{i,j}^{n-1} + 34p_{i,j}^{n-2} - 24p_{i,j}^{n-3} + 8p_{i,j}^{n-4} - p_{i,j}^{n-5}).\end{aligned} \tag{2}$$

The absorption and nonlinear terms used backward-time differences. The spatial differences were computed using a fourth order accurate, $\mathcal{O}(\Delta x^4, \Delta r^4)$, centered differencing,

$$\begin{aligned}\frac{\partial p}{\partial r} &\approx \frac{1}{12\Delta r}(-p_{i,j+2}^{n} + 8p_{i,j+1}^{n} - 8p_{i,j-1}^{n} + p_{i,j-2}^{n}),\\ \frac{\partial^2 p}{\partial r^2} &\approx \frac{1}{12(\Delta r)^2}(-p_{i,j+2}^{n} + 16p_{i,j+1}^{n} - 30p_{i,j}^{n} + 16p_{i,j-1}^{n} - p_{i,j-2}^{n}),\\ \frac{\partial^2 p}{\partial x^2} &\approx \frac{1}{12(\Delta x)^2}(-p_{i+2,j}^{n} + 16p_{i+1,j}^{n} - 30p_{i,j}^{n} + 16p_{i-1,j}^{n} - p_{i-2,j}^{n}).\end{aligned} \tag{3}$$

We found that by using a higher order for the spatial derivatives the effects of numerical dispersion (artificial phase velocity) were reduced. A discussion of numerical stability and dispersion is beyond the scope of this article but is discussed elsewhere.[8]

4. Tissue heating by ultrasound

Bioeffects of ultrasound have been studied in the laboratory for some time.[9] However, experiments can be costly and time-consuming. In addition, data can be collected only where instruments are placed invasively. Thus, modeling of bioeffects is useful in making predictions for clinical applications.

As sound propagates through tissue, some of its energy is absorbed and is manifest as a temperature increase. It has been shown that heating from high-intensity ultrasound is greater than linear models predict.[1,2] This is because as an acoustic signal propagates nonlinear distortion pumps energy from the signal into its higher harmonics. In most fluids absorption increases with frequency; therefore higher harmonics are absorbed more strongly than the fundamental, leading to increased heating.

The temperature increase in the tissue can be modeled by a diffusion type equation. The "bioheat equation" is commonly used to describe the thermal effects in tissue,[10]

$$\frac{\partial T}{\partial t} = \frac{k_t}{\rho C_t}\nabla^2 T - \frac{W_b C_b}{\rho C_t}(T - T_a) + \frac{Q}{\rho C_t}, \tag{4}$$

where T is the temperature in the tissue, k_t is the thermal conductivity of the tissue, C_t and C_b are the heat capacity of the tissue and the blood respectively, W_b is the perfusion rate (cooling by blood flow), T_a is the ambient (arterial) temperature (37°C), and Q is the heat deposition source term due to the acoustic field.

The bioheat equation was solved using the FDTD scheme; the pressure and temperature fields were calculated simultaneously. The heat source term was calculated as described by Pierce[11],

$$Q = \frac{2\alpha}{\rho_0 c_0 \omega^2}\left(\frac{\partial p}{\partial t}\right)^2. \tag{5}$$

In a thermoviscous fluid, the absorption α is related to δ and $\omega = 2\pi f$ by

$$\delta = \frac{2c_0^2\alpha}{\omega^2}. \tag{6}$$

Empirical results indicate that absorption in tissue follows a power law which varies from $\omega^{1.1}$ to $\omega^{1.5}$ rather than ω^2 as observed in a thermoviscous fluid. However, it has been shown that for finite-amplitude propagation the acoustic intensity is approximately the same using either power law[12] and hence the heat deposition should be only mildly sensitive to the exact power law relationship used.

5. Results

Simulation results are shown in this section to illustrate the output of the numerical code described above. The example output was for a focused bowl source array of 64 simple sources having azimuthal symmetry. The source was driven by a 1 MHz sinusoidal burst of 6 cycles modulated by a Gaussian envelope in time. The geometric focus of the array was situated 3 cm from the array face. The source aperture was 4 cm; the computational domain spanned an area of 5.12 cm $\times$ 5.12 cm. The grid spacing was $\Delta x = \Delta r = 0.1$ mm and $\Delta t = 10$ ns.

The propagation medium was modeled as a tissue-like material, having properties similar to those reported in the literature for soft tissue.[13] The parameters used in the acoustic problem were: $c_0 = 1600$ m/s, $\rho_0 = 1100$ kg/m^3, $\alpha = 4.5$ Np/m, and $\beta = 5.5$. For the bioheat equation the following parameters were used: $k_t = 0.6$ W/(m·K), $C_t = C_b = 3800$ J/(kg·K) and $W_b = 0.5$ kg/(m^3·s). Figure 1 shows some snapshots of the pressure and temperature fields resulting from nonlinear propagation in the medium.

Mm. 1. Animated pressure and temperature fields (460Kb)

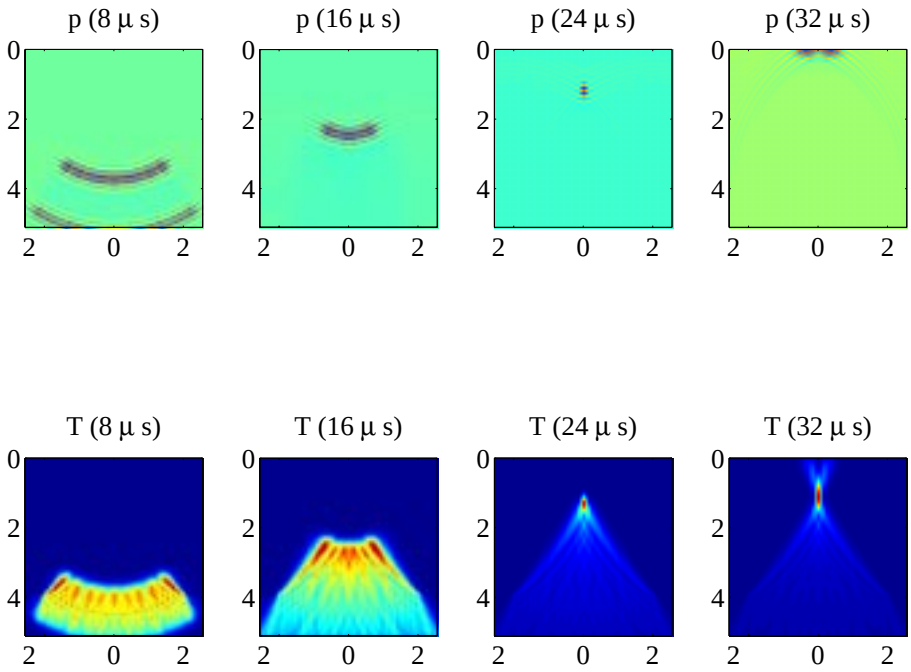

Fig. 1. Snapshots of the pressure (top row), and temperature (bottom row) for the 1 MPa nonlinear simulation. The axes are labeled in cm. Those reading the print version should refer to the color version of this figure in the online archival version.

Figure 2 shows axial slices of the temperature fields at 32 μs for linear and nonlinear simulations at source pressures ranging from 1 MPa to 10 MPa. The linear simulations were achieved by setting β to zero. Temperature elevation increased with source pressure. For nonlinear simulations excess heating increased dramatically for source pressures above 5 MPa. For the 1 MPa nonlinear simulation the the heating was only 2% above the linear predictions and at 2 MPa the excess heating was 4%. However, at 5 MPa excess heating was 27% and at 10 MPa it was 80%. High source levels were required to observe excess heating because the entire propagation path was modeled as tissue. Tissue has a relatively large absorption and prevents steep shocks, with significant harmonic content, from forming. For propagation through water, which is much less absorbing, steep shocks occur much more readily and consequently excess heating becomes important at lower source levels.

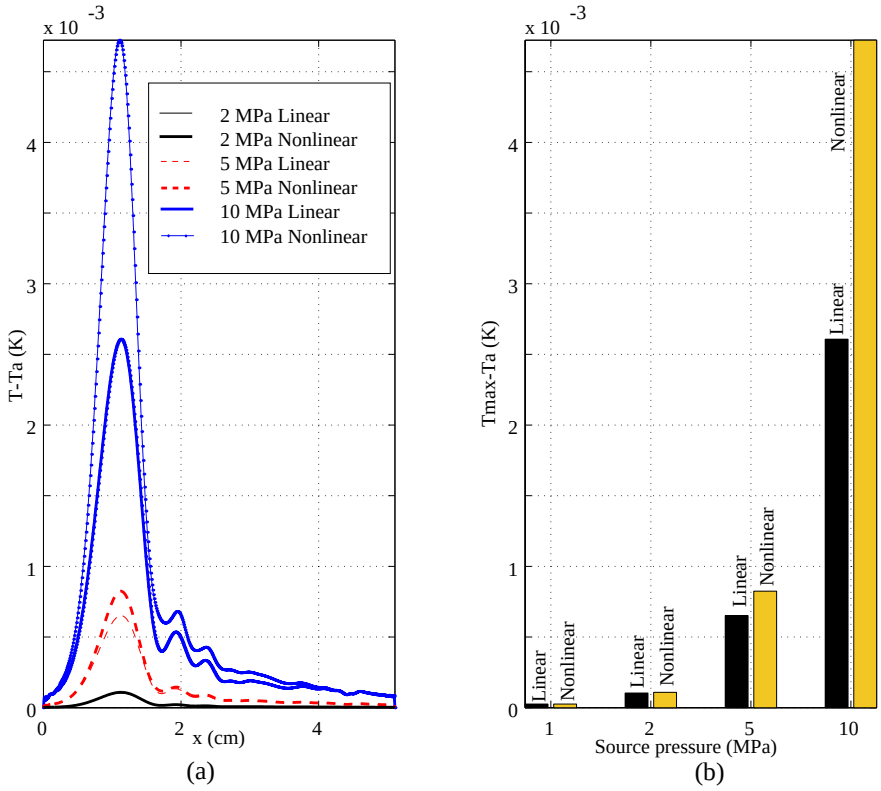

Fig. 2. (a) Axial slices of the temperature at 32 μs for various source pressures with and without nonlinearity. (b) Peak temperature elevation for several source conditions, showing the increasing effect of nonlinear distortion.

6. Conclusions

Accurate knowledge of the behavior of ultrasonic beams in tissue allows for better prediction of bioeffects of ultrasound, and improved treatment and device design. The FDTD method for simulation of transient finite-amplitude acoustic fields has been described with an application in medical ultrasound used as an example. Heating in tissue, modeled as a thermoviscous fluid, was obtained for a short acoustic pulse from a focused bowl source. Peak temperature rises from a 1 MHz ultrasonic pulse propagating nonlin-

early through a tissue-like material was observed to depend on the degree of nonlinear distortion and ranged from 2% to 80% excess temperature rise for 1 MPa to 10 MPa source pressure conditions.

Acknowledgments

This work was supported in part by the Office of Naval Research (code 321TS). The authors wish to thank Steven Kargl and Ron Roy for valuable discussions.

References and Links

[1] D. R. Bacon, E. L. Carstensen, "Increased heating by diagnostic ultrasound due to nonlinear propagation," J. Acoust. Soc. Am. **88**, 26-34 (1990).
[2] E. L. Carstensen, N. D. McKay, D. Dalecki, T. G. Muir, "Absorption of finite amplitude ultrasound in tissues," Acustica **51**, 116-123 (1982).
[3] J. Wu, G. Du, "Temperature elevation in tissues generated by finite-amplitude tone bursts of ultrasound," J. Acoust. Soc. Am. **88**, 1562-1577 (1990).
[4] T. D. Mast, L. M. Hinkleman, M. J. Orr, V. W. Sparrow, R. C. Waag, "Simulation of ultrasonic pulse propagation through the abdominal wall," J. Acoust. Soc. Am. **102**, 1177-1190 (1997).
[5] I. M. Hallaj, R. O. Cleveland, S. G. Kargl, "Two-dimensional nonlinear propagation of pulsed ultrasound through a tissue-like material", *Proceedings of the* 16^{th} *Int. Congress on Acoust. and the 135th Meeting of the Acoust. Soc. Am., Seattle, June 1998.*, (American Institute of Physics, New York, 1998) vol. 3, pp. 1863-1864.
[6] M. F. Hamilton, C. L. Morfey, "Model equations", in *Nonlinear Acoustics*, edited by M. F. Hamilton and D. T. Blackstock (Academic Press, San Diego, 1998) Chap. 3.
[7] K. S. Yee, "Numerical solution of initial boundary value problems involving Maxwell's equations in isotropic media," IEEE Trans. Antennas and Propagation **14**, 302-307 (1996).
[8] S. Nakamura, *Applied Numerical Methods With Software*, (Prentice Hall, New Jersey, 1991).
[9] G. ter Haar, "Ultrasound focal beam surgery," Ultrasound in Med. and Biol. **21**, 1089-1100 (1995).
[10] C. A. Damianou, K. Hynynen, X. Fan, . "Evaluation of accuracy of a theoretical model for predicting the necrosed tissue volume during focused ultrasound surgery," IEEE Trans. Ultrasonics, Ferroelec. Freq. Contr. **42**, 182-187 (1995).
[11] A. D. Pierce, *Acoustics, An Introduction to its Physical Principles and Applications*, (Acoustical Society of America, New York, 1991) pp. 515-519.
[12] M. A. Averkiou, L. A. Crum, V. A. Khokhlova, O. V. Rudenko, "Nonlinear waveform distortion and energy attenuation of intense acoustic waves in biological tissue," *Proceedings of the World Congress of Ultrasonics, 1995, Part I.*.
[13] S. Yongchen, D. Yanwu, T. Jie, T. Zhensheng, "Ultrasonic propagation parameters in human tissues," *Proceedings of Ultrasonics Symposium, 1986.*

ACOUSTICAL NEWS—USA

Elaine Moran
Acoustical Society of America, 500 Sunnyside Boulevard, Woodbury, New York 11797

Editor's Note: *Readers of this Journal are asked to submit news items on awards, appointments, and other activities about themselves or their colleagues. Deadline dates for news items and notices are 2 months prior to publication.*

The 136th meeting of the Acoustical Society of America held in Norfolk, Virginia

The 136th meeting of the Acoustical Society of America was held 12–16 October 1998 at the Norfolk Waterside Marriott Hotel in Norfolk, Virginia. This was the second time the Society has met in this city, the previous meeting being held in 1984.

The meeting drew a total of 712 registrants. There were 108 nonmembers registered and 137 students were in attendance.

Attesting to the international ties of our organization, 43 of the registrants were from outside North America, the United States, Canada, and Mexico, which accounted for 645, 23, 1, respectively. There were 8 registrants from Japan, 6 each from Germany and Sweden, 5 from France, 4 from Italy, 3 each from Australia and Russia, 2 from People's Republic of China, and 1 each from Denmark, Greece, The Netherlands, Spain and the United Kingdom.

A total of 501 papers organized into 64 sessions covered the areas of interest of all 12 Technical Committees and 1 Technical Group. The meeting also included 17 different meetings dealing with standards, indicating a healthy level of activity in this area of our endeavors.

The local meeting committee arranged technical tours to NASA Langley Research Center and an organ concert and demonstration tour to two local Norfolk churches.

The tutorial lecture was continued at the Norfolk meeting. Seth Putterman of UCLA lectured on ''Probing the Unknowns of Sonoluminescence'' to an audience of about 75 attesting to the broad interest of the subject.

The meeting also included a Sonic Boom Symposium cosponsored by NASA. The Symposium provided a forum for government, industry, and university participants to present and discuss the current state of the art in sonic boom technology.

A Gallery of Acoustics was presented which included several interesting images resulting from various signal processing techniques. Two short courses were also presented including a Short Course on Auralisation and a Short Course on Sonic Boom.

The plenary session included the presentation of awards, announcement of newly elected Fellows of the Society, and recognition to the meeting organizers. The President presented five Society awards (see Figs. 1–5) and announced the election of 23 new Fellows. The Science Writing Award in Acoustics for Journalists was awarded to Jennifer Ouellette for her article in the September 1997 issue of *The Industrial Physicist* titled ''Science and Art Converge in Concert Hall Acoustics.'' The Science Writing Award for Professionals in Acoustics was awarded to Mathias Fink for his article in the March 1997 issue of *Physics Today* titled ''Time Reversed Acoustics.'' Dr. Fink was not able to be present at the meeting. The Silver Medal in Animal Bioacoustics was presented to Whitlow W. L. Au of the Hawaii Institute of Marine Biology ''for contributions to the fundamental knowledge of the acoustics of dolphin sonar.'' The Silver Medal in Engineering Acoustics was presented to Richard H. Lyon of RH Lyon Corp, Cambridge, Massachusetts ''for contributions to noise reduction of products through design and to Statistical Energy Analysis.'' The Silver Medal in Musical Acoustics was presented to Neville H. Fletcher of Australia ''for contributions to understanding sound production, and especially the role of nonlinear processes

FIG. 1. President James E. West (r) presents the Science Writing Award in Acoustics to Jennifer Ouelette.

FIG. 2. President James E. West (r) presents the Silver Medal in Animal Bioacoustics to Whitlow W. L. Au.

 0001-4966/99/105(5)/2539/3/$15.00

FIG. 3. President James E. West (r) presents the Silver Medal in Engineering Acoustics to Richard H. Lyon.

FIG. 4. President James E. West (r) presents the Silver Medal in Musical Acoustics to Neville H. Fletcher.

FIG. 5. President James E. West (r) presents the von Békésy Medal to Murray B. Sachs.

in string, wind, and percussion musical instruments. The von Békésy Medal was presented to Murray B. Sachs of Johns HopkinsUniversity ''for contributions to understanding the neural representation of complex acoustic stimuli.'' Election of the following persons to Fellow grade was announced: Jan D. Achenbach, Peter G. Cable, Robert P. Carlyon, Dale E. Chimenti, Sheryl Coombs, David J. Evans, Katherine W. Ferrara, Oded Ghitza, James Greenleaf, Frank Henyey, Daniel Juve, Armin Kohlrausch, Vladimir A. Krasilnikov, Frederic L. Lizzi, Rudolph Martinez, John Middlebrooks, Edward Monahan, Andrew J. Norris, Kevin J. Parker, Oleg V. Rudenko, Neil A. Shaw, Yoichi Tohkura, and Barry Uscinski.

The President expressed the Society's thanks to the Local Committee for the excellent execution of the meeting, which clearly required meticulous planning. He introduced the Chair of the Meeting, Kevin P. Shepherd, who acknowledged the contributions of the members of his committee including: Clemans A. Powell, Technical Program Chair; John Cline, Administrative Chair; Lori Jones, Secretary; Gary Gibbs, Audio-Visual; Dan Palumbo and Travis Turner, Facilities; Sheri Brown, Paper Copying Service; Brenda Sullivan, Signs; and Maureen Tracey, Technical Tours.

The President also extended thanks to the members of the Technical Program Organizing Committee: Clemans A. Powell, Technical Program Chair; Darrell R. Jackson, Acoustical Oceanography; Peter M. Scheifele, Animal Bioacoustics; Noral D. Stewart and George E. Winzer, Architectural Acoustics; T. Douglas Mast, Biomedical Ultrasound/Bioresponse to Vibration; Victor W. Sparrow, Education in Acoustics; James F. Tressler, Engineering Acoustics; Charles E. Schmid, Musical Acoustics; Richard J. Peppin, Noise; Bart Lipkens and Victor W. Sparrow, Physical Acoustics; Gary R. Wilson, Signal Processing in Acoustics; Steven A. Zahorian and Matthew Zimmer, Speech Communication, Gerard P. Carroll, Structural Acoustics and Vibration; Ralph R. Goodman, Underwater Acoustics.

JAMES E. WEST
President 1998–1999

USA Meetings Calendar

Listed below is a summary of meetings related to acoustics to be held in the U.S. in the near future. The month/year notation refers to the issue in which a complete meeting announcement appeared.

1999

4–6 June — International Hearing Aid Conference V, Iowa City, IA [Rich Tyler, Dept. of Otolaryngology, Head and Neck Surgery, The University of Iowa, 200 Hawkins Dr., #E230 GH, Iowa City, IA 52242-1078, Tel.: 319-356-2471; Fax: 319-353-6739, E-mail: rich-tyler@uiowa.edu, WWW: http://www.medicine.uiowa.edu/otolaryngology/news/news.html].

6–7 June — 1999 SEM Spring Conference, Cincinnati, OH [Katherine M. Ramsay, Conference Manager, Society for Experimental Mechanics, Inc., 7 School St., Bethel, CT 06801; Tel.: 203-790-6373; Fax: 203-790-4472; E-mail: meetings@sem1.com].

25–26 June — 1999 Biomedical Imaging Symposium: Visualizing the Future of Biology and Medicine, Bethesda, MD [BECON Symposium Website http://www.nih.gov/grants/becon/meeting99/index.htm].

27–30 June — ASME Mechanics and Materials Conference, Blacksburg, VA [Mrs. Norma Guynn, Dept. of Engineering Science and Mechanics, Virginia Tech, Blacksburg, VA 24061-0219; Fax: 540-231-4574; E-mail: nguynn@vt.edu; WWW: http://www.esm.vt.edu/mmconf/].

6–11 July — 1999 Clarinetfest, Ostend, Belgium [International Clarinet Association, Keith Koons, Music Dept., Univ. of Central Florida, P.O. Box 161354, Orlando, FL 32816-1354].

30 Sept.–1 Oct. — Seventh Annual Conference on the Management of the Tinnitus Patient, Iowa City, IA [Rich Tyler, Dept. of Otolaryngology, Head and Neck Surgery, The University of Iowa, 200 Hawkins Dr., #E230 GH, Iowa City, IA 52242-1078, Tel.: 319-356 2471; Fax: 319-353-6739, E-mail: rich-tyler@uiowa.edu, WWW: http://www.medicine.uiowa.edu/otolaryngology/news/news.html].

7–10 Oct. — Symposium on Occupational Hearing Loss, Philadelphia, PA [American Institute for Voice and Ear Research, Attn: Barbara-Ruth Roberts, 1721 Pine St., Philadelphia, PA 19103, Tel.: 215-545-2068; Fax: 215-735-2725.

1–5 Nov. — 138th meeting of the Acoustical Society of America, Columbus, OH [Acoustical Society of America, 500 Sunnyside Blvd., Woodbury, NY 11797, Tel.: 516-576-2360; Fax: 516-576-2377; E-mail: asa@aip.org; WWW: asa.aip.org].

2–4 Dec. — ACTIVE 99, Fort Lauderdale, FL [Institute of Noise Control Engineering, P.O. Box 3206 Arlington Branch, Poughkeepsie, NY 12603, Tel.: 914-462-4006; Fax: 914-463-020; E-mail: INCEUSA@aol.com;/users.aol.com/inceusa/ince.html].

6–8 Dec. — INTER-NOISE 99, Fort Lauderdale, FL [Institute of Noise Control Engineering, P.O. Box 3206 Arlington Branch, Poughkeepsie, NY 12603, Tel.: 914-462-4006; Fax: 914-463-020; E-mail: INCEUSA@aol.com;/users.aol.com/inceusa/ince.html].

BOOK REVIEWS

James F. Bartram
94 Kane Avenue, Middletown, Rhode Island 02842

These reviews of books and other forms of information express the opinions of the individual reviewers and are not necessarily endorsed by the Editorial Board of this Journal.

Editorial Policy: *If there is a negative review, the author of the book will be given a chance to respond to the review in this section of the Journal and the reviewer will be allowed to respond to the author's comments. [See ''Book Reviews Editor's Note,'' J. Acoust. Soc. Am.* ***81****, 1651 (May 1987).]*

A reply to Daniel R. Raichel's ''Review of Architectural Acoustics, Blending Sound Sources, Sound Fields, and Listeners'' [J. Acoust. Soc. Am. 104, 3151 (1998)]

Yoichi Ando

Graduate School of Science and Technology, Kobe University, Rokkodai, Nada, Kobe 657-8501, Japan

I am thankful that Daniel R. Raichel wrote the review of my book, *Architectural Acoustics, Blending Sound Sources, Sound Fields, and Listeners* (AIP Press/Springer Verlag, New York, 1998). I hope that most of the technical comments may be accepted.

However, I am unhappy on two parts as mentioned below. Taking this opportunity in replying to his review, I would like to offer further information:

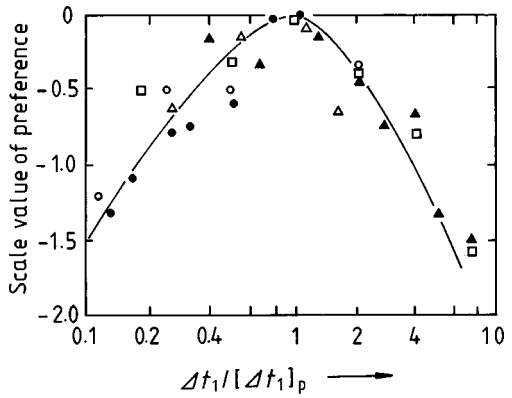

FIG. 1. Scale value of preference as a function of the delay time normalized by its preferred delay time given by Eq. (4.1) in the book. Different symbols indicate scale values obtained by subjects from different nations with different music motifs. ○ ●: Music motif A; △ □: Music motif B; ▲: Music motif C; ● ▲: 7 Korean subjects; ○ □: 13 German subjects; △: 10 Japanese subjects.

(1) In the last part in his review he stated: ''In view of the subjective nature of Ando's thesis, a question remains: is aural subjectivity a variant according to culture and nationality?'' My book describes scientific approaches using only the paired-comparison tests asking which of two sound fields they preferred to hear music and speech. His comments are concerned with culture and nationality. As a matter of fact, we tested many acousticians and students of American, German, Korean, and Japanese including participants to the MCHA95 Symposium, and found no significant differences. As matter of fact, as is cited in my book, experiments as a function of the delay time of single reflection on the subjective preference for different national subjects had been performed in the beginning of the 1980's.[1] As is shown in Fig. 1, we may not find any fundamental differences between the scale values of subjective preference with different national subjects. In this figure, the delay time of single reflection is normalized by the preferred delay time. I understand to some extent ''a cultural difference.'' However, I am basically interested in the individual differences; age, sex, music education, and other relevance related to the individuals. I hope readers will deeply understand that the sentences that I mentioned on page 220 in my book, i.e., ''So far, we have discussed that a meeting place of art and science may help discover individual preference or personality as the minimum unit of society. A lasting peace on earth may be achieved by release of each personality given by Nature.'' A war or a fight was/is occurring to release nations, races, religions, and human specified groups, but not to release individual personality, that is the final goal of education.

(2) He said, ''The text is not an easy read . . . .'' As I mentioned on the back cover, the second paragraph, beginning with ''In writing this book, the author has paid special attention to stimulating readers' left and right hemisphere of the brain with both text and illustration, . . . '', almost all of the mathematical expressions are illustrated. Thus architectural students may understand with figures (right hemisphere) without knowledge of the mathematics (left hemisphere). Therefore, if readers have two hemispheres, then they can understand the book deeply.

[1] S. H. Kang and Y. Ando, ''Comparison between subjective preference judgments for sound fields by different nations,'' Memoirs of the Graduate School of Science and Technology Kobe University, **3-A**, 71–76 (1985).

 0001-4966/99/105(5)/2547/1/$15.00

Architectural Acoustics: Principles and Practice

William J. Cavanaugh and Joseph A. Wilkes

John Wiley & Sons, Inc., New York, NY, 1999.
xvii+332 pp. Price: $69.95.

The new textbook *Architectural Acoustics: Principles and Practice* by William J. Cavanaugh and Joseph A. Wilkes is an exceptionally welcome addition to the limited number of textbooks specifically written to teach architects the basic principles of building acoustics.

Each of the six chapters is authored or co-authored by a practicing acoustic consultant with expertise in specific areas of architectural acoustic design. Mr. Cavanaugh and Mr. Wilkes have assembled an impressive team of individuals who offer the reader an opportunity to understand both the principles of the subject as well as how to apply these principles.

The key introductory chapter is written by William Cavanaugh, former Director of BBN's Architectural Technology Division and currently the principal and founder of Cavanaugh Tocci Associates, Inc. of Sudbury, Massachusetts, one of the country's leading consultancies in architectural acoustics. Having taught and lectured on the subject for over 30 years, Mr. Cavanaugh is well aware of the need to differentiate between teaching architects and teaching engineers or physicists. His Introductory Chapter on Basic Concepts and Design Criteria is extremely clear and concise. Both the text and graphics are well organized and within the 54 page Introduction, I counted only 4 simple algebraic equations. Nothing quite scares an architecture student as much as opening an engineering textbook on acoustics and being faced with page after page of equation derivations. The material in this textbook is primarily explained through the use of text, charts, graphs, tables and nomograms.

Subjects covered are basic measurements of sound, wavelengths, the audible frequency range, and units of sound intensity. The design criteria portion explains NC curves, STC numbers, and other typical architectural criteria. In addition, Mr. Cavanaugh emphasizes the importance of involving the acoustic specialist at the beginning of the design process in order to meet required program objectives such as privacy, speech intelligibility and musical liveness, warmth and definition.

Chapter two, written by Rein Pirn of Acentech, Inc. of Cambridge Massachusetts, is devoted to descriptions of construction materials and their ability to absorb, reflect, or transmit sound. Mr. Pirn was the acoustician who first advised his colleagues that the power of musical sources must determine the volume of recital halls rather than the amount of absorption represented by seated audience members. Also, in researching rehearsal and recital hall usage, he found that musicians preferred lowering the reverberation times in these spaces through added absorption when the power levels of source ensembles were too high. Mr. Pirn begins his section with the acoustician's anthem to architects. Materials that absorb sound cannot be used to isolate sound. Fiberglass batts, boards, and ceiling tiles, as well as lightweight panels, have very low transmission loss characteristics and must not be used as sound isolation partitions. A particularly valuable section of this chapter is 12 pages of construction details with corresponding tables of Sound Transmission Class, Surface Weight, Overall Thickness, and Fire-Resistive Ratings. A brief overview of vibration isolation devices is included here, although more detailed information regarding this subject can be found in the next chapter.

The third chapter, authored by Greg Tocci, co-founder of Cavanaugh Tocci Associates, Inc. and currently the Associate Editor of *Noise Control Engineering Journal*, is devoted to noise and vibration control. Mr. Tocci analyzes noise from its multiple sources through their paths to the ultimate receivers and describes the controls necessary to assure privacy and acoustical comfort. Systems described include building partitions, floor/ceiling construction, building envelopes, and HVAC mechanical systems and their distribution networks. It is a shame that the acoustics profession as well as the Standards Committees of a number of our learned societies have not arrived at a single standard to measure steady state background noise in rooms. The section of this chapter devoted to explaining the differences between NC (Noise Criteria), RC (Room Criteria), and NCB (Balanced Noise Criteria) may tend to confuse the architect rather than assist him in his design efforts. On the other hand, Mr. Tocci's explanations and graphics depicting the differences between these criteria will be of great assistance to practicing acousticians who may be somewhat befuddled by the controversy on this subject now raging in our midst.

David Klepper and L. Gerald Marshall, co-founders with Larry King of KMK Associates, were brave enough to tackle chapter four, Room Acoustics. They did an excellent job in explaining how sound reflection patterns in a listening room affect musical quality and speech intelligibility, and describe why the reproduction of these patterns determines the acoustic quality of a space rather than its geometric shape.

There are a few comments with which one might take issue. I do not believe that the authors are correct in stating that poor orchestral balance will be found behind the orchestra platform in a surround hall. It is the high power levels and uni-directional characteristics of horns, trumpets, and trombones that are more likely to create orchestral imbalance in shoebox concert halls when the rear wall of the room reinforces the brass sections to the detriment of the lower powered string instruments. I might have expected a little more historical transition from the Greek and Roman Theatres to those of the Court Theatres of the Italian Renaissance and Elizabethan England. These latter building types are gaining great favor with Contemporary theatre consultants and are causing acousticians to rethink acoustic criteria for multi-use performance facilities. On the whole, an A plus for this section.

The fifth chapter of the book covers sound reinforcement systems and describes how they must be tailored to match the acoustical design of public rooms. J. Jacek Figwer, an independent consultant from Concord, Massachusetts, wrote this section and provides the reader with a clear description of the type of systems required to meet the program uses of a variety of different spaces (Theatres, Meeting Rooms, Plenary Halls, Churches, Music Schools, Sports Arenas, etc.). I am not sure the numerous system schematic drawings shown in the Case Studies portion of the chapter will be of use to architects. However, practicing sound system design professionals will find them of immense value.

One topic I found missing from this chapter is a warning to architects that loudspeakers are three-dimensional objects which must be integrated into an architectural design at the earliest possible moment. Dreaming of recreating the proscenium arch of the La Scala Opera House is an invitation to aesthetic disaster. Rooms such as La Scala were built well before the era of electronic sound reinforcement. Once pictures of your new facility have been taken for the architectural press, the theatre crew (doing whatever is necessary to develop good speech intelligibility in the room), will hang loudspeakers helter skelter all over your beautiful proscenium arch.

The final chapter was written by Professors Gary S. Siebein and Bertram Y. Kinsey of the University of Florida. Both men played key roles in setting up the Architectural Technology Research Center at the school and have established independent consultancies in the State. This section of the book seeks to record the most recent progress in acoustic research in developing methods of evaluating, modeling and predicting the acoustical characteristics of buildings. Here, again, we may find design professionals better able to evaluate these tools and determine when to use them than architects or students of architecture. We are at an early stage in the development of these techniques and one cannot overemphasize the importance of adding a skilled, knowledgeable, and experienced practitioner to the design team in order to insure the successful culmination of acoustically sensitive building projects.

One is hesitant to offer superlatives when addressing scientists and engineers. However, this book deserves all our accolades. It is a welcome addition to every architect's and acoustician's bookshelf and is a must for every University and College library here and abroad.

DR. J. CHRISTOPHER JAFFE
Jaffe Holden Scarbrough Acoustics, Inc.
114A Washington Street
Norwalk, Connecticut 06854

 0001-4966/99/105(5)/2548/1/$15.00

REVIEWS OF ACOUSTICAL PATENTS

The purpose of these acoustical patent reviews is to provide enough information for a Journal reader to decide whether to seek more information from the patent itself. Any opinions expressed here are those of reviewers as individuals and are not legal opinions. Printed copies of United States Patents may be ordered at $3.00 each from the Commissioner of Patents and Trademarks, Washington, DC 20231.

Reviewers for this issue:

RONALD B. COLEMAN, *BBN Acoustic Technologies, 70 Fawcett Street, Cambridge, Massachusetts 02138*
D. LLOYD RICE, *11222 Flatiron Drive, Lafayette, Colorado 80026*
KEVIN P. SHEPHERD, *M.S. 436, NASA Langley Research Center, Hampton, Virginia 23681*
ERIC E. UNGAR, *Bolt, Beranek and Newman Incorporated, 50 Moulton Street, Cambridge, Massachusetts 02238*

5,760,348

43.50.Gf NOISE ATTENUATING APPARATUS

Stephen Glen Heuser, Lawrence, MI
2 June 1998 (Class 181/272); filed 15 August 1996

This muffler, intended primarily for small internal combustion engines, consists of a series of chambers that enclose each other. The engine exhaust is fed into the innermost chamber via a pipe that penetrates all of the chambers. Each chamber communicates with the one that encloses it via a series of conical orifice tubes whose smaller ends extend into the outer chamber. The purpose of these tubes is explained in the patent as follows: ''The compression of the sound wave will cause an inverted resonance and if the terminating impedance is not totally restricted . . . wave components of a substantially homogeneously reflected sound wave approaching the point of resonance are blurred and canceled by the superposition with any oncoming sound waves.'' It is claimed that these attenuators can be designed both to attenuate noise and to control backpressure.—EEU

5,799,479

43.50.Gf WEAR-RESISTING LOW NOISE CHAIN

Koji Tanaka, assignor to Tsubakimoto Chain Company
1 September 1998 (Class 59/4); filed in Japan 13 February 1996

A chain used for power transmission is described in which the inner surface of the inner plate of each link is shaped such that it conforms with the socket tooth shape. The chain and tooth thus contact smoothly, reducing both wear and noise.—KPS

5,809,770

43.50.Gf SILENCER FOR A GAS FLOW

Darrell D. Jahn, assignor to Donaldson Company, Incorporated
22 September 1998 (Class 60/39.33); filed 31 July 1995

A silencer for reducing the noise emitted by the venting of a gas flow is described with particular application to bleed air from gas turbines used to generate electricity. The silencer consists of a tubular gas flow member having a sidewall, an open end for connection to a gas supply, a closed second end, and an opening in the sidewall for passage of gas. The tubular gas flow member is surrounded by a porous noise reducing member in the location of the opening in the sidewall. A shell surrounds the noise reducing member. The noise reducing member can be wire mesh which is wrapped around the tubular gas flow member. Guidance is provided regarding the size of openings, choice of materials, and porosity of the noise reduction member.—KPS

5,801,344

43.50.Gf SOUND ATTENUATOR WITH THROAT TUNER

Andrew J. Herold, assignor to Arvin Industries, Incorporated
1 September 1998 (Class 181/272); filed 24 February 1997

A muffler for the exhaust of an internal combustion engine is described in which a key feature is two concentric pipes whose lengths overlap. Attenuation is achieved at a selected frequency which is determined by the relative radii of pipes **134** and **135**, the overlap length **188**, and the

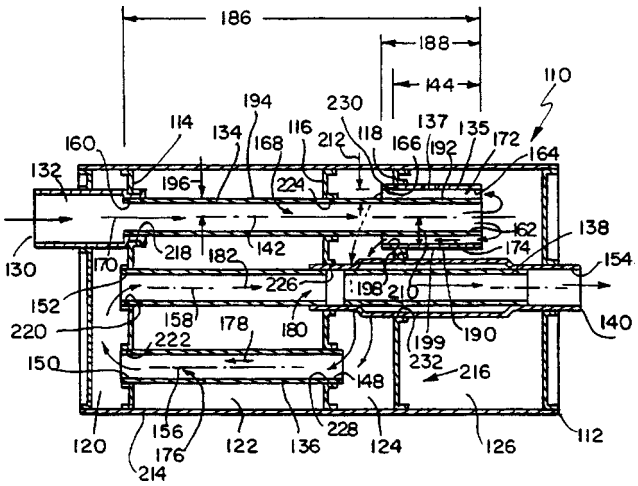

volume of the chamber **126**. Example calculations for a particular geometrical configuration are given, as are attenuation spectra. The cited example yields practical geometries, but appears to rely on the speed and sound being 2405 in. per s!—KPS

5,810,566

43.50.Gf PULSE DAMPER OR ACOUSTIC OUTLET PIECE FOR A COMPRESSOR AND COMPRESSOR EQUIPPED THEREWITH

Raphael Pauwels, assignor to Atlas Copco Airpower, Belgium
22 September 1998 (Class 417/312); filed in Belgium 15 November 1996

A device for attenuating pressure pulses from displacement-type compressors is described. The outlet pipe from the compressor is surrounded by a conical layer of sound absorbing material, arranged such that the material thickness gradually increases along the flow direction, thus achieving broadband absorption. Materials are proposed which are suitable for the high temperatures commonly encountered with these types of flows.—KPS

 0001-4966/99/105(5)/2551/6/$15.00

5,774,565

43.50.Ki ELECTRONIC CANCELLATION OF AMBIENT NOISE IN TELEPHONE HEADSET

Roger D. Benning *et al.*, assignors to Lucent Technologies, Incorporated
30 June 1998 (Class 381/83); filed 28 October 1996

An active control circuit for use inside telephone receivers such as headsets and handsets is described. The purpose of this circuit is to reduce the effects of ambient noise on the intelligibility of incoming voice signals. The circuit is basically a classic feedback loop with equalization of the transfer function between the handset speaker and an error microphone response (representing the listener's ear). The electronic voice signal and ambient noise enter the feedback loop at different points. In this way, the microphone output tracks the voice signal (servo system) while attenuating the noise signal (disturbance rejection). The incoming voice signal is bandpass filtered between 500 and 3000 Hz to amplify frequencies important for speech intelligibility. Finally, an auxiliary circuit is included to periodically open the feedback loop in the event that the feedback loop starts to go unstable.—RBC

5,790,673

43.50.Ki ACTIVE ACOUSTICAL CONTROLLED ENCLOSURE

William E. Gossman, assignor to Noise Cancellation Technologies, Incorporated
4 August 1998 (Class 381/71.1); filed 9 April 1997

The author claims an approach for controlling tonal noise from a noise source within an enclosure. The approach uses an assortment of microphones and speakers to control the sound radiated from a tonal source.—RBC

5,802,184

43.50.Ki ACTIVE NOISE AND VIBRATION CONTROL SYSTEM

Michael C. Heath, assignor to Lord Corporation
1 September 1998 (Class 381/71.4); filed 15 August 1996

A system is described for controlling tonal vibrations. The purpose is to reduce noise within a vehicle interior, such as an aircraft fuselage. The system employs a pulse width modulated amplifier operating at a switching frequency much higher than the tonal frequency being controlled. The output of the amplifier is passed through a ''power dissipation reduction circuit'' to reduce heat-generating eddy currents from passing to the actuator.—RBC

5,809,152

43.50.Ki APPARATUS FOR REDUCING NOISE IN A CLOSED SPACE HAVING DIVERGENCE DETECTOR

Mitsuru Nakamura *et al.*, assignors to Hitachi, Limited and Nissan Motor Company, Limited
15 September 1998 (Class 381/71.8); filed in Japan 11 July 1991

An active control system is presented for controlling tonal engine noise reaching the interior of a vehicle. The system described is similar to many others that have been reviewed. It uses a filtered-X LMS adaptive control algorithm to generate drive signals to loudspeakers for the purpose of minimizing the mean-square response at one or more microphone locations. The controller is also equipped with a ''divergence prediction algorithm'' to determine if the system is going unstable. The divergence prediction is based on monitoring time-averaged power of the actuator drive signals. The control system shuts off if this power estimate violates one of several threshold-based criteria. Instabilities are possible since the plant estimate in the filtered-X algorithm is *not* updated to account for changes in the transfer functions from the speakers to the residual microphones.—RBC

5,809,843

43.50.Ki ACTIVE CANCELLATION OF NOISE AT GEAR MESH FREQUENCIES FOR A GEAR ASSEMBLY UNDER LOAD

James E. Barger *et al.*, assignors to BBN Corporation
22 September 1998 (Class 74/574); filed 7 January 1997

A method and apparatus are described to cancel gear vibration and noise by introducing a canceling torque or force on a driven gear set. The residual metric to be controlled is from either a vibration sensor characterizing the structural response at the gear mesh frequency and harmonics, or the power supply current to the prime mover of the gear set. The latter response is shown to exhibit significant tonal response at the gear mesh frequency and harmonics, and can be measured inductively. The control output can be used to modify the drive current to the prime mover, or as an input to an auxiliary torque motor.—RBC

5,812,684

43.50.Ki PASSENGER COMPARTMENT NOISE ATTENUATION APPARATUS FOR USE IN A MOTOR VEHICLE

Joseph S. Mark, assignor to Ford Global Technologies, Incorporated
22 September 1998 (Class 381/86); filed 5 July 1995

An active control system is described to attenuate noise in the passenger compartment of a vehicle caused by turbulent boundary layer excitation of the windows. The preferred embodiment of the system uses four piezoelectric actuators and sensors mounted on the side windows below the beltline of the door. The sensors monitor vibration of the window and serve as the input signals to a PID controller. The output of the controller is used to drive the actuators to reduce window vibration.—RBC

5,812,682

43.50.Ki ACTIVE VIBRATION CONTROL SYSTEM WITH MULTIPLE INPUTS

Colin F. Ross and Graham P. Eatwell, assignors to Noise Cancellation Technologies, Incorporated
22 September 1998 (Class 381/71.11); filed 6 February 1996

An algorithm is described for providing active vibration control when using two or more reference sensor responses that may be highly correlated. The application is claimed to be effective when two sources cause excitations at the same, or nearly the same, frequency. Examples of this are when two machines are connected by a clutch that can slip, when they are governed to run at the same nominal speed, or when they are linked with a control system such as a synchrophaser for aircraft propellers. The approach relies on estimating the cross-spectral density matrices between the reference and residual sensors. The authors state that this algorithm will allow for convergence of the control filters when the cross-spectral density matrix of the reference signals is ill-conditioned.—RBC

5,801,341

43.50.Lj MECHANISM OF NOISE SUPPRESSION SYSTEM FOR A SUPERSONIC AIRCRAFT

John Keith Newell and Gregory Zwernemann, assignors to Northrop Grumman Corporation
1 September 1998 (Class 181/215); filed 9 September 1996

A noise suppression system for a jet engine exhaust is described in which part of the exhaust gas is diverted into a plurality of small exhaust streams, thus shifting the noise to a higher frequency which is more readily absorbed by the atmosphere. The system is designed for aircraft engines

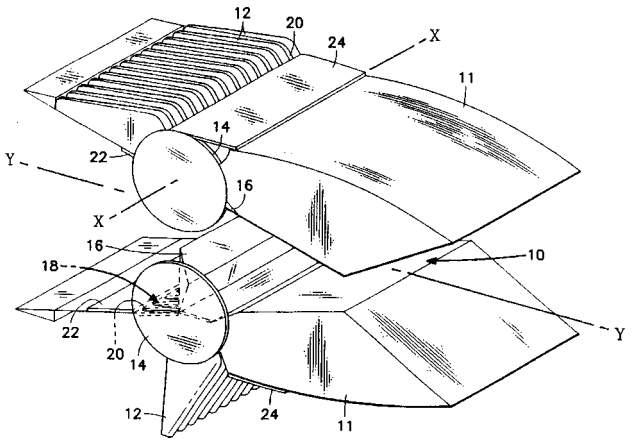

with rectangular exhaust nozzles. The arrangement is deployed only when needed, such as on landing or takeoff. The upper half of the figure illustrates the system in a stowed position; the lower half shows the system deployed for noise suppression.—KPS

5,774,559

43.50.Yw METHOD AND APPARATUS FOR DETERMINING PERCEIVED ROUGHNESS OF POWERTRAIN SOUNDS

Ben John Feng, assignor to Ford Global Technologies, Incorporated
30 June 1998 (Class 381/56); filed 3 February 1997

A method to calculate the psychoacoustic parameter termed roughness is described, with particular application to the sound generated by automobile powertrains. The narrow-band spectrum of the sound is distributed into auditory critical bands, roughness is calculated within each band, and these are then combined into a single roughness value. An interesting aspect of the method is that the critical bands are centered on each half and whole integer of the powertrain's fundamental frequency and adapt as the frequencies change. Methods to incorporate effects of masking of one frequency band by another are also described.—KPS

5,806,028

43.71.Gv METHOD AND DEVICE FOR RATING OF SPEECH QUALITY BY CALCULATING TIME DELAYS FROM ONSET OF VOWEL SOUNDS

Bertil Lyberg, assignor to Telia AB
8 September 1998 (Class 704/231); filed in Sweden 14 February 1995

A technique is presented for estimating speech quality or naturalness without requiring large numbers of listeners to make subjective judgements. The method relies on having one or more persons attempt to imitate the test materials, and then compare specific acoustic measurements such as vowel onset times between the test items and the human spoken items.—DLR

5,806,031

43.72.Ar METHOD AND RECOGNIZER FOR RECOGNIZING TONAL ACOUSTIC SOUND SIGNALS

Adam B. Fineberg, assignor to Motorola
8 September 1998 (Class 704/254); filed 25 April 1996

This linguistic tone analyzer extracts pitch-related features consisting of long-lag cepstral coefficients to track the tone patterns of a tonal language. It is well known that the cepstral vector is an excellent domain for extracting pitch information. This analyzer does not do a full typical pitch analysis, but rather compares the tone trends from frame to frame.—DLR

5,809,455

43.72.Ar METHOD AND DEVICE FOR DISCRIMINATING VOICED AND UNVOICED SOUNDS

Masayuki Nishiguchi and Jun Matsumoto, assignors to Sony Corporation
15 September 1998 (Class 704/214); filed in Japan 15 April 1992

This speech voicing detector performs statistical measurements on speech subframes to make voiced/unvoiced/silence decisions. Measured

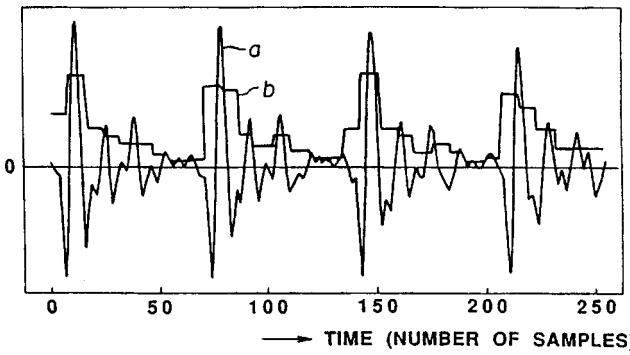

features include peak level, standard deviation, and spectral energy distribution.—DLR

5,809,461

43.72.Bs SPEECH RECOGNITION APPARATUS USING NEURAL NETWORK AND LEARNING METHOD THEREFOR

Mitsuhiro Inazumi, assignor to Seiko Epson Corporation
15 September 1998 (Class 704/232); filed in Japan 30 March 1992

This patent reads like a proposal for the use of recursive neural networks for speech recognition. A number of feedback path arrangements are

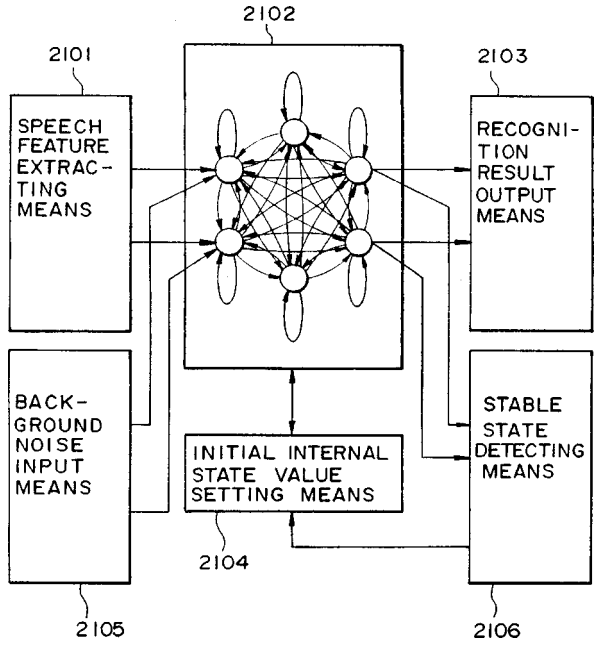

considered. The training method seems to be essentially back-propagation, although several alternate training strategies are described.—DLR

5,809,462

43.72.Bs METHOD AND APPARATUS FOR INTERFACING AND TRAINING A NEURAL NETWORK FOR PHONEME RECOGNITION

Paul A. Nussbaum, assignor to Ericsson Messaging Systems, Incorporated
15 September 1998 (Class 704/232); filed 24 April 1995

The patent describes a development system for use in configuring speech recognition systems based on neural network technology. A variety of network connection schemes are supported as are several training methods. Graphic displays include extracted speech acoustical data, network-detected segment boundaries, and other recognition system performance indicators.—DLR

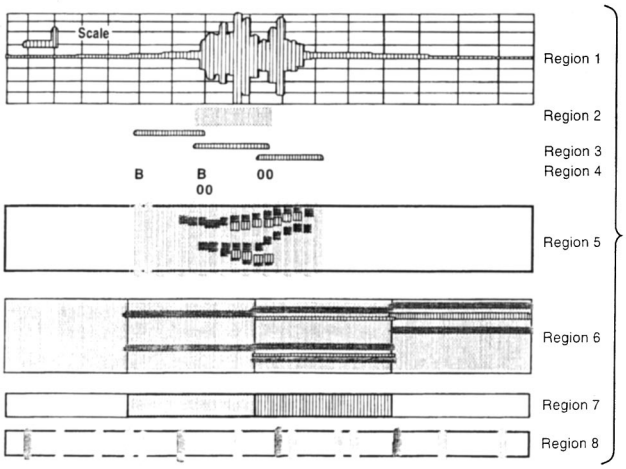

5,806,025

43.72.Dv METHOD AND SYSTEM FOR ADAPTIVE FILTERING OF SPEECH SIGNALS USING SIGNAL-TO-NOISE RATIO TO CHOOSE SUBBAND FILTER BANK

Marvin L. Vis and Aruna Bayya, assignors to U S West, Incorporated
8 September 1998 (Class 704/226); filed 7 August 1996

This speech noise reduction system is designed to reduce background noise and static in a mobile, wireless environment. The method consists of dividing the speech spectrum into subbands and selectively filtering each subband according to the signal-to-noise ratio and prediction error measured in each subband.—DLR

5,799,131

43.72.Gy SPEECH CODING AND DECODING SYSTEM

Tomohiko Taniguchi and Mark Johnson, assignors to Fujitsu Limited
25 August 1998 (Class 395/2.13); filed in Japan 18 June 1990

This code-excited (CELP) vocoder uses Gram–Schmidt Orthogonalization to solve a problem caused by correlations between the optimized gains for adaptive and stochastic codebooks in a typical CELP vocoder. An optimum code vector is derived from the adaptive codebook. The code vector from the stochastic codebook is then orthogonalized with respect to the adaptive vector. This results in reducing the dependencies between the adaptive and stochastic gain values.—DLR

5,799,272

43.72.Gy SWITCHED MULTIPLE SEQUENCE EXCITATION MODEL FOR LOW BIT RATE SPEECH COMPRESSION

Qinglin Zhu, assignor to ESS Technology, Incorporated
25 August 1998 (Class 704/223); filed 1 July 1996

This linear prediction vocoder uses excitations from both an adaptive codebook search result and a generated pulse train. The pulse sequences vary in amplitude, pulse spacing, and number of pulses. A linear prediction spectral vector is tested with all excitation forms once each subframe. This is said to allow an encoding bitrate as low as 4 K bps.—DLR

5,806,037

43.72.Ja VOICE SYNTHESIS SYSTEM UTILIZING A TRANSFER FUNCTION

Akira Sogo, assignor to Yamaha Corporation
8 September 1998 (Class 704/268); filed in Japan 29 March 1994

The patent describes a formant-based speech synthesizer for use in games and karaoke systems. The design uses a long-term inverse predictor

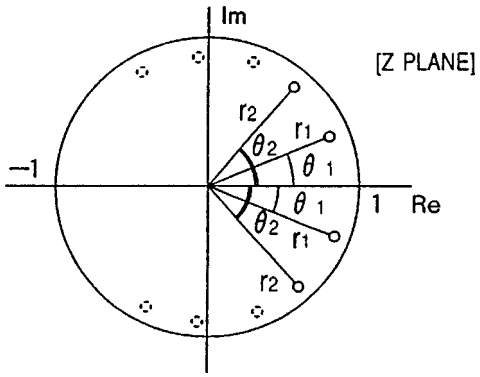

to generate pulse excitations and a codebook system for generating unvoiced excitation waveforms.—DLR

5,799,274

43.72.Ne SPEECH RECOGNITION SYSTEM AND METHOD FOR PROPERLY RECOGNIZING A COMPOUND WORD COMPOSED OF A PLURALITY OF WORDS

Masaru Kuroda, assignor to Ricoh Company, Limited
25 August 1998 (Class 704/239); filed in Japan 9 October 1995

This speech recognition system is extended to handle compound words by recognizing the component word elements and by checking the overall duration of the compound word. Feature vectors from each partial-word

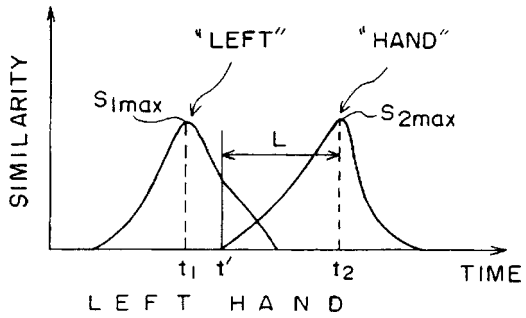

element are stored as references. As features are extracted from the input speech, they are tested for similarity to the stored references. The best matching similarity sequences are used to locate compound words.—DLR

5,799,277

43.72.Ne ACOUSTIC MODEL GENERATING METHOD FOR SPEECH RECOGNITION

Junichi Takami, assignor to Victor Company of Japan, Limited
25 August 1998 (Class 704/256); filed in Japan 25 October 1994

This speech recognizer based on hidden Markov models uses a novel method of training said to produce accurate models which are robust across speech variations with only limited training materials. During training passes, particular feature sequences may be split into distinct sequences, either along the time axis or along a phonetic context difference. Alternatively, multiple feature sequences may be merged into single sequences. The modifications optimize the likelihoods of state matching better than standard training procedures.—DLR

5,806,030

43.72.Ne LOW COMPLEXITY, HIGH ACCURACY CLUSTERING METHOD FOR SPEECH RECOGNIZER

Jean-Claude Junqua, Santa Barbara, CA
8 September 1998 (Class 704/245); filed 6 May 1996

The patent describes a method of clustering of hidden Markov models to reduce the complexity of a speech recognition system. Initial HMMs are formed for all phonetic elements of a labeled training set. The HMMs are then combined into triphone sets having a common center element. Distri-

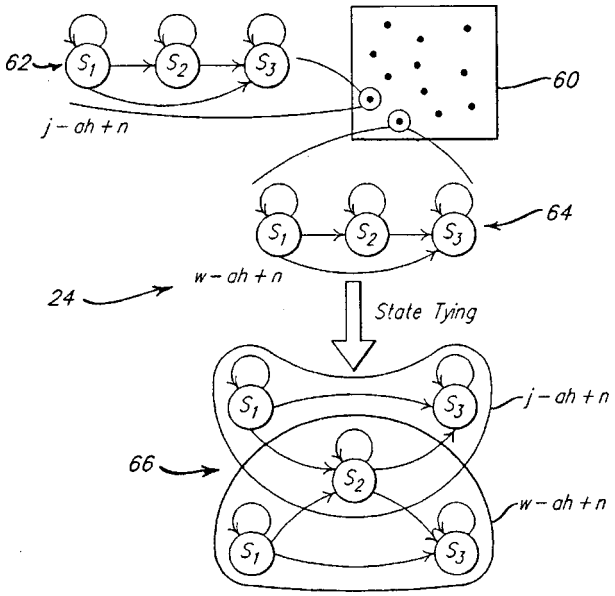

butions for the center elements are tied and all HMMs are retrained. The new HMMs are ranked by the number of each triphone example in the training data, merging little-trained models into more robustly trained models and all HMMs are again retrained.—DLR

5,802,488

43.72.Ne INTERACTIVE SPEECH RECOGNITION WITH VARYING RESPONSES FOR TIME-OF-DAY AND ENVIRONMENTAL CONDITIONS

Isao Edatsune, assignor to Seiko Epson Corporation
1 September 1998 (Class 704/231); filed in Japan 1 March 1995

This invention enhances the performance of a speech recognition system by detecting external factors such as the time-of-day and environmental conditions and using that information to set weights on the possible decoded recognition results. The example is given where ''good morning'' would be more likely to be uttered before noon than in the evening. The acceptance weights for that utterance are modified accordingly.—DLR

5,806,022

43.72.Ne METHOD AND SYSTEM FOR PERFORMING SPEECH RECOGNITION

Mazin G. Rahim and Jay Gordon Wilpon, assignors to AT&T Corporation
8 September 1998 (Class 704/205); filed 20 December 1995

Speech processing for telephone transmission often includes various forms of signal enhancement, such as power level adjustments, designed to improve listener acceptance. This speech recognition system, designed for use with the telephone network, compensates for such adjustments by modifying cepstral and mel frequency features so that the recognition features more nearly match the features present in the training data.—DLR

5,806,029

43.72.Ne SIGNAL CONDITIONED MINIMUM ERROR RATE TRAINING FOR CONTINUOUS SPEECH RECOGNITION

Eric Rolfe Buhrke *et al.*, assignors to AT&T Corporation
8 September 1998 (Class 704/244); filed 15 September 1995

This patented method for training a speech recognition system provides improved modeling of the training data in the presence of additive noise or channel bias conditions. As hidden Markov model probability distributions are built up, cluster analysis is performed on the distributions and the resulting clusters are used to detect and adjust or adapt outliers which occur in the training data.—DLR

5,806,033

43.72.Ne SYLLABLE DURATION AND PITCH VARIATION TO DETERMINE ACCENTS AND STRESSES FOR SPEECH RECOGNITION

Bertil Lyberg, assignor to Telia AB
8 September 1998 (Class 704/255); filed in Sweden 16 June 1995

This speech analysis method is intended to augment an existing recognition system by measuring duration and pitch change effects to extract prosodic information from the input speech signal. Emphasis is placed on the processing of segment and syllable durations, aided by pitch detection, to locate word stress and tone patterns such as the Swedish accent 1 and accent 2.—DLR

5,806,034

43.72.Ne SPEAKER INDEPENDENT SPEECH RECOGNITION METHOD UTILIZING MULTIPLE TRAINING ITERATIONS

Joe A. Naylor *et al.*, assignors to ITT Corporation
8 September 1998 (Class 704/256); filed 2 August 1995

The patent describes a more or less typical HMM-based speech recognition system. During recognition operations, in addition to the standard utterance decoding function, a mean vector range is accumulated across all speech frames. This information is used to provide a form a speaker recognition in addition to the normal speech recognition function.—DLR

Variational formulation using integral equations to solve sound scattering above an absorbing plane

C. Granat and M. Ben Tahar
LG2mS, UPRESA CNRS 6066, Université Technologique de Compiègne, BP 20529, 60205 Compiègne Cedex, France

T. Ha-Duong
D.M.A. Université Technologique de Compiègne, Centre de Recherche de Royallieu, 60200 Compiègne, France

(Received 20 May 1998; accepted for publication 25 January 1999)

The boundary element method is used to model two-dimensional acoustic radiation and scattering from a body of arbitrary shape above an infinite plane of flat surface and homogeneous impedance. The particularity of the study is the use of an indirect integral representation of the solution, given in terms of the jumps of pressure and its normal derivative through the boundaries. A variational formulation is associated with the boundary indirect integral equations modeling our problem. The major difficulty in the formulation is the infinite feature of the plane, which is avoided by introducing an appropriate Green's function. Numerical results of the attenuation of sound by noise barriers are presented. They show good agreement with other results in the literature. © *1999 Acoustical Society of America.* [S0001-4966(99)00405-1]

PACS numbers: 43.20.−f, 43.20.Fn [DEC]

INTRODUCTION

Acoustic emissions levels take an increasingly important part in environmental problems. In particular, road traffic is increasingly becoming a major noise source. In order to reduce this noise many solutions are under study. One of these studies, represented by noise barriers, is now in common use. In addition to noise barriers, the development of absorbing road surfaces is also an interesting contribution to road noise control.

In 1976 Thomasson,[1] following and correcting Ingard's works,[2] gave the three-dimensional solution of the scalar wave field produced by a point source in the presence of an infinite and homogeneous absorbing boundary. Later on, for the same problem, Kawaï *et al.*[3] derived an asymptotic solution in the far field, by a modified saddle point method. They get an asymptotic solution that is more accurate than Thomasson's. Nobile and Hayek[4] also obtained an asymptotic solution for the field. It is expressed in the form of an asymptotic series that is accurate even for relatively low values of its parameter, and for a wide range of incident angles. These former papers were motivated by the assessment of an adapted Green's function which is built to satisfy the impedance boundary condition on the infinite ground plane.

In the 1980's, the boundary element method (BEM) was applied in several investigations concerned with the sound field above an inhomogeneous impedance plane.[5,6] For example, in 1985, Habault[5] described sound propagation above an inhomogeneous plane made of a rigid strip, in the case of a two-dimensional problem (respectively, a rigid square for a three-dimensional problem) embedded in an infinite absorbing plane. The previous adapted of Green's function[1–3] has been employed and the boundary integral equations (BIE) have been solved using a collocation technique. Habault showed that the prediction of the sound field above an inhomogeneous plane is not correct if the plane is not accurately modeled (as a locally reacting surface or as an extended reaction surface). This aspect has been pointed out by Park and Eversman.[7] Concurrent with Habault, Chandler-Wilde and Hothersall[6] dealt with the same problem, but with a more general approach regarding the ground admittance: The ground is a normally reacting ground in which a strip of a variable admittance is embedded. In their numerical examples, the admittance model of Delany and Bazley[8] was used. In a first step, by considering the cylindrical wave source as a superposition of plane waves (using the analysis given in Ref. 9) and in a second step, following the work of Kawaï *et al.*,[3] they obtained the Green's function for a horizontal line source above an impedance plane. They showed that soft ground near the source (and by reciprocity the receiver) may be particularly important in reducing noise levels.

More recently, in 1991 Hothersall *et al.*,[10] considered a more complicated case: instead of dealing with a strip embedded in the ground, they considered a single noise barrier of arbitrary cross-sectional shape and arbitrary surface cover, lying on the ground. A two-dimensional BEM was used to provide a solution of the sound field around barriers, to predict their performance and to develop a more efficient design. The obtained results in noise level attenuation depended on the relative positioning of the source, receiver, and noise barrier. They showed that parameters such as the maximum height of the barrier, the type of ground cover, or the barrier surface, and the cross-sectional shape of the barrier were main factors affecting the attenuation.

Recently, Jean[11] dealt with an identical physical problem applied to railway noise barriers. A variational approach is developed, instead of using a collocation method to solve numerical boundary elements model as the previously quoted authors[1–3,5–7,10] did. Moreover, he showed that assessment of

barrier efficiency could be improved by introducing the train profiles and using a 3D transformation.[12] This transformation consists of a Fourier transform to transpose results for infinite coherent line source to infinite incoherent line source.

The purpose of this paper is to analyze the same type of scattering problem from a barrier as studied by Hothersall *et al.*[10] and Jean.[11] However, the mathematical formulation is different: An indirect representation of the field is developed, whereas the authors[10,11] gave a direct representation with the pressure on the surface as single unknown. Our formulation, based on the jumps of the pressure and its normal derivative through the surface, allows consideration of boundaries on which the admittance is discontinuous. On the other hand, as indicated in Ref. 13, the BIE obtained with this method, proved to be well-posed for every frequency.

The geometry and the governing equations of the problem are presented in Sec. I. Since the domain is infinite, a boundary integral equation method will be used to model this problem in Sec. II to Sec. IV. First, a half-plane Green's function, constructed to satisfy the impedance boundary condition,[6] is incorporated into the BIE. Thus, there is no need to model the infinite absorbing plane. Then, as in Ref. 11, a variational formulation is associated with the BIE. This avoids the explicit computation of the finite part of singular integrals and leads to a symmetrical linear algebraic system, after discretization by boundary finite elements. This final system can be solved by conventional numerical algorithms. Finally, some examples are presented in Sec. V, and the results are compared to those[10] obtained by a collocation method.

I. GEOMETRY AND GOVERNING EQUATIONS OF THE PROBLEM

A two-dimensional problem of outdoor sound propagation and its attenuation using noise barriers, sketched in Fig. 1, is considered. We deal with the propagation of a wave emitted by a monofrequency and harmonic time dependence ($e^{-i\omega t}$) line source, situated in a homogeneous, perfect, and quiescent fluid medium Ω, above an infinite and absorbing plane Γ. The domain Ω is assumed to be free from temperature variations and wind effect. The plane Γ is a locally reacting one. It has a homogeneous specific admittance β^g defined by $\rho \cdot c/Z$, where ρ is the air density, c is the sound speed, and Z the specific acoustic impedance of the locally reacting surface. Different models[8,14] can be suggested for the computation of the specific admittance depending on certain properties of the plane. The model used in this paper is the Delany–Bazley's model.[8] It depends only on the frequency flow resistivity and thickness of the absorptive layer.

Throughout the present work, it will be assumed that either $\beta^g = 0$ (rigid boundary) or $\mathrm{Re}(\beta^g) > 0$ (energy-absorbing boundary). At the same time, the noise barrier is bounded by two different types of surfaces. These are denoted by S_2 and S_3 in Fig. 1. On S_2 the normal derivative of the pressure is known, whereas on S_3 the specific surface admittance β^+ is known on the outside (side +). An admittance condition (β^-) is added to the inside (side −) of S_3 for convenience in the analysis of the problem,[13] as will be explained in Sec. I C. Let $Y_0(x_0, y_0)$ denote the source position and $Y(x,y)$ the receiver position. P_0 represents the amplitude of the source.

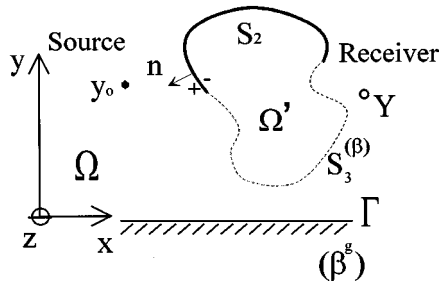

FIG. 1. Geometry of the problem.

A. The total pressure field

The total pressure field p satisfies: the Helmholtz equation

$$\nabla^2 p(Y) + k^2 p(Y) = P_0 \cdot \delta(Y - Y_0) \quad \forall Y \in \Omega, \tag{1}$$

and the following boundary conditions:

on the surface of the obstacle

$$\frac{\partial p(Y)}{\partial n} = \overline{V}_n(Y) \ \text{ on } \ S_2, \tag{2}$$

$$\frac{\partial}{\partial n} p^+(Y) + ik\beta^+ p^+(Y) = 0 \ \text{ on } \ S_3^+; \tag{3}$$

on the infinite ground of homogeneous admittance

$$\left(\frac{\partial}{\partial y} + ik\beta^g \right) p(Y) = 0 \ \text{ on } \ \Gamma; \tag{4}$$

and the Sommerfeld radiation conditions at infinity

$$\lim_{r \to \infty} \sqrt{r} \cdot \left(\frac{\partial}{\partial r} - ik \right) p(r) = 0 \ \text{ with } \ r = |Y|, \tag{5a}$$

$$\lim_{r \to \infty} \sqrt{r} \cdot p(r) = 0, \tag{5b}$$

where $\vec{n}$ is the unit normal vector drawn out of the barrier to the fluid medium. We recall that β^+ represents the admittance of the outside barrier surface, whereas β^g represents the ground admittance. For convenience, the total pressure field p is expressed as the sum of the scattered field p^{sc} and a field in absence of the barrier p^I:

$$p = p^{sc} + p^I. \tag{6}$$

B. The pressure field in absence of barrier

In the absence of barrier or any scattering obstacle, as sketched in Fig. 2, the pressure field in the upper half-plane satisfies the Helmholtz equation

$$(\nabla^2 + k^2) p^I(Y) = P_0 \cdot \delta(Y - Y_0) \ \text{ in } \ \Omega, \tag{7}$$

the boundary condition,

$$\left(\frac{\partial}{\partial y} + ik\beta^g \right) p^I(Y) = 0 \ \text{ on } \ \Gamma, \tag{8}$$

and the Sommerfeld radiation condition at infinity.

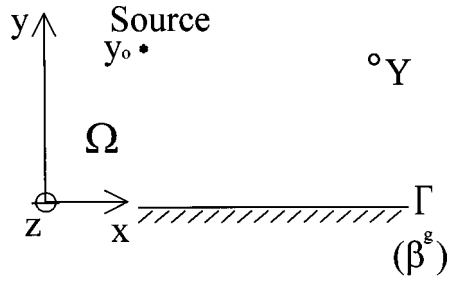

FIG. 2. Geometry with no barrier.

C. The scattered pressure field

Considering the boundary values problems of p [Eqs. (1)–(4)] and p^I [Eqs. (7) and (8)], using Eq. (6), the scattered pressure p^{sc} evidently satisfies the Helmholtz equation

$$(\nabla^2+k^2)p^{sc}(Y)=0 \quad \text{in} \quad \Omega; \tag{9}$$

the boundary conditions

$$\frac{\partial p^{sc+}(Y)}{\partial n}=\overline{V}_n(Y)-\frac{\partial p^I(Y)}{\partial n}\equiv V_0(Y) \quad \text{on} \quad S_2, \tag{10}$$

$$\frac{\partial}{\partial n}p^{SC+}(Y)+ik\beta^+p^{SC+}(Y) = -\left(\frac{\partial}{\partial n}p^I(Y)+ik\beta^+p^I(Y)\right) \quad \text{on} \quad S_3^+, \tag{11}$$

$$\left(\frac{\partial}{\partial y}+ik\beta^g\right)p^{sc}(Y)=0 \quad \text{on} \quad \Gamma, \tag{12}$$

and the Sommerfeld radiation conditions at infinity.

In order to solve this problem, the boundary integral equations method (BIEM) has been chosen to determine an integral representation of the fields p^I, p^{sc}. Consequently a fundamental solution has to be established.

An interior problem is automatically introduced in this BIEM, and may produce some irregular frequencies. In the interior problem, p^{sc} satisfies the Helmholtz equation

$$(\nabla^2+k^2)p^{sc}(Y)=0 \quad \text{in} \quad \Omega', \tag{13}$$

the boundary conditions

$$\frac{\partial p^{sc-}(Y)}{\partial n}=V_0(Y) \quad \text{on} \quad S_2 \tag{14}$$

$$\frac{\partial}{\partial n}p^{SC-}(Y)-ik\beta^-p^{SC-}(Y) = -\left(\frac{\partial}{\partial n}p^I(Y)-ik\beta^-p^I(Y)\right) \quad \text{on} \quad S_3^-. \tag{15}$$

Knowing Eq. (15), one then gets the following boundary condition for the total pressure field:

$$\frac{\partial}{\partial n}p^-(Y)-ik\beta^-p^-(Y)=0 \quad \text{on} \quad S_3^-. \tag{16}$$

To avoid the outcome of irregular frequencies, the boundary condition (15) [resp. Eq. (16)] is associated to the system of Eqs. (9)–(12) [resp. Eqs. (1)–(4)].[13]

II. FUNDAMENTAL SOLUTION

The major difficulty in the present formulation is the infinite feature of the absorbing plane Γ. In order to avoid the discretization of this plane in the boundary element method (BEM), we used a special half-plane Green's function.[6] This Green's function satisfies:

$$\nabla^2G(X,Y)+k^2G(X,Y)=\delta(X-Y) \quad \forall (X,Y)\in\Omega\times\Omega, \tag{17}$$

$$\frac{\partial G(X,Y)}{\partial y}+ik\beta^g\cdot G(X,Y)=0 \quad \forall Y\in\Gamma, \tag{18}$$

and the Sommerfeld radiation conditions in two dimensions

$$\lim_{R\to\infty}\sqrt{R}\cdot\left(\frac{\partial}{\partial R}-ik\right)G(X,Y)=0 \quad \text{with} \quad R=|Y-X|, \tag{19a}$$

$$\lim_{R\to\infty}\sqrt{R}\cdot G(X,Y)=0. \tag{19b}$$

It is built in Ref. 6 as the sum of three terms:

$$G(X,Y)=\frac{-i}{4}\cdot(H_0^1(kR)+H_0^1(kR'))+P_\beta(X,Y), \tag{20}$$

with $R=|Y-X|$ and $R'=|Y-X'|$. Here X' is the image of X with respect to Γ and H_0^1 is the Hankel function of the first kind of order zero. The first and second terms in Eq. (20) correspond to the direct and reflected waves, respectively. They are easily obtained using the method of images, since they satisfy the boundary condition of free surface $\beta^g=0$ on the infinite plane. The third term, $P_\beta(X,Y)$, represents a correction term corresponding to the radiated wave. It accounts for the acoustical properties of the infinite absorbent plane. It is obtained by an inverse Fourier transform resulting in a contour integral in the complex plane. Since this integral cannot be integrated analytically, it is transformed to a suitable form for effective evaluation using the steepest descent method.[3,15] Thereby, it has the following representation:[6,10]

$$P_\beta(X,Y)=\frac{i\beta^g}{2\pi} \cdot\int_{-\infty}^{\infty}\frac{\exp(ik(\sqrt{1-s^2}\cdot(y+y_0)+s\cdot|x-x_0|)}{\sqrt{1-s^2}(\sqrt{1-s^2}+\beta^g)}\cdot ds, \tag{21}$$

where $\text{Re}\sqrt{1-s^2}\geqslant 0$ and $\text{Im}\sqrt{1-s^2}\geqslant 0$.

III. INTEGRAL REPRESENTATIONS

In this section, an integral formulation is developed in order to determine the total pressure at any receiver point of the domain Ω.

A. Integral representation of p^I

Via Green's theorem, the boundary values problem satisfied by p^I can be reformulated as the boundary integral equation

$$p^I(X)=\int_\Omega G(X,Y)\cdot P_0\cdot\delta(Y-Y_0)\cdot dV(Y)$$
$$=P_0\cdot G(X,Y_0), \tag{22}$$

where G is the special Green's function given in Sec. II. At this step, the determination of the scattered pressure is missing in order to find out the total pressure field.

B. Indirect integral representation of p^{sc}

To find an integral representation of the scattered pressure, we use an indirect method based on single and double layer potentials.[16] Writing Eqs. (9) and (13) in a distribution sense and convoluting them by the former special Green's function satisfying the impedance boundary condition on the surface ground and the Sommerfeld conditions, the scattered pressure admits the following indirect integral representation:

$$-\int_{S_2}\frac{\partial G(x,y)}{\partial n_y}\cdot\mu_2(y)\cdot dS_2(y)+\int_{S_3}G(x,y)\cdot\sigma_3(y)dS_3(y)$$
$$-\int_{S_3}\frac{\partial G(x,y)}{\partial n_y}\cdot\mu_3(y)\cdot dS_3(y)$$
$$=\begin{cases}p^{sc}(x) & \forall x\in\Omega \quad (23a)\\ \frac{1}{2}(p^{sc+}(x)+p^{sc-}(x)) & \forall x\in S_2 \text{ or } S_3' \quad (23b)\end{cases}$$

where μ_2 (respectively μ_3) represents the jump of p^{sc} through the surface S_2 (respectively S_3); also denoting the double layer density on S_2 (respectively S_3). σ_3 represents the jump of the normal derivative of p^{sc} through the surface S_3; also denoting the simple layer density on S_3. These variables have the following expressions:

$$\mu_2(y)=(p^{sc^+}(y)-p^{sc^-}(y)) \text{ on } S_2,$$
$$\mu_3(y)=(p^{sc^+}(y)-p^{sc^-}(y)) \text{ on } S_3, \tag{23c}$$
$$\sigma_3(y)=\left(\frac{\partial p^{sc^+}(y)}{\partial n_y}-\frac{\partial p^{sc^-}(y)}{\partial n_y}\right) \text{ on } S_3.$$

In the latter integral representation [Eq. (23b)], if $x\in S_2$ (respectively S_3), the first (respectively the third) integral has to be understood as a Cauchy principal value. It should be noted that, as $p^{SC}(y)$ and $G(x,y)$ satisfy the impedance boundary condition on Γ and the Sommerfeld radiation conditions, the integration contour is reduced to $S_2\cup S_3$. The integral representation [(23a), (23b)] shows that the scattered pressure at any point in the domain Ω or on the barrier surface can be evaluated from the values of the jump of the pressure and the jump of its normal derivative through the boundaries only. The next step then consists in determining theses unknowns densities (μ_2,σ_3,μ_3).

C. Integral equations system

Applying the boundary conditions [Eqs. (10) and (14)] on the surface S_2, to the integral representation of the scattered pressure Eq. (23b), one gets

$$V_0(x)=-\text{F.P.}\int_{S_2}\frac{\partial^2 G(x,y)}{\partial n_x\partial n_y}\cdot\mu_2(y)dS_2(y)$$
$$+\int_{S_3}\left(\frac{\partial G(x,y)}{\partial n_x}\cdot\sigma_3(y)\right.$$
$$\left.-\frac{\partial^2 G(x,y)}{\partial n_x\partial n_y}\cdot\mu_3(y)\right)dS_3(y), \quad \forall x\in S_2, \tag{24}$$

where the integral corresponding to the second derivative of the Green's function should be taken as a Hadamard's finite part (F.P.).

Before applying the boundary conditions [Eqs. (11) and (15)] on the surface S_3, they need to be rewritten in terms of simple and double layer densities. From one part, subtracting Eq. (15) from Eq. (11), and from another part adding Eq. (15) multiplied by β^+ to Eq. (11) multiplied by β^-, the impedance boundary conditions on S_3 [Eqs. (11) and (15)] can be reformulated as follows:

$$\beta^+p^{SC+}(y)+\beta^-p^{SC-}(y)=\frac{i}{k}\sigma_3(y)-(\beta^++\beta^-)p^I(y), \tag{11bis}$$

$$\beta^-\frac{\partial}{\partial n}p^{SC+}(y)+\beta^+\frac{\partial}{\partial n}p^{SC-}(y)$$
$$=-ik\beta^-\beta^+\mu_3(y)-(\beta^++\beta^-)\frac{\partial}{\partial n}p^I(y). \tag{15bis}$$

Hence, applying these boundary conditions to the integral representation Eq. (23b), one finds

$$p^I(x)=\frac{1}{S\beta}\left(\frac{i}{k}\cdot\sigma_3(x)-\frac{1}{2}\Delta\beta\cdot\mu_3(x)\right)+\int_{S_2}\frac{\partial G(x,y)}{\partial n_y}$$
$$\cdot\mu_2(y)\cdot dS_2(y)-\int_{S_3}G(x,y)\cdot\sigma_3(y)dS_3(y)$$
$$+\text{P.V.}\int_{S_3}\frac{\partial G(x,y)}{\partial n_y}\cdot\mu_3(y)\cdot dS_3(y) \quad \forall x\in S_3, \tag{25}$$

$$\frac{\partial p^I(x)}{\partial n_x}=\frac{1}{S\beta}\left(\frac{1}{2}\Delta\beta.\sigma_3(x)-ik\beta^+\beta^-\mu_3(x)\right)$$
$$+\int_{S_2}\frac{\partial^2 G(x,y)}{\partial n_x\partial n_y}\cdot\mu_2(y)\cdot dS_2(y)$$
$$-\text{P.V.}\int_{S_3}\frac{\partial G(x,y)}{\partial n_x}\cdot\sigma_3(y)dS_3(y)$$
$$+\text{F.P.}\int_{S_3}\frac{\partial^2 G(x,y)}{\partial n_x\partial n_y}\cdot\mu_3(y)\cdot dS_3(y) \quad \forall x\in S_3, \tag{26}$$

where $S\beta=\beta^++\beta^-$ and $\Delta\beta=\beta^+-\beta^-$. The sign P.V. indicates its interpretation as a Cauchy principal value. At this step, a system of the three integral equations (24), (25), and (26) with three unknowns which are the simple layer density σ_3 on S_3, the double layer densities μ_2 on S_2 and μ_3 on S_3,

is obtained. Usually this system is solved using collocation technique, but this has two disadvantages. First, the double layer term contains an hypersingular integral which is difficult to compute and second, the final algebraic system is not necessarily symmetric. To overcome these two difficulties, a variational formulation[11,16] is associated with the integral equations system [Eqs. (24), (25), and (26)], although such an approach is less straightforward to write than a collocation method.

IV. VARIATIONAL FORMULATION

A. The associated variational formulation

The associated variational formulation has the following expression:

$$
\begin{aligned}
&A((\mu_2,\sigma_3,\mu_3),(\mu_2',\sigma_3',\mu_3')) \\
&\quad = \int_{S_2}\int_{S_2} \mu_2'(x)\,\frac{\partial^2 G(x,y)}{\partial n_x \partial n_y}\,\mu_2(y)\cdot dS_2(y)\,dS_2(x) \\
&\qquad + \int_{S_2}\int_{S_3}\left(\mu_2'(x)\,\frac{\partial^2 G(x,y)}{\partial n_x \partial n_y}\,\mu_3(y) - \mu_2'(x)\,\frac{\partial G(x,y)}{\partial n_x}\,\sigma_3(y)\right)\cdot dS_3(y)\,dS_2(x) \\
&\qquad + \int_{S_3}\int_{S_2}\left(\mu_3'(x)\,\frac{\partial^2 G(x,y)}{\partial n_x \partial n_y}\,\mu_2(y) - \sigma_3'(x)\,\frac{\partial G(x,y)}{\partial n_y}\,\mu_2(y)\right)\cdot dS_2(y)\,dS_3(x) \\
&\qquad + \int_{S_3}\int_{S_3}\left(\sigma_3'(x)\cdot G(x,y)\cdot\sigma_3(y) + \mu_3'(x)\,\frac{\partial^2 G(x,y)}{\partial n_x \partial n_y}\,\mu_3(y) - \sigma_3'(x)\,\frac{\partial G(x,y)}{\partial n_y}\,\mu_3(y)\right. \\
&\qquad \left. - \mu_3'(x)\,\frac{\partial G(x,y)}{\partial n_x}\,\sigma_3(y)\right)\cdot dS_3(y)\,dS_3(x) \\
&\qquad + \int_{S_3}\left(\frac{1}{ik\cdot S\beta}\,\sigma_3'(x)\cdot\sigma_3(x) + \frac{1}{2}\,\frac{\Delta\beta}{S\beta}\,(\sigma_3'(x)\cdot\mu_3(x) + \mu_3'(x)\cdot\sigma_3(x)) - ik\,\frac{\beta^+\cdot\beta^-}{S\beta}\,\mu_3'(x)\cdot\mu_3(x)\right)\cdot dS_3(x). \qquad (28)
\end{aligned}
$$

The arbitrary regular test functions σ_3', μ_3' and μ_2' are defined on S_3 and S_2, respectively. Thereby, through a second integration, all the integrals have a meaning in the variational formulation Eq. (27).

B. The resulting matrix system

Using the property of symmetry of Green's function and the convergence of the double integrals, it can be derived that the bilinear form $A((\mu_2,\sigma_3,\mu_3),(\mu_2',\sigma_3',\mu_3'))$ is symmetrical. Therefore, the solution of Eq. (27) is given by the stationarity of the functional

$$
\begin{aligned}
F(\mu_2,\sigma_3,\mu_3) = \tfrac{1}{2}A((\mu_2,\sigma_3,\mu_3),(\mu_2,\sigma_3,\mu_3)) &+ \int_{S_2}\mu_2(x)\cdot V_0(x)\cdot dS_2(x) \\
&+ \int_{S_3}\sigma_3(x)\cdot p^I(x)\cdot dS_3(x)
\end{aligned}
$$

$$
\begin{aligned}
&A((\mu_2,\sigma_3,\mu_3),(\mu_2',\sigma_3',\mu_3')) \\
&\quad = -\int_{S_2}\mu_2'(x)\cdot V_0(x)\cdot dS_2(x) \\
&\qquad - \int_{S_3}\sigma_3'(x)\cdot p^I(x)\cdot dS_3(x) \\
&\qquad + \int_{S_3}\mu_3'(x)\cdot\frac{\partial p^I(x)}{\partial n_x}\cdot dS_3(x), \qquad (27)
\end{aligned}
$$

where the bilinear form $A((\mu_2,\sigma_3,\mu_3),(\mu_2',\sigma_3',\mu_3'))$ is written as

$$
- \int_{S_3}\mu_3(x)\,\frac{\partial p^I(x)}{\partial n_x}\,dS_3(x). \qquad (29)
$$

C. Transformation of the double layer integrals

Before going further on the discretization of the functional Eq. (29), the way the explicit computation of the double layer integrals is avoided is examined below. In fact, only the integrals in which the operator $[\partial^2 G(x,y)]/(\partial n_x \partial n_y)$ should happen to be singular, have to be considered. These double layer integrals have the following representation:

$$
\int_S\int_S \mu(x)\cdot\frac{\partial^2 G(x,y)}{\partial n_x \partial n_y}\cdot\mu(y)\cdot dS(y)\cdot dS(x), \qquad (30)
$$

where S and μ are given for S_2 and μ_2 (respectively, S_3 and μ_3) if the double layer integral over S_2 (respectively, S_3) is considered. The fundamental solution G can be expressed as:

$$
G(x,y) = G_0(x,y) + G_i(x',y) + P^{\beta}(x,y), \qquad (31)
$$

where after identification with Eq. (20),

$$G_0(x,y) = -\frac{i}{4} H_0^1(k \cdot R)$$

and

$$G_i(x,y) = -\frac{i}{4} H_0^1(k \cdot R') \equiv G_0(x',y).$$

In a first step of the transformation of Eq. (30), the transformation given in Ref. 16 is employed to avoid the computation of the finite part of the integral associated to the second normal derivative of the kernel G_0 in Eq. (30). Next, a similar transformation process is applied on the kernel G_i which is not singular except when S cuts Γ. Hence, one finds as a result of these two transformations,

$$\begin{aligned}
&\int_S \int_S \mu(x) \cdot \frac{\partial^2 G(x,y)}{\partial n_x \partial n_y} \cdot \mu(y) \cdot dS(y) \cdot dS(x) \\
&= \int_S \int_S \mu(x) \cdot \Bigg(k^2 [(\mathbf{n}_x \cdot \mathbf{n}_y) \cdot G_0(x,y) \\
&\quad + (\mathbf{n}_x \cdot T \cdot \mathbf{n}_y) \cdot G_0(x',y)] + \frac{\partial^2 P^\beta(x,y)}{\partial n_x \partial n_y} \Bigg) \mu(x) \\
&\quad \cdot dS(y) dS(x) \\
&\quad - \int_S \int_S \frac{\partial \mu(x)}{\partial S} (G_0(x,y) - G_0(x',y)) \\
&\quad \cdot \frac{\partial \mu(y)}{\partial S} \cdot dS(y) dS(x), \qquad (32)
\end{aligned}$$

where $T = \left[\begin{smallmatrix} 1 & 0 \\ 0 & -1 \end{smallmatrix}\right]$ is the transformation matrix in the image method. The original relations given in Refs. 16 and 17 also have integrals above ∂S. But since our model problem is bidimensional ∂S_2 (respectively, ∂S_3), represents the initial (respectively, final) and the final (respectively, initial) point of the curve S_2 (respectively, S_3). When ∂S is sufficiently regular, $\mu(x) = 0 \ \forall x \in \partial S$. Thus assuming $\mu(x) = 0$ on ∂S, the integrals above ∂S in Refs. 16 and 17 are null. Therefore, the general transformations[16,17] can be simplified to the relation (32) for our problem. Thereby, all integrals in Eq. (29) are well-defined and their numerical computation is conventional.

D. Discretization by a finite element method

Taking into account the transformation of both double layer integrals on S_2 and S_3, and using straight linear isoparametric finite elements for the discretization of the boundaries S_2 and S_3, one gets the following discretized functional after assembly:

$$\begin{aligned}
F(\mu_2, \sigma_3, \mu_3) = \tfrac{1}{2} (&\langle \mu_2 \rangle D_2 \{\mu_2\} + \langle \sigma_3 \rangle A_3 \{\sigma_3\} \\
&+ \langle \mu_3 \rangle D_3 \{\mu_3\}) + \langle \mu_2 \rangle C_{23} \{\sigma_3\} \\
&+ \langle \sigma_3 \rangle C_{33} \{\mu_3\} + \langle \mu_2 \rangle D_{23} \{\mu_3\} \\
&+ \langle \mu_2 \rangle \{V_0\} + \langle \sigma_3 \rangle \{p^I\} - \langle \mu_3 \rangle \left\{ \frac{\partial p^I}{\partial n} \right\}. \qquad (33)
\end{aligned}$$

Since in a first step, the functional Eq. (29) has been discretized on each boundary element and in a second step, it has been assembled over the whole set of boundary elements, $\{\mu_2\}$, $\{\sigma_3\}$, and $\{\mu_3\}$ represent the vectors of the nodal values of μ_2, σ_3 and μ_3.

The stationarity of the discretized functional (33) leads to the linear matrix system:

$$\begin{bmatrix} D_2 & C_{23} & D_{23} \\ C_{23}^T & A_3 & C_{33} \\ D_{23}^T & C_{33}^T & D_3 \end{bmatrix} \cdot \begin{Bmatrix} \{\mu_2\} \\ \{\sigma_3\} \\ \{\mu_3\} \end{Bmatrix} = \begin{Bmatrix} -\{V_0\} \\ -\{p^I\} \\ \left\{ \frac{\partial p^I}{\partial n} \right\} \end{Bmatrix}, \qquad (34)$$

where the global matrix is symmetrical since A_3, D_2, and D_3 are symmetrical matrixes. A_3 represents the single layer matrix, whereas D_2, D_3, and D_{23} represent the double layer matrixes. C_{23} and C_{33} are the coupling matrixes between the simple and the double layer. The resolution of system (34) permits to determine μ_2, σ_3, and μ_3 on each node of the barrier boundary. Since this system is symmetrical, it can easily be solved using conventional algorithms. Finally, the application of the integral representation (23a) gives the scattered pressure at any receiver point in the fluid medium Ω.

V. NUMERICAL EXAMPLES

The special Green's function presented in Sec. II is implemented in a BEM code RAYON2D, solving integral equations with a variational approach. For the validation, results of insertion loss (IL) or excess attenuation (EA) around noise barriers of arbitrary cross-sectional shape, using a BEM and the variational formulation given above for the discretization will be compared to those obtained by a collocation method.[10] The computation of the excess attenuation (EA) and the insertion loss (IL) at a receiver point x are given by:

$$\mathrm{EA} = -20 \log_{10} \left| \frac{p(x)}{p_{FF}(x)} \right|, \qquad (35a)$$

$$\mathrm{IL} = -20 \log_{10} \left| \frac{p(x)}{p_{WB}(x)} \right| \ \text{in dB}, \qquad (35b)$$

where p, p_{FF}, and p_{WB} denote the total acoustic pressure at x with the barrier present, in free field conditions, and with only the flat ground present, respectively.

The numerical computations have been carried out using a point source of unit amplitude. The admittance of the infinite ground surface and of the barrier surfaces is either zero or is defined by the Delany–Bazley model.[8] In the latter case, the absorbent material is characterized by its flow resistivity (σ). The dependence of the normalized surface admittance (β) upon frequency (f) is given through this expression:

$$\frac{1}{\beta} = 1 + 9.08 (10^3 f/\sigma)^{-0.75} + i \cdot 11.9 (10^3 f/\sigma)^{-0.73}. \qquad (36)$$

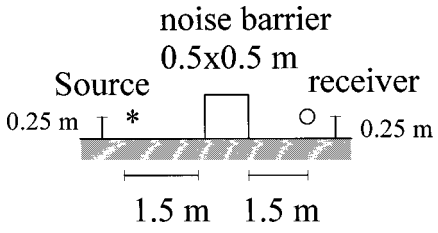

FIG. 3. Geometry of a noise barrier of a square cross section. The admittance of the barrier surfaces is zero and the admittance of the ground surface is defined by $\sigma = 250 \times 10^3$ Nsm^{-4}.

A. Excess attenuation for a noise barrier of a square cross section

For this first numerical example, the geometry of the barrier, the location of the receiver, and the source are given in Fig. 3. The computed excess attenuation (EA) is presented in Fig. 4, for the configuration indicated in Fig. 3. To perform our computation, a minimum of four boundary elements is taken per wavelength. In this example, in order to reach 4 kHz, 75 elements are required for the discretization.

In Fig. 4, we can see that our numerical results obtained with a special Green's function and a variational formulation for the resolution of the integral equations are in good agreement both with results obtained in Ref. 10 using the same Green's function and a collocation technique, and with an outdoor experiment.[18]

B. Excess attenuation for a wedge noise barrier

In this example, the source and the receiver are located on the ground surface as it is shown in Fig. 5. Thus no interference effects due to ground reflections will be considered.

The external surface of the wedge, as well as the ground either have an admittance variation with frequency given by Eq. (36), or are perfectly reflecting. Whereas the internal surface admittance of the wedge is prescribed to one, when the wedge is not rigid. For the admittance variation, the value $\sigma = 300\,000$ Nsm^{-4}, has been used in this example as characteristic of grassland.

Through the plots in Fig. 6 the effect of ground and or surface barrier admittance can be assessed. Note that the ef-

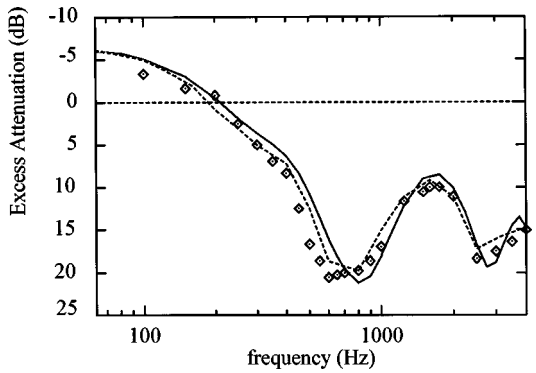

FIG. 4. Comparison of numerical results using a variational formulation (–) with numerical results using collocation method (Ref. 10) (– – –) and measurements (Ref. 18) (◇) calculated at one-third octave band center frequencies.

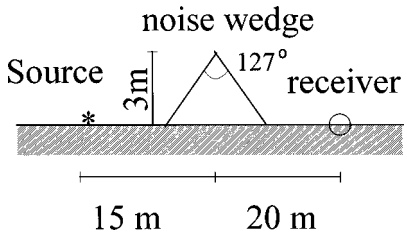

FIG. 5. Geometry of a wedge noise barrier. The admittance of the ground and the barrier surfaces is either zero or defined by $\sigma = 300 \times 10^3$ Nsm^{-4}.

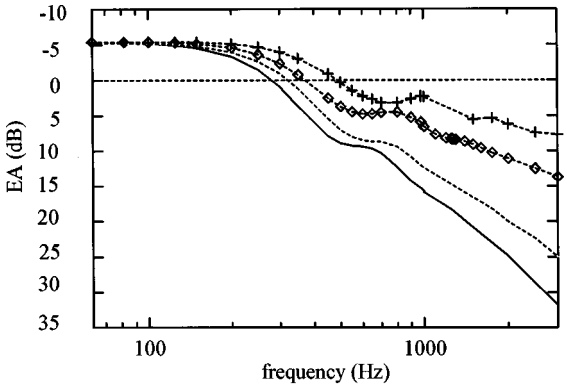

FIG. 6. Comparison of the EA in four different configurations of the admittances of the ground and the wedge surfaces: wedge surface and ground with admittance (–); wedge surface with admittance and rigid ground (-◇-); rigid wedge surface and ground with admittance (– – –); rigid wedge surface and rigid ground (-+-).

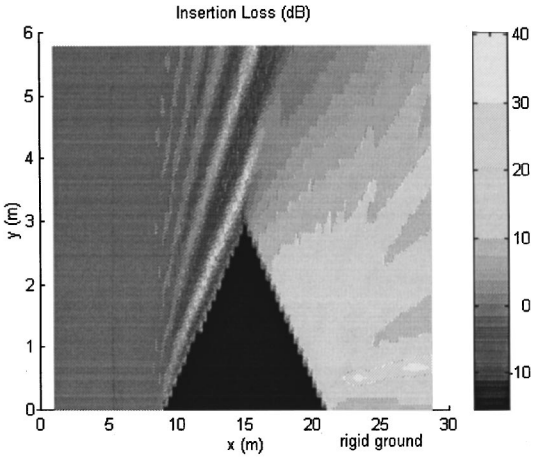

FIG. 7. IL mapping for a rigid ground and a barrier surface admittance defined by $\sigma = 300 \times 10^3$ Nsm^{-4}.

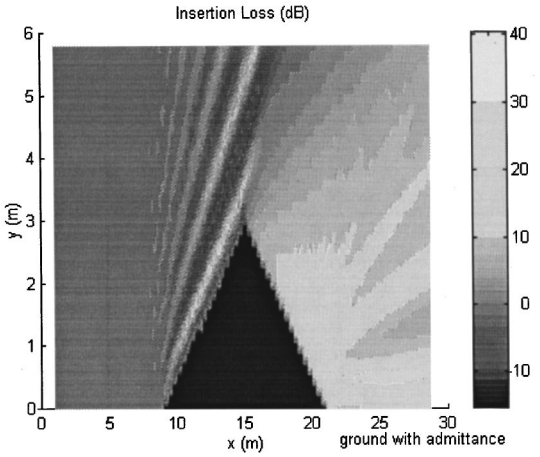

FIG. 8. IL mapping for a ground and a barrier surface admittance defined by $\sigma = 300 \times 10^3$ Nsm^{-4}.

fect of changing from rigid ground to grassland produces an excess attenuation which increases much more rapidly with increasing frequency.

C. Insertion loss around a wedge noise barrier

The geometry of the wedge is represented by black areas of the mappings Figs. 7 and 8. The point source is located at the origin. The external surface of the wedge has an admittance defined by $\sigma = 300 \times 10^3\ \mathrm{Nsm}^{-4}$ and the internal surface admittance is assumed to be equal to one. The ground either has the same admittance variation as the external surface of the barrier, or is rigid. Computations of the insertion loss have been performed at the frequency of 500 Hz, for a rigid ground (Fig. 7) and a ground with admittance characteristic of grassland (Fig. 8).

VI. CONCLUSION

This paper has presented a variational formulation using indirect integral equations for the solution of outdoor sound propagation scattered by a noise barrier of arbitrary shape lying above an infinite impedance ground. The developed formulation in terms of indirect integral equations allows modeling of a scattering body with an admittance on its inside surface. This avoids the outcome of irregular frequencies whereas the use of a variational approach itself does not permit it. The solution of the problem occurs first in the special Green's function, which incorporates the boundary condition at the ground, and second, in the use of a variational approach leading after discretization to a symmetrical linear system. Therefore, substantial computer time and memory are saved during the resolution of this system. On the other hand, the computation of an elementary matrix with a variational formulation requires more time than a collocation method, because of double integrations. The results of our numerical model using a variational formulation have shown good agreement with published results using a classical collocation method found in the literature[10] and with experimental results.[18]

ACKNOWLEDGMENT

The authors would like to acknowledge the financial support provided by the ''Conseil Regional de Picardie'' under the regional group of modeling (project N 94-8).

[1] S. I. Thomasson, ''Reflection of waves from a point source by an impedance boundary,'' J. Acoust. Soc. Am. **59**, 780–785 (1976).
[2] U. Ingard, ''On the reflection of a spherical sound wave from an infinite plane,'' J. Acoust. Soc. Am. **23**, 329–335 (1951).
[3] T. Kawai, T. Hidaka, and T. Nakajima, ''Sound propagation above an impedance boundary,'' J. Sound Vib. **83**, 125–138 (1982).
[4] M. A. Nobile and S. I. Hayek, ''Acoustic propagation over an impedance plane,'' J. Acoust. Soc. Am. **78**, 1325–1336 (1985).
[5] D. Habault, ''Sound propagation above an inhomogeneous plane boundary integral equation method,'' J. Sound Vib. **100**, 55–67 (1985).
[6] S. N. Chandler-Wilde and D. C. Hothersall, ''Sound propagation above an inhomogeneous impedance plane,'' J. Sound Vib. **98**, 475–491 (1985).
[7] J. M. Park and W. Eversman, ''A boundary element method for propagation over absorbing boundaries,'' J. Sound Vib. **175**, 197–218 (1994).
[8] M. E. Delany and E. N. Bazley, ''Acoustical properties of fibrous absorbent materials,'' Appl. Acoust. **3**, 105–116 (1970).
[9] L. M. Brekhovskiski, *Waves in Layered Media* (Academic, New York, 1960).
[10] D. C. Hothersall, S. N. Chandler-Wilde, and M. N. Hajmirzae, ''Efficiency of single noise barriers,'' J. Sound Vib. **146**, 303–322 (1991).
[11] P. Jean, ''A variational approach for the study of outdoor sound propagation and application to railway noise,'' J. Sound Vib. **212**, 275–294 (1998).
[12] D. Duhamel, ''Efficient calculation of the three-dimensional sound pressure field around a noise barrier,'' J. Sound Vib. **197**, 547–571 (1996).
[13] T. Ha-Duong, ''A system of boundary integral equations for the problem of acoustic scattering by an absorbing wall,'' in *Proceedings of the 8th International Conference on Boundary Element Method* (Springer Verlag, Tokyo, 1986).
[14] K. Attenborough, ''Acoustical impedance models for outdoor ground surfaces,'' J. Sound Vib. **99**, 521–544 (1985).
[15] G. Arfken, *Mathematical Methods for Physicists* (Academic, New York, 1985).
[16] M. Ben Tahar, ''Formulation variationnelle par équations intégrales pour le rayonnement acoustique en présence d'un écoulement non uniforme,'' Ph. D. dissertation, Dept AVI, Université de Technologie de Compiègne, Compiègne, France (1991).
[17] M. A. Hamdi and J. M. Ville, ''Sound radiation from ducts theory and experiment,'' J. Sound Vib. **107**, 231–246 (1986).
[18] K. B. Rasmussen, ''Sound propagation over non flat terrain,'' The Danish Academy of Technical Sciences, Danish Acoustical Laboratory Report **35** (1982).

On the radiation of ultrasound into an isotropic elastic half-space via wavefront expansions of the impulse response

Dmitri Gridin
School of Electrical, Electronic and Information Engineering, South Bank University, 103 Borough Road, London SE1 0AA, United Kingdom

(Received 6 June 1998; accepted for publication 22 January 1999)

The problem of propagation of pulses in the radiating near zone of a large circular normal transducer directly coupled to a homogeneous and isotropic elastic half-space is re-visited. It is shown that for certain observation angles the impulse response approach is computationally inefficient. A new method based on the so-called wavefront expansions of the impulse response is developed instead. The expansions are obtained by the analytical harmonic synthesis of the high-frequency asymptotics of the transducer field. Unlike these asymptotics the wavefront expansions are expressed in terms of elementary functions only. The direct *P*, edge *P* and *S* waves as well as the transition regions (penumbra and axial region) are described. The uniform asymptotic expansions applicable throughout the radiating near zone are derived as well. The code based on the time convolution of the pressure input function with the wavefront expansions is compared to a direct numerical code. It is thousands of times faster but practically just as accurate except that the phenomena related to the head waves are not described. Formulas pertaining to the far field are also offered. © *1999 Acoustical Society of America.* [S0001-4966(99)01205-9]

PACS numbers: 43.20.Bi, 43.20.Dk, 43.35.Zc [DEC]

INTRODUCTION

Simulating the propagation of pulses radiated by surface loads into an elastic half-space is a first step toward the system model of ultrasonic nondestructive evaluation (NDE) of industrial materials. The most interesting surface loads from the theoretical point of view and in some industrial applications are a point source and a circular transducer (see, e.g., Miller and Pursey, 1954; Ilan and Weight, 1990). The field radiated by a point source is the Green's function for 3D Lamb's problem and can be utilized in calculating the elastic fields radiated by ultrasonic transducers.

The case of a *time-harmonic* pointlike transducer acting on the surface of a homogeneous and isotropic elastic half-space has been considered in Miller and Pursey (1954). The solutions were obtained in the integral form using Fourier or Hankel transforms, and then the far-field asymptotics of the compressional and shear waves were found. The *transient* response of an elastic half-space can be found using the Laplace–Hankel transform technique (e.g., Achenbach, 1973). The corresponding solution for the *step-function* response has been used by Knopoff and Gilbert (1959) and Gakenheimer and Miklowitz (1969) to find the so-called wavefront expansions for the compressional, shear and head waves.

In the past two decades the propagation of ultrasonic pulses radiated by *circular transducers* into elastic solids has been intensively studied by various full numerical schemes (e.g., Ilan and Weight, 1990; Djelouah and Baboux, 1992) and approximate methods (e.g., Weight, 1987; Schmerr and Sedov, 1989; Lhémery, 1994). The full numerical schemes are extremely time consuming and do not produce any explicit dependence of the radiated waves upon the model parameters. The approximate models elucidate the physics of the problem in terms of the direct compressional and edge compressional and shear waves. However, in some regions the assumptions behind the models of Weight (1987) and Lhémery (1994) lead to disagreement with an exact solution (see discussion below). For the uniform normal load Lhémery's model also gives nonphysical pulse of the direct *S* wave. The method of Schmerr and Sedov (1989) describes the field inside the axial region or far from the axis only. None of the above approximate models describe the head waves and the field in the vicinity of the critical rays.

Recently, a new method has been developed for simulating the transient field of a large circular normal transducer. Fradkin *et al.* (1998) have proposed a two-tier approach to description of the radiating near field of a time-harmonic transducer based on the short-wavelength diffraction theory involving asymptotic approximation of integrals (see references therein): First, they obtain the far-field asymptotics of a point source acting on the surface of an elastic half-space (that is, of the Green's function). Then they integrate these asymptotics over the transducer surface and find the radiating near-field asymptotics of the transducer, including the asymptotics which are applicable inside the penumbra and the axial region. Gridin (1998) has complemented their results by applying the uniform stationary phase method (Borovikov, 1994) to obtain the high-frequency asymptotics of the head waves and the field in the vicinity of the critical rays as well. It has been shown that the high-frequency asymptotic method combined with the Fast Fourier Transform is 100–1000 times faster but practically as accurate as a direct numerical solution (Gridin and Fradkin, 1998).

Several researchers have studied the *impulse* response to a circular normal transducer radiating into solids. Bresse and Hutchins (1989) have used the Cagniard–de Hoop method and expressed the response in terms of double integrals. Djelouah and Baboux (1992) have computed it by taking the

inverse Fourier transform of the integral representation of the time-harmonic transducer field. McNab *et al.* (1990) have used the abovementioned Green's function obtained by Gakenheimer and Miklowitz (1969) and performed the spatial convolution with a circular load of arbitrary apodization using the discrete numerical procedure. Laturelle (1990), who worked with uniform loads of step-function excitation, transformed the inverse Laplace–Hankel integral to separate the contributions of the static solution, the Rayleigh and other elastic waves. Weight (1987) and then Lhémery (1994) have extended an impulse response approach developed by Stepanishen (1971) for the transient radiation into fluids to the case of an elastic half-space. Their approach will be called the impulse response approach throughout the paper. The Fourier inversion of the high-frequency asymptotics has been used by Schmerr and Sedov (1989) to obtain the asymptotic representation for the impulse response. However, only the normal component in the axial region and far from the axis has been described. None of the approximate models (Weight, 1987; Schmerr and Sedov, 1989; Lhémery, 1994) take into consideration that for certain angles of propagation shear wave arrivals are *two-sided* phenomena [see Knopoff and Gilbert, 1959; Miklowitz, 1978, pp. 319–328, 340–347; and, e.g., Eq. (11) below].

In this paper a new fast method is proposed for simulating the transient field radiated by a circular normal transducer directly coupled to a homogeneous and isotropic elastic half-space. We obtain the wavefront expansions of the impulse response, and then perform its numerical time convolution with the pressure input function. The paper is organized as follows: First, the time-domain Green's function for 3D Lamb's problem is considered and a disadvantage of the impulse response approach at certain observation angles are discussed. Then, the wavefront expansions for the *P* and *S* fields radiated by a circular normal transducer are obtained. The outputs of the asymptotic and direct numerical codes for simulating the propagation of pulses are compared next. At the end of the paper, the far field of a circular normal transducer is briefly discussed.

I. GREEN'S FUNCTION FOR 3D LAMB'S PROBLEM

A. Formulation

Let us consider the transient motion of a homogeneous and isotropic elastic half-space caused by a normal impulsive point load. The displacement field $\mathbf{u}$ inside the medium is described by the elastodynamic equation

$$\frac{\partial^2 \mathbf{u}}{\partial t^2} + c_S^2 \nabla \times (\nabla \times \mathbf{u}) - c_P^2 \nabla (\nabla \cdot \mathbf{u}) = \mathbf{0}, \tag{1}$$

where c_P is a speed of *P* (also known as compressional or longitudinal) wave and c_S, of *S* (also known as shear or transverse) wave. The cylindrical coordinates (r,φ,z), with the origin at the point of excitation and the *z*-axis directed into the solid, are used below. The boundary conditions due to a normal impulsive point load are:

$$\sigma_{zr}|_{z=0} = 0, \quad \sigma_{zz}|_{z=0} = -\frac{\delta(t)\,\delta(r)}{2\pi r} \tag{2}$$

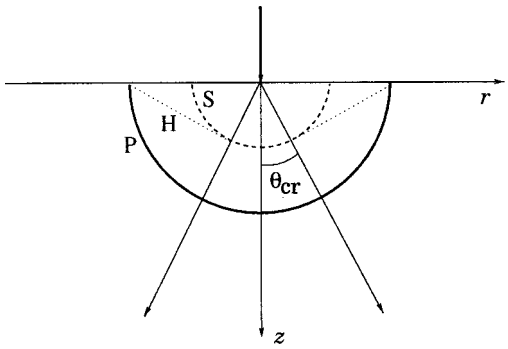

FIG. 1. Point source acting normally on the surface of an elastic half-space. Solid line is the front of the *P*, dashed line, of the *S*, and dotted line, of the head wave. Arrowed segments are the critical rays.

[cf. Achenbach, 1973, Eq. (7.209)], where δ is the Dirac delta function. The half-space is assumed to be at rest prior to $t=0$, and the boundedness condition at infinity is imposed.

B. Wavefront expansions

A *wavefront expansion* is a series of the type

$$\mathbf{u}(t,\mathbf{s}) \sim \begin{cases} \displaystyle\sum_{n=0}^{\infty} \frac{[t-\tau(\mathbf{s})]^{n+\nu}}{(n+\nu)!} C_n(\mathbf{s}), & t > \tau(\mathbf{s}); \\ 0, & t < \tau(\mathbf{s}), \end{cases} \tag{3}$$

where eikonal (or the front of pulse) $\tau(\mathbf{s})$ and the amplitude functions $C_n(\mathbf{s})$ depend on the coordinates of the observation point $\mathbf{s}$ only, and ν is a different constant for different waves (e.g., Friedlander, 1958, p. 63; Borovikov, 1966, p. 24). The Fourier transform of Eq. (3) gives the usual *ray* asymptotic series in inverse powers of the circular frequency ω:

$$\mathbf{u}(\omega,\mathbf{s}) \sim e^{i\omega\tau(\mathbf{s})} \sum_{n=0}^{\infty} \left(\frac{i}{\omega}\right)^{n+\nu+1} C_n(\mathbf{s}) \tag{4}$$

(e.g., Babič and Buldyrev, 1991). Expansion (3) converges as $t \to \tau$, i.e., only for times close to the arrival time. This condition corresponds to the high-frequency limit, $\omega \to \infty$, for the ray series (4).

It is well-known that a point source acting normally on the surface of an elastic half-space radiates a spherical *P* and *S* and a conical head wave (Fig. 1). For this problem the leading terms of the wavefront expansions have been obtained by Knopoff and Gilbert (1959) who applied the method of steepest descent and Tauberian theorems to the Laplace–Hankel integral representation for the displacements. They noticed that for the observation angles $\theta > \theta_{\rm cr}$, where

$$\theta_{\rm cr} = \arcsin\gamma, \quad \gamma = c_S/c_P, \tag{5}$$

the *S* wave arrivals are two-sided singularities, i.e., the disturbance exists both before and after the *S* front. There is nothing nonphysical in such behavior since the *S* front is preceded by the head front. Gakenheimer and Miklowitz (1969) have used the Cagniard–de Hoop method and the expressions for the step-function response were obtained in terms of single integrals. These were used to find the wave-

front expansions. The logarithmic singularity of the S wave arrival was detected. Below, similar results are derived using the analytical harmonic synthesis of the far-field asymptotics of the time-harmonic Green's function.

The leading terms of the far-field asymptotics for the P and S waves radiated by a point source are given, respectively, by

$$\mathbf{G}_0^P \simeq -\frac{1}{2\pi\varrho c_S^2 s} A^P(\theta) e^{ik_P s} \mathbf{n}^P(\theta), \tag{6}$$

and

$$\mathbf{G}_0^S \simeq -\frac{1}{2\pi\varrho c_S^2 s} A^S(\theta) e^{ik_S s} \mathbf{n}^S(\theta) \tag{7}$$

(e.g., Miller and Pursey, 1954), where

$$s=(r^2+z^2)^{1/2},\ \sin\theta = r/s. \tag{8}$$

Here ϱ is the density of the solid and the wave numbers of the P and S waves are $k_P=\omega/c_P$ and $k_S=\omega/c_S$, respectively. The directivity functions $A^P(\theta)$ and $A^S(\theta)$ and the unit displacements vectors $\mathbf{n}^P(\theta)$ and $\mathbf{n}^S(\theta)$ are given in Appendix A.

The leading term of the time-domain Green's function can be obtained directly from Eqs. (6) and (7) by using the harmonic synthesis (inverse Fourier transform):

$$\mathbf{g} = \frac{1}{\pi}\mathrm{Re}\int_0^{+\infty} \mathbf{G} e^{-i\omega t}\, d\omega, \tag{9}$$

to give

$$\mathbf{g}_0^P \simeq -\frac{1}{2\pi\varrho c_S^2 s} A^P \mathbf{n}^P \delta(t-t^P), \tag{10}$$

and

$$\mathbf{g}_0^S \simeq -\frac{1}{2\pi\varrho c_S^2 s} \mathbf{n}^S \left[\mathrm{Re}\, A^S \delta(t-t^S) + \frac{1}{\pi}\mathrm{Im}\, A^S (t-t^S)^{-1} \right], \tag{11}$$

where $t^\alpha = s/c_\alpha$, $\alpha = P, S$; and Table I from Lighthill (1958) has been used. Note that for $\theta > \theta_{\mathrm{cr}}$ Eq. (11) involves the $(t-t^S)^{-1}$-term because at these angles $\mathrm{Im}\, A^S \neq 0$ while A^P is real everywhere. This term demonstrates that for $\theta > \theta_{\mathrm{cr}}$ the S wave arrival is a two-sided singularity. It corresponds to the logarithmic singularity in the step-function response [Gakenheimer and Miklowitz, 1969, Eq. (79)] which has been mentioned above.

The leading term of the wavefront expansion for the head wave is an order smoother than for the spherical P or S wave [Knopoff and Gilbert, 1959, Eq. (14)]. A similar result may be obtained by the harmonic synthesis of the far-field asymptotics of the head wave (e.g., Gridin, 1998). In the regions surrounding the critical ray the fronts of the S and head waves come tangentially close to each other and the above expansion for the S wave is inapplicable. Directly on the critical ray the fronts make a tangential contact and the corresponding singularity is one-fourth of the order smoother than that of the spherical S wave. Note that this conclusion differs from the one made by Knopoff and Gilbert (1959).

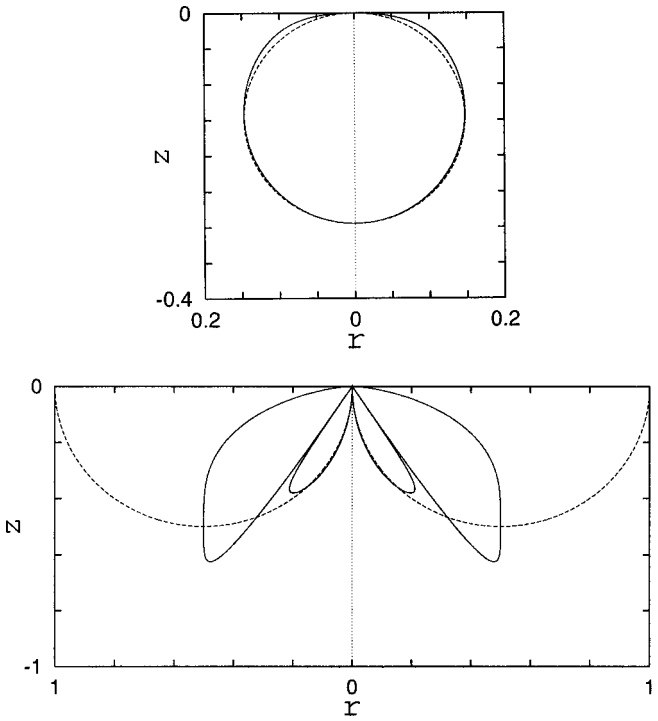

FIG. 2. Comparison of directivity diagrams $A^P(\theta)$ (a) and $\mathrm{Re}\, A^S(\theta)$ (b) (solid lines) with those used by Lhémery (1994) and given by Eqs. (12) and (13) (dashed lines), respectively.

C. One disadvantage of the impulse response approach

To make use of Stepanishen's impulse response approach, Lhémery (1994) has approximated the Green's function for 3D Lamb's problem by the sharp-wave part of the infinite solid Green's function multiplied by a factor of 2 to obtain:

$$\mathbf{g}^P = \frac{1}{2\pi\varrho c_S^2 s} \gamma^2 \cos\theta \mathbf{n}^P \delta(t-t^P), \tag{12}$$

and

$$\mathbf{g}^S = -\frac{1}{2\pi\varrho c_S^2 s} \sin\theta \mathbf{n}^S \delta(t-t^S). \tag{13}$$

The continuous-wave part of the infinite solid Green's function has been taken into account by Lhémery and Stacey (1995). However, from the point of view of the analysis of wave arrivals in the far field of a point source this part is relatively small.

The differences between Eqs. (12) and (13) on the one hand and Eqs. (10) and (11) on the other may be summarized as follows: The Lhémery's formula for the P wave contains the $-\gamma^2\cos\theta$ factor instead of the directivity function $A^P(\theta)$. As seen in Fig. 2(a), the discrepancy is insignificant. The formula for the S wave contains the $\sin\theta$ factor instead of $\mathrm{Re}\, A^S(\theta)$. Figure 2(b) shows that this discrepancy is insignificant only for $\theta < \theta_{\mathrm{cr}}$ but for $\theta > \theta_{\mathrm{cr}}$ it cannot be ignored. Moreover, at these observation angles $\mathrm{Im}\, A^S \neq 0$, and the $(t-t^S)^{-1}$ singularity should be taken into account. This singularity leads to the impulse response for a circular transducer being a double integral, and thus makes the impulse

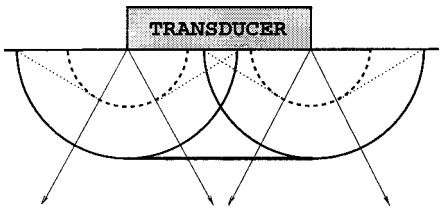

FIG. 3. Circular transducer acting normally on the surface of an elastic half-space. Solid lines are the fronts of the direct and edge *P*, dashed line, of the edge *S*, and dotted line, of the edge head waves. Arrowed segments are the critical rays.

response approach computationally inefficient for describing the *S* waves at the observation angles $\theta > \theta_{cr}$. However, the Lhémery's model is accurate and efficient at all observation angles in describing *P* waves, and in describing *S* waves at observation angles $\theta < \theta_{cr}$.

II. PULSED CIRCULAR NORMAL TRANSDUCER

A. Formulation

Let us consider transient motion of a homogeneous and isotropic elastic half-space caused by a directly coupled circular normal transducer. The cylindrical coordinates (r,φ,z), with the origin at the transducer center and the *z*-axis directed into the solid, are used below. The displacements are again described by Eq. (1) and the idealized boundary conditions are those of the normal pressure uniformly applied over a disk of radius *l*. Thus we have

$$\sigma_{zr}|_{z=0}=0, \quad \sigma_{zz}|_{z=0}=\begin{cases} -p_0(t), & r\leqslant l; \\ 0, & r>l, \end{cases} \tag{14}$$

where $p_0(t)$ is a pressure input function. As above, the half-space is at rest prior to $t=0$, and the boundedness condition at infinity is imposed. Since realistic pulses used in NDE contain mostly intermediate and high frequencies, we assume that so does the initial waveform p_0.

B. Wavefront expansions of the impulse response

The well-known picture of wavefronts underneath a circular normal transducer is shown in Fig. 3. The front of the direct *P* wave is plane, and the fronts of the edge *P* and *S* waves are toroidal. Our purpose is to find wavefront expansions for these waves including the so-called transition regions, the penumbra or shadow boundary where the front of the direct *P* wave is tangentially close to the front of the edge *P* wave, and the axial region where the focusing of the fronts of the toroidal edge *P* and *S* waves takes place. We neglect the head waves and the regions surrounding the critical rays.

The time-harmonic counterpart of the problem formulated above has been treated in Fradkin *et al.* (1998), where the leading terms of the high-frequency asymptotics of the direct *P* and edge *P* and *S* waves as well as the field inside the penumbra and the axial regions have been found. These formulas may be utilized to find the leading terms of the wavefront expansions of the impulse response up to a smooth function by means of the analytical harmonic synthesis [analogously to Eq. (9)]. The results are given below, where the arrival times are as follows:

$$t_0^P=z/c_P, \; t_1^\alpha=s_1/c_\alpha, \; t_2^\alpha=s_2/c_\alpha, \; t_*^\alpha=s_*/c_\alpha, \tag{15}$$

with $\alpha=P,S$, and the corresponding distances and angles are given by

$$s_1=[z^2+(r-l)^2]^{1/2}, \quad s_2=[z^2+(r+l)^2]^{1/2}, \quad s_*=(z^2+l^2)^{1/2}, \tag{16}$$

and

$$\sin\theta_1=|l-r|/s_1, \; \sin\theta_2=(l+r)/s_2, \; \sin\theta_*=l/s_*. \tag{17}$$

The direct *P* wave is described by a step-function singularity:

$$\mathbf{u}_0^P=C_0^P\mathbf{e}_z\begin{cases} 0, & r>l; \\ 0, & t<t_0^P, \, r<l; \\ 1, & t>t_0^P, \, r<l, \end{cases} \tag{18}$$

where C_0^P and all the coefficients used below depend on the coordinates of the observation point only and are listed in Appendix B. For the leading terms of the edge *P* wave arriving respectively from the nearest and farthest edge point we obtain the square-root singularities

$$\mathbf{u}^{P_1}\simeq C_1^P\mathbf{n}_1^P\begin{cases} 0, & t<t_1^P; \\ (t-t_1^P)^{1/2}, & t>t_1^P; \end{cases} \tag{19}$$

and

$$\mathbf{u}^{P_2}\simeq C_2^P\mathbf{n}_2^P\begin{cases} (t_2^P-t)^{1/2}, & t<t_2^P; \\ 0, & t>t_2^P \end{cases} \tag{20}$$

(for the acoustical case see Stepanishen, 1976).

The *z*-component of Eq. (19) is not applicable inside the penumbra where the direct and edge *P* fronts are tangentially close to each other. Here we obtain

$$u_z^{P_1(\text{penumbra})} \simeq C_0^P\begin{cases} 0, & t<t_1^P; \\ \dfrac{1}{\pi}\arctan\left\{-\operatorname{sgn}(l-r)\dfrac{(t-t_1^P)^{1/2}}{(t_1^P-t_0)^{1/2}}\right\}, & t>t_1^P, \end{cases} \tag{21}$$

where $\operatorname{sgn}x=1$, if $x>0$, and -1, if $x<0$. Note that for $l=r$ (or $t_1^P=t_0$) Eqs. (18) and (21) become

$$u_0^P+u_z^{P_1(\text{penumbra})}\simeq C_0^P\begin{cases} 0, & t<t_1^P; \\ 1/2, & t>t_1^P. \end{cases} \tag{22}$$

An expression similar to Eq. (21) has been obtained for the acoustic scattering by a wedge by Keller and Blank (1951) without a recourse to the frequency domain (see also Friedlander, 1958, p. 125; Borovikov, 1966, p. 72).

In the axial region, where the focusing of the edge *P* waves takes place, neither Eqs. (19) nor (20) are applicable. They are replaced by the following expressions:

$$u_z^{P(\text{axial})} \simeq C_*^P \cos\theta_* \begin{cases} \arcsin\dfrac{t_*^P - t}{t_r^P}, & |t-t_*^P| < t_r^P; \\ \dfrac{\pi}{2}\operatorname{sgn}(t_*^P - t), & |t-t_*^P| > t_r^P \end{cases} \tag{23}$$

[see also Schmerr and Sedov, 1989, Eq. (58)] and

$$u_r^{P(\text{axial})} \simeq C_*^P \sin\theta_* \begin{cases} \left\{1 - \left(\dfrac{t_*^P - t}{t_r^P}\right)^2\right\}^{1/2}, & |t-t_*^P| < t_r^P; \\ 0, & |t-t_*^P| > t_r^P, \end{cases} \tag{24}$$

where $t_r^P = r\sin\theta_*/c_P$. Directly on the transducer axis Eqs. (23) and (24) become

$$\mathbf{u}^{P(\text{axial})} \simeq C_*^P \cos\theta_* \mathbf{e}_z \frac{\pi}{2}\operatorname{sgn}(t_*^P - t), \tag{25}$$

i.e., we obtain a singularity of the same order as the direct P wave.

The leading terms of the edge S waves are the square-root singularities

$$\mathbf{u}^{S_1} \simeq \mathbf{n}_1^S \begin{cases} \operatorname{Im} C_1^S (t_1^S - t)^{1/2}, & t < t_1^S; \\ \operatorname{Re} C_1^S (t - t_1^S)^{1/2}, & t > t_1^S, \end{cases} \tag{26}$$

and

$$\mathbf{u}^{S_2} \simeq \mathbf{n}_2^S \begin{cases} \operatorname{Re} C_2^S (t_2^S - t)^{1/2}, & t < t_2^S; \\ -\operatorname{Im} C_2^S (t - t_2^S)^{1/2}, & t > t_2^S. \end{cases} \tag{27}$$

Note that the S wave arrivals are two-sided singularities for $\theta_{1,2} > \theta_{\text{cr}}$. There is no penumbra in the S field, since there is no direct S wave.

In the axial region neither Eq. (26) nor (27) are applicable where we obtain the following formulas:

$$u_z^{S(\text{axial})} \simeq \sin\theta_* \begin{cases} \operatorname{Re} C_*^S \arcsin\dfrac{t - t_*^S}{t_r^S}, & |t-t_*^S| < t_r^S; \\ \operatorname{Re} C_*^S \dfrac{\pi}{2}\operatorname{sgn}(t - t_*^S) + \operatorname{Im} C_*^S \operatorname{arccosh}\dfrac{|t_*^S - t|}{t_r^S}, & |t-t_*^S| > t_r^S, \end{cases} \tag{28}$$

and

$$u_r^{S(\text{axial})} \simeq \cos\theta_* \begin{cases} \operatorname{Re} C_*^S \left\{1 - \left(\dfrac{t_*^S - t}{t_r^S}\right)^2\right\}^{1/2} - \operatorname{Im} C_*^S \dfrac{t_*^S - t}{t_r^S}, & |t-t_*^S| < t_r^S; \\ -\operatorname{Im} C_*^S \dfrac{t_r^S \operatorname{sgn}(t_*^S - t)}{|t_*^S - t| + \{(t_*^S - t)^2 - (t_r^S)^2\}^{1/2}}, & |t-t_*^S| > t_r^S, \end{cases} \tag{29}$$

where $t_r^S = r\sin\theta_*/c_S$. Directly on the transducer axis Eqs. (28) and (29) become

$$\mathbf{u}^{S(\text{axial})} \simeq \sin\theta_* \mathbf{e}_z \left[\operatorname{Re} C_*^S \frac{\pi}{2}\operatorname{sgn}(t - t_*^S) + \operatorname{Im} C_*^S \log|t - t_*^S|\right], \tag{30}$$

i.e., we have the singularity of the same order as the direct P wave.

Similarly to the point source case, the leading term of the head wavefront expansion is an order smoother than for the P or S wave. In the regions surrounding the critical rays the S and head fronts become tangentially close to each other and the above expansions for the S wave are inapplicable. Directly on the critical ray the fronts make a tangential contact and the corresponding singularity is one fourth of the order smoother than that of the S wave.

C. Uniform asymptotics

By matching the asymptotics which are applicable inside a geometrical region to those applicable inside a transition region one can obtain *uniform* asymptotics which are applicable both inside and outside. The procedure is demonstrated below for the z-component of the total P field.

First, let us consider the penumbral region. The total P field there is expressed as

$$u_z^P \simeq u_0^P + u_z^{P_1(\text{penumbra})} + u_z^{P_2}. \tag{31}$$

On the other hand, inside the geometrical region this field is given by

$$u_z^P \simeq u_0^P + u_z^{P_1} + u_z^{P_2}. \tag{32}$$

Expanding $u_z^{P_1(\text{penumbra})}$ [see Eq. (21)] for small arguments of the arctan, which corresponds to the transition to the geometrical region, we obtain the leading term

$$u_3 = C_3 \begin{cases} 0, & t < t_1^P; \\ (t - t_1^P)^{1/2}, & t > t_1^P. \end{cases} \tag{33}$$

Then the wavefront expansion which is applicable both inside and outside the penumbra can be written as

$$u_z^P \simeq (u_0^P + u_z^{P_1} + u_z^{P_2}) + (u_z^{P_1(\text{penumbra})} - u_3). \tag{34}$$

In the geometrical and penumbral region Eq. (34) gives Eqs. (32) and (31), respectively, up to smoother terms.

The asymptotics which are applicable both inside and outside the axial region may be derived analogously. Moreover, the uniform wavefront expansion which is applicable throughout all zones may be obtained. It has the form

$$u_z^{P(\text{uniform})} \simeq (u_0^P + u_z^{P_1} + u_z^{P_2}) + (u_z^{P_1(\text{penumbra})} - u_3) + (u_z^{P(\text{axial})} - u_4 - u_5), \tag{35}$$

where we have

$$u_4 = C_4 \begin{cases} 0, & t < t_*^P - t_r^P; \\ \{t - (t_*^P - t_r^P)\}^{1/2}, & t > t_*^P - t_r^P, \end{cases} \tag{36}$$

and

$$u_5 = -C_4 \begin{cases} \{(t_*^P + t_r^P) - t\}^{1/2}, & t < t_*^P + t_r^P; \\ 0, & t > t_*^P + t_r^P. \end{cases} \tag{37}$$

D. Discussion and numerical results

The limits of applicability of the above expansions are determined by some characteristic time τ_0, e.g., $\tau_0 = 1/2f_0$, where f_0 is the central frequency of the pressure input function p_0. First of all, the expansions are applicable for

$$|t - t_i^\alpha| < \tau_0, \tag{38}$$

that is, for the times which are close to the corresponding wave arrival t_i^α. Also, we should have

$$t_0^P > \tau_0, \quad t_1^P - t_0^P > \tau_0. \tag{39}$$

The first condition in Eq. (39) requires that the direct P wave arrives no earlier than τ_0, and the second, that the direct and edge P arrivals on the transducer axis are separated by at least τ_0. Conditions (39) are approximately equivalent to

$$\lambda_P/2 < z < l^2/\lambda_P, \tag{40}$$

where λ_P is a P wavelength. This defines the so-called radiating near zone of a circular normal transducer (see Fradkin *et al.*, 1998). For a typical frequency 5 MHz and the transducer radius $l = 10$ mm this region extends in steels from about 0.5 mm to about 80 mm. The numerical experiments have demonstrated that the wavefront expansions give reasonable agreement with the direct numerical solution in the intermediate zone as well. The far field of a circular normal transducer is briefly discussed in Sec. II E.

All of the above asymptotic formulas have been validated against a direct numerical solution similar to the one described in Djelouah and Baboux (1992). The test parameters have been chosen as follows: $c_P = 5840$ m/s, $c_S = 3170$ m/s, $\varrho = 7770$ kg/m^3 and $l = 10$ mm.

1. Impulse response

For simplicity, only the P wave contributions to the impulse response are shown in Fig. 4. At point $r = 3$ mm and $z = 5$ mm which lies in the geometrical region the arrivals are well separated [Fig. 4(a)]. The solid line represents the direct numerical solution, and the dashed and dotted lines represent the wavefront expansions. These are (from left to right): The step-function singularity of the direct P wave (18), the square-root singularity of the edge P wave arriving from the nearest edge point (19) and the square-root singularity of the P wave from the farthest edge point (20). It can be seen that the expansions give a correct description of the singularities of the impulse response. As it has been pointed out above [see Eq. (38)], the expansions are applicable for times close to the corresponding wave arrivals. In practice, their ''tails'' can be left in, since they are smooth, and thus do not affect the results of the time convolution, provided that the pulses contain mostly high and intermediate frequencies.

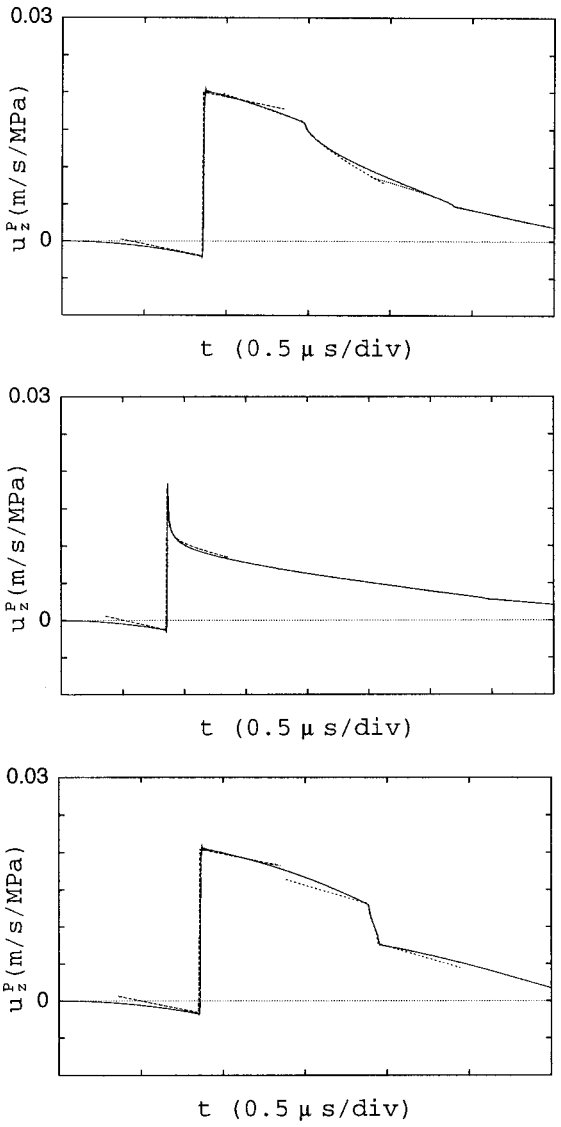

FIG. 4. The P-wave contribution to the z-component of impulse response at $z = 5$ mm and various r: (a) geometrical region—$r = 3$ mm; (b) penumbra—$r = 9.5$ mm; (c) axial region—$r = 0.2$ mm. Solid line is the direct, and dashed and dotted lines are the asymptotic solutions.

At the penumbral point $r = 9.5$ mm and $z = 5$ mm [Fig. 4(b)] the arrival of the direct and nearest edge P waves are close to each other and we have the sum of step-function

singularity (18) and arctan singularity (21). The amplitude of the next arrival, which is due to the *P* wave arriving from the farthest edge point, is very small.

At point $r=0.2$ mm and $z=5$ mm [Fig. 4(c)], which lies in the axial region, the first singularity is the same as in Fig. 4(a). The second, which is due to the focusing of the edge *P* waves, is the arcsin-type Eq. (23). It can be seen that directly on the axis this arrival becomes a step-function type.

A transition from the nonuniform expansion applicable inside the geometrical region to the penumbral expansion may be made when the difference between the direct and edge *P* arrival times is less than the characteristic time τ_0. In the case of the axial region the difference between the arrival times of the edge *P* waves arriving from the nearest and the farthest edge point should be smaller than τ_0. However, using the uniform asymptotics Eq. (35) allows one to avoid both transitions.

2. Pulse propagation

The trains of pulses may be obtained by the time convolution of the pressure input function $p_0(t)$ with the impulse response. Below, we consider the particle velocity because this is the quantity measured by the receiving probes (Weight, 1987). It can be expressed as follows:

$$v(t)=\frac{\partial}{\partial t}\{p_0(t)*u(t)\}, \tag{41}$$

where the ''star'' denotes the time convolution. In the numerical calculations the pressure input function has been chosen to be one cycle of sine of frequency $f_0=5$ MHz and amplitude $P_0=1$ MPa, so that we have

$$p_0(t)=\begin{cases} P_0\sin(2\pi f_0 t), & 0<t<1/f_0; \\ 0, & \text{otherwise.} \end{cases} \tag{42}$$

The *z*-component of the particle velocity at the same observation points as used in Fig. 4(a)–(c) is shown in Fig. 5(a)–(c), respectively, with the *S* wave included.

In the geometrical region [Fig. 5(a)] all pulses are well separated. The first is due to the direct *P* wave. This pulse restores the initial waveform (cf. Weight, 1987). Its amplitude is obtained simply by multiplying of the amplitude of the step function in Eq. (18) by the amplitude of the pressure input function P_0. The other pulses are due to the edge *P* and *S* waves (the direct solution contains the small head pulses as well). The shapes of these pulses are expressed as fractional Weyl's or Riemann–Liouville's integrals of the order one-half of the initial waveform (Erdélyi, 1954, pp. 181–212) since the corresponding wavefront singularities are the square-root functions. These results may be derived directly in the time domain by applying to the problem in hand the general technique developed in Chapman (1992) and Prentice (1994), although the technique requires further development for the *S* waves.

In the penumbra the pulses of the direct and nearest edge *P* waves overlap and the amplitude of the resulting pulse diminishes [Fig. 5(b)]. Straight underneath the transducer

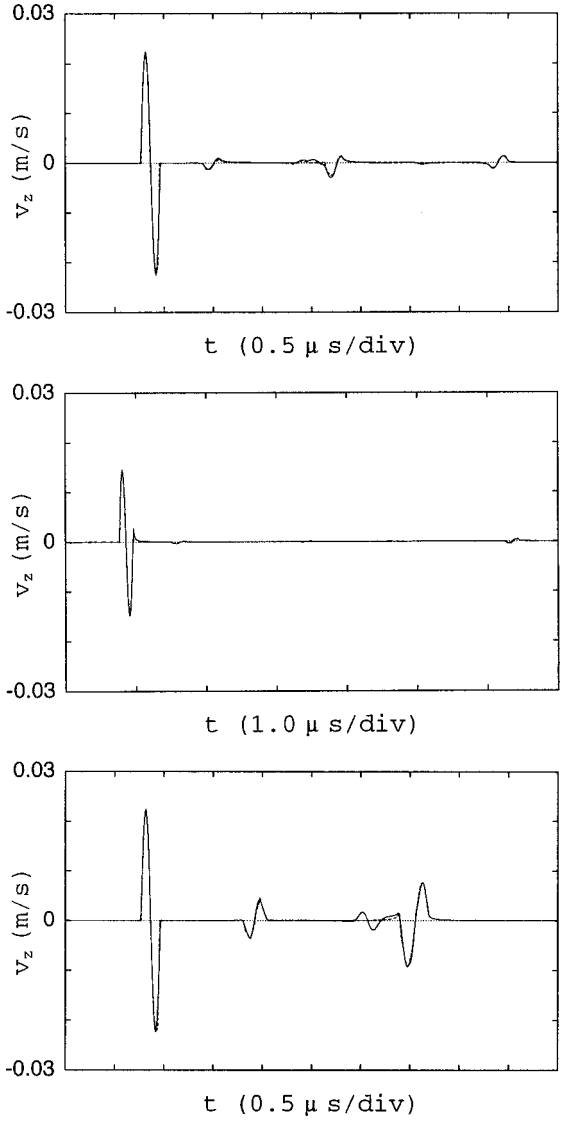

FIG. 5. The *z*-component of the particle velocity at $z=5$ mm and the same *r* as in Fig. 4(a)–(c), respectively. Solid line is the direct, and dashed line is the asymptotic solution.

rim this amplitude is one-half of the amplitude of the direct *P* wave (cf. Weight, 1987). The other discernible pulses are those of the edge *S* waves.

In the axial region [Fig. 5(c)] the first pulse is the same as in Fig. 5(a). The second is due to the focusing of the edge *P* waves. Note that directly on the axis this pulse also restores the initial waveform (cf. Weight, 1987) but is inverted and has a smaller amplitude compared to the direct *P* pulse. The head pulse which is neglected in our analysis arrives next. The last pulse is due to the focusing of the edge *S* waves. Note that directly on the axis the shape of this pulse coincides with the initial *only* for $\theta_*<\theta_{cr}$ (or $z>l/\tan\theta_{cr}$). For $\theta_*>\theta_{cr}$ the pulse shape is distorted from the initial due to the presence of the logarithmic singularity in Eq. (30).

This situation is illustrated in Fig. 6 which shows the *S*-wave pulse at the axial point $r=0$ mm and $z=3$ mm. We compare the pulse obtained by using Eq. (30) both with and without the log term with the exact. It can be seen that if we neglect the logarithmic singularity, the corresponding pulse restores the initial waveform. If we take the singularity into

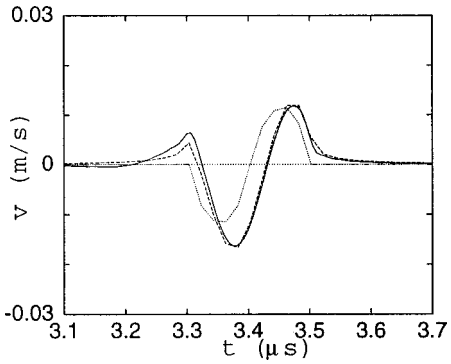

FIG. 6. The *S*-wave pulse at the axial point $r=0$ mm and $z=3$ mm. Solid line is the direct, and dashed and dotted line is the asymptotic solution with and without the log term, respectively.

account there is a distortion and the resulting pulse practically coincides with the exact. This distortion, although present in the direct numerical results computed by the finite-difference method [Ilan and Weight, 1990, Fig. 10(a); Lhémery and Stacey, 1995, Fig. 2(III)], has not been noticed and explained before.

All the figures demonstrate good agreement between the asymptotic and direct numerical method but the former is thousands times faster. Moreover, the wave-front expansions have an explicit physical interpretation and allow an easy prediction of the amplitudes and shapes of the radiated pulses. A further discussion of the transient field radiated by a circular normal transducer into an elastic half-space may be found, for instance, in Djelouah and Baboux (1992) or Gridin and Fradkin (1998).

E. Far field of a circular transducer

The far-field asymptotics of a time-harmonic large circular normal transducer are well-known and differ from those of a point source by factors of the type $2J_1(k_\alpha l \sin\theta)/k_\alpha l \sin\theta$ (e.g., Tang *et al.*, 1994). In the time domain the corresponding expansions for the *P* and *S* waves are given by

$$u^P(t)\simeq C^P\mathbf{n}^P\begin{cases}\left\{1-\left(\dfrac{t^P-t}{t_l^P}\right)^2\right\}^{1/2}, & |t-t^P|<t_l^P;\\ 0, & |t-t^P|>t_l^P,\end{cases} \tag{43}$$

and

$$u^S(t)\simeq\mathbf{n}^S\begin{cases}\operatorname{Re}C^S\left\{1-\left(\dfrac{t^S-t}{t_l^S}\right)^2\right\}^{1/2}-\operatorname{Im}C^S\dfrac{t^S-t}{t_l^S}, & |t-t^S|<t_l^S;\\ -\operatorname{Im}C^S\dfrac{t_l^S\operatorname{sgn}(t^S-t)}{|t^S-t|+\{(t^S-t)^2-(t_l^S)^2\}^{1/2}}, & |t-t^S|>t_l^S,\end{cases} \tag{44}$$

respectively, with $t^\alpha=s/c_\alpha$, and $t_l^\alpha=l\sin\theta/c_\alpha$. On the axis they coincide with the point-source asymptotics similar to Eqs. (10) and (11) but with the unit force replaced by the unit pressure. For the radiation into fluid media expressions similar to Eq. (43) have been obtained by Stepanishen (1974) [see also Schmerr and Sedov, 1989, Eq. (60)].

III. CONCLUSIONS

A new method based on the wavefront expansions of the impulse response has been developed to describe the pulse propagation in the radiating near zone of a circular normal transducer. The nonuniform expansions of the direct *P* and edge *P* and *S* waves have been obtained by the analytical harmonic synthesis of the high-frequency asymptotics. The uniform asymptotic expansions have been also derived. The resulting formulas are expressed in terms of elementary functions only. The wavefront expansions have an explicit physical interpretation and allow an easy prediction of the amplitudes and shapes of the radiated pulses. The asymptotic code based on the expansions has been fully tested against the direct numerical solution. It is thousands times faster but practically just as accurate. The method may be extended to deal with nonuniform loads without increase in the computation time.

ACKNOWLEDGMENTS

The author gratefully acknowledges a South Bank Research Scholarship. He is much indebted to Professor V. A. Borovikov and Dr. C. J. Chapman for bringing the time-domain diffraction methods to his attention, and to Dr. L. J. Fradkin for the careful reading of the manuscript and useful discussions. Comments of Dr. J. P. Weight are also appreciated.

APPENDIX A: DIRECTIVITY DIAGRAMS FOR A NORMAL POINT SOURCE

The directivity diagrams for the *P* and *S* spherical waves in the far field of a point source acting normally on the surface of a homogeneous and isotropic elastic half-space are as follows:

$$A^P(\theta)=\frac{2\sin^2\theta-\gamma^{-2}}{R^P(\sin\theta)}\cos\theta, \tag{A1}$$

and

$$A^S(\theta)=\frac{2\sin\theta(\gamma^2-\sin^2\theta)^{1/2}}{R^S(\sin\theta)}\cos\theta, \tag{A2}$$

with the Rayleigh-type functions

$$R^P(\xi)=(2\xi^2-\gamma^{-2})^2+4\xi^2(1-\xi^2)^{1/2}(\gamma^{-2}-\xi^2)^{1/2}, \tag{A3}$$

and

$$R^S(\xi)=(2\xi^2-1)^2-4\xi^2(\xi^2-1)^{1/2}(\xi^2-\gamma^2)^{1/2}. \tag{A4}$$

The unit displacement vectors are given by

$$\begin{aligned}\mathbf{n}^P(\theta)&=\sin\theta\mathbf{e}_r+\cos\theta\mathbf{e}_z,\\ \mathbf{n}^S(\theta)&=\cos\theta\mathbf{e}_r-\sin\theta\mathbf{e}_z.\end{aligned} \tag{A5}$$

APPENDIX B: COEFFICIENTS OF THE WAVEFRONT EXPANSIONS

The coefficients of the wavefront expansions given in Sec. II B are as follows (the unit pressure is assumed):

$$C_0^P = \frac{1}{\varrho c_P}, \tag{B1}$$

$$C_1^P = -\frac{\sqrt{2}}{\pi \varrho c_S^{1/2} \gamma^{3/2}} A^P(\theta_1) \frac{1}{|l-r|} \left(\frac{l s_1}{r} \right)^{1/2}, \tag{B2}$$

$$C_2^P = -\frac{\sqrt{2}}{\pi \varrho c_S^{1/2} \gamma^{3/2}} A^P(\theta_2) \frac{1}{l+r} \left(\frac{l s_2}{r} \right)^{1/2}, \tag{B3}$$

$$C_1^S = -\frac{\sqrt{2}}{\pi \varrho c_S^{1/2}} A^S(\theta_1) \frac{1}{|l-r|} \left(\frac{l s_1}{r} \right)^{1/2}, \tag{B4}$$

$$C_2^S = -\frac{\sqrt{2}}{\pi \varrho c_S^{1/2}} A^S(\theta_2) \frac{1}{l+r} \left(\frac{l s_2}{r} \right)^{1/2}, \tag{B5}$$

$$C_*^P = -\frac{1}{\pi \varrho c_S \gamma} A^P(\theta_*), \tag{B6}$$

and

$$C_*^S = -\frac{1}{\pi \varrho c_S} A^S(\theta_*). \tag{B7}$$

The unit displacement vectors are given by

$$\begin{aligned} \mathbf{n}_1^P &= -\operatorname{sgn}(l-r)\cos\theta_1 \mathbf{e}_z + \sin\theta_1 \mathbf{e}_r, \\ \mathbf{n}_2^P &= \cos\theta_2 \mathbf{e}_z + \sin\theta_2 \mathbf{e}_r, \\ \mathbf{n}_1^S &= \operatorname{sgn}(l-r)\sin\theta_1 \mathbf{e}_z + \cos\theta_1 \mathbf{e}_r, \\ \mathbf{n}_2^S &= -\sin\theta_2 \mathbf{e}_z + \cos\theta_2 \mathbf{e}_r. \end{aligned} \tag{B8}$$

The coefficients used in the uniform asymptotic expansion in Sec. II C can be expressed as

$$C_3 = -\frac{1}{\pi \varrho c_P^{1/2}} \operatorname{sgn}(l-r) \frac{1}{(s_1 - z)^{1/2}}, \tag{B9}$$

and

$$C_4 = \frac{\sqrt{2}}{\pi \varrho c_S^{1/2} \gamma^{3/2}} A^P(\theta_*) \cos\theta_* \left(\frac{s_*}{rl} \right)^{1/2}. \tag{B10}$$

The coefficients for the far-field wavefront expansions of a circular normal transducer are given by

$$C^P = -\frac{l}{\pi \varrho c_S \gamma r} A^P(\theta), \tag{B11}$$

and

$$C^S = -\frac{l}{\pi \varrho c_S r} A^S(\theta). \tag{B12}$$

Achenbach, J. D. (**1973**). Wave Propagation in Elastic Solids (North-Holland, New York).

Babič, V. M., and Buldyrev, V. S. (**1991**). *Short-Wavelength Diffraction Theory: Asymptotic Methods* (Springer-Verlag, Heidelberg).

Borovikov, V. A. (**1966**). *Diffraction by Polygons and Polyhedra* (Nauka, Moscow).

Borovikov, V. A. (**1994**). *Uniform Stationary Phase Method* (IEE Electromagnetic Series, London), Vol. 40.

Bresse, L. F., and Hutchins, D. A. (**1989**). ''Transient generation of elastic waves in solids by a disk-shaped normal force source,'' J. Acoust. Soc. Am. **86**, 810–817.

Chapman, C. J. (**1992**). ''Time-domain asymptotics and the method of stationary phase,'' Proc. R. Soc. London, Ser. A **437**, 25–40.

Djelouah, H., and Baboux, J. C. (**1992**). ''Transient ultrasonic field radiated by a circular transducer in a solid medium,'' J. Acoust. Soc. Am. **92**, 2932–2941.

Erdélyi, A. (Ed). (**1954**). *Tables of Integral Transforms*, Vol. II (McGraw-Hill, New York).

Fradkin, L. J., Kiselev, A. P., and Krylova, E. (**1998**). ''The radiating near field asymptotics of a time-harmonic circular normal ultrasonic transducer in an elastic half-space,'' J. Acoust. Soc. Am. **104**, 1178–1187.

Friedlander, F. G. (**1958**). *Sound Pulses* (Cambridge University Press, Cambridge).

Gakenheimer, D. C., and Miklowitz, J. (**1969**). ''Transient excitation of an elastic half space by a point load travelling on the surface,'' J. Appl. Mech. **36**, 505–515.

Gridin, D. (**1998**). ''High-frequency asymptotic description of head waves and boundary layers surrounding critical rays in an elastic half-space,'' J. Acoust. Soc. Am. **104**, 1188–1197.

Gridin, D., and Fradkin, L. J. (**1998**). ''High-frequency asymptotic description of pulses radiated by a circular normal transducer into an elastic half-space,'' J. Acoust. Soc. Am. **104**, 3190–3198.

Ilan, A., and Weight, J. P. (**1990**). ''The propagation of short pulses of ultrasound from a circular source coupled to an isotropic solid,'' J. Acoust. Soc. Am. **88**, 1142–1151.

Keller, J. B., and Blank, A. (**1951**). ''Diffraction and reflection of pulses by wedges and corners,'' Commun. Pure Appl. Math. **4**, 75–94.

Knopoff, L., and Gilbert, F. (**1959**). ''First motion method in theoretical seismology,'' J. Acoust. Soc. Am. **31**, 1161–1168.

Laturelle, F. G. (**1990**). ''The stresses produced in an elastic half-space by a normal step loading over a circular area: analytical and numerical results,'' Wave Motion **12**, 107–127.

Lhémery, A. (**1994**). ''A model for the transient ultrasonic field radiated by an arbitrary loading in a solid,'' J. Acoust. Soc. Am. **96**, 3776–3786.

Lhémery, A., and Stacey, R. (**1995**). ''Transient field radiated by nonuniform transducers in a solid calculated by an approximate model and the finite-difference method,'' *Review of Progress in Quantitative Nondestructive Evaluation*, Vol. 14, edited by D. O. Thompson and D. E. Chimenti (Plenum, New York), pp. 997–1004.

Lighthill, M. J. (**1958**). *Fourier Analysis and Generalized Functions* (Cambridge University Press, Cambridge).

McNab, A., Cochran, A., and Campbell, M. A. (**1989**). ''The calculation of acoustic fields in solids for transient normal surface force sources of arbitrary geometry and apodization,'' J. Acoust. Soc. Am. **87**, 1455–1465.

Miklowitz, J. (**1978**). *The Theory of Elastic Waves and Waveguides* (North-Holland, Amsterdam).

Miller, G. F., and Pursey, H. (**1954**). ''The field and radiation impedance of mechanical radiators on the free surface of a semi-infinite isotropic solid,'' Proc. R. Soc. London, Ser. A **223**, 521–541.

Prentice, P. R. (**1994**). ''Time-domain asymptotics. I. General theory for double integrals,'' Proc. R. Soc. London, Ser. A **446**, 341–360.

Schmerr, L. W., and Sedov, A. (**1989**). ''An elastodynamic model for compressional and shear wave transducers,'' J. Acoust. Soc. Am. **86**, 1988–1999.

Stepanishen, P. R. (**1971**). ''Transient radiation from pistons in an infinite planar battle,'' J. Acoust. Soc. Am. **49**, 1629–1638.

Stepanishen, P. R. (**1974**). ''Acoustic transients in the far-field of a baffled circular piston using the impulse response approach,'' J. Sound Vib. **32**, 295–310.

Stepanishen, P. R. (**1976**). ''Asymptotic behavior of the acoustic nearfield of a circular piston,'' J. Acoust. Soc. Am. **59**, 749–754.

Tang, X. M., Zhenya, Z., and Toksöz, M. N. (**1994**). ''Radiation patterns of compressional and shear transducers at the surface of an elastic half-space,'' J. Acoust. Soc. Am. **95**, 71–76.

Weight, J. P. (**1987**). ''A model for the propagation of short pulses of ultrasound in a solid,'' J. Acoust. Soc. Am. **81**, 815–826.

The full-field equations for acoustic radiation and scattering

Martin Ochmann[a)]
Technische Fachhochschule Berlin, Fachbereich Mathematik, Physik und Chemie, Luxemburger Strasse 10, 13353 Berlin, Germany

(Received 9 September 1998; revised 8 January 1999; accepted 12 January 1999)

The source simulation technique or related approaches like the multipole method, the superposition method, etc. are used for calculating the sound field radiated (or scattered) from complex-shaped structures. However, it is known that these techniques can lead to ill-conditioned systems of equations, and their numerical treatment requires extreme care. A new stabilized variant of the source simulation technique—called the full-field method—has been developed by using the exterior instead of the interior Helmholtz integral formulation or, equivalently, by expanding the sound field into special trial and weighting functions. These functions are chosen in such a way that the resulting matrix becomes more diagonally dominant. The full-field method is applied to the acoustic radiation from a pulsating sphere and to the high-frequency scattering from a cylinder and a nonconvex structure. The numerical results are compared with calculations obtained from other methods. It is shown that the improved method leads to better conditioned sets of equations which can be solved directly without singular-value decomposition, since the associated condition numbers are decreased strongly, in some cases by a few orders of magnitude. © *1999 Acoustical Society of America.* [S0001-4966(99)01504-0]

PACS numbers: 43.20.Fn, 43.20.Rz, 43.30.Gv, 43.30.Jx [ANN]

INTRODUCTION

The source simulation technique or multipole method is widely used for the analysis of radiation and scattering problems. The basic idea of the method is to replace the radiating or scattering body by a system of multipoles, called sources, located within the envelope of the radiator. The better the system of sources satisfies the boundary condition on the surface of the structure, the closer the agreement between the original and the simulated sound field. A detailed investigation about the source simulation technique, its different variants, the underlying mathematical basis, strategies for minimizing the boundary error, etc., including a comprehensive list of references, can be found in Ref. 1. For many technical applications, numerical calculations based on the source simulation technique are faster than conventional boundary element calculations. However, the numerical realization of the source simulation technique could lead to ill-conditioned systems of linear equations. These instabilities are mainly caused by three facts assuming that the finite element model of the vibrating surface is fine enough with regard to the vibration pattern and frequency range considered. First, the wide-spread use of spherical wave functions leads to instabilities if the shape of the structure strongly deviates from a spherical shape like, for example, a long cylinder. This instability can easily be removed by taking into account several source locations in the interior of the structure. In other words, the multi-point multipole method must be applied instead of the one-point multipole method.[1–3] In Ref. 1, a detailed discussion can be found on how to select the source locations. Also, some references were given concerning the numerical optimization of the source positions for the multi-point multipole method. Second, symmetries of the structure and the boundary conditions can cause an badly conditioned system. Such an instability can be avoided by taking into account a source system with the same symmetry as the original problem.[1]

The main point of the present investigation concerns the third type of instability and an approach to remove it: Some variants of the source simulation technique like, for example, the null-field method[4,5] or the superposition method[6,7] are related to the interior Helmholtz integral equation,[5] which is an ill-posed integral equation of the first kind.[8,9] Also, the internal source density method of Stepanishen for radiation and scattering problems from bodies of revolution (see Ref. 10, where more references to related papers can be found) leads to an integral equation of the first kind. Often such unstable linear systems are solved by employing singular-value decomposition[10,11] which needs considerable computer time. To overcome this instability without an additional increase of computer time due to the singular-value decomposition, a new stabilized variant of the source simulation technique has been developed. This variant can be derived from the exterior Helmholtz integral formulation and is called full-field method or full-field equations of the first kind (FFE1), whereas the null-field equations (NFE) are based on the interior Helmholtz integral formulation.[4,5] As an alternative, the method of weighted residuals can also be used for obtaining a very clear derivation of the FFE1. It is well-known that the source simulation technique is equivalent to the NFE, if spherical wave functions are used as trial and also as weighting functions.[1,3] Such equations were also derived by Waterman for the solution of scattering problems and became well-known under the name T-matrix method.[12] Also in this context, several attempts were made to overcome the ''numerical instabilities associated with the T-matrix method.'' [13] In the present paper it is shown that the FFE1

[a)]Electronic mail: ochmann@tfh-berlin.de

 0001-4966/99/105(5)/2574/11/$15.00

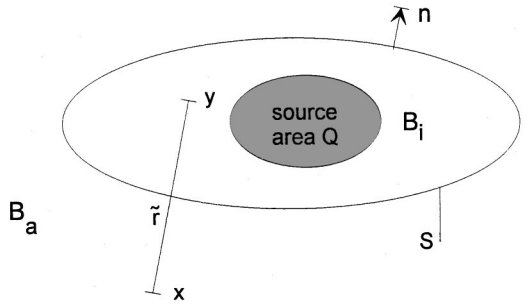

FIG. 1. Geometry of the radiation or scattering problem.

are obtained if the real parts of the spherical wave functions are used as weighting functions. However, to avoid difficulties at certain critical frequencies, it is recommended that the complex conjugate spherical wave functions be used as weighting functions. The resulting equations are called full-field equations of the second kind (FFE2).

The two variants of the full-field equations are applied to calculate the acoustic radiation from a pulsating sphere and the high-frequency scattering from a finite cylinder and a nonconvex structure. The condition numbers of the resulting matrices and the directivity diagrams in the far-field are presented and compared with the results of the null-field method and the least-squares approximation. It is shown that especially the FFE2 leads to better conditioned sets of equations which can be solved directly without singular-value decomposition, since the associated condition numbers are decreased remarkably.

The paper is organized as follows. The radiation and scattering problem is presented in Sec. I. In Sec. II, the theory of the full-field equations is described in detail. In Sec. III, numerical results are presented for the three structures mentioned above. In Sec. IV, we finish with some concluding remarks.

I. DESCRIPTION OF THE RADIATION AND SCATTERING PROBLEM

A radiating or scattering structure B with a closed surface S is considered. The interior of B is called B_i and the exterior B_a. The interior B_i is assumed to be nonzero, since the application of the source simulation technique requires to place equivalent sources in B_i. However, structures with very thin components like the blades of a propeller can also be treated successfully by using the source simulation technique.[1] The surface normal n should be directed into the exterior B_a as shown in Fig. 1. In the following, only exterior problems will be investigated. In the exterior region B_a, the complex sound pressure p has to satisfy the Helmholtz equation

$$\Delta p + k^2 p = 0, \tag{1}$$

where $k=\omega/c$ is the wave number, ω is the angular frequency, c the speed of sound, and Δ is the Laplace operator. All time-varying quantities should obey the time dependence $\exp(-j\omega t)$ with $j=\sqrt{-1}$. Since sound radiation into the free three-dimensional space is considered, the pressure p has to satisfy the Sommerfeld radiation condition

$$\lim_{R\to\infty} R\left[\frac{\partial p}{\partial R} - jkp\right] = 0, \tag{2}$$

which can be interpreted as a boundary condition at infinity. Here, $R=\|x\|=\sqrt{x_1^2+x_2^2+x_3^2}$ denotes the distance from x to the origin, where points in space are denoted by simple letters like $x=(x_1,x_2,x_3)$. Solutions of Eqs. (1) and (2) are called *radiating wave functions*. In general, such functions contain singularities located in the interior B_i, and hence, they can be considered sources of the exterior sound field. Therefore, radiating wave functions will simply be called *sources*. For a complete description of the problem, boundary conditions on the surface of the radiator or scatterer are needed. For simplicity, only the Neumann boundary value problem will be considered, where the normal velocity v and therefore the gradient of the pressure

$$\frac{\partial p}{\partial n} = j\omega\rho v \quad \text{on} \quad S \tag{3a}$$

is prescribed. Here, ρ is the fluid density and $\partial/\partial n$ is the derivative in the direction of the outward normal n. The radiation problem is obtained if a normal velocity $v\neq 0$ is given at the surface S. Hence, Eq. (3a) is an inhomogeneous boundary condition. Equations (1), (2), and (3a) describe the radiation problem for the radiated pressure p. For the related scattering problem, an incident wave p_i is impinging on the body S and causes a scattered wave p_s. The scattering problem for the scattered pressure p_s is again described by Eqs. (1) and (2), where p has to be substituted by p_s in both equations. Now the boundary condition

$$\frac{\partial p}{\partial n} = 0 \tag{3b}$$

for a sound-hard scatterer becomes homogeneous and must be formulated for the total pressure $p=p_i+p_s$.

The scattering problem can be formulated as an equivalent radiation problem by the following procedure: The normal velocity v_i of the incident pressure wave p_i will be evaluated at the surface S where the scatterer is assumed to be sound transparent. If B is now vibrating with the negative normal velocity $(-v_i)$, the radiated sound pressure is identical with the pressure p_s scattered from B due to the incident wave p_i. Hence, instead of Eq. (3b), we simply have to use

$$\frac{\partial p_s}{\partial n} = j\omega\rho(-v_i) \tag{3c}$$

for the scattering problem, which again is an inhomogeneous boundary condition like Eq. (3a). Equations (1), (2), and (3c) describe the scattering problem as an equivalent ''radiation problem'' for the scattered pressure p_s. In conclusion, both types of problems can be treated by the source simulation technique in a uniform way.

II. THEORY OF THE FULL-FIELD METHOD

A. Spherical wave functions and symmetry relations

The full-field method (FFM) is a variant of the source simulation technique, which was described in Ref. 1 in detail. The basic idea of the source simulation technique con-

sists in replacing the radiator or scatterer by a system of radiating wave functions placed in the interior of the body. Hence, the so-called source region Q (see Fig. 1) is fully contained in B_i and embodies all sources. In the three-dimensional space, the spherical wave functions present the simplest form of radiating wave functions. Hence, they are the most often used type of sources, and they are given by

$$\psi_{nm}^{c,s}(x)=\Gamma_{nm}h_n^{(1)}(kr)P_n^m(\cos\vartheta)\cdot\begin{cases}\cos m\varphi\\ \sin m\varphi\end{cases}, \tag{4}$$

where the P_n^m are the associated Legendre polynomials.[14] Here, spherical coordinates are introduced by $x=(r\sin\vartheta\cos\varphi, r\sin\vartheta\sin\varphi, r\cos\vartheta)^T$, where T denotes transposition. The superscript c (or s) indicates that the cosine (or sine) is used. The cylindrical functions $h_n^{(1)}$ are the spherical Hankel functions of the first kind.[14] The normalizing factors

$$\Gamma_{nm}=\left[\frac{\epsilon_m}{4\pi}(2n+1)\frac{(n-m)!}{(n+m)!}\right]^{1/2},\quad \epsilon_m=\begin{cases}1, & m=0\\ 2, & \text{otherwise}\end{cases} \tag{5}$$

are chosen in such a way that the spherical harmonics

$$y_{nm}^{c,s}(x)=\Gamma_{nm}P_n^m(\cos\vartheta)\cdot\begin{cases}\cos m\varphi\\ \sin m\varphi\end{cases} \tag{6}$$

are orthonormal with respect to the integration over the unit sphere

$$\int_0^{2\pi}\int_0^{\pi}y_{mn}^{\alpha}y_{\mu\nu}^{\beta}\sin\vartheta\,d\vartheta\,d\varphi =\begin{cases}1, & \text{if } \alpha=\beta,\ \mu=m,\ \text{and } v=n\\ 0, & \text{otherwise}\end{cases}, \tag{7}$$

where α and β stands for c or s, respectively. Taking into account that there are only wave functions of cosine type for $m=0$, it is easy to check that the number of different spherical wave functions up to an index n_0 is given by

$$\sum_{j=0}^{n_0}(2j+1)=(n_0+1)^2. \tag{8}$$

For simplicity we denote the $\psi_{nm}^{c,s}$ by ψ_l where the index $l=0,1,2,...$ runs through all combinations of m and n for c and s. The regular wave functions

$$\chi_l=\mathrm{Re}\{\psi_l\} \tag{9}$$

present standing waves, where Re{} denotes the real part of the quantity in brackets. The regular wave functions contain spherical Bessel functions instead of Hankel functions like the radiating wave functions. For deriving the full-field equations, the following symmetry relations are very important:

$$\int\int_S\left(\psi_l\frac{\partial\psi_m}{\partial n}-\psi_m\frac{\partial\psi_l}{\partial n}\right)ds=0, \tag{10a}$$

$$\int\int_S\left(\chi_l\frac{\partial\psi_m}{\partial n}-\psi_m\frac{\partial\chi_l}{\partial n}\right)ds=\delta_{lm}\frac{j}{k}, \tag{10b}$$

$$\int\int_S\left(\psi_l^*\frac{\partial\psi_m}{\partial n}-\psi_m\frac{\partial\psi_l^*}{\partial n}\right)ds=\delta_{lm}\frac{2j}{k}, \tag{10c}$$

where the asterisk denotes the complex conjugate, and δ_{lm} is the Kronecker Delta. Equation (10a) is even valid for all radiating wave functions as shown in Ref. 3. Equation (10b) can be proved by using the second Green's theorem for the domain $S\cup K_i$ where K_i is a sphere lying completely in B_i.[1,15] Finally, Eq. (10c) is easily obtained by using $\psi_l^*=2\chi_l-\psi_l$, and combining Eqs. (10a) and (10b) in a suitable manner. For obtaining Eqs. (10), S is assumed to be a Lyapunov surface.[1] Its essential property is that the normal vector n to the surface exists at each point. In practice, structures with corners or edges (like the finite cylinder or the cat's eye in Sec. III) can be treated as well, since such edges can be considered as curves with a small radius of curvature.

B. Derivation of the full-field equations by expanding the free-space Green's function in the Helmholtz integral equation

This first way of derivation is not as short and elegant as the second way described in subsection C, but it shows very clearly the idea of the method and the reason for the higher stability of the full-field equations. The starting point is the Helmholtz integral equation (HIE) for the exterior space

$$\int\int_S\left[p(y)\frac{\partial g(x,y)}{\partial n(y)}-\frac{\partial p(y)}{\partial n(y)}g(x,y)\right]ds =\begin{cases}p(x), & x\in B_a \quad (11a)\\ \frac{1}{2}p(x), & x\in S \quad (11b)\\ 0, & x\in B_i, \quad (11c)\end{cases}$$

where

$$g(x,y)=\frac{1}{4\pi\tilde{r}}e^{jk\tilde{r}}\quad\text{with}\quad \tilde{r}=\|x-y\| \tag{12}$$

is the free-space Green's function, and y is a spatial point on the structural surface S. The starting point for the well-known boundary element method is the surface HIE equation (11b) which is an integral equation of the second kind with satisfactory numerical stability.[9] The null-field equations are based on the interior HIE equation (11c) which produces a ''null-field'' in the interior of the structure. The null-field equations can lead to numerical instabilities, since the interior HIE is an integral equation of the first kind, which may lead to ill-conditioned sets of algebraic equations[1,9] (see also Ref. 16, where numerical instabilities were observed). The reason is the following: The surface S is divided into boundary elements for the numerical solution. Then, due to the ''null-field'' on the right-hand-side of Eq. (11c), the diagonal terms in the corresponding matrix tend to zero if the subdivision of the surface S is refined for obtaining better approximations. On the other hand, the null-field equations or the strongly related source simulation technique can have advantages over the boundary element solvers (see Sec. III A). To avoid the instability problem, we start with the exterior HIE equation (11a) as a basis for a source simulation technique with diagonally dominant matrices. In analogy to the derivation of the NFE[5] the free-space Green's function is expanded into spherical wave functions[15]

$$g(x,y)=jk\sum_{m=0}^{\infty}\psi_m(x)\chi_m(y)\quad\text{for}\quad x\in B_a,\quad y\in S. \tag{13}$$

This expansion is substituted into the exterior HIE equation (11a), multiplied by a spherical harmonic $y_l(\approx y_{nm}^{c,s})$ for an arbitrary index l and integrated over an exterior sphere ∂K_R with centroid at the origin. The radius R of the sphere is assumed to be large enough such that $S\subset\partial K_R$. This leads to the equation

$$\int\int_{\partial K_R}p(x)y_l\,dk_R=jk\sum_{m=0}^{\infty}\int\int_{\partial K_R}\psi_m y_l\,dk_R \times\int\int_S\left(p\frac{\partial\chi_m}{\partial n}-\chi_m\frac{\partial p}{\partial n}\right)ds. \tag{14a}$$

The orthonormal relations (7) together with definitions (4) and (6) can be written as

$$\int\int_{\partial K_R}\psi_m y_l\,dk_R=R^2\int_0^{2\pi}\int_0^{\pi}\psi_m y_l\sin\vartheta\,d\vartheta\,d\varphi =\delta_{ml}h_{\tilde{m}}^{(1)}(kR)R^2, \tag{14b}$$

where the index notation $\psi_m(x)=h_m^{(1)}y_m(x)$ is used.

By combining Eqs. (14a) and (14b) the following equations are obtained:

$$\int\int_{\partial K_R}p(x)y_l\,dk_R=jkh_{\tilde{l}}^{(1)}(kR)R^2 \times\int\int_S\left(p\frac{\partial\chi_l}{\partial n}-\chi_l\frac{\partial p}{\partial n}\right)ds. \tag{14c}$$

In contrast to the derivation of the NFE, the integration was performed over an *exterior* sphere so that the regular wave functions, instead of the radiating wave functions, appear in the right-hand side of Eq. (14c). Now by applying the main idea of the source simulation technique, the sound pressure p is developed into a series of radiating spherical wave functions

$$p(x)=\sum_{m=0}^{\infty}c_m\psi_m(x) \tag{15}$$

with unknown coefficients c_m and substituted into Eq. (14c). Using again the orthonormal relations (14b) together with the boundary condition (3a), we get the equations

$$\frac{j}{k}c_l+\sum_{m=0}^{\infty}c_m\int\int_S\psi_m\frac{\partial\chi_l}{\partial n}ds=j\omega\rho\int\int_S v\chi_l\,ds, \qquad l=0,1,2,..., \tag{16}$$

which are called full-field equations (FFE), since they are based on the ''full-field'' equation (11a) with nonzero right-hand side instead of the ''null-field'' equation (11c). To distinguish them from different but similar types of equations, we more accurately call Eqs. (16) the full-field equations of the first kind (FFE1).

C. Derivation of the full-field equations using the method of weighted residuals

This derivation is simpler than the one before and can be better generalized. Expansion (15) for the acoustic pressure satisfies the Helmholtz equation and the radiation condition by definition of the radiating wave functions. Consequently, the solution of the radiating or scattering problem is found if the series also satisfies the boundary condition (3a) [or (3c)]. Therefore, series (15) is substituted into Eq. (3a) which gives

$$\sum_{m=0}^{\infty}c_m\frac{\partial\psi_m}{\partial n}=j\omega\rho v\quad\text{on}\quad S. \tag{17}$$

For minimizing the boundary error, the method of weighted residuals[1,3] is used. Equation (17) is multiplied by weighting functions w_l and integrated over the surface S, which yields

$$\sum_{m=0}^{\infty}c_m\int\int_S\frac{\partial\psi_m}{\partial n}w_l\,ds=j\omega\rho\int\int_S v w_l\,ds, \qquad l=0,1,2,.... \tag{18}$$

The weighting functions $\{w_l\}$ should constitute a linearly independent and complete family of functions. If the regular wave functions χ_l are chosen as weighting functions and the symmetry relation (10b) is taken into account, Eq. (18) exactly leads to the full-field equations (16). Hence, the FFE1 can be interpreted as a special boundary residual method in which the pressure is expanded into spherical radiating wave functions and the resulting boundary error is minimized by employing the regular wave functions.

D. Numerical behavior and generalization of the full-field equations

The first term on the left-hand side of Eq. (16) contributes the quantity

$$\text{Diag}\,1=j/k$$

to the diagonal elements of the corresponding matrix. It only depends on the wave number and does not depend on the way how the integrals in Eq. (16) will be approximated numerically or on the order l of the wave functions, etc. Hence, this term is responsible for the diagonal dominance of the system of equations and will have an stabilizing effect. Waterman[12] already gave a similar argument in his derivation of the T-matrix method. He explained that for $l\gg ka$ (a equals the maximum radius of the structure) all elements of his ''Q-matrices'' tend to zero which leads to ill-conditioned systems. Then he applied the divergence theorem to get explicit diagonal terms. This procedure seems to be similar to the use of the symmetry relation (10b).

Diag 1 disappears if the radiating wave functions ψ_l are used as weighting functions. In this case, the symmetry relation (10a) has to be applied, and the null-field equations are obtained. Numerical problems associated with the NFE or the related T-matrix method are mentioned in many publications (see, for example, Ref. 13). In fact, the numerical stability might be improved dramatically if the FFE are used instead of the NFE. This will be shown in Sec. III. However, full-field equations in the present form (FFE1) suffer from

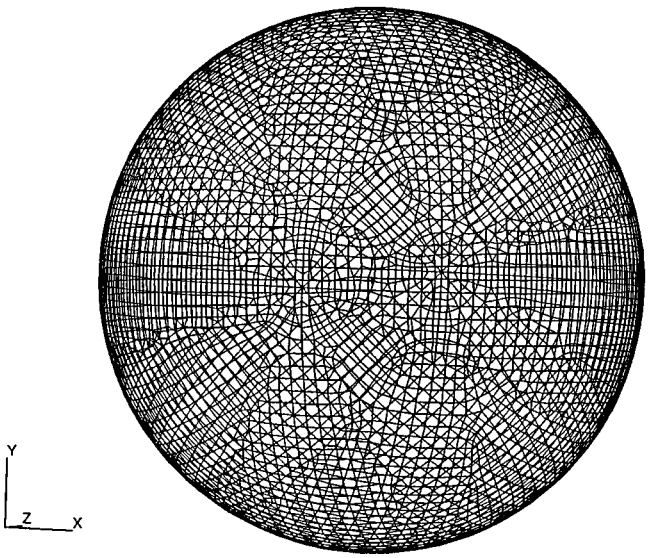

FIG. 2. Finite-element model of the sphere.

two disadvantages. First, the family of weighting functions $\{\chi_l\}$ is not complete and does not constitute a basis for the Hilbert space $L_2(S)$ of square integrable functions over the surface S whenever k is an eigenvalue of the interior Dirichlet problem (see Ref. 12, Appendix A). This problem is similar to the appearance of critical frequencies in the boundary element method.[9] However, the completeness of weighting functions is necessary for inverting the system of Eqs. (18) (see Ref. 15, p. 134). To avoid such difficulties at certain critical frequencies, we recommend the use of the complex conjugate spherical wave functions

$$w_l = \psi_l^* \tag{19}$$

as weighting functions. These functions are known to be complete and constitute a basis for $L_2(S)$ for every wave number k.[1] On the other hand, the symmetry relation (10c) contains a diagonal element on the right-hand side as in Eq. (10b). Hence the same procedure as in subsection C leads to the equations

$$\frac{2j}{k} c_l + \sum_{m=0}^{\infty} c_m \int\int_S \psi_m \frac{\partial \psi_l^*}{\partial n}\, ds = j\omega\rho \int\int_S v\, \psi_l^*\, ds, \qquad l = 0,1,2,\ldots . \tag{20}$$

We call Eqs. (20) the full-field equations of the second kind (FFE2). Again, the diagonal elements

$$\text{diag } 2 = 2 \text{ diag } 1 = 2j/k, \tag{21}$$

arising from the application of Eq. (10c) have a stabilizing effect. This will be demonstrated in Sec. III. The idea of using the complex conjugate functions for constructing energy expressions goes back to Cremer and Wang.[17]

The second disadvantage of the FFE stems from the fact that spherical wave functions are used. These functions correspond to spherical sources with a singularity in the origin of the coordinate system as defined in Eq. (4). Hence, the method is also called one-point multipole method[1] and gives good results for spherelike radiators. But the more the shape of the body deviates from a sphere the worse the results get. For this reason, it was recommended to use spherical wave functions with different source locations x_q located in the interior B_i of the body (multi-point multipole method):[1–3]

$$\psi_l^q(x) = \psi_l(x - x_q), \quad q = 1,\ldots,Q.$$

Hence, instead of Eq. (15) the pressure is expanded into the series

$$p(x) = \sum_{q=1}^{Q} \sum_{m=0}^{\infty} c_m^q \psi_m^q(x). \tag{22}$$

By choosing the weighting functions $\chi_l^s = \mathrm{Re}\{\psi_l^s\}$, the procedure of subsection II C can be applied. However, some care is needed, since the symmetry relations (10) are only valid for wave functions with the same source location. For example, instead of Eq. (10b) we get

$$\int\int_S \left(\chi_l^s \frac{\partial \psi_m^q}{\partial n} - \psi_m^q \frac{\partial}{\partial n} \chi_l^s \right) ds$$

$$= \begin{cases} j/k & \text{for } l = m \text{ and } s = q \quad (23a) \\ 0 & \text{for } l \neq m \text{ and } s = q \quad . \quad (23b) \\ ? & \text{for } s \neq q \quad (23c) \end{cases}$$

Equations (23a) and (23b) follow directly from Eq. (10b), which does not depend on the special choice of the source location $x_q \in B_i$. For wave functions with different source locations, the present author has not found analogous symmetry relations. This does not matter since the symmetry relations have only to be applied on the diagonal $l = m$ and $s = q$ which yields the generalized FFE1

$$\frac{j}{k} c_l^s + \sum_{q=1}^{Q} \sum_{m=0}^{\infty} c_m^q \int\int_S g_{l,m}^{s,q}\, ds = j\omega\rho \int\int_S v\, \chi_l^s\, ds, \qquad s = 1,\ldots,Q; \quad l = 0,1,2,\ldots \tag{24a}$$

with

$$g_{l,m}^{s,q} = \begin{cases} \psi_m^q \dfrac{\partial \chi_l^s}{\partial n}, & \text{for } l = m \text{ and } s = q \\ \dfrac{\partial \psi_m^q}{\partial n} \chi_l^s, & \text{elsewhere} \end{cases} . \tag{24b}$$

Analogously, the weighting functions $(\psi_l^s)^*$ lead to the generalized FFE2

$$\frac{2j}{k} c_l^s + \sum_{q=1}^{Q} \sum_{m=0}^{\infty} c_m^q \int\int_S h_{l,m}^{s,q}\, ds = j\omega\rho \int\int_S v (\psi_l^s)^* ds, \qquad s = 1,\ldots,Q; \quad l = 0,1,2,\ldots , \tag{25a}$$

$$h_{l,m}^{s,q} = \begin{cases} \psi_m^q \dfrac{\partial (\psi_l^s)^*}{\partial n}, & \text{for } l = m \text{ and } s = q \\ (\psi_l^s)^* \dfrac{\partial \psi_m^q}{\partial n}, & \text{elsewhere} \end{cases} . \tag{25b}$$

Equations (25) are the main result of the present investigation. The diagonal terms Diag 2 are responsible for an improved stability. No critical frequencies occur, and arbitrary surface geometries can be treated if the source locations are chosen in an appropriate manner.[1,3] In practical calculations, only a finite number $N_w=(N+1)\cdot Q$ of wave functions can be used, i.e., the index l runs from 0 to N. For example, if only monopoles ($N=0$) and two source locations ($Q=2$) are used, the system of equations has the form $A\mathbf{c}=\mathbf{f}$ with

$$A=\begin{pmatrix} 2j/k+\int\int_S \psi_0^1 \frac{\partial(\psi_0^1)^*}{\partial n}\,ds & \int\int_S \frac{\partial \psi_0^2}{\partial n}(\psi_0^1)^*\,ds \\ \int\int_S \frac{\partial \psi_0^1}{\partial n}(\psi_0^2)^*\,ds & 2j/k+\int\int_S \psi_0^2 \frac{\partial(\psi_0^2)^*}{\partial n}\,ds \end{pmatrix}, \tag{26a}$$

$$\mathbf{c}=\begin{pmatrix} c_0^1 \\ c_0^2 \end{pmatrix}, \quad \text{and} \quad \mathbf{f}=j\omega\rho\int\int_S \begin{pmatrix} v(\psi_0^1)^* \\ v(\psi_0^2)^* \end{pmatrix} ds. \tag{26b}$$

In the following numerical analysis also the weighting functions

$$w_l=\partial\psi_l^*/\partial n$$

are used which implies that the surface velocity error is minimized in the least squares sense by using the quadratic L_2-norm.[1,3] Hence, this approach is called the L2M (L2-method) and leads to the equations

$$\sum_{m=0}^{\infty} c_m \int\int_S \frac{\partial\psi_m}{\partial n}\frac{\partial\psi_l^*}{\partial n}\,ds = j\omega\rho\int\int_S v\frac{\partial\psi_l^*}{\partial n}\,ds, \qquad l=0,1,2,\ldots, \tag{27}$$

which are formulated with one source location at the origin for simplicity.

The L2M often leads to good results, but it also might suffer from instability, since no diagonal terms like Diag 1 or Diag 2 are produced. The L2M has the advantage that the matrix of the discretized version is Hermitian.

III. NUMERICAL ANALYSIS

A. Numerical implementation and condition number of a linear system

The full-field equations (24) or (25) can be evaluated numerically for a body of arbitrary shape by dividing the surface S into M boundary elements. While performing the integration we assume that the surface pressure and the surface normal velocity are constant over each boundary element. If the total number of wave functions used is N_w, a linear system of equations $Ax=b$ with an $N_w\times N_w$ coefficient matrix A must be solved. One main advantage of the source simulation technique is that in general the number of equations N_w is much smaller than the number of boundary elements ($N_w \ll M$), especially if fine-meshed surface grids are used for the purpose of high-frequency calculations. Hence, the method may lead to faster numerical algorithms than boundary element techniques which work with $N_w=M$.

Instead of using the spherical wave functions directly, it has a favorable numerical effect to work with normalized functions $\psi_l^q(x)/K_l^q$ where we have chosen the Hankel functions $h_n^{(1)}(ka)$ as normalizing constants in most calculations (a is a typical length of the structure). The condition number of the linear system of equations $Ax=b$ is defined by[18,19]

$$\kappa=\mathrm{cond}(A)=\|A\|\|A^{-1}\|, \tag{28}$$

where $\|\ \|$ is a matrix norm. κ is a real number greater or equal to one. The condition number measures the sensitivity of the solution x with respect to perturbations in A or in b. An unstable or badly conditioned system has a large condition number.[18,19] The condition number depends on the chosen matrix norm. The Euclidean (or spectral) condition number κ_{spec} is defined as the ratio of the largest and the smallest singular value of A. As suggested from Tobocman,[20] we have also used the matrix norm

$$\kappa_F=\frac{1}{n}\|A\|_F\|A^{-1}\|_F, \tag{29a}$$

which is based on the Frobenius norm

$$\|A\|_F=\sqrt{\sum_{i=1}^{N_w}\sum_{j=1}^{N_w}|a_{ij}|^2}. \tag{29b}$$

Here again, $A=(a_{ij})$ is the abovementioned $N_w\times N_w$-matrix.

B. Radiation of a pulsating sphere

Results are presented for a sphere consisting of 6096 boundary elements (see Fig. 2). The radius R of the sphere is 1 m with the centroid at the origin. For investigations in air, a frequency up to 1100 Hz can be chosen to ensure that six elements are available per wave length. The simplest radiation pattern is considered, in which the sphere is pulsating with a constant radial surface velocity $v=v_R=\mathrm{const}$.

As a first simple test a monopole source was put at the origin, and, as expected, we get a condition number of 1 for the NFE, FFE1, FFE2, and the L2M. Also, the relative quadratic error of the normal velocity integrated over the surface

$$F_{\mathrm{rel}}=\int\int_S |v-v_s|^2\,ds \Big/ \int\int_S |v|^2\,ds \tag{30}$$

is smaller than 4×10^{-6}. Here v_s is the normal surface velocity simulated by the source system (i.e., by the test monopole). The remaining error is only caused by the discretiza-

TABLE I. Results for the pulsating sphere with five monopoles on an auxiliary surface.

Method	NFE	FFE1	FFE2	L2M
κ_{spec}	4.7	2.5	1.5	1.5
F_{rel} [%]	169	101	79	79

TABLE II. Results for the pulsating sphere with 30 monopoles on an auxiliary surface.

Method	NFE	FFE1	FFE2	L2M
κ_{spec}	199.2	170.7	169.3	157
F_{rel} [%]	0.1	0.1	0.065	0.064

TABLE III. Results for the pulsating sphere with 125 monopoles on an auxiliary surface.

Method	NFE	FFE1	FFE2	L2M
κ_{spec}	2.4×10^{7}	8×10^{4}	4.2×10^{4}	1.4×10^{7}
κ_F	7.6×10^{5}	3.5×10^{3}	2.5×10^{3}	7.2×10^{5}
F_{rel} [%]	7.2×10^{-4}	3.2×10^{-5}	6×10^{-5}	2.4×10^{-4}

TABLE IV. Results for the pulsating sphere with 280 monopoles on an auxiliary surface.

Method	NFE	FFE1	FFE2	L2M
κ_{spec}	8.6×10^{8}	3.2×10^{6}	1.4×10^{6}	2.1×10^{9}
κ_F	1.3×10^{7}	3.4×10^{4}	2.1×10^{4}	2.7×10^{7}
F_{rel} [%]	17	~0	~0	59

tion of the surface, the numerical integration, and rounding errors, since a monopole exactly produces a pulsating sphere. It is remarkable that the boundary error [Eq. (30)] is a measure for the accuracy of the solution depending on the number and on the locations of the sources. For every calculation the boundary error can be computed, even if the solution is not known *a priori*. This is an important advantage of the general source simulation technique and of the full-field method too. As a more interesting source system, monopoles are chosen [i.e., $m=n=0$ in Eq. (4)] which are nearly equidistantly distributed on an inner auxiliary surface. This auxiliary surface, too, is a sphere like the original sphere, but with radius $r_i=0.9R$. Now, the condition number is studied for the different variants of the multipole method and for an increasing number N_0 of monopoles. The frequency is always 500 Hz ($kR=9.2$). Tables I–IV show the results for an increasing number of monopoles used. In Fig. 3, it can be seen that the condition number starts at 1 and increases with increasing N_0. The condition number for the FFE1 and FFE2 is 2–3 orders of magnitude smaller then the one for the NFE and the L2-method if 280 monopoles are used. The velocity error decreases with increasing N_0; however, Table IV shows that F_{rel} changes from decrease to increase, but only for the NFE and the L2M due to high condition numbers. Since all calculations were made with single precision, the system is ill-conditioned if $\kappa_{\text{spec}}>10^{6}$. Note that the Frobenius condition number κ_F is always smaller than κ_{spec}.

C. Scattering from finite cylinder

Second, the scattering of a plane wave from a cylinder is studied. The finite-element model of the cylinder is shown in Fig. 4. The axis of the cylinder is located on the *z*-axis of the coordinate system. The cylinder consists of 3620 boundary elements and has a length to width ratio $l/(2a)=3.73$. The scattering from such cylinders was also calculated by using an iterative boundary element solver[21] and the multipole method.[22] The surface of the cylinder is assumed to be rigid. The frequency was chosen so that $ka=8.4$. This corresponds approximately to the condition of six elements per wavelength. At five source positions, multipoles with different orders (monopoles+dipoles+quadrupoles+$\cdots$) were placed on the axis in the interior of the cylinder. In Fig. 5 the condition number κ_{spec} is shown as a function of the number of sources for the different methods. As expected, FFE1 and FFE2 lead to much lower condition numbers than the NFE and the L2M. For example, if multipoles with orders up to nine are used at each of the five source locations, the total number of sources is 500 [see Eq. (8)], and we obtain: $\kappa_{\text{spec}}=3\times10^{9}$ for the NFE and $\kappa_{\text{spec}}=3\times10^{4}$ for the FFE2, a difference of five orders of magnitude!

Similar to Tables I–IV, the Frobenius condition number is always smaller than the spectral condition number but both show the same tendency. In Fig. 6 the relative error F_{rel} [see Eq. (30)] is presented. In general, the error decreases with increasing source number. For example, the error of the FFE2 goes down to 7% if 500 sources are used. The L2M directly minimizes this boundary error, and hence it decreases to 6% in spite of the high condition number. The error for the NFE first decreases, but grows dramatically between 400 and 500 sources due to the increase of the condition number. The error of the FFE1 shows a somewhat strange behavior: It also decreases, but at 405 sources it has a singular high value. Up until now, an explanation was missing.

Directivity patterns are shown in the following figures. For the purpose of comparison, the solution of the plane wave approximation (PWA)[23] is also presented which gives a good approximation in the high-frequency range if multiple

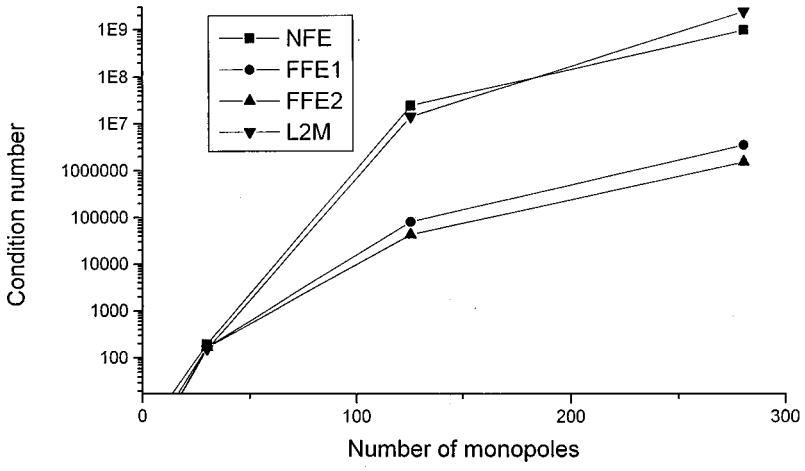

FIG. 3. Condition number as a function of the number of monopoles for the pulsating sphere at 500 Hz.

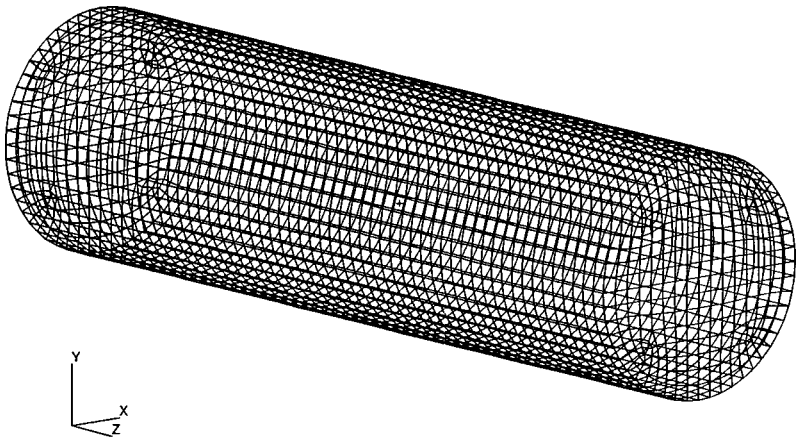

FIG. 4. Finite-element model of cylinder.

reflections do not occur. In Figs. 7–9 the target strength *TS*,[24]

$$TS = 10 \log \left. \frac{I_r}{I_i} \right|_{r=1m}, \tag{31}$$

is shown in several planes and for different incidence directions n_i of the single frequency plane wave p_i, where I_i is the incident intensity and I_r is the intensity of return at 1 m. (The target strength was calculated in the far-field and then projected back to the distance of 1 m from the scatterer.) The incident direction n_i is defined by

$$n_i = \begin{pmatrix} -\cos\alpha\cos\beta \\ -\cos\alpha\sin\beta \\ -\sin\alpha \end{pmatrix},$$

where the incident angles are $\alpha = 90° - \vartheta$ and $\beta = \varphi$ (ϑ and φ are the spherical coordinates defined above). All calculations were performed with 500 sources.

In Fig. 7(a) the directivity pattern is shown for $(\alpha, \beta) = (0°, 0°)$ (i.e., the incidence direction n_i is along the negative *x*-axis) in the *xy*-plane, which is formed from the *x*- and the *y*-axis. (The system of coordinates is presented in Fig. 4.) The results of the NFE, the FFE1 and the PWA agree very well, and the maximum of forward-scattering is clearly seen.

Figure 7(b) shows the directivity pattern in the *xz*-plane: Again, the curves of the FFE1 and of the PWA agree well, but the curve of the NFE is obviously incorrect: The exploding behavior is caused by the poorly conditioned system of equations. Nearly the same figure is obtained for the *yz*-plane.

Figure 8(a) and 8(b) show the results for $(\alpha, \beta) = (75°, 0°)$. Now the NFE produces exploding curves in all planes, whereas the FFE1 and the PWA agree much better. The results of the FFE2, the PWA and the L2M are very similar in all planes.

For $(\alpha, \beta) = (90°, 0°)$ the direction of incidence is along the axis of the cylinder. As expected, the data of the FFE1 and the PWA agree and constitute a circle around the cylinder, whereas the NFE yields a bigger jagged circle [Fig. 9(a)]. On the other hand, the L2M also gives a jagged circle [Fig. 9(b)], which is smaller than the ones obtained from the PWA and the FFE2.

D. High-frequency scattering from a nonconvex cat's eye structure

In Fig. 10, the finite-element model of the nonconvex scatterer considered is shown. It consists of a sphere where the positive octant (i.e., the part corresponding to $x > 0$, $y > 0$, $z > 0$) is cut out. The region of the missing octant is called ''cat's eye,'' since it acts like a three-dimensional reflector. The cat's eye structure consists of 7911 boundary elements to guarantee about six wavelengths per element at

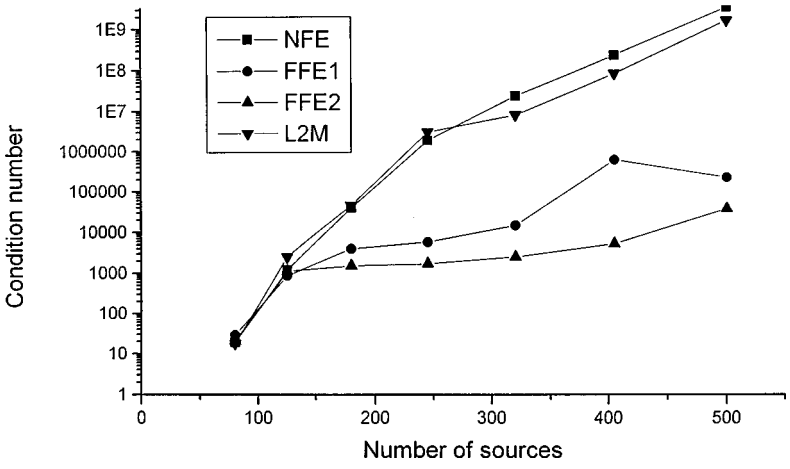

FIG. 5. Condition number as a function of the number of sources for the cylinder at $ka = 8.4$.

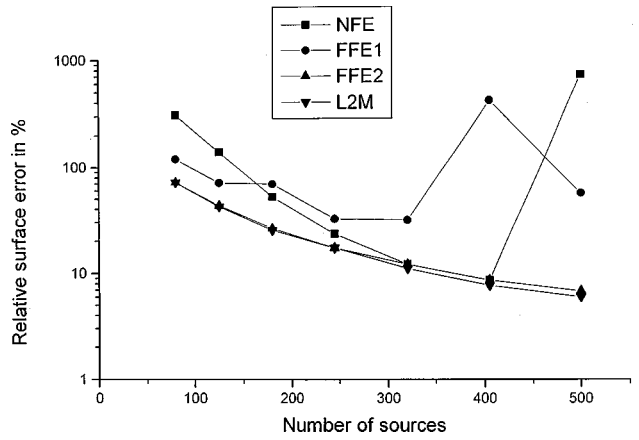

FIG. 6. Relative velocity error F_{rel} as a function of the number of sources for the cylinder at $ka=8.4$.

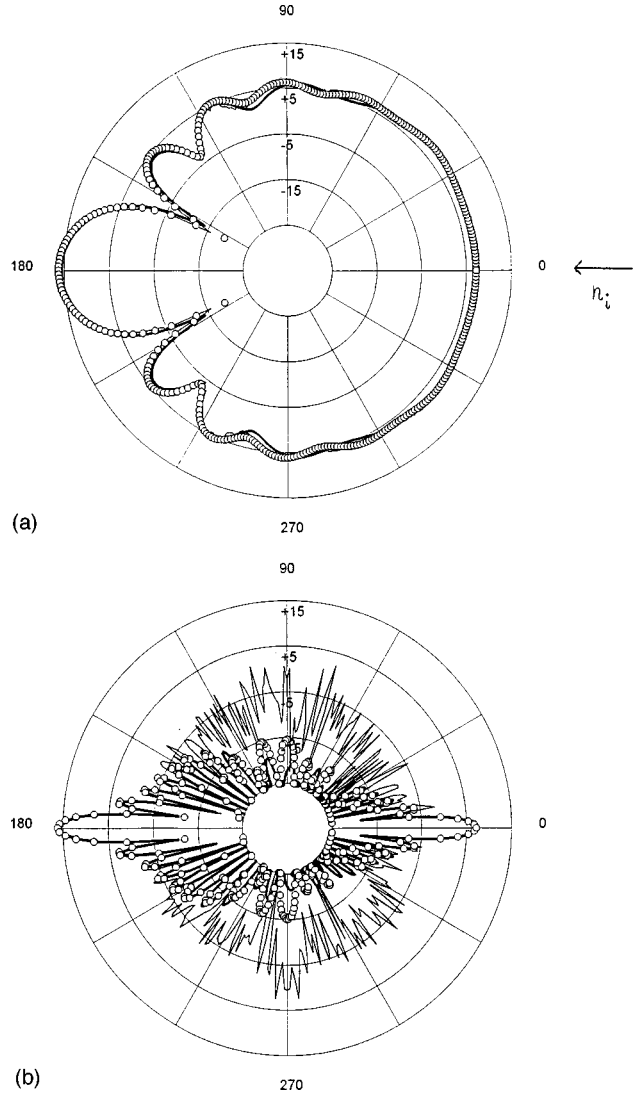

FIG. 7. Directivity pattern for the cylinder at $ka=8.4$. Vertical scaling gives the target strength *TS* in dB; direction of incidence $n_i=-x$ corresponding to $(\alpha,\beta)=(0°,0°)$; thick curve: PWA, thin curve: NFE, circles: FFE1; (a) *xy*-plane, (b) *xz*-plane.

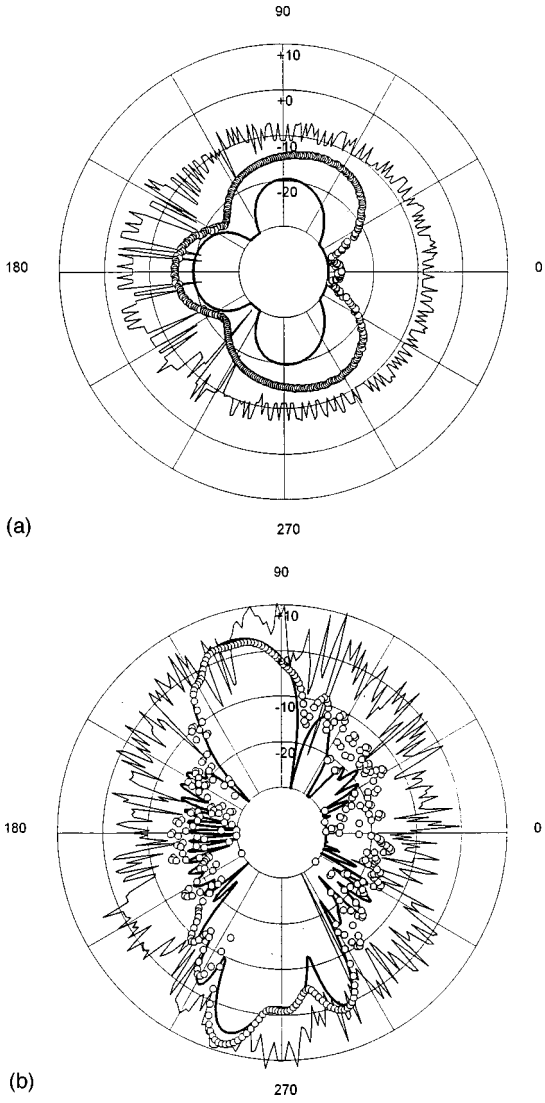

FIG. 8. Directivity pattern for the cylinder at $ka=8.4$. Vertical scaling gives the target strength *TS* in dB; direction of incidence is $(\alpha,\beta)=(75°;0°)$; thick curve: PWA, thin curve: NFE, circles: FFE1; (a) *xy*-plane, (b) *xz*-plane.

$ka=20.9$ (a is the radius of the corresponding sphere). The surface is rigid. The incident angles are $(\alpha,\beta)=(45°,45°)$ or $(\alpha,\beta)=(0°,45°)$. Hence, the incident wave illuminates the reflecting area of the cat's eye which leads to multiple reflections.

The scattering from such structures was also calculated using an iterative boundary element solver and the PWA.[21] Multipoles with different orders were placed at seven source positions lying in the middle of each of the seven octants. In Fig. 11 the condition number κ_{spec} is shown as a function of the number of sources for the four different methods. The incident angles are $(\alpha,\beta)=(45°,45°)$, which is most difficult to calculate due to the multiple scattering. Similar as for the cylinder, FFE1 and FFE2 lead to much lower condition numbers than the NFE and the L2M. For example, if multipoles with orders up to ten are used at each of the seven source locations, the total number of sources is 847 [see Eq. (8)], and we obtain: $\kappa_{\text{spec}}=2.8\times10^{9}$ for the L2M and κ_{spec}

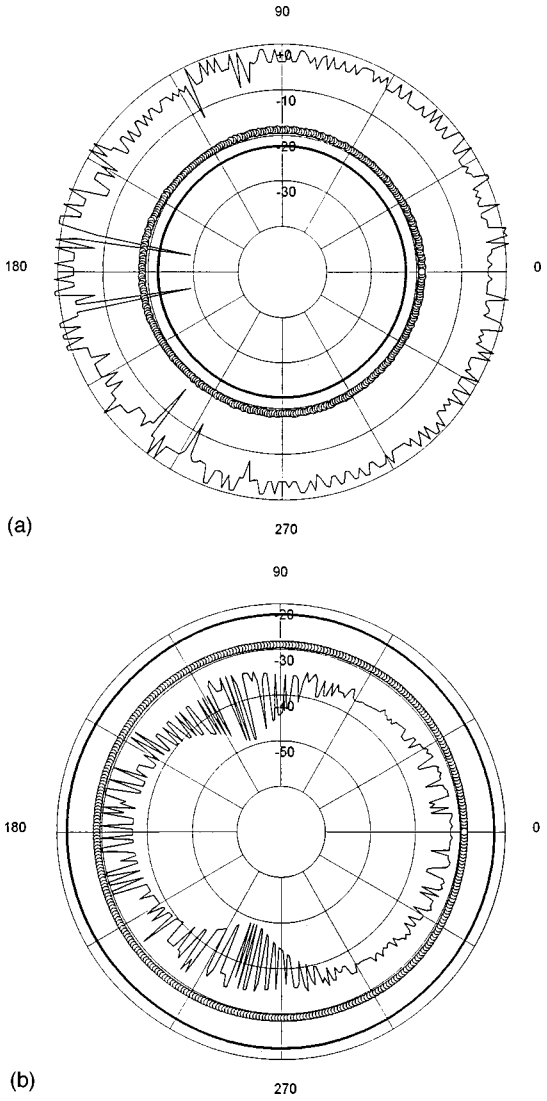

FIG. 9. Directivity pattern for the cylinder at $ka=8.4$. in the *xy*-plane. Vertical scaling gives the target strength *TS* in dB; direction of incidence is $(\alpha,\beta)=(90°;0°)$; (a) thick curve: PWA, thin curve: NFE, circles: FFE1. (b) thick curve: PWA, thin curve: LM2, circles: FFE2.

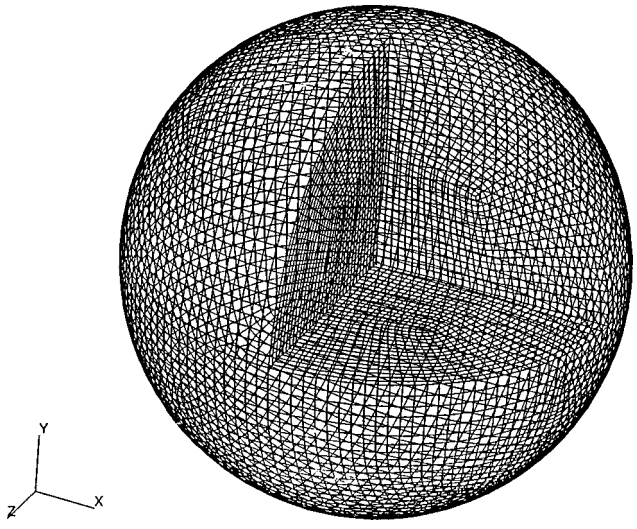

FIG. 10. Finite-element model of the cat's eye structure.

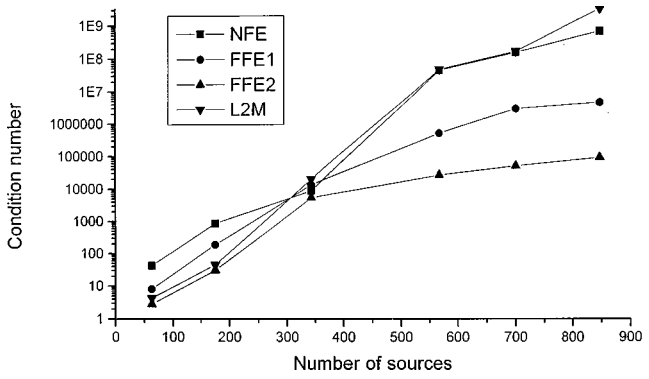

FIG. 11. Condition number as a function of the number of sources for the cat's eye structure at $ka=20.9$.

$=8.1\times10^4$ for the FFE2. This is again a difference of nearly five powers of ten.

In Fig. 12 the relative error F_{rel} [see Eq. (30)] is presented. In general, the error decreases with increasing source number. For example, the error of the FFE2 goes down to 33% if 1008 sources (multipoles with order up to ten) are used, whereas the L2M leads to wrong results ($F_{\mathrm{rel}}=1290\%$) due to the high condition number. The errors for the NFE and surprisingly also for the FFE1 could not be minimized for this scattering situation.

In Fig. 13 the directivity pattern of the *TS* is shown in the *xy*-plane (the system of coordinates is shown in Fig. 10). The calculations were performed with 700 sources (multipoles with orders up to nine at each of the seven source locations). The incident angles $(\alpha,\beta)=(0°,45°)$ were chosen so that the maxima of the forward and backward scattering can be seen in the *xy*-plane.

The curves of the PWA, the NFE and the FFE2 agree well at forward scattering. But only the FFE2 ($\kappa_{\mathrm{spec}}=4{,}6\times10^4$, $F_{\mathrm{rel}}=23\%$) could predict a clear backscattering maximum caused by multiple reflections. In contrast, the PWA does not find any backscattering maximum, whereas the NFE produces too large results in this area, since we have $\kappa_{\mathrm{spec}}=1{,}1\times10^8$ and $F_{\mathrm{rel}}=700\%$.

IV. CONCLUSIONS

The radiation and scattering calculations presented show that the full-field equations of the first and the second kind

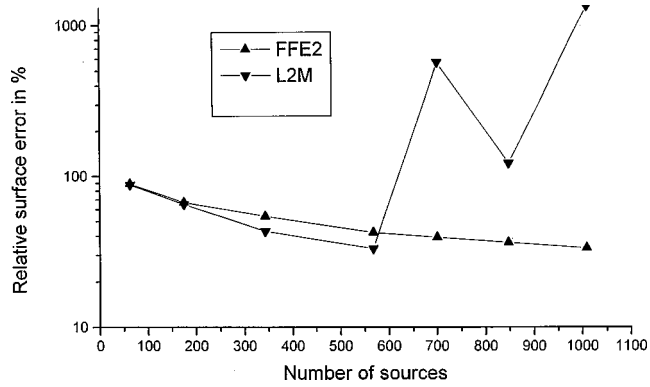

FIG. 12. Relative velocity error F_{rel} as a function of the number of sources for the cat's eye structure at $ka=20.9$.

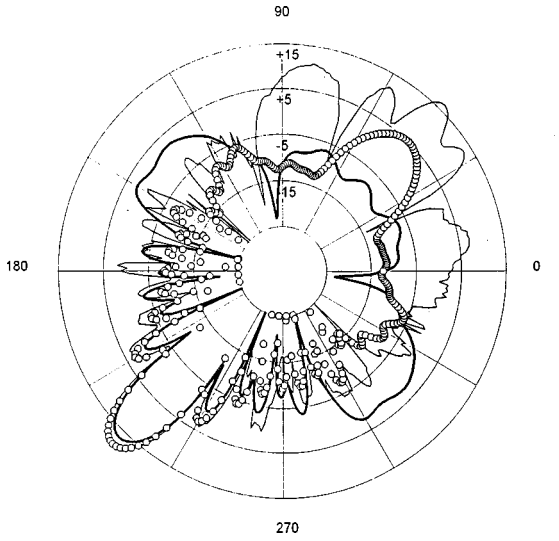

FIG. 13. Directivity pattern for the cat's eye structure at $ka=20.9$ in the *xy*-plane. Vertical scaling gives the target strength *TS* in dB; direction of incidence is $(\alpha,\beta)=(0°;45°)$; thick curve: PWA, thin curve: NFE, circles: FFE2.

are better conditioned than the null-field equations or the source simulation technique with least-squares approximation, since the associated condition numbers are decreased up to five orders of magnitude. In most cases, the full-field equations of the second kind lead to smaller boundary errors as the equations of the first kind. The full-field equations can be solved directly without the time-consuming singular-value decomposition, and they produce reasonable results. The directivity patterns in the far-field are in good agreement with approximate solutions at high frequencies like the plane wave approximation, whereas the null-field equations may lead to unstable and incorrect results with an exploding behavior.

ACKNOWLEDGMENTS

The author is grateful to Dr. H. G. Schneider and A. Homm from the Forschungsanstalt der Bundeswehr für Wasserschall and Geophysik (FWG), Kiel (Germany) for putting the structural models at his disposal. Also, I am grateful to Professor Dr. K. Brod from Fachhochschule Wiesbaden for looking over the manuscript.

[1] M. Ochmann, ''The source simulation technique for acoustic radiation problems,'' Acustica **81**, 512–527 (1995).
[2] M. Heckl, ''Remarks on the calculation of sound radiation using the method of spherical wave synthesis,'' Acustica **68**, 251–257 (1989), in German.
[3] M. Ochmann, ''Multiple radiator synthesis—An effective method for calculating the radiated sound field of vibrating structures of arbitrary surface configuration,'' Acustica **72**, 233–246 (1990), in German.
[4] P. A. Martin, ''Acoustic scattering and radiation problems, and the null-field method,'' Wave Motion **4**, 391–408 (1982).
[5] D. Colton and R. Kress, *Integral Equation Methods in Scattering Theory* (Wiley-Interscience, New York, 1983).
[6] G. H. Koopmann, L. Song, and J. B. Fahnline, ''A method for computing acoustic fields based on the principle of wave superposition,'' J. Acoust. Soc. Am. **86**, 2433–2438 (1989).
[7] R. Jeans and I. C. Mathews, ''The wave superposition method as a robust technique for computing acoustic fields,'' J. Acoust. Soc. Am. **92**, 1156–1166 (1992).
[8] R. Kress and A. Mohsen, ''On the simulation source technique for exterior problems in acoustics,'' Math. Methods Appl. Sci. **8**, 585–597 (1986).
[9] H. A. Schenck, ''Improved integral formulation for acoustic radiation problems,'' J. Acoust. Soc. Am. **44**, 41–58 (1968).
[10] P. R. Stepanishen, ''A generalized internal source density method for the forward and backward projection of harmonic pressure fields from complex bodies,'' J. Acoust. Soc. Am. **101**, 3270–3277 (1997).
[11] J. B. Fahnline and G. H. Koopmann, ''A numerical solution for the general radiation problem based on the combined methods of superposition and singular-value decomposition,'' J. Acoust. Soc. Am. **90**, 2808–2819 (1991).
[12] P. C. Waterman, ''New formulation of acoustic scattering,'' J. Acoust. Soc. Am. **45**, 1417–1429 (1969).
[13] D. J. N. Wall, ''Methods of overcoming numerical instabilities associated with the T-matrix method,'' in *Acoustics, Electromagnetic and Elastic Wave Scattering—Focus on the T-Matrix Approach*, edited by V. V. Varadan and V. K. Varadan (Pergamon, New York, 1980), pp. 269–286.
[14] M. Abramowitz and I. A. Stegun, *Handbook of Mathematical Functions*, 9th ed. (Dover, New York, 1972).
[15] R. E. Kleinman, G. F. Roach, and S. E. G. Ström, ''The null field method and modified Green functions,'' Proc. R. Soc. London, Ser. A **394**, 121–136 (1984).
[16] K. A. Cunefare, G. H. Koopmann, and K. Brod, ''A boundary element method for acoustic radiation valid for all wavenumbers,'' J. Acoust. Soc. Am. **85**, 39–48 (1989).
[17] L. Cremer and M. Wang, ''Synthesis of spherical wave fields to generate the sound radiated from bodies of arbitrary shape, its realisation by calculation and experiment,'' Acustica **65**, 53–74 (1988), in German.
[18] W. H. Press, B. P. Flannery, S. A. Teukolsky, and W. T. Vetterling, *Numerical Recipes, the Art of Scientific Computing*, 2nd ed. (Cambridge U.P., Cambridge, 1990).
[19] E. Pärt-Enander, A. Sjöberg, B. Melin, and P. Isaksson, *The MATLAB® Handbook* (Addison-Wesley, Harlow, 1996).
[20] W. Tobocman, ''Comparison of the T-matrix and Helmholtz integral equation methods for wave scattering calculations,'' J. Acoust. Soc. Am. **77**, 369–374 (1985).
[21] S. N. Makarov and M. Ochmann, ''An iterative solver of the Helmholtz integral equation for high-frequency acoustic scattering,'' J. Acoust. Soc. Am. **103**, 742–750 (1998).
[22] A. Homm and M. Ochmann, ''Sound scattering of a rigid test cylinder using the source simulation technique for numerical calculations,'' in *Proceedings of the 4th International Congress on Sound and Vibration*, edited by M. J. Crocker and N. I. Ivanov (International Scientific Publications, Auburn, 1996), pp. 133–138.
[23] M. C. Junger and D. Feit, *Sound, Structures, and Their Interaction* (MIT, Cambridge, 1972).
[24] R. J. Urick, *Principles of Underwater Sound*, 3rd ed. (McGraw-Hill, New York, 1983).

Interface conditions for Biot's equations of poroelasticity

Boris Gurevich
The Geophysical Institute of Israel, P.O. Box 2286, Holon 58122, Israel

Michael Schoenberg
Schlumberger-Doll Research, Old Quarry Road, Ridgefield, Connecticut 06877-4108

(Received 27 February 1997; accepted for publication 15 February 1999)

Interface conditions at a boundary between two porous media are derived directly from Biot's equations of poroelasticity by replacing the discontinuity surface with a thin transition layer, in which the properties of the medium change rapidly yet continuously, and then taking the limit as the thickness of the transition layer approaches zero. The interface conditions obtained in this way, the well known ''open-pore'' conditions, are shown to be the only ones that are fully consistent with the validity of Biot's equations throughout the poroelastic continuum, including surfaces across which the medium properties are discontinuous. But partially blocked or completely impermeable interfaces exist; these may be looked upon as the case of a thin layer with its permeability taken to be proportional to the layer thickness, again in the limit as layer thickness approaches zero. This approach can serve as a simple recipe for modeling such an interface in any heterogeneous numerical scheme for poroelastic media.
[S0001-4966(99)03605-X]

PACS numbers: 43.20.Gp [DEC]

INTRODUCTION

The linear mechanics of porous elastic solids saturated with compressible viscous fluids is described by Biot's equations of poroelasticity.[1–3] To be used for piecewise homogeneous media, these equations must be complemented by interface conditions which relate the field variables on both sides of a surface of discontinuity in the material properties which are involved in the coefficients appearing in Biot's equations.

Such conditions were suggested by Deresiewicz and Skalak;[4] they require the continuity across an interface of the total (normal and tangential) stress traction, of the fluid pressure p (for the case when the two media are in perfect hydraulic contact), of the solid particle velocity $\mathbf{v}$, and of the normal component of the relative fluid velocity. The relative flow $\mathbf{w}$ of the fluid relative to the solid is defined as

$$\mathbf{w}=\phi(\mathbf{V}-\mathbf{v}), \tag{1}$$

where $\mathbf{V}$ is the fluid particle velocity and ϕ is the porosity.

When the hydraulic contact between two porous materials is imperfect, the condition for the jump in pressure p may be written

$$-(p^{+}-p^{-})=\frac{1}{\beta_s}w_n, \tag{2}$$

where β_s is sometimes called interface hydraulic permeability and subscript n denotes the component normal to the interface. For perfect hydraulic contact, $\beta_s=\infty$ and $p^{+}=p^{-}$, i.e., p is continuous. On the other hand, for no hydraulic contact across the interface, $\beta_s=0$ and condition (2) reduces to $w_n=0$, implying no motion of the fluid relative to the solid.

The interface conditions of Deresiewicz and Skalak are now widely used in modeling wave propagation in layered poroelastic media, porous media with inclusions, and other kinds of piecewise homogeneous porous materials.[5–8] Bourbié *et al.*[5] have given a proof of these conditions on the basis of Hamilton's principle. For some situations the boundary conditions of Deresiewicz and Skalak have been confirmed experimentally.[9,10] However, some issues related to the interface conditions in porous media are still under discussion. In particular, this relates to the value of the interface permeability β_s, which has to be assigned for every interface in the medium. Furthermore, the newly developed algorithms for numerical simulation of elastic wave propagation in poroelastic media[11,12] use so-called heterogeneous numerical schemes, which are applicable to porous media with spatially variable coefficients. For piecewise homogeneous media these schemes assume no explicit conditions at a surface of discontinuity. Then, the question arises, which boundary conditions are implied (or simulated) by these algorithms.[13] Moreover, de la Cruz and Spanos[14] have expressed doubts about the physical validity of the boundary conditions of Deresiewicz and Skalak, and proposed altogether different boundary conditions for porous media; see also Ref. 15. Their concern, if justified, could throw into doubt all the theoretical and numerical results based on the interface conditions of Deresiewicz and Skalak, and thus needs to be addressed.

On the other hand, it has long been known in mathematical physics that interface conditions at an internal discontinuity in a medium described by a linear system of partial differential equations can be derived from those equations if they are written for a general inhomogeneous medium. For Maxwell's equations, for example, this method is discussed in great detail in The Feynman Lectures on Physics.[16] As noted once by S. L. Lopatnikov,[17] this method may be applied to Biot's equations of poroelasticity to derive the interface conditions consistent with these equations.

This note employs the idea of using the equations for a general inhomogeneous medium to end the controversy over interface conditions in porous media. Biot's equations are assumed to hold not only in continuous regions, but also at a discontinuity. By replacing the discontinuity surface with a thin transition layer, in which the properties of the medium change rapidly yet continuously, we arrive at interface conditions that are identical to the open-pore conditions of Deresiewicz and Skalak. We then consider a closed or partially open interface, and show that such an interface may be looked upon as the limiting case of a thin layer, as layer thickness approaches zero, with permeability proportional to the layer thickness.

I. INTERFACE CONDITIONS AT A DISCONTINUITY SURFACE

The linear dynamics of an inhomogeneous porous medium of porosity ϕ saturated with a viscous fluid of density ρ_f and viscosity η can be described by Biot's equations of poroelasticity,[3] which, in Cartesian coordinates x_i, $i=1,2,3$ with summation implied by repeated indices and with the time derivative of function f denoted by $\dot{f}$, have the form

$$\frac{\partial \tau_{ij}}{\partial x_j} = (\rho \dot{v}_i + \rho_f \dot{w}_i), \tag{3}$$

$$-\frac{\partial p}{\partial x_i} = \frac{\eta}{\kappa} \hat{F} w_i + (\rho_f \dot{v}_i + m \dot{w}_i), \tag{4}$$

where the field variables are the τ_{ij} which are the components of total stress in the porous saturated medium, p which is fluid pressure, and v_i and w_i which are components of particle velocity **v** and relative fluid velocity **w**, respectively; see Eq. (1). As for material parameters, ρ is bulk density of the saturated rock,

$$\rho = (1-\phi)\rho_s + \phi \rho_f, \tag{5}$$

where ρ_s is the density of the solid grain material, and

$$m = \frac{\rho_f \alpha}{\phi}, \tag{6}$$

with α denoting the tortuosity coefficient, a dimensionless number. Low frequency permeability is given by κ, and the operator $\hat{F}$ is a linear integral convolution operator with respect to time, which in the Fourier transform domain becomes a frequency dependent multiplier $F(\omega)$, implying frequency dependent permeability $\tilde{\kappa}(\omega) = \kappa / F(\omega)$ (so-called dynamic permeability[2,18]). This operator is defined so that its transform approaches unity as frequency becomes very low. At higher frequencies this operator accounts for the deviation of the fluid flow in pores from the Poiseuille flow. Note that all material properties, including the operator $\hat{F}$, are in general functions of position.

The total stresses and fluid pressure are linearly related to solid and fluid velocity derivatives by

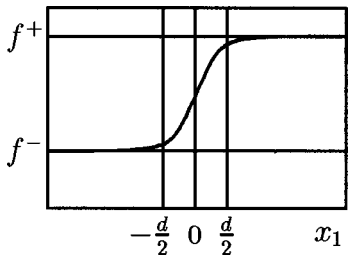

FIG. 1. Behavior of a parameter of the porous medium, say, porosity ϕ, across the transition region around the discontinuity.

$$\dot{\tau}_{ij} = \mu \left(\frac{\partial v_i}{\partial x_j} + \frac{\partial v_j}{\partial x_i} \right) + \delta_{ij} \left[\lambda_c \frac{\partial v_k}{\partial x_k} + \left(1 - \frac{K}{K_s} \right) M \frac{\partial w_k}{\partial x_k} \right], \tag{7}$$

$$-\dot{p} = \left(1 - \frac{K}{K_s} \right) M \frac{\partial v_k}{\partial x_k} + M \frac{\partial w_k}{\partial x_k}, \tag{8}$$

where λ_c and μ are Lame constants of the saturated rock, K and K_s are bulk moduli of the dry (empty) solid matrix and solid grain material, respectively; M is the ''pore space modulus,'' defined by

$$\frac{1}{M} = \frac{\phi}{K_f} + \frac{(1-\phi-K/K_s)}{K_s}, \tag{9}$$

with K_f the fluid bulk modulus. In Eq. (7), δ_{ij} is the Kronecker symbol. Equations (3), (4), (7), and (8) form a system of 13 partial differential equations for 13 unknown functions: 6 independent components τ_{ij} of the total stress, fluid pressure p, 3 components of the solid velocity v_i, and 3 components of the relative fluid velocity w_i.

Now, assume that in the porous medium there is a discontinuity surface, across which the properties of the medium undergo a jump. Let P be a point on the discontinuity surface, and assume that this surface is smooth in the vicinity of P. Consider a Cartesian coordinate system with its origin at point P and its x_1 axis normal to the discontinuity surface, and with values on the positive side denoted by superscript ''+'' and on the negative side, with a superscript ''−''. We wish to obtain relationships between the limiting values of the field variables (stresses, pressure, and velocities) as $x_1 \to 0$ through negative and positive values of the x_1 coordinate. These relationships will be seen to derive from the requirement that Biot's equations are valid throughout the medium *including* the discontinuity (and hence, at point P as well).

Following the procedure described in Ref. 16, we replace the discontinuity by a thin transition layer of the thickness d, in which the Biot's coefficients, including porosity, change rapidly but smoothly, as shown in Fig. 1. The thickness d is taken small enough to ensure that the derivatives with respect to x_1 of the Biot's coefficients in the layer are much larger than the derivatives with respect to x_2, x_3, and also much larger than any spatial derivatives in the regions of continuity of the coefficients. Thus terms containing derivatives with respect to x_1 are the terms of interest. Note that of the 13 scalar equations corresponding to Eqs. (3), (4), (7) and (8), 10 of them have terms containing a derivative with respect to x_1. As $d \to 0$, all terms that do not contain a

derivative with respect to x_1 are bounded in the d-vicinity of P, and we can write these ten equations in the form

$$\frac{\partial \tau_{i1}}{\partial x_1} = \mathcal{O}(1), \tag{10}$$

$$-\frac{\partial p}{\partial x_1} = \mathcal{O}(1), \tag{11}$$

$$\mu \frac{\partial v_i}{\partial x_1} + \delta_{i1}\left[(\lambda_c + \mu)\frac{\partial v_1}{\partial x_1} + \left(1 - \frac{K}{K_s}\right) M \frac{\partial w_1}{\partial x_1}\right] = \mathcal{O}(1), \tag{12}$$

$$\lambda_c \frac{\partial v_1}{\partial x_1} + \left(1 - \frac{K}{K_s}\right) M \frac{\partial w_1}{\partial x_1} = \mathcal{O}(1), \tag{13}$$

$$\left(1 - \frac{K}{K_s}\right) M \frac{\partial v_1}{\partial x_1} + M \frac{\partial w_1}{\partial x_1} = \mathcal{O}(1). \tag{14}$$

Note this is actually a set of 9 scalar equations since Eq. (13) comes from Eq. (7) as $d \to 0$ for both ij set to 22 and to 33. Equations (12), (13), and (14) can be satisfied if and only if

$$\frac{\partial v_i}{\partial x_1} = \mathcal{O}(1), \tag{15}$$

$$\frac{\partial w_1}{\partial x_1} = \mathcal{O}(1). \tag{16}$$

Now by replacing each derivative of the form $\partial f / \partial x_1$ with the corresponding finite difference $(f^+ - f^-)/d$, multiplying both sides of each of the Eqs. (10), (11), (15), and (16) by d, and taking the limit as $d \to 0$, we obtain,

$$\tau_{i1}^+ - \tau_{i1}^- = 0, \tag{17}$$

$$p^+ - p^- = 0, \tag{18}$$

$$v_i^+ - v_i^- = 0, \tag{19}$$

$$w_1^+ - w_1^- = 0, \tag{20}$$

a set of eight independent interface conditions. Recalling that subscript 1 refers to the normal component of the field variables, we conclude that the interface conditions require the continuity, across the interface, of (1) normal and tangential components of the total stress traction acting on the interface, (2) fluid pressure, (3) the solid velocity vector, and (4) the normal component of the relative fluid velocity vector. These conditions follow directly from Biot's equations if the latter are satisfied at the discontinuity.

Comparing these boundary conditions with those of Deresiewicz and Skalak mentioned in the Introduction, we immediately see that interface conditions (17)–(20) are identical to a particular case of the standard conditions of Deresiewicz and Skalak, the open-pore conditions, namely Eq. (2) with interface permeability $\beta_s \to \infty$. In other words, out of the choice allowed by the standard conditions of Deresiewicz and Skalak, only the open-pore conditions are consistent with Biot's equations, if the latter are to be valid throughout the poroelastic continuum, including surfaces across which the medium properties are discontinuous. These are the interface conditions that must be used in any numerical modeling scheme, if that scheme is to properly handle Biot's equations when the porous medium is piecewise continuous.

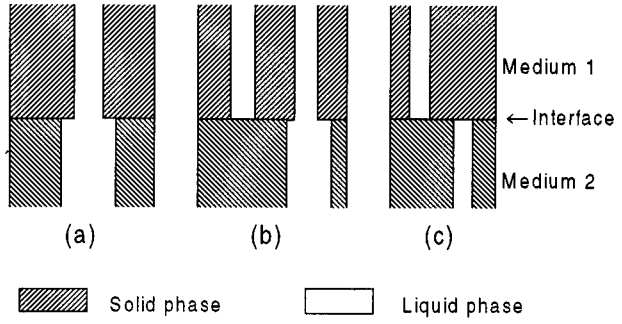

FIG. 2. Diagram of an interface between two porous media on a microscopic scale: (a) open interface ($\beta_s = \infty$); (b) partially open interface ($0 < \beta_s < \infty$); (c) closed interface ($\beta_s = 0$) (after Deresiewicz and Skalak, Ref. 4).

We emphasize that, in line with Biot theory the above derivation of the interface conditions has been carried out exclusively from the macroscopic standpoint, without considering microscopic details of the interface.

II. CLOSED AND PARTIALLY OPEN INTERFACES

The result of the previous section that the only interface conditions consistent with Biot theory are the open-pore conditions may seem unphysical, since in a real medium one can always imagine an impermeable, or partially permeable contact between two permeable media.[9] Folklore has it that, if one looks at an interface from the microscopic standpoint, such a situation may occur if the cross sections of pores of two media do not match at the interface, as shown in Fig. 2. This, however, seems a highly unlikely scenario for a natural interface, based on preliminary experiments carried out by Rasolofosaon and Schoenberg in 1996. Their results showed that the presence of a fracture in a piece of sandstone did not change the decrease of the rock's permeability normal to the fracture whether the two pieces of the rock were held together such that the two pieces ''fit'' one another at the fracture surface, or whether one piece of the rock was offset slightly relative to the other piece such that the two pieces did not fit at the fracture surface.

A more likely scenario for partial or total blockage of flow across a fracture is one in which clays, muds, or ground up grain materials clog the pores in the vicinity of the interface or fracture surface.

At this point the question arises as to how partially open or closed interfaces can be handled in the context of Biot theory. Following an approach used in Ref. 19, we can solve this problem by replacing the interface with a thin poroelastic layer of thickness d, and letting its permeability to viscosity ratio κ/η be proportional to the thickness d, i.e.,

$$\frac{\kappa}{\eta} \equiv \beta d, \tag{21}$$

keeping in mind that open pore conditions of *perfect hydraulic contact* must hold on both sides of the layer. Then Eq. (4) becomes

$$-\frac{\partial p}{\partial x_i}=\frac{1}{\beta d}\,\hat{F}w_i+(\rho_f\dot{v}_i+m\dot{w}_i). \tag{22}$$

After replacement of $\partial p/\partial x_1$ with its finite difference approximation $(p^+-p^-)/d$ and the multiplication of both sides of the equation by d, taking the limit as $d\to 0$ yields

$$-(p^+-p^-)=\frac{1}{\beta}\,\hat{F}w_1. \tag{23}$$

Comparing this result with Eq. (2) we see that a layer of small thickness d with low permeability $\kappa=\beta\eta d$ and operator $\hat{F}$ is equivalent to an interface with a finite frequency dependent interface permeability. In the time domain, one over the interface permeability is an integral operator, such that

$$\frac{1}{\beta_s}=\frac{\hat{F}}{\beta}. \tag{24}$$

At low frequencies $\hat{F}\approx 1$, and hence $\beta_s\approx\beta$. However, at higher frequencies, the interface permeability operator $\hat{F}$ becomes, in the frequency domain, simply multiplication by $F(\omega)$, the Fourier transform of the kernel function of $\hat{F}$. This means that the interface permeability to be used in the interface condition must involve the limiting value (as $d\to 0$) of the frequency dependent permeability $\tilde{\kappa}(\omega)=\kappa/F(\omega)$ of the inserted layer, rather than its quasi-static permeability κ[18]

$$\frac{1}{\beta_s}=\frac{F(\omega)}{\beta}=\lim_{d\to 0}\frac{F(\omega)\,\eta d}{\kappa}=\lim_{d\to 0}\frac{\eta d}{\tilde{\kappa}}, \tag{25}$$

proving the intuitive surmise of Rosenbaum[20] that the interface permeability as defined by Deresiewicz and Skalak[4] might be frequency dependent.

Equation (24) provides a simple recipe for numerical modeling algorithms. An interface with frequency independent inverse permeability $1/\beta_s$ can be simulated by a layer of small thickness d and inverse permeability

$$1/\kappa=1/\beta_s\,\eta d. \tag{26}$$

An impermeable interface, instead of being simulated by letting $w_n=0$ on the interface, can be modeled by a thin layer of small β, small enough so that the length corresponding to a typical background permeability to viscosity ratio divided by β is $\gg$ than layer thickness d. Clearly, an interface with frequency dependent inverse permeability can be modeled in similar fashion by the inclusion of $\hat{F}$ in the time domain or $F(\omega)$ in the frequency domain.

One can also observe that the permeability of the transition layer that simulates a partially impermeable interface depends not only on the interface permeability, but also on the fluid viscosity. This fact may look suspicious, since permeability is a property of the solid frame, and must not be affected by fluid properties. To explain this, one needs to recall the definition of interface permeability, Eq. (2). Indeed, Eq. (2) is nothing more than a form of the quasi-static Darcy law, which, for a homogeneous medium with a rigid frame is usually written as

$$V=-\frac{\kappa}{\eta}\nabla p, \tag{27}$$

where V denotes fluid particle velocity. Comparing Eq. (27) with (2) one can conclude that the interface permeability is not a purely geometrical characteristic of the interface, but is inversely proportional to the fluid viscosity. This shows that in the right-hand side of Eq. (26) the fluid viscosity cancels out and hence the permeability of the transition layer is in fact independent of fluid properties.

III. CONCLUSIONS

Interface conditions at a boundary between two porous media have been derived directly from Biot's equations of poroelasticity. These conditions are identical to a particular variant of the class of interface conditions of Deresiewicz and Skalak, namely to the open-pore conditions. In other words, we have proved that only the open-pore interface conditions are fully consistent with the validity of Biot's equations of poroelasticity at the interface. These are the conditions that should be expected to hold in any heterogeneous numerical modeling scheme, if that scheme is to properly handle Biot's equations in an inhomogeneous poroelastic continuum.

Interface conditions for closed or partially open interfaces may also be used, whether the interface is along a surface of discontinuity or not. Such conditions violate Biot's equations at the interface, but we have shown that a partially open or impermeable interface may be looked upon as a limiting case of a thin layer with small permeability proportional to the layer thickness, where the open-pore conditions do apply on both sides of this thin layer. This can serve as a simple recipe for modeling such an interface in any heterogeneous numerical scheme for poroelastic media. Further experimental and numerical studies are needed to analyze the importance of fully or partially impermeable interfaces in different porous materials.

ACKNOWLEDGMENTS

The work of Boris Gurevich was carried out under a project supported by the Earth Science Research Administration of the Israel Ministry of Infrastructure. Boris Gurevich also thanks S. L. Lopatnikov of Moscow University for productive discussions. Michael Schoenberg would like to express appreciation to Patrick Rasolofosaon of IFP for being his host for two weeks of discussion and experiments in Paris during summer 1996.

[1] M. A. Biot, ''Theory of propagation of elastic waves in a fluid-saturated porous solid. I. Low-frequency range,'' J. Acoust. Soc. Am. **28**, 168–178 (1956).
[2] M. A. Biot, ''Theory of propagation of elastic waves in a fluid-saturated porous solid. II. Higher frequency range,'' J. Acoust. Soc. Am. **28**, 179–191 (1956).
[3] M. A. Biot, ''Mechanics of deformation and acoustic propagation in porous media'' J. Appl. Phys. **33**, 1482–1498 (1962).
[4] H. Deresiewicz and R. Skalak, ''On uniqueness in dynamic poroelasticity,'' Bull. Seismol. Soc. Am. **53**, 783–788 (1963).
[5] T. Bourbié, O. Coussy, and B. Zinszner, *Acoustics of Pourous Media* (Technip, Paris, 1987).

[6] J.-F. Allard, R. Bourdier, and C. Depollier, ''Biot waves in layered media,'' J. Appl. Phys. **60**, 1926–1929 (1986).
[7] J. G. Berryman, ''Scattering by a spherical inhomogeneity in a fluid-saturated porous medium,'' J. Math. Phys. **26**, 1408–1419 (1985).
[8] B. Gurevich, A. P. Sadovnichaja, S. L. Lopatnikov, and S. A. Shapiro, ''The Born approximation in the problem of elastic wave scattering by a spherical inhomogeneity in a fluid-saturated porous medium,'' Appl. Phys. Lett. **61**, 1275–1277 (1992).
[9] P. N. J. Rasolofosaon, ''Importance of the interface hydraulic condition on the generation of second bulk compressional wave in porous media'' Appl. Phys. Lett. **52**, 780–782 (1988).
[10] B. Gurevich, ''Numerical simulation of ultrasonic experiments on poroelastic samples,'' European Association of Geoscientists and Engineers, Extended Abstracts, Paper C032 (1996).
[11] N. Dai, A. Vafidis, and E. R. Kanasewich, ''Wave propagation in heterogeneous, porous media: A velocity-stress, finite difference method'' Geophysics **60**, 327–340 (1995).
[12] J. M. Carcione, ''Full frequency-range transient solution for compressional waves in a fluid-saturated viscoacoustic porous medium,'' Geophys. Prosp. **44**, 99–129 (1996).
[13] G. Guiroga-Goode and J. M. Carcione, ''Heterogeneous modelling behaviour at an interface in porous media,'' European Association of Geoscientists and Engineers, Extended Abstracts, Paper C005 (1996).
[14] V. de la Cruz and T. J. T. Spanos, ''Seismic boundary conditions for porous media,'' J. Geophys. Res. B **94**, 3025–3029 (1989).
[15] B. Gurevich, ''Discussion of 'Reflection and transmission of seismic waves at the boundaries of porous media,'' by V. de la Cruz, J. Hube, and T. J. T. Spanos (Wave Motion **16**, 323–338, 1992) with reply by the authors, Wave Motion **18**, 303–304 (1993).
[16] R. P. Feynman, R. B. Leighton, and M. Sands, *The Feynman Lectures on Physics, Vol. 2* (Addison–Wesley, Reading, MA, 1964).
[17] S. L. Lopatnikov, personal communication (1985).
[18] D. L. Johnson, J. Koplik, and R. Dashen, ''Theory of dynamic permeability and tortuosity in fluid-saturated porous media,'' J. Fluid Mech. **176**, 379–402 (1987).
[19] M. Schoenberg, ''Elastic wave behavior across linear slip interfaces,'' J. Acoust. Soc. Am. **68**, 1516–1521 (1980).
[20] J. H. Rosenbaum, ''Synthetic microseismograms: Logging in porous formations,'' Geophysics **39**, 14–32 (1974).

Multimode radiation from an unflanged, semi-infinite circular duct

Phillip Joseph and Christopher L. Morfey
Institute of Sound and Vibration Research, University of Southampton, Southampton SO17 1BJ, United Kingdom

(Received 15 February 1998; accepted for publication 29 January 1999)

Theoretical expressions for sound radiation from a single incident duct mode, arriving at the open end of a semi-infinite circular unflanged duct with rigid walls, are used to obtain numerical results for (1) the single-mode sound power transmission coefficient, and (2) the multimode far-field directivity factor. For the multimode calculations the modes are assumed incoherent, and a weighting model is adopted which includes, as special cases, equal power per mode (above cutoff), and excitation by incoherent monopoles or axial dipoles uniformly distributed over a duct cross section. High-frequency asymptotic features of the results are explored in detail and analytical approximations are given. The findings have practical application to sound power measurement from tall exhaust stacks. © *1999 Acoustical Society of America.* [S0001-4966(99)00705-5]

PACS numbers: 43.20.Mv, 43.20.Rz [DEC]

INTRODUCTION

A. Background: Duct sound power estimation from limited far-field data

Various common noise sources radiate sound into finite-length ducts, from which the sound escapes into the far field via radiation from an unbaffled open end. Examples are exhaust mufflers, large exhaust stacks, and aircraft turbofan engines. Often one wishes to determine the sound power radiated from the duct opening, either as an index of insertion loss in order to assess silencer performance, or as a means of quantifying and ranking the total noise output for predicting community annoyance.

The sound power may, in principle, be determined by integrating the normal component of sound intensity over a surface enclosing the duct exit. However, sometimes not all measurement locations required to perform the integration are easily accessible, as in the case of large exhaust stacks which may be tens of meters high. In this example, the only measurements which are easy to make are close to the ground, corresponding to the rear-arc or backward-radiated sound radiated at angles approaching 180° to the duct axis. It is clear that a method of inferring the radiated power, at any frequency, from a small number of far-field mean square pressure measurements would be extremely useful to the noise control engineer.

B. Scope of investigation

This paper presents a theoretical and numerical study of the nondimensional directivity factor $Q(ka,\theta)$ for multimode sound radiation from the open end of a semi-infinite duct, in the absence of flow. The directivity factor relates the mean square far-field pressure, at any polar angle θ to the duct axis including the rear arc, to the net sound power transmitted along the duct.[1] The nondimensional frequency ka equals $2\pi fa/c$, where f is the frequency, a is the duct radius, and c is the sound speed. For calculating $Q(ka,\theta)$ we use the exact theoretical expressions for modal sound radiation from a semi-infinite, hard-walled, unflanged circular duct as presented by Homicz and Lordi[2] and summarized in Appendix A. These are based on the earlier classical work of Levine and Schwinger[3] for incident plane waves, and of Weinstein[4] for the higher-order modes.

The single-mode analysis of Ref. 2 is applied in what follows to a particular family of mode amplitude weighting functions, which includes the following three special cases: (1) equal incident in-duct power per mode above cutoff; (2) excitation of incident modes by incoherent monopoles uniformly distributed over a duct cross section (Fig. 1); and (3) excitation by incoherent axial dipoles uniformly distributed over a duct cross section. In each case, the individual modes are incoherently excited, and the contribution of evanescent modes is neglected. The omission of cutoff modes is a simplifying approximation that is adopted throughout; it becomes progressively more accurate as kL increases (where L is the length of duct between the source plane and the open end). For these three incident-mode weighting models in turn, we present graphs of $Q(ka,\theta)$ as a function of nondimensional frequency ka $(0.1 \leqslant ka \leqslant 60.0)$ for a number of representative angles in both the forward and rear arc. The possibility of extending the results to include mean flow is briefly examined in Appendix B.

The paper concludes by deriving a high-frequency asymptotic expression for $Q(ka,\theta)$, valid under the same conditions of multimode excitation, using the concept of a continuum of duct modes. Because scattering at the edge of the duct opening is neglected in the high-frequency model, this analysis is limited to the forward arc.

C. Previous work

Most of the literature concerned with the radiation from ducts is restricted to individual modes. Comparatively little work appears to have been published which is aimed at understanding the radiation due to a specified distribution of modes. One of the earliest such studies is due to Rice[5] whose approach is similar in principle to that presented in this pa-

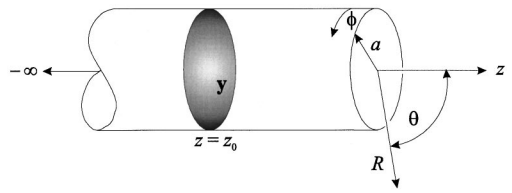

FIG. 1. Semi-infinite, hard-walled unflanged circular duct with associated coordinate system and continuous source distribution represented by the shaded region.

per; a difference in detail is that Rice used baffled-duct radiation patterns, calculated via the Kirchhoff approximation. Rice's innovation was to introduce a mode-amplitude weighting function proportional to the cutoff ratio raised to an exponent that could be varied to include, as a special case, equal power per mode. This weighting function is justified empirically, insofar as it matches the multimode radiation characteristics of certain ducted aircraft-engine fans;[5] on the other hand, the weighting function proposed in the present paper is based on physical source models, as outlined in Sec. B above. For the special case of equal incident power per mode, the far-field directivity predicted by Rice[5] in the high-frequency limit agrees with that predicted here in the same limit.

Snakowska[6] also investigated multimode radiation from unflanged ducts under the assumption of equal power per mode, but with the excitation limited to axisymmetric $m=0$ modes. Her paper goes beyond the work presented here by including a calculation of the acoustic resistance and reactance for the duct termination. One of her main conclusions is that when all the cut-on axisymmetric modes are excited with equal incident power, the influence of an individual mode on the multimode directivity is strongest at frequencies just above that mode's cutoff. This contradicts one of the findings presented in the present paper. Here, it is shown that if the power in a mode incident on the duct termination is held constant as cutoff is approached, the pressure amplitude of the incident mode tends to infinity, but the modal transmission function tends to zero more rapidly. The far-field pressure in that mode therefore equals zero, in the limit as the cutoff frequency is approached from above.

I. IN-DUCT TO FAR-FIELD TRANSFER FUNCTION

The nondimensional single-mode transfer function $H_{mn}(ka,\theta)$, defined in Eq. (3) below, relates the far-field acoustic pressure $p_{mn,f}(R,\theta,\phi,t)$ at any far-field point (R,θ,ϕ) to the pressure amplitude of the incident (m,n) duct mode arriving at the duct termination. In this section we show how $H_{mn}(ka,\theta)$ follows from the classical Wiener–Hopf solution,[2–4] mentioned above, for sound radiation from a semi-infinite, hard-walled circular unflanged duct (Fig. 1).

The in-duct sound field can be expressed as the sum of modal components $p=\Sigma_{m=-\infty}^{\infty}\Sigma_{n=0}^{\infty}(p_{mn}^{+}+p_{mn}^{-})$, where the $(+,-)$ superscripts denote the forward (incident) and reflected waves, respectively, and (m,n) are the usual circumferential and radial mode indices. Above its cutoff frequency at angular frequency ω, a single incident mode is described by

$$p_{mn}^{+}(r,\phi,z,t)=e^{j\omega t}a_{mn}\Psi_{mn}(r,\phi)e^{-j\alpha_{mn}kz},$$
$$\text{where}\quad \alpha_{mn}=\sqrt{1-(\kappa_{mn}/k)^2}. \tag{1}$$

The wave numbers κ_{mn} are the modal transverse wave numbers; they satisfy the hard-walled boundary condition $J_m'(\kappa_{mn}a)=0$, where J_m denotes the Bessel function of the first kind of order m, the prime signifies differentiation with respect to the argument, and a is the duct radius. Similarly, reflections from the open end produce waves traveling back up the duct, with typical term $p_{ml}^{-}=e^{j\omega t}b_{ml}\Psi_{ml}e^{j\alpha_{ml}kz}$. Here a_{mn} and b_{ml} are the modal amplitudes, k is the free space wave number, and Ψ_{mn} are the normalized mode shape functions given by

$$\Psi_{mn}(r,\phi)=\frac{1}{N_{mn}}J_m(\kappa_{mn}r)e^{-jm\phi}. \tag{2}$$

The modal normalization constants N_{mn} are introduced above to satisfy the normalization condition, $S^{-1}\int_S|\Psi_{mn}|^2\,dS=1$.

We now define the dimensionless in-duct to far-field transfer function $H_{mn}(ka,\theta)$, by writing

$$p_{mn,f}(R,\theta,\phi,t)=\left(\frac{a}{R}\right)a_{mn}H_{mn}(ka,\theta)e^{j(\omega t-m\phi)}e^{-jkR}. \tag{3}$$

Note that the (m,n) subscript on $p_{mn,f}$ means that the far-field pressure corresponds to an (m,n) incident mode in the duct. Homicz and Lordi[2] present explicit expressions for the modal far-field pressure radiated from an unflanged duct, in a similar form to Eq. (3); these are listed in Appendix A, together with some additional results we have found to be essential for numerical evaluation and which are omitted from Ref. 2. Their transfer function D_{mn} differs from ours by a simple factor; it is defined by

$$p_{mn,f}(R,\theta,\phi,t)=\frac{1}{R}a_{mn}N_{mn}^{-1}D_{mn}(k,a,\theta)e^{j(\omega t-m\phi)}e^{-jkR}. \tag{4}$$

Two features of Eqs. (3) and (4) are noteworthy. First, the radiated sound field is expressed in terms of the incident-mode pressure amplitude arriving at the open end of the duct. The factor H_{mn} (or D_{mn}) therefore automatically incorporates the reflection process at the duct termination, unlike the corresponding expression for a flanged circular duct derived by Tyler and Sofrin.[7] Second, the dimensionless transfer function $H_{mn}(ka,\theta)$ depends only on (ka,θ) and the mode indices (m,n). Comparing Eqs. (3) and (4) gives the following relationship between $H_{mn}(ka,\theta)$ and $D_{mn}(k,a,\theta)$ for a single incident mode:

$$H_{mn}(ka,\theta)=\frac{1}{a}\frac{D_{mn}(k,a,\theta)}{N_{mn}}. \tag{5}$$

II. MULTIMODE RADIATION DIRECTIVITY AS A FUNCTION OF MODAL WEIGHTING

A. Objectives

The radiation pattern of far-field rms pressure, p_f, due to a set of incident modes with pressure amplitudes a_{mn} as given by Eq. (1), is determined from Eq. (6) below:

$$p_f(R,\theta,\phi)=\frac{a}{\sqrt{2}R}\left|\sum_{m,n} a_{mn}H_{mn}(ka,\theta)e^{-jm\phi}\right|. \tag{6}$$

For incoherent excitation of the incident modes, we treat the amplitudes a_{mn} as random variables, and average the mean square far-field pressure p_f^2 over multiple realizations. The modal contributions add to give

$$E\{p_f^2(R,\theta,\phi)\}=\frac{1}{2}\left(\frac{a}{R}\right)^2\sum_{m,n}|H_{mn}(ka,\theta)|^2E\{|a_{mn}|^2\}, \tag{7}$$

where $E\{\}$ is the expectation operator. Averaging the radiated field in this way removes any azimuthal dependence; the radiated far field is therefore axisymmetric and a function of the polar angle θ only, as indicated in Eq. (7). In practice, the required averaging will generally be achieved by taking a time average of the signal power in a narrow frequency band.

Starting from Eq. (7), we now explore the multimode radiation patterns produced by the following three types of source in a semi-infinite unflanged duct:

(1) Equal power per mode incident on the open end.
(2) Incoherent monopoles uniformly distributed over a duct cross section.
(3) Incoherent axial dipoles uniformly distributed over a duct cross section.

These three source models are shown below to belong to the general family

$$E\{|a_{mn}|^2\}\propto\alpha_{mn}^{-q}\quad(\text{for real }\alpha), \tag{8}$$

where $q=1$, 2, and 0 for cases (1), (2), and (3), respectively; the dimensionless modal wave number α_{mn} is defined in Eq. (1). It follows that the far-field radiation pattern for mean square pressure can be modeled in all three cases by

$$\left(\frac{R}{a}\right)^2E\{p_f^2\}\propto\sum_{m,n}|H_{mn}(ka,\theta)|^2\alpha_{mn}^{-q}. \tag{9}$$

The concept of relating the modal weighting to α is similar to that used earlier by Rice,[5] whose family of modal weighting models was based on powers of $\kappa_{mn}/k=\zeta_{mn}$ (which we shall call cut-on ratio; its inverse k/κ_{mn} is the usual cutoff ratio). Note that $\alpha_{mn}^2+\zeta_{mn}^2=1$.

B. Modal weighting models

1. Equal power per mode incident on open end

The sound power $W^+(ka)$ incident at the open termination of the duct is given to within a constant factor by

$$W^+\propto\mathrm{Re}\int_S d\mathbf{y}[p^+(\mathbf{y})]^*\frac{\partial p^+(\mathbf{y})}{\partial z},\quad \mathbf{y}\in S. \tag{10}$$

Here $p^+(\mathbf{y})=\Sigma_{m,n}p_{mn}^+(\mathbf{y})$, and $\mathbf{y}$ is a two-dimensional vector that specifies the position over a duct cross section. The integration can be performed using the orthogonality property of the mode shape functions, to give the expected value of the incident sound power in terms of the mode pressure amplitudes:

$$E\{W^+\}\propto\sum_{m,n}E\{|a_{mn}|^2\}\alpha_{mn}\quad(\alpha_{mn}\ \text{real}). \tag{11}$$

If the sound power in each of the incident modes is equal, it follows that the square of the mode pressure amplitudes varies as

$$E\{|a_{mn}|^2\}\propto\alpha_{mn}^{-1}\quad(\alpha_{mn}\ \text{real}), \tag{12}$$

which corresponds to Eq. (8) with the index q equal to 1.

2. Incoherent monopoles uniformly distributed over a cross section

Let $q(\mathbf{y})$ denote a volume velocity distribution over the duct cross section $z=z_0$ (Fig. 1), with time factor $e^{j\omega t}$ understood. Modal components of $q(\mathbf{y})$ are defined by

$$q(\mathbf{y})=\sum_{m,n}q_{mn}\Psi_{mn}(\mathbf{y}); \tag{13}$$

$$q_{mn}=\frac{1}{S}\int_S d\mathbf{y}\Psi_{mn}^*(\mathbf{y})q(\mathbf{y}), \tag{14}$$

where $\Psi_{mn}(\mathbf{y})$ are the orthonormal mode shape functions and S is the cross-sectional area. Now let the duct in Fig. 1 extend from $z=0$ to $z=-\infty$. The forward-wave modal pressures in $z_0<z<0$ are given by[8]

$$a_{mn}=\frac{\rho c}{2\alpha_{mn}}q_{mn}e^{jk\alpha_{mn}(z_0-z)}. \tag{15}$$

It follows from Eqs. (14) and (15) that above cutoff,

$$|a_{mn}|^2=\left(\frac{\rho c}{2\alpha_{mn}}\right)^2\int_S d\mathbf{y}\Psi_{mn}^*(\mathbf{y})\int_S d\mathbf{y}'\Psi_{mn}(\mathbf{y}')q^*(\mathbf{y})q(\mathbf{y}'). \tag{16}$$

To model a uniform distribution of incoherent monopoles over the plane $z=z_0$, we write

$$E\{q^*(\mathbf{y})q(\mathbf{y}')\}=A\delta(\mathbf{y}-\mathbf{y}'),\quad \mathbf{y}\in S, \tag{17}$$

where A is a constant and δ is the Dirac delta function. Substituting Eq. (17) in Eq. (16) gives

$$E\{|a_{mn}|^2\}\propto\alpha_{mn}^{-2}\quad(\alpha_{mn}\ \text{real}), \tag{18}$$

which is the required result. It corresponds to Eq. (8) above, with the index q equal to 2.

3. Incoherent axial dipoles uniformly distributed over a cross section

Replacing $q(\mathbf{y})$ by an axial-dipole distribution $f_z(\mathbf{y})$, where f_z represents an axial force per unit area, introduces an extra axial derivative in the pressure solution. In place of Eq. (15), we find

$$a_{mn}=\tfrac{1}{2}(f_z)_{mn}e^{jk\alpha_{mn}(z_0-z)}, \tag{19}$$

which leads to the result

$$E\{|a_{mn}|^2\}\propto\alpha_{mn}^{-0}\quad(\alpha_{mn}\ \text{real}). \tag{20}$$

The axial-dipole weighting corresponds to Eq. (8), but with $q=0$; thus equal mode pressure amplitudes are predicted for all the incident modes above cutoff.

III. MULTIMODE DIRECTIVITY FACTOR $Q(ka,\theta)$: DEPENDENCE ON WEIGHTING MODEL

A dimensionless directivity factor, $Q(ka,\theta)$, that relates the net sound power incident on the open end of the duct to the mean square far-field pressure $p_f^2(ka,\theta)$ is defined by

$$Q(ka,\theta)=p_f^2(ka,\theta)/\langle p_f^2(ka)\rangle_\Omega, \tag{21}$$

where $\langle p_f^2(ka)\rangle_\Omega$ is the average of the radiated mean square pressure over solid angle,

$$\langle p_f^2(ka)\rangle_\Omega=\frac{1}{2}\int_0^\pi d\theta\; p_f^2(ka,\theta)\sin\theta. \tag{22}$$

Here and in what follows, the expectation operator $E\{\}$ has been omitted for brevity. Combining Eqs. (9), (21), and (22) gives the exact expression for $Q(ka,\theta)$ as

$$Q(ka,\theta)=\frac{\Sigma_{m,n}|H_{mn}(ka,\theta)|^2\alpha_{mn}^{-q}}{\frac{1}{2}\int_0^\pi d\theta\sin\theta\;\Sigma_{m,n}|H_{mn}(ka,\theta)|^2\alpha_{mn}^{-q}}. \tag{23}$$

The usefulness of a $Q(ka,\theta)$ prediction such as Eq. (23) is that it replaces the difficult measurement of radiated sound power, $W(ka)$, by a single measurement of far-field mean square sound pressure, $p_f^2(ka,\theta)$, through the relationship

$$p_f^2(ka,\theta)=Q(ka,\theta)\,\frac{\rho c W(ka)}{4\pi R^2}, \tag{24}$$

where ρ and c denote the ambient density and sound speed. In practice, the sound power would be better taken as an average from acoustic pressure measurements at several different azimuthal and polar angles, but the point is that prior knowledge of $Q(ka,\theta)$ obviates the need for a complete set of p_f^2 measurements over the entire 4π solid angle range.

In order to understand the frequency dependence of the directivity factor $Q(ka,\theta)$, and the way this depends on the modal weighting exponent q, it is helpful to examine the behavior of the single-mode transfer function $H_{mn}(ka,\theta)$ as cutoff is approached. The related directivity function D_{mn}, given by Eq. (A3) in Appendix A, contains α_{mn} as a multiplicative factor; at frequencies approaching cutoff ($\alpha_{mn}\to 0$), this factor dominates the frequency dependence. For a single mode near cutoff, therefore, the asymptotic dependence of H_{mn} on ka is

$$H_{mn}(\theta,\,ka)\sim\alpha_{mn},\quad \alpha_{mn}\to 0, \tag{25}$$

and at cutoff, the transfer function equals zero. This is analogous to sound transmission across a plane interface between two media, where—as at the duct termination—the transmitted wave approaches zero as the grazing angle of the incident plane wave tends to zero.

Numerical confirmation of the dependence predicted in Eq. (25) is provided by Fig. 2, for the representative angles of θ=45°, 89.9°, and 135°. This shows very close agreement, as $\alpha_{mn}\to 0$, between the rates at which $|H_{mn}(\theta,ka)|^2$ and the function α_{mn}^2 fall to zero, for the (30, 4) mode (chosen arbitrarily).

Note that a curious anomaly in the behavior of $|H_{mn}|^2$ very close to cutoff appears at exactly θ=90°. This is likely to be an artefact of the numerical computation, since the asymptotic behavior predicted by Eq. (25) is closely followed at the slightly different angle of θ=89.9°.

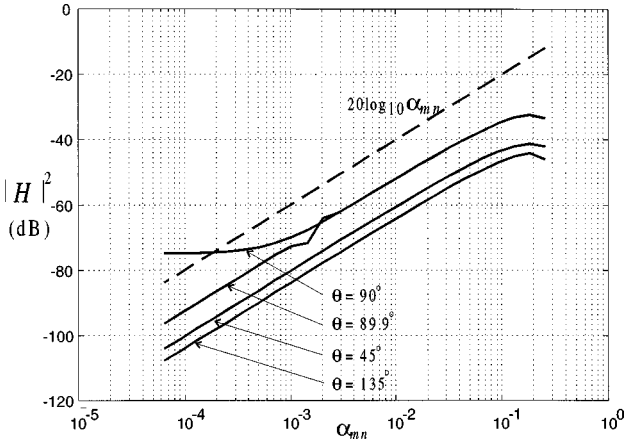

FIG. 2. Variation of $|H_{mn}|^2$ as $\alpha_{mn}\to 0$ for some representative angles, compared with α_{mn}^2. Mode $m=30$, $n=4$.

The tendency of $|a_{mn}|^2$ to approach infinity as $k\to\kappa_{mn}$, as predicted by Eq. (8) for $q>0$, is therefore opposed by the tendency of $|H_{mn}(ka,\theta)|^2$ to approach zero. The radiated mean square pressure is proportional to the product of these terms. For a single mode close to cutoff, we obtain the simple power law

$$p_{mn,f}^2(ka,\theta)\propto\alpha_{mn}^{2-q}\quad(\alpha_{mn}\ll 1;\;\;\theta=\text{constant}). \tag{26}$$

Equation (26) identifies three categories of behavior:

(i) $q<2$ (including a distribution of incoherent axial dipole sources, and equal incident power per mode). Modes close to cutoff make a negligible contribution to the total radiated field compared with the other modes, and zero contribution identically at cutoff.

(ii) $q=2$ (a distribution of incoherent monopole sources). Modes close to cutoff, and modes precisely at cutoff, make contributions to the total radiation field which are comparable to those of other modes.

(iii) $q>2$. Modes close to cutoff dominate the total radiated acoustic field. Exactly at the cutoff frequency of a particular mode, the radiated power and far-field mean square pressure become infinitely large. As the (m,n) cutoff is approached, Eq. (23) becomes

$$Q(ka,\theta)\to\frac{|H_{mn}(\kappa_{mn}a,\theta)|^2}{\frac{1}{2}\int_0^\pi d\theta\sin\theta\,|H_{mn}(\kappa_{mn}a,\theta)|^2},\qquad ka\to\kappa_{mn}a; \tag{27}$$

this result is independent of q in the range $q>2$.

IV. DIRECT EVALUATION OF $Q(ka,\theta)$ AT LOW ka

In the forward arc, the variation of $|H_{mn}(ka,\theta)|^2$ with angle θ tends to be highly oscillatory for individual modes when ka is large. However, provided the value of ka is not too large, the expression for $Q(ka,\theta)$ can be evaluated directly without approximation, with the summation in the denominator of Eq. (23) being performed first and the integration second: the summation over many modes has the effect, exactly like integration, of smoothing out the rapid fluctua-

tions to produce relatively slow angular variations in $Q(ka,\theta)$. In order to achieve a given integration accuracy for $Q(ka,\theta)$, the number of angles between 0 and π at which $|H_{mn}(ka,\theta|^2$ must be computed can therefore be much smaller, particularly at high ka, than that required to achieve the same accuracy in a single mode. (We have experienced insignificant degradation in integration accuracy by sampling the radiated field every 15°, compared with the original 1° interval used to produce the graphs presented as Figs. 3–11 in Secs. V and VI.)

Direct modal summation has been used to generate most of the numerical $Q(ka,\theta)$ results in Sec. VI, specifically up to $ka=35$. However, with the total number of modes increasing as $(ka)^2$, the computational effort required by direct modal summation and integration eventually becomes excessive at high ka. At that stage some simplification is therefore necessary and is the subject of the next section.

V. INDIRECT EVALUATION OF $Q(ka,\theta)$ AT HIGH ka: THE ENERGY TRANSMISSION COEFFICIENT APPROACH

An alternative expression for $Q(ka,\theta)$ is developed below in terms of the energy transmission coefficient T_{mn} for an individual mode. Given a single-mode incident field as in Eq. (1), the sound power arriving at the open end is

$$W_{mn}^{+}=\frac{|a_{mn}|^2 S\alpha_{mn}}{2\rho c}. \tag{28}$$

The power transmitted to the far field in this case, denoted by $W_{mn,f}$, can be related to the incident modal power W_{mn}^{+} through a modal energy transmission coefficient T_{mn} defined as

$$T_{mn}=\frac{W_{mn,f}}{W_{mn}^{+}}. \tag{29}$$

Substituting Eqs. (3), (22), (24), and (28) into (29) gives

$$T_{mn}=2\alpha_{mn}^{-1}\int_0^{\pi} d\theta \sin\theta |H_{mn}(ka,\theta|^2, \tag{30}$$

which can be calculated exactly using Appendix A.[9] In terms of T_{mn}, the multimode expression for $Q(ka,\theta)$ in Eq. (23) becomes

$$Q(ka,\theta)=\frac{4\Sigma_{m,n}|H_{mn}(ka,\theta)|^2\alpha_{mn}^{-q}}{\Sigma_{m,n}\alpha_{mn}^{1-q}T_{mn}}. \tag{31}$$

Note that incoherent excitation of modes is a necessary condition on Eq. (31), as it is for Eq. (23). At this stage, Eqs. (30) and (31) are simply a restatement of Eq. (23); but if a rapid method of approximating T_{mn} can be devised in place of Eq. (30), then Eq. (31) offers a simpler way to estimate the multimode directivity factor at high ka values.

One such method is suggested by Fig. 3. It shows the energy transmission coefficient T_{mn} plotted against κ_{mn}/k for all the propagating modes at $ka=35$, with T_{mn} calculated from Eq. (30). At this high frequency, well cut-on modes (represented by points with $\kappa_{mn}/k\ll 1$) beam directly from the duct with very little energy reflection; whereas modes close to cutoff approach the duct termination at near-zero

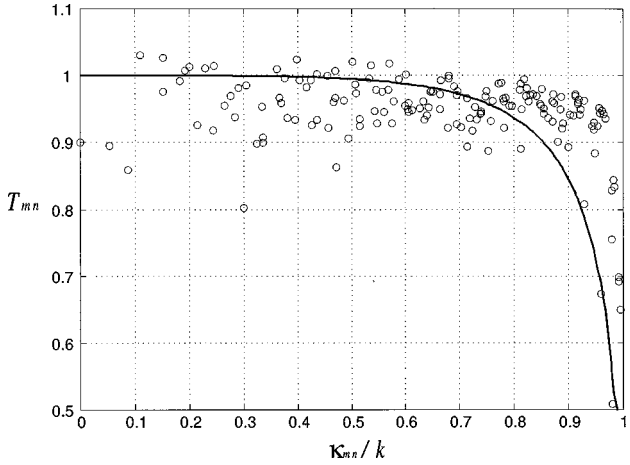

FIG. 3. Comparison between the numerically computed energy transmission coefficient $T_{mn}=2\alpha_{mn}^{-1}\int_0^{\pi} d\theta |H_{mn}(\theta)|^2 \sin\theta$ evaluated for all propagating modes at $ka=35$ (denoted by ''○''), and the high-frequency asymptotic result $T_{mn}=4\alpha_{mn}(1+\alpha_{mn})^{-2}$ (solid curve). The horizontal axis is the cut-on ratio, κ_{mn}/k.

grazing angles, which leads to significant energy reflection back along the duct. An approximate model for the energy reflection process is obtained by representing the duct termination as an impedance boundary; there is then no conversion of the incident (m,n) mode into reflected (m,l) modes of different radial order. The energy transmission coefficient is related to the modal resistance ratio τ_{mn} and reactance ratio χ_{mn} at the termination, through[8]

$$T_{mn}=\frac{4\alpha_{mn}\tau_{mn}}{(1+\alpha_{mn}\tau_{mn})^2+(\alpha_{mn}\chi_{mn})^2} \quad \text{(above cutoff)}. \tag{32}$$

At sufficiently high frequency τ_{mn} and χ_{mn} tend, respectively, to unity and zero; the approximate energy transmission coefficient asymptotes to

$$T_{mn}\rightarrow\frac{4\alpha_{mn}}{(1+\alpha_{mn})^2} \quad \text{(above cutoff; } ka\gg 1). \tag{33}$$

Equation (33) is plotted in Fig. 3 as the smooth curve. It can be seen to provide a reasonable first approximation to the exact results of Eq. (30), for the propagating modes at $ka=35$.

Note that some values of T_{mn} greater than unity appear in Fig. 3; these violate energy conservation, and are caused by numerical inaccuracy. Computation of the modal directivity function from Eq. (A3) at high ka involves multiplying a very small (exponential) term with a very large θ-dependent product term. Errors of a few percent are therefore easily acquired. Nevertheless, the broad agreement between the asymptotic estimate above and the exact T_{mn} from Eq. (30) is sufficiently close, for high-order modes well above cutoff, to make it attractive to use Eqs. (31) and (33) rather than carry out computationally intensive evaluations of $H_{mn}(ka,\theta)$ over all θ, as would be required by the exact expression for $Q(ka,\theta)$. The resulting high-ka approximation, parameterized on α, is

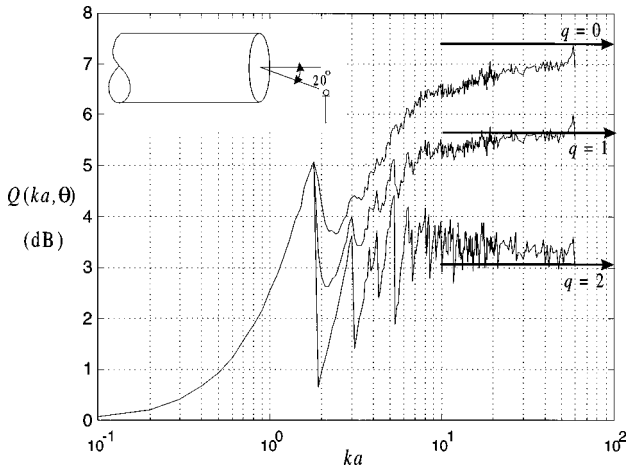

FIG. 4. Variation of Q with ka at $\theta=20°$ for the three source models $q=0$, 1, and 2. The horizontal arrows ''→'' denote the high-frequency asymptotes computed from Eq. (42).

$$Q(ka,\theta)\approx\frac{\Sigma_{m,n}|H_{mn}(ka,\theta)|^2\alpha_{mn}^{-q}}{\sum_{m,n}\left(\frac{\alpha_{mn}}{1+\alpha_{mn}}\right)^2\alpha_{mn}^{-q}},\quad ka\gg 1. \tag{34}$$

VI. RESULTS

A. Forward-arc directivity factor as a function of frequency, for fixed angles to the axis

The multimode directivity factor $Q(ka,\theta)$ has been computed for $ka=0.1(0.1)35$ using the exact expression of Eq. (23), and for $ka=36(1)60$ using the approximate expression of Eq. (34). Integration of $|H_{mn}(ka,\theta)|^2$ required by the exact expression was performed using trapezoidal integration between 0° and 180° in 1° increments. Modal summations in Eq. (23) were restricted to nonnegative values of the circumferential mode index m, and contributions to the summation of from modes with $m=0$ were halved, to take account of symmetry between modes that have the same m value, but spin in opposite directions.

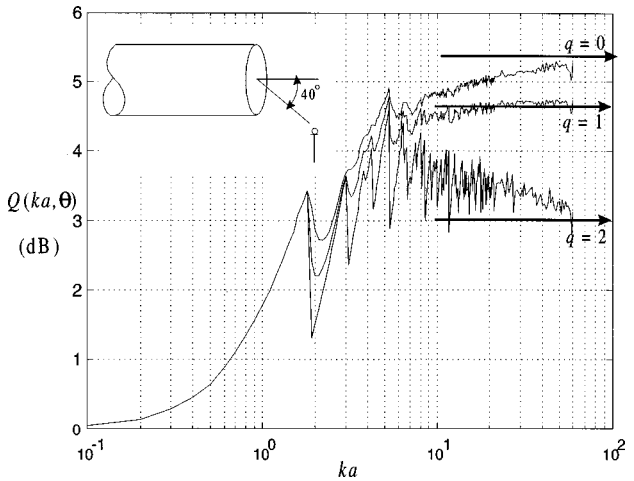

FIG. 5. Variation of Q with ka at $\theta=40°$ for the three source models $q=0$, 1, and 2. The horizontal arrows '→' denote the high-frequency asymptotes computed from Eq. (42).

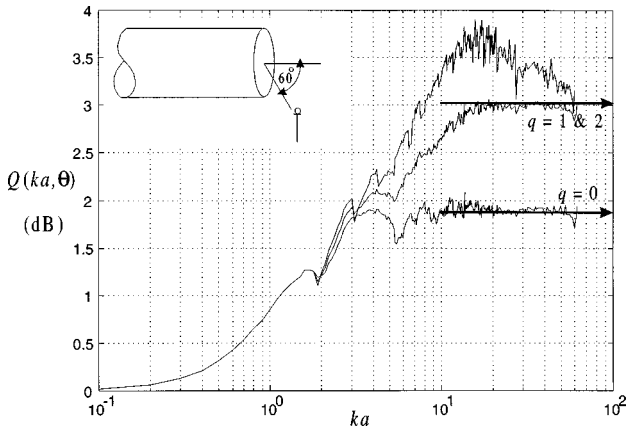

FIG. 6. Variation of Q with ka at $\theta=60°$ for the three source models $q=0$, 1 and 2. The horizontal arrows '→' denote the high-frequency asymptotes computed from Eq. (42).

The angles chosen for graphical presentation are $\theta=20°$, 40°, 60°, and 80° in the forward arc and 100°, 120°, 140°, and 160° in the rearward arc; at each angle, $Q(ka,\theta)$ has been calculated for source model indices $q=0$, 1 and 2. Results for the four forward-arc angles are presented in Figs. 4–7; the arrows indicate high-frequency asymptotes, computed using the theory presented in Sec. VII below. (No high-frequency asymptote is indicated in Fig. 7 for $\theta=80°$, since the model of Sec. VII breaks down at angles larger than about 70° for the range of ka values under investigation here; cf. Fig. 13 below.) Note that the approximate results ($ka>35$) merge smoothly, at all angles, with the exact results ($ka\leqslant 35$).

At frequencies below the first modal cutoff frequency ($ka\approx 1.841$), Figs. 4–7 show that $Q(ka,\theta)$ is independent of the mode excitation model; this result is expected, since only the plane wave is involved. Note on the other hand how at $\theta=80°$, the three source models diverge with increasing ka, indicating a marked sensitivity of $Q(ka,\theta)$ to the modal weighting index q. Farfield measurements confined to angles close to the sideline direction evidently reveal little about the radiated sound power, in situations where the type of source in the duct is unknown; this aspect of the problem is discussed in greater detail in Sec. VIII.

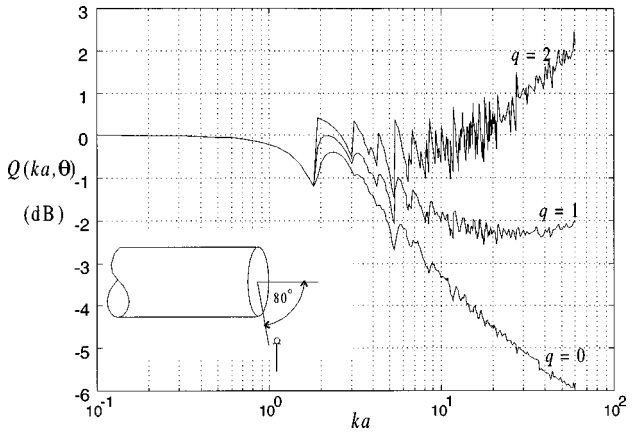

FIG. 7. Variation of Q with ka at $\theta=80°$ for the three source models $q=0$, 1, and 2.

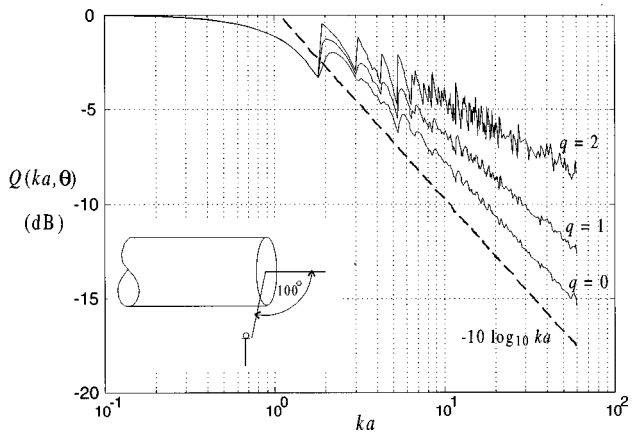

FIG. 8. Variation of Q with ka at $\theta=100°$ for the three source models $q=0$, 1, and 2.

Because of the assumption that cutoff modes do not contribute to the far-field radiation (equivalent to assuming that the source of sound is several duct diameters from the open end), the $Q(ka,\theta)$ curves for $q=2$ show discontinuities as each new mode cuts on. The reasons for this, and for the more gradual fluctuations in $Q(ka,\theta)$ when $q<2$, were briefly indicated in Sec. III [see comments following Eq. (26)]. A fuller explanation is presented in Sec. VIII.

B. Rear-arc diffraction

Results for the angles 100°, 120°, 140°, and 160° in the rear arc are plotted in Figs. 8–11. The underlying variation of $Q(ka,\theta)$ with ka for values of θ in the rear arc, away from the sideline direction, appears to be close to the simple frequency power law $Q(ka,\theta)\propto(ka)^{-1}$ represented by the dashed lines in Figs. 8–11. A speculative explanation can be obtained by comparing duct radiation in the rear arc to the classical problem of plane wave diffraction by a semi-infinite rigid half-plane,[10] on the hypothesis that above the first cutoff frequency the duct wall curvature ceases to be important. In the shadow zone of the half-plane, the field appears to be generated by a line source located along its edge. This source radiates into the shadow zone as cylindrical waves, with characteristic frequency dependence $k^{-1/2}$ for the far-field pressure.

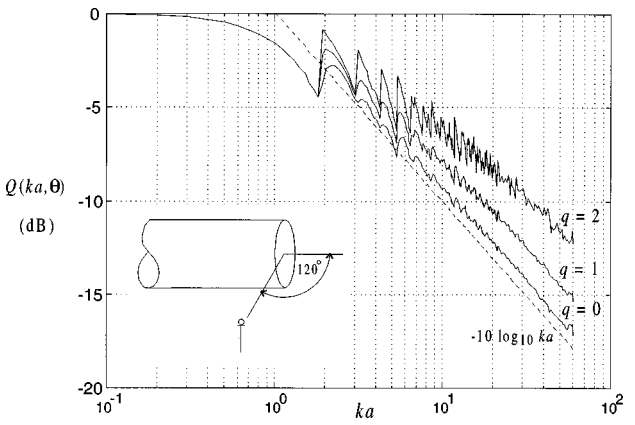

FIG. 9. Variation of Q with ka at $\theta=120°$ for the three source models $q=0$, 1, and 2.

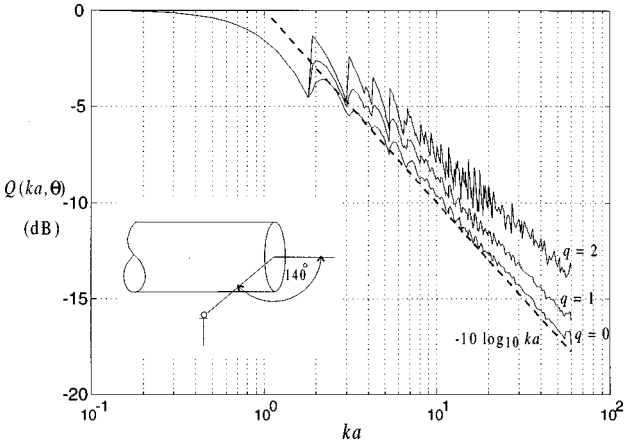

FIG. 10. Variation of Q with ka at $\theta=140°$ for the three source models $q=0$, 1, and 2.

For high frequencies ($ka>10$), Figs. 8–11 show that fluctuations in Q about the general trend $Q(ka,\theta)\propto(ka)^{-1}$ are typically 1 dB or less for q equal to 1 or 0, and 3 dB or less for q equal to 2. A more accurate description of the rear-arc directivity factor was obtained by fitting $Q(ka,\theta)$, at each of the rear-arc angles $\theta=90°(1°)170°$, to a linear regression model of the form

$$\hat{L}_Q(ka,\theta)=a(\theta)+b(\theta)\log_{10} ka \quad \text{(dB)}, \tag{35}$$

where $\hat{L}_Q$ represents the least-squares best fit to the directivity index L_Q, defined as $10\log_{10} Q$. The coefficients $a(\theta)$ and $b(\theta)$, computed for the dimensionless frequency range $3\leqslant ka\leqslant 35$, are plotted in Fig. 12 below. Note that Fig. 12, while useful for estimating the rear-arc directivity index for finite ka, does not answer the question of how $Q(ka,\theta)$ behaves as ka tends to infinity; according to the hypothesis of the previous paragraph, $b(\theta)$ would equal -10 for all rear-arc angles in this limit.

VII. HIGH-FREQUENCY BEHAVIOUR OF THE FORWARD-ARC RADIATED FIELD

At sufficiently high frequencies, the summation over discrete modes which appears in the expression for $Q(ka,\theta)$

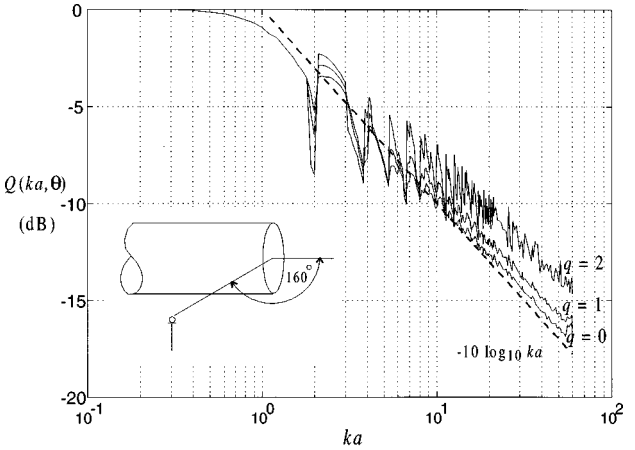

FIG. 11. Variation of Q with ka at $\theta=160°$ for the three source models $q=0$, 1, and 2.

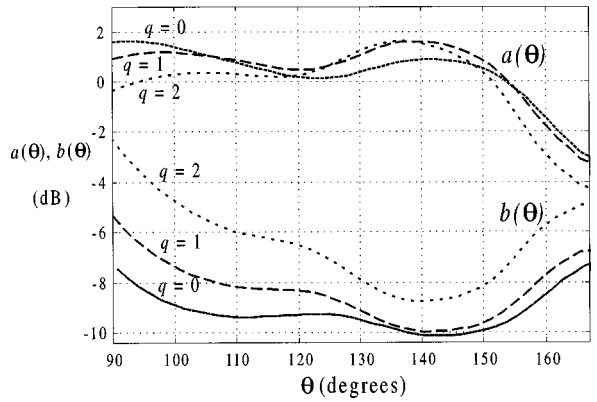

FIG. 12. Variation of the coefficients $a(\theta)$ and $b(\theta)$ in the regression line $\hat{L}_Q = a(\theta) + b(\theta)\log_{10} ka$, obtained as a least squares best fit to the directivity index $L_Q = 10\log_{10} Q$ computed exactly from Eq. (23) over the frequency range $3 \leqslant ka \leqslant 35$.

may be replaced by an integral over a continuous modal distribution function. For the particular incident-mode weighting function given by Eq. (8), the resulting integral can be solved in closed form. By means of this approach we shall demonstrate that the field radiated by either the monopole or the dipole source distribution into the forward hemisphere ($\theta < 90°$) corresponds in the high ka limit to that radiated into a free field, as if the duct were acoustically transparent.[11]

Consider the solid-angle distribution of transmitted sound power with respect to $\cos\theta$, which determines the directivity of far-field radiation from the axisymmetric duct. Assuming no energy reflection, which we have shown to be accurate in the high ka limit except for modes close to cutoff, the radiated and incident sound powers are equal. At sufficiently high ka the summation of sound power in individual modes may be replaced by the integral

$$W = \frac{S}{\rho c} \int \alpha \, d\langle p^2 \rangle, \quad ka \to \infty, \tag{36}$$

where $\langle p^2 \rangle$ is the spatial average of the in-duct mean squared pressure over the duct cross section. With the modes excited incoherently, this mean square pressure average is the sum of the modal contributions. In the high ka limit the incident-mode weighting model of Eq. (8) gives the contribution to $d\langle p^2 \rangle$ from a small number of neighboring modes, whose transverse wave numbers lie between κ and $\kappa + d\kappa$, as

$$d\langle p^2 \rangle \propto \alpha^{-q} \, dN(\kappa) \quad (0 < \kappa < k, \ \ ka \to \infty); \tag{37}$$

here $N(\kappa)$ is the number of duct modes having transverse wave numbers in the range 0 to κ, and $N(\kappa)$ and κ are being treated as continuous. Now introduce the mode count density function $n(\zeta, ka)$, defined as the ζ-derivative of the normalized mode count $N(\kappa)/N(k)$ for a fixed value of ka: thus

$$n(\zeta, ka) d\zeta = \frac{dN(\kappa)}{N(k)}, \quad \text{with} \quad \int_0^1 n(\zeta) d\zeta = 1, \tag{38}$$

where $\zeta = \kappa/k$ is the cut-on ratio introduced earlier. In the high ka limit, the density function may be replaced by the asymptotic expression (cf. Ref. 12)

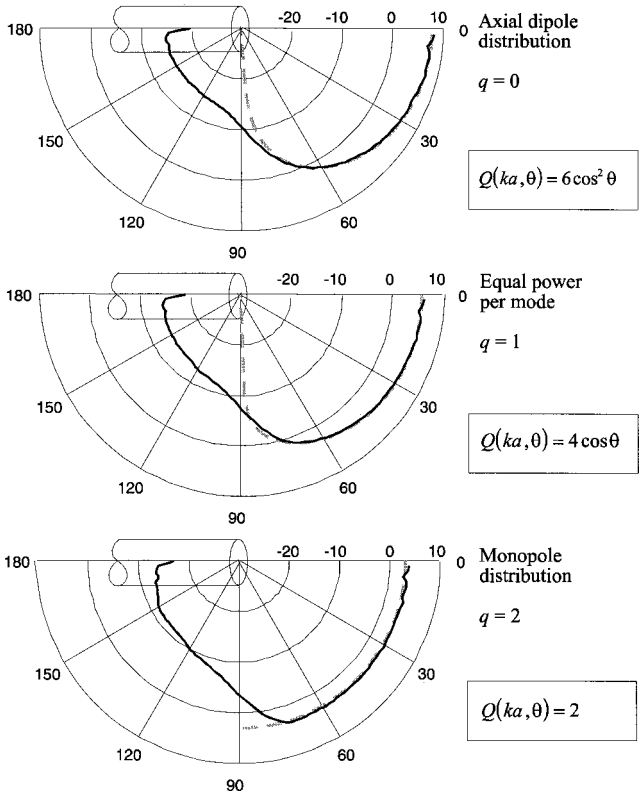

FIG. 13. Comparison of the numerically computed variation of Q with θ at $ka = 35$ with high-frequency asymptotic values (dashed line), for the three source models $q = 0$, 1, and 2.

$$n(\zeta, ka) \approx 2\zeta, \quad ka \to \infty. \tag{39}$$

In terms of the angle θ, the parameters ζ and α are equivalent to $\sin\theta$ and $\cos\theta$, respectively, and Eq. (37) leads to the following distribution of incident in-duct sound power with respect to $\cos\theta$:

$$dW \propto (\cos\theta)^{2-q} \, d(\cos\theta), \quad ka \to \infty. \tag{40}$$

In the absence of reflections, the transmitted and radiated sound power are equal, and since $dW \propto p_f^2 \, d(\cos\theta)$, Eq. (40) identifies the high-frequency far-field directivity of mean squared pressure as

$$p_f^2(ka, \theta) \propto \cos^{2-q}\theta \quad (0 \leqslant \theta \leqslant \pi/2, \ \ ka \to \infty). \tag{41}$$

Evaluating Eq. (41) for $q = 1$ yields exact agreement with the far-field directivity function predicted by Rice for equal power per mode,[5] although Rice's work was based on a different radiation model (the flanged-duct Kirchhoff directivity functions[7]). For $q = 2$, the radiated field due to the monopoles is omnidirectional; while for $q = 0$, the radiated field due to the axial dipoles is the well-known free-field dipole radiation pattern. The last two radiation patterns are the same as if the duct were absent.

Finally, substituting Eq. (41) into Eq. (23) for $Q(ka, \theta)$ and confining the integration to the forward arc ($0 \leqslant \theta \leqslant \pi/2$) yields the general, high ka asymptotic result

$$Q(ka, \theta) \approx Q_\infty(\theta) = 2(3-q)\cos^{2-q}\theta \quad (0 \leqslant \theta \leqslant \pi/2, \ \ ka \to \infty). \tag{42}$$

In Fig. 13 the asymptotic expression above, evaluated for the

three source models at $ka=35$, is compared with the exact $Q(ka,\theta)$ obtained by summing all the modes according to Eq. (23). At this value of ka, Fig. 13 indicates agreement between the exact results (in which about 160 modal terms are summed) and their high ka approximation, to within a fraction of 1 dB for values of θ less than about 70°. Beyond 70°, the agreement breaks down since the sound field is dominated by modes near cutoff, and these modes violate the assumption of no energy reflection which is implicit in the high-frequency model (cf. Fig. 3).

VIII. SENSITIVITY OF Q TO THE SOURCE MODEL INDEX q

It is interesting to note that over the entire ka range and for any angle in the forward arc from 20° to 60°, the values of $Q(ka,\theta)$ for the three source models ($q=0$, 1, and 2) differ by less than 6 dB (see Figs. 4–7 earlier). The rear-arc calculations show that the same is true for angles of 120° and greater (see Figs. 8–11). This behavior suggests that an average value of $Q(ka,\theta)$—obtained from the results for $q=0$, 1, and 2—may be applied as a first approximation at these angles to any ducted source which conforms to Eq. (8), with the only restriction on q being that $0\leqslant q\leqslant 2$.

A measure, ϵ_Q, of the spread in the values of Q across the three source models $q=0$, 1, and 2 is defined by Eq. (43) below:

$$\epsilon_Q(ka,\theta)=10\log_{10}\frac{Q(ka,\theta)|_{q=2}}{Q(ka,\theta)|_{q=0}}. \tag{43}$$

The justification for Eq. (43) as a suitable measure of variability is that values of Q for $q=1$, corresponding to equal incident power per mode, almost always lie between those for $q=0$ and $q=2$ (see Figs. 4–11). The exceptions occur between angles $\cos^{-1}\frac{2}{3}$ and $\cos^{-1}\frac{1}{2}$ (i.e., 48° and 60°, respectively), where the maximum deviation between the three Q values does not exceed 1.2 dB. The high-frequency asymptotic behavior of ϵ_Q in the forward arc, not too close to the sideline direction, is obtained by substituting the asymptotic expression Eq. (42) into Eq. (43) to give

$$\epsilon_Q(ka,\theta)=-10\log_{10}(3\cos^2\theta)\quad(0\leqslant\theta\leqslant\pi/2,\ ka\to\infty). \tag{44}$$

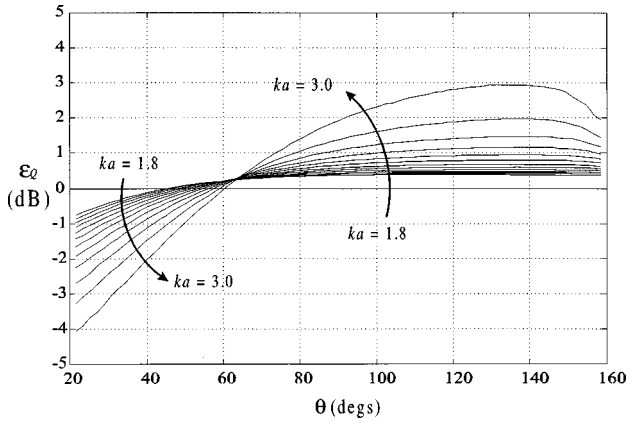

FIG. 14. Plot of the spread parameter ϵ_Q defined by Eq. (43) versus angle θ for $ka=1.8(0.1)3.0$.

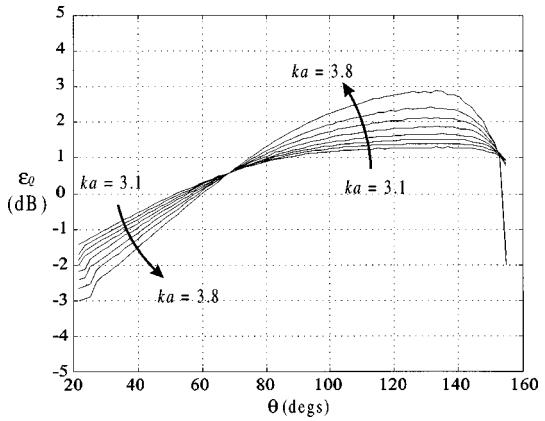

FIG. 15. Plot of the spread parameter ϵ_Q defined by Eq. (43) versus angle θ for $ka=3.1(0.1)3.8$.

The spread parameter ϵ_Q defined by Eq. (43) has been computed exactly, by direct modal summation, for three sets of ka values: $ka=1.9$ (0.1) 3.0; $ka=3.1$ (0.1) 3.8; and $ka=4$, 8, 16, 32, 80. The results are plotted in Figs. 14, 15, and 16, respectively. Also shown, as a dashed line in Fig. 16, is the high-frequency asymptotic prediction of Eq. (44).

Figure 14 spans the frequency range between the (1,0) and (2,0) mode cutoff points: note that at θ=20° the spread $|\epsilon_Q|$ is greatest at $ka=1.9$, and decreases monotonically up to $ka=3.0$, whereas at θ=120° the trend is reversed. A similar—although less pronounced—trend is observed in Fig. 15, which spans the range between the (2,0) and (0,1) mode cutoff points. In both cases the family of curves ''pivots'' about an angle close to 60°; at this angle the spread in directivity index, $|\epsilon_Q|$, between the $q=0$ and $q=2$ source models is minimal. The same ''pivoting'' phenomenon may be seen in Fig. 16 at higher frequencies: here all the curves pass through 0 dB within a few degrees of the high ka asymptote, Eq. (44), which goes to zero at the angle $\theta=\cos^{-1}(1/\sqrt{3})\approx 55°$. At this angle Eq. (42) predicts $L_Q=3$ dB for $q=0$ and 2, and 3.6 dB for $q=1$.

The sensitivity of $Q(ka,\theta)$ to the in-duct modal weighting, for the family of weighting functions specified by Eq. (8), is therefore a minimum around θ=55°. This conclusion has practical implications for sound power estimation. It suggests that a single measurement of far-field pressure at

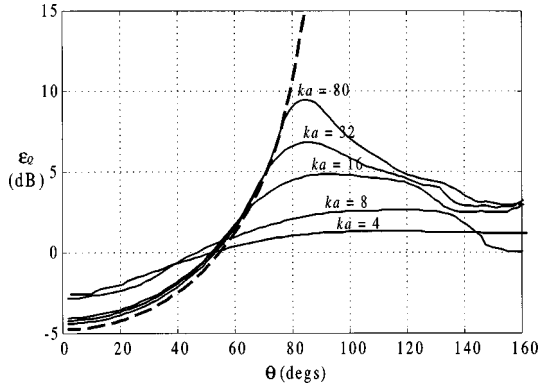

FIG. 16. Plot of the spread parameter ϵ_Q defined by Eq. (43) versus angle θ, for ka values from 4 to 80. Dashed curve indicates the high-frequency asymptotic prediction, $\epsilon_Q=-10\log_{10}3\cos^2\theta$.

$\theta=55°$ can be used to obtain an approximation of the sound power, even if the exact source type is unknown. Figure 16 clearly identifies the angle of 55° to the duct axis as the best single position to measure sound pressure for the purpose of inferring radiated sound power, when the source characteristics are uncertain. Measurement angles close to 90° are the worst for this purpose. Furthermore, rear-arc radiation is likely to be relatively sensitive to departures of the duct edge radius from the idealized knife-edge geometry implicit in the theory of Appendix A. Any attempt to infer sound power radiation from single-point far-field measurements should therefore only be made in the forward arc, as proposed above.

IX. CONCLUSIONS

(1) The sound power transmission coefficient for a single mode, $T_{mn}(ka)$, has been computed for modes incident at the open end of a semi-infinite circular hard-walled duct using theoretical expressions due to Homicz and Lordi.[2] The value of $T_{mn}(ka)$ increases with ka, from zero at the mode cutoff to an asymptotic limit of unity at large ka. A simple approximate expression, Eq. (33), provides an estimate which becomes increasingly accurate at high frequencies.

(2) A generalized multimode excitation model has been used to compute the directivity factor $Q(ka,\theta)$ for far-field radiation from the open end, with three different assumptions for the source:

(1) Equal incident in-duct power per mode, above cutoff;
(2) Excitation by incoherent monopoles uniformly distributed over a duct cross section;
(3) Excitation by incoherent axial dipoles uniformly distributed over a duct cross section.

Values of $Q(ka,\theta)$ are presented for the ka range 0.1 to 60, at angles of 20°(20°)160° from the duct axis.

(3) Modes excited close to cutoff contribute differently to the multimode directivity factor $Q(ka,\theta)$, according to which of the models (1)–(3) is adopted. The incoherent monopole model gives roughly equal prominence to all modes above cutoff, while the other models de-emphasize modes near cutoff.

(4) At large values of ka, the computation of $Q(ka,\theta)$ is made much faster by using the $T_{mn}(ka)$ approximation of Eq. (33). This leads to a simplified expression for $Q(ka,\theta)$, Eq. (34), which has been used in this paper to extend the numerical results beyond $ka=35$. Good agreement is found at the junction of the two methods, since individual-mode errors in $T_{mn}(ka)$ tend to cancel.

(5) At angles deep into the rear arc ($\theta>100°$), the multimode directivity factor varies asymptotically with frequency as $Q(ka,\theta)\propto(ka)^{-1}$ $(ka\to\infty)$.

(6) In the forward arc, at angles of 60° or less to the axis, $Q(ka,\theta)$ approaches a high-frequency asymptotic limit, $Q_\infty(\theta)$, which depends on the modal power weighting as well as the angle. Equation (42) provides a simple analytical expression for this limit; it is obtained by neglecting reflections and diffraction at the duct termination. The approximation is equivalent, for the monopole and axial-dipole source models, to removing the duct and allowing the source distribution to radiate into the free field.

(7) At $ka=35$, the asymptotic expression of Eq. (42) for $Q(ka,\theta)$ is within 1 dB of the exact result, for each of the source models described above, and for angles up to about 70° from the duct axis. Beyond this angle the agreement breaks down; the sound field in the range $70°<\theta<90°$ is dominated by modes near cutoff, whose reflection at the open end is not allowed for in Eq. (42).

(8) The rear-arc behavior of $Q(ka,\theta)$ becomes progressively less sensitive to the source model as θ increases toward 180°.

(9) Values of the multimode directivity factor $Q(ka,\theta)$ for the three source model indices $q=0$, 1, and 2 differ by only 0.7 dB at $\theta=55°$, over the entire ka range. At angles close to 90°, on the other hand, the respective values of Q diverge with increasing ka.

ACKNOWLEDGMENTS

The authors would like to express their gratitude to Dr. Homicz, for allowing access to his notes on the derivation of the unflanged duct directivity functions presented in Ref. 2. The contributions of Dr. D.A.K. Hewlett and of M. Evans (Rolls Royce plc, Ansty) are gratefully acknowledged. The authors have also benefited from discussions with Dr. C.J. Chapman.

APPENDIX A: MODAL DIRECTIVITY FUNCTION OF FAR-FIELD RADIATION FROM A SEMI-INFINITE, HARD-WALLED CIRCULAR UNFLANGED DUCT

This Appendix is a summary of the results presented by Homicz and Lordi[2] for computing the magnitude of the far-field pressure $|p_{mn,f}(k,a,\theta)|$ radiated from a semi-infinite, hard-walled circular unflanged duct. A single incident mode arriving at the duct termination,

$$p^+_{mn}(r,\phi,z,t)=P_{mn}e^{j(\omega t-m\phi-k\alpha_{mn}z)}J_m(\kappa_{mn}r), \tag{A1}$$

with α_{mn} real (i.e., above cutoff), radiates far-field acoustic pressure

$$p_{mn,f}(R,\theta,\phi,t)=\frac{P_{mn}}{R}J_m(\kappa_{mn}a)e^{j(\omega t-m\phi-kR)}D_{mn}(k,a,\theta). \tag{A2}$$

Only the magnitude of the directivity function D_{mn} is of interest here; it is given by

$$\begin{aligned}|D_{mn}(k,a,\theta)| &= \left|\frac{J_m(\kappa_{mn}a)\alpha_{mn}}{\alpha_{mn}-\cos\theta}\right| \\ &\times\sqrt{\frac{(\kappa_{mn}a)^2-m^2}{\pi\kappa^2_{mn}}}\sin[\Omega(ka\sin\theta)]\prod_{s=0}^{n_0}{}'\frac{\alpha_{ms}+\alpha_{mn}}{\alpha_{ms}-\alpha_{mn}} \\ &\times\sqrt{\prod_{q=0}^{n_0}\frac{\alpha_{mq}-\cos\theta}{\alpha_{mq}+\cos\theta}} \\ &\times\exp[S(\alpha_{mn},ka)-S(\cos\theta,ka)],\end{aligned} \tag{A3}$$

where the integer n_0 denotes the highest radial mode order that can propagate with azimuthal index m, and the prime on the first product means that $s=n$ is excluded. [In our notation, the zero index $(n=0)$ denotes the mode of lowest radial order for each m, and modes are numbered 0,1,2, . . . in ascending sequence of transverse wavenumber.]

The functions Ω and S (note that our S is redefined to simplify the notation) are given by

$$\Omega(\nu)=\tan^{-1}\frac{Y'_m(\nu)}{J'_m(\nu)}\mp\frac{\pi}{2},\quad \left.\begin{cases}-, & m>0\\ +, & m=0\end{cases}\right\}, \tag{A4}$$

$$S(\eta,ka)=\frac{1}{2\pi}\int_{-1}^{1}\frac{\Omega(ka\sqrt{1-\xi^2})}{\xi-\eta}\,d\xi, \tag{A5}$$

where the integral over ξ is to be evaluated in the principal value sense. In Eq. (A4), the function Ω represents the phase of the Hankel function derivative; negative m values are not required in the numerical calculation. An important condition on Ω, not stated explicitly but essential to computing D, is that it is a continuous function and must consequently be unwrapped for phase: when the argument equals the dimensionless transverse wave number—which means that $Y'_m(\nu)/J'_m(\nu)$ becomes singular—the function Ω is given by

$$\Omega(\nu_{mn})=n\pi \quad (\text{where } \nu_{mn}=\kappa_{mn}a;\ \text{note that } \nu_{00}=0). \tag{A6}$$

APPENDIX B: EXTENSION OF THE SINGLE-MODE TRANSFER FUNCTION ANALYSIS TO INCLUDE MEAN FLOW

Extension of the $H_{mn}(ka,\theta)$ result in Appendix A to include mean flow effects, at either the inlet or exhaust end of a duct, would be a useful generalization. A complicating factor is that the two flow directions must be considered separately, because the mean flow fields are quite different in general; the exception is when the duct is immersed in a uniform flow parallel to its axis. A further complication arises from the shedding of vorticity fluctuations at a trailing edge, which occurs when incident sound is scattered by the edge in the presence of flow. This invalidates any attempt to infer $H_{mn}(ka,\theta)$ for a duct outlet based on applying a transformation to the zero-flow result; compare Section 6 of Ref. 2. At a leading edge, however, no vortex shedding occurs provided the mean flow does not separate, and this is the one case where the zero-flow $H_{mn}(ka,\theta)$ expression can easily be generalized.[2]

A detailed discussion of the trailing-edge scattering problem in a uniform mean flow has been given by Rienstra[13] for an axisymmetric duct; it would therefore be possible to calculate uniform-flow values of $H_{mn}(ka,\theta)$ for a cylindrical duct, based on Ref. 2 for the inlet case and on Ref. 13 for the exhaust case, with the flow Mach number M as a parameter. However, modeling more realistic inlet and exhaust flows is problematic: the most promising option appears to be to represent the exhaust jet by a cylindrical vortex sheet, following Munt[14,15] and Cargill.[16] Their predictions of the plane wave end reflection coefficient on this basis have been shown by Peters *et al.*[17] to agree well with experimental data. Extension of Refs. 14–16 to include higher-order azimuthal modes would be a first step toward a multimode description of radiation from flow ducts. The resulting transfer function, $H_{mn}(ka,\theta,M>0)$, could then be combined with a generalized version of the modal weighting models in Sec. II B; it is a straightforward matter to extend the latter to include a mean flow Mach number M in the duct, based on the theory given in Ref. 18.

[1] Details are given in Sec. III, Eqs. (21), (22), and (24).
[2] G. F. Homicz and J. A. Lordi, ''A note on the radiative directivity patterns of duct acoustic modes,'' J. Sound Vib. **41**, 283–290 (1975).
[3] H. Levine and J. Schwinger, ''On the radiation of sound from an unflanged circular pipe,'' Phys. Rev. **73**, 383–406 (1948).
[4] L. A. Weinstein, *The Theory of Diffraction and the Factorization Method* (Golem, Boulder, CO, 1969).
[5] E. J. Rice, ''Multimodal far-field acoustic radiation pattern using mode cutoff ratio,'' AIAA J. **16**, 906–911 (1978).
[6] A. Snakowska, ''On the principle of equipartition of energy in the sound field inside and outside a circular duct,'' Acustica **79**, 155–160 (1993).
[7] J. M. Tyler and T. G. Sofrin, ''Axial flow compressor noise studies,'' SAE Transactions **70**, 309–332 (1962).
[8] C. L. Morfey, ''Rotating pressure patterns in ducts: their generation and transmission,'' J. Sound Vib. **1**, 60–87 (1964).
[9] One could also determine T_{mn} by calculating the matrix of modal reflection coefficients at the duct termination, $R_{nl}(ka,m)$, and using the relation $T_{mn}=1-\Sigma_{l=0}^{\infty}|R_{nl}(ka,m)|^2$. Note that for any given azimuthal order m, the reflected modal pressure amplitudes b_{ml} are related to the incident modal amplitudes a_{mn} by $b_{ml}=a_{mn}R_{nl}$. However, calculation of end reflection coefficients is not considered in this paper.
[10] P. M. Morse and K. U. Ingard, *Theoretical Acoustics*, 2nd ed. (Princeton University Press, Princeton, NJ, 1986), pp. 450–453.
[11] For a more detailed discussion of ''duct transparency'' conditions, see C. J. Chapman, J. Fluid Mech. **313**, 367–380 (1996).
[12] E. J. Rice, ''Modal density function and number of propagating modes in ducts,'' NASA TM X-73539 (1976).
[13] S. W. Rienstra, ''Acoustic radiation from a semi-infinite annular duct in a uniform subsonic mean flow,'' J. Sound Vib. **94**, 267–288 (1984).
[14] R. M. Munt, ''The interaction of sound with a subsonic jet issuing from a semi-infinite cylindrical pipe,'' J. Fluid Mech. **83**, 609–640 (1977).
[15] R. M. Munt, ''Acoustic transmission properties of a jet pipe with subsonic jet flow: I, the cold jet reflection coefficient,'' J. Sound Vib. **142**, 413–436 (1990).
[16] A. M. Cargill, ''Low frequency acoustic radiation from a jet pipe—a second order theory,'' J. Sound Vib. **83**, 339–354 (1982).
[17] M. C. A. M. Peters, A. Hirschberg, A. J. Reijnen, and A. P. J. Wijnands, ''Damping and reflection coefficient measurements for an open pipe at low Mach and low Helmholtz numbers,'' J. Fluid Mech. **256**, 499–534 (1993).
[18] C. L. Morfey, ''Sound transmission and generation in ducts with flow,'' J. Sound Vib. **14**, 37–55 (1971).

Dispersion of longitudinal waves propagating in liquid-filled cylindrical shells

Hegeon Kwun, Keith A. Bartels, and Christopher Dynes
Southwest Research Institute, 6220 Culebra Road, San Antonio, Texas 78238-5166

(Received 15 May 1998; accepted for publication 1 February 1999)

The dispersion of the first two longitudinal wave modes, $L(0,1)$ and $L(0,2)$, was experimentally investigated for a cylindrical shell (such as a pipe or tube) that was completely filled with a liquid. It was observed that the presence of a liquid inside the cylinder dramatically alters the dispersion curve for the $L(0,2)$ mode by dividing (or branching) the curve into approximately equally spaced regions separated by cutoff-type behavior. This branching was attributed to coupling between the unperturbed $L(0,2)$ mode in the shell and the unperturbed longitudinal modes in a liquid cylinder with rigid boundaries, $L_L(0,2N)$, where N is an integer. The physical mechanism for the mode coupling was determined to be radial resonances in the combined liquid/pipe system. In time domain, the liquid effects on the dispersion are manifested as a long-duration signal or a series of short-duration pulses, depending on the pulse length of the transmitted signal relative to the reciprocal of the frequency interval between branching. © *1999 Acoustical Society of America.* [S0001-4966(99)01405-8]

PACS numbers: 43.20.Mv, 43.40.At [CBB]

INTRODUCTION

In previous publications,[1,2] we reported on a simple method for experimentally observing dispersion characteristics of elastic longitudinal wave modes in structures such as cylindrical shells over a relatively wide frequency range (up to approximately 350 kHz). The method involved (1) transmitting a short-duration, elastic-wave pulse into the material using a device called a ''magnetostrictive sensor (MsS),'' (2) detecting the transient wave forms at a different position along the material using another MsS, (3) performing a time–frequency transformation of the detected signals, and (4) analyzing the time evolution of the spectral components.

Using this method, we experimentally investigated the effects of liquid on the dispersion properties of the first two longitudinal wave modes in a cylindrical shell. The investigation was spurred by a need to understand some effects that occurred while applying MsS to the nondestructive evaluation (NDE) of piping in processing plants such as refineries and chemical plants.[3,4] In this application, a longitudinal-mode pulse is launched at a location along the length of a pipe. Signals reflected from defects such as corrosion or cracks are detected from the same location where the initial wave was transmitted. Since these guided waves fill the whole pipewall cross sections, and they can propagate a long distance along the pipe, this technique has offered a very efficient and fast means of inspecting a long segment of piping (typically, more than 30 meters). To apply this technique in on-line processing plants, where the majority of pipes carries some type of liquid product, it was necessary to understand the effects that liquids have on the dispersion properties of the longitudinal wave modes in a cylindrical shell. Most of the previous work on wave propagation in cylindrical shells that has been reported in the literature by other researchers deals with empty shells, and only a very limited number of reports considered liquid-filled cylindrical shells.[5,6]

This paper describes the experimental arrangement used in the investigation and the data obtained from pipe samples before and after filling them with water, as well as data obtained from liquid-filled pipes in a refinery. The results are then discussed and compared with theory.

I. EXPERIMENTAL ARRANGEMENT

A general description of the MsS instrumentation setup and its operational procedures has been given in previous papers[1–4] along with a description of the technical background of MsS technology and the method for observing the dispersion properties of elastic waves. Therefore, no additional description is given in this paper.

The primary sample used for the investigation was a nominal 4.5-in. (114.3-mm)-outside diameter (OD), schedule 80 (0.337-in. or 8.6-mm wall thickness) seam-welded carbon steel pipe. The sample was approximately 168 ft (55.44 m) long, and was made by welding four 42-ft (13.86-m)-long pipe joints. To allow for filling and draining the pipe, the sample was flanged on both ends with suitable couplings for letting water and air in and out. The sample was placed on wooden support beams spaced at approximately 10 ft (3 cm) along the sample length.

A transmitting and a receiving MsS were placed at two locations along the pipe length separated by approximately 11 meters. MsS data were then collected before and after filling the pipe with water so that a direct comparison between the two experiments could be made.

In addition, data were acquired from other pipes in the laboratory as well as from operating plants. These pipes ranged in size from 3.5 to 16 in. (88.9 to 406.4 mm) in OD and contained liquids such as water, diesel, gasoline, and olefins.

II. RESULTS AND DISCUSSION

A. Data from a 4.5-in.-OD, schedule 80, water-filled pipe sample

Figure 1(a) and (b) show the MsS signals detected from the 4.5-in.-OD, schedule 80 (0.337-in. or 8.6-mm wall thick-

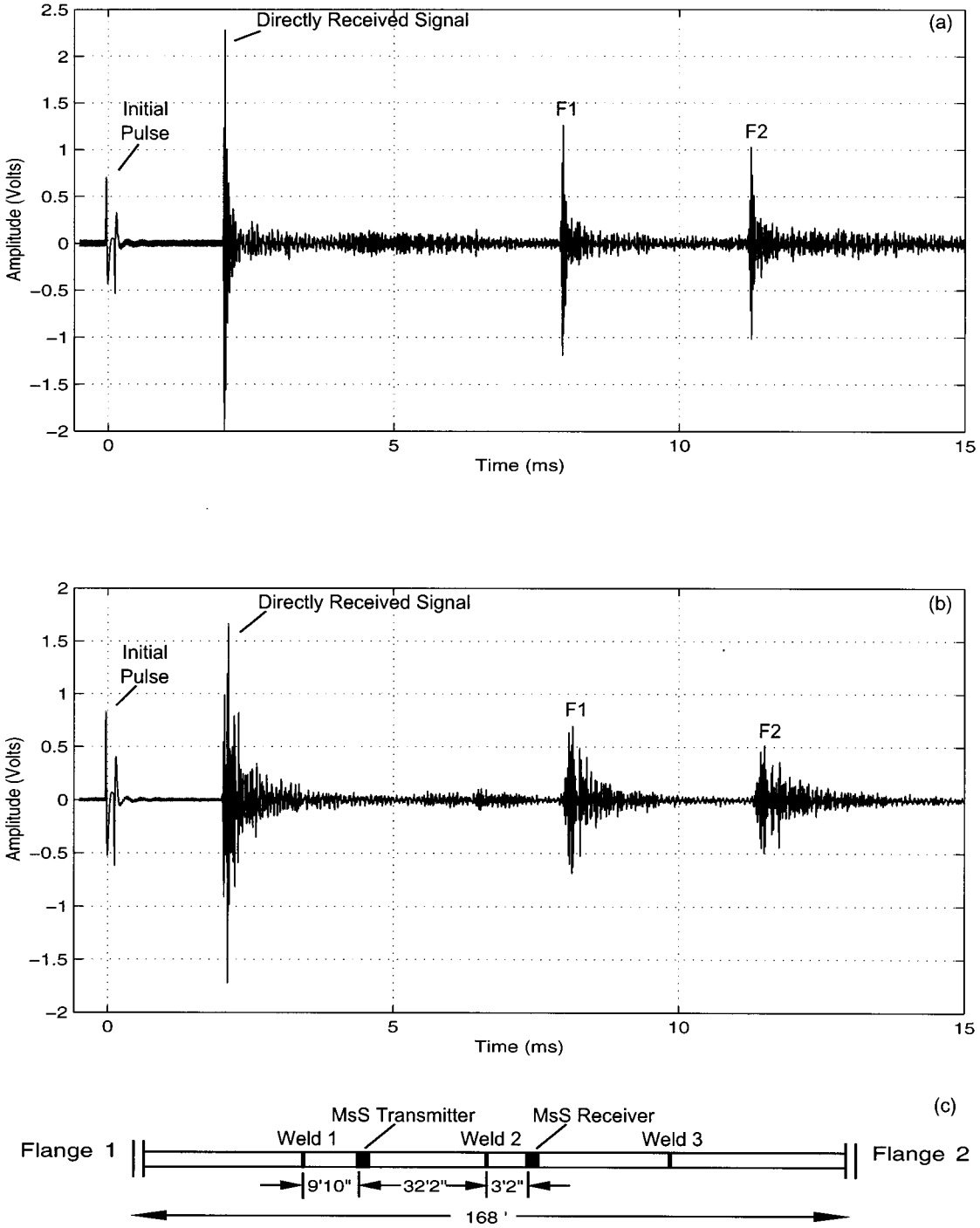

FIG. 1. Detected signals from a 4.5-in. (114.3-mm)-OD, schedule 80, steel pipe sample when the pipe was filled with air (a) and with water (b). The configuration of the pipe sample is shown in (c).

ness), pipe sample filled with air and water, respectively. The configuration of the pipe sample and MsS transmitter and receiver locations used for data acquisition are illustrated in Fig. 1(c). The first signal in these figures is the initial pulse (which was a single cycle of 60-kHz sinusoidal pulse) applied to the transmitting MsS that leaked electrically to the receiver side of the instrumentation. The elastic wave pulse generated in the pipewall by the transmitting MsS propagated in both directions along the pipe. The second signal in the data shows the wave that traveled directly from the transmitting MsS to the receiving MsS. The third signal (indicated as $F1$) shows the wave that traveled to flange 1, was reflected, and traveled back to the receiving MsS. The fourth signal (indicated as $F2$) shows the wave that traveled to flange 2, was reflected, and traveled back to the receiving MsS.

The two sets of data in Fig. 1 apparently showed no significant difference except that, in the water-filled pipe, the attenuation was somewhat higher (increased from 0.13 dB/m in the air-filled pipe to 0.22 dB/m), the velocity of wave propagation was slightly lower (decreased from 5.36×10^5 cm/s in the air-filled pipe to 5.31×10^5 cm/s), and the

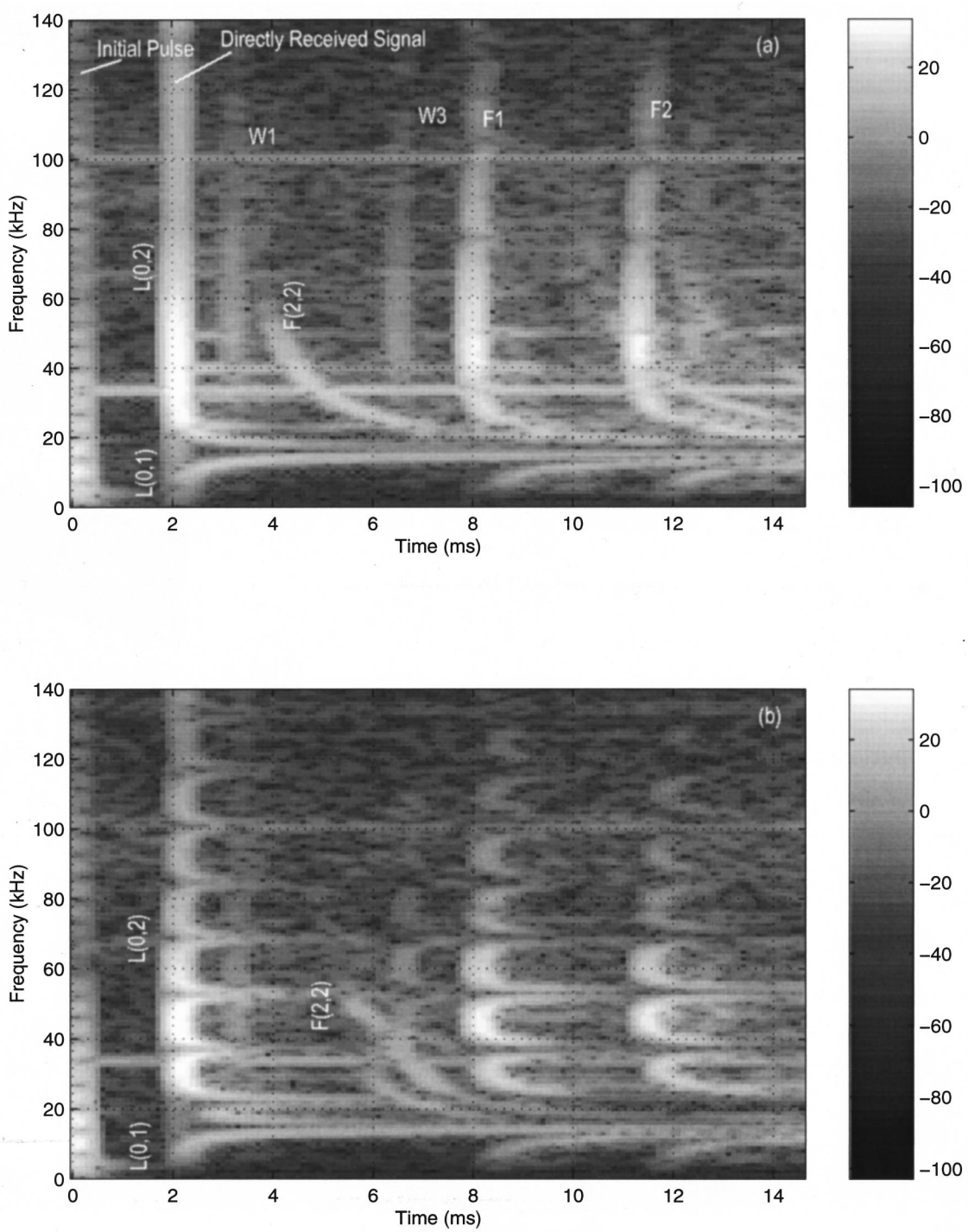

FIG. 2. A time–frequency representation of the data given in Fig. 1(a) and (b), respectively. The gray scale is in dB.

signals were longer in duration. As will be shown below, the water in the pipe dramatically alters the dispersion properties of the $L(0,2)$ mode and the spectral content of the signals. These spectral effects, however, were not easily recognizable in the time-amplitude data shown in Fig. 1.

The data in Fig. 1(a) and (b) were analyzed using a short-time Fourier transform[7] (STFT). The logarithms of the absolute values of the STFT are shown as gray-scale images in Fig. 2(a) and (b), respectively. A 0.9-ms Hanning window was used in the computations of the STFT. From the STFT images, the time evolution of each frequency component of the detected signals (up to approximately 140 kHz) can be easily seen. The STFT presentation[2] (discussed in a previous paper) gives the arrival time of each frequency component and, therefore, gives a direct portrayal of the group velocity as a function of frequency. The dispersion properties of the first two longitudinal wave modes, $L(0,1)$ and $L(0,2)$, can be observed in the STFT along with those of a flexural mode which was identified as $F(2,2)$. As reported previously,[1,2] Fig. 2(a) shows that the elongation of the signals (or namely, their persistence over a long period of time) in Fig. 1(a) was due to the dispersion of the $L(0,1)$ and $L(0,2)$ modes near

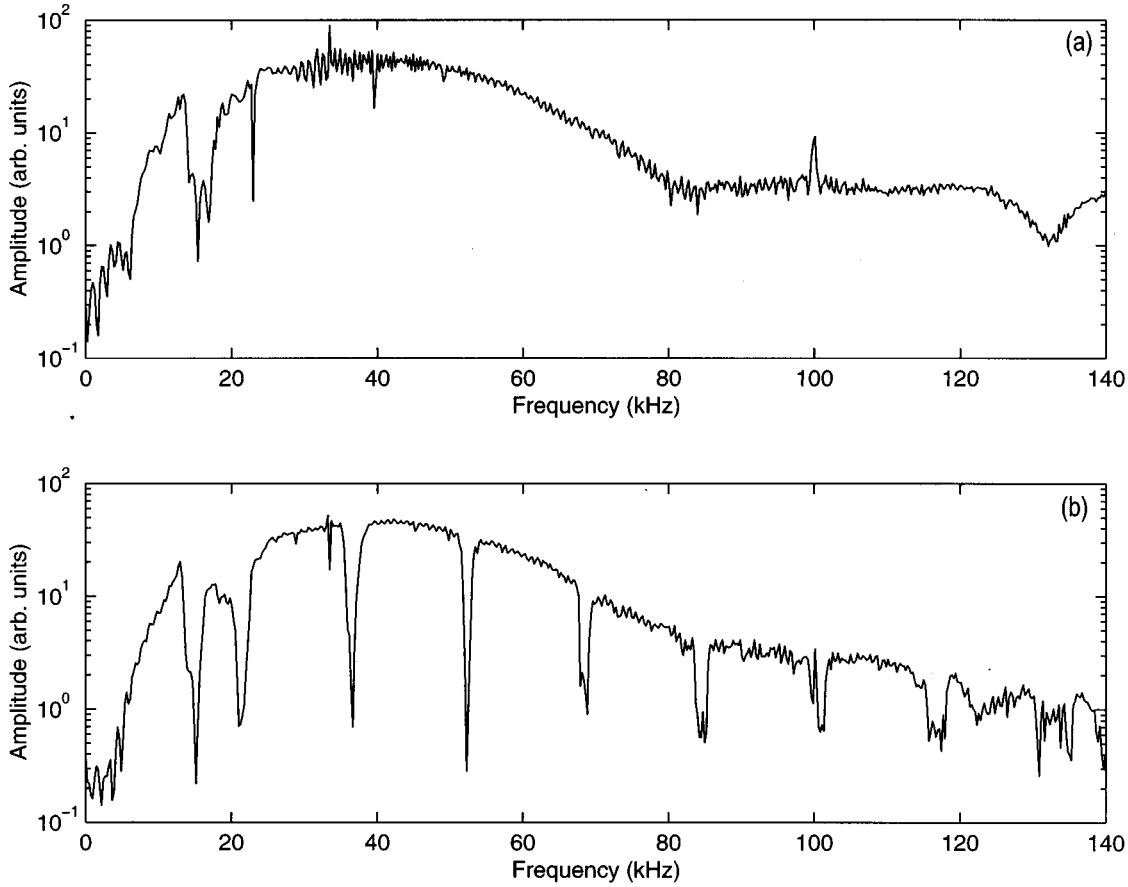

FIG. 3. FFT data of the signals over an approximately 3-ms time span around the directly received signal in Fig. 1(a) and (b), respectively.

their cutoff frequencies. (Constant frequencies such as at 35 and 100 KHz that occur over all times in Fig. 2 are electromagnetic interference signals picked up by the receiver coils from communication towers in the area.) The mode designation in this paper follows the notations used by Meitzler[8] and Zemanek,[9] which appear to be used as a standard system in the literature. The first index in this notation, starting from 0, refers to the circumferential order of the mode. All longitudinal modes are of 0 circumferential order because their displacements are constant around the circumference. The second index, consecutively numbered from 1, refers to the order in which a mode occurs counting from the mode that propagates at 0 frequency. For comparison purposes, the designation used for modes in the air-filled pipe is also used for modes in the water-filled pipe in this paper.

When the STFTs of Fig. 2(a) and (b) were compared, the effects of water in the pipe on the dispersion properties of longitudinal wave modes in the shell could be clearly recognized. The most dramatic change caused by the water occurred in the dispersion curve for the $L(0,2)$ mode, which branched into approximately equally spaced regions, separated by cutoff-type behavior. In addition to the branching, the group velocity of the unperturbed section of $L(0,2)$ mode in each branch was somewhat decreased; for example, at 45 kHz from approximately 5.36 to 5.31×10^5 cm/s and at 108 kHz from approximately 5.28 to 5.08×10^5 cm/s. This slowdown in velocity was already noted in the data in Fig. 1(a) and (b). Additionally, a branching and slowdown in velocity also occurred for $F(2,2)$, whereas no noticeable change was observable in the dispersion curve for the $L(0,1)$ mode. [In addition to the prominent signals directly received and reflected from $F1$ and $F2$, the signals reflected from welds 1 and 3 ($W1$ and $W3$), that were difficult to recognize in Fig. 1(a) and (b), are also visible in Fig. 2(a) and (b). STFT data processing is thus utilized in NDE applications to enhance the detectability of signals as well as to identify their wave modes.]

The cutoff frequencies for $L(0,1)$[10] and $L(0,2)$ modes together with the frequencies at which branching occurs (these will be called ''branching frequencies'' in the rest of this paper) could be determined by manually locating their positions in the image data in Fig. 2(a) and (b). The cutoff frequencies determined by this process may be somewhat inaccurate because of the difficulty in accurately reading the precise shade of the gray scale. To more accurately determine the cutoff and the branching frequencies, an alternative method was used that involved (1) windowing the directly received signal (the first signal) in Fig. 1(a) and (b) over a span of approximately 3 ms and (2) performing a discrete Fourier transformation (DFT) on the windowed data. Figure 3(a) and (b) show the magnitude of the DFT for the case of pipes filled with air and water, respectively. The dips in the DFT are those caused by the cutoff behavior that is observed in the dispersion curves. The cutoff and the branching frequencies could be determined more accurately from these dips than was possible from the STFT images in Fig. 2. The other spikes and dips in Fig. 3(a) are due to electromagnetic interference noise. The experimentally determined dispersion

TABLE I. A comparison of experimentally determined and calculated wave dispersion properties in a 4.5-in. (114.3-mm)-OD, 0.337-in. (8.6-mm)-wall, carbon steel pipe.

	Group velocity 10^5 cm/s				Cutoff frequencies (kHz)				Branching frequencies in $L(0,2)$ (kHz) Due to water							
	45 kHz		108 kHz		$L(0,1)$		$L(0,2)$									
	air	water	air	water	air	water	air	water	1st	2nd	3rd	4th	5th	6th	7th	8th
Experimental	5.36	5.31	5.28	5.08	14.5	13.8	17.1	15.4	21.3	36.4	52.3	68.3	84.5	100.9	116.6	132.9
Calculated	5.39	5.32	5.31	5.18[a]	15.1	14.5	16.5	14.9	21.3	36.1	51.6	67.5	83.2	99.1	115.0	131.0

[a]At 105 kHz, where the velocity peaks in that branch.

properties are tabulated in Table I. In addition to the branching and the slowing of the group velocity of the $L(0,2)$ mode, the cutoff frequency of the $L(0,2)$ mode was decreased somewhat when the pipe was filled with water.

For comparison with the experimental data in Fig. 2(a) and (b), calculated dispersion curves of the group velocity of the two longitudinal modes in the pipe are shown in Fig. 4(a) and (b) for the cases where the pipe is in a vacuum (which, for all practical purposes, should be the same as in air) and the pipe is filled with water, respectively. The curves found below the curves for $L(0,2)$ in Fig. 4(b) are curves for the longitudinal modes in the water cylinder, $L_L(0,2N)$ where N is an integer, near their respective cutoff frequencies. (The curves shown in Fig. 4(b) are for $N=1$ through 8. The notations used here are similar to those used for longitudinal modes in cylindrical shells except that the second index refers to the number of ''half wavelengths'' over the diameter of the liquid cylinder.[11]) These calculations were performed using the general-purpose software package called DISPERSE,[12] developed by Imperial College, University of London. The dispersion curves in these figures were computed using the automated tracing routine available in this software with the default material constants (for example, in steel, 7.932 g/cm^3 for density, 5.96×10^5 cm/s for compressional velocity, and 3.26×10^5 cm/s for shear velocity; in water, 1.0 g/cm^3 for density and 1.483×10^5 cm/s for compressional velocity). A detailed description of the theoretical model employed in the program can be found in the user's manual[13] and in other publications of the Imperial College group.[14]

The calculated dispersion curves showed all the main features of the experimentally observed liquid effects, including the branching and the slowing of the group velocity of the $L(0,2)$ mode. The quantitative agreement between the experimental and calculated dispersion properties was also excellent, as shown in Table I. The small discrepancies between the calculated and experimental data can be attributed to the use of the default material constants for computation instead of the actual material constants of the samples. Since the purpose of the experiment was not to test the accuracy of DISPERSE but to understand the general effects of the liquid on the dispersion properties, no attempt was made to measure material constants of the actual pipe sample for use in computation.

The branching of the $L(0,2)$ in Fig. 4(b) occurred at frequencies where the phase velocity of the unperturbed $L(0,2)$ mode in the pipewall (or shell) coincided with that of the unperturbed $L_L(0,2N)$ modes of the water cylinder in the pipe.[13] It is also known that when the phase velocity curves of two modes intersect, a mode coupling takes place at the frequency of the intersection.[8] This shows that the observed branching in $L(0,2)$ mode is a result of mode coupling between the unperturbed $L(0,2)$ and $L_L(0,2N)$ modes.

According to the computed results in Fig. 4(b), the group velocity of the perturbed $L(0,2)$ mode at the branching frequencies does not go to zero but reaches a minimum. In comparison, the group velocity at cutoff frequencies goes to zero. The presence of this minimum could not be confirmed from the experimental data because of the lack of signal components at the branching frequencies. Also, the computed data show that the group velocity of $L_L(0,2N)$ modes undergoes a spike-like change at the branching frequencies. It would be of scientific interest to confirm this behavior of $L_L(0,2N)$ modes experimentally. The data in Fig. 4(b) suggest that the coupling of two modes pulls down the group velocity dispersion curve of one mode and pulls up that of the other mode.

To gain additional insight into the effects of liquid on wave dispersion properties in cylindrical shells, other existing theories were reviewed and their implications evaluated.

The cutoff frequencies of the unperturbed $L(0,1)$ and $L(0,2)$ modes in the cylindrical shell are given as $v_0/2\pi b$ and $Kv_p/2\pi b$, respectively,[15] where v_0 and v_p are, respectively, the longitudinal wave velocities in a rod and in a plate at very low frequencies ($v_0<v_p<$ the compressional velocity in the material[16]), K is a constant that is approximately 1 in a relatively thin shell, and b is the mean radius of the cylindrical shell. [Using $v_0=5.15\times10^5$ cm/s and $v_p=5.33\times10^5$ cm/s, the above expressions yield cutoff frequencies of approximately 15.5 and 16.1 kHz for $L(0,1)$ and $L(0,2)$ modes, respectively, which match well with the values given in Table I.]

The unperturbed longitudinal modes in a liquid cylinder with rigid boundaries (water in a pipe belongs to this case) are $L_L(0,0)$ and $L_L(0,2N)$ where N is an integer.[11] The $L_L(0,0)$ mode is nondispersive, and its phase and group velocities are the same as the compressional velocity of a plane wave in the liquid. The $L_L(0,2N)$ modes are dispersive, and their cutoff frequencies, f_N, are given as $v_L j_{1N}/2\pi a$, where v_L is the compressional velocity in the liquid, j_{1N} is a root of the Bessel function $J_1(x)=0$, and a is the radius of the liquid cylinder.[11] The first several values for j_{1N} are 3.8317, 7.0156, 10.1735, 13.3237, 16.4706, etc., for $N=1,2,3,4,5$, etc. With $v_L=1.483\times10^5$ cm/s in water, the corresponding

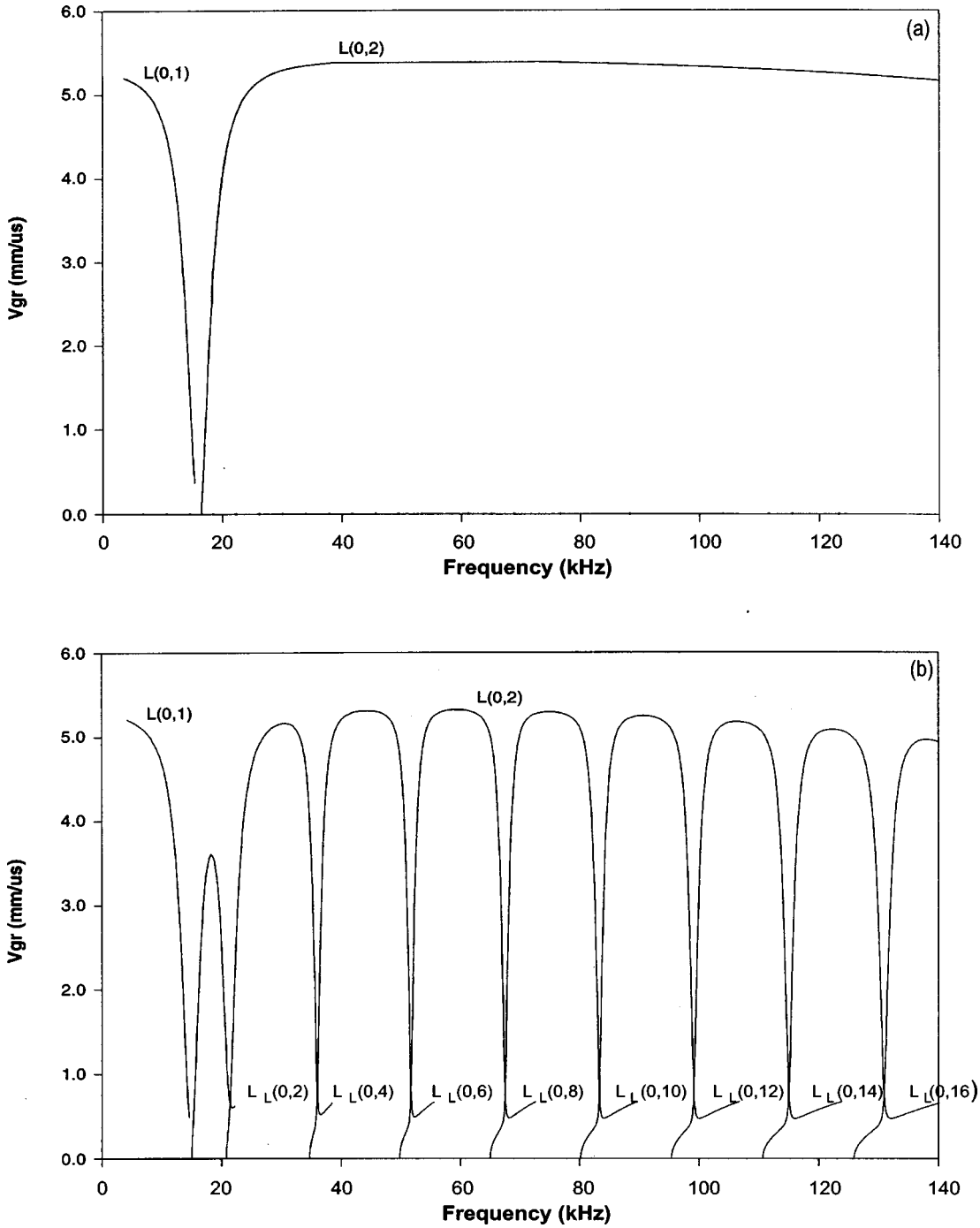

FIG. 4. Calculated dispersion curves for the $L(0,1)$ and $L(0,2)$ modes in a 4.5-in. (114.3 mm)-OD, schedule 80 pipe; (a) when the pipe was filled with air, (b) with water.

f_N in the water cylinder in the pipe sample are 18.62, 34.08, 49.42, 64.72, 80.01 kHz, etc., respectively. The above agrees well with the cutoff frequencies of $L_L(0,2N)$ modes indicated in Fig. 4(b).

The $L_L(0,0)$ mode is nondispersive, and its phase velocity cannot intersect the phase velocity curves of the unperturbed $L(0,1)$ and $L(0,2)$ modes in the pipewall except, perhaps, in the region very close to the cutoff frequency of $L(0,1)$. Therefore, it is not possible to couple the $L_L(0,0)$ mode with the two longitudinal modes in the shell. On the other hand, the $L_L(0,2N)$ modes are dispersive, and their phase velocity curves can intersect with those of $L(0,1)$ and $L(0,2)$ modes in the shell, thus allowing mode coupling. Since this intersection, if it occurs, will take place at a frequency higher than f_N, the corresponding branching frequency will be always higher than f_N, as can be seen in Fig. 4(b). (Over the frequency range investigated, the branching frequency was approximately 6 percent higher than f_N.) In the water-filled pipe sample used in this experiment, $f_{N=1}$ is greater than $Kv_p/2\pi b$, the cutoff frequency of the $L(0,2)$ mode. Consequently, the coupling of $L_L(0,2N)$ modes can only occur with the $L(0,2)$ mode in the shell. This explains the absence of any observable liquid effect on the $L(0,1)$ mode in the experimental data. From the above argument, it

can be deduced that if $av_0/bv_L > 3.8317$, then $f_{N=1}$ is smaller than $v_0/2\pi b$, the cutoff frequency of $L(0,1)$ mode. In this case, the mode coupling between the $L_L(0,2N)$ modes in the liquid cylinder and the $L(0,1)$ mode in the shell can occur, and thus a branching of the $L(0,1)$ mode will take place. It would also be of scientific interest to experimentally confirm this hypothesis using a setup that satisfies the required condition. (The required condition can be satisfied by filling a relatively thin-walled pipe with a liquid, such as methyl or ethyl alcohol, whose velocity is significantly lower than the velocity in water.)

B. Data from other liquid-filled pipes

As mentioned in the introduction, MsS technology has also been applied to the NDE of piping in processing plants such as refineries and chemical plants. During the course of an on-line inspection of pipelines carrying various liquids, a new phenomenon was encountered that was not observed during the experimental investigation described in Sec. II A.

To describe this new phenomenon, data acquired from a nominal 6 5/8-in. (168.3-mm)-OD, schedule 40 (0.28-in. or 7.1-mm wall), seamless carbon steel pipeline carrying diesel fuel are shown in Fig. 5(a), together with their time–frequency representation in Fig. 5(b). The data shown in Fig. 5(a) were taken by following a typical MsS operating procedure used in NDE applications that involves (1) exciting the MsS transmitter with a 2-cycle, 60-kHz pulse, (2) detecting signals reflected from geometric irregularities in the pipeline such as girth welds and corrosion defects with the MsS receiver placed adjacent to the transmitter (called the pulse-echo technique in ultrasonics), and (3) conditioning the detected signals using a 60-kHz bandpass filter with a 30-kHz bandwidth at -3 dB point.

The relatively large amplitude signals in Fig. 5(a) are those reflected from girth welds in the pipeline that were at a distance of approximately 4.37, 13.21, and 25.55 m from the sensor. Normally, long-duration signals such as those shown in Fig. 1(b) are expected because of liquid-induced dispersion. In this case, the signal reflected from each girth weld appeared to consist of a series of short-duration pulses. These pulses were found to be separated by a constant time interval (in this case, approximately 0.117 m). The occurrence of this series of short-duration pulses, initially though to be a new phenomenon, was not observed during the experiments described in Sec. II A.

Despite this different signal pattern, the corresponding time–frequency representation (obtained via a 0.9-ms, Hanning-windowed STFT) plotted in Fig. 5(b) showed no difference in the behavior of the liquid-induced dispersion properties, exhibiting the same type of branching in the $L(0,2)$ mode as that shown in Fig. 2(b). Within the frequency range covered by the signal conditioner used to acquire the data (that is, from approximately 35 to 85 kHz), the branching occurred at 45.2, 53.6, 62.0, 70.7, and 79.3 kHz, respectively. From the calculated values for f_N with 1.28×10^5 cm/s as the compressional wave velocity in diesel fuel, those branching frequencies were identified as those caused by the coupling between the $L(0,2)$ mode in the pipewall and the $L_L(0,2N)$ modes in the diesel for $N=5$ to 9, respectively.

Series of short-duration pulses were also observed in pipes carrying other liquids such as water, olefins, and gasoline whenever the inside diameter (ID) of the pipe was greater than v_L times the pulse length of the signal. In contrast, signals such as those shown in Fig. 1(b) were only observed when the ID of the pipe was less than v_L times the pulse length of the signal. It appeared that the same branching of the dispersion curve could lead to two very different signal patterns, depending on the size of the pipe's ID. Several hypotheses were made about the source of these trailing pulses, and several experiments (described below) were run to test these hypotheses. It was eventually concluded that these trailing pulses were simply a different manifestation in the time domain of the same liquid-induced dispersion described in Sec. II A.

Initially, to investigate the generation of these pulses and to understand their cause, additional tests were conducted in the laboratory using relatively large-sized pipe samples. Figure 6(a) and (b) show the MsS data obtained from a nominal 10 3/4-in. (273.1-mm)-OD, schedule 40 (0.365-in. or 9.3-mm-wall), seam-welded pipe sample which was filled with air and water, respectively. The sample was approximately 6 m long and flanged at both ends. The data were taken with the MsS transmitter and the MsS receiver placed at approximately 1/4 and 1/2 of the length of the pipe and by exciting the MsS transmitter with a pulse consisting of a single cycle from a 60-kHz sinusoid. The first two signals in these plots were, respectively, the initial pulse and the tail end of an electronic gate signal employed to block the initial pulse that was coupled directly to the receiver side of the instrumentation. The third signal was the longitudinal wave mode in the pipewall that traveled 1/4 length of the pipe (from the MsS transmitter location to the MsS receiver location). Since the cutoff frequency of the $L(0,2)$ mode in this pipe sample was low (calculated to be approximately 6.4 kHz), the longitudinal waves generated and detected were almost exclusively $L(0,2)$ mode. The fourth signal in Fig. 6(a) was identified as the $F(2,2)$ wave mode that traveled the same distance as the previous $L(0,2)$ mode signal. The last signal in Fig. 6(a) is the $L(0,2)$ mode that traveled 3/4 of the length of the pipe (from the MsS transmitter location to the nearest flanged end and then back to the MsS receiver location after reflection from the flanged end). Because of the complex interaction of the wave with the flanged end, the last signal showed a complicated signal pattern.

The data in Fig. 6(b), taken after the pipe sample was filled with water, showed two short-duration pulses subsequent to the $L(0,2)$ mode signal that traveled 1/4 of the length of the pipe (from the MsS transmitter location to the MsS receiver location). The time between the adjacent pulses was approximately 0.161 ms. Test data (not shown in this paper) obtained from a water-filled, 16-in. (406.4-mm)-OD, schedule 30 (0.375-in. or 9.5-mm-wall) pipe sample also showed an extra pulse that trailed the first signal by approximately 0.254 ms. The experimental data obtained from this laboratory test thus confirmed the phenomenon of the generation of a series of short-duration pulses brought about by the presence of liquid in the pipe, as already observed from liquid-filled pipes in plants. In addition, the time between the

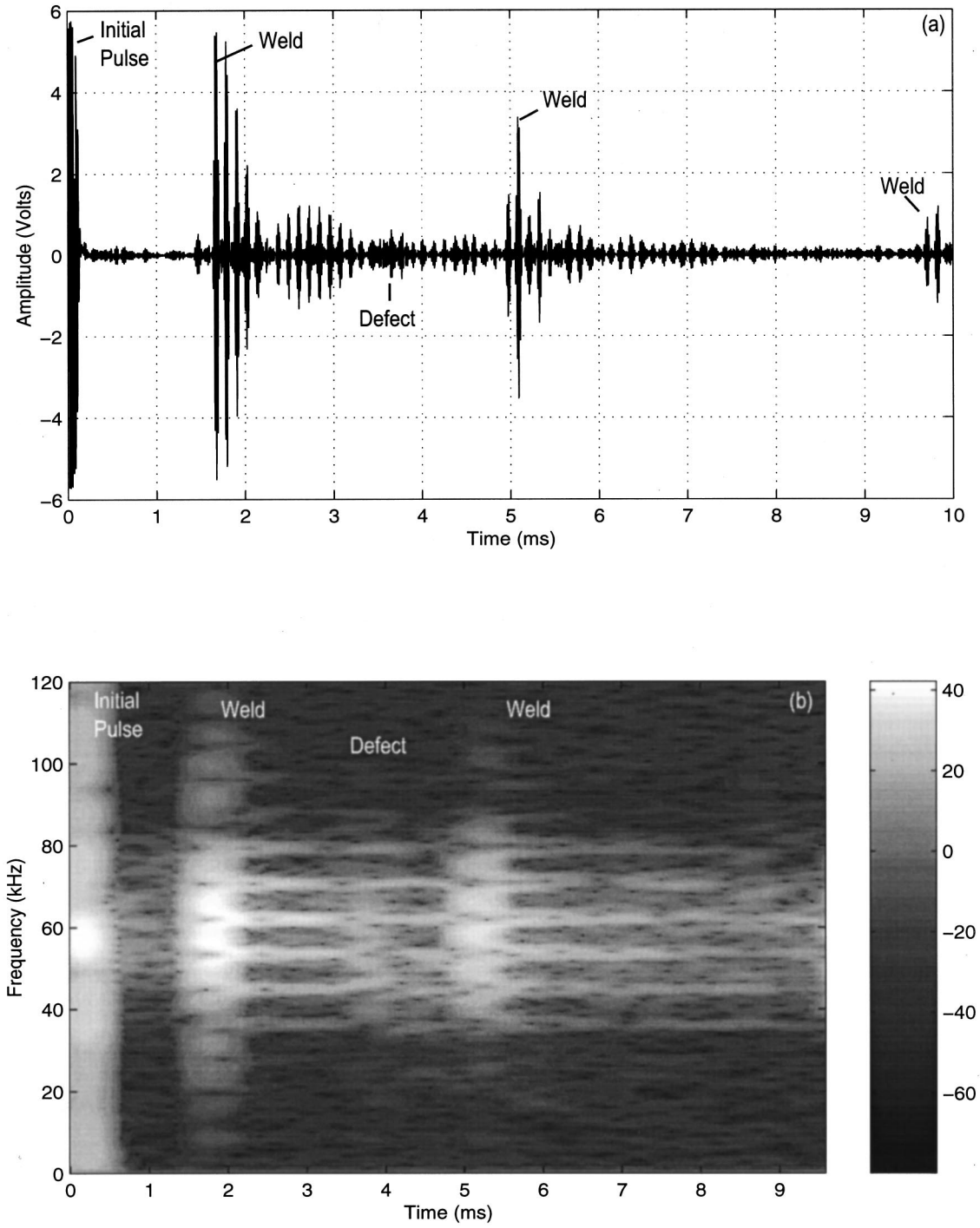

FIG. 5. Data acquired from a nominal 6 5/8-in. (168.3-mm)-OD, schedule 40, steel pipeline carrying diesel in a refinery: (a) detected signals and (b) a time–frequency representation of the detected signals. The gray scale is in dB.

adjacent pulses was proportional to the ID of pipe. [In Fig. 6(b), the $F(2,2)$ mode signal occurred substantially later in time than when the pipe was filled with air. This slowing of the velocity of the flexural wave modes was observed previously and discussed in Sec. II A.] The time–frequency plot (not shown in this paper) of the waveform in Fig. 6(b) showed the branching in the $L(0,2)$ dispersion curve at intervals of approximately 6 kHz, indicating the same general liquid effects discussed in Sec. II A.

The shape of the trailing pulses was very similar to that of the transmitted signal in the pipewall, and the time interval between the adjacent pulses was approximately equal to the time required for the compressional wave in the liquid to travel diametrically across the ID of the pipe. These observations seemed consistent with the well-known ''trailing pulse'' generation phenomenon accompanying a pulsed-compressional-wave propagation in solid waveguides.[17] In that case, the trailing pulses are generated by shear waves produced via mode conversion at the free boundary of the solid waveguide. These shear waves propagate across the

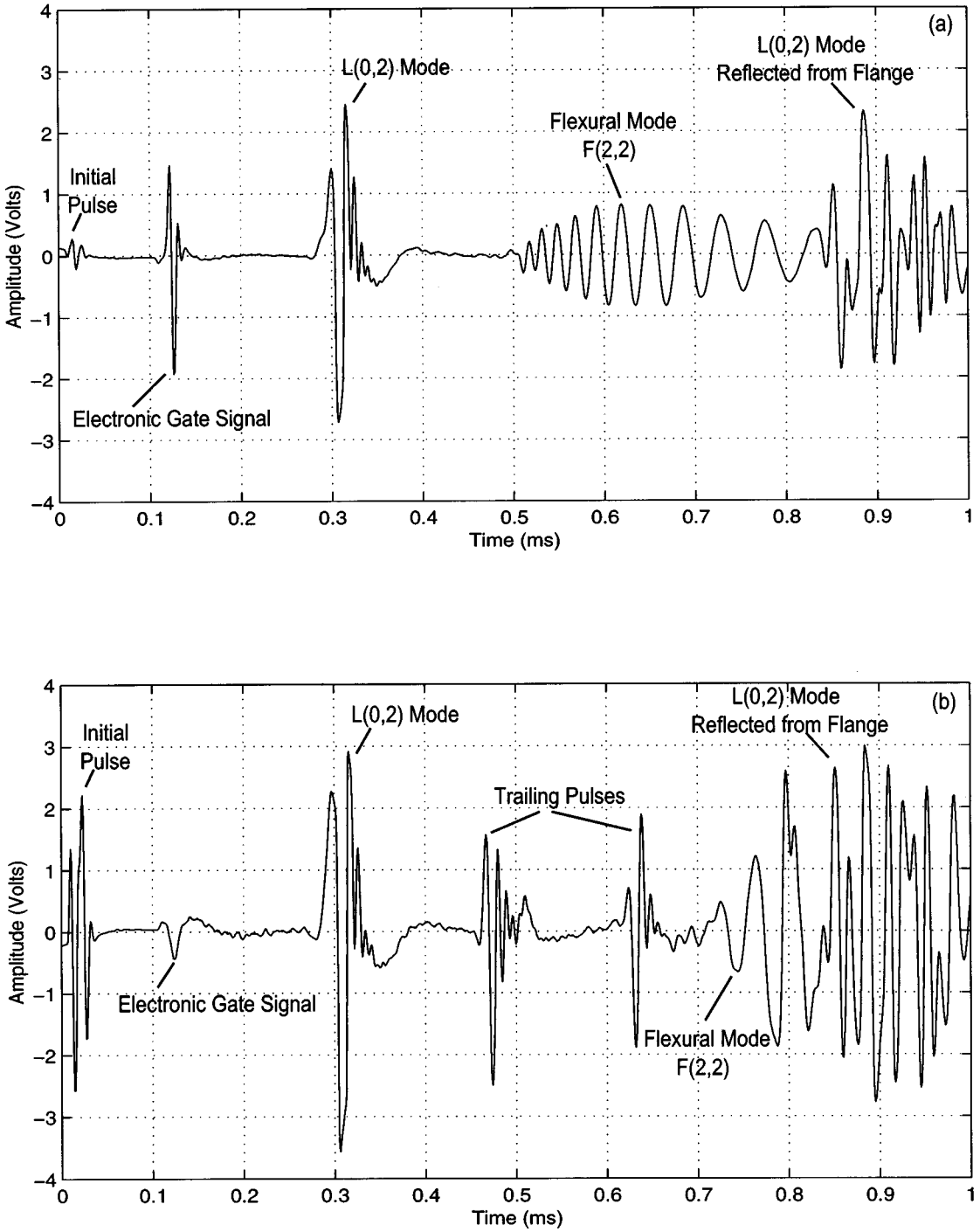

FIG. 6. Detected signals from a 10 3/4-in. (273.1-mm)-OD, schedule 40, steel pipe sample when the pipe was filled with air (a) and with water (b).

waveguide and are then mode converted back to a compressional wave. Therefore, it was hypothesized that the $L(0,2)$ wave in the pipewall was in some way converted to the $L_L(0,0)$ mode in the liquid, and then traveled diametrically with v_L, with an angle θ, that satisfies Snell's law, $\sin\theta = v_L/v_{\text{ph}}$, where v_{ph} is the phase velocity of the $L(0,2)$ mode in the shell. Upon reaching the other side of the ID, the $L_L(0,0)$ mode was converted back to the $L(0,2)$ mode in the shell. The $L_L(0,0)$ mode reverberating diametrically within the liquid cylinder in this fashion then generated the series of pulses that would be separated by a time interval, $\Delta t = D[(v_L \cos\theta)^{-1} - v_g^{-1}\tan\theta]$, where D is the ID of the pipe and v_g is the group velocity of the $L(0,2)$ mode in the shell. According to this hypothesis, the time interval between the pulses in Fig. 6(b) would be approximately 0.159 ms, which, in fact, agrees well with the measured value. Despite this agreement, however, the hypothesis was discarded because the observed branching in the dispersion curve could not be explained. Furthermore, the modeling data showed no evidence of interaction between the $L(0,2)$ mode in the shell and the $L_L(0,0)$ mode in the liquid filling the shell.

In the time–frequency data found in Fig. 5(b), the spectral content of the leading portion of the signal is missing frequency components near the branching, whereas the trail-

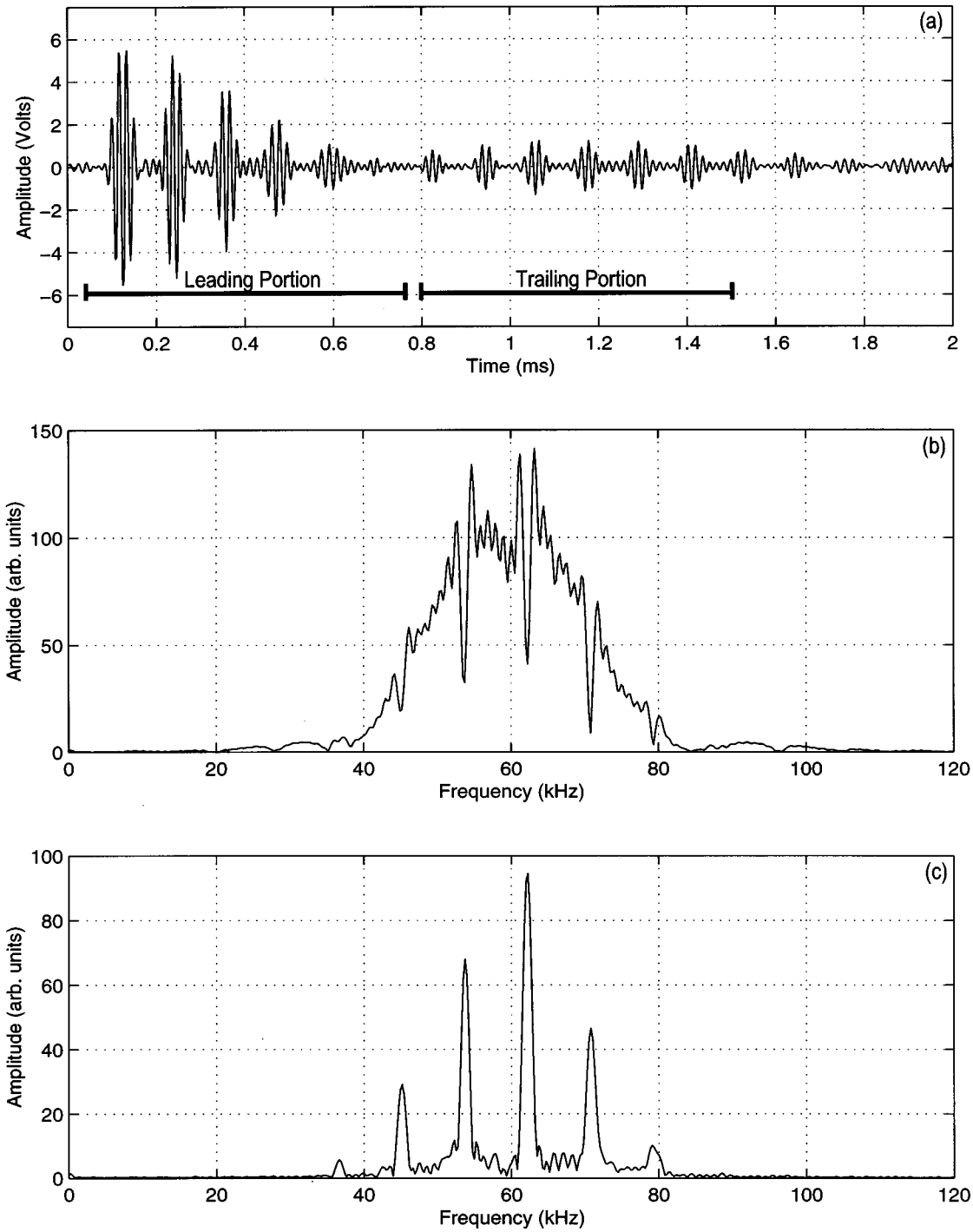

FIG. 7. Expanded view of a series of pulses of the first weld signal in Fig. 5 (a) and DFT data of the leading (b) and trailing (c) portions of the signal.

ing portions of the signal consist of only those missing frequency components. This is a natural consequence of wave dispersion near the branching, where the frequency components travel at a significantly lower velocity than those components comprising the leading portion of the signal [as described in Fig. 4(b)]. For a closer examination of the frequency content of the leading and trailing portions of the signal, the part of the data that covers the first weld signal in Fig. 5(a) is replotted in Fig. 7(a), together with the magnitude of the DFT of the leading and trailing portions of the signal in Fig. 7(b) and (c), respectively. [The data in Fig. 7(b) and (c) correspond to the signals from approximately 0.06 to 0.76 ms and from approximately 0.8 to 1.5 ms in Fig. 7(a).] The DFT of the leading portion showed missing components around the branching frequencies, while the DFT of the trailing portion showed mainly those missing components. Actually, each peak in the DFT data of Fig. 7(c) should be split into two parts, since information from very near the branching frequency had not yet arrived. This splitting could not be observed in the data because of insufficient frequency resolution. The peaks in Fig. 7(c) correspond to the branching frequencies discussed earlier in this section. The interval between branching frequencies in this case was 8.5 kHz, the inverse of which is exactly the 0.117-ms time

interval observed between the adjacent pulses. The time interval between the adjacent pulses was thus directly linked to the frequency interval between the branching frequencies. The pulse-like behavior is expected, actually, since a property of the Fourier transform is that a series of pulses in frequency [Fig. 7(c)] must produce a series of pulses in time [Fig. 7(a)].

The signal pattern and the difference in the spectral contents of the leading and trailing signals described in Fig. 7 are essentially identical to the phenomenon associated with ultrasonic-wave backscattering from a plate immersed in water.[18] The cause of this phenomenon was shown to be the resonances of the plate in its Lamb wave modes.[18,19] As discussed in Sec. II A, the branching in the dispersion curve for the $L(0,2)$ mode in liquid-filled cylindrical shells was attributed to the mode coupling between the unperturbed $L(0,2)$ mode in the shell and the unperturbed $L_L(0,2N)$ modes in the liquid. The striking similarity between the two phenomena suggests that the coupling between $L(0,2)$ and $L_L(0,2N)$ modes involves physical resonances of the liquid cylinder set on by $L(0,2)$ propagating in the shell, and that the basic reason for the series of branching frequencies is radial resonances in the liquid/pipe system. It is believed, therefore, that analytical expressions describing the liquid-induced effects on the longitudinal wave propagation in a shell can be formulated in a similar manner to that used to describe the ultrasonic-wave backscattering from a plate.[19]

By considering all the experimental observations and relevant theories and phenomena, it was concluded that radial resonances in the liquid/pipe system lead to (1) the branching of the dispersion curve of the $L(0,2)$ mode, and (2) the generation of a series of short-duration pulses when the pulse length of the transmitted signal is less than the inverse of the frequency interval between the branching frequencies.

III. SUMMARY

The effects of a liquid that completely fills a cylindrical shell such as pipe or tube on the dispersion properties of the first two longitudinal wave modes in the shell, $L(0,1)$ and $L(0,2)$, were investigated experimentally. Liquid was found to induce a branching in the dispersion curve for the $L(0,2)$ mode via a coupling between the unperturbed $L(0,2)$ mode in the shell and the unperturbed longitudinal modes in the liquid, $L_L(0,2N)$, where N is an integer. The physical mechanism for the mode coupling is determined to be radial resonances in the combined liquid/pipe system. When the pulse length of the transmitted signal is less than the inverse of the frequency interval between the branching frequencies, the dispersion effects caused by liquid are manifested as a series of ''trailing'' pulses that follow the leading signal. In addition, liquid was found to slightly reduce the group velocities and cutoff frequencies of longitudinal modes in the shell, as well as to increase wave attenuation.

ACKNOWLEDGMENTS

The work described in this paper was supported by (in no specific order) Chevron, Texaco, Gas Research Institute, TEAM Inc., CTI Alaska Inc., Mitsubishi Chemical Engineering, CXR Co. Ltd., Tokyo Gas Company, Japan Energy, and Southwest Research Institute (SwRI). The authors wish to thank Jerry L. Jackson of SwRI for his comments and discussions on this work.

[1] H. Kwun and K. A. Bartels, ''Experimental Observation of Wave Dispersion in Cylindrical Shells Via Time-Frequency Analysis,'' J. Acoust. Soc. Am. **97**, 3905–3907 (1995).

[2] H. Kwun and K. A. Bartels, ''Experimental Observation of Elastic-Wave Dispersion in Bounded Solids of Various Configurations,'' J. Acoust. Soc. Am. **99**, 962–968 (1996).

[3] H. Kwun, J. J. Hanley, and A. E. Holt, ''Detection of Corrosion in Pipe Using the Magnetostrictive Sensor Technique,'' Proc. International Society for Optical Engineering (SPIE), on ''Nondestructive Evaluation of Aging Maritime Applications,'' edited by R. B. Mignogna, SPIE Vol. 2459, 140–148 (1995).

[4] H. Kwun and K. A. Bartels, ''Magnetostrictive Sensor Technology and Its Applications,'' Ultrasonics **36**, 171–178 (1998).

[5] T. J. Plona, B. K. Sinha, S. Kostek, and S. K. Chang, ''Axisymmetric Wave Propagation in Fluid-Loaded Cylindrical Shells. II. Theory Versus Experiment,'' J. Acoust. Soc. Am. **92**, 1144–1155 (1992).

[6] L. D. Lafleur and F. D. Shields, ''Low-Frequency Propagation Modes in a Liquid-Filled Elastic Tube Waveguide,'' J. Acoust. Soc. Am. **97**, 1435–1445 (1995).

[7] B. Boashash, *Time-Frequency Signal Analysis* (Wiley, New York, 1992).

[8] A. H. Meitzler, ''Mode Coupling Occurring in the Propagation of Elastic Pulses in Wires,'' J. Acoust. Soc. Am. **33**, 435–445 (1961).

[9] J. Zemanek, ''An Experimental and Theoretical Investigation of Elastic Wave Propagation in a Cylinder,'' J. Acoust. Soc. Am. **51**, 265–283 (1972).

[10] Strictly speaking, the $L(0,1)$ mode has no cutoff frequency. The cutoff frequency here refers to a ''membrane model'' cutoff described in Ref. 15, where the dispersion curve exhibits a cutoff-like behavior.

[11] M. Redwood, *Mechanical Waveguides, The Propagation of Acoustic and Ultrasonic Waves in Fluids and Solids with Boundaries* (Pergamon, New York, 1960), pp. 73–76.

[12] DISPERSE, A System for Generating Dispersion Curves, Version 1.0 (Imperial College, University of London, 1997).

[13] B. Pavlakovic and M. Lowe, DISPERSE User's Manual (Imperial College, University of London, 1997).

[14] B. Pavlakovic, M. Lowe, D. Alleyne, and P. Cawley, ''DISPERSE: A General Purpose Program for Creating Dispersion Curves,'' in *Review of Progress In Quantitative Nondestructive Evaluation*, Vol. 16, edited by D. O. Thompson and D. E. Chimenti (Plenum, New York, 1997), pp. 185–192.

[15] M. C. Junger and F. J. Rosato, ''The Propagation of Elastic Waves in Thin-Walled Cylindrical Shells,'' J. Acoust. Soc. Am. **26**, 709–713 (1954).

[16] M. Redwood, *Mechanical Waveguides, The Propagation of Acoustic and Ultrasonic Waves in Fluids and Solids with Boundaries* (Pergamon, New York, 1960), pp. 128, 144.

[17] M. Redwood, *Mechanical Waveguides, The Propagation of Acoustic and Ultrasonic Waves in Fluids and Solids with Boundaries* (Pergamon, New York, 1960), Chap. 9.

[18] O. Lenoir, P. Rembert, J. L. Izbicki, and P. Pareige, ''The Im/Re Spectrum Method: A New Method of Detection of Resonances of Plane or Cylindrical Targets,'' J. Appl. Phys. **71**, 2129–2135 (1992).

[19] R. Fiorito, W. Madigosky, and H. Uberall, ''Resonance Theory of Acoustic Waves Interacting with An Elastic Plate,'' J. Acoust. Soc. Am. **66**, 1857–1866 (1979).

Comparison of acoustic fields radiated from piezoceramic and piezocomposite focused radiators

D. Cathignol
INSERM, Unité 281, 151 Cours Albert Thomas, 69424 Lyon Cedex 03, France

O. A. Sapozhnikov
Department of Acoustics, Physics Faculty, Moscow State University, Moscow 119899, Russia

Y. Theillère
INSERM, Unité 281, 151 Cours Albert Thomas, 69424 Lyon Cedex 03, France

(Received 8 November 1998; accepted for publication 18 February 1999)

The acoustic field radiated from piezoelectric transducers is usually predicted supposing that the transducer vibrates in thickness mode. However, different reports have shown that not only thickness vibrations were excited, but also plate waves. These waves are responsible for discrepancy between the experimental acoustic fields and those predicted by the Rayleigh integral. It could be supposed that the plate waves are strongly attenuated in piezocomposite materials, as mechanical cross-talk between neighboring elements of the composite structure is fairly weak. A similar effect could be achieved in piezoceramic material by employing a heavy backing, which partially damps the plate waves. These opportunities of plate wave damping are investigated in the present paper. Three transducers are studied, which have identical geometrical characteristics, but are made from different materials. The plate waves in these transducers are indirectly compared by measuring corresponding ultrasound fields and comparing them with theoretically predicted field. It is shown that plate wave patterns are strongly material dependent and that it is only for piezocomposite sources (even when highly focused) that Rayleigh integral modeling can accurately predict the pressure field distribution. © *1999 Acoustical Society of America.* [S0001-4966(99)04105-3]

PACS numbers: 43.20.Rz, 43.20.Bi, 43.20.Px, 43.38.Fx [JEG]

INTRODUCTION

Piezoelectric sources made in the form of spherical caps are widely used both to radiate focused ultrasound beams for medical imaging and therapy or nondestructive testing and to receive acoustic signals from a given spatial region.[1–3] The Rayleigh integral is usually used to calculate the corresponding ultrasound pressure-field pattern.[4,5] It expresses the acoustic pressure at a given spatial point by taking into account the velocity distribution over the radiator surface. For the thickness vibration mode, this distribution is uniform (pistonlike motion) which significantly simplifies the calculations.[6] However, different reports have shown that for plane transducers, not only are the thickness vibrations excited, but also the plate waves.[7–9] More recently, we have shown that the impact of such waves is more pronounced for piezoelectric focused radiators.[10] It is these waves which are responsible for the discrepancies observed between experimental acoustic fields and Rayleigh integral predictions. Unfortunately, it is almost impossible to model these waves as their structure depends on a variety of poorly characterized factors such as the mechanical properties of the backing material, piezoceramic characteristics, the matching layers, how the bowl is attached in the transducer casing, etc. Plate wave-induced modification of the resultant field can be very significant; in some cases, the amplitude of additional side lobes may even exceed that of the main (focal) lobe.[11] As a result, piezoceramic transducers may be unsuitable for some applications like HIFU therapy.[12,13] In addition, a quasi-perfect on-axis pressure amplitude distribution is of major interest for the $V(z)$ technique used in nondestructive evaluation.

It could be supposed that plate waves might be strongly attenuated in piezocomposite materials as mechanical cross-talk between neighboring elements of the composite structure is fairly weak.[14,15] A similar effect could be achieved in piezoceramic materials by using a heavy backing which would damp plate waves to some extent.

The goal of this paper is to investigate the potential of this kind of plate wave damping. Three transducers are studied: their geometrical characteristics are identical, but each is made from a different material. The plate waves in these transducers will be indirectly compared by measuring corresponding ultrasound fields and comparing them with theoretically predicted field.

I. MATERIALS AND METHODS

A. The three radiators

The three sources tested were spherical bowls with a radius of curvature of $F=100$ mm and an aperture diameter of $d=100$ mm. The resonance frequency of each transducer was approximately 1 MHz.

The first transducer was constructed using 1.87 mm thickness piezoelectric ceramic (piezoceramic P1-60, Quartz et Silice, Nemours, France). The piezoceramic bowl was flush-mounted in a thick brass ring, which acted as a rigid baffle. A gap of 0.2 mm between this ring and the bowl wall was filled with silicone cement. It was mounted with air backing and without any matching layer on its front face. The main electromechanical properties of this piezoceramic material are: acoustical impedance 28 MRayl, longitudinal

 0001-4966/99/105(5)/2612/6/$15.00

velocity $c_L = 3740$ m/s, dielectric loss factory $\tan(\delta_e) = 0.6\%$, mechanical loss factory $\tan(\delta_m) = 1{,}2\%$. Further details on assembly and on the pressure field distribution can be found in Ref. 10.

The second radiator was also made from a piezoceramic material. The material used and the assembly were the same, apart from the fact that the backing, instead of being air, was a heavy silica bead-containing epoxy resin (STYCAST 2850 FT, Emerson et Cuming, France). The backing was sufficiently thick (70 mm), to delay and thus eliminate any waves reflected by the rear face beyond the 50 μs temporal window used in the measurements. Moreover, at 1 MHz, this thickness afforded an attenuation of about 70 dB. The elasticity module of the backing material was 7.7×10^4 kg/cm^2.

The third radiator was made of a piezoelectric ceramic/polymer composite material (piezocomposite) of 1–3 connectivity manufactured by a dice-and-fill process (Imasonic Besançon, France). The volume fraction of piezoceramic material was 30%. Care was taken to attenuate spurious resonant lateral modes by: (i) selecting the PZT element aspect ratio and the spacing so that the interelement mode frequencies were well above those of the thickness mode; (ii) by introducing interelement spacing variations to eliminate constructive interference; (iii) and finally by adjusting the polymer stiffness to reduce cross coupling between elements while maintaining an even surface response.[15] The main electromechanical properties of this piezocomposite are: acoustical impedance 11 MRayl, longitudinal velocity $c_L = 3550$ m/s, relative dielectric constant $\varepsilon_{33}^s = 220$, electromechanical coupling factor $k_t = 0.534$, dielectric loss factor $\tan(\delta_e) = 3.5\%$, mechanical loss factor $\tan(\delta_m) = 3.4\%$. The 1.68 mm thickness of the material corresponds to a resonance frequency of 1.1 MHz. The transducer was backed with 3.4 MRayl impedance material. This material comprised an epoxy resin matrix containing aluminum beads and hollow, 35 mm thick, microspheres (STYCAST MM2651, Emerson et Cuming, France). The attenuation coefficient at 1 MHz was 9 dB/mm. The front face of the transducer was in direct contact with water (no matching layer) so that propagation conditions would be comparable with those of the two piezoceramic transducers.

B. Experimental apparatus

The experimental design is shown in Fig. 1. The tested focused transducer was placed in a $0.75 \times 0.6 \times 0.5$ m tank filled with degassed and demineralized water. The transducer was supplied by a sinusoidal waveform generator (8116A from Hewlett-Packard). The pressure field was sampled by a needle hydrophone with a 0.25 mm active element diameter [PZTZ44, Specialty Engineering Associates (SEA), USA]. The hydrophone was connected to an oscilloscope (Tektronix 2430A) via a preamplifier (A17DB, SEA). An x-y-z micropositioning system was used to move the hydrophone in three orthogonal directions with an accuracy of 0.01 mm (Micro-Contrôle, France). This system was controlled by a personal computer with the help of a stepper controller. The computer was also used to record the hydrophone signal transferred from the oscilloscope.

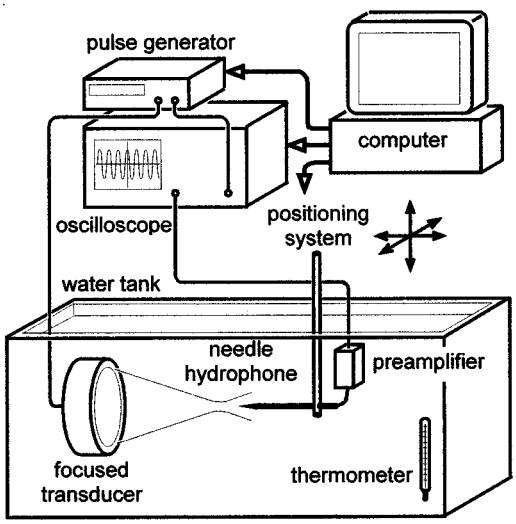

FIG. 1. Experimental setup.

C. Experimental procedure

As shown in a preceding article,[10] plate wave effects are stronger along the transducer axis of symmetry (the acoustic axis), so only the pressure at points on this axis were measured. When a transducer is placed into the bath, its acoustic axis does not necessarily coincide with the spatial coordinates of the three-dimensional micropositioning system and a specific procedure[10] is necessary to define the x, y, and z coordinates of two points on the acoustic axis. These two points are used by the computer to translate the hydrophone along the acoustic axis. The origin of the axes (x,y,z) was derived by carefully translating the hydrophone along the acoustic axis as far as the transducer face. Pressure measurements were made at room temperature (24 °C) for two different modes: pulsed and continuous.

The pulsed mode separates the different types of wave generated by the transducer in time domain. To do this, the generator emitted one cycle at 1 MHz.

To simulate a continuous wave (cw), the transducer was driven by tone burst at three different frequencies (0.8, 1, 1.2 MHz). The gate of the oscilloscope was adjusted to sample the signal after cw behavior had been established but before any reflections had returned (from the hydrophone casing, the back of the tank, etc.). The peak-to-peak hydrophone voltage was used to characterize the acoustic pressure amplitude.

To avoid nonlinear effects, the voltage applied to the transducer was kept low. The pressure amplitude near the radiator surface was less than 0.1 bar, which is well below that required to generate significant nonlinear effects.

II. RESULTS AND DISCUSSION

A. Pulsed mode

As mentioned above, pulsed regime allows to identify and quantify plate waves in the time domain. Figure 2 shows the signal over time for $z = 20$ mm for each of the three types of transducers. The temporal waveform is the resultant of three different waves: the direct wave (D); the edge wave (E); and the head wave (H).[7,10] As explained in Ref. 10, the

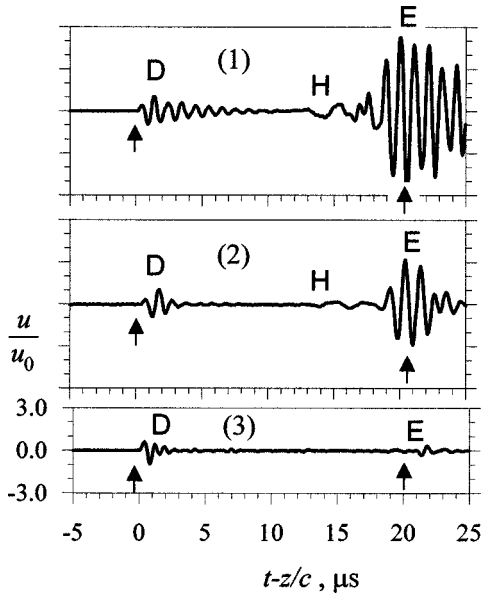

FIG. 2. Waveforms in pulsed regime at $z=20$ mm for different radiators: (1) piezoceramic transducer without backing, (2) piezoceramic transducer with backing, and (3) piezocomposite transducer. The hydrophone signal u is normalized by the peak value of the direct wave u_0. Letters D, H, and E denote direct, head, and edge waves correspondingly. Arrows mark theoretical arrival times for the direct and edge waves.

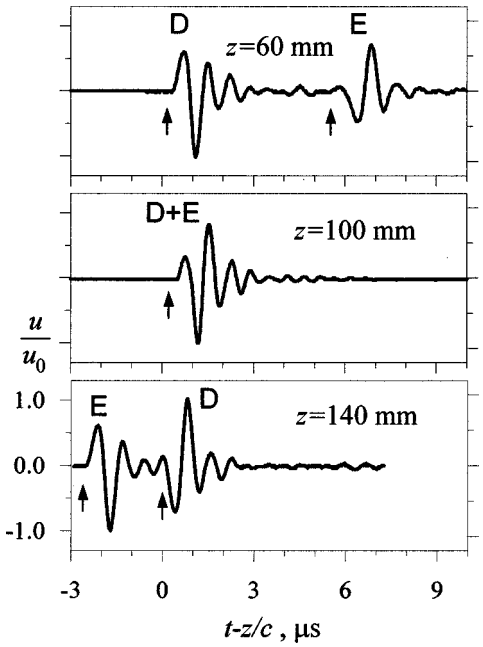

FIG. 4. On-axis pressure waveforms in pulsed regime at different distances z from the piezocomposite transducer. Symbols are the same as in Fig. 2.

head waves are generated into the liquid as soon as the plate wave phase velocity exceeds the speed of the sound in water. Figure 3 shows the path of each of the three waves (D), (E), and the wave (H).

As it is seen, the direct wave arrives at the time $t_D = z/c$, the edge wave arrives at the time $t_E = r/c$, and the head wave arrives at the time $t_H = l/c_* + r_*/c$. Here, c is the speed of sound in water, c_* is the maximum propagation velocity of the plate waves (r_* and l are defined in Fig. 3).

In Figs. 2 and 4, the time zero is taken as the time of arrival of the direct wave (D) which corresponds to the relevant speed of sound $c=1490$ m/s. It can be seen in Fig. 2 that the head wave (H) arrives later, at time $t_H > t_D$. The beginning of the head wave corresponds to a plate wave with a propagation velocity in ceramic material of 3500 m/s, as we have shown.[10] This corresponds to the low frequency group velocity of the zeroth order Lamb mode.

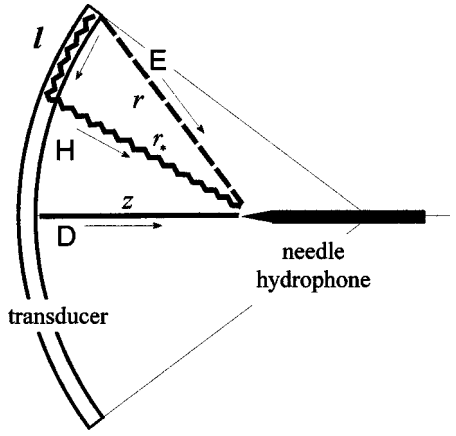

FIG. 3. Acoustic paths for edge (E), head (H), and direct (D) waves.

As expected, the duration of the direct wave is longer for the piezoceramic transducer with no backing (10 cycles instead of the 2–3 of the other transducers), because there is no damping at the rear face and because of the absence of matching layer at the front face.

The direct wave is followed by the head wave which subsequently interferes with the edge wave. In a previous article, we showed that, for airbacked piezoceramic transducers, the head wave spread out over a period of about 10 μs, initially having the form of a low frequency and small amplitude signal and later a higher frequency and increased amplitude signal. If it is assumed that the amplitude of the edge wave is the same as that of the direct wave (with the transducer resonating in piston mode), it could be estimated from Fig. 2-1 that, for a piezoceramic transducer without any backing, the amplitude of the head wave is between 4 and 5 times greater than that of the direct wave. This ratio would be no more than 3 for backed piezoceramic material (Fig. 2-2) and it seems that, for backed piezocomposite materials, the head wave completely disappears (Fig. 2-3). Therefore, it can be concluded that backing reduces but does not eliminate head waves with piezoceramic materials, whereas it completely eliminates them for piezocomposite materials.

In theory, for purely piston mode vibrations, the edge wave should be a delayed inverted replica of the direct wave and should arrive at the time t_E. However, as can be seen in Fig. 2-3, the actual time of arrival is slightly different from the predicted time and moreover, the amplitude of the edge wave is smaller than that of the direct wave. This can be explained by the fact that the normal velocity distribution near the edge of the transducer's surface changes continuously rather than suddenly, unlike in a perfect piston model. Because the edge wave may be interpreted by the non uniform distribution of the normal velocity on the transducer surface, the hydrophone will receive not only the main edge

wave issued from the transducer rim but also, before the arrival of this main wave, a lot of edge waves issued from a ring situated at the periphery of the transducer. In addition, the directivity properties of the hydrophone contributes to the reduction in the received off-axis signal.

Both of these effects should be less significant for larger magnitude z distances. In order to check this, the signal was measured at three different distances as shown in Fig. 4: in front of the focal point (60 mm), at the focal point (100 mm), and beyond the focal point (140 mm). The difference in amplitude and shape between the direct and edge waves steadily diminishes as the distance z increases. At the focal point, both waves (direct and edge) cannot be distinguished because they are arriving together. Therefore, referring to Eq. (1), the resultant waveform is the time derivative of the waveform of the isolated direct wave on the axis. Beyond the focal point, it is seen that the two waves are again separated, but the edge wave arrives before the direct wave. As can be seen, the two effects mentioned above are no longer very important and the two waves have the same amplitude and shape but are opposite in phase as predicted by the piston source theory. This confirms that the velocity distribution at a piezocomposite surface is uniform.

B. Continuous mode

As shown by O'Neil, for sinusoidally vibrating focusing transducers with uniform normal velocity distribution along their surfaces, a simple theoretical expression for wave amplitude follows from the Rayleigh integral:[4]

$$p=\frac{\rho c u_n e^{-i\omega t}}{1-z/F}(e^{ikz}-e^{ikR}). \tag{1}$$

Here u_n is the normal velocity amplitude on the radiator surface, ρ and c are the density and sound velocity of the medium, ω is the angular frequency, $k=\omega/c$ is the wave number, z is the distance along the axis, F is the radius of the radiator's curvature, $R=F\sqrt{1+(1-z/F)^2-2(1-z/F)\cos\alpha_{\max}}$ is the distance between the observation point and the radiator edge, where $\alpha_{\max}$ is the half-aperture angle of the radiator. Equation (1) gives the axial pressure distribution in the case of a purely thickness transducer vibration and is convenient for making comparisons with experimental results.

Figure 5(a), (b), (c) shows plots of axial pressure distribution at three different frequencies (0.8, 1, and 1.2 MHz) for the three transducers. Thick lines represent experimental measurements and the thin lines correspond to Eq. (1). It can be seen that the most pronounced discrepancies occur with the piezoceramic transducer without backing (curves number 1). The experimental curves contain additional spikes in the prefocal region. It has been shown in our previous work that these deviations between theory and reality are due to Lamb waves originating at the transducer rim and propagating toward its center.[10] It is also seen that the effect of Lamb waves on the pressure field is frequency dependent. This can be explained by dispersion of the Lamb waves.[16] When a heavy backing is used in the piezoceramic transducer (curves number 2), the effect of plate waves is less significant than that seen if the transducer is only air-backed. This should not be surprising because elastic waves in the piezoelectric plate lose energy through radiation into the backing material which is directly in contact with the plate. Therefore, these waves predominate only in the small annular region near the radiator rim and do not noticeably distort the uniform normal velocity distribution at the transducer surface. The curves number 3 in Fig. 5 correspond to the piezocomposite transducer. It is very important that no additional peaks were noticed in the prefocal region. Compared with pressure fields for piezoceramic transducers, the experimental results for the composite material coincide very well with the O'Neil theory for all distances. This indicates that no significant plate waves were excited in the piezocomposite transducer, i.e., only thickness vibrations were present in the piezocomposite plate.

However, some discrepancies between the theory and the measured values are detected even for the curves numbered 3 which correspond to the piezocomposite material (Fig. 5). In particular, no predicted zero pressure points were observed in the focal region. These discrepancies between curves calculated on the basis of O'Neil relationship and the experimental results can be attributed either to imperfect curvature or to nonuniformity of the normal velocity distribution. Since the signals generated by the piezocomposite transducer in pulsed mode were not associated with plate waves, we thought that it was the curvature problem which was the more significant. Therefore, we checked the curvature of the piezocomposite and piezoceramic transducers by measuring bowls' shape along a series of planes passing through the acoustic axis and separated by angles of 15°. For each arc, the measurements of points' coordinates were made with a step of 1 mm. For the piezoceramic material, it appeared that all the measurements fell to a 100 mm radius sphere within an accuracy of 10 μm. In contrast, the piezocomposite shell was less perfect: the best fit spherical radius was of $F=99.797$ mm with a standard deviation of 0.027 mm. Figure 6 represents the deviation $\Delta(i)$ between the calculated radius r_i and F for each measurement in three dimensions, i.e.,

$$\Delta(i)=F-r_i. \tag{2}$$

In light of Fig. 6, it can be seen that the bowl remains axisymmetric but with a bulge at its center of the order of 0.09 mm and an inverted bulge of the order of 0.06 mm between the center and the edge. Although these values are much smaller than the wavelength (1.5 mm), they are not negligible. Whereas the piezoceramic bowl was ground, the piezocomposite was heat-cast, so it is possible that some deformations occurred during the cooling process.

Taking the actual geometry into account, the ultrasound field can be recalculated using the Rayleigh integral as given below:

$$p=-\rho c\frac{ik}{2\pi}\int u_n\frac{e^{ikR_a}}{R_a}dS. \tag{3}$$

R_a is the distance between the observation point to the element dS and the integral is calculated over the transducer surface. Supposing that only the thickness vibration is

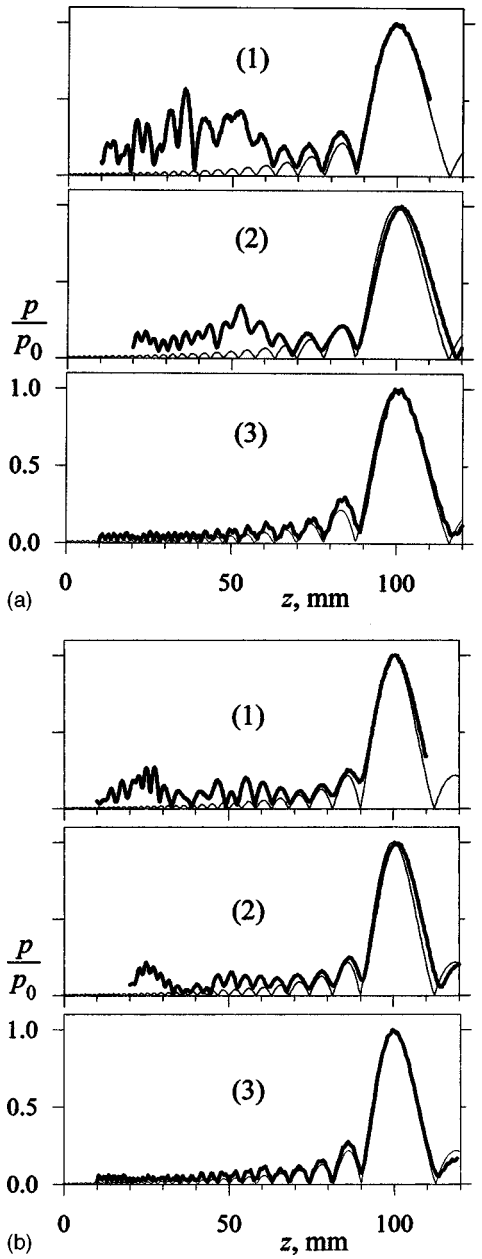

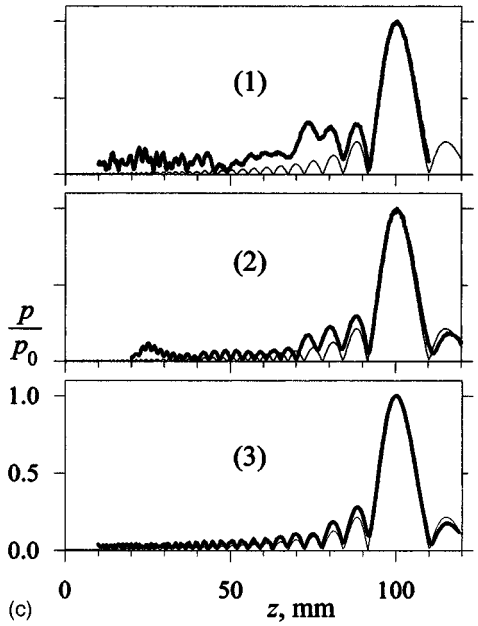

FIG. 5. Experimental pressure amplitude distribution along the axis of transducer symmetry (thick lines), compared with the corresponding results of the O'Neil theory (thin lines), for different radiators: (1) piezoceramic transducer without backing, (2) piezoceramic transducer with backing, and (3) piezocomposite transducer. The pressure amplitude, p, is normalized by its maximum value, p_0. (a), (b), and (c) correspond to the frequencies $f = 0.8$, 1, and 1.2 MHz.

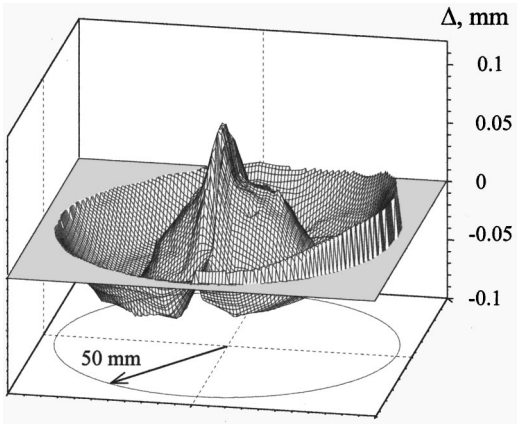

FIG. 6. Deviation of the piezocomposite bowl shape from the best fit sphere: Δ presents the difference $F - r_i$, where F is the sphere radius, r_i is the distance between the transducer surface and the sphere center.

present, the normal velocity can be considered as a constant and factored out from the integral. Thus the calculated amplitude distribution along the axis is shown in Fig. 7 by a thin line. The thick line represents the actual measurements. It is seen that the theoretical and experimental values are almost indistinguishable. In particular, the theoretical curve does not yield any ''real'' zero values thereby showing the significance of imperfect curvature, even when minimal. The two curves coincide closely for each of the three frequencies.

III. CONCLUSIONS

In a previous article, it was shown that the ultrasound field generated by a spherical piezoceramic bowl was perturbed by plate waves which induced additional side lobes and made certain applications like imaging and therapy im

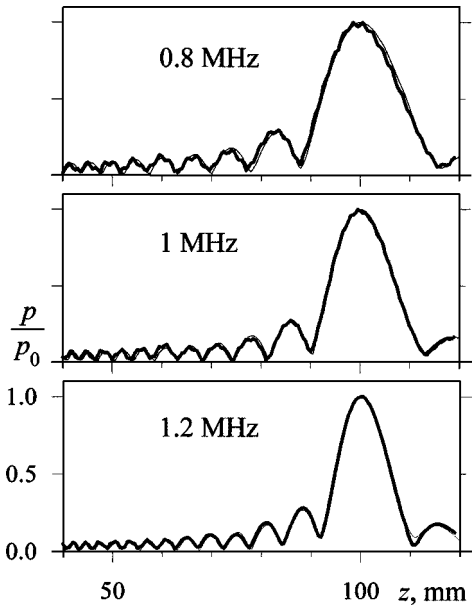

FIG. 7. Axial distribution of acoustic field amplitude at different frequencies (piezocomposite transducer). Thick lines present the experiment, thin lines are the theoretical curves obtained using the Rayleigh integral with account for transducer nonsphericity (see Fig. 6).

practicable. This series of experiments was undertaken in order to test the hypothesis that plate waves could be reduced by either radiating of their energy into a heavy backing or by using a material such as a piezocomposite which would dissipate their energy. It was demonstrated that only piezocomposite material could completely eliminate these plate waves. Therefore, for piezocomposite radiators with known shape, it is possible to accurately calculate the ultrasound field pattern using the Rayleigh integral and, in doing so, the normal velocity distribution along the radiator surface can be taken as being uniform.

Piezocomposite materials are known to have the following advantages: low acoustical impedance, high coupling coefficient, and large bandwidth, as well as being easy to cast. Another advantage must be added to those mentioned: because of the absence of plate waves, the radiated ultrasound field of piezocomposite transducers can be precisely predicted.

ACKNOWLEDGMENTS

This work was funded in part by l'action spécifique pour les Pays d'Europe Centrale et Orientale (PECO) de l'Institut National de la Santé Et de la Recherche Médicale (INSERM).

[1] *New Techniques and Instrumentation in Ultrasonography*, edited by P. N. T. Wells (Churchill Livingstone, New York, 1980).
[2] A. J. Coleman, M. J. Choi., J. E. Saunders, and T. G. Leighton, ''Acoustic emission and sonoluminescence due to cavitation at the beam focus of an electrohydraulic shockwave lithotripter,'' Ultrasound Med. Biol. **18**, 267–281 (1992).
[3] D. Cathignol, J. Tavakkoli, A. Birer, and A. Arefiev, ''Comparison between the effects of cavitation induced by two different pressure-time shock waveform pulses,'' IEEE Trans. Ultrason. Ferroelectr. Freq. Control **45**, 788–499 (1998).
[4] A. O. Williams, Jr., ''Acoustic intensity distribution from a ''piston'' source.—II. The concave piston,'' J. Acoust. Soc. Am. **17**, 219–227 (1946).
[5] H. T. O'Neil, ''Theory of focusing radiators,'' J. Acoust. Soc. Am. **21**, 516–526 (1949).
[6] P. R. Stepanishen, ''The time-dependent force and radiation impedance on a piston in a rigid infinite planar baffle,'' J. Acoust. Soc. Am. **49**, 841–849 (1970).
[7] J. C. Baboux, F. Lakestani, and M. Perdrix, ''Theoretical and experimental study of the contribution of radial modes to the pulsed ultrasonic field radiated by a thick piezoelectric disk,'' J. Acoust. Soc. Am. **75**, 1722–1731 (1984).
[8] E. Riera-Franco de Sarabia, A. Ramos-Fernandez, and F. Rodriguez-Lopez, ''Temporal evolution of transient transverse beam profiles in near-field zones,'' Ultrasonics **32**, 47–56 (1994).
[9] B. Delannoy, C. Bruneel, F. Haine, and R. Torguet, ''Anomalous behavior in the radiation pattern of piezoelectric transducers induced by parasitic Lamb wave generation,'' J. Appl. Phys. **51**, 3942–3948 (1980).
[10] D. Cathignol, O. A. Sapozhnikov, and J. Zhang, ''Lamb waves in piezoelectric focused radiator as a reason for discrepancy between O'Neil's formula and experiment,'' J. Acoust. Soc. Am. **101**, 1286–1297 (1997).
[11] D. Cathignol, O. A. Sapozhnikov, and J. Zhang, ''Lamb waves in piezoelectric focused sources,'' Proc. World Congress 1995 on Ultrasonics, part 2, pp. 1091–1093 (1995).
[12] J. Y. Chapelon, J. Margonari, F. Vernier, F. Gorry, R. Ecochard, and A. Gelet, ''*In vivo* effects of high-intensity ultrasound on prostatic adenocarcinoma dunning R3327,'' Cancer Res. **52**, 6353–6357 (1992).
[13] F. J. Fry, G. Kossof, and R. C. Eggleton, ''Threshold ultrasonic dosages for structural changes in mammalian brain,'' J. Acoust. Soc. Am. **48**, 1413–1417 (1970).
[14] W. A. Smith, ''Design of piezocomposites for ultrasonic transducers,'' Ferroelectrics **91**, 155–162 (1989).
[15] B. G. Pazol, L. G. Bowen, R. L. Gentilman, H. T. Pham, and W. J. Serwatka, ''Ultrafine scale piezoelectric composite materials for high frequency ultrasonic imaging arrays,'' IEEE Ultrasonic Symposium, 1263–1268 (1995).
[16] I. A. Viktorov, *Rayleigh and Lamb Waves* (Plenum, New York, 1967).

Extension of the angular spectrum approach to curved radiators

Ping Wu and Tadeusz Stepinski
Uppsala University, Department of Materials Science, Signals and Systems, Box 528, S-751 20 Uppsala, Sweden

(Received 22 September 1998; accepted for publication 7 January 1999)

The angular spectrum approach (ASA) is conventionally applied to the evaluation of acoustic fields from planar radiators because it is usually based on the 2-D Fourier transform (or the zero-order Hankel transform in the axisymmetrical case) which is implemented only in a plane. The present paper is intended to extend the ASA to more general cases where radiators have curved surfaces. For this purpose, two approaches are developed. The first one is the extended ASA and is derived in a general way. From this approach, the angular spectrum of a curved radiator is given by a double integral that does not take the 2-D Fourier transform form, and thus cannot be implemented using 2-D fast Fourier transform (FFT) but by numerical integration. The second approach is the indirect ASA that gives the angular spectrum via 2-D Fourier transforming an initial field pre-calculated in a plane. The method for calculating the initial field is proposed based on the method developed by Ocheltree and Frizzell for planar sources. An example is given of a linear array with a cylindrically concave surface, and in this case, the angular spectrum (the double integral) from the extended ASA reduces to a single integral. The angular spectra of the array are calculated using both approaches and compared. The comparison has shown that the angular spectra obtained from both approaches are in excellent agreement. The accuracy and efficiency of the two approaches are studied in the numerical implementation. In this example, the extended ASA has been shown to be more efficient and more accurate than the latter approach. Both approaches can be applied to arbitrarily curved transducers. In the general case where the double integral cannot be reduced to a single integral, the latter approach can be more efficient.
[S0001-4966(99)01304-1]

PACS numbers: 43.20.Rz, 43.20.Bi [DEC]

INTRODUCTION

The angular spectrum approach (ASA) has found wide applications in modeling wave propagating fields in optics,[1,2] electromagnetics,[3] acoustics and ultrasonics.[4–18] The ASA is usually implemented based on the two-dimensional (2-D) spatial Fourier transform, or Hankel transform in the axisymmetrical case. It is well known that the 2-D Fourier transform (or the Hankel transform) is implemented in a plane. Thus the ASA is usually restricted to dealing with the radiation of *planar* radiators,[1–8] and the backpropagation of ultrasonic fields in *planes*.[9,10] In this paper, we extend the ASA to more general cases where the radiators are curved. The motivation of the present work is our intention to use the ASA to simulate elastic fields in immersed solids (e.g., copper) radiated by a linear array that we have in our laboratory and use in immersion test[15] because this approach is easily applied to the immersion case.[16] The main target of the paper is the angular spectra of curved radiators because an angular spectrum of a source is the basis that is necessary for synthesizing the elastic fields radiated by the source into an immersed solid.

Ultrasonic beam focusing is commonly employed to attain fine spatial resolution and is usually realized by means of either curved transducers or planar transducers coupled to focusing lenses. A large body of literature is available dealing with the radiation of the focused transducers of both types. Our attention is focused on transducers of the first type, i.e., transducers with curved surfaces, because they are in our present interest. Concave transducers and arrays with concave surfaces have become more and more common nowadays since piezocomposite materials have been available. Among the most commonly used are spherically concave and cylindrically concave transducers, as well as various ultrasonic arrays which have either linearly, or cylindrically, or curvilinearly aligned elements. The arrays, in addition to performing electronic focusing in azimuth, often have cylindrically curved surfaces for geometrical focusing in elevation. Acoustic fields from curved transducers have been studied extensively by means of different methods, but most of the methods were used to treat spherically concave transducers[11–14,19–26] and focused transducers with arbitrary axisymmetric surface velocity distributions.[27] The ASA is one of the methods used, modeling spherically curved transducers, however, mostly in the applications of acoustic microscopy, e.g., in Refs. 11–14, where the angular spectra were obtained only in the focal plane. Moreover, due to axisymmetry of the transducers, the 2-D problem could be simplified into the 1-D problem. However, it is not possible for curved transducers that are not axisymmetrical, e.g., cylindrically concave transducers and linear or phased arrays with cylindrically curved surfaces. The ASA has also been used to the transducers coupled to focusing lenses. Two relevant papers by Guyomar and Powers,[17,18] are worth mentioning here. In these two papers, they studied and extended the angular spectrum approach to the case of transient fields from curved transducers. It should be pointed out that the

extension made was the time extension of the angular spectrum giving the time impulse response. The curved transducers were essentially treated as planar transducers having time-delay excitations or, equivalently, coupled to lenses with various focusing surfaces such as spherical concave, spherical convex, conical, parabolic, and cylindrical surfaces. The thin lens approximation was implicitly employed in the formulation. Thus the 2-D Fourier transform was applicable and used in their case. In our case the transducers and the linear arrays studied are cylindrically curved. To our knowledge, little work has been reported exploring the ASA for the calculation of acoustic fields from such curved transducers and arrays.

In the present work two angular spectrum approaches are developed to calculate the angular spectrum of a curved transducer. The first one is the extended ASA, that is, the conventional ASA extended in space from the planar sources to the curved sources. The starting point is the Rayleigh integral describing the radiation from a curved transducer, and then a general form of the angular spectrum is derived that is a double integral not possessing the 2-D Fourier transform form, which means the angular spectrum cannot be implemented using 2-D fast Fourier transform (FFT) but by numerical integration. The second approach is the one that indirectly gives the angular spectrum via 2-D Fourier transforming an initial field pre-calculated in a plane, and is therefore referred to as indirect ASA in this paper. Theories of these approaches will be presented in Sec. I. The method used for calculating ultrasonic fields from a linear array with a cylindrical concave surface (referred to as Ocheltree-based method in sequel) was developed based on the idea proposed by Lee and Benkeser[28] who extended to the circular array case the method developed by Ocheltree and Frizzell for planar sources,[29] and the Ocheltree-based method is given in detail in the Appendix. In Sec. II, both approaches are applied to the specific case of a linear array with a cylindrically concave surface. In Sec. III, calculations and comparison of the angular spectra of the linear array are made using both approaches.

I. THEORY

A. General consideration

A curved transducer having a rigid baffle and radiating acoustic fields into lossless fluids is considered here. It is well known that a sound field from a rigid baffled planar piston source in a fluid can be rigorously depicted by the Rayleigh integral. For a curved source the Rayleigh integral can approximately represent the radiation of the source under certain conditions.[19,24,25] Following O'Neil,[19] the velocity potential can be approximately expressed by the Rayleigh integral if the normal velocity of the source on the curved surface S is represented by $\tilde{v}_n(\mathbf{r})$ at frequency ω,

$$\phi(\mathbf{r}) = -\frac{1}{2\pi}\int\int_S \tilde{v}_n(\mathbf{r}')\frac{\exp(jkr_s)}{r_s}dS, \tag{1}$$

where $r_s = |\mathbf{r}-\mathbf{r}'|$ is the distance from source point $\mathbf{r}'$ on surface S to field point $\mathbf{r}$ in the medium. Equation (1) treats each surface element dS as a point source of strictly hemispherical waves, and in the limiting case where S is a plane radiator with an infinite baffled plane, the equation is rigorously correct. If S is curved, waves radiated from any part of the curved surface are diffracted by other parts of this surface, but the integral in Eq. (1) neglects this fact. When the surface S is only slightly curved, this secondary diffraction becomes relatively unimportant. The resultant effects due to the secondary disturbances which originate at different parts of S will be further reduced by phase differences if the extent of S is large relative to the wavelength. Also, with this restriction on the dimension, most of the energy will be radiated in a central beam, which will be affected very little by the presence or the absence of a baffle around the radiator.[25] Hence, if the diameter or breadth of a slightly curved source surface S is large compared with the wavelength, the velocity potential at points in or near the main beam will be represented approximately by the integral in Eq. (1). This is often called O'Neil theory. This theory has been used by many researchers dealing with curved transducers, such as Penttinen and Luukkala,[20] Arditi *et al.*,[21] Fink and Cardoso,[25] Schmerr,[26] etc. A number of experimental studies (e.g., Refs. 22 and 23) and numerical investigations[24] have demonstrated that the O'Neil theory agrees very well with experiments and with more exact models for curved transducers. An important conclusion from Coulouvrat's work[24] states that the conditions of validity of the O'Neil theory are much less stringent than expected, and this work also derived more precise conditions for the applicability of the O'Neil theory. Thus the O'Neil theory does seem to be a good basis for evaluating focused transducers. From the relation of pressure with velocity potential, $\tilde{p}(r) = -\rho\partial\phi(r)/\partial t = jk\rho c\phi(r)$ where ρ is the density, c is the sound velocity, and $k=\omega/c$ is the wave number, one obtains the Rayleigh integral in terms of pressure in the following manner:

$$\tilde{p}(\mathbf{r}) = -\frac{jk\rho c}{2\pi}\int\int_S \tilde{v}_n(\mathbf{r}')\frac{\exp(jkr_s)}{r_s}dS. \tag{2}$$

Two angular spectrum approaches, the extended ASA and the indirect ASA, are derived from this Rayleigh integral.

B. The extended angular spectrum approach

Consider a source with surface S that is represented by $z=f(x,y)$ under the Cartesian coordinates. Assuming that $z=f(x,y)$ is continuous and has the first-order derivatives, the elementary surface dS can be expressed by $dS = dx'dy'/\cos\theta_z$, where $\cos\theta_z$ is the direction cosine of the normal with respect to the z-axis. $\cos\theta_z$ can be obtained from

$$\cos\theta_z = \frac{1}{\sqrt{(f_x(x,y))^2+(f_y(x,y))^2+1}}, \tag{3}$$

where $f_x(x,y)$ and $f_y(x,y)$ are the partial derivatives with respect to x and y, respectively. From Eqs. (2) and (3), the pressure in the Cartesian coordinates can be easily derived as

$$\tilde{p}(x,y,z) = -\frac{jk\rho c}{2\pi}\int\int_{S_{xy}} \tilde{v}_n(x',y',f(x',y')) \times \frac{\exp(jkr_s)}{r_s}\frac{dx'\,dy'}{\cos\theta_z}$$

$$= -\frac{jk\rho c}{2\pi}\int\int_{S_{xy}} \tilde{v}_z(x',y',f(x',y')) \times \frac{\exp(jkr_s)}{r_s}dx'\,dy', \quad (4)$$

where S_{xy} is the area of the projection of the surface S onto the x-y plane, $\tilde{v}_z = \tilde{v}_n/\cos\theta_z$, and $r_s = \sqrt{(x-x')^2+(y-y')^2+[z-f(x',y')]^2}$.

In the case of a planar piston source, its angular spectrum can be obtained by applying the convolution theorem to the Rayleigh integral[1,2] and it is given by a 2-D spatial Fourier transform of the normal velocity on the source surface.[4–8] For a planar piston source located in the $z=z_0$ plane, its angular spectrum is denoted by $V(k_x,k_y;z=z_0)$. For an acoustic field from the planar source propagating forward in the $+z$-direction to a plane at z_1 ($\geqslant z_0$), the angular spectrum of the field can be derived from the relation[1]

$$V(k_x,k_y;z=z_1) = V(k_x,k_y;z=z_0)\exp(j(z_1-z_0)k_z), \quad (5)$$

where $k_x = kn_x$, $k_y = kn_y$, $k_z = \sqrt{k^2-k_x^2-k_y^2} = k\sqrt{1-n_x^2-n_y^2}$ are the spatial frequencies in the x-, y-, and z-directions in the medium, respectively. However, the above relation does not apply to a curved source. Now we divide the surface S of the curved source into a set of such small elementary sources with surface δS that each of them can be approximated by a plane. Then we obtain the angular spectrum of the whole source by the superposition of the angular spectra of elementary sources. Supposing that δS_{xy} is the projection of δS onto the x-y plane, the angular spectrum of the small elementary source on surface S at (x',y',z') where $z' = f(x',y')$ can be approximated by

$$\delta V(k_x,k_y;z') = \int\int_{\delta S_{xy}} \tilde{v}_z(x',y',z') \times \exp[-j(x'k_x+y'k_y)]dx'\,dy' \approx \tilde{v}_z(x',y',z')\exp[-j(x'k_x+y'k_y)]\,\delta S_{xy}.$$

Thus at the plane $z=z_1$ ($\geqslant\max[f(x',y')]$) the angular spectrum of the whole source can be obtained from superposition of the spectra of all elementary sources in the following manner:

$$V(k_x,k_y;z=z_1) = \lim_{\delta S_{xy}\to 0}\sum_{S_{xy}} \delta V(k_x,k_y;z') \times \exp(j(z_1-z')k_z) = \int\int_{S_{xy}} \tilde{v}_z(x',y',f(x',y')) \times \exp[-j(x'k_x+y'k_y)] \times \exp[j(z_1-f(x',y'))k_z]dx'\,dy', \quad (6)$$

where the condition $z_1 \geqslant \max[f(x',y')]$ must be met in order to ensure that $V(k_x,k_y;z=z_1)$ is always finite for all k_x and k_y. Equation (6) is the final form for the angular spectrum of a curved source and is derived, based on the Rayleigh integral of curved surface (the O'Neil's theory) and the ASA in the case of planar sources, without any approximation. Obviously, the angular spectrum of the curved source is not of the form of the 2-D spatial Fourier transform. Since $k_z = \sqrt{k^2-k_x^2-k_y^2} = k\sqrt{1-n_x^2-n_y^2}$, evanescent waves show up when $k_x^2+k_y^2 > k^2$ or $n_x^2+n_y^2 > 1$. When z_1 is chosen to be so large that $z_1 \geqslant \max[f(x',y')]$ plus a few wavelengths, e.g., $z_1 \geqslant \max[f(x',y')]+2\lambda$, the evanescent waves are strongly attenuated and thus can be neglected without loss of accuracy.[4–9] Therefore, $V(k_x,k_y;z=z_1)$ in the range of $k_x^2+k_y^2 \leqslant k^2$ is usually used for synthesizing the acoustic field. In general, the double integral in Eq. (6) is very difficult to directly solve. But, in some special cases, the integral can be simplified to a significant extent. One of the cases is linear arrays with cylindrically curved surfaces, which will be studied in the following section.

C. The indirect angular spectrum approach

In the indirect ASA, the angular spectrum of a curved transducer is obtained via 2-D Fourier transforming an initial field pre-calculated in a plane. Since the 2-D Fourier transform can be implemented very efficiently using FFT, the method for calculating the initial field is most essential to the indirect ASA. For a linear array with a cylindrically curved surface, we have developed the Ocheltree-based method for calculating its ultrasonic fields, based on the method developed by Ocheltree and Frizzell for planar sources[29] and the appropriate coordinate transformation. This Ocheltree-based method is derived from the Rayleigh integral in Eq. (2) and the derivation is presented in the Appendix. Although it is developed for the linear array with a cylindrically curved surface, the method can be adapted to the cases of circular arrays[28] and transducers with conical and spherical surfaces,[30] or perhaps the case of a transducer with an arbitrarily curved surface. Consider a source with a curved surface S, represented by $z=f(x,y)$ under the Cartesian coordinates, as in Sec. I B. An initial velocity field of z-component radiated by the source is calculated in a plane at $z=z_1$, and represented by $\tilde{v}_{0z}(x,y,z_1)$. Performing the 2-D Fourier transform on the initial field that can be thought of as a secondary source with normal velocity $\tilde{v}_n(x,y,z_1) = \tilde{v}_{0z}(x,y,z_1)$, we obtain the angular spectrum of the curved source at the plane $z=z_1$ (refer to the Appendix for the procedure).

II. THE ANGULAR SPECTRUM AND THE ACOUSTIC FIELD OF A LINEAR ARRAY WITH A CYLINDRICALLY CONCAVE SURFACE

The ultrasonic linear array considered here has a cylindrical concave surface performing geometrical focusing in elevation, i.e., in the y-z plane (see Fig. 1). Calculation of the angular spectrum and the fields from this type of array is presented in this section. For the indirect ASA, the angular spectrum of the array is just the 2-D Fourier transformed

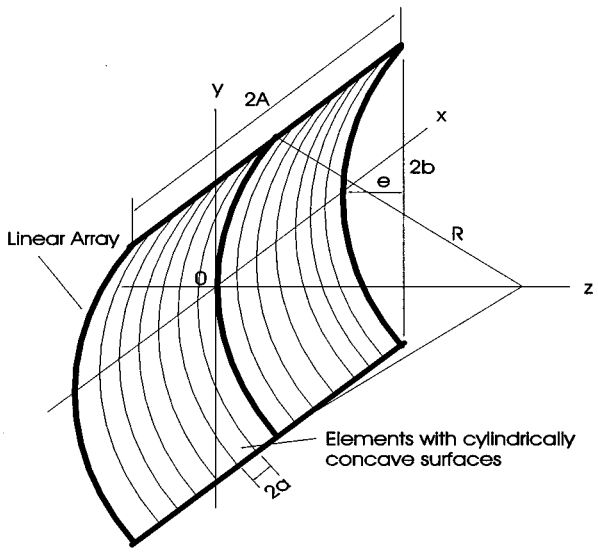

FIG. 1. Geometry and notation of the array with a cylindrically concave surface.

initial field in a plane radiated by the array. The initial field is calculated by the Ocheltree-based method that has been presented in the Appendix. Here we only consider the extended ASA used for the linear array case.

Referring to Fig. 1, we assume that the array has N' elements (N' is assumed to be even) and its surface is cylindrically concave and expressed by the following equation:

$$y^2+(z-R)^2=R^2, \quad \text{or} \quad z=R-\sqrt{R^2-y^2}, \qquad \{x_i-a\leqslant x\leqslant x_i+a, \quad -b\leqslant y\leqslant b\}, \tag{7}$$

where R is the radius of the curvature, $2a$ and $2b$ define the width and length of each element, respectively, $x_i=(i-1/2)d$ is the position of the center of the ith element on the x axis, $i=-N'/2+1,\ldots,0,1,2,\ldots,N'/2$, and $z=e$ for $y=\pm b$. The direction cosine of the normal of the array surface with respect to the z-axis is easily found from Eqs. (2) and (7) as follows:

$$\cos\theta_z=\sqrt{R^2-y^2}/R. \tag{8}$$

Consider the array with all the elements having uniform normal velocity distribution on the surface. For the ith element, the normal velocity excitation at frequency ω is supposed to be

$$\tilde{v}_{ni}(x,y,z)=\tilde{v}_i(\omega)\exp(j\omega\tau_i), \tag{9}$$

where $\tilde{v}_i$ is the complex amplitude, and τ_i is the delay time, which, in the time-harmonic case, creates phase shift $\omega\tau_i$ for beam steering and focusing.[16] Inserting Eqs. (7)–(9) into Eq. (6), we obtain the angular spectrum for the ith element of the array centering at $(x,y,z)=\{(i-1/2)d,0,0\}$ and having the dimension $\{(i-1/2)d-a\leqslant x\leqslant(i-1/2)d+a, \quad -b\leqslant y\leqslant b\}$, as follows:

$$V_i(k_x,k_y;z=z_1)=\tilde{v}_i(\omega)\exp(j\omega\tau_i)\int_{(i-1/2)d-a}^{(i-1/2)d+a}\exp(-jx'k_x)dx'\int_{-b}^{b}\frac{\exp[-j(y'k_y+(R-\sqrt{R^2-y'^2}-z_1)k_z)]}{\sqrt{R^2-y'^2}/R}dy'$$

$$=\tilde{v}_i(\omega)\exp[j\omega\tau_i-j(i-1/2)dk_x]2a\,\mathrm{sinc}(ak_x)\int_0^b\frac{2R\cos(y'k_y)\exp(j(z_1-R+\sqrt{R^2-y'^2})k_z)}{\sqrt{R^2-y^2}}dy', \qquad (z_1\geqslant e), \tag{10}$$

where $\mathrm{sinc}(x)=\sin(x)/x$. From Eq. (10) and by superposition, the angular spectrum of the array can be obtained,

$$V(k_x,k_y;z=z_1)=\sum_{i=-N'/2+1}^{N'/2}V_i(k_x,k_y;z=z_1). \tag{11}$$

Inserting Eq. (10) into Eq. (11), it is easy to find that $2a\,\mathrm{sinc}(ak_x)$ and the integral can be factored out from the sum in Eq. (11). Therefore, in the cases of a cylindrically concave, rectangular transducer, and an array consisting of such linearly aligned transducers, the double integral of the angular spectrum can be reduced into a single integral. The single integral will be numerically implemented, which will be further studied in next section (Sec. III).

Based on the angular spectrum in Eq. (11), the pressure field from the array can be synthesized,

$$\tilde{p}(x,y,z)=k\rho c\int_{-\infty}^{\infty}\int_{-\infty}^{\infty}V(k_x,k_y,z=z_1)\times\frac{\exp[j(xk_x+yk_y+(z-z_1)k_z)]}{k_z}dk_x\,dk_y, \qquad (z\geqslant z_1). \tag{12}$$

In the transient case, the pulse normal velocity of the ith element is represented by $v_{ni}(x,y,z;t)$ and its temporal Fourier transform is $\tilde{v}_{ni}(x,y,z)$ defined by Eq. (9). The transient pressure field can, thus, be obtained by the inverse Fourier transform, that is, $p(x,y,z;t)=(1/2\pi)\int_{-\infty}^{\infty}\tilde{p}(x,y,z)\exp(-j\omega t)d\omega$.

III. NUMERICAL CALCULATION AND COMPARISON IN THE CASE OF THE LINEAR ARRAY

In this section, we present some calculations of angular spectra using the extended and the indirect ASA for a spe-

cific linear array similar to the one used in our lab for the inspection of electron beam welds in copper.[15] The programs for both approaches were written in C and run on a PC with Pentium 133 MHz. The array has the geometrical parameters: $2a=1$ mm, $2b=30$ mm, $R=100$ mm, and $N'=22$. No gaps between the adjacent elements is assumed. The medium in which waves propagate is water whose sound speed and density are 1500 m/s and 1000 kg/m^3, respectively. Here the considered array is not electronically focused. In this case, both the angular spectrum and the radiated field are symmetrical with respect to the x- and the y-axis, respectively.

From the extended ASA, that is, using Eqs. (10) and (11), we calculate the angular spectrum for $z_1=e+5$ mm (where $e=R-\sqrt{R^2-b^2}=1.13$ mm). The evanescent waves are neglected in this case without affecting the accuracy (see Sec. I) and thus $V(k_x,k_y;z=z_1)$ in the range of $-1\leqslant n_x$, $n_y\leqslant 1$ is of interest. The computational accuracy of the approach completely depends on the numerical integration, which obviously depends on the integration interval dy (or spatial sampling interval), that is, the smaller the dy the more accurate the integration and meanwhile the more time consuming the computation. With consideration of both accuracy and efficiency for the numerical integration in Eq. (10), the most important thing is choosing an appropriate spatial sampling interval. Since $R\gg b$ (the upper limit of y'), $1/\sqrt{R^2-y'^2}$ varies very slowly in a small range from $1/R$ to $1/\sqrt{R^2-b^2}$ as y' changes from 0 to b, and either does $R-\sqrt{R^2-y'^2}$ in the range from 0 to $R-\sqrt{R^2-b^2}$ ($\approx b^2/(2R)$). Due to the small-range variation of $R-\sqrt{R^2-y'^2}$, $\exp(j(z_1-R+\sqrt{R^2-y^2})k_z)$ oscillates only with a few cycles even for $k_z=k$. Thus $\cos(y'k_y)$ in the integral is the dominant term for choosing an appropriate sampling interval for the integration. Taking into account that the spatial frequency $k_y=n_y 2\pi/\lambda$ varies from 0 to $2\pi/\lambda$ as n_y goes from 0 to 1, the three different sampling intervals are used for the integration that are $\lambda/5$ for n_y in the range 0–0.33, $\lambda/10$ for n_y in the range 0.33–0.66, and $\lambda/15$ for n_y in the range 0.66–1. In this way, the angular spectrum with dimension of 257×257 in the first quadrant ($0\leqslant n_x$, $n_y\leqslant 1$) was calculated with consideration of its symmetry, and the computational time used was 99 s. The calculated angular spectrum is shown in Fig. 2 as a bold dotted curve.

Using the indirect ASA, i.e., using the Ocheltree-based method to calculate an initial field in the plane at $z=e+5$ mm and then performing the 2-D FFT of the initial field, we obtained the angular spectrum of the array in the plane at $z=e+5$ mm. The accuracy of this approach depends on the accuracy of the initial field, the spatial interval of the field points, and the size (the spatial truncation) of the field. For a good accuracy of the initial field, the condition is taken into account that determines the limitation on the width and length of each subelement into which each array element is divided [see Eq. (A7) in the Appendix]. Setting $F=80$ and $z=5$ mm in $\sqrt{4\lambda z/F}$ and then taking appropriate integer numbers [refer to Eq. (A3)], each element in the array is divided into 3×85 subelements whose widths and lengths satisfy Eq. (A7). Thus the 22-element array is divided into 66×85 subelements altogether. Due to the symmetry of the array, only one-fourth of the initial field is calculated that is in the first quadrant ($x\geqslant 0$, $y\geqslant 0$) of the plane at z_1. To reduce the aliasing error in the transform domain, a spatial interval of half-wavelength ($\lambda/2$) (Nyquist interval) is used. Concerning the initial field size, the field is calculated only in the first quadrant with size of 129×129 points that makes 32 mm$\times$32 mm, and then it is mirrored to the other three quadrants so as to form a 257×257 matrix. The amplitudes of the field points along the four sides of the square matrix are less than 0.55% maximum of the field. Finally, zero-padding is done to the 257×257 field so as to create a 512×512 matrix for the 2-D FFT. For obtaining such a 512×512 angular spectrum the whole computational time was 877 s. The angular spectrum obtained from the indirect ASA (solid curves) is also shown in Fig. 2 in comparison with the one obtained from the extended ASA (bold dotted curves).

The comparison in Fig. 2 shows that in the on-axis case [see Fig. 2 (a)–(d)] the results from the two approaches agree excellently except that some small discrepancies exist in the range of large n_x and n_y (around 0.95–1), and that in the off-axis case [Fig. 2(e)–(h)] the results agree very well except that some small discrepancies exist in the range of small n_x and n_y (around 0) and in the range of large n_x and n_y (around 0.5).

To figure out the reason for these discrepancies, we used the indirect ASA to re-calculate the angular spectrum with the initial field size increased to 64 mm$\times$64 mm, that resulted in 257×257 field points. Then the 257×257 field was mirrored to the other three quadrants so as to form a 512×512 matrix for 2-D FFT. The computational time in this case was 2850 s, almost four times long as for the computation of the 32 mm$\times$32 mm initial field. The results calculated in such a way have been shown to be closer to those obtained from the extended ASA. This can be demonstrated by comparing the normalized root-mean-square (rms) difference between the results obtained from the extended ASA and the indirect ASA in the above two cases, respectively. The normalized rms difference is here defined as

$$\Delta_{\mathrm{rms}}=\frac{\{\Sigma_{m=1}^{M}[V_{\mathrm{ind}}(m)-V_{\mathrm{ext}}(m)]^2/M\}^{1/2}}{\{\Sigma_{m=1}^{M}[V_{\mathrm{ext}}(m)]^2/M\}^{1/2}},$$

where $V_{\mathrm{ext}}(m)$ and $V_{\mathrm{ind}}(m)$ are the real or imaginary part of the discrete angular spectra from the extended ASA and the indirect ASA for given n_x or n_y. Take the real part of the angular spectrum for $n_x=0$ [like the one in Fig. 2(a)] as an example. In the case of the 32 mm$\times$32 mm initial field, Δ_{rms} for the results in Fig. 2(a) is 0.0387, and in the case of the 64 mm$\times$64 mm initial field, Δ_{rms} reduces to 0.0297. This reveals that the extended ASA is more accurate than the indirect ASA, and that the spatial truncation of the initial field has an effect on the computation accuracy of the indirect ASA, i.e., the larger the initial field size the better the computational accuracy. Obviously, computation of an initial field with a larger size requires much longer computational time.

From the above calculation, comparison, and analysis, it is concluded that the ASA can be extended to directly solve

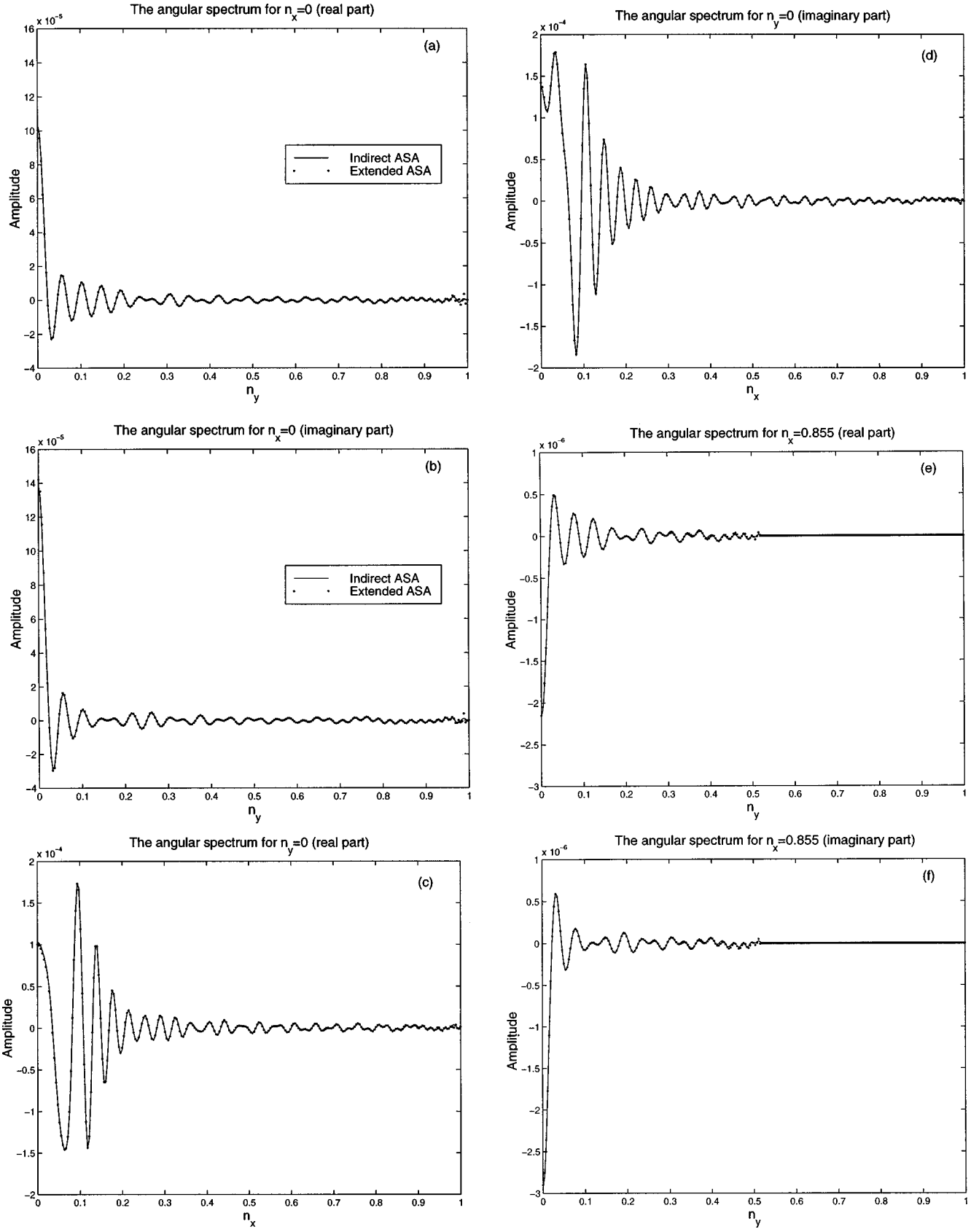

FIG. 2. The angular spectra from the extended ASA (dotted line) and the indirect ASA (solid line). (a) The real and (b) the imaginary part for $n_x=0$; (c) the real and (d) the imaginary part for $n_y=0$; (e) the real and (f) the imaginary part for $n_x=0.855$; (g) the real and (h) the imaginary part at $n_y=0.855$. Note that the vertical axes are different in scale.

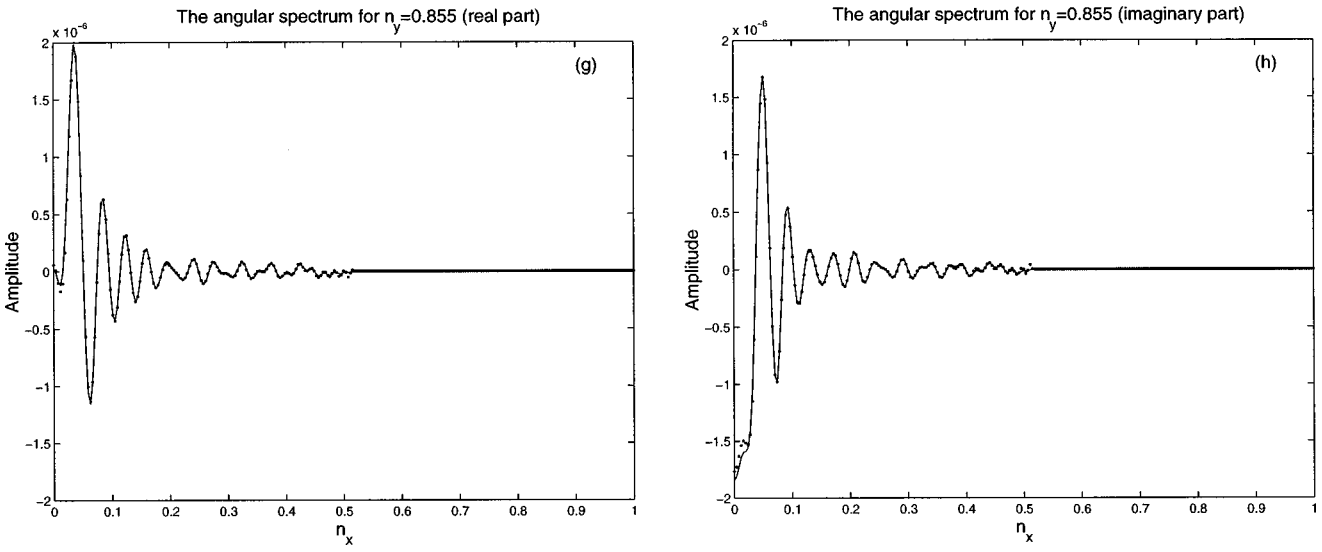

FIG. 2. (*Continued.*)

the fields from curved sources based on Eq. (6). In the case of a linear array with a cylindrically concave surface, the double integral in Eq. (6) reduces to the single integral in Eq. (10). In this case, the extended ASA has been shown to be more accurate and more efficient than the indirect ASA (the efficiency of the extended ASA is better by a factor of 8 or more), and for the similar computational accuracy, the extended ASA is much more efficient than the indirect ASA (the efficiency of the extended ASA is better by a factor of 28 or more).

However, in the general case where the double integral of the extended ASA cannot be reduced to a single integral, the double integral must be evaluated, and the extended ASA may not be so efficient as the indirect ASA. For example, if we had directly evaluated the double integral in Eq. (6) for the above-studied linear array case using the sampling interval $dx=\lambda/5$ for all n_x (so as to make 110 integration intervals in the x-direction), the computational time could have been about 100 times the computational time (99 s) for the evaluation of the single integral in Eq. (11), instead of 28 times 99 s—the computational time for the indirect ASA. Therefore, in this general case, the indirect ASA can be a better alternative.

Using the angular spectrum calculated from the extended ASA and Eq. (12), we simulated an acoustic field from the array (see Fig. 3). The acoustic field is in the y-z plane at $x=0$ and its focal zone is seen around 95 mm.

IV. CONCLUSIONS

The ASA which is conventionally applicable to the case of planar transducers has been extended to treat the case of curved transducers, and thus two approaches, namely, the extended ASA and indirect ASA, have been developed.

The extended ASA has been derived without any approximation in a general way starting from the Rayleigh integral of curved surface (O'Neil's theory) and using the conventional ASA theory for the case of planar sources. A general form of the angular spectrum has been obtained that is given by a double integral that does not have the 2-D Fourier transform form. Therefore, the extended ASA is implemented by numerical integration instead of using the 2-D FFT. This approach has been applied to the case of a linear array with a cylindrically curved surface, and it has been shown that in this case the double integral reduces to a single integral.

The indirect ASA gives the angular spectrum of a curved source via the 2-D FFT of an initial field precalculated in a plane. The method for calculating the initial field from a linear array with a cylindrically concave surface has been established based on the method developed by Ocheltree and Frizzell.[29] This Ocheltree-based method is the most essential part of the indirect ASA.

A specific example has been given of a linear array with a cylindrically concave surface similar to that used in our lab

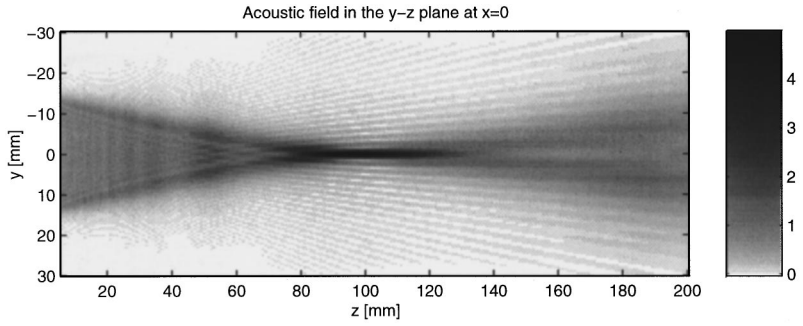

FIG. 3. Simulated acoustic field (pressure magnitude) in water from the linear array with a cylindrically concave surface, based on the extended ASA. The field is normalized by multiplying by the acoustic impedance of water.

for the inspection of weld in copper. An efficient way for the numerical implementation of the extended ASA has been proposed. The angular spectra of the array were calculated using the two approaches and compared. The comparison has shown that the angular spectra calculated from both approaches are in excellent agreement.

The accuracy and efficiency of both approaches have been discussed in detail. From the example of the linear array, the extended ASA has been shown to be more efficient and more accurate than the indirect ASA, especially in the range of large direction cosines (n_x and/or n_y). However, in the general case where the double integral of the extended ASA cannot be reduced to a single integral, the double integral must be evaluated, and the extended ASA may not be as efficient as the indirect ASA. Therefore, in this general case, the indirect ASA can be a better alternative.

In principle, both approaches can be applied to arbitrarily curved transducers provided that the secondary diffraction due to the curvature of a transducer does not yield significant errors in calculation. In practice, the secondary diffraction is usually unimportant and its effect can be neglected, as stated in Sec. I.

ACKNOWLEDGMENTS

This work was sponsored by the Swedish Nuclear Fuel and Waste Management Co. (SKB) under Contract No. 61230-97-52. The authors are thankful to the anonymous reviewers for their valuable comments on this paper.

APPENDIX: THE METHOD FOR THE CALCULATION OF FIELDS FROM A LINEAR ARRAY WITH A CYLINDRICALLY CONCAVE SURFACE

This method was developed based on the idea proposed by Lee and Benkeser[28] who extended to the circular array case the method developed by Ocheltree and Frizzell for planar sources.[29] Unlike the circular array dealt with by Lee and Benkeser, the array in our case is a linear array with a cylindrically concave surface, their idea has been adapted to our case. Therefore, we name it Ocheltree-based method.

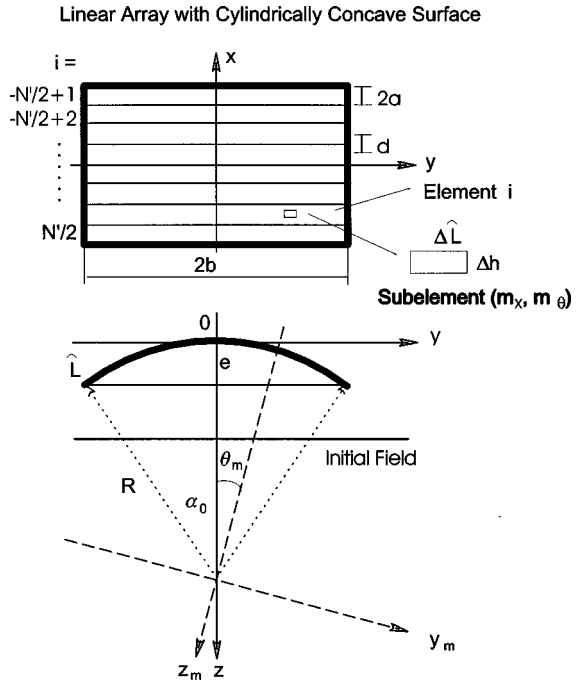

FIG. A1. Geometry for calculating acoustic field from the linear array with a cylindrically concave surface based on Ocheltree's method (Ref. 29).

To facilitate the calculation of fields from such a linear array using Ocheltree-based method, we re-arrange Fig. 1 and use two coordinate systems (see Fig. A1). The first one is the x-y-z coordinate system which is the same as in Fig. 1, and the other is x_m-y_m-z_m coordinate system which is a rotating system. Their relation will be given below.

The half angle, α_0, subtended by chord $2b$ (see Fig. A1) can easily be found to be

$$\alpha_0 = \arcsin(b/R). \tag{A1}$$

Thus, the arc length spanning over chord $2b$ is

$$\hat{L} = 2\alpha_0 R. \tag{A2}$$

When each element is divided into such $M_x \times M_\theta$ small subelements with width Δh and length $\Delta\hat{L}$ (see Fig. A1) that the curvature of the subelements can be neglected, the subelements can be thought of as plane piston sources. The subelements are indicated by (m_x, m_θ), where $m_x = 1, \ldots, M_x$ and $m_\theta = 1, \ldots, M_\theta$. Thus the width and the length of each subelement are

$$\Delta h = 2a/M_x, \quad \Delta\hat{L} = \Delta\alpha R = 2\alpha_0 R/M_\theta, \tag{A3}$$

respectively, where

$$\Delta\alpha = 2\alpha_0/M_\theta \tag{A4}$$

is the angle subtended by the arc spanning the centers of adjacent subelements in the y-direction. The angle subtended by the arc from the center of subelement (m_x, m_θ) to the z-axis is

$$\theta_{m_\theta} = -\alpha_0 + \Delta\alpha(m_\theta - 1/2), \quad (m_\theta = 1, \ldots, M_\theta). \tag{A5}$$

To facilitate the calculation, we shall use the second set of coordinates, (x_m, y_m, z_m), for all subelements with θ_{m_θ}. The (x_m, y_m, z_m) coordinates are a system rotating around point $(x,y,z) = (0,0,R)$ and are related to the x-y-z coordinates through the following transformation:

$$\begin{bmatrix} x_m \\ y_m \\ z_m \end{bmatrix} = \begin{bmatrix} 1 & 0 & 0 \\ 0 & \cos\theta_{m_\theta} & \sin\theta_{m_\theta} \\ 0 & -\sin\theta_{m_\theta} & \cos\theta_{m_\theta} \end{bmatrix} \begin{bmatrix} x \\ y \\ z - R \end{bmatrix}. \tag{A6}$$

Equation (A6) means that the x_m-y_m-z_m coordinate system is obtained in such a way that the x-y-z coordinates first translate by R in the z-direction, and then rotate clockwise by an angle θ_{m_θ}.

Following Ocheltree and Frizzell for planar sources,[29] each subelement has such a small size $\Delta A = \Delta h \times \Delta\hat{L}$ that Δh and $\Delta\hat{L}$ meet the condition

$$\Delta h, \ \Delta\hat{L} \leqslant \sqrt{4\lambda z/F}, \tag{A7}$$

in which the constant F represents the distance from the source to the field point relative to the distance to the near-field–far-field transition for a source of size $\Delta A = \Delta h$

$\times \Delta\hat{L}$, and thus, the Fraunhofer approximation can be applied.

For such a small subelement that has a uniform normal velocity v_0 and is located at point (0, 0, 0) under the x-y-z coordinates, corresponding to point (0, 0, $-R$) under the x_m-y_m-z_m coordinates with $\theta_{m_\theta}=0$, the acoustic field from the subelement can be approximated by[29]

$$\begin{aligned}\delta p_{0,0}(x_0,y_0,z_0) &= -\frac{j\rho c}{\lambda}\int\int_{\Delta A} v_n(x_0',y_0',z_0')\frac{e^{-jkr_{s0}}}{r_{s0}}dS_0 \\ &\approx \frac{j\rho c\Delta A v_0}{\lambda}\operatorname{sinc}\left(\frac{kx_0\Delta h}{2R_{s0}}\right)\operatorname{sinc}\left(\frac{ky_0\Delta\hat{L}}{2R_{s0}}\right),\end{aligned} \tag{A8}$$

where $dS_0=dx_0'\,dy_0'$,

$$r_{s0}=\sqrt{(x_0-x_0')^2+(y_0-y_0')^2+(z_0+R)^2}$$

and $R_{s0}=\sqrt{x_0^2+y_0^2+(z_0+R)^2}$.

For such a subelement that is located at point $(x,y,z)=(x_{m_x},R\sin\theta_{m_\theta},R-R\cos\theta_{m_\theta})$, where

$$x_{m_x}=-a+\Delta h(m_x-1/2)\quad (m_x=1,\ldots,M_x), \tag{A9}$$

we can obtain the same formula as in Eq. (A8) by transforming the x-y-z coordinates into the x_m-y_m-z_m coordinates by means of Eq. (A6). The pressure field from subelement (m_x,m_θ) under the x_m-y_m-z_m coordinates is expressed as

$$\begin{aligned}\delta p_{m_x,m_\theta}(x_m,y_m,z_m) &= -\frac{j\rho c}{\lambda}\int\int_{\Delta A} v_n(x_m',y_m',z_m')\frac{e^{-jkr_{sm}}}{r_{sm}}dS_m \\ &\approx \frac{j\rho c\Delta A v_0}{\lambda}\operatorname{sinc}\left(\frac{k(x_m-x_{m_x})\Delta h}{2R_{sm}}\right)\operatorname{sinc}\left(\frac{ky_m\Delta\hat{L}}{2R_{sm}}\right),\end{aligned} \tag{A10}$$

where $dS_m=dx_m'\,dy_m'$,

$$r_{sm}=\sqrt{(x_m-x_m'-x_{m_x})^2+(y_m-y_m')^2+(z_m+R_0)^2},$$

and $R_{sm}=\sqrt{(x_m-x_{m_x})^2+y_m^2+(z_m+R_0)^2}$.

The pressure field from an element centered at $(x,y,z)=(0,0,0)$ is the summation of $\delta p_{m_x,m_\theta}(x_m,y_m,z_m)$, that is,

$$\begin{aligned}\tilde{p}_{00}(x,y,z) &= \sum_{m_\theta=1}^{M_\theta}\sum_{m_y=1}^{M_x}\delta p_{m_x,m_\theta}(x_m,y_m,z_m) \\ &= \frac{j\rho c\Delta A v_0}{\lambda}\sum_{m_\theta=1}^{M_\theta}\sum_{m_x=1}^{M_y}\operatorname{sinc}\left(\frac{k(x_m-x_{m_x})\Delta h}{2R_{sm}}\right) \\ &\quad\times\operatorname{sinc}\left(\frac{ky_m\Delta\hat{L}}{2R_{sm}}\right),\end{aligned} \tag{A11}$$

where x_m, y_m, z_m depend on m_θ via Eq. (A6). The pressure field from the array with N' elements is, therefore, obtained by the summation of $\tilde{p}_i(x,y,z)$, the field from the ith array element, in the manner

$$\tilde{p}(x,y,z)=\sum_{i=-N'/2+1}^{N'/2}\tilde{p}_i(x,y,z)=\sum_{i=-N'/2+1}^{N'/2}\tilde{p}_{00}(x+x_i,y,z), \tag{A12}$$

where $x_i=(i-1/2)d$. Choosing a plane $z=z_1$ parallel to the x-y plane and using the relation $\tilde{v}_z(x,y,z_1)=-(1/jk\rho c)\partial\tilde{p}(x,y,z)/\partial z\big|_{z=z_1}$, we calculate an initial velocity field of z-component, denoted by $\tilde{v}_{0z}(x,y,z_1)$, in the plane $z=z_1$ via Eq. (A12). Based on the initial field, which can be thought of as a secondary source with normal velocity $\tilde{v}_n(x,y,z_1)=\tilde{v}_{0z}(x,y,z_1)$, the angular spectrum of the array at the plane $z=z_1$ can be obtained using the 2-D FFT.

Although the method is established for the case of a cylindrically curved, rectangular transducer, and a linear array consisting of such transducers, it can be extended to the case of transducers with conical and spherical surfaces[30] or perhaps the general case where a transducer has an arbitrarily curved surface.

[1] J. W. Goodman, *Introduction to Fourier Optics* (McGraw-Hill, New York, 1968).
[2] G. C. Sherman, ''Generalization of the angular spectrum of plane waves and the diffraction transform,'' J. Opt. Soc. Am. **59**, 146–156 (1969).
[3] P. C. Clemmow, *The Plane Wave Spectrum Representation of Electromagnetic Fields* (Pergamon, London, 1966).
[4] E. G. Williams and J. D. Maynard, ''Numerical evaluation of the Rayleigh integral for planar radiators using the FFT,'' J. Acoust. Soc. Am. **72**, 2020–2030 (1982).
[5] D. P. Orofino and P. C. Pedersen, ''Efficient angular spectrum decomposition of acoustic sources—Part I. Theory, and Part II. Results,'' IEEE Trans. Ultrason. Ferroelectr. Freq. Control **40**, 238–257 (1993).
[6] P. T. Christopher and K. J. Parker, ''New approaches to the linear propagation of acoustic fields,'' J. Acoust. Soc. Am. **90**, 507–521 (1991).
[7] P. Wu, R. Kazys, and T. Stepinski, ''Analysis of the numerically implemented angular spectrum approach based on the evaluation of two-dimensional acoustic fields—Part I: Errors due to the discrete Fourier transform and discretization, and Part II: Characteristics as a function of angular range,'' J. Acoust. Soc. Am. **99**, 1339–1359 (1996).
[8] P. Wu, R. Kazys, and T. Stepinski, ''Optimal selection of parameters for the angular spectrum approach to numerically evaluate acoustic fields,'' J. Acoust. Soc. Am. **101**, 125–134 (1997).
[9] D.-L. Liu and R. C. Waag, ''Propagation and backpropagation for ultrasonic wavefront design,'' IEEE Trans. Ultrason. Ferroelectr. Freq. Control **44**, 1–13 (1997).
[10] M. E. Schafer, ''Transducer characterization using the angular spectrum method,'' J. Acoust. Soc. Am. **85**, 2202–2214 (1996).
[11] K. K. Liang, G. S. Kino, and B. T. Khuri-Yakub, ''Material characterization by the inversion of $V(z)$,'' IEEE Trans. Sonics Ultrason. **SU-32**, 213–225 (1985).
[12] C.-H. Chou and G. S. Kino, ''The evaluation of $V(z)$ in a type II reflection microscope,'' IEEE Trans. Ultrason. Ferroelectr. Freq. Control **34**, 341–345 (1987).
[13] V. S. Ardebili and A. N. Sinclair, ''A new angular spectrum approach for modelling the acoustic microscope response with high attenuation coupling fluids,'' Proc. 1995 IEEE Ultrason. Symp. (IEEE Cat. No. 95CH35844), Vol. 2, 873–876 (1995).
[14] Y. Sugara, J. Kushibiki, and N. Chubachi, ''Performance of concave transducers in acoustic microscopy,'' Proc. 1988 IEEE Ultrason. Symp. (IEEE Cat. No. 88CH2578-3), Vol. 2, 751–756 (1988).
[15] T. Stepinski and P. Wu, *Inspection of Copper Canisters for Spent Nuclear Fuel by Means of Ultrasonic Array System*, SKB Projektrapport 97-08 (SKB, Stockholm, August 1997).
[16] P. Wu and T. Stepinski, ''Elastic fields in immersed isotropic solids from phased arrays: The time harmonic case,'' Res. Nondestruct. Eval. **10**, 185–204 (1998).
[17] D. Guyomar and J. P. Powers, ''Transient fields radiated by curved surfaces—Application to focusing,'' J. Acoust. Soc. Am. **76**, 1564–1572 (1984).
[18] D. Guyomar and J. Powers, ''Transient radiation from focused transduc-

ers,'' Proc. IEEE 1984 Ultrason. Symp. (IEEE Cat. No. 84CH2112-1), Vol. 2, 979–982 (1984).
[19] H. T. O'Neil, ''Theory of focusing radiators,'' J. Acoust. Soc. Am. **21**, 516–526 (1949).
[20] A. Penttinen and M Luukkala, ''The impulse response and pressure nearfield of a curved radiator,'' J. Phys. D **9**, 1547–1557 (1976).
[21] M. Arditi, F. S. Foster, and J. M. Hunt, ''Transient fields of concave annular arrays,'' Ultrason. Imaging **3**, 37–61 (1981).
[22] E. L. Madsen, M. M. Goodsitt, and J. A. Zagzebski, ''Continuous waves generated by focused radiators,'' J. Acoust. Soc. Am. **70**, 1508–1517 (1981).
[23] H. Djelouah, J. C. Baboux, and M. Perdix, ''Theoretical and experimental study of the field radiated by ultrasonic focused transducer,'' Ultrasonics **29**, 188–200 (1991).
[24] F. Coulouvrat, ''Continuous field radiated by a geometrically focused transducer: Numerical investigation and comparison with an approximate model,'' J. Acoust. Soc. Am. **94**, 1663–1675 (1993).
[25] M. A. Fink and J.-F. Cardoso, ''Diffraction effects in pulse-echo measurement,'' IEEE Trans. Sonics Ultrason. **SU-31**, 313–329 (1984).
[26] L. W. Schmerr, Jr., A. Sedov, and T. P. Lerch, ''A boundary diffraction wave model for a spherically focused ultrasonic transducer,'' J. Acoust. Soc. Am. **101**, 1269–1277 (1997).
[27] W. A. Verhoef, M. J. T. M. Cloostermans, and J. M. Thijsssen, ''The impulse-response of a focused source with an arbitrary axisymmetric surface velocity distribution,'' J. Acoust. Soc. Am. **75**, 1716–1720 (1984).
[28] C. Lee and P. J. Benkeser, ''Computationally efficient sound field calculations for a circular array transducer,'' IEEE Trans. Ultrason. Ferroelectr. Freq. Control **39**, 43–47 (1992).
[29] K. B. Ocheltree and L. A. Frizzell, ''Sound field calculation for rectangular sources,'' IEEE Trans. Ultrason. Ferroelectr. Freq. Control **36**, 242–248 (1989).
[30] C. Lee and P. J. Benkeser, ''A computationally efficient method for the calculation of the transient field of acoustic radiators,'' J. Acoust. Soc. Am. **96**, 545–551 (1994).

Modeling of scattering by partially buried elastic cylinders

J. A. Fawcett[a)]
Saclant Undersea Research Centre, Viale San Bartolomeo 400, 19138 San Bartolomeo, La Spezia, Italy

(Received 17 March 1998; accepted for publication 22 January 1999)

The work of a previous paper on the modeling of scattering by a partially buried cylinder is extended to allow the cylinder to have full elasticity (and not just be a fluid structure as in the previous work). The results of computations showing the effects of increasing burial on the backscattered field, both in the spectral and temporal domains, are given. A shelled and a solid aluminum cylinder are considered for a grazing angle of incidence which is subcritical. © *1999 Acoustical Society of America.* [S0001-4966(99)02805-2]

PACS numbers: 43.30.Gv, 43.20.Fn [DLB]

INTRODUCTION

The effect of burial in the seabed on the spectrum of the energy backscattered from an elastic object is an area of current research.[1–3] In an earlier paper[1] we presented a Boundary Integral Equation Method (BIEM) which could be used to model the scattering from proud (above the seabed), partially buried, or fully buried cylindrical structures. In that paper the cylinder was taken to be a fluid structure; shear was not modeled. In this paper we describe a simple modification to allow the cylinder to be elastic in nature and we present computational examples of the effect of burial on the energy (both in the spectral and temporal domains) backscattered from an evacuated steel-shelled cylinder and from a solid aluminum cylinder as they are increasingly buried in a sediment layer.

I. THEORY

We consider an infinitely long cylinder and use two-dimensional modeling. In Ref. 1 the pressure field within the cylinder, at the outer radius, was taken to have the form

$$p=\sum_{m=-N}^{N} a_m e^{im\theta}, \tag{1}$$

$$p_r=\sum_{m=-N}^{N} \alpha_m a_m e^{im\theta}, \tag{2}$$

where p_r is the radial derivative of the pressure (the range being measured from the center of the cylinder). The form of the coefficients α_m can be determined from the form of the solution in the interior of the cylinder. For example, in the case that the cylinder was a homogeneous fluid, then

$$\alpha_m=\frac{1}{J_m(k_{\rm int}r)}\frac{dJ_m(k_{\rm int}r)}{dr}, \tag{3}$$

where the subscript ''int'' refers to the interior of the cylinder. In the case that the interior is a layered fluid, then the interior continuity equations can be used to derive an expression for α_m. We now indicate the approach we take if the cylinder is a shelled elastic cylinder with some interior fill (a solid cylinder is a subcase of this). The outer radius of the cylinder is $r=a$ and the interior radius is $r=b$. We seek to express the stress and displacement fields within the cylinder in terms of one unknown coefficient for each azimuthal order. To do this, we consider the equations of continuity that the acoustic/elastic fields must satisfy at the interfaces of the cylinder; in particular, we will consider the equations involving only the potentials in the interior of the cylinder. These equations do not depend upon the form of the exterior fields; for simplicity, we will consider the elastic cylinder in a fluid free space.

In the exterior fluid, at a particular angular order m, there is a single unknown compressional coefficient $h_p^{\rm ex}$ for the Hankel function of order m, $H_m^1(kr)$. In the shell there are four unknowns $h_p^{\rm es}$, $j_p^{\rm es}$, $h_s^{\rm es}$, and $j_s^{\rm es}$ (''es'' denotes elastic shell) where these are the coefficients for the Hankel and Bessel functions for the compressional and shear potentials, respectively. Finally, within the innermost section of the cylinder we have $j_p^{\rm int}$ and $j_s^{\rm int}$. For a specified incident field, there is a 7×7 system of equations for the unknown coefficients γ,

$$A\boldsymbol{\gamma}=\mathbf{r}, \tag{4}$$

where

$$\boldsymbol{\gamma}\equiv(h_p^{\rm ex},j_p^{\rm es},h_p^{\rm es},j_s^{\rm es},h_s^{\rm es},j_p^{\rm int},j_s^{\rm int})^T, \tag{5}$$

and $\mathbf{r}$ is the known incident excitation.

There are three equations at the exterior shell/water interface ($r=a$); the continuity of the stress component σ_{rr}, the radial particle displacement u_r, and the vanishing of the stress component $\sigma_{r\theta}$. There are equations for the continuity of σ_{rr}, $\sigma_{r\theta}$, u_r, and u_θ at the interior shell/solid interface ($r=b$). Only the first two continuity equations for σ_{rr} and u_r at the exterior shell/water interface involve the incident and scattered potential in the exterior water. The third equation for $\sigma_{r\theta}$ involves only shell potentials (this stress component automatically vanishes in the water due to the absence of shear in a fluid). Because of this, $\mathbf{r}$ has the form

$$(r_1,r_2,0,0,0,0,0)^T, \tag{6}$$

where r_1 and r_2 are expressions involving the incident compressional potential. Thus the last five equations in the system of Eq. (4) do not depend upon the exterior incident or

[a)]Now at Defence Research Establishment Atlantic, P.O. Box 1012, Dartmouth, NS B2Y 3Z7, Canada.

scattered fields. We will not give the individual elements of matrix A. The detailed form of this matrix for elastic cylinders can be found in the literature; for example, the matrix for a fluid-filled, elastic-layered cylinder can be found in Ref. 4.

If we consider the bottom righthand 5×6 submatrix of A (i.e., the last five rows and six columns), A_b, and the last six coefficients of γ, we can write from Eqs. (4) and (6) that

$$A_b\gamma_b=\mathbf{0}. \tag{7}$$

Arbitrarily setting j_p^{es} equal to unity we can write

$$\hat{A}_b\hat{\gamma}_b=-\mathbf{a}_1, \tag{8}$$

where $\hat{A}_b$ is the right 5×5 submatrix of A_b, $\hat{\gamma}_b$ are the five unknown interior coefficients (assuming that $j_p^{\mathrm{es}}=1$), and $\mathbf{a}_1$ is the first column of A_b. Thus we can express the radial stress component, σ_{rr}, and the radial displacement, u_r, within the shell at $r=a$ in terms of the unknown coefficient for j_p^{es}. In particular,

$$\begin{aligned}&\sigma_{rr}\propto(f_1+\hat{\gamma}_{b,1}f_2+\hat{\gamma}_{b,2}f_3+\hat{\gamma}_{b,3}f_4),\\&u_r\propto(g_1+\hat{\gamma}_{b,1}g_2+\hat{\gamma}_{b,2}g_3+\hat{\gamma}_{b,3}g_4),\end{aligned} \tag{9}$$

where

$$\begin{aligned}f_1&=\frac{-\lambda\omega^2}{c_p^2}J_m(k_pa)+2\mu J_m''(k_pa),\\f_2&=\frac{-\lambda\omega^2}{c_p^2}H_m(k_pa)+2\mu H_m''(k_pa),\\f_3&=2\mu i\frac{m}{a}\left(J_m'(k_sa)-\frac{1}{a}J_m(k_sa)\right),\\f_4&=2\mu i\frac{m}{a}\left(H_m'(k_sa)-\frac{1}{a}H_m(k_sa)\right),\\g_1&=J_m'(k_pa),\quad g_2=H_m'(k_pa),\\g_3&=\frac{im}{a}J_m(k_sa),\quad g_4=\frac{im}{a}H_m(k_sa).\end{aligned} \tag{10}$$

The prime symbol denotes a derivative with respect to r and $\gamma_{b,i}$ denotes the ith element of the solution vector γ_b. We note that σ_{rr} and u_r are continuous across the cylinder surface and that in the surrounding fluids $p=-\sigma_{rr}$ and $p_r=-\rho\omega^2u_r$. Thus we can write for the pressure p and its normal derivative p_r on the exterior of the cylinder's surface,

$$\begin{aligned}p&=\sum_{m=-N}^{N}-a_mt_me^{im\theta},\\p_r&=\sum_{m=-N}^{N}-\rho\omega^2a_mu_me^{im\theta},\end{aligned} \tag{11}$$

where t_m and u_m are the expressions in brackets in Eq. (9) and the expansion coefficients a_m are to be determined. The remainder of the BIEM approach follows that of Ref. 1 for the fluid cylinder. The basic BIEM now takes the form

$$2\pi a_m=i_m-A_{mk}t_ka_k+B_{mk}\omega^2u_ka_k, \tag{12}$$

where

$$A_{mk}\equiv a\lim_{\epsilon\to0}\int_0^{2\pi}\int_0^{2\pi}G_{r'}(a+\epsilon,\theta;a,\theta')\times e^{-im\theta}e^{ik\theta'}\,d\theta\,d\theta', \tag{13}$$

$$B_{mk}\equiv a\lim_{\epsilon\to0}\int_0^{2\pi}\int_0^{2\pi}G(a+\epsilon,\theta;a,\theta')\times e^{-im\theta}e^{ik\theta'}\rho(\theta)d\theta\,d\theta', \tag{14}$$

and G is the half-space Green's function. The details of computing these integrals are given in Ref. 1. If the object is totally above or below the interface, then there exist generalized T-matrix formulations (for example, a cylindrical adaptation in Ref. 5 of the spherical method of Ref. 6) or plane-wave decomposition methods[7] for these problems. We verified that the BIEM of this paper gave results which agreed with those of these other methods.

There is a problem with the BIEM approach of this paper (and also in Ref. 1) in the case that the cylinder is partially buried. Because the fluid approximation is used for the surrounding environment, the tangential component of displacement is not continuous across the water-basement interface. Thus the displacement in the radial direction (defined with respect to the cylinder center) is also not continuous. Hence where the cylinder's surface intersects the interface (we denote the corresponding angles as $\pm\theta_c$) we expect the series expansion of p and p_r [Eq. (11)] to behave poorly. This problem is improved by the fact that the series are involved in integrals, Eqs. (13) and (14). However, for cases where the values of p_r near θ_c are particularly important in the total scattering solution, there may be poor convergence with respect to the series expansion. In particular, for the case where the cylinder is almost totally buried (for example, 90% or 95%), there were sometimes convergence problems at various frequencies. This is because the upper surface of the cylinder in the water is close to and almost tangential to the interface, and it is in this region that one expects the series convergence to be poorest. One would expect that this problem would also depend upon the medium properties (for example, if there are only very small jumps in the density at the interface, then there should be only small discontinuities in the solution's derivatives across the interface), and the grazing angle of the incident energy, which controls the structure of the incident field upon the surface of the cylinder.

One ad hoc solution to this problem is to compute the numerical solution for N. Fourier coefficients and then for a larger number (say $N+10$) (by saving the integral results for the N case, the increased computation is not large) and see if the solutions are sufficiently converged. If they are not, this computed value should be ignored or replaced by a smoothed value.

II. NUMERICAL EXAMPLES

A. Steel-shelled cylinder with an evacuated interior

As a numerical example, we first consider a steel-shelled cylinder (6 mm thick) with an evacuated interior (which we

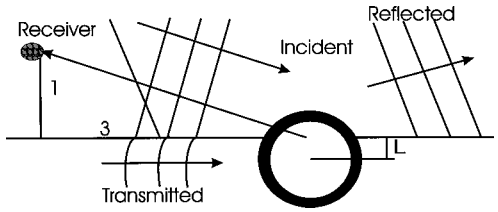

FIG. 1. Schematic of geometry for partially buried cylinder with direct and reflected planes waves incident in the water column and evanescent wave in the bottom.

model by using near zero values of c_p, c_s, and ρ) and an outer radius of 0.25 m. We consider the water with sound speed 1500 m/s and $\rho=1$ g/cm^3 overlying the basement with sound speed 1700 m/s and $\rho=1.5$ g/cm^3. The steel has parameters: $c_p=5950$ m/s, $c_s=3240$ m/s, and $\rho=7.7$ g/cm^3. We consider an incident plane wave, comprised of the direct and reflected wave in the water column and the transmitted wave in the basement. The grazing angle of incidence is 18.4° which is significantly subcritical. A receiver is in the water column at a range of 3.16 m at an angle of 18.4° with respect to the origin on the interface (see Fig. 1).

In Fig. 2 we present a waterfall plot of the spectra of the backscattered power in dB ($20\log_{10}|P|$) for 16 levels of burial of the cylinder, starting at a burial of $-1.5a$ (the center of the cylinder is positioned $0.375m=1.5a$ above the water/basement interface) and ending with a burial depth of $1.5a$. There is, however, no problem in using the method of this paper for much larger cylinder offsets from the interface. The curves have been offset 30 dB from each other and the points have been computed at a 50-Hz spacing. Because of the evanescent nature of the incident wave for the buried cylinder, we would expect the backscattered levels to fall rapidly as a function of burial in this case. Equivalently, if we consider a cylinder which is totally buried, a significant decrease in backscattered power as a function of frequency would be expected since the incident wave field in the bottom is evanescent; this can be seen in the last three curves of Fig. 2. The curves representing partial burial from 25% to 75% (curves 6–11) burial are fairly similar to each other in character, although the locations of the nulls in the spectra (particularly, the first null) changes as a function of burial fraction. The curves on either side of this range of burial values show more variation with respect to burial depth. However, it should be noted that the spectra are very much reduced in amplitude for the higher frequencies, so although there are differences in the features of these curves, these differences are, in fact, small in amplitude.

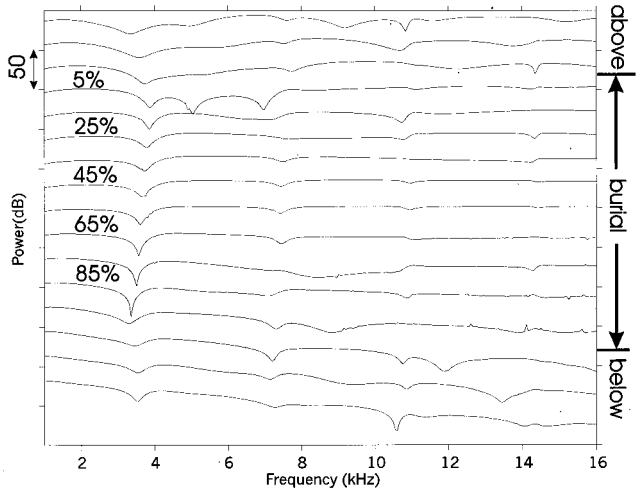

FIG. 2. Waterfall plot of backscattered power spectra from steel-shelled cylinder as a function of fractional burial, from $1.5a$ above the seabed interface to burial $1.5a$ below the interface.

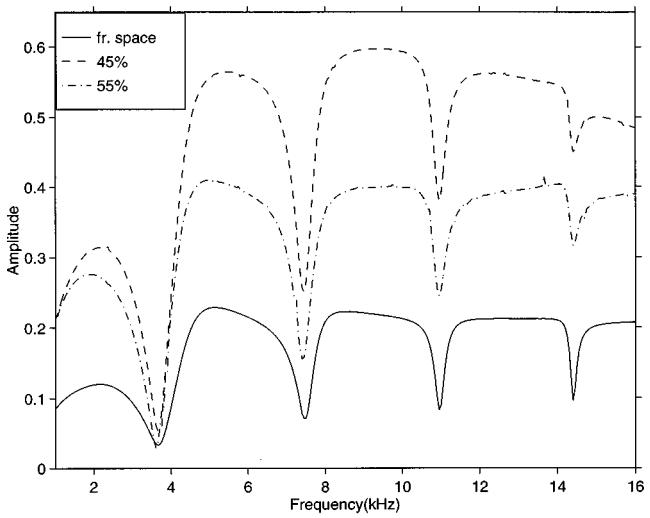

FIG. 3. Backscattered power levels from steel-shelled cylinder 45%, 55% buried, and in free-space surrounded by water.

In Fig. 3 we show the spectral curves as a function of frequency for the cylinder 45% buried, 55% buried, and for the cylinder in free space, surrounded by water. As can be seen, the three curves look qualitatively very similar but are different in amplitude levels. The curves for the partially buried cylinder show enhanced levels of backscatter with respect to the free-space curve. This is due to the fact that there is constructive interference between direct and seabed reflected wave fields. For the subcritical grazing angle considered here for the incident plane wave, the reflection coefficient has unity amplitude and a phase shift. Thus when the direct incident and reflected incident wave fields are added together, there can be an increase of amplitude in the area of constructive interference, from that of the direct incident field (up to a factor of 2). Similarly, the interference of the direct path and reflected scattered energy can produce further amplitude enhancements at the receiver. As the cylinder becomes increasingly buried, this amplitude enhancement disappears. The surface of the cylinder, from which reflections for this backscatter geometry take place, becomes increasingly buried in the seabed. The incident wave field in the sediment is exponentially decaying with depth from the interface for a subcritical grazing angle of incidence. Thus for total or almost total burial, the backscattered levels will be less than that for the free-space case.

We note that the spectra shown in Fig. 3 have a series of broad peaks and fairly sharp troughs. This type of spectra is caused by the interference of energy from the specular reflection and a sequence of Lamb waves which propagate cir-

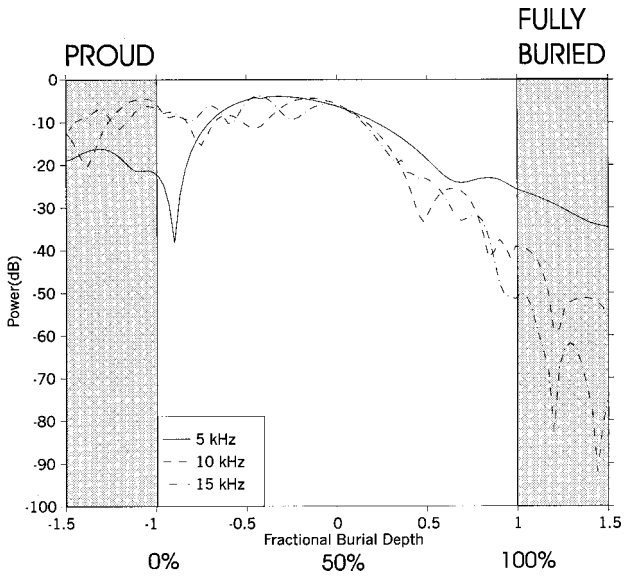

FIG. 4. Backscattered power levels from steel-shelled cylinder as a function of fractional burial for 5, 10, and 15 kHz.

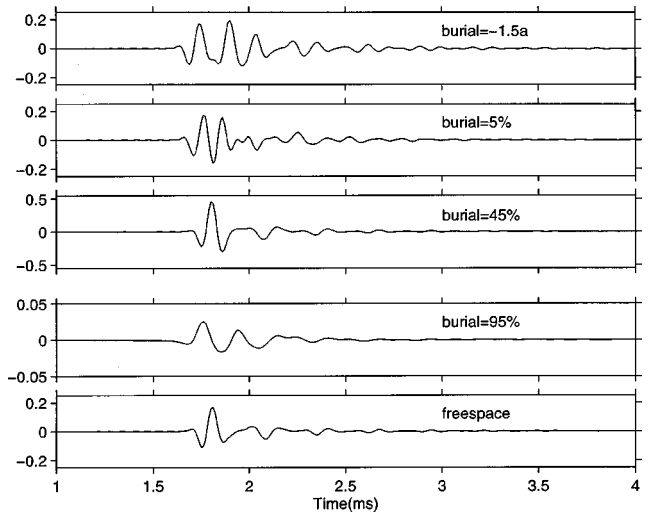

FIG. 5. Backscattered time series from steel-shelled cylinder as a function of fractional burial. (Please note the scale change in plots 3 and 4.)

cumferentially around the shell. The study of these types of waves and the related resonance spectra are described, for example, in Ref. 8. Some of the features in the spectra shift very slightly as a function of burial. This is not surprising; the surrounding medium properties have an effect on the spectral properties of the backscattered field in free space and hence also in the case of partial or total burial of an object, where the medium above the interface is different from that below. Second, when an object is totally above or below an interface, the multiple interactions of the object's scattered field with the interface can produce an effective shift to the free-space resonant frequencies of the object.[6] This type of phenomena should also be present in the case of partial burial. As discussed above, there are also additional interference effects introduced into the spectra due to the combination of direct and seabed reflected wave fields.

We now give a different presentation of the spectral information. We consider the frequency fixed at 5, 10, and 15 kHz and in Fig. 4 show the variation of the backscattered level with respect to the fraction of burial. We have computed these curves for 101 depths of burial. As can be seen for fractions of burial, slightly less than 0 (50% burial), the fall-off of amplitude is rapid, more rapid with increasing frequency, as one would expect due to the evanescent nature of the energy in the bottom.

Thus far we have dealt with the amplitude or power of the backscattered spectra. However, the phase of the spectra is also important when Fourier synthesizing the time domain scattered pulse. We construct the scattered pulse in the time domain by multiplying the complex-valued Fourier spectra with the source spectrum for a 7-kHz Ricker wavelet. The resulting time series are shown in Fig. 5 for different amounts of fractional burial: 1.5*a* above the interface, burial of 5%, burial of 45%, and burial of 95%. Also shown is the time series for the cylinder surrounded only by water. For the first two curves there is coherent combination of the direct and reflected wave fields for both the incident and scattered wave fields. This has the effect of producing a sequence of overlapping pulses for the top time series. These pulses become increasingly merged in time until, for values of burial near 50%, the resultant pulse is similar to that scattered by the cylinder in freespace but there is an amplitude enhancement by a factor of almost 2.5. For 95% burial, the amplitude of the backscattered time series has decreased significantly.

B. Solid aluminum cylinder

We now repeat many of the previous computations for the cylinder being solid aluminum with the acousto-elastic parameters: $c_p = 6380$ m/s, $c_s = 3100$ m/s, and $\rho = 2.79$ g/cm^3. In Fig. 6 we present the waterfall plot of the backscattered spectra for the 16 levels of burial. The trend is the same as for the previous example. For the top curves, there are additional nulls and peaks in the curves due to interference effects caused by the underlying seabed. These effects disappear as the object becomes partially buried and there is an enhancement of backscattered levels. As the cylinder becomes increasingly buried, the level of backscatter decreases

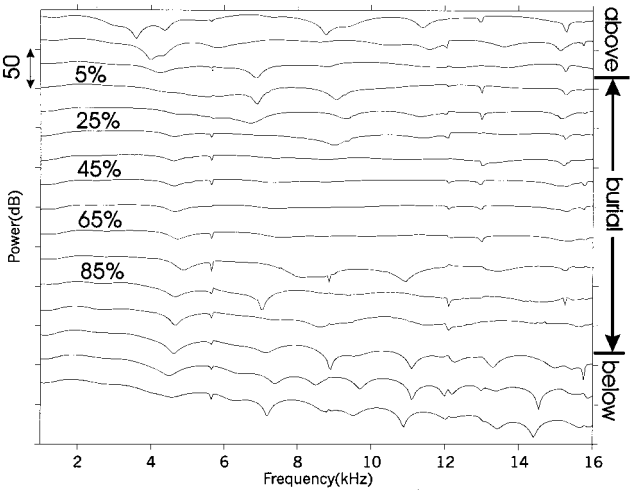

FIG. 6. Waterfall plot of backscattered power spectra from solid aluminum cylinder as a function of fractional burial, from 1.5*a* above the seabed interface to burial 1.5*a* below the interface.

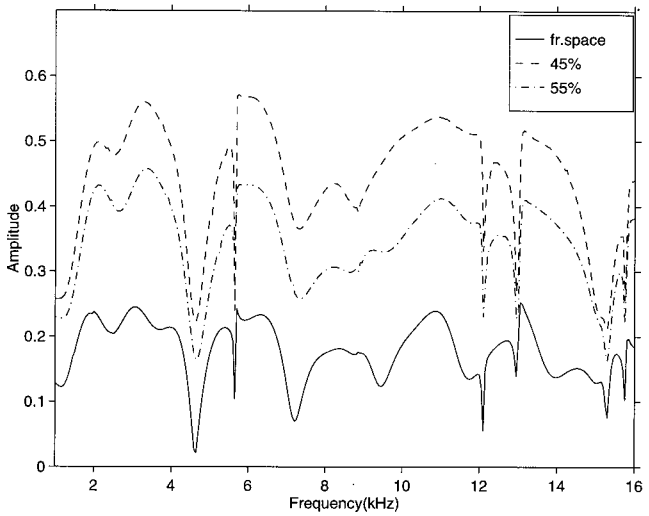

FIG. 7. Backscattered power levels from solid aluminum cylinder 45%, 55% buried, and in free-space surrounded by water.

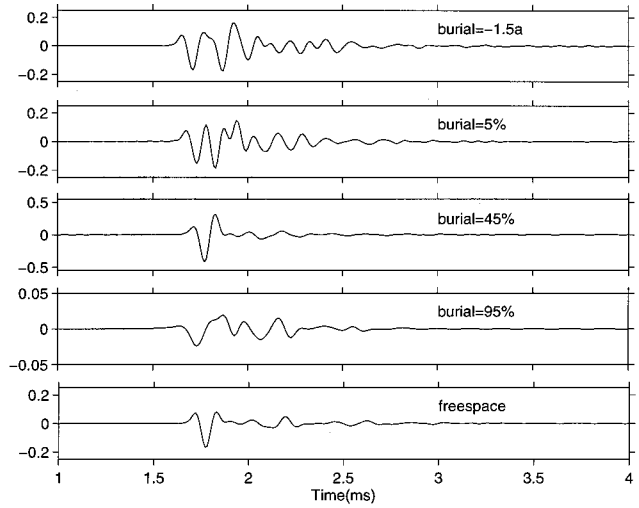

FIG. 9. Backscattered time series from solid aluminum cylinder as a function of fractional burial. (Please note the scale change and plots 3 and 4.)

significantly and there is now additional interference effects in the spectra, but at a low amplitude level. The position of the null in the spectra at about 4.5 kHz changes slightly as a function of burial.

In Fig. 7 we show the backscattered spectra in linear amplitude for the cylinder 45% buried, 55% buried, and the free-space result. We notice that the spectra are similar but that the amplitude of the two partially buried curves are significantly higher than the free-space curve. The sharp peaks and troughs, due to resonance effects, are evident in these curves. As discussed for the previous example, these features may shift slightly as a function of the fraction of burial.

As in the previous example, we now compute the amplitude of the backscattered field for 5, 10, and 15 kHz as the cylinder's location varies from 1.5*a* above the seabed interface to 1.5*a* below. Although some of the details are different than for the steel shell case, the general features in Fig. 8 are the same; there is some variation in amplitude for the cylinder buried less than 50% and a rapid decrease in amplitude, especially for the 10- and 15-kHz curves after 50% burial. Finally we compute the backscattered time series for the different amounts of burial (Fig. 9). For this cylinder the specular reflection of the pulse has positive polarity because the solid cylinder ''appears'' rigid to the incident pulse (in contrast to the shell case where the interior was a pressure release surface). Above or partially above the seabed, the results of reflections from the seabed can be seen in the time series. These features disappear as the cylinder becomes approximately 50% buried. For 95% burial the backscattered series is diminished in amplitude and the arrival at approximately 2 ms, which appeared weakly in the 45% curve and in the free-space curve, is now almost equal in amplitude to the specular reflection.

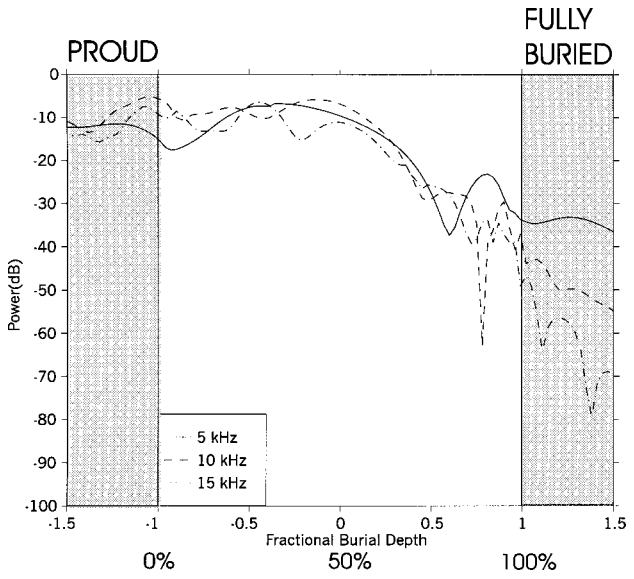

FIG. 8. Backscattered power levels from solid aluminum cylinder as a function of fractional burial for 5, 10, and 15 kHz.

III. SUMMARY

We have presented a method for computing exactly the scattering from a partially buried elastic cylinder. The form of the solution within the cylinder is utilized to specify the relation between the coefficients for the internal radial stress and the radial displacement. This relation is then used in the external BIEM to obtain a system of equations for the Fourier coefficients of the pressure field on the cylinder surface. There are some situations where the method may have difficulties due to the poor convergence properties of the series expansions (as discussed in Sec. I) but, in general, the method performed well.

The backscattered spectra for a shelled and a solid cylinder as well as backscattered time series were computed for various amounts of burial. The incident field was a generalized plane wave (i.e., direct, effect, and transmitted components) with a subcritical grazing angle. For the cylinder above the seabed or only slightly buried, the spectra and the time series were complicated by the interferences between direct and seabed reflected paths. As the cylinder became close to 50% buried, the spectra and time series became simpler in structure, and the amplitudes were larger than for the

corresponding free-space result. After approximately 50% burial, the levels began to decrease rapidly with greater loss for higher frequencies. This is expected from the evanescent behavior of the incident field in the bottom. The time series became smaller in amplitude for burial amounts greater than 50% with the higher frequency components of the incident spectrum being stripped out.

[1] J. A. Fawcett, ''Acoustic scattering from cylindrical objects embedded between two half-spaces,'' J. Acoust. Soc. Am. **100**, 3053–3060 (1996).

[2] R. Lim, J. L. Lopes, R. H. Hackman, and D. G. Todoroff, ''Scattering by objects buried in underwater sediments: Theory and experiment,'' J. Acoust. Soc. Am. **93**, 1762–1783 (1993).

[3] R. Lim, ''Acoustic scattering by a partially buried three-dimensional elastic obstacle,'' J. Acoust. Soc. Am. **104**, 769–782 (1998).

[4] L. Flax and W. G. Neubauer, ''Acoustic reflection from layered elastic absorptive cylinders,'' J. Acoust. Soc. Am. **61**, 307–312 (1977).

[5] J. A. Fawcett, W. L. J. Fox, and A. Maguer, ''Modeling of scattering by objects on the seabed,'' J. Acoust. Soc. Am. **104**, 3296–3304 (1998).

[6] R. H. Hackman and G. S. Sammelmann, ''Multiple-scattering analysis for a target in an oceanic waveguide,'' J. Acoust. Soc. Am. **84**, 1813–1825 (1988).

[7] J. A. Fawcett, ''A plane-wave decomposition method for modeling scattering from objects and bathymetry in a waveguide,'' J. Acoust. Soc. Am. **100**, 183–192 (1996).

[8] N. D. Veksler, *Resonance Acoustic Spectroscopy* (Springer-Verlag, New York, 1993).

Highly resolved detection and selective focusing in a waveguide using the D.O.R.T. method

Nicolas Mordant, Claire Prada, and Mathias Fink
Laboratoire Ondes et Acoustique, Université Paris 7, CNRS UMR C7587, ESPCI, 10 rue Vauquelin, 75352, Paris Cedex 05, France

(Received 28 July 1998; accepted for publication 22 January 1999)

The D.O.R.T. method (French acronym for Decomposition of the Time Reversal Operator) is a scattering analysis technique using an array of transducers. The method is effective to achieve detection and selective focusing on pointlike scatterers through inhomogeneous media [J. Acoust. Soc. Am. **99**, 2067–2076 (1996)]. Laboratory measurements in a water waveguide are presented. Taking advantage of the multiple reflections at the interfaces of the guide, high resolution is achieved with the D.O.R.T. method. The separation of two scatterers and the selective focusing are obtained with a transverse resolution at least nine times better than the free-space limit prediction. The detection of a scatterer from the water/air interface of the guide is also achieved with high resolution (1/20 of the free space diffraction spot). The effect on the D.O.R.T. method of surface waves produced at one interface of the guide is measured. Finally, the impulse response function of each scatterer to the array is computed as a combination of the eigenvectors of the time-reversal operator obtained at each frequency. Using these impulse Green's functions, selective focusing with high temporal and spatial compression is performed. © *1999 Acoustical Society of America.* [S0001-4966(99)00505-6]

PACS numbers: 43.30.Pc, 43.30.Re, 43.30.Gr [DLB]

INTRODUCTION

The problem of optimum signal transmission and source location in a waveguide has been the subject of many theoretical and experimental works. The propagation of an acoustic pulse inside a waveguide is a complex phenomenon. This complexity renders the detection and imaging process very difficult. Because of multiple path effects, the Green's function that is used in matched field processing is nontrivial and its calculation requires accurate knowledge of the medium. Several studies have shown how to take advantage of this complexity. In waveguide transmission, the guide can be considered as a linear filter. This concept can be applied in the ocean. Parvulescu *et al.*[1,2] reported a matched filter experiment in the ocean between a source and a receiver. They recorded the reception of an impulsive transmission and replayed the time-reversed signal through the source. They obtained a high temporal compression, which was explained by the coherent recombination of the energy received over different multiple paths. They also showed high sensitivity to small displacements of the source, suggesting that this property should be used to locate the source.

The ability to achieve temporal and spatial focusing is even more striking in complex medium such as a chaotic reflecting cavity. C. Draeger *et al.*[3] put this in evidence in a time-reversal experiment with a single source and a single receiver in silicone wafer.

As proposed by C. S. Clay and S. Li,[4,5] the combination of array matched filter and time domain matched signal techniques improve the accuracy in source localization. They reported a laboratory experiment where they achieved focusing in the receive mode using the time-reversed version of the calculated impulse responses of the waveguide. They demonstrated an improvement of the spatial resolution due to the multiple images of the receiver with respect to the waveguide interfaces. In these papers, focusing is explained in terms of matched signal: The waveguide plays the role of a correlator. The possibility to take advantage of the invariance of acoustic wave equation under time reversal in order to achieve spatial and temporal focusing arose afterward. In 1989, we built the first time-reversal mirror that was able to time reverse a wave field with an array of transducers.[6] At the beginning, this system was aimed to compensate for distortions induced by sound speed fluctuations and for misalignment of the transducers in the array. In 1991, D. R. Jackson *et al.*[7] showed that time-reversal mirror should be used in underwater sound to achieve highly resolved focusing. They provided a theoretical analysis of the time-reversal process in a water channel.

Focusing experiments inside a water waveguide with a time-reversal mirror were first achieved in 1995 by P. Roux *et al.*[8,9] They demonstrated how to refocus an incident acoustic field back to its origin and to achieve high temporal and spatial compression by time reversal of the wave field. They obtained a 6-dB focal width that was nine times narrower than the free-space diffraction limit prediction. In 1996, an impressive experiment was realized by Kuperman and his team in the Mediterranean Sea.[10] They have implemented a time-reversal mirror and have shown that the time-reversal process allows refocusing at 6-km distance in a 120-m deep water channel.

In the abovementioned papers, only transmission from sources to receivers is considered. A natural question is how to use this super focusing property to detect scatterers in an echographic mode. This question is of practical concern for nondestructive evaluation as well as underwater acoustics. In echographic mode, the signal reflected from a scatterer is

extremely complex for it has undergone a double path through the guide. We propose to apply the D.O.R.T. method to this particular problem. This method was first presented in 1994 in a paper entitled ''Eigenmodes of the time-reversal operator: A solution to selective focusing in multiple target media.''[11] Since then it has been used to make detection and selective focusing through aberrating media,[12,13] and also to separate Lamb modes propagating around a thin hollow cylinder.[14] As will be shown in this paper, the method can also take advantage of the matched filter property of the waveguide in order to separate the echoes from different scatterers with high resolution.

In Sec. I, the principle of the D.O.R.T. method is recalled; then an example of highly resolved detection and selective focusing in a water waveguide is presented. The detection of a scatterer placed near an interface of the guide is studied in Sec. II.

In Sec. III, the imaging problem is addressed by adding an *a priori* knowledge on the guide. The field produced by transmission of the conjugate eigenvectors is calculated with a simple ray model where the guide parameters are determined by an iterative optimization procedure.

The consequences of fluctuations of the medium on the performance of the D.O.R.T. method are studied in Sec. IV. The considered waveguide is a water layer delimited by steel and air interfaces. Surface waves are produced at the water/air interface.

In Secs. I–IV, the analysis of the transfer function is done at a single frequency. In the last section, it is shown that in some cases the eigenvectors obtained at each frequency can be combined to obtain the time domain Green's function for each scatterer.

I. SELECTIVE HIGHLY RESOLVED FOCUSING IN A WAVEGUIDE

The D.O.R.T. method was widely described in several papers.[13,14] For the detection part it consists in the following steps. First, the inter-element impulse response functions, $k_{lm}(t)$, are measured. Second, the transfer matrix is calculated at one chosen frequency (more often the central frequency of the transducers). Finally, the time-reversal operator, $K^*(\omega)K(\omega)$, is diagonalized. In practice, it is convenient to calculate the singular value decomposition of the transfer matrix: $K(\omega)=U(\omega)\Lambda(\omega)V^+(\omega)$, where $\Lambda(\omega)$ is a real diagonal matrix of the singular values, and $U(\omega)$ and $V(\omega)$ are unitary matrices. The eigenvalues of $K^*(\omega)K(\omega)$ are the squares of the singular values of $K(\omega)$, and its eigenvectors are the columns of $V(\omega)$. We shall use this decomposition in the following.

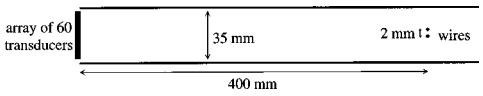

FIG. 1. Geometry of the experiment.

For pointlike scatterers, the general result that was shown is that the number of ''nonzero'' singular values is equal to the number of well-resolved scatterers. Furthermore, if the scatterers have different ''apparent'' reflectivities, each eigenvector provides the phase and amplitude to be applied to the transducers in order to focus on one particular scatterer. For the detection part, the D.O.R.T. method shares some of the principles of eigenvector decomposition techniques that are used in passive source detection,[15,16] however, it should not be considered as a competing technique as it is active and deterministic.

A. Experimental geometry

The experiment is performed in a two-dimensional water waveguide, delimited by two water/steel plane interfaces. In a good approximation, the reflections at the interfaces can be considered as total. The water layer is 35 mm thick. The array consists of 60 transducers with a central frequency of 1.5 MHz, it spans the whole height of the guide with a pitch equal to 0.58 mm. The scatterers are two wires of diameters 0.1 mm and 0.2 mm, spaced 2 mm and placed perpendicular to the array axis at a distance of 400 mm (Fig. 1). As the average wavelength is 1 mm, both wires behave almost like point scatterers. For this range and this frequency, the free-space diffraction focal width is 12 mm so that the two wires are not resolved by the system.

The echographic signals recorded after a pulse is applied to one transducer of the array are very complex with low signal-to-noise ratio. The inter-element response $k_{28\,40}(t)$ is a typical example (Fig. 2). After approximately five reflections at the interfaces, the signal can no longer be distinguished from noise. The echoes of the two wires are superimposed and cannot be separated in a simple manner.

B. Eigenvectors and singular values

The 60×60 impulse response functions are measured and the transfer matrix is calculated at frequency 1.5 MHz. Decomposition reveals two singular values that are separated

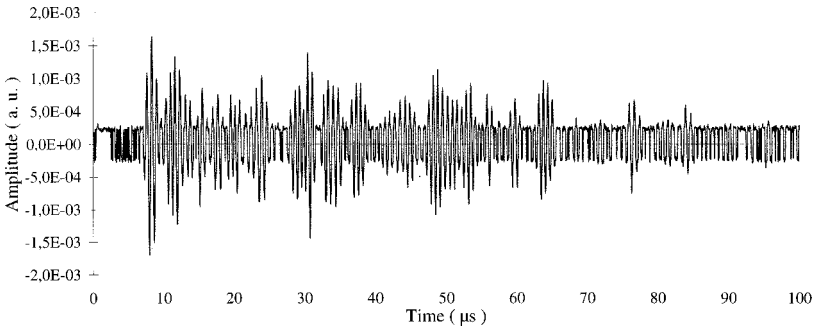

FIG. 2. Typical echo of the wires: inter-element impulse responses $k_{28\,40}(t)$.

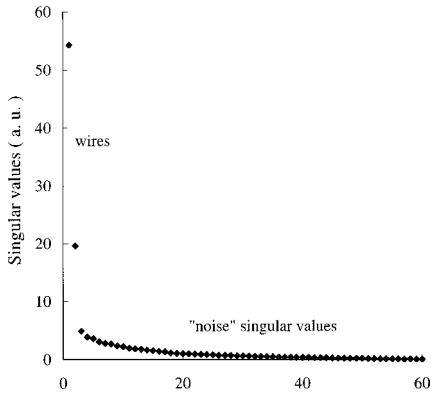

FIG. 3. Singular values of the transfer matrix calculated at 1.5 MHz.

from the 58 ''noise'' singular values (Fig. 3). The ''noise'' singular values are partly explained by electronic and quantization noises. However, different second order acoustical phenomena that are not taken into account in the model probably contribute to these singular values: among them, the defects of the interfaces, the elastic responses of the wires, the multiple echoes between the wires, and also coupling between the transducers.

C. Selective focusing in monochromatic mode

The eigenvectors V_1 and V_2 have a complicated phase and amplitude distribution and it is impossible to tell to which scatterer each of them corresponds. These distributions are applied to the array of transducers. Namely, if $V_1=(A_1e^{i\varphi_1},A_2e^{i\varphi_2},\cdots,A_ne^{i\varphi_n})$ is the first eigenvector, then the signal $s_p(t)=A_p\cos(\omega t-\varphi_p)$ is applied to transducer number p. A needle probe is used to scan the so produced pressure field across the guide at the range of the wires (Fig. 4). For each eigenvector, the wave is focused at the position of one wire. In both cases the residual level is lower than -18 dB and the -6 dB focal width is 1.4 m. In fact, the width is overestimated because the width of the probe is 0.5 mm, and the real focal width is probably around 1.2 m which is ten times thinner than the theoretical free-space focal width.

For comparison, the same experiment is achieved after removing the guide. In this case the wires are not resolved and only the first singular value is significant. The pressure pattern is measured for transmission of the first eigenvector, and the focal width is 13 mm (Fig. 4). Consequently, the guide allows us to achieve a focusing at least 10 times thinner than in free space. The angular directivity of each transducer limits the number of reflections at the guide interfaces that can be recorded. This induces an apodization of the virtual array made of the set of images of the real one. Taking this phenomenon into account, the focal width roughly corresponds to a virtual aperture consisting of eight pairs of images of the array.

II. DETECTION NEAR THE INTERFACE

In many problems, the detection of a defect near an interface is difficult, especially if the reflectivity coefficient of the interface is close to -1, which is the case for the water/air interface. Indeed, in this situation, the virtual image of the defect with respect to the interface behaves as a source in opposite phase with the defect. The real source and the virtual source interfere in a destructive way so that the reflected signal is very low. Here we analyze the ability of the D.O.R.T. method to detect a wire that is close to a water/air interface.

The experiment is done in a water waveguide of 35-mm width limited by air at the surface and steel at the bottom. A wire of 0.2 mm diameter is placed inside the guide at 400 mm from the array. The wire is moved step by step from the bottom to the surface and for each position the transfer matrix is measured and decomposed. The two first singular values are displayed versus the distance to the surface (Fig. 5). The first singular value represents the signal level and the second one represents the noise level. When the wire reaches the bottom, the singular value increases rapidly by a factor of 2: The echoes from the scatterer and from its image add constructively. Conversely, when the wire gets to the surface the singular value decreases rapidly. It remains well separated from the noise singular values until the distance between the wire and the interface reaches $\lambda/5$.

To illustrate the role played by multiple reflections at the interfaces, a simple model is used to calculate the theoretical singular values for different numbers of reflections. The reflection coefficients are taken equal to 1 at the bottom and equal to -1 at the surface. According to the theory,[13,14] the singular value of the transfer matrix is $\lambda_1=c\Sigma_l|H_l|^2$, where c is the reflectivity coefficient of the scatterer and H_l is the response from the scatterer to transducer number l. For a

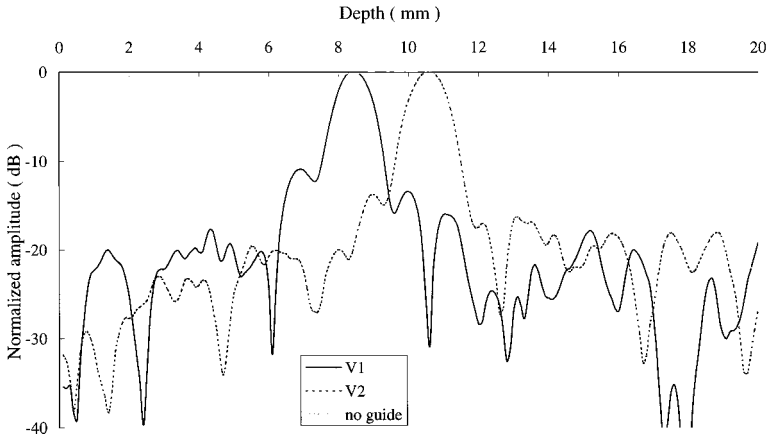

FIG. 4. Pressure pattern measured across the guide at the range of the wires after transmission of the eigenvectors. First (solid) and second (dot) eigenvectors obtained with the guide, first (gray) eigenvector without the guide.

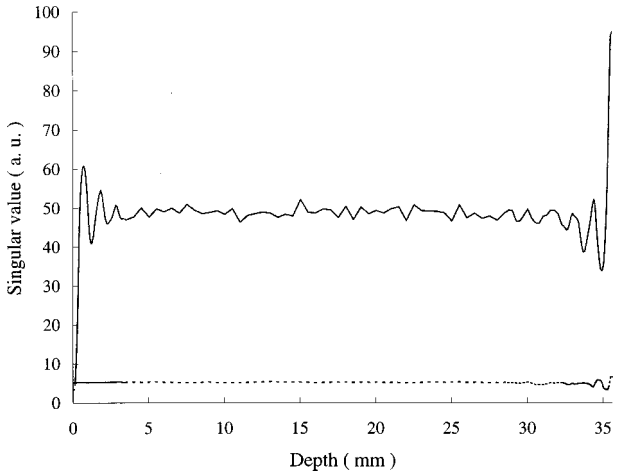

FIG. 5. Experiment: Dependence of the singular values of the transfer matrix versus the distance to the surface (solid: first, dashed: second).

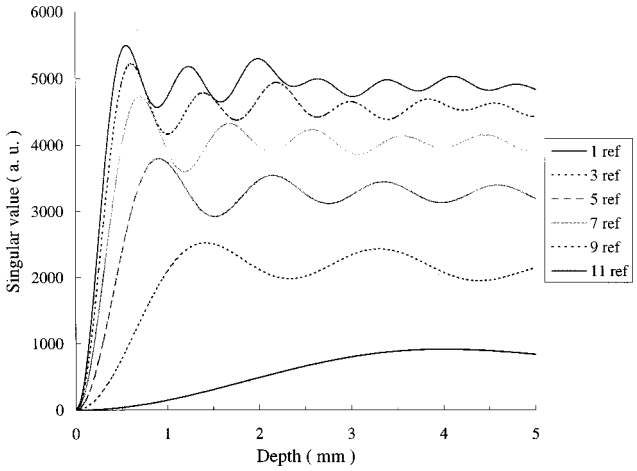

FIG. 7. Theoretical first singular value as a function of the distance to the interface calculated for different numbers of reflections at the interface.

scatterer close to the upper interface the images have to be taken into account by pairs: (S,I_1), (I_{-1},I_{-2}), (I_2,I_3), and so on. Each pair corresponds to adjacent acoustic paths (Fig. 6).

There is a qualitative agreement between theoretical (Fig. 7) and experimental curves (Fig. 5). The abovementioned phenomenon can be seen: The singular value decreases to zero when the wire reaches the surface. Again, the more reflections are taken into account the closer to the surface the wire can be detected. The minimum distance to the surface under which the wire is no longer detected is the distance where the first singular value is at the level of noise singular values. It depends on the number of images that are taken into account. For example, assuming that the noise singular values level is 500 (this corresponds roughly to the experimental noise singular values), for one image the minimum distance is 2 mm, for three images it is 0.4 mm, and for five images it is less than 0.2 mm. This is another illustration of the ability of the D.O.R.T. method to provide high resolution by taking advantage of multiple paths.

III. IMAGING THE SCATTERERS

In the experiment of Sec. I, the eigenvectors were used to focus selectively on each scatterer. Of course, this procedure is not sufficient to make an image or a localization of the scatterers. Imaging requires us to backpropagate numerically the data with an appropriate beamformer, which assumes a precise knowledge of the parameters of the waveguide.[17] Here, we give a simple example using an optimization procedure to approximate parameters of the guide. The water guide is delimited by two parallel water/steel interfaces as in Sec. I. In a first approximation, the distance between the interfaces is $H=35$ mm, the transducers array is perpendicular to the guide ($\alpha=0°$), and the distance from the center of the array to one interface is $d_0=17.5$ mm. Four scatterers of diameters up to 0.2 mm are placed at range $r_1=r_2=388$ mm, $r_3=r_4=398$ mm, and depth $h_1=12$ mm, $h_2=26$ mm, $h_3=17$ mm, and $h_4=22$ mm (Fig. 8). At 1.5 MHz, the theoretical free space focal spot is 12 mm in the transverse direction and 900 mm in range. Consequently, the wires are not resolved in a classical monochromatic approach.

The singular value decomposition of the transfer matrix is calculated at frequency 1.5 MHz. Four singular values are separated from the noise singular values, which reveals the presence of the four scatterers (Fig. 9). However, at this stage it is impossible to tell to which wire each eigenvector corresponds. To localize the wires, it is necessary to backpropagate the eigenvectors in the modeled waveguide.

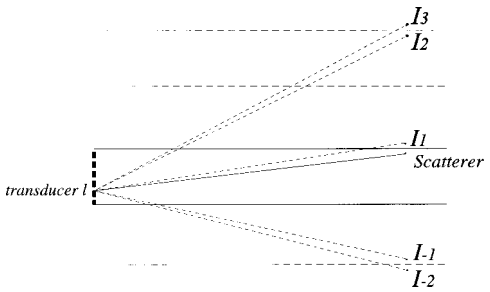

FIG. 6. Pairs of images used to calculate the singular values for a scatterer close to the surface.

A. Optimization of the guide parameters

Since the measurement of the parameters of the guide is not precise enough to backpropagate numerically the eigenvectors, we developed a self-adaptive method to optimize the values of the three parameters. A calibration wire is placed half-way between the four wires and the array of transducers. The distance between the reference and the targets is long enough so that the last measurable echo from the reference wire arrives before the first echo from the four wires.

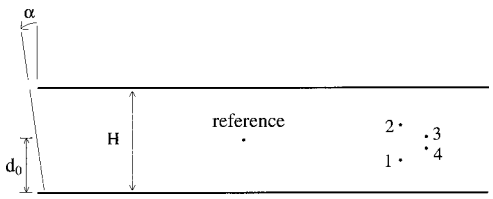

FIG. 8. Experimental setup and parameters used in the optimization procedure.

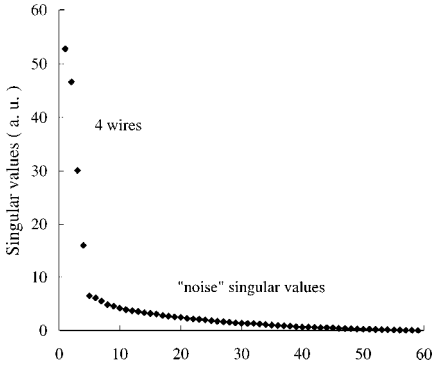

FIG. 9. Singular values of the transfer matrix obtained with the four wires.

The inter-element impulse responses of this wire are measured and the first eigenvector of the corresponding time reversal operator is calculated. As we know from the preceding results, the transmission of this eigenvector focuses on the reference wire. Thus the idea is to calculate the field produced by transmission of this eigenvector at the depth of the reference wire and to maximize the quality of the focusing. The parameters H, d_0, and α are varied until the best focusing is obtained. Namely, the function to be maximized is

$$M_P = \frac{\max_D(|P(\alpha,H,d_0)|)}{\text{mean}_D(|P(\alpha,H,d_0)|)},$$

where D is the section of the guide at the range of the reference wire, and P is the pressure field calculated by transmission of the first eigenvector. This eigenvector is obtained taking into account all the measurable reflections. In order to avoid the problem of secondary maxima, backpropagation is first computed taking into account only two reflections on the guide interfaces. With fewer reflections the focal width is larger and the absolute maximum is easier to localize. Once the best parameters are obtained for two reflections, the procedure is iterated starting from the new parameters and adding one more reflections at each step. This process is iterated until the parameters converge.

After such an optimization of the focused pattern, the parameters are found to be $H=34.77\,\text{mm}\pm0.05\,\text{mm}$, $\alpha=0.27°\pm0.01°$, and the position of the array center $d_0=17.77\,\text{mm}\pm0.05\,\text{mm}$.

B. Images provided by each eigenvector

The estimated values of the parameters H, d_0, and α are used to calculate the pressure patterns for transmission of eigenvectors 1 to 4 corresponding to the responses of the four wires. The images are calculated in the range 375 mm to 414 mm on the whole height of the guide. Each eigenvector leads to a focusing at the position of one of the wire (Fig. 10). The resolution at -6 dB is 1.2 mm in depth and 10 mm in range, which corresponds to an effective aperture of 595 mm. The level of the side lobes reaches -4 dB. The four scatterers are well separated in this decomposition.

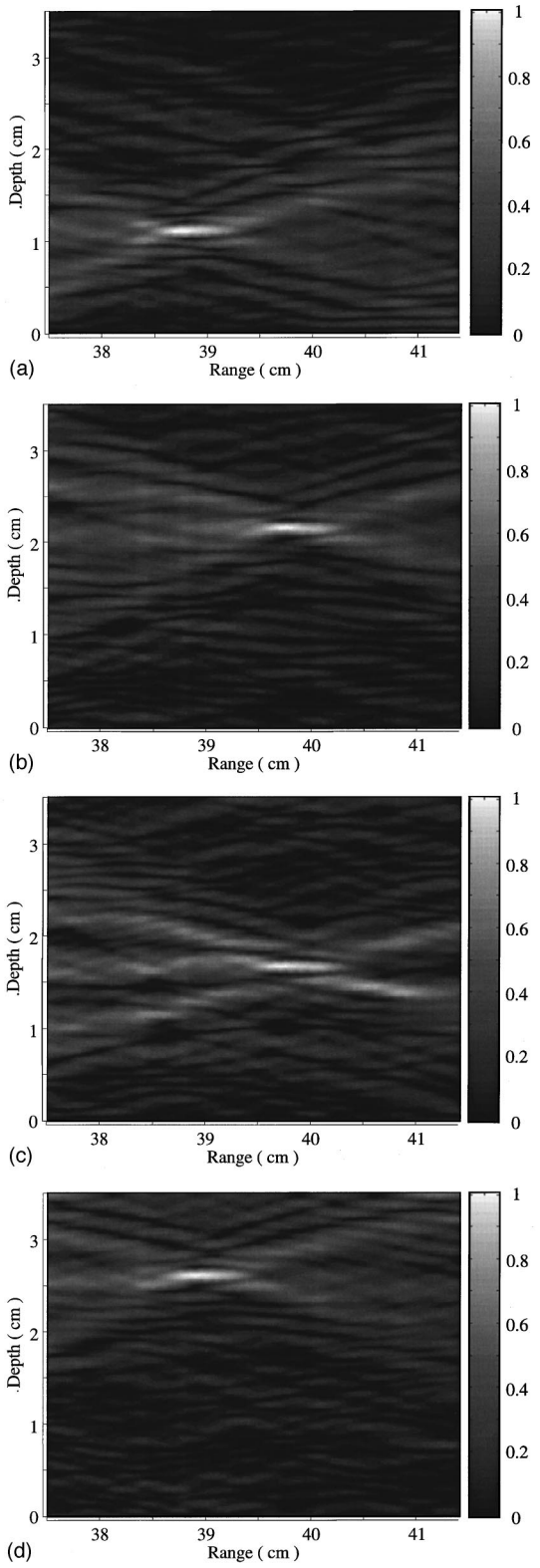

FIG. 10. Pressure field calculated by numerical propagation of eigenvectors 1 to 4.

C. Comparison with phase conjugation

To illustrate the efficiency of this method, we calculate the image obtained by the phase conjugation of an echo of the wires. As explained in different papers,[6,7,11] the phase conjugate of an echo of the wires should refocus on each wire simultaneously, the amplitude of each focal spot de-

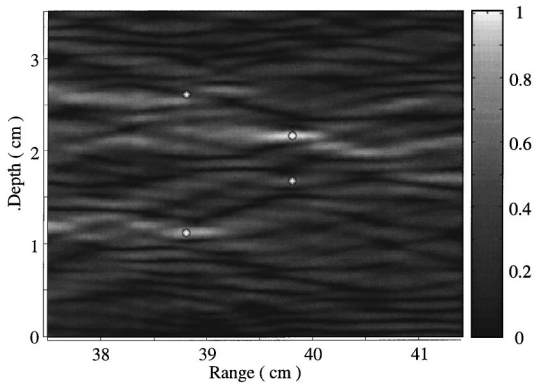

FIG. 11. Pressure field calculated by numerical propagation of the phase conjugated of the response of the wires obtained after transmission by ten elements in the center of the transducer array.

pending on the first insonification, and on the apparent reflectivity of the wires. In order to increase the signal-to-noise ratio, we choose to insonify the wires with ten adjacent transducers in the middle of the array. The Fourier component of the received echo is calculated at 1.5 MHz. This provides a complex vector V that is phase conjugated and numerically transmitted in the modeled wave guide.

On the phase conjugate image (Fig. 11), only the first and second most reflective wires can be distinguished. The energy refocused on the two other wires is at the same level as secondary lobes and thus cannot be distinguished. This result illustrates the efficiency of the D.O.R.T. method to detect weak scatterers among stronger ones, and thus to find more details of the scattering medium.

IV. STUDY OF A TIME VARYING WAVEGUIDE

To analyze the robustness of the method, we now propose to make measurements in a steel/water/air waveguide in the presence of surface waves. We study the dependence of the singular values distribution and the focusing obtained by transmission of the eigenvectors with respect to the root mean square height of the waves.

A vertical plate with horizontal oscillations at 6 Hz produces the surface waves. This displacement produces waves of typical wavelength of 30 mm. The height of the waves is varied using a diaphragm placed between the plate and the guide (Fig. 12). A transducer put on the bottom and focused at the surface measures the time of flight to the surface, which provides the height of the waves. The root mean square height h_{rms} of the waves is varied from 0 to 1.7 mm. This corresponds to $0<kh_{\mathrm{rms}}<10$. A copper wire and a tungsten wire of diameter 0.2 mm are placed at 500 mm from the array and spaced 5 mm.

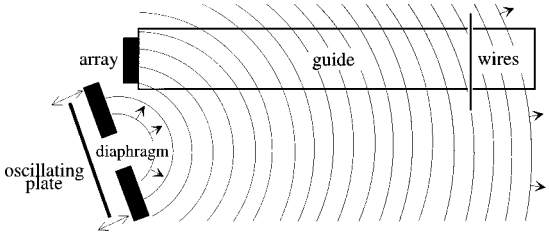

FIG. 12. Experimental setup built to produce surface waves.

For a given wave height, the transfer matrix K is measured and decomposed. While kh_{rms} is lower than 1.5, the two singular values corresponding to the wires are well separated from noise singular values. For $kh_{\mathrm{rms}}=1.5$, the two first eigenvectors were transmitted into the guide and the field measured at range 500 mm (Fig. 13). The eigenvectors focus at the position of the wires, however, the main lobes are approximately 1.6 times larger and the residual level twice higher than in the absence of waves (see Fig. 4).

At this stage, it is important to recall that the measurement of the matrix K takes 5 min. For our system the matrix is measured column by column so that each column corresponds to one realization of the medium. Consequently, the transfer matrix K corresponds to a sort of average medium. This may partly explain why the result of the backpropagation is good for one realization of the matrix K.

For higher waves, it is necessary to average the interelement impulse responses over several realizations. The singular values of the ten times averaged matrix K_{10} are calculated for h_{rms} varying from 0 to 1.7 mm. The two greatest singular values decrease rapidly with the height of the waves while the noise singular values increase (Fig. 14). In fact, the main effect of the averaging is to lower the ''noise'' singular values so that the signal singular values better emerge from noise. This phenomenon is illustrated in the case of $h_{\mathrm{rms}}=1.7\,\mathrm{mm}\,(kh_{\mathrm{rms}}=10)$. The results obtained with one real-

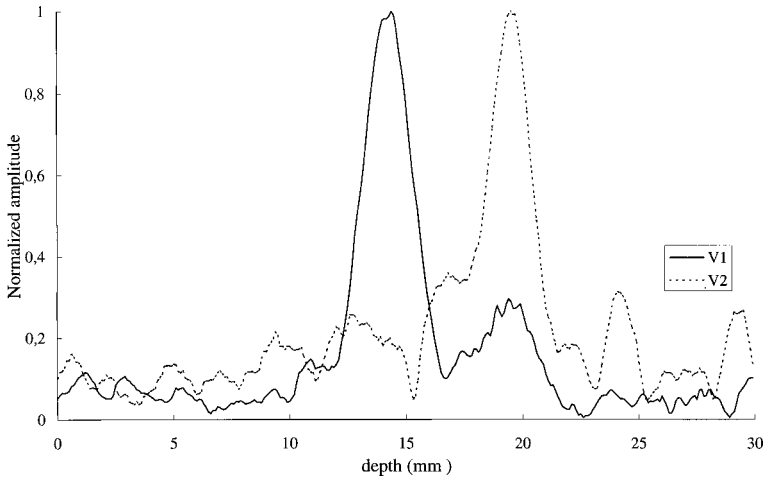

FIG. 13. Pressure field measured for transmission of eigenvectors 1 and 2 calculated with a nonaveraged transfer matrix obtained with surface waves of $h_{\mathrm{rms}}=0.23$ mm.

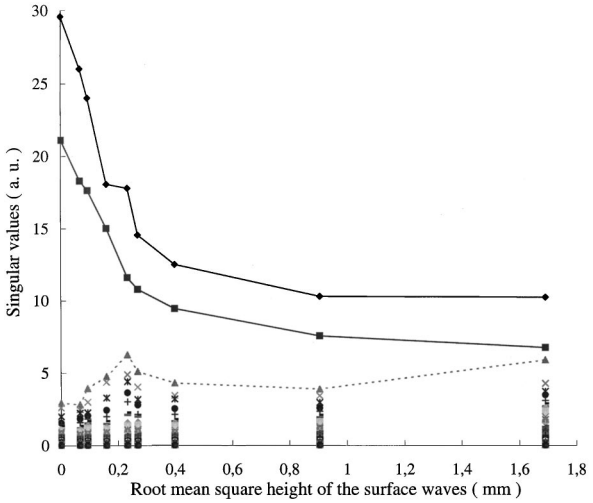

FIG. 14. Singular values of the ten times average transfer matrix versus the root mean square height of the waves (◆ first, ▲ second, ■ third).

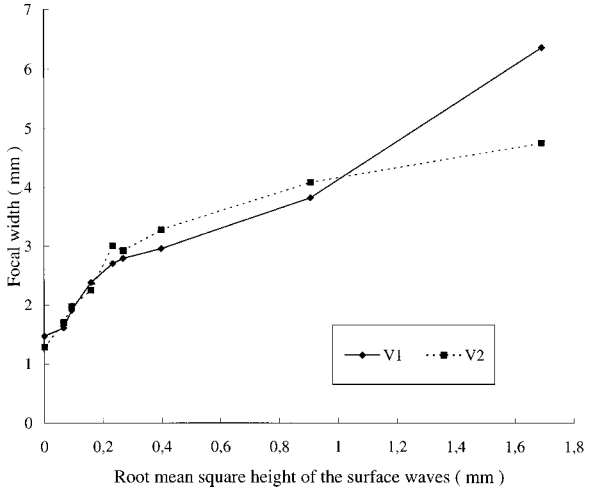

FIG. 16. Width of the focal spot versus the root mean square height of the surface waves measured for the ten times averaged transfer matrix.

ization of the inter-element impulse responses (matrix K_1) and with the average of ten realizations (matrix K_{10}) are compared. The corresponding eigenvectors are transmitted into the guide and the so-produced field measured. For the first eigenvector, the averaging does not make any significant difference on the focus pattern [Fig. 15(a)]. This is probably due to the fact that the signal corresponding to the strongest scatterer is above noise even without averaging. Conversely, the focus pattern obtained with the second eigenvector calculated with K_1 is poor and noisy, whereas the focusing on the second wire is recovered with K_{10} [Fig. 15(b)].

The focus pressure pattern was measured for different h_{rms}. The -6 dB focal width was plot versus h_{rms} (Fig. 16). It varies from 1.2 mm to 6 mm for waves with $h_{\mathrm{rms}}=1.7$ mm. For this height, the separation of the two wires corresponds to a resolution almost three times thinner than in free space. Such a resolution was necessarily obtained with a significant contribution of the wave reflected at the surface.

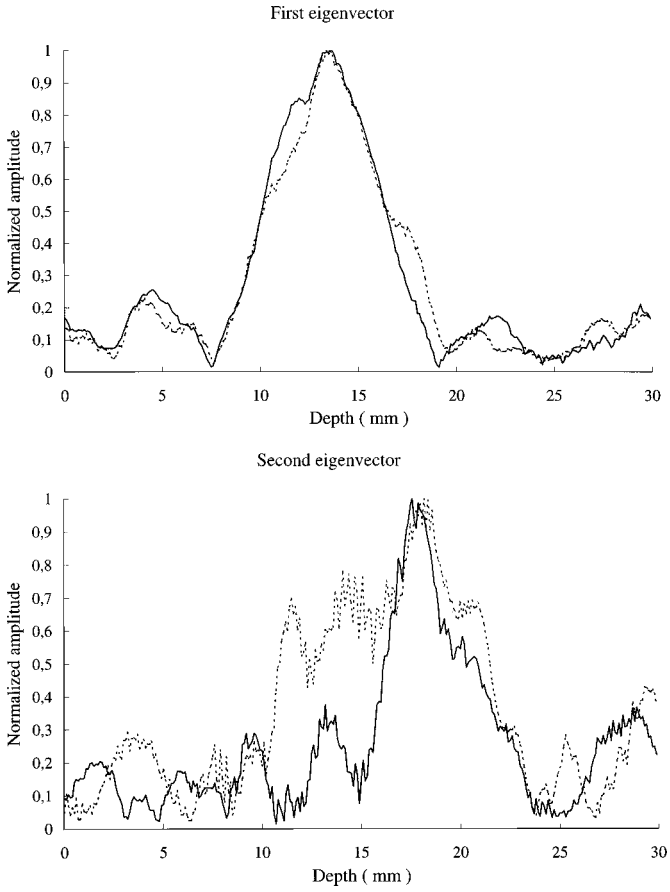

FIG. 15. Pressure field measured for transmission of the first eigenvector (a) and the second eigenvector (b) calculated with a nonaveraged transfer matrix (dot) and of a ten times averaged transfer matrix (solid) for surface waves of $h_{\mathrm{rms}}=1.7$ mm.

V. D.O.R.T. METHOD IN THE TIME DOMAIN

In the preceding sections, all of the results were obtained with the eigenvectors calculated at the central frequency of the transducers. Only a small part of the information contained in the inter-element impulse response functions has been used. In fact, decomposition of the time reversal operator can be done at any frequency. In order to get temporal signals, it would be natural to calculate the eigenvectors in the whole band of the transducers and to perform an inverse Fourier transform of the eigenvector function of frequency. In fact, this operation is nontrivial. The main reason is that the scatterers' reflectivity generally depends on frequency, so that at one frequency the first eigenvector can be associated to one scatterer while it is associated to another one at another frequency. However, if the strengths of the scatterers are different enough then the first eigenvector may correspond to the same scatterer in the whole frequency band of the transducers. In this case, it is possible to build temporal signals from the eigenvectors. If the first eigenvector corresponds to one pointlike scatterer, then the temporal signal will provide the impulse Green's function connecting the scatterer with the array. The details of this procedure will be discussed in another paper entirely devoted to what we call the extended D.O.R.T. method.

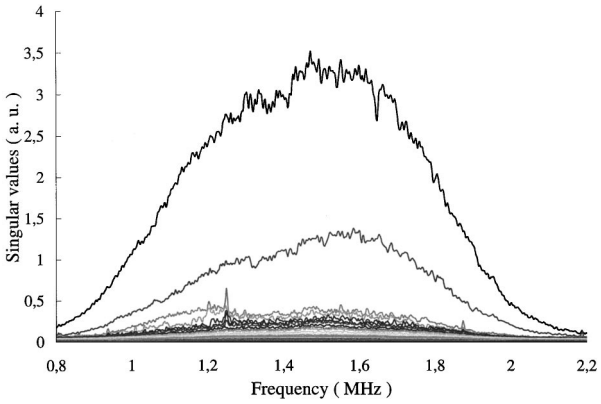

FIG. 17. Singular values of the transfer matrix versus frequency.

A. Construction of the temporal Green's functions

The abovementioned conditions are satisfied in the following example. The array of transducers and the waveguide are the same as in the Introduction. The range of the scatterers is 400 mm, the distance between the scatterers is 2 mm, and their reflectivities differ by a factor of 3 in the frequency band of the transducers. The SVD of the transfer matrix is calculated at each frequency of the discrete spectrum from 0.8 to 2.2 MHz. The singular values distribution versus frequency is shown Fig. 17: two singular values are apart from the 58 noise singular values and well separated from each other.

The impulse response function from the strong scatterer to the array can be reconstructed from the eigenvectors $\sqrt{\lambda_1(\omega)}V_1(\omega)$. Assuming the reflectivity of the scatterer is independent of frequency, this response is the temporal Green's function connecting the scatterer to the array convoluted by the acousto-electrical response of the transducer (Fig. 18, top). The same procedure applied to $\sqrt{\lambda_2(\omega)}V_2(\omega)$ provides the impulse Green's function from the second scatterer to the array (Fig. 18, bottom). This result is of particular interest in a complex propagating medium like a waveguide. Indeed, the low signal-to-noise ratio due to the length of the multiple path and the complexity of the echographic response of scatterer due to the double paths along the guide

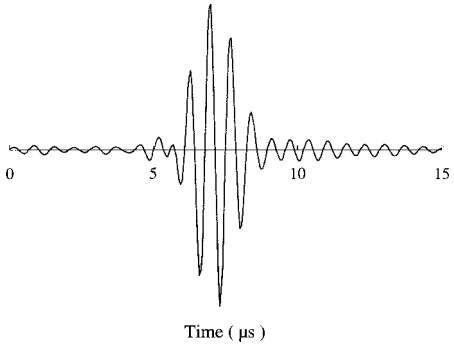

FIG. 19. Time domain compression: signal received at the position of the first wire after transmission of the first temporal eigenvector.

renders the determination of the impulse responses of the scatterers very difficult.

B. Selective focusing in the pulse mode

These signals are then transmitted from the array and the so-produced field is recorded along a line at the initial depth of the wires. One can observe an excellent temporal compression at the position of the wires: The transmitted signals are 165 μs long while the signal received at the wire position is a pulse 3 μs long (Fig. 19). The transverse peak pressure pattern of the first and second eigenvectors at the depth of the wire (Fig. 20) can be compared with the one obtained in monochromatic transmission (Sec. I, Fig. 4). The improvement in spatial focusing is undeniable (Fig. 21). The secondary lobes decrease to -30 dB while in the monochromatic transmission they remained around -18 dB.

VI. CONCLUSION

The echographic detection of scatterers in a simple water waveguide was studied. It was shown that the D.O.R.T. method provides information on the scattering medium that was not yet available. Taking advantage of the multiple reflections at the guide interfaces, the method was used to separate the signal coming from different scatterers and then to focus a wave field at anyone of them. The obtained resolution was nine times thinner than the free-space diffraction

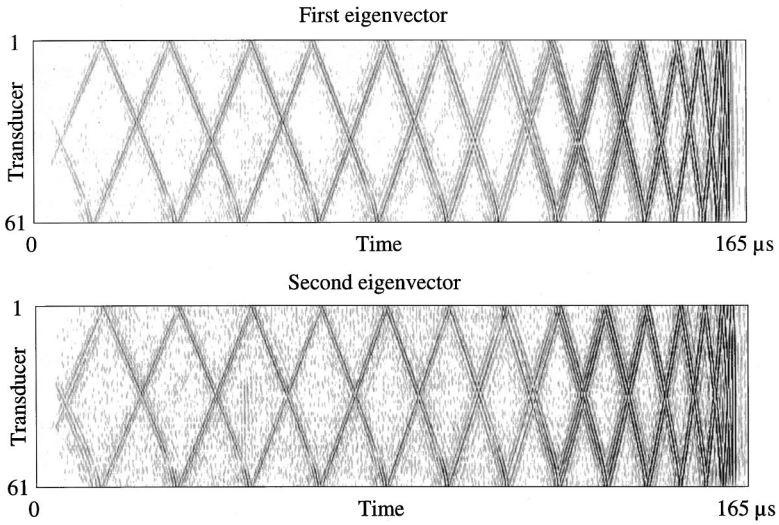

FIG. 18. Signals reconstructed from the first eigenvector (a) and from the second eigenvector (b). These signals correspond to the impulse response from each wire to the array.

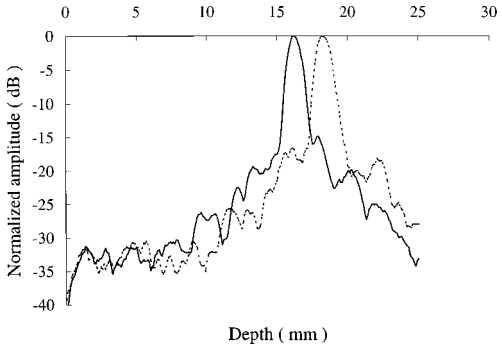

FIG. 20. Maximum of the pressure field measured at the depth of the wires across the guide after transmission of eigenvectors 1 and 2.

prediction. The method was also applied to the detection of a scatterer near the water/air interface, the distance under which the scatterer is no more detectable was shown to be less than $\lambda/5$ at a range of 400λ.

The efficiency of the method in a nonstationary guide with surface waves at the water/air interface was studied. For high waves ($kh_{\mathrm{rms}}=10$), averaging of the transfer matrix allowed to reduce the noise singular values and to keep a resolution almost three times thinner than in free space. Finally, it was shown that a combination of the eigenvectors found at each frequency provided the impulse responses of each scatterer to the array.

These experimental results open several axis of research. The D.O.R.T. method could be applied to nondestructive testing in solid waveguides. This is of particular interest for defects that are close to the interfaces. The results presented in a nonstationary guide are promising and motivate further studies of underwater applications such as mine countermeasures. A perturbation analysis of the transfer matrix in the presence of surface waves should be carried on. The time domain D.O.R.T. method could be used in detection to reduce sidelobe effects such as false location problem. Furthermore, the ability to achieve spatial and temporal compression may be applied to acoustic communication in shallow water.

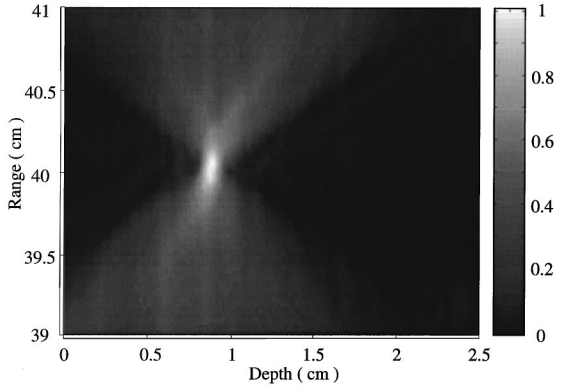

FIG. 21. 2D map of the maximum of the pressure field measured after transmission of the first eigenvector.

ACKNOWLEDGMENTS

We wish to express our gratitude to Julien de Rosny for programing the procedures that allowed us to operate the electronic devices in a very convenient manner. This research was supported by the DRET Contract No. 96-1213.

[1] A. Parvulescu and C. S. Clay, ''Reproducibility of signal transmissions in the ocean,'' Radio Electron. Eng. **29**, 223–238 (1965).
[2] A. Parvulescu, ''Matched—signal ('MESS') processing by the ocean,'' J. Acoust. Soc. Am. **98**, 943–960 (1995).
[3] C. Draeger and M. Fink, ''One-channel time reversal of elastic waves in a chaotic 2D silicon cavity,'' Phys. Rev. Lett. **79**, 407–410 (1997).
[4] C. S. Clay, ''Optimum time domain signal transmission and source location in a waveguide,'' J. Acoust. Soc. Am. **81**, 660–664 (1987).
[5] S. Li and C. S. Clay, ''Optimum time domain signal transmission and source location in a waveguide: Experiments in an ideal wedge waveguide,'' J. Acoust. Soc. Am. **82**, 1409–1417 (1987).
[6] M. Fink, C. Prada, and F. Wu, ''Self focusing in inhomogeneous media with time reversal acoustic mirrors,'' Proc. IEEE Ultrason. Symp. 1989, edited by B. R. McAvoy, Vol. 2, pp. 681–686 (1989).
[7] D. R. Jackson and D. R. Dowling, ''Phase conjugation in underwater acoustics,'' J. Acoust. Soc. Am. **89**, 171–181 (1991).
[8] P. Roux, B. Roman, and M. Fink, ''Transmissions acoustiques sous-marines dans les milieux à petits fonds: application du miroir à retournement temporel,'' 3ième journées d'Etude en Acoustique Sous-Marine, Brest (1995).
[9] P. Roux, B. Roman, and M. Fink, ''Time-reversal in an ultrasonic waveguide,'' Appl. Phys. Lett. **70**, 1811–1813 (1997).
[10] W. A. Kuperman, W. S. Hodgkiss, H. C. Song, T. Akal, C. Ferla, and D. R. Jackson, ''Phase conjugation in the ocean: Experimental demonstration of an acoustic time-reversal mirror,'' J. Acoust. Soc. Am. **103**, 25–40 (1998).
[11] C. Prada and M. Fink, ''Eigenmodes of the time reversal operator: A solution to selective focusing in multiple target media,'' Wave Motion **20**, 151–163 (1994).
[12] C. Prada, J. L Thomas, and M. Fink, ''The iterative time reversal process: Analysis of the convergence,'' J. Acoust. Soc. Am. **97**, 62–71 (1995).
[13] C. Prada, S. Manneville, D. Spoliansky, and M. Fink, ''Decomposition of the time reversal operator: Detection and selective focusing on two scatterers,'' J. Acoust. Soc. Am. **99**, 2067–2076 (1996).
[14] C. Prada and M. Fink, ''Separation of interfering acoustic scattered signals using the invariant of the time-reversal operator. Application to Lamb waves characterization,'' J. Acoust. Soc. Am. **104**, 801–807 (1998).
[15] G. Bienvenu and L. Kopp, ''Optimality of high resolution array processing using the eigensystem approach,'' IEEE Trans. Acoust., Speech, Signal Process. **31**, 1235–1247 (1983).
[16] Ralph O. Schmidt, ''Multiple Emitter Location and Signal Parameter Estimation,'' IEEE Trans. Antennas Propag. **AP-34**, 276–281 (1986).
[17] A. B. Baggeroer, W. A. Kuperman, and P. N. Mikhalevsky, ''An overview of matched field methods in ocean acoustics,'' IEEE J. Ocean Eng. **18**, 401–424 (1993).

Passive acoustic methods applied to fin whale population density estimation

Mark A. McDonald
2535 Sky View Lane, Laramie, Wyoming 82070

Christopher G. Fox
National Oceanic and Atmospheric Administration, Pacific Marine Environmental Laboratory, Hatfield Marine Science Center, Newport, Oregon 97365

(Received 20 July 1998; accepted for publication 28 January 1999)

Assessing the size of cetacean populations in the open ocean has traditionally relied on visual surveys alone. The addition of acoustic monitoring can complement these surveys if reliable protocols can be formulated and calibrated with visual techniques. A study is presented to estimate fin whale population statistics based on near-continuous recording from a single hydrophone. Range to calling animals is estimated by transmission loss and multipath methods to provide a minimum population density estimate. Results are derived from recordings at a hydrophone site north of Oahu, Hawaii that have been the focus of earlier studies. The average calling whale density is 0.027 animals/1000 km^2, while the seasonal maximum calling whale density is about three times the average, or 0.081 animals/1000 km^2. Over 30 fixed hydrophone sites are available around the Worlds Oceans from which such statistics could be generated. © *1999 Acoustical Society of America.* [S0001-4966(99)01005-X]

PACS numbers: 43.30.Sf, 43.80.Ka [WA]

INTRODUCTION

Most species of large cetaceans in the open ocean are currently considered endangered and are protected by international agreement. Assessing the viability of marine mammal populations in the pelagic environment requires reliable methods of assessing size, density, and distribution of various population stocks, or at the least relative decline or recovery of a population through time. Both the National Oceanic and Atmospheric Administration, which has responsibility for managing and protecting this resource, and the United States Navy, which operates acoustic and other systems during routine operations, require reliable information on marine mammal stocks in the open ocean. Stock assessment has traditionally relied almost exclusively on visual surveys from surface vessels. Although the technique is well developed and reliable when adequate sampling is available, results suffer in open ocean applications where animal densities are low. Often observations are quite difficult to collect in high-latitude regions during certain times of the year. In addition, the presence of the surface ship carrying the observers can affect the behavior of the animals and influence the results. Underwater acoustics offers a complementary method for assessing cetacean populations that, when combined with other information, can improve population estimates. In many parts of the world's oceans, the seasonality and population density of fin and blue whales are unknown, thus even with significant errors, acoustic surveys are likely to provide a useful contribution. Previous whale acoustic studies have estimated seasonality for fin and blue whales (Clark and Charif, 1998; Moore *et al.*, 1998; Thompson and Friedl, 1982), but have not addressed the potential for minimum or relative population abundance estimation.

Long-duration low-frequency digital recordings are potentially available from more than 30 deep ocean hydrophones deployed around the world's oceans by the U.S. military. These hydrophone systems were designed either to track Soviet submarines or monitor missile impacts and nuclear tests in the central Pacific, but the recordings also contain many natural sounds produced by earthquakes, volcanic activity, and whales. Of particular interest are sounds produced by large baleen whales since these animals spend much of their lives in pelagic environments, making their assessment difficult by traditional means. Fin whales (*B. physalus*) and blue whales (*B. musculus*) produce calls with the lowest-frequency and highest source levels of all cetaceans (Richardson *et al.*, 1995). Estimating absolute abundance directly from acoustic recordings requires understanding the acoustic behavior of the whales to a degree beyond our present state of knowledge. In most cases, the signal level of the marine mammal call is too low and the spacing of the available hydrophones too great to allow direct localization. However, minimum abundance estimates can be derived from an isolated hydrophone if the range for each of the calling whales can be accurately estimated. Absolute abundance estimates may ultimately be achieved by deriving empirical calibrations from acoustic recordings obtained from areas where population density is known from visual census efforts.

In this paper, a method of population assessment based on acoustic techniques is applied to the study of fin whales (*B. physalus*) using a seafloor hydrophone located off the island of Oahu, Hawaii, an area where so few fin whales have been seen that their density has not been previously estimated (Mobley *et al.*, 1996). Based on acoustic data from this one hydrophone, a minimum density estimate of fin whales at this site (0.081 animals/1000 km^2) during peak season is derived. Finally, criteria are proposed by which call

 0001-4966/99/105(5)/2643/9/$15.00

abundance at a site can be measured to ultimately provide an empirically calibrated population density estimate.

I. METHODS AND RESULTS

A. Point transect surveys

The point transect population survey method consists of measuring call density at multiple geographic locations to estimate average density for a region. Each call density estimate consists of the number of acoustic detections, with associated ranges, per time period. In contrast to visual fin whale distance sampling data where detection rates decrease with range out to a maximum of about 6 km (Clark and Fristrup, 1997) because it is more difficult to see more distant animals, ocean acoustic data for fin whales from a deep-water hydrophone have a relatively constant detection rate out to about 20 km where variability in ambient noise levels and in call source levels combine to obscure some calls. Given the long-duration continuous observation periods of seafloor recordings, enough detections are recorded, even in a low density area such as our example, to allow data from beyond about 20 km to be truncated such that we assume all calling animals are detected in the reduced survey area. In our data the detection ranges were scored at the closest point of approach, resulting in a bias towards more detections at short range. While this bias might be treated statistically based on speed of travel calculations, the observed increase in detections at short ranges is not so large as to believe the intermediate and long range data has a significant bias.

The two primary questions which this paper addresses are how to define a detection and how to determine the range to each detection. The observer disturbance problem, so common in visual distance sampling surveys, is nonexistent for moored hydrophones, but the problems of clustering, animal movement, and multiple counting of the same animal remain. The most obvious problem with estimating population density using single hydrophone data is that if only one point, the hydrophone location, is sampled, a few resident whales could produce the vast majority of the calls. Multiple hydrophone locations are needed before extrapolating such a population density estimate to a much larger area.

B. Kaneohe hydrophone data

Near-continuous recordings were analyzed from a hydrophone in 800 m of water north of the island of Oahu, Hawaii (Fig. 1) covering the period August 12, 1992 to April 1, 1993 (232 days). These recordings were originally collected for seismic studies and were digitally sampled at 100 Hz having a low-pass filter applied with frequency response rolloff starting near 20 Hz, the frequency response below 20 Hz being such that the ocean ambient noise spectrum appears flat down to about 2 Hz. The longest gap in data recording was about five days and only three breaks lasted more than one day, with overall coverage of 94%. This is one of the same hydrophones used by previous researchers (Northrup *et al.*, 1971; Thompson and Friedl, 1982) to plot the time distribution of whale calls. One difference between this study and previous work is that earlier researchers recorded on analog tape and relied primarily on listening to the sounds

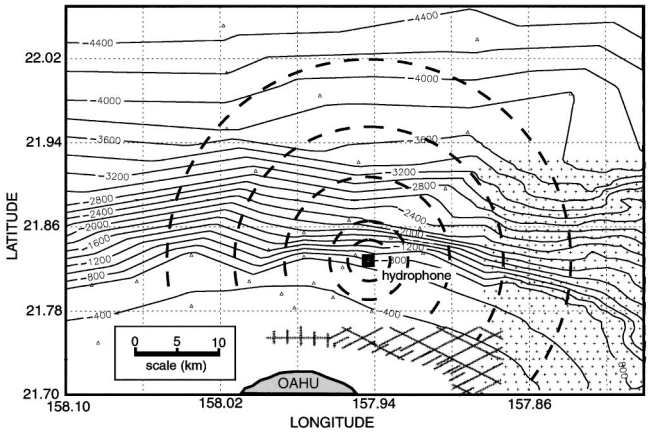

FIG. 1. The location of the Kaneohe hydrophone is shown off the north coast of Oahu, Hawaii. The bathymetry is contoured in meters, the plus symbols indicating digital data points from hydrographic surveys and the triangles indicating data transferred from published nautical charts. The arcs overlain on the map define the zones into which the acoustic survey data was divided.

played back at higher speeds to identify whale calls, while in this study spectrograms were reviewed visually for all data. Only detections which have a signal-to-noise ratio (SNR) greater than 1.0, over the 2–25 Hz band as measured from a waveform plot, are scored. The details of software and spectrogram parameters used in viewing the data are irrelevant as any reasonable choices can detect signals with a waveform SNR below 1.0. One of the authors (M.A.M.) reviewed and scored all 232 days of data in its entirety, a task which required three week's effort.

For comparison purposes, the same percent occurrence scaling used by Thompson and Friedl (1982) is plotted in Fig. 2. This plot scaling, where a day was scored if a call was heard during that day, was more logical for their data, where only about 8 h of data were analyzed per day and there were many gaps in the data. Fin whale calls were observed for 627 h (~12.5%) of the more than 5000 h of data from the 232 days we analyzed, where breaks in calling of less than 1 h were regarded as continuous fin whale calls. Most of the occurrence data from the Thompson and Friedl (1982) study utilized data from two hydrophones, 11.6 km apart monitored for about 8 h per day, while only one of those two hydrophones was available for this study. Differences in occurrence percentages are likely due to the use of one hydrophone versus two, the increased hours per day of observation and the different methods of detecting whale calls (listening versus spectrogram review). The increased percentage of fin whale calls detected is not useful in relative abundance terms because of these differences, even if we assumed call behavior were the same through the years. Seasonality is similar to that observed by others (Northrup *et al.*, 1971; Thompson and Friedl, 1982), although the increased number of observations provides a more precise measure of occurrence than the previous studies.

C. Call description

The relatively short duration of fin whale calls (about 0.8 s) makes them well suited to range estimation with mul-

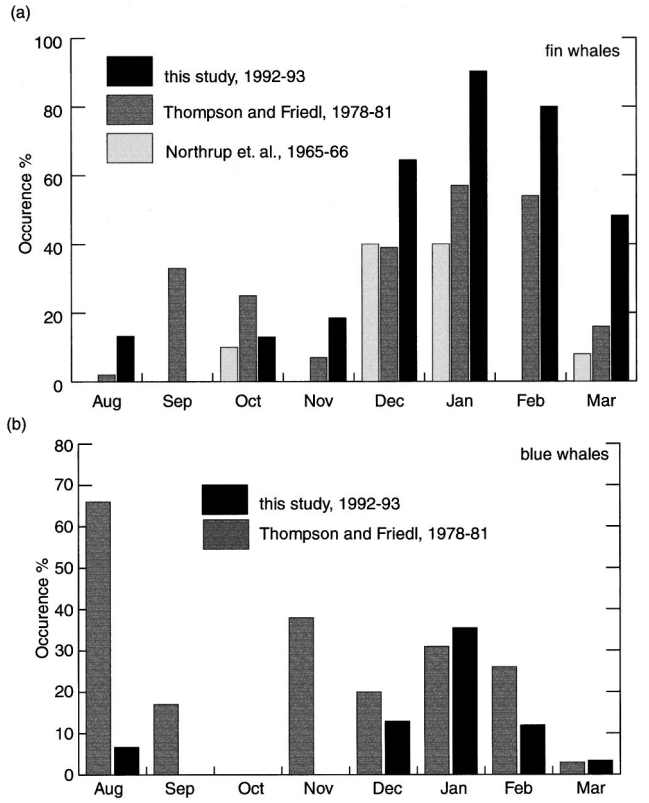

FIG. 2. (a) The occurrence of fin whales from August 1992 to March 1993. Occurrence is expressed as the percentage of each month's total recording days on which fin whale calls were received. The results of studies undertaken from 1965 to 1966 and 1978 to 1981 are plotted for comparison. (b) The occurrence of blue whales plotted as above.

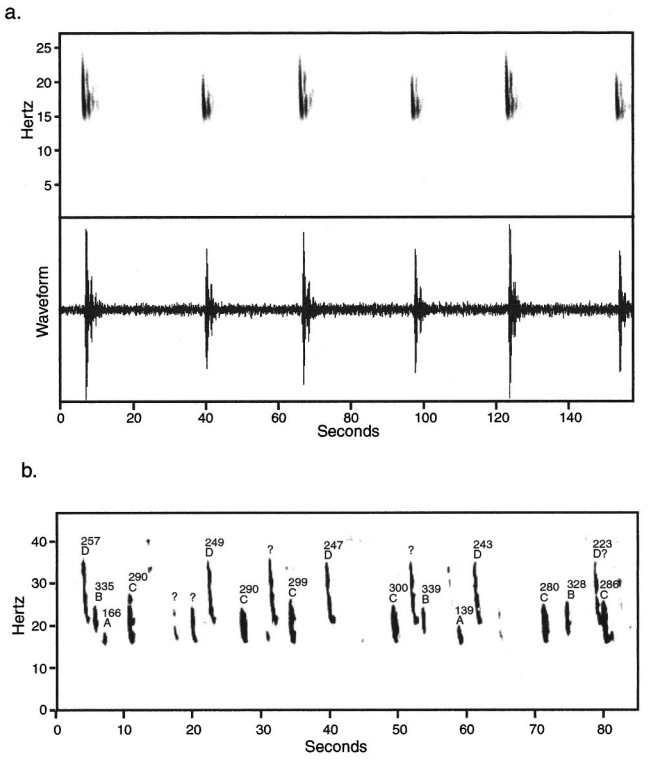

FIG. 3. (a) A typical fin whale call series of the ''20-Hz doublet'' type is shown in spectrogram and waveform. The direct path arrivals are loudest in this example with a SNR of about 12, measured as the ratio of the loudest arrivals to the background noise level on the waveform display. (b) The ''20- to 35-Hz irregular repetition interval'' call type as recorded on a DIFAR sonobuoy October 12, 1997 off Southern California. The compass bearing to the whale is shown above most calls as computed from DIFAR processing. The calls are labeled A through D to suggest that at least four individuals are involved as inferred from call character and bearings. At least three fin whales and one blue whale were visually seen generally to the northwest of the sonobuoy within 1.5 miles.

tipath (echo) techniques. Fin whale calls from the area of this study have been previously categorized into three types, based on the pattern and frequency range of the 0.8-s pulses (Thompson *et al.*, 1992; Thompson and Friedl, 1982). The ''doublet 20-Hz'' calls are well known from both Atlantic and Pacific Oceans and are the dominant call in lower latitudes, making up more than 90% of the calls recorded in this study. An example of typical ''doublet 20-Hz'' calls from this study is shown in Fig. 3(a). Field observations indicate the individuals producing such calls to be smaller (female fin whales are generally larger than males), which together with the seasonality of the calls has led to the suggestion this is a male breeding call (Watkins *et al.*, 1987).

The second call type, sometimes called the ''20- to 35-Hz irregular repetition interval'' type, has been confirmed by analyzing several hours of field data collected with sonobuoy arrays where simultaneous visual observations confirm these calls to be produced by fin whales. Review of hundreds of hours of unpublished fin whale call data recorded on seismology and military systems indicates that at higher North Pacific latitudes in summer more than 90% of fin whale calls are of this higher-frequency countercall type. An example of this second call type is shown in Fig. 3(b), from a recording made with a DIFAR sonobuoy deployed to the southeast of a group of at least three fin whales which were very active though changing swim directions often over an area of about 1.5 miles diameter. Visual position tracks for each whale could not be maintained as it was impossible to keep individual fin whales separated. One blue whale was also present. This recording was made off Southern California (33°31.96′ N 119°44.54′ W) on October 12, 1997. The compass bearings to the whale are shown in the figure for most calls, as computed from post-cruise DIFAR processing (D'Spain, 1994). The call character appears to be a ''signature'' correlated to individuals, as the bearings are nearly the same or smoothly varying for each call character yet different between each call character.

The third call type, ''30- to 90-Hz shorter and more irregular repetition intervals'' call, represents a small fraction of the total in both seasons and all latitudes. Other known fin whale call types include a variety of relatively quiet moans and belches, as well as single 20–35 Hz pulses or series of just a few 20–35 Hz pulses. These less common calls were ignored in this analysis because of the uncertainty whether a fin whale or another species produced the sound. The spectral character of fin whale pulse sounds consistently shows a downward sweep in frequency through the typical 0.8-s duration (Edds, 1988; Thompson *et al.*, 1992; Watkins, 1981).

Essential to our approach to counting fin whale detections is our belief that the loudest calls typical of each sequence of ''20-Hz doublets'' have source levels consistent (within a few dB) from one encounter to the next or have a

variability which can be statistically characterized. Knowledge of absolute source levels is not critical to our method. Source levels for fin whale calls of the ''doublet 20-Hz'' type have been reviewed by others (Payne and Webb, 1971; Watkins *et al.*, 1987), reporting wide ranges which have little relevance to our problem as we only score typical, not unusual fin whale calls as detections. A typical detection consists of hundreds of calls in total and dozens of calls which are used to estimate an average for scoring the highest SNR. Of more interest is the median source level which has been reported as 80 dB *re*: dyne/cm^2 at one yard which translates to 179 dB *re*: μPa @ 1 m (Payne and Webb, 1971). In our observations and that of others (Patterson and Hamilton, 1964), source level is consistently louder on the alternately occurring wider bandwidth pulse of the patterned ''doublet 20-Hz'' type calls. We score only the louder of these two types. The initial and final few calls of a series are commonly less loud.

D. Range estimates from call echoes (multipath ranging)

When the typical 0.8-s duration fin whale calls are recorded in water deeper than about 600 m, the received sound consists of three or more distinct multipath arrivals corresponding to the direct path and the echoes which are reflections between the sea surface and seafloor. Localization of sound sources using multipath information from single hydrophone data is a well-established method (Frazier and Pecholcs, 1990; Hassab, 1976; Westwood and Knobles, 1997), although it has generally not been applied to whale calls. Using pre-existing bathymetric knowledge in the vicinity of the deep-sea hydrophones, ray-tracing methods can be used to calculate the time separation between successive multipath arrivals as a function of range and of the bathymetry between the hydrophone and the calling whale. Examples of fin whale calls recorded from different ranges are shown in Fig. 4. A suggestion that fin whale ''doublets'' may be caused by reflections from inside the earth, as deep as the mantle (Premus and Spiesberger, 1997), is not supported by our own transmission loss estimates, the long time intervals (greater than 30 s) common in our data or by the variability in such intervals at a single site. Because of the considerable effort involved in estimating range by this method for each whale call series, this technique may best be applied as a calibration check for the transmission loss method of range estimation.

Recordings from a deep-sea hydrophone on a flat seafloor would be the simplest to analyze in terms of translating echo arrival time differences to ranges. The time differences would be relatively large because of the deep water and independent of azimuth because of the flat seafloor. An example of such multipath time differences is plotted in Fig. 5 for a hypothetical hydrophone on a flat seafloor in 4000 m of water, a typical seafloor depth. A simple ray-tracing algorithm (Coates, 1989) using a constant velocity sound speed profile was used to calculate this example. As arrival time differences can be readily picked to an accuracy of less than 0.1 s, either visually or by cross correlation with a representative call, the range accuracy is on the order of a few tenths

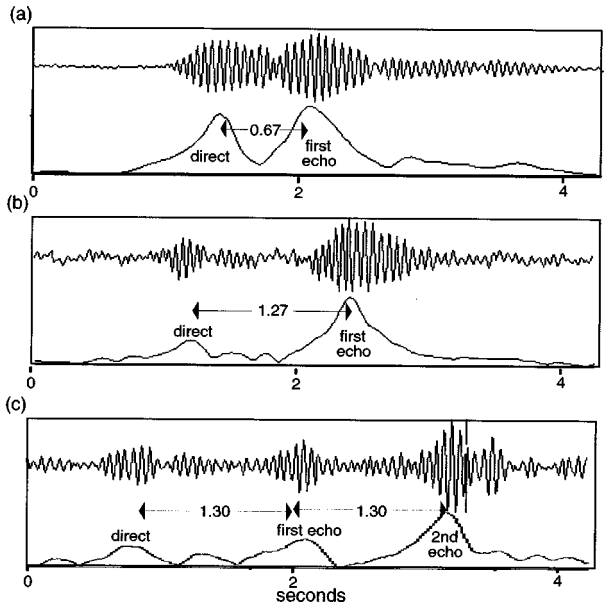

FIG. 4. (a) A time series and a cross correlation of that time series with a representative fin whale pulse are plotted where the fin whale is located upslope of the seafloor hydrophone at about one km horizontal range. The two distinct pulses are the direct arrival and the first seafloor→surface→hydrophone echo path arrival. Other echoes are seen later. (b) The time series and cross correlation is plotted for a whale downslope at about the 4-km range. The first or direct arrival has diminished more than the reflected path because of refraction within the water column. (c) The time series and cross correlation are plotted for a whale downslope at about the 10-km range. The direct arrival is not apparent.

of one kilometer over the first ten kilometers with decreasing accuracy at longer ranges (Fig. 5). In deep water, seafloor recordings typically show a direct arrival and three or more separate bounce path arrivals when ranges are less than 10 km (McDonald *et al.*, 1995). At ranges between 10 and 25 km in lower latitude waters, the direct path arrival is greatly diminished because of refraction within the water column, but the reflected path arrivals remain, thus detectability of the signal changes little. In high-latitude waters, the multipath method is expected to work better than in lower latitudes because shadow zones are less prominent.

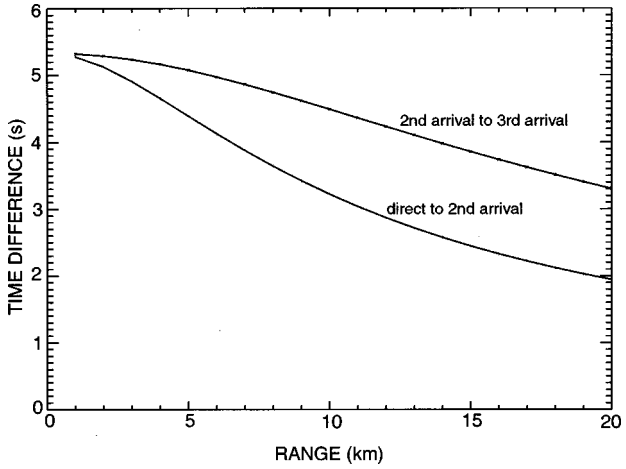

FIG. 5. The differences in arrival times for the direct path and first two bounce paths are plotted for a hypothetical receiver in 4000 m of water with a flat seafloor.

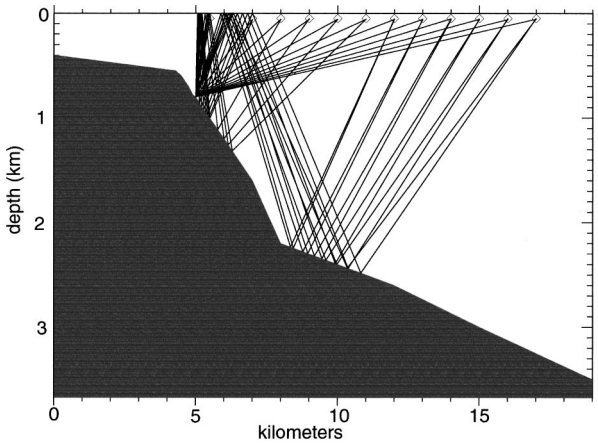

FIG. 6. A bathymetric profile is shown across the Kaneohe hydrophone with the isotropic acoustic travel paths shown for the direct and first two bounce paths shown from evenly spaced source positions.

The rapidly changing bathymetry in the vicinity of the Kaneohe hydrophone makes range determinations using multipath methods much more complicated than would be the case in a flat seafloor environment. Figure 6 graphically shows echo travel paths for a bathymetric profile extending offshore from the Kaneohe hydrophone, an area of steeply sloping bathymetry. Irregular bathymetry opens the possibility of inverting the travel time difference data for a unique position or track for the calling whale, but complicates the estimation of range. Figure 7 shows the two contour maps of time differences for the first three acoustic travel paths. The accuracy of these maps is controlled by our knowledge of the bathymetry, which in this case was largely taken from the nautical charts. Inversion of echo time differences from a single hydrophone for a unique whale position would require better knowledge of bathymetry than provided by the nautical charts for this area. Multipath analysis of some of the nearer whale calls shows that the whales are about as commonly found inshore of the hydrophone as offshore from it. Because of the difficulties presented by the rugged and poorly known bathymetry, we have only used multipath techniques for validation of transmission loss range estimates out to about the 5-km range, a region where spherical spreading losses would be expected in any case. The multipath technique has allowed us to determine that the loudest whales were nearly above the hydrophone (less than several hundred meters horizontal offset), allowing us to transform the transmission loss curve to a range versus SNR plot. In the case of a more ideal hydrophone, the multipath data should be able to verify the spreading loss assumptions out to about 20 km.

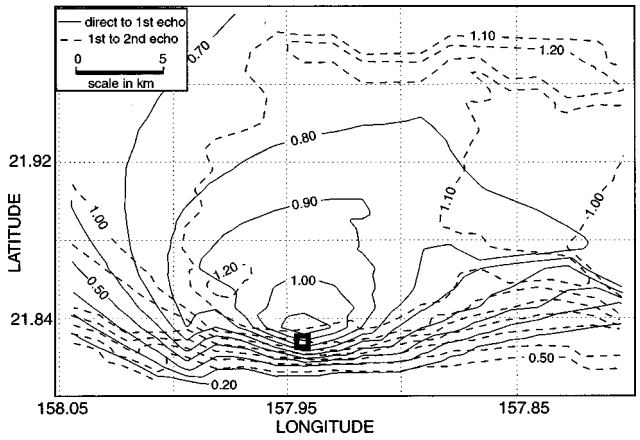

FIG. 7. Two time difference isochron maps are overlain for the area around the Kaneohe hydrophone. Because of the rugged bathymetry the contours are not symmetric as they would be in the case shown in Fig. 5.

E. Range estimates from received sound level (transmission loss ranging)

Estimation of range from received level of whale calls can be accomplished with little effort and independently of multipath methods, although multipath methods can provide a valuable check on the results. Estimation of range to sound sources in the ocean using amplitudes alone requires a reliable sound transmission loss model and the assumption that all the calling whales have about the same maximum source levels during a bout of calling or a statistically characterized variability in source levels. A bout is defined as a series of stereotyped pulses separated by at least 2 h from any other bout (Watkins *et al.*, 1987). Given these assumptions the distribution of the received amplitude data can be used to develop a transform between received level and range. Recording system calibration is not needed nor is any knowledge of the animals' source levels as the relative received levels alone provide sufficient information to fit the data to a transmission loss model, assuming some of the animals pass relatively near the hydrophone. The primary advantage of the relative amplitude and transmission loss approach is that it simplifies the task of evaluating ranges for very large numbers of calls, directly correlating amplitude to range while using the multipath method only to verify the accuracy of the transform.

Theoretical transmission loss calculations such as those performed with parabolic equation methods using the RAM software (Collins, 1993) require knowledge of the sound speed profile within the water column, a bathymetric profile, receiver depth, source depth, and of lesser importance the seafloor characteristics. The source depth, or depth of calling whales, has been reported to be about 50 m for fin whales (Watkins *et al.*, 1987), and analogous blue whale call depths have been precisely measured at depths near 40 m (D'Spain *et al.*, 1995). An earlier report of a single fin whale call at 1200 ft (Patterson and Hamilton, 1964) is believed to be in error because of the difficulty of producing such sounds when the whale's air volume is compressed so small (McDonald *et al.*, 1998). Because the receiving hydrophone is at or below sound channel depths, convergence zone effects are much diminished and water-column sound velocities become less critical to the problem than for a shallow source and receiver. In most cases, transmission loss can be reasonably approximated by simple spherical spreading out to about 15-km range. It may be that a transition from spherical to cylindrical spreading loss occurs beyond 15 km, or it may never occur considering time stretching (Urick, 1983), which is the spreading of the pulse by multipaths as is evident in Fig. 4.

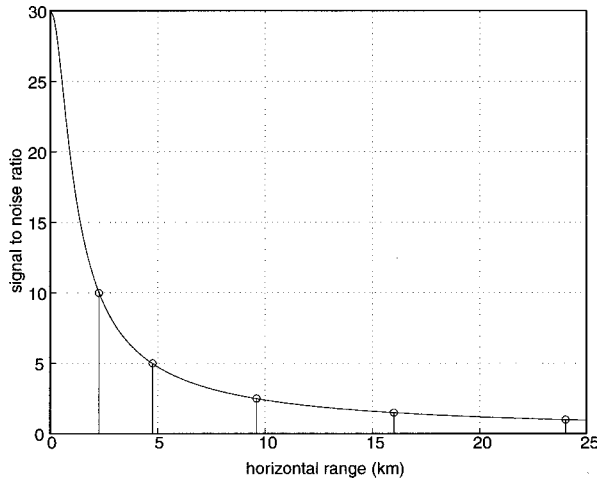

FIG. 8. Spherical-spreading loss ($20 \log R$) is plotted such that the whale calls directly above the hydrophone have the observed SNR of 30. The range of each of the SNR data bins used in the Kaneohe study is shown by vertical lines.

In addition to the assumption of constant or at least predictable source levels there will be a predictable bias associated with changing ambient noise conditions. While ambient noise studies were not conducted for the hydrophone site used in this study, analogous data from near Wake Island (McCreery *et al.*, 1993) suggest ambient noise at 20 Hz increases about 3 dB as wind increases from calm to 13 m/s. At least one other study (Morris, 1978) suggests there is no change in ambient noise levels at 20 Hz in the deep sound channel where the Kaneohe hydrophone is placed. A 3-dB change in ambient noise is equivalent to shifting P–P (peak-to-peak) SNR (signal-to-noise ratio) from 1.4 to 1.0 or from 5.0 to 4.6, thus is significant only for low SNR data. Assuming the transmission loss range data are truncated at an SNR of 1.5, a 3-dB change in ambient equates to SNR variation from 1.7 to 1.3, or a detection range shift from 14 to 18.5 km, assuming spherical spreading loss. This would correspond to a 75% increase in area for our outer survey zone, but this represents the maximum variability rather than the statistical bias. To estimate statistical bias we have assumed a normal distribution for the occurrence of each wind state, with a center at 6.5 m/s based on the number of spectra used for each wind state at Wake (McCreery *et al.*, 1993). The weighted average range for a 1.2 SNR with a nominal 20-km range becomes about 20.5 km corresponding to only about a 5% increase in area. At shorter ranges the effect of ambient noise variability is less, thus we have ignored the bias for all ranges in our analysis.

Transmission losses were calculated for a variety of cases with RAM using typical environmental parameters for this site, an 800-m hydrophone depth, and a source depth of 50 m. A simple spherical spreading loss provides a reasonable estimate of the calculated average results. While transmission loss is usually plotted with log–log scaling using straight lines fitted through the data, it is more useful for our purpose to plot in linear space (Fig. 8). The whales passing nearly overhead the 800-m-deep hydrophone as determined by multipath methods had a SNR of 30, thus defining the range transform for all other calls.

A rough confirmation of the accuracy of our range-amplitude transform is provided by the examination of fin whale acoustic call tracks derived from similar travel time methods and similar arrays of seafloor hydrophones. An array off Bermuda has been able to track fin whales out to 20 km when ship noise is low and the azimuth is favorable (Patterson and Hamilton, 1964); this range corresponds to a SNR of 1.2 by our transform. An array of ocean bottom seismometers in 2400-m water depths found the SNR typically approached unity in the 15–20 km range (McDonald *et al.*, 1995), again similar to our range transform as presented in Fig. 8. Speculations of communication among fin whales over hundreds of miles (Payne, 1995; Payne and Webb, 1971) rely on detection of an omni-directional SNR much less than 1, and thus are not relevant to the methods used here. If a typical whale source level of 176 dB @ 1 m is assumed, the average ambient noise band level at the Kaneohe hydrophone is 88 dB rms *re*: 1 μPa, similar to what is expected from previous studies (Bannister, 1986; Kibblewhite *et al.*, 1976). Hydrophone systems such as used in this study and at Wake Island have electronic noise levels well below ocean ambient levels.

F. Number of calling whales (detection time constant)

For this study, a statistical approach to counting the number of acoustic whale detections using fixed-time duration is proposed. Frequently, multiple whales are calling within the acoustically monitored area, but it is difficult to count each and not double count the passage of a single whale through the area. Using a time constant scoring system, the time periods that include any number of calls are treated as detections over a given time-interval constant. For example, 6 h of continuous calling could be scored as six detections with a 1-h time constant, two detections with a 4-h time constant, or one detection with an 8-h time constant. A typical recording might have 2 h of calling followed by 4 h of silence and 3 h more of calling, a sequence which would score five with a 1-h time constant, two with a 4-h time constant, and two with an 8-h time constant. Based on observations of the duration of call series, a 4- to 8-h time constant appears to represent a good balance between multiply counting a single animal and missing calling animals. In some circumstances it may be possible to separate multiple callers by recognizing multiple ranges, but the inclusion of such information greatly increases the analysis effort required. The detection time constant method provides an easily calculated statistic which can then be calibrated by more rigorous visual or detailed acoustic surveys.

G. Minimum population density estimation

Scoring the number of detections using different time constants provides a range of calling whale density estimates. Call detection numbers and density are shown in Table I for each of the SNR bins. The SNR bins were arbitrarily chosen at levels we judged convenient for separating call series. The areas are computed as the area between range circles except that at ranges beyond 4.75 km, the areas are

TABLE I. Relation of average call density estimate to time constant and range.

		Number of detections		Call density/1000 km^2	
SNR	Range (km)	$TC=4$ h	$TC=8$ h	$TC=4$ h	$TC=8$ h
1.0–1.5	16.0–24.0	143	85	0.042	0.025
1.5–2.5	9.6–16.0	54	36	0.031	0.020
2.5–5.0	4.75–9.6	15	10	0.016	0.011
5.0–10	2.25–4.75	11	8	0.038	0.027
>10	0–2.25	9	7	0.106	0.083
Average Call Density/1000 km^2 Weighted by number of detections				0.040	0.027

cut off at the 400-m depth to account for the shallow water and onshore zones where whales would not be detected (Fig. 1).

The shortest-range zone will have a higher error due to the relatively small number of detections within that zone and will have a bias toward a higher density because the scoring system assigns the whale to the closest zone it swims through while calling. Using longer time constants increases the bias in detection range estimation toward shorter ranges because the animals have had more time to swim across multiple zones. The longest-range zone may have a larger area surveyed than assumed if the transmission loss does in fact transition from spherical loss to some lesser transmission loss at less than the 24-km range. The intermediate zones between 2.25 and 16 km might be expected to have the most reliable data. The call densities in Table I are averaged throughout the 232 days of the study although the call density varies greatly with season (Fig. 2). The average calling whale density, weighted by number of detections, is 0.027 animals/1000 km^2, for our best estimate 8-h time constant, while the seasonal maximum call density is about three times the average, or 0.081 animals/1000 km^2. The data for a 4-h time constant is shown to provide a sense of the error associated with the choice of time constant. Given that animals producing calls have usually been observed to be part of a group (Watkins, 1981), it may also be appropriate to apply a cluster size to each detection before calibration, further increasing the estimate of acoustic population density.

Limitations of the suggested approach include acoustic saturation, such as has been seen in the California Channel Islands where blue whale calls sometimes continuously overlap each other throughout the day. Our experience with the study site off Oahu and with seafloor recorders off Washington State suggests that the saturation problem is rarely encountered in the deep ocean, the busiest days at the Kaneohe hydrophone having 16 h of calling.

II. DISCUSSION

A. Comparisons with other population density estimates

The best known fin whale population density is that within 100 miles of the coast of California, where extensive visual line transect surveys indicate a population density of 1.1 animals/1000 km^2 (Barlow, 1995; Forney *et al.*, 1995). Several permanent seafloor hydrophones are present off Monterey (Chiu *et al.*, 1997) and off San Nicolas Island (Hildebrand, 1998) which could help to provide calibration for the transform between acoustic call density and absolute population density.

Aerial and ship visual surveys for whales off Hawaii have encountered relatively few fin whales, suggesting fin whale density to be considerably less than that off California (Leatherwood *et al.*, 1988; Miyashita *et al.*, 1995; Mobley *et al.*, 1996; Norris, 1998). As an exercise in estimating the minimum percentage of whales detected acoustically versus actually being present, let us assume the peak density off Oahu equals that off California, although we believe it actually to be much lower. The acoustically detected peak fin whale density off Hawaii (0.081 animals/1000 km^2) then represents greater than 7% of the animals present, a minimum bound. Given that the actual fin whale density off Hawaii is considered to be much lower, we expect we are acoustically counting much more than 7% of the whales present.

B. Detection time constant

A more theoretical approach to estimating the average time constant incorporates swim speed into the calculation. Examination of the multipath information from call series off Oahu reveals the animals to be always or nearly always moving. If the average speeds and monitored area are known, then average transit time can be calculated. Off Bermuda in winter, 117 h of acoustic fin whale tracks were analyzed and yielded speeds of 1.1–4.4 knots (2.0–8.1 km/h) averaged over whole tracks, with the most frequent speeds between 2 and 3 knots (3.7–5.6 km/h) (Patterson and Hamilton, 1964). Calling fin whales in the Northeast Pacific in summer have been seen to travel an average of 8.6 km/h, based on three whales traveling together analyzed over a 1.5-h period (McDonald *et al.*, 1995). There is one report of calling whales in the fall off George's bank which ''move little'' (Watkins *et al.*, 1987).

The Bermuda data are similar to the Kaneohe hydrophone data in call type, season, and setting (near an island), thus tracks from this study are used to estimate average transit time. The average travel speed at Bermuda was 4.65 km/h, but this is reduced to an average straight-line transit speed of 3.25 km/h to account for the zigzag character of the tracks. Assuming a 20-km radius survey zone, the average straight-line transit for whales entering the observation zone is then 9.8 h, but most calling bouts will be of shorter duration resulting in a time constant less than 9.8 h in agreement with our choices of 4 or 8 h as a time constant.

With more data on the call rates of individual fin whales it may be possible to devise a method better than the ''detection time constant,'' but counting the hours during which calling occurs and noting the typical signal-to-noise ratio during those hours have the advantages of simplicity and mimimal analyses time. More sophisticated future approaches might incorporate ''cue counting'' methods (Buckland *et al.*, 1993) which rely on data collected by following individual animals.

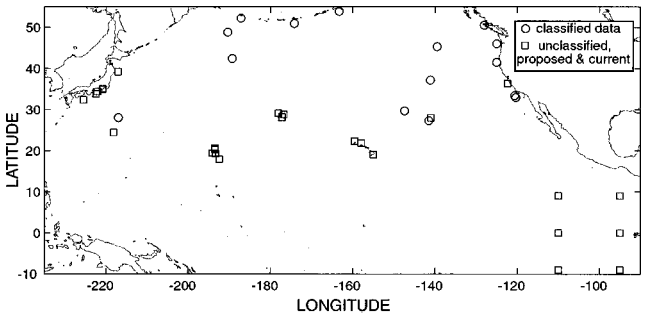

FIG. 9. Permanent and semi-permanent, existing and planned hydrophone locations in the Pacific are shown. Locations of the classified hydrophones are approximate as plotted by Howe and Mercer (1997).

C. The ideal deep sea hydrophone for acoustic whale census

Since the hydrophone sites currently available for marine mammal studies were designed for other tasks, it is worthwhile to consider the ideal configuration for a hydrophone deployed specifically for marine mammal studies. This ideal hydrophone would be below the critical depth (typically about 2000 m for intermediate latitudes) in an area where there is little bathymetric relief within the more or less 20-km range to be surveyed. The reflectivity of the seafloor may also be a factor in the preservation of more or fewer multipath arrivals, a high reflectivity being desirable, although any site will probably work. The location of the H2O seismology station (IRIS, 1998) on a submarine cable between Hawaii and California or the TPC2 hydrophone on a cable between Japan and Guam, in 4000–4200 m of water approaches the ideal. The advantage of being well below the critical depth is noise levels which are 10–20 dB lower (Kibblewhite *et al.*, 1976; Morris, 1978; Shooter *et al.*, 1990), where the distant noise, including distant whale calls, are eliminated and the whale calls within 20 km are more clearly heard. The lack of bathymetric relief allows a simple transform between multipath arrival separations and range (Fig. 5).

III. CONCLUSIONS

Accurate estimation of global whale populations remains a difficult problem that must be addressed using complementary techniques to be successful. This study presents a simple, robust method, although it does include numerous assumptions and caveats, by which acoustic call density can be related to minimum whale population density and later calibrated by proven visual survey techniques. The advantage of acoustic methods is the relatively low cost of placing a self-contained recording instrument at a site where visual observations are often difficult, such as the Antarctic, to obtain a long-term, continuous record of call activity. Recent advancements in the technology of self-contained recording systems make acoustic monitoring an underutilized resource (Fox and Stafford, 1998). Many refinements could be applied to the approach developed here, but calibration of acoustic data with visual survey data is expected to be the most important advance. This approach would work equally well for blue whales except that multipath ranging is complicated by the longer call duration, requiring the application of signal processing techniques (Spiesberger, 1998). The North Pacific alone has over 30 permanent hydrophones either in place or planned (Fig. 9) (Howe and Mercer, 1997; Kinoshita, 1997) and there are many more around the world (Richelson, 1998). If the data from these hydrophones were made readily available, the effort required to establish baseline call densities is relatively small. A crude and simple minimum estimate of fin and blue whale densities around the world's oceans based on acoustic detection could soon become a reality.

ACKNOWLEDGMENTS

Kahneohe hydrophone data were collected by Dr. Dan Walker at the Hawaii Institute of Geophysics. This project was funded through the Office of Naval Research Marine Mammal Office by the Strategic Environmental Research and Development Program, with additional support from the NOAA VENTS Program. The recording illustrated in Fig. 3(a) was made with the assistance of John Calambokidis and Art Teranishi. This manuscript has benefited from reviews by Charles R. Greene, Jr. and three anonymous reviewers. PMEL Contribution #1978.

Bannister, R. W. (**1986**). ''Deep sound channel noise from high-latitude winds,'' J. Acoust. Soc. Am. **79**, 41–48.

Barlow, J. (**1995**). ''The abundance of cetaceans in California waters. Part 1: Ship surveys in summer and fall of 1991,'' Fish. Bull. **93**, 1–14 plus errata.

Buckland, S. T., Anderson, D. R., Burnham, K. P., and Laake, J. L. (**1993**). *Distance Sampling* (Chapman & Hall, London).

Chiu, C., Collins, C. A., Hager, C. A., Miller, C. W., Moore, T. C., Rocheleau, M. R., Lashkari, K., and Hayes, S. (**1997**). ''A feasibility study of monitoring blue whales using the Pt. Sur ocean acoustic observatory,'' J. Acoust. Soc. Am. **102**, 3213.

Clark, C. W., and Charif, R. A. (**1998**). ''Acoustic Monitoring of large whales to the west of Britain and Ireland using bottom-mounted hydrophone arrays,'' October 1996–September 1997, Joint Nature Conservation Committee, Report # 281, Peterborough.

Clark, C. W., and Fristrup, K. M. (**1997**). ''Whales '95: A Combined Visual and Acoustic Survey of Blue and Fin Whales off Southern California,'' pp. 583–600, Rep. Int. Whal. Comm., 47.

Coates, R. F. W. (**1989**). *Underwater Acoustic Systems* (Macmillan, London).

Collins, M. D. (**1993**). ''A split step Padé solution for parabolic equation method,'' J. Acoust. Soc. Am. **93**, 1736–1742.

D'Spain, G. L. (**1994**). ''Relationship of underwater acoustic intensity measurements to beamforming,'' Can. Acoust. **22**, 157–158.

D'Spain, G. L., Kuperman, W. A., Hodgkiss, W. S., and Berger, L. P. (**1995**). ''3-D localization of a blue whale,'' technical memorandum, Marine Physical Laboratory, Scripps Institution of Oceanography, University of California, San Diego.

Edds, P. L. (**1988**). ''Characteristics of finback *Balaenoptera physalus* vocalizations in the St. Lawrence estuary,'' Bioacoustics **1**, 131–149.

Forney, K. A., Barlow, J, and Carretta, J. V. (**1995**). ''The abundance of cetaceans in California waters. Part II: Aerial surveys in winter and spring of 1991 and 1992,'' Fish. Bull. **93**, 15–26.

Fox, C. G., and Stafford, K. M. (**1998**). ''A new technology for long-term acoustic monitoring of the open ocean,'' *48th Rep. Int. Whal. Comm.*, App. 2.

Frazier, L. N., and Pecholcs, P. I (**1990**). ''Single hydrophone localization,'' J. Acoust. Soc. Am. **88**, 995–1002.

Hassab, J. C. (**1976**). ''Passive tracking of a moving source by a single observer in shallow water,'' J. Sound Vib. **44**, 127–145.

Hildebrand, J. A. (**1998**). personal communication.
Howe, B. M., and Mercer, J. A. (**1997**). ''Cabled sources and receivers for ATOC,'' in *International Workshop on Scientific Use of Submarine Cables*, pp. 163–168, Okinawa.
IRIS (**1998**). Global Seismic Network station list, http://www.iris.washington.edu/GSN/GSNstations.
Kibblewhite, A. C., Shooter, J. A., and Watkins, S. L. (**1976**). ''Examination of attenuation at very low frequencies using the deep-water ambient noise field,'' J. Acoust. Soc. Am. **60**, 1040–1047.
Kinoshita, H. (**1997**). ''Cable-Connected Submarine Environment Monitor System,'' in *International Workshop on Scientific Use of Submarine Cables*, pp. 119–125, Okinawa.
Leatherwood, S., Reeves, R. R., Perrin, W. F., and Evans, W. E. (**1988**). *Whales, Dolphins and Porpoises of the Eastern North Pacific and adjacent Arctic Waters, A Guide to their Identification* (Dover, New York).
McCreery, C. S., Duennebeir, F. K., and Sutton, G. H. (**1993**). ''Correlation of deep ocean noise (0.4–30 Hz) with wind, and the Holu Spectrum—A worldwide constant,'' J. Acoust. Soc. Am. **93**, 2639–2648.
McDonald, M. A., Hildebrand, J. A., and Webb, S. C. (**1995**). ''Blue and fin whales observed on a seafloor array in the Northeast Pacific,'' J. Acoust. Soc. Am. **98**, 712–721.
McDonald, M. A., Webb, S. C., Hildebrand, J. A., Clark, D., Reidenberg, J. S., and Laitman, J. T. ''On the physics of sound production in the blue whale,'' in *Hearing in whales and Dolphins*, edited by W. W. L. Au (Springer-Verlag, New York) (in press).
Miyashita, T., Kato, H., and Kasuya, T. (**1995**). *Worldwide Map of Cetacean Distribution, Based on Japanese Sighting Data (Vol. 1)* (National Research Institute of Far Seas Fisheries, Shizuoka, Japan).
Mobley, J. R. J., Smultea, M., Norris, T., and Weller, D. (**1996**). ''Fin whale sighting north of Kaua'i, Hawai'i,'' Pacific Science **50**, 230–233.
Moore, S. E., Stafford, K. M., Dahlheim, M. E., Fox, C. G., Braham, H. W., Polovina, J. J., and Bain, D. E. (**1998**). ''Seasonal variation in reception of fin whale calls at five geographic areas in the North Pacific,'' Marine Mammal Science **14**, 617–627.
Morris, G. B. (**1978**). ''Depth dependence of ambient noise in the northeastern Pacific ocean,'' J. Acoust. Soc. Am. **64**, 581–590.
Norris, T. F. (**1998**). Personal Communication.
Northrup, J. W., Cummings, W. C., and Morrison, M. F. (**1971**). ''Underwater 20-Hz signals recorded near Midway Island,'' J. Acoust. Soc. Am. **49**, 1909–1910.
Patterson, B., and Hamilton, G. R. (**1964**). ''Repetitive 20 cycle per second biological hydroacoustic signals at Bermuda,'' in *Marine Bio-Acoustics*, Vol. One, edited by W. N. Tavolga (Pergamon, Oxford), pp. 125–145.
Payne, R. (**1995**). *Among Whales* (Scribner, New York).
Payne, R., and Webb, D. (**1971**). ''Orientation by means of long range acoustic signaling in baleen whales,'' Ann. (N.Y.) Acad. Sci. **188**, 110–141.
Premus, V., and Spiesberger, J. L. (**1997**). ''Can acoustic multipath explain finback (*B. physalus*) 20-Hz doublets in shallow water?,'' J. Acoust. Soc. Am. **101**, 1127–1138.
Richardson, W. J., Greene, Jr., C. R., Malme, C. I., and Thomson, D. H. (**1995**). *Marine Mammals and Noise* (Academic, San Diego).
Richelson, J. T. (**1998**). ''Scientists in Black,'' Sci. Am. **278**, 48–55.
Shooter, J. A., DeMary, T. E., Wittenborn, A. F. (**1990**). ''Depth dependence of noise resulting from ship traffic and wind,'' IEEE J. Ocean Eng. **15**, 292–298.
Spiesberger, J. L. (**1998**). ''Linking auto- and cross-correlation functions with correlation equations: Application to estimating the relative travel times and amplitudes of multipath,'' J. Acoust. Soc. Am. **104**, 300–312.
Thompson, P. O., Findley, L. T., and Vidal, O. (**1992**). ''20 Hz pulses and other vocalizations of fin whales, Balaenoptera physalus, in the Gulf of California, Mexico,'' J. Acoust. Soc. Am. **92**, 3051–3057.
Thompson, P. O., and Friedl, W. A. (**1982**). ''A long term study of low frequency sounds from several species of whales off Oahu, Hawaii,'' Cetology **45**, 1–19.
Urick, R. J. (**1983**). *Principles of Underwater Sound* (McGraw-Hill, New York).
Watkins, W. A. (**1981**). ''Activities and underwater sounds of fin whales,'' Sci. Rep. Whales Res. Inst. **33**, 83–117.
Watkins, W. A., Tyack, P., Moore, K. E., and Bird, J. E. (**1987**). ''The 20-Hz signals of finback whales (*Balaenoptera physalus*),'' J. Acoust. Soc. Am. **82**, 1901–1912.
Westwood, E. K., and Knobles, D. P. (**1997**). ''Source track localization via multipath correlation matching,'' J. Acoust. Soc. Am. **102**, 2645–2654.

Experimental study of a radial mode thermoacoustic prime mover

Jay A. Lightfoot
Dynetics, Inc., 1000 Explorer Boulevard, Huntsville, Alabama 35759

W. Patrick Arnott
Atmospheric Science Center, Desert Research Institute, P.O. Box 60220, Reno, Nevada 89506

Henry E. Bass and Richard Raspet
National Center for Physical Acoustics and Department of Physics and Astronomy, University of Mississippi, University, Mississippi 38677

(Received 10 June 1998; revised 10 December 1998; accepted 11 December 1998)

The purpose of this research is to branch out from thermoacoustics in the plane wave geometry to study radial wave thermoacoustic engines. The radial wave prime mover is described. Experimental results for the temperature difference at which oscillations begin are compared with theoretical predictions. Predictive models often assume a uniform pore size and temperature continuity between the stack and heat exchangers; however, stacks of nonuniform pore size and temperature discontinuities between the stack and heat exchangers are common imperfections in experimental devices. The radial engine results are explained using a theoretical model which takes into account these prevalent construction flaws. Theory and experiment are shown to be in agreement after the complications are included. Spectral measurements show that an additional feature of the radial geometry is the anharmonicity of the resonant modes which significantly reduces nonlinear harmonic generation. © *1999 Acoustical Society of America.* [S0001-4966(99)05603-9]

PACS numbers: 43.35.Ud, 43.20.Bi [ANN]

INTRODUCTION

The primary goal of this paper is to examine an experimental radial wave thermoacoustic engine, taking into account existing radial wave thermoacoustic theory and the common imperfections of nonuniform pore size and temperature discontinuities between the stack and heat exchangers. Swift briefly mentioned thermoacoustics in the radial mode of a cylindrical resonator,[1] and developed the radial mode thermoacoustic wave equation. Arnott *et al.* derived coupled first-order differential equations for pressure and specific acoustic impedance in a stack with a temperature gradient, and pressure and impedance translation equations for open resonator sections and heat exchangers.[2] Numerical implementation of these equations as described in Ref. 2 allows for the prediction of the onset temperature difference (ΔT_{onset}), the temperature difference across the stack at which acoustic oscillations are observed.

ΔT_{onset} is an important quantity in thermoacoustic engines for several reasons. The total power generated by a prime mover is the power generated by the stack (which is proportional to the temperature difference across the stack, ΔT) minus the thermal and viscous losses in the stack. A prime mover will begin to make sound when the total power generated in the stack overcomes other losses in the heat exchangers and the resonator.[3,4] Therefore, ΔT_{onset} is proportional to the ratio of the acoustic power dissipated in the entire system (including the stack, heat exchangers, and any external load) to the acoustic power generated by the stack. Second, from an experimental vantage point, ΔT_{onset} measurements are relatively easy to make, so that predictions and measurements can be compared to determine the accuracy of the numerical model.

An outgrowth of this research was the need to elucidate experimental deviations from the theoretical ideal—a distribution of pore sizes within the stack rather than a uniform pore size and temperature discontinuities between the stack and the heat exchangers. Elementary methods of accounting for these complications are presented which bring experiment and theory into agreement.

I. RADIAL WAVE THERMOACOUSTIC PRIME MOVER DESIGN

A schematic of the resonator portion of the radial thermoacoustic prime mover is shown in Fig. 1. The outer ring (A) is constructed of steel with inner and outer diameters of 148.6 cm and 156.2 cm. The top and bottom lids (B) have an outer diameter of 158.75 cm and a thickness of 2.54 cm. The center hole in B, for access to the thermoacoustic elements, has a diameter of 35.6 cm. All seals were made with o-rings. The caps (C) are constructed of stainless steel and have a groove cut at the location of the stack, leaving a $\frac{1}{4}$-in. plate over this region, to reduce thermal conduction of heat in the radial direction across the stack region of the resonator. When the caps (C) are placed into the holes in B, the inner faces of the caps are flush with the inner faces of the lids. The height of B, and thus the inner height of the resonator, is 10.2 cm. The assembled resonator has a mass of about 1360 kg. It should be noted that measures can be taken to significantly reduce the mass of the resonator.

The heat exchangers[5] are constructed of four standard $\frac{1}{4}$-in. copper tubes bent into circles, with copper plates (each

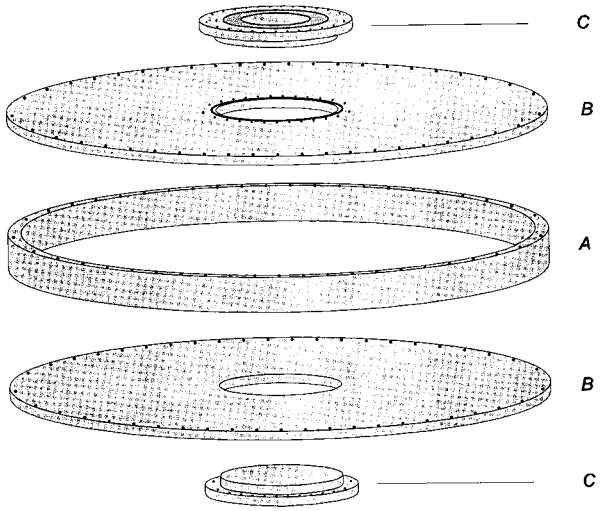

FIG. 1. Unassembled view of the resonator used for the large radial wave thermoacoustic prime mover. Pieces C are stainless steel caps which allow access to the inner thermoacoustic elements. Pieces A and B are plain carbon steel.

having four $\frac{1}{4}$-in. pre-punched holes to fit snugly over the tubing) fed onto the copper tubes. Steel washers were placed between the copper plates to maintain the correct spacing. The individual copper plates are 10 cm tall, 1.3 cm wide (radial dimension), and 0.76 mm thick. The washer spacers are also 0.76 mm thick, and the porosity or ratio of open area to total area of the heat exchangers is 0.32, where blockage by heat exchanger tubing and washer spacers has been taken into account. The inner (hot) heat exchanger was heated by dissipation of electrical current in 80% Nickel, 20% chromium wire inserted into the copper tubing and electrically insulated from the tubing with temperature resistant ceramic beads. The outer (cold) heat exchanger was cooled using tap water. The hot heat exchanger has an outer diameter of 23.8 cm and an inner diameter of 21.2 cm when fitted to the stack, while the cold heat exchanger has an outer diameter of 28.8 cm and an inner diameter of 26.3 cm when fitted to the stack.

The silicon bonded mica paper stack, with inner and outer diameters of 23.8 cm and 26.3 cm, was sandwiched between the two heat exchangers. The thickness of the individual stack pieces is 0.015 cm. Mica was chosen because of its high temperature tolerance (up to 773 K) and its low thermal conductivity of 0.163 W/(m*K). The stack was formed by placing 183 of these pieces on top of each other with 8 smaller mica washers between each of the larger mica pieces to maintain the proper spacing. The spacer washers were 0.64 cm in diameter and 0.038 cm thick. The overall stack height was 10.2 cm. In an attempt to further maintain proper spacing in the stack, 0.015 cm diameter temperature resistant teflon thread was used between each pair of mica washer spacers to provide a total of 16 support locations equally spaced about the circumference of the stack.

A line drawing of the entire system is shown in Fig. 2. The Endevco 8510B microphone used for detection of the acoustic wave was located at a pressure antinode next to the outer wall of the resonator. It would be preferable to have the microphone at the center of the resonator, since the highest sound pressure levels (SPL) occur there, but high temperatures precluded such a placement of the microphone. All other inlets to the resonator (i.e., plumbing, heating, gas valve, and thermocouples) are located at the pressure node in order to reduce losses due to any leaks at these junctures.

II. MEASUREMENTS AND ASSOCIATED ERRORS

All temperature measurements were taken with type K thermocouples having a precision of ± 1 K. Test measurements with multiple thermocouples of the heat exchanger temperature varied by a maximum of 2 K, therefore temperature measurements were taken using a single thermocouple for each heat exchanger. The thermocouples were placed between plates of the heat exchangers and coupled to the heat exchangers using high temperature–high thermal conductivity paste. At ΔT_{onset} the sound in the tube, initiated by a small tap on the resonator, increased instead of decaying. The error associated with the measurement of ΔT_{onset} is estimated to be ± 2 K (the difference between the earliest ΔT_{onset} after tapping and the ΔT_{onset} obtained without tapping), so that the total error in temperature measurements is ± 5 K.

SPL was measured with an Endevco 8510B piezoresistive microphone which was calibrated using a pistonphone. The microphone output was routed to a dynamic signal analyzer for viewing the SPL as a function of frequency. The error associated with SPL measurements was less than 0.2 dB, and the frequency step size was 0.25 Hz.

III. EXPERIMENTAL RESULTS AND COMPARISON TO THEORY

Several questions required measurements with the radial wave prime mover. The first had to do with theoretical predictions; can we predict the behavior of radial wave prime movers using radial wave thermoacoustic theory? The second was whether the radial modes reduce harmonic generation. Originally we were interested in the effect of sloped stacks in radial wave thermoacoustic engines, but theory has shown that the effect in radial prime movers with a natural slope between plates is minimal.[6]

A. Initial comparison of experimental and theoretical onset temperatures

Measurements of ΔT_{onset} have been made on the above described radial wave prime mover. Thermocouples were placed in the heat exchangers (attempts to measure the temperature at the face of the stack gave ambiguous results due to the short radial length of the stack and an inability to precisely position the thermocouple). Figures 3 and 4 show the lowest experimental ΔT_{onset} results (solid circles) achieved as a function of ambient pressure, for air and argon, respectively. The ambient temperature in both cases was 293 K. Also shown are the theoretical predictions for the hot side temperature (dashed line) *assuming that the stack faces maintain the same temperature as theheat exchangers*. For the present discussion, the dotted lines in Figs. 3 and 4 should be ignored. It is obvious that theory and experiment

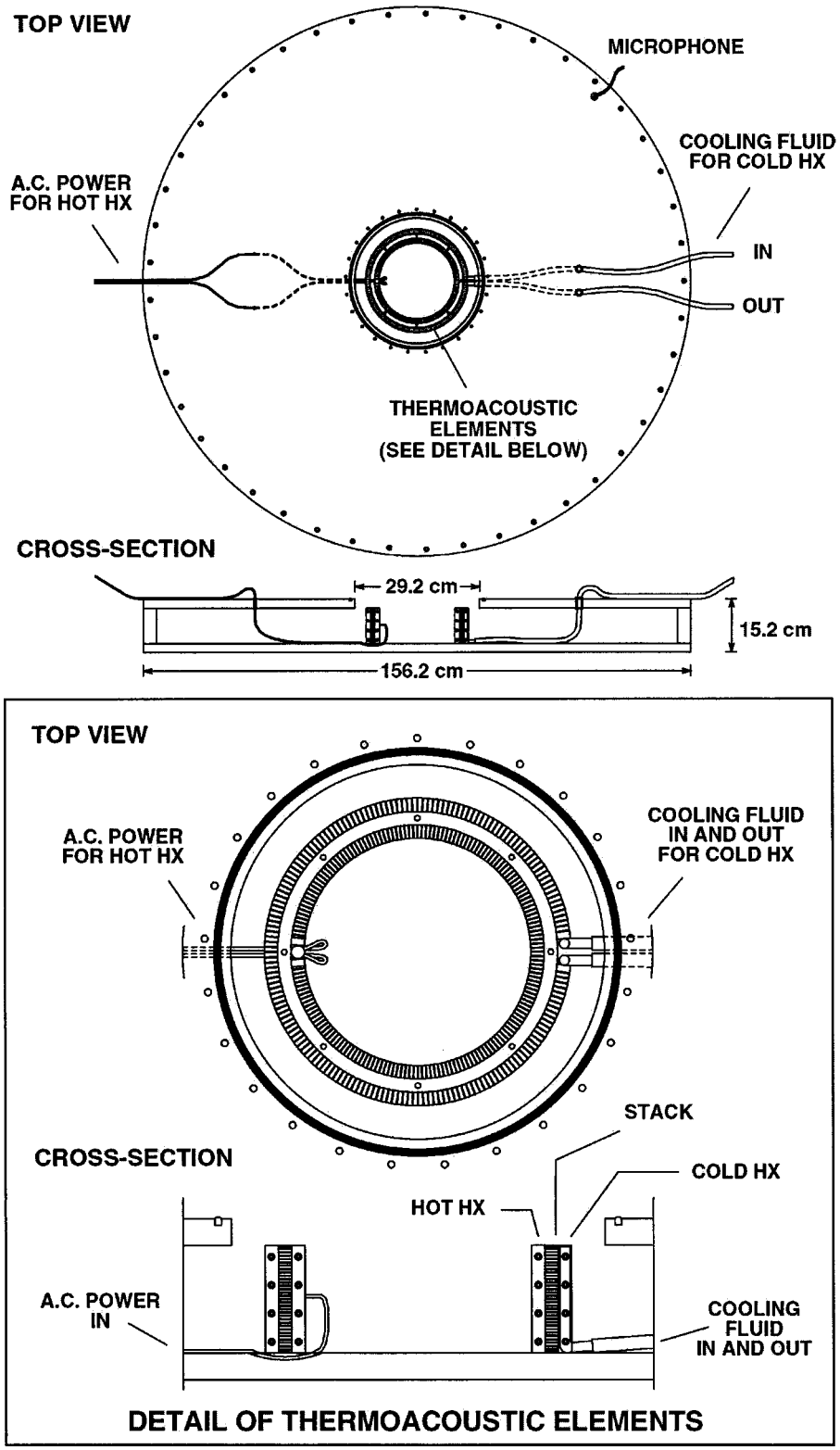

FIG. 2. Line drawing of the radial wave thermoacoustic prime mover.

are not at all in agreement, with the experimental onset temperatures being significantly higher than predicted for both gases.

There are several complicating features of our radial engine. First, for computations the stack was assumed to have a fixed pore size or plate spacing, but measurements show that a distribution of pore sizes exists. Second, ΔT_{onset} is sensitive to the ''fit'' of the heat exchangers around the stack, a fact which is enhanced by the short radial length of the stack as will be shown later. The heat exchanger ''fit'' is not as difficult in the plane wave case, since the manufacture of a flat heat exchanger surface is easily achieved so that the stack surfaces can be flush against heat exchangers with no alteration of the stack pore shape, so that direct thermal contact is sustained between the stack and the heat exchanger. Such a fit is more difficult in the radial case since the heat exchanger surfaces must maintain perfect curvature to provide the best possible thermal contact between stack and heat

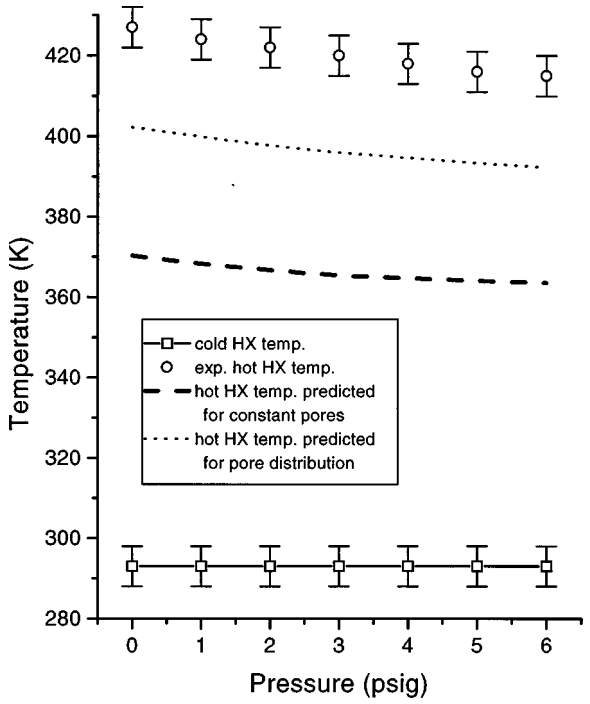

FIG. 3. Onset temperatures for the radial wave prime mover with air as the working fluid, assuming no temperature discontinuity between the stack and heat exchangers. Solid line shows cold heat exchanger temperature; dashed line is the predicted hot heat exchanger temperature for a stack with a single pore size; dotted line is the predicted hot heat exchanger temperature for the stack with the pore distribution shown in Fig. 5; and circles show experimental results.

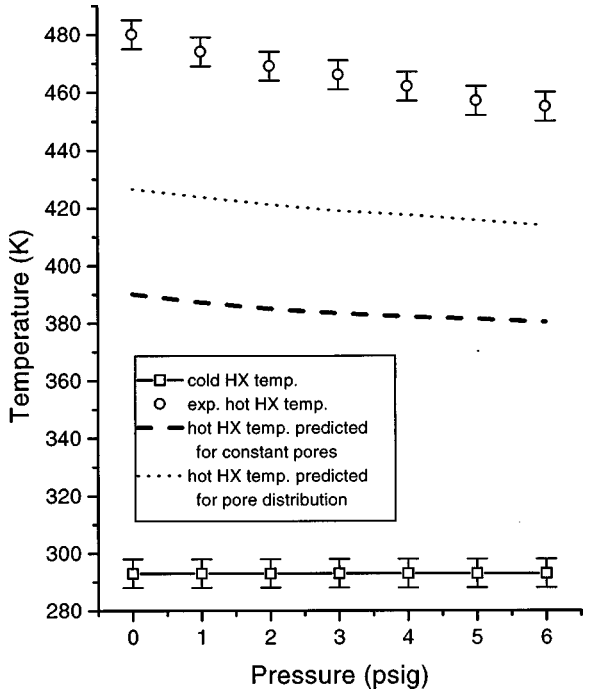

FIG. 4. Onset temperatures for the radial wave prime mover with argon as the working fluid, assuming no temperature discontinuity between the stack and heat exchangers. Solid line shows cold heat exchanger temperature; dashed line is the predicted hot heat exchanger temperature for a stack with a single pore size; dotted line is the predicted hot heat exchanger temperature for the stack with the pore distribution shown in Fig. 5; and circles show experimental results.

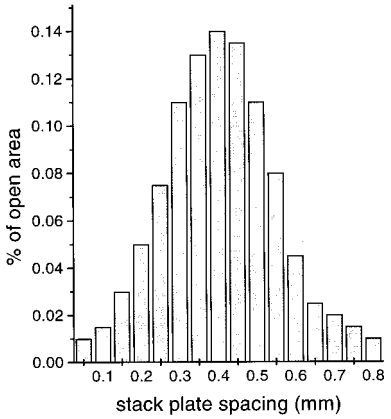

FIG. 5. Area distribution of plate spacing in the radial prime mover stack.

exchanger. Attempts to force the heat exchangers against the stack, thus creating the necessary curvature in the heat exchangers, tend to distort the stack plate spacing. Since the heat exchanger is much more rugged than the stack, a point is reached where the stack conforms to the heat exchanger shape via warping of the stack plates rather than the heat exchanger conforming to the stack shape. For identical gas compositions and pressures, results for ΔT_{onset} varied depending upon the proximity of the heat exchangers to the stack and the stack distortion.

B. Nonuniform stack plate spacing

As mentioned previously, attempts were made to maintain a constant plate spacing throughout the stack by using mica washer spacers and later by adding teflon thread to maintain the correct spacing. In hindsight, it would have been much better to use thicker (and thus more rigid) mica plates in the stack at the expense of reducing the stack porosity (this would also have prevented additional distortion of the stack spacing due to pressure from the heat exchangers). In order to characterize the present stack, measurements of the plate spacing were taken over the entire height of the stack, assuring that the average spacing is equal to the originally expected constant spacing. Radial variations in plate spacing were negligible. Over 500 measurements were made to ensure an accurate representation of the axial/azimuthal pore size distribution. The measurements were by necessity taken without the heat exchangers in place, such that no plate warping was introduced by pressure from the heat exchangers. Ideally, measurements would have been repeated with the heat exchangers in place. However, since ΔT_{onset} measurements in the following sections were taken for cases in which the heat exchangers were pressed as tightly as possible against the stack *without* distorting it, pore measurements of the stack alone should be sufficient. Figure 5 shows the measured distribution in terms of the percent of the total open area in the stack occupied by each gap size.

Prediction of ΔT_{onset} for a stack with a distribution of pore sizes is accomplished by treating the various pore sizes as having parallel impedances. The electrical analog would be parallel resistors. Beginning with a known impedance and pressure amplitude at the hot, rigid end of the resonator, the

pressure and impedance at the hot face of the stack may be determined using translation theorems, Eqs. (5) and (6) of Ref. 2. The boundary conditions at the hot face of the stack are continuity of pressure and volume velocity, so

$$P_{1j}=P_H, \tag{1}$$

and

$$\sum_j A_j V_{1j}=A_H V_H, \tag{2}$$

where j represents quantities for a particular pore size, subscript 1 denotes that the quantity is evaluated at the hot end of the stack, P_{1j} is the complex acoustic pressure at the hot side of an individual pore, P_H is the pressure at the hot face of the stack determined by translation, A_j is the stack cross-section occupied by a particular pore size, A_H is the resonator cross-sectional area at the hot face of the stack, $V_{1\mathrm{j}}$ is the bulk particle velocity averaged over the cross-section of the stack having a given plate spacing at the hot side, and V_{H} is the velocity at the hot face of the stack determined by translation.

To obtain a full numerical solution to the problem, it would be necessary to guess the complex pressure P_C and the various pore velocities at the cold side of the stack, integrate backward to the hot side of the stack checking to see if the conditions in Eqs. (1) and (2) had been met, and repeat the process with new guesses until the solution converged. This would require scanning an extremely large parameter space. Therefore, the method of Raspet *et al.* for approximating thermoacoustic calculations using a single step[7] has been utilized to reduce computation times. The single step method was shown to be accurate for $|kL|\leqslant 0.3$, where L is the stack length and k is the wave number. The radial prime mover certainly meets this criterion since $|kL|\approx 0.065$.

Assumptions are that the acoustic pressure is constant across the pore cross section and is a function only of the radial distance along the pore, and that the transverse velocity is small relative to the radial velocity. The relevant equations describing the fluid motion in the pore are taken from Eqs. (7) and (8) of Ref. 2 [with porosity accounted for such that $v_r(r)=V_j/\Omega_j$, where Ω_j is the porosity for a given pore size and $V_j=P_j/Z_j$] and are given by

$$V_j=\frac{\Omega_j F_j(\lambda_j)}{i\omega\rho_0}\frac{dP_j}{dr} \tag{3}$$

and

$$\frac{dV_j}{dr}+\frac{1}{T}\frac{dT}{dr}\left[\frac{F_j(\lambda_{Tj})/F_j(\lambda_j)1}{1-N_{\mathrm{Pr}}}\right]V_j+\frac{V_j}{r}+\frac{\Omega_j F_j(\lambda_j)}{i\omega\rho_0}k_j^2 P_j=0, \tag{4}$$

where $k_j{}^2$ is given by Eq. (4) of Ref. 2. The finite difference forms of these equations are given by

$$iC_j\frac{V_{1j}+V_{2j}}{2}=\frac{P_{1j}-P_{2j}}{L} \tag{5}$$

and

$$iC_j\frac{V_{1j}-V_{2j}}{L}+iC_jD_j\frac{V_{1j}+V_{2j}}{2}+k_j^2\frac{P_{1j}+P_{2j}}{2}=0, \tag{6}$$

where

$$C_j=\frac{\omega\rho_0}{\Omega_j F_j(\lambda_j)}, \tag{7}$$

and

$$D_j=\frac{1}{T}\frac{dT}{dr}\left[\frac{F(\lambda_{Tj})/F(\lambda_j)-1}{1N_{\mathrm{Pr}}}\right]+\frac{1}{r}. \tag{8}$$

The subscript 2 refers to pore quantities at the cold side of the stack, subscript 1 to pore quantities at the hot side of the stack, subscript j to pores of a particular size, and all parameters are evaluated at the center of the stack. Note that the volume coefficient of expansion, β, in Eq. (8) has been replaced by the ideal gas result, $1/T$.[8] Equations (5) and (6) may be combined to eliminate V_{2j} so we are left with V_{1j} in terms of P_{1j} and P_{2j}

$$V_{1j}=\frac{1}{iC_jL}\left\{P_{1j}\left[1-\frac{D_jL}{2}-\frac{k_j^2L^2}{4}\right]-P_{2j}\left[1-\frac{D_jL}{2}+\frac{k_j^2L^2}{4}\right]\right\}. \tag{9}$$

Now we need only to guess the magnitude and phase of P_{2j}, and use the known pressure P_{1j} to determine V_{1j}. These values of V_{1j} are then tested to see if the condition in Eq. (2) holds. If the requirement is not met, P_{2j} is adjusted and the process is repeated. When the requirement is met, Eq. (5) is rearranged to give V_{2j} using the now known values for V_{1j}, P_{1j}, and P_{2j}. The pressure and velocity at the cold side of the stack are then determined by requiring conservation of pressure and volume velocity

$$P_C=P_{2j} \tag{10}$$

and

$$A_CV_C=\sum_j A_jV_{2j}, \tag{11}$$

where P_C is the pressure in the tube at the cold face of the stack, A_C is the resonator cross-section at the cold face of the stack, and V_C is the area averaged particle velocity in the tube at the cold face of the stack.

Using the method outlined above, $\Delta T_{\mathrm{onset}}$ was determined for a stack having a distribution of pore sizes. The dotted lines in Figs. 3 and 4 show corrections, using the measured pore distribution of Fig. 5, to the constant pore size results represented by dashed lines for the hot side temperature at onset in air and argon, respectively. Physically, the reason for the increased $\Delta T_{\mathrm{onset}}$ as a result of the pore distribution is due to the fact that only the pore spacings in the middle of the distribution have the correct ratio of penetration depth to pore size, while the pores with other sizes are not acting as efficiently. It is obvious that the pore distribution in the stack explains a significant portion of the discrepancy between experiment and theory, but further interpretation is required to account for the remaining disparity.

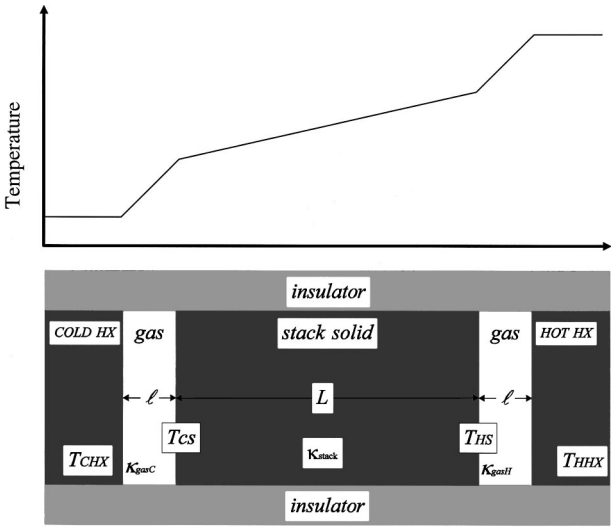

FIG. 6. Illustration of the gaps present between the radial stack and heat exchangers. The upper plot shows a representative temperature distribution over the heat exchanger–gap–stack–gap–heat exchanger system. Temperature is constant in the heat exchangers, while the gradient is larger in the gaps than in the stack.

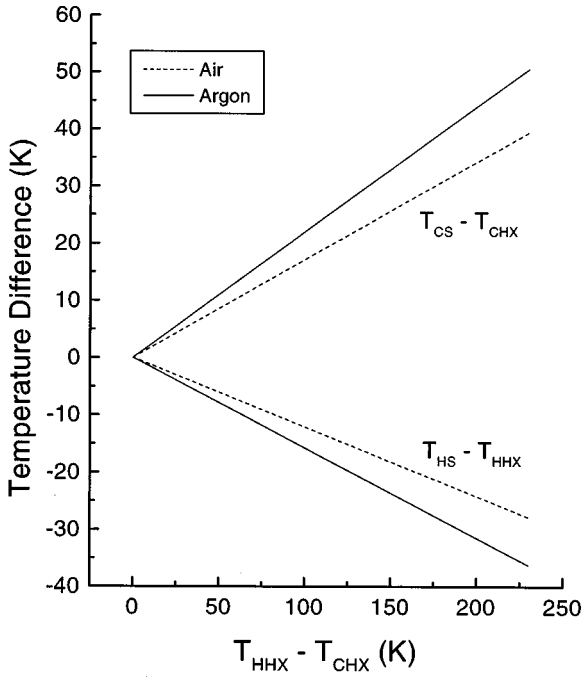

FIG. 7. Demonstration of the temperature discontinuity between the stack and heat exchanger face for $\ell/L=0.036$. The various temperature locations are shown pictorially in Fig. 6.

C. Temperature discontinuities between the heat exchanger and the stack face

As the stack in a thermoacoustic prime mover becomes very short, the temperature gradient necessary for onset of oscillations increases, which in turn raises the amount of heat flowing via thermal conduction from the hot side to the cold side of the stack. In addition, any small gap between the stack and the heat exchanger becomes a more appreciable percentage of the stack length, so that heat which is conducted across the gap may no longer be ignored by assuming that the stack face and the heat exchanger maintain the same temperature. Rather, it becomes necessary to account for conduction through the fluid across gaps between the stack and heat exchanger as well as for normal thermal conduction through the stack, when determining the temperatures at the faces of the stack which ultimately cause onset.

A simple model may be used to explain the remaining difference between experiment and theory, and why the difference is much more noticeable for the radial engine than for a plane wave device. Consider the heat exchanger–stack–heat exchanger pictured in Fig. 6. Perfect insulators have been placed on top and bottom to confine heat flows to the horizontal direction. The hot and cold heat exchangers are held at temperatures T_{HHX} and T_{CHX}. Rather than assuming that the stack face and the heat exchanger are in physical contact and at the same temperature, they are separated by a small gap of length ℓ filled with gas. The stack length is denoted by L. Assumptions are: heat is transported only by conduction, κ_C (the thermal conductivity of the gas in the gap near the cold heat exchanger) is evaluated at a temperature of T_{CHX}, κ_H (the thermal conductivity of the gas in the gap near the hot heat exchanger) is evaluated at a temperature of T_{HHX}, κ_S (the thermal conductivity of the solid stack material) is assumed to be constant and is evaluated at a temperature of $\frac{1}{2}(T_{\mathrm{HHX}}+T_{\mathrm{CHX}})$. Our goal is to find the hot and cold side stack temperatures, T_{HS} and T_{CS}, in terms of the known quantities ℓ, L, T_{CHX}, T_{HHX}, κ_C, κ_H, and κ_S. Assuming linear temperature gradients within the three regions and requiring heat flow to be continuous at all boundaries, application of the 1D steady state heat equation yields

$$T_{HS}=\frac{\kappa_H T_{\mathrm{HHX}}+\kappa_C T_{\mathrm{CHX}}\kappa_C T_{\mathrm{CS}}}{\kappa_H} \tag{12}$$

and

$$T_{\mathrm{CS}}=\frac{[\kappa_C\kappa_H+\kappa_C\kappa_S(\ell/L)]T_{\mathrm{CHX}}+\kappa_H\kappa_S T_{\mathrm{HHX}}(\ell/L)}{\kappa_H\kappa_C+\kappa_H\kappa_S(\ell/L)+\kappa_C\kappa_S(\ell/L)}. \tag{13}$$

Examining Eqs. (12) and (13), it is evident that as $\ell/L\rightarrow 0$, $T_{\mathrm{HS}}\rightarrow T_{\mathrm{HHX}}$ and $T_{\mathrm{CS}}\rightarrow T_{\mathrm{CHX}}$ as expected. In the case of the radial wave prime mover, $L=1.25$ cm and a good average estimate for ℓ (determined by physical measurement of the gaps between the heat exchangers and the stack) is $\ell=0.45$ mm, producing a ratio of $\ell/L=0.036$. For the typical 5.08 cm plane wave stack of Ref. 9, a conservative estimate would be $\ell=0.025$ mm so that $\ell/L=0.002$.

Figures 7 and 8 show deviations of the stack face temperatures from the heat exchanger temperatures over a range of heat exchanger temperature differences for the above values of ℓ/L for air and argon. From these figures we see that the radial prime mover does a poor job of establishing the expected temperature difference across the stack due to the short radial length of the stack and the presence of non-negligible gaps between the stack and heat exchanger. For a 150 K difference across the heat exchangers, the actual difference across the stack is only 106 K for air and 94 K for argon, while a conservative estimate for the 5.08 cm stack of Ref. 9 gives differences of 147 K for air and 144 K for

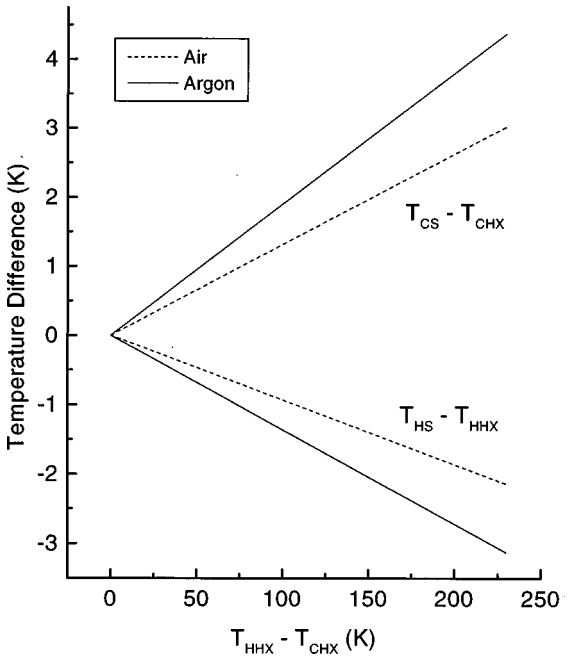

FIG. 8. Demonstration of the temperature discontinuity between the stack and heat exchanger face for $\ell/L=0.002$. The various temperature locations are shown pictorially in Fig. 6.

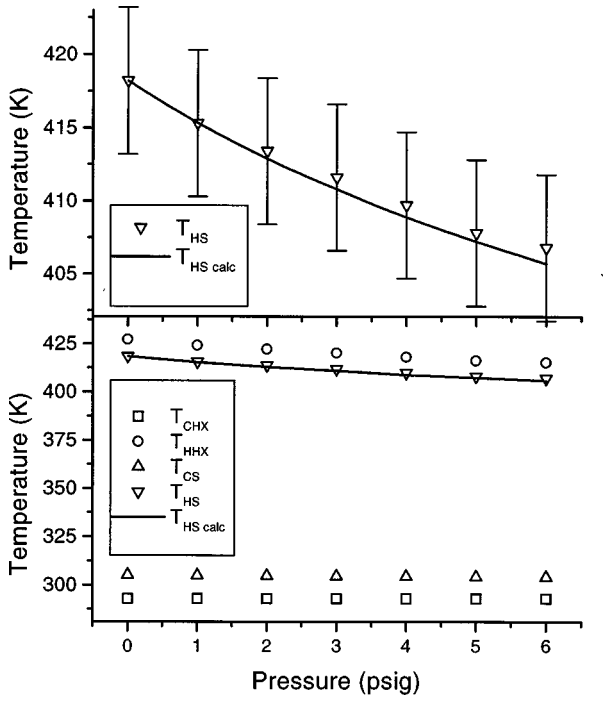

FIG. 9. Air results for $\ell_{eff}=0.2$ mm. The upper plot is a blown up version of T_{HS} and $T_{HS\ calc}$ in the lower plot, where $T_{HS\ calc}$ is the numerically predicted onset temperature using T_{CS} as the temperature at the cold side of the stack. Measured temperatures are represented by circles and squares, while triangles represent calculations. Errors in the lower plot are smaller than the data points.

argon. These results indicate that assuming the heat exchanger temperature was equivalent to the stack face temperature was not appropriate.

Previously, it was mentioned that experimental measurements of ΔT varied depending upon the ''fit'' of the heat exchangers to the stack. Measurements of the gap between the heat exchangers and the stack range from 0 to 0.6 mm when the heat exchangers are tightened and pressed against the stack. The upper end of this range can be reduced to about 0.4 mm by lightly hammering the heat exchanger against the stack. Measurements have been made for a forced (hammered) and an unforced (only tightened and pressed) fit of the heat exchangers against the stack. In both cases, ℓ should be close to the average measured gap value, although a slight variance due to azimuthal heat flows in the fluid and the stack may do a better job of modeling the experimental results. Therefore, an effective gap length, ℓ_{eff}, is defined to simulate the effect that the entire gap distribution has on ΔT_{onset}.

In order to compare experiment with theory using the measured distribution of pore sizes and accounting for a gap between the stack and heat exchangers, T_{CS} and T_{HS} are calculated using the measured values for T_{CHX} and T_{HHX} for a guessed ℓ_{eff} in air, the initial guess being the average measured gap size. T_{CS} is then used as the cold side stack temperature in the ΔT_{onset} calculation to determine the predicted hot side temperature required for onset, denoted by $T_{HS\ calc}$. This predicted value is compared with T_{HS}. ℓ_{eff} is then adjusted and the process repeated until $T_{HS\ calc}$ and T_{HS} best match up over a range of pressures. Admittedly, this process is backward, since ℓ_{eff} is adjusted to give the best possible results for a given gas (air). However, if the theory is correct, then the resulting ℓ_{eff} for one gas should be applicable to other gases as well. Therefore, the ℓ_{eff} determined for air is used to determine T_{CS} and T_{HS} for the prime mover filled with argon, and the resulting T_{HS} is compared with $T_{HS\ calc}$ for argon.

Figures 9 and 10 show T_{CHX}, T_{CS}, T_{HS}, T_{HHX}, and $T_{HS\ calc}$ for air and argon, respectively. Note that measured temperatures are represented by the squares and circles, while triangles represent calculated values. The experimental results are the same as those shown in Figs. 3 and 4, and again represent the configuration giving the lowest ΔT_{onset}. Keep in mind that T_{CHX} and T_{HHX} are experimental results, however, the comparison will be between the calculated-from-experiment T_{HS} and the predicted hot side stack temperature $T_{HS\ calc}$. In the upper plot of Fig. 9, we see that a chosen value of $\ell_{eff}=0.2$ mm produces nice agreement for air. Applying this value of ℓ_{eff} to the argon data, we see in the upper plot of Fig. 10 that T_{HS} and $T_{HS\ calc}$ are within 5 K of each other over the pressure range tested, and appear to be following the same general trend. It should be mentioned at this point that it would have been nice to extend the pressure range over which measurements were made, however, due to the large flat surface area of the resonator, increasing the pressure beyond 6 psig would have placed an exorbitant amount of force upon the bolts holding the resonator together, and could have caused the steel plates to bow outward.

Measurements were also made which gave higher onset temperatures due to a looser fitting of the heat exchangers. Figures 11 and 12 show the results for air and argon, respectively. $\ell_{eff}=0.41$ mm provides good agreement between T_{HS} and $T_{HS\ calc}$ in air. Applying this ℓ_{eff} to the argon data also

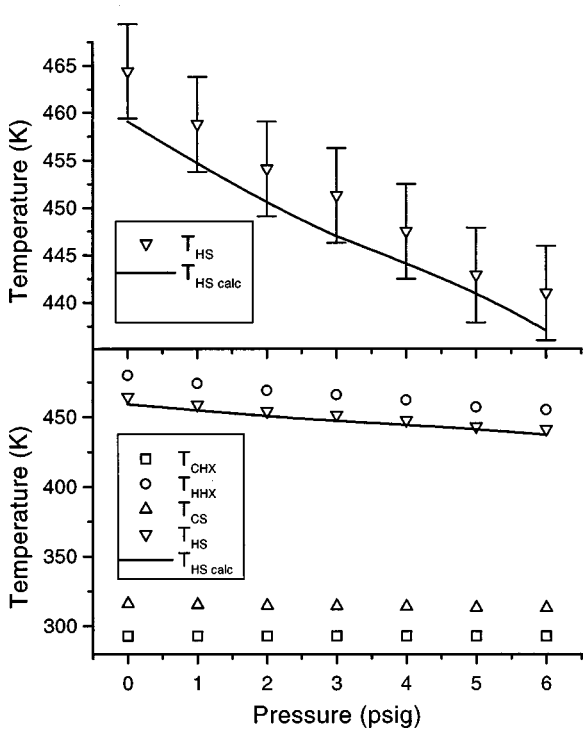

FIG. 10. Argon results for ℓ_{eff}=0.2 mm. The upper plot is a blown up version of T_{HS} and $T_{HS\ calc}$ in the lower plot, where $T_{HS\ calc}$ is the numerically predicted onset temperature using T_{CS} as the temperature at the cold side of the stack. Measured temperatures are represented by circles and squares, while triangles represent calculations. Errors in the lower plot are smaller than the data points.

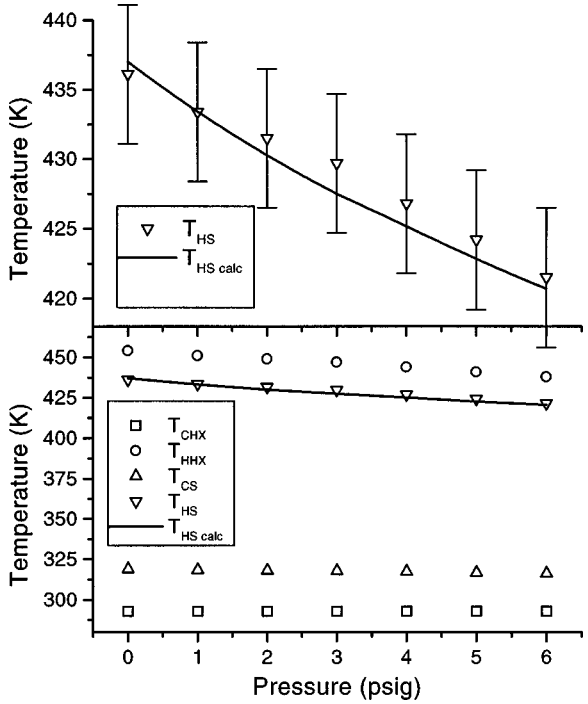

FIG. 11. Air results for ℓ_{eff}=0.41 mm. The upper plot is a blown up version of T_{HS} and $T_{HS\ calc}$ in the lower plot, where $T_{HS\ calc}$ is the numerically predicted onset temperature using T_{CS} as the temperature at the cold side of the stack. Measured temperatures are represented by circles and squares, while triangles represent calculations. Errors in the lower plot are smaller than the data points.

gives good results, such that T_{HS} and $T_{HS\ calc}$ are within 8 K of each other, and again the general trend of the curves are the same. The agreement is not as good as in the previous case, due to a larger distribution of gaps between the stack and heat exchangers. In particular, we have assumed that ℓ_{eff} is the same at the hot and cold sides of the stack. For a looser fit of the heat exchangers on the stack, this assumption becomes less valid than in the case where the heat exchangers were fit as tightly as possible *without disfiguring the stack.*

D. Radial prime mover harmonic generation

In most cases, the linear acoustic wave equation suffices to describe the behavior of a system. However, when the acoustic pressure amplitude becomes large, higher order terms must be taken into account. Coppens and Sanders accounted for nonlinear effects for finite-amplitude standing waves in a resonance tube by modifying the linear equations of state and continuity to allow for second-order effects.[10] Chen included an additional second-order term in the momentum equation for the same problem and found the correction to be small,[11] as would be expected since good agreement was shown between theory and experiment using the Coppens and Sanders approximation.

The general behavior of a prime mover was effectively described by Atchley *et al.*[12]

> ''Once onset of self oscillation is reached, the acoustic amplitude in the tube immediately assumes a large value, typically about 1% of the ambient pressure. The observed waveform is noticeably nonsinu-

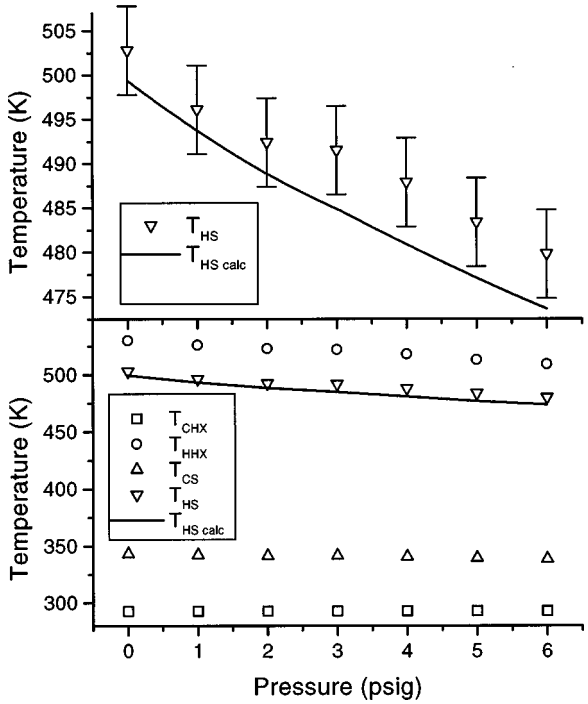

FIG. 12. Argon results for ℓ_{eff}=0.41 mm. The upper plot is a blown up version of T_{HS} and $T_{HS\ calc}$ in the lower plot, where $T_{HS\ calc}$ is the numerically predicted onset temperature using T_{CS} as the temperature at the cold side of the stack. Measured temperatures are represented by circles and squares, while triangles represent calculations. Errors in the lower plot are smaller than the data points.

soidal. As more energy is supplied to the hot end of the stack, the temperature of that end increases only slightly while the acoustic amplitude in the tube increases rapidly... Unfortunately, as the acoustic amplitude increases, an increasing fraction of the acoustic energy appears as higher harmonics–harmonic distortion increases.''

The authors presented results for a constant cross-section plane wave prime mover immediately after onset and also when the hot end temperature was raised 43 K beyond the necessary temperature for onset. In both cases, nonlinear generation of higher harmonics was demonstrated. The experimental results for the relative amplitudes of the harmonics to the fundamental in the prime mover just beyond onset provided nice agreement with the theory of Ref. 10.

It is desirable in a prime mover to minimize the generation of higher harmonics so that more acoustic energy is channeled into the fundamental. In a plane wave resonator, one of the ways to accomplish this is to vary the cross-section of the tube.[13] This detuning causes the natural modes of the resonator to be anharmonic. Gaitan and Atchley,[14] following the method outlined by Coppens and Sanders[15] in a later paper, investigated higher harmonic generation in tubes with harmonic and anharmonic natural modes for application to thermoacoustic engines. The anharmonic tubes were made by varying the cross-section in the center of the tube to a size different than at the ends. Experimental results for the amplitudes of the harmonics for a given amplitude of the fundamental were in excellent agreement with theory for both tube types. In the case of the harmonic tube, the amplitude of the first harmonic was only 10–20 dB below the fundamental, depending upon the acoustic pressure amplitude of the fundamental. However, in two separate anharmonic tubes (one with a larger center cross-section than at the ends and one with a smaller center cross-section) the amplitude of the first harmonic was reduced 30–40 dB below the fundamental.

The generic nonlinear wave equation presented in Ref. 1 is

$$\sum_n \left(c_n^2 \nabla^2 - \frac{\partial^2}{\partial t^2} + \frac{n\omega}{Q_n} \frac{\partial}{\partial t} \right) \frac{p_n}{\rho_0 c^2} \doteq -\frac{\partial^2}{\partial t^2} \left[\left(\frac{u}{c} \right)^2 + \frac{\gamma - 1}{2} \left(\frac{p}{\rho_0 c^2} \right)^2 \right], \tag{14}$$

where c_n and Q_n are the sound speed and quality factor of the nth resonance of the tube, ω is the angular driving frequency (the fundamental resonance for a prime mover), p_n is the acoustic pressure of the nth harmonic of the driving frequency, u and p are the total acoustic velocity and pressure and are functions of radial location r in radial systems (or longitudinal position z in plane systems) and time t. Equation (18) is valid near resonance and assumes the total standing wave to be of the form

$$p = \sum_{n=1}^{\infty} p_n = \sum \rho_0 c^2 M R_n \cos(nkz) \sin(n\omega t + \phi_n), \tag{15}$$

where M is the peak Mach number of the fundamental, R_n is the nondimensional amplitude of the nth harmonic, k is the wave number of the driving frequency, and ϕ_n is the temporal phase of the nth harmonic. For a radial system, Eq. (15) would have J_0 in place of cosine. The harmonic amplitudes, R_n, are shown in Refs. 14 and 15 to be directly proportional to

$$R_n \propto Q_n \cos\left(\tan^{-1}\left(2Q_n \frac{n\omega\omega_n}{\omega_n} \right) \right), \tag{16}$$

where ω_n denotes normal modes of the resonator, so that the harmonic amplitudes are maximized when the normal modes correspond exactly to the harmonics of the fundamental frequency. Therefore, a detuned resonator leads to a reduction in the amplitudes of the harmonics.

With the existing radial wave prime mover, we are limited to examination of the behavior of the system just above onset. The reason for this is that when attempts are made to increase the temperature beyond onset, the following cycle ensues. When the necessary temperature difference is reached, sound is produced. The system responds with an increased acoustic pressure amplitude and thus increased acoustic heat transport from the hot side to the cold side of the stack. The cold heat exchanger, unable to sustain its temperature with the increased heat load, begins to heat up such that the temperature difference across the stack falls below the necessary difference for oscillations to be maintained. When the acoustic wave ceases, the acoustic heat transport also ceases, and the cold heat exchanger returns to its original cooler temperature. Once again the temperature difference reaches the critical onset value, the acoustic wave is regenerated, and the cycle is repeated. A similar effect was observed by Olson and Swift in a plane wave prime mover.[16] Although it would be nice to get a comparison of plane and radial prime movers at lower and higher acoustic pressure amplitudes, the results for temperatures just above onset should give some insight into the reduction of higher harmonic generation which occurs in radial systems as compared to constant cross-section plane systems.

Figure 13 shows a spectrum from the previously described radial wave prime mover. The hot heat exchanger temperature is 427 K and the ambient heat exchanger temperature is 293 K, giving a temperature difference of 134 K. The fundamental frequency of oscillation is 288 Hz in air at atmospheric pressure. The sound pressure level (SPL) at the microphone is 153 dB. The SPL at the center of the resonator is estimated to be 161 dB. The first radial wave harmonic occurs at 526 Hz, but there is no noticeable signal at this frequency. The first nonlinear harmonic occurs at twice the fundamental, or 584 Hz. There is a significant harmonic generation at this frequency, with an SPL of 115 dB. However, this is 38 dB below the fundamental. These results are very similar to those of Ref. 14 for a detuned plane wave resonator driven by a piston. In both cases, the first harmonic is nearly 40 dB below that of the fundamental, and there is no noticeable sound production at the other normal modes of the tubes. In the radial prime mover, the second and third nonlinear harmonics occur at three and four times the fundamen-

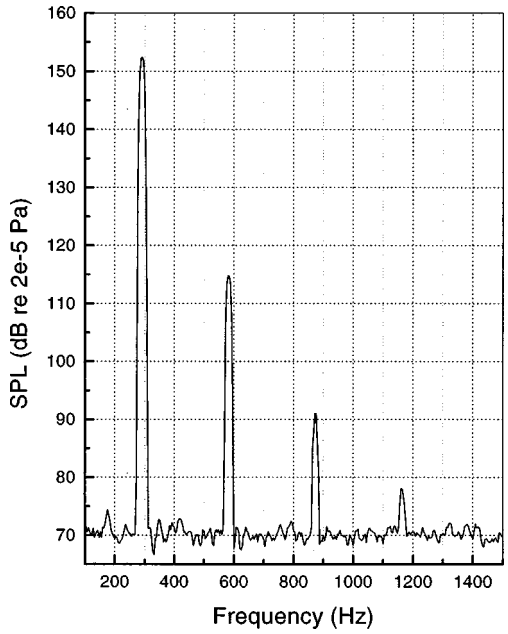

FIG. 13. Acoustic spectrum from the radial wave prime mover in air at atmospheric pressure.

tal, 876 Hz and 1.168 kHz, and are 63 dB and 75 dB below the fundamental, respectively.

For comparison, a constant cross-section plane wave prime mover was constructed and the spectrum is shown in Fig. 14. A schematic of the prime mover, which is similar in design to that described by Belcher,[9] is shown in Fig. 15. The hot heat exchanger temperature was 410 K and the ambient heat exchanger temperature was 300 K for a temperature difference of 110 K. The frequency of operation was the same as in the radial case, 288 Hz, and the thermoacoustic elements were located at the position predicted to give the lowest temperature difference necessary to produce sound. A ceramic square pore stack and parallel-plate copper heat exchangers were used. The microphone was located at the ambient end of the tube. The sound pressure level (SPL) at the microphone was 156 dB. The first harmonic occurs at twice the fundamental frequency, or 576 Hz. There is a large contribution at this frequency, with an SPL of 137 dB, only 19 dB below the fundamental (compared to a first harmonic which was 38 dB below the fundamental in the radial prime mover). The first through sixth harmonics give noticeable contributions in the plane engine compared to only the first through third harmonics in the radial engine. The results of the plane wave prime mover are similar to those of Ref. 12 for a prime mover just beyond onset, and Ref. 14 for a harmonic resonator driven by a piston. In all three cases, the first harmonic has an amplitude about 20 dB below the fundamental with more harmonics having significant amplitudes than in the radial and detuned plane resonators.

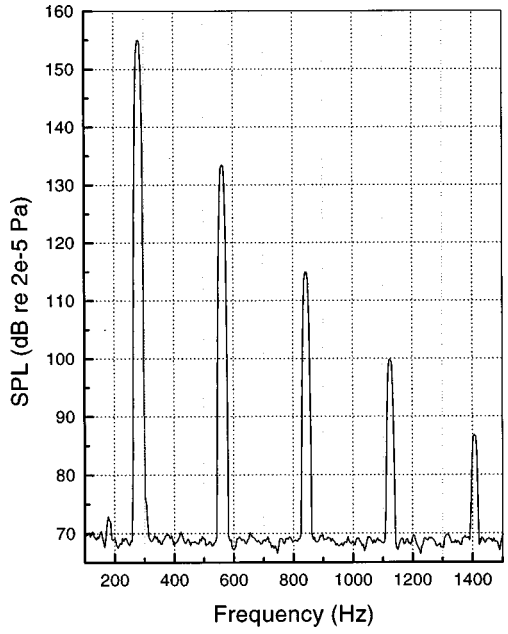

FIG. 14. Acoustic spectrum from the plane wave prime mover in air at atmospheric pressure.

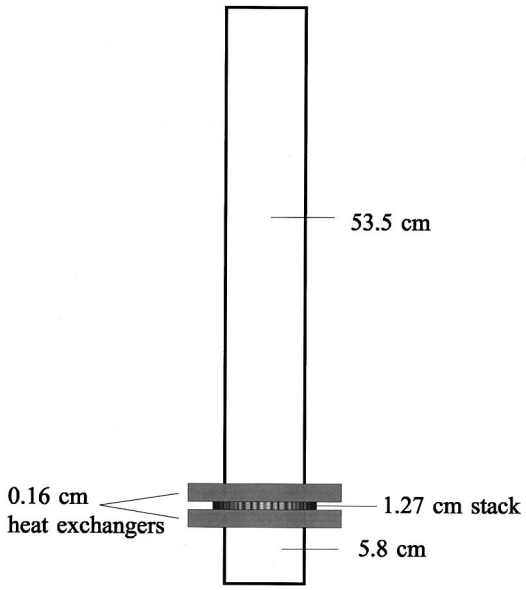

FIG. 15. Plane wave model with dimensions similar to the proposed large radial wave thermoacoustic prime mover. All lengths shown are in the vertical direction. The tube diameter is 8.5 cm.

The reduction in higher harmonic generation for the radial engine is understood qualitatively by considering the proximity of the nonlinear higher harmonics to the natural modes or overtones of the resonator. In general, the nonlinear harmonics have a very narrow bandwidth[12] while the overtones have a wider bandwidth. In the case of the plane resonator the nonlinear harmonics are not exactly the same as the overtones, since a very slight detuning of the overtones occurs due to dissipation in the resonator and the thermoacoustic elements; however, the two are in the same vicinity so that the nonlinear harmonics certainly fall within the bandwidth of the overtones, thus enhancing the higher harmonic generation. The radial engine and detuned plane resonators, by contrast, have no overtones in the vicinity of the nonlinear harmonics so that these systems do not enhance the generation of higher harmonics. A convenience of a radial system is that no variation in tube shape is necessary to make the resonator anharmonic.

IV. CONCLUSIONS

The primary goal of this research was to test the radial wave thermoacoustic theory. Although some satisfaction is

lost in not being able to directly compare measured onset temperatures with predicted values due to unforeseen physical constraints on the system (i.e., significant gaps between stack and heat exchanger), with these constraints included, it has been shown that the existing radial wave theory is accurate and useful for prediction of engine performance.

A secondary goal was to test the generation of higher harmonics in a radial mode prime mover. The expected result was attained. Comparison of harmonic generation in the radial prime mover and a similar plane prime mover showed that the radial prime mover does not enhance the generation of higher harmonics, since the resonator harmonics are not in the vicinity of multiples of the fundamental. In addition, sound pressure levels of the higher harmonics in the radial prime mover were found to be similar to those produced by a detuned plane prime mover.

We identified several areas in which care should be taken in future research, and developed some useful tools for understanding these problem areas. In radial engines, stack plates which are rigid enough to provide a constant plate spacing should be used. Since the radial stack was characterized by a distribution of pore sizes rather than a constant pore size, a method was developed for analyzing pore distributions in the stack. This should be a useful first step in the analysis of inhomogeneous stacks (i.e., steel wool, fiberglass, etc.). In addition, some difficulties with short stacks have been discovered and understood. It was shown that the fit of the heat exchanger to the stack is much more important when short stacks are used.

ACKNOWLEDGMENT

The authors wish to gratefully acknowledge the support of the Office of Naval Research.

[1] G. W. Swift, ''Thermoacoustic engines,'' J. Acoust. Soc. Am. **84**, 1145–1180 (1988).
[2] W. P. Arnott, J. A. Lightfoot, R. Raspet, and Hans Moosmüller, ''Radial wave thermoacoustic engines: Theory and examples for refrigerators and high-gain narrow-bandwidth photoacoustic spectrometers,'' J. Acoust. Soc. Am. **99**, 734–745 (1996).
[3] J. Wheatley, ''Intrinsically irreversible or natural engines,'' in *Frontiers in Physical Acoustics* (Elsevier, New York, 1986).
[4] W. P. Arnott, J. R. Belcher, R. Raspet, and H. E. Bass, ''Stability analysis of a helium-filled thermoacoustic engine,'' J. Acoust. Soc. Am. **96**, 370–375 (1994).
[5] The heat exchangers were constructed by W. Patrick Arnott, Robert Abbott, and Michael Ossofsky at the Desert Research Institute, Reno, NV.
[6] J. A. Lightfoot, ''Thermoacoustic engines in alternate geometry resonators,'' Ph. D. Dissertation, The University of Mississippi (1997).
[7] R. Raspet, J. Brewster, and H. E. Bass, ''A new approximation method for thermoacoustic calculations,'' J. Acoust. Soc. Am. **103**, 2395–2402 (1998).
[8] F. Reif, *Fundamentals of Statistical and Thermal Physics* (McGraw-Hill, New York, 1965), pp. 166–169.
[9] J. R. Belcher, ''A study of element interactions in thermoacoustic engines,'' Ph.D. Dissertation, The University of Mississippi (1996).
[10] A. B. Coppens and J. V. Sanders, ''Finite-amplitude standing waves in rigid-walled tubes,'' J. Acoust. Soc. Am. **43**, 516–529 (1968).
[11] R. Chen, ''Time averaged pressure distributions for finite amplitude standing waves,'' Master's Thesis from Pennsylvania State University, Graduate Program in Acoustics (December 1994)
[12] A. A. Atchley, H. E. Bass, and T. J. Hofler, ''Development of nonlinear waves in a thermoacoustic prime mover,'' in *Frontiers of Nonlinear Acoustics: Proceedings of 12th ISNA*, edited M. F. Hamilton and D. T. Blackstock (Elsevier, New York, 1990), pp. 603–608.
[13] G. W. Swift, ''Analysis and performance of a large thermoacoustic engine,'' J. Acoust. Soc. Am. **92**, 1551–1562 (1992).
[14] D. F. Gaitan and A. A. Atchley, ''Finite amplitude standing waves in harmonic and anharmonic tubes,'' J. Acoust. Soc. Am. **93**, 2489–2495 (1993).
[15] A. B. Coppens and J. V. Sanders, ''Finite-amplitude standing waves within real cavities,'' J. Acoust. Soc. Am. **58**, 1133–1140 (1975).
[16] J. R. Olson and G. W. Swift, ''Similitude in thermoacoustics,'' J. Acoust. Soc. Am. **95**, 1405–1412 (1994).

Acoustic study of texture in polycrystalline brass

K. Foster, S. L. Fairburn, and R. G. Leisure
Department of Physics, Colorado State University, Fort Collins, Colorado 80523-1875

S. Kim, D. Balzar, G. Alers, and H. Ledbetter
Materials Science and Engineering Laboratory, NIST, Boulder, Colorado 80303

(Received 21 July 1998; revised 19 January 1999; accepted 26 January 1999)

Resonant ultrasound spectroscopy was used to measure the orthorhombic elastic constants of rolled, polycrystalline plates of Cu, Cu–5% Zn, and Cu–15% Zn. The experimental results were fit to theoretical expressions to determine the orientation-distribution coefficients W_{400}, W_{420}, and W_{440}. These coefficients are related to texture (the nonrandom orientation of crystallites). The experimental results were in good agreement with theory for the Cu and the Cu–15% Zn materials. The agreement was not as good for the more anisotropic Cu–5% Zn material, especially for the in-plane compressional constants C_{11} and C_{22}. The ultrasonically derived W's were compared to those obtained from neutron measurements for the Cu–Zn alloys. Pole plots based on the two types of measurements, using W_{400}, W_{420}, and W_{440}, were in excellent agreement for the 15% Zn material, and in qualitative agreement for the 5% Zn material. The results support the idea that acoustic methods can be used to measure the low-order W's in polycrystalline materials. [S0001-4966(99)00605-0]

PACS numbers: 43.35.Cg [HEB]

INTRODUCTION

The elastic constants of single crystals reflect the symmetry of the crystalline lattice. In the case of cubic-symmetry materials, three independent elastic constants are required to describe the linear elasticity. The number of independent elastic constants increases with decreasing symmetry, e.g., nine elastic constants are required for crystals with orthorhombic symmetry. In contrast, polycrystalline materials are often assumed to be elastically isotropic with only two independent elastic constants. Isotropy results when the grains composing the material are small compared to the length scale used in the measurement and are randomly oriented. In many cases of practical interest, however, the grains have a statistically preferred orientation as a result of mechanical processing or heat treatment. Such preferred orientation, called texture, results in elastic anisotropy of polycrystalline aggregates, and has practical implications including effects on formability and nondestructive testing. In principle, any physical-mechanical property not representable as a scalar depends on the aggregate's texture.

Texture has been described theoretically[1–3] in terms of an orientation-distribution function (ODF) w, where $w(\xi,\psi,\phi)d\xi\,d\psi\,d\phi$ is the probability of finding crystallites with orientations between (ψ,θ,ϕ) and $(\psi+d\psi,\theta+d\theta,\phi+d\phi)$. Here $\xi=\cos\theta$, and θ, ψ, and ϕ are Euler angles[2] describing the orientation of the crystallite axes with respect to the specimen axes. The orientation-distribution function may be expanded in terms of generalized spherical harmonics. The expansion coefficients W_{lmn} are called orientation-distribution coefficients (ODCs). Detailed information about the W's can be obtained from x-ray diffraction and neutron-diffraction measurements; however, these techniques are not convenient for nondestructive testing or process control. As a result, there is interest in the use of ultrasonic methods to provide information about texture.[4–8] The present objective is to investigate anisotropic elasticity in textured materials and compare the results to theoretical expressions previously derived.[4,6,8] Although the effects of texture on the propagation of Rayleigh and Lamb waves have been studied in the past,[6,8] the interpretation was complicated because of dispersive effects associated with the Rayleigh-wave and Lamb-wave propagation in plates. Some of the W_{lmn} have also been obtained from acoustic shear-wave birefringence measurements.[5,7] The present paper presents a study of the complete set of anisotropic elastic constants resulting from texture in plates.

I. THEORETICAL BACKGROUND

A. Anisotropic elasticity and ODCs

We studied the effects of texture on rolled plates. It is assumed that the macroscopic properties of the rolled plates have three mutually perpendicular mirror planes. Thus the resulting elastic-constant matrix is expected to exhibit orthorhombic symmetry (nine independent C_{ij}),[6] as illustrated in Fig. 1, where x_1, x_2, and x_3 refer to the plate rolling, transverse, and normal directions, respectively. X_1, X_2, and X_3 designate the principal-axis system of the crystallite. The Euler angles give the orientation of (X_1,X_2,X_3) with respect to (x_1,x_2,x_3).[6] It is straightforward to transform the elastic-constant matrix from the crystallite coordinate system to the specimen coordinate system.[9] The results obviously depend on the symmetry and orientation of the crystallite with respect to the specimen. To obtain the aggregate results, the transformed elastic constants are averaged over all orientations using the W's discussed above. For the case of crystallites with cubic symmetry and a specimen with orthorhombic symmetry (rolled-plate case) the results are[6,8]

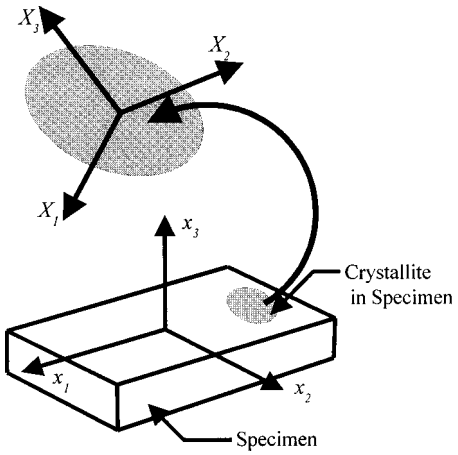

FIG. 1. The coordinate systems used to describe the rolled-plate specimen (x_1,x_2,x_3) and a crystallite in the sample (X_1,X_2,X_3). For the specimen, x_1=plate-rolling direction, x_2=plate-transverse direction, and x_3=plate-normal direction.

$$
\begin{aligned}
C_{11} &= \lambda + 2\mu + \left(\frac{12\sqrt{2}c\pi^2}{35}\right) \\
&\quad \times \left[W_{400} - \left(\frac{2\sqrt{10}}{3}\right) W_{420} + \left(\frac{\sqrt{70}}{3}\right) W_{440} \right], \\
C_{22} &= \lambda + 2\mu + \left(\frac{12\sqrt{2}c\pi^2}{35}\right) \\
&\quad \times \left[W_{400} + \left(\frac{2\sqrt{10}}{3}\right) W_{420} + \left(\frac{\sqrt{70}}{3}\right) W_{440} \right], \\
C_{33} &= \lambda + 2\mu + \left(\frac{32\sqrt{2}c\pi^2}{35}\right) W_{400}, \\
C_{44} &= \mu - \left(\frac{16\sqrt{2}c\pi^2}{35}\right) \left(W_{400} + \sqrt{\frac{5}{2}} W_{420} \right), \\
C_{55} &= \mu - \left(\frac{16\sqrt{2}c\pi^2}{35}\right) \left(W_{400} - \sqrt{\frac{5}{2}} W_{420} \right), \\
C_{66} &= \mu + \left(\frac{4\sqrt{2}c\pi^2}{35}\right) (W_{400} - \sqrt{70} W_{440}), \\
C_{23} &= \lambda - \left(\frac{16\sqrt{2}c\pi^2}{35}\right) \left(W_{400} + \sqrt{\frac{5}{2}} W_{420} \right), \\
C_{13} &= \lambda - \left(\frac{16\sqrt{2}c\pi^2}{35}\right) \left(W_{400} - \sqrt{\frac{5}{2}} W_{420} \right), \\
C_{12} &= \lambda + \left(\frac{4\sqrt{2}c\pi^2}{35}\right) (W_{400} - \sqrt{70} W_{440}),
\end{aligned}
\tag{1}
$$

where λ and μ are the Lamé constants for the texture-free material and c is an anisotropy parameter for the crystallite. Different averaging methods (Voigt, Reuss, Hill, other) are reflected only in the values of λ, μ, and c; the ODCs contribute in the same way for each mehod.[6] In principle λ, μ, and c can be obtained from the single-crystal elastic constants using one of these averaging methods. For copper, Ledbetter[10] compared nine averaging methods and found that

TABLE I. Single-crystal elastic constant data (Ref. 11) used to compute the anisotropy parameter.

	c_{11}(GPa)	c_{12}(GPa)	c_{44}(GPa)
Copper(100.0)	168.40	121.40	75.50
Copper(95.9)–Zinc(4.1)	163.20	117.60	74.40
Copper(82.9)–Zinc(17.1)	149.90	109.70	71.50

Kröner's method gives best measurement theory agreement. The absolute value of c depends on the chosen averaging method. For copper, for the Voigt, Hill, and Reuss cases we found $c=-104.4$, -99.0, and -94.0 GPa, respectively. The Kröner value falls between the Hill and Voigt results. Thus a difference in c of about 2% would produce no significant effect on the present results and conclusions. We avoided the problem of choosing an averaging method for λ and μ by measuring all nine elastic constants for textured plates, and fitting Eq. (1) to the results to obtain the five parameters λ, μ, W_{400}, W_{420}, and W_{440}. As can be seen from Eq. (1), c always occurs as a multiplier of the W's, thus the W's and c cannot be determined independently from these experiments. We calculate c from single-crystal c_{ij} using the usual anisotropy relationship $c=c_{11}-c_{12}-2c_{44}$, where the c_{ij} are the single-crystal values[11] (Table I). The relative values of the W's will not be affected by the choice of c. In our experience, the laboratory–laboratory variation in measured single-crystal c_{ij} is about 1 in 10^3, thus insignificant for present purposes.

B. Acoustic pole plots

The distribution of orientations of the crystallites is conveniently expressed in terms of a distribution function for reciprocal-lattice vectors. Figure 2 illustrates the situation for a particular reciprocal-lattice vector $\mathbf{t}_i$. The orientation of $\mathbf{t}_i$ in the *crystallite* coordinate system is specified by the angles Θ_i and Φ_i. For example, these angles are $\pi/2$ and $\pi/4$, respectively, for a [110] reciprocal-lattice vector. This vector is specified by the angles χ_i and η_i in the *plate* coordinate system. Let $q_i(\zeta,\eta)d\zeta\,d\eta$ be the probability to find $\mathbf{t}_i$ between (χ,η) and $(\chi+d\chi,\eta+d\eta)$ where $\zeta=\cos(\chi)$. It has been shown[4,6] that

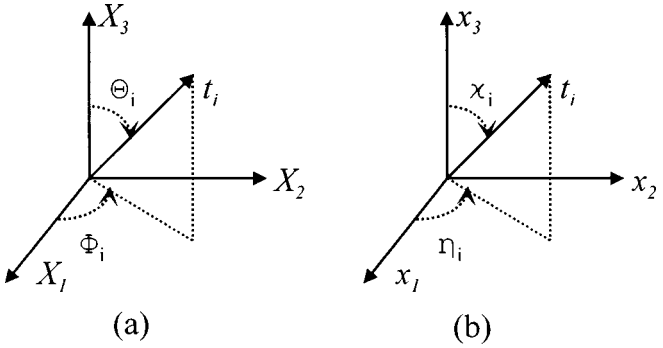

FIG. 2. The angles used to describe the orientation of a particular reciprocal lattice vector $\mathbf{t}_i$ in a crystallite (Θ_i,Φ_i) and in the rolled-plate sample (χ_i,η_i).

FIG. 3. Microstructure of Cu–5% Zn alloy. Reference bar equals 20 μm. Mechanical deformation converted originally equiaxed grains into aligned spheriods. Rolling direction is horizontal. Plate-normal direction is vertical.

$$q_i(\zeta,\eta)=\frac{1}{4\pi}+S(\Xi_i,\Phi_i)[P_4^0(\zeta)W_{400}+2P_4^2(\zeta)\times\cos(2\eta)W_{420}+2P_4^4(\zeta)\cos(4\eta)W_{440}]+\text{higher order terms}, \quad (2)$$

where

$$S(\Xi_i,\Phi_i)=\frac{2\sqrt{2\pi}}{3}\left[P_4^0(\Xi_i)+\frac{10}{\sqrt{70}}P_4^4(\Xi_i)\cos(4\Phi_i)\right], \quad (3)$$

with $\Xi_i=\cos(\Theta_i)$. The $P_l^m(z)$ are the normalized associated Legendre functions. It is convenient to display the information about the distribution of reciprocal-lattice vectors as pole plots, which are projections of $4\pi q_i(\zeta,\eta)$ onto the x_1-x_2 plane. Such plots are presented below.

II. EXPERIMENTAL DETAILS

The study was carried out on Olin Corporation copper and copper–zinc alloys (brass). The specimens used for the study were cut from 3.17-mm-thick plates. Three types of materials were studied: Olin type 110 copper containing 0.021-wt. % oxygen; Olin type 210 copper–5% zinc alloy; and, Olin type 230 copper–15% zinc alloy. These alloys have the same crystal structure as copper: face-centered cubic. Copper dissolves zinc substitutionionally up to about 40%. Optical microstructures (Fig. 3) revealed that the grain morphology was quite uniform through the thickness of the plates. The grain size was approximately 0.01 mm in the 110 and 210 materials, and somewhat smaller in the 230 material. The Cu–5% Zn alloy appeared to have been heavily deformed. The microstructure strongly suggests (but does not prove) strong texture in this material; microstructural evidence for texture was less obvious for the Cu and the Cu–15% Zn alloys. The neutron-diffraction pole figures (Fig. 4) confirm this. The texture index[12] for Cu–5% Zn was determined as 4.7 and for Cu–15% Zn as 1.6. Room temperature elastic-constant measurements were carried out at Colorado State University (CSU) and at the National Institute for Standards and Technology (NIST). Measurements on a number of specimens for each type of material were carried out at CSU using Resonant Ultrasound Spectroscopy (RUS).[13–15] The different specimens varied somewhat in size, but each was an accurate parallelepiped approximately 2 mm on an edge, with the specimen axes aligned with the original plate axes so as to maintain the orthorhombic symmetry. Similar resonance measurements were carried out at NIST for the 110 copper material and the 210 alloy. These specimens were larger: $3\times4\times8$ mm^3 and $3\times5\times8$ mm^3. Specimen dimensions were measured to an accuracy of 0.1% or better. Careful specimen preparation procedures were used[14] to ensure that the parallepiped-shaped specimens had parallel/orthogonal faces. The elastic constants were determined from the measured frequencies by an iterative procedure.[14] Starting with an initial set of estimated elastic constants, the frequencies were computed and compared to the measured frequencies. The elastic constants were varied so as to minimize the difference between measured and computed frequencies. A typical rms difference between measured and computed frequencies for the first 50 frequencies was 0.1%–0.2%. In addition to the resonance measurements, elastic constants for all three materials were measured at NIST using a pulse-echo

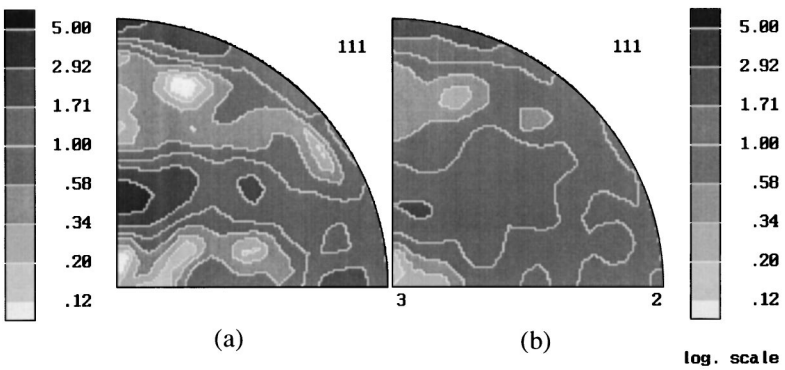

FIG. 4. [111] pole figures were obtained from time-of-flight neutron-diffraction measurements at the High Intensity Powder Diffractometer at the Manuel Lujan Jr. Neutron Scattering Center at Los Alamos National Laboratory: (a) Cu–5% Zn; (b) Cu–15% Zn.

TABLE II. Orthorhombic elastic constants for Cu–x% Zn alloys. ''±'' indicates the standard deviation of the measurements as a percentage of the mean. x_1=plate rolling direction, x_2=transverse direction, x_3=plate-normal direction.

x	0	5%	15%
C_{11}(GPa)	201.2±0.59%	203.3±0.38%	193.6±0.72%
C_{22}(GPa)	201.0±0.39%	200.8±1.53%	191.8±0.10%
C_{33}(GPa)	199.4±1.38%	196.0±0.32%	191.2±0.34%
C_{44}(GPa)	45.50±0.12%	41.84±0.33%	46.80±0.02%
C_{55}(GPa)	45.79±0.25%	45.30±0.21%	44.39±0.03%
C_{66}(GPa)	45.43±0.24%	44.12±3.24%	43.63±0%
C_{23}(GPa)	110.2±0.04%	101.9±3.94%	102.5±1.41%
C_{13}(GPa)	111.2±2.42%	104.8±1.09%	100.2±0.67%
C_{12}(GPa)	109.6±1.71%	99.53±1.57%	101.0±0%
ρ(g/cm^3)	8.903±0.05%	8.852±0.05%	8.730±0.05%

method and a Marx-oscillator technique.[16] Densities were determined by the Archimedes method using distilled water as a standard, where a typical uncertainty is about 5 in 10^4 for the specimen sizes used here.

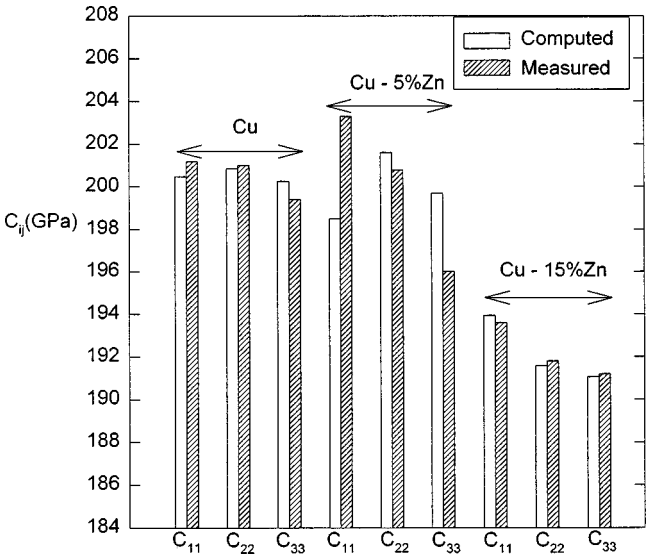

FIG. 5. Comparison of measured and computed values of the elastic constants C_{11}, C_{22}, and C_{33} for Cu, and two Cu–Zn alloys. The computations used the parameters of Table II.

III. RESULTS AND DISCUSSION

Table II presents the results for the orthorhombic elastic constants from a large number of measurements on the Cu–x% Zn system. The ''±'' in Table II indicates the standard deviation of the measurements as a percentage of the mean. If there were no preferred orientation (no texture) then, as Eq. (1) shows, we would expect: $C_{11}=C_{22}=C_{33}$; $C_{44}=C_{55}=C_{66}$; $C_{23}=C_{13}=C_{12}$; and $C_{44}=1/2(C_{11}-C_{12})$. By these measures, an inspection of Table II shows that the Cu–5% Zn material is the most anisotropic, the Cu–15% Zn the second most anisotropic, while the Cu showed a small anisotropy. These observations agree with the microstructures (Fig. 3) and the neutron-diffraction pole figures (Fig. 4). (Figure 4 shows the [111] pole figure because this figure is used most often for interpretations. Our [111] pole figure differs slightly from ''textbook'' figures because of the lower plastic deformation in our specimens.) For a more detailed comparison of the experimental results with the theoretical expressions we did a least-squares fit of the data of Table II to the theoretical expressions of Eq. (1) to determine the five parameters, W_{400}, W_{420}, W_{440}, λ, and μ. For the parameter c we used Table I[11] to calculate the following values: −104.0 GPa for Cu, −103.2 GPa for Cu–5% Zn, and −102.8 GPa for Cu–15% Zn. The results of this fitting are presented in Table III. The ''rms error'' is the rms difference between the measured elastic constants and those calculated by Eq. (1) using the parameters of Table III. The derived W's indicate that Cu–5% Zn is significantly more anisotropic than the other materials, in qualitative agreement with the microstructure and neutron diffraction pole figures. Table III also lists the W's determined from neutron-diffraction measurements on the same alloys. It can be seen that the ultrasound and neutron values are in rough agreement.

Figures 5–7 present a comparison of the measured C_{ij} and the computed C_{ij} using the parameters of Table III. The two sets of values agree well with each other, except for C_{11} and C_{33} for the 5% Zn material. To further explore the comparison of theory and measurement we note that Eq. (1) indicates various relations among the elastic constants. For example, it is expected that $C_{11}-C_{22}=C_{44}-C_{55}=C_{23}-C_{13}$. Of course, these numbers would all equal zero for an isotropic material. The experimental numbers for these three quantities are, respectively (in GPa): (Cu) +0.2, −0.29, −1.0; (Cu–5% Zn) +7.3, −3.46, −2.95; (Cu–15% Zn) +1.80, +2.41, +2.27. These numbers are all in excellent accord with the theoretical expressions *except* for the value of $C_{11}-C_{22}$ for the Cu–5% Zn alloy. These numbers also make clear that the Cu material is the most nearly isotropic, while the Cu–5% Zn material is the most anisotropic. The discrep-

TABLE III. ODCs (W's), and Lamé constants (λ and μ) for Cu–x% Zn alloys obtained by fitting the experimental results of Table I to Eq. (1). ''rms'' indicates the rms difference between the measured elastic constants and those computed using the parameters of Table II. Also listed are W's obtained from neutron-diffraction measurements for the 5% Zn and 15% Zn material.

x	0	5% Ultrasound	5% Neutron	15% Ultrasound	15% Neutron
W_{400}	4.93×10^{-4}	-2.98×10^{-3}	-1.73×10^{-3}	5.34×10^{-4}	9.95×10^{-5}
W_{420}	-1.76×10^{-4}	-1.53×10^{-3}	-1.91×10^{-3}	1.14×10^{-3}	9.77×10^{-4}
W_{440}	6.72×10^{-6}	-2.05×10^{-3}	-3.17×10^{-3}	-9.18×10^{-4}	-8.44×10^{-4}
λ (GPa)	110.1	104.1		101.5	
μ (GPa)	45.38	45.83		45.15	
rms	0.31%	1.50%		0.39%	

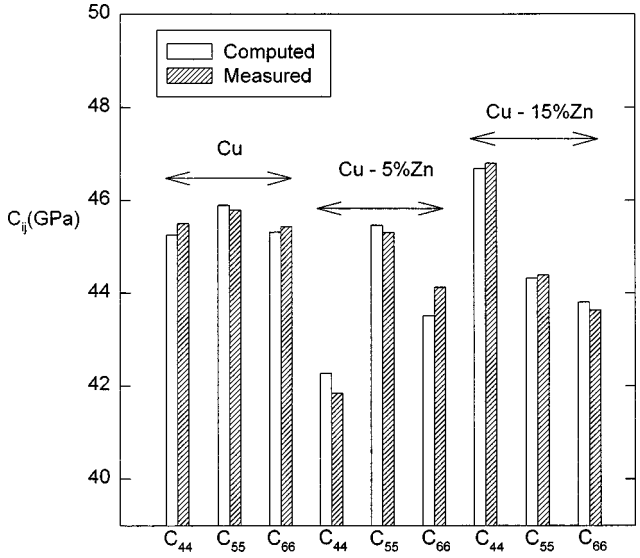

FIG. 6. Comparison of measured and computed values of the elastic constants C_{44}, C_{55}, and C_{66} for Cu, and two Cu–Zn alloys. The computations used the parameters of Table II.

ancy of $C_{11}-C_{22}$ in the Cu–5% Zn alloy suggests possible departures from the assumed orthorhombic symmetry.

For a visual comparison of the W's determined acoustically with low-order W's determined by neutron diffraction we turn to pole plots. Figures 8 and 9 are contour plots of $4\pi q_i(\zeta,\eta)$ for the [100] reciprocal-lattice vector projected onto the x_1-x_2 plane. Light represents high intensity and dark represents low intensity. Figure 8 is for the Cu–15% Zn alloy: Figs. 8(a) and 8(b) are derived from ultrasonic and neutron measurements, respectively. It is seen that, to the resolution presented in the figures, the two plots are almost identical. The quantity $4\pi q_{[100]}(\zeta,\eta)$ is maximum in the plane of the plate at approximately 50° to the rolling direction. The maximum (minimum) values of $4\pi q_{[100]}(\zeta,\eta)$ are 1.21 (0.74) for the ultrasonic results and 1.17 (0.80) for the neutron results. A value of unity corresponds to an isotropic

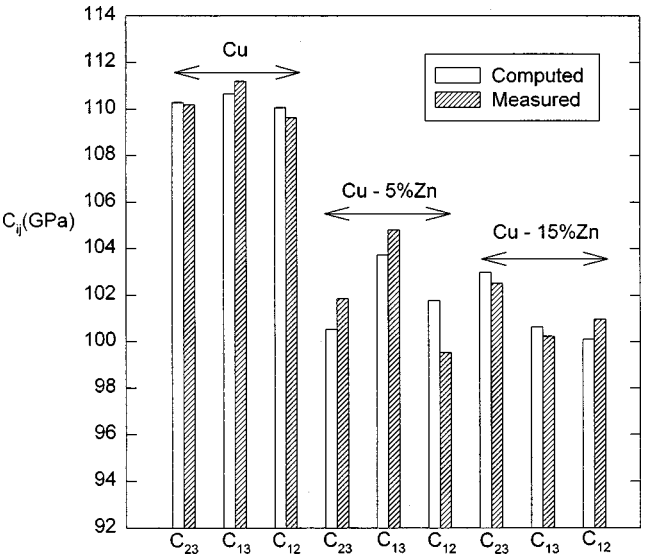

FIG. 7. Comparison of measured and computed values of the elastic constants C_{23}, C_{13}, and C_{12} for Cu, and two Cu–Zn alloys. The computations used the parameters of Table II.

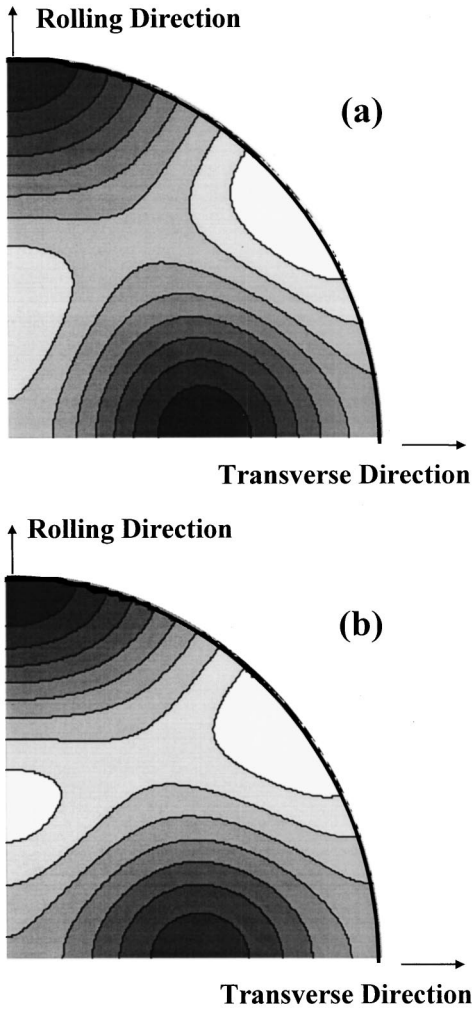

FIG. 8. [100] pole plots for the Cu–15% Zn material. Light (dark) represents high (low) intensity. (a) Derived from acoustic measurements. The intensity ranges from 0.74 to 1.21. (b) Derived from neutron measurements. The intensity ranges from 0.80 to 1.17. Note that these plots, for both the acoustic and neutron-diffraction cases, are based only on the lower-order W_{lmn}: W_{400}, W_{420}, and W_{400}. The complete pole plot based on all the W_{lmn} may differ considerably. Here, we show the [100] pole figures instead of the [111] figure as in Fig. 4 because using the principle crystal axis facilitates texture visualization.

distribution. Figure 9 presents similar results for the Cu–5% Zn alloy. Although the ultrasonic and neutron results are qualitatively similar in Fig. 9, the correspondence is certainly not as close as in the case of Fig. 8. The maximum (minimum) values in Fig. 9 are 1.39 (0.25) for the ultrasonic results and 1.46 (0.08) for the neutron results.

Previous workers[5,7] have compared ultrasonic and neutron results for W_{420} and W_{440}. The agreement we find between the neutron-derived and acoustic-derived results for these two parameters is comparable to that found previously. The ultrasonic methods often do not determine W_{400}. As has been discussed by Hirao *et al.*,[6] the ultrasonic result for W_{400} is critically dependent on the averaging method used to compute the isotropic parameters from the single-crystal data. Our method is different. We compute only the anisotropy parameter c from the single-crystal data, and the results are not critically dependent on c.

Comparison of the acoustic and neutron-diffraction

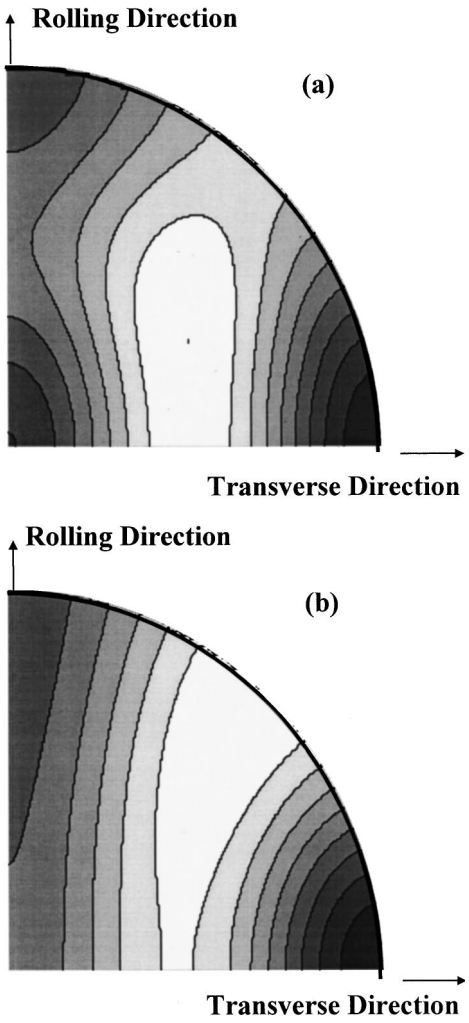

FIG. 9. [100] pole plots for the Cu–5% Zn material. Light (dark) represents high (low) intensity. (a) Derived from acoustic measurements. The intensity ranges from 0.25 to 1.39. (b) Derived from neutron measurements. The intensity ranges from 0.08 to 1.46. See note in caption for Fig. 8.

ODFs in Figs. 8 and 9 deserves additional discussion. These pole figures are constructed using only the low-order ODF coefficients W_{400}, W_{420}, and W_{440}. As such, they clearly do not represent the complete pole figures. For example, the measured neutron-diffraction [100] pole figures (Fig. 4) show considerably more detail than the pole figures in Figs. 8(b) and 9(b). Nevertheless, in terms of the effect of the ODF on overall polycrystal physical and mechanical properties, the low-order ODF coefficients play the leading role. In fact, for tensorial properties, only the low-order ODF coefficients come into play. This result, known as the truncation theorem,[12,17] is evident in Eq. (1) where only W_{lmn} through order 4 enter the averaging of the elastic constants, which are fourth-rank tensors. Likewise, for second-rank tensorial properties such as thermal expansion and thermal conductivity, only W_{lmn} through order 2 enter the averaging process.

IV. CONCLUSIONS

Acoustic methods have been used to obtain the elastic constants of rolled plates of Cu, Cu–5% Zn, and Cu–15% Zn polycrystalline materials. It was assumed that the macroscopic properties of the rolled plates have orthorhombic symmetry. The experimental results were compared to theoretical expressions to obtain the ODCs. The results for Cu exhibited little, if any, anisotropy and thus were not a test of the theory. The results for the Cu–15% Zn material showed considerable elastic anisotropy. The results were in good agreement with the theoretical expressions, and the ODCs were in good agreement with neutron measurements for W_{400}, W_{420}, and W_{440}. The acoustic and neutron pole plots for W_{ijk} through order 4 were almost identical. The ultrasonic results indicated that the Cu–5% Zn material is the most anisotropic, in qualitative agreement with microstructures; however, the agreement between theory and measurements was not as good for this material, especially for C_{11} and C_{22}. The reasons for this disagreement are not known; perhaps this material possesses less than orthorhombic macroscopic symmetry, which would then require additional W_{ijk}. The analysis was based, of course, on orthorhombic symmetry, the usual assumed macroscopic symmetry for a rolled plate. One can imagine rolled plates with less than orthorhombic symmetry, caused for example by nonhomogeneous deformation. Nevertheless, the acoustic and neutron pole plots for this material were in qualitative agreement. Overall, the results presented here support the idea that ultrasonic methods may be used for quantitative texture corrections of tensorial physical quantities.

ACKNOWLEDGMENTS

The work at Colorado State University was supported by the National Science Foundation under Grant No. DMR-9501550 and by the Colorado Advanced Materials Institute. This work has benefitted from the use of the Los Alamos Neutron Science Center at the Los Alamos National Laboratory. This facility is funded by the U.S. Department of Energy under Contract No. W-7405-ENG-36.

[1] R.-J. Roe and W. R. Krigbaum, J. Chem. Phys. **40**, 2608 (1964).
[2] R.-J. Roe, J. Appl. Phys. **36**, 2024 (1965).
[3] R.-J. Roe, J. Appl. Phys. **37**, 2069 (1966).
[4] C. M. Sayers, J. Phys. D **15**, 2157 (1982).
[5] C. M. Sayers, D. R. Allen, G. E. Haines, and G. G. Proudfoot, Philos. Trans. R. Soc. London, Ser. A **320**, 187 (1986).
[6] M. Hirao, K. Aoki, and H. Fukuoka, J. Acoust. Soc. Am. **81**, 1434 (1987).
[7] A. V. Clarke, Jr., R. C. Reno, R. B. Thompson, J. F. Smith, G. V. Blessing, R. J. Fields, P. P. Delsanto, and R. B. Mignogna, Ultrasonics **26**, 189 (1988).
[8] Y. Lee and R. B. Thompson, J. Acoust. Soc. Am. **91**, 1298 (1992).
[9] F. I. Fedorov, *Theory of Elastic Waves in Crystals* (Plenum, New York, 1968).
[10] H. Ledbetter, in *Dynamic Modulus Measurements* (ASTM, Philadelphia, 1990), pp. 135–148.
[11] J. A. Rayne, Phys. Rev. **112**, 1125 (1958).
[12] H. Bunge, *Texture Analysis in Materials Science* (Butterworths, London, 1982).
[13] A. Migliori, J. L. Sarrao, W. M. Visscher, T. M. Bell, Ming Lei, Z. Fisk, and R. G. Leisure, Physica B **183**, 1 (1993).
[14] A. Migliori and J. L. Sarrao, *Resonant Ultrasound Spectroscopy* (Wiley, New York, 1997).
[15] R. G. Leisure and F. A. Willis, J. Phys.: Condens. Matter **9**, 6001 (1997).
[16] H. Ledbetter, Cryogenics **20**, 637 (1980).
[17] M. Ferrari and G. Johnson, Mech. Mater. **8**, 67 (1989).

Time-frequency analysis of the dispersion of Lamb modes

W. H. Prosser and Michael D. Seale
NASA Langley Research Center, MS 231, Hampton, Virginia 23681-2199

Barry T. Smith
Norfolk Academy, 1585 Wesleyan Drive, Norfolk, Virginia 23502

(Received 13 October 1997; accepted for publication 15 January 1999)

Accurate knowledge of the velocity dispersion of Lamb modes is important for ultrasonic nondestructive evaluation methods used in detecting and locating flaws in thin plates and in determining their elastic stiffness coefficients. Lamb mode dispersion is also important in the acoustic emission technique for accurately triangulating the location of emissions in thin plates. In this research, the ability to characterize Lamb mode dispersion through a time-frequency analysis (the pseudo-Wigner–Ville distribution) was demonstrated. A major advantage of time-frequency methods is the ability to analyze acoustic signals containing multiple propagation modes, which overlap and superimpose in the time domain signal. By combining time-frequency analysis with a broadband acoustic excitation source, the dispersion of multiple Lamb modes over a wide frequency range can be determined from as little as a single measurement. In addition, the technique provides a direct measurement of the group velocity dispersion. The technique was first demonstrated in the analysis of a simulated waveform in an aluminum plate in which the Lamb mode dispersion was well known. Portions of the dispersion curves of the A_0, A_1, S_0, and S_2 Lamb modes were obtained from this one waveform. The technique was also applied for the analysis of experimental waveforms from a unidirectional graphite/epoxy composite plate. Measurements were made both along and perpendicular to the fiber direction. In this case, the signals contained only the lowest order symmetric and antisymmetric modes. A least squares fit of the results from several source to detector distances was used. Theoretical dispersion curves were calculated and are shown to be in good agreement with experimental results. [S0001-4966(99)02705-8]

PACS numbers: 43.35.Cg, 43.40.Le, 43.35.Zc, 43.20.Mv [HEB]

INTRODUCTION

In propagating through solid materials, acoustic waves may have velocities that are dependent on their frequency. This dispersion may be due to the material behavior, such as in viscoelastic materials. It can also be caused by the influence of specimen geometry on the wave propagation. This is the case for waves propagating in plates, rods, and shells. Accurate knowledge of this dispersion is important for many acoustic based nondestructive evaluation techniques. In ultrasonic testing, the velocity and its dispersion are used to determine the depth or location of flaws. It is also used in measurements of elastic properties. Related techniques such as laser generated ultrasonics and acousto-ultrasonics also require information about the dispersion for interpretation of data. In acoustic emission (AE), the velocity is needed to determine the location of the source of emission. As pointed out by Ziola and Gorman,[1] if not taken into account, highly dispersive propagation can lead to large errors in source location in AE testing.

In this study, the ability to determine group velocity dispersion of Lamb modes by using a time-frequency analysis method, the pseudo-Wigner–Ville distribution (PWVD), was demonstrated. The technique was first applied to a simulated broadband acoustic waveform in an aluminum plate. The technique was then applied to experimental waveforms from a unidirectional graphite/epoxy (AS4/3502) laminate. The broadband acoustic waves were generated by a pencil lead fracture (Hsu–Neilsen source) and were detected with broadband, contact, ultrasonic transducers. Measurements were made at several source-to-detector distances. A least squares fit was used to calculate the velocity for the lowest order symmetric and antisymmetric modes contained in the waveforms. Results are presented for propagation along, and perpendicular to, the fiber direction. Theoretical dispersion curves were also calculated and compared to the experimental measurements.

Time-frequency analyses such as the PWVD can offer several advantages for velocity dispersion measurements in comparison to more traditional techniques. For example, they can be applied to broadband signals so that as little as one measurement may be required to determine the velocity of multiple modes over a wide range of frequencies. This can be of significant importance when access time to specimens for measurements is limited, or when measurements are required for a large number of specimens. Another important advantage is the ability to analyze signals containing multiple propagation modes and/or reflections which superimpose and interfere in the time domain. These multiple modes and reflections can be separated in time-frequency space. The PWVD also provides a direct measurement of group velocity dispersion which may be the desired quantity in certain applications such as the recently developed AE source location technique from Ziola and Gorman.[1] Although, in theory, the group velocity can be obtained from

phase velocity dispersion measurements, small measurement errors in the phase velocity can propagate into significant errors in the calculated group velocity.

For Lamb mode dispersion measurements, there is another advantage in that immersion of the plate is not required. Direct contact ultrasonic sensors can be used. This is in contrast to corner reflection and leaky Lamb measurement techniques which have been widely used by Mal *et al.*,[2] Chimenti and Nayfeh,[3] and Balasubramaniam and Rose.[4] These techniques also require a number of measurements with the wave incident to the plate at different angles to map out the dispersion curves.

The difficulty of phase unwrapping, which occurs in the Fourier phase dispersion measurement technique,[5–7] is not present in time-frequency based analysis. The Fourier phase technique also cannot be used when multiple modes or reflections are superimposed in time. However, another technique which overcomes these limitations is the two-dimensional Fourier transform method which was presented by Alleyne and Cawley[8] and applied by Costley and Berthelot.[9] A difficulty of the two-dimensional Fourier transform technique is that a large number of closely spaced measurements is required to avoid aliasing when Fourier transforming from the spatial domain. However, instead of the Fourier transform, alternative spectral estimation techniques such as Prony's method can be used. A review of such techniques is provided by Kay and Marple.[10] Alternative spectral estimation techniques can be used when the spatial data are undersampled, and thus requires fewer measurements at different locations. However, these methods are somewhat susceptible to noise, requiring input data with a high signal-to-noise level. Lang *et al.*,[11] Leslie and Randall,[12] and McClellan[13] have applied these techniques to measure the dispersion of acoustic waves for geophysical applications.

More recently, another time-frequency analysis method, the short-time Fourier transform, has been used to characterize dispersion by Kwun and Bartels.[14] They evaluated the group velocity dispersion of the first and second modes of the axisymmetric longitudinal wave in cylindrical steel shells. The signals were generated and detected with magnetostrictive sensors and measurements made at frequencies below 100 kHz.

I. PWVD THEORY

Time-frequency distributions provide a method for examining how the frequency content of a given signal changes as a function of time. The output of these distributions is the energy density, or intensity, of various frequency components of a signal at given points in time. Cohen[15] has provided a detailed review of time-frequency distributions and discusses their numerous applications. Grade and Gram-Hansen[16] compare the Wigner–Ville distribution to the short-time Fourier transform (STFT) and wavelet transform (WT) for the analysis of nonstationary signals. It is pointed out that the Wigner–Ville distribution offers an advantage in that it is a more general transform which is not limited by the uncertainty relationship on simultaneous time and frequency resolution. However, this advantage comes at the expense of a couple of limitations. First, computational complexity is much greater for the Wigner–Ville distribution. Also, negative energy levels and cross terms may appear in the Wigner–Ville distribution which do not have physical meaning. This problem is discussed in more detail below.

From Cohen,[15] the general equation for a time-frequency distribution, $w(t,\omega)$, for an input time signal $s(t)$ is given by

$$w(t,\omega)=\frac{1}{2\pi}\int\int\int e^{-i\theta t-i\tau\omega-i\theta u}\phi(\theta,\tau)\times s^*\left(u-\frac{\tau}{2}\right)s\left(u+\frac{\tau}{2}\right)du\,d\tau\,d\theta, \tag{1}$$

where the integrals are evaluated from $-\infty$ to ∞. In this equation, s^* is the complex conjugate and $\phi(\theta,\tau)$ is an arbitrary function known as the kernel. Time and frequency are represented by t and ω respectively. For the Wigner distribution,[17] which is discussed in detail by Jeon and Shin[18] and Wahl and Bolton,[19] the kernel function has a value of 1. Upon this substitution, Eq. (1) reduces to

$$w(t,\omega)=\int s^*\left(t-\frac{\tau}{2}\right)s\left(t+\frac{\tau}{2}\right)e^{-i\tau\omega}\,d\tau. \tag{2}$$

For application to digitized or sampled signals, this equation must be modified to a discrete form. This is given by

$$w(m\Delta t,k\Delta\omega)=2\Delta t\sum_{n=0}^{2N-1}s[(m+n)\Delta t]\times s^*[(m-n)\Delta t]e^{-i2\pi nk/2N}, \tag{3}$$

where Δt is the sampling interval and $\Delta\omega=\pi/(2N\Delta t)$. The discrete Wigner distribution has several characteristics which limit its usefulness in this form. The first is a higher sampling requirement than the conventional discrete Fourier transform (DFT) to avoid aliasing. According to Boashash,[20] the sampling frequency must be four times that of the highest frequency content of the signal as opposed to the usual Nyquist criteria for the DFT which requires it to be only twice that of the highest frequency content. Other considerations discussed by Jeon and Shin[18] include the fact that the frequency resolution is only 1/4 of that obtained by the DFT. Additionally, the Wigner distribution produces complicated and unexpected results when more than one frequency component is contained in a signal. ''Noise,'' or the appearance of signal in the Wigner distribution at frequencies and times not actually contained in the waveform, is produced. It is caused by interference which consists of cross terms from the multiple frequency components and makes interpretation of results very difficult. The final undesirable characteristic is that this distribution may take on negative values which do not have physical meaning. This most often occurs as a result of the interference discussed above.

A couple of solutions are available to overcome the first limitation, that is, the more restrictive sampling frequency requirement. The first and most obvious is to sample at the higher frequency. Hardware limitations in some situations may make this impractical. Also, once the data have been acquired at a given sample rate, it may not be possible to

reacquire it at a faster rate. Thus another solution was proposed by Ville[21] and is discussed by Jeon and Shin[18] and Boashash,[20] among others. This approach involves the calculation of the Wigner distribution using the analytic signal. The analytic signal is a complex signal where the real component is the original signal and the imaginary component is its Hilbert transform. When the Wigner distribution is performed on the analytic signal, the requirement to avoid aliasing is now reduced to that of the Nyquist criteria. The resulting time-frequency distribution is known as the Wigner–Ville distribution. Boashash[20] provides an intuitive rationale on why this approach reduces the sampling requirement based on the fact that a single sample of the analytic signal provides two effective samples (the real and imaginary parts) of the original signal.

Another approach is used to minimize the effects of interference terms or ''noise'' in the distribution. This is the application of smoothing to the distribution. According to Jeon and Shin,[18] this emphasizes deterministic components and reduces those due to interference. A Gaussian window function, $G(t,\omega)$, is convolved with the Wigner–Ville distribution resulting in the pseudo-Wigner–Ville distribution, where

$$G(t,\omega)=\frac{1}{2\pi\sigma_t\sigma_\omega}e^{-(t^2/2\sigma_t^2+\omega^2/2\sigma_\omega^2)}. \tag{4}$$

It has been shown that if σ_t^2 and σ_ω^2 are both greater than zero and if

$$\sigma_t\sigma_\omega\geqslant\tfrac{1}{2}, \tag{5}$$

then the pseudo-Wigner–Ville distribution will contain only positive values. For application to the discrete Wigner–Ville distribution, the Gaussian window function is sampled over the region $\pm 2\sigma_t$ and $\pm 2\sigma_\omega$. It is given by

$$G(p,q)=\frac{1}{2\pi jk\Delta t\Delta\omega}e^{-(p^2/2j^2+q^2/2k^2)}, \tag{6}$$

where p and q are integer values that range over $\pm 2j$ and $\pm 2k$, respectively. The resulting sampled pseudo-Wigner–Ville distribution, $w'(r,m)$, is given by

$$w'(r,m)=\frac{\Delta t\Delta w}{2\pi}\sum_{p=r-j}^{r+j}\sum_{q=m-k}^{m+k}w(p,q)G(p-r,q-m). \tag{7}$$

II. DISPERSION FROM A SIMULATED WAVEFORM

The ability to measure Lamb mode dispersion from time-frequency analysis was first tested on a simulated acoustic waveform.[22] A finite element method, developed by Hamstad and Gary[23,24] for the prediction of acoustic emission signals in plates, was used to generate the simulated signal. A two-dimensional finite element formulation was used to model a surface loading source at the center of a circular plate. The radius of the plate was 0.5715 m, the thickness was 6.35 mm, and the receiver was at a distance of 0.254 m from the source. The force time response was linear with a rapid rise time of 0.1 μs, rising to a constant peak value of 1 N. The material properties of aluminum from

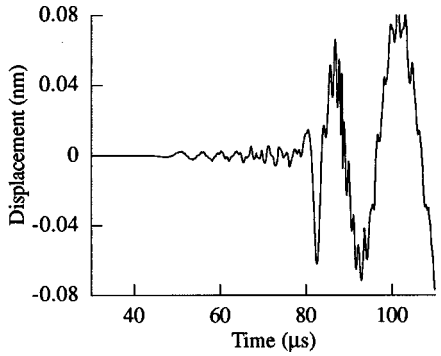

FIG. 1. Early signal arrivals in the filtered, simulated acoustic waveform in aluminum plate.

Kolsky[25] were used. These were a density of 2700 kg/m^3, longitudinal wave velocity of 6320 m/s, and shear wave velocity of 3100 m/s. In the finite element model, 100 cells were used through the plate thickness providing an equiaxial cell size of 0.0635 mm. The resulting simulated signal was sampled at 10 MHz.

As discussed by Gorman and Prosser,[26] sources normal to the plate surface, such as that modeled in this calculation, and the pencil lead break used in the experiments, produce signals with very large, low frequency A_0 mode components. These large amplitude components make it difficult to detect and analyze the higher frequency, smaller amplitude, components of other modes. In the analysis of the simulated waveform, a 20-kHz high-pass Bessel (fourth order) digital filter was used to reduce these large amplitude, low frequency components. The early portion of this filtered waveform is shown in Fig. 1. The full waveform is shown in Fig. 2 along with the corresponding PWVD image which is discussed later. Arriving first in the simulated waveform are the lower frequency components of the S_0 mode. The larger amplitude, lower frequency component of the signal is that of the A_0 mode. Superimposed on these modes are components

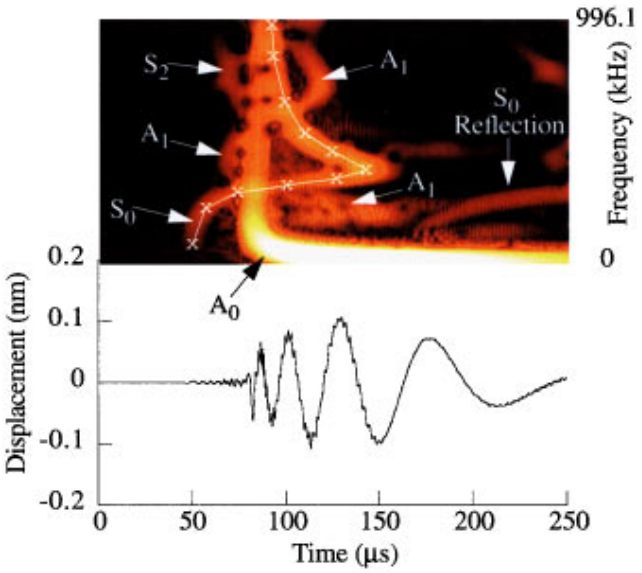

FIG. 2. Pseudo-Wigner–Ville distribution image and corresponding time domain signal for simulated acoustic waveform in aluminum plate.

of the A_1 and S_2 modes, as well as a reflection of the S_0 mode from the outer edge of the plate.

The original Fortran source code for the PWVD calculation from Jeon and Shin[18] was modified for these dispersion measurements. The maximum number of points in the input signal and the maximum number of points in the calculated distribution were increased to provide enhanced time and frequency resolution. Zero padding of the signal was used to increase the frequency resolution of the PWVD calculation with 1024 zeroes padded onto the front of the signal. Additional zeroes were padded onto the end of signal to bring the total number of points to 4096. The PWVD, calculated from the 4096 point waveforms, provided 1024×1024 point resolution in the time-frequency domain. The smoothing parameters for the PWVD calculation, j and k from Eq. (6), were set based on the criterion that the distribution have no negative values. This occurs when

$$j \cdot k \geq \frac{P}{\pi}, \tag{8}$$

where P is the number of points in the original waveform. A square smoothing window was used with j and k both set equal to 37 to satisfy this equation.

The resulting three-dimensional data of the distribution can be visualized in a number of ways. It can be displayed as contour plots, 3D surface plots, or as gray-scale or false color images. The latter approach was used in this work, where the color at a given x and y point in the image represents the amplitude of the distribution at a particular time and frequency. Due to the large amplitude difference between the different modes, the values were first compressed, by raising all values to the 1/4 power, to more clearly show the multiple modes in the same image. An image processing program (NIH Image) was then used to adjust the contrast to provide the best visualization of the image data. The resulting PWVD image for the simulated acoustic signal in aluminum is shown in Fig. 2, along with the original time domain waveform. The different modes are labeled in the PWVD image.

For a given mode of propagation, the arrival time was determined as a function of frequency from the corresponding peak in the PWVD. However, there were several factors which affected the accuracy of this peak determination. First, for a given frequency, there were often several peaks in the PWVD, which corresponded to the arrivals of different modes of propagation. These peaks sometimes had significantly different amplitudes. A simple, amplitude based peak determination routine was insufficient for these calculations. Instead, an image processing approach was used to initially determine the approximate value of peaks at different frequency points for a given mode. A point and click selection tool (in NIH image) was used to obtain approximate peak locations at selected frequency points. These frequency and time values were saved into a text file which was then used as input for a peak determination program. In the peak determination program, linear interpolation was used to provide an estimate of the peak times for all of the frequency values between those selected with the image processing program. In the PWVD image for the simulated waveform in Fig. 2, the peak values selected for the S_0 mode along with the linear interpolations between the points are also shown. Then, for each mode and at each frequency point, a simple peak search routine was used to find the time for the actual peak within a predefined neighborhood of the approximate value. For these calculations, a window of ±15 points in time (±6 μs) was used to define the allowable neighborhood for the peak search routine.

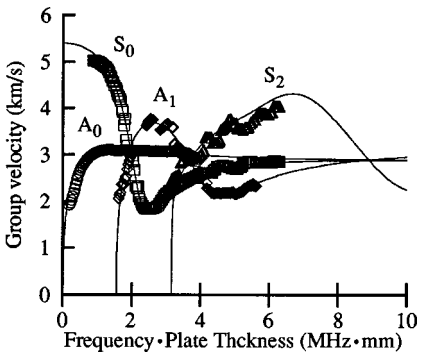

FIG. 3. Group velocity of Lamb modes measured from PWVD analysis of a simulated waveform in aluminum plate compared to theoretical Lamb dispersion curves.

Another problem in determining the time for the peak was the limited time resolution of the PWVD. The reduction from the 4096 point, 0.1-μs sampled waveform, to 1024 points in time resulted in a resolution of only 0.4 μs for the PWVD. To improve the resolution in determining the peak, and thus the arrival time and resultant group velocity, a seven point cubic spline fit was used. The final problem in peak determination was background ''noise'' in the PWVD calculation. Smoothing reduced, but did not entirely eliminate, the problem of cross terms from multiple frequency components. This background ''noise'' made the peak determination more difficult, particularly for smaller amplitude signal components.

The group velocity dispersion was then calculated using the measured peak times (i.e., arrival times) as a function of frequency for the different modes, together with the known propagation distance. For the simulated waveform, the propagation distance was known exactly with no experimental uncertainty. The results are plotted in Fig. 3, along with the known group velocity dispersion curves for these modes in aluminum. As can be seen in this figure, the agreement between the PWVD calculated dispersion and theoretical curves for the S_0 and A_0 modes was excellent. For the A_1 and S_2 modes, the agreement was not quite as good. The effect of the background noise in the PWVD calculation, together with the much smaller amplitudes of these modes, resulted in larger discrepancies between calculated and theoretical velocities.

III. EXPERIMENTAL RESULTS FOR A COMPOSITE PLATE

The time-frequency dispersion measurement technique was further demonstrated with experimental measurements in a graphite/epoxy composite plate. Although this technique can be used on a single waveform, as demonstrated in the

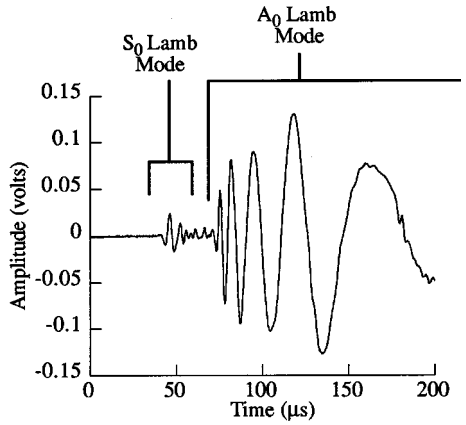

FIG. 4. Typical signal generated by a lead break source in a gr/ep plate identifying S_0 and A_0 Lamb mode components.

previous section, these experimental results were obtained from several measurements. The added uncertainty in position measurements, along with the already coarse time determination in the PWVD analysis, provided the motivation for using additional measurements. Otherwise, the same image processing based analysis for approximate peak determination, followed by peak searching with a cubic spline fit, was used.

The measurements were performed on a 16 ply unidirectional plate of AS4/3502 graphite/epoxy. The nominal plate thickness was 2.26 mm with lateral dimensions of 0.508 m along the fiber direction (0° direction) and 0.381 m along the 90° direction. Signals were generated by fracturing a 0.5-mm-diameter pencil lead on the surface of the plate (Hsu–Neilsen source). This source mechanism produces broadband, transient acoustic waves and is often used to simulate acoustic emission signals. Figure 4 shows a typical waveform produced by this source mechanism in the thin composite plate. The distance of propagation from source to receiver for this signal was 12.1 cm along a direction perpendicular to the fibers. Identified are the lowest order symmetric and antisymmetric Lamb mode components. No higher order modes were observed in the experimental waveform because of the smaller thickness plate used and the large attenuation of high frequency acoustic waves in this composite material.

Another factor which may have prevented observation of higher order modes was the large aperture (1.27 cm diameter) of the sensor used. The sensor was a 3.5-MHz ultrasonic sensor (Panametrics V182). This sensor is heavily damped to optimize its performance in thickness gaging in its intended use. It was operated far off-resonance in detecting these signals which had maximum frequency contents below 500 kHz. In this mode of operation, this sensor provides high fidelity, flat frequency, displacement sensitive response. This has been demonstrated by Prosser[27] by comparing its response to a wide band, displacement sensitive, optical interferometer. Gorman[28] and Ziola and Gorman[1] have previously used a similar type of 5-MHz sensor for studying plate mode AE signals. Papadakis[29] discussed why this type of sensor provides high fidelity, flat frequency response when operated off-resonance. However, the phase cancellation across the large aperture of the sensor can limit its response at higher frequencies. Point contact sensors such as the pinducer and the NIST conical sensor do not suffer from this limitation, but were not available for these experiments. In addition, the overall sensitivity of these point contact sensors is typically less than those with larger sensor area.

The signals were digitized at a sampling frequency of 10 MHz with 12 bit vertical resolution (Digital Wave Corporation F4012). The 2048 point waveforms were padded with 1024 zeros in front of the signal to increase the frequency resolution of the PWVD. Starting at the last zero crossing of the experimental signals, the remaining values were set to zero to eliminate a big discontinuity at the end of the waveform. Such a discontinuity would provide an appearance of high frequency signal content in the PWVD images. Padding these zero values toward the end of the waveform also eliminated the reflection components of the A_0 mode. However, the signals still contained very small amplitude S_0 reflection components. An additional 1024 zeroes were also padded onto the end of the waveform to increase the number of points to 4096.

To improve accuracy, seven measurements were taken at different distances of propagation in 1.27-cm increments over a range of 8.89 cm–16.51 cm. A least squares fit of arrival time versus distance was used to calculate the velocity. The source position was kept fixed for all measurements and the receiver was moved to different positions. At the largest distance, the source and receiver were centered in the plate. Waveform acquisition was triggered by a narrow band, 150-KHz resonant sensor (Physical Acoustics Corporation R15) positioned adjacent to the source.

Images of the PWVD along with the corresponding time domain signals for two distances of propagation along the 90° direction are shown in Fig. 5. The large dispersion of the A_0 mode is clearly seen in both the time domain signals and the PWVD images. The measured Lamb mode dispersion results for propagation perpendicular to the fiber direction are shown in Fig. 6. The uncertainties in the measured velocity values as determined from the uncertainty of the slope in the least squares fit are displayed as error bars on the measured data. Theoretical Lamb mode phase and group velocity dispersion curves for these anisotropic, laminated composite plates were generated using a method from Dong and Huang[30] and Data *et al.*[31] For these theoretical dispersion calculations, nominal material properties, which were obtained from the manufacturer and are listed in Table I, were used. Comparison with theoretical curves shows good agreement, particularly for the A_0 mode. The measured values for the S_0 mode are slightly higher than predicted. Similar results were obtained in phase velocity measurements in this material in an earlier study by Prosser.[6,27] A possible explanation for this slight discrepancy is that the nominal material properties obtained from the manufacturer and used in the theoretical calculations are somewhat different from those of the actual material. Material property variations are not uncommon in graphite/epoxy and may be caused by fiber volume variations, differences in cure processing conditions, and variations in resin chemistry.

The results for propagation along the fiber direction are

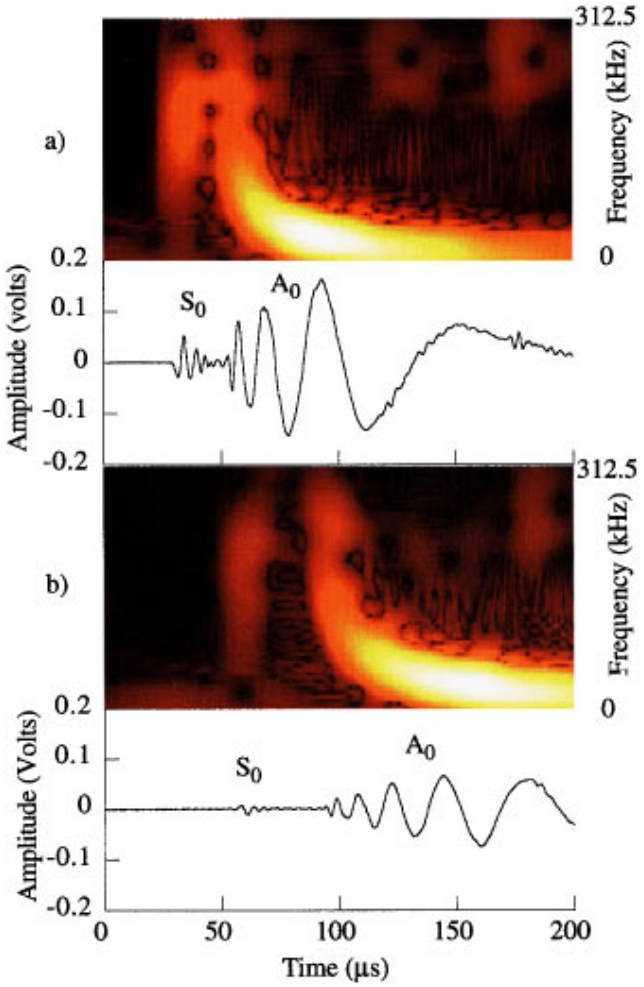

FIG. 5. Pseudo-Wigner–Ville distribution images and corresponding time domain signals for propagation perpendicular to the fiber direction at distances of (a) 8.89 cm and (b) 15.24 cm.

shown in Fig. 7. Comparison with theoretical curves again shows good agreement for the A_0 mode. For the S_0 mode, the measured values in this case are slightly lower than predicted. These results are again consistent with the previous phase velocity measurements[6,27] which showed good agreement between theory and experiment for the A_0 mode, and slightly elevated measured values for the S_0 mode. Again,

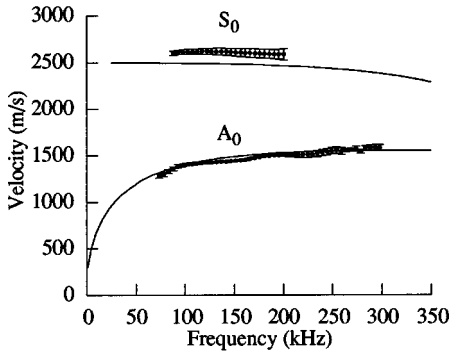

FIG. 6. Measured S_0 and A_0 mode group velocities and comparison with theoretical predictions (solid lines) for propagation perpendicular to the fiber direction.

TABLE I. Properties of AS4/3502 used in theoretical dispersion calculations.

Elastic modulus	(GPa)
c_{11}	10.59
c_{12}	3.09
c_{13}	4.11
c_{33}	147.1
c_{44}	5.97

the discrepancy was attributed to variations in actual material properties from the nominal properties used in the theoretical calculations.

IV. CONCLUSIONS

A time-frequency analysis method using the pseudo-Wigner–Ville Distribution (PWVD) was developed to characterize Lamb mode group velocity dispersion from broadband acoustic signals in plates. The technique was first demonstrated on a simulated waveform. This simulated signal was generated with a two-dimensional, dynamic finite element method to model propagation in an isotropic, aluminum plate. The simulated waveform contained multiple Lamb modes, as well as a reflection from a boundary, which were superimposed in the time domain waveform. The PWVD was able to separate these modes in time-frequency space to allow dispersion measurements. In this analysis, the arrival times, as a function of frequency, for the different modes are determined from the times of the corresponding peaks in the PWVD. These peak times were first estimated using an image processing program. Then the actual peak times were determined with a peak detection routine based on the image processor based estimates. The resolution of peak time determination was then further improved with a cubic spline fit to the peak. The arrival times were then used with the known propagation distance to calculate the group velocity dispersion. From the simulated waveform, portions of the group velocity dispersion for the S_0, A_0, A_1, and S_2 Lamb modes were determined. The agreement between the time-frequency measured dispersion and the known theoretical dispersion curves for aluminum was excellent for the S_0 and A_0 modes. The agreement for the A_1 and S_2 modes was adequate, but less than that for the other two modes. The

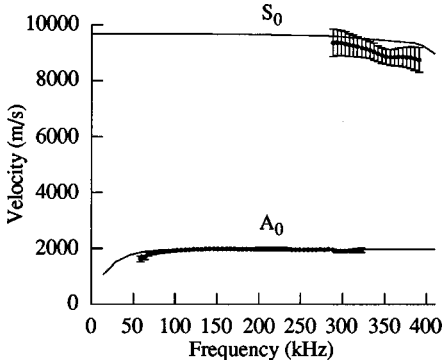

FIG. 7. Measured S_0 and A_0 mode group velocities and comparison with theoretical predictions (solid lines) for propagation along the fiber direction.

amplitude of the A_1 and S_2 modes was much smaller in the time domain signal and the resulting PWVD. The peak detection was therefore much more susceptible to ''noise'' in the PWVD. This ''noise'' is the result of the interaction of multiple frequency components in the time-frequency calculation which is reduced, but not entirely eliminated, by the smoothing used in the PWVD calculation.

The time-frequency dispersion measurement technique was further demonstrated on experimental data. Broadband acoustic signals were acquired in anisotropic, unidirectional graphite/epoxy composite plates. Measurements were made for propagation both along, and perpendicular to the fiber direction. A pencil lead fracture (Hsu–Neilsen source) on the surface of the plate was used to generate the acoustic signals. Broadband contact ultrasonic sensors were used to acquire the waveforms. The signals contained only the lowest order symmetric and antisymmetric Lamb modes. The same process was used to determine the arrival times for these two modes from the peaks in the PWVD. However, in this case, a least squares fit from a number of propagation distances was used to calculate the dispersion. The added uncertainty in the distance measurement, along with the limited time resolution for the PWVD analysis, was the motivation for using the least square approach. Higher frequency sampling of the waveform could be used to increase the time resolution. However, the resulting increased number of points would significantly increase the time required for the PWVD calculation. The measured dispersion was compared with theoretical predictions. The agreement was good with discrepancies consistent with previous phase velocity dispersion measurements in this material. These discrepancies have been attributed to a lack of knowledge of the exact material properties for this composite. The nominal properties from the manufacturer were used in the theoretical dispersion calculations. It is widely known that actual material properties for a composite can vary as a result of a number of factors including resin chemistry variations, different processing conditions, and different fiber volume ratios.

Dispersion measurement from time-frequency analysis can offer a number of advantages in comparison to more traditional velocity measurement techniques. The first is that when a broadband acoustic source is used, few measurements, possibly only one, may be required to characterize dispersion for multiple modes over a wide frequency range. This can be particulary important when access time to specimens is limited, or when testing of a large number of specimens is required. The ability to analyze complex waveforms in which multiple modes and/or reflections are superimposed is also an advantage. Additionally, this method provides a direct measurement of the group velocity dispersion which is sometimes the desired quantity. Significant errors can occur when calculating group velocity from measured phase velocity data.

ACKNOWLEDGMENTS

The authors would like to acknowledge Jae-Jin Jeon and Young S. Shin of the Department of Mechanical Engineering, Naval Postgraduate School, who provided the original computer source code for performing the pseudo-Wigner–Ville Distribution. The authors would also like to acknowledge the efforts of William Winfree of the Nondestructive Evaluation Science Branch at NASA Langley Research Center who provided computer code which aided in determining the peaks of the distributions and displaying the images of the pseudo-Wigner–Ville distributions. Dr. Winfree also provided useful editorial comments in the preparation of this manuscript.

[1] S. M. Ziola and M. R. Gorman, ''Source location in thin plates using cross-correlation,'' J. Acoust. Soc. Am. **90**, 2551–2556 (1991).
[2] A. K. Mal, C.-C. Yin, and Y. Bar-Cohen, ''The influence of material dissipation and imperfect bonding on acoustic wave reflection from layered solids,'' Rev. Prog. Quant. Nondestr. Eval. **7B**, 927–934 (1988).
[3] D. E. Chimenti and A. H. Nayfeh, ''Leaky Lamb waves in fibrous composite laminates,'' J. Appl. Phys. **58**, 4531–4538 (1985).
[4] K. Balasubramaniam and J. L. Rose, ''Physically based dispersion curve feature analysis in the NDE of composites,'' Res. Nondestruct. Eval. **3**, 41–67 (1991).
[5] W. Sachse and Y. H. Pao, ''On the determination of phase and group velocities of dispersive waves in solids,'' J. Appl. Phys. **49**, 4320–4327 (1978).
[6] W. H. Prosser and M. R. Gorman, ''Plate mode velocities in graphite/epoxy plates,'' J. Acoust. Soc. Am. **96**, 902–907 (1994).
[7] N. A. Schumacher, C. P. Burger, and P. H. Gien, ''A laser-based investigation of higher-order modes in transient lamb waves,'' J. Acoust. Soc. Am. **93**, 2981–2984 (1993).
[8] D. Alleyne and P. Cawley, ''A two-dimensional Fourier transform method for the measurement of propagating multimode signals,'' J. Acoust. Soc. Am. **89**, 1159–1168 (1991).
[9] R. D. Costley, Jr. and Y. H. Berthelot, ''A laser based technique to resolve mode propagation of Lamb waves in plates,'' Second International Conference on Acousto-Ultrasonics: Acousto-Ultrasonic Materials Characterization, pp. 85–94 (June 24–25, 1993).
[10] S. M. Kay and S. L. Marple, Jr., ''Spectrum analysis—A modern perspective,'' Proc. IEEE **69**, 1380–1419 (1981).
[11] S. W. Lang, A. L. Kurkjian, J. H. McClellan, C. F. Morris, and T. W. Parks, ''Estimating slowness dispersion from arrays of sonic logging waveforms,'' Geophysics **52**, 530–544 (1987).
[12] H. D. Leslie and C. J. Randall, ''Multipole sources in boreholes penetrating anisotropic formations: Numerical and experimental results,'' J. Acoust. Soc. Am. **91**, 12–27 (1992).
[13] J. H. McClellan, ''Two-dimensional spectrum analysis in sonic logging,'' IEEE ASSP Magazine 12–18 (1988).
[14] H. Kwun and K. A. Bartels, ''Experimental observation of wave dispersion in cylindrical shells via time-frequency,'' J. Acoust. Soc. Am. **97**, 3905–3907 (1995).
[15] L. Cohen, ''Time-frequency distributions—A review,'' Proc. IEEE **77**, 941–981 (1989).
[16] S. Grade and K. Gram-Hansen, ''The analysis of nonstationary signals,'' Sound Vib. 30th Anniversary Issue **31**, 40–46 (1997).
[17] E. Wigner, ''On the quantum correction for thermodynamic equilibrium,'' Phys. Rev. **40**, 749–759 (1932).
[18] J. Jeon and Y. S. Shin, ''Pseudo Wigner–Ville distribution, computer program and its applications to time-frequency domain problems,'' Naval Postgraduate School Report NPS-ME-93-002 (1993).
[19] T. J. Wahl and J. S. Bolton, ''The application of the Wigner distribution to the identification of structure-borne noise components,'' J. Sound Vib. **163**, 101–122 (1993).
[20] B. Boashsah, ''Note on the use of the Wigner distribution for time-frequency signal analysis,'' IEEE Trans. Acoust., Speech, Signal Process. **36**, 1518–1521 (1988).
[21] J. Ville, ''Theorie et Applications de la Notion de Signal Analytique,'' Cables Transm. **2a**, 61–74 (1948).
[22] M. A. Hamstad, private communication (1998).
[23] J. Gary and M. A. Hamstad, ''On the far-field structure of waves generated by a pencil lead break on a thin plate,'' J. Acoust. Emiss. **12**, 157–170 (1994).
[24] M. A. Hamstad, J. Gary, and A. O'Gallagher, ''Far-field acoustic emission waves by three-dimensional finite element modeling of pencil-lead breaks on a thick plate,'' J. Acoust. Emiss. **14**, 103–114 (1996).
[25] H. Kolsky, *Stress Waves in Solids* (Dover, New York, 1953).

[26] M. R. Gorman and W. H. Prosser, ''AE source orientation by plate wave analysis,'' J. Acoust. Emiss. **9**, 283–288 (1991).
[27] W. H. Prosser, ''The propagation characteristics of the plate modes of acoustic emission waves in thin aluminum plates and thin graphite/epoxy composite plates and tubes,'' NASA Technical Memorandum 104187 (November, 1991).
[28] M. R. Gorman, ''Plate wave acoustic emission,'' J. Acoust. Soc. Am. **90**, 358–364 (1990).
[29] E. P. Papadakis, ''Broadband flaw detection transducers: Application to acoustic emission pulse shape and spectrum recording based on pulse echo response spectrum corrected for beam spreading,'' Acustica **46**, 293–298 (1980).
[30] S. B. Dong and K. H. Huang, ''Edge vibrations in laminated composite plates,'' J. Appl. Mech. **52**, 433–438 (1985).
[31] S. K. Datta, A. H. Shah, and W. Karunasena, ''Wave propagation in composite media and material characterization,'' in *Elastic Waves and Ultrasonic Nondestructive Evaluation*, edited by S. K. Datta, J. D. Achenbach, and Y. S. Rajapakse (Elsevier Science, North-Holland, 1990), pp. 159–167.

Working gases in thermoacoustic engines

James R. Belcher
Jackson State Community College, 2046 North Parkway, Jackson, Tennessee 38301

William V. Slaton, Richard Raspet, Henry E. Bass, and Jay Lightfoot[a)]
Department of Physics and Astronomy, University of Mississippi, University, Mississippi 38677

(Received 10 February 1998; accepted for publication 17 February 1999)

The best working gases for thermoacoustic refrigeration have high ratios of specific heats and low Prandtl numbers. These properties can be optimized by the use of a mixture of light and heavy noble gases. In this paper it is shown that light noble gas–heavy polyatomic gas mixtures can result in useful working gases. In addition, it is demonstrated that the onset temperature of a heat driven prime mover can be minimized with a gas with large Prandtl number and small ratio of specific heats. The gas properties must be optimized for the particular application of thermoacoustics; it cannot be assumed that high specific heat ratio and low Prandtl number are always desirable. © *1999 Acoustical Society of America.* [S0001-4966(99)04205-8]

PACS numbers: 43.35.Ud [DEC]

INTRODUCTION

Research in thermoacoustics has been largely driven by the design and construction of mechanically driven refrigerators.[1,2] Large heat flows and temperature spans are desirable in such devices. In his review article, Swift[3] shows that the acoustically driven heat flux is proportional to $\gamma-1$, where γ is the ratio of specific heats of the working gas and that the heat flux is approximately proportional to $1/(1-\sqrt{N_{\rm pr}})$, where $N_{\rm pr}$ is the Prandtl number of the gas. Therefore, a low Prandtl number and high ratio of specific heats are desirable for mechanically driven refrigeration. The best gas mixtures for these devices are binary mixtures of noble gases, the best stable mixture being helium and xenon. However, xenon is a relatively expensive gas.[4]

In this paper it is shown that molar averages of gas properties can be used for quick estimates of the gas properties of mixtures of gases. Next the gas properties of monatomic and polyatomic gases are calculated using collision integral theory to investigate whether such mixtures may produce acceptable gas properties at lower expense.

Then the theory of minimum temperature gradient for the onset of a thermoacoustic prime mover is presented and used to demonstrate that maximum specific heat ratio and minimum Prandtl number are not universally desirable for all thermoacoustic devices. Measurements of onset temperature difference with sulfur-hexafluoride–helium mixtures and argon–helium mixtures show good agreement with theory and compare the use of nonnoble gases in thermoacoustic mixtures to the results with noble gas mixtures.

I. THEORY

A. Estimation of gas properties

The viscosity and thermal conductivity of a gas are similar in that they involve the transport of some physical property through the gas and depend upon the same intermolecular collisions. A good description of the transport properties of viscosity and thermal conductivity may be obtained if the following assumptions are made:[5]

(1) The molecules are rigid, nonattracting spheres with diameter σ and the total scattering cross section is $\sigma_0=4\pi\sigma^2$.
(2) The average molecular speed is $\bar{v}=\sqrt{8kT/\pi m}$, where k is Boltzmann's constant, m is the mass of the molecule, and T is the temperature in Kelvin.
(3) All molecules travel in a direction parallel to one of the coordinate axes.

The proportionality constant for the associated momentum or energy flux yields the viscosity and the thermal conductivity.

Based upon these assumptions, the viscosity and thermal conductivity for pure gases can be written as[5–7]

$$\eta=\frac{5}{16}\frac{\sqrt{\pi MkT}}{\sigma_0} \tag{1}$$

and

$$\kappa=\frac{\eta}{M}\left(C_v+\frac{9R}{4}\right), \tag{2}$$

where the gas constant $R=1.99$ cal/mol K, C_v is the molar specific heat at constant volume, and M is the molecular weight of the gas. This is the Eucken corrected thermal heat conductivity as appears in Ref. 5, Equation (8.2-33). This expression may be rewritten as $\kappa=\eta c_v(9\gamma-5)/4$, where c_v is the specific heat per unit mass at constant volume.

Gamma can be approximated by $\gamma\cong 1+2/N$, where N is the number of degrees of freedom for the gas (see Fig. 1). For a monatomic gas $N=3$ and $\gamma\cong 5/3$, while for other gases $N>3$ and $\gamma<5/3$. The Prandtl number can be written as $N_{\rm pr}=c_p\eta/\kappa\cong 4\gamma/(9\gamma-5)$, where c_p is the specific heat per

[a)]Present address: Dynetics, Inc., 1000 Explorer Blvd., Huntsville, AL 35806.

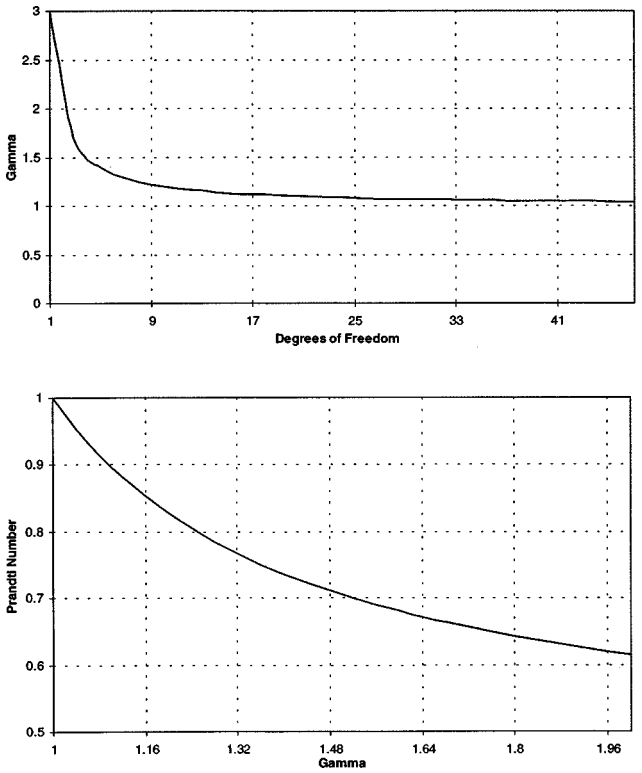

FIG. 1. Dependence of gamma on the degrees of freedom and the Prandtl number versus gamma for pure gases.

unit mass at constant pressure, η is the viscosity, and κ is the thermal conductivity of the gas. The relationship between Prandtl number, gamma, and degrees of freedom is displayed in Fig. 1. $N_{\mathrm{pr}} \cong 0.68$ for monatomic gases, and approaches one as γ approaches one for a more complicated gas.

B. Estimation of binary gas mixture properties

The molar specific heats for a binary gas mixture can be written as a linear combination of the individual component's capacities[6,8]

$$C_{p_{12}} = x_1 C_{p_1} + x_2 C_{p_2} \tag{3}$$

and

$$C_{v_{12}} = x_1 C_{v_1} + x_2 C_{v_2}, \tag{4}$$

where x_1 is the mole fraction of species one, x_2 the mole fraction of species two, C_{p_1} and C_{v_1} are the heat capacities for species one, and C_{p_2} and C_{v_2} are the heat capacities for species two. Gamma for the binary gas mixture can thus be computed by the ratio of Eqs. (3) and (4).

The specific heat per unit mass at constant pressure for a binary mixture can be expressed as

$$c_{p_{12}} = \frac{x_1 C_{p_1} + x_2 C_{p_2}}{x_1 M_1 + x_2 M_2}, \tag{5}$$

where M_1 is the molecular weight (g/mol) of species one and M_2 is the molecular weight (g/mol) of species two.

To a first approximation the viscosity can be written as

$$\eta_{12} = x_1 \eta_1 + x_2 \eta_2,$$

where η_1 is the viscosity of species one and η_2 is the viscosity of species two. This can be expanded using Eq. (1) to give

$$\eta_{12} = \frac{5}{64} \sqrt{\frac{kT}{\pi}} \left\{ x_1 \frac{\sqrt{M_1}}{\sigma_1^2} + x_2 \frac{\sqrt{M_2}}{\sigma_2^2} \right\}, \tag{6}$$

where σ_1 is the diameter of a molecule of species one, and σ_2 is the diameter of a molecule of species two.

The thermal conductivity for a binary mixture can similarly be written as $\kappa_{12} = x_1 \kappa_1 + x_2 \kappa_2$ and from Eq. (2),

$$\kappa_{12} = \frac{5}{64} \sqrt{\frac{kT}{\pi}} \left\{ \frac{x_1}{\sqrt{M_1}} \frac{C_{v_1} + \frac{9R}{4}}{\sigma_1^2} + \frac{x_2}{\sqrt{M_2}} \frac{C_{v_2} + \frac{9R}{4}}{\sigma_2^2} \right\}. \tag{7}$$

These formulas for the viscosity and thermal conductivity assume constant molecular cross section with temperature and do not account for the dependence of the average cross section on the mixture composition. For more accurate empirical formula see Eqs. (7) and (16) of Ref. 8.

TABLE I. Gas properties.

Gas	Ref. 9 Mass (g/mol)	Ref. 5 ϵ/κ (°K)	Ref. 5 σ (Å)	Ref. 9 c_p (cal/mol °K)	Ref. 9 c_v (cal/mol °K)	Ref. 9 γ	Ref. 9 κ (cal/s cm °C)	Ref. 9 η 10^{-4} poise
Helium	4	10.22	2.566	4.968	3.0478	1.63	0.000 35	1.96
Neon	20.18	35.7	2.789	4.968	3.026	1.642	0.000 117	3.173
Argon	39.94	124	3.418	5.000	2.996	1.668	0.000 0415	2.2638
Krypton	83.80	190	3.61	5.328	3.1968	1.67	0.000 022 8	2.53
Xeon	131.3	229	4.055	5.016	3.02	1.66	0.000 013 0	2.31
Air	29	84	3.698	6.96	4.97	1.4	0.000 062	1.846
SF_6	146	200.9	5.51	23.26	22.36	1.04	0.000 033	1.53
O_2	32	113	3.433	7.019	5.028	1.396	0.000 063 9	2.063

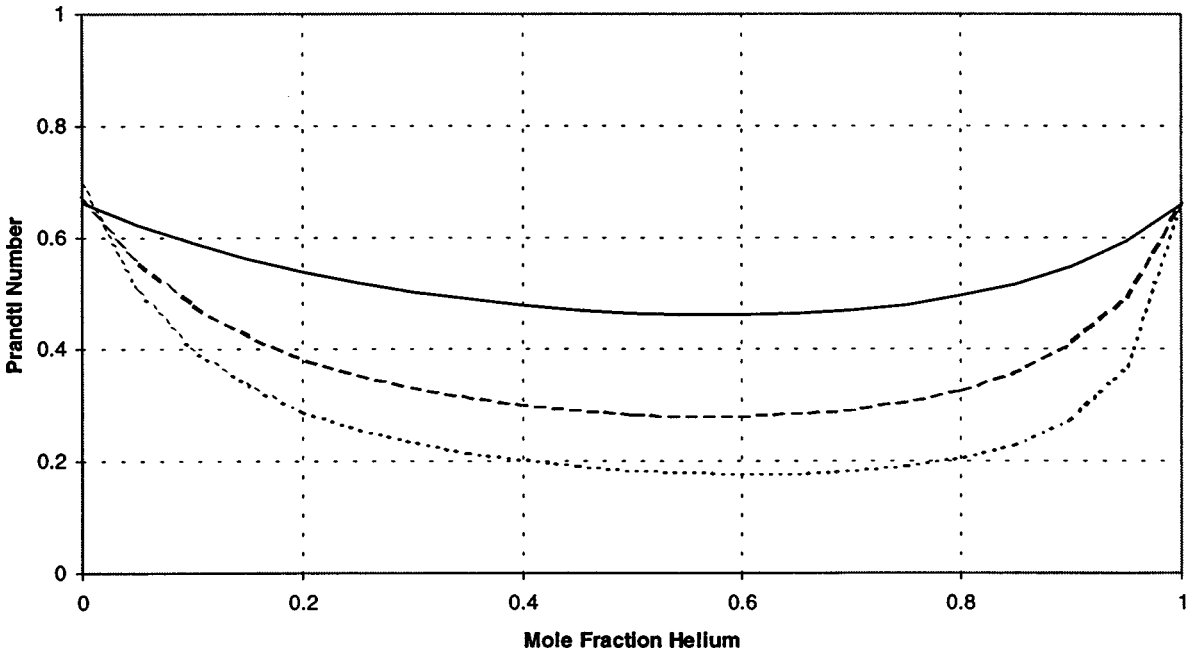

FIG. 2. Binary gas mixtures using the simplified model. Helium–Neon (solid line); Helium–Argon (large dashed line); Helium–Krypton (small dashed line).

To this level of approximation the Prandtl number can be calculated from Eqs. (5), (6), and (7) as $[N_{\mathrm{pr}}]_{\mathrm{mix}} = (c_{p_{12}}\eta_{12})/\kappa_{12}$:

$$[N_{\mathrm{pr}}]_{\mathrm{mix}} = \frac{(x_1(C_{p_1}-C_{p_2})+C_{p_2})}{(x_1(M_1-M_2)+M_2)} \times \frac{\left(x_1\left(\frac{\sqrt{M_1}}{\sigma_1^2}-\frac{\sqrt{M_2}}{\sigma_2^2}\right)+\frac{\sqrt{M_2}}{\sigma_2^2}\right)}{\left(x_1\left(\frac{C_{v_1}+\frac{9R}{4}}{\sigma_1^2\sqrt{M_1}}-\frac{C_{v_1}+\frac{9R}{4}}{\sigma_2^2\sqrt{M_2}}\right)+\frac{C_{v_1}+\frac{9R}{4}}{\sigma_2^2\sqrt{M_2}}\right)}. \tag{8}$$

Equation (8) shows the dependence of the Prandtl number on the ratio of the molecular weights of the gases present in the mixture. The parameters necessary to compute the Prandtl numbers for the different gases considered for thermoacoustic devices are presented in Table I.[9] The Prandtl number for binary mixtures of helium–neon, helium–argon, and helium–krypton calculated with the simple model are shown in Fig. 2. These monatomic gases have approximately the same Prandtl number and gamma in their pure states. Binary mixtures produce a decrease in the Prandtl number with a minimum occurring when the lighter gas is approximately 66% by volume. The mixture of helium–neon has a mass ratio of 5 and provides the smallest change to the Prandtl number. The mixture of helium–krypton has a mass ratio of 16 and has the largest effect on the Prandtl number.

The viscosity and thermal conductivity for a gas mixture composed of n components is presented by Hirshfelder *et al.*[5] Equations (8.2-25), (8.2-36), and (8.2-40) of Ref. 5 contain the full transport theory calculation for the viscosity and thermal conductivity, respectively. These equations require knowledge of the force constants for the assumed interaction potential, Lennard–Jones in this case, and collision integrals, $\Omega^{(l,s)}$ which are a function of temperature. The force constants that were used in this calculation can be found in Table I.

Theoretical predictions of the Prandtl number for helium mixed with argon, krypton, and xenon are shown in Fig. 3 for 300 K. A mixture containing approximately 60% helium and 40% of any of the other gases produces a minimum in the Prandtl number. The maximum decrease of 67% occurs for a helium–xenon mixture. The simplified model [Eq. (9)] produces the same general trend in the Prandtl number as the more complicated transport theory calculations. This is shown in Figs. 2 and 3. Figure 4 shows little change in the ratio of specific heats (gamma) with concentration since all gases are monatomic.

Figure 5 shows Prandtl number predictions for mixture of air with helium, argon, neon, and krypton at 300 K. Air is assumed to be diatomic. The Prandtl number varies very little for air mixed with argon, neon, and krypton, but varies by 34% for a 42% air–58% helium mixture. Gamma decreases linearly from the noble gas value of 1.67 to the 1.4 value for air.

Comparing the Prandtl numbers for a helium–argon mixture from Fig. 3 and the air–helium mixture from Fig. 5 shows that the two closely resemble each other. The minimum in the air–helium mixture curve is shifted by 2%, with a minimum Prandtl number of 0.44 compared to 0.42 for helium–argon mixtures. Comparing values for helium–neon mixtures and air–krypton mixtures, the difference in the Prandtl number is negligible. This observation suggests that the Prandtl number for binary gas mixtures is mass ratio

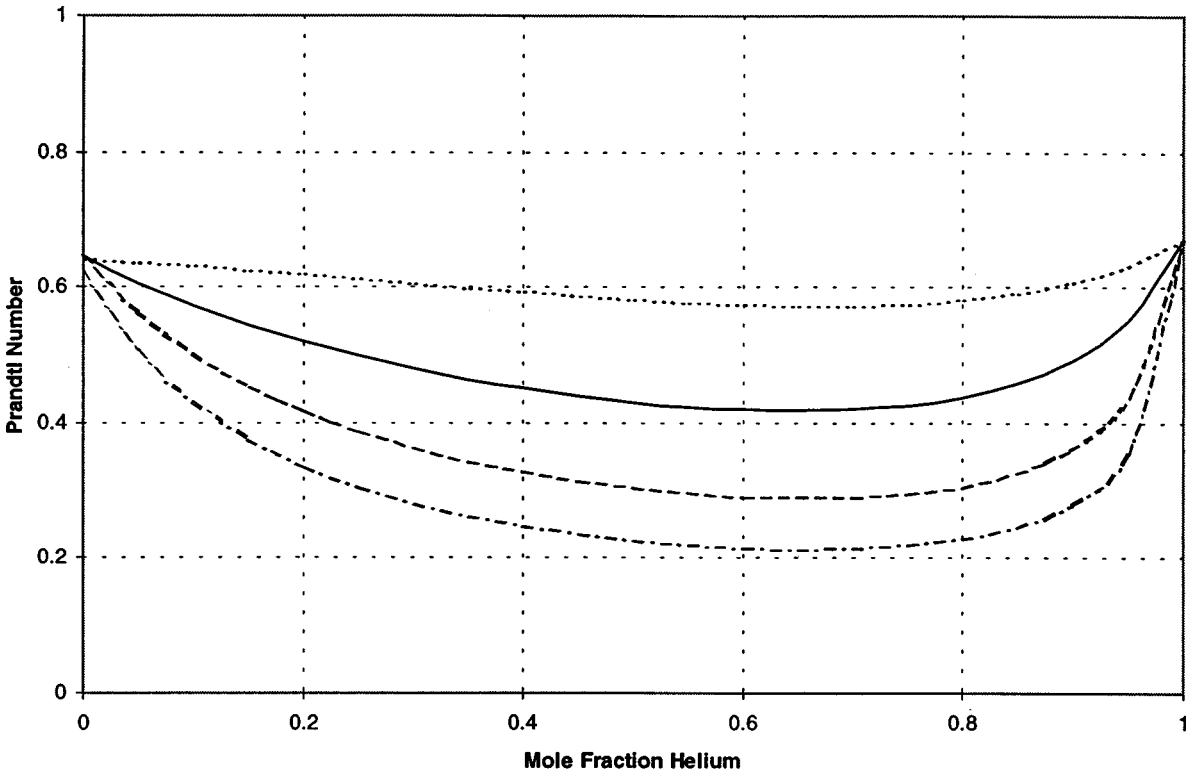

FIG. 3. The Prandtl number for binary mixtures at 1 atm and temperature of 300 K calculated using the theory of Ref. 5. Helium–Neon (dotted line); Helium–Argon (solid line); Helium–Krypton (dashed line); Helium–Xenon (dot-dash line).

dependent as was suggested in Fig. 2. The larger species' mass should be a minimum of five times larger than the smaller species in the mixture for any significant effect on the Prandtl number.

The larger the molecular mass of the heavier species the smaller the amount needed to decrease the Prandtl number. Figure 6 shows the Prandtl number and gamma for a gas mixture of helium and sulfur hexafluoride (SF_6), which is 36.5 times heavier than helium. A mixture containing 10% SF_6 decreases the Prandtl number by 45% with gamma only decreasing by 16%. The minimum Prandtl number occurs for a mixture of 35% SF_6 and 65% helium.

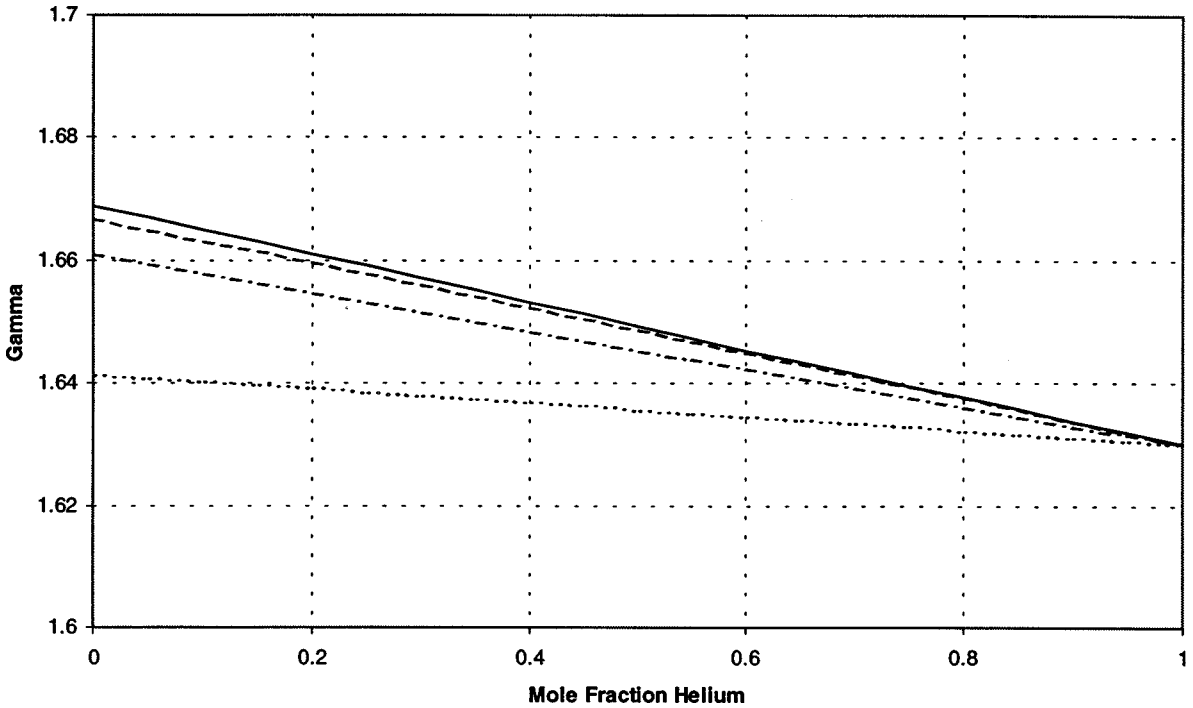

FIG. 4. The ratio of the specific heats for binary mixtures at 300 K and 1 atm. Helium–Neon (dotted line); Helium–Argon (solid line); Helium–Krypton (dashed line); Helium–Xenon (dot-dash line).

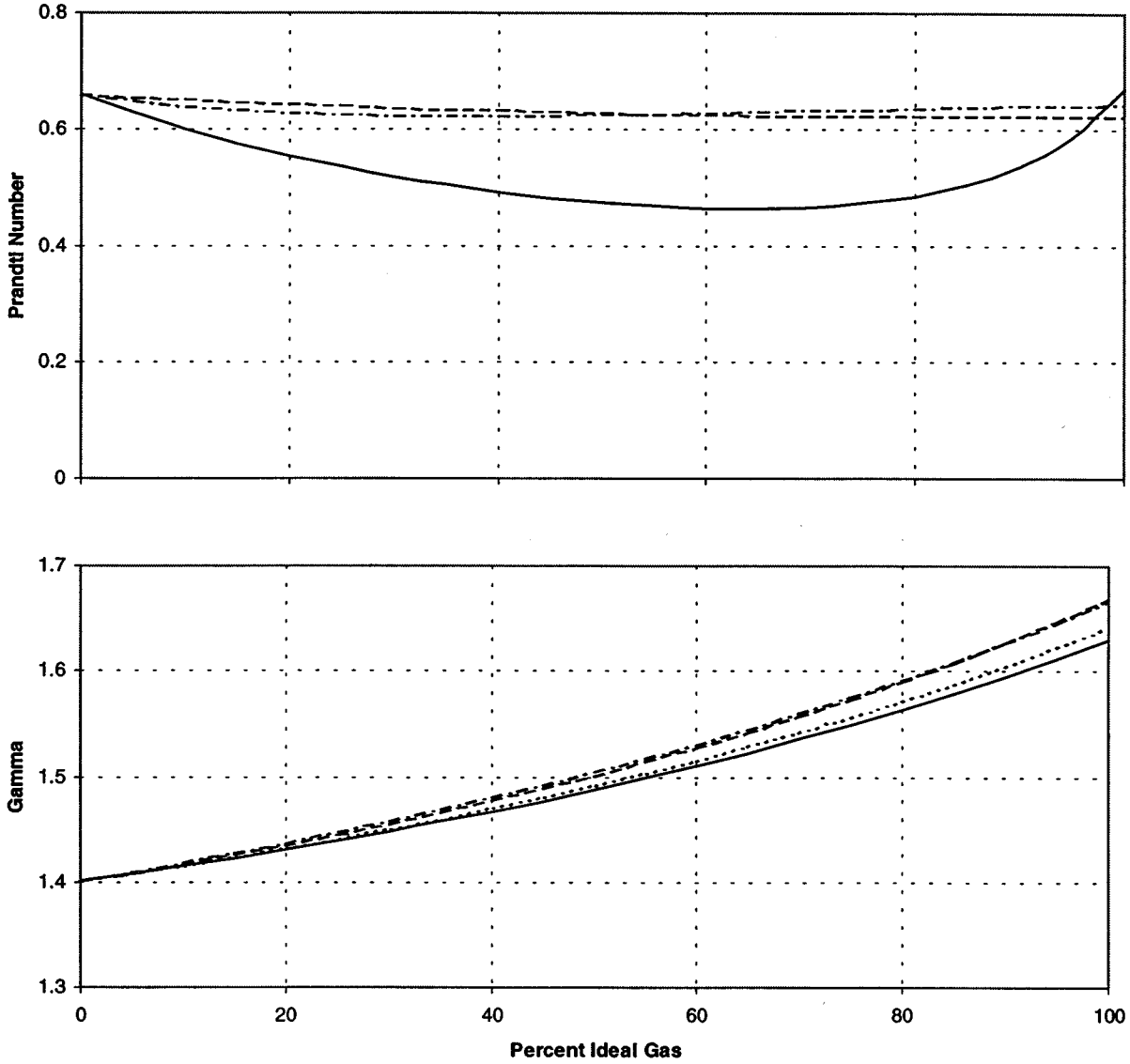

FIG. 5. Prandtl Number and ratio of specific heats for air mixed with different ideal gases calculated using the theory of Ref. 5. Air–Helium (solid line); Air–Argon (dashed line); Air–Neon (dotted line); Air–Krypton (dash-dot line).

C. Prime mover onset

The minimum nondimensional temperature difference necessary for spontaneous oscillation can be written as[10]

$$\tau_{\min}=\frac{\Omega(1-N_{\mathrm{pr}})}{\mathrm{Im}\{F^*(\lambda_T)/F^*(\lambda)\}}\sqrt{[(\gamma-1)\mathrm{Im}\,F^*(\lambda_T)+\bar{\dot{w}}_{\mathrm{ext}}][\mathrm{Im}\,F^*(\lambda)/|\Omega F(\lambda)|^2+\bar{\dot{w}}_{\mathrm{ext}}]},\tag{9}$$

where Ω is the stack porosity. Thermoacoustic gain and thermoviscous dissipation of sound in porous materials may be described theoretically with the use of a thermoviscous dissipation function.[11] Viscous effects are then expressed in terms of $F(\lambda)$, where λ is the shear wave number $=R(\rho_0\omega/\eta)^{1/2}$ and thermal effects are expressed in terms of $F(\lambda_T)$, where λ_T is the thermal disturbance number $=R(\rho_0\omega C_p/\kappa)^{1/2}$. $\bar{\dot{w}}_{\mathrm{ext}}$ is the nondimensional form of $\bar{\dot{W}}_{\mathrm{ext}}$, the total rate of energy loss in the heat exchangers and the rest of the resonator other than the stack. We can see that the gas properties play an important role in determining the temperature difference necessary for spontaneous oscillations.

If there were no losses or work outside the stack, the minimum temperature difference would be proportional to $\sqrt{\gamma-1}$ and a minimum onset temperature would occur for γ close to one, which is characteristic of a polyatomic gas. The dependence on Prandtl number is not as clear. There is a multiplicative factor of $(1-N_{\mathrm{pr}})$, which would indicate that Prandtl numbers near one are optimal for low onset temperature, but there are implicit dependencies on N_{pr} contained in the thermoviscous functions $F(\lambda_T)$ and $F(\lambda)$.

In a real prime mover, the heat exchangers and resonator

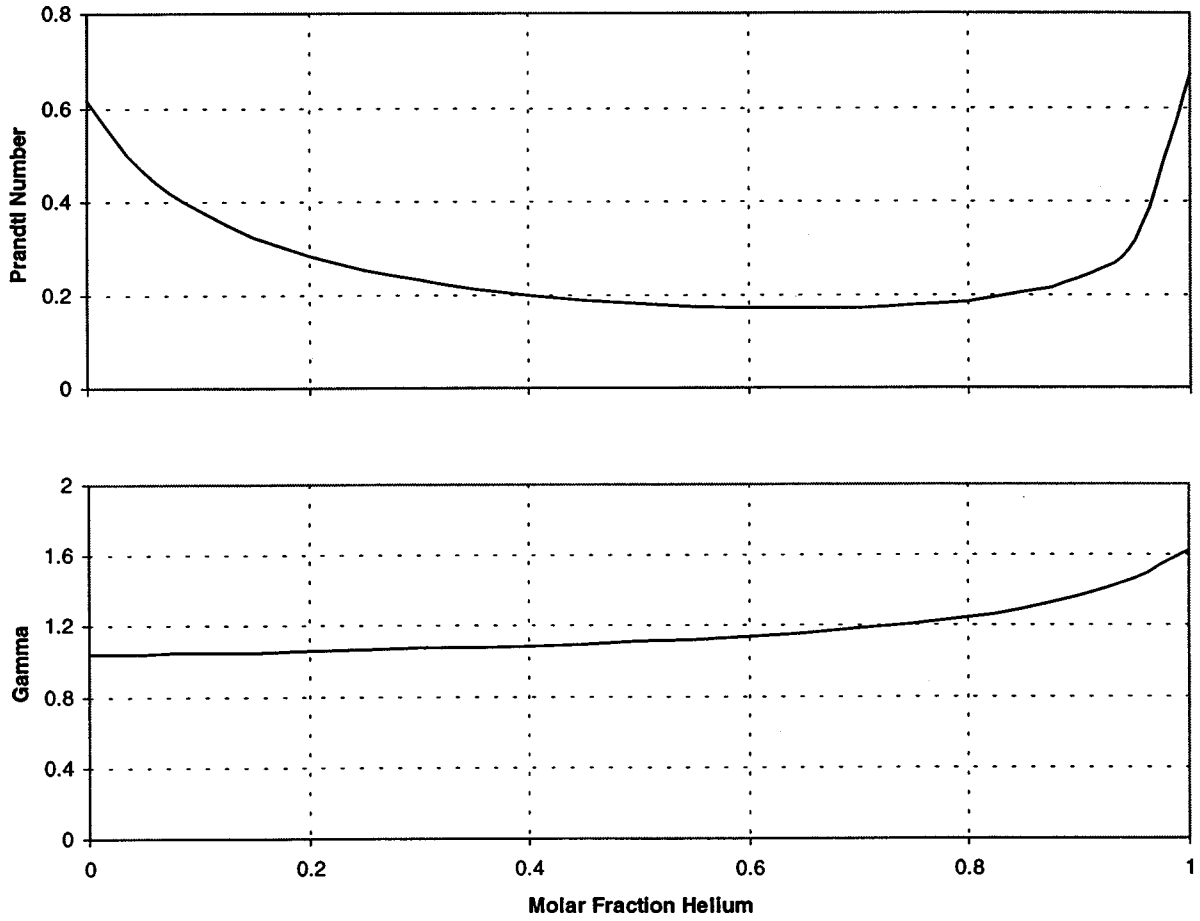

FIG. 6. The Prandtl number and ratio of specific heats for mixtures of helium and SF_6 at 300 K and 1 atm calculated using the theory of Ref. 5.

represent losses to the acoustic wave and contribute to the external work $\dot{\overline{w}}_{\text{ext}}$. The actual gas properties which minimize the onset temperature are a compromise between the ideal case where large Prandtl number and small ratio of specific heats are desirable and the loaded case where small Prandtl number and large ratio of specific heats are desirable.

II. EXPERIMENTAL CONFIGURATION AND MEASUREMENTS

The prime mover shown in Fig. 7 was used to experimentally observe changes in onset temperature for different binary mixtures. The prime mover is an aluminum tube 129 cm in length with an inner diameter of 8.52 cm. The tube is flanged on both ends with a 1.27 cm thick aluminum sleeve. One end is capped with a 1.27 cm thick aluminum disk with a 0.635 cm microphone port. The heat exchangers are 0.05 cm thick parallel plate copper fins spaced 0.102 cm apart encased in a 15.24 cm square copper block that is 0.32 cm thick. The hot heat exchanger has a 0.635 cm hole drilled on each side perpendicular to the fins. Rod heaters are inserted to supply heat. The cold heat exchanger has a an additional 0.635 cm hole drilled parallel to the fins to allow cooling fluid to be circulated through the ends of the fins. The stack is a 5.08 cm long ceramic pore material containing 200 pores per square in. The individual pores have square boundaries

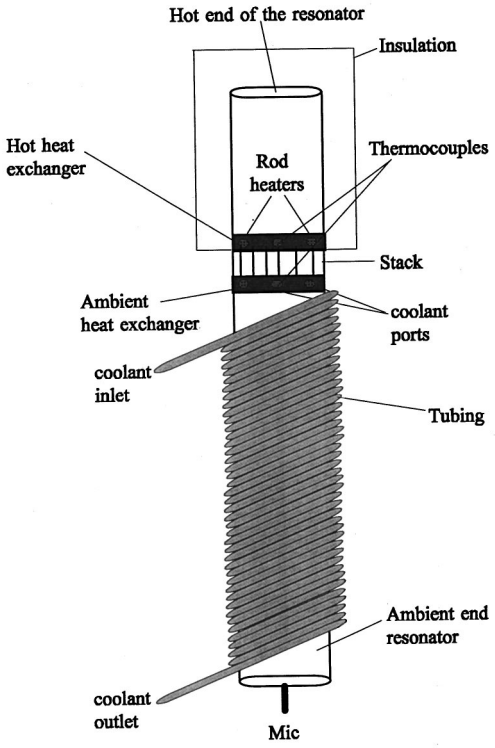

FIG. 7. The prime mover used in the binary gas mixture experiments.

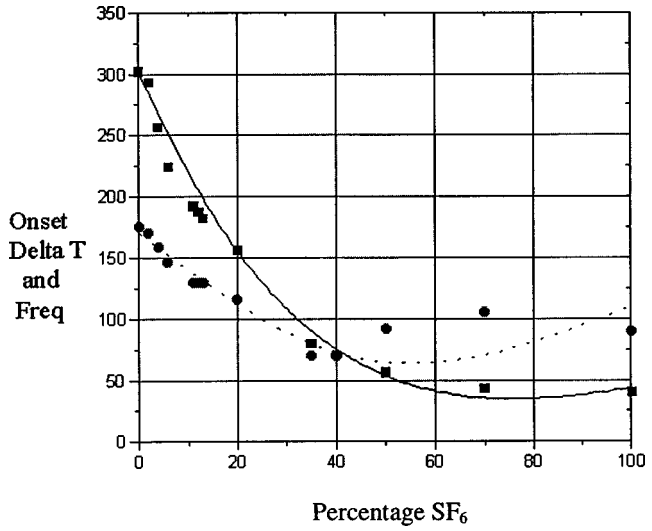

FIG. 8. The onset temperature difference in Kelvin (solid circle experiment, dotted line theory) and frequency in hertz (solid squares experiment, solid line theory) versus the percentage of SF_6 mixed with helium at 1 atm. The temperatures were measured in the heat exchangers.

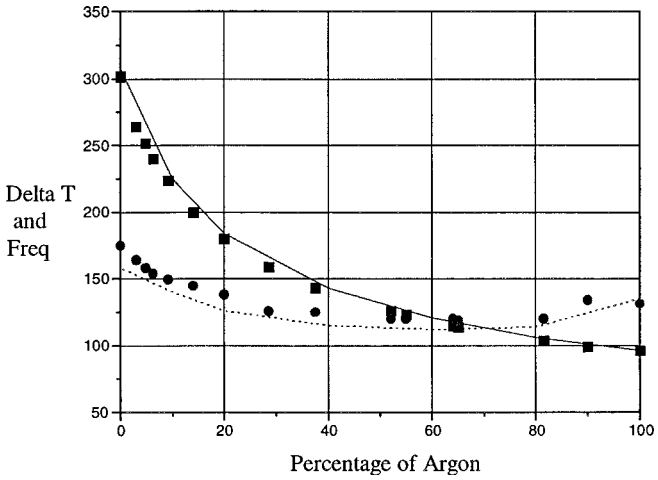

FIG. 9. The onset temperature difference in Kelvin (solid circle experiment, dotted line theory) and frequency in hertz (solid squares experiment, solid line theory) versus the percentage of argon mixed with helium at 1 atm. The temperatures were measured in the heat exchangers.

of 1.54 mm and extend the entire length of the stack. The stack has a diameter of 8.4 cm and is encased in a stainless steel cylinder flanged at both ends.

The temperature of the heat exchangers was measured with type K thermocouples embedded in the heat exchangers midway between the heaters or coolant ports. The distance between the thermocouple and the nearest fin was 0.05 cm. The temperature measured at that location differed from the measured temperature of the fins by at most 3 °C at the maximum rate of heat input. Slowly increasing the heat input and allowing the temperature to reach steady state decreases the error to approximately 0.5 °C.

The prime mover was evacuated and filled with helium. The second gas was added until the desired percentage was reached using the law of partial pressures. The gases were allowed to mix then excess pressure was released. The temperature gradient was then increased until onset of self-oscillation was detected. The temperature, frequency, and percentage of the gases were recorded. The prime mover was then cooled to room temperature and the process repeated.

Pressurizing the prime mover above the desired pressure during mixing was done for two reasons. First, it allowed for greater accuracy in the calculation of the percentages of each gas. Second, if the frequency shifted while venting the excess pressure, we concluded that the gases were not thoroughly mixed and the procedure was repeated.

III. RESULTS FOR BINARY GAS MIXTURES

Figure 8 shows the theoretical[10] and experimental onset temperature and frequency for various mixtures of helium and SF_6. The agreement between theory and experiment is quite good for low percentages of SF_6, but at high percentages, the two values deviate considerably. This may be a result of the way we have included temperature dependence of the properties of the mixture from one end of the stack to the other. In the calculations, we assumed that the viscosity and thermal conductivity varied as $T^{1/2}$ which is the correct temperature dependence for the properties of helium but may not be correct for the mixture used. The minimum measured onset temperature difference occurs at around 40% SF_6, while the minimum predicted onset temperature difference occurs at 60% SF_6. From Fig. 6 the gas mixture is optimized for onset in this prime mover when the gas has low Prandtl number and low gamma. The low ratio of specific heats lowers the critical temperature gradient, while the low Prandtl number lowers the losses outside the stack.

Figure 9 shows the theoretical and experimental onset temperature and frequency for various mixtures of helium and argon. The minimum value for the Prandtl number occurs in the range of 35%–45% argon, which corresponds to a minimum onset temperature difference of 125 K. Theoretical calculations and experimental data are in good agreement with the largest difference of 5% for Delta T (the temperature difference across the stack) and 3% for frequency.

Figures 8 and 9 show that the temperature difference across the stack needed for self-oscillation is 170 K in pure helium, 130 K in pure argon, and 108 K in pure SF_6. With a Prandtl number equal to 0.73 and gamma of 1.04, pure SF_6 has the lowest onset temperature for pure gases.

IV. CONCLUSIONS

The optimum mixture of gases in a thermoacoustic engine depends upon the application and design goals. If a small temperature difference across the stack for the initiation of self-oscillation is an important goal, mixtures containing polyatomic gases with a small gamma might be superior to monatomic gases. The important thing to keep in mind is that the dependence of thermoacoustic gains and losses depends in a complex way on all the thermodynamic properties of the working fluid. The gas mixture properties must be optimized for the particular thermoacoustic application.

ACKNOWLEDGMENT

The authors gratefully acknowledge the support of the Office of Naval Research.

[1] T. J. Hofler, ''Thermoacoustic refrigeration design and performance,'' Ph.D. dissertation, Physics Department, University of California at San Diego (1986).
[2] S. L. Garrett, J. A. Adeff, and T. J. Hofler, ''Thermoacoustic refrigerator for space applications,'' J. Thermophys. Heat Transfer **7**, 595 (1993).
[3] G. W. Swift, ''Thermoacoustic engines,'' J. Acoust. Soc. Am. **84**, 1145 (1988).
[4] Xenon ($35.38/liter), SF_6 ($0.21/liter) NexAir, 363 Walnut, Memphis, TN 38126.
[5] J. Hirschfelder, C. Curtiss, and R. Bird, *Molecular Theory of Gases and Liquids*, 2nd ed. (Wiley, New York, 1964).
[6] S. Chapman and T. Cowling, *The Mathematical Theory of Non-uniform Gases*, 3rd ed. (Cambridge University Press, Cambridge, 1970).
[7] F. Reif, *Fundamentals of Statistical and Themal Physics* (McGraw-Hill, New York, 1965).
[8] F. W. Giacobbe, ''Estimation of Prandtl numbers in binary mixtures of helium and other noble gases,'' J. Acoust. Soc. Am. **96**, 3568 (1994).
[9] W. Braker and A. L. Mossman, *Matheson Gas Data Book*, 5th ed., (Matheson, Lyndhurst, NJ, 1971).
[10] W. P. Arnott, James R. Belcher, Henry E. Bass, and Richard Raspet, ''Stability analysis of a helium-filled thermoacoustic engine,'' J. Acoust. Soc. Am. **96**, 370 (1994).
[11] W. P. Arnott, Henry E. Bass, and Richard Raspet, ''General formulation of thermoacoustics for stacks having arbitrarily-shaped pore cross-sections,'' J. Acoust. Soc. Am. **91**, 3228 (1991).

Photoacoustic detection and localization of small gas leaks

Serdar H. Yönak and David R. Dowling[a)]
Department of Mechanical Engineering and Applied Mechanics, University of Michigan, Ann Arbor, Michigan 48109-2121

(Received 21 August 1998; accepted for publication 5 February 1999)

Leak detection and localization are critical manufacturing quality-control processes. Many industrial and domestic machines use or convey pressurized gases or liquids. Unintended leaks from machine components may be detrimental to consumers, manufacturers, and the environment. This paper describes a leak detection technique based on photoacoustic sounds produced by the interaction of a carbon dioxide (CO_2) laser tuned to 10.6 micrometers and a photoactive tracer gas, sulfur hexaflouride (SF_6), emitted by calibrated leak sources. Acoustic signals generated by a high-speed scan of the laser beam through the cloud of tracer gas formed near the leak are recorded in a bandwidth from 3 to 52 kHz by multiple microphones. From the recorded signals, the presence or absence of a leak may be deduced by comparison with the background noise level at the signal frequencies, which occur at the harmonics of the scan rate. When a leak is present, its location is determined from a simple model of the acoustic environment and matched field processing (MFP). Current results show that a gas leak of 1 cm^3 per day can be detected and localized to within ± 3 mm in a few seconds using four microphones, placed 0.41 m from the leak location, and an incoherent average of the MFP ambiguity surfaces at eight signal frequencies. Comparisons of the Bartlett and minimum-variance-distortionless matched field processors are also presented. © *1999 Acoustical Society of America.* [S0001-4966(99)01905-0]

PACS numbers: 43.38.Zp, 43.35.Sx, 43.60.Gk [SLE]

INTRODUCTION

Photoacoustics is the excitation of acoustic waves by unsteady heat addition from a light source. Bell (1880, 1881) discovered this phenomenon more than a century ago. Following Bell's initial discovery, others such as Rayleigh (1880), Tyndall (1881), Preece (1881), and Mercadier (1881) presented observations of their own. After this initial enthusiasm, the field lay dormant for about 90 years. In the 1970's, physical chemists and molecular physicists started using photoacoustics for spectroscopy (Rosencwaig, 1980). Not long after, environmental chemists and engineers applied photoacoustic spectroscopy to trace gas detection and gas emission monitoring (Kreuzer and Patel, 1971; Claspy, 1977; Dewey, 1974; Dewey *et al.*, 1973; and Goldan and Goto, 1974). More recently, the work of Brassington (1982), was combined with some new observations to produce a photoacoustic leak detection system (McRae and Dewey, 1992; McRae, 1994). At present, photoacoustics has been used primarily for spectroscopy and most measurements have been made in closed acoustically resonant cells. This paper presents photoacoustic measurements made in an open environment and documents their utility for leak detection and localization under ordinary laboratory conditions.

Many industrial and domestic products use or convey pressurized gases or liquids. Unintended leaks of these gases or liquids may cause warranty problems, or even health and environmental hazards. Current leak detection and localization techniques such as bubble visualization, sniffing devices, or helium-mass spectrometers are either subjective, time consuming, ill-suited to a factory environment, require vacuum pumps, or not easily automated. Optical methods such as scanning a laser over the object that is leaking and looking for hot spots or backscatter absorption (McRae, 1989; McRae and Kulp, 1993) work well for leaks larger than 3×10^{-4} cm^3/s, but fail for leaks smaller than this, mainly because gases are optically thin. Photoacoustic techniques, which can be used at ordinary room temperature and pressure, may provide significant improvements in speed and localization accuracy. Here, the component under test is pressurized above atmospheric pressure with a photoactive tracer gas and (if necessary) an inert diluent gas. If a leak is present, a small tracer gas cloud will form near the leak. The beam from a laser tuned to a spectral absorption line of the tracer gas is scanned across the area of the suspected leak. When the laser beam contacts the tracer-gas cloud, the tracer gas is rapidly heated and expands, launching an acoustic wave. Previous photoacoustic leak detection efforts (McRae and Dewey, 1992; McRae, 1994) used a single microphone and narrow-band filtering to detect photoacoustic sound. This paper describes an enhancement of McRae's work to include multiple microphones, multiple signal frequencies, and matched-field processing (MFP) to determine the leak location.

MFP is a signal-processing technique originally developed for use in underwater acoustics for the localization of unknown sources in known acoustic environments. Bucker (1976) laid the foundation for the use of MFP in underwater applications over 20 years ago. Since then, many investigators have added to the development of MFP and review articles and monographs covering the various implementations are available (Baggeroer *et al.*, 1993; Tolstoy, 1993; Jensen *et al.*, 1994). At a basic level, measured acoustic signals are

a)Author to whom correspondence should be addressed.

compared to predicted acoustic signals to produce an ambiguity surface based on a computational model of the acoustic environment with a variable test source location. When there is a good match between the predicted and measured acoustic signals, the ambiguity surface achieves a maximum and the test source is presumed to be at or near the location of the actual acoustic source. In this sense, the MFP ambiguity surface can be thought of as a spatial correlation, which when normalized properly gives a probability map for the source location. The accuracy of the MFP-determined sound-source location is strongly dependent on the accuracy of the acoustic model of the environment and the signal-to-noise ratio of the measurements. Hence, source localization to better than a wavelength may be possible with a good environmental model at high signal-to-noise ratios. Generally, MFP has been developed as a narrow-band technique, but broadband source localization by incoherently combining MFP results from several frequencies is a straightforward extension (Baggeroer *et al.*, 1988). This paper explores two particular implementations of MFP which do not require *a priori* information about background noise: the Bartlett processor (Bucker, 1976) which is technically equivalent to back propagation or time inversion of the received signals (Jackson and Dowling, 1991), and the minimum variance (MV) distortionless processor (described in Jensen *et al.*, 1994), which typically provides better side lobe control than the Bartlett processor when the signal-to-noise ratio comfortably exceeds 0 dB. Although more sophisticated MFP schemes exist (Collins and Kuperman, 1991; Collins *et al.*, 1994; Fialkowski *et al.*, 1997), the two chosen for this study are relatively easy to implement and provide important baseline results for photoacoustic leak localization.

In the present study, a carbon dioxide laser tuned to 10.6 micrometers and the tracer gas sulfur hexaflouride (SF_6) are used to produce photoacoustic sounds. The laser beam is rapidly scanned across a flat plate with a leak of known-rate present or absent along the scan. Acoustic measurements are made with two or four microphones and the recorded signal is Fourier analyzed and compared to a previously measured background sound level at the harmonics of the scan rate (the signal frequencies). If the recorded signal exceeds the background level by more than a factor of 3, a positive detection is made and a leak is presumed to be present. Since the source has broadband characteristics, MFP is performed at the main signal frequencies and the ambiguity surfaces from the various frequencies are incoherently averaged. The peak of the resultant multiple-frequency ambiguity surface is used to determine the location of the leak. Reflecting boundaries and frequency-dependent microphone directionality are accounted for in the processing.

The remainder of the paper is divided into four sections. Section I describes the details of the experimental setup. Section II discusses the generation of photoacoustic sound, photoacoustic signal characteristics, and the detection limitations presented by coherent noise. In Sec. III, the localization results are presented and a range of comparisons is made between the Bartlett and minimum-variance (MV) distortionless matched field processors. Two and four microphone results are also compared. In addition, error in source localization due to microphone-placement and speed-of-sound-measurement errors are discussed. The conclusions drawn from this research are given in Sec. IV.

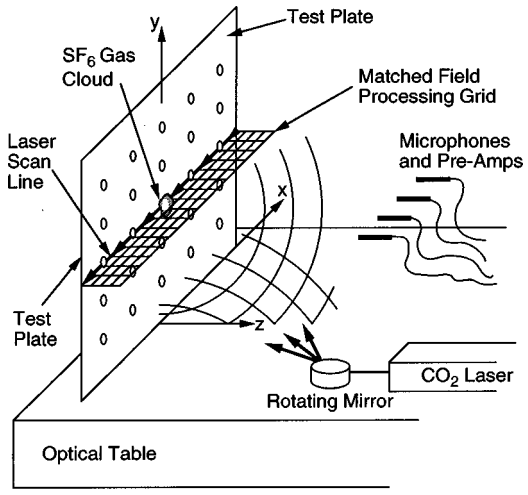

FIG. 1. Experimental setup. The test plate lies in the $x-y$ plane. The four microphones are 14.6 cm above the optical table top and 0.41 m from the plate. The CO_2-laser beam traverses the plate in the x-direction at a rate of 6.25 kHz. Photoacoustic leak detection and localization was investigated in the lowest row of holes on the plate, which were 10.5 cm above the optical table top.

I. EXPERIMENTS

The current experimental setup, shown in Fig. 1, is for one-dimensional detection and localization of leaks along a line parallel to the x-axis on a flat aluminum plate mounted on top of and perpendicular to an optical table. The laboratory environment, consisting primarily of painted cinder block walls with a concrete ceiling and a tile floor, was not acoustically treated. Laboratory temperature was monitored to $\pm 1\,^{\circ}\mathrm{C}$ using a T-type thermocouple and an electronic signal conditioner. The test plate measures 0.61 by 0.61 m and has holes which are spaced evenly on 7.62-cm centers. For the experiments presented here, leak detection and localization was only investigated on the bottom row of holes, located 10.5 cm above the table surface. For detection and localization in a factory on a two-dimensional surface, the second in-plane dimension (corresponding to the y-coordinate) would be interrogated by assembly-line motion. A known-rate leak of the tracer gas, SF_6, may be mounted in any of the holes in the test plate. The x and z coordinates of this leak are unknowns in the signal-processing routines.

Three leak rates (q) were investigated: $q=10^{-2}\,\mathrm{cm}^3/\mathrm{s}$ (large enough to produce visible bubbles in a dunk tank), $q=1.22\times10^{-5}\,\mathrm{cm}^3/\mathrm{s}$ (approximately 1 cm^3 per day), and $q=6.38\times10^{-7}\,\mathrm{cm}^3/\mathrm{s}$ (approximately 1 cm^3 every 2 1/2 weeks). The $10^{-2}\,\mathrm{cm}^3/\mathrm{s}$ leak was obtained using a needle valve from Leybold. The two smaller leaks are fixed-volume, fixed-orifice calibrated leaks from Vacuum Instruments Corporation. The row of holes on the plate is interrogated using a Synrad grating-tuned 12-watt CO_2 laser tuned to 10.6 micrometers, which corresponds to a strong spectroscopic absorption band of SF_6 (Lymann *et al.*, 1986). Since the ap-

proach is based on the spectroscopic resonant absorption of laser light by a gas, any laser–gas combination can be used so long as the wavelength of the laser light corresponds to a molecular absorption band for the gas. The nominal beam spot diameter of the CO_2 laser at the plate surface was 7 mm. Since the CO_2 laser is invisible, it was combined with a 5-mW red He–Ne laser (not shown in Fig. 1) using a Zn–Se beam combiner to visualize the potentially hazardous CO_2 beam. The laser beams are initially perpendicular to one another, and each forms an incidence angle of 45 deg with the beam combiner. The combined beams are then incident on a Lincoln Laser Company beam scanner consisting of a 20-sided polygonal mirror mounted on the shaft of a high-speed motor that can rotate up to 37 500 rpm. For the current experiments, the scanner motor is run at 18 750 rpm yielding a beam-scan rate of 6.25 kHz with a sweep angle of 30 deg. The scanner sets up a line scan that is centered at normal incidence on the aluminum test plate located 0.84 m away. The scanned laser beams traverse the plate horizontally in the negative *x*-direction.

When the laser beam illuminates the tracer-gas cloud formed near the test leak, photoacoustic sound is generated at frequencies which are harmonics of the scan rate. This sound is then measured using two or four Brüel & Kjær Model 4136 quarter-inch broadband microphones. The microphones have a nominal bandwidth from a fraction of a hertz to about 80 kHz. The microphone sensitivity did exhibit directional behavior at the higher frequencies, and their directional response was measured at the frequencies of interest for use in MFP. In this study, for the greatest angle of incidence, which was approximately 30 deg, the microphone response at 50 kHz was 70% of that for normal incidence. The microphones form a linear array parallel to the *x*-axis and 0.41 m away from the plate 14.6 cm above the optical table top. This vertical position allows the scanned laser beams to travel an unobstructed path beneath the microphones. The intended microphone spacing is 25.4 mm, slightly less than half of a wavelength at 6.25 kHz, with a nominal placement error of ± 1 mm. The measured sound from each microphone is high-pass filtered with a cutoff frequency of 3 kHz by a Krohn-Hite model 3364 analog filter and acquired using a PC-based data acquisition system at a rate of 104.667 kHz per channel for a 0.629-s data record duration. The acquired time-domain signals are fast-Fourier transformed, and the amplitude and phase of the signal at the harmonics of the scan rate are passed to the MFP routines to determine the location of the leak. MFP is carried out using the Bartlett processor, $B_B(\mathbf{r})$, the usual gauge in MFP studies, and the MV processor $B_{\mathrm{MV}}(\mathbf{r})$, a nonlinear processor that has the ability to reject correlated noise from locations other than the source location (Jensen *et al.*, 1994). These processors were chosen for this study because neither require *a priori* knowledge of background noise, and because they are representative of the two classes of matched-field processors: linear and nonlinear (or adaptive).

For the present application, with *m* microphones located at positions $\mathbf{r_i}=(x_i,y_i,z_i)$, the narrow-band version of either the Bartlett processor or minimum-variance-distortionless (MV) processor at a frequency ω (rad/s) and location $\mathbf{r}=(x,y,z)$, can be cast into the same form:

$$B(\mathbf{r};\omega)=\sum_{i=1}^{m}\sum_{j=1}^{m} w^*(\mathbf{r},\mathbf{r_i};\omega)K_{ij}(\omega)w(\mathbf{r},\mathbf{r_j};\omega), \tag{1a}$$

where $B(\mathbf{r},\omega)$ is the processor output or ambiguity function, $w(\mathbf{r},\mathbf{r_i};\omega)$ is the weighting for each microphone, $K_{ij}(\omega)$ is the measured cross-spectral density matrix of the microphone measurements $M_i(\omega)$ at frequency ω

$$K_{ij}(\omega)=\frac{M_i^*(\omega)M_j(\omega)}{\Sigma_{n=1}^{m}|M_n(\omega)|^2}, \tag{1b}$$

and the asterisk denotes complex conjugation. In some applications of MFP, $K_{ij}(\omega)$ is determined from an ensemble average of several independent sets of measurements (Baggeroer *et al.*, 1993).

For the Bartlett processor, the microphone weights are determined from

$$w_B(\mathbf{r},\mathbf{r_i})=G(\mathbf{r},\mathbf{r_i};\omega)/|G(\mathbf{r},\mathbf{r_i};\omega)|, \tag{2}$$

where $G(\mathbf{r},\mathbf{r_i};\omega)$ is the appropriate Green's function for the Helmholtz equation at frequency ω. The current experimental step-up approximates a quarter space ($y>0,z>0$) with two hard walls at $y=0$ (the optical table top) and $z=0$ (the test plate), so the following Green's function based on the method of images was used:

$$G(\mathbf{r},\mathbf{r_i};\omega)=\frac{S_1e^{ikr_1}}{4\pi r_1}+\frac{S_2e^{ikr_2}}{4\pi r_2}+\frac{S_3e^{ikr_3}}{4\pi r_3}+\frac{S_4e^{ikr_4}}{4\pi r_4}, \tag{3a}$$

where

$$r_1=\sqrt{(x-x_i)^2+(y-y_i)^2+(z-z_i)^2}, \tag{3b}$$

$$r_2=\sqrt{(x-x_i)^2+(y+y_i)^2+(z-z_i)^2}, \tag{3c}$$

$$r_3=\sqrt{(x-x_i)^2+(y-y_i)^2+(z+z_i)^2}, \tag{3d}$$

$$r_4=\sqrt{(x-x_i)^2+(y+y_i)^2+(z+z_i)^2}, \tag{3e}$$

k is the acoustic wave number, and S_1 through S_4 are the frequency- and direction-dependent microphone sensitivities. The environmental model of (3) treats the plate and table top as infinite in extent. Thus (3) remains valid as long as the leak is several fundamental-frequency wavelengths from the edge of the plate or the table. Simpler environmental models that neglect reflections from the plate and/or the optical table proved useless. More complicated models that account for reverberation within the laboratory were not found necessary. For the Bartlett processor, the weight vectors do not depend on M_i, so the processor is considered to be linear with respect to the received signals.

For the MV processor, the received signals are used in the construction of the microphone weights to minimize the output of the processor for all locations except the location of the acoustic source. The MV weights explicitly depend on the measurements which renders this processor nonlinear

$$w_{\mathrm{MV}}(\mathbf{r},\mathbf{r_i};\omega) = \frac{\Sigma_{j=1}^{m}[K_{ij}(\omega)]^{-1} w_B(\mathbf{r},\mathbf{r_j};\omega)}{\Sigma_{i=1}^{m}\Sigma_{j=1}^{m} w_B(\mathbf{r},\mathbf{r_i};\omega)[K_{ij}(\omega)]^{-1} w_B(\mathbf{r},\mathbf{r_j};\omega)}. \quad (4)$$

Here, $[\ ]^{-1}$ implies a matrix inverse which becomes problematic when K_{ij} does not have full rank. This problem occurs when $m>1$ but only one set of measurements $M_i(\omega)$ is used to construct $K_{ij}(\omega)$. In the current investigations, this matrix inversion problem was overcome by diagonal loading of K_{ij} (Baggeroer *et al.*, 1993) with 0.01 times the identity matrix (δ_{ij}).

The approach to finding a suitable diagonal loading was to look at the magnitude of the diagonal element of the K_{ij} matrix (note that the data vectors are normalized so that the trace of the matrix was equal to 1) and select an optimum loading. The value used was 0.01, which is large enough to keep the matrix numerically nonsingular but small compared to the magnitude of the diagonal elements. It was observed that for diagonal loading greater than 1 the MV processor output became essentially the same as the output from the Bartlett processor (with an offset and scale change). As the loading was decreased from 1 to 0.01, the MV processor peak became sharper and the spatial side lobes were suppressed more. As the diagonal loading was decreased from 0.01 to 1×10^{-7}, the width of the localization peak and the main lobe to side lobe ratio remained constant. As the loading was decreased further to 1×10^{-8}, the largest peak would occur at ambiguous locations that did not correspond to true source locations because of numerical error due to finite precision computer arithmetic.

For both processors, the extension from narrow-band to multiple frequencies is accomplished by incoherently averaging the narrowband ambiguity functions

$$B(\mathbf{r}) = \frac{1}{N}\sum_{n=1}^{N} B(\mathbf{r},\omega_n), \quad (5)$$

where the number of signal frequencies is N.

II. SIGNALS AND DETECTION

As was mentioned previously, photoacoustics is the excitation of acoustic waves by unsteady heating from a light source. This unsteady heating shows up as a source term in the Helmholtz equation (Morse and Ingard, 1968), which has an integral solution of the following form:

$$\tilde{p}(\mathbf{r},\omega) = \frac{i\omega}{4\pi}\frac{\gamma-1}{c^2}\int_{\text{all }\mathbf{r}'} \tilde{H}(\mathbf{r},\omega)G(\mathbf{r},\mathbf{r}';\omega)d^3r'. \quad (6)$$

Here $\tilde{p}$ is the complex pressure field, $\mathbf{r}$ is the field point, γ is the ratio of specific heats of the ambient gas, c is the ambient speed of sound, and $\tilde{H}(\mathbf{r},\omega)$ is the temporal Fourier transform of the rate of heat produced per unit volume by the absorption of light. The integral is performed over the source coordinate $\mathbf{r}'$. Increased absorption of light by the gas or increased light intensity leads to an increase in the source strength, which in turn leads to an increase in the magnitude of the photoacoustic sound. In addition, higher frequencies are clearly favored through the leading factor in (6). Details of how the spectroscopic properties of a photoactive gas and its interaction with the light influence the heating term can be found in Kreuzer (1977) and Rosencwaig (1980).

The spatial extent of $\tilde{H}(\mathbf{r},\omega)$ determines whether or not a leak leads to an acoustic point source. The size of the concentrated portion of the gas cloud affects the localization accuracy, since it is the excited gas cloud that is the true acoustic source regardless of laser-beam spot size. For the largest leak that was examined (10^{-2} cm^3/s), the gas does diffuse and even flow from the source so this leak is far from point-like. Localization and imaging of larger leaks is the focus of further investigation. For the localization study with the considerably smaller leaks (1.22×10^{-5} cm^3/s and 6.38×10^{-7} cm^3/s) presented in this article, the gas does diffuse from the source. However, the concentrated portion of the leak lies well within the boundary layer of any reasonable airflow over the test plate. Thus, the concentrated portion of the leaking gas is not convected from the leak source and its behavior can be considered point-like.

This contention is based on a comparison of boundary layer and gas diffusion length scales. For a 2-m/s airflow across the plate (typical of an air circulation fan), the Blasius boundary layer (Fox and McDonald, 1992) is approximately 7.5 mm thick after a development length of 30.5 cm (the distance from the edge of the test plate to its center). An effective leak radius can be found by considering the radially symmetric species conservation equations in a semi-infinite domain for air (7a) and SF_6 (7b) and the radially symmetric Fick's law of diffusion [(7c) and (7d)] with constant diffusivity (adapted from Bird *et al.*, 1960)

$$\frac{1}{r^2}\frac{\partial}{\partial r}(r^2 C X_{\mathrm{air}} u_r + r^2 \dot{n}_{\mathrm{air}}) = 0, \quad (7a)$$

$$\frac{1}{r^2}\frac{\partial}{\partial r}(r^2 C X_{\mathrm{SF_6}} u_r + r^2 \dot{n}_{\mathrm{SF_6}}) = 0, \quad (7b)$$

$$\dot{n}_{\mathrm{air}} = -C D_{\mathrm{SF_6-air}}\frac{\partial X_{\mathrm{air}}}{\partial r}, \quad (7c)$$

$$\dot{n}_{\mathrm{SF_6}} = -C D_{\mathrm{SF_6-air}}\frac{\partial X_{\mathrm{SF_6}}}{\partial r}, \quad (7d)$$

where r is the radial coordinate, u_r is the bulk radial velocity, C is the molar concentration, X_{air} is the mole fraction or air, $X_{\mathrm{SF_6}}$ is the mole fraction of SF_6, $D_{\mathrm{SF_6-air}}$ is the diffusivity of SF_6 in air, $\dot{n}_{\mathrm{air}}$ is the molar flux of air, and $\dot{n}_{\mathrm{SF_6}}$ is the molar flux of SF_6. These equations with boundary conditions, $X_{\mathrm{SF_6}}\to0$ and $X_{\mathrm{air}}\to1$ as $r\to\infty$ and $X_{\mathrm{SF_6}}\to1$ and $X_{\mathrm{air}}\to0$ as $r\to0$, can be solved in a half/space to find

$$X_{\mathrm{SF_6}} = 1-\exp\left(\frac{-q}{2\pi D_{\mathrm{SF_6-air}} r}\right), \quad (8)$$

where q is the volumetric leak rate.

Setting $X_{\mathrm{SF_6}}=1/2$ determines the half-concentration radius, $r_{1/2}$, of the gas cloud. For a 1.22×10^{-5} cm^3/s leak with diffusivity for SF_6 in air equal to 0.0934 cm^2/s at 298 K, this effective leak radius is approximately 0.0003 mm, which is considerably smaller than the thickness of the boundary layer

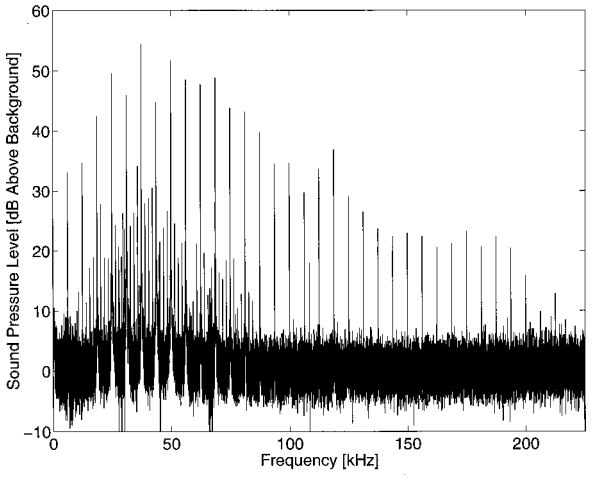

FIG. 2. FFT amplitude spectrum of the photoacoustic sound from a 10^{-2} cm^3/s leak measured by one microphone at a sampling frequency of 500 kHz normalized by an equivalent spectrum of background noise. The main photoacoustic signal frequencies occur at integer multiples of 6.25 kHz. Minor signal frequencies (evident between 10 and 80 kHz) are believed to be caused by speed modulation of the rotating polygonal mirror.

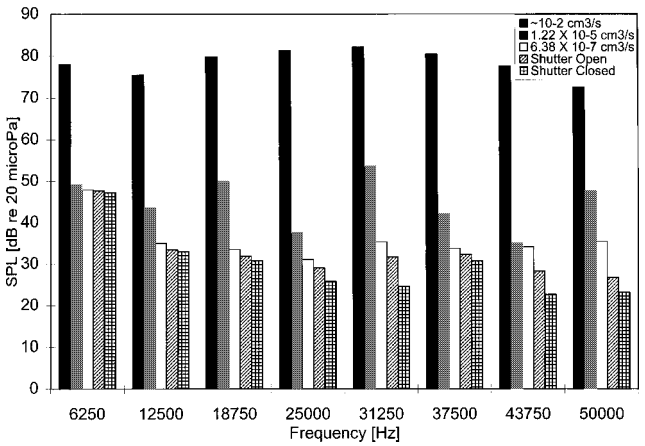

FIG. 3. Average photoacoustic signal amplitudes for the first eight signal harmonics under five different experimental conditions, three with leaks present and two without. The largest leak is the loudest and the background noise with the CO_2-laser shutter closed is the quietest. The 6.38 $\times 10^{-7}$ cm^3/s leak lies near the detection limit for this system.

of the flow across the plate. Hence, an exterior gas flow is likely to have little or no influence on the high-concentration part of the SF_6 gas cloud. This contention has been verified by preliminary experiments with a room fan and the calibrated leaks used in this study. It should be noted that all localization studies with the small leaks were done with the leaks at steady state. The fixed-volume, fixed-orifice leaks from Vacuum Instruments Corporation are always *on* so the leak being interrogated was not turned on immediately before an experiment. Finally, note that the steady-state species conservation equations are sufficient in this case since the diffusive time scale for the leak cloud to establish itself, $r_{1/2}^2/D_{\mathrm{SF_6-air}}$, is of order 10^{-8} s.

For the experiments presented here, photoacoustic sound is generated by rapidly scanning the CO_2-laser beam over the leaking gas. As the laser passes over the gas cloud formed near the leak, the gas absorbs the laser light and rapidly expands. This rapid expansion launches an acoustic wave relieving the local pressure. Once the beam has passed, the local temperature is reduced mainly through thermal conduction. This causes the gas to cool down and contract. The diffusing and expanding SF_6 is replenished by the leak itself. The beam comes by again and the process is repeated. The acoustic waves are launched at the frequency of the scan rate. Thermal conduction does set a limit to the frequency of photoacoustic sound. Fortunately, for the small leaks used in this study, this limit (which is proportional to $D_{\mathrm{SF_6-air}}/r_{1/2}^2$) lies in the multiple megahertz range, too high to be of concern for this study. Rosencwaig (1980) and Kreuzer (1977) give a full description of the photoacoustic effect not only for gases, but for solids and liquids as well.

A normalized FFT amplitude spectrum for the photoacoustic signal from the largest leak in this study, 10^{-2} cm^3/s, is displayed in Fig. 2. These measurements were made with a single microphone 0.41 m from the leak at a sampling rate of 500 kHz with the leak at $x=z=0$ (the middle of laser scan). The spectrum in Fig. 2 is normalized by an equivalent-length and bandwidth background noise spectrum measured with the whole experiment in operation but without a leak mounted on the plate. Hence, spectral values near 0 dB correspond to the noise level. The fluctuations of ± 5 dB near 0 dB result from nonrepeatability in the noise and are not statistically significant. The fundamental frequency of the photoacoustic sound is 6.25 kHz (the laser beam scan rate). Figure 2 shows that the dominant tones of the photoacoustic signal are this fundamental frequency and its first 35 harmonics up to approximately 225 kHz. The bias toward the higher-frequency harmonics predicted by (6) can be deduced from Fig. 2, where tonal signal components are clearly evident well beyond the nominal microphone bandwidth of 80 kHz. These high-frequency signal tones must be loud enough to overcome the loss of microphone sensitivity. The secondary signal tones that occur between the main signal harmonics from approximately 10 to 80 kHz are believed to be caused by modulation of the spinning speed of the rotating-polygonal-mirror laser scanner which is driven by a four-pole motor. These secondary tones are spaced at intervals that are one-fourth of the fundamental frequency, which is consistent with scan-rate modulation produced by the rotational-speed fluctuation characteristics of a four-pole motor.

Through repeated trials, it was found that the photoacoustic signal frequencies are stable within the limits set by the motor controller for the rotating polygonal mirror. However, the signal amplitudes and the phase relationship between signal harmonics varied from trial to trial, making it impossible to exploit any form of coherent broadband processing. These signal fluctuations are believed to be caused by motion and deformation of the tracer gas cloud formed near the leak, and are the subject of ongoing investigation.

The leak-rate dependence of the average amplitude received by the four-microphone array at the first eight signal frequencies is shown in Fig. 3 along with two measurements of the background noise. In all five cases shown in Fig. 3, the FFT amplitudes from the four microphones are converted to sound-pressure amplitude using the manufacturer's calibra-

tion of microphone sensitivity, averaged, and converted to sound-pressure level (dB *re* 20 μPa). Both of the background sound measurements were made without a leak mounted on the plate, but with all of the other experimental components switched on. In one case, the CO_2-laser shutter is open, and in the other it is closed. The second noise check is made to quantify the photoacoustically generated background noise from the laser beam scanning over the plate alone. The shutter-open noise level is the more important from a leak-detection performance standpoint. Figure 3 clearly shows the 10^{-2} cm^3/s leak to be the loudest, and this leak is easily audible in the laboratory. The two smaller leaks produce average signal amplitudes still exceeding, but much closer to, the background noise level.

Based on these results, it should be possible to use the amplitude of the recorded sounds at several of the dominant signal frequencies to determine whether or not a leak is present by simple thresholding. The 10^{-2} cm^3/s leak is 30 dB or more above the shutter-open noise level at every signal frequency. The 1.22×10^{-5} cm^3/s leak is more than 10 dB above the shutter-open noise level at five of the eight signal frequencies. The 6.38×10^{-7} cm^3/s leak is only a few dB above the shutter-open noise level at the eight signal frequencies. Hence, a detection threshold of several dB above background at selected signal frequencies should provide satisfactory detection performance for leaks larger than 10^{-5} cm^3/s. For the present experiments, a 9-dB threshold applied at signal frequencies of 18.75, 31.25, 37.5, and 50.0 kHz detected the two larger leaks without the fail or false detection for more than 50 trials. However, with this simple threshold scheme the smallest leak could not be detected about half the time, and the false detection probability also approached 50%. Improved detection capability at the lowest leak rate may be possible with more microphones, shorter path lengths, or use of a more sophisticated signal-detection scheme, such as that described for the leak localization in the next section.

It should be noted that there is significant background photoacoustic sound generated by the interaction of the laser and aluminum plate alone. For example, by comparing the two background sound levels in Fig. 3, the photoacoustic sound (noise) at 31.25 kHz generated by scanning the CO_2 laser across the plate alone is 7.1 dB above the noise level when the CO_2-laser shutter is closed. Ultimately, any leak-detection limit will be set by correlated noise generated by the target device on which the leak resides.

III. LOCALIZATION

Once the presence of a leak is determined, the next step is to find its location. As discussed at the end of Sec. I, this was approached using the measured photoacoustic signals and the Bartlett and MV matched field processors. The computation of the necessary replica fields was done using (3) for the eight lowest signal frequencies. The higher signal harmonics reside beyond the capability of the current data acquisition system when four input channels are used. The eight single-frequency ambiguity surfaces were averaged according to (5). The rest of this section describes how microphone number, processor type, leak rate, and microphone geometry influence photoacoustic leak localization.

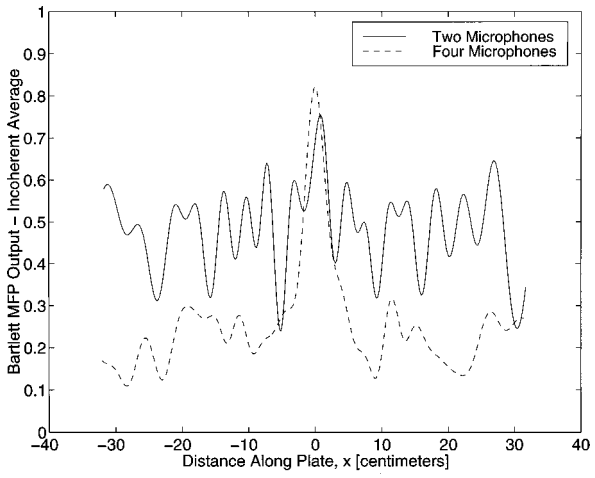

FIG. 4. Multiple-frequency Bartlett MFP results at $z=0$ versus the cross plate coordinate, x, using two and four microphones for a 1.22×10^{-5} cm^3/s leak at the center of the plate. The four microphone results show significant suppression of the spatial side lobes compared to the two microphone results.

The first comparison is drawn between the use of two and four microphones for the Bartlett processor with the 1.22×10^{-5} cm^3/s leak located at the center of the plate. The intersection of the multiple-frequency ambiguity surface with the plane of the plate ($z=0$) is displayed in Fig. 4. The horizontal axis is the distance along the plate with $x=0$ denoting the plate center. Here, the leak is known to lie on the surface of the plate so only results from $z=0$ need to be examined. The peak value of these MFP results gives the processor-determined location of the leak along the line of the laser scan (the x-direction). Although Fig. 4 shows that x-direction localization is possible with two microphones, the four microphone results are clearly superior. The two-microphone side lobes are 13% below the peak, while the four microphone side lobes are 62% below the peak. Moreover, the two microphone results indicate a leak location that is 6 mm to the right of center, while the four-microphone localization agrees with actual leak location to within less than 1 mm.

A comparison of the differences between single- and multiple-frequency MFP is shown in Fig. 5, which displays the various single-frequency and the incoherent-average ambiguity surfaces for variable x at $z=0$ for the 1.22×10^{-5} cm^3/s leak located at $x=0$ when four microphones are used. For the Bartlett processor [Fig. 5(a)], the leak is unambiguously localized at the center of the plate at 6.25 and 18.75 kHz, but the spatial resolution at these frequencies is relatively low, yielding broad ambiguity peaks. At frequencies 25 kHz and higher, the ambiguity peaks are narrower but there are now significant spatial side lobes. In fact, at 43.75 kHz the side lobe magnitude is greater than that of the main lobe. The incoherent average [the top trace in Fig. 5(a)] reduces spatial side lobes yet partially retains the spatial resolution associated with the higher frequencies. For the MV processor in Fig. 5(b), the peaks are narrower and the side lobe suppression is usually better. However, the main

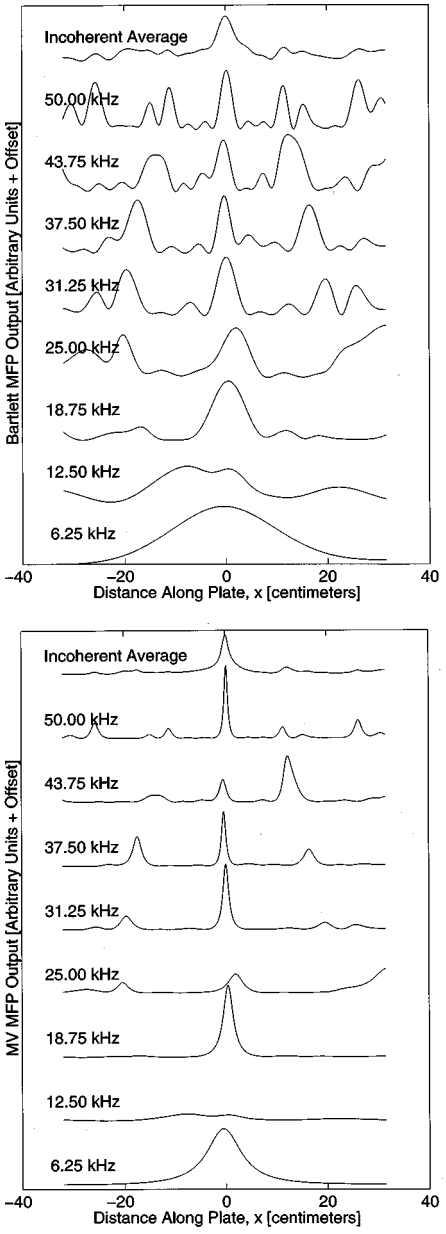

FIG. 5. Frequency by frequency and incoherent-average MFP results at $z=0$ using four microphones for a 1.22×10^{-5} cm^3/s leak at the center of the plate versus the cross plate coordinate, x, for (a) the Bartlett processor, and (b) the minimum-variance (MV) distortionless processor. The Bartlett processor produces many side lobes at the four higher frequencies, but these are suppressed in the incoherent average. The MV processor has better spatial resolution at every frequency and superior side lobe suppression, but fails to consistently produce a main lobe.

peak is sometimes suppressed in favor of a side lobe.

The array spacing was chosen based on the lowest frequency or the fundamental frequency of the harmonics that were used in the processing. Since the array is sparse for the higher frequencies, the single-frequency localization results at these higher frequencies would lead to deleterious aliasing effects. Incoherent averaging suppresses the deleterious aliasing effects that would arise from using only single-frequency results. The higher frequencies are used to increase the spatial resolution and are advantageous, as the signal-to-noise-ratio is typically higher at those frequencies.

Figure 6 shows the effect of leak size and provides a

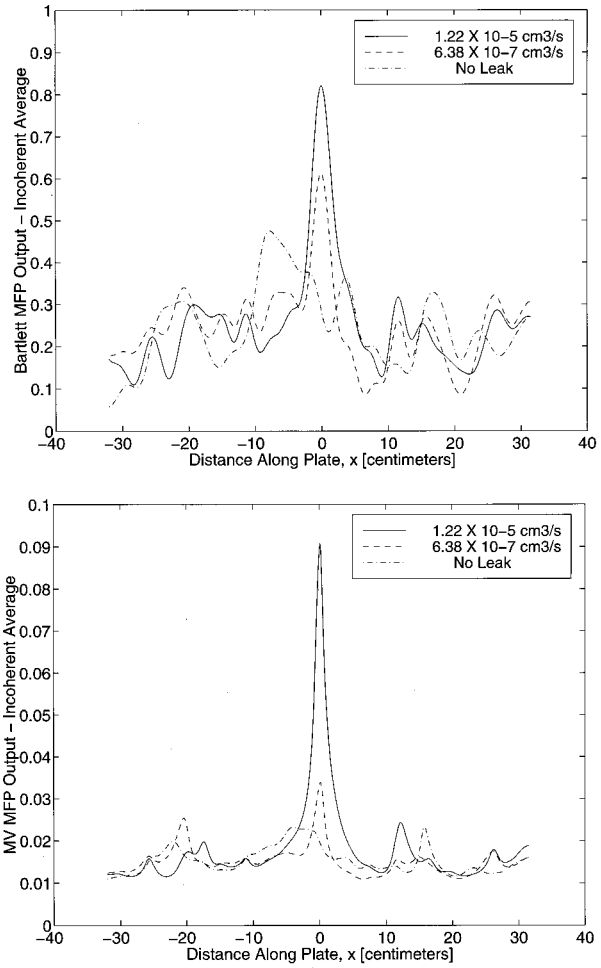

FIG. 6. A comparison of incoherently averaged MFP results at $z=0$ for 1.22×10^{-5} cm^3/s and a 6.38×10^{-7} cm^3/s leaks, and for a no-leak case versus the cross-plate coordinate, x, for (a) the Bartlett processor, and (b) the minimum-variance (MV) distortionless processor. Both processors find both leaks, although the peak in the Bartlett ambiguity function is degraded less rapidly by the decrease in leak rate.

comparison of the Bartlett [Fig. 6(a)] and MV [Fig. 6(b)] processors for variable x at $z=0$. In both Fig. 6(a) and (b), MFP output for the 1.22×10^{-5} cm^3/s and the 6.38×10^{-7} cm^3/s leaks placed at $x=0$ are each compared to a representative case when no leak is present. The no-leak results vary from trial to trial because of noise fluctuations. Note that the vertical scale of Fig. 6(b) is expanded relative to that of Fig. 6(a) The 1.22×10^{-5} cm^3/s leak is easily localized by both processors, with the main ambiguity peak at least twice as high as any false-localization peak of the no-leak case. The MV results for this leak exhibit a narrower main lobe, implying a finer localization resolution. The smaller 6.38×10^{-7} cm^3/s leak is also found by both processors. However, the main lobe magnitude for both processors is reduced: by 25% for the Bartlett processor, and by almost 70% for the MV processor.

All the results in Figs. 2 through 6 have been for leaks located at $x=0$. Figure 7 displays the intersection of the incoherent-average ambiguity surfaces with the plate surface $(z=0)$ for the Bartlett [Fig. 7(a)] and MV [Fig. 7(b)] processors when all four microphones are used and the 1.22×10^{-5} cm^3/s leak is located at seven different locations: x

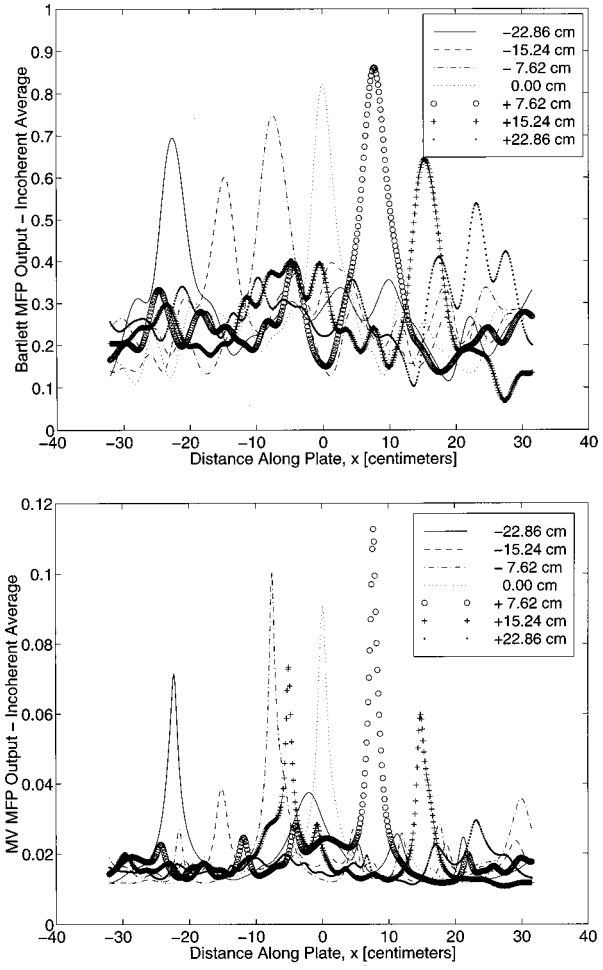

FIG. 7. Incoherently averaged MFP results at $z=0$ with the 1.22×10^{-5} cm^3/s leak placed at seven different x-locations for (a) the Bartlett processor, and (b) the minimum-variance (MV) distortionless processor. The Bartlett processor finds the leak every time, while the MV processor fails when the leak is located at $x=-15.42$ cm because of a side peak at $x=6$ cm.

$=-22.86$, -15.24, -7.62, 0, $+7.62$, $+15.24$, $+22.86$ cm. The Bartlett processor locates this leak at all seven positions to within ±3 mm. The MV processor locates the leak successfully in six of the seven locations. It fails when the leak is placed at $x=+15.24$ cm because of a side lobe near $x=-6$ cm. In addition, the main lobe maxima when the leak is at $x=-22.86$; -15.24 cm and $+22.86$ cm are all lower than the side lobe maximum when the leak is at $x=+15.24$ cm. Main-lobe/side-lobe amplitude overlap of this kind have thus far prevented the development of a leak-detection criterion based on MFP, although investigations are continuing and improvements may be possible with other processors.

As a further illustration of the results given in Fig. 7, Figs. 8 and 9 show $x-z$ ambiguity surface plots for the Bartlett and MV processors, respectively, for four cases when the 1.22×10^{-5} cm^3/s leak is located at $x=-22.86$, -15.24, -7.62, and 0 cm. For both processors, the results are somewhat symmetric about $x=0$. The views shown are those obtained by looking down upon the processing grid shown in Fig. 1. A comparison of Figs. 8 and 9 reveals that the MV processor generally provides better spatial resolution than the

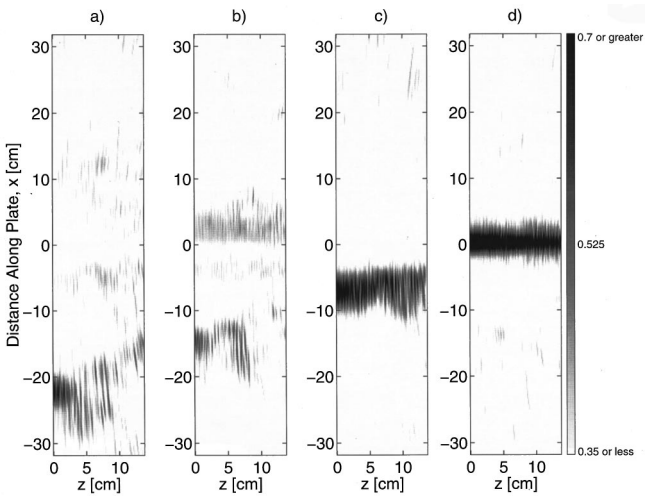

FIG. 8. Bartlett MFP ambiguity surfaces computed in the $x-z$ plane with the 1.22×10^{-5} cm^3/s leak placed at four different x-locations for: (a) $x=-22.86$ cm, (b) $x=-15.24$ cm, (c) $x=-7.62$ cm, and (d) $x=0.0$ cm. For the most symmetrical case (leak at $x=0$), the processor is unable to localize the leak in the z direction. For all of the off-center cases, the asymmetry in the environment allows localization in the z, as well as the x, directions.

Bartlett processor, which is consistent with its performance in underwater applications (Jensen *et al.*, 1994). For both processors, as the leak is moved away from the center of the plate, the z-coordinate of the leak is determined in addition to its x-coordinate. This shows that asymmetry and complexity in the acoustic environment actually aids leak localization, a phenomena previously described in underwater acoustics as environmental signal processing (Perkins and Kuperman, 1990).

The comparison between the Bartlett and MV processors presented in Figs. 5 through 9 can be summarized as follows. The MV processor has greater side-lobe suppression capability and a narrower main lobe than the Bartlett processor at single frequencies when the photoacoustic signal is strong enough. However, when the results are incoherently aver-

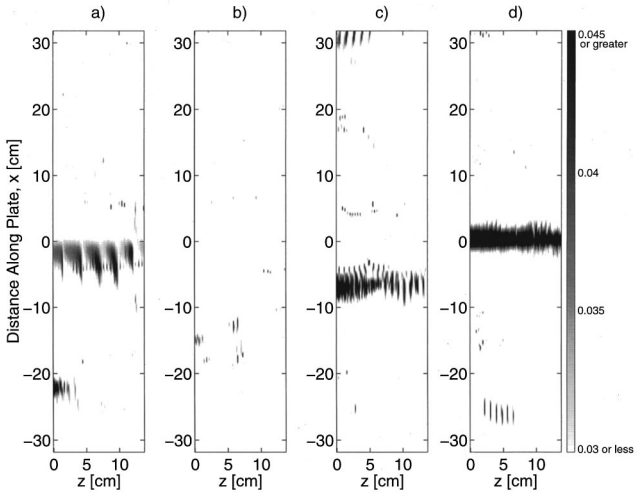

FIG. 9. Same as Fig. 8 for the minimum-variance distortionless processor. Here, some localization capability is shown in both the x and z directions for all leak/microphone-array geometries tested.

aged the side-lobe suppression capability of both processors is essentially equal but the MV processor continues to have a narrower main lobe than the Bartlett processor. The multiple-frequency Bartlett processor appears to have an advantage at low signal-to-noise ratios because its side lobe structure remains benign.

To determine the sensitivity of leak-location error to random error in microphone placement and speed of sound mismatch, Monte Carlo simulations of the experiment with the Bartlett processor were performed. The results of the simulation show that a root-mean-square (rms) error in microphone placement of 1 mm in each coordinate direction leads to approximately 6-mm rms error in leak location. The sensitivity to mismatch between the actual sound speed in the lab during an experiment, and the computed sound speed based on the measured temperature is predicted to be less important. A mismatch of 0.6 m/s (corresponding to a temperature error 1.0 °C in air at ordinary room conditions), should lead to an rms error of 1 mm in the leak location. Hence, the observed leak-location accuracy of ± 3 mm for the 1.22×10^{-5} cm^3/s leak easily falls within the bounds of the microphone placement error, but is larger than that likely to be caused by mismatch in the speed of sound.

IV. SUMMARY AND CONCLUSIONS

This investigation was undertaken to determine the capabilities of a photoacoustic leak detection and localization system based on a CO_2 laser and SF_6 as a tracer gas. The findings to date indicate that leaks with rates as low as 10^{-5} cm^3/s can be accurately detected and located using photoacoustic sounds. The results also lead to several additional conclusions. The ultimate limit for photoacoustic leak detection and localization will be the correlated noise produced by the moving laser beam as it interacts with the target surface. This limit may be lowered from its current value, which probably lies between 10^{-5} and 10^{-6} cm^3/s, through the use of MFP processors with enhanced noise rejection capabilities. Alternately, a surface-skimming laser scan system may reduce the correlated noise, but such a system would only be useful for interrogating leaks on planar components. Unfortunately, the details of the sound production mechanism have not yet been illuminated well enough to be able to explain the observed amplitude and phase fluctuations of the photoacoustic signal. However, the stability of the signal frequencies is certainly sufficient for photoacoustic leak detection and localization for leak rates of 10^{-5} cm^3/s and higher. It can also be concluded that multiple-frequency matched-field processing with either a linear or nonlinear processor produces enhanced side-lobe rejection over single-frequency processing. This is important for photoacoustic leak localization since almost any type of laser scanning system will produce photoacoustic sounds having a rich harmonic content that begs for exploitation. And finally, multiple-frequency Bartlett processing appears to be more robust than multiple-frequency, minimum-variance-distortionless processing, especially at low signal-to-noise ratios. As expected, however, the minimum-variance-distortionless processor provides higher spatial resolution at high signal-to-noise ratios, and would be the tool of choice for applications involving photoacoustic imaging of large tracer gas clouds.

ACKNOWLEDGMENT

This project has been funded by Ford Motor Company, Advanced Manufacturing Technology Development.

Baggeroer, A. B., Kuperman, W. A., and Schmidt, H. (**1988**). ''Matched Field Processing: Source Localization in Correlated Noise as an Optimum Parameter Estimation Problem,'' J. Acoust. Soc. Am. **83**, 571–587.

Baggeroer, A. B., Kuperman, W. A., and Mikhalevsky, P. N. (**1993**). ''An Overview of Matched Field Methods in Ocean Acoustics,'' IEEE J. Ocean Eng. **18**, 401–424.

Bell, A. G. (**1880**). ''On the Production and Reproduction of Sound by Light,'' Am. J. Sci. **20**, 305–324.

Bell, A. G. (**1881**). ''Upon the Production of Sound by Radiant Energy,'' Philos. Mag. **11**, 510–528.

Bird, R. B., Stewart, W. E., and Lightfoot, E. N. (**1960**). *Transport Phenomena* (Wiley, New York), pp. 527–529.

Brassington, D. J. (**1982**). ''Photo-acoustic Detection and Ranging-A New Technique for the Remote Detection of Gases,'' J. Phys. D **15**, 219–228.

Bucker, H. P. (**1976**). ''Use of Calculated Sound Fields and Matched-Field Detection to Locate Sound Sources in Shallow Water,'' J. Acoust. Soc. Am. **59**, 368–373.

Claspy, P. C. (**1977**). ''Infrared Optoacoustic Spectroscopy and Detection,'' in *Optoacoustic Spectroscopy and Detection*, edited by Y.-H. Pao (Academic, New York), pp. 133–166.

Collins, M. D., and Kuperman, W. A. (**1991**). ''Focalization: Environmental Focusing and Source Localization,'' J. Acoust. Soc. Am. **90**, 1410–1422.

Collins, M. D., Makris, N. C., and Fialkowski, L. T. (**1994**). ''Noise cancellation and source localization,'' J. Acoust. Soc. Am. **96**, 1773–1776.

Dewey, Jr., C. F. (**1974**). ''Opto-Acoustic Spectroscopy,'' Opt. Eng. (Bellingham) **13**, 483–488.

Dewey, Jr., C. F., Kamm, R. D., and Hackett, C. E. (**1973**). ''Acoustic Amplifier for Detection of Atmosphetic Pollutants,'' Appl. Phys. Lett. **23**, 633–635.

Fialkowski, L. T., Collins, M. D., and Perkins, J. S. (**1997**). ''Source localization in Noisy and Uncertain Ocean Environments,'' J. Acoust. Soc. Am. **101**, 3539–3545.

Fox, R. W., and McDonald, A. T. (**1992**). *Introduction to Fluid Mechanics* (Wiley, New York), p. 419.

Goldan, P. D., and Goto, K. (**1974**). ''An Acoustically Resonant System for Detection of Low-Level Infrared Absorption in Atmospheric Pollutants,'' J. Appl. Phys. **45**, 4350–4355.

Jackson, D. R., and Dowling, D. R. (**1991**). ''Phase Conjugation in Underwater Acoustics,'' J. Acoust. Soc. Am. **89**, 171–181.

Jensen, F. B., Kuperman, W. A., Porter, M. B., and Schmidt, H. (**1994**). *Computational Ocean Acoustics* (American Institute of Physics, New York), Chap. 10.

Kreuzer, L. B. (**1977**). ''The Physics of Signal Generation and Detection,'' in *Optoacoustic Spectroscopy and Detection*, edited by Y.-H. Pao (Academic, New York), pp. 1–25.

Kreuzer, L. B., and Patel, C. K. N. (**1971**). ''Nitric Oxide Air Pollution: Detection by Optoacoustic Spectroscopy,'' Science **173**, 45–47.

Lymann, J. L., Quigley, G. P., and Judd, O. P. (**1986**). ''Single-infrared-frequency Studies of Multiple Photon Excitation and Dissociation of Polyatomic Molecules,'' in *Multiple-Photon Excitation and Dissociation of Polyatomic Molecules*, edited by C. D. Cantrell (Springer, Berlin), pp. 9–94.

McRae, T. G. (**1989**). ''Remote Sensing Technique for Leak Testing of Components and Systems,'' Mater. Eval. **47**, 1308–1312.

McRae, T. G. (**1994**). ''Photo Acoustic Leak Location and Alarm on the Assembly Line,'' Mater. Eval. **52**, 1186–1190.

McRae, T. G., and Dewey, A. H. (**1992**). ''Photo-acoustic Leak Detection System and Method,'' US Patent No. 5,161,408.

McRae, T. G., and Kulp, T. J. (**1993**). ''Backscatter Absorption Gas Imaging: A New Technique for Gas Visualization,'' Appl. Opt. **32**, No. 21, 4037–4050.

Mercadier, M. E. (**1881**). ''On Radiophony,'' Philos. Mag. **11**, 78–80.

Morse, P. M., and Ingard, K. U. (**1968**). *Theoretical Acoustics* (Princeton University Press, Princeton, NJ), p. 783.

Perkins, J. S., and Kuperman, W. A. (**1990**). ''Environmental Signal Processing: Three Dimensional Matched Field Processing with a Vertical Array,'' J. Acoust. Soc. Am. **87**, 1553–1556.
Preece, W. H. (**1881**). ''On the Conversion of Radiant Energy into Sonorous Vibrations,'' Proc. R. Soc. London **31**, 506–520.
Lord Rayleigh (**1881**). ''The Photophone,'' Nature (London) **23**, 274–275.
Rosencwaig, A. (**1980**). *Photoacoustics and Photoacoustic Spectroscopy* (Wiley, New York), pp. 15–30.
Tolstoy, A. (**1993**). *Matched Field Processing For Underwater Acoustics* (World Scientific, River Edge, NJ).
Tyndall, J. (**1881**). ''Action of an Intermittent Beam of Radiant Heat upon Gaseous Matter.'' Proc. R. Soc. London **31**, 307–317.

Counteracting moment device for reduction of earthquake-induced excursions of multi-level buildings

Kosuke Nagaya,[a] Toshiyuki Fukushima, and Yasuhiro Kosugi
Department of Mechanical Engineering, Gunma University, Kiryu Gunma 376-8515, Japan

(Received 27 March 1998; revised 16 December 1998; accepted 4 February 1999)

A vibration-control mechanism for beams and columns was presented in our previous report in which the earthquake force was transformed into a vibration-control force by using a gear train mechanism. In our previous report, however, only the principle of transforming the earthquake force into the control force was presented; the discussion for real structures and the design method were not presented. The present article provides a theoretical analysis of the column which is used in multi-layered buildings. Experimental tests were carried out for a model of multi-layered buildings in the frequency range of a principal earthquake wave. Theoretical results are compared to the experimental data. The optimal design of the control mechanism, which is of importance in the column design, is presented. Numerical calculations are carried out for the optimal design. It is shown that vibrations of the column involving the mechanism are suppressed remarkably. The optimal design method and the analytical results are applicable to the design of the column. [S0001-4966(99)02105-0]

PACS numbers: 43.40.Cw, 43.55.Vj, 43.20.Ks [CBB]

INTRODUCTION

During the Hansin–Awaji earthquake in Japan, a number of buildings were destroyed. In particular, buildings and structures having large open spaces, such as parking garages, were destroyed due to lack of stiffened walls. To suppress vibrations of structures and buildings, much research has been done. Xue *et al.*[1] discussed an intelligent passive vibration-control system, in which an ordinary passive system is combined with an additional intelligent passive part. Prendergast[2] presented a base isolation system, and discussed vibration isolation of bridges. A numerical simulation was also carried out to assess the effectiveness of a passive isolator, an active vibration absorber, and an integrated passive/active control in the paper by Lee-Glause *et al.*[3] Villaverde and Koyama[4] discussed a tuned-mass-spring-dashpot system. In their paper, they show that the displacement of the roof is reduced by up to about 40% for a ten-story building. A method of tuned-mass dampers for seismic applications was also discussed by Sadek *et al.*[5] Utku *et al.*[6] presented a method in which the gravitational energy of the mass of the building is used to achieve active vibration control. Active control of flexural structures were discussed by Ohsumi and Sawada.[7] They also discussed a method for computing an optimal control system. Chuang *et al.* showed the LQR control method.[8] Feng and Mita[9] presented an innovative vibration-control system for reducing the dynamic response of tall buildings due to wind and seismic load.

Earthquakes contain large amounts of energy. If their energies can be transformed into vibration-control energies, vibrations from the earthquake can be suppressed without increasing the thickness of members of buildings. Studies based on this point of view have not been reported in previous papers. This paper presents a beam or column with a vibration-control device which transforms the vibration force into a vibration-control force. The column or beam is made of a hollow steel pipe into which a gear train mechanism is inserted. In this mechanism, an inertia force at the tip of the column is transformed into a control moment. Theoretical analysis of the multi-layered column or beam has been developed for the proposed vibration-control system. To validate the method and analysis, experimental tests were carried out for a multi-layered column with a vibration-control device present. The optimal design is of importance for the structures, so an optimal design method is also developed.

I. ANALYSIS OF A COLUMN OR BEAM WITH A VIBRATION-CONTROL DEVICE

A. Vibration-control device and its principle at operation

Figure 1 shows the geometry of a three layered structure (column or beam) having the proposed vibration-control device in each element layer. The structure consists of a hollow pipe (column) in which a gear train is installed. The numbers in Fig. 1 indicate the element and the floor; for example, the number 12 means gear 1 on the second floor. Consider the first floor in Fig. 1. An upper end of the rigid arm 01 is rigidly connected to the top of the column of the first floor. The other end of the arm is rigidly connected to shaft B that is rigidly connected to the gear 11. Thus the upper end of the arm is rigidly connected to the top of the column, and the lower end is rigidly connected to gear 11. Shaft B of gear 11 is free from the column, so if the arm moves in the horizontal direction, gear 11 also moves in the horizontal direction like a rack. Gears 11, 21, and 31 engage each other as shown in Fig. 1. The shaft of middle gear 21 is connected to the column, but gear 21 can rotate freely around its shaft. The shaft

[a]Author to whom correspondence should be addressed.

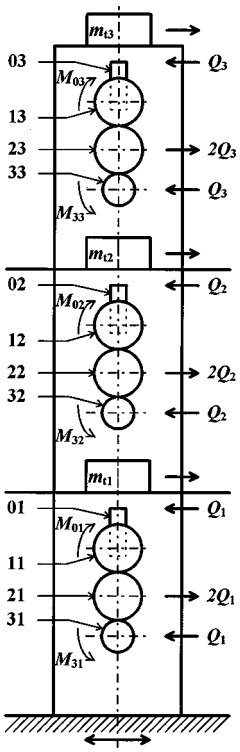

FIG. 1. Geometry of the present column.

of gear 31 is rigidly connected to both the column and gear 31. Thus gear 31 is rigidly connected to the column. The structure is subjected to bending vibrations due to inertia forces of the masses on the floors under an earthquake. In the system when the upper end of the column (the second floor) moves in the right direction due to the inertia forces, gear 11, which is connected to the rigid arm, moves to the right, and gear 21 rotates corresponding with the movement of gear 11. The rotation of gear 21 is transferred to gear 31. Since the rotating direction of gear 31 is opposite to that of the column displacement, and the shaft is rigidly connected to both gear 31 and the column, a restoring moment M_{31} is generated. The restoring moment M_{31} can be increased by using larger gear ratios in the gear train. Since gear 11 does not rotate in this system, a rack gear can also be used instead of the pinion gear. When the column just described is used in the construction of parking garages, its strength is increased by the restoring moment.

B. Analytical model

A three layered column is divided into a number of segments as shown in Fig. 2. The transfer matrix method is applied in the analysis. The cross section of the column is moderately thick in a practical column, so shear deformation is included. It is assumed that the effect of axial forces is small compared to the bending moments. Thus the bending deformation is included, but the effect of axial forces is neglected in the analysis. For a small element of the column without mass, the field transfer matrix for the beam element i is:

$$\{z\}_i=[T_f]_i\{z\}_{i-1}, \tag{1}$$

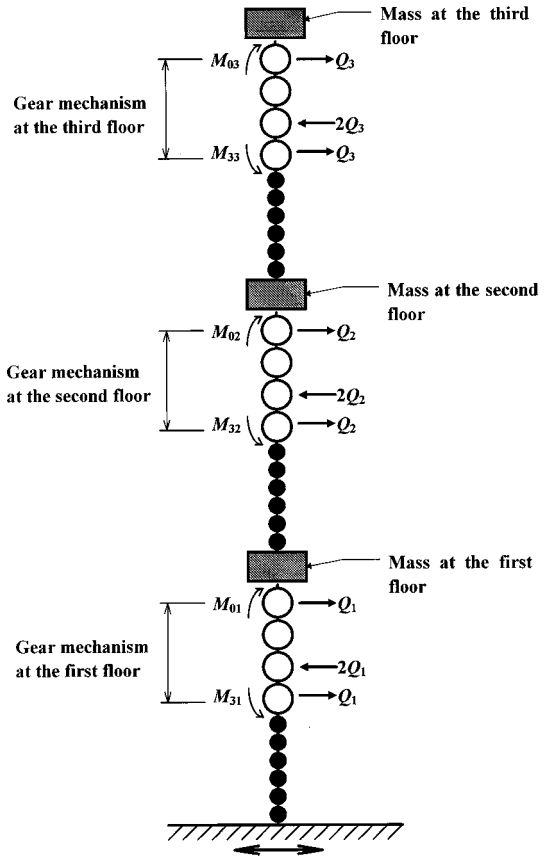

FIG. 2. Analytical model of the present multi-layered column.

where

$$\{z\}=\begin{Bmatrix} -w \\ \varphi \\ M \\ V \\ Q_1 \\ Q_2 \\ Q_3 \end{Bmatrix}, \quad [T_f]=\begin{bmatrix} 1 & l & \frac{l^2}{2EJ} & \frac{l^3}{6EJ}-\frac{l}{GA_s} & 0 \\ 0 & 1 & \frac{l}{EJ} & \frac{l^2}{2EJ} & 0 \\ 0 & 0 & 1 & l & 0 \\ 0 & 0 & 0 & 1 & 0 \\ 0 & 0 & 0 & 0 & 1 \end{bmatrix},$$

and where w is the displacement, φ is the bending slope, M is the bending moment, V is the shearing force, Q is the force acting to the gear, l is the element length in m, EJ is the flexural rigidity in $\mathrm{N\cdot m^2}$, $GA_s=GA/K_s$ is the shear rigidity in N, and K_s is the shear coefficient. Subscripts 1–3 depict the floor number.

The point transfer matrix for the element between the right side, R, and the left side, L, at the ith mass is:

$$\{z\}_i^R=[T_p]_i\{z\}_i^L, \tag{2}$$

where

$$[T_p]=\begin{bmatrix} 1 & 0 & 0 & 0 & 0 \\ 0 & 1 & 0 & 0 & 0 \\ 0 & 0 & 1 & 0 & 0 \\ m\omega^2 & 0 & 0 & 1 & 0 \\ 0 & 0 & 0 & 0 & 1 \end{bmatrix},$$

where m_i in kg is the concentrated mass involving the element mass at point i, and ω is the forced angular frequency in rad/s.

The point transfer matrix for rigid arms 01–03 is written:

$$[T_p]=\begin{bmatrix} 1 & 0 & 0 & 0 & 0 \\ 0 & 1 & 0 & 0 & 0 \\ 0 & 0 & 1 & 0 & l_0 \\ m_0\omega^2 & 0 & 0 & 1 & 1 \\ 0 & 0 & 0 & 0 & 1 \end{bmatrix}. \tag{3}$$

For gears 11, 12, and 13, the point transfer matrix is

$$[T_p]=\begin{bmatrix} 1 & 0 & 0 & 0 & 0 \\ 0 & 1 & 0 & 0 & 0 \\ 0 & 0 & 1 & 0 & 0 \\ m_1\omega^2-jc_1\omega & 0 & 0 & 1 & 0 \\ 0 & 0 & 0 & 0 & 1 \end{bmatrix}. \tag{4}$$

For gears 21, 22, and 23 it becomes

$$[T_p]=\begin{bmatrix} 1 & 0 & 0 & 0 & 0 \\ 0 & 1 & 0 & 0 & 0 \\ 0 & 0 & 1 & 0 & 0 \\ m_2\omega^2-jc_2\omega & 0 & 0 & 1 & -2 \\ 0 & 0 & 0 & 0 & 1 \end{bmatrix} \tag{5}$$

and it is written for gears 31, 32, and 33 as

$$[T_p]=\begin{bmatrix} 1 & 0 & 0 & 0 & 0 \\ 0 & 1 & 0 & 0 & 0 \\ 0 & 0 & 1 & 0 & -r_3 \\ m_3\omega^2-jc_3\omega & 0 & 0 & 1 & 1 \\ 0 & 0 & 0 & 0 & 1 \end{bmatrix}, \tag{6}$$

where the upper line of each variable has complex values, and m_0, m_1, m_2, and m_3 are the masses in kg including the gears and arms at gear 1, gear 2, and gear 3, respectively. l_0 is the length of the rigid arm in m for each floor, r_3 is the radius of the gear 3 in m, and c_1, c_2, and c_3 are damping coefficients for the floors 1, 2, and 3 due to friction between gears in N·s/m .

The state vector at point n is given by the following transfer equations:

$$\{z\}_n=[T_f]_n[T_p]_{n-1}[T_f]_{n-1}[T_p]_{n-2}\cdots[T_p]_1[T_f]_1\{z\}_0. \tag{7}$$

Thus when the base at floor 0 (ground) is taken to be point 0, and the mass at the top of the third floor to be point T, the matrix equation is written as follows by using the transfer matrix $\overline{B}$ between 0 through N:

$$\begin{bmatrix} -\overline{w} \\ \overline{\varphi} \\ \overline{M} \\ \overline{V} \\ \overline{Q_1} \\ \overline{Q_2} \\ \overline{Q_3} \end{bmatrix}_N = \begin{bmatrix} B_{11} & \cdots & \cdots & B_{14} & \cdots & \cdots & B_{17} \\ \vdots & \ddots & & & & & \vdots \\ \vdots & & \ddots & & & & \vdots \\ B_{41} & & & B_{44} & & & B_{47} \\ \vdots & & & & \ddots & & \vdots \\ \vdots & & & & & \ddots & \vdots \\ B_{71} & \cdots & \cdots & B_{74} & \cdots & \cdots & B_{77} \end{bmatrix} \times \begin{bmatrix} -\overline{w} \\ \overline{\varphi} \\ \overline{M} \\ \overline{V} \\ \overline{Q_1} \\ \overline{Q_2} \\ \overline{Q_3} \end{bmatrix}_0, \tag{8}$$

where B_{11} through B_{77} are the elements of the transfer matrix obtained by Eq. (7), where n is replaced with N. Each variable has a complex value, so the upper bar indicates a complex value.

C. Boundary conditions

Since the column is built-in at floor 0, the boundary conditions at point 0 are

$$-w_0^r=u_0, \quad w_0^i=0, \quad \varphi_0^r=0, \quad \varphi_0^i=0. \tag{9a}$$

At the right point of the tip mass at point N (upper surface of the mass attached to the top of the column) in the above equation, there is no restriction, so the boundary conditions are

$$M^r=0, \quad M^i=0, \quad V^r=0, \quad V^i=0, \tag{9b}$$

where superscript r denotes the real part, i the imaginary part, and u_0 is the base displacement in the horizontal direction.

Substituting Eq. (9) into (8), one obtains the value of each state variable at point 0:

$$-w_0=\overline{u_0}, \quad \overline{\varphi_0}=0$$

$$\overline{M_0}=\frac{1}{B_{33}B_{44}-B_{34}B_{43}} \times\left\{\begin{array}{l}(B_{34}B_{41}-B_{31}B_{44})\overline{u_0}+(B_{34}B_{45}-B_{35}B_{44})\overline{Q_1} \\ +(B_{34}B_{46}-B_{36}B_{44})\overline{Q_2}+(B_{34}B_{47}-B_{37}B_{44})\overline{Q_3}\end{array}\right\}, \tag{10}$$

$$\overline{V_0}=\frac{1}{B_{33}B_{44}-B_{34}B_{43}} \times\left\{\begin{array}{l}(B_{31}B_{43}-B_{33}B_{41})\overline{u_0}+(B_{35}B_{43}-B_{33}B_{45})\overline{Q_1} \\ +(B_{36}B_{43}-B_{33}B_{46})\overline{Q_2}+(B_{37}B_{43}-B_{33}B_{47})\overline{Q_3}\end{array}\right\}.$$

Substituting Eq. (10) into (7) gives the state variables at an arbitrary point in the column.

D. Derivation of the shearing force Q_{1-3}

The above equations involve the unknown shearing forces $\overline{Q}_1-\overline{Q}_3$. They will be found from the relations between the displacements of the structure and the rotation angles of the gears. Figure 3 shows the relation between the displacements at the gears and the rotation angles θ_{31-33} of the gears. The angles of rotation for gears 31–33 are written as follows with reference to Fig. 3:

$$\begin{aligned}
\overline{\theta}_{31}&=(r_{21}/r_{31})\{(1/r_{21})(\overline{w}_{11}-r_{11}\overline{\varphi}_{11})-\overline{\varphi}_{21}-\overline{w}_{21}/r_{21}\}-\overline{\varphi}_{31},\\
\overline{\theta}_{32}&=(r_{22}/r_{32})\{(1/r_{22})(\overline{w}_{12}-r_{12}\overline{\varphi}_{12})-\overline{\varphi}_{22}-\overline{w}_{22}/r_{22}\}-\overline{\varphi}_{32},\\
\overline{\theta}_{33}&=(r_{23}/r_{33})\{(1/r_{23})(\overline{w}_{13}-r_{13}\overline{\varphi}_{13})-\overline{\varphi}_{23}-\overline{w}_{23}/r_{23}\}-\overline{\varphi}_{33},
\end{aligned} \tag{11}$$

where r_{11-33}[m] are the radii of gears 13–33, w_{13-23}[m] are the displacements of column, and φ_{13-33}[rad] are the bending slopes of the column. Gear 3 for each floor is rigidly connected to the column, so the rotation angle should be zero; but in the practical system, the shaft is made of elastic material. Hence, the elasticity of the shaft has to be considered. The relations between the control torque and the restoring torque due to the shaft are:

$$\begin{aligned}
r_{31}\overline{Q}_1-\overline{K}_{\theta 1}\overline{\theta}_{31}&=0,\\
r_{32}\overline{Q}_2-\overline{K}_{\theta 2}\overline{\theta}_{32}&=0,\\
r_{33}\overline{Q}_3-\overline{K}_{\theta 3}\overline{\theta}_{33}&=0,
\end{aligned} \tag{12}$$

where $\overline{K}_{\theta 1}$, $\overline{K}_{\theta 2}$, $\overline{K}_{\theta 3}$ are the spring constants for rotation of the shafts. The shear forces and the angles of rotation have complex values, so the above equations have to be satisfied for each real and imaginary part:

$$\begin{aligned}
X(1)&=\mathrm{Re}(r_{31}\overline{Q}_1-\overline{K}_{\theta 1}\overline{\theta}_{31})=0\\
X(2)&=\mathrm{Im}(r_{31}\overline{Q}_1-\overline{K}_{\theta 1}\overline{\theta}_{31})=0\\
X(3)&=\mathrm{Re}(r_{32}\overline{Q}_2-\overline{K}_{\theta 2}\overline{\theta}_{32})=0\\
X(4)&=\mathrm{Im}(r_{32}\overline{Q}_2-\overline{K}_{\theta 2}\overline{\theta}_{32})=0\\
X(5)&=\mathrm{Re}(r_{33}\overline{Q}_3-\overline{K}_{\theta 3}\overline{\theta}_{33})=0\\
X(6)&=\mathrm{Im}(r_{33}\overline{Q}_3-\overline{K}_{\theta 3}\overline{\theta}_{33})=0.
\end{aligned} \tag{13}$$

Equations (13) are nonlinear simultaneous equations, so it is difficult to derive analytical results. The equations are solved by the numerical method known as Brent's method.[10] Using Eqs. (13), the six values of the shearing forces can be determined, then the state variables can be calculated.

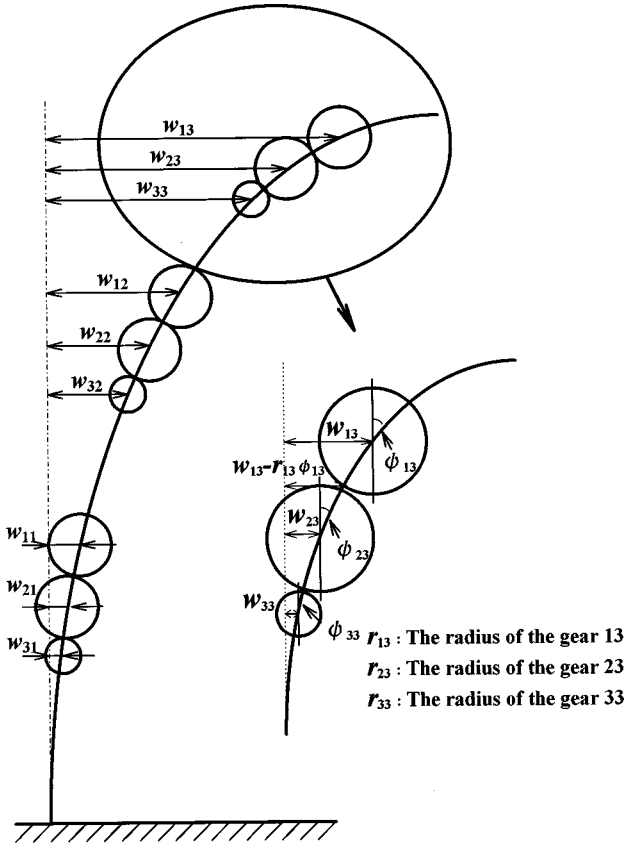

FIG. 3. Relation between displacements of the column and bending slope.

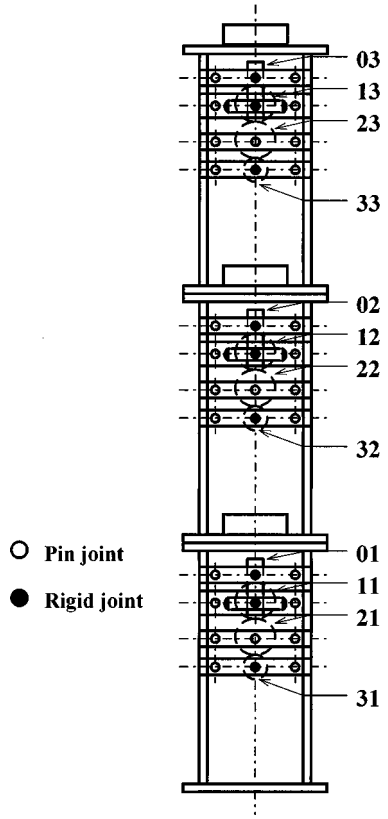

FIG. 4. Geometry of the column used in the experiment.

TABLE I. Dimensions of the present column with hollow square cross section.

Length in the axial direction	[mm]	300
Length of the cross section	[mm]	106
Width of the cross section	[mm]	106
Thickness of the column	[mm]	3
Diameters of pitch circle	[mm]	60 (gear 1)
		60 (gear 2)
		16 (gear 3)
		10 (Shaft for gear 1)
Radii of the shaft	[mm]	10 (Shaft for gear 2)
		8 (Shaft for gear 3)
Module of gears	[mm]	1.0
Mass on each foor	[kg]	1.1
Mass of the column	[kg]	5.7

TABLE II. Dimensions used in the numerical simulation.

Masses of the present column [kg]	Mass upper the gear mechanism	$m_i=0.031$
	Mass under the gear mechanism	$m_i=0.199$
	Rigid arm	$m_0=0.743$
	Gear 1	$m_1=1.170$
	Gear 2	$m_2=1.170$
	Gear 3	$m_3=0.313$
Radii of the gears [mm]	Gear 1	$r_1=30.0$
	Gear 2	$r_2=30.0$
	Gear 3	$r_3=8.00$
Equivalent damping coefficients between the gears [N·s/m]	Gear 1	$c_1=5.0$
	Gear 2	$c_2=5.0$
	Gear 3	$c_3=18.8$
Torsional rigidity of the shaft for the gear 3 [N·m/rad]	$K_\theta=5.0$	
Base displacement [mm]	1.50	
Size [mm×mm×mm]	300×100×100	

II. NUMERICAL CALCULATION AND EXPERIMENT

A. Experimental model

Figure 4 depicts the geometry of the column used in the experiment. The column is made of two steel plates of 3 mm thickness. In the figure, the arm (the rigid lever) made of steel with high rigidity is rigidly connected to the top of the column, and the shaft of gear 3 is rigidly connected to the plates and gear 3. There is a slit for the support plates which support the shaft of gear 1, so gear 1 moves in the horizontal direction with the arm. Gear 2 can rotate around its axis freely, so the movement of gear 1 is transmitted to gear 3 through gear 2, but the direction of rotation is changed by the middle gear 2. The height of each column is 300 mm, and the cross section is square with each length being 106 mm. The dimensions of the column is depicted in Table I. Three columns are connected to each other, and the three layered column is constructed as shown in Fig. 4.

B. Numerical examples

Numerical calculations are carried out for the column described above. The dimensions used in the calculation are the same as in Table I. Additional dimensions are shown in Table II. Figure 5 shows the frequency response of vibration amplitude of the displacement at the tip of the three layered column. The base is excited by a sinusoidal function with amplitude 1.5 mm. The solid line is the result when the column has the control device present. The result for the case of an ordinary column without a control device is shown by the dotted line.

The bending moment is of importance because columns generally fail in bending. Figure 6 shows the response curve for the bending moment at the base of the column.

C. Experiment

Figure 7 shows the geometry of the experimental setup. The three layered column lies on a horizontal exciting table ② which vibrates in the horizontal direction. Laser gap sensors ④ detect displacements at the top of the column and the base. To detect moments in the column, two strain gauges ③ are pasted on the surface of the column plate near the base and the middle point as shown in Fig. 7. The detected signals are input to an oscilloscope. The wave in the oscilloscope is stored in memory, then it is written to the printer.

Experimentally obtained results are depicted by white and black dots in Fig. 5 and Fig. 6. In these figures, the white square dots denote the experimental result without a control device, and the black triangle dots show the result with the control device present.

In Fig. 5, the displacement of the column with the control device at the resonant frequency is only 4% of that without the device. The displacement at low frequency (at 3.5 Hz) with the device is also suppressed within 40% of that without the device. Almost the same suppression ratios are found for the bending moment in Fig. 6. In this system, the shearing force (the contact force between gear teeth) increases with the amplitude of vibration of the column because the gear rotation is the sliding motion between gear teeth. When the friction force between gear teeth becomes large, the resonance peak decreases. Although a damper is not used, large damping can be obtained by using the friction

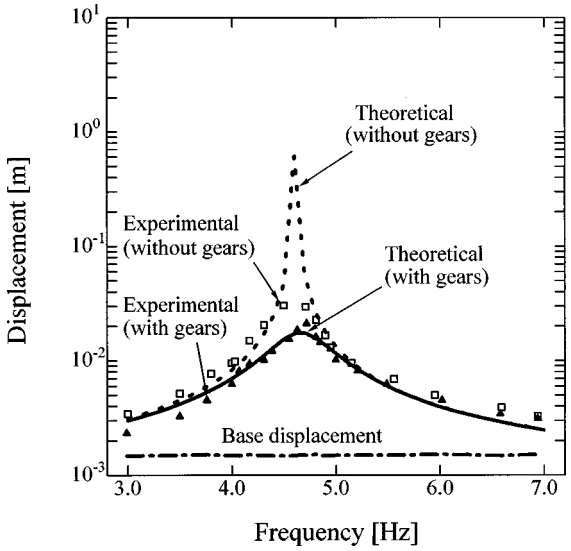

FIG. 5. Comparison between frequency response of the displacements for the present column with gears and ordinary column without gears.

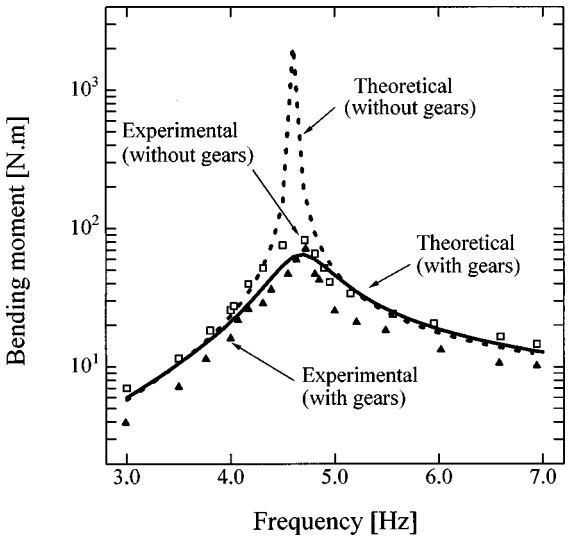

FIG. 6. Comparison between frequency response of the bending moments at the base of the first floor for the present column with gears and ordinary column without gears.

between gear teeth in this system. This is the merit of this device. The other interesting phenomena are the amplitudes in the low frequency region. For ordinary buildings, designs are made under the first resonance frequency, and only the first mode is considered. Therefore, small stresses in the low frequency region are desirable. In the present system, the stresses in the low frequency region are smaller than those without control device, as mentioned above.

Since the experimental column was constructed by using many bolts, as shown in Fig. 4, there were some differences between the column and the analytical model. Thus there were a few discrepancies between the experimental and the theoretical results. However, the analysis can be used from a design engineering point of view.

III. OPTIMAL DESIGN

In the above discussion, the present theoretical analysis has enough accuracy from a design engineering point of view. The column used in the experiment is only a model to verify the present system and the theoretical analysis. It is not a optimal design. There will be optimal values for the location of gears, gear ratios, and lengths of arms which minimize vibrations of column. Therefore, we considered this optimal design next.

A. Model of optimal design

In the optimal design problem, a column is chosen whose sizes are close to those of real columns. We consider a column with 3000 mm height whose cross section is square with 520 mm on sides made of 3 mm thick steel pipe. A mass of 700 kg is assumed to be on the top of each column. Table III depicts the dimensions of the column used in the optimal design. A three layered column is constructed by combining the columns with these dimensions.

In the design of the gears, Ni–Cr–Mo steel (SNCM616) is used for the gear shaft. If we use a safety factor at 3, the allowable normal stress, σ_b, and allowable shear stress, τ_b, are as follows: $\sigma_b = 1177/3 \fallingdotseq 392\ \mathrm{N/mm^2}$, $\tau_a = 294/3 \fallingdotseq 98\ \mathrm{N/mm^2}$. The shafts sizes are given by using the usual design methods. These values are depicted in Table III.

TABLE III. Dimensions of the present column with hollow square cross section.

Length in the axial direction	[mm]	3000
Length of the cross section	[mm]	520
Width of the cross section	[mm]	520
Thickness of the column	[mm]	10
Thickness of the gear	[mm]	350
Radii of the shaft	[mm]	100 (Shaft for gear 1) 100 (Shaft for gear 2) 90 (Shaft for gear 3)
Module of gears	[mm]	12
Mass on each floor	[kg]	700
Mass of each column	[kg]	1193

In the optimal design, the gears are installed inside the hollow pipe, so there are lower and upper limits for the sizes of the gears.

From the strength of gear design, the minimum diameters for the gears are $D_1, D_2 = 192, D_3 = 180$. The maximum diameter is 380 mm (Z=31). Thus there are the following limitations:

$$192 \leqq D_1, D_2 \leqq 372, \quad 180 \leqq D_3 \leqq 372.$$

There is also a geometric limitation for the arm:

$$1.5 \leqq location\ of\ rigid\ arm \leqq 2.8.$$

The bending moment is of importance, because the column will fail at the point of maximum bending moment. Tall buildings can be designed for higher modes, but ordinary buildings are designed for the first mode. The principal frequencies of earthquakes in Japan are in the range 2–4 Hz, so the stress at the base has to be smaller than the allowable stress in this frequency region. Then the bending moments in the first mode (for frequencies less than the first resonance frequency) are minimized by choosing optimal values of the arm location and gear ratios. For this reason, the following cost function is considered:

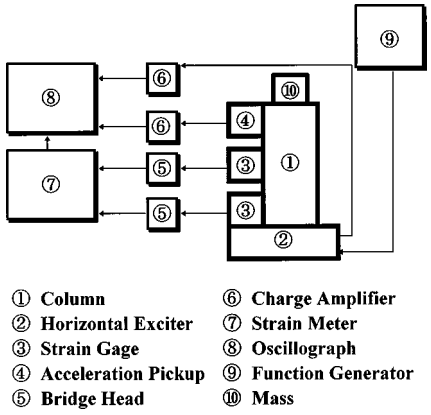

FIG. 7. Experimental setup for measuring vibration response.

TABLE IV. Optimal parameters obtained for the gear mechanism.

		Before optimization	After optimization
First floor	Diameter of pitch circle of gear 1 [mm]	300	372
	Diameter of pitch circle of gear 2 [mm]	300	192
	Diameter of pitch circle of gear 3 [mm]	204	180
	Location of the rigid arm [mm]	2000	2800
Second floor	Diameter of pitch circle of gear 1 [mm]	300	372
	Diameter of pitch circle of gear 2 [mm]	300	372
	Diameter of pitch circle of gear 3 [mm]	204	180
	Location of the rigid arm [mm]	2000	2055
Third floor	Diameter of pitch circle of gear 1 [mm]	300	372
	Diameter of pitch circle of gear 2 [mm]	300	192
	Diameter of pitch circle of gear 3 [mm]	204	180
	Location of the rigid arm [mm]	2000	1500

$$J=\alpha_1\int_{\omega_1}^{\omega_2}|M(\omega)|d\omega+\int_{\omega_1}^{\omega_2}\{\alpha_2|Q_1(\omega)|+\alpha_3|Q_2(\omega)| + \alpha_4|Q_3(\omega)|\}d\omega, \tag{14}$$

where $M(\omega)$ is the bending moment at the base, $Q_i(\omega)$ is the force acting on the gear teeth at the ith floor, α_{1-4} are the weights, ω is the forced angular frequency, and ω_1 and ω_2 are the lower and upper angular frequencies, respectively, in the considered frequency range. (In this paper, a frequency range up to 4 Hz is used.) Since it is difficult to design the gears when the force acting on the gear tooth is significantly large, the force Q_{1-3} is also involved in the cost function. By minimizing the cost function given in Eq. (14), we find optimal values of arm and gears under the minimum moments and minimum forces. The optimal values can be calculated by using the form:

$$X_{sj+1}=X_{sj}-\eta(\partial J/\partial X_{sj}) \quad (s=1,2,\ldots,12,\ j=1,2,\ldots,\infty), \tag{15}$$

where X_{sj} is the sth parameter for obtaining optimal value, η is the coefficient of weight, and j is the iteration. Repeating the calculation of Eq. (15), we find the optimal value for each parameter. The obtained optimal values are given in Table IV. Initial values are also shown.

B. Numerical simulations for the optimal column

In the numerical calculation, the rotation spring constant K_θ for a shaft is given by

$$K_\theta=(G\pi d^4/32l)$$

under the assumption that there is no backlash, where G is the shear modulus, d is the diameter of the shaft of gear 3, l is the length of the shaft, and c_1, c_2, and c_3 are the damping coefficients due to friction between the gear teeth. The damping coefficients are determined from the experimental data. Table V shows the coefficients used in the simulation.

TABLE V. Parameters used in the optimal problem.

Masses of the present column [kg]	First floor	Mass upper the gear mechanism	$m_i=4.54$
		Mass under the gear mechanism	$m_i=11.50$
		Rigid arm	$m_0=98.10$
		Gear 1	$m_1=105.0$
		Gear 2	$m_2=99.10$
		Gear 3	$m_3=82.60$
	Second floor	Mass upper the gear mechanism	$m_i=4.54$
		Mass under the gear mechanism	$m_i=11.50$
		Rigid arm	$m_0=98.10$
		Gear 1	$m_1=105.0$
		Gear 2	$m_2=99.10$
		Gear 3	$m_3=82.60$
	Third floor	Mass upper the gear mechanism	$m_i=4.54$
		Mass under the gear mechanism	$m_i=11.50$
		Rigid arm	$m_0=98.10$
		Gear 1	$m_1=105.0$
		Gear 2	$m_2=99.10$
		Gear 3	$m_3=82.60$
Radii of the gears [mm]	First floor	Gear 1	$r_1=114.0$
		Gear 2	$r_2=108.0$
		Gear 3	$r_3=90.0$
	Second floor	Gear 1	$r_1=114.0$
		Gear 2	$r_2=108.0$
		Gear 3	$r_3=90.0$
	Third floor	Gear 1	$r_1=114.0$
		Gear 2	$r_2=108.0$
		Gear 3	$r_3=90.0$
Equivalent damping coefficients between the gears [N·sm] (used to all floors)		Gear 1	$c_1=6.00\times10^3$
		Gear 2	$c_2=6.00\times10^3$
		Gear 3	$c_3=7.60\times10^3$
Torsional rigidity of the shaft for the gear 3 [N·m/rad] (used to all floors)			$K_\theta=1.68\times10^6$
Base displacement [mm]			15.0

C. Response of the optimal column

Figure 8 shows the frequency response of the tip displacement of the three layered column. The solid line shows the result after optimization, and the chain line shows the result before optimization. The result without gears is also shown by the dashed line. The amplitude of tip displacement with the device at 3.5 Hz is suppressed within 40% of that without control in the case of the optimal device. Tip displacement in the case of the optimal device at the frequency is also suppressed to within 70% of that with the device before optimization. Displacement at the resonance frequency compared to that of the column without gears is re-

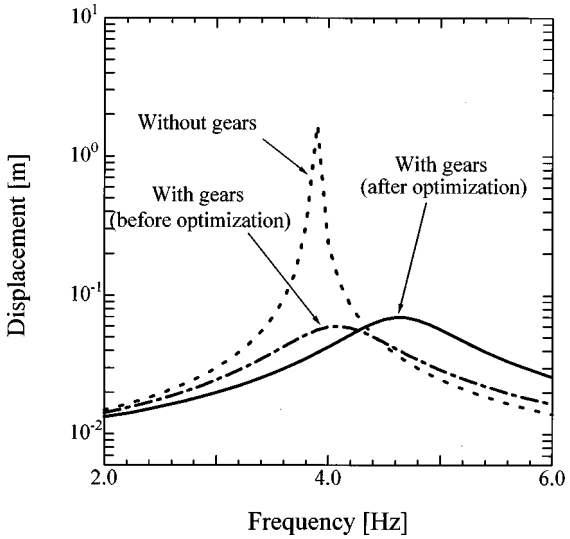

FIG. 8. Comparison between frequency response of the displacements at the tip of the third floor for the optimal problem.

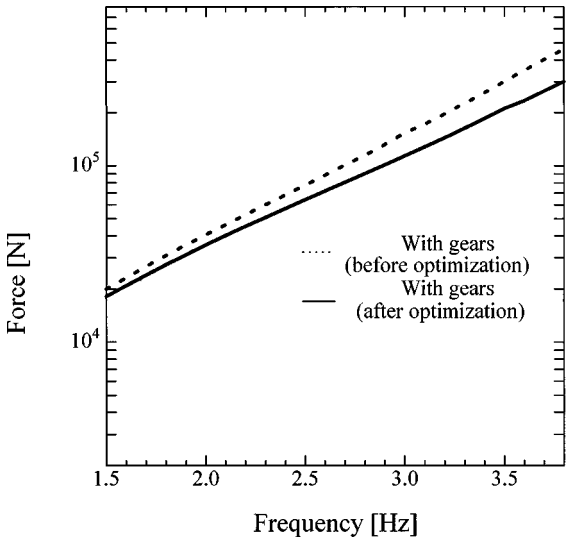

FIG. 10. Comparison between the reaction force $|Q_3|$ before optimization and that after optimization.

duced due to friction forces between the gear teeth. The resonance frequency of the optimal column increases compared to that of the column before optimization. The displacement in the designed frequency range (from 0 to 4 Hz) is especially reduced. Figure 9 shows the amplitudes of bending moment at the base of the column versus the forced frequency. The moment at 3.5 Hz is also suppressed to within 40% of the value without control device. The bending moments in the designed frequency range have to be small to prevent failure of the column. Figure 10 depicts the reaction force of gear 3 at the third floor. The force after optimization is smaller than that before optimization. For a 3.5 Hz frequency, the force after optimization is suppressed to within 66% of the force with the device before optimization. Thus the controlled columns have advantages over columns without gears. In addition, the present method of optimal design is applicable.

Since the gear train is installed in the column mentioned above, if the large gear can be placed outside the column, a more significant effect can be obtained because the effect of vibration suppression increases with the gear ratio.

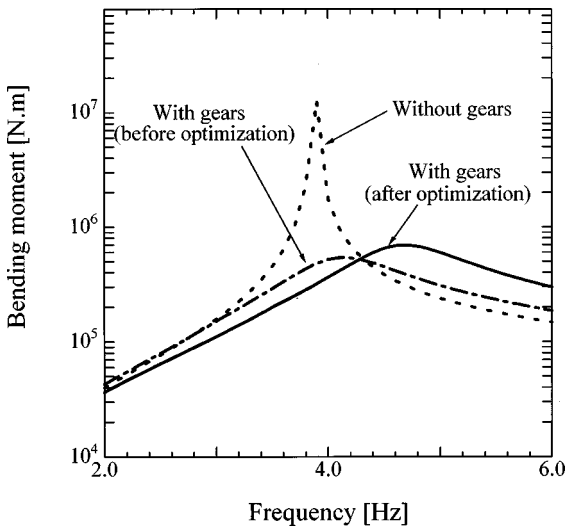

FIG. 9. Comparison between frequency response of the bending moments at the base of the first floor for the optimal problem.

IV. CONCLUSIONS

A multi-layered intelligent column is presented in which the earthquake force is transformed into a vibration-control force. The column is constructed with three element columns with gear mechanisms. Each column transforms the earthquake force to a control force. Hence, the control forces act on each floor.

Analytical expressions for the response of the column are presented. To validate the present system and theoretical result, experimental tests have been carried out on a model of the multi-layered column.

A method of optimal design for the column is also presented, and numerical calculations are carried out for some important cases.

It is ascertained that the displacements and the bending moments for the column with the control device are suppressed to within 40% of those without the device. By making use of the optimal design, the vibration displacements and the bending moments can be suppressed to within 70% of those for the column with the device before optimization. Hence, the present column has advantages compared with the columns without control devices, and it can be used for the columns in parking garages.

[1] S. Xue, J. Tobita, and S. Kurita, ''Mechanics and dynamics of intelligent passive vibration system,'' Journal of Engineering Mechanics **123**, 322–327 (1997).
[2] J. Prendergast, ''Seismic isolation in bridges,'' Civil Engineering **65**, 58–61 (1995).
[3] G. Lee-Glauser, G. Ahmadi, and Lucas G. Horta, ''Integrated passive/active vibration absorber for multistory buildings,'' Journal of Structural Engineering **123**, 499–504 (1997).
[4] R. Villaverde Koyama and A. Leslie, ''Damped resonant appendages to increase damping in buildings,'' Earthquake Engineering and Structural Dynamics **22**, 491–507 (1993).
[5] F. Sadek, B. Mohraz, and Andrew W. Taylor, ''A method of estimating the parameters of tuned dampers for seismic applications,'' Earthquake Engineering and Structural Dynamics **26**, 617–635 (1997).

[6] S. Utku, B. Utku, and Ben K. Wada, ''A readily available energy source for active vibration-control in buildings,'' Earthquake Engineering and Structural Dynamics **22**, 823–827 (1993).
[7] A. Ohsumi and Y. Sawada, ''Active control of flexible structures subject to distributed and seismic disturbances,'' J. Dyn. Syst., Meas., Control **115**, 649–657 (1993).
[8] C.-H. Chung, D.-N. Wu, and Q. Wang, ''LQR for state-bounded structural control,'' J. Dyn. Syst., Meas., Control **118**, 113–119 (1996).
[9] Marita Q. Feng and A. Mita, ''Vibration control of tall buildings using mega-subconfiguration,'' Journal of Engineering Mechanics **121**, 1082–1088 (1995).
[10] I. J. More and M. Y. Cosnard, ACM Trans. Math. Softw. **5**, 64–85 (1979).

Circumferential waves on an immersed, fluid-filled elastic cylindrical shell

X. L. Bao and P. K. Raju
Department of Mechanical Engineering, Auburn University, Auburn, Alabama 36849-5341

H. Überall
Department of Physics, Catholic University of America, Washington, DC 20064

(Received 18 March 1997; revised 2 November 1998; accepted 20 November 1998)

The existence of various types of circumferential waves, both predominantly shell or fluid borne, and the repulsion of their dispersion curves is discussed here for an infinite, thin elastic, circular-cylindrical shell immersed in a fluid and filled with another fluid. The study is based on an analytic calculation of the partial-wave resonances in the acoustic scattering amplitude of a normally incident plane wave. A large number of cases of repulsion are found in the phase-velocity dispersion curves of the various types of circumferential waves due to the shell–fluid coupling. © *1999 Acoustical Society of America.* [S0001-4966(99)02003-2]

PACS numbers: 43.40.Ey, 43.40.Fz [CBB]

INTRODUCTION

The phase-velocity dispersion curves and acoustic excitation of propagating circumferential waves on thin elastic cylindrical shells immersed in water; have been discussed in the literature in various stages.[1–10] For a thin metal shell (such as aluminum), the dispersion curves of these waves are similar to those of the Lamb waves $S_0, A_1, S_1, A_2, S_2, \ldots$ on a free plate of the same thickness, or even on a water-loaded plate. An exception here is the lowest antisymmetric plate-borne wave A_0 which, when the plate is fluid loaded on one side, gets joined by a fluid-borne wave (called a Scholte–Stoneley wave, A wave, or $l=0$ wave) with which it interacts as seen in Fig. 1. The two dispersion curves both rise from the origin at zero frequency with different slopes, then approach each other as if about to cross at the critical frequency (point P) where the phase velocities get close to the fluid sound speed c_0 (i.e., $c_0/c_T=0.486$), but then veer away from each other again, one dispersion curve asymptoting to c_0 from below for frequency $\rightarrow\infty$, the other one to the (higher) Rayleigh speed c_R on a half-space of the plate material, again from below. This is discussed in a recent study of waves on fluid-loaded plates,[11] as well as in a review paper[12] which also discusses the analogous cases of (evacuated) cylindrical and spherical[13,14] shells.

This ''curve-repulsion'' phenomenon is shown in Fig. 1 for an aluminum plate of thickness d, water loaded on one side, with the phase velocity c_p of the two interacting lowest-order waves on the plate plotted versus the frequency–thickness product fd. The light-dotted curve shows the lowest Lamb wave A_0 for a free plate. If water loaded on one side, two interacting waves exist as shown by the other curves. In the literature (e.g., Ref. 12), these are called A_0 for the upper curve, and A for the lower curve. (For the analogous spherical-shell case, they were named a_{0+} and a_{0-}, respectively,[13] the appearance of the second branch a_{0-} being referred to as ''bifurcation.'' This notation is entered in Fig. 1 as an alternative.) It was then shown[12] that at the near-crossover point P, the physical nature of the waves gets exchanged, A_0 to the right of P (on the curve portion marked a_0) being the plate-borne wave (i.e. a pseudo-Lamb wave) and A (on the curve portion marked a) the fluid-borne (Scholte–Stoneley) wave, while in the low-frequency part of Fig. 1 to the left of P, A_0 is now fluid borne on the curve portion marked a here, and A is plate-borne on the curve portion marked a_0 here (see also Ref. 15 for the analogous phenomenon in the higher-order free Lamb waves).

This introductory discussion referring to plate waves was given here in order to prepare the state for analogous cases of cylindrical shells (see Ref. 12 for one-sided water-loaded cylindrical and even spherical shells), helping to understand the similarities here. For empty immersed shells, the dispersion curves of low-order circumferential waves were found very similar to those of the plate, Fig. 1, as strikingly shown by Fig. 3 of Ref. 4. The fluid-borne wave was first found here by Subrahmanyam[2] (see Fig. 6 of Ref. 8, where his results are reproduced, for a complete picture). Other investigations[3,9] only describe portions of the shell-equivalent curves of Fig. 1. It appears to us that the findings of Refs. 2, 4, and 8 have completed the formal classification of the two lowest circumferential waves on an empty, immersed thin cylindrical shell, while the above discussion, aided by the use of the markings a and a_0 indicating the physical nature of the waves, has clarified this nature (fluid-borne or shell-borne) of the waves. We should only add that in a transition region for the plate around point P of Fig. 1 (as well as for the shells), since the curve repulsion is gradual rather than abrupt, each wave will have a mixed nature there, with some of the other physical character admixed to it.

The next step, taken in the following, is to consider immersed shells that in addition to immersion are filled with (another) fluid. Here the shell vibrations are coupled to both fluids, which generates additional waves that propagate circumferentially in the interior fluid filler, and which interact with the A_0 and A waves present on the shell and in the external fluid, causing additional phenomena of dispersion curve repulsions. An earlier step towards the shell loaded

 0001-4966/99/105(5)/2704/6/$15.00

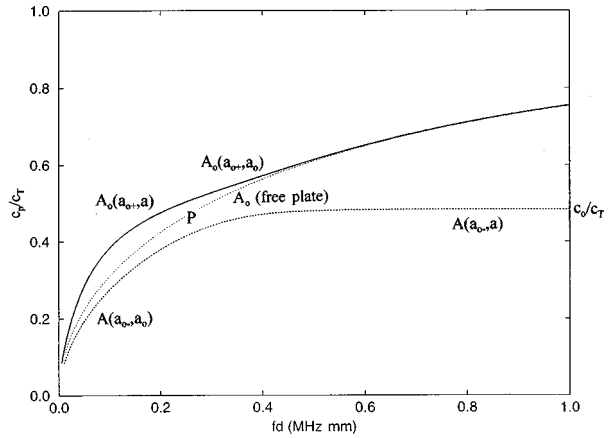

FIG. 1. Phase velocity dispersion curves of lowest-order waves propagating on an aluminum plate (material parameters of Al: density $\rho=2.7$ g/cm^3, compressional bulk speed $c_L=6350$ m/s, shear speed $c_T=3050$ m/s. Free plate: A_0 wave (light-dotted curve). Plate water loaded on one side (material parameters of water: density $\rho_0=1.0$ g/cm^3, sound speed $c_0=1483$ m/s): A wave, heavy-dotted curve; A_0 wave: solid curve, with near-crossover at point P. The symbols a and a_0 designate the water-borne and the plate-borne portions of these curves, respectively.

with two fluids was taken by Ref. 10, but it was based on resonance analysis mainly of experimental results (as well as on arrival times of scattered pulses), thus providing a somewhat incomplete picture. Our present results are obtained by the calculation of partial-wave resonances in acoustic scattering amplitudes which furnishes both the amplitudes and widths of the resonances, as well as the circumferential wave dispersion curves. (It should be mentioned here that for a solid body or a thick shell, the scattering phenomenon will generate both circumferential surface waves and those that penetrate the body, being referred to as ''through waves.''[16] For thin shells, however, as they are considered here, all propagating wave modes in the shell can, by geometry, be referred to as ''circumferential.'')

I. CALCULATION OF SCATTERING RESONANCES AND DISPERSION CURVES

The far-field backscattering amplitude (form function) f_∞ can be written for a spherical shell immersed and fluid loaded, at normal incidence, as[1]

$$f_\infty(\pi)=2/(i\pi x)^{1/2}\sum_{n=0}^{\infty}\varepsilon_n(-1)^n R_n(x), \tag{1}$$

where $x=ka$, $k=2\pi f/c_0$, c_0=sound speed in the ambient fluid, a=external shell radius (the internal radius is called b), $\varepsilon_n=2-\delta_{n0}$ with the Kronecker symbol used here being $\delta_{n0}=1(n=0),\ 0(n\neq 0)$,

$$R_n(x)=-\frac{J_n(x)F_n(x)-xJ_n'(x)}{H_n^{(1)}(x)F_n(x)-xH_n^{(1)\prime}(x)}, \tag{2a}$$

where $J_n(x)$ and $H_n^{(1)}(x)$ are the Bessel and Hankel (first kind) functions, respectively, and the prime denotes the derivative with respect to the argument x. Further,

$$F_n(x)=\frac{\rho_0}{\rho_{cy}}x_T^2\frac{D_n^{(1)}(x)}{D_n^{(2)}(x)}, \tag{2b}$$

with ρ_0 the density of the ambient fluid, ρ_{cy} that of the shell material, $x_T=k_Ta$, $k_T=2\pi f/c_T$, c_T being the shear speed in the shell material, and $D_n^{(1)}(x)$, $D_n^{(2)}(x)$ are 5×5 determinants that contain all other parameters of the shell and the internal fluid; they are given, e.g., in Ref. 1.

The nth term in Eq. (1) is called ''nth partial wave,'' and it exhibits resonances associated with the mode number n. We find these resonances from a plot of the nth partial wave amplitude which also displays the resonance width. The scattering amplitude, as well as the individual partial waves, also contain a nonresonant background term corresponding to specular reflection,[17] and in order to exhibit the resonances clearly this background term should be coherently subtracted. For a thick shell, one can use as a background term the scattering amplitude for a rigid shell[17] obtained from $F_n(x)\to\infty$. However, for a thin shell an ''intermediate background'' must be used, which can be obtained from a pragmatic approach based on the value of the scattering amplitude between resonances,[18] or simply from the scattering amplitude from a (fluid) shell[19,20] in which one sets $c_T=0$. (Note that a very detailed derivation and discussion of the intermediate background was given by Werby,[21,22] where it is shown under what conditions this background must be used, and when for a thick shell the rigid background, and for a thin shell the soft background, is applicable). In the first approach, described in Ref. 18 and which is appropriate for the fairly thin shells (0.92%) that will be considered here, the resonant partial waves are obtained from the subtraction

$$f_n^{\rm res}(x)=f_n(x)-f_n^b(x), \tag{3a}$$

$$f_n(x)=2/(i\pi x)^{1/2}\varepsilon_n(-1)^n R_n, \tag{3b}$$

$$f_n^b(x)=2/(i\pi x)^{1/2}\varepsilon_n(-1)^n R_n^b, \tag{3c}$$

$$R_n^b(x)=-\frac{J_n(x)F_n^b(x)-xJ_n'(x)}{H_n^{(1)}(x)F_n^b(x)-xH_n^{(1)\prime}(x)} \tag{3d}$$

with F_n^b corresponding to the background values chosen according to Ref. 18. (The fluid–shell subtraction method was successfully used by us for the case of empty cylindrical shells.)

We present our results in the form of ''Regge trajectories,''[23] i.e., plots of the resonant frequencies along the abscissa, versus the mode number of the resonance n on the ordinate. As a new feature, however, we superimpose on these graphs, for each value of n, a plot of the modulus of the partial-wave amplitude versus frequency. This shows not only the resonance locations, but also their widths, which furnishes additional insight into previously noticed experimental observabilities of the corresponding circumferential waves.

II. EVACUATED ALUMINUM SHELL IMMERSED IN WATER

Before applying our approach to the immersed shell filled with a fluid, we shall demonstrate its use for the immersed evacuated shell. We show results for an aluminum shell of thickness parameter b/a immersed in water. Figure 2 presents our augmented Regge diagram for $b/a=0.92$, the

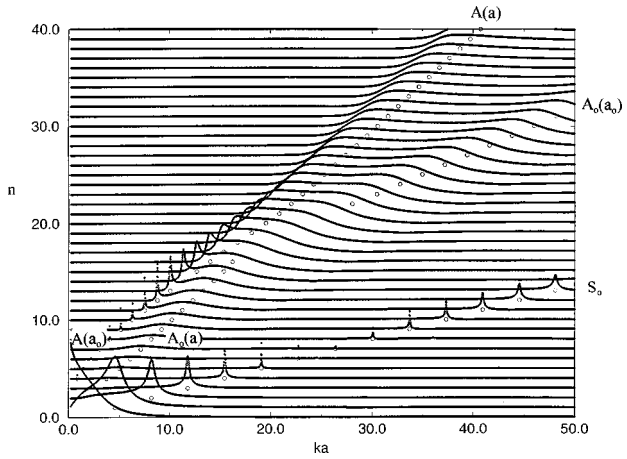

FIG. 2. Regge diagram showing resonance frequencies of A, A_0 (or alternately, showing the physical indicators a, a_0), and S_0 waves for given mode numbers n, with superimposed nth partial-wave scattering amplitude moduli versus frequency, for an evacuated, water-immersed aluminum shell of thickness parameter $b/a=0.92$.

points being located underneath the partial-wave maxima at the value of n of the partial wave. The several maxima in each partial wave show two families A and A_0 of interacting waves, and, incidentally, also a third family corresponding to the S_0 Lamb wave.[3,4] The designations for the waves are obtained from converting Fig. 2 into a phase velocity dispersion diagram, via[24]

$$c_p/c_0=(ka)^*_{nl}/n, \tag{4}$$

$(ka)^*_{nl}$ being the resonance value of ka. Figure 3 shows the corresponding results, as well as the A_0 curve of the free shell (stars), and one can see that these immersed-shell results agree closely with those of the A and A_0 curves of the plate water loaded on one side (Fig. 1).

Similar results are shown in the following figures for a somewhat thicker ($b/a=0.88$) Al shell: Fig. 4 corresponds to Fig. 3 for the thinner shell but here we have also entered the S_0 wave dispersion curve. Figure 5 shows the entire resonant part of the form function (summed coherently over n),

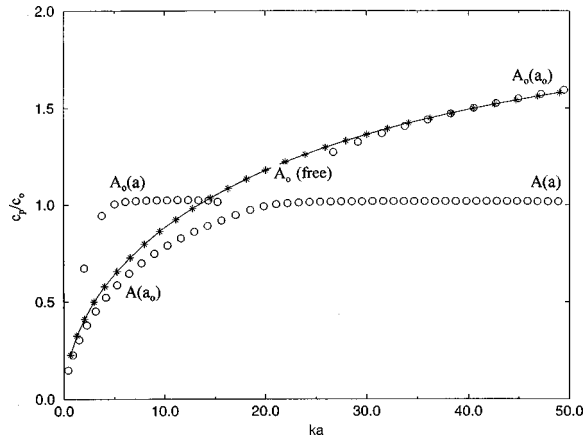

FIG. 3. Phase velocity dispersion curves of A and A_0 (with physical indicators a and a_0) waves for the case of Fig. 2 (circles), and of the A_0 wave on a free aluminum shell (solid curve with asterisks).

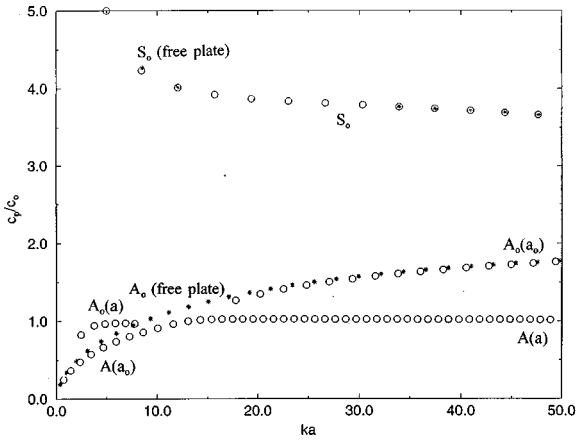

FIG. 4. Phase velocity dispersion curves of A, A_0 (a,a_0) waves and also the S_0 wave for the case of shell thickness $b/a=0.88$ (circles), and of the A_0 and S_0 wave on a free aluminum shell (asterisks).

the resonant peaks being identified by (n,l) where $l=0$ is the A wave, $l=2$ the S_0 wave, and the (experimentally often noted) absence of any observation of the A_0 wave in very thin shells is explained by the large widths of the corresponding resonance peaks (Fig. 2) which makes these peaks hard to see. Note that the A_0 wave has recently been seen[25] in an experiment based on Schlieren observations, rather than on an observation of the resonance peaks. Another forthcoming paper[26] shows, in figures similar to the present Fig. 5, how the A_0 wave manifests itself through observable resonances for shell thicknesses $b/a<0.9$, but that these resonances disappear from observation for thinner shells, $b/a>0.9$. In the same reference,[26] analytical discussions are given to explain details of the dispersion curve repulsion phenomena for evacuated shells, such as in the present Figs. 3 and 4. The fluid-filled cylindrical shells, to be studied in the following section, exhibit dispersion curves additional to these (labeled F_i) which are due to waves in the internal fluid (with repulsion phenomena of their own) (as will be seen in Fig. 7).

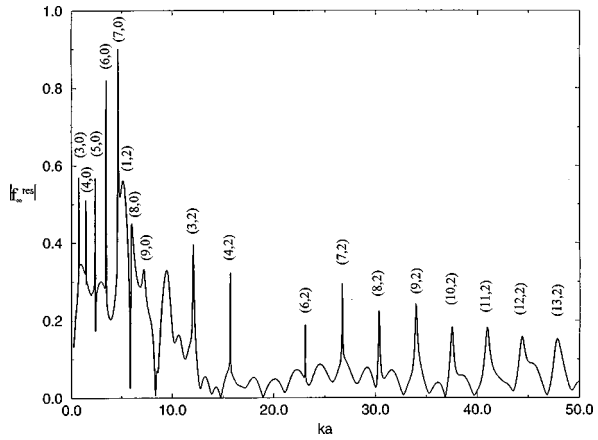

FIG. 5. Complete resonance spectrum of the backscattering amplitude modulus of an evacuated, water-loaded Al shell with $b/a=0.88$.

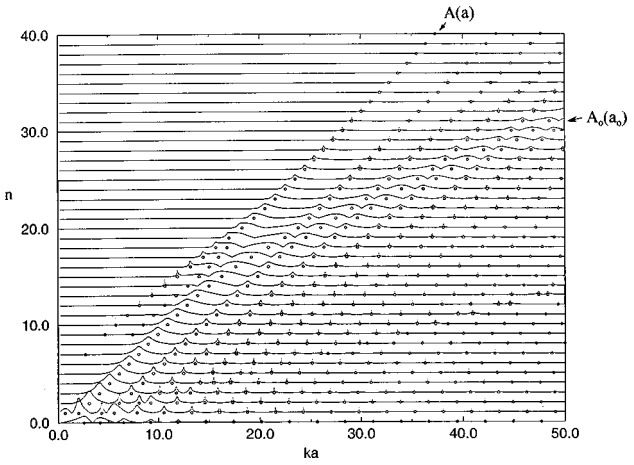

FIG. 6. Regge diagram of resonance frequencies for given n, with superimposed nth partial-wave scattering amplitude moduli versus frequency, for a water-immersed, alcohol-filled aluminum shell with $b/a=0.92$.

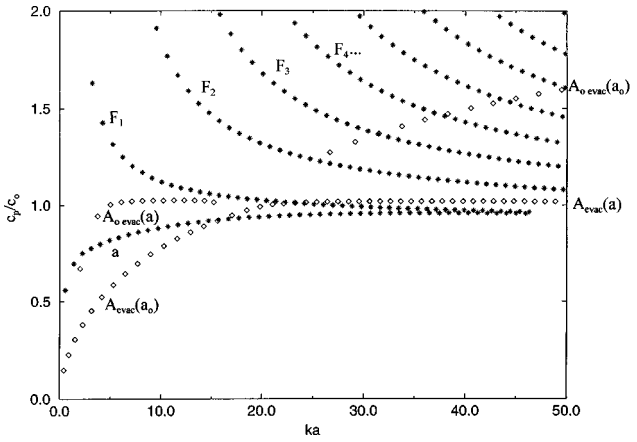

FIG. 8. Phase velocity dispersion curves of shell- or fluid-borne waves for a water-immersed, alcohol-filled ''liquid aluminum'' shell with $b/a=0.92$ in which c_T was taken as zero.

III. ALUMINUM SHELL IMMERSED IN WATER, AND FILLED WITH ANOTHER FLUID

The Regge plots, corresponding to the case where a shell of $b/a=0.92$ is filled with alcohol, are shown in Fig. 6, and the corresponding dispersion curves in Fig. 7; the latter figure also indicates the free-shell dispersion curve as a dashed line. Compared to the case of the evacuated shell, a much larger amount of activity is seen to occur now. Additional waves are present, and many cases of curve veering are evident. In order to better understand the situation, we shall first consider Fig. 8 in which the aluminum shell is replaced by a ''liquid'' shell with the same density and compressional speed but where the shear speed is set equal to zero: here the curve veering does not occur. The diamonds correspond to A_0 and A curves of the evacuated Al shell shown earlier (Fig. 3), and the asterisks to the case of the ''liquid'' shell. New waves were introduced by the fluid filling, and thus are filler-borne waves of various orders, which we shall designate by $F_1,F_2,\ldots$ (with $c_{F1},c_{F2},\ldots$ starting out at corresponding cutoff frequencies). The first of these waves, however, which starts out at the origin, can be attributed to the a wave on the outer periphery of the (liquid) shell. Looking back to Fig. 7,

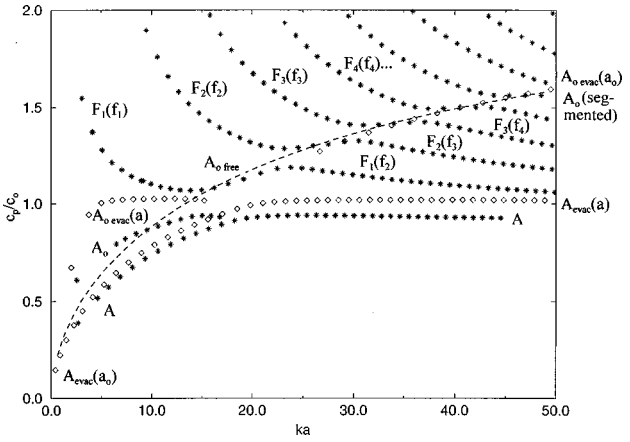

FIG. 7. Phase velocity dispersion curves of shell- or fluid-borne waves for the case of Fig. 6 (asterisks), for the evacuated shell (diamonds), and for the free shell (dashed curve).

where the evacuated, water-immersed elastic-Al shell dispersion curves are indicated by diamonds, and those of the water-immersed, alcohol-filled elastic-Al shell by asterisks, we see that the strong coupling that is in evidence between the shell and the filler fluid has had the consequence of producing strong curve-veering (repulsion) effects between the corresponding dispersion curves. We clearly see that all the curves A_0–$A(a)$, $F_1,F_2,\ldots$ of Fig. 8 are still there. The shell–filler coupling, however, has caused them, upon their passing from left to right through the region of the (dashed) free-shell curve, to veer upwards from the former (Fig. 8) $F_1,F_2,F_3,\ldots$ curve positions to those of the former $F_2,F_3,F_4,\ldots$ curves, undergoing curve-repulsion phenomena in this process. Similarly as in the plate case of Fig. 1, we now use indicator labels $f_1,f_2,f_3,\ldots$ in order to suggest curves (waves modes) of the same physical modal identity that, due to the shell–filler coupling, have been broken up into segments. (Note that the higher-order pseudo-Lamb waves $S_0,A_1,S_1,\ldots$ would not lie inside the present graphs and thus are not considered here.)

The segmentation effects caused by the shell–filler coupling are seen to have the following forms:

(i) The A_0 wave is present in its former shape but is interrupted at its near-cross-over point with the A wave.

(ii) From this point onwards, the A_0 wave, while following along the $A_{0\ \mathrm{free}}$ curve, is broken up into many segments due to its curve repulsions at the crossovers with the F_i waves.

(iii) Each of the F_i waves is divided into two segments at the same crossover points with the A_0 wave (and if the f_i designations are employed, the f_i curves can be considered as broken into two segments each).

(iv) Following a given continuous F_i dispersion curve, we see that descending from its cutoff, it starts out as the f_i curve, then takes over a portion of the A_0 curve, finally turning into the f_{i+1} curve. (Corresponding effects among the dispersion curves of the higher-order Lamb waves are discussed in Ref. 15.) The continuation of the f_1 curve to the right of its first veering-off

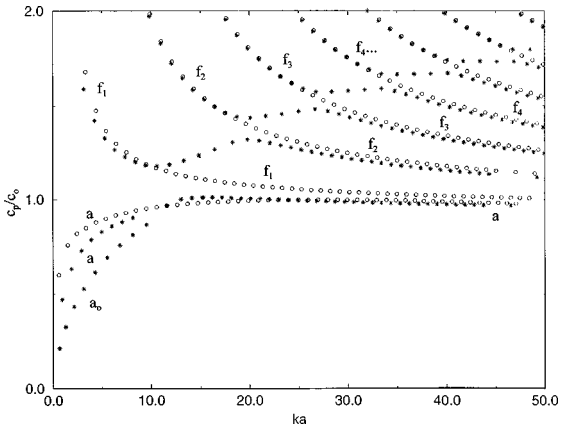

FIG. 9. Phase velocity dispersion curves for an alcohol-filled (asterisks) aluminum shell with $b/a=0.88$, and for a ''liquid aluminum'' shell with $c_T=0$.

point, however, is not evident in Fig. 7. If present here, it could possibly have been not registered by our method of resonance search; the same applies to an apparent absence in Fig. 7 of the analog of the *S* wave of the plate bounded by two dissimilar liquids, Fig. 2 of Ref. 11.

It is seen, thus, that strong coupling effects between shell and filler fluid (caused mathematically by shear terms in the boundary conditions) modify the otherwise continuous dispersion curves of shell waves and fluid-filler waves so as to break them up into disjoint segments at their intersection points, due to curve repulsions.

The last figure (Fig. 9) shows the dispersion curves for a $b/a=0.88$ aluminum shell immersed in water and filled with alcohol (asterisks); these are compared with those of the ''liquid ($c_T=0$) aluminum'' shell (circles) where the veering of the former (solid aluminum) curves from one to the neighboring one of the latter (liquid aluminum) curves is exhibited. All these results are qualitatively the same as in Figs. 7 and 8. (For simplicity, only the notation with lower-case letters is retained in Fig. 9 so as not to overburden the figure.)

IV. SUMMARY

Our study of the dispersive circumferential waves that can exist on a thin circular-cylindrical shell immersed in water, and filled with another fluid, has demonstrated the existence of shell-borne waves (only the lowest-order Lamb-type waves were considered here), of an external-fluid-borne, Scholte–Stoneley (A) type wave (most clearly if the shell is evacuated), and of a variety of highly dispersive, filler-fluid-borne waves. The interaction between these waves that exists due to the boundary conditions is such that the individual waves have their dispersion curves undergoing curve repulsions at the points where they would intersect each other, a given dispersion curve veering off from its uncoupled direction, and taking on the direction of the dispersion curve it would intersect with (''curve repulsion''). This takes place once between the A_0 and A waves, but twice between the A_0 and F_i waves. The physical nature of the waves (fluid borne versus shell borne), however, remains the same along the now segmented (disjointed) course of the previously uncoupled waves, but it changes over if one chooses to follow along any of the continuous but veering dispersion curves; these do not uniformly represent a wave of one given physical nature along their course.

[1] J. D. Murphy, E. D. Breitenbach, and H. Überall, ''Resonance scattering of acoustic waves from cylindrical shells,'' J. Acoust. Soc. Am. **64**, 677–683 (1978).
[2] J. V. Subrahmanyam, ''Creeping wave analysis through frequency plane for an obliquely incident plane wave on an elastic scatterer,'' Ph.D. thesis, Catholic University of America, Washington, DC, 1983.
[3] E. D. Breitenbach, H. Überall, and K. B. Yoo, ''Resonant acoustic scattering from elastic cylindrical shells,'' J. Acoust. Soc. Am. **74**, 1267–1273 (1983).
[4] J. L. Rousselot, ''Comportement acoustique d'un tube cylindrique mince en basse fréquence,'' Acustica **58**, 291–297 (1985).
[5] N. Veksler, ''The analysis of peripheral waves in the problem of plane acoustic pressure wave scattering by a circular cylindrical shell,'' Acustica **69**, 63–72 (1989).
[6] G. Quentin and M. Talmant, ''Plane plate model applied to the scattering of the ultrasonic waves from cylindrical shells,'' in *Elastic Wave Propagation*, edited by M. F. McCarthy and M. A. Hayes (Elsevier, North-Holland, Amsterdam, 1989), pp. 477–482.
[7] M. Talmant and G. Quentin, ''Backscattering of a short ultrasonic pulse from thin shells,'' J. Appl. Phys. **63**, 1857–1863 (1988).
[8] M. Talmant, G. Quentin, J. L. Rousselot, J. V. Subrahmanyam, and H. Überall, ''Acoustic resonances on thin cylindrical shells and the resonance scattering theory,'' J. Acoust. Soc. Am. **82**, 681–699 (1988).
[9] N. D. Veksler, J. L. Izbicki, and J. M. Conoir, ''Bending A wave in the scattering by a circular cylindrical shell: Its relation with the bending free modes,'' J. Acoust. Soc. Am. **96**, 287–293 (1994).
[10] J. P. Sessarego, J. Sageloli, C. Gazanhes, and H. Überall, ''Two Scholte–Stoneley waves on doubly fluid-loaded plates and shells,'' J. Acoust. Soc. Am. **101**, 135–142 (1997).
[11] X. L. Bao, H. Franklin, P. K. Raju, and H. Überall, ''The splitting of dispersion curves for plates fluid-loaded on both sides,'' J. Acoust. Soc. Am. **102**, 1246–1248 (1997).
[12] H. Überall, A. Gérard, A. Guran, J. Duclos, M. El H. Khelil, X. L. Bao, and P. K. Raju, ''Acoustic scattering resonances: Relation to external and internal surface waves,'' Appl. Mech. Rev. **49**, S63–S71 (1996).
[13] G. S. Sammelmann, D. H. Trivett, and R. H. Hackman, ''Acoustic scattering by a submerged spherical shell. I. The bifurcation of the dispersion curve for the spherical antisymmetric Lamb wave,'' J. Acoust. Soc. Am. **85**, 114–124 (1989).
[14] M. Talmant, H. Überall, R. D. Miller, M. F. Werby, and J. W. Dickey, ''Lamb waves and fluid-borne waves on water-loaded, air-filled thin spherical shells,'' J. Acoust. Soc. Am. **86**, 278–289 (1989).
[15] H. Überall, B. Hosten, M. Deschamps, and A. Gérard, ''Repulsion of phase velocity dispersion curves and the nature of plate vibrations,'' J. Acoust. Soc. Am. **96**, 908–917 (1994).
[16] D. Brill and H. Überall, ''Acoustic waves transmitted through solid elastic cylinders,'' J. Acoust. Soc. Am. **50**, 921–939 (1977).
[17] L. Flax, L. R. Dragonette, and H. Überall, ''Theory of elastic resonance excitation by sound scattering,'' J. Acoust. Soc. Am. **63**, 723–731 (1978).
[18] J. D. Murphy, J. George, A. Nagl, and H. Überall, ''Isolation of the resonant component in acoustic scattering from fluid-loaded elastic spherical shells,'' J. Acoust. Soc. Am. **65**, 368–373 (1979).
[19] N. D. Veksler, ''Intermediate background in problems of sound wave scattering by elastic shells,'' Acustica **76**, 1–9 (1992).
[20] S. G. Kargl and P. L. Marston, ''Longitudinal resonances in the form function for backscattering from a spherical shell: Fluid shell case,'' J. Acoust. Soc. Am. **88**, 1114–1122 (1990).
[21] M. F. Werby, ''The acoustic background for a submerged elastic shell,'' J. Acoust. Soc. Am. **90**, 3279–3287 (1991).
[22] M. F. Werby, ''Recent developments in scattering from submerged elastic and rigid targets,'' in *Acoustic Resonance Scattering*, edited by H. Überall (Gordon and Breach, Philadelphia, 1992), pp. 277–303.
[23] J. Ripoche and G. Maze, ''New Acoustic Spectroscopy: The resonance scattering spectroscopy, by the Method of Isolation and Identification of Resonances (MIIR),'' in *Acoustic Resonance Scattering*, edited by

H. Überall (Gordon and Breach, Philadelphia, 1992), pp. 69–103.
[24] H. Überall, L. R. Dragonette, and L. Flax, ''Relation between creeping waves and normal modes of vibration of a curved body,'' J. Acoust. Soc. Am. **61**, 711–715 (1977).
[25] A. C. Ahyi, P. Pernod, O. Gatti, V. Latard, A. Merlen, and H. Überall, ''Experimental demonstration of the pseudo-Rayleigh (A_0) wave,'' J. Acoust. Soc. Am. **104**, 2727–2732 (1998).
[26] G. Maze, F. Léon, J. Ripoche, and H. Überall, ''Repulsion phenomena in the phase-velocity dispersion curves of circumferential waves on elastic cylindrical shells,'' J. Acoust. Soc. Am. **105**, 1695–1701 (1999).

Applications of the causality condition to one-dimensional acoustic reflection problems

J. Gregory McDaniel
Department of Aerospace and Mechanical Engineering, Boston University, 110 Cummington Street, Boston, Massachusetts 02215

(Received 2 November 1998; revised 9 January 1999; accepted 19 February 1999)

The causality condition is examined as a means of determining frequency-domain information about a submerged object from a partial knowledge of its acoustic reflection characteristics. A one-dimensional problem is considered in which an acoustic wave reflects from an object that is described by the impedance it presents to the fluid. Two new applications of the causality condition to the frequency-domain analysis of this problem are investigated and illustrated by numerical examples. In each application, the causality condition is used to find the object's complex impedance from a knowledge of the reflected wave's magnitude. The first application is to experimental studies where one desires a knowledge of an object's complex impedance but practical limitations only allow a measurement of the reflected wave amplitude. Analysis shows that the causality condition may be used to determine the phase of the reflected wave, and hence the object's impedance, if the reflection coefficient is minimum phase. When this is true, examples suggest that the phase of the reflection coefficient may be accurately determined from the causality condition even in the presence of noise and band-limited data. The second application is to design situations, where one wishes to create an object that reflects sound with a specified frequency-dependent magnitude. The causality condition may aid the designer by providing a knowledge of all causal object impedances that produce the same reflection coefficient magnitude. A numerical example is presented in which a variety of causal object impedances produce the same reflection coefficient magnitude over an infinite frequency range.
[S0001-4966(99)04405-7]

PACS numbers: 43.40.Fz [CBB]

INTRODUCTION

This paper presents applications of the causality condition to problems in which acoustic waves reflect from submerged objects. For simplicity we shall restrict our attention to the one-dimensional system shown in Fig. 1, however, extensions of the concepts to multi-dimensional scattering problems are discussed in Sec. IV. The system consists of an object that presents an impedance to the fluid through a rigid massless piston. The impedance defines the ratio of force to velocity such that $Z=F/V$ where F is the force applied to the piston in the direction of the velocity V indicated in the figure. An acoustic wave reflects from the object when there is any difference between the fluid impedance $\rho_f c_f A$ and the object impedance Z, where ρ_f and c_f are the fluid's mass density and sound speed, respectively, and A is the area of the piston.

If the pressure due to the incident wave is zero for $t<0$, then one would expect that the piston velocity and the pressure due to the reflected wave would also be zero for $t<0$. This expectation is known as the causality condition, which in more general terms states that a response cannot precede its cause. In time-domain analysis and in experimental data, the condition is implicit in the solution. However, in the frequency domain the condition is much more subtle and powerful. In particular, it allows one to relate the real and imaginary parts and, in some cases, the magnitude and phase of the Fourier transform of a causal response.

We shall present two applications of the causality condition in the frequency domain. In both applications, the frequency dependence of the reflected wave's magnitude is known and one desires a knowledge of the object's complex impedance. A key issue in both applications is the nonuniqueness of the reflected wave's phase in the absence of other knowledge about the system. In particular, the causality condition allows one to compute the minimum phase from the magnitude of the response's Fourier transform. However, the actual phase may not be the minimum phase and there is no definitive way of knowing this from only a knowledge of the magnitude. Nonetheless, the minimum phase is useful as a starting point for constructing other phases that satisfy the causality condition.

Some of the earliest applications of the causality condition were made by Kronig[1] in 1926 and Kramers[2] in 1927 and involved the dispersion of X-rays. Their work led to integral relations between the index of refraction and the atomic absorption coefficient. Since then, the causality condition has been applied to many engineering problems, perhaps the most notable being the design of feedback amplifiers by Bode.[3] The concept was so critical to amplifier designs that it appeared in a design patent (U.S. Patent Number 2,123,178), and a corrected form of his causality equations appeared in Terman's *Radio Engineer's Handbook*.[4] This and other work in circuit analysis and design is discussed by Guillemin.[5] In addition, there is a large body of work which involves applications of the causality condition to electromagnetic scattering matrices. An introduction is

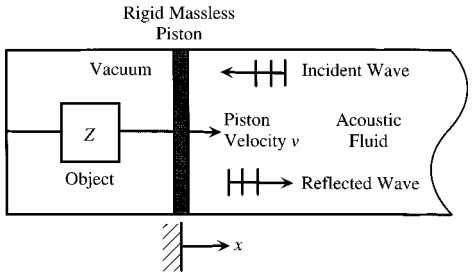

FIG. 1. A schematic showing the system under consideration, which consists of a rigid massless piston of area A connected to ground by a complex impedance Z that reflects acoustic waves.

given by Holbrow and Davidon;[6] more detailed treatment is found in Refs. 7 and 8. The present work differs in that it uses the causality condition to find properties of the scatterer in the frequency domain, such as its impedance, that directly relate to its construction.

Before stating the mathematical implications of the causality condition, let us define $f(t)$ as the response of a linear system to an excitation $g(t)$ that is zero for $t<0$. Furthermore, let us define the complex Fourier transform $\tilde{f}(\omega)$ and its inverse transform as:

$$\tilde{f}(\omega)=\int_{-\infty}^{\infty} f(t)e^{i\omega t}\,dt \tag{1}$$

and

$$f(t)=\frac{1}{2\pi}\int_{-\infty}^{\infty}\tilde{f}(\omega)e^{-i\omega t}\,d\omega. \tag{2}$$

The causality condition in the time domain leads to Hilbert transform relations between the real and imaginary parts of the complex Fourier transform of the response. Discussions and proofs of these relations are found in various texts,[9–13] and in an article by MacDonald and Brachman.[14] Writing $\tilde{f}(\omega)=\tilde{f}_r(\omega)-i\tilde{f}_i(\omega)$, the Hilbert transform relations are

$$\tilde{f}_i(\omega)=-\frac{1}{\pi}\mathcal{P}\int_{-\infty}^{\infty}\frac{\tilde{f}_r(x)}{\omega-x}\,dx, \tag{3}$$

and

$$\tilde{f}_r(\omega)=\frac{1}{\pi}\mathcal{P}\int_{-\infty}^{\infty}\frac{\tilde{f}_i(x)}{\omega-x}\,dx, \tag{4}$$

where $\mathcal{P}$ indicates the principal value of the integral. These may be derived by either invoking the convolution theorem in the time domain or by contour integration in the frequency domain (see Ref. 10 with j replaced by $-i$).

The relationships between magnitude and phase of $\tilde{f}(\omega)$ may be derived from Eqs. (3) to (4) if $\tilde{f}(\omega)$ is analytic and has no zeros in the upper half of the complex plane (henceforth referred to as the causal half-plane). The assumption of analyticity guarantees causality while the assumption of no zeros in the causal half-plane is known as the *minimum phase condition*. This condition will be discussed in more detail below. Magnitude and phase relations are derived by writing $\tilde{f}(\omega)=\exp[-\alpha(\omega)+i\theta(\omega)]$ and taking the natural logarithm, which yields

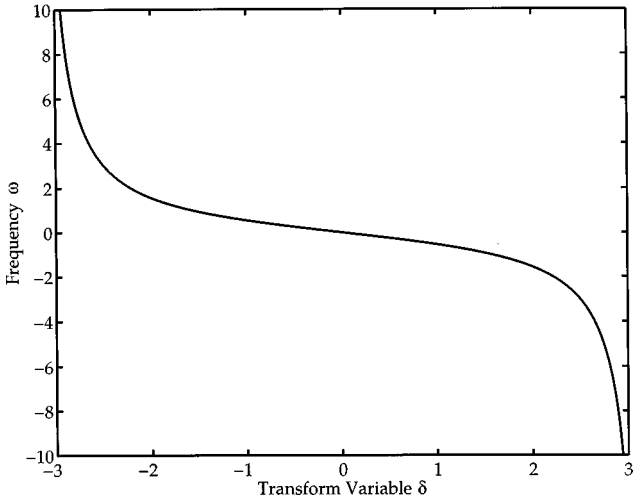

FIG. 2. A plot illustrating the Wiener–Lee transform, which maps an infinite frequency domain defined by $-\pi<\delta<\pi$.

$$\theta(\omega)=\frac{\omega}{\pi}\mathcal{P}\int_{-\infty}^{\infty}\frac{\alpha(x)}{x^2-\omega^2}\,dx, \tag{5}$$

and

$$\alpha(\omega)=\alpha(0)-\frac{\omega^2}{\pi}\mathcal{P}\int_{-\infty}^{\infty}\frac{\theta(x)}{x(x^2-\omega^2)}\,dx. \tag{6}$$

The phase θ found from Eq. (5), which is the phase of $\tilde{f}$ that satisfies the minimum phase condition, is known as the *minimum phase*.

Direct numerical evaluation of either Eq. (6) or (5) is complicated by the singularities at $x=\pm\omega$. A more straightforward and robust numerical procedure is made possible by the Wiener–Lee transform[15–16] defined as $\omega=-\tan(\delta/2)$ and illustrated in Fig. 2. From Eqs. (5) and (6), we find that the transformed magnitude and phase, $\overline{\alpha}(\delta)$ and $\overline{\theta}(\delta)$, may be expressed in terms of the following Fourier series

$$\overline{\alpha}(\delta)=\sum_{n=0}^{\infty} d_n\cos(n\delta) \tag{7}$$

and

$$\overline{\theta}(\delta)=\sum_{n=1}^{\infty} e_n\sin(n\delta), \tag{8}$$

where

$$d_n=-e_n. \tag{9}$$

This transform will be used in numerical examples to determine the minimum phase $\overline{\theta}$ by expanding the magnitude $\overline{\alpha}$ in the cosine series in Eq. (7), finding e_n from Eq. (9), and then evaluating the sine series in Eq. (8). This approach has been applied to a related problem involving phase reconstruction from uniform fiber Bragg gratings,[17–18] in which the amplitude was measured from power measurements and the phase was reconstructed by the Wiener–Lee transform.

The minimum phase condition is subtle and, as pointed out by Victor,[19] has been missed by previous researchers. For both of the applications considered here, an understand-

ing of the condition and its implications is critical. Let us briefly review a key analytical result presented by Victor, which states that the Fourier transform $\tilde{f}(\omega)$ of a causal response may be decomposed as follows:

$$\tilde{f}(\omega)=e^{i\omega D}Q(\omega)\prod_{q=1}^{Q}P(\omega,\omega_q), \tag{10}$$

where $e^{i\omega D}$ is a phase shift which accounts for delays between excitation and response. The delay D is the largest value for which the time-domain response $f(t+D)$ is causal. The factor $P(\omega,\omega_q)$ is defined as

$$P(\omega,\omega_q)=\frac{\omega-\omega_q}{\omega-\omega_q^{\star}}, \tag{11}$$

where ω_q lies in the causal half-plane and $\omega_q^{\star}$ is its complex conjugate. Like the phase-shift factor, $P(\omega,\omega_q)$ has unit magnitude so that $|\tilde{f}(\omega)|=|Q(\omega)|$. The factor $Q(\omega)$ possesses the minimum phase and therefore has no zeros in the causal half-plane.

If the magnitude $|\tilde{f}(\omega)|$ is known over an infinite frequency range, then its minimum phase may be found from Eq. (5). Whether or not this corresponds to the actual phase cannot be known without further assumptions on $\tilde{f}(\omega)$. In this regard, certain assumptions relevant to the system in Fig. 1 will be explored in Sec. II. If one is interested in finding all causal transforms $\tilde{f}(\omega)$ given $|\tilde{f}(\omega)|$ over an infinite frequency range, then the minimum phase may be found from Eq. (5). Equation (10) may then be used to find all possible transforms of causal responses by choosing any number of values for the ω_q under the condition that each ω_q lie in the causal half-plane.

I. APPLICATION OF THE CAUSALITY CONDITION TO THE ACOUSTIC REFLECTION PROBLEM

In addition to placing requirements on the Fourier transform of the response, the causality condition may be used to infer dynamic properties of a system such as the one shown in Fig. 1. In the frequency domain, linear systems obey the algebraic relationship $\tilde{f}(\omega)=\tilde{g}(\omega)H(\omega)$, where $\tilde{g}(\omega)$ is the Fourier transform of the excitation and $H(\omega)$ is generally known as the *system* or *transfer function* and obeys the Hilbert transform relations given in Eqs. (3)–(6). To see this, consider an impulsive excitation described by $g(t)=\delta(t)$, so that $\tilde{g}(\omega)=1$ and $\tilde{f}(\omega)=H(\omega)$. From this equality, we see that the Hilbert transform relations in Eqs. (3)–(6) also apply to the system function $H(\omega)$. This recognition, which will be used extensively in the present work, is significant in that the system function is independent of excitation and often leads directly to the design of the system.

It shall be expedient to derive the system function from the steady-state complex amplitudes of a time-harmonic response and excitation. If the steady-state response and excitation are written as $f_{ss}(t)=\Re\{F(\omega)e^{-i\omega t}\}$ and $g_{ss}(t)=\Re\{G(\omega)e^{-i\omega t}\}$, respectively, then the system function is $H(\omega)=F(\omega)/G(\omega)$. The application of the causality condition to a system function derived from steady-state response is a source of confusion in that steady-state responses are assumed to exist for all time. We must keep in mind only the mathematical equivalence.

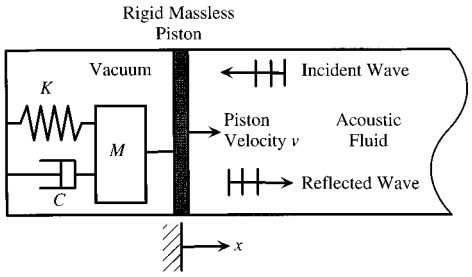

FIG. 3. A schematic showing an object impedance that consists of a rigid massless piston connected to a mass-spring-dashpot system.

Turning to the particular problem illustrated in Fig. 1, we identify the incident and reflected pressures at $x=0$ as the excitation and response, respectively. Other response variables, such as the velocity of the piston, may be chosen but our interest here is in the reflected pressure because it is most often experimentally measured or specified in a design problem. The incident and reflected pressures satisfy the acoustic wave equation and have the form of forward and backward propagating waves, respectively, given by

$$p_{\text{inc}}(x,t)=P_{\text{inc}}(\omega)e^{-i(\omega t-kx)} \tag{12}$$

and

$$p_{\text{ref}}(x,t)=P_{\text{ref}}(\omega)e^{-i(\omega t+kx)}. \tag{13}$$

The acoustic wave number is given by $k=\omega/c_f$.

The complex reflection coefficient, defined as $R(\omega)=P_{\text{ref}}(\omega)/P_{\text{inc}}(\omega)$ may be interpreted as the system function because it is the ratio of the response to the excitation. The problems considered here involve the determination of the object's impedance Z, which represents the ratio of force on the piston to its velocity, from a specification of the magnitude of the reflection coefficient over an infinite frequency range. In the frequency domain, the impedance and reflection coefficient are algebraically related by[20]

$$z=\frac{1+R}{1-R}\quad\text{or}\quad R=\frac{z-1}{z+1}, \tag{14}$$

where $z=Z/(\rho_f c_f A)$ is the specific acoustic impedance of the object. The applications described in the following two sections proceed by applying the causality condition to determine the phase of R from a knowledge of $|R|$, and then using Eq. (14) to find the complex-valued impedance z.

II. IMPEDANCES THAT CREATE MINIMUM PHASE REFLECTION COEFFICIENTS

The reflection coefficient is minimum phase when none of its zeros are in the causal half-plane. If this condition is satisfied and the magnitude of R is known over an infinite frequency range, then the phase may be uniquely determined from Eq. (5). In this section, we shall illustrate the implications of this condition by examining the system shown in Fig. 3, in which the object impedance Z shown in Fig. 1 has been replaced by a mass-spring-dashpot system. The param-

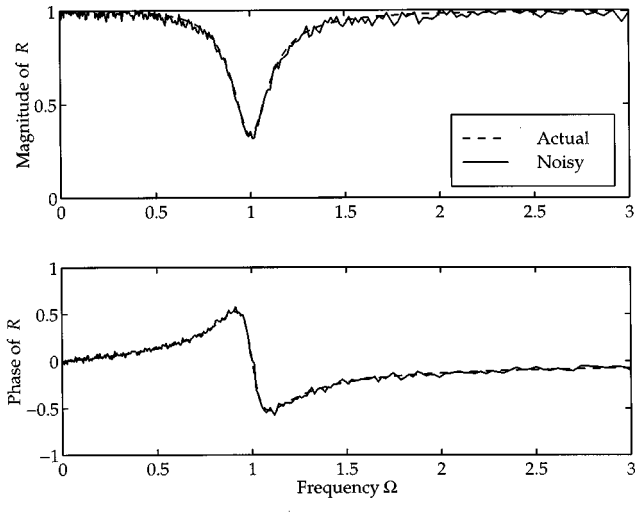

FIG. 4. Plots showing frequency dependencies of the magnitude and phase of a noise-corrupted minimum phase reflection coefficient R for the case $c=2$ and $\beta=10$.

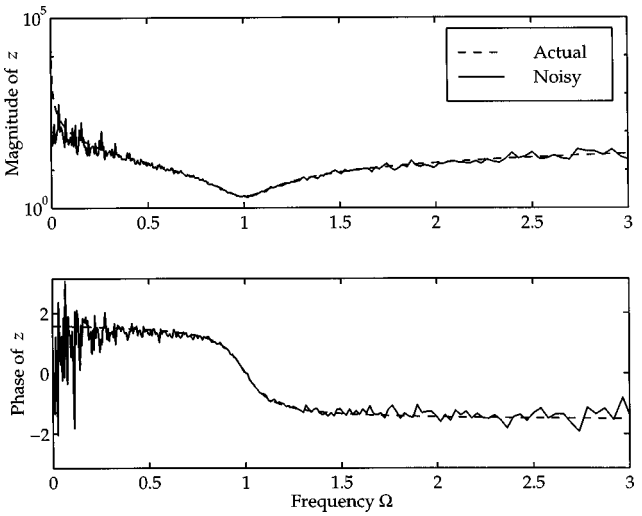

FIG. 5. Plots showing the frequency dependencies of the magnitude and phase of the specific object impedance z that creates the reflection coefficient shown in Fig. 4.

eters K, C, and M represent the usual spring, mass, and dashpot elements. The specific impedance of this system is

$$z=\frac{Z}{\rho_f c_f A}=c+i\beta\left(\frac{1}{\Omega}-\Omega\right), \tag{15}$$

where $\Omega=\omega/\sqrt{K/M}$, $c=C/(\rho_f c_f A)$, and $\beta=\sqrt{KM}/(\rho_f c_f A)$.

For this impedance, the zeros of R are given by

$$\Omega_{1,2}=-i\left(\frac{(c-1)\pm\sqrt{(c-1)^2-4\beta^2}}{2\beta}\right). \tag{16}$$

Neither of these zeros are in the causal half-plane when $c>1$, but both zeros are in the causal half-plane when $c<1$. Therefore, we conclude that R will be minimum phase when $c>1$ or $C>\rho_f c_f A$. Physically, this means that the reflection coefficient is minimum phase when the damping of the object, which is represented by the dashpot constant C, is larger than the impedance $\rho_f c_f A$ of the fluid.

Let us further illustrate this concept and the computation of the minimum phase from Eqs. (7) to (9) by way of two numerical examples. In both examples, it is assumed that the magnitude of the reflection coefficient is known and one is interested in finding its phase. The impedance in Eq. (15) was computed at frequencies defined by 315 values of the transform variable δ that ranged from $-\pi$ to -0.001 in equal steps of 0.01. The sine series in Eq. (7) was truncated at 315 terms and the d_n were found by a collocation technique that required that equation to hold at each value of δ.

In the first example, the parameters of the object impedance were taken as $c=2$ and $\beta=10$ so that R is minimum phase. The magnitude of the reflection coefficient for this system is shown in Fig. 4 and is labeled ''actual.'' In order to simulate what one might measure in an experiment, noise was added to the reflection coefficient magnitude to produce the curve labeled ''noisy'' in the same plot. The noise was taken to be normally distributed about zero with a maximum amplitude of 0.01. The noisy data was used to reconstruct the phase from Eqs. (7) to (9). This phase approximates the actual phase very well as shown in Fig. 4 because the system is minimum phase. In Fig. 5, the impedances computed from the noisy reflection coefficient are compared to the actual impedance of the structure. The agreement is good except at low frequencies where the impedance approaches infinity and its phase is very sensitive to errors in the reflection coefficient, as may be seen by Eq. (14).

An important practical concern is the bandwidth over which the reflection coefficient magnitude must be measured in order to determine its phase by causality. The results shown in Figs. 4 and 5 required a knowledge of the reflection coefficient magnitude at 315 frequencies with the maximum frequency of $\Omega=3{,}375$. Is such a large bandwidth required when the magnitude and phase of R appear to vary only slightly for $\Omega>2$? To investigate this question, the calculation was performed with the noisy data truncated above $\Omega=1$ and $\Omega=2$. Above each upper limit, the magnitude was extrapolated to the constant value given at the upper limit. From Fig. 4, we see that this is a reasonable approximation to the actual reflection coefficient when the upper limit is $\Omega=2$ but not when it is $\Omega=1$. Using the same sampled frequencies which were used in the first example, the causality condition was used to reconstruct the phases.

The phases are plotted in Fig. 6 and, as expected, the $\Omega=2$ truncation agrees very well with the actual phase, which is replotted for reference, but the $\Omega=1$ truncation does not approximate the actual phase. Considering only the $\Omega=2$ truncation, this plot indicates that if a reflection coefficient is measured over a finite frequency band in the presence of noise, its phase may be accurately determined by the causality condition if the magnitude is accurately extrapolated outside of the measurement band. We expect this to be true in general when the measurement band contains the resonances of the system, as shown here for measurements up to $\Omega=2$.

In the second example, the parameters $c=1/2$ and $\beta=10$ were chosen, so that the system was not minimum phase. The magnitude of the reflection coefficient of this system is shown in Fig. 7. The minimum phase of the reflec-

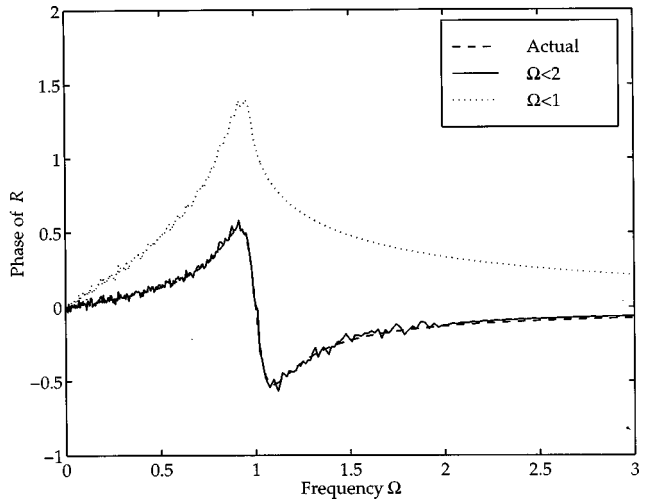

FIG. 6. A plot of the phase of the reflection coefficient predicted by causality and a knowledge of the magnitude of the reflection coefficient over a finite frequency range.

tion coefficient, determined from the magnitude and Eqs. (9), is plotted along with the actual phase. The difference between the two phases is due to the fact that the actual phase is not the minimum phase. The actual reflection coefficient R_a is related to the minimum phase reflection coefficient R_{mp} by the following form of Eq. (10):

$$R_a = e^{i\omega D} R_{mp}(\omega) \prod_{q=1}^{Q} P(\omega, \omega_q). \tag{17}$$

These observations can be generalized to an object with an arbitrary impedance, as shown in Fig. 1, by writing the object's specific impedance as $z(\omega) = z_r(\omega) + iz_i(\omega)$. From Eq. (14), the zeros of R satisfy

$$z_r(\omega_n) - 1 + iz_i(\omega_n) = 0, \quad \text{for} \quad n = 1,2,\ldots,N. \tag{18}$$

Whenever all of the ω_n lie in the lower half of the complex plane, the reflection coefficient will be minimum phase and

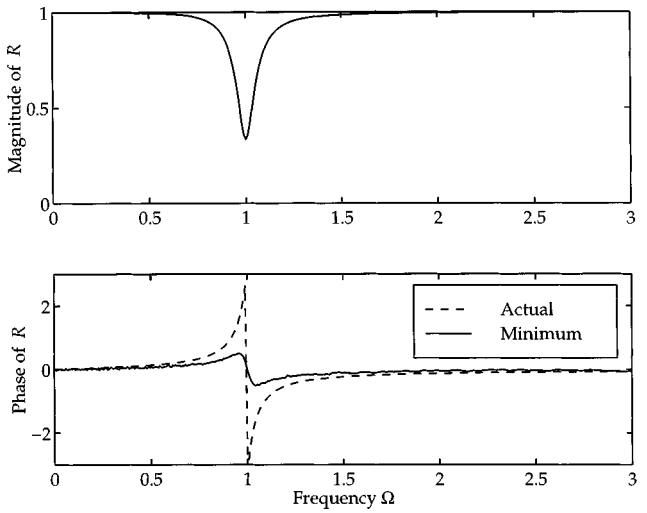

FIG. 7. Plots of the magnitude and phase of a nonminimum phase reflection coefficient. The minimum phase in the lower plot was computed by Eqs. (7)–(9).

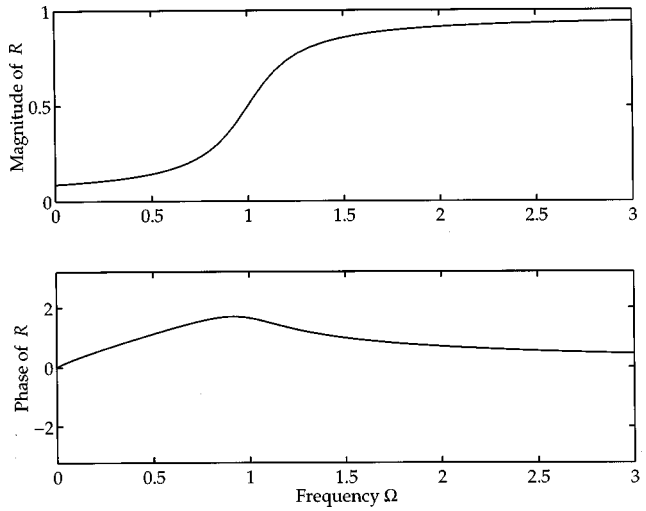

FIG. 8. A plot showing the desired reflection coefficient, given in Eq. (19), and the minimum phase computed by Eqs. (7)–(9).

the causality condition may be used to uniquely recover the phase of R from its magnitude.

III. CAUSAL IMPEDANCES FROM A REFLECTION COEFFICIENT MAGNITUDE

In this section, the nonuniqueness of the reflection coefficient's phase is exploited to find all causal object impedances that reflect waves with the same magnitude over an infinite frequency band. The analysis is expected to aid design studies by identifying very different conceptual designs that have the same acoustic properties. As an example, we shall consider the system in Fig. 1 and assume that one desires the magnitude of the reflection coefficient to be

$$|R| = 0.3 \tan^{-1}[5(\Omega - 1)] + 0.5. \tag{19}$$

The magnitude is shown in the upper plot of Fig. 8. This assumed form is meant to represent a structure that is essentially a ''high-pass filter,'' reflecting very little sound at low frequencies and giving almost perfect reflection at higher frequencies. The minimum phase of R found from Eqs. (7) to (9) is shown in the lower plot.

Other causal phases are indicated by a form of Eq. (10):

$$R = e^{i\omega D} R_{mp}(\omega) \prod_{n=1}^{N} P(\Omega, \Omega_n), \tag{20}$$

where R_{mp} is the minimum phase reflection coefficient, whose magnitude and phase are shown in Fig. 8. To illustrate the various object impedances produced by choices of Ω_n, let us limit the product in Eq. (20) to one term ($N=1$) and compute causal reflection coefficients for the cases $\Omega_1 = i$, $10i$, and $1+i$. The unwrapped phases of the reflection coefficient for these cases are shown in Fig. 9, where the minimum phase is indeed always lower than the nonminimum phases. The corresponding impedances are shown in Fig. 10.

Every impedance shown in Fig. 10 represents a physically realizable object that obeys the causality condition. In design situations one typically faces constraints and objectives in choosing an impedance. For example, limiting the total mass of the object may be expressed as a constraint on

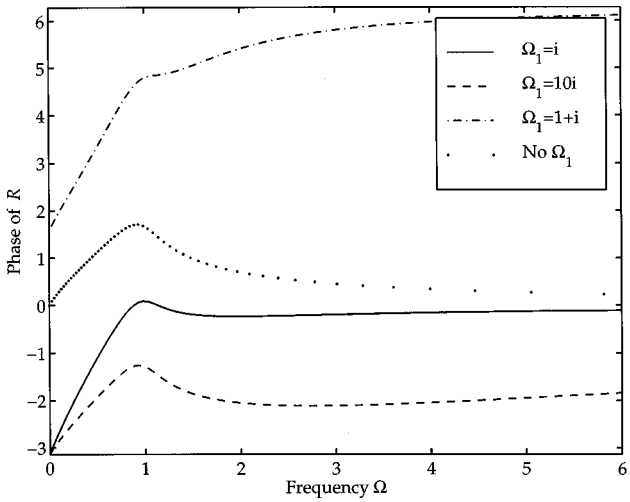

FIG. 9. A plot showing causal nonminimum phases of the desired reflection coefficient given in Eq. (20).

impedance. Eq. (20), as illustrated in Fig. 10, offers the possibility of considering many impedances that give the same magnitude of reflected sound. Given a set of design constraints and objectives, one could proceed by applying optimization procedures that vary the number and values of Ω_n to achieve a desired impedance, as calculated from Eqs. (14) and (20).

IV. CONCLUSIONS

The analyses presented here indicate the conditions under which the causality condition allows one to determine an object's impedance from a knowledge of the reflected wave's magnitude. When the reflection coefficient is minimum phase, the causality condition may be useful in experimental studies in which the impedance of an object is to be determined by measuring only the magnitude of the reflected wave. When this is true, numerical examples suggest that calculations of the object's impedance from a knowledge of the reflection coefficient magnitude may be accurate even when noise is present and when the magnitude is only specified over a finite frequency band. In design problems, the causality condition may be used to find a class of causal object impedances that produce the same reflection coefficient magnitude. The designer may then choose the most desirable object based on other considerations, such as ease of construction. The Wiener–Lee transform has suggested a robust and efficient computational algorithm for implementing the causality condition in the examples presented here.

In principle, these applications may be extended to multi-dimensional scattering. For example, consider a time-harmonic scattering problem in which the incident pressure amplitude $\{P_{\text{inc}}\}$ at locations on an object is related to the scattered pressure amplitude $\{P_{\text{sc}}\}$ at a set of locations in the acoustic medium. Writing this relationship as $\{P_{\text{sc}}\}=[S]\times\{P_{\text{inc}}\}$, we note that each element of the scattering matrix $[S]$ may be interpreted as a system function in the same way as the reflection coefficient R in the one-dimensional problem. In particular, the (i,j) element of $[S]$ represents the scattered pressure at the ith field point caused by a unit incident pressure at the jth location on the body with no incident pressure at the other points. Therefore, if only the magnitudes of the scattered pressures were measured at the field points, the causality condition could be used to reconstruct the minimum phases of every element of $[S]$. It may be possible to develop conditions to insure that the actual phases are the minimum phases by placing assumptions on the impedance of the scattering body, as was done for the one-dimensional case in Sec. II.

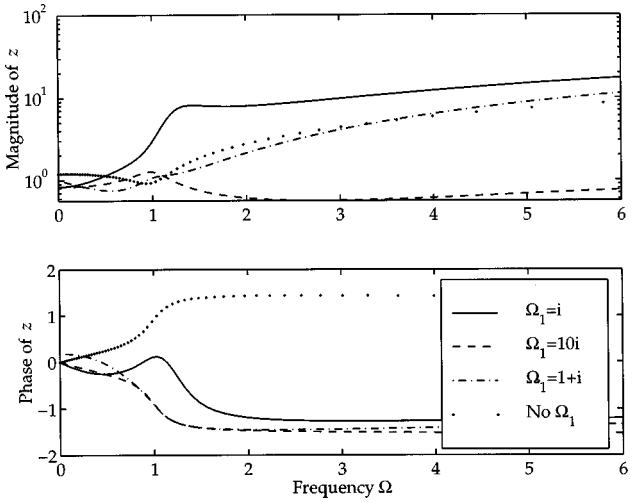

FIG. 10. Plots of the magnitude and phase of some causal object impedances that create the magnitude of reflection coefficient shown in the upper plot of Fig. 8.

ACKNOWLEDGMENTS

The author would like to thank Professor Allan Pierce and Professor Richard Weaver for many helpful comments and insights that expanded the scope of the paper.

[1] R. de L. Kronig, ''On the theory of the dispersion of x-rays,'' J. Opt. Soc. Am. **12**, 547–557 (1926).
[2] H. A. Kramers, ''La diffusion de la lumiere par les atomes,'' Estratto dagli Atti del Congresso Internazionale de Fisici Como, **2**, 545–557 (1927).
[3] H. W. Bode, *Network Analysis and Feedback Amplifier Design* (Van Nostrand, New Jersey, 1945).
[4] F. E. Terman, *Radio Engineer's Handbook* (McGraw-Hill Book, New York, 1943).
[5] E. A. Guillemin, *The Mathematics of Circuit Analysis* (Wiley, New York, 1949).
[6] C. H. Holbrow and W. C. Davidon, ''An introduction to dispersion relations,'' Am. J. Phys. **32**, 762–774 (1964).
[7] N. G. van Kampen, ''S-matrix and causality condition. I. Maxwell field,'' Phys. Rev. **89**, 1072–1079 (1953).
[8] John S. Toll, ''Causality and the dispersion relation: Logical foundations,'' Phys. Rev. **104**, 1760–1770 (1956).
[9] W. C. Titchmarsh, *Introduction to the Theory of Fourier Integrals* (Oxford University Press, Oxford, 1937), pp. 119–151.
[10] A. Papoulis, *The Fourier Integral and Its Applications*, Electronic Science Series (McGraw-Hill, New York, 1962), pp. 192–222.
[11] H. M. Nussenzveig, *Causality and Dispersion Relations* (Academic, New York, 1972), Chap. 1.
[12] R. Bracewell, *The Fourier Integral and Its Applications*, 2nd ed. (McGraw-Hill, New York, 1978).
[13] E. B. Saff and A. D. Snider, *Fundamentals of Complex Analysis for Mathematics, Science, and Engineering*, 2nd ed. (Prentice-Hall, New Jersey, 1993), pp. 415–429.
[14] J. Ross MacDonald and Malcolm K. Brachman, ''Linear-system integral transform relations,'' Rev. Mod. Phys. **28**, 393–422 (1956).

[15] Y. W. Lee, ''Synthesis of electric networks by means of the Fourier transforms of Laguerre's functions,'' J. Math. Phys. 83–113 (1932).
[16] A. Papoulis, *The Fourier Integral and Its Applications*, Electronic Science Series (McGraw-Hill, New York, 1962).
[17] Miguel A. Muriel and Alejandro Carballar, ''Phase reconstruction from reflectivity in uniform fiber Bragg gratings,'' Opt. Lett. **22**, 93–95 (1997).
[18] D. Pastor and J. Capmany, ''Experimental demonstration of phase reconstruction from reflectivity in uniform fibre Bragg gratings using the Wiener-Lee transform,'' J. Math. Phys. 83–113 (1998).
[19] Jonathan D. Victor, ''Temporal impulse response from flicker sensitivities: Causality, linearity, and amplitude data do not determine phase,'' J. Opt. Soc. Am. **6**, 1302–1303 (1989).
[20] Allan D. Pierce, *Acoustics, An Introduction to Its Physical Principles and Applications* (The Acoustical Society of America, New York, 1989).

Fluid flow imaging by means of wide-band diffraction tomography

Stephen J. Norton[a)]
Oak Ridge National Laboratory, Oak Ridge, Tennessee 37831-6200

(Received 1 July 1998; revised 21 January 1999; accepted 21 January 1999)

The problem of reconstructing a two-dimensional distribution of fluid flow from wide-band scattering measurements is considered. Reciprocal scattering measurements are employed, meaning that scattered waves are recorded between a source and receiver, and again with the source and receiver interchanged. As shown, such measurements allow the reconstruction of a fluid flow image separate from that of a distribution of stationary acoustic velocity inhomogeneities.
[S0001-4966(99)00105-8]

PACS numbers: 43.60.Pt, 43.60.Rw, 43.30.Pc [JCB]

INTRODUCTION

We examine the problem of reconstructing a map of two-dimensional (2-D) fluid flow by propagating broadband acoustic pulses through the flow region. In the following, we shall consider diffraction (or scattering) of the pulses by velocity inhomogeneities created by the flow. We remark that approaches to this problem based on ray theory, in which diffraction is neglected, were proposed years ago in the areas of medical ultrasound and oceanography. In this case, travel-time measurements are made over many overlapping paths and, under the assumption of a ray-propagation model, the problem reduces to that of tomographically reconstructing a 2-D vector field (the fluid velocity field) from observations of its line integrals through the region of flow. The latter technique was first proposed by Johnson *et al.*;[1] later oceanographers attempted to employ the same principle to map 2-D ocean current flow from reciprocal acoustic travel-time measurements.[2] By a ''reciprocal travel-time measurement'' we mean the following: the travel time of a pulse is measured between two points, **a** and **b**, and again in the opposite direction (from **b** to **a**). The difference in travel time is sensitive to flow, but is insensitive (to first order) to stationary inhomogeneities. Conversely, the sum of the travel-time measurements is sensitive to stationary inhomogeneities, but insensitive to flow.

In the remainder of this section, we briefly review the ray-based approach, which will be seen to have certain parallels to the scattering approach. Consider a region with fluid flow defined by the 2-D vector velocity field $\mathbf{v}(\mathbf{R})$, where $\mathbf{R}$ is a 2-D position vector. For generality, we also allow the possibility that the medium has a stationary *acoustic* velocity inhomogeneity, denoted by $c(\mathbf{R})$. Under these conditions, the above ''reciprocal'' travel-time measurement (i.e., the difference in travel times between **a** and **b** and **b** and **a**), denoted by $\tau(\mathbf{a},\mathbf{b})$, can be shown to reduce to the following form under the assumption of a ray-propagation model:[3]

$$\tau(\mathbf{a},\mathbf{b}) = \int_{\mathbf{a}}^{\mathbf{b}} \mathbf{V}(\mathbf{R}) \cdot d\mathbf{l}, \tag{1}$$

where $\mathbf{V}(\mathbf{R}) \equiv -2\mathbf{v}(\mathbf{R})/c(\mathbf{R})^2$ and $d\mathbf{l}$ is a (vector) element of path length along the propagation path between **a** and **b**. Thus Eq. (1) is seen to be the line integral of the *component* of $\mathbf{V}(\mathbf{R})$ along the propagation path. The vector-field tomographic reconstruction problem can then be defined as follows: Given a boundary enclosing some region of a vector field, $\mathbf{V}(\mathbf{r})$, and given observations of its line integrals defined by Eq. (1) joining all possible pairs of points **a** and **b** on the boundary, reconstruct $\mathbf{V}(\mathbf{R})$ in the region enclosed by the boundary. (This is not a physical boundary, but an imaginary boundary on which the acoustic sources and receivers reside. We also need to assume that the boundary is convex, so that all ray paths lie within the boundary's interior.) Unfortunately, this problem as just posed is underdetermined because an arbitrary 2-D vector field is defined by two independent component functions $V_x(\mathbf{R})$ and $V_y(\mathbf{R})$, and one set of ''scalar'' tomographic data is insufficient to recover both $V_x(\mathbf{R})$ and $V_y(\mathbf{R})$. Despite this, progress can be made by noting that an arbitrary vector field can be expressed as the sum of irrotational and solenoidal components, $\mathbf{V}(\mathbf{R}) = \nabla\Phi(\mathbf{R}) + \nabla\times\boldsymbol{\Psi}(\mathbf{R})$, where $\Phi(\mathbf{R})$ and $\boldsymbol{\Psi}(\mathbf{R})$ are spatially dependent scalar and vector potentials. Norton[3] was the first to observe that the problem defined by Eq. (1) can be used to recover uniquely the solenoidal component, $\nabla\times\boldsymbol{\Psi}(\mathbf{R})$, of the vector field $\mathbf{V}(\mathbf{R})$, but not its irrotational component, $\nabla\Phi(\mathbf{R})$. He went on to note that if the field is divergenceless (i.e., $\nabla\cdot\mathbf{V}=0$) within the region of interest, then the scalar potential, $\Phi(\mathbf{R})$, solves Laplace's equation, $\nabla^2\Phi = 0$, in that region and can, in principle, be recovered from observations of the flow velocity on the *boundary* of the domain of interest.[3,4] In Ref. 3 a projection-slice theorem for vector fields analogous to the one used in conventional (scalar) tomography was derived.

The time-of-flight approach to fluid flow reconstruction works well when the scale of the flow inhomogeneities is large compared to a wavelength, so that ray theory provides a reasonable description of propagation. This is generally a valid assumption for the tomographic reconstruction of ocean current flow, but may not hold at higher frequencies and smaller scales, such as in the ultrasonic regime. In the latter case, an approach based on diffraction tomography may be more appropriate. Solutions to the fluid flow recon-

[a)]Current address: Geophex, Ltd., 605 Mercury Street, Raleigh, NC 27603.

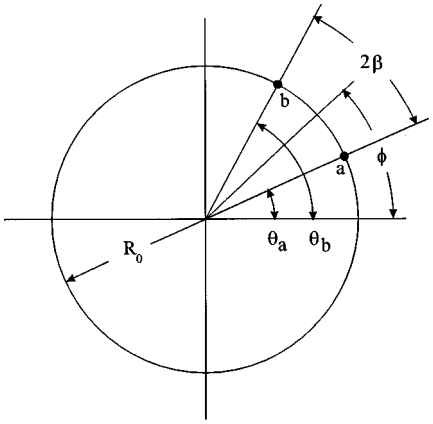

FIG. 1. Imaging geometry; the source/receiver points are **a** and **b**.

struction problem based on diffraction tomography were independently developed by Rouseff and Winters[5] and Rychagov and Ermert.[6] These authors made the notable discovery that both components of an arbitrary 2-D vector field can be recovered using diffraction tomography, unlike time-of-flight vector-field tomography. The diffraction approach is again based on ''reciprocal'' measurements, meaning that a *scattering* measurement is recorded between a source and receiver, and again with the source and receiver interchanged. The reciprocal scattering technique was earlier proposed for reconstructing stratified fluid flow in Ref. 7.

The abovementioned work on vector-field diffraction tomography[5,6] is based on a single frequency formulation, analogous to the case of traditional (scalar) diffraction tomography.[8] In this formulation, if there are, say, N sources and N receivers, then $2N^2$ measurements of the complex scattered field are required (the factor of 2 arising from the two reciprocal measurements). The current paper investigates an approach to fluid flow reconstruction based on wideband diffraction tomography, in which case only $2N$ measurements are needed, two from each of N source/receiver pairs. In particular, we consider the following geometry: we assume a source resides on a circular boundary enclosing the region of interest and a receiving point is displaced at a fixed angular distance around the circle from the source point (Fig. 1). Both source and receiver rotate together at fixed angular separation around the circumference of the circular boundary. At each angular position of the source/receiver pair, a reciprocal scattering measurement is performed; that is, a pulse is transmitted from the source, the scattered field recorded by the receiver, and the measurement repeated with the source and receiver interchanged. The recorded amplitudes are then subtracted. The advantage of the broadband approach is that only two transducers (one source/receiver pair) are needed, rather than a source and/or receiving transducer array, as required in the cw formulation. Thus broadband data acquisition is, in principle, significantly more efficient than single frequency tomography which requires a much larger number of source/receiver combinations. We shall show, however, that the broadband approach again loses the irrotational component, $\nabla\Phi$, of the vector flow field, as was the case in ray-based tomography. An explicit wide-band analytical inversion formula can, however, be derived for the solenoidal component, $\nabla\times\mathbf{\Psi}$, as shown in the next section. But, as was the case for the ray-based formulation, if the field $\mathbf{V}$ is divergenceless, then the irrotational component can again in principle be recovered from boundary measurements of $\mathbf{V}$. The formula for the scalar potential, Φ, in terms of the normal component of $\mathbf{V}$ on the boundary is given at the end of the next section.

I. ANALYSIS

Suppose we have a region of fluid flow defined by the velocity field $\mathbf{v}(\mathbf{r})$. [Much of the development up to Eq. (17) is similar to that in Section 1 of Ref. 7; we repeat it here for completeness.] For the moment, we allow $v(\mathbf{r})$ to be an arbitrary 3-D vector field (where $\mathbf{r}$ is a 3-D position vector); later we specialize to the two-dimensional case. We further assume that the medium has stationary inhomogeneities in the sound speed, denoted by $c(\mathbf{r})$. Let c_0 denote the mean sound speed and define the normalized fluid velocity field $\mathbf{u}(\mathbf{r})$ by

$$\mathbf{u}(\mathbf{r})\equiv\mathbf{v}(\mathbf{r})/c_0, \tag{2}$$

and the sound speed perturbation by

$$\gamma(\mathbf{r})\equiv[c_0/c(\mathbf{r})]^2-1. \tag{3}$$

We shall assume that both $|\mathbf{u}(\mathbf{r})|$ and $\gamma(\mathbf{r})$ are much less than unity so the Born approximation can be invoked. If the time-dependent wave equation is Fourier transformed, with ω the frequency variable, we obtain the Helmholtz equation[3]

$$\nabla^2 p_k(\mathbf{r})+k^2 p_k(\mathbf{r})=-k^2\gamma(\mathbf{r})p_k(\mathbf{r})-2ik\mathbf{u}(\mathbf{r})\cdot\nabla p_k(\mathbf{r}), \tag{4}$$

where $p_k(\mathbf{r})$ is acoustic pressure and $k\equiv\omega/c_0$. This equation is valid to first order in $|\mathbf{v}|/c_0$.

Suppose we illuminate the region of flow from a point source at $\mathbf{r}_a$. In a homogeneous medium with sound speed c_0 and in the absence of fluid flow, the incident field, $p_{ki}(\mathbf{r})$, obeys

$$\nabla^2 p_{ki}(\mathbf{r})+k^2 p_{ki}(\mathbf{r})=-S(k)\,\delta(\mathbf{r}-\mathbf{r}_a), \tag{5}$$

where $S(k)$ represents the frequency dependence of the source, and $\delta(\cdot)$ denotes the 3-D Dirac delta function. We introduce the Green's function

$$g_k(\mathbf{r}|\mathbf{r}')=\frac{1}{4\pi|\mathbf{r}-\mathbf{r}'|}e^{ik|\mathbf{r}-\mathbf{r}'|}, \tag{6}$$

which obeys

$$\nabla^2 g_k(\mathbf{r}|\mathbf{r}')+k^2 g_k(\mathbf{r}|\mathbf{r}')=-\delta(\mathbf{r}-\mathbf{r}'). \tag{7}$$

Comparing Eqs. (5) and (7), we see that

$$p_{ki}(\mathbf{r})=S(\mathbf{r})g_k(\mathbf{r}|\mathbf{r}_a). \tag{8}$$

Now using standard techniques, Eq. (4) can be converted into integral form:

$$p_k(\mathbf{r})=p_{ki}(\mathbf{r})+\int\int\int[k^2\gamma(\mathbf{r}')p_k(\mathbf{r}')+2ik\mathbf{u}(\mathbf{r}')\cdot\nabla p_k(\mathbf{r}')]g_k(\mathbf{r}|\mathbf{r}')d^3\mathbf{r}'. \tag{9}$$

In the Born approximation, we replace $p_k(\mathbf{r}')$ in the integrand with the incident field $p_{ki}(\mathbf{r}')$, given here by Eq. (8). Now let $\mathbf{r}_b$ denote the observation point. Invoking the Born approximation and setting $\mathbf{r}=\mathbf{r}_b$, Eq. (9) becomes

$$p_{ks}(\mathbf{r}_a,\mathbf{r}_b)=\int\int\int [k^2\gamma(\mathbf{r})g_k(\mathbf{r}|\mathbf{r}_a) + 2ik\mathbf{u}(\mathbf{r})\cdot\nabla g_k(\mathbf{r}|\mathbf{r}_a)]g_k(\mathbf{r}|\mathbf{r}_b)d^3\mathbf{r}, \quad (10)$$

where we have defined for convenience

$$p_{ks}(\mathbf{r}_a,\mathbf{r}_b)\equiv\frac{1}{S(k)}[p_k(\mathbf{r}_b)-p_{ki}(\mathbf{r}_b)], \quad (11)$$

and the reciprocity of the Green's function was used to write $g_k(\mathbf{r}|\mathbf{r}_b)=g_k(\mathbf{r}_b|\mathbf{r})$.

In a moment, we show how to eliminate the term involving $\gamma(\mathbf{r})$ in the integrand of Eq. (10) by exploiting the nonreciprocity of fluid flow.[3] First, however, we demonstrate how the first term in Eq. (10) can be isolated by eliminating the second term involving $\mathbf{u}(\mathbf{r})$, in which case one can invert for the sound speed perturbation, $\gamma(\mathbf{r})$. Define

$$p_s^{(+)}(k)\equiv p_{ks}(\mathbf{r}_a,\mathbf{r}_b)+p_{ks}(\mathbf{r}_b,\mathbf{r}_a), \quad (12)$$

$$p_s^{(-)}(k)\equiv p_{ks}(\mathbf{r}_a,\mathbf{r}_b)-p_{ks}(\mathbf{r}_b,\mathbf{r}_a). \quad (13)$$

Here $p_{ks}(\mathbf{r}_b,\mathbf{r}_a)$ means that the positions of the source and receiver have been interchanged. We will see that $p_s^{(+)}(k)$ depends only on the sound speed perturbation, $\gamma(\mathbf{r})$, whereas $p_s^{(-)}(k)$ will depend only on the fluid flow field $\mathbf{u}(\mathbf{r})$.

First consider $p_s^{(+)}(k)$; substituting Eq. (10) into (12), we see that

$$p_s^{(+)}(k)=2k^2\int\int\int \gamma g_a g_b\, d^3\mathbf{r} + 2ik\int\int\int [(\mathbf{u}\cdot\nabla g_a)g_b+(\mathbf{u}\cdot\nabla g_b)g_a]d^3\mathbf{r}, \quad (14)$$

where for brevity, $g_a\equiv g_k(\mathbf{r}|\mathbf{r}_a)$ and $g_b\equiv g_k(\mathbf{r}|\mathbf{r}_b)$. We now show that the second integral vanishes. To see this, note that the integrand can be written

$$(\mathbf{u}\cdot\nabla g_a)g_b+(\mathbf{u}\cdot\nabla g_b)g_a=\nabla\cdot(\mathbf{u}g_a g_b)-g_a g_b\nabla\cdot\mathbf{u}. \quad (15)$$

We shall assume that the velocity field is divergenceless, so that $\nabla\cdot\mathbf{u}=0$. In the case of fluid flow, this follows under the assumption of an incompressible fluid and that no sources or sinks reside in the region of interest. Thus the second integral in Eq. (14) reduces to the volume integral of the divergence $\nabla\cdot(\mathbf{u}g_a g_b)$. Using the divergence theorem, the volume integral can be converted to a surface integral, which vanishes upon allowing the surface to expand to infinity, leaving

$$p_s^{(+)}(k)=2k^2\int\int\int \gamma g_a g_b\, d^3\mathbf{r}. \quad (16)$$

Methods based on standard (scalar) diffraction tomography could be used to reconstruct $\gamma(\mathbf{r})$ using Eq. (16), which contains no contribution due to flow (to first order).

We next see that, on substituting Eq. (10) into (13), the contribution due to the stationary inhomogeneity, γ, cancels, leaving

$$p_s^{(-)}(k)=2ik\int\int\int [(\mathbf{u}\cdot\nabla g_a)g_b-(\mathbf{u}\cdot\nabla g_b)g_a]d^3\mathbf{r}. \quad (17)$$

We now use the Helmholtz theorem to decompose the vector field $\mathbf{u}$ into solenoidal and irrotational components:

$$\mathbf{u}(\mathbf{r})=\nabla\Phi(\mathbf{r})+\nabla\times\boldsymbol{\Psi}(\mathbf{r}), \quad (18)$$

where, for the moment, $\Phi(\mathbf{r})$ and $\boldsymbol{\Psi}(\mathbf{r})$ are unknown scalar and vector potentials. We show in Appendix A that, when Eq. (18) is substituted into Eq. (17), the contribution due to the irrotational component, $\nabla\Phi$, vanishes identically. On the other hand, Appendix B shows that the contribution due to the solenoidal component, $\nabla\times\boldsymbol{\Psi}(\mathbf{r})$, in Eq. (18) is nonzero. In particular, the results of the two appendices show that on substituting Eq. (18) into (17), we obtain

$$p_s^{(-)}(k)=-4ik\int\int\int \boldsymbol{\Psi}\cdot[\nabla g_a\times\nabla g_b]d^3\mathbf{r}. \quad (19)$$

Our next objective is to solve this equation for the vector potential $\boldsymbol{\Psi}(\mathbf{r})$. This can be easily accomplished if we assume that the source and receiver are sufficiently far from the region of nonvanishing flow so that the incident wavefronts may be regarded as plane over this region. In this case, we may assume that $r\ll r_a$ and $r\ll r_b$ (where $r\equiv|\mathbf{r}|$, etc.) for $\mathbf{r}$ confined to the region of nonzero flow. Then the Green's functions can be written

$$g_a\equiv g_k(\mathbf{r}|\mathbf{r}_a)=\frac{1}{4\pi|\mathbf{r}-\mathbf{r}_a|}e^{ik|\mathbf{r}-\mathbf{r}_a|}\approx\frac{1}{4\pi r_a}e^{ik(r_a-\mathbf{r}\cdot\hat{n}_a)}, \quad (20)$$

$$g_b\equiv g_k(\mathbf{r}|\mathbf{r}_a)=\frac{1}{4\pi|\mathbf{r}-\mathbf{r}_b|}e^{ik|\mathbf{r}-\mathbf{r}_b|}\approx\frac{1}{4\pi r_b}e^{ik(r_b-\mathbf{r}\cdot\hat{n}_b)}, \quad (21)$$

where $\hat{n}_a=\mathbf{r}_a/r_a$ and $\hat{n}_b=\mathbf{r}_b/r_b$ are unit vectors pointing in the direction of $\mathbf{r}_a$ and $\mathbf{r}_b$. Then

$$\nabla g_a\times\nabla g_b=\left(\frac{k}{4\pi}\right)^2\frac{\hat{n}_a\times\hat{n}_b}{r_a r_b}e^{ik(r_a+r_b)}e^{-ik(\hat{n}_a+\hat{n}_b)\cdot\mathbf{r}},$$

and Eq. (19) becomes

$$p_s^{(-)}(k)=\frac{ik^3}{(2\pi)^2 r_a r_b}e^{ik(r_a+r_b)} \times\int\int\int \boldsymbol{\Psi}(\mathbf{r})\cdot(\hat{n}_a\times\hat{n}_b)e^{-ik(\hat{n}_a+\hat{n}_b)\cdot\mathbf{r}}d^3\mathbf{r}. \quad (22)$$

Note that Eq. (22) looks like a Fourier transform of the quantity $\boldsymbol{\Psi}(\mathbf{r})\cdot(\hat{n}_a\times\hat{n}_b)$. At this point we shall assume that the flow is two-dimensional and confined to the plane of the unit vectors $\hat{n}_a$ and $\hat{n}_b$. The vector potential $\boldsymbol{\Psi}$ will then be perpendicular to this plane since the solenoidal component, $\nabla\times\boldsymbol{\Psi}$, lies within the plane. Let the x-y plane be the plane of flow; then writing $\mathbf{R}=(x,y)$ as a 2-D vector in this plane, we have $\boldsymbol{\Psi}(\mathbf{R})=\hat{z}\Psi(\mathbf{R})$, with $\hat{z}$ the z unit vector, and $\Psi(\mathbf{R})$

is to be determined. Equation (22) then becomes

$$p_s^{(-)}(k)=\frac{ik^3}{(2\pi)^2 r_a r_b}e^{ik(r_a+r_b)}(\hat{n}_a\times\hat{n}_b)\cdot\hat{z}\int\int\Psi(\mathbf{R})e^{-ik(\hat{n}_a+\hat{n}_b)\cdot\mathbf{R}}d^2\mathbf{R}, \tag{23}$$

where we have neglected an unimportant constant resulting from the integration with respect to z. (Or, alternatively, since the integrand is independent of z, we can merely assume, for convenience, that the range of the z-integration is unity.)

Let θ_a and θ_b represent the angular positions of the points $\mathbf{r}_a$ and $\mathbf{r}_b$ on the circumference of a large circle of radius R_0 surrounding the region of flow, so that $\mathbf{r}_a=R_0\hat{n}_a$ and $\mathbf{r}_b=R_0\hat{n}_b$. The units vectors may be written

$$\hat{n}_a=(\cos\theta_a,\sin\theta_a), \tag{24}$$

$$\hat{n}_b=(\cos\theta_b,\sin\theta_b). \tag{25}$$

We now assume that $\hat{n}_a$ and $\hat{n}_b$ are separated by a fixed angle 2β, that is, we allow the source/receiver points $\mathbf{r}_a$ and $\mathbf{r}_b$ to rotate together around the circular boundary at the fixed angular separation 2β (Fig. 1). We thus define

$$\beta\equiv\tfrac{1}{2}(\theta_b-\theta_a)\quad\text{and}\quad\phi\equiv\tfrac{1}{2}(\theta_a+\theta_b).$$

Then

$$\hat{n}_a+\hat{n}_b=(\cos\theta_a+\cos\theta_b,\sin\theta_a+\sin\theta_b)=2\cos(2\beta)(\cos\phi,\sin\phi), \tag{26}$$

$$\hat{n}_a\times\hat{n}_b=\hat{z}\sin(\theta_b-\theta_a)=\hat{z}\sin(2\beta). \tag{27}$$

Now write $\mathbf{R}=(R\cos\theta,R\sin\theta)\equiv(R,\theta)$, so that from Eq. (26),

$$(\hat{n}_a+\hat{n}_b)\cdot\mathbf{R}=2R\cos\beta\cos(\theta-\phi).$$

Then Eq. (23) becomes

$$p_s^{(-)}(k,\phi)=\frac{ik^3}{(2\pi)^2R_0^2}e^{i2kR_0}\sin(2\beta)\int_0^{2\pi}d\theta\times\int_0^{\infty}R\,dR\Psi(R,\theta)e^{-i2kR\cos\beta\cos(\theta-\phi)}. \tag{28}$$

The double integral on the right of Eq. (28) is the 2-D Fourier transform of $\Psi(R,\theta)$ in polar form. Taking the inverse 2-D Fourier transform of both sides of Eq. (28) gives

$$\Psi(R,\theta)=C_\beta\int_0^{2\pi}d\phi\int_0^{\infty}dk e^{-i2kR_0}\frac{p_s^{(-)}(k,\phi)}{k^2}e^{i2kR\cos\beta\cos(\theta-\phi)}, \tag{29}$$

where

$$C_\beta\equiv\frac{4R_0^2\cos^2\beta}{i\sin(2\beta)} \tag{30}$$

is a constant. This is our fundamental reconstruction formula which allows us to compute $\Psi(R,\theta)$ from the broadband reciprocal scattering data, $p_s^{(-)}(k,\phi)$, recorded as a function of frequency, k, and the angular position, ϕ, of the source/receiver pair.

The solenoidal component of $\mathbf{u}(R,\theta)$ of the velocity field in Eq. (18) can then be computed from

$$\mathbf{u}_S(R,\theta)\equiv\nabla\times\boldsymbol{\Psi}(R,\theta)=\frac{1}{R}\frac{\partial\Psi}{\partial\phi}\hat{R}-\frac{\partial\Psi}{\partial R}\hat{\phi}, \tag{31}$$

where $\hat{R}$ and $\hat{\phi}$ are unit vectors.

The irrotational component of the velocity field, given by

$$\mathbf{u}_I(\mathbf{R})\equiv\nabla\Phi(\mathbf{R}), \tag{32}$$

can be recovered from boundary measurements since Φ obeys Laplace's equation

$$\nabla^2\Phi(\mathbf{R})=0. \tag{33}$$

This follows from the assumption of a divergenceless field ($\nabla\cdot\mathbf{u}=0$). The 2-D Green's function for the Laplacian, $G(\mathbf{R}|\mathbf{R}')$, which solves

$$\nabla^2G(\mathbf{R}|\mathbf{R}')=-\delta(\mathbf{R}-\mathbf{R}'), \tag{34}$$

is given by

$$G(\mathbf{R}|\mathbf{R}')=-\frac{1}{4\pi}\ln(|\mathbf{R}-\mathbf{R}'|). \tag{35}$$

One can then show that[3]

$$\Phi(\mathbf{R})=\oint G(\mathbf{R}|\mathbf{R}')\mathbf{u}(\mathbf{R}')\cdot\hat{n}\,ds, \tag{36}$$

where the integration is around the boundary of the region under study, and $\hat{n}$ represents the outward unit normal to this boundary. The irrotational component of the flow is given by the gradient of Eq. (36), that is,

$$\mathbf{u}_I(\mathbf{R})\equiv\nabla\Phi(\mathbf{R})=\oint\nabla G(\mathbf{R}|\mathbf{R}')\mathbf{u}(\mathbf{R}')\cdot\hat{n}\,ds. \tag{37}$$

Equations (31) and (37) define the total vector field: $\mathbf{u}(\mathbf{R})=\mathbf{u}_S(\mathbf{R})+\mathbf{u}_I(\mathbf{R})$.

II. DISCUSSION AND CONCLUSION

The purpose of this paper is to show that a closed form broadband reconstruction formula can be derived for the solenoidal component of the vector flow field under study from acoustic scattering measurements. It is worth remarking that no particulate matter is needed in the fluid to provide scattering centers, which contrasts with Doppler based approaches for the measurement of flow. Thus the technique is not subject to the range Doppler uncertainty principle. Whether this approach has other advantages over Doppler systems is open to question. Indeed, the method should work best in the absence of particulate matter carried with the fluid, since this will affect the wide-band response in a manner that is not easy to predict. Further study will be needed to address these and other practical issues in implementing this technique.

APPENDIX A

Here we show that the first term in Eq. (18), that is $\nabla\Phi$, when substituted in Eq. (16), is identically zero. That is, we wish to show that

$$\int\int\int [(\nabla\Phi\cdot\nabla g_a)g_b-(\nabla\Phi\cdot\nabla g_b)g_a]d^3\mathbf{r}=0. \quad \text{(A1)}$$

To see this, we use the following vector identity:

$$\nabla\cdot[\Phi g_b\nabla g_a-\Phi g_a\nabla g_b]=(\nabla\Phi\cdot\nabla g_a)g_b-(\nabla\Phi\cdot\nabla g_b)g_a + \Phi g_b\nabla^2 g_a-\Phi g_a\nabla^2 g_b, \quad \text{(A2)}$$

which can be verified by expanding the left-hand side. Using the fact that $\nabla^2 g_a=-k^2 g_a$ and $\nabla^2 g_b=-k^2 g_b$ from Eq. (7), since $\mathbf{r}\neq\mathbf{r}_a$ and $\mathbf{r}\neq\mathbf{r}_b$, the last two terms cancel, leaving

$$\nabla\cdot[\Phi g_b\nabla g_a-\Phi g_a\nabla g_b]=(\nabla\Phi\cdot\nabla g_a)g_b - (\nabla\Phi\cdot\nabla g_b)g_a. \quad \text{(A3)}$$

Substituting Eq. (A3) into (A1) and using the divergence theorem, Eq. (A1) becomes a surface integral of $\Phi g_b\nabla g_a - \Phi g_a\nabla g_b$; allowing the surface to expand to infinity, the integral vanishes, as required.

APPENDIX B

Here we prove that Eq. (19) follows on substituting Eq. (18) into (17). Inserting Eq. (18) into (17) and using Eq. (A1), we have

$$p_s^{(-)}(k)=2ik\int\int\int [(\nabla\times\boldsymbol{\Psi}\cdot\nabla g_a)g_b - (\nabla\times\boldsymbol{\Psi}\cdot\nabla g_b)g_a]d^3\mathbf{r}. \quad \text{(B1)}$$

First note the identity

$$(\nabla\times\boldsymbol{\Psi})\cdot\nabla g_a=\nabla\cdot(\boldsymbol{\Psi}\times\nabla g_a)+\boldsymbol{\Psi}\cdot(\nabla\times\nabla g_a) =\nabla\cdot(\boldsymbol{\Psi}\times\nabla g_a),$$

since $\nabla\times\nabla g_a\equiv 0$. Similarly,

$$(\nabla\times\boldsymbol{\Psi})\cdot\nabla g_b=\nabla\cdot(\boldsymbol{\Psi}\times\nabla g_b),$$

and the integrand of Eq. (B1) becomes

$$g_b\nabla\cdot(\boldsymbol{\Psi}\times\nabla g_a)-g_a\nabla\cdot(\boldsymbol{\Psi}\times\nabla g_b). \quad \text{(B2)}$$

Now note the identity

$$g_b\nabla\cdot(\boldsymbol{\Psi}\times\nabla g_a)=\nabla\cdot(g_b\boldsymbol{\Psi}\times\nabla g_a)-\nabla g_b\cdot(\boldsymbol{\Psi}\times\nabla g_a),$$

so Eq. (B2) becomes

$$\begin{aligned} &g_b\nabla\cdot(\boldsymbol{\Psi}\times\nabla g_a)-g_a\nabla\cdot(\boldsymbol{\Psi}\times\nabla g_b)\\ &\quad=\nabla\cdot[g_b\boldsymbol{\Psi}\times\nabla g_a-g_a\boldsymbol{\Psi}\times\nabla g_b]-\nabla g_b\cdot(\boldsymbol{\Psi}\times\nabla g_a)\\ &\qquad+\nabla g_a\cdot(\boldsymbol{\Psi}\times\nabla g_b)\\ &\quad=\nabla\cdot[g_b\boldsymbol{\Psi}\times\nabla g_a-g_a\boldsymbol{\Psi}\times\nabla g_b]-\boldsymbol{\Psi}\cdot\nabla g_a\times\nabla g_b\\ &\qquad+\boldsymbol{\Psi}\cdot\nabla g_b\times\nabla g_a\\ &\quad=\nabla\cdot[g_b\boldsymbol{\Psi}\times\nabla g_a-g_a\boldsymbol{\Psi}\times\nabla g_b]-2\boldsymbol{\Psi}\cdot\nabla g_a\times\nabla g_b. \end{aligned} \quad \text{(B3)}$$

Substituting Eq. (B3) into (B1), the first term vanishes on account of the divergence theorem, leaving Eq. (19), as desired.

[1] S. A. Johnson, J. F. Greenleaf, C. R. Hansen, W. F. Samayoa, M. Tanaka, A. Lent, D. A. Christensen, and R. L Woolley, ''Reconstructing three-dimensional fluid velocity vector fields from acoustic transmission measurements,'' in *Acoustical Holography*, edited by L. W. Kessler (Plenum, New York, 1977), Vol. 7, pp. 307–326.

[2] W. Munk, P. Worchester, and C. Wunsch, *Ocean Acoustic Tomography* (Cambridge University Press, New York, 1995), and references therein.

[3] S. J. Norton, ''Tomographic reconstruction of 2-D vector fields: application to flow imaging,'' Geophys. J. **97**, 161–168 (1988).

[4] S. J. Norton, ''Unique tomographic reconstruction of vector fields using boundary data,'' IEEE Trans. Image Process. **IP-1**, 406–412 (1992).

[5] D. Rouseff and K. B. Winters, ''Two-dimensional vector flow inversion by diffraction tomography,'' Inverse Probl. **10**, 687–697 (1994).

[6] M. N. Rychagov and H. Ermert, ''Reconstruction of fluid motion in acoustic diffraction tomography,'' J. Acoust. Soc. Am. **99**, 3029–3035 (1996).

[7] S. J. Norton, ''Reconstructing stratified fluid flow from reciprocal scattering measurements,'' J. Acoust. Soc. Am. **89**, 2567–2572 (1991).

[8] A. J. Devaney, ''A filtered backpropagation algorithm for diffraction tomography,'' Ultrason. Imaging **4**, 336–350 (1982).

Group delays of distortion product otoacoustic emissions in the guinea pig

Sandra Schneider, Vera F. Prijs, and Ruurd Schoonhoven
Leiden University Medical Center, Department of ENT/Audiology, PO Box 9600, 2300 RC Leiden, The Netherlands

(Received 29 October 1998; accepted for publication 10 February 1999)

This paper presents a comprehensive set of experimental data on group delays of distortion product otoacoustic emissions (DPOAEs) in the guinea pig. Group delays of the DPOAEs with frequencies $2f_1-f_2$, $3f_1-2f_2$, $4f_1-3f_2$, and $2f_2-f_1$ were measured with the phase gradient method. Both the f_1- and the f_2-sweep paradigm were used. Differences between the two sweep paradigms were investigated for the four DPOAEs, as well as the group delay differences between the DPOAEs. Analysis revealed larger group delays with the f_2-sweep paradigm, but only for the lower sideband DPOAEs (with $f_{dp}<f_1,f_2$). For the lower sideband cubic distortion product $2f_1-f_2$, the f_2-sweep delays were a factor of 1.17–1.54 larger than the f_1-sweep delays, depending on frequency. The upper sideband DPOAE $2f_2-f_1$ showed no significant difference between f_1- and f_2-sweep group delays, except for the highest and lowest f_2 frequencies. Comparing the group delays of the DPOAEs for each sweep paradigm separately, equal group delays were found for all four DPOAEs measured with the f_1-sweep. With the f_2-sweep paradigm on the other hand, the group delays of the three lower sideband DPOAEs occurred to be larger than the group delays of the upper sideband DPOAE $2f_2-f_1$. A tentative interpretation of the data in the context of proposed explanatory hypotheses on DPOAE group delays is given.
[S0001-4966(99)03505-5]

PACS numbers: 43.64.Jb, 43.64.Kc [BLM]

INTRODUCTION

Distortion product otoacoustic emissions (DPOAEs) are a product of nonlinear processes in the inner ear and form an important tool to study cochlear mechanics. Upon stimulating the ear with two pure tones of slightly different frequency f_1 and f_2 (the primaries), combination tones are generated in the cochlea with frequencies $f_{DP}=mf_1+nf_2$ (given that $f_1<f_2$ and m,n integers). Only the strongest combination tones are measurable in the outer ear canal as DPOAEs (Kemp, 1979). The emission with frequency $2f_1-f_2$, known as the cubic distortion product, usually has the highest amplitude and therefore is the one most frequently studied (Probst *et al.*, 1991). The definitions lower sideband (LSB) and upper sideband (USB) DPOAE are used to indicate whether the DP frequency is lower or higher than the primary frequencies, respectively.

The distortion products are assumed to be generated in the region where the f_1 and f_2 excitation patterns show substantial overlap (Kim, 1980; Kim *et al.*, 1980; Siegel *et al.*,1982). Within that region, the place where f_2 reaches its maximum basilar membrane displacement (x_2) is supposedly the largest contributor to the generation of a DPOAE. Suppression experiments support this view by showing that the amplitude of the cubic distortion product $2f_1-f_2$ is most effectively decreased by a tone close to f_2 (Brown and Kemp, 1984; Kummer *et al.*, 1995) or between f_1 and f_2 (Martin *et al.*, 1987).

There is evidence from neural recordings in cats (Smoorenburg *et al.*, 1976; Kim *et al.*, 1980) and basilar membrane velocity measurements (Robles *et al.*, 1991) that the $2f_1-f_2$ distortion product reaches its own characteristic place x_{DP} apically from the generation site x_2. Recently, several studies showed that there is a contribution from this characteristic place to the $2f_1-f_2$ DPOAE in the ear canal of human subjects (Kummer *et al.*, 1995; Brown *et al.*, 1996; Heitmann *et al.*, 1998).

The upper sideband DPOAE with frequency $2f_2-f_1$ differs from the lower sideband DPOAEs ($2f_1-f_2$, $3f_1-2f_2$, $4f_1-3f_2$, etc.) in several ways. Its amplitude is considerably smaller than the amplitude of the $2f_1-f_2$ DPOAE, and its characteristic frequency place is located basally from the primary frequency regions. Therefore, a distortion product with frequency $2f_2-f_1$ generated close to x_2 is not likely to reach the ear canal. Suppression experiments have shown that the $2f_2-f_1$ level is best suppressed by a tone with a frequency close to $2f_2-f_1$, not to f_2 (Martin *et al.*, 1987, 1998). This supports the idea that the contribution of the $2f_2-f_1$ characteristic frequency place is larger than that of x_2.

While early studies mostly focused on DPOAE amplitude under various stimulus conditions, more recently several authors have also considered the phase of the ear canal response. The interest here is that a measure of the mechanical delay in the cochlea can be obtained by determining the group delay of the DPOAEs with the phase-gradient method (Kimberley *et al.*, 1993; O'Mahoney and Kemp, 1995), fixing one of the primaries while varying the other. The f_1-sweep paradigm refers to varying the f_1 frequency at fixed values of f_2, while the f_2-sweep paradigm refers to the opposite situation. Under the assumption that the DPOAEs are generated at x_2, the first is easier to interpret, since the

generation site will not move during the f_1-sweep. Several studies reported larger group delays when determined with the f_2-sweep method as opposed to the f_1-sweep in humans (O'Mahoney and Kemp, 1995; Moulin and Kemp, 1996b; Bowman *et al.*, 1997) and in rabbits (Whitehead *et al.*, 1996). Moulin and Kemp (1996b) have shown that this only holds true for the lower sideband DPOAEs. They reported no significant difference between f_1- and f_2-sweep for the $2f_2-f_1$ group delays in human subjects. In the attempts to explain the differences found between the group delays obtained with f_1- and f_2-sweeps, two hypotheses have been proposed, concerning the way the DPOAE generation site moves with the changing primary frequencies: the place- and the wave-fixed model (Kemp, 1986; O'Mahoney and Kemp, 1995; Moulin and Kemp, 1996a,b). The place-fixed model for the generation of DPOAEs is based on the assumption that the generation place does not move during the f_1- or f_2-sweep. In the wave-fixed description, however, the generation place x_2 is fixed to the peak of the traveling wave, which means that it shifts in the f_2-sweep paradigm. Bowman *et al.* (1997, 1998) ascribed the differences between f_1- and f_2-sweep group delays to the level-dependent filter build-up time. In their view, which is based on the place-fixed model, the f_2-sweep paradigm includes a larger portion of the filter build-up time in the group delay than does the f_1-sweep.

In this report we present a comprehensive set of DPOAE group delay data for the guinea pig. In this animal, as well as in other rodents, DPOAE amplitudes are substantially higher than in human subjects (Brown, 1987; Brown and Gaskill, 1990). This gives the possibility to measure several DPOAE components with a good signal-to-noise ratio. As part of a larger study of distortion products in the guinea pig, we measured the amplitudes and phases of the four DPOAEs with frequencies $2f_1-f_2$, $3f_1-2f_2$, $4f_1-3f_2$, and $2f_2-f_1$, with both the f_1- and the f_2-sweep paradigm. In this paper we focus on the phase data, from which the group delays were calculated. A comparative evaluation is presented of group delays of different DP components when measured with the same sweep paradigm, and of group delays obtained with the f_1-sweep versus the f_2-sweep paradigm. Finally, a tentative analysis is made of the interpretation of the data in terms of the place-fixed and wave-fixed models, proposed to explain the differences of DPOAE group delays in different paradigms (Kemp, 1986; O'Mahoney and Kemp, 1995; Moulin and Kemp, 1996a,b).

I. METHODS

A. Subjects

Five pigmented female guinea pigs, weighing between 500 and 700 g, were tested. Otoscopic inspection revealed no abnormalities in any of the ears. The animals were anesthetized with an intramuscular injection of ketamine hydrochloride (Ketalar, 20 mg/kg) and xylazine (Rompun, 15 mg/kg). Their body temperature was maintained at 38 °C with a heating blanket. During each experimental session, lasting between 1 and 2 h, one ear was tested. Each ear was measured twice, on different days, except one ear, which was only tested once. This resulted in a total of 19 sessions.

B. Material

The stimulus tones were generated on a DSP board (Ariel DSP 16+) and delivered to the ear canal via two ER2 transducers (Etymotic Research). These were connected to an ER10B probe system (Etymotic Research), housing a low noise miniature microphone for the recording of ear canal sound pressure levels. The microphone signal was amplified 40 dB. The probe system was sealed into the external auditory meatus with a plastic earplug. All recordings were made in a sound-treated booth. We used modified versions of CUBDIS© software, which enabled us to record several other distortion products in addition to the $2f_1-f_2$ component, over a wide range of f_2/f_1 values, with both the f_1- and the f_2-sweep paradigm.

C. DPOAE recording paradigms

1. Ear canal calibration

Prior to each f_1- or f_2-sweep measurement, an ear canal calibration was performed to set the level and starting phase of the primaries. The responses to 50 swept tones (''chirps''), generated at a constant voltage and presented in a continuous mode, were averaged and the amplitude and phase spectra were computed. From these spectra, the voltage, and the starting phase of each frequency, necessary to obtain the desired primary level and zero phase at the place of the microphone, were calculated. The amplitude spectra of the ear canal calibrations were also used to check the probe fit. Whenever the spectrum showed signs that the probe was no longer sealing the ear canal, the probe was replaced and calibration was done again.

2. f_1- and f_2-sweeps

Amplitudes and phases of the following DPOAE components were recorded as a function of DPOAE frequency: $2f_1-f_2$, $3f_1-2f_2$, $4f_1-3f_2$, and $2f_2-f_1$. Two different methods were used to modify the DPOAE frequency: the f_1-sweep paradigm, with frequency f_2 fixed and f_1 varied, and the f_2-sweep paradigm, with f_1 fixed and f_2 varied. The fixed f_2 frequencies were between 1.5 and 11 kHz, the fixed f_1 values a factor of 1.25 lower. The step-size of the varying primary frequency was 24.4 or 48.8 Hz. During each sweep, the f_2/f_1 ratio varied over a broad range of at most 1.01–1.70. Primary levels in all sweep experiments were constant at $L_1, L_2 = 65$, 55 dB SPL. Noise levels were determined from the average amplitudes of the six frequency bins closest to the DPOAE frequency bin.

D. Data analysis

The phase-frequency relations were unwrapped to eliminate 2π discontinuities. Group delays were calculated from the slope of the unwrapped phase curves according to the following equation:

$$D = -\frac{1}{2\pi}\frac{d\varphi_{DP}}{df_{DP}} \quad (1)$$

with D, the group delay, in ms; φ_{DP}, the DPOAE phase, in radians; and f_{DP}, the DPOAE frequency, in kHz. Since the phase-frequency curve is linear only over a small range of f_2/f_1 (Moulin and Kemp, 1996a), the slope was determined from a regression line fitted through a small part of the curve, consisting of 11 points. Those points corresponded to the frequencies centered on the maximum in the DPOAE amplitude versus frequency relation. This implies that for each f_1- or f_2-sweep measurement, the group delay is determined at the primary frequency separation that yields the maximum DPOAE level, which can be different for all four DP components. All group delays in this study are referenced to f_2 frequency. In case of f_1-sweeps this is the fixed primary, but group delays measured with the f_2-sweep method are given as a function of the f_2 belonging to the maximum in DPOAE level, where the phase-frequency gradient was computed. Group delays were excluded from further analysis when one or more of the data points used for group delay calculation had a signal-to-noise ratio smaller than 10 dB.

Using the method as described above, the group delay was not determined when there was no clear maximum in the DPOAE level. Together with the 10-dB noise criterion, this resulted in unequal numbers of group delay data points for the different DP components and for the two sweep paradigms. Since the group delays were determined at the primary frequencies yielding the maximum DPOAE level, we found f_2-sweep group delays in each individual ear at many slightly different f_2 values instead of at a few fixed values (as for the f_1-sweep paradigm). Therefore, instead of paired statistical tests, an alternative test was used to compare the f_1- and f_2-sweep group delay values, which consists of comparing the linear fits through the pooled data.

The group delay versus f_2 curves were fitted with the following regression equation:

$$\log(D) = a + b\cdot\log(f_2) + c\cdot S + d\cdot\log(f_2)\cdot S, \quad (2)$$

with S as the ''dummy'' variable, which is 0 or 1 in case of f_1-sweep and f_2-sweep, respectively. This results in the two regression lines $\log(D_1) = a + b\cdot\log(f_2)$ and $\log(D_2) = (a + c) + (b + d)\cdot\log(f_2)$ for the two sweep paradigms, which are exactly the same lines as two separate linear fits would have given (Draper and Smith, 1981). Subtracting these lines yields $\log(D_2/D_1) = c + d\cdot\log(f_2)$. Plotting D_2/D_1 as a function of f_2, with the 95% confidence interval, shows the frequency areas where D_1 is significantly different from D_2 ($p < 0.05$).

II. RESULTS

As an illustrative example of the raw data, the amplitude and phase-frequency relations of a representative measurement, obtained with the f_1-sweep paradigm and f_2 fixed at 8 kHz, are shown in Fig. 1. The f_2-sweep results, at $f_1 = 6$ kHz, of the same ear are plotted in Fig. 2. The upper panels show the levels of the four DPOAEs with frequencies $2f_1 - f_2$, $3f_1 - 2f_2$, $4f_1 - 3f_2$, and $2f_2 - f_1$ as a function

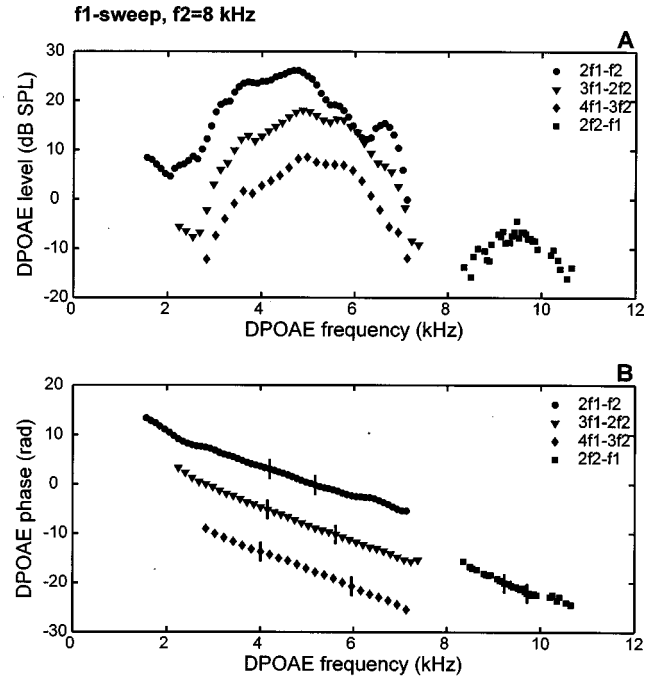

FIG. 1. DPOAEs measured in an individual guinea pig ear, with the f_1-sweep paradigm at $f_2 = 8$ kHz. (A) DPOAE level as a function of DPOAE frequency ($\bullet = 2f_1 - f_2$, $\blacktriangledown = 3f_1 - 2f_2$, $\blacklozenge = 4f_1 - 3f_2$, $\blacksquare = 2f_2 - f_1$). All data points shown have signal-to-noise ratio >10 dB. (B) Corresponding DPOAE phase as a function of DPOAE frequency. The region from which the group delays are calculated, consisting of 11 points around the maximum in DPOAE level, is indicated with vertical lines.

of the distortion product frequency f_{DP}. Only data points with signal-to-noise ratio >10 dB are plotted. The three lower sideband DPOAEs all peak at approximately the same f_{DP}, which implies that the ratio f_2/f_1 at maximum DP level

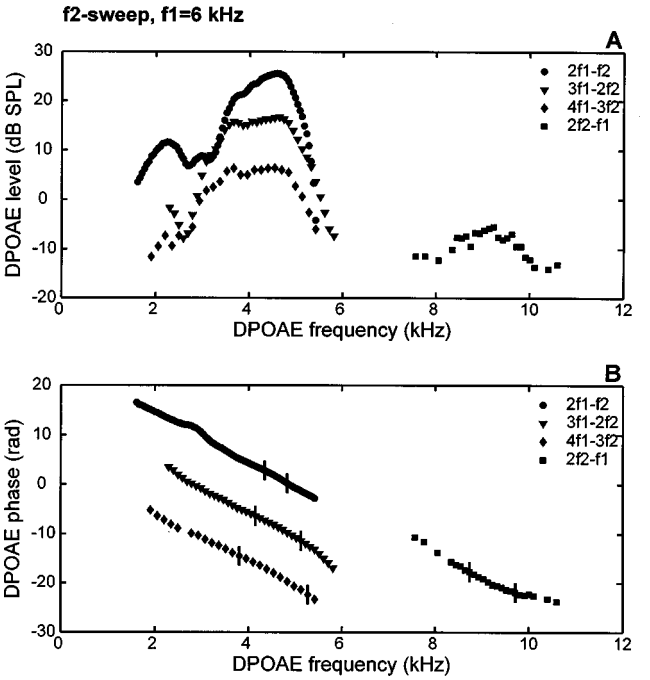

FIG. 2. DPOAEs measured in an individual guinea pig ear (the same ear as in Fig. 1), with the f_2-sweep paradigm at $f_1 = 6$ kHz. See caption for Fig. 1.

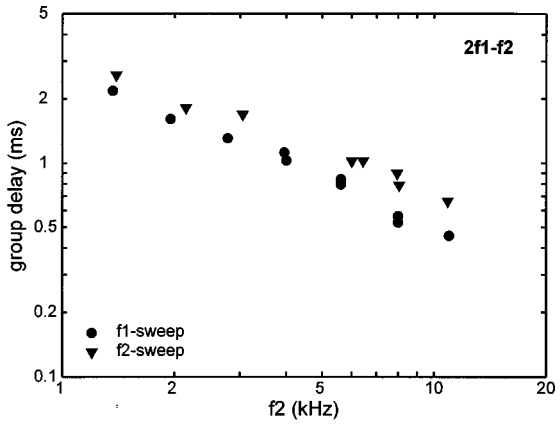

FIG. 3. Group delays of the $2f_1-f_2$ DPOAE as a function of f_2 frequency, measured in one individual ear (●= f_1-sweep group delays, ▼= f_2-sweep group delays).

decreases with increasing DP order. The $2f_2-f_1$ DPOAE has its maximum at a higher f_{DP}. The lower panels of Figs. 1 and 2 show the corresponding DPOAE phases. The curves are shifted arbitrarily with a multiple of 2π. The region where the regression line was fitted to determine the slope is indicated in each phase curve.

All group delays of the $2f_1-f_2$ DPOAE from one measurement (one ear) are plotted on a double-logarithmic scale in Fig. 3, as a function of the f_2 frequency. For the f_1-sweep group delays, this is the fixed f_2 frequency, and for the f_2-sweep group delays this is the f_2 frequency belonging to the maximum in DPOAE level, at which the group delay was determined. The f_1 and f_2-sweep group delays (D_1 and D_2, respectively) are indicated with different symbols. The group delay decreases as a function of frequency, and the f_2-sweep group delays are larger than those obtained with the f_1-sweep paradigm.

TABLE I. Coefficients of the regression lines $\log(D)=a+b\log(f_2)$, for the four DPOAEs and the two sweep paradigms.

	f_1-sweep			f_2-sweep		
	a	b	R^2	a	b	R^2
$2f_1-f_2$	0.45	−0.77	0.93	0.51	−0.64	0.91
$3f_1-2f_2$	0.42	−0.73	0.91	0.48	−0.68	0.91
$4f_1-3f_2$	0.34	−0.61	0.85	0.44	−0.64	0.85
$2f_2-f_1$	0.41	−0.72	0.52	0.24	−0.43	0.76

Figure 4 shows the pooled group delay data from all measurements, for the DPOAEs with frequency $2f_1-f_2$, $3f_1-2f_2$, $4f_1-3f_2$, and $2f_2-f_1$. The data are fitted with regression lines according to Eq. (2). The dashed and solid lines represent the fits through the f_1-sweep and the f_2-sweep group delays, respectively. The lower sideband DPOAEs all show the same effect: f_2-sweep group delays

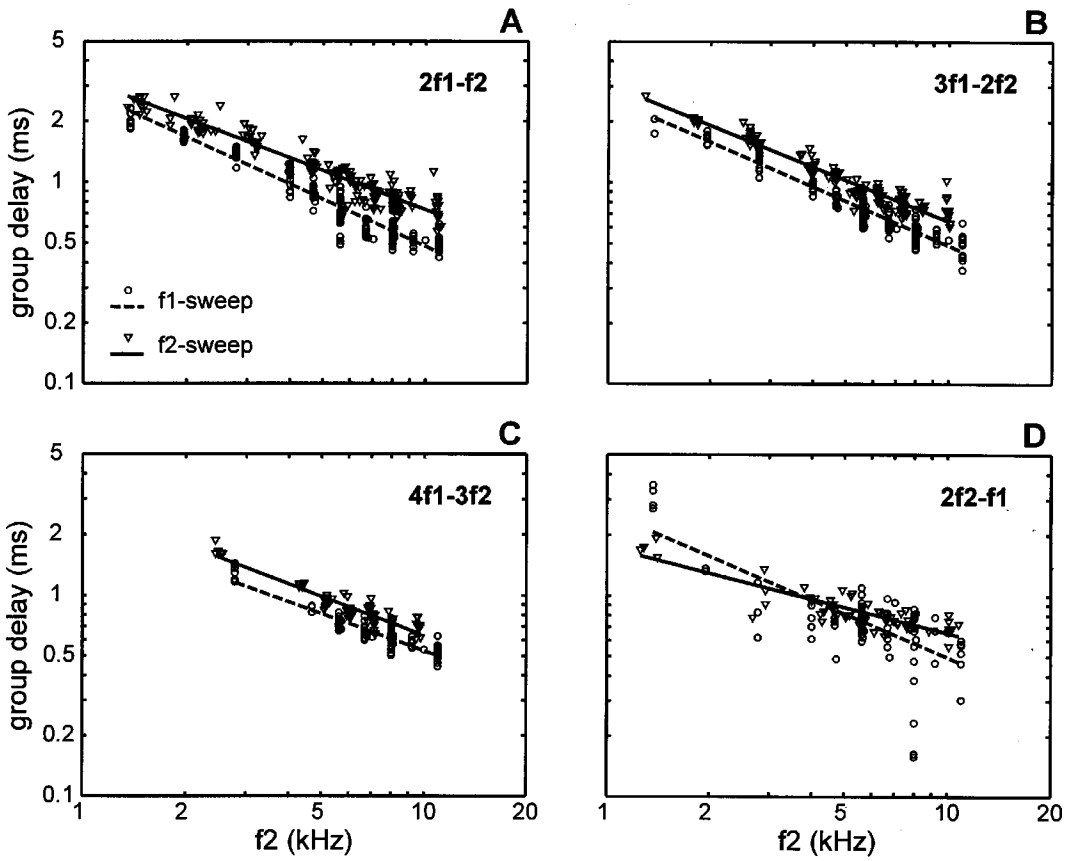

FIG. 4. Pooled group delay data from all measurements. Group delays are plotted as a function of f_2 frequency, for both sweep paradigms. For each sweep paradigm and DPOAE component, the regression line is fitted [Eq. (2)] and plotted with a dashed line (f_1-sweep, ○) or a solid line (f_2-sweep, ▽). (A) Group delays of the $2f_1-f_2$ DPOAE. (B) Group delays of the $3f_1-2f_2$ DPOAE. (C) Group delays of the $4f_1-3f_2$ DPOAE. (D) Group delays of the $2f_2-f_1$ DPOAE.

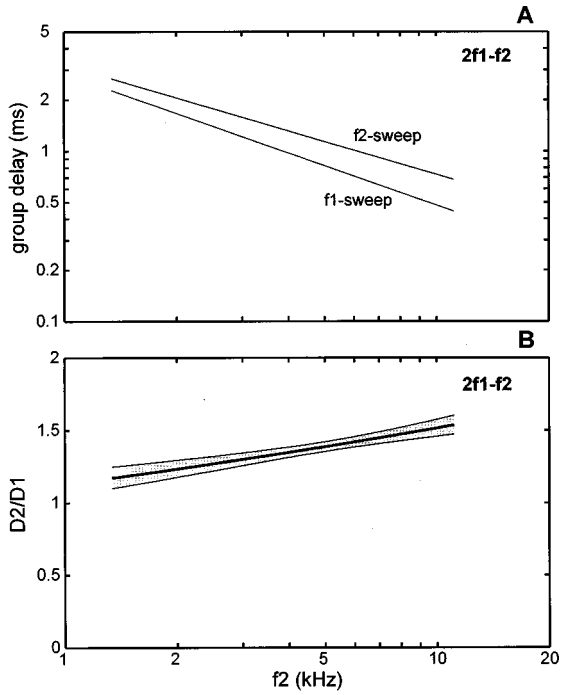

FIG. 5. Comparison of the f_1-sweep group delays (D_1) and the f_2-sweep group delays (D_2). (A) Regression lines of the f_1- and f_2-sweep group delays for the $2f_1-f_2$ DPOAE, as in Fig. 4A. (B) Subtracting the lines of (A) results in the ratio D_2/D_1 as a function of f_2. The 95% confidence interval of the group delay ratio is indicated with the shaded area.

are larger than the group delays determined with the f_1-sweep paradigm. The DPOAE with frequency $2f_2-f_1$, in the lower right panel, behaves differently. At the lowest frequencies, the f_1-sweep delays seem to be larger, while in the higher frequency region the f_2-sweep method gives larger group delays.

In Table I, the coefficients are given of the regression lines that were plotted in Fig. 4, together with the goodness of fit R^2.

In order to evaluate whether, and in which frequency range, the f_1- and f_2-sweep group delays are significantly different, the regression lines were compared as described in Sec. I. This method is illustrated in Fig. 5 for the $2f_1-f_2$ DPOAE. The upper panel shows again the two logarithmic regression lines for the f_1- and f_2-sweep group delays as a function of f_2 (the same as in Fig. 4A). Subtracting these, results in the ratio of f_1- and f_2-sweep group delays D_2/D_1. This ratio is plotted in the lower panel, as a function of f_2 with the 95% confidence interval. From Fig. 5B it is clear that the group delays of the $2f_1-f_2$ DPOAE measured with f_2-sweeps are significantly larger than the f_1-sweep group delays, at all frequencies.

The same procedure was followed with the group delays of the other DPOAEs. Figure 6 shows the ratio between f_1- and f_2-sweep group delays for all four DPOAEs. For the lower sideband DPOAEs $2f_1-f_2$, $3f_1-2f_2$, and $4f_1-3f_2$, the delays obtained with the f_2-sweep method are

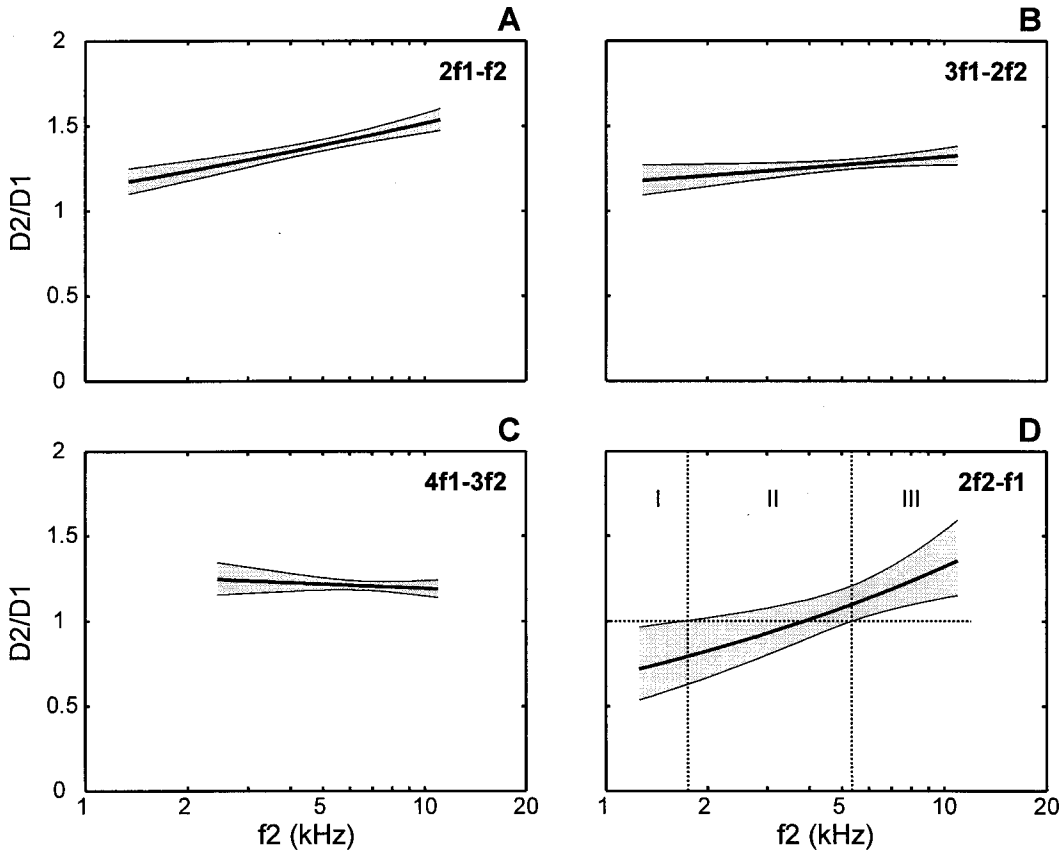

FIG. 6. Ratio of f_1-sweep and f_2-sweep group delays D_2/D_1 as a function of f_2 with 95% confidence interval. Results for the three lower sideband DPOAEs $2f_1-f_2$ (A), $3f_1-2f_2$ (B), $4f_1-3f_2$ (C), and for the upper sideband DPOAE $2f_2-f_1$ (D). Area I indicates the frequency region below 1.8 kHz, where $D_1>D_2$, in area II D_1 and D_2 are not significantly different and in area III, above 5.4 kHz, $D_2>D_1$.

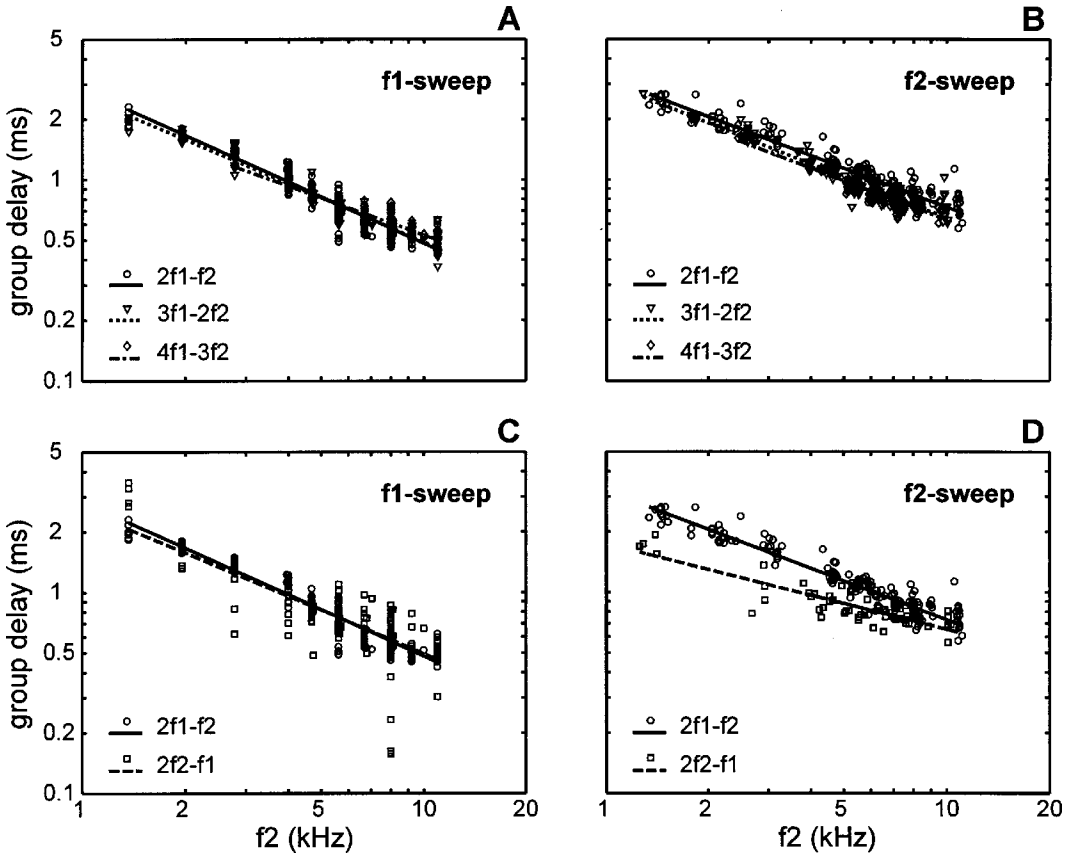

FIG. 7. Pooled group delay data as a function of f_2 frequency. Same data points as in Fig. 4. (A) f_1-sweep group delays of the three lower sideband DPOAEs with regression lines (○ solid, $2f_1-f_2$; ▽ dotted, $3f_1-2f_2$; ◇ dashed-dotted, $4f_1-3f_2$). (B) f_2-sweep group delays of the three lower sideband DPOAEs. (C) f_1-sweep group delays of $2f_1-f_2$ (○, solid) and $2f_2-f_1$ (□, dashed). (D) f_2-sweep group delays of $2f_1-f_2$ and $2f_2-f_1$.

significantly larger than those measured with an f_1-sweep, at all measured frequencies (Fig. 6A, B, and C). The $2f_2-f_1$ group delays show no significant difference between f_1- and f_2-sweep for f_2 in the range 1.8–5.4 kHz (the confidence interval overlaps the $D_2/D_1=1$ line, area II in Fig. 6D). For $f_2<1.8$ kHz, the f_1-sweep paradigm produces the largest group delays (area I), while at $f_2>5.4$ kHz, the f_2-sweep group delays are larger (area III).

In Fig. 7, the same group delay data from Fig. 4 are plotted again, although grouped differently. In this case not the sweep paradigms are compared, but the DPOAE components. This is done for the f_1- and the f_2-sweep method separately. Again, these are pooled data from all measurements. In Fig. 7A, the group delays of the lower sideband DPOAEs obtained with f_1-sweeps are plotted, together with the regression lines (see Table I). The same method of comparing regression lines was used to determine whether the fits differ significantly. There appear to be no significant differences between the group delays of the three lower sideband DPOAEs obtained with the f_1-sweep in the observed frequency region. Figure 7B shows the group delays of the same lower sideband DPOAEs, obtained with the f_2-sweep method. The only significant difference is found between the $2f_1-f_2$ and the $4f_1-3f_2$ group delays. The latter are slightly smaller. A comparison between the $2f_1-f_2$ and the $2f_2-f_1$ group delays is shown in Fig. 7C, for the f_1-sweep data. There is no significant difference. However, when the f_2-sweep data of the same DPOAEs are compared (Fig. 7D), there appears to be a large significant difference for all measured frequencies. The group delays of the $2f_2-f_1$ DPOAE are smaller than of the $2f_1-f_2$ DPOAE, when obtained with the f_2-sweep paradigm.

III. DISCUSSION

The amplitudes of DPOAEs are larger in guinea pigs than in human subjects, which made it possible to measure several DP components with a good signal-to-noise ratio, in order to compare their group delays. We have shown that the group delays of the distortion products $2f_1-f_2$, $3f_1-2f_2$, $4f_1-3f_2$, and $2f_2-f_1$ can be successfully recorded in the guinea pig, with both the f_1- and the f_2-sweep paradigm. Comparing the group delays of the two sweep paradigms, and in addition of the four different DP components in one study, can add to the discussion about the generation sites of the DPOAEs and the difference between the sweep paradigms. Note that in this study one pair of stimulus levels was used ($L_1, L_2=65,55$ dB SPL) due to limited measuring time in each session. General validity of the given interpretation of the data is not proved here.

A. Comparison of the two sweep paradigms for the lower sideband DPOAEs

The fact that the f_2-sweep paradigm gives larger group delays than the f_1-sweep paradigm for the lower sideband

DPOAEs is in agreement with other studies. O'Mahoney and Kemp (1995) reported f_1-sweep group delays that were on average 21.5% smaller than the f_2-sweep group delays for the $2f_1-f_2$ DPOAE in humans (with $L_1,L_2=70,60$ dB SPL). This corresponds with a D_2/D_1 of 1.27, which is in the range of the values we found for the guinea pig (Fig. 6A). Whitehead *et al.* (1996) reported an average D_2/D_1 of 1.6 in humans (with $L_1=L_2=75$ dB SPL). In the same study, the ratio of the f_1- and f_2-sweep group delays of the $2f_1-f_2$ DPOAE in rabbits appeared to depend on the stimulus levels. At high levels (75 dB SPL) D_2/D_1 was close to one. Bowman *et al.* (1997) reported group delay values for f_1- and f_2-sweep measurements of the $2f_1-f_2$ DPOAE in humans, which correspond to values for D_2/D_1 between 1.30 and 1.93. They reported a dependence of D_2-D_1 on stimulus level. This has led them to conclude that the f_2-sweep delay consists of a larger part of the filter build-up time, which is level dependent, than the f_1-sweep delay. The ratio D_2/D_1 based on the fits of the group delays that Moulin and Kemp (1996a,b) found for the $2f_1-f_2$ DPOAE in humans, ranges from 1.28 to 1.62, for f_2 from 1 to 6 kHz, which is close to our values for the guinea pig. For the next lower sideband DPOAE $3f_1-2f_2$, Moulin and Kemp (1996b) reported fits that correspond to D_2/D_1 of 1.23 to 1.37, for f_2 from 1 to 6 kHz. Results for the $4f_1-3f_2$ group delays have not been reported so far. We conclude that the ratios of f_1- versus f_2-sweep group delays we have found for the lower sideband DPOAEs in the guinea pig are in the same range as those found in other species. Additionally, our data show that the ratio D_2/D_1 decreases with increasing order of the lower sideband distortion product.

B. Comparison of the two sweep paradigms for the upper sideband DPOAE $2f_2-f_1$

With respect to group delay differences between the f_1- and the f_2-sweep paradigm, the upper sideband DPOAE with frequency $2f_2-f_1$ does not behave like the lower sideband DPOAEs. We found no significant difference between D_1 and D_2 for frequencies in the range 1.8–5.4 kHz. For $f_2<1.8$ kHz, the f_1-sweep group delays were larger than the f_2-sweep group delays, and for $f_2>5.4$ kHz the group delays obtained with an f_2-sweep were larger. Other studies report similar results. Whitehead *et al.* (1996) found ''little difference'' between f_1- and f_2-sweep group delays for the $2f_2-f_1$ DPOAE in humans and in rabbits. Moulin and Kemp (1996a,b) saw no significant difference between f_1- and f_2-sweep group delays for the $2f_2-f_1$ DPOAE in humans, except at 4 kHz, where the f_2-sweep group delay was larger. So, the results of our study in the guinea pig are similar to those reported for humans and rabbits, regarding the dependence of the group delays of the upper sideband DPOAE $2f_2-f_1$ on sweep paradigm.

The fact that the group delays of the upper sideband DPOAE do not depend on which primary is swept, at least in the mid-frequency range, while the group delays of the lower sidebands do, indicates that there is no common generation site for upper and lower sideband DPOAEs. The same conclusion can be drawn from the results of suppression experiments (Martin *et al.*, 1987, 1998). In addition, onset latencies and amplitude correlation functions also strongly suggest that the $2f_2-f_1$ DPOAE is generated basal to the primary frequency region on the basilar membrane (Martin *et al.*, 1998).

C. Group delay differences between DPOAEs

The group delay differences between the four DP components appear to depend on the sweep paradigm that is used. The f_1-sweep method gives the same group delay values for all DP components. In contrast, the group delays that were measured with f_2-sweeps show a small but significant difference between $2f_1-f_2$ and $4f_1-3f_2$, and in particular a large disparity between the two cubic distortion products $2f_1-f_2$ and $2f_2-f_1$. The latter upper sideband DPOAE has 12% (at 11 kHz) to 46% (at 1.5 kHz) smaller group delays than the lower sideband DPOAE $2f_1-f_2$. Several other studies showed the same effect of the $2f_2-f_1$ group delays being smaller than the $2f_1-f_2$ group delays, when measured with the f_2-sweep, in humans (Wable *et al.*, 1996; Moulin and Kemp, 1996b; Whitehead *et al.*, 1996). Moulin and Kemp (1996b) reported values corresponding with an average percentage of 27%, which is in the same range as our values. In addition, Whitehead *et al.* (1996) and Martin *et al.* (1998) reported onset latencies that were shorter for $2f_2-f_1$ than for $2f_1-f_2$ in rabbits and humans. In gerbils, $2f_2-f_1$ group delays were shorter than $2f_1-f_2$ group delays when measured with the f_1-sweep paradigm at an f_2 of 4 kHz and stimulus levels of 50 dB and higher (Brown and Kemp, 1985). This is in contrast with our f_1-sweep data for the guinea pig. We conclude that our findings for the two cubic distortion products are qualitatively similar to those reported in man and rabbit.

D. Place- and wave-fixed DPOAE generation models

So far, two hypotheses have been proposed in literature that link the changing frequency of the primaries with the presumed DPOAE generation site: the place-fixed and the wave-fixed model (Kemp, 1986; O'Mahoney and Kemp, 1995; Moulin and Kemp, 1996b). Both models assume a common generation site for all distortion products. This site is fixed to a place near x_2 at the cochlear partition in the place-fixed model, for small changes in the primary frequencies. In the wave-fixed model, the generation site is assumed to be fixed to the f_2 traveling wave, the amplitude and phase profile of which are invariant apart from a translation along the basilar membrane. Considering the f_1-sweep, both the place- and wave-fixed model represent the same situation, where the DPOAE generation site x_2 is place fixed even for the wave-fixed model since the f_2 frequency is constant. In this case, the group delay will only depend on the change in the phase of the changing f_1 primary, at the fixed generation site. For the f_2-sweep paradigm, the place- and wave-fixed models describe two different situations. In the place-fixed model, the group delay will depend on the phase change of the changing f_2 primary at the fixed generation site. In the wave-fixed model, the place of generation x_2 will move along with the changing f_2 in case of an f_2-sweep, and the group delay only depends on the phase change of the fixed f_1

primary at the generation place, due to the movement of x_2. The phase of f_2 will have no influence, since it is constant at its own characteristic frequency place (Kemp, 1986).

Both the place- and the wave-fixed model predict the group delays of the lower sideband DPOAEs measured with the f_2-sweep paradigm to be longer than the f_1-sweep group delays (Moulin and Kemp, 1996b). So here our data are in accordance with both the place- and the wave-fixed hypothesis. When the comparison of the group delays of the different lower sideband DPOAEs is considered, we can distinguish between place- and wave-fixed. The place-fixed model predicts the group delays of all lower sideband DPOAEs to be equal, with either sweep paradigm. The wave-fixed model, on the other hand, predicts a difference between group delays of the lower sideband DPOAEs, depending on the order of distortion product, only for the f_2-sweep paradigm: the higher the order of the distortion product, the smaller the f_2-sweep group delay would be (Moulin and Kemp, 1996b). Our data agree with this concept, since the group delay measured with f_2-sweep decreases with increasing DPOAE order, although the effect was only small. The only significant difference is between the $2f_1-f_2$ and $4f_1-3f_2$ group delays. We conclude that our lower sideband group delay data are in favor of the wave-fixed model.

Our results for the upper sideband DPOAE $2f_2-f_1$, as well as those of Moulin and Kemp (1996b), disagree with the place-fixed model. When x_2 is the assumed generation site, the place-fixed model predicts a difference in $2f_2-f_1$ group delay between the two sweep paradigms, for all frequencies. This is not observed in the present data, which show no significant difference between the two sweep paradigms for the $2f_2-f_1$ group delay, in the frequency range 1.8–5.4 kHz. Again, this suggests that the hypothesis that the $2f_2-f_1$ has the same generation place as the lower sideband DPOAEs is not valid, as also suggested by, e.g., Moulin and Kemp (1996b).

E. Contribution from the x_{DP} place to the generation of the $2f_1-f_2$ DPOAE

Several studies have suggested a second place contributing to the cubic distortion product $2f_1-f_2$ measured in the ear canal, namely its characteristic frequency place x_{DP} which is located apically from the primary frequency region (Gaskill and Brown, 1996; Brown *et al.*, 1996; Heitmann *et al.*, 1998). In a study by Stover *et al.* (1996), indications were found for the existence of multiple DPOAE generators. Brown *et al.* (1996) have shown that the cubic distortion product measured in the human ear canal can be described as a vector summation of two components originating from x_2 and x_{DP}. They suggest that the component from x_{DP} gives rise to the fine structure observed in the DPOAE amplitude. Heitmann *et al.* (1998) found additional proof for this view in the results of suppression experiments, which showed a decrease in the fine structure when the suppressor tone had a frequency close to $2f_1-f_2$. However, the amplitude versus frequency characteristics of guinea pig DPOAEs do not show fine structure (Brown and Gaskill, 1990). This could indicate that the contribution of the x_{DP} place to the generation of the lower sideband DPOAEs is relatively small in the guinea pig. As a result, we can conclude that the assumption made in the place- and wave-fixed model, of a place (close to) x_2 being the only contributor to the generation of the lower sideband DPOAEs, is probably closer to the truth in guinea pig than in human.

IV. CONCLUSIONS

For the lower sideband DPOAEs measured in the guinea pig, the f_2-sweep gave larger group delays than the f_1-sweep paradigm. The ratio between f_2-sweep and f_1-sweep group delay D_2/D_1 decreases with increasing order of the lower sideband DPOAE. In contrast with the lower sideband DPOAEs, the upper sideband DPOAE $2f_2-f_1$ showed no difference in group delay measured with f_1- or f_2-sweep between 1.8 and 5.4 kHz. This indicates that, at least below 5.4 kHz, there is no common generation site for upper and lower sideband DPOAEs.

The f_1-sweep method gives the same group delay values for all DPOAE components with our stimulus conditions. Group delays measured with the f_2-sweep method, however, show a small but significant difference between the $2f_1-f_2$ and the $4f_1-3f_2$ DPOAE, and a large difference between the $2f_1-f_2$ and $2f_2-f_1$, with the group delays of the latter being the smallest. Most aspects of these results are better described by the wave-fixed than by the place-fixed model for DPOAE generation.

ACKNOWLEDGMENTS

This work, which was part of a collaboration program with the University of Groningen, was supported by the Netherlands Organization for Scientific Research (NWO) and the Heinsius Houbolt Fund.

Bowman, D. M., Brown, D. K., Eggermont, J. J., and Kimberley, B. P. (**1997**). ''The effect of sound intensity on f_1-sweep and f_2-sweep distortion product otoacoustic emissions phase delay estimates in human adults,'' J. Acoust. Soc. Am. **101**, 1550–1559.

Bowman, D. M., Eggermont, J. J., Brown, D. K., and Kimberley, B. P. (**1998**). ''Estimating cochlear filter response properties from distortion product otoacoustic emission (DPOAE) phase delay measurements in normal hearing adults,'' Hearing Res. **119**, 14–26.

Brown, A. M. (**1987**). ''Acoustic distortion from rodent ears: A comparison of responses from rats, guinea pigs and gerbils,'' Hearing Res. **31**, 25–38.

Brown, A. M., and Gaskill, S. A. (**1990**). ''Measurement of acoustic distortion reveals underlying similarities between human and rodent mechanical responses,'' J. Acoust. Soc. Am. **88**, 840–849.

Brown, A. M., and Kemp, D. T. (**1984**). ''Suppressibility of the $2f_1-f_2$ stimulated acoustic emissions in gerbil and man,'' Hearing Res. **13**, 29–37.

Brown, A. M., and Kemp, D. T. (**1985**). ''Intermodulation distortion in the cochlea: Could basal vibration be the major cause of round window CM distortion?,'' Hearing Res. **19**, 191–198.

Brown, A. M., Harris, F. P., and Beveridge, H. A. (**1996**). ''Two sources of acoustic distortion products from the human cochlea,'' J. Acoust. Soc. Am. **100**, 3260–3267.

Draper, N. R., and Smith, H. (**1981**). *Applied Regression Analysis*, 2nd ed. (Wiley, New York).

Gaskill, S. A., and Brown, A. M. (**1996**). ''Suppression of human acoustic distortion product: Dual origin of $2f_1-f_2$,'' J. Acoust. Soc. Am. **100**, 3268–3274.

Heitmann, J., Waldmann, B., Schnitzler, H.-U., Plinkert, P. K., and Zenner, H.-P. (**1998**). ''Suppression of distortion product otoacoustic emissions (DPOAE) near $2f_1-f_2$ removes DP-gram fine structure—Evidence for a secondary generator,'' J. Acoust. Soc. Am. **103**, 1527–1531.

Kemp, D. T. (**1979**). ''Evidence of mechanical nonlinearity and frequency selective wave amplification in the cochlea,'' Arch. Otorhinolaryngol. **224**, 37–45.
Kemp, D. T. (**1986**). ''Otoacoustic emissions, travelling waves and cochlear mechanisms,'' Hearing Res. **22**, 95–104.
Kim, D. O. (**1980**). ''Cochlear mechanics: Implications of electrophysiological and acoustical observations,'' Hearing Res. **2**, 297–317.
Kim, D. O., Molnar, C. E., and Matthews, J. W. (**1980**). ''Cochlear mechanics: Nonlinear behavior in two-tone responses as reflected in cochlear-nerve-fiber responses and in ear-canal sound pressure,'' J. Acoust. Soc. Am. **67**, 1704–1721.
Kimberley, B. P., Brown, D. K., and Eggermont, J. J. (**1993**). ''Measuring human cochlear traveling wave delay using distortion product otoacoustic emission phase responses,'' J. Acoust. Soc. Am. **94**, 1343–1350.
Kummer, P., Janssen, T., and Arnold, W. (**1995**). ''Suppression tuning characteristics of the $2f_1-f_2$ distortion product otoacoustic emission in humans,'' J. Acoust. Soc. Am. **98**, 197–210.
Martin, G. K., Jassir, D., Stagner, B. B., Whitehead, M. L., and Lonsbury-Martin, B. L. (**1998**). ''Locus of generation for the $2f_1-f_2$ vs $2f_2-f_1$ distortion-product otoacoustic emissions in normal-hearing humans revealed by suppression tuning, onset latencies, and amplitude correlations,'' J. Acoust. Soc. Am. **103**, 1957–1971.
Martin, G. K., Lonsbury-Martin, B. L., Probst, R., Scheinin, S. A., and Coats, A. C. (**1987**). ''Acoustic distortion products in rabbit ear canal. II. Sites of origin revealed by suppression contours and pure-tone exposures,'' Hearing Res. **28**, 191–208.
Moulin, A., and Kemp, D. T. (**1996a**). ''Multicomponent acoustic distortion product otoacoustic emission phase in humans. I. General characteristics,'' J. Acoust. Soc. Am. **100**, 1617–1639.
Moulin, A., and Kemp, D. T. (**1996b**). ''Multicomponent acoustic distortion product otoacoustic emission phase in humans. II. Implications for distortion product otoacoustic emissions generation,'' J. Acoust. Soc. Am. **100**, 1640–1662.
O'Mahoney, C. F., and Kemp, D. T. (**1995**). ''Distortion product otoacoustic emission delay measurement in human ears,'' J. Acoust. Soc. Am. **97**, 3721–3735.
Probst, R., Lonsbury-Martin, B. L., and Martin, G. K. (**1991**). ''A review of otoacoustic emissions,'' J. Acoust. Soc. Am. **89**, 2027–2067.
Robles, L., Ruggero, M. A., and Rich, N. C. (**1991**). ''Two-tone distortion in the basilar membrane of the cochlea,'' Nature (London) **349**, 413–414.
Siegel, J. H., Kim, D. O., and Molnar, C. E. (**1982**). ''Effects of altering organ of Corti on cochlear distortion products f_2-f_1 and $2f_1-f_2$,'' J. Neurophysiol. **47**, 303–328.
Smoorenburg, G. F., Morton Gibson, M., Kitzes, L. M., Rose, J. E., and Hind, J. E. (**1976**). ''Correlates of combination tones observed in the response of neurons in the anteroventral cochlear nucleus of the cat,'' J. Acoust. Soc. Am. **59**, 945–962.
Stover, L. J., Neely, S. T., and Gorga, M. P. (**1996**). ''Latency and multiple sources of distortion product otoacoustic emissions,'' J. Acoust. Soc. Am. **99**, 1016–1024.
Wable, J., Collet, L., and Chéry-Croze, S. (**1996**). ''Phase delay measurements of distortion product otoacoustic emissions at $2f_1-f_2$ and $2f_2-f_1$ in human ears,'' J. Acoust. Soc. Am. **100**, 2228–2235.
Whitehead, M. L., Stagner, B. B., Martin, G. K., and Lonsbury-Martin, B. L. (**1996**). ''Visualization of the onset of distortion-product otoacoustic emissions, and measurement of their latency,'' J. Acoust. Soc. Am. **100**, 1663–1679.

Response magnitude and timing of auditory response initiation in the inferior colliculus of the awake chinchilla

Dennis P. Phillips[a)]
Department of Psychology, Dalhousie University, Halifax, Nova Scotia B3H 4J1, Canada

Robert Burkard
Center for Hearing and Deafness, State University of New York at Buffalo, 215 Parker Hall, Buffalo, New York 14214

(Received 15 June 1998; revised 1 February 1999; accepted 8 February 1999)

Recent single-unit studies in anesthetized cats have revealed that the latency and strength of transient responses to tone burst stimuli are determined largely by stimulus events in the first few ms of the signal. The present study sought to extend these findings by studying the inferior colliculus potential (ICP) in unanesthetized chinchillas. The ICP magnitude and latency were studied as a function of the plateau amplitude and rise time of noise burst stimuli. ICP amplitude increased with stimulus amplitude and decreased with stimulus rise time. ICP latency decreased with stimulus amplitude and increased with stimulus rise time. The absolute values of the ICP latencies confirmed that it is only the first few ms of the stimulus which determine the timing of response initiation, and therefore, that it is not the plateau level of the stimulus that directly determines the latent period. These data constitute a direct link between earlier single-unit studies in anesthetized animals and brainstem-evoked potential data in animals and man. © *1999 Acoustical Society of America.* [S0001-4966(99)03705-4]

PACS numbers: 43.64.Qh, 43.64.Ri [RDF]

INTRODUCTION

There has been considerable recent interest in the timing and magnitude of central auditory responses evoked by aperiodic stimuli (e.g., Heil, 1997a, b; Heil and Irvine, 1996; Phillips, 1988, 1998; Phillips and Hall, 1990; Phillips *et al.*, 1995). Part of this interest stems from curiosity about the temporal precision with which a sound's time structure is represented in the central auditory system (e.g., Phillips and Hall, 1990). More recently, there has been some question as to precisely what feature of a tone- or noise burst stimulus is encoded by the response timing. It has long been assumed that the electrophysiological response latency reflects the time after the acoustic stimulus onset that the signal amplitude exceeds the threshold for spike generation (e.g., Kitzes *et al.*, 1978; Phillips, 1988; Suga, 1971). Despite this, it has been convention to display the effect of stimulus amplitude on response latency by plotting the latter as a function of the *plateau* level of the stimulus. Heil and Irvine (1996,1997; Heil, 1997a,b) recently provided evidence that the timing of response initiation in central neurons was probably driven by the rate of change of peak stimulus pressure (for linear rise-time signals) or maximum acceleration of pressure (for cosine-squared rise function signals), rather than by the plateau level of the signal, and that this relationship arises in the cochlea.

Almost all of the recent evidence on these issues has come from single-neuron recording studies in anesthetized animals (e.g., Heil and Irvine, 1996, 1997; Heil, 1997a,b; Phillips, 1988, 1998). This raises two further issues. One is the extent to which the responses described in those studies are representative of those that would be seen in an unanesthetized animal. The second is the extent to which the single-neuron observations are reflected in gross evoked responses, because there are well-documented effects of rise time on the human scalp-recorded auditory brainstem response (e.g., Suzuki and Horiuchi, 1981; Hecox and Deegan, 1983; Barth and Burkard, 1993). The purpose of the present study was to examine the magnitude and latency of the evoked potential recorded directly from electrodes in the inferior colliculi (IC) of unanesthetized chinchillas. Our specific goal was to describe the effects of noise burst rise time and amplitude on response amplitude and latency. This was because the pattern of data seen in the factorial combination of these stimulus parameters provides the opportunity to tease out whether it is peak stimulus level, or some dynamic property of sound onset, that determines the response. Noise bursts were used to eliminate the confounding factor of bandwidth changes with manipulations of the stimulus envelope when using tonal carriers (Burkard, 1991; Barth and Burkard, 1993). Our data provide a direct link between earlier studies of single neurons in anesthetized animals and brainstem-evoked response studies in animals and man.

I. METHODS

Six adult chinchillas (three male, three female) ranging in weight from 537 to 666 gm were anesthetized with ketamine (60 mg/kg) and acepromazine (0.6 mg/kg) for surgical implantation of tungsten electrodes. The skin over the posterior cranium was cut and the electrode was stereotaxically placed into the left inferior colliculus (IC). A reference electrode was placed subdurally at a site roughly 1 cm anterior to

[a)]Author to whom all correspondence should be addressed. Electronic mail: ears@is.dal.ca

the IC electrode. During advancement of the IC electrode, the right ear was acoustically stimulated with a tone burst and the inferior colliculus potential (ICP) was monitored until a large-amplitude response was observed.

Experimental data collection occurred several weeks following surgery. Each unanesthetized chinchilla was placed in a custom-designed animal restraint (Snyder and Salvi, 1994) in a single-walled sound-isolating chamber. Electrical activity from the IC (active) was referenced to the frontal electrode and was amplified (5000 to 10 000 gain) and filtered (100–3000 Hz) by a Stanford Research Systems model SR560 bioamplifier. This activity was digitized at a 5000-Hz sampling frequency for a time window of 51.2 ms by the 16-bit analog-to-digital converter of a TMS320C25 board housed in a Pentium-based microcomputer. Each evoked response was the sum of 200 artifact-free sweeps. Stimuli were generated by the digital-to-analog converter of a TMS320C25 board at a sampling rate of 25 kHz, routed through a custom-built programmable attenuator to an Etymotic ER2 earphone and presented to the right ear. The output of the earphone was calibrated in a 0.5-cc volume and monitored with an Etymotic ER-7C probe microphone that was threaded through the insert foam plug used to couple the earphone to the chinchilla's ear. All sound-pressure level (SPL) values refer to the rms SPL (dB *re* 20 μPa) of the noise burst plateau.

Stimuli were noise bursts with a constant 2-ms plateau time. For all conditions, noise burst rise time and fall time were equal, and each was shaped with a raised cosine function. That is, the slope of the function was 0 at 0 deg and gradually increased to 1 at 90 deg and then decreased to 0 at 180 deg. Noise burst rise times and fall times included 0 (fast), 1, 2, 4, 8, 16, and 32 ms. There was 100 ms off-time between the offset of one noise burst and the onset of the next noise burst. Hence, the interstimulus interval was 102, 104, 106, 110, 118, 134, and 166 ms for rise times of 0, 1, 2, 4, 8, 16, and 32 ms rise times, respectively. Noise bursts were presented at levels ranging from 0 to 78 dB SPL in 6-dB steps. The order of rise time condition was randomized. For all rise times, data were collected in order of ascending noise burst amplitude.

The dependent variables were the latency of the initial positive peak of the ICP response with respect to stimulus onset, and the peak to following trough amplitude. The Etymotic ER2 earphone introduced an acoustic delay of 0.9 ms. The data shown herein are corrected for this delay.

II. RESULTS

A. ICP responses

Figure 1 plots a rise-time intensity series from one chinchilla for the 0-ms rise time noise burst (left panel) and the 32-ms rise time noise burst (right panel). Response latency was the interval between noise burst onset and the initial positive peak of the ICP. ICP amplitude of each response was from this positive peak to the following negative trough. For what follows, note that the latencies are longer, and the threshold stimulus level was higher, for the long rise time stimuli.

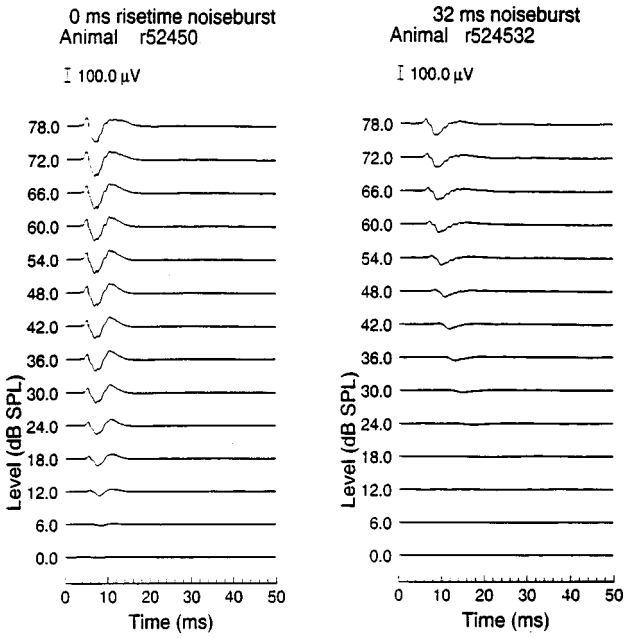

FIG. 1. ICP level series from one chinchilla for two noise burst rise times are shown. On the right are responses to noise bursts with a 0-ms rise time, while on the left are responses to noise bursts with a 32-ms rise time.

B. ICP threshold across rise time

The lowest level at which an ICP was observed at each noise burst rise time is shown in Fig. 2. There is little or no effect of rise time on mean ICP threshold until rise time is increased to 8 ms and larger. Threshold is 5–7 dB SPL for noise burst rise times of 4 ms and less, increasing to 10, 14, and 21 dB SPL for rise times of 8, 16, and 32 ms, respectively.

C. ICP amplitude

Mean ICP amplitude is plotted across noise burst level in Fig. 3. The parameter is noise burst rise time. Data points are only shown if at least three of six animals showed a response for a given rise time and level condition. There are

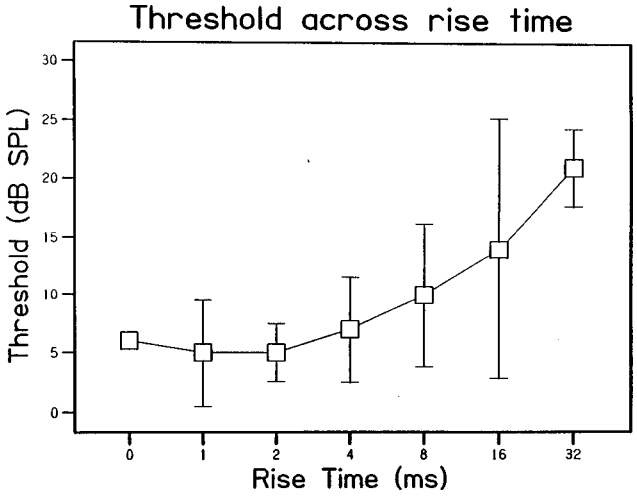

FIG. 2. Mean ICP threshold is plotted against noise burst rise time. Each value is the mean threshold for six chinchillas, and the vertical bars represent one standard deviation.

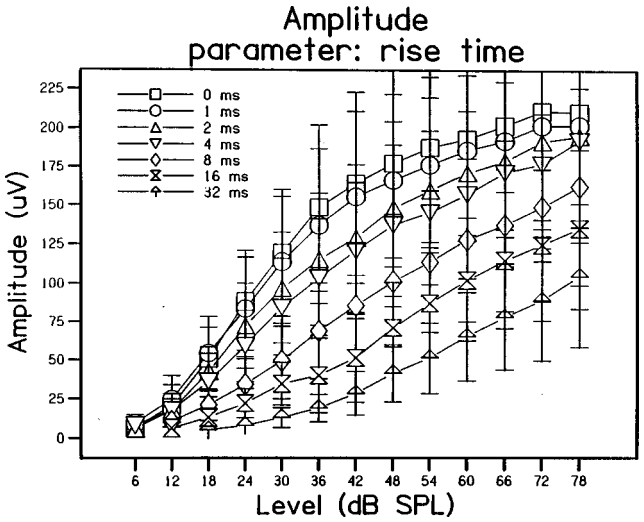

FIG. 3. Mean ICP amplitude is plotted across noise burst level. The parameter is noise burst rise time. Each data point is the mean value of no less than three values.

increases in mean ICP amplitude with increasing noise burst level. For shorter rise times (0, 1, and 2 ms), mean amplitude saturates for noise burst levels above 72 dB SPL, while at longer rise times there is a monotonic increase in amplitude with increasing noise burst rise time. For a given noise burst level, there is a decrease in mean ICP amplitude with increasing noise burst rise time.

D. ICP latency

Figure 4 plots mean ICP latency across noise burst level. The parameter is noise burst rise time. These latency values have been corrected for the 0.9-ms acoustic delay produced by the ER2 earphone. Mean ICP latency decreases with increasing noise burst level. Also, for a given noise burst level, there is an increase in ICP latency with increasing noise burst rise time.

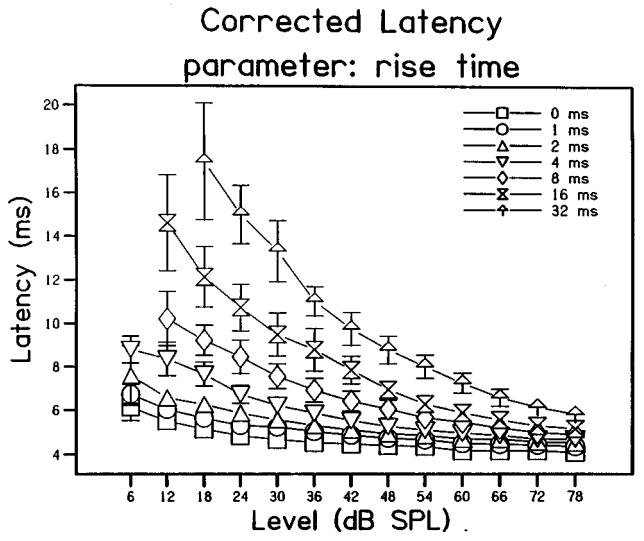

FIG. 4. Mean ICP latency is plotted across noise burst level. The parameter is noise burst rise time. Each data point is the mean value of no less than three values.

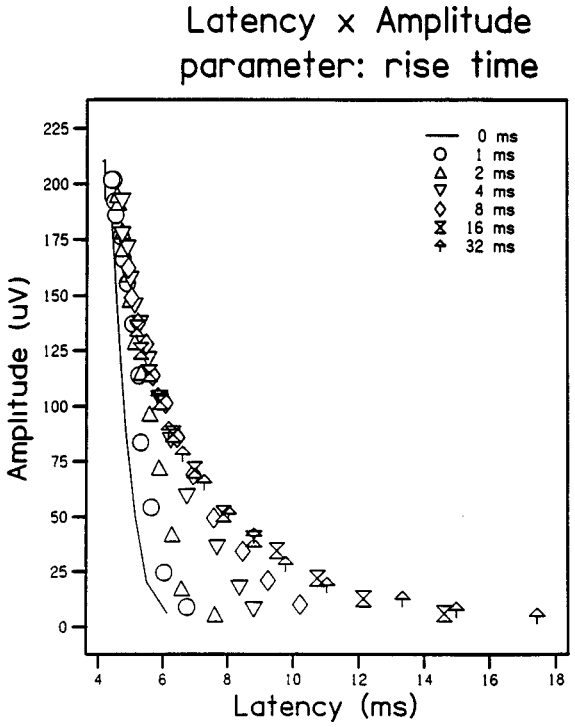

FIG. 5. Mean ICP amplitude is plotted across ICP latency. The solid line shows data from the 0-ms rise time noise burst level series, showing the decrease in ICP latency and the increase in ICP amplitude with increasing noise burst level. The individual data points represent latency-amplitude values for noise bursts with longer rise times.

E. Are ICP changes with increasing rise time equivalent to changes with decreasing level?

Increasing noise burst rise time and decreasing noise burst level both produce increased response latency and decreased response amplitude. This raises the question of whether the effects of the two stimulus variables are equivalent. If this were so, then increasing rise time would produce changes in the latency-amplitude response space that paralleled the changes in this space to a reduction in noise burst level. Figure 5 plots mean ICP amplitude across mean ICP latency. The solid line shows data for the 0-ms noise burst rise time, with the upper left-hand portion of the function depicting the short-latency, large-amplitude responses produced by high-level noise bursts, and the lower-right portion of the function showing the long-latency, low-amplitude responses produced by low-level stimuli. The individual data points show mean ICP amplitude-latency data points for nonzero rise time data for various stimulus levels. Different rise times are represented by unique symbols. If increasing noise burst rise time were equivalent to decreasing stimulus level, then we would expect all data points to fall on the solid line, or to be randomly scattered on both sides of the line. There is a clear bias in these data, i.e., all data points fall above/to-the-right of the line, indicating that compared to changes in noise burst level, there are greater changes in response latency than response amplitude with manipulations of noise burst rise time.

F. Quantitative changes in response latency

Figure 6 presents the raw latency data obtained from each of the six animals, with ID numbers indicated. ICP

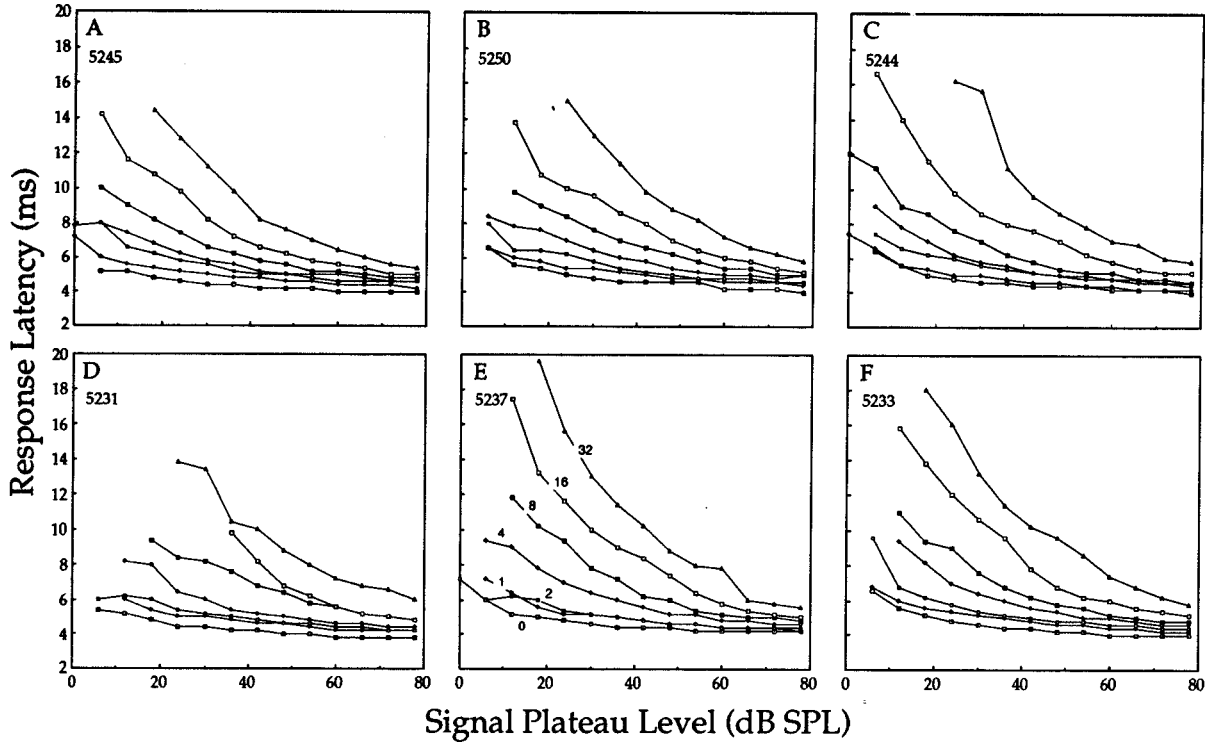

FIG. 6. Latency-vs-intensity functions, plotted separately for each animal used in the study (A–F). Animal ID number is indicated. In each panel, noise burst rise time is the parameter. Key in E applies to A–F. Description in text.

latency has been plotted as a function of the plateau level of the stimulus. The parameter in each case is the rise time (in ms) of the stimulus, as indicated in panel E.

In each animal, mean response latency declined as a function of stimulus amplitude, and did so for stimuli of all rise times. The rates of change of the slopes of these functions were, however, greater for stimuli with long rise times than for stimuli with short ones. This had the consequence that the curves tended to converge at high SPLs. Note that at these high SPLs, latencies were typically under 7.0 ms even when the stimulus had a rise time of 32 ms. Given the additional factor of a minimum neural transmission time from the cochlea (see below), this means that the stimulus event(s) responsible for the timing of response initiation were necessarily restricted to those in the very earliest few ms of the stimulus.

Following Burkard (1991) and Heil and Irvine (1996), the data in Fig. 6 have been replotted in Fig. 7, with latency expressed as a function of rise time, and thus with SPL as the parameter. In each animal, it is apparent that latency increases with stimulus rise time, and that this effect is greater for signals of low amplitude than for intense signals. That is, the slope of the latency-vs-rise time function is steeper for low amplitude sounds.

III. DISCUSSION

The present study confirmed that both response magnitude and response latency are sensitive functions of the amplitude and rise time of a noise burst stimulus. It did so in the auditory midbrain of unanesthetized chinchillas, and thus extends the earlier single-unit work conducted in anesthetized cats. Further, the response we studied was a gross-evoked potential rather than single units; our data thus constitute a bridge between the single unit and the scalp-recorded evoked potential studies (see below). Before proceeding with these comparisons, we must briefly address the effects that our stimulus paradigm might have had on the data. The main concern is that stimulus duration (and therefore total stimulus energy) covaried with rise time, raising the question of precisely which parameter or parameters were driving the responses. Recall that among the main findings was that increases in rise time caused increases in noise burst response threshold (Fig. 2), and reductions in response amplitude (Fig. 3) and lengthenings of response latency (Fig. 4) for noise bursts of any specified plateau SPL. These effects are in the direction opposite that expected were it to have been total stimulus energy driving the responses. It is also the case that a constant stimulus off-time was used, so that there was an inverse relation between interstimulus interval and rise time. Again, the effects observed were then in the direction opposite those expected if the shorter interstimulus intervals were responsible for the effects (e.g., through adaptation). That is, the stimulus conditions with the shortest interstimulus intervals were the ones associated with the strongest and shortest-latency responses.

The present data complement those presented by Burkard *et al.* (1997) for ICP responses to click stimuli. With increasing noise burst level, there is an increase in ICP amplitude. For stimuli with short rise times, the mean amplitude saturates above 72 dB SPL, while for the longer rise times (4 ms and above), there was no evidence of saturation up to 78 dB SPL, the highest noise burst level used herein. For stimuli with these longer rise times, ICP threshold is elevated (see Fig. 2). We would need to have obtained responses to higher

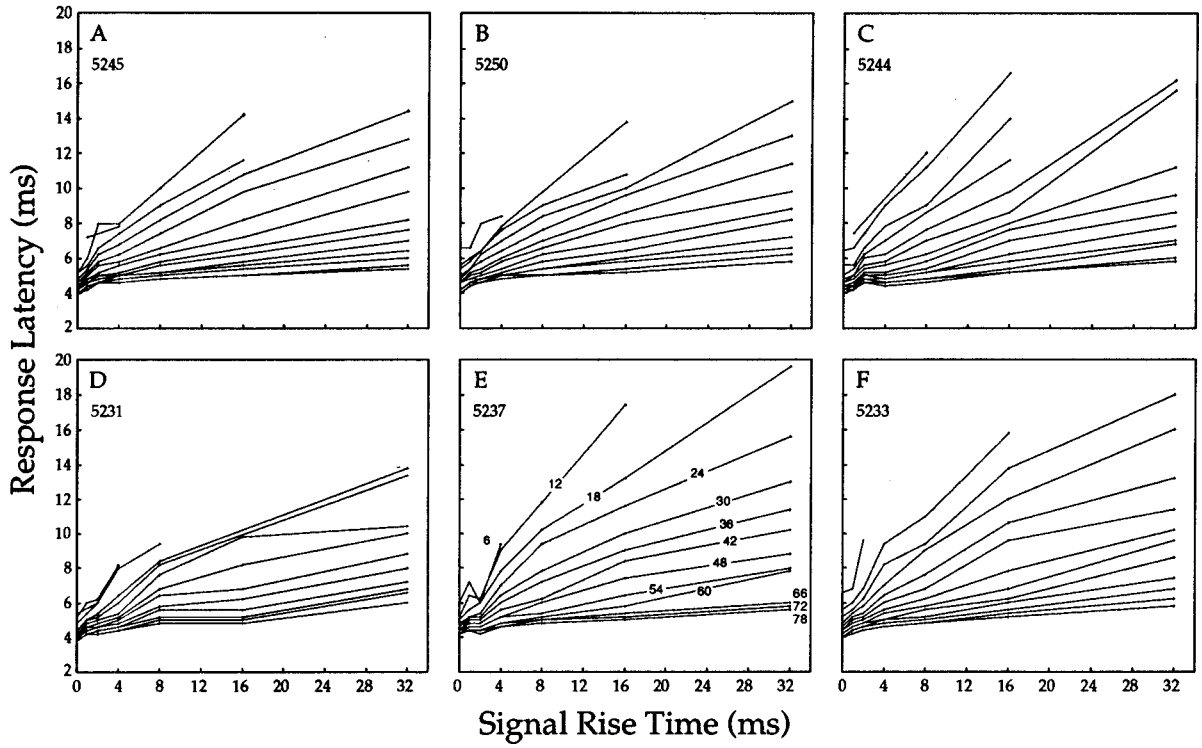

FIG. 7. Same data as in Fig. 6, but with latency plotted as a function of noise burst rise time, with SPL as the parameter. Other details as for Fig. 5.

noise burst levels in order to determine whether there is a greater dynamic range for ICP amplitude for longer noise burst rise times. All that can be definitively stated on the basis of the present data is that there is no decrease in the ICP amplitude dynamic range with increasing noise burst rise time. There are no published data on ICP response amplitude to changes in noise burst rise time or level. ICP amplitude does increase in amplitude with increasing click level, saturating for click levels above 70 dB pSPL (Burkard *et al.*, 1997). We observed this amplitude saturation for the short-rise time data in the present study, but these data are not directly comparable, as the click thresholds in Burkard *et al.* (1997) were roughly 30 dB pSPL, as compared to the 5–7-dB SPL noise burst thresholds reported herein. Differences in stimuli and calibration procedures likely contribute to these threshold differences. Nonetheless, the ICP amplitude appears to have a smaller dynamic range for clicks than for noise bursts.

The present data are consistent with previous single-cell recording studies of central neurons. First, the present finding that ICP threshold increases with stimulus rise time (Fig. 2) is in agreement with descriptions of cortical neurons (Heil, 1997b; Phillips, 1988; Phillips *et al.*, 1995), cells in the bat's inferior colliculus (Suga, 1971), and some cells in the frog's dorsal medullary nucleus (Hall and Feng, 1991). The single-unit data, at least for neurons with a monotonic rate response, reveal that long rise-time tones evoke responses whose rate-response functions are sometimes shallower than those for short rise-time tones (Heil, 1997b), as was also seen in the present data (Fig. 3). Interestingly, both of these effects seem to be stronger in central neurons and in the present ICP data than in data presented for cat cochlear-nerve fibers (cf. Heil and Irvine, 1997). There are at least two potential reasons for this. One lies in the fact that cochlear neurons have sustained discharges; the contribution of the transient response to the total spike count generated by a long tone is relatively less than that seen in central neurons, whose responses are often dominated by onset transients. A second possibility is that specifically central mechanisms underlie these effects, i.e., that the threshold shifts and shallower rate-intensity slopes reflect some afferent convergence that is not available to cochlear neurons.

Second, there are also strong similarities between the latency behavior of the ICP and that of single central neurons. First, single neurons have latency-intensity functions whose negative slopes decline with increases in SPL (e.g., Aitkin *et al.*, 1970; Brugge *et al.*, 1969; Kitzes *et al.*, 1978; Heil, 1997a; Phillips, 1998; Phillips and Hall, 1990; Phillips *et al.*, 1995). In central neurons, mean response latencies for tones of any given SPL are longer for long rise-time stimuli, but latencies decline more quickly with increases in SPL, so that the latency functions for tones of different rise times tend to converge somewhat at high SPLs (Heil and Irvine, 1996; Phillips *et al.*, 1995). The same properties were seen in the ICP latency behavior in the present study (Figs. 4 and 6). These similarities in the effects of stimulus SPL and rise time on single-unit and ICP response strengths and latencies strongly suggest that the unit and ICP responses are shaped by the same mechanisms. Note, however, that while the effects of rise time on the *timing* of responses might be determined in large part by peripheral mechanisms (after Heil and Irvine, 1997), the effects of rise time on response *strength* may also be influenced by central processes (see above).

Several studies have investigated the effects of noise burst rise time and level on the brainstem auditory-evoked response (BAER) in both humans (Hecox *et al.*, 1976; He-

cox and Deegan, 1983; Barth and Burkard, 1993; Folsom and Aurich, 1987) and gerbils (Burkard, 1991). With increasing noise burst level, there is the expected decrease in BAER peak latencies and an increase in peak amplitudes (Barth and Burkard, 1993; Folsom and Aurich, 1987; Burkard, 1991). With increasing noise burst rise time, there are increases in BAER peak latencies (Hecox *et al.*, 1976; Hecox and Deegan, 1983; Barth and Burkard, 1993; Folsom and Aurich, 1987; Burkard, 1991). The effects on noise burst rise time on BAER peak amplitudes varies across study. For the various waves of the gerbil BAER, response amplitude decreases with increasing noise burst rise time (Burkard, 1991). For human BAER wave V, several studies report little effect of rise time on wave V amplitude (Hecox *et al.*, 1976; Hecox and Deegan, 1983), while other studies report the expected decrease in amplitude with increasing noise burst rise time (Folsom and Aurich, 1987; Barth and Burkard, 1993). The analyses shown in Fig. 5 demonstrate that the effects of increasing rise time on ICP latency and amplitude are not quantitatively equivalent to a simple reduction in noise burst level. Specifically, the latency shift is greater than the amplitude change when the reference is the 0-ms rise time noise burst ICP latency/amplitude response space. These effects are similar to those seen in wave V of the human BAER (Barth and Burkard, 1993) and waves i and v of the gerbil BAER (Burkard, 1991). These findings suggest that the timing to response initiation is affected by such factors as: (1) the time of the noise burst onset ramp in which the stimulus is below threshold, (2) the slope defining the noise burst envelope at onset (i.e., Pa/ms), and/or (3) a critical integration time, in which the response only integrates energy over a finite time from some critical trigger onset time (Brinkman and Scherg, 1979; Suzuki and Horiuchi, 1981). Importantly, scalp-recorded BAERs show some of the same effects on response latency and response magnitude that are seen in single units and the present ICP data (e.g., Barth and Burkard, 1993; Burkard, 1991; Hecox and Galambos, 1974; Suzuki and Horiuchi, 1981). It is in this sense that the present ICP data form a link between the antecedent single-unit data in anesthetized animals and the BAER data in unanesthetized human beings.

The minimal latencies seen at high SPLs were almost always under 7 ms, despite the fact that the rise time of the stimuli eliciting those responses was often considerably longer (up to 32 ms). Now, there is a fixed minimal transmission time of the neural signal from the cochlea to the IC, which is probably in the order of 4 ms, based on response latency to higher-level noise bursts with fast (nominally 0-ms) rise times. Taken together, these observations have two related implications. The first implication is that the stimulus event(s) responsible for the initiation of the response were those in the very first few ms of the signal. This conclusion is in agreement with the earlier observations of Suzuki and Horiuchi (1981) on the human BAER and of the later findings of Heil and Irvine (1996, 1997; Heil, 1997a,b) and Phillips (1998) on feline cortical neurons.

The second implication is that it is not the plateau level of the stimulus which itself determines the timing of response initiation (see also Suzuki and Horiuchi, 1981; Heil and Irvine, 1996; Heil, 1997a; Phillips, 1998). In the context of the present data, this seems like an obvious point, but it is probably not the assumption usually made when one adopts the convention of plotting response latency as a function of stimulus SPL (e.g., present study, Figs. 4 and 6). There are at least two ways in which plateau level might influence response latency. One is through its effect on the timing of some ''trigger'' or ''threshold'' level for response, so that the trigger level occurs earlier for high-amplitude stimuli. The other is that neurons respond directly to the rate of change of stimulus pressure. Heil (1997a) recently showed for cortical neurons in anesthetized cats that the dynamic property of sound onset which determined latency varied with the shape of the rise function. When stimuli were gated with cosine-squared rise times, latency was an inverse function of the maximum acceleration of peak pressure at stimulus onset; when gated with linear rise times, latency was determined by the rate of change of peak pressure. The present data were obtained with cosine rise times (the only ones available at the time of the study), which have different dynamics from either of those used by Heil (1997a). A detailed comparison of ICP or other data from unanesthetized animals, with the existing single-unit data at this level of analysis, therefore awaits a future study.

ACKNOWLEDGMENTS

This research was supported by NIH-NIDCD Grant No. R01DC00166 to R. Salvi, and by Grants from NSERC of Canada to D.P.P. Special thanks are due to Carrie Secor for assistance with data acquisition, and to Susan Hall for assistance with the data analysis.

Aitkin, L.M., Anderson, D. J., and Brugge, J. F. (**1970**). ''Tonotopic organization and discharge characteristics of single neurons in nuclei of the lateral lemniscus of the cat,'' J. Neurophysiol. **33**, 421–440.

Barth, C. D., and Burkard, R. (**1993**). ''Effects of noise burst rise time and level on the human brainstem auditory evoked response,'' Audiology **32**, 225–233.

Brinkman, R., and Scherg, M. (**1979**). ''Human auditory on- and off-potentials of the brainstem,'' Scand. Audiol. **8**, 27–32.

Brugge, J. F., Dubrovsky, N. A., Aitkin, L. M., and Anderson, D. J. (**1969**). ''Sensitivity of single neurons in the auditory cortex of cat to binaural stimulation: effect of varying interaural time and intensity,'' J. Neurophysiol. **32**, 1005–1024.

Burkard, R. (**1991**). ''Effects of noise burst rise time and level on the gerbil brainstem auditory evoked response,'' Audiology **30**, 47–58.

Burkard, R., Trautwein, P., and Salvi, R. (**1997**). ''The effects of click level, click rate, and level of background masking noise on the inferior colliculus potential (ICP) in the normal and carboplatin-treated chinchilla,'' J. Acoust. Soc. Am. **102**, 3620–3627.

Folsom, R., and Aurich, C. (**1987**). ''Auditory brainstem responses from human adults and infants: Influence of stimulus onset,'' Audiology **26**, 117–122.

Hall, J. C., and Feng, A. S. (**1991**). ''Temporal processing in the dorsal medullary nucleus of the northern leopard frog (*Rana pipiens pipiens*),'' J. Neurophysiol. **66** 955–973.

Hecox, K., and Deegan, D. (**1983**). ''Rise–fall time effects on the brainstem auditory evoked response: Mechanisms,'' J. Acoust. Soc. Am. **73**, 2109–2116.

Hecox, K., and Galambos, R. (**1974**). ''Brainstem auditory evoked responses in human infants and adults,'' Arch. Otolaryngol. **99**, 30–33.

Hecox, K., Squires, N., and Galambos, R. (**1976**). ''Brainstem auditory evoked responses in man. I. Effect of stimulus rise–fall time and duration,'' J. Acoust. Soc. Am. **60**, 1187–1192.

Heil, P. (**1997a**). ''Auditory cortical onset responses revisited. I. First-spike timing,'' J. Neurophysiol. **77**, 2616–2641.
Heil, P. (**1997b**). ''Auditory cortical onset responses revisited. II. Response strength,'' J. Neurophysiol. **77**, 2642–2660.
Heil, P., and Irvine, D. R. F. (**1996**). ''On determinants of first-spike latency in auditory cortex,'' NeuroReport **7**, 3073–3076.
Heil, P., and Irvine, D. R. F. (**1997**). ''First-spike timing of auditory-nerve fibers and comparison with auditory cortex,'' J. Neurophysiol. **78**, 2438–2454.
Kitzes, L. M., Gibson, M. M., Rose, J. E., and Hind, J. E. (**1978**). ''Initial discharge latency and threshold considerations for some neurons in cochlear nuclear complex of the cat,'' J. Neurophysiol. **41**, 1165–1182.
Phillips, D. P. (**1988**). ''Effect of tone-pulse rise time on rate-level functions of cat auditory cortex neurons: Excitatory and inhibitory processes shaping responses to tone onset,'' J. Neurophysiol. **59**, 1524–1539.
Phillips, D. P. (**1998**). ''Factors shaping the response latencies of neurons in the cat's auditory cortex,'' Behav. Brain Res. **93**, 33–41.
Phillips, D. P., and Hall, S. E. (**1990**). ''Response timing constraints on the cortical representation of sound time structure,'' J. Acoust. Soc. Am. **88**, 1403–1411.
Phillips, D. P., Semple, M. N., and Kitzes, L. M. (**1995**). ''Factors shaping the tone level sensitivity of single neurons in posterior field of cat auditory cortex,'' J. Neurophysiol. **73**, 674–686.
Snyder, D., and Salvi, R. (**1994**). ''A novel chinchilla restraint device,'' Lab Animal **23**, 42–44.
Suga, N. (**1971**). ''Responses of inferior colliculus neurons of bats to tone bursts with different rise times,'' J. Physiol. (London) **217**, 159–177.
Suzuki, T., and Horiuchi, K. (**1981**). ''Rise time of pure-tone stimuli in brain stem response audiometry,'' Audiology **20**, 101–112.

Influence of speech stimuli intensity on the activation of auditory cortex investigated with functional magnetic resonance imaging

Cécile M. Mohr
Department of Nuclear and Radiological Engineering Science, University of Florida, P.O. Box 100245, Gainesville, Florida 32610

Wayne M. King
Department of Communication Sciences and Disorders, University of Florida, 335 Dauer Hall, Gainesville, Florida 32611

Alan J. Freeman
SMIS Limited, Alan Turing Road, Surrey Research Park, Guildford, Surrey, GU23 5YF, England

Richard W. Briggs
Departments of Radiology, Chemistry, and Molecular Biology & Biochemistry, University of Florida, P.O. Box 100374, J.H. Miller Health Center, Gainesville, Florida 32610

Christiana M. Leonard
Department of Neuroscience, University of Florida Brain Institute, P.O. Box 100244, Gainesville, Florida 32611

(Received 30 April 1998; revised 9 December 1998; accepted 11 January 1999)

Understanding the impact of variations in the acoustic signal is critical for the development of auditory and language fMRI as an experimental tool. We describe the dependence of the BOLD signal and speech intelligibility on the intensity of auditory stimuli. Eighteen subjects were imaged on a 1.5-T MRI scanner. Speech stimuli were English monosyllabic words played at five intensity levels. Intrasubject reproducibility was measured on one subject by presenting the stimulus five times at the same intensity level. Intelligibility was measured during data acquisition as subjects signaled when hearing two targets. Each functional trial consisted of four cycles (30 s off–30 s on). Five oblique slices covering primary and association auditory areas were imaged. Activated voxels were identified by cross-correlation analysis and their percent signal change (ΔS) was measured. Intersubject differences in activation extent, asymmetry, and dependence on intensity were striking. Volume of activation was significantly greater in the left than in the right hemisphere. Intrasubject reproducibility for ΔS was higher than for volume of activation. ΔS and intelligibility showed a similar dependence on intensity suggesting that not only intensity but also intelligibility affect the fMRI signal. © *1999 Acoustical Society of America.* [S0001-4966(99)01404-6]

PACS numbers: 43.64.Sj, 43.64.Ri, 43.66.Ba, 43.66.Yw [RDF]

LIST OF SYMBOLS AND ABBREVIATIONS

IL	intensity level
IL_{max}	higher intensity level at which activation is observed
IL_{min}	lower intensity level at which activation is observed
ΔS	percent signal change
ΔS_{3rep}	percent signal change of voxels activated in three or more of the five trials
ΔS_{4rep}	percent signal change of voxels activated in four ore more of the five trials
ΔS_{5rep}	percent signal change of voxels activated in all trials
$\Delta S_{5rep,i}$	value at trial ''i'' of percent signal change of voxels activated in all trials
ΔS_{3rep} @ IL_{max}	percent signal change at IL_{max}
ΔS_{3rep} @ IL_{min}	percent signal change at IL_{min}
ΔR	change in response
V	volume of activation (in μl)
V_i	volume of activation at trial i ($i=1-5$)
V_{3rep}	volume of activation (in μl) common to three or more of the five trials
V_{4rep}	volume of activation (in μl) common to four or more of the five trials
V_{5rep}	volume of activation (in μl) common to the five trials
TR/TE/FA	repetition time/echo time/flip angle
mm^3	cubic millimeter
s	second
μl	micro-liter
°	degree

 0001-4966/99/105(5)/2738/8/$15.00

INTRODUCTION

Brain activity is characterized by increases in regional cerebral glucose metabolism (rCMRgl), oxygen consumption ($rCMRO_2$), cerebral blood flow (rCBF), and cerebral blood volume (rCBV). Changes in $rCMRO_2$, rCBF, and rCBV affect the signal in magnetic resonance (MR) images[1–6] and therefore neuronal activation can be detected by MRI. These discoveries have lead to the development of a noninvasive neuroimaging tool called functional magnetic resonance imaging (fMRI).

Although there have been many fMRI studies of oral language and auditory processing, the effects of simple auditory stimulus manipulations such as intensity, frequency, and rate have been largely ignored. In view of the level of auditory noise in the scanner, it seems essential to characterize optimal auditory stimulus presentation. Of the few studies which have addressed basic stimulus parameters issues, several have investigated the influence of presentation rate on the fMRI response.[7–9] Stimulus presentation rate had been shown to increase rCBF using positron emission tomography (PET). When this parameter was varied in a fMRI experiment, the percent signal change of activated areas increased with increasing rate.[7] Similarly, sound intensity was shown to increase rCMRgl in central auditory structures in animals.[10] Still, the dependence of the fMRI signal on stimulus intensity has not been described except for two studies by Millen *et al.* and Strainer *et al.*[11,12] Both studies used two levels of sound intensity (sensation level, 20 dB and 50 dB) and a limited number of subjects ($n=8$ and $n=10$, respectively). Millen *et al.* found no influence of speech intensity on the volume of fMRI activation. Strainer *et al.* presented pure tone stimuli and showed an increased volume of activation at higher sound intensity when imaging the primary auditory cortex.

In this study, to address the issue of optimal stimulus presentation in language studies, intensity was varied and intelligibility (i.e., the understanding of the words) was monitored during the experiment to assess its effect on the fMRI response. Speech stimuli were presented at five intensity levels (IL) to 18 subjects. Reproducibility of the activation was measured for one subject and the influence of IL on the percent signal change in fMRI data was assessed.

I. METHODS

A. Subjects

Eighteen volunteers (17 males, 1 female; 21–40 years old) participated in a 1-h scanning session. Handedness was assessed in 16 of the 18 subjects with the Edinburgh handedness inventory.[13] Eight of these subjects were classified as dextral and eight as adextral (scores <0.75). Participants were recruited on a voluntary basis and signed an informed consent form that had been approved by the University of Florida Institutional Review Board.

B. Selection of stimuli and sound delivery setup

The speech stimuli used in this experiment were monosyllabic English words taken from the Northwestern University word lists (NU-6).[10] The NU-6 lists were chosen because they contain a large number of words (200), have high intertest reliability, and are in widespread clinical use as a measure of word discrimination ability. The word lists were digitally filtered with a finite impulse response function to ensure spectral stability and then recorded on magnetic tape for playback to the subjects. The rate of presentation was kept constant at 30 words per minute.

Auditory stimuli were delivered binaurally through a custombuilt sound delivery system. The audio system consisted of an amplifier coupled to an 18-ft length of 0.5-in.-diameter rigid plastic tubing. A 0.25-in.-thick foam insulated the tube from sound impinging on its outside. At the chest of the subject the tube split into two smaller 0.1-in.-diameter tubes, which ended in tightly occluding foam inserts for the ears. A vent was placed at the tubing fork to attenuate low frequencies, which dominate an acoustic stimulus at the distal end of a tube. The subjects were also fitted with protective headphones (average noise reduction rating: 20 dB) to provide additional attenuation of scanner noise. The output of the sound delivery system was verified by measuring the output of the inserts in a 2-cc coupler and verified on one volunteer by placing a probe-tube microphone in the ear canal approximately 5 mm away from the tympanic membrane. All sound levels were measured on a C-weighted scale and ranged from 65 to 110 dB.

C. Selection of intensity levels and experimental fMRI design

Prior to the experiment, the stimulus intensities were individually determined to cover a range from low to perfect intelligibility for each subject. The subject listened to the tape while a dummy scan replicated the true fMRI experiment noise conditions. Initially, the tape was played at 70 dB and 100 dB (C-weighted scale) and the number of words correctly identified was recorded as a percent of total words presented. Three additional sound levels were then chosen so as to cover a range of subject performance from poor (0%–20% correct) to perfect (100% correct). The sound levels used for individual subjects ranged on a C-weighted scale from 65 to 70 dB at IL 1, 70 to 80 dB at IL 2, 80 to 90 dB at IL 3, 90 to 95 dB at IL 4, and 100 dB to 110 dB at the fifth IL.

In experiment 1, the five individualized intensity levels (IL) were then presented in a randomized order for each of the 18 subjects. To assess stability of the intra-subject fMRI signal (i.e., reproducibility within a subject in the absence of intensity changes) a second experiment was conducted with one individual, in which the stimulus was presented five times at a constant IL (90 dB on a C-weighted scale) (experiment 2).

Each of the five functional trials lasted 4 min, alternating 30 s of stimulus on and off. During functional scanning, subjects were instructed to mentally rehearse the words and to lie still. Additionally, to measure intelligibility and to ensure the subjects' attention, they were instructed to indicate with a push button whenever they heard one of two target words. The target words were the same for all subjects and each of them occurred four times during the 2 min of stimu-

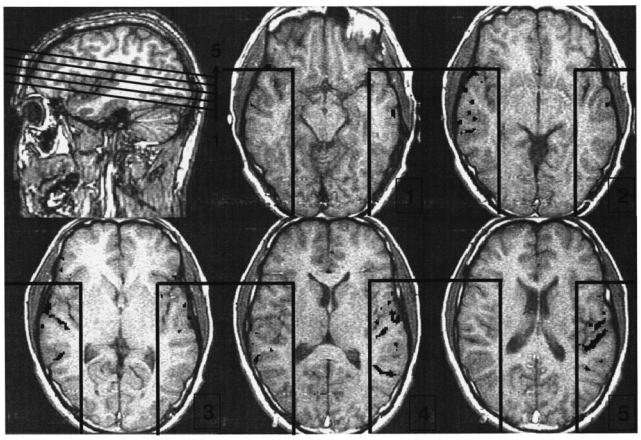

FIG. 1. Location of the five oblique functional slices on a sagittal view of the brain (top left hand corner). Images 1–5 display activation maps (black dots) overlaid onto anatomical images and are presented from the most inferior to the most superior location of functional slices. The bilateral ROIs used for data analysis are presented. They start 30-mm lateral to the midline and extend from 10-mm anterior to the AC to the occipital pole. Coordinates were defined on ''Talairached'' brains.

lus presentation. Subject response was monitored to evaluate the true positive fraction (i.e., fraction of target words accurately detected to the total of target words) and false positive fraction (i.e., fraction of nontarget words detected to the total number or words).

D. Imaging protocol

All subjects were imaged on a 1.5-T GE Signa scanner (General Electric Medical Systems, Milwaukee, WI) using the standard GE birdcage head coil. To restrict motion, subjects' heads were stabilized with foam padding. Functional images were acquired using a multislice spiral scan[14] technique (TR/TE/FA=750 ms/40 ms/45°, 4 interleaves, 128 $\times$128 matrix, voxel size=1.4$\times$1.4$\times$5 mm^3, 1.5-mm gap) resulting in a temporal resolution of 3 s. Five oblique slices covering Heschl's gyrus (HG), the planum temporale (PT), and the posterior superior temporal sulcus (STS) were selected from a sagittal view in the left hemisphere (Fig. 1, top left hand corner). For each functional trial, this acquisition protocol yielded 80 time-point images at each slice location. High-resolution anatomical images were obtained using a 3D-SPGR sequence (TR/TE/FA=27 ms/7 ms/45°, 256$\times$256 $\times$128, voxel size=0.94$\times$0.94$\times$1.3 mm^3).

E. Data processing

Functional images were reconstructed and corrected for in-plane motion by aligning them to the last image of the functional run using the AFNI package (MCW).[15] Each voxel signal intensity time course was correlated to a square reference waveform phase shifted by 6 s to create a map of correlation coefficients. The phase shift simulated an average delay in activation after stimulus onset, caused by the hemodynamic response time of the brain.[2,16,17] The voxel percent signal changes ΔS between on and off periods were also calculated.

Correlation coefficients and percent signal change (ΔS) maps were overlaid onto the anatomic 3D data set, transformed to Talairach coordinates, and interpolated to 3$\times$3$\times$3 mm^3 (or 27 μl) voxels using AFNI.[15] Voxels were defined as active when their correlation coefficient was greater than 0.5. This threshold ensured that the response of the voxel was related to the stimulus with a statistical significance of $p < 0.001$.[18] Additionally, voxels with a ΔS greater than 20% were eliminated to exclude voxels representing large blood vessels and voxels at the edge of the brain where slight motion can create large signal changes. Using the three-dimensional visualization tools of AFNI, three different regions of auditory cortex, HG (which contains primary auditory cortex), and secondary auditory cortex which includes PT and the STS, were identified on a sagittal view. The number of subjects with activation in these areas was recorded. Additionally, two large regions of interest (ROI) that encompassed left and right primary and association auditory cortices were selected. Each ROI extended laterally beginning at 30-mm lateral to the midline, and ranged in the anterior/posterior direction from 10-mm anterior to the anterior commissure (AC)[19,20] to the occipital pole (Fig. 1, images 1–5).

F. Data analysis

Using data from experiment 1, the total volume of activation in this region and the mean percent signal change in that area (V_i and ΔS_i; $i=1-5$) was measured as well as $V_{3\text{rep}}$, $V_{4\text{rep}}$, $V_{5\text{rep}}$, the volume of brain tissue activated at least 3, 4, or 5 times of the five presented IL. Two methods were adopted to analyze these data.

First, voxels *activated at 3 or more stimulus intensity levels* were combined and analyzed as ''repeated voxels.'' Their percent signal change, $\Delta S_{3\text{rep}}$, was calculated at each IL and their Talairach coordinates were recorded. To assess the influence of stimulus intensity on the signal change $\Delta S_{3\text{rep}}$, the highest and the lowest stimulus IL ($\text{IL}_{\max}$ and $\text{IL}_{\min}$) at which each voxel was activated were identified. The change in response ΔR was calculated by subtracting the $\Delta S_{3\text{rep}}$ at the lowest stimulus intensity ($\Delta S_{3\text{rep}} @ \text{IL}_{\min}$) from that at the highest stimulus intensity ($\Delta S_{3\text{rep}} @ \text{IL}_{\max}$). Positive ΔR indicates an increase in percent signal change between lowest and highest stimulus intensity, while negative ΔR indicates a decrease in percent signal change as stimulus intensity increased. The hypothesis that ΔR was significantly different from zero was tested using a paired-sample *t*-test. Secondly, voxels *activated at all five presentations of the stimulus* were counted ($V_{5\text{rep}}$). Then, influence of intensity on their percent signal change, $\Delta S_{5\text{rep}}$, was investigated using a five-factor repeated measures ANOVA.

Using data from experiment 2, activated voxels at each of the five trials (V_i where $i=1-5$) and voxels activated in all the trials ($V_{5\text{rep}}$) were counted. The ratio of $V_{5\text{rep}}$ to V_i was calculated for each trial as a measure of the intra-subject stability of the fMRI volume of activation. In addition $\Delta S_{5\text{rep},i}$, the percent signal change at each trial *i*, of $V_{5\text{rep}}$ was measured and compared to assess its stability.

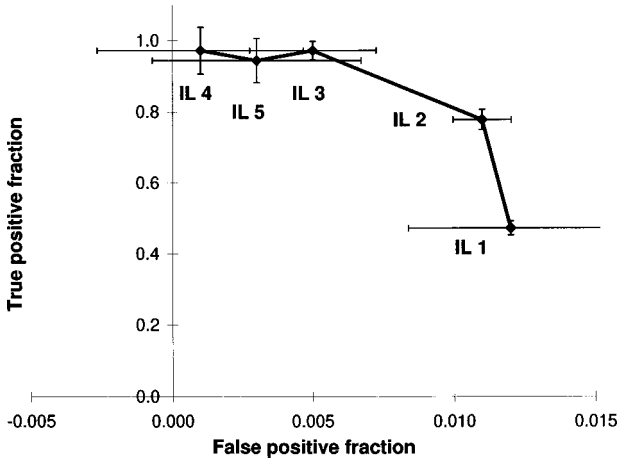

FIG. 2. Mean subject performance at each intensity level (IL). True positive fraction is plotted versus false positive fraction at each of the five IL values. Mean value and standard error of the mean are displayed ($n=18$). Large error bars result from the low number of target words used to compute the true and false positive fractions. Intelligibility increases with sound intensity up to IL 4 and the decreases slightly.

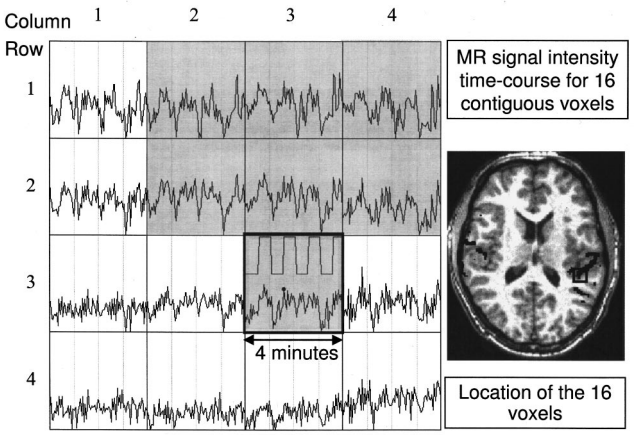

FIG. 3. Time courses of 16 activated and nonactivated contiguous voxels of one subject at IL 4. Each of the 16 ''boxes'' displays the MR signal from one voxel as a function of time. The stimulus paradigm is presented in the highlighted voxel (row 3, column 3): it consists of four cycles during which the stimulus is alternatively 30 s off and 30 s on. The location of the 16 contiguous voxels is shown on the MR image and corresponds to the left planum temporale. Activated voxels (shaded) can be identified in rows 1 and 2, as well as at the center voxel location (row 3, column 3). For these voxels, the time course of the MR signal exhibits a periodic pattern that follows the stimulus paradigm.

II. RESULTS

A. Intensity level and intelligibility

Figure 2 displays the mean true positive fraction (TPF) versus the mean false positive fraction (FPF) obtained at each intensity level during the fMRI experiments. Intelligibility is characterized by a high TPF and a low FPF.

Performance became progressively better in going from IL 1 to IL 2 and IL 3, as reflected by decreased FPF and increased TPF. Two subjects performed worse at IL 4 than at IL 3, and the remaining increased their performance. Four did worse at IL 5 than at IL 4, while all others performed equally well. On average, intelligibility increased from IL 1 to IL 4 and then slightly decreased at IL 5.

B. Reproducibility

Table I shows results of experiment 2 when stimulus intensity was not varied but kept at a constant level (90 dB-C, or the average IL 4). The volume of activation V_i at each trial i, the ratio $(V_{5\text{rep}}/V_i)$ as well as the percent signal change of five times repeated voxels $(\Delta S_{5\text{rep}})$ are presented. V_i can quadruple from one trial to another [range: 1701 μl–7992 μl; mean: 4185 μl; standard deviation: 2538 μl or coefficient of variation (COV) 61%]. The 594 μl activated in all the trials $(V_{5\text{rep}})$, represented only 7% of the largest total activation (in trial 2), to about 33% of the smallest activation volume (in trials 1 and 5). Despite this variability, visual inspection showed that the locus of activation was similar for each trial. The average $\Delta S_{5\text{rep}}$ ranged from 3.8% to 5.3%. The mean $\Delta S_{5\text{rep}}$ over the five trials was 4.4% (standard deviation: 0.6% or COV 13.4%).

In the two worst cases, activation inside the ROI represented 35%–50% of the total activation. This occurred for the two subjects with the lowest number of voxels activated (two and six, respectively). For the remaining subjects, activation in the combined ROIs represented on the average 86% of the total activation.

TABLE I. Results of experiment 2, testing reproducibility of activation: for each trial i, activated volume V_i in μl, relative volume of activation common to all trials ($V_{5\text{rep}}=594$ μl) compared to the total activation volume sat each trial (V_i) and average percent signal change $\Delta S_{5\text{rep},i}$ for activated voxels common to all five trials $(V_{5\text{rep}})$. Note that in experiment 2, the intensity level was kept constant in all five trials.

	Trial 1 $i=1$	Trial 2 $i=2$	Trial 3 $i=3$	Trial 4 $i=4$	Trial 5 $i=5$
V_i (in μl)	1917	7992	4590	4725	1701
$V_{5\text{rep}}/V_i$	0.31	0.07	0.13	0.13	0.35
$\Delta S_{5\text{rep},i}$	4.2%	5.3%	4.6%	3.8%	4.1%

C. Activation pattern

Figure 1 (images 1–5) illustrates the typical pattern of activation. More voxels are activated in the left than in the right hemisphere and the location of the activation corresponds to auditory cortex in the superior temporal gyrus. Figure 3 shows the MR signal intensity time course for 16 contiguous voxels for one subject at IL 4. Activated voxels exhibit a regular pattern that follows the 4-min stimulation cycles of alternating periods of 30 s off and 30 s on.

Most of the subjects demonstrated activation in auditory cortex, namely the planum temporale (PT), Heschl's gyrus (HG), and the superior temporal sulcus (STS). Table II dis-

TABLE II. Number of subjects demonstrating activation in the superior temporal sulcus (STS), the planum temporale (PT), and Heschl's gyrus (HG) per hemisphere.

Anatomical region	Right hemisphere	Left hemisphere
Planum temporale (PT)	17/18	15/18
Heschl's Gyrus (HG)	8/18	11/18
Superior temporal sulcus (STS)	14/18	14/18

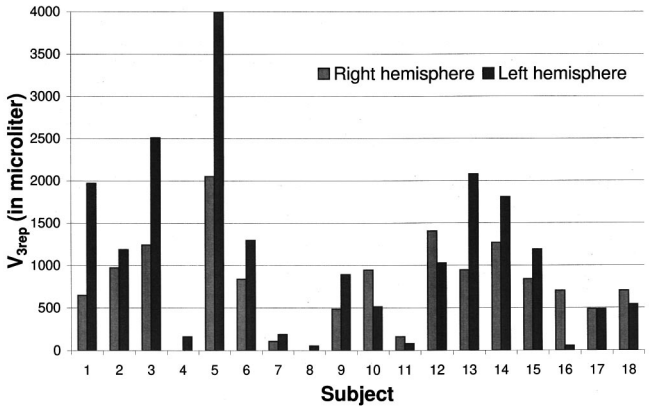

FIG. 4. V_{3rep} as a function of hemisphere for all subjects. V_{3rep} was significantly greater in the left hemisphere than in the right (paired sample *t*-test; $df=17$; $p=0.046$).

plays the number of subjects with ''repeated'' activation in the right and left PT, STS, and HG. Figure 4 shows V_{3rep} for each subject in both left and right hemispheres. V_{3rep} varied considerably among subjects: four subjects had very small repeated volumes of activation (less than 405 μl), nine subjects had activation volumes between 540 and 2700 μl, and five subjects had activation volumes greater than 2700 μl. These differences could not be attributed to obvious characteristics such as age or dextrality. All 18 subjects activated voxels in the left hemisphere and 16 activated in the right. V_{3rep} was greater in the left than in the right hemisphere for 12 subjects, smaller in the left than in the right for 5, and the same in both hemispheres for the remaining subject. V_{3rep} was significantly greater in the left than in the right hemisphere (paired sample *t*-test, $df=17$: $p=0.046$).

D. Effect of intensity level

Table III presents $\Delta S_{3rep}@\mathrm{IL}_{min}$, $\Delta S_{3rep}@\mathrm{IL}_{max}$, and the resulting ΔR ($\Delta S_{3rep}@\mathrm{IL}_{max}-\Delta S_{3rep}@\mathrm{IL}_{min}$) for each subject in each hemisphere. Table IV presents the mean and standard deviation of the same quantities per hemisphere. Since subjects exhibited a great difference in V_{3rep}, the mean ΔR for all 18 subjects was calculated by weighting each individual ΔR by the corresponding V_{3rep}. In the right hemisphere, 16 subjects had repeated activation. ΔR is positive for all of these subjects (range: $+0.33\%-+2.41\%$) and significant for 15 of them ($p<0.05$). In the left hemisphere, all subjects showed repeated activation and ΔR ranged from -0.11 to $+4.70\%$. For two subjects, the small number of voxels did not allow calculation of a *p*-value. Of the remaining 16, 12 showed a significant positive ΔR. The mean weighted ΔR was 1.11% (standard deviation: 0.64%) in the right and 0.85% (standard deviation: 0.80%) in the left hemisphere. Despite the large standard deviations of these measurements, the mean ΔR was significant and positive in both hemispheres (paired-sample *t*-test, $df=17$: $p<0.001$ in the right and the left hemispheres).

Figure 5 shows the mean ΔS_{5rep} weighted by V_{5rep}, the individual repeated volume of activation, versus intensity level in both hemispheres. These data were obtained for the nine and eight subjects having voxels activated five times in the left and right hemisphere, respectively. With an initial value of 5% at IL 1, ΔS_{5rep} increases to 6.5% at IL 4, and then decreases to 6% at IL 5. Stimulus intensity has an effect on ΔS_{5rep} in both hemispheres (repeated measures, ANOVA: right hemisphere $p=0.039$, left hemisphere $p=0.049$). No significant difference between right and left hemisphere was observed.

TABLE III. Average percent signal change for ''repeated'' voxels at the lowest stimulus intensity ($\Delta S_{3rep}@\mathrm{IL}_{min}$) and at the highest stimulus intensity ($\Delta S_{3rep}@\mathrm{IL}_{max}$) per hemisphere and per subject. ΔR, the change in response, is the difference between $\Delta S_{3rep}@\mathrm{IL}_{max}$ and $\Delta S_{3rep}@\mathrm{IL}_{min}$. *P*-values are obtained by doing a paired sample *t*-test on $\Delta S_{3rep}@\mathrm{IL}_{min}$ and $\Delta S_{3rep}@\mathrm{IL}_{max}$ for all ''repeated'' voxels of each subject. Significant *p*-values at the 0.050 level are highlighted. ''NA'' (nonapplicable) applies either when no voxels are activated or when there are not enough voxels to do a paired-sample *t*-test.

	Right hemisphere				Left hemisphere			
Subject	$\Delta S_{3rep}@\mathrm{IL}_{min}$	$\Delta S_{3rep}@\mathrm{IL}_{max}$	ΔR	*p*-value	$\Delta S_{3rep}@\mathrm{IL}_{min}$	$\Delta S_{3rep}@\mathrm{IL}_{max}$	ΔR	*p*-value
1	6.17	7.14	0.97	**0.002**	4.93	5.36	0.43	**0.012**
2	3.95	4.28	0.33	0.054	5.05	5.74	0.69	**0.050**
3	5.34	6.01	0.67	**0.001**	4.94	5.69	0.75	**0.001**
4	NA	NA	NA	NA	3.87	8.57	4.70	**0.005**
5	5.58	6.18	0.60	**0.001**	4.83	5.37	0.54	**0.003**
6	4.72	5.84	1.12	**0.008**	4.31	4.20	−0.11	0.351
7	2.93	3.28	0.35	**0.027**	4.01	4.21	0.20	0.558
8	NA	NA	NA	NA	7.40	10.90	3.50	NA
9	3.27	3.92	0.65	**0.022**	2.85	3.70	0.85	**0.001**
10	3.54	4.03	0.49	**0.020**	4.86	5.19	0.33	**0.030**
11	6.10	8.40	2.30	**0.020**	3.43	4.60	1.17	0.115
12	4.82	6.57	1.75	**0.001**	4.85	5.87	1.02	**0.001**
13	4.54	6.95	2.41	**0.001**	4.70	6.61	1.91	**0.001**
14	3.87	5.62	1.75	**0.001**	3.34	3.91	0.57	**0.001**
15	3.30	4.35	1.05	**0.001**	2.89	5.86	2.97	**0.001**
16	4.37	6.30	1.93	**0.001**	2.50	3.00	0.50	NA
17	3.86	5.16	1.30	**0.001**	3.32	4.44	1.12	**0.001**
18	3.29	3.78	0.49	**0.005**	4.04	4.50	0.46	0.215

TABLE IV. Weighted mean ΔS_{3rep} @ IL_{min}, ΔS_{3rep} @ IL_{max}, ΔR, and respective weighted standard deviation over the 18 subjects. Each mean value was weighted for each subject by V_{3rep}, the volume of repeated activation. The *p*-value was obtained by testing the hypothesis that ΔR was significantly different than zero. For both hemispheres, ΔR was positive and significantly greater than zero, which demonstrates that increasing intensity level causes an increase in the percent signal change of three times or more activated voxels, V_{3rep}.

	Right hemisphere				Left hemisphere			
	ΔS_{3rep} @ IL_{min}	ΔS_{3rep} @ IL_{max}	ΔR	*p*-value	ΔS_{3rep} @ IL_{min}	ΔS_{3rep} @ IL_{max}	ΔR	*p*-value
Weighted mean (std. deviation)	4.50 (0.88)	5.61 (1.10)	1.11 (0.64)	0.001	4.35 (0.74)	5.20 (0.82)	0.85 (0.80)	0.001

III. DISCUSSION

A. Intelligibility and sound intensity

Performance increased significantly from IL 1 to IL 4: Intelligibility increased with increasing sound intensity. A relatively insensitive measure was used (detection of 8 words out of 60) and there was no clear distinction between IL 4 and IL 5. Still, four subjects showed a decrease in TPF at IL 5 versus IL 4. These results suggest a decrease in intelligibility between IL 4 and IL 5 while sound intensity was increased.

B. Intra- and inter-subject variability

From experiment 2, three quantitative results on reproducibility can be drawn. First, up to four-fold variations in activated volumes can occur from one experiment to another within the same individual. Second, only 7%–35% of the volume of activation for one experiment will also be activated in all replicate experiments. Last, for voxels activated in two identical experiments, the percent signal change will be within 15% of the mean value in 68% of the time. These results were obtained at near optimal intensity conditions and considered the effects of speech stimuli on only one individual. Therefore these values might not be representative of a whole population and with stimuli of different type and intensity. Still the reported intra-subject variability estimates agree with the results of a fMRI experiment on visual cortex published by Moser *et al.*[21] Our data confirm their conclusion that percent signal change ΔS is a more stable measure of activity than volume of activation.

Intra-subject reproducibility in fMRI has been the topic of many papers.[21–23] Recent statistical models[24,25] have presented an experimental method for estimating the specificity and sensitivity of a fMRI protocol. This method requires repeating each experiment 2–4 times and could not be implemented retrospectively in this study. Such an approach in future fMRI experiments will allow estimating better margins of errors.

Consistent with other studies,[21] large inter-subject variations were observed. How much of this variation is attributable to the low intra-subject reproducibility of the activated volume, and how much is due to individual physiological differences is unknown. None of the information gathered from the subjects correlated with the observed variations. Attention has been shown to increase activity in auditory cortex[26] and could have contributed to the variability of the results. The level of concentration addressed to identifying the target words varied with IL and probably among the subjects.

C. Lateralization of activation

Language is lateralized to the left hemisphere for the majority of right-handers. In this study, the data showed a slight but significant ($p = 0.046$) asymmetry in the activation volume toward the left hemisphere, which confirmed the expected asymmetry. However, this result was not significant at the 0.001 level. A mismatch negativity study[27] demonstrated that if speech stimuli were presented with a noisy background, the left/right activation asymmetry decreased. Therefore, our weak lateralization could be due to the noisy MR scanner environment, as well as the variability of handedness in the subject population.

The right auditory cortex is shifted slightly anterior relative to the left. It is possible that the choice of ROI might have excluded a small part of the right auditory cortex and resulted in an artifactual predominant activation in the left hemisphere. This would corroborate the many previous functional imaging studies,[12,28–32] which have failed to find significant lateralization in activation following speech processing tasks.

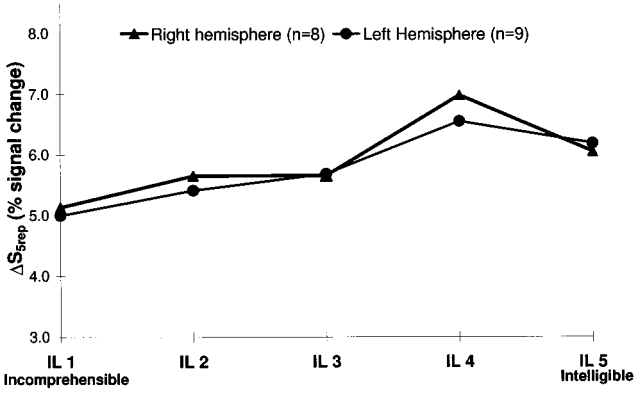

FIG. 5. ΔS_{5rep}, the percent signal change of the five times activated voxels, in both hemispheres as a function of intensity level. The mean ΔS_{5rep} values over subjects having voxels activated at all five ILs have been calculated: 8/18 subjects had at least one voxel activated at all trials in the right hemisphere and 9/18 in the left. In both hemispheres, ΔS_{5rep} increases with increasing IL, up to IL 4 where it reaches its maximum.

D. Influence of stimulus intensity or intelligibility

Two previous studies investigated the influence of sound intensity on the fMRI response.[11,12] Meaningful speech stimuli[11] and pure tones[12] were presented at 2 sound intensities, 20- and 50-dB sensation level. The volume of activation in the primary auditory cortex was greater when pure tone stimuli were presented at higher sound levels. With speech stimuli, the activation volume in several brain regions did not differ in the two conditions. As stated previously, the volume of activation is a more variable quantity than percent signal change. In our study, ΔR, the percent signal change between the lowest and highest intensity levels, was chosen as a preferable measure.

Results show an increase in ΔR with increasing IL, which suggests an increase in neuronal activity in auditory cortex between low and high intensity levels. Other factors than can modulate brain response are (a) sound intensity, (b) the level of attention, and (c) speech intelligibility. (a) Increasing sound intensity has been shown to increase glucose metabolism in central auditory structures[10] and could explain the observed increase in fMRI signal change. Additional support for the importance of sound intensity as a determinant of brain activity comes from the increase of $\Delta S_{5\text{rep}}$ with increasing IL. The percent signal change of around 5% at IL 1 also supports the effects of intensity on fMRI activation since intelligibility is close to zero at this intensity level. If our data reflect the effects of sound intensity rather than intelligibility, auditory stimuli should be presented at high amplitude to produce optimum activation of the brain. (b) As intensity and intelligibility increase, attention and effort are expected to decrease. If our result reflected attention level, a response decrease with increasing IL would have been expected. Our data did not confirm this hypothesis. (c) Intelligible stimuli could produce increased activation, which would be expected to occur in association cortex. To distinguish effects of intensity and intelligibility, a separate analysis of primary and association cortex might be useful. It is expected that intensity would affect primary auditory cortex and probably association cortex while intelligibility is expected to affect mainly association cortex. Our analysis did not distinguish between these areas, as primary auditory cortex is small considering the fMRI spatial resolution. The decrease of percent signal change between IL 4 and IL 5 supports an effect of intelligibility. Such a decrease could also reflect habituation or ''saturation.'' An effect of habituation is unlikely since the presentation order was randomized for all subjects. Saturation can be defined as leveling off of brain performance and brain response: As sound intensity increases with IL, the brain could reach the limits of its dynamic capabilities. As the stimuli were played at a reasonably loud intensity, saturation of the auditory system seems unlikely, although background scanning noise has been shown to reduce the dynamic range of the auditory system.[33] Saturation effects have been observed in other fMRI auditory experiments investigating the influence of word presentation rate,[7,9] and were also reported while studying the influence of luminance on activation in the visual cortex.[34] If there is truly saturation, auditory stimuli should be presented at an intermediate sound level.

Our data do not permit a definite conclusion about the relative contribution of intensity and intelligibility, and it is likely that both affected the fMRI signal as intensity changes caused intelligibility changes.

IV. CONCLUSION

In summary, intelligibility levels were varied by changing the stimulus intensity. Increased brain activation was observed when intensity level was increased. In both hemispheres a significant positive change in the response ΔR between lowest and highest IL was noted. Sound intensity influenced the baseline of the fMRI signal. Intensity level influenced the percent signal change of voxels activated at all 5 ILs, which reached its maximum value at IL 4. Intelligibility varied in a similar pattern. Intra-subject variability in volumes of activation and patterns of asymmetry was large. Areas of repeated activation were located in auditory cortex and were significantly greater in the left hemisphere than in the right. In designing fMRI studies, special care should be taken in controlling possible sources of variability such as attention. Functional trials should also be repeated at least twice in order to determine the specificity and sensitivity of the implemented protocol.

Future fMRI studies of auditory cortex need to address the contribution of intelligibility and intensity. Intelligibility could be varied by changing a background noise while keeping sound intensity constant. Experiments with a better spatial resolution are needed in order to distinguish primary and association areas, along with a separate analysis of these areas. Combined with these results, such experiments will guide the optimal presentation for future auditory and language fMRI studies.

ACKNOWLEDGMENTS

This work was supported by the National High Magnetic Field Laboratory (Tallahasee, Florida), the University of Florida (UF) Brain Institute, the UF Center for Structural Biology, the UF Department of Radiology, and an Interdisciplinary Research Initiative grant from UF awarded to Dr. Thomas Oakland. The authors also thank Dr. Doug Noll for the spiral scan sequence, Dr. Gareth Barker for some processing programs, Dr. Bruce Crosson for his help with AFNI, Dr. Carl Crandell for the use of his audio equipment, as well as Dr. David Buckley and Dr. Stephen Blackband for useful discussions.

[1] S. Ogawa, R. S. Menon, D. W. Tank, S. G. Kim, H. Merkle, J. M. Ellermann, and K. Ugurbil, ''Functional brain mapping by blood oxygenation level-dependent contrast magnetic resonance imaging. A comparison of signal characteristics with a biophysical model,'' Biophys. J. **64**, 803–812 (1993).

[2] E. A. DeYoe, P. Bandettini, J. Neitz, D. Miller, and P. Winans, ''Functional magnetic resonance imaging (FMRI) of the human brain,'' J. Neurosci. Methods **54**, 171–187 (1994).

[3] R. B. Buxton, E. C. Wong, and L. R. Frank, ''A biomechanical interpretation of the BOLD signal time course: The Balloon model,'' *Proceedings of the 5th ISMRM Meeting*, Vol. 1, 1997 (Abstract).

[4] T. L. Davis, K. K. Kwong, P. A. Bandettini, R. M. Weisskoff, and B. R. Rosen, ''Mapping the dynamics of oxidative metabolism by functional MRI,'' *Proceedings of the 5th ISMRM Meeting*, Vol. 1, 1997 (Abstract).

[5] P. A. Bandettini, W. M. Luh, T. L. Davis, J. Van Kylen, H. V. Forster, S.

M. Rao, E. C. Wong, A. Jesmanowicz, and J. S. Hyde, ''Simultaneous measurement of cerebral perfusion and oxygenation changes during neuronal activation and hypercapnia,'' *Proceedings of the 5th ISMRM Meeting*, Vol. 1, 1997 (Abstract).
[6] R. B. Buxton, E. C. Wong, and L. R. Frank, ''A comparison of perfusion and BOLD changes during brain activation,'' *Proceedings of the 5th ISMRM Meeting*, Vol. 1, 1997 (Abstract).
[7] J. R. Binder, S. M. Rao, T. A. Hammeke, J. A. Frost, P. A. Bandettini, and J. S. Hyde, ''Effects of stimulus rate on signal response during functional magnetic resonance imaging of auditory cortex,'' Brain Res. Cogn. Brain Res. **2**, 31–38 (1994).
[8] A. Dhankhar, B. E. Wexler, R. K. Fulbright, T. Halwes, A. M. Blamire, and R. G. Shulman, ''Functional magnetic resonance imaging assessment of the human brain auditory cortex response to increasing word presentation rates,'' J. Neurophysiol. **77**, 476–483 (1997).
[9] G. E. Rees, A. M. Howseman, O. Josephs, C. Frith, K. J. Friston, and R. Turner, ''Characterizing the relationship between BOLD fMRI contrast and cerebral blood flow by varying stimulus presentation rate,'' *Proceedings of the 5th ISMRM Meeting*, Vol. 1, 1997 (Abstract).
[10] R. M. Abrams, A. A. Hutchison, and K. J. Gerhardt, ''Effect of high-intensity sound on local cerebral glucose utilization in fetal sheep,'' Brain Res. Dev. Brain Res. **48**, 1–10 (1989).
[11] S. J. Millen, V. M. Haughton, and Z. Yetkin, ''Functional magnetic resonance imaging of the central auditory pathway following speech and pure-tone stimuli,'' Laryngoscope **105**, 1305–1310 (1995).
[12] J. C. Strainer, J. L. Ulmer, F. Z. Yetkin, D. L. Daniels, and S. J. Millen, ''Functional MR of the primary auditory cortex: An analysis of pure tone activation and tone discrimination,'' AJNR, **18**, 601–610 (1997).
[13] G. G. Briggs and R. D. Nebes, ''Patterns of hand preference in a student population,'' Cortex **11**, 230–238 (1975).
[14] D. C. Noll, J. D. Cohen, C. H. Meyer, and W. Schneider, ''Spiral *K*-space MR imaging of cortical activation,'' J. Magn. Reson. Imaging. **5**, 49–56 (1995).
[15] R. W. Cox, ''AFNI: software for analysis and visualization of functional magnetic resonance neuroimages,'' Comput. Biomed. Res. **29**, 162–173 (1996).
[16] J. W. Belliveau, K. K. Kwong, D. N. Kennedy, J. R. Baker, C. E. Stern, R. Benson, D. A. Chesler, R. M. Weisskoff, M. S. Cohen, R. B. Tootell *et al.*, ''Magnetic resonance imaging mapping of brain function. Human visual cortex,'' Invest. Radiol. **27**, S59–65 (1992).
[17] S. G. Kim, W. Richter, and K. Ugurbil, ''Limitations of temporal resolution in functional MRI,'' Magn. Reson. Med. **37**, 631–636 (1997).
[18] P. A. Bandettini, A. Jesmanowicz, E. C. Wong, and J. S. Hyde, ''Processing strategies for time-course data sets in functional MRI of the human brain,'' Magn. Reson. Med. **30**, 161–173 (1993).
[19] P. V. Penhune, ''Interhemispheric anatomical differences in human primary auditory cortex: Probabilistic mapping and volume measurements from magnetic resonance scans,'' Cerebral Cortex **6**, 661–672 (1997).
[20] C. M. Leonard, C. Puranik, J. M. Kuldau, and L. J. Lombardino, ''Normal variations in the frequency and location of human auditory cortex landmarks: Heschl's gyrus: Where is it?,'' Cerebral Cortex **8**, 397–406 (1998).
[21] E. Moser, C. Teichtmeister, and M. Diemling, ''Reproducibility and post-processing of gradient-echo functional MRI to improve localization of brain activity in the human visual cortex,'' Magn. Reson. Imaging **14**, 567–579 (1996).
[22] E. Bullmore, M. Brammer, S. C. R. Williams, S. Rabe-Hesketh, N. Janot, A. David, J. Mellers, R. Howard, and P. Sham, ''Statistical methods of estimation and inference for functional MR image analysis,'' Magn. Reson. Med. **35**, 261–277 (1996).
[23] F. Z. Yetkin, T. L. McAuliffe, R. W. Cox, and V. M. Haughton, ''Test–retest precision of functional MR in sensory and motor task activation,'' AJNR. Am. J. Neuroradiol. **17**, 95–98 (1996).
[24] C. R. Genovese, D. C. Noll, and W. F. Eddy, ''Estimating test-retest reliability in functional MR Imaging I: Statistical methodology,'' Magn. Reson. Med. **38**, 497–507 (1997).
[25] D. C. Noll, C. R. Genovese, L. E. Nystrom, A. L. Vazquez, S. D. Forman, W. F. Eddy, and J. D. Cohen, ''Estimating test–retest reliability in functional MR Imaging II: Application to motor and cognitive studies,'' Magn. Reson. Med. **38**, 508–517 (1997).
[26] J. R. Binder, J. A. Frost, T. A. Hammeke, S. M. Rao, and R. W. Cox, ''Function of the left planum temporale in auditory and linguistic processing,'' Brain **119**, 1239–1247 (1996).
[27] Y. Shtyrov, T. Kujala, J. Ahveninen, M. Tervaniemi, P. Alku, R. J. Ilmoniemi, and R. Naatanen, ''Background acoustic noise and the hemispheric lateralization of speech processing in the human brain: magnetic mismatch negativity study,'' Neurosci. Lett. **251**, 141–144 (1998).
[28] J. C. Mazziotta, M. E. Phelps, R. E. Carson, and D. E. Kuhl, ''Tomographic mapping of human cerebral metabolism: auditory stimulation,'' Neurology **32**, 921–937 (1982).
[29] S. E. Petersen, P. T. Fox, M. I. Posner, M. Mintun, and M. E. Raichle, ''Positron emission tomographic studies of the cortical anatomy of single-word processing,'' Nature (London) **114**, 585–589 (1988).
[30] R. Wise, F. Chollet, U. Hadar, K. Friston, E. Hoffner, and K. Frackowiak, ''Distribution of cortical neural networks involved in word comprehension and word retrieval,'' Brain **114**, 1805–1817 (1991).
[31] R. J. Zatorre, A. C. Evans, E. Meyer, and A. Gjedde, ''Lateralization of phonetic and pitch discrimination in speech processing,'' Science **256**, 846–849 (1992).
[32] J. R. Binder, S. M. Rao, T. A. Hammeke, F. Z. Yetkin, A. Jesmanowicz, P. A. Bandettini, E. C. Wong, L. D. Estkowski, M. D. Goldstein, V. M. Haughton, and J. S. Hyde, ''Functional magnetic resonance of human auditory cortex,'' Ann. Neurol. **35**, 662–672 (1994).
[33] T. M. Talavage and W. B. Edminster, ''Saturation and nonlinear responses in auditory cortex,'' Neuroimage, **7**, S362 (1998) (Abstract).
[34] B. G. Goodyear and R. S. Menon, ''The effect of absolute luminous intensity on BOLD MRI response in primary visual cortex,'' *Proceedings of the 5th ISMRM Meeting*, Vol. 1, 1997 (Abstract).

Temporal resolution and temporal masking properties of transient stimuli: Data and an auditory model

Lutz Wiegrebe
Zoologisches Institut, Universität München, Luisenstr. 14, 80333 München, Germany

Katrin Krumbholz
MRC Centre for the Neural Basis of Hearing, Department of Physiology, University of Cambridge, Downing Street, Cambridge CB2 3EG, United Kingdom

(Received 14 May 1998; revised 21 July 1998; accepted 29 January 1999)

Temporal resolution is often measured using the detection of temporal gaps or signals in temporal gaps embedded in long-duration stimuli. In this study, psychoacoustical paradigms are developed for measuring the temporal encoding of transient stimuli. The stimuli consisted of very short pips which, in two experiments, contained a steady state portion. The carrier was high-pass filtered, dynamically compressed noise, refreshed for every stimulus presentation. The first experiment shows that, with these very short stimuli, gap detection thresholds are about the same as obtained in previous investigations. Experiments II and III show that, using the same stimuli, temporal-separation thresholds and duration-discrimination thresholds are better than gap-detection thresholds. Experiment IV investigates the significance of residual spectral cues for the listeners' performance. In experiment V, temporal separation thresholds were measured as a function of the signal-pip sensation level (SL) in both forward- and backward-masking conditions. The separation thresholds show a strong temporal asymmetry with good separation thresholds independent of signal-pip SL in backward-masking conditions and increasing separation thresholds with decreasing signal-pip SL in forward-masking conditions. A model of the auditory periphery is used to simulate the gap-detection and temporal-separation thresholds quantitatively. By varying parameters like auditory-filter width and transduction time constants, the model provides some insight into how the peripheral auditory system may cope with temporal processing tasks and thus represents a more physiology-related complement to current models of temporal processing. [S0001-4966(99)01805-6]

PACS numbers: 43.66.Ba, 43.66.Dc, 43.66.Fe, 43.66.Jh [JWH]

INTRODUCTION

The temporal resolution of the human auditory system is often measured by the detection of silent gaps in white or narrow-band noise (for example Plomp, 1964; Buunen and Valkenburg, 1979; Forrest and Green, 1987). Using wide-band or high-pass filtered noise, gap detection thresholds were shown to be approximately 2 ms. The gap-detection paradigm was modified in several ways to obtain a measure of the rate of decay of auditory sensation. In a gap-detection experiment, Plomp (1964) decreased the level of the noise burst following the gap relative to that of the first burst. He suggested that the gap-detection threshold measured as a function of the level of the second noise burst traces the rate of decay of auditory sensation. Penner (1977) showed that the gap-detection paradigm is related to forward masking. When the noise burst following the silent gap was shortened to 2 ms, and thereby, the gap-detection paradigm was transferred into a forward-masking paradigm, performance remained constant. Penner also pointed out that Plomp's (1964) measure of the rate of decay does not depend on the duration of the first noise burst.

Ronken (1970) and Henning and Gaskell (1981) followed a different approach to investigate the temporal resolution of the auditory system. Ronken examined the discriminability of stimuli which differed only in their phase spectra. He used pairs of 250-μs clicks. The results indicated that the auditory system can discriminate between a weak click followed by a strong click and the time reversed signal (a strong click followed by a weak one) when the two were about 1 ms apart. Henning and Gaskell (1981) repeated Ronken's (1970) experiment using 20-μs clicks. They obtained resolution thresholds down to 200 μs. The difference in resolution threshold relative to the gap-detection experiments of one order of magnitude has been unexplained so far (Green, 1985).

Penner *et al.* (1972) introduced the ''critical masking interval,'' a temporal analog of the critical band concept. They determined click-detection thresholds as a function of the duration of a broadband noise masker where the click was temporally centered in the noise. The idea of a temporal analog of spectral processing also inspired Moore *et al.* (1988) and Plack and Moore (1990) to measure the ''temporal window,'' a temporal analog of the psychophysically determined auditory filter. In analogy to the notched-noise method to evaluate auditory-filter shapes (Patterson, 1976), the experimental task was the detection of a tone pip presented at a variable position in the temporal gap of a broadband noise. As in the derivation of auditory filters, a rounded-exponential or exponential function was fitted to the data to produce a temporal window. The temporal-window model was successfully used to predict the results of a vari-

ety of temporal resolution tasks, however, it has not been tested with the data obtained by Henning and Gaskell (1981) or by Ronken (1970).

Although the temporal-window model predicts gap-detection data well, it does not provide insight into how the auditory system might perform the temporal analysis and into which physiological parameters influence temporal resolution. Here, we introduce an auditory model of temporal processing based on Meddis' and Hewitt's (1991a,b) computer model of the auditory periphery. In order not to restrict model performance by assuming a (naturally artificial) decision criterion, the ''optimal detector'' strategy proposed by Dau *et al.* (1996) was employed to simulate psychophysical thresholds in the auditory model. By varying parameters of the auditory model like the auditory-filter bandwidth or time constants associated with mechano-neural transduction, some insight can be gained into which physiological processing stages may influence temporal processing.

Three exploratory experiments were performed (experiments I–III). In experiment I, listeners had to perform a gap-detection task but with very short signals before and after the gap. Experiment II investigated nonsimultaneous masking by a noise pip using another noise pip as the signal. In experiment III, listeners had to detect an increase in the duration of a single noise pip.

Experiment IV was designed as a control experiment to investigate the relevance of spectral magnitude information for the current experimental tasks. In experiment V, we used the paradigm of experiment II and measured temporal-separation thresholds as a function of signal-pip sensation level (SL) in backward- and forward-masking conditions.

I. EXPERIMENTS

A. Experiments I–III: Gap detection, nonsimultaneous masking, and duration discrimination for transient stimuli

The following experiments are designed to investigate auditory temporal processing using transient stimuli. Starting with a repetition of the gap-detection paradigm using very short noise pips before and after the gap, temporal processing thresholds in tasks more similar to those of Ronken (1970) and Henning and Gaskell (1981) are investigated (experiment II). The third experiment tries to relate the results of experiment II to a duration-discrimination paradigm.

1. Stimuli

The stimuli consisted of pips with a 6-dB down duration of 0.3 ms and a Gaussian envelope. In experiments I and III, the pip in one interval included a steady state portion of variable duration. The amplitude spectrum of a pair of short *tone* pips shows peaks at frequencies corresponding to the reciprocal of the peak-to-peak temporal separation and spectral troughs midway between the peaks. As this spectral ripple does not occur in the spectrum of a single pip, a two-pips vs one-pip discrimination may be based on spectral cues instead of the temporal cues addressed in this study. Accordingly, we used noise as a carrier. Using a stimulus envelope with a 6-dB down duration of only 0.3 ms, a Gaussian noise carrier with its inherent random envelope fluctuation may ''fill'' the stimulus envelope to a highly variable extent. To ensure a proper representation of the stimulus envelope, the noise carrier was dynamically compressed in the following way. First the noise was digitally band-pass filtered between 6 and 18 kHz, second it was scaled to values between -1 and 1; and third the amplitude fluctuations of the noise were dynamically compressed by processing each amplitude value with the function,

$$Ac = \frac{2}{e^{-12A}+1} - 1. \tag{1}$$

Ac is the compressed amplitude value, and A is the uncompressed value of the amplitude. A 10-ms burst of compressed noise is shown in Fig. 1A while Fig. 1B shows a burst of Gaussian noise with equal energy. The noise was refreshed for each stimulus presentation. All stimuli were generated digitally and played back at a sampling frequency of 50 kHz on a DSP32c System board (Loughborough Sound Images).

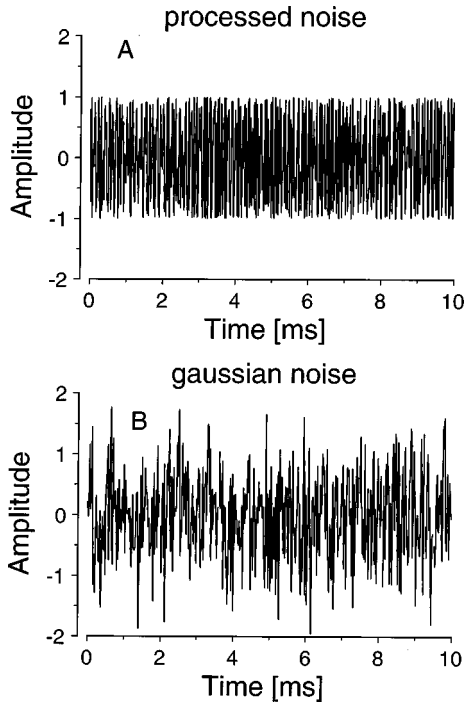

FIG. 1. Comparison between a 10-ms sample of noise processed as described in the Stimuli section (upper panel A) and a sample of Gaussian noise (lower panel B). The high-pass filtering and the dynamic compression limit the range of amplitude fluctuations strongly. Nevertheless, the processed noise sounds ''noisy'' and does not have any tonality.

The overall stimulus energy was equalized for the two intervals and a ± 5-dB roving level was used to prevent listeners from using possible residual loudness cues (average level=25 dB SL for a single noise pip). Although equating energy does not necessarily give equal loudness of the stimuli presented in the two intervals, all listeners confirmed that loudness did not serve as a reliable cue to perform the desired task, due to the roving-level paradigm.

For experiments I–III, stimuli were presented in the free sound field in a room ($5\times10\times3.5$ m) which was echo free above 200 Hz. The speaker was a Technics EAS 10 TH800B with a flat frequency response from 5 kHz to >100 kHz. It

was positioned 1 m above the walking grid at a distance of 3.1 m from the listener who was seated on a chair that ensured a fixed head position. Free-field stimulation was initially used because, with a fixed head position, it provides the most reliable stimulus presentation which was verified with a B&K 4165 microphone mounted at the head position.

2. Procedure

An adaptive, two-alternative, forced-choice task was used with a three-down one-up rule which estimates the 79.4% correct value of the psychometric function (Levitt, 1971). The independent variable was either the temporal separation within the pip pair (experiments I and II) or the pip duration (experiment III). To mark the beginning of an observation interval, each interval was preceded by a faint 200-ms 3-kHz pure tone and a 500-ms gap. The listeners' task was to indicate the interval which contained the stimulus with the temporal gap (experiment I), the interval containing the two noise pips (signal plus masker pip, experiment II) or the interval with the longer-duration stimulus (experiment III). Visual feedback was provided in all experiments. In an experimental run, 11 reversals according to the three-down, one-up rule were obtained. Temporal separations were changed in steps of 50% for reversals 1 and 2, in steps of 10% for reversals 3–5, and in steps of 5% for reversals 6–11. The average of reversals 6–11 was taken as the threshold temporal separation for this run. Thresholds presented here were derived from a minimum of three runs obtained on different days.

3. Listeners

Three listeners aged 25–31 took part in the experiments I–III. Listener LW was the first author; listener KK was the second author. All listeners had absolute thresholds within 10 dB of the 1969 ANSI standard at audiometric frequencies between 250 Hz and 8 kHz. Before data collection, listeners were given several hours of training until stable performance was achieved.

4. Experimental tasks and results

Experiment I is a replication of the classical gap-detection experiment using transient stimuli and compressed noise. Listeners had to discriminate between a noise pip with a steady state portion and a pair of noise pips with a peak-to-peak temporal separation of the same duration as the steady state portion of the pip in the other observation interval. Figure 2A shows an example of the two stimuli to be discriminated with the peak-to-peak temporal separation set to the average perceptual threshold of 1.99 ms. For the individual thresholds and standard deviations, see Table I, row 1.

In experiment II, the detection of a second (signal) noise pip was measured as a function of the peak-to-peak temporal separation between the signal and masker pip (see Fig. 2B). As in experiment I the total energy for the two intervals was equalized and the presentation level was again roved by ± 5 dB. The average threshold peak-to-peak separation time in the pip pair was 0.76 ms, that is, considerably less than in experiment I. An example of the two intervals with the average threshold separation is given in Fig. 2B; individual data and standard deviations are given in Table I.

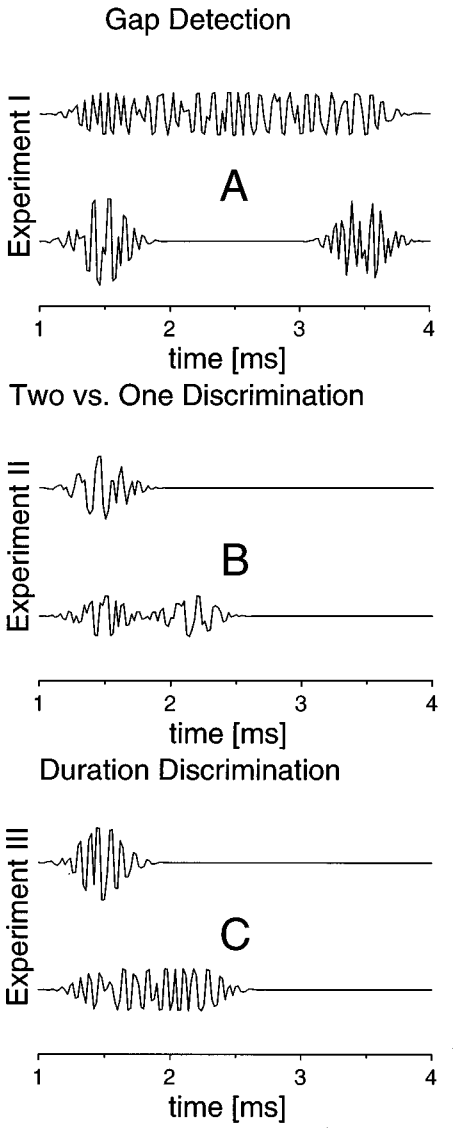

FIG. 2. Examples of stimuli for experiments I–III. Panel A corresponds to experiment I, panel B to experiment II, and panel C to experiment III. The stimuli are plotted with a temporal separation or steady state duration in which the upper and lower stimulus were just discriminable. The upper and lower stimuli are shown with equal energies.

Experiment III was designed as a duration-discrimination experiment. Listeners had to discriminate between a standard noise pip with a 6-dB duration of 0.3 ms and a noise pip with a steady state portion of variable duration. On average, listeners could just discriminate between a noise pip without a steady state portion and a pip with a 0.67-ms steady state portion. Two intervals with the steady state portion set to the threshold duration are shown in Fig. 2C. Again, individual data and standard deviations are given in Table I.

5. Interim discussion

The result of experiment I shows that the stimuli used in our study give rise to gap-detection thresholds that are very similar to those reported for broadband noise (Forrest and

TABLE I. Results of experiments I–III. The table shows threshold values and standard deviations for the three listeners as well as the averaged thresholds and derived standard deviations. Experiment I is a gap-detection experiment; experiment II involves discrimination of a pair of noise pips from a single pip. Experiment III involves discrimination of a single noise pip from a noise pip with a steady state portion of variable duration.

Subj.	KK	TB	LW	Average
Exp. I	1.96±0.37 ms	2.54±0.33 ms	1.47±0.39 ms	1.99±0.33 ms
Exp. II	0.68±0.18 ms	0.89±0.31 ms	0.71±0.12 ms	0.76±0.20 ms
Exp. III	0.53±0.19 ms	0.88±0.22 ms	0.60±0.12 ms	0.67±0.16 ms

Green, 1987). The experiment confirms the finding of Forrest and Green (1987) that gap-detection performance is largely independent of the duration of the preceding and following noise bursts. In experiments II and III, the thresholds were significantly below those of experiment I.

It is interesting to compare this pattern of thresholds in the different experiments with the listeners' reports about which perceptual cues they used in the different tasks. In experiments II and III, listeners reported that the single noise pip sounded sharp and temporally well-defined. Any blurring of the sharpness was interpreted as either the pip pair or the longer pip. In experiment I, listeners reported that the single noise pip with the steady state portion caused a noisy (hiss) sensation whereas the two noise pips produced a double-transient perception. The difference in the listeners' reports about the perceptual cues used in experiment I on the one hand, and in experiments II and III, on the other hand, may be related to the threshold differences. In the modeling section, we will show that the auditory model also predicts different thresholds for experiment I on the one hand, and experiments II and III, on the other hand (see below).

Although the thresholds found in experiments II and III are considerably lower than those of experiment I, they are longer than those reported by Henning and Gaskell (1981) for the discrimination of two double clicks with either the first or the second one of each pair attenuated by 6 dB. This difference may be due to a difference in stimulus duration: Henning and Gaskell's transients were rectangular clicks with a duration of only 20 μs which is considerably shorter than our 300-μs noise pips. The strong influence of the duration of the transient stimuli is also reflected in the divergence of the results of the original experiment by Ronken (1970) from those obtained by Henning and Gaskell (1981).

B. Experiment IV: The perceptual significance of spectral cues

Although the stimuli used in the current experiments consisted of noise as a carrier, the occurrence of spectral ripple cannot be prevented completely. The magnitude spectrum of a pair of noise pips sometimes had a ripple corresponding to the temporal separation of the two pips. The following experiment was designed to investigate the significance of these spectral cues for the paradigms used in experiments I and II.

1. Stimuli

For this experiment, stimuli were generated which preserved the spectral magnitude information of the noise pips but the phase spectra were randomized. Thus the temporal stimulus properties were manipulated in a way that prevents a meaningful use of temporal cues in the experimental task. In condition I, listeners had to detect a pair of noise pips as opposed to a single noise pip as a function of the peak-to-peak temporal separation within the pip pair. Thus the task was the same as in experiment II. In condition II, stimuli were produced exactly in the same way as in condition I and then their magnitude spectra were calculated using a 10.24-ms rectangular window centered around the masker pip for the standard interval or around the masker plus signal pip for the signal interval. A random-phase spectrum was produced and, using the inverse fast Fourier transform, a 10.24-ms noise burst was generated for each interval. The noise burst has the same magnitude spectrum as the masker pip or the masker plus signal pip from which it was derived but, unlike in condition I, the stimuli do not differ in duration or temporal envelope. Stimuli were generated digitally online at a sampling rate of 50 kHz using the Tucker Davis Technologies System II. As in all other experiments, the presentation level was roved over a 10-dB range to remove possible residual loudness cues after the stimuli in each interval had been equalized in energy. The average SL for a single noise pip or a noise burst was 25 dB. After comparing free-field results of experiment II with a replication of the experiment using headphones, experiment IV was performed in a strongly sound attenuated booth using Sennheiser HD540 Reference headphones and diotic stimulation.

2. Procedure and listeners

Here, psychometric functions for the discrimination of two noise pips versus a single pip were obtained in condition I. The independent variable was the peak-to-peak temporal separation between the masker and the signal pip. In condition II, the procedure was the same with the stimuli manipulated to preserve the magnitude spectra while the phase and duration information was manipulated so that it did not provide useful cues for the discrimination. Listeners were given an equal amount of training for the two conditions. The training consisted of 200 presentations of intervals with a fixed temporal separation between the signal and masker pip of 0.5, 1, 2, and 5 ms. For training purposes the first interval always contained both signal and masker pip and the second interval always contained the masker pip only. The training for condition II was performed in exactly the same way but with the stimuli manipulated as described above. During the training sessions, listeners were asked to establish their own perceptual criterion to do the task based on the feedback provided. Data collection immediately followed the training

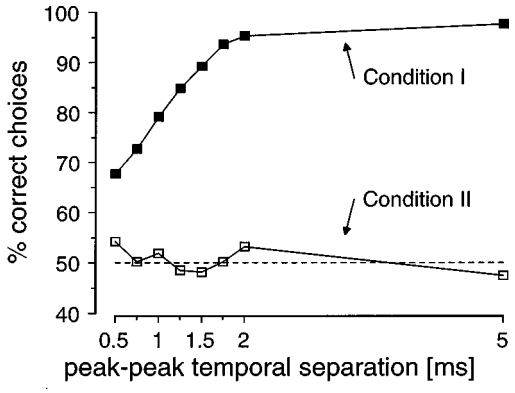

FIG. 3. Average psychometric functions for the detection of a signal noise pip masked by another, equal-level noise pip as a function of the peak-to-peak temporal separation between the signal and masker pip. Filled symbols show the performance for the pips (condition I); open symbols show the performance for noise bursts (condition II), where the magnitude spectra of the bursts are identical to those of the masker pip or signal plus masker pip in condition I.

session. Training and data collection was done first for condition I and then for condition II. Each point of the psychometric functions shown is derived from 99 trials distributed over 3 runs. Within each run, the temporal separation for each trial was chosen randomly from the range tested with the constraint that each separation was presented 33 times. Three listeners aged 24–40 took part in the experiment. Listener I was the first author; the other two listeners took part in the control experiment only. All listeners had absolute thresholds within 10 dB of the 1969 ANSI standard for audiometric frequencies between 250 Hz and 8 kHz.

3. Results and discussion

Psychometric functions for the two conditions are plotted in Fig. 3. Individual psychometric functions were very similar and thus, data were pooled across listeners. The filled symbols show performance for the detection of the signal pip as a function of the peak-to-peak temporal separation between signal and masker pip (condition I). The open symbols show performance for the discrimination of noise bursts (condition II) which provide the same spectral magnitude cues as the stimuli in condition I. For condition I, performance rises rapidly with increase in temporal separation. For condition II, performance is at chance level for all temporal separations tested. These results show that the spectral magnitude information which is fully preserved in condition II compared to condition I does not provide perceptual cues to do the temporal-processing task. The shape of the psychometric function in condition I is in agreement with the listeners' performance being based on temporal cues which become more salient as the temporal separation between the noise pips is increased.

C. Experiment V: Temporal separation thresholds for a noise pip masker as a function of signal-pip SL

In experiment II, we measured the detection of a noise pip masked by another, equal-level noise pip as a function of the peak-to-peak temporal separation between the signal and masker pip. It is not clear, however, which of the noise pips in the signal interval is the masker pip and which is the signal pip. If the level of either the first or the second noise pip is decreased relative to the other, the fainter noise pip can be regarded as the signal and the unattenuated pip as the masker. Thus it is possible to determine the temporal separation threshold as a function of the signal-pip SL.

1. Stimuli

The stimuli used for experiment V were very similar to those of experiment II. They consisted of a single (masker) noise pip in one observation interval and two noise pips (signal plus masker) in the other interval. In the latter interval, one of the pips was attenuated in steps of 5 dB relative to the other. Overall stimulus energy was equalized for the two intervals and then the presentation level was roved by ± 5 dB. Experiment V was performed in a strongly sound attenuated booth using AKG K240DF headphones and diotic stimulation.

2. Procedure

An adaptive, two-alternative forced-choice task was used with a three-down one-up rule which estimates the 79.4% correct value of the psychometric function (Levitt, 1971). The independent parameter was the peak-to-peak temporal separation between the signal and masker noise pip. In an experimental run, 11 reversals according to the three-down one-up rule were obtained. Temporal separations were changed in steps of 50% for reversals 1 and 2, in steps of 10% for reversals 3–5, and in steps of 5% for reversals 6–11. The average of reversals 6–11 was taken as the threshold for this run. Thresholds presented here were derived from a minimum of four runs on different days.

3. Listeners

Four listeners took part in this experiment; two of them were the authors, the other two were students aged 23 and 28 who were paid for their participation. All listeners had normal audiometric thresholds for pure tones between 250 and 8000 Hz according to the 1969 ANSI standard.

4. Results

Averaged temporal separation thresholds and standard deviations for the four listeners are shown in Fig. 4. Separation thresholds were obtained as a function of the signal-pip SL either when the signal pip preceded the masker pip (backward masking) or when the signal pip followed the masker pip (forward masking). At a signal-pip SL of 25 dB, masker and signal pip have the same SL. This condition cannot be interpreted as only forward or backward masking but must be seen as a weighted combination of the two. In backward-masking conditions, temporal-separation thresholds were on average below 1 ms. This was true for signal-pip SLs down to 10 dB SL. Even when the signal pip was only 5 dB SL on average, separation thresholds were only about 1.3 ms. In forward-masking conditions, however, separation thresholds increased rapidly with decreasing signal-pip SL.

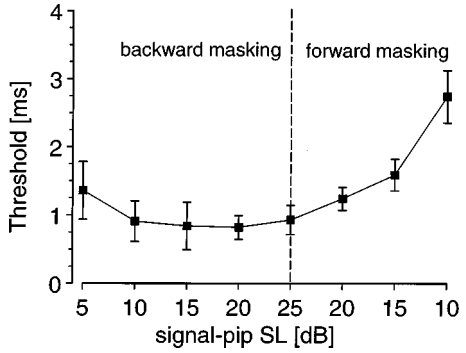

FIG. 4. Temporal-separation thresholds as a function of the signal-pip SL. The masker pip is always at 25 dB SL. SLs are given before level randomization. Backward masking refers to conditions where the signal pip precedes the masker pip; forward masking refers to conditions where the signal pip follows the masker pip. The central value at a pip SL of 25 dB (vertical dashed line) is the separation threshold when masker and signal pip have the same SL of 25 dB. Data are averaged over four subjects; the error bars represent standard deviations.

II. GENERAL DISCUSSION

Experiments I–III revealed that the transient stimuli we designed to investigate the limits of temporal resolution give gap-detection thresholds in agreement with previous studies. Experiments II and III showed that, in a different experimental setup, the use of transient stimuli can lead to considerably shorter temporal-processing thresholds than those obtained from gap detection. The experimental paradigm of experiment II was used in experiment V to obtain temporal-separation thresholds as a function of the position and SL of the signal pip relative to the masker pip. Temporal-separation thresholds are asymmetric with generally low thresholds in the backward-masking conditions and increasing separation thresholds with decreasing signal-pip SL in the forward-masking conditions.

Penner (1974) measured backward and forward masking produced by a 1-ms noise burst. The signal was a 0.1-ms rectangular click. Unlike in the current study, the independent variable in these experiments is the temporal separation of the signal and masker and the dependent variable is the signal level. Translated into the temporal-separation thresholds as obtained here, thresholds obtained in Penner's study were nonmonotonic and generally higher than those presented here. Several factors may account for the discrepancies between Penner's results and ours: First, in Penner's study, signals were filtered between 100 and 5000 Hz, whereas our signals were filtered between 6 and 18 kHz. Eddins *et al.* (1992) found that gap detection improves with increasing stimulus bandwidth. Second, Penner used Gaussian noise. For masker durations as short as 1 ms, fluctuations in the noise temporal envelope (Fig. 1) would cause large variability in the actual presentation level of the noise from one presentation to the next. These fluctuations were minimized in our study by using compressed noise. Third, it cannot be ruled out that the rectangular-click signal produces a more systematic spectral interference with the noise masker than the two noise signals we used. This may be a cause for the nonmonotonicity found in her backward- and forward-masking thresholds.

III. MODELING AUDITORY TEMPORAL PROCESSING

A. Current models of temporal resolution

Viemeister (1979) introduced a model of temporal processing designed to explain the limits of modulation detection. It consists of a broadband band-pass filter with a bandwidth of several kilohertz, half-wave rectification, and a first-order, low-pass filter with a cutoff frequency of about 60 Hz. This model was subsequently used by Forrest and Green (1987) to model the results of decrement and increment detection. Moore *et al.* (1988) and Plack and Moore (1990) presented a temporal analog of the auditory filter referred to as the ''temporal window.'' In the following, we present a simulation of the experiments based on a computer model of the auditory periphery as opposed to the current functional models.

B. Temporal resolution in an auditory model

The abovementioned models account well for gap and modulation detection data. To our knowledge, however, the results of the click-pair experiments by Ronken (1970) and Henning and Gaskell (1981) have not been simulated. Moreover, the current models do not provide insight into how temporal resolution is limited in the auditory system. Peripheral auditory filtering is known to be much more selective than implied by a band-pass filter with a bandwidth in the range of several kilohertz. Even more important, the low-pass cutoff frequency of mechanoelectrical transduction in inner hair cells is known to be at least one order of magnitude higher (cutoffs between 600 and 2000 Hz, cf. Palmer and Russell, 1986) than the one used in Viemeister's (1979) model. These higher cutoff frequencies allow for much more of the temporal fine structure of sounds to be processed in the auditory system; this fine structure appears to be involved in the perception of, for example, complex tones (Shackleton and Carlyon, 1994), iterated rippled noise (Yost *et al.*, 1996), and in the encoding of pure-tone frequency (Moore, 1997).

1. Model structure

The model introduced here is based on the computer model of the auditory periphery by Meddis and Hewitt (1991a,b). The model consists of broadband filtering to simulate the outer- and middle-ear transfer functions (second-order butterworth filters with cutoff frequencies of 450 and 8000 Hz, cf. Meddis and O'Mard, 1997) and a fourth-order gammatone filterbank with a variable number of filters per critical band. The filterbank is followed by a bank of simulated inner hair cells (Meddis, 1988). The output of this stage is spike probability as a function of time for each frequency channel defined by the filterbank. For the simulations, 24 channels equally spaced on a equivalent rectangular bandwidth (ERB) scale (Moore and Glasberg, 1987; Glasberg and Moore, 1990) between 1 and 15 kHz were used. The multi-channel output of the hair-cell bank is then summed over all frequency channels. This seems justified because (1) as shown in the control experiment, performance is based on temporal not spectral processing and (2) cochlear-nucleus onset units which supposedly play an im-

portant role for the coding of transient stimuli are known to receive input from a very wide frequency range (Winter and Palmer, 1995).

2. Modeling procedure and decision criterion

The auditory model was included in a threshold estimation procedure that precisely simulated the psychoacoustical experiment including the refreshing of the noise for each presentation and the roving level. In an adaptive 2AFC procedure, two stimuli were presented to the auditory model in each trial and the decision process had to select one of them according to a decision mechanism.

The output of the auditory model as outlined above is spike probability as a function of time summed over all frequency channels. The decision mechanism which works on the auditory-model output is based on the ''optimal detector'' strategy introduced into psychoacoustical modeling by Dau *et al.* (1996): Using this decision process, one does not have to specify in which respect the spike-probability function is supposed to differ between the two observation intervals of an experimental trial. By calculating correlations between the model outputs for the two observation intervals and a ''template,'' the decision mechanism derives its own ''optimal'' decision variable. The template was derived by presenting the model with 20 presentations of the standard interval in a clearly above-threshold condition (Dau *et al.*, 1996): For the simulation of gap-detection thresholds (experiment I), this standard interval was a noise pip with a 4-ms steady state portion. For the simulation of experiments III and V, this standard interval was a single noise pip. The 20 model responses to the standard interval were averaged to form the template. The template was normalized to unity. In the adaptive 2AFC paradigm, the correlation between the template and the output of the model for each of the two observation intervals is calculated. For the simulation of gap detection, the interval which gives a higher correlation with the template is interpreted as the stimulus without a gap; in the simulation of experiments III and V, the interval which gives a higher correlation with the template is interpreted as the interval which contains the pip without a steady state portion (experiment III) or as the interval which contains the masker pip only (experiment V). The decision reached in this way is used in the adaptive procedure to estimate the model threshold. The overall sensitivity of the decision mechanism can be manipulated by adding noise to the model output for both observation intervals.[1] The variance of this *internal* noise was adjusted in the simulation of experiment V to give the right temporal separation threshold when the first and the second noise pip are at the same level. The internal-noise variance and thus the model sensitivity was fixed for all simulations presented here.

3. Modeling results and discussion

Temporal-separation thresholds in Fig. 4 are replotted as a solid line in Fig. 5. The simulation using the auditory model is shown by the dashed line. The auditory model produces temporal-separation thresholds in good agreement with the experimental data.

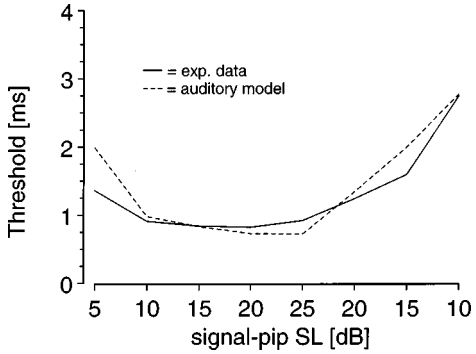

FIG. 5. Comparison of the temporal-separation thresholds obtained experimentally (solid line) with the simulation results of the auditory model (dashed line). Apart from the backward-masking data for a signal-pip SL of 5 dB, where the model performance is worse than the experimental data, model results are in good agreement with the data of experiment V.

The auditory model was then tested in experiment III, where the task was to discriminate between a single noise pip and a noise pip with a variable steady state duration. All model parameters remained unchanged. The threshold steady state portion necessary to discriminate a noise pip from an elongated noise pip was 0.69 ms, which is again in good agreement with the value of 0.67 ms found in experiment III (Table I).

The next test for the auditory model was a simulation of experiment I which was the gap-detection task. All model parameters including the internal-noise variance remained unchanged; the template was derived as described above. The template is always derived from an above-threshold standard interval which, in this case was a 4-ms noise burst without a temporal gap.

The experimental threshold averaged over four listeners was 1.99 ms. The auditory model revealed a gap-detection threshold of 1.7 ms which is in reasonable agreement with experiment I. Thus the difference in temporal thresholds for experiment I on the one hand and experiments II, III, and V on the other hand is preserved in the auditory simulation. This results from the fact that the auditory simulation (and presumably also the listener) uses different templates derived from the different standard intervals to make a decision. One might ask why not use the template for experiments III and V for experiment I because thresholds are lower in experiments III and V than in experiment I. However, if one used the single-pip template of experiments III and V for the gap detection in experiment I, both the standard interval (noise burst without gap) and the signal interval (two noise pips with temporal gap) differ strongly from the template which does not help to discriminate the two. The template as it is used here is optimized to discriminate between signal and standard interval in a specific experimental paradigm by deriving the template from the corresponding standard interval in this experiment.

C. Test of different auditory-model parameters

In this section, we investigate how specific changes to parameters of the auditory model influence performance of the model in a temporal-processing task. These simulations may provide some insight into which physiological stages of

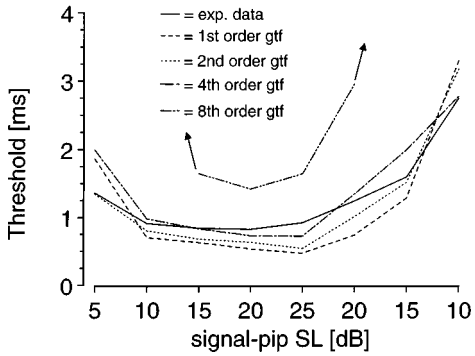

FIG. 6. Model performance as a function of the order of the gammatone filters used to simulate peripheral filtering (parameter *n* in the impulse response). The solid line shows the experimental data; the other temporal separation thresholds are for a filter order of one (dashed line), two, (dotted line), four (dash-dotted line equals standard filter order) and eight (dash-dot-dotted line).

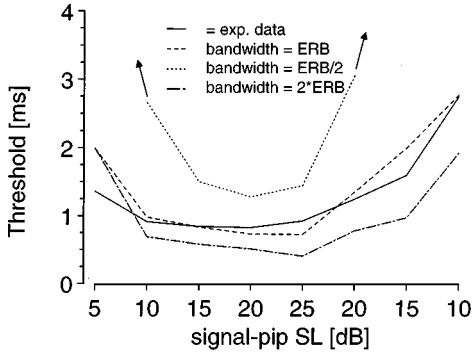

FIG. 7. Model performance as a function of the gammatone-filter bandwidth (parameter *b* in the impulse response). The solid line shows the experimental data; the other temporal-separation thresholds are for half the standard bandwidth (dotted line), standard bandwidth, (dashed line), and double the standard bandwidth (dash-dotted line). With increasing filter bandwidth, the temporal-separation thresholds improve indicating the trade-off between spectral and temporal selectivity.

peripheral auditory processing influence temporal resolution in the auditory system. Specifically, we investigate the influence of the sharpness of auditory filters, their bandwidths, and time constants associated with the simulated inner hair-cell/synapse transduction.

1. Auditory-filter order and bandwidth

In the auditory model, peripheral auditory filtering is simulated with a gammatone filterbank. The impulse response of a gammatone filter, $gt(t)$, is

$$gt(t) = at^{(n-1)} e^{-2\pi bt} \cos(2\pi f_c t + \phi),$$

where *n* is the filter order and fc is the filter center frequency (Patterson, 1994). The parameter *b* determines the bandwidth of the filter; it is related to the filter center frequency via the equivalent rectangular bandwidth (ERB) by

$$\mathrm{ERB} = 24.7 + 1.018 * fc,$$

$$b = 1.019 * \mathrm{ERB},$$

(Patterson, 1994). The gammatone filter can be manipulated by changing *n* or *b*. Both of these manipulations influence the filter bandwidth. However, whereas *n* determines the rising slope of the filter impulse response, *b* determines the falling slope and thus a different influence of the two manipulations on the temporal separation thresholds in backward- and forward-masking conditions may be expected. First, we varied the filter order, *n*, from one to eight in doublings while leaving all other model parameters constant. The simulated temporal separation thresholds are plotted in Fig. 6 for a filter order of one (dashed line), two (dotted line) four (dash-dotted line; standard filter order), and eight (dash-dot-dotted line). Experimental data are replotted from Fig. 4 (solid line). With decreasing filter order, temporal separation thresholds improve while the frequency selectivity of the gammatone filters deteriorates. Changing the filter order does not change exclusively backward or forward masking but seems to affects both.

For the next simulations, we fixed the gammatone-filter order at a value of four but varied the filter bandwidth. In the standard condition, the ERB of the gammatone filters corresponds to the values determined psychophysically (Moore and Glasberg, 1987; Glasberg and Moore, 1990). In variation I, we halved the auditory-filter bandwidth relative to the standard condition; in variation II, we doubled the bandwidth. The simulation results are shown in Fig. 7 in the same format as in the previous figure. Experimental data are shown by the solid line; the simulation with ERB bandwidths as suggested by Glasberg and Moore (1990) is shown by the dashed line (standard condition); the simulation with half the suggested bandwidths is shown by the dotted line and the simulation with double the suggested bandwidths is shown by the dash-dotted line. As the filter order, the filter bandwidth influences temporal-separation thresholds in a systematic way. Spectrally narrower filters lead to increased temporal-separation thresholds; filters that are spectrally broader than the values used in the standard condition lead to lower temporal-separation thresholds.

Separation thresholds obtained with a filter order of eight and an ERB bandwidth are almost identical to the thresholds obtained with a filter order of four and a bandwidth of half the ERB. Figure 8 shows the impulse and frequency response of an auditory filter centered at 6 kHz with these sets of parameters. Whereas the two filters have the same $Q_{80\,\mathrm{dB}}$ widths, their impulse responses look slightly different with the eighth-order filter (upper row) having a delayed but then steeper upward slope. The outcome of the simulations suggests that the shape of the impulse response is not critical as long as the filter bandwidth is similar.

2. Inner hair-cell/synapse time constants

In the following simulations, we investigated the influence of different parameter sets for the simulated inner hair-cell/synapse transduction. Apart from the standard parameter set used here, we tested model performance with two additional sets of parameters which simulated synapse properties of either high spontaneous rate (HSR) auditory nerve fibers (Meddis, 1988) or medium spontaneous rate (MSR) fibers (Meddis *et al.*, 1990). Parameter sets for the standard condition and for the two variations are given in Table II. Model performance using these variations are plotted in Fig. 9. As in Figs. 6 and 7, the solid line is a replot from the experi-

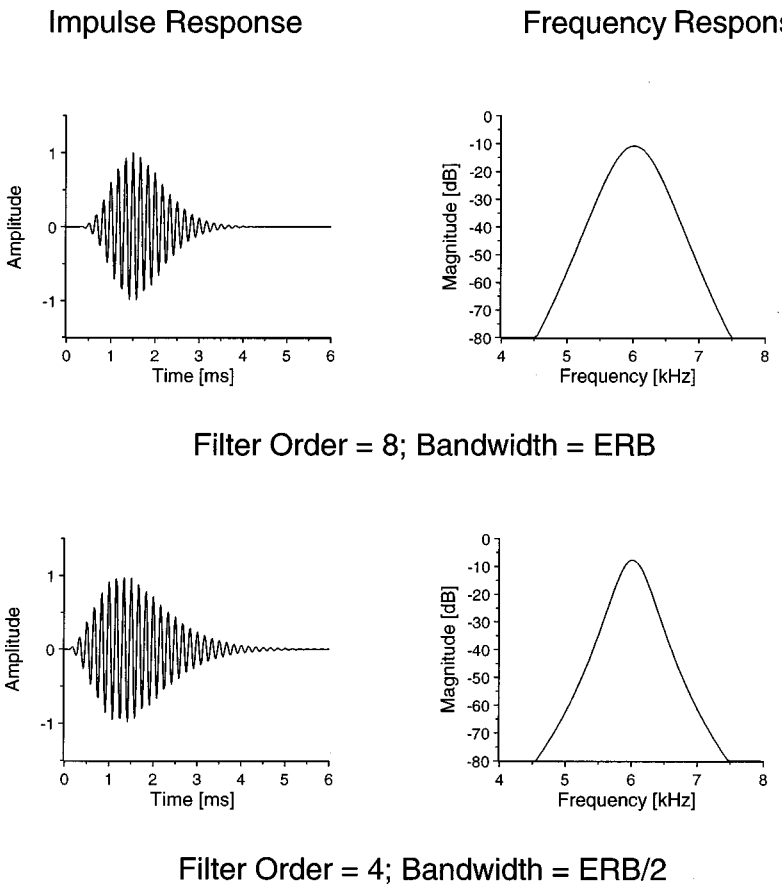

FIG. 8. Impulse and frequency response of a gammatone filter centered at 6 kHz. The upper row shows the response for an eighth-order filter with *b* derived from the ERB, the lower row shows the response of a fourth-order filter with *b* derived from half the ERB. The two filters show a similar bandwidth although changing the filter order affects mainly the rising slope and changing *b* affects mainly the falling slope of the impulse response. The temporal-separation thresholds are not significantly affected by the different shapes of the impulse response.

mental data. The dashed line shows the standard-model performance, the dotted line shows the model performance using a parameter set for an HSR nerve fiber, and the dash-dotted line shows the response with parameters for an MSR fiber. The difference in nerve-fiber type is reflected strongest in the forward-masking conditions. The simulations suggest that HSR fibers may be less accurate in their encoding of the envelope of transient stimuli than MSR fibers. This result is supported by physiological recordings from cat auditory-nerve fibers which show that HSR fibers are less accurate in their encoding of temporal stimulus features than MSR and LSR fibers (Silkes and Geisler, 1991; Joris *et al.*, 1994a,b).

TABLE II. Parameter sets of the simulated inner hair-cell/synapse transduction used for the auditory simulations. The standard condition refers to the parameter set used for all simulations unless otherwise specified. Variation I is based on Meddis (1988) for a high spontaneous rate auditory-nerve fiber and variation II is based on Meddis *et al.* (1990) for a medium spontaneous rate fiber.

	Standard	Variation I (Meddis, 1988)	Variation II (Meddis *et al.*, 1990)
constant *A*	100	5	10
constant *B*	6000	300	3000
release rate	2000	2000	1000
replenishment rate	5.05	5.05	5.05
loss rate	2500	2580	2500
reprocessing rate	66.31	66.31	66.31
recovery rate	6580	6580	6580
M	1	1	1
h	50 000	50 000	50 000

3. Summary of the influence of different auditory-model parameters

The simulations in the last sections show that temporal processing in a computer model of the auditory periphery is influenced by parameters of auditory filtering and by parameters associated with the generation of pre- and post-synaptic potentials in inner hair cells. Generally, increasing the auditory-filter width and thus shortening the filter-impulse response leads to improvement in temporal processing and a narrowing of the filter width leads to a deterioration in tem-

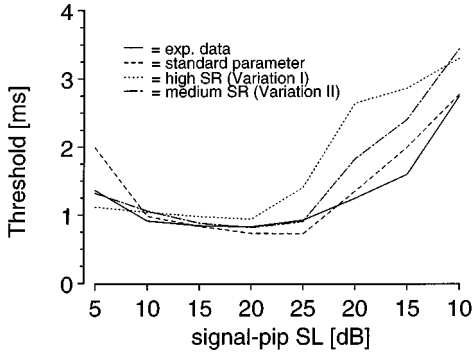

FIG. 9. Model performance for different sets of parameters for the simulated inner hair-cell/synapse transduction. As in the previous figures, the solid line shows the experimental data. The dashed line shows the simulated separation thresholds with the standard parameter set. The dotted line shows temporal-separation thresholds derived with a parameter set specified to simulate synapse properties for a high spontaneous-rate auditory-nerve fiber; the dash-dotted line shows thresholds derived with a parameter set specified to simulate a medium spontaneous-rate fiber. Parameters were taken from Meddis *et al.* (1990); a full listing of the parameter sets is found in Table II.

poral processing. Auditory-filter width can be changed by either changing the filter order or the bandwidth. Although changing the filter order affects only the rising part of the impulse response and changing the bandwidth affects only the falling part of the impulse response, no differential contributions of these model manipulations could be observed. This may result from the presence of an additional limitation on temporal processing associated with the generation of synaptic potentials in the simulated inner hair cells. In line with physiological findings, the current simulations suggest that MSR fibers provide a more accurate encoding of temporal stimulus features than HSR fibers. Thus based on the current simulation results, an influence of hair-cell synaptic properties and auditory-nerve fiber type on temporal processing may be assumed. The pronounced difference between temporal-separation thresholds in backward- and forward-masking conditions appears to be closely related to the temporal asymmetry observed in the auditory-filter impulse response and in the synaptic transmission.

In the current simulations, the best fit to the experimental data was always achieved using the standard model. This is not meant to imply that the standard-model parameter set is the only ''correct'' set. It may be possible to achieve equally good model performance with another set of parameters and/or by changing the internal-noise variance, i.e., the overall model sensitivity. The aim of the model manipulations presented here is only to investigate the influence of crucial parameters in the auditory model, not to specify their best values.

IV. CONCLUSIONS

The current experiments provide psychophysical measures of temporal processing. With the same transient stimuli, it was possible to replicate gap-detection experiments but, using a paradigm more similar to experiments on phase sensitivity with click pairs, considerably shorter thresholds for temporal processing were obtained. A control experiment showed that residual spectral information did not provide reliable detection cues. The stimuli used here enabled us to measure temporal-separation thresholds in backward- and forward-masking conditions. The separation thresholds show a strong temporal asymmetry with low thresholds in backward-masking conditions and increasing thresholds with decreasing signal-pip SL in forward-masking conditions. The different temporal-processing thresholds obtained in the different experimental paradigms can be quantitatively predicted using an auditory model of peripheral processing.

The auditory model is not designed to challenge current functional models of temporal resolution but to establish an auditory complement which may provide some insight into which properties of temporal processing are determined by peripheral stages of auditory processing and which properties reflect more central limitations. The current simulations suggest that auditory-filter bandwidth affects the temporal-separation thresholds which improve the lower the filter order and the broader their bandwidths. In line with physiological recordings from auditory-nerve fibers, the auditory model indicates that temporal processing is more accurate in medium spontaneous-rate fibers than in high spontaneous-rate fibers. Based on the current simulations, it appears that the acuity with which transient stimuli are perceived may be largely determined by features of the peripheral auditory system. The current auditory model is intended to illustrate the limitations of temporal processing based on general physiological properties of the auditory periphery. Although the model predicts the current data reasonably well, it may be the case that, for more complex temporal-processing tasks with longer-duration stimuli, more central limitations of auditory processing start to take over and the auditory model would need additional processing stages. This is suggested by properties of the temporal-window model by Moore *et al.* (1988) and Plack and Moore (1990) which shows much shallower upward and downward slopes than indicated by the temporal-separation thresholds measured here. Their data imply that detecting a tone pip within a temporal gap in broadband noise represents a more complex temporal-processing task which presumably involves higher-order auditory processing (Moore, personal communication). Thus for longer-duration stimuli and more complex experimental paradigms, central processing may impose further limits on the temporal processing of the human auditory system.

ACKNOWLEDGMENTS

We thank Dipl.-Ing. Wolfgang Schmid and Professor Hugo Fastl from the ''Technische Universität Muenchen'' for extensive experimental and technical support in experiments I–III. We thank our listeners for their participation in the experiments, and Dr. R.D. Patterson, Dr. R.P. Carlyon, and Professor B.C.J. Moore for helpful discussions and comments on earlier versions of the manuscript. We thank Dr. Van Summers and an unknown reviewer for very helpful comments on earlier versions of this manuscript. This study was supported by the Deutsche Forschungsgemeinschaft SFB 204 ''Gehör,'' Muenchen and the Medical Research Council, U.K.

[1]Instead of actually adding noise to the model output, the calculations can be performed in a less time-consuming way by accounting for the internal-noise variance in the decision module (see Appendix to Dau *et al.*, 1996).

Buunen, T. J. F., and Valkenburg, D. A. (**1979**). ''Auditory detection of a single gap in noise,'' J. Acoust. Soc. Am. **65**, 534–537.

Dau, T., Pueschel, D., and Kohlrausch, A. (**1996**). ''A quantitative model of the ''effective'' signal processing in the auditory system. I. Model structure,'' J. Acoust. Soc. Am. **99**, 3615–3622.

Eddins, D. A., Hall, J. W., and Grose, J. H. (**1992**). ''Detection of temporal gaps as a function of frequency region and absolute bandwidth,'' J. Acoust. Soc. Am. **91**, 1069–1077.

Forrest, T. G., and Green, D. M. (**1987**). ''Detection of partially filled gaps in noise and the temporal modulation transfer function,'' J. Acoust. Soc. Am. **82**, 1933–1943.

Glasberg, B. R., and Moore, B. C. J. (**1990**). ''Derivation of auditory filter shapes from notched-noise data,'' Hearing Res. **47**, 103–138.

Green, D. M. (**1985**). ''Temporal factors in psychoacoustics,'' in *Time Resolution in Auditory Systems*, edited by A. Michelsen (Springer, New York), pp. 122–140.

Henning, G. B., and Gaskell, H. (**1981**). ''Monaural phase sensitivity with Ronken's paradigm,'' J. Acoust. Soc. Am. **70**, 1669–1673.

Joris, P. X., Carney, L. H., Smith, P. H., and Yin, T. C. T. (**1994a**). ''Enhancement of neural synchronization in the anteroventral cochlear nucleus. I. Responses to tones at the characteristic frequency,'' J. Neurophysiol. **71**, 1022–1036.

Joris, P. X., Smith, P. H., and Yin, T. C. T. (**1994b**). ''Enhancement of neural synchronization in the anteroventral cochlear nucleus. II. Responses in the tuning curve tail,'' J. Neurophysiol. **71**, 1037–1051.

Levitt, H. (**1971**). ''Transformed up–down methods in psychoacoustics,'' J. Acoust. Soc. Am. **49**, 467–477.

Meddis, R. (**1988**). ''Simulation of auditory-neural transduction: Further studies,'' J. Acoust. Soc. Am. **83**, 1056–1063.

Meddis, R., and Hewitt, M. J. (**1991a**). ''Virtual pitch and phase sensitivity of a computer model of the auditory periphery. I: Pitch identification,'' J. Acoust. Soc. Am. **89**, 2866–2882.

Meddis, R., and Hewitt, M. J. (**1991b**). ''Virtual pitch and phase sensitivity of a computer model of the auditory periphery. II: Phase sensitivity,'' J. Acoust. Soc. Am. **89**, 2883–2894.

Meddis, R., and O'Mard, L. (**1997**). ''A unitary model of pitch perception,'' J. Acoust. Soc. Am. **102**, 1811–1820.

Meddis, R., Hewitt, M. J., and Shackleton, T. M. (**1990**). ''Implementation details of a computer model of the inner hair-cell/auditory-nerve synapse,'' J. Acoust. Soc. Am. **87**, 1813–1816.

Moore, B. C. J. (**1997**). *An Introduction into the Psychology of Hearing* (Academic, London), pp. 178–185.

Moore, B. C. J. (**1998**). Personal communication.

Moore, B. C. J., and Glasberg, B. R. (**1987**). ''Formulae describing frequency selectivity as a function of frequency and level and their use in calculating excitation patterns,'' Hearing Res. **28**, 209–225.

Moore, B. C. J., Glasberg, B. R., Plack, C. J., and Biswas, A. K. (**1988**). ''The shape of the ear's temporal window,'' J. Acoust. Soc. Am. **83**, 1102–1116.

Palmer, A. R., and Russell, I. J. (**1986**). ''Phase locking in the cochlear nerve of the guinea pig and its relation to the receptor potential of inner hair cells,'' Hearing Res. **24**, 1–15.

Patterson, R. D. (**1976**). ''Auditory filter shapes derived with noise stimuli,'' J. Acoust. Soc. Am. **59**, 640–654.

Patterson, R. D. (**1994**). ''The sound of a sinusoid: Spectral models,'' J. Acoust. Soc. Am. **96**, 1409–1418.

Penner, M. J., Robinson, C. E., and Green, D. M. (**1972**). ''The critical masking interval,'' J. Acoust. Soc. Am. **52**, 1661–1668.

Penner, M. J. (**1974**). ''Effect of masker duration and masker level on forward and backward masking,'' J. Acoust. Soc. Am. **56**, 179–182.

Penner, M. J. (**1977**). ''Detection of temporal gaps in noise as a measure of the decay of auditory sensation,'' J. Acoust. Soc. Am. **61**, 552–557.

Plack, C. J., and Moore, B. C. J. (**1990**). ''Temporal window shape as a function of frequency and level,'' J. Acoust. Soc. Am. **87**, 2178–2187.

Plomp, R. (**1964**). ''Rate of decay of auditory sensation,'' J. Acoust. Soc. Am. **36**, 277–282.

Ronken, D. (**1970**). ''Monaural detection of a phase difference between clicks,'' J. Acoust. Soc. Am. **70**, 1091–1099.

Shackleton, T. M., and Carlyon, R. P. (**1994**). ''The role of unresolved harmonics in pitch perception and frequency modulation detection,'' J. Acoust. Soc. Am. **95**, 3529–3540.

Silkes, S. M., and Geisler, C. D. (**1991**). ''Responses of ''lower-spontaneous-rate'' auditory-nerve fibers to speech syllables presented in noise. I: General characteristics,'' J. Acoust. Soc. Am. **90**, 3122–3139.

Viemeister, N. F. (**1979**). ''Temporal modulation transfer functions based upon modulation thresholds,'' J. Acoust. Soc. Am. **66**, 1364–1380.

Winter, I. M., and Palmer, A. R. (**1995**). ''Level dependence of cochlear nucleus onset unit responses and facilitation by second tones or broadband noise,'' J. Neurophysiol. **73**, 141–159.

Yost, W. A., Patterson, R. D., and Sheft, S. (**1996**). ''A time-domain description for the pitch strength of iterated rippled noise,'' J. Acoust. Soc. Am. **99**, 1066–1078.

Factors affecting the loudness of modulated sounds

Brian C. J. Moore, Deborah A. Vickers, and Thomas Baer
University of Cambridge, Department of Experimental Psychology, Downing Street, Cambridge CB2 3EB, England

Stefan Launer
Phonak AG, Laubisrutistrasse 28, CH-8712 Stafa, Switzerland

(Received 15 June 1998; revised 30 November 1998; accepted 22 February 1999)

Loudness matches were obtained between unmodulated carriers and carriers that were amplitude modulated either periodically (rates between 2 and 32 Hz, modulation sinusoidal either on a linear amplitude scale or on a dB scale; the latter is called dB modulation) or with the envelope of the speech of a single talker. The carrier was a 4-kHz sinusoid, white noise, or speech-shaped noise. Both normally hearing subjects and subjects with cochlear hearing loss were tested. Results were expressed as the root-mean-square (rms) level of the modulated carrier minus the level of the unmodulated carrier at the point of equal loudness. If this difference is positive, this indicates that the modulated carrier has a higher rms level at the point of equal loudness. For normally hearing subjects, the results show: (1) For a 4000-Hz sinusoidal carrier, the difference was slightly positive (averaging about 0.7 dB). There was no significant effect of modulation rate or level over the range 20–80 dB SL. (2) For a speech-shaped noise or white noise carrier, the difference was close to zero, although for large modulation depths it tended to be negative. There was no clear effect of level (over the range 35–75 dB SPL) or modulation rate. For the hearing-impaired subjects, the differences were small, but tended to be slightly negative for both the 4000-Hz carrier and the noise carriers, when the modulation rate was above 2 Hz. Again, there was no clear effect of overall level. However, for dB modulation, the differences became more negative with increasing modulation depth. For modulation rates in the range 4–32 Hz, the results could be fitted reasonably well using the assumption that the loudness of modulated sounds is based on the rms value of the time-varying intensity of the response of the basilar membrane (taking into account the compression that occurs in the normal cochlea). The implications of the results for the fitting of multi-band compression hearing aids and for the design of loudness meters are discussed. [S0001-4966(99)04705-0]

PACS numbers: 43.66.Cb, 43.66.Mk, 633.66.Sr, 43.66.Ts [RVS]

INTRODUCTION

There have been many studies of the loudness of steady, long-duration sounds; see for example, Scharf (1978) and Plack and Carlyon (1995). Also, models exist which can predict the loudness of steady sounds with reasonable accuracy (Zwicker and Scharf, 1965; Zwicker and Fastl, 1990; Moore *et al.*, 1997). However, there are only a few studies of the loudness of sounds which fluctuate over time (Bauch, 1956; Zwicker, 1977; Fastl, 1993; Zhang and Zeng, 1997). This question is of both theoretical and practical interest. The theoretical interest stems from the possible influence of basilar-membrane nonlinearity on loudness perception. The input–output function of the normal basilar membrane shows a strongly compressive response for stimuli with frequencies close to the characteristic frequency (CF) of the place being studied (Sellick *et al.*, 1982; Robles *et al.*, 1986; Ruggero, 1992; Ruggero *et al.*, 1997). The compression is fast acting, and it is strongest at mid-range levels (30–80 dB SPL), becoming weaker at very low levels, and perhaps at very high levels (Robles *et al.*, 1986; Ruggero, 1992). It seems likely that the loudness perception of fluctuating sounds would be affected by this fast-acting compression. In particular, sounds with the same rms level but with different peak factors might have a different loudness, since their ''effective'' excitation levels would differ after the compression was applied (Carlyon and Datta, 1997). Also, the variation of the compression with overall level could affect the loudness of modulated sounds.

The practical interest lies in two applications. The first is the design of meters intended to indicate the subjective loudness of sounds, as opposed to the physical intensity (Fastl, 1993; Stone *et al.*, 1997). While such meters can give a reasonable indication of the loudness of sounds and of how loudness varies with duration, it is not clear how well the meters work for modulated sounds. Further data on the loudness of modulated sounds are needed for comparison with the readings of the meters.

The second practical application is the design and fitting of hearing aids intended to compensate for the effects of loudness recruitment. Many current hearing aids have multiple channels, with independent compression (automatic gain control) applied in each channel. One stated goal of such aids is to amplify sounds for a hearing-impaired person in such a way as to restore perceived loudness to normal (Allen and Jeng, 1990; Pluvinage, 1989; Cox, 1995; Kiessling, 1997; Cornelisse *et al.*, 1995). Procedures for fitting hearing aids based on this concept have been developed (Cox, 1995; Cornelisse *et al.*, 1995). The required level-dependent gain in each channel is often deduced from loudness scaling data obtained using stationary signals, such as

bursts of sinusoidal tones or bandpass noise (Kiessling, 1997; Allen and Jeng, 1990; Kollmeier and Hohmann, 1995). An alternative approach is to use loudness models (Moore and Glasberg, 1997; Launer, 1995) or empirical data relating loudness to absolute threshold (Killion and Fikret-Pasa, 1993) to predict the required level-dependent gains from absolute thresholds (Moore *et al.*, 1999a,b). Again, the loudness models and the empirical data have been based on the loudness of stationary sounds only. However, in natural listening conditions, many sounds, most notably speech, vary markedly over time. Therefore it is questionable whether gain values deduced using stationary signals are appropriate.

Data on the loudness of amplitude-modulated sinusoidal carriers were presented by Bauch (1956); see also Zwicker and Fastl (1990). Subjects were required to adjust the level of a steady tone to match the loudness of a modulated tone; a switch was provided so that subjects could listen to each tone for as long as they liked before making a match. For very low modulation rates, below about 10 Hz, the loudness of the modulated tone corresponded to its peak level. For higher rates, up to about one-half of the critical bandwidth, the loudness decreased, and corresponded to the rms level. For rates larger than about one-half of the critical bandwidth, the loudness increased, as the spectral components were resolved by the auditory system. Results were similar for carrier frequencies from 400 to 4000 Hz and for levels ranging from 30 to 70 dB SPL.

There are, however, some problems with the data of Bauch. First, it appears that data were obtained for only two subjects, and results were presented for only one. It is well known that loudness judgments can vary markedly across subjects, so several subjects are needed to obtain reasonably representative results. Second, the raw data were not presented. Rather, only idealized curves were presented. Third, only the steady tone was adjusted in level. In studies of this type it is important to obtain matches with both the steady tone varied and the modulated tone varied, to reduce bias effects; examples of such bias effects are given later in this paper.

Moore *et al.* (1998b) also presented data on the loudness of amplitude-modulated tones. Loudness matches were made between a steady 4000-Hz sinusoid and a 4000-Hz sinusoidal carrier that was amplitude modulated at various rates and depths. The modulated and steady sounds were presented in regular alternation, and matches were made with both the steady tone varied and the modulated tone varied (the same method was used in this paper, and is described in more detail later on). The mean results differed from those of Bauch (1956). For modulation rates above 4 Hz, at the point of equal loudness the modulated tone had a slightly higher rms level than the steady tone and a markedly higher peak level. For modulation rates of 4 Hz and below, the modulated and steady tones had almost equal rms levels at the point of equal loudness. There was no significant effect of overall level or of modulation depth. Thus, in contrast to the claim of Bauch (1956), loudness was not determined by the peak level, even for the lower modulation rates.

Zhang and Zeng (1997) attempted to replicate some of the results of Bauch (1956), as reported in Zwicker and Fastl (1990), but using a more modern method. They tested both normally hearing subjects, and subjects with cochlear implants who were electrically stimulated, but only the results for the former will be discussed here. They used an adaptive procedure with two interleaved staircases to determine the point of equal loudness (Jesteadt, 1980). Only the steady tone was adjusted in level. They used both a two-tone complex (i.e., a pair of beating tones) and a three-tone complex with components added in two different starting phases, producing either amplitude modulation or quasi-frequency modulation. All sounds were centered at 1000 Hz. For intermediate modulation rates, at the point of equal loudness the steady sound had a slightly lower rms level than the modulated sound, as was also reported by Moore *et al.* (1998b). However, for very low modulation rates (below 10 Hz), the steady sound had a slightly higher rms level than the modulated sound at the point of equal loudness. The results for very low rates fell between those reported by Bauch (1956) and those reported by Moore *et al.* (1998b).

Zhang and Zeng (1997) also estimated points of equal loudness for a steady white noise and a white noise that was amplitude modulated at various rates and depths. If loudness is determined by the peak level for low modulation rates, then for a modulation index of 1.0 the steady sound should have a rms level 4.2 dB higher than the modulated sound at the point of equal loudness. For modulation rates up to about 100 Hz, the rms level of the steady sound at the matching point was higher than that of the modulated sound. However, the difference was generally much less than 4.2 dB. The biggest difference was about 3.5 dB for a modulation rate of 10 Hz and an overall level of 45 dB SPL. For an overall level of 30 dB SPL, the difference reached about 2 dB for modulation rates of 40 Hz and below, while for an overall level of 70 dB SPL the difference was generally less than 1 dB for all modulation rates.

From this brief survey, it is apparent that data on the loudness of modulated sounds differ somewhat across studies and are far from conclusive in determining the main factors that influence loudness for such sounds. In this paper, we present a series of studies of the loudness of modulated sounds, using both normally hearing and hearing-impaired subjects. The method was designed to reduce bias effects as far as possible. The following questions were addressed: (1) Which measure of level is relevant for the perception of loudness; the overall rms level, the peak level, or some other quantity? (2) Does the relevant quantity depend on overall level? (3) Does the relevant quantity depend on the modulation waveform? (4) How is loudness influenced by modulation with the envelope of speech rather than by periodic modulation? (5) Is the effect of modulation rate and depth on loudness influenced by the type of carrier used (sinusoid or noise)? (6) Are the answers to questions 1–5 different for normal-hearing and for hearing-impaired subjects? One would expect differences in loudness perception between normally hearing subjects and subjects with cochlear hearing loss if it is indeed the case that the loudness of fluctuating sounds is influenced by compression on the basilar membrane; cochlear hearing loss is associated with reduced compression (Moore, 1995; Moore and Oxenham, 1998).

I. GENERAL METHOD

A. Procedure

The modulated and steady sounds were presented in regular alternation to one ear with 500-ms silent intervals between successive sounds. Within a given run, either the steady or the modulated sound was fixed in level and the level of the other sound was varied to determine the level corresponding to equal loudness. The starting level of the variable sound was chosen randomly from within a certain range. In early experiments, the range was from 10 dB above absolute threshold (10 dB SL) to 90 dB SPL. However, in some cases, this meant that the starting level was far from the final matching level. In later experiments, the starting level was chosen randomly from within a range of ± 10 dB around the level of the fixed sound. Some conditions were run choosing the starting level in both ways. No systematic discrepancies were found between the mean results for the two cases. However, the differences between the results for the two types of match (steady sound varied or modulated sound varied) tended to be larger when the range of starting levels was larger.

The levels of the sounds were adjusted using a programmable attenuator (Tucker-Davis PA4; see below for details). Subjects were told to press button ''1'' if the modulated sound appeared louder. Whenever this button was pressed, either the level of the modulated sound was decreased for the next presentation or the level of the steady sound was increased (depending on which sound was being varied). They were told to press button ''2'' if the steady sound appeared louder; this button had the opposite effect. If no button was pressed, then the level stayed the same indefinitely. A change from pressing button 1 to pressing button 2, or vice versa, was called a turnaround. The step size for the change in level of the variable tone was 3 dB until two turnarounds had occurred and was 1 dB thereafter. Subjects were instructed to ''bracket'' the point of equal loudness several times, by making the modulated sound clearly louder than the steady sound and then clearly softer, and then to use the buttons to make the sounds equal in loudness. When subjects were satisfied with a match, they indicated this by pressing a third button, and the level at this point was taken as the matching level. To reduce bias effects, for each condition five trials were run with the steady tone varied, and five trials were run with the modulated tone varied.

B. Stimuli

The steady and modulated sounds each had 20-ms raised-cosine rise/fall ramps. The overall duration varied across experiments (between 500 and 2000 ms) and will be given for each experiment. The carrier was a 4-kHz sinusoid, a white noise or a speech-shaped noise; more details of this are given later. The relatively high frequency for the sinusoidal carrier was chosen so that spectral sidebands would not be resolved even for the highest modulation rate used. Modulation rates ranged from 2 to 32 Hz, chosen to cover the range of prominent modulations in speech (Houtgast *et al.*, 1980). The overall level ranged from 20 to 80 dB SL for the normally hearing subjects. Levels will be given individually for hearing-impaired subjects. The modulation was either sinusoidal on a linear amplitude scale or sinusoidal on a dB scale (Moore *et al.*, 1996). For convenience, we will refer to these as ''linear'' modulation and ''dB'' modulation. The equation specifying the stimulus waveform for the latter is

$$F(t) = a10^{r[\sin(2\pi f_m t + \theta) - 1]/40} \sin(2\pi f_c t), \quad (1)$$

where a is the peak amplitude, r is the modulation depth (peak-to-valley ratio in dB), f_m is the modulator frequency, θ is a starting phase for the modulator, which was randomly selected on each trial, and f_c is the carrier frequency.

This form of modulation was used as it allows the peak value of the envelope relative to the rms value to be manipulated over a wide range. This was intended to allow a clearer assessment of whether loudness at low modulation rates is related to the peak level or the rms level. For example, for dB modulation with $r = 60$ dB, the ratio of the peak value of the envelope to the rms value of the envelope is 8.1 dB. Figure 1 shows waveforms for linear modulation with $m = 0.5$ (top left) and 1 (top right). With $m = 0.5$, the ratio of the level at the peak to the level at the valley is 9.54 dB. The figure also shows waveforms for dB modulation with $r = 9.54$ dB (bottom left) and 60 dB (bottom right). For moderate modulation depths the waveforms for linear and dB modulation are rather similar when the peak-to-valley ratios are equated. However, at large modulation depths, dB modulation gives a waveform with a high peak factor; brief high-amplitude portions occur with near-silent intervals between. The modulation depths used, for both linear and dB modulation, will be specified separately for each experiment. In some experiments, the envelope of the speech of a single talker was used as a modulator; more details are given later.

Stimuli were digitally generated using a Tucker-Davis Technologies (TDT) AP2 array processor in a host PC connected via an optical interface to a 16-bit digital-to-analog converter (TDT DD1, 50 kHz sampling rate). Stimulus levels were controlled by a TDT PA4 programmable attenuator. Stimuli were delivered using Sennheiser HD414 earphones. Subjects were tested in a double-walled sound attenuating chamber.

C. Subjects

Both normally hearing and hearing-impaired subjects were used. The former all had thresholds no greater than 10 dB HL at the standard audiometric frequencies. Their ages ranged from 20 to 53 years. No consistent effect of age on the results was found. The numbers of subjects and the characteristics of the individual hearing-impaired subjects will be given with the descriptions of the individual experiments. All subjects were given at least 2 h of training to familiarize them with the task.

D. Measurement of absolute thresholds

Absolute thresholds for the steady sounds were measured using an adaptive two-interval, two-alternative forced-choice procedure, with a three-down one-up stepping rule tracking the 79.4% correct point on the psychometric func-

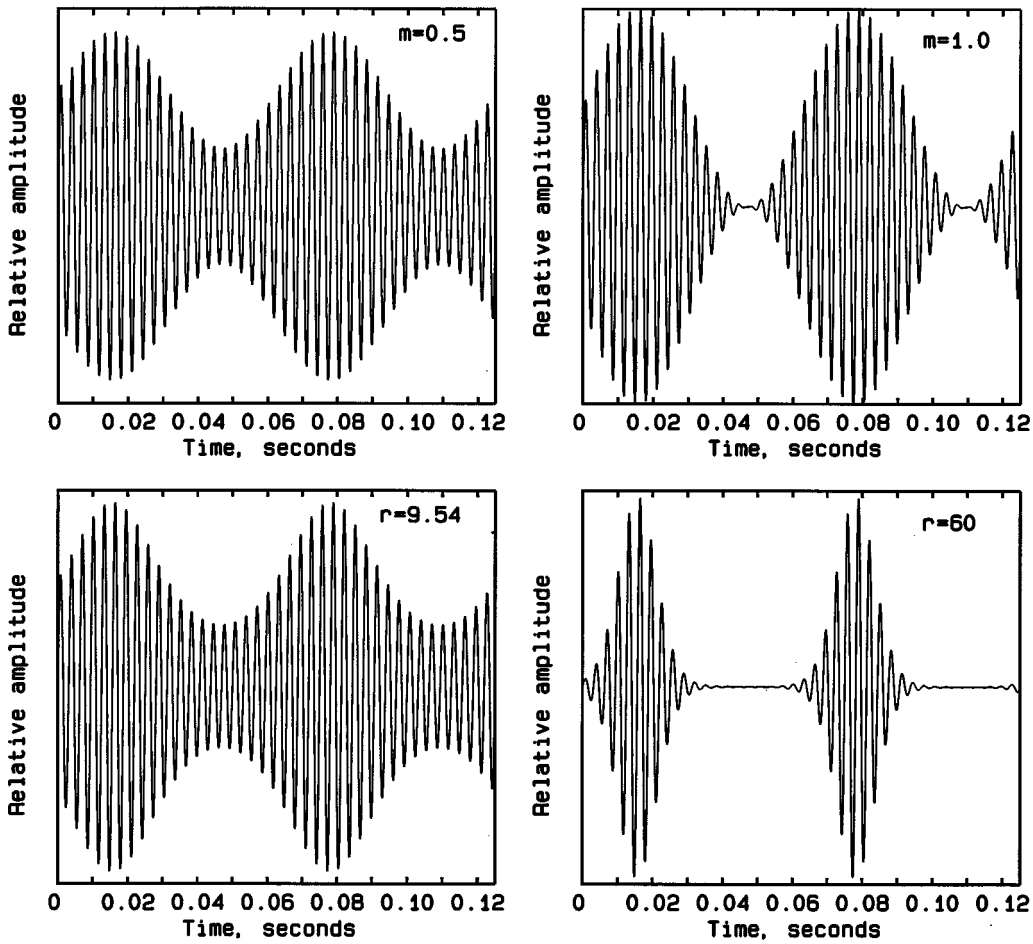

FIG. 1. Waveforms for linear modulation with $m=0.5$ (top left) and 1 (top right); dB modulation with $r=9.54$ dB (bottom left) and 60 dB (bottom right).

tion. The step size was 5 dB up to the first four reversals, and 2 dB thereafter. Twelve reversals were obtained and threshold was estimated as the mean level at the last eight. Each threshold reported is the mean of at least three runs.

II. EXPERIMENT 1. EFFECTS OF LEVEL, MODULATION RATE, AND MODULATION DEPTH USING A 4-kHz CARRIER AND NORMALLY HEARING SUBJECTS

A. Conditions and subjects

When the steady sound was fixed in level, the level was either 20, 40, 60, or 80 dB above absolute threshold (20 to 80 dB SL). When the modulated sound was fixed in level, rms levels were the same as for the fixed levels of the steady sounds. Modulation rates of 2, 8, and 32 Hz were used. Modulation depths were $m=0.5$ and 1.0 for linear modulation and $r=9.54$, 20, and 60 dB for dB modulation. The depth of $r=9.54$ dB was chosen as it gave the same peak-to-valley ratio as for linear modulation with $m=0.5$. For the rates of 8 and 32 Hz, the duration of each sound, including the 20-ms rise/fall times, was 500 ms. For the 2-Hz rate, the duration of each sound was increased to 1000 ms, so that two full cycles of modulation were included within the overall duration of the stimulus. Four normally hearing subjects were tested in all conditions, with the exception that one subject reported that the stimuli at 80 dB SL were uncomfortably loud, and she was not tested at that level. Four additional subjects were tested in some conditions with large modulation depths, and gave essentially the same results as the first four subjects.

B. Results

All overall levels were expressed as root-mean-square (rms) values. To display the results, we have calculated the difference in level between the modulated and steady tones at the point of equal loudness, i.e., the level of the modulated tone minus the level of the steady tone. If the loudness were determined by rms level, the difference would be 0 dB. In the figures that follow, a dashed line is plotted at 0 dB to indicate where the points would lie in this case. If the loudness were determined by the peak level, the difference would be negative, the points would lie below the dashed line.

The pattern of results was similar across the four subjects and Fig. 2 shows mean results for linear modulation. Results are plotted separately for the case when the modulated sound was varied (open circles) and the case where the steady sound was varied (filled circles). Error bars indicate $\pm$ one standard error (SE) across subjects. The solid lines show the mean for these two cases. There are clear bias effects related to whether the modulated or steady sound was varied. At low SLs, subjects avoided adjusting the variable sound to a very low level; therefore, the open circles lie above the

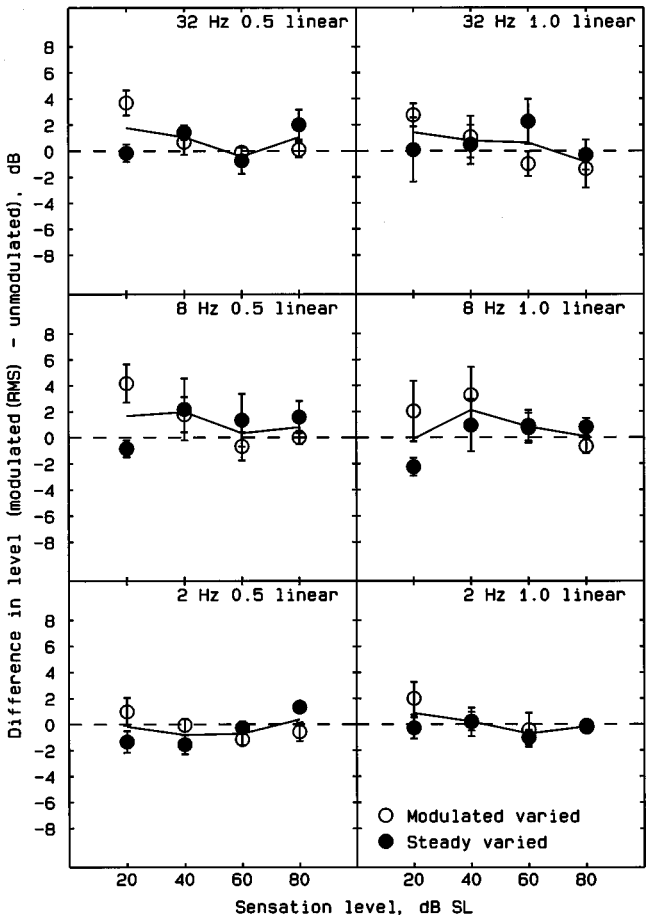

FIG. 2. Mean results of the normally hearing subjects for linear modulation of a 4000-Hz sinusoidal carrier. The figure shows the difference in level between the modulated and steady tones at the point of equal loudness, i.e., the level of the modulated tone minus the level of the steady tone. Results are plotted separately for the case when the modulated sound was varied (open symbols) and the case where the steady sound was varied (filled symbols). The solid line shows the mean for these two cases. Error bars indicate ± one standard error (SE) across subjects. Scores are plotted as a function of sensation level (SL); each panel shows results for one modulation depth and one modulation rate.

filled circles. At high SLs, subjects avoided adjusting the variable sound to a very high level; therefore the open circles lie mostly below the filled circles. Discounting these bias effects (i.e., looking at the mean for the conditions with the modulated tone varied and the steady tone varied—indicated by the solid line), most of the results lie close to 0 dB; the tones are equally loud when their rms levels are roughly equal. There is no clear effect of SL, although there is a slight trend for the differences to decrease slightly with increasing level; the mean differences (excluding the results for AO, who was not tested at 80 dB SL) are 1.2, 1.1, 0.5, and 0.2 dB for levels of 20, 40, 60, and 80 dB SL, respectively. There is a small effect of modulation rate; values tend to be slightly positive for rates of 8 and 32 Hz, but to lie close to zero for the 2-Hz rate. There is no clear effect of modulation depth.

For each subject, the data were averaged across conditions with the steady tone varied and with the modulated tone varied, and the resulting averages were subjected to a within-subjects analysis of variance (ANOVA) with factors modulation depth, modulation rate, and level. The results for subject AO were not included in the analysis as she was not tested at the highest level. None of the main effects or interactions was significant at the 0.05 level. The grand mean score (excluding the data for AO) was 0.74 dB, i.e., at the point of equal loudness the modulated tone was 0.74 dB higher in rms level than the steady tone. Based on a *t*-test, this is significantly greater than zero ($p<0.001$).

Figure 3 shows results for dB modulation. As for linear modulation, there are clear bias effects related to which sound was varied. Discounting these bias effects (i.e., looking at the mean indicated by the solid line), most of the results lie close to 0 dB; the tones are equally loud when their rms levels are roughly equal. There is a slight trend for the differences to decrease slightly with increasing level; the mean differences (excluding the results for AO) are 1.3, 1.5, 0.7, and −0.1 dB for levels of 20, 40, 60, and 80 dB SL, respectively. There is a small effect of modulation rate; values tend to be slightly positive for rates of 8 and 32 Hz, but to lie close to zero for the 2-Hz rate. There is no clear effect of modulation depth, even though changing the modulation depth resulted in large changes in the ratio of the peak value of the envelope to the rms value of the envelope.

For each subject, the data were averaged across conditions with the steady tone varied and with the modulated tone varied, and the resulting averages were subjected to a within-subjects ANOVA with factors modulation depth, modulation rate, and level (again, excluding the results for subject AO). None of the main effects or interactions was significant at the 0.05 level. The grand mean score (excluding AO) was 0.82 dB, which is significantly greater than zero ($p<0.001$).

The results for dB modulation with $r=9.54$ dB are very similar to those for linear modulation with $m=0.5$ (compare the left columns in Figs. 2 and 3), as would be expected from the physical similarity of the stimuli in these two cases. Also, the results for these two cases are very similar to those reported by Moore *et al.* (1998b). Moore *et al.* used a somewhat wider range of modulation rates (4 to 128 Hz) than in the present study, and they did find a significant effect of modulation rate; for linear modulation with $m=0.5$, the difference averaged across level increased from 0.4 to 1.5 dB as the modulation rate increased from 4 to 128 Hz, while for dB modulation with $r=9.54$ dB, the difference increased from 0.3 to 1.4 dB. Our results show a trend in the same direction. For linear modulation, the difference averaged across level and across the two modulation depths increased from 0.1 to 0.69 dB as the rate increased from 2 to 32 Hz. For dB modulation, the difference averaged across level and across the three modulation depths increased from 0.49 to 0.93 dB as the rate increased from 2 to 32 Hz. However, as noted above, the effects of modulation rate in the present study were not statistically significant.

C. Discussion

The results show that amplitude modulation had only a small effect on loudness; roughly, equal rms levels lead to equal loudness for steady and modulated carriers. The results for linear modulation differ from those presented by Bauch

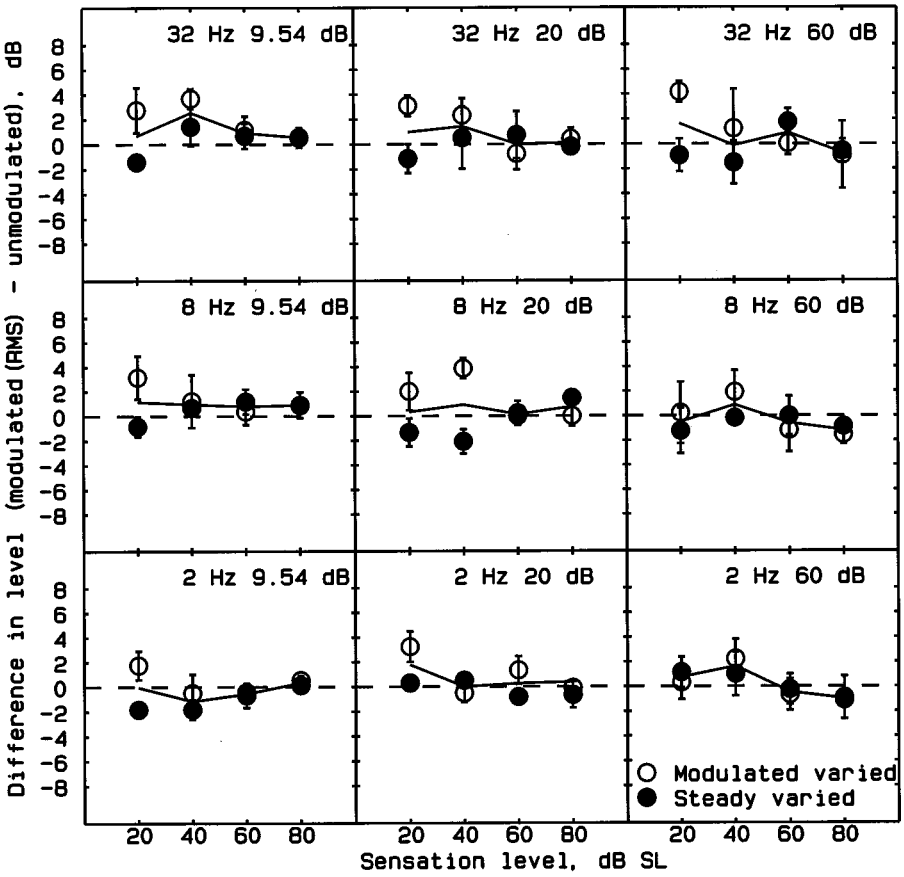

FIG. 3. As Fig. 2, but for dB modulation.

(1956). As described in the Introduction, he reported that, for modulation rates from about 25 Hz to one-half of the critical bandwidth, equal loudness occurred when the modulated and steady tones were equal in rms level, while for very low rates the steady tone had to be 3 dB (for $m=0.5$) or 4 dB (for $m=1$) higher in rms level than the modulated tone to achieve equal loudness. If plotted in the same way as in Fig. 2, this would give a score of -3 dB for the bottom-left panel and -4 dB for the bottom right panel. Like the results of Moore *et al.* (1998b), our results are not consistent with his suggestion that for very low modulation rates the loudness is determined by the peak level rather than the rms level.

Moore *et al.* (1998b) offered an explanation for the finding that for moderate modulation rates the modulated tone had to be slightly higher in level than the steady tone at the point of equal loudness, based on the compression that occurs on the basilar membrane. Zhang and Zeng (1997) have also suggested that the loudness of modulated sounds might be influenced by basilar-membrane compression (see also Carlyon and Datta, 1997). The argument of Moore *et al.* was as follows. Assume that the basilar-membrane input–output function for a tone close to CF has the form shown in Fig. 4. The absolute values on the ordinate are arbitrary, but they have been chosen so that a 100-dB input gives a 100-dB output, consistent with the idea that the compression arises from an active mechanism that plays no role at high levels (100 dB and above).

We have calculated the effects of applying this transfer function to the envelopes of our stimuli, assuming that the compression acts instantaneously. Consider as examples, two sounds, one steady and the other dB modulated with a depth of 9.54 dB, each with a rms level of 60 dB. For the steady sound, the output is 80 dB, i.e., the active mechanism is assumed to provide 20 dB of gain. For the modulated sound, the peak output level is 81.1 dB, the minimum is 78.5 dB, the rms value is 79.8 dB, and the mean value (calculated on an amplitude scale and then converted to dB) is also 79.8 dB. To make the rms value of the output 80 dB (the same as for the steady sound) the rms input level has to be increased to 60.8 dB. To make the mean value of the output equal to 80 dB, the rms value of the input has to be increased to 61 dB. Hence, if equal loudness occurred when the mean level of the output of the basilar-membrane transfer function was the same for the two sounds, the modulated sound would have to be about 1 dB higher in level than the steady sound. This

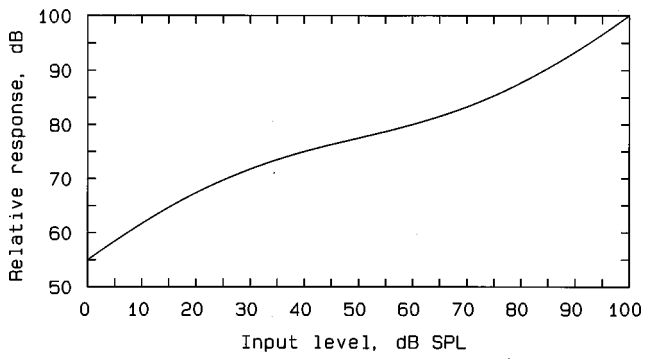

FIG. 4. Schematic basilar membrane input-output function for a tone with frequency close to CF.

TABLE I. Illustration of the calculated effects of basilar-membrane compression on dB-modulated tones, based on the input–output function shown in Fig. 4. All calculations were based on the envelopes of the stimuli. The first three columns show, in order, the input level of the steady tone, the modulation depth (r in dB) of the modulated tone, and the rms input level of the modulated tone required for equal loudness (averaged for modulation rates of 8 and 32 Hz). The final four columns show the rms input level of the modulated tone required to match the output for the steady tone, using the following measures of the output: the rms value, the mean value, the rms value of the intensity, and the mean of the intensity.

			rms input level for a match based on output			
Input, steady	r	Level of modulated tone for equal loudness	rms	Mean	rms of intensity	Mean of intensity
20	9.54	20.9	20.7	20.9	20.1	20.7
	20	20.7	22.3	23.6	20.3	22.3
	60	20.6	26.4	34.3	20.6	26.5
40	9.54	41.8	41.1	41.2	40.7	41.0
	20	41.2	43.6	44.4	42.1	43.6
	60	40.4	51.9	58.0	45.1	51.9
60	9.54	60.9	60.8	60.8	60.4	60.7
	20	60.1	62.4	63.1	61.2	62.4
	60	60.9	67.6	72.1	62.8	67.6
80	9.54	80.7	80.5	80.8	79.9	80.4
	20	80.4	81.4	82.6	79.7	81.4
	60	79.1	83.6	88.1	79.5	83.6

corresponds very well to the observed results, at least for modulation rates of 8 and 32 Hz.

For larger modulation depths, the results cannot be accounted for in terms of the rms or mean level after compression on the basilar membrane. This is illustrated in Table I. The first column shows the input level of the steady tone. The second column the modulation depth (r in dB) of the modulated tone, and the third column shows the rms input level of the modulated tone required for equal loudness to the steady tone at the specified level (averaged for modulation rates of 8 and 32 Hz). The fourth and fifth columns show the rms input level of the modulated tone needed to match the rms and mean output levels produced by the steady tone.

For $r = 9.54$ dB, the level of the modulated tone needed to produce the same output as the steady tone nearly matches the experimentally obtained value (column 3) for both the rms and mean measures; this is true for all four input levels of the steady tone (20–80 dB SL). In other words, equal rms or mean levels after compression give equal loudness. However, for higher modulation depths, the levels of the modulated tone required for equal rms or mean outputs as for the steady tone lie well above the experimentally obtained values. Conversely, the levels of the modulated tone required to give equal peak outputs as for the steady tone would lie well below the experimentally obtained values (not shown in the table).

Some researchers have suggested that, in the determination of loudness, the output of the cochlea is subjected to an expansive nonlinearity, such as exponentiation (Zeng and Shannon, 1994) or squaring (Schlauch *et al.*, 1998). Other research has also suggested that the auditory system processes an intensitylike quantity after basilar-membrane compression has been applied (Oxenham and Moore, 1995; Oxenham and Plack, 1997; Moore and Oxenham, 1998). To assess whether such a process might account better for our results, we investigated the effect of squaring the envelope of the output of the compressive nonlinearity prior to calculating the rms and mean values. The final two columns of Table I shows the rms input level of the modulated tone needed to achieve the same rms or mean value of the *squared* output as obtained for the steady tone. It may be seen that the levels so obtained using the rms measure match the experimentally obtained values reasonably well. The largest discrepancy is 4.7 dB for an input level of 40 dB and a modulation depth of 60 dB. All other discrepancies are less than 2 dB.

We conclude that, at least for modulation rates of 8 and 32 Hz, the loudness of modulated sounds is related to the rms value of the squared output of the basilar membrane, taking into account the compressive nonlinearity. In other words, it is related to the rms value of the time-varying intensity of the response of the basilar membrane. If this is correct, then the pattern of results should be different for subjects with cochlear hearing loss, since for them basilar-membrane compression is typically reduced or absent (Moore and Oxenham, 1998; Moore, 1995; Oxenham and Moore, 1995; Oxenham and Plack, 1997). If compression is absent, then equal loudness should be achieved when the modulated and steady sounds are matched for rms *intensity* (rather than rms amplitude). Thus the modulated tone should have a lower rms level than the steady tone at the point of equal loudness. The difference should become progressively more negative as the modulation depth increases. The next experiment tests this prediction.

III. EXPERIMENT 2. EFFECTS OF LEVEL, MODULATION RATE, AND MODULATION DEPTH USING A 4-kHz CARRIER AND HEARING-IMPAIRED SUBJECTS

A. Conditions and subjects

Five subjects with moderate to severe cochlear hearing loss were tested. Their absolute thresholds in dB HL for the ears tested are given in Table II (the table also shows the audiogram for subject AW, who was tested in later experi-

TABLE II. Audiometric thresholds in dB HL for the test ears of the six hearing-impaired subjects.

	Frequency						
	250	500	1000	2000	4000	6000	8000
DB (age 46)	5	5	10	30	60	70	80
DT (age 73)	20	10	5	60	65	60	60
AW (age 82)	66	81	67	67	63	64	81
PY (age 69)	35	40	45	55	55	65	70
AR (age 70)	35	45	45	40	50	55	60
VW (age 71)	40	45	55	55	60	60	80

ments). The hearing impairments were diagnosed as being of cochlear origin on the basis of lack of an air–bone gap, the presence of loudness recruitment, normal tympanograms, normal acoustic reflex thresholds, and lack of tone decay. The cause of the hearing loss was unknown for all subjects except DT, who had a noise-induced loss. The hearing loss at the test frequency ranged from 50 to 65 dB. The absolute thresholds in dB SPL ranged from 59 to 74. Subjects were tested at levels of 80 and 95 dB SPL, in the following conditions: (1) linear modulation with $m=0.5$ and 1.0 and modulation rates of 2, 4, 8, and 32 Hz; and (2) dB modulation with $r=10$, 30, 50, and 60 dB, and rates of 2, 4, 8, and 32 Hz. Durations were the same as for experiment 1.

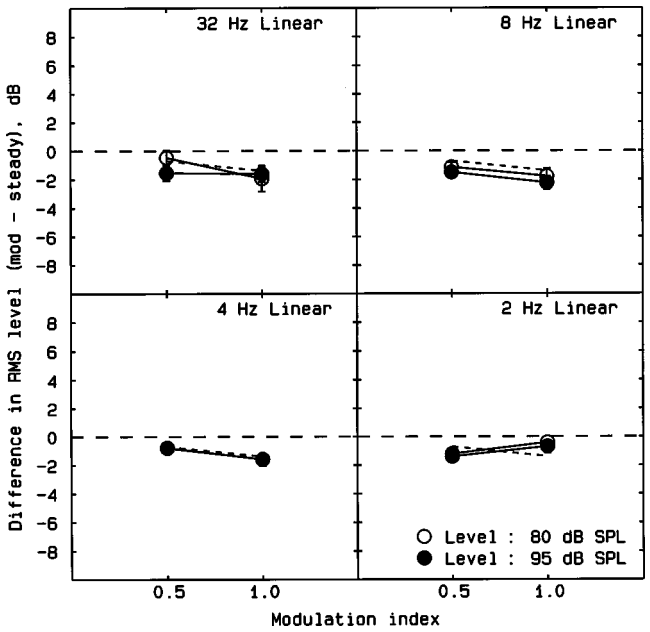

FIG. 5. Mean results of four hearing-impaired subjects for linear modulation of a 4000-Hz carrier. Difference scores are plotted as a function of modulation depth with overall level as parameter. Each panel shows results for one modulation rate. Error bars indicate ± one standard error (SE) across subjects. The dashed lines show predictions assuming that basilar membrane compression was absent and that equal loudness corresponded to equal rms intensities for the steady and modulated tones.

B. Results

All subjects gave results which were reasonably consistent and reproducible. Also, the results were similar across subjects. Bias effects, i.e., differences in the matches depending on whether the steady tone or the modulated tone was varied in level to determine the point of equal loudness, were similar in magnitude to those reported for the normally hearing subjects of experiment 1. In the figures that follow, only the mean results for these two cases (modulated varied or steady varied) will be presented. Figures 5 and 6 show the results for linear modulation and dB modulation, respectively. Error bars indicate ± one standard error (SE) across subjects; the small error bars indicate the consistency of results across subjects. For linear modulation, most of the values are slightly negative (−1 to −2 dB). There is no clear effect of modulation index, modulation rate, or sound level. For dB modulation, the values again tend to be slightly negative. For modulation rates of 32, 8, and 4 Hz, the values become slightly more negative with increasing modulation depth. Values are typically −1 dB for the 10-dB modulation depth, decreasing to −2 to −3 dB for the 60-dB depth. The dashed lines in Figs. 5 and 6 show predictions based on the analysis given earlier, assuming that the compressive nonlinearity on the basilar membrane was completely absent, and that equal loudness corresponded to equal rms intensities of the steady and modulated tones. For the modulation rates of 32, 8, and 4 Hz, the results fit the predictions very well. However, for the 2-Hz modulation rate there is no clear effect of modulation depth, and, for dB modulation, the obtained differences lie above the predicted differences.

For each subject, the data were averaged across conditions with the steady tone varied and with the modulated tone varied, and the resulting averages were subjected to a within-subjects ANOVA with factors modulation depth, modulation rate and level. For linear modulation, none of the main factors was significant at the 0.05 level, but the interaction of depth and rate was significant; $F(3,12)=3.85$, $p=0.038$. This reflects the finding that the difference became more negative with increasing modulation depth for rates of 32, 8, and 4 Hz, but it became more positive with increasing modulation depth for the 2-Hz rate. None of the other inter-

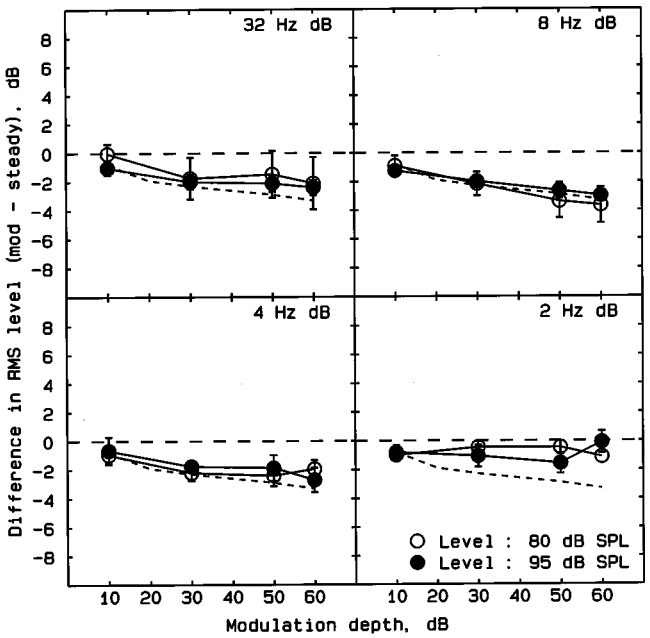

FIG. 6. As Fig. 5, but for dB modulation.

actions was significant. The grand mean score was −1.29 dB. Based on a *t*-test, this is significantly less than zero ($p < 0.001$). For dB modulation, the main effect of modulation depth was highly significant; $F(3,12) = 11.48$, $p < 0.001$. None of the other main effects was significant. The interaction of depth and rate was significant; $F(9,36) = 3.25$, $p = 0.005$. This reflects the finding that the difference became more negative with increasing modulation depth for rates of 32, 8, and 4 Hz, but did not change markedly with modulation depth for the 2-Hz rate. The grand mean score was −1.66 dB. This is significantly less than zero ($p < 0.001$).

Overall, the results are consistent with the prediction made earlier, that loss of basilar-membrane compression associated with cochlear hearing loss would lead to the modulated tone having a lower rms level than the steady tone at the point of equal loudness. They are also consistent with the idea that the loudness of modulated sounds is determined by a quantity related to the rms intensity of the response of the basilar membrane for modulation rates of 4 Hz and above.

IV. EXPERIMENT 3. LOUDNESS MATCHES FOR A 4000-Hz SINUSOID MODULATED WITH THE ENVELOPE OF SPEECH

A. Stimuli and subjects

In this experiment, rather than using periodic modulation, we used as a modulator the envelope of the speech from a single female talker. We did this to improve the chances of finding an influence of the peak factor on loudness; such a modulator leads to a very high peak-to-rms ratio. Also, we thought that loudness judgments might be more related to the peak value of the envelope when the modulator is not periodic. The speech was taken from a compact disc (CD) of test sounds recorded by ReSound Corporation. The passage lasts approximately 1 min. The passage was digitized and pauses longer than 250 ms were edited out by hand, giving a file of duration 50 s. The envelope was extracted by calculating the rms amplitude of the speech in a 10-ms long sliding temporal window. The ratio of the peak value of the envelope to the rms value was 13.9 dB. The carrier was a 4000-Hz sinusoid. Although the modulator was derived from speech, the modulated carrier did not sound speechlike.

Pilot experiments indicated that, to get an impression of the overall loudness of the modulated sinusoid, a reasonably long sample had to be presented. However, the use of stimuli with very long durations required trials that were excessively long. We chose to use a duration of 2 s for the speech-modulated carrier, including the 20-ms raised-cosine rise/fall ramps. The 2-s envelope sample was selected randomly from the complete envelope waveform file. On average, the ratio of the peak value of the envelope to the rms value for a 2-s sample was 10.4 dB. The comparison sound was an unmodulated 4000-Hz carrier with a duration of 500 ms. We did not use a 2-s duration for the comparison sound as loudness does not seem to change with duration once the duration exceeds about 200 ms (Scharf, 1978). Seven normally hearing subjects and three hearing-impaired subjects, AW, VW, and DT, were tested. For the normally hearing subjects, carrier levels of 20, 40, 60, and 80 dB SL were used; corresponding levels in dB SPL were about 9 dB higher. However, two subjects, LW and JP, found the highest level to be unpleasant, and so they were not tested at that level. For the hearing-impaired subjects, levels of 80, 85, 90, and 95 dB SPL were used for all subjects. Absolute thresholds at the test frequency in dB SPL were 72, 69, and 74 dB SPL, for AW, VW, and DT, respectively, so the lowest SL used was 6 dB. Subject VW was also tested using a level of 75 dB SPL.

B. Results

The results differed somewhat across the normally hearing subjects, so individual results are shown in Fig. 7. The group average results are also shown. In this case error bars represent the standard error across subjects. For four subjects, the differences in level lie close to the dashed line, indicating that, at the point of equal loudness, the speech-modulated carrier had a similar rms level to the unmodulated carrier. For two subjects, DV and SR, the points tend to lie above the dashed line, indicating that, at the point of equal loudness, the speech-modulated carrier had a slightly higher rms level than the unmodulated carrier. For the remaining subject, LW, the points tend to lie below the dashed line. For the mean results, the points lie close to the dashed line, but on average are slightly above it. The average difference was 0.74 dB. Based on a *t*-test, this is significantly greater than zero ($p < 0.01$). The effect of level varied across subjects, but overall there was a slight trend for the difference to become more negative with increasing level. A within-subjects ANOVA was conducted with factor level, excluding the data for the two subjects who were not tested at the highest level. This showed a significant effect of level; $F(3,12) = 5.05$, $p = 0.017$.

Individual results for the hearing-impaired subjects are shown in Fig. 8. The results for subject AW showed more variability than those for the other two subjects, and bias effects were also larger. The points for AW lie close to the dashed line, indicating that, at the point of equal loudness, the speech-modulated carrier had a similar rms level to the unmodulated carrier. For the other two subjects, the points lie below the dashed line, indicating that, at the point of equal loudness, the speech-modulated carrier had a slightly lower rms level than the unmodulated carrier. This effect is in the same direction as found for periodic linear modulation and dB modulation. A within-subjects ANOVA with factor level showed no significant effect of level. The grand mean score was −1.83 dB. This is significantly less than zero ($p < 0.001$).

Overall, the results with the speech-modulated carrier are similar to those for the carrier that was modulated with periodic functions; for normally hearing subjects, equal rms levels lead roughly to equal loudness, but there is a small trend for the modulated sound to have a higher rms level than the unmodulated sound at the point of equal loudness. For hearing-impaired subjects, the reverse trend is found (except for AW). The difference between the normal and

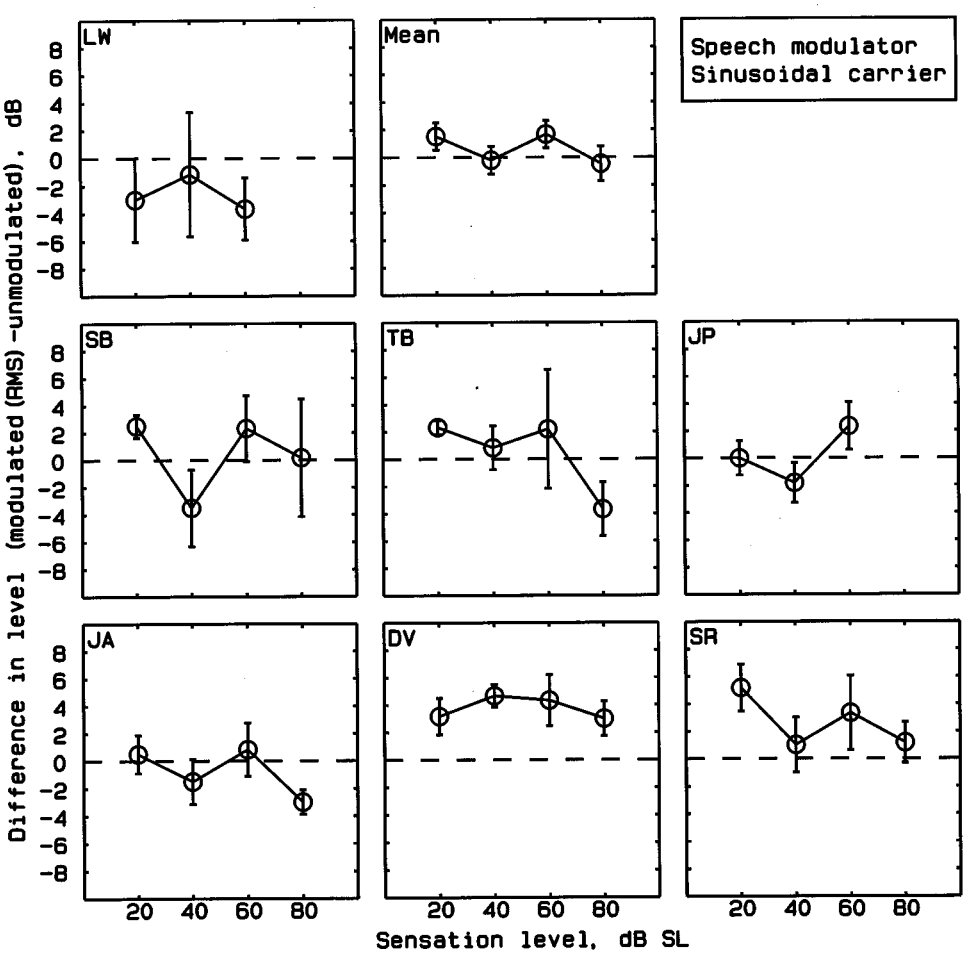

FIG. 7. Individual results for seven normally hearing subjects using a 4000-Hz sinusoidal carrier modulated with the envelope of speech from a single talker. Error bars show ± one standard deviation (s.d.) across runs. The group mean data are also shown (middle, top). In this case, error bars indicate ± one SE across subjects.

hearing-impaired subjects can be explained in terms of the loss of basilar-membrane compression for the latter.

V. EXPERIMENT 4. LOUDNESS MATCHES FOR PERIODICALLY MODULATED WHITE NOISE AND SPEECH-SHAPED NOISE

As described in the Introduction, Zhang and Zeng (1997) obtained loudness matches between unmodulated and modulated white noise. They found that the unmodulated noise had a slightly higher rms level than the modulated noise at the point of equal loudness, although the difference was small (usually less than 3 dB) and it varied with modulation rate and with level. This effect is opposite in direction to that found by us for the 4000-Hz sinusoidal carrier. To determine whether the discrepancy was due to the different carrier (sinusoid versus noise) or due to the different method used, we obtained loudness matches between modulated and unmodulated noise, using the same method as described earlier. To extend the generality of the results, we used both white noise and speech-shaped noise as the carrier.

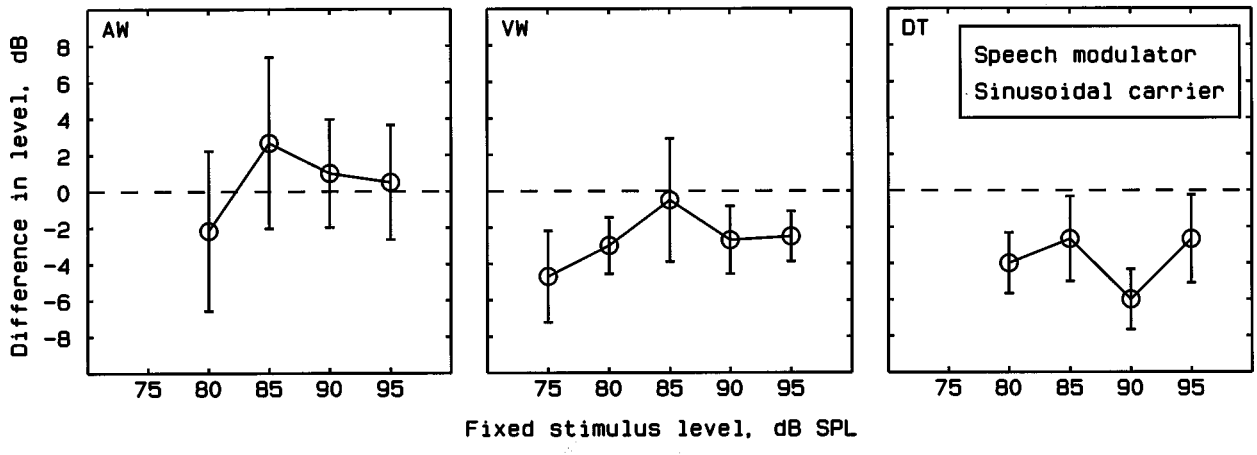

FIG. 8. Individual results for three hearing-impaired subjects using a 4000-Hz sinusoidal carrier modulated with the envelope of speech from a single talker. Error bars show ± one s.d. across runs.

A. Stimuli and subjects

The modulators were periodic with rates of 2, 8, and 32 Hz. The modulation was linear with $m=0.5$ and 1, and dB with $r=9.54$ and 60 dB. The white noise carrier was low-pass filtered at 8 kHz. The speech-shaped noise carrier had the same long-term average spectrum as the HINT sentences (Nilsson *et al.*, 1994), and it was identical to that specified in Peters *et al.* (1998). For the rates of 8 and 32 Hz, the duration of each sound, including the 20-ms rise/fall times, was 500 ms. For the 2-Hz rate, the duration of each sound was increased to 1000 ms. Five normally hearing subjects were tested. For them, the overall level of the fixed sound was 35, 55, and 75 dB SPL, for both types of noise. Three hearing-impaired subjects, AW, VW, and DT, were tested. For VW and DT, overall levels of 75 and 90 dB SPL were used. For AW, the level of 75 dB was judged to be too quiet, and overall levels of 85 and 90 dB were used.

B. Results

Results were similar across the normally hearing subjects, and mean results for the five subjects are shown in Figs. 9 and 10. For the white noise carrier with linear modulation (Fig. 9, open symbols), the difference scores for all conditions lie close to 0 dB, i.e., equal rms levels lead roughly to equal loudness. For $m=1$, the mean scores are all slightly negative, but the size of the effect is very small. The grand mean score is -0.44 dB. Based on a *t*-test, this is significantly less than zero ($p<0.01$). For the speech-shaped noise carrier with linear modulation (Fig. 9, filled symbols), the difference scores for all conditions again lie close to 0 dB. For $m=1$, the mean scores tend to be slightly negative, especially for the 8- and 32-Hz modulation rate. The grand mean score is -0.94 dB. This is significantly less than zero ($p<0.001$). These effects are in the same direction as reported by Zhang and Zeng (1997), but they are smaller in magnitude. For example, using a white noise modulator and linear modulation with $m=1$, and a modulation rate of 10 Hz, they found differences (expressed in the same way as us) of about -2, -3.5, and -1 dB for overall levels of 30, 45, and 70 dB SPL.

The difference scores for linear modulation were subjected to a within-subjects ANOVA with factors noise type, modulation depth, level, and rate. The main effects of noise type, level, and rate were not significant. The main effect of modulation depth was significant; $F(1,4)=137.5$, $p<0.001$, reflecting the fact that the mean difference was more negative for $m=1(-1.12)$ than for $m=0.5(-0.26)$. None of the interactions was significant.

For the white noise carrier with dB modulation (Fig. 10, open symbols), the difference scores lie close to 0 dB, but for $r=60$ dB and for the two lower levels at rates of 8 and 2 Hz, they tend to be negative. The grand mean score is -0.41 dB. This is not significantly different from zero. For the speech-shaped noise with dB modulation (Fig. 10, filled symbols), the scores are slightly negative for $r=60$ dB for the two lower overall levels, but not for the level of 75 dB. The grand mean score is -1.07 dB. This is significantly less than zero ($p<0.001$). The difference scores for dB modulation were subjected to a within-subjects ANOVA with factors type of noise, modulation depth, level, and rate. None of the main effects was significant. The interaction of noise type and level was significant [$F(2,8)=6.76$, $p=0.019$], although it accounted for only a small proportion of the variance in the data. The four-way interaction was also significant [$F(4,16)=6.39$, $p=0.003$], but again it accounted for only a small proportion of the variance in the data.

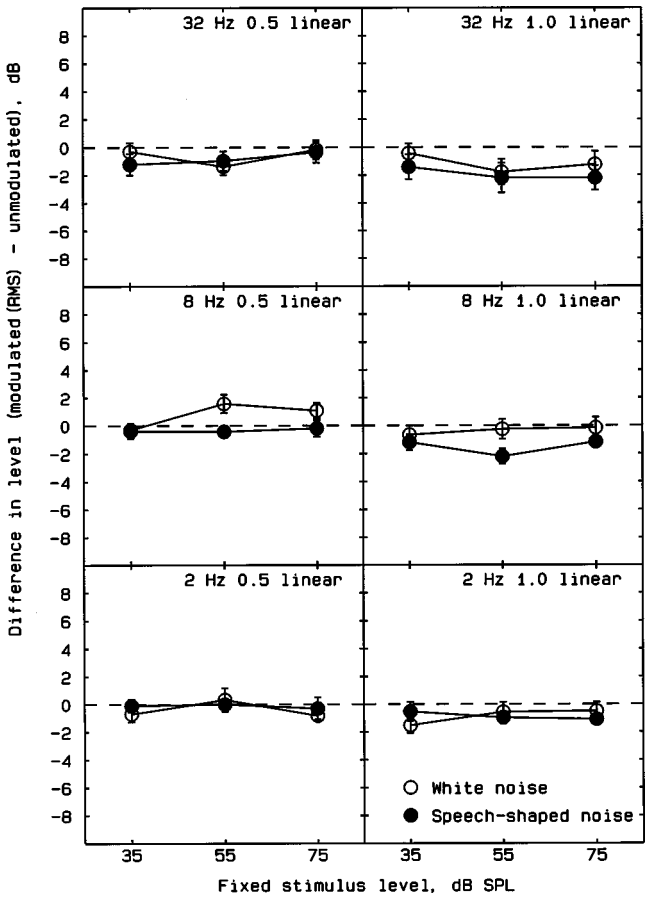

FIG. 9. Mean results for five normally hearing subjects for a white noise carrier (open symbols) or a speech-shaped noise carrier (filled symbols), using linear modulation. Error bars indicate ± one SE across subjects. Each panel shows results for one modulation depth and one modulation rate.

The results did not vary markedly across the hearing-impaired subjects, and mean data for them are presented in Figs. 11 and 12. At the level identified as ''low'' subject AW was tested at 85 dB SPL, while the other two subjects were tested at 75 dB SPL, but results were similar for all these cases. For the white noise carrier with linear modulation (Fig. 11, open symbols), the difference scores were mostly slightly negative, especially for $m=1$. The grand mean score was -0.8 dB. This is significantly less than zero ($p<0.001$). For the speech-shaped noise with linear modulation (Fig. 11, filled symbols), scores were also mostly negative. The grand mean score was -0.94 dB. This is significantly less than zero ($p<0.001$). For dB modulation (Fig. 12), scores were again mostly negative at the higher modulation depth for both white noise (open symbols) and speech-shaped noise (filled symbols). The grand mean score for the white noise was -1.1 dB. This is significantly less than zero ($p<0.001$). The grand mean score for the speech-shaped

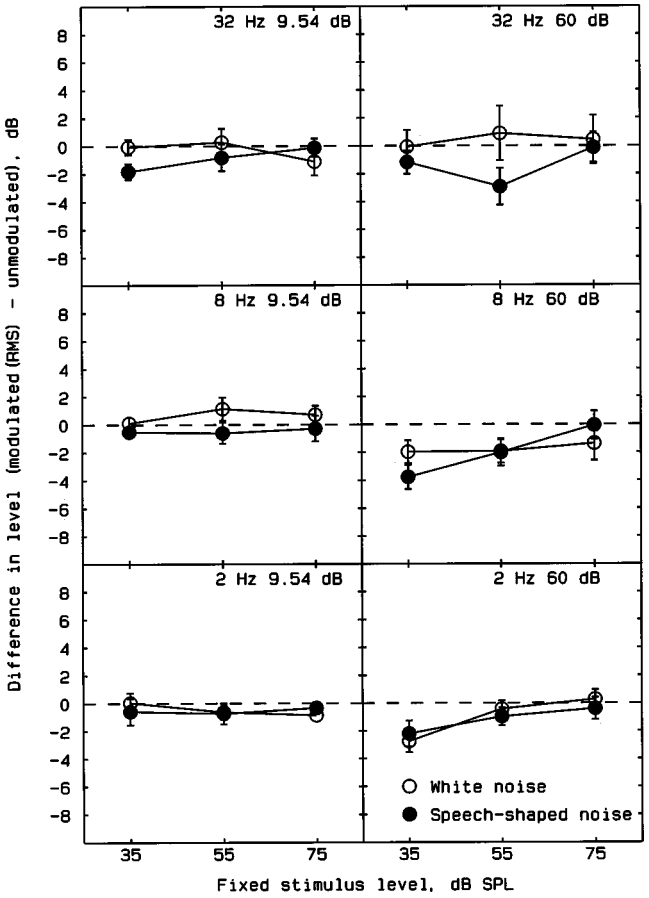

FIG. 10. As Fig. 9, but for dB modulation.

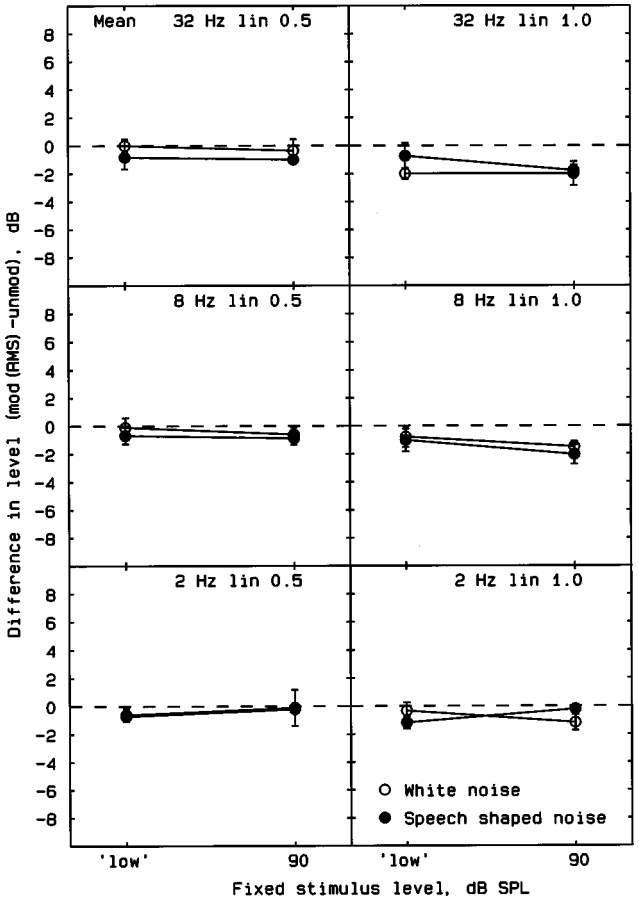

FIG. 11. Mean results for three hearing-impaired subjects for a white noise carrier (open symbols) or a speech-shaped noise carrier (filled symbols), using linear modulation. Error bars indicate ± one SE across subjects. Each panel shows results for one modulation depth and one modulation rate. The level identified as ''low'' was 85 dB SPL for AW and 75 dB SPL for the other two subjects.

noise was −1.5 dB. This is significantly less than zero ($p < 0.001$). There was no consistent overall effect of level.

A within-subjects ANOVA was conducted on the data for linear modulation, with factors type of noise, modulation depth, level, and rate. To include the data of all subjects, the level was simply labeled as ''high'' or ''low,'' for each subject. The main effect of modulation depth was significant; $F(1,2)=21.44$, $p=0.044$. This reflects the fact that the mean difference for $m=1(-1.23)$ was more negative than the mean difference for $m=0.5(-0.5)$. None of the other main effects or interactions was significant. A similar ANOVA on the data for dB modulation just failed to give a significant effect of modulation depth, $F(1,2)=10.39$, $p=0.084$, and the main effects of the other factors were also nonsignificant. The interaction of modulation depth and rate was marginally significant [$F(2,4)=7.2$, $p=0.047$], reflecting the fact that scores were more negative for the higher modulation depth at rates of 2 and 32 Hz, but not at 8 Hz. None of the other interactions was significant.

VI. EXPERIMENT 5. LOUDNESS MATCHES FOR A SPEECH MODULATOR AND SPEECH-SHAPED NOISE CARRIER

A. Stimuli

In this experiment we tried to create stimuli that were as speechlike as possible, but without the spectral fluctuations characteristic of speech. The modulator was based on the envelope of the speech of a single talker, as described for experiment 3, and the carrier was the speech-shaped noise used in experiment 4. As in experiment 3, the duration of the speech-modulated stimulus was 2 s, while the duration of the unmodulated stimulus was 500 ms (including the 20-ms rise/fall times). Seven normally hearing subjects were tested for overall levels of the fixed stimulus of 35, 55, and 75 dB SPL. Three hearing-impaired subjects were tested. Overall levels were 85 and 90 dB SPL for AW, 75, 80, 85, and 90 dB SPL for VW, and 70, 75, 80, 85, and 90 dB SPL for DT.

B. Results

The results differed somewhat across the normally hearing subjects, so individual results are shown in Fig. 13. The group average results are also shown. For two subjects, JA and DV, the differences in level lie close to the dashed line. For one subject, SR, the points lie above the dashed line. For the remaining four subjects, the points tend to lie below the dashed line. For the mean results, the points lie close to the dashed line, but on average are very slightly below it. The average difference was −0.23 dB. This is not significantly different from zero. Excluding the results for SR, the mean difference was −0.73 dB, which is significantly less than zero ($p<0.01$). A within-subjects ANOVA with factor level showed no significant effect of level.

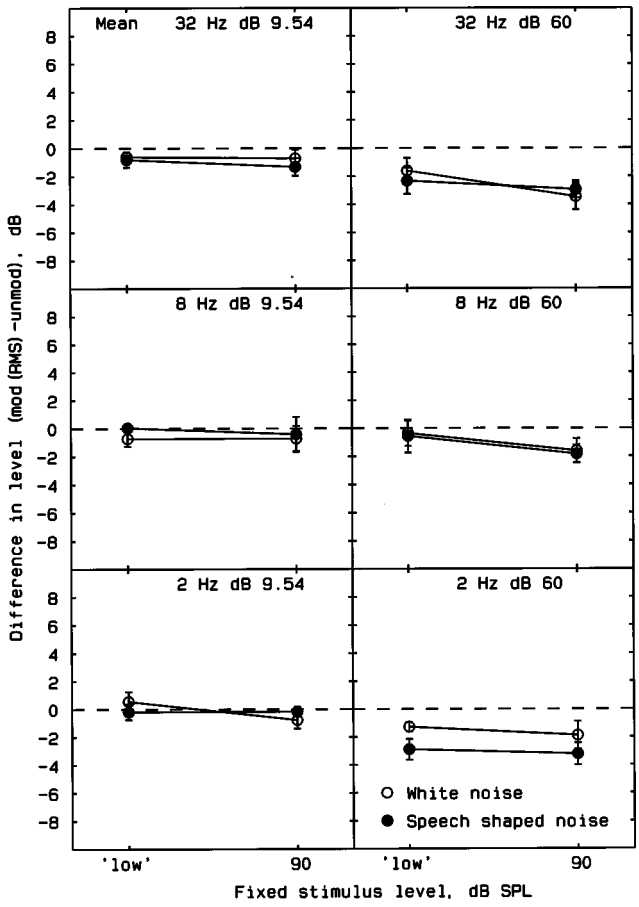

FIG. 12. As Fig. 11, but for dB modulation.

Comparing the result for the noise carrier (Fig. 13) and for the sinusoidal carrier (Fig. 7), it is apparent that the results for the former are somewhat more orderly; variations across level are smaller for the noise carrier than for the sinusoidal carrier. For some subjects, the differences have the same sign for the noise and sinusoidal carriers; for example, SR consistently shows positive differences, while LW shows negative differences. However, for other subjects there are discrepancies. For example, TB shows mostly positive differences for the sinusoidal carrier, but negative differences for the noise carrier.

The individual results for the hearing-impaired subjects are shown in Fig. 14. For subject AW, the differences scores lie close to the dashed line. For the other two subjects, the scores are clearly below the dashed line, indicating that, at the point of equal loudness, the speech-modulated noise had a lower rms level than the steady noise. The grand mean score was -2.1 dB. This is significantly less than zero ($p < 0.001$). There is no clear effect of level. For each individual subject, the pattern of results for the noise carrier is similar to that for the sinusoidal carrier (Fig. 8); differences are close to zero for AW and negative for VW and DT.

VII. DISCUSSION

We have investigated the influence of temporal fluctuations of sounds on the perception of loudness for normally hearing and hearing-impaired subjects. We used modulated narrow-band and broadband sounds with different modulation rates, type of modulation, and modulation depths as stimuli. The results showed that, to a first approximation, equal rms levels led to equal loudness of steady and modulated sounds, both for normal and for hearing-impaired subjects. However, there were some small but systematic deviations from this rule. For normally hearing subjects, and for a 4000-Hz sinusoidal carrier, modulated sounds had a slightly higher rms level than unmodulated sounds at the point of equal loudness. This was true, on average, for both periodic modulation and modulation with the envelope of speech from a single talker. A similar effect for periodic modulation was reported by Moore *et al.* (1998b). Zhang and Zeng (1997) also observed a similar effect, for modulation rates between 10 and 50 Hz for a two-tone (beating) complex and for rates between 50 and 100 Hz for a three-tone complex. For lower modulation rates they found that the modulated sounds had a slightly lower rms level than the unmodulated sounds at the point of equal loudness. These findings differ from those reported by Bauch (1956). As described in the Introduction, he found that, for modulation rates between about 20 Hz and half the critical bandwidth at the carrier frequency, the modulated and unmodulated sounds had equal rms levels at the point of equal loudness. Several factors may have contributed to the discrepancy. First, there was probably a bias in Bauch's procedure, as only the steady tone was adjusted to determine a match. Second, individual differences may have played a role, as Bauch tested only two subjects. Finally, Bauch allowed his subjects to listen to each sound for as long as they wanted. This may have resulted in subjects using a different criterion to that used with shorter stimuli.

Our results showed that, for normally hearing subjects and for noise carriers, modulated sounds had slightly lower rms levels than unmodulated sounds at the point of equal loudness. A similar, but slightly larger effect was reported by Zhang and Zeng (1997). This effect is in the opposite direction to that found for sinusoidal carriers. The difference between sinusoidal and noise carriers might reflect differences in basilar-membrane compression for sinusoids and for noise, which could result from level-dependent compressive interactions between noise components in different frequency regions (Ruggero, 1973; Schalk and Sachs, 1980). However, there is little direct evidence to support or refute the idea that input-output functions on the basilar membrane differ for sinusoids and for noise. Moore and Glasberg (1983) found that the rate of growth of forward masking with masker level does not differ for sinusoidal and broadband noise maskers when adequate cues are available to reduce ''confusion'' of the signal with the sinusoidal masker, which suggests that input–output functions on the basilar membrane are not greatly different for sinusoids and broadband noise. On the other hand, Florentine *et al.* (1996) found that the effect of level on temporal integration of loudness differed between 1-kHz tones and broadband noise, which could be interpreted in terms of differences in basilar membrane input–output functions for sinusoids and for noise.

For hearing-impaired subjects, and for a 4000-Hz sinusoidal carrier, we found that modulated sounds had a slightly lower rms level than unmodulated sounds at the point of

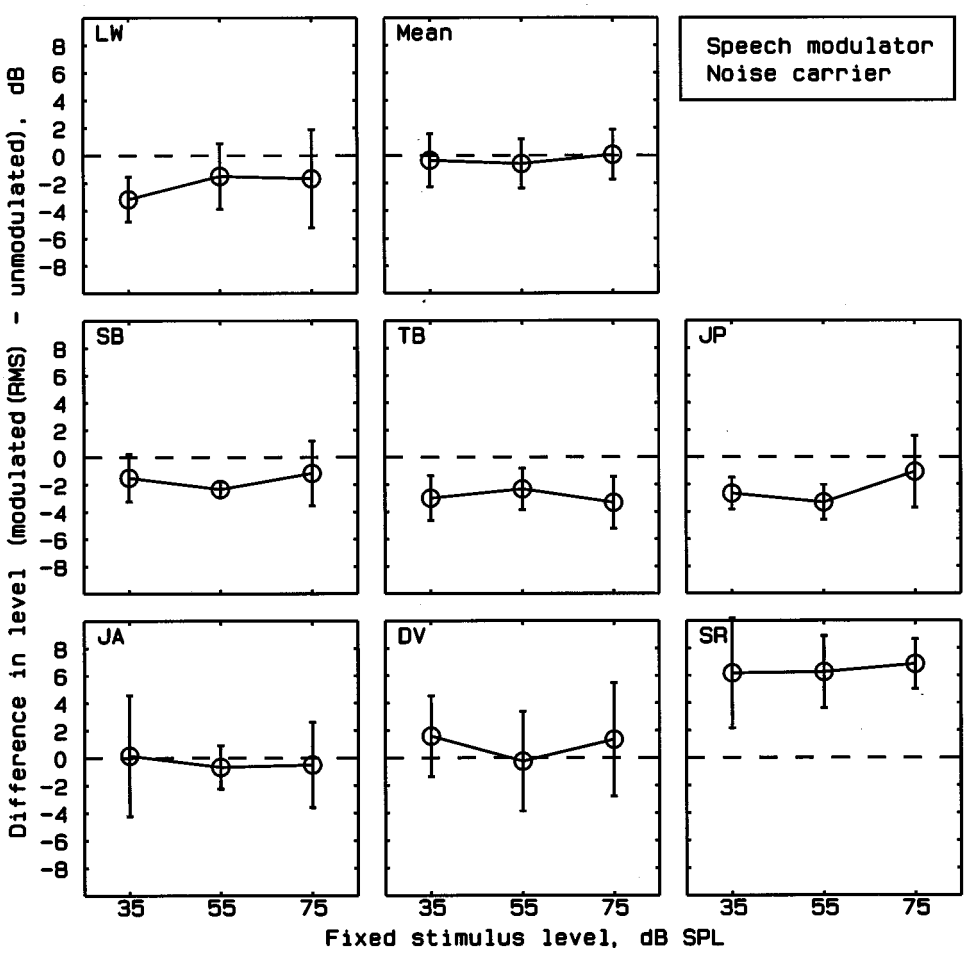

FIG. 13. Individual results for seven normally hearing subjects using a speech-shaped noise carrier modulated with the envelope of speech from a single talker. Otherwise, as Fig. 7.

equal loudness. However, this was not true for all subjects, especially for a speech modulator. For hearing-impaired subjects and for noise carriers, the modulated sounds had a slightly lower rms level than unmodulated sounds at the point of equal loudness. As described earlier, the differences between normally hearing and hearing-impaired subjects may reflect reduced basilar-membrane compression in hearing-impaired subjects. For the sinusoidal carrier and for modulation rates of 4 Hz and above, the results for both normally hearing and hearing-impaired subjects could be fitted quite well based on the assumption that loudness corresponds to the rms value of the intensity of the basilar-membrane response.

Evidence that fast-acting compression on the basilar membrane plays a role in loudness perception has been presented previously by Carlyon and Datta (1997). They used as stimuli complex tones with equal-amplitude components added either in Schroeder-positive or Schroeder-negative phase (Schroeder, 1970). There is evidence that the former produces waveforms on the basilar membrane with high peak factors, while the latter produces waveforms with rather flat envelopes (Kohlrausch and Sander, 1995; Carlyon and

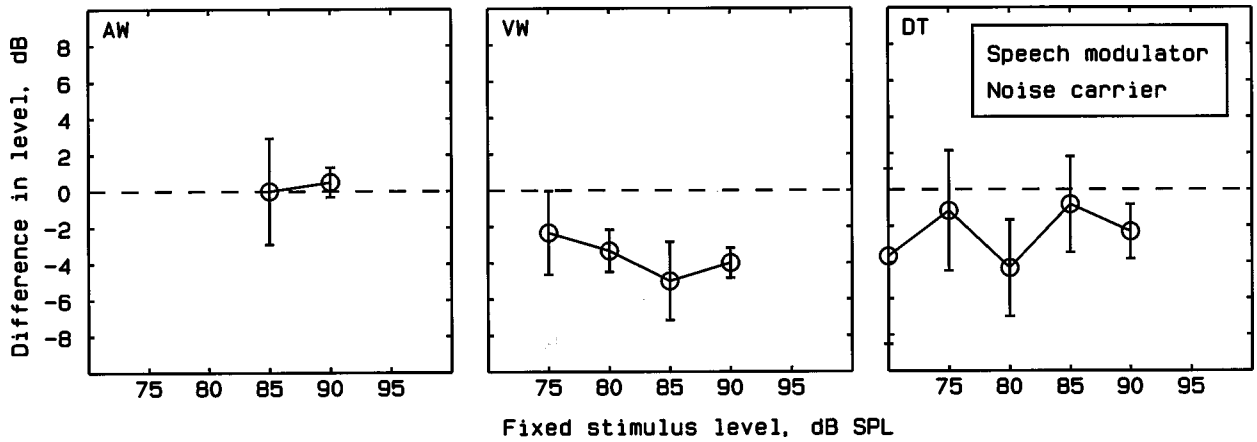

FIG. 14. Individual results for three hearing-impaired subjects using a speech-shaped noise carrier modulated with the envelope of speech from a single talker. Error bars show ± one s.d. across runs.

Datta, 1997). Carlyon and Datta found that when the two sounds had equal rms levels, Schroeder-positive phase gave a lower loudness than Schroeder-negative phase. They argued that this happened because fast-acting compression on the basilar membrane would lead to lower average excitation for the former than for the latter.

In the Introduction, we described the use of loudness scaling procedures in the fitting of multi-band compression hearing aids, so as to restore loudness perception to ''normal.'' We suggested that it is questionable whether gain values deduced using stationary signals are appropriate for predicting the gain required for time-varying sounds such as speech. The present results suggests that, in practice, these gain values would be appropriate, at least to a first approximation. However, for hearing-impaired subjects, our results show that the modulated carriers, including the speech-shaped noise carrier modulated with the envelope of speech, were slightly lower in rms level than the unmodulated carriers, at the point of equal loudness. Therefore, the amount of gain required to restore loudness to ''normal'' would be slightly less for modulated sounds such as speech than for the steady sounds typically used to measure loudness growth functions. Given the inherent variability typically associated with measures of loudness growth, the small differences in gain required for steady and modulated sounds are unlikely to be of great importance, although the 5-dB effects found for VW and DT might be clinically relevant.

In practice, the situation is complicated, because the level-dependent gains required might depend upon the attack and release times of the compression circuits used in the hearing aids. In principle, fast-acting compression is needed to restore dynamic aspects of loudness perception to normal. For example, Moore *et al.* (1996) showed that the perceived fluctuation of loudness associated with amplitude modulation of a sinusoidal carrier was effectively ''magnified'' by loudness recruitment. This effect occurred for modulation rates up to 32 Hz (the highest tested). To restore the perceived fluctuation of loudness to normal would require release times less than about 20 ms, shorter than those used in most commercial hearing aids. Our results are not really applicable to the fitting of such systems, since they were based on judgments of the overall loudness impression, not the amount of loudness fluctuation. Our results are more applicable to aids with multi-band compression in which the gain changes more slowly with time.

In any case, it should be noted that the goal of restoring loudness perception to normal is not universally accepted (Moore *et al.,* 1998a). We certainly do not advocate such a goal. However, *if* this goal is accepted, then our results show that loudness judgments obtained using steady sounds should be adequate for determining the gains appropriate for time-varying sounds, as least in systems with reasonably long time constants.

In the Introduction, we mentioned the application of this work to the design of meters intended to indicate the subjective loudness of sounds as opposed to the physical intensity. Current loudness meters (Fastl, 1993; Stone *et al.,* 1997) predict that a modulated sound should have a somewhat higher loudness than a comparable steady sound of equal rms level. Our results are not generally consistent with this prediction. Hence the design of the meters needs modification. Probably, the accuracy of the predictions could be improved by incorporating a simulation of the fast acting compression that occurs on the basilar membrane.

VIII. CONCLUSIONS

Loudness matches were obtained between unmodulated carriers and carriers that were amplitude modulated. Results were expressed as the rms level of the modulated carrier minus the level of the unmodulated carrier at the point of equal loudness. If this difference is positive, this indicates that the modulated carrier has a higher rms level at the point of equal loudness. The main results are as follows:

(1) The effect of modulation on the perception of overall loudness was rather weak; equal rms levels led to *approximately* equal loudness for steady and modulated tones.
(2) For a 4-kHz sinusoidal carrier and normally hearing subjects, the mean difference was slightly positive; modulated sounds had a slightly higher rms level than steady sounds, at the point of equal loudness. This was true both for periodic modulation and modulation with the envelope of a single talker.
(3) For a speech-shaped or white noise carrier and normally hearing subjects, the mean difference was slightly negative, although this effect was not significant for modulation with the envelope of a single talker.
(4) For normally hearing subjects, there was no clear effect of level or modulation waveform (linear or logarithmic).
(5) For periodic modulation of a 4-kHz sinusoidal carrier, hearing-impaired subjects gave a negative mean difference. The difference increased with increasing modulation depth for rates of 4, 8, and 32 Hz, but not for a rate of 2 Hz. There was no clear effect of level.
(6) For modulation of a 4-kHz sinusoidal carrier or speech-shaped noise carrier with the envelope of a single talker, two out of three hearing-impaired subjects showed a negative difference.
(7) For a speech-shaped or white noise carrier with periodic modulation, hearing-impaired subjects showed a negative difference.
(8) For the sinusoidal carrier, the results for both normally hearing and hearing-impaired subjects could be fitted quite well based on the assumption that loudness corresponds to the rms value of the time-varying intensity of the basilar-membrane response.

ACKNOWLEDGMENTS

This work was supported by Phonak AG, the Medical Research Council and the EU (SPACE project). We thank Sarah Barratt for gathering some of the data, Brian Glasberg for assistance with statistics, and Fan-Gang Zeng and an anonymous reviewer for helpful comments on an earlier version of this paper. We thank Fan-Gang Zeng in particular for suggesting that we evaluate the effect of squaring the basilar-membrane response.

Allen, J. B., and Jeng, P. S. (**1990**). ''Loudness growth in 1/2-octave bands (LGOB); a procedure for the assessment of loudness,'' J. Acoust. Soc. Am. **88**, 745–753.
Bauch, H. (**1956**). ''Die Bedeutung der Frequenzgruppe für die Lautheit von Klängen,'' Acustica **6**, 40–45.
Carlyon, R. P., and Datta, A. J. (**1997**). ''Excitation produced by Schroeder-phase complexes: Evidence for fast-acting compression in the auditory system,'' J. Acoust. Soc. Am. **101**, 3636–3647.
Cornelisse, L. E., Seewald, R. C., and Jamieson, D. G. (**1995**). ''The input/output formula: A theoretical approach to the fitting of personal amplification devices,'' J. Acoust. Soc. Am. **97**, 1854–1864.
Cox, R. M. (**1995**). ''Using loudness data for hearing aid selection. The IHAFF approach,'' Hear. J. **48(10)**, 39–44.
Fastl, H. (**1993**). ''Loudness evaluation by subjects and by a loudness meter,'' in *Sensory Research—Multimodal Perspectives*, edited by R. T. Verrillo (Erlbaum, Hillsdale, NJ).
Florentine, M., Buus, S., and Poulsen, T. (**1996**). ''Temporal integration of loudness as a function of level,'' J. Acoust. Soc. Am. **99**, 1633–1644.
Houtgast, T., Steeneken, H. J. M., and Plomp, R. (**1980**). ''Predicting speech intelligibility in rooms from the modulation transfer function. I. General room acoustics,'' Acustica **46**, 60–72.
Jesteadt, W. (**1980**). ''An adaptive procedure for subjective judgments,'' Percept. Psychophys. **28**, 85–88.
Kiessling, J. (**1997**). ''Scaling methods for the selection, fitting and evaluation of hearing aids,'' in *Psychoacoustics, Speech and Hearing Aids*, edited by B. Kollmeier (World Scientific, Singapore).
Killion, M. C., and Fikret-Pasa, S. (**1993**). ''Three types of sensorineural hearing loss: Loudness and intelligibility considerations,'' Hear. J. **46**, 31–36.
Kohlrausch, A., and Sander, A. (**1995**). ''Phase effects in masking related to dispersion in the inner ear. II. Masking period patterns of short targets,'' J. Acoust. Soc. Am. **97**, 1817–1829.
Kollmeier, B., and Hohmann, V. (**1995**). ''Loudness estimation and compensation employing a categorical scale,'' in Advances in Hearing Research, edited by G. A. Manley, G. M. Klump, C. Köppl, H. Fastl, and H. Oeckinghaus (World Scientific, Singapore).
Launer, S. (**1995**). ''Loudness perception in listeners with sensorineural hearing impairment,'' Ph.D. thesis, Oldenburg, Germany.
Moore, B. C. J. (**1995**). *Perceptual Consequences of Cochlear Damage* (Oxford U.P., Oxford).
Moore, B. C. J., and Glasberg, B. R. (**1983**). ''Growth of forward masking for sinusoidal and noise maskers as a function of signal delay: implications for suppression in noise,'' J. Acoust. Soc. Am. **73**, 1249–1259.
Moore, B. C. J., and Glasberg, B. R. (**1997**). ''A model of loudness perception applied to cochlear hearing loss,'' Aud. Neurosci. **3**, 289–311.
Moore, B. C. J., and Oxenham, A. J. (**1998**). ''Psychoacoustic consequences of compression in the peripheral auditory system,'' Psychol. Rev. **105**, 108–124.
Moore, B. C. J., Alcántara, J. I., and Glasberg, B. R. (**1998a**). ''Development and evaluation of a procedure for fitting multi-channel compression hearing aids,'' Br. J. Audiol. **32**, 177–195.
Moore, B. C. J., Glasberg, B. R., and Baer, T. (**1997**). ''A model for the prediction of thresholds, loudness and partial loudness,'' J. Audio Eng. Soc. **45**, 224–240.
Moore, B. C. J., Glasberg, B. R., and Stone, M. A. (**1999b**). ''Use of a loudness model for hearing aid fitting. III. A general method for deriving initial fittings for hearing aids with multi-channel compression,'' Br. J. Audiol. (in press).
Moore, B. C. J., Wojtczak, M., and Vickers, D. A. (**1996**). ''Effect of loudness recruitment on the perception of amplitude modulation,'' J. Acoust. Soc. Am. **100**, 481–489.
Moore, B. C. J., Alcántara, J. I., Stone, M. A., and Glasberg, B. R. (**1998a**). ''Use of a loudness model for hearing aid fitting. II. Hearing aids with multi-channel compression,'' Br. J. Audiol. (in press).
Moore, B. C. J., Launer, S., Vickers, D., and Baer, T. (**1998b**). ''Loudness of modulated sounds as a function of modulation rate, modulation depth, modulation waveform and overall level,'' in *Psychophysical and Physiological Advances in Hearing*, edited by A. R. Palmer, A. Rees, A. Q. Summerfield, and R. Meddis (Whurr, London).
Nilsson, M., Soli, S. D., and Sullivan, J. A. (**1994**). ''Development of the Hearing in Noise Test for the measurement of speech reception thresholds in quiet and in noise,'' J. Acoust. Soc. Am. **95**, 1085–1099.
Oxenham, A. J., and Moore, B. C. J. (**1995**). ''Additivity of masking in normally hearing and hearing-impaired subjects,'' J. Acoust. Soc. Am. **98**, 1921–1935.
Oxenham, A. J., and Plack, C. J. (**1997**). ''A behavioral measure of basilar-membrane nonlinearity in listeners with normal and impaired hearing,'' J. Acoust. Soc. Am. **101**, 3666–3675.
Peters, R. W., Moore, B. C. J., and Baer, T. (**1998**). ''Speech reception thresholds in noise with and without spectral and temporal dips for hearing-impaired and normally hearing people,'' J. Acoust. Soc. Am. **103**, 577–587.
Plack, C. J., and Carlyon, R. P. (**1995**). ''Loudness perception and intensity coding,'' in *Hearing*, edited by B. C. J. Moore (Academic, Orlando, FL).
Pluvinage, V. (**1989**). ''Clinical measurement of loudness growth,'' Hear. Inst. **39**, 28–29, 32.
Robles, L., Ruggero, M. A., and Rich, N. C. (**1986**). ''Basilar membrane mechanics at the base of the chinchilla cochlea. I. Input-output functions, tuning curves, and response phases,'' J. Acoust. Soc. Am. **80**, 1364–1374.
Ruggero, M. A. (**1973**). ''Response to noise of auditory nerve fibers in the squirrel monkey,'' J. Neurophysiol. **36**, 569–587.
Ruggero, M. A. (**1992**). ''Responses to sound of the basilar membrane of the mammalian cochlea,'' Curr. Opin. Neurobiol. **2**, 449–456.
Ruggero, M. A., Rich, N. C., Recio, A., Narayan, S. S., and Robles, L. (**1997**). ''Basilar-membrane responses to tones at the base of the chinchilla cochlea,'' J. Acoust. Soc. Am. **101**, 2151–2163.
Schalk, T. B., and Sachs, M. B. (**1980**). ''Nonlinearities in auditory-nerve fiber responses to bandlimited noise,'' J. Acoust. Soc. Am. **67**, 903–913.
Scharf, B. (**1978**). ''Loudness,'' in *Handbook of Perception, Volume IV. Hearing*, edited by E. C. Carterette and M. P. Friedman (Academic, New York).
Schlauch, R. S., DiGiovani, J. J., and Ries, D. T. (**1998**). ''Basilar membrane nonlinearity and loudness,'' J. Acoust. Soc. Am. **103**, 2010–2020.
Schroeder, M. R. (**1970**). ''Synthesis of low peak-factor signals and binary sequences with low autocorrelation,'' IEEE Trans. Inf. Theory **IT-16**, 85–89.
Sellick, P. M., Patuzzi, R., and Johnstone, B. M. (**1982**). ''Measurement of basilar membrane motion in the guinea pig using the Mössbauer technique,'' J. Acoust. Soc. Am. **72**, 131–141.
Stone, M. A., Moore, B. C. J. and Glasberg, B. R. (**1997**). ''A real-time DSP-based loudness meter,'' in *Contributions to Psychological Acoustics*, edited by A. Schick and M. Klatte (Bibliotheks- und Informationssystem der Universität Oldenburg, Oldenburg).
Zeng, F. G., and Shannon, R. V. (**1994**). ''Loudness-coding mechanisms inferred from electric stimulation of the human auditory system,'' Science **264**, 564–566.
Zhang, C., and Zeng, F.-G. (**1997**). ''Loudness of dynamic stimuli in acoustic and electric hearing,'' J. Acoust. Soc. Am. **102**, 2925–2934.
Zwicker, E. (**1977**). ''Procedure for calculating loudness of temporally variable sounds,'' J. Acoust. Soc. Am. **62**, 675–682.
Zwicker, E., and Fastl, H. (**1990**). *Psychoacoustics—Facts and Models* (Springer-Verlag, Berlin).
Zwicker, E., and Scharf, B. (**1965**). ''A model of loudness summation,'' Psychol. Rev. **72**, 3–26.

Two phase effects in roughness perception[a)]

Daniel Pressnitzer
Institut de Recherche et de Coordination Acoustique/Musique (IRCAM), 1 place Igor Stravinsky, F-75004 Paris, France

Stephen McAdams
Laboratoire de Psychologie Expérimentale (CNRS), Université René Descartes, EPHE, 28 rue Serpente, F-75006 Paris, France and IRCAM, 1 place Igor Stravinsky, F-75004 Paris, France

(Received 20 February 1998; accepted for publication 13 February 1999)

The respective influences of spectral and temporal aspects of sound in roughness perception are examined by way of phase manipulations. In a first experiment, the phase of the central component of three-component signals is shown to modify perceived roughness, for a given amplitude spectrum, regardless of whether it modifies the waveform envelope. A second experiment shows that the shape of the waveform envelope, for a given amplitude spectrum and a given modulation depth, also influences perceived roughness. We interpret both of these results by considering the envelope of an internal representation that is deduced from the physical signal by taking into account peripheral auditory processing. The results indicate that the modulation depth of such an internal representation is not the only determinant of roughness, but that an effect of temporal asymmetry is also to be taken into account.
[S0001-4966(99)03805-9]

PACS numbers: 43.66.Jh, 43.66.Ki, 43.66.Nm [DWG]

INTRODUCTION

Auditory roughness is a term that was introduced by von Helmholtz (1877) to describe the percept experienced when two sounds with proximal frequency components are heard simultaneously. He proposed that this attribute was linked to musical dissonance: for instance, an interval of a minor second played in the medium register of the piano produces roughness. The understanding of what kinds of sensory mechanisms are responsible for roughness perception is of interest when considered in the light of recent experimental results in the fields of developmental and comparative psychology. Babies (Schellenberg and Trainor, 1996) and members of other species (Fay, 1994; Hulse *et al.*, 1995) also seem to be sensitive to auditory roughness.

Experimental studies seeking to quantify roughness perception have often studied the effects of the frequency composition of stimuli (Plomp and Levelt, 1965; Plomp and Steeneken, 1968; Kameoka and Kuriyagawa, 1969). The presence of frequency components within the limits of a critical band is considered, in these studies, to be the source of the beats that produce the percept of roughness. Consequently, models of roughness perception have been proposed that are based on the spectral composition of energy falling within critical bands (Hutchinson and Knopoff, 1978).

A different approach to roughness is to study the influence of temporal parameters by means of amplitude-modulated stimuli (Mathes and Miller, 1947; Terhardt, 1974; Fastl, 1977). A dependence of roughness on the frequency and depth of the modulation was demonstrated. The interpretation proposed is that roughness is determined by the envelope fluctuations of the signal within an auditory filter. These results have inspired another kind of model in which roughness estimates are based on the rms value of the signal envelope after auditory filtering and after a modulation-frequency bandpass filter (Aures, 1985; Daniel and Weber, 1997).

These two approaches generally produce similar predictions as proximal frequency components give rise to amplitude beats and amplitude modulation gives rise to proximal frequency components. A method to pit them against each other is to use phase manipulations. This was done by Mathes and Miller (1947) who compared the roughness produced by Sinusoidally Amplitude-Modulated (SAM) tones and Quasi-Frequency-Modulated (QFM) tones. QFM tones have the same amplitude spectrum as SAM tones but display almost no amplitude modulation. The QFM tones were judged less rough than the SAM tones. This finding, confirmed by Terhardt (1974), has been interpreted in terms of differences in envelope rms after auditory filtering (Mathes and Miller, 1947; Terhardt, 1974).

Some authors claimed that this interpretation was flawed, as roughness differences could be heard for sounds having the same waveform envelope and frequency composition but different phase spectra (cf. discussion among Smoorenburg and Terhardt in Terhardt, 1970). In these cases, differences in temporal fine structure on the one hand or differences in the phases of the combination tones (Buunen *et al.*, 1974) on the other hand could influence the resulting percepts. However, to our knowledge, no experimental data have been produced to support this claim. The aim of the present study is to provide such quantitative experimental data and to discuss them in relation to the different models of roughness perception.

[a)]Portions of these results were first presented at the 4th French Acoustics Conference (Pressnitzer and McAdams, 1997) and at the 11th International Symposium on Hearing (Pressnitzer and McAdams, 1998).

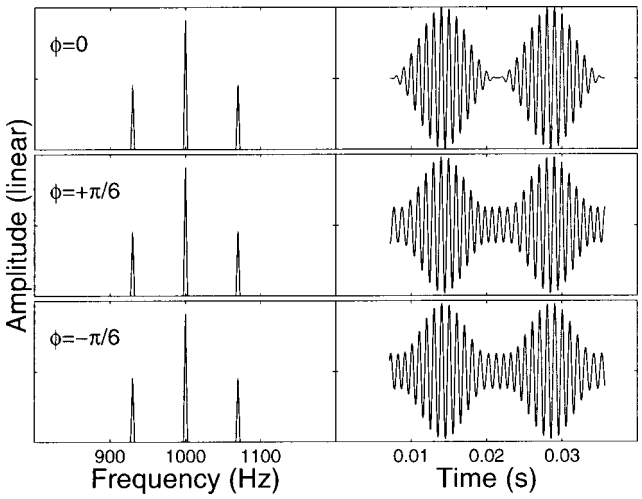

FIG. 1. Stimuli for Experiment 1. Amplitude spectra and waveforms of a pAM tone are plotted for three phase conditions at (f_c, f_m)=(1000 Hz, 70 Hz).

I. EXPERIMENT 1

A. Experimental hypotheses

Consider three spectral components with frequencies $(f_c),(f_c-f_m),(f_c+f_m)$ and with relative amplitudes of 1,1/2, and 1/2, respectively. In order to study the influence of phase relations among these components, it suffices to set the starting phase of the sidebands to zero and to vary the starting phase ϕ of the central component (Goldstein, 1967b). For $\phi=0$, a SAM tone with frequency f_c modulated at a frequency f_m with a modulation depth of 100% is obtained. By varying ϕ, we can produce a family of sounds that have the same amplitude spectrum as SAM tones but different temporal waveforms. We will refer to these as ''pseudo-AM'' (pAM) tones:

$$\mathrm{pAM}(t)=\tfrac{1}{2}\cos[2\pi(f_c-f_m)t]+\cos(2\pi f_c t+\phi)+\tfrac{1}{2}\cos[2\pi(f_c+f_m)t]. \quad (1)$$

If the only determinant of roughness was the distribution of energy across frequency, all pAM tones with identical amplitude spectra should be equally rough.

If ϕ is nonzero, the envelope of the pAM tone is generally not sinusodal anymore. If ϕ takes for instance the value of $+\pi/6$, the envelope looks ''flatter'' (Fig. 1). The envelope actually gets flatter and flatter as ϕ is varied from 0 to $+\pi/2$, where a QFM tone is obtained (the analytical expression of the envelope is derived in Appendix A). By systematically varying ϕ we can therefore investigate the relation between envelope rms magnitude and roughness for a given amplitude spectrum.

Finally, pAM sounds with opposite phase values have the same amplitude spectrum and waveform envelope but different temporal fine structures (Fig. 1, bottom two panels). If only the characteristics of the envelope contribute to roughness, these two sounds should be identically rough.

B. Method

1. Stimuli and Apparatus

Seven series of pAM stimuli were used in which a given center frequency and a ''modulation'' frequency were paired: (f_c, f_m)=(125 Hz, 30 Hz), (250, 40), (500, 50), (1000, 70), (2000, 70), (4000, 70), and (8000, 70). In each case, f_m was chosen to produce maximum roughness for a pure tone of frequency f_c amplitude-modulated sinusoidally at f_m (Zwicker and Fastl, 1990). The phase ϕ of the central component was varied from $-\pi/2$ to $+\pi/2$ in steps of $\pi/6$. Each sound was 1 s in duration and had raised-cosine onset and offset ramps of 50 ms. The stimuli were obtained by additive synthesis with a 16-bit resolution and a sampling rate of 44.1 kHz. The signals were played by a NeXT station through an ISPW DSP card, Pro IO digital-to-analog converters, and Canford power amplifier. They were presented over Sennheiser HD 520 II headphones at 60 dB (A-weighted), as measured by a Bruel & Kjaer 2209 sound-level meter with a flat-plate coupler. This level has generally been used in past studies of roughness. The distortion products of the whole sound reproduction chain for our stimuli were less than 60 dB below signal amplitude as measured by a Bruel & Kjaer spectral analyzer. Subjects were seated in a Soluna S1 double-walled sound-isolation booth and responded by clicking with a mouse on a graphic interface.

2. Procedure

The notion of roughness was first introduced to listeners by means of a demonstration. A SAM tone with a carrier of 1000 Hz and a modulation frequency of 70 Hz was presented. Listeners could vary its modulation depth in a continuous fashion, thus changing concomitantly its amplitude spectrum and its envelope (the level of the carrier was kept constant). Listeners were instructed that the change in the quality of the tone they heard was called roughness. This example is considered to produce no roughness if the modulation depth is zero and the maximum roughness obtainable with a single SAM tone if the modulation depth is one (Zwicker and Fastl, 1990). Further demonstrations were given with SAM tones at the carrier and modulation frequencies used in the experiment. Following this familiarization phase, the experiment began. The stimuli were presented in separate blocks corresponding to the different f_c's. In each block, all 21 pairs of nonidentical stimuli were presented in both orders in a randomized fashion, giving a total of 42 trials per block. For each trial, listeners were asked to decide which sound was rougher (2AFC). No feedback was given. After a few practice trials (5 to 10), all blocks were run just once.

3. Subjects

A first group of 15 subjects ran the conditions f_c =500,1000,2000 Hz. Subsequently, another group of 15 subjects ran the conditions f_c=125,250,4000,8000 Hz. The listeners consisted of 17 men and 13 women with ages varying from 24 to 32 (mean=27). They all had self-reported normal hearing and were not queried about musical training or previous experience in psychoacoustic experiments.

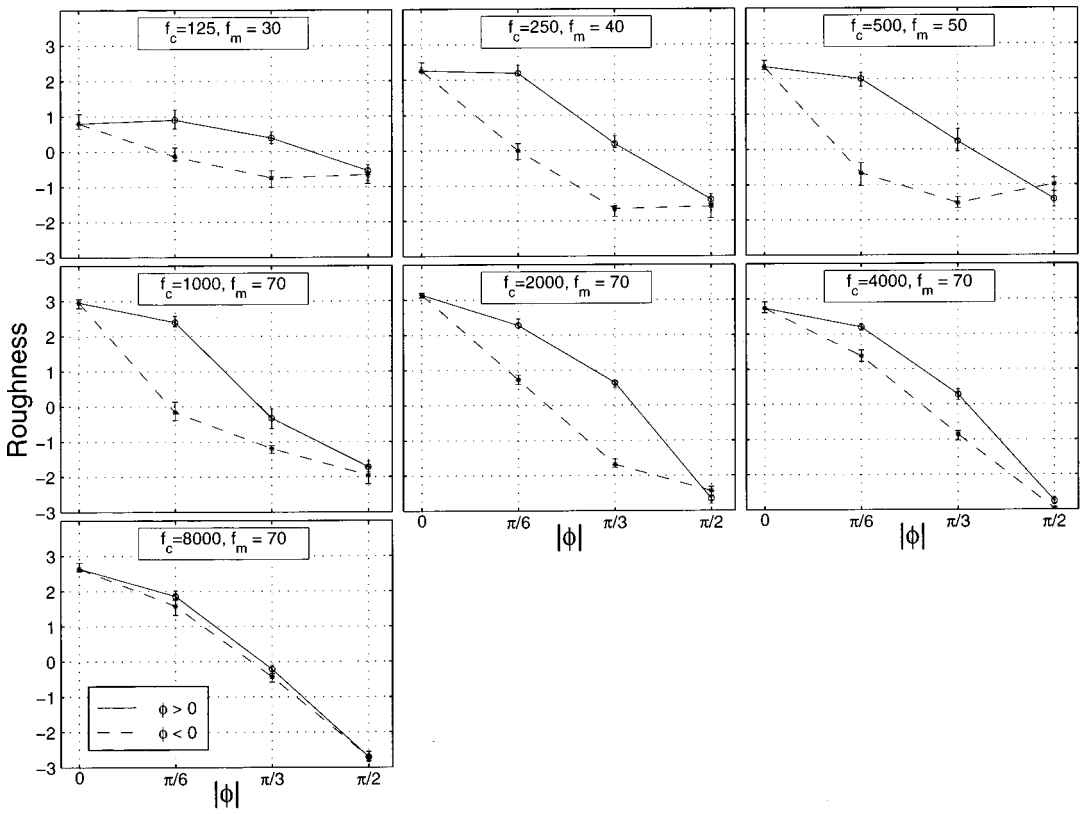

FIG. 2. Results of Experiment 1. The different panels correspond to the seven (f_c, f_m) conditions, as indicated (in Hz) on top of each panel. The roughness values estimated by the BTL method and the standard deviations estimated by bootstrap are plotted as a function of the phase ϕ of the central component. Solid lines represent $\phi>0$ and dashed lines represent $\phi<0$.

4. Statistical analyses

The Bradley–Terry–Luce (BTL) method was used to construct a psychophysical scale from the binary paired-comparison judgments (David, 1988). The basic hypothesis for this method is that the stimuli can be arranged along a linear scale, roughness in our case. When presented with two sounds, listeners do not compare their ''true'' roughnesses but rather two random variables centered on the real values. Therefore, different outcomes are expected for the same comparison between two sounds, across listeners but also with repetitions for a same listener. It can then be shown that, with certain hypotheses on the random distributions, the proportion of times one sound is judged rougher than another is linked to the distance separating them on the perceptual scale (Bradley, 1953). The BTL method uses this principle to combine all comparison judgments across all listeners to produce a single *relative* scale that represents the contrast perceived between sounds in terms of roughness. The scale is normalized so that the sum of the values is equal to zero, hence the presence of negative values in the scale.

In order to test whether roughness differences were significant, they must be compared to the standard deviations of the results. These standard deviations are not readily available with the BTL method because judgments from all listeners are collapsed into proportions to build the scale. They were estimated by the bootstrap technique (Efron and Tibshirani, 1993). An empirical distribution was generated by resampling with replacement from the data set: a 100 sets of 15 samples were drawn. As a sample corresponds to the data matrix for a given subject, each set can be thought of as a simulated subject group. For each set, the BTL analysis was performed anew, giving in the end a distribution of estimated roughness values for each stimulus. These distributions were used to estimate the standard deviations displayed in the figures. The standard deviations were finally used to test for the significance of the difference between any two stimuli at a given risk, here $p<0.05$ (Efron and Tibshirani, 1993).

C. Results

The results for the seven series of stimuli are presented in Fig. 2 in which the estimated roughness values are plotted as a function of ϕ. The most obvious factor contributing to roughness is the absolute value of ϕ, greater $|\phi|$ producing smaller roughness. This effect is similar in range across most f_c's tested, except for $f_c=125$ Hz where a significant decrease in range is observed. However, for f_c's at or below 4 kHz, there is also a strong effect of the sign of the phase ϕ for stimuli with a same amplitude spectrum and a same waveform envelope. This effect is consistent for the intermediate phase conditions for which the positive phase condition results in significantly higher roughness than the negative phase condition. This effect disappears for all f_c's at $\phi=\pm\pi/2$ and for all phase differences at $f_c=8$ kHz. Another

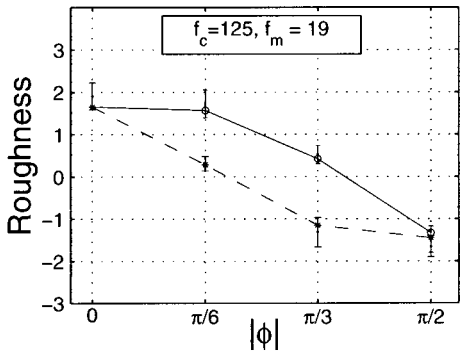

FIG. 3. Results of the control block of Experiment 1. This condition is to be compared with the top left panel of Fig. 2 that has the same f_c.

feature of the data to note is the relatively small size of the standard deviations, indicating a strong agreement across subjects.

D. Discussion

1. Dependency of roughness on the phase absolute value

The influence of $|\phi|$ reflects the effect of waveform envelope for a given amplitude spectrum. It can be interpreted by considering that the rms value of the envelope of the physical stimulus decreases as $|\phi|$ increases, and that this decrease is preserved after auditory filtering (Appendix C).

The overall reduction of variation range at $f_c = 125$ Hz could then be explained in terms of a critical band effect. At $f_c = 2$ kHz, the pAM stimuli cover 140 Hz, which is clearly less than the width of the auditory filter as estimated in terms of equivalent rectangular bandwidth (ERB=240 Hz; Glasberg and Moore, 1990). At $f_c = 125$ Hz, the stimuli cover 60 Hz which exceeds the ERB of 38 Hz at this center frequency. In this case, interactions occur mainly between adjacent components (separated by 30 Hz).

A control block was included in the experiment for 15 subjects. In this block, the modulation frequency was chosen so that the ratio f_m/ERB was identical to the one used for the condition $f_c = 1$ kHz. A series of pAM sounds with $(f_c, f_m) = (125,19)$ Hz was thus generated. We expected the effect of $|\phi|$ to be more pronounced in this case as all components could interact within an auditory filter. The results obtained are presented in Fig. 3. The global contrast increases, confirming our hypothesis. The greater variability in the results is probably due to the weak roughness produced by such a low modulation frequency; experimental judgments are harder to make in this case. The lessened contrast at this f_c in the original data suggests that the effect of waveform envelope, when manipulated by phase relationships, is more pronounced if the three components can interact within a single auditory filter. This is in agreement with previous findings (Mathes and Miller, 1947; Goldstein, 1967b; Terhardt, 1974).

The effect of $|\phi|$ is therefore in good agreement with the hypothesis of the dependency of roughness on envelope fluctuation after auditory filtering as measured by envelope rms magnitude.[1] However, the significant influence of phase for a given waveform envelope and amplitude spectrum is not expected with this hypothesis. Let us examine different factors that may underlie the observed differences.

2. Combination tones

Combination tones generated by the three components of the pAM stimuli may have played a role in the roughness judgments. Several studies have shown that among these tones, the most important is the first-order cubic difference tone (CDT) that is situated at $2(f_c)-(f_c+f_m)=f_c-f_m$ and that can interact with the acoustic component at the same frequency in our stimuli (Goldstein, 1967a; Plomp, 1976; Greenwood, 1991). Studying the influence of phase on the residue pitch of a three-component signal resembling the pAM tones, Buunen *et al.* (1974) proposed that the lower acoustic component was internally modified by a vector sum with the CDT. The phase of the CDT was found to vary as a function of the phase of the primaries, which may explain the differences observed in perceived roughness when ϕ varies.

A rule was derived to predict the phase change of the CDT if the phases of the primaries change (Buunen *et al.*, 1974). In the case of the pAM tones, the phase change of the CDT reduces to two times the change in ϕ. Therefore, between the conditions $\phi=\pi/2$ and $\phi=-\pi/2$ the phase of the CDT should shift by 2π. This is consistent with the fact that both $\pm\pi/2$ conditions produced an equivalent roughness.

However, an interpretation based on CDT faces two problems. First, the phase effect disappears at $f_c = 8$ kHz, whereas combination tones are likely to be still present, even with a lessened amplitude (Greenwood, 1991). Second, even if the phase change of the CDT could be summed up in a consistent rule by Buunen *et al.* (1974), the relation between the absolute phase of the CDT and the absolute phases of the primaries varies widely between subjects (Buunen *et al.* 1974; Zurek and Leishowitz, 1976). This is true to the extent that individual data had to be presented to report the effect. Our results display on the contrary a remarkable agreement among listeners.

3. Asymmetry of the internal envelope

Temporal factors can alternatively be considered to interpret the observed roughness differences between positive and negative phase conditions. Even if these conditions correspond to a same physical envelope, the temporal fine structure of the stimuli are not the same. These physical differences could modify an ''internal envelope'' that would take into account the effects of auditory peripheral filtering.

A computational model was used to investigate the effect of peripheral auditory filtering (Giguère and Woodland, 1994). It is an active (Davis, 1983) basilar membrane model that displays a realistic phase behavior. It has been successfully used to interpret previous experimental data demonstrating the influence of phase on internal envelope (Carlyon, 1996; Carlyon and Datta, 1997b). The details of the implementation we used are described in Appendix C.

Overall, the filters centered at frequencies higher than the stimulus f_c are expected to produce most of the perceived roughness because of the spread of the excitation pat-

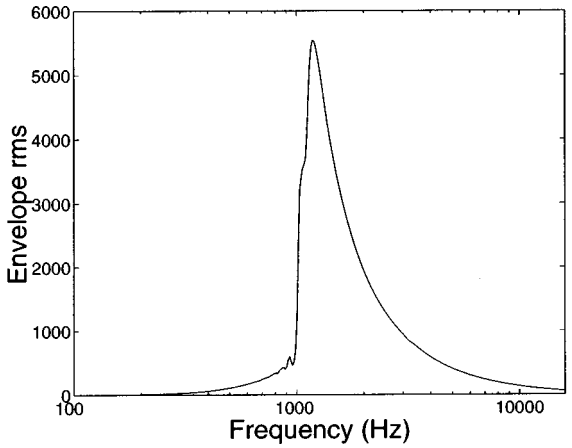

FIG. 4. Envelope modulation of the pAM tone with $(f_c, f_m) = (1000,70)$ Hz and $\phi = 0$ after auditory filtering. The filtering is simulated by the Giguère and Woodland (1994) model. The rms value of the Hilbert envelope of the signal present in each filter is displayed as a function of filter center frequency, in model's units.

terns toward high frequencies. This can be confirmed by computing the envelope rms value in individual channels of the auditory filtering simulation (Fig. 4).

The output of the filter that produces the highest envelope rms for the pAM tones with $(f_c, f_m) = (1000,70)$ Hz is displayed in Fig. 5, as an example of the output of the filters located above stimulus f_c. For all phases except $\phi = \pm\pi/2$, the modulations introduced by opposite phases reveal different shapes. In the positive phase conditions, the modulation shows an abrupt rise and a slow decay. This pattern is inverted for the negative conditions. This conversion of temporal fine-structure differences into envelope shape differences is for instance illustrated by the conditions $\phi = \pm\pi/6$, whose physical waveforms look very similar (Fig. 1, bottom panels), but whose filtered waveforms display asymmetrical envelopes (Fig. 5, top panels). These two sounds produced different roughnesses (Fig. 2).

The envelope asymmetry is actually introduced by the attenuation of the lower component of the pAM by auditory filtering, as we show in Appendix B. Therefore, it is not a critically dependent on the computational model used to simulate auditory filtering. In this Appendix, we show as well that the asymmetry has to disappear for the $\pm\pi/2$ conditions for all carrier frequencies. It also disappears progressively as the carrier frequency increases; the width of the critical band then becomes very large compared to the frequency span of the pAM tones and the auditory filters do not attenuate the lower component significantly more than the other components. The asymmetry is therefore present when significant differences in roughness were perceived and absent when the same roughnesses were judged.

It is important to note that the rms value of the modulation envelope after simulated auditory filtering cannot explain the observed results. It would lead to predict no effect of phase sign in most conditions, or even in some conditions a higher rms value for negative phase (see Appendix C). This precludes an interpretation in terms of the existing temporal models. The exploration of the effect of auditory filtering on positive and negative phase conditions therefore points to the

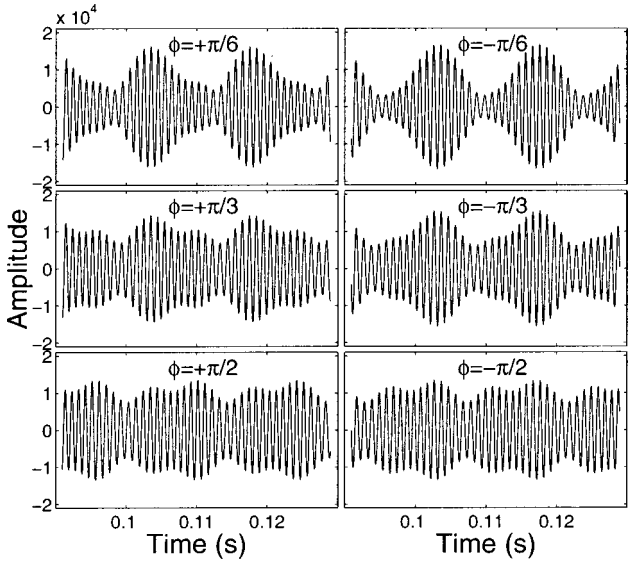

FIG. 5. Filtering of the pAM tones with $(f_c, f_m) = (1000,70)$ Hz by the Giguère and Woodland (1994) model. The output of the auditory filter that has the highest envelope rms (centered at 1180 Hz) is displayed for different values of ϕ. Amplitude is in model's units.

hypothesis that the shape of the envelope could have an influence on roughness perception. Another experiment was designed to address directly this hypothesis.

II. EXPERIMENT 2

A. Experimental hypotheses

This experiment proposes to study the roughness produced by pure tones modulated with asymmetrical envelopes. A modulation resembling a sawtooth waveform, with a slow rise and an abrupt decay, was chosen. We chose not to use a real sawtooth to modulate our stimuli as the spectrum of such a waveform consists theoretically of an infinite number of harmonically related spectral components. In addition to the aliasing problems that the sampling of such a wave may cause (Stilson and Smith, 1996), resolved spectral components could appear in the lower auditory channels that might confuse listeners in their judgments. We rather constructed envelopes by truncating the spectrum of a sawtooth of frequency f_m. For a given center frequency f_c, only the spectral components that lay within a frequency distance of 1/2 ERB (Glasberg and Moore, 1990) of f_c were retained:

$$E_{\text{sawtooth}}(t) = \sum_{n=1}^{n=N} \frac{1}{n} \cos(2\pi n f_m t - \pi/2) \quad \text{with } N \cdot f_m \leqslant \tfrac{1}{2}\,\text{ERB}(f_c). \tag{2}$$

The actual stimuli were then obtained by amplitude modulating a cosine wave at frequency f_c with the corresponding envelope:

$$x_{\text{sawtooth}}(t) = \left(1 + m \cdot \frac{E_{\text{sawtooth}}(t)}{\max[E_{\text{sawtooth}}(t)]}\right) \cdot \cos(2\pi f_c t - \pi/2). \tag{3}$$

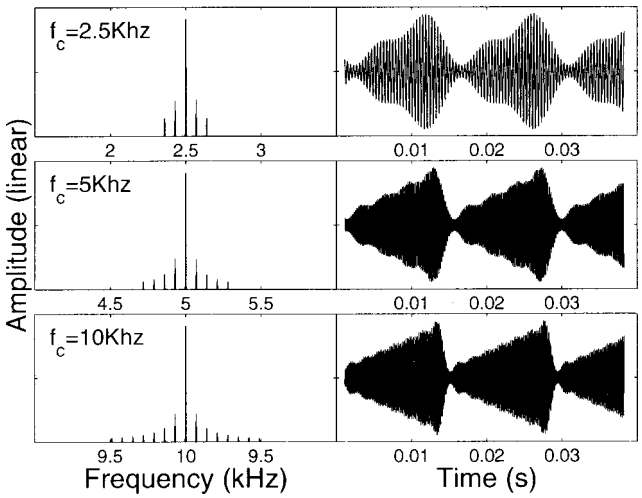

FIG. 6. Stimuli for Experiment 2. Amplitude spectra and waveforms are plotted for the ''sawtooth'' conditions with a modulation depth of $m=0.8$.

Such sounds look like sawtooth amplitude-modulated tones (see Fig. 6) and will therefore be referred to as ''sawtooth'' stimuli. Another set of stimuli was generated by inverting the starting phases of all components (envelope and carrier) to $+\pi/2$. These sounds are in fact a time reversal of the ''sawtooth'' ones and will be referred to as ''reversed'' stimuli. This phase manipulation allows us to compare stimuli with a given amplitude spectrum and a given modulation depth, but different physical envelope shapes. These differences in shape resemble those hypothesized to have been introduced by auditory filtering in Experiment 1. We checked that they should also be preserved after auditory filtering with a model simulation shown in Fig. 7 (Giguère and Woodland, 1994). If envelope asymmetry has an effect on roughness perception, a change in roughness should be observed between the ''sawtooth'' and ''reversed'' conditions.

B. Method

1. Stimuli

The modulation frequency f_m was chosen to be 70 Hz. The first center frequency for which $E_{\text{sawtooth}}(t)$ could have more than one spectral component according to the band-limiting criterion was 2500 Hz. In order to make the stimuli as similar as possible to those of the first experiment, various carrier frequencies were tested and for a given carrier frequency different values of modulation depth m were used. Three series of amplitude-modulated tones were generated: $(f_c, f_m)=$(2500 Hz; 70 Hz), (5000; 70), (10 000; 70). Three modulation depths were used: $m=0.4$, 0.6, 0.8. An experimental block therefore includes sounds with varying modulation depth, and for a given amplitude spectrum and modulation depth ''sawtooth'' and ''reversed'' modulations are present.

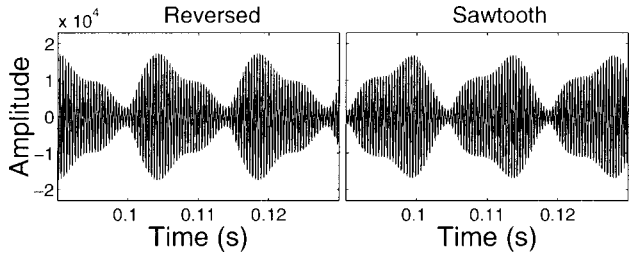

FIG. 7. Filtering of the ''reversed'' and ''sawtooth'' tones, with $(f_c, f_m)=(2500,70)$ Hz and $m=0.8$, by the Giguère and Woodland (1994) model. The output of the auditory filter with the highest envelope rms (centered at 2818 Hz) is displayed. Amplitude is in model's units.

2. Apparatus and procedure

The apparatus and procedure remained identical to those in Experiment 1, except that the headphones were changed to Sennheiser 420 (the headphones used in experiment 1 being no longer available). For a given f_c block, all 15 possible pairs of nonidentical stimuli were presented in both orders in a randomized fashion, giving a total of 30 trials. All blocks were run once by each subject.

3. Subjects

Ten subjects participated in the experiment. The listeners consisted of 6 men and 4 women with ages varying from 24 to 45 (mean=28). All listeners had self-reported normal hearing and were not queried about musical training or previous experience in psychoacoustic experiments.

C. Results

The results are displayed in Fig. 8. The influence of modulation depth is visible for all center frequencies; a higher modulation depth introduces more roughness. A significant effect of the shape of the waveform envelope is also observed. For a given amplitude spectrum and a given modulation depth, the ''reversed'' stimulus is systematically

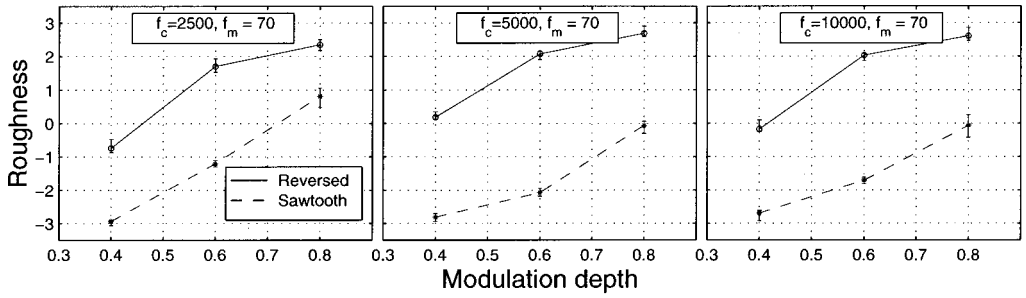

FIG. 8. Results of Experiment 2. The different panels correspond to the three (f_c, f_m) conditions, as indicated (in Hz) on top of each panel. The roughness values are displayed as a function of modulation depth m. Solid lines represent the ''reversed'' modulation, dashed lines the ''sawtooth'' modulation.

judged rougher than the ''sawtooth'' stimulus. This effect is highly significant at all f_c's for all modulation depths. It is, however, significantly smaller for the stimuli centered on $f_c = 2.5$ kHz.

D. Discussion

1. Effect of modulation depth

The increase in roughness with modulation depth can be explained by both spectral and temporal arguments. Indeed, in contrast to Experiment 1, the stimuli used here differ according to their amplitude spectra when the modulation depth increases; a greater modulation depth is accompanied by greater envelope rms, but also by greater sideband energy. This all leads to predict higher roughness. However, for a given modulation depth the signals have the same amplitude spectrum and waveform envelope rms. In this situation, the ''reversed'' and ''sawtooth'' conditions display equivalent envelope rms values after auditory filtering, as estimated by the model used for experiment 1 (Appendix C). An effect of the shape of the envelope is nevertheless observed.

2. Effect of envelope shape

The significant effect of envelope shape is consistent with our previous hypotheses. ''Reversed'' sawtooth modulations that display an abrupt rise and a slow decay resemble the signals obtained after auditory filtering of the positive phase conditions of Experiment 1. They are rougher than ''sawtooth'' modulations that resemble the negative phase conditions.

This effect is more pronounced for high f_c's. This is also consistent with our hypotheses. The asymmetry of the waveform envelope is less sharp for the lowest f_c because of the small number of spectral components in the modulation. This could provide the basis for the reduction in the perceptual effect observed. In Experiment 1, the phase effect disappeared for high f_c's as the asymmetry in the internal envelope disappeared. Here, the asymmetry is imposed on the acoustical stimulus and the effect remains. All this suggests that the phase effects are linked to characteristics of the envelope and not to details in the temporal fine structure of the stimuli, since the representation of such details would become progressively less reliable at high f_c's due to the loss of phase locking.

III. GENERAL DISCUSSION

A. Spectral and temporal models

The effect of phase on roughness perception of sounds that have the same amplitude spectrum has been used as an argument against spectral models (Plomp and Steeneken, 1968; Terhardt, 1974). The only possibility to spectrally account for our results would be to consider the influence of combination tones on the ''internal spectrum,'' as the phase of the first-order cubic distortion product changes with the phase of its primaries (Buunen *et al.*, 1974). Such an effect cannot totally be ruled out as a contribution to the results of Experiment 1, even if we argued that these effects averaged out across listeners because of their variability. The effect of combination tones on the results of Experiment 2 is harder to imagine, however.

In contrast, the temporal models' hypothesis of the link between roughness and characteristics of the envelope can readily explain some of the features of our experimental data, namely the effect of $|\phi|$ in Experiment 1 and of m in Experiment 2. However, these models fall short of explaining another major feature of the results, in that sounds with the same amplitude spectrum and rms envelope magnitude can produce different roughnesses.

B. Phase dispersion

Phase effects have previously been reported for sounds with the same amplitude spectrum and waveform envelope. Thresholds of pure tones masked by harmonic sounds in positive Schroeder phase or negative Schroeder phase exhibited an influence of phase (Smith *et al.*, 1986; Kohlrausch and Sander, 1995; Carlyon and Datta, 1997a,b). The proposed explanation was that the phase-dispersive properties of the basilar membrane introduced differences in the modulation depth of the internal envelope near the resonance frequency of the masked tone. The model we used to simulate auditory filtering in the discussion of the results of Experiment 1 (Giguère and Woodland, 1994) has a realistic phase behavior and was able to predict the results of these former studies. However, in our case the envelope rms differences that appeared between some positive and negative phase conditions were very small and sometimes even went against the experimental results. The lack of large differences in envelope rms probably comes from the fact that the stimuli we used were narrowly band limited. The model, however, introduced an asymmetry in the filtered waveforms, that could be predicted by considering very general characteristics of auditory filtering. The phase effects we observed in both experiments for sounds with the same amplitude spectrum and envelope rms magnitude were therefore not attributed to a decrease in internal modulation depth but rather to a temporal asymmetry of the internal representation following auditory filtering.

C. Ramped and damped sinusoids

Temporal asymmetry effects have been reported by Patterson (1994a,b) with sounds resembling the stimuli of Experiment 2. In these studies, exponentially modulated sinusoids and their time reversals were compared. Various combinations of carrier and modulation frequencies were tested. ''Ramped'' conditions sounded generally more pure-tone-like than ''damped'' conditions. The interpretation proposed by Patterson relies on the distribution of time intervals across auditory channels, more intervals corresponding to the period of the carrier being present in the ramped conditions. Therefore, the effect is less pronounced at high frequencies because of loss of phase locking. However, such an interpretation in terms of time intervals could not explain all the features of the results of Experiment 2 because the envelope shape effect persists (and increases) at high carrier frequen-

cies. We hypothesize that in our case subjects might have ''listened to the envelope'' rather than the carrier to make the roughness judgments.

D. Roughness and envelope perception

Our results lead us to propose that roughness is linked to envelope fluctuations after auditory filtering. We also argue that the extraction of features relevant to roughness perception cannot be reduced to a simple bandpass filtering of the envelope followed by rms evaluation, but that an effect of envelope asymmetry has to be taken into account. Why such an asymmetry might translate into more or less roughness is still unclear. The recently reported influence of temporal asymmetry on latter stages of auditory processing (Winter and Patterson 1998) may ultimately provide a way to understand this effect.

IV. CONCLUSION

This study aimed to estimate the influence of some phase manipulations on roughness perception. We confirmed that phase changes that affect a signal's envelope rms magnitude while leaving its amplitude spectrum constant can have a clear effect on roughness perception, all the more so as the signals have a limited bandwidth compared to the auditory critical band. Differences in roughness between signals having the same amplitude spectrum and envelope rms magnitude across auditory filters were also found. We interpreted these differences on the basis of the shape of the modulation after auditory filtering: Modulations with an abrupt rise and a slow decay produce more roughness than modulations with a slow rise and an abrupt decay.

ACKNOWLEDGMENTS

The authors would like to thank Bennett K. Smith for his insights on the effects of phase dispersion. We also thank Ian M. Winter and Roy D. Patterson for discussing with us some of their recent data. Finally, we thank Wes Grantham and two anonymous reviewers who provided helpful comments on a previous version of this manuscript. Part of this work was completed thanks to a Fyssen Foundation grant to the first author.

APPENDIX A

Let us consider a signal composed of the sum of N cosine waves with amplitudes A_i, angular frequencies w_i, and phases ϕ_i, with $i \in [1, N]$. The envelope $E(t)$ of this signal may be obtained by taking the absolute value of its Hilbert transform (Hartmann, 1997):

$$E(t)^2 = \sum_{i=1}^{N} A_i^2 + 2 \sum_{\substack{j>i \\ i=1}}^{N} A_i A_j \cos[(\omega_i - \omega_j)t + (\phi_i - \phi_j)]. \tag{A1}$$

In the case of the pAM stimuli given in Eq. (1), this envelope can be simplified as in Eq. (A2):

$$E(t)^2 = \underbrace{3/2}_{dc} + \underbrace{1/2 \cos(2\omega_m t)}_{a(t)} + \underbrace{2|\cos(\phi)|\cos(\omega_m t)}_{b(t)}. \tag{A2}$$

Three terms participate in the square of the envelope: a dc offset, a component $a(t)$ at angular frequency $2w_m$ that does not depend on ϕ, and a component $b(t)$ at angular frequency w_m. If $\phi = 0$, then $b(t)$ has maximum amplitude and Eq. (A2) simplifies to a cosinusoidal modulation. The rms value of the envelope is then $\sqrt{2}/2$. If $\phi = \pm \pi/2$, then only $a(t)$ remains and the envelope has an rms value of $(1 - \sqrt{2}/2)/2$. As $b(t)$ depends only on the absolute value of ϕ, two opposite phase conditions will produce the same envelope.

APPENDIX B

Let us examine the influence on the pAM tones of an ideal bandpass filter that is phase linear and that halves the amplitude of the lower component without affecting the amplitude of the other components. In this case, simplifications of Eq. (A1) lead to the following expression of the envelope:

$$E(t)^2 = \mathrm{dc} + a(t) + b(t)$$

with

$$\begin{aligned} &\mathrm{dc} = 11/8 \\ &a(t) = 1/4 \cos(2\omega_m t) \\ &b(t) = \sqrt{1/4 + 2\cos^2(\phi)}\cos(\omega_m t + \theta) \\ &\theta = \begin{cases} \arctan[-1/3 \tan(\phi)] & \text{if } (\phi \neq \pm \pi/2) \\ -\phi & \text{if } (\phi = \pm \pi/2) \end{cases}. \end{aligned} \tag{B1}$$

The important thing to notice here, disregarding the numerical values specific to the example given, is that the phase of $b(t)$ depends on ϕ. If $\phi > 0$, then $\theta < 0$ and $b(t)$ will be slightly delayed compared to $a(t)$. Since $b(t)$ has a larger amplitude than $a(t)$, this will result in an asymmetry in the shape of the envelope (a rapid rise and a slow decay). If $\phi < 0$, the sign of θ and therefore the shape of the envelope is reversed, producing a slow rise and an abrupt decay. If $\phi = \pm \pi/2$, the delay θ is equal to $\pm \pi/2$. The absolute phase difference between these two conditions corresponds to π, half a period of $b(t)$, therefore a complete period of $a(t)$; the envelope remains the same between positive and negative phase conditions if $\phi = \pm \pi/2$. This same pattern of dependency of the envelope on the phase ϕ will always be observed if the lower component of the pAM has a smaller amplitude than the higher one.

This example aims to illustrate what happens in the auditory filters of center frequency above f_c, since for such filters the lower component is more attenuated than the higher one (additional attenuation of the central component does not change the reasoning). The actual filtering at the level of the basilar membrane is not phase linear, but the small frequency span of the pAM allows one to make a linearization of phase around f_c without introducing much error—such a linearization was also proposed by Goldstein (1967b) for comparing AM and QFM envelopes within a

single auditory filter. Therefore, any model of auditory filtering should introduce an asymmetry similar to the one we just described.

The asymmetry is reversed for filters centered below f_c; however, these filters will contain much less activity because of the spread of the excitation patterns toward high frequencies. At the level of gross activity at the input to the auditory nerve, we thus hypothesize that the critical-band filtering has the global effect of sharpening the leading slope of the modulation envelope for positive ϕ and flattening it for negative ϕ.

APPENDIX C

To simulate the effect of auditory filtering, we used the model of Giguère and Woodland (1994) as implemented in the AIM Release 8 software platform (Patterson *et al.*, 1995). All parameters were set to default values, except for the quality factor Q_n, which was increased from 2 to 8. In doing this we followed the suggestion made by Carlyon (1996, 1997b) that the original value leads to too broad tuning curves when compared to psychophysical data. The wave input level was set to 60 dB SPL. All simulations were made with 320 segments between 100 Hz and 16 kHz at a sampling rate of 71 680 Hz (Giguère *et al.*, 1997).

In order to test if the transformation made by the filtering could account for the effect of phase observed in Experiment 1, we extracted the Hilbert envelope of the signals present in each channel, computed their rms value, and then summed up these values across channels. This does not give a perfect roughness estimate as a power function probably relates rms and roughness (Terhardt, 1974). In addition, the problem of roughness addition across channels is not taken into account here. However, all existing temporal roughness models would predict a monotonic link between overall rms value and perceived roughness.

The results of the computation for some representative f_c and f_m conditions are presented in Fig. C1. They can be compared to the experimental results of Fig. 2. The envelope rms value decreases with increasing $|\phi|$, which corresponds to the experimental results. However, the simulations are at clear variance concerning the effect of the sign of ϕ.

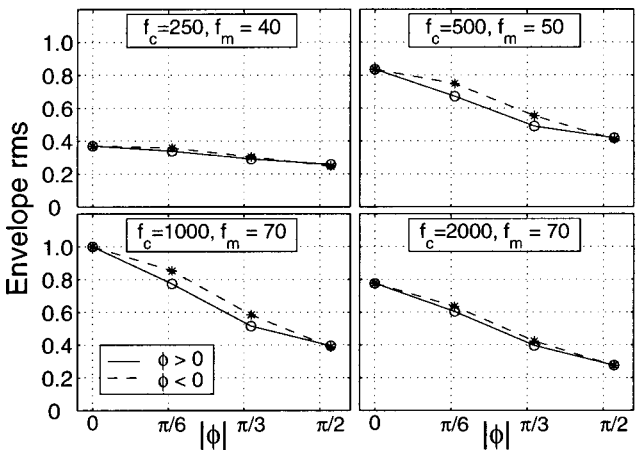

FIG. C1. Model simulation for the stimuli of Experiment 1. The sum of the rms value of the envelope of the signals present in each auditory filter is displayed as a function of ϕ. The rms values have been normalized to their maximum across stimuli.

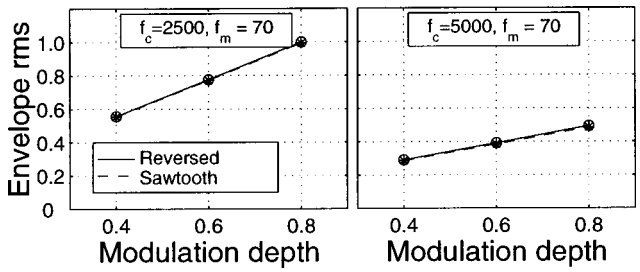

FIG. C2. Model simulation for the stimuli of Experiment 2. The sum of the rms value of the envelope of the signals present in each auditory filter is displayed as a function of *m*. The rms values have been normalized to their maximum across stimuli.

The same model was used with the stimuli of Experiment 2. The results of the computation for some representative f_c and f_m conditions are shown in Fig. C2. The increase of the rms value of the envelope with modulation depth generally goes with the perceived increase in roughness. However, the large effect of envelope asymmetry between the ''reversed'' and ''sawtooth'' conditions observed experimentally is not reproduced by the model.

[1]An aspect of the stimuli other than the envelope rms could be thought to have influenced the perceived roughness when $|\phi|$ is varied. In the conditions $|\phi|=\pi/2$ the envelope period is halved (see Appendix A). This change makes the apparent modulation frequency higher than the frequency that produces maximum roughness and could contribute to the small roughness values observed in these cases. However, the fact that the main contribution to roughness judgments came from variations of envelope rms and not of envelope period is suggested by two distinct points. For all f_c conditions, the halving of the envelope period is only fully present for $|\phi|=\pi/2$. For the other phase values, the period remains the same but the observed roughness value decreases along with the envelope rms. For the control block at $f_c=125$ Hz and $f_m=19$ Hz, the modulation frequency is below that which produces maximum roughness. The halving of the envelope period, leading to an apparent modulation frequency of 38 Hz, should actually tend to produce more roughness in this particular case. However, the observed roughness values when the halving takes place are still small, in agreement with the low envelope rms value.

Aures, W. (**1985**). ''Ein Berechnungsverfahren der Rauhigkeit [A roughness calculation method],'' Acustica **58**, 268–281.

Bradley, R. A. (**1953**). ''Some statistical methods in taste testing and quality evaluation,'' Biometrics **9**, 22–39.

Buunen, T. J. F., Festen, J. M., Bilsen, F. A., and van den Brink, G. (**1974**). ''Phase effects in a three-component signal,'' J. Acoust. Soc. Am. **55**, 297–303.

Carlyon, R. P. (**1996**). ''Spread of excitation produced by maskers with damped and ramped envelopes,'' J. Acoust. Soc. Am. **99**, 3647–3655.

Carlyon, R. P., and Datta, A. J. (**1997a**). ''Excitation produced by Schroeder-phase complexes: Evidence for fast-acting compression in the auditory system,'' J. Acoust. Soc. Am. **101**, 3636–3647.

Carlyon, R. P., and Datta, A. J. (**1997b**). ''Masking period patterns of Schroeder-phase complexes: Effects of level, number of components, and phase of flanking components,'' J. Acoust. Soc. Am. **101**, 3648–2657.

Daniel, P., and Weber, R. (**1997**). ''Psychoacoustical roughness: Implementation of an optimized model,'' Acustica **83**, 113–123.

David, H. A. **(1988)**. *The Method of Paired Comparisons*, 2nd ed. (Oxford University Press, New York).

Davis, H. (**1983**). ''An active process in cochlear mechanics,'' Hearing Res. **9**, 79–90.

Efron, B., and Tibshirani, R. J. **(1993)**. *An Introduction to the Bootstrap* (Chapman & Hall, London).

Fastl, H. **(1977)**. ''Roughness and temporal masking patterns of sinusoidally amplitude modulated broadband noise,'' in Evans, E. F. and Wilson, J. P. (Eds.), *Psychophysics and Physiology of Hearing*, edited by E. F. Evans and J. P. Wilson (Academic, London), pp. 403–415.

Fay, R. R. (**1994**). ''Perception of temporal acoustic patterns by the goldfish (Carassius auratus),'' Hearing Res. **76**, 158–172.

Giguère, C., Smoorenburg, G. F., and Kunov, H. (**1997**). ''The generation of psychoacoustic combination tones in relation to two-tone suppression effects in a computational model,'' J. Acoust. Soc. Am. **102**, 2821–2830.

Giguère, C., and Woodland, P. C. (**1994**). ''A computational model of the auditory periphery for speech and hearing research. I. Ascending path,'' J. Acoust. Soc. Am. **95**, 331–342.

Glasberg, B. R., and Moore, B. C. J. (**1990**). ''Derivation of auditory filter shapes from notched-noise data,'' Hearing Res. **47**, 103–138.

Goldstein, J. L. (**1967a**). ''Auditory nonlinearity,'' J. Acoust. Soc. Am. **41**, 676–689.

Goldstein, J. L. (**1967b**). ''Auditory spectral filtering and monaural phase perception,'' J. Acoust. Soc. Am. **41**, 458–479.

Greenwood, D. D. (**1991**). ''Critical bandwidth and consonance: Their operational definitions in relation to cochlear nonlinearity and combination tones,'' Hearing Res. **54**, 209–246.

Hartmann, W. M. **(1997)**. *Signals, Sound, and Sensation* (AIP Press, Woodbury, New York).

von Helmholtz, H. L. F. **(1877)**. *On the Sensations of Tone as the Physiological Basis for the Theory of Music*, 2nd ed., translated by A. J. Ellis (1885), 4th ed. (Dover, New York, 1954; from German).

Hulse, S. H., Bernard, D. J., and Braaten, R. F. (**1995**). ''Auditory discrimination of chord-based spectral structures by European starlings (Sturnus Vulgaris),'' J. Exp. Psychol. **124**, 409–423.

Hutchinson, W., and Knopoff, L. (**1978**). ''The acoustic component of Western consonance,'' Interface **7**, 1–29.

Kameoka, A., and Kuriyagawa, M. (**1969**). ''Consonance theory Part I,'' J. Acoust. Soc. Am. **45**, 1451–1458.

Kohlrausch, A., and Sander, A. (**1995**). ''Phase effects in masking related to dispersion in the inner ear. II. Masking period pattern of short sound targets,'' J. Acoust. Soc. Am. **97**, 1817–1829.

Mathes, R. C., and Miller, R. L. (**1947**). ''Phase effects in monaural phase perception,'' J. Acoust. Soc. Am. **19**, 780–797.

Patterson, R. D. (**1994a**). ''The sound of a sinusoid: Spectral models,'' J. Acoust. Soc. Am. **96**, 1409–1418.

Patterson, R. D. (**1994b**). ''The sound of a sinusoid: Time-interval models,'' J. Acoust. Soc. Am. **96**, 1419–1428.

Patterson, R. D., Allerhand, M. H., and Giguère, C. (**1995**). ''Time-domain modelling of peripheral auditory processing: A modular architecture and a software platform,'' J. Acoust. Soc. Am. **98**, 1890–1894.

Plomp, R. **(1976)**. *Aspects of Tone Sensation* (Academic, London).

Plomp, R., and Levelt, W. (**1965**). ''Tonal consonance and critical bandwidth,'' J. Acoust. Soc. Am. **38**, 548–560.

Plomp, R., and Steeneken, H. J. M. (**1968**). ''Interference between two simple tones,'' J. Acoust. Soc. Am. **43**, 883–884.

Pressnitzer, D., and McAdams, S. (**1997**). ''Influence de la phase sur la perception de rugosité de sons complexes,'' Actes du 4ème Congrès Français d'Acoustique **1**, 535–538.

Pressnitzer, D., and McAdams, S. **(1998)**. ''Phase effects in roughness perception,'' in *Psychophysical and Physiological Advances in Hearing*, edited by A. R. Palmer, A. Rees, A. Q. Summerfield, and R. Meddis (Whurr, London), pp. 286–292.

Schellenberg, E. G., and Trainor, L. J. (**1996**). ''Sensory consonance and the perceptual similarity of complex-tone harmonic intervals: Test of adult and infant listeners,'' J. Acoust. Soc. Am. **100**, 3321–3328.

Smith, B. K., Sieben, U. K., Kohlrausch, A., and Schroeder, M. R. (**1986**). ''Phase effects in masking related to dispersion in the inner ear,'' J. Acoust. Soc. Am. **80**, 1631–1637.

Stilson, T., and Smith, J. **(1996)**. ''Alias-free digital synthesis of classic analog waveform,'' in *Proceedings of 1996 International Computer Music Conference*, Hong Kong, edited by L. Ayers and A. Norner.

Terhardt, E. **(1970)**. ''Frequency analysis and periodicity detection in the sensation of roughness and periodicity pitch,'' in *Frequency Analysis and Periodicity Detection in Hearing*, edited by R. Plomp and G. Smoorenburg (A. W. Sijthoff, Leiden), pp. 278–287.

Terhardt, E. (**1974**). ''On the perception of periodic sound fluctuation (roughness),'' Acustica **30**, 201–212.

Winter, I. M., and Patterson, R. D. **(1998)**. ''Comparisons of the responses from neurones in the cochlear nucleus and inferior colliculus encoding to ramped and damped sinusoids,'' in *Assoc. Res. Oroloryngol. Abs.*, edited by G. R. Popelka, St. Petersburg Beach, FL., p. 99.

Zurek, P. M., and Leishowitz, B. H. (**1976**). ''Measurement of the combination tones $f2$-$f1$ and $2f2$-$f1$,'' J. Acoust. Soc. Am. **60**, 155–168.

Zwicker, E., and Fastl, H. **(1990)**. *Psychoacoustics, Facts and Models* (Springer-Verlag, Berlin).

Syllable intelligibility for temporally filtered LPC cepstral trajectories

Takayuki Arai
Sophia University, 7-1 Kioi-cho, Chiyoda-ku, Tokyo, Japan

Misha Pavel
AT&T Labs West, 75 Willow Road, Menlo Park, California 94025

Hynek Hermansky
Oregon Graduate Institute of Science & Technology, P.O. Box 91000, Portland, Oregon 97291-1000

Carlos Avendano
CIPIC, University of California, Davis, California 95616

(Received 19 December 1996; accepted for publication 29 January 1999)

The intelligibility of syllables whose cepstral trajectories were temporally filtered was measured. The speech signals were transformed to their LPC cepstral coefficients, and these coefficients were passed through different filters. These filtered trajectories were recombined with the residuals and the speech signal reconstructed. The intelligibility of the reconstructed speech segments was then measured in two perceptual experiments for Japanese syllables. The effect of various low-pass, high-pass, and bandpass filtering is reported, and the results summarized using a theoretical approach based on the independence of the contributions in different modulation bands. The overall results suggest that speech intelligibility is not severely impaired as long as the filtered spectral components have a rate of change between 1 and 16 Hz. © *1999 Acoustical Society of America.* [S0001-4966(99)01705-1]

PACS numbers: 43.66.Mk, 43.71.Es, 43.72.Ar [JH]

INTRODUCTION

One of the main objectives of front-end processing in robust automatic speech recognition (ASR) is to preserve critical linguistic information while suppressing such irrelevant information as speaker-specific characteristics, channel characteristics, and additive noise. The information suppressed in the front end of the recognizer is lost for the recognition process. To determine information to be preserved, we need to identify those features of the signal that are necessary for human speech recognition. One way to identify the useful features is to suppress a given feature, reconstruct the speech, and determine its intelligibility through perceptual experiments.

Temporal processing, or filtering the time trajectories, of the logarithmic spectrum or cepstral coefficients is becoming a common procedure in current ASR. One reason for this type of processing is that the convolutional distortion, such as the frequency characteristics of a communications channel, is an additive component in the logarithmic spectrum and the cepstrum domains. These channel characteristics are often fixed or only slowly varying in time. Therefore, cepstral mean subtraction (CMS) is often used to eliminate the channel characteristics by subtracting the mean (or dc component) of the time trajectory of each cepstral coefficient.[1] The delta features are calculated as linear regression coefficients over a short segment of a time trajectory to emphasize the dynamic characteristics of the original features.[2] This delta technique is effectively equivalent to applying a finite impulse response (FIR) bandpass filter which eliminates the dc component of the time trajectory and applies 6 dB/oct emphasis on changes up to approximately 12 Hz.

The RelAtive SpecTrAl (RASTA) technique suppresses the spectral components that change more slowly or quickly than the typical range of change of spectral envelope.[3] (Please note that throughout this paper, we address the rate of change of spectral envelope, i.e., the rate at which the source signal is being modulated, by changes in the vocal tract shape, not the rate of change of the signal itself.) The RASTA technique is implemented by the following steps: (1) compute the spectral amplitude, (2) transform the spectral amplitude through a compressing static nonlinear transformation, (3) filter the time trajectory of each transformed spectral component, (4) transform the filtered speech representation through an expanding static nonlinear transformation, and (5) perform optional processing. The logarithmic function is often used for the nonlinear transformation. RASTA processing also eliminates the dc component but, unlike the delta feature computation, it passes components between 1 and 12 Hz unattenuated. Both delta and RASTA techniques appear to achieve some degree of robustness to channel variations.

Thus, the front end suppresses some information from the speech signal by filtering the time trajectories of the cepstral coefficients. The relatively slow rates of cepstral change, or low-modulation frequencies, include such information as channel characteristics, speaker information, and voice quality, which are assumed not crucial for human speech communication. Similarly, the relatively fast rates of cepstral change, or high-modulation frequencies, might be less important for human speech communication.

To justify this approach, it is essential to identify the

contribution of different modulation frequency bands of cepstral coefficients to human speech recognition. In this paper, we used the LPC-based approach for at least two reasons. First, LPC is the most common technique in speech engineering; therefore, our results are directly applicable to many LPC-based ASR systems. Second, the results can enhance our understanding of the temporal properties of the speech signals. This is due to the fact that, at least in theory, the LPC analysis separates speech information into two components: the sound source and the vocal tract. Hence, the LPC technique allows us to manipulate these components independently and permits us to study the dynamics of each.

The goal of this study is to examine the effect of filtering the time trajectories of the spectral envelope on the intelligibility of the reconstructed speech.

Drullman[4,5] reported the effect of temporal filtering of the spectral envelope on the intelligibility of speech. In his study, the original speech was split into a series of frequency bands. The magnitude envelope of the analytic signal for each band was then low-pass and high-pass filtered. He concluded that low-pass filtering below 16 Hz or high-pass filtering above 4 Hz does not appreciably reduce speech intelligibility.

Drullman's results showed that the low- and high-modulation frequencies of the magnitude spectrum are not essential for the intelligibility of speech. These results are, in principle, consistent with RASTA processing.

In this paper, we will focus on the following question: ''How will speech intelligibility be affected if:

(1) filtering is done in the cepstral trajectories,
(2) the filters are bandpass filters, and
(3) the energy contour is unmodified?''

Prior work does not address these questions for the following reasons. First, Drullman applied the filtering to the magnitude envelope of the analytic signal, which effectively implies filtering of the magnitude spectrum of the speech. It is not obvious that Drullman's results generalize to other features, such as cepstrum, that are typically used for speech recognition. Filtering in a different domain might affect human speech perception differently. This is particularly true if the filtering is performed on a nonlinear transformation of the signal, e.g., the logarithmic function. In contrast to Drullman's study, we examined the effects of temporal filtering of the time trajectories of the LPC cepstrum. Thus, our results have direct implications for cepstrum-based ASR systems.

Second, it is not obvious whether his results for the low-pass and the high-pass experiments can be used to draw any conclusions about bandpass filtering because of a nonlinearity of the human auditory system. Therefore, we investigated empirically the effect of bandpass filtering.

Third, because the temporal change of the magnitude envelope was filtered in Drullman's experiment, the energy contour and the temporal change of the spectrum were both affected. Instead, we focus only on the modification of the spectral change; in our experiment, the energy contour of the modified signal is kept the same as that of the original signal.

In this paper, we first describe the signal processing based on a residual-excited LPC vocoder. This signal processing consists of the LPC cepstral analysis of the speech signal, temporal filtering of the cepstrum, and reconstruction of the speech. The stimuli for the perceptual experiments are described in Sec. II. In the same section, the experimental procedure, subjects, and data analysis are described. We then describe two experiments with low-pass and high-pass conditions (experiment 1), and bandpass conditions (experiment 2). Finally, we discuss further issues based on the experimental results, including the information for intelligibility using a density function over the modulation frequency (in Sec. IV).

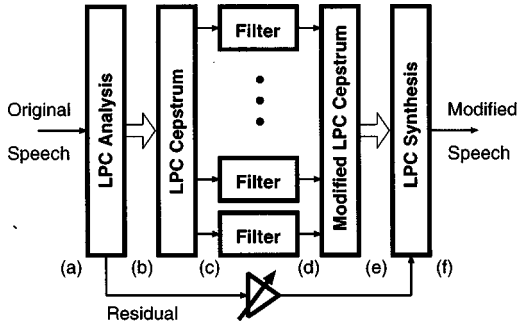

FIG. 1. Block diagram of the speech-processing system.

I. SIGNAL PROCESSING

An overview of our signal-processing method is illustrated in Fig. 1. It consists of applying a frame-by-frame LPC analysis to the original speech, then filtering the time trajectories of the resulting LPC cepstral coefficients. Subsequently, the modified speech signal is reconstructed by an LPC synthesis technique. The filters used in this study were either low-pass, high-pass, or bandpass, with different cutoff frequencies covering the frequency band of interest.

The signal-processing technique was based on a residual-excited LPC vocoder. This approach permits the construction of the entire continuum from the nonfiltered signal to the complete removal of all LPC information. In the range between those two extremes, we were able to examine speech intelligibility as a function of the frequency content of the temporal trajectories of the LPC cepstral coefficients.

Figure 2 shows an example of an utterance: (a) the original speech, and (b) its spectrogram, the time trajectory of the first LPC cepstral coefficient (c) before and (d) after filtering, and (f) the modified speech and (e) its spectrogram. In the original time trajectory, one can see very high modulation frequencies as well as the dc component [Fig. 2(c)]. After bandpass filtering between 1 and 16 Hz, fast and slow modulations are removed, but the major components remain [Fig. 2(d)]. A comparison of the spectrograms of Fig. 2(b) and (e) indicates that the major spectral transitions were preserved.

A. LPC cepstral representation

The speech signals were first analyzed by a 12th-order linear prediction technique, with pre-emphasis. The energy and the 12 LPC coefficients were calculated at each frame using the parameters shown in Table I. Following the LPC

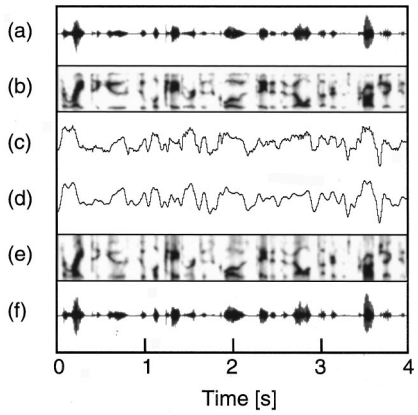

FIG. 2. Signals and spectrograms of an utterance. Each plot corresponds to the letter marked in Fig. 1. (a) Original speech. (b) LPC-based spectrogram of the original speech. (c) Time trajectory of the first LPC cepstral coefficient. (d) Bandpass filtered time trajectory of (c) with bandpass filter between 1 and 16 Hz. (e) LPC-based spectrogram of the modified speech. (f) Modified speech.

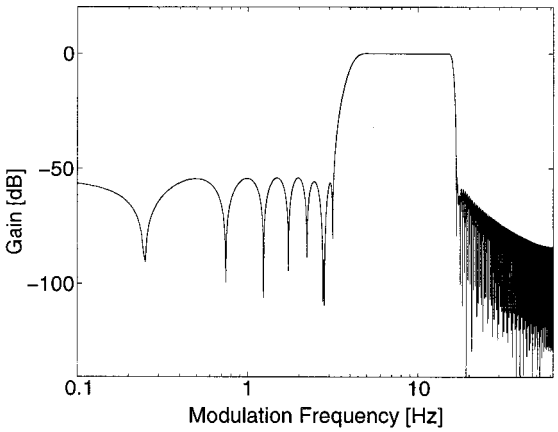

FIG. 3. The frequency characteristics of a bandpass filter designed by the windowing method. For this plot, the cutoff frequencies are 4 and 16 Hz.

analysis, the LPC coefficients were converted to cepstral coefficients. To achieve a logarithmic spectrum with a sufficiently high resolution, we calculated all cepstral coefficients up to quefrency of 16 ms.

B. Filtering of the cepstral coefficients

The time trajectory of each cepstral coefficient was processed by a temporal filter. The filters were identical at all quefrencies except that the coefficient at zero quefrency was discarded. The bandpass filters (BPFs) were implemented as 257-tap finite impulse response (FIR) filters with linear phase. Their coefficients were designed by the windowing method (Hamming window). For each filter, the slope within the transient band is approximately 48 dB/Hz. Figure 3 shows the magnitude frequency characteristics of a sample bandpass filter.

C. Reconstruction of the speech

The filtered LPC cepstral coefficients were used to compute the modified power spectrum at each frame. A 12th-order LPC filter was calculated from the autocorrelation function obtained by applying the inverse Fourier transform of the power spectrum. In the last stage of the signal processing, we reconstructed speech sounds using the modified LPC coefficients together with the residual signal.

Ideally, the residual signal would contain only the sound source information. In practice, however, the residual signal may also contain some information about the vocal tract shape, so the LPC residual sometimes yields a relatively intelligible signal. In the first half of this study (experiment 1), we further whitened the residual signal to reduce the intelligibility. The whitening was not as helpful as we expected, so we did not whiten the residual signal in the second half of this study (experiment 2).

Finally, to avoid measuring the effect of modifying the energy contour, we matched the total energy in each frame of the reconstructed speech to the energy in the related frame of the original speech. Thus, our reconstructed speech had the same energy contour as the original speech, but its spectral envelope structure was modified.

TABLE I. Conditions for LPC analysis.

Order of LPC analysis	12
Window	Hamming
Frame length	32 ms
Frame period	8 ms
Pre-emphasis	0.98

II. STIMULUS

A. Speech samples

The original speech sounds were obtained from a Japanese syllable database used for articulation tests at NTT Japan. To generate stimuli for this study, we selected the voice of a 24-year-old female. Each sentence contained a target Japanese syllable in the carrier phrase ''Kankonbai ——— oruso.'' The original speech signal was quantized with a 16-bit resolution and sampled at 48 kHz. Our stimuli were processed and presented at an 8-kHz sampling rate.

The original data set contained 100 Japanese syllables. We selected a subset of 31 syllables covering the three corner vowels /a/, /i/, and /u/, and Japanese consonants /p/, /b/, /t/, /d/, /k/, /g/, /s/, /ʃ/, /ts/, /tʃ/, /dz/, /dʒ/, /n/, /m/. The 31 syllables are shown in Table II. Each syllable is a vowel (V) or consonant–vowel (CV) syllable.

TABLE II. Japanese syllables used in this study.

	Unvoiced consonants			Voiced consonants		
Vowels	/a/	/i/	/u/			
Stops +Vowels	/pa/	/pi/	/pu/	/ba/	/bi/	/bu/
	/ta/			/da/		
	/ka/	/ki/	/ku/	/ga/	/gi/	/gu/
Fricatives +Vowels	/sa/	/ʃi/	/su/			
Affricates +Vowels		/tʃi/	/tsu/	/dza/	/dʒi/	/dzu/
Nasals +Vowels				/ma/	/mi/	/mu/
				/na/	/ni/	/nu/

B. Stimulus conditions

Stimuli were divided into conditions according to the amount of low-pass, high-pass, and bandpass filtering of the LPC cepstral coefficients.

For experiment 1, the time trajectories of the LPC cepstral coefficients were filtered with low-pass and high-pass filters with cutoff frequencies f_C, where $f_C = \{0,1,2,3,4,5,6,8,12,24,48,f_N\}$ [Hz], where f_N is equal to half of the frame rate, i.e., $f_N = 62.5$ Hz. A complete set of the 13 conditions (including clean speech) applied to all 31 syllables was presented to our subjects in a session consisting of 403 ($=13\times31$) stimuli.

For experiment 2, the time trajectories of the LPC cepstral coefficients were filtered with bandpass filters. The bandpass filters had lower cutoff frequencies f_L and upper cutoff frequencies f_U, where $f_L = \{0,1,2,4,8,16,32,f_N\}$ [Hz] and $f_U = \{0,1,2,4,8,16,32,f_N\}$ [Hz] ($f_L \leq f_U$). Note that when $f_L = 0$ the filter is a low-pass filter, and when $f_U = f_N$ the filter is a high-pass filter. A complete set of the 30 conditions (including clean speech) applied to all 31 syllables was presented to our subjects in a session consisting of 930 ($=30\times31$) stimuli.

C. Procedure

We used the method of constant stimuli, with stimuli presented in random order. Each subject participated in four sessions. Combinations of syllables and filtering conditions were randomized across sessions and subjects.

The stimuli were generated by the digital-to-analog (D/A) converter of a SPARC-20 workstation at 8-kHz sampling rate and presented using high-quality headphones (Sennheiser HD 250 II) at a comfortable listening level. On each trial, the subject heard an isolated syllable preceded and followed by 1-s intervals of silence. Following each stimulus presentation, subjects indicated their answer and then initiated the next trial. Each stimulus was presented only once.

Subjects interacted with the experimental setup using a graphical user interface and a mouse input device. As shown in Fig. 4, the monitor screen showed icons for all 31 possible stimuli, and subjects were asked to select the icon of the most likely stimulus. In addition to the stimulus icons, there were buttons to allow corrections and to indicate completion of trials.

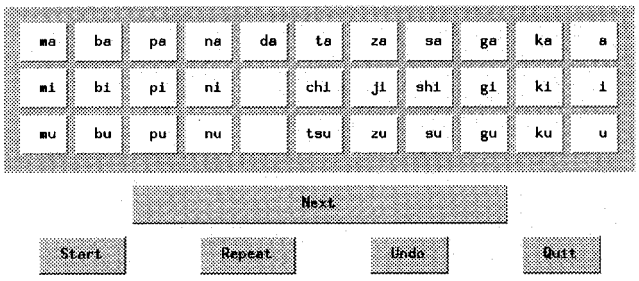

FIG. 4. Graphical user interface for the experiments.

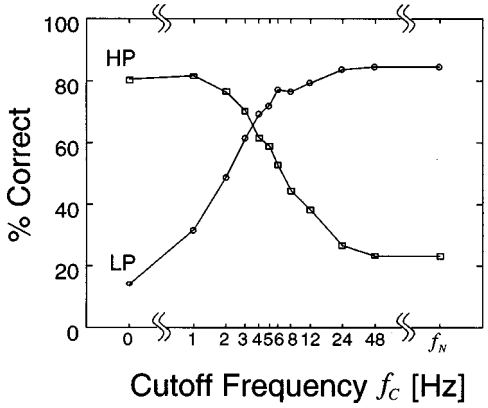

FIG. 5. Results for low-pass (LP) and high-pass (HP) filtering.

D. Subjects

A total of 20 Japanese native speakers participated in the study. The subjects were paid for their participation. Of the 20 subjects, 16 participated in experiment 1 and four in experiment 2. No subject reported having any previous hearing problem.

E. Data analysis

We summarized the data for each condition and each stimulus in terms of the proportion of correct responses to total responses. The proportion of correct CV syllables is defined as P_c(CV), and a response was scored as correct only if both constituents (phonemes)—vowel and consonant—were recognized correctly. The resulting overall proportions of correct responses were averaged over all stimuli for each condition. In addition, we analyzed the results for each phonetic category. The proportion correct for each category is denoted as P_c(category), e.g., P_c(C) for consonants and P_c(V) for vowels.

III. EXPERIMENTAL RESULTS

A. Experiment 1

Experiment 1 consisted of low-pass and high-pass filtering of the LPC cepstral trajectories. The overall summary of the results averaged over stimuli and subjects is shown in Fig. 5. The abscissa of the graph shows cutoff frequencies and the ordinate represents the proportion of correct responses P_c(CV) of each CV. Each point is an average of 31 stimuli, 8 subjects, and 4 sessions for a total of 992 ($=31\times8\times4$) trials. Assuming a binomial distribution of responses, the largest standard error of the estimates is less than 2%. The corresponding error bars were omitted for clarity.

The performance for the original speech averaged over the four subjects was 85.8% and ranged from 75.8% to 99.2%. The average score for the residual signal was 18.5% and ranged from 7.3% to 27.4%. The useful range of the information in the LPC cepstral trajectories was therefore 18.5%–85.8%.

In the low-pass condition, the performance begins to decrease gradually below 24 Hz. In the high-pass condition, the decrease in performance begins above 1 Hz. The low-pass

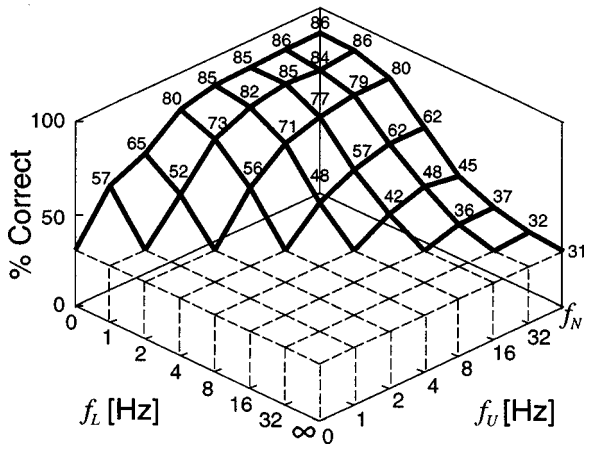

FIG. 6. Results on 31 syllables (full set) for bandpass filtering. The number at each node shows the proportion of correct responses.

and high-pass curves intersect between 3 and 4 Hz. This modulation frequency indicates the center of information, where the information is equally divided into lower and higher modulation bands. This modulation frequency is consistent with the average syllabic rate of speech.[6]

B. Experiment 2

Four native Japanese subjects participated in experiment 2. Each subject participated in four experimental sessions. Each session consisted of 930 stimuli.

The results for the bandpass condition are shown in Fig. 6. The vertical axis is the proportion of correct responses P_c(CV), while the other two axes are the cutoff frequencies, f_L and f_U. Each point is an average of 31 stimuli, 4 subjects, and 4 sessions for a total of 496 ($=31\times4\times4$) trials. The largest standard error of a binomial distribution with the same number of trials is less than 2%.

In experiment 2, the performance for the original speech averaged over four subjects was 86.1% and ranged from 84.7% to 89.5%. The average score for the residual signal was 30.6% and ranged from 17.7% to 41.9%. The useful range of the information in the LPC cepstral trajectories was therefore 30.6%–86.1%.

The data from this experiment are also consistent with those of the low-pass and high-pass conditions in experiment 1.

Table III is the confusion matrix for the original signal in experiment 2. As shown in this table, there are several syllables for which the original signal is hard to understand. This could be attributed to the low sound quality of the 8-kHz sampled stimuli. Misperception of the consonant of the syllables was common, while most of the vowels were perceived correctly. Figure 7 shows the proportion of correct responses for the 21 CV syllables which are perceived perfectly for the original signal (/ka/, /ki/, /ku/, /ga/, /gi/, /gu/, /sa/, /ʃi/, /su/, /dza/, /dzu/, /tʃi/, /tsu/, /da/, /na/, /ni/, /nu/, /pi/, /ba/, /bi/, /ma/).

As can be seen in Fig. 7 (subset) and Fig. 6 (full set), the global trends in both cases are the same. As in Fig. 6, the trend in Fig. 7 is not affected when the time trajectories have components between 1 and 16 Hz.

TABLE III. Reduced confusion matrix of responses for the original signal in the bandpass experiment. Syllables that were perceived perfectly were omitted from the matrix. The total number of responses for each syllable is 16.

	Response								
Stimulus	/u/	/ka/	/ku/	/gi/	/gu/	/ta/	/ni/	/nu/	Total
/dʒi/				3					3
/ta/		12							12
/pa/						7			7
/pu/			10		2				12
/bu/					6			2	8
/mi/							11		11
/mu/	2							12	14

C. Cue trading

To maintain the original phonetic information for human perception, a decrease in one feature can be offset by an increase in another cue; this tradeoff is known as cue trading.[7] To illustrate the phenomenon of cue trading, we projected Fig. 7 onto two different planes. The two planes are shown in Fig. 8: (a) the proportion of correct syllables P_c(CV) versus f_U, and (b) the proportion of correct syllables P_c(CV) vs f_L. In Fig. 8(a), the graphs of $f_L=0$ Hz and $f_L=1$ Hz match when $f_U>4$ Hz, while the graphs of $f_L=0$ Hz and $f_L=1$ Hz do not match when $f_U\leqslant4$ Hz. That is, if we have components at 4 Hz and above, then we can compensate for the lost cues below 1 Hz, but if we lose the components at 4 Hz and above, then we cannot compensate for those lost cues. Similarly, in Fig. 8(b) the graphs of $f_U=16$ Hz and $f_U=f_N$ match when $f_L<4$ Hz, while the graphs of $f_U=16$ Hz and $f_U=f_N$ do not match when $f_L\geqslant4$ Hz. That is, if we have the components at 4 Hz and below, then we can compensate for the lost cues above 16 Hz, but if we lose the components at 4 Hz and below, then we cannot. This suggests that the component at 4 Hz is necessary for cue trading. A modulation frequency of 4 Hz corresponds to the average syllabic rate of speech.[6]

Figure 9 shows the results in terms of proportion of

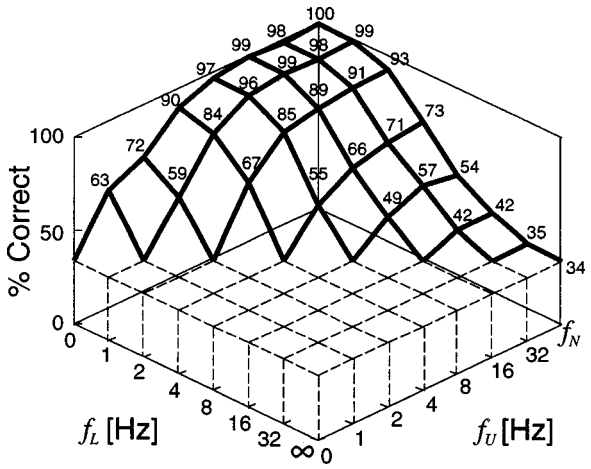

FIG. 7. Results on 21 CV syllables (subset) for bandpass filtering. The number at each node shows the proportion of correct responses.

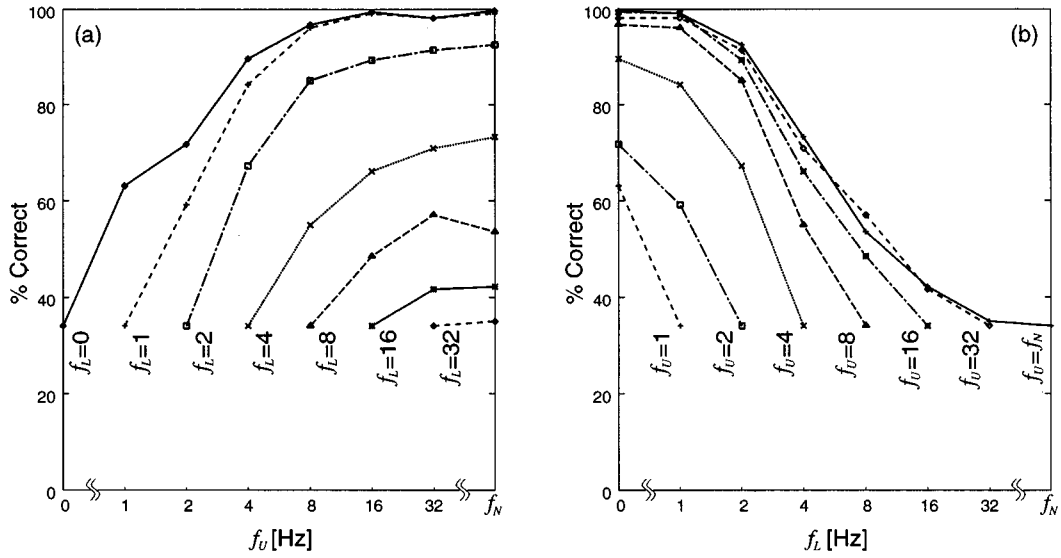

FIG. 8. Projection of Fig. 6 onto two different planes. (a) A plot of the proportion correct versus f_U. (b) A plot of the proportion correct versus f_L.

correct CV syllables P_c(CV), consonants P_c(C), and vowels P_c(V). As can be seen in Fig. 9(a), P_c(C) is sensitive to higher-modulation frequency components and is lower than P_c(V) when $f_U<16$ Hz. On the other hand, as shown in Fig. 9(b), P_c(V) is sensitive to lower-modulation frequency components and is lower than P_c(C) when $f_L>1$ Hz.

As can be seen in Fig. 9, P_c(CV) is larger than the product of P_c(C) and P_c(V). Fletcher showed that the articulation probability of a CV syllable will be the product of the articulation probabilities of the C and the V.[8] The results in our domain, however, suggest that consonants and vowels do not contribute to intelligibility independently.

The results for each consonant category were analyzed as shown in Fig. 10. The proportion of correct responses for each category drops when $f_U<16$ Hz, and P_c(stops) and P_c(nasals) are sensitive to higher-modulation frequency components [Fig. 10(a)]. As shown in Fig. 10(b), the proportion of correct responses for each category drops when $f_L>2$ Hz, and P_c(fricatives) and P_c(affricates) are sensitive to lower-modulation frequency components. We observed that the modulation frequency component at 4 Hz is essential for the sounds having longer duration, such as fricatives, and that the much higher-modulation frequency components are essential for the sounds having shorter duration, such as stops.

IV. DISCUSSION

In Drullman's experiment, the temporal change of the magnitude envelope was filtered. As a result, both the energy

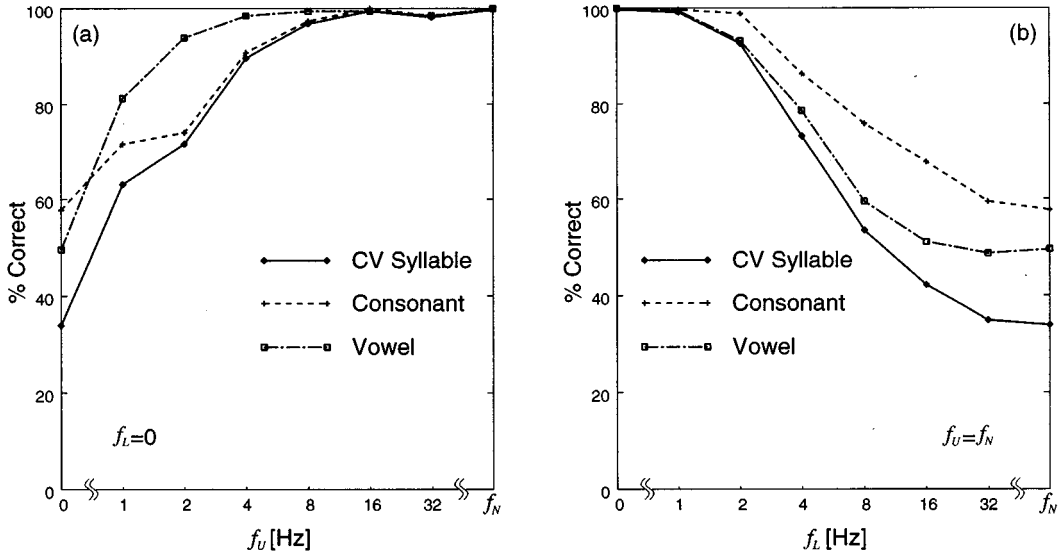

FIG. 9. The result in terms of CV (syllable), C (consonant), and V (vowel). (a) The proportion correct versus f_U when $f_L=0$. (b) The proportion correct versus f_L when $f_U=f_N$.

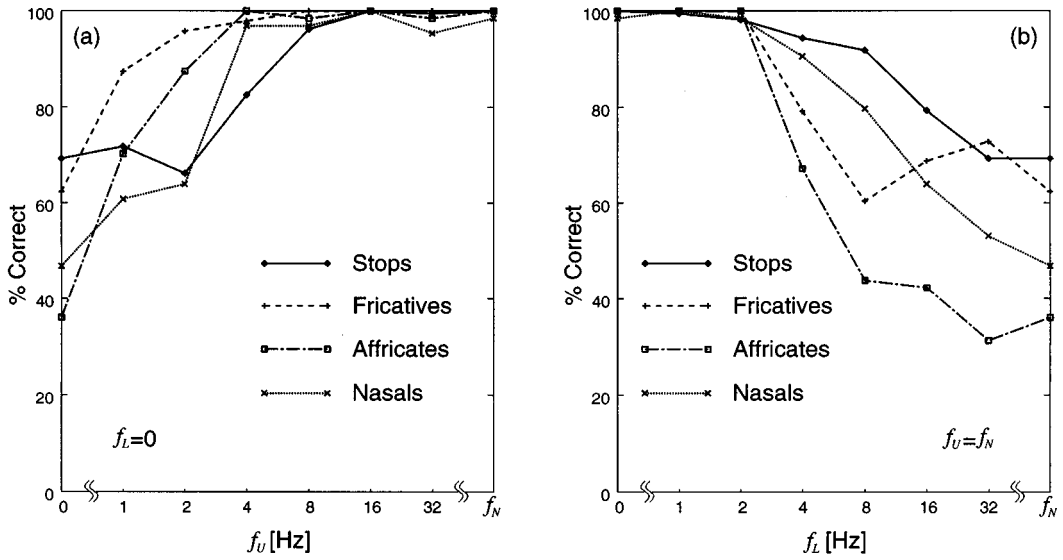

FIG. 10. The result for each consonant category. (a) The proportion correct versus f_U when $f_L=0$. (b) The proportion correct versus f_L when $f_U=f_N$.

contour and the temporal change of the spectrum were affected. We primarily modified the rate of change of the spectral components but kept the LPC residual and the energy contour unchanged.

The LPC residual contains timing information such as plosive bursts, fricative onset, and vowel onset. Therefore, the modified speech signal also contains such timing information as seen in the spectrogram, Fig. 2(e). This technique, however, effectively smears the formant structure of speech as well as the formant transitions. Thus, both vowel and consonant intelligibilities were affected, as seen in Fig. 9. For the residual signal itself, the proportion of correct CV syllables was 34%, whereas for the original signal the proportion of correct CV syllables was 100%. Therefore, our results are valid in the range between those two extremes, and we focus on the relative importance of the modulation frequency.

Figure 6 shows that the modified speech is more intelligible when $f_L \leqslant 1$ Hz and $f_U \geqslant 16$ Hz. The lower limit of 1 Hz suggests that the slowly varying and static components, such as channel characteristics, do not contribute significantly to human speech communication. Similarly, the very fast-changing components above 16 Hz seem to have little effect on intelligibility. In fact, the upper limit of the modulation frequency has important implications for parametric speech coding, particularly for defining how fast we can sample the speech envelope for efficient transmission of speech signals.[9]

In this study, only a target syllable was presented during the experiments. Those syllables were extracted from a longer carrier phrase after temporal filtering. We also conducted a small separate experiment in which we included the carrier phrase as well as the target syllable to see the effect of environmental cues on speech intelligibility. Two native Japanese subjects participated in one experimental session

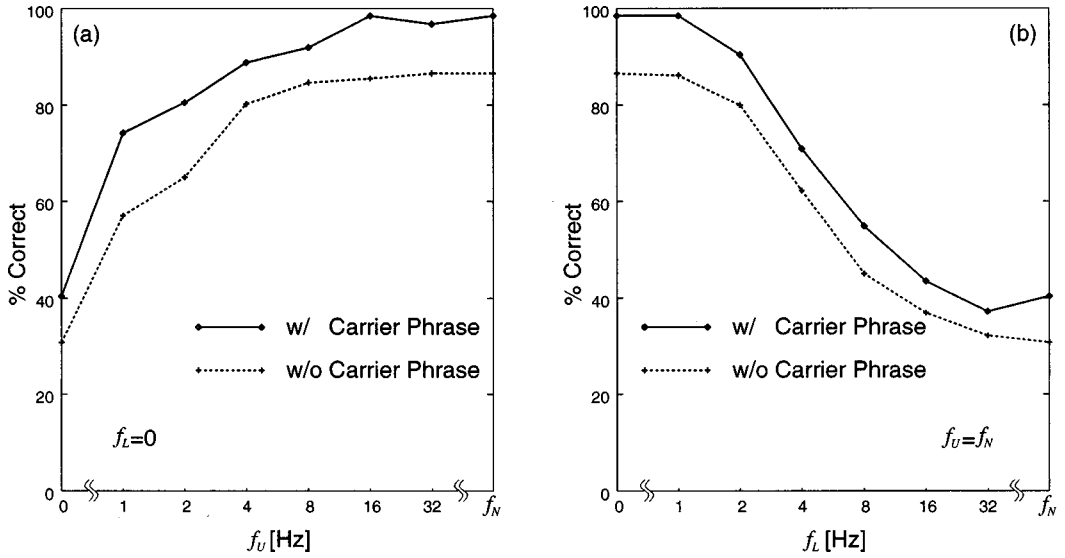

FIG. 11. With and without the carrier phrase. (a) The proportion correct versus f_U when $f_L=0$. (b) The proportion correct versus f_L when $f_U=f_N$.

consisting of 465 stimuli. Figure 11 shows the results in terms of proportion of correct responses with and without the carrier phrase. From Fig. 11 there is approximately 10% gain on average when the target is presented with the carrier phrase. It appears that this gain is due to formant transitions into the consonants of the target syllables. However, the general trend remains the same.

A. Theoretical analysis

The regularity of the relationship between the cutoff frequencies and intelligibility suggests that the information relevant for speech communication is distributed over the temporal modulation frequency range. In this section, we develop a quantitative model that relates the intelligibility and information density as a function of the energy at different modulation frequencies. This model was motivated by the model of the articulation index developed by Fletcher.[8]

The general notion is that each modulation-frequency component contributes independently to the collection of features that are necessary for recognition. In particular, if the information in two nonoverlapping bands A and B is combined, the resulting intelligibility, i.e., the probability of a correct response, P_c, is given by

$$P_c(A+B)=1-[1-P_c(A)][I-P_c(B)], \tag{1}$$

where the intelligibility of each band separately is given by $P_c(A)$ and $P_c(B)$. Moreover, if $P_c(A+B)$ is an additive function of information I_A and I_A, then P_c has the form

$$P_c=1-e^{-(I_A+I_B)}. \tag{2}$$

Given this formulation, we need to determine the relationship between the information measure I and the intervals of the modulation frequency. We assume that the amount of information in a small neighborhood of frequency f, $I(f,f+\Delta f)$, is proportional to a continuous density function D so that $I(f+\Delta f)=D(f)\Delta f$. The amount of information in a band (interval) of frequencies $f_1<f_2$ is then given by the integral

$$I(f_1,f_2)=\int_{f_1}^{f_2} D(f)df. \tag{3}$$

The information density function $D(\cdot)$ must be determined empirically.

Given this model, we can compute the probability of correct identification of the syllables in experiment 2 (shown in Fig. 7) by integrating information between low- and high-frequency limits f_L and f_U. Thus,

$$P_c(f_L,f_U)=1-e^{-I(f_L,f_U)}, \tag{4}$$

$$=1-e^{-\int D(f)df}. \tag{5}$$

We found empirically that the following function:

$$D(f)=1\Big/\left[1+\left(\frac{f-f_{\max}}{\alpha}\right)^2\right], \tag{6}$$

where $f_{\max}$ and α are constants to be determined. Then, by integrating Eq. (6)

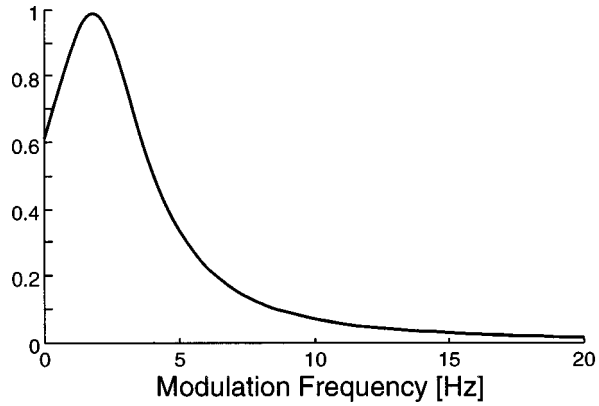

FIG. 12. Density function $D(f)$.

$$I(f_L,f_U)=\alpha\left[\tan^{-1}\left(\frac{f_U-f_{\max}}{\alpha}\right)-\tan^{-1}\left(\frac{f_L-f_{\max}}{\alpha}\right)\right]. \tag{7}$$

The estimated P_c, or $\hat{P}_c$, is obtained by minimizing χ^2, where $f_{\max}$ and α are parameters. Because P_c in Fig. 7 is ranging over the interval $P_0\leqslant P_c<1$, we use the following definition instead of (4):

$$\hat{P}_c(f_L,f_U)=\gamma(1-e^{-\beta I(f_L,f_U)})+P_0. \tag{8}$$

Then, the optimal fit gives us:

$$f_{\max}=1.789,\quad \alpha=2.255,\quad \beta=0.487,$$

$$\gamma=0.726,\quad P_0=0.333,$$

and $D(f)$ is shown in Fig. 12. In this case, χ^2 is 61. Figure 13 shows the fit between P_c and $\hat{P}_c$.

The information distribution function with normalization is defined as the accumulative curve of the density function $D(f)$ as follows:

$$\overline{I}(f)=\int_0^f D(f)df\Big/\int_0^\infty D(f)df. \tag{9}$$

Figure 14 shows $\overline{I}(f)$ as a function of the modulation frequency f in the optimal case. As shown in this figure, 10%,

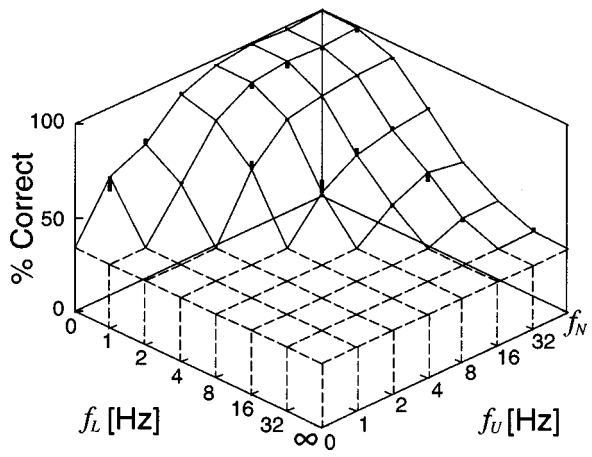

FIG. 13. Fit between P_c and $\hat{P}_c$. The vertical bars show the difference $\hat{P}_c(f_L,f_U)-P_c(f_L,f_U)$ from each $P_c(f_L,f_U)$.

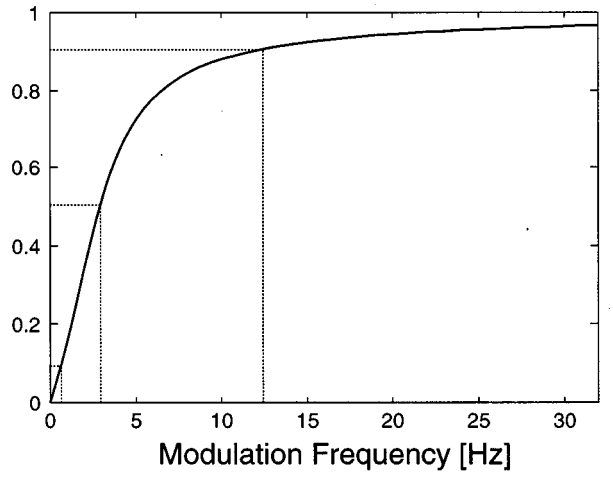

FIG. 14. Distribution function $\overline{I}(f)$.

50%, and 90% percentiles are at 0.7, 2.9, and 11.7 Hz, respectively. The information function shows that most of the information is involved within the range between 1 and 12 Hz. These low-modulation frequencies are, therefore, essential for the human auditory system to extract and recognize speech information.[10]

V. CONCLUSION

The intelligibility of speech with filtered time trajectories of the spectral envelope was investigated. We extended previous research[4,5] to the logarithmic domain and applied bandpass filters in addition to low-pass and high-pass filters. For the result of the perceptual experiments, the information for intelligibility was described by a density function over modulation frequency. The results of these experiments suggest that speech intelligibility is not severely impaired as long as the filtered LPC cepstral coefficients have a rate of change between 1 and 16 Hz.

In contrast to Drullman's study, the effects of temporal filtering of the time trajectories of the cepstrum were examined in this study. In particular, we determined the effect of bandpass filtering. Thus, our results may have direct implications for cepstrum-based ASR systems, and they are important as a benchmark of how the spectral representations used in ASR relate to human speech recognition.

Recently, Kanedera showed that the performance of the speech recognition for the 13-word Bellcore digit database task and the 216 Japanese word-recognition task had the highest recognition rate when the bandpass filter between 1 and 16 Hz was used.[11] This result is consistent with that of our perceptual experiment. The results provide additional support for RASTA-like processing of cepstral features in ASR.

ACKNOWLEDGMENTS

We acknowledge the assistance of Yonghong Yan, Troy Bailey, Brian Mak, and Ronald Cole of the Oregon Graduate Institute of Science & Technology (OGI), who helped with the setup of the initial perceptual experiment; Steven Greenberg of the International Computer Science Institute (Berkeley, California), Robert Damper of the University of Southampton and Pieter Vermeulen of OGI, who gave us useful comments; and Karen Ward of OGI, who helped us to proofread this manuscript. Thanks to Sadaoki Furui of the Tokyo Institute of Technology and the former members of his laboratory at NTT for lending their speech database and for their helpful comments. We would also like to thank the subjects who participated in the experiments. Finally, we would like to thank the two anonymous reviewers, who gave us many valuable suggestions. This research was supported in part by grants from the DoD under Grant No. MDA-904-94-C-6169 and the NSF/ARPA under Grant No. IRI-9314959, with additional funding provided by the member companies of the Center for Spoken Language Understanding (CSLU).

[1] B. S. Atal, ''Effectiveness of Linear Prediction Characteristics of the Speech Wave for Automatic Speaker Identification and Verification,'' J. Acoust. Soc. Am. **55**, 1304–1312 (1974).
[2] S. Furui, ''Speaker-Independent Isolated Word Recognition Using Dynamic Features of Speech Spectrum,'' IEEE Trans. Acoust., Speech, Signal Process. **ASSP34**, 52–59 (1986).
[3] H. Hermansky and N. Morgan, ''RASTA Processing of Speech,'' IEEE Trans. Speech Audio Process. **2**, 578–589 (1999).
[4] R. Drullman, J. M. Festen, and R. Plomp, ''Effect of Temporal Envelope Smearing on Speech Reception,'' J. Acoust. Soc. Am. **95**, 1053–1064 (1994).
[5] R. Drullman, J. M. Festen, and R. Plomp, ''Effect of Reducing Slow Temporal Modulations on Speech Reception,'' J. Acoust. Soc. Am. **95**, 2670–2680 (1994).
[6] T. Houtgast and H. J. M. Steeneken, ''A Review of the MTF Concept in Room Acoustics and its Use for Estimating Speech Intelligibility in Auditoria,'' J. Acoust. Soc. Am. **77**, 1069–1077 (1985).
[7] B. C. J. Moore, *An Introduction to the Psychology of Hearing* (Academic, New York, 1989).
[8] H. Fletcher, *Speech and Hearing in Communication* (Krieger, Huntington, NY, 1953).
[9] J. L. Flanagan, ''Parametric Coding of Speech Spectra,'' J. Acoust. Soc. Am. **68**, 412–419 (1980).
[10] S. Greenberg, ''Understanding Speech Understanding: Towards a Unified Theory of Speech Perception,'' in *Proceedings of the ESCA Tutorial and Advanced Research Workshop on the Auditory Basis of Speech Perception*, edited by W. A. Ainsworth and S. Greenberg (Keele University, Staffordshire, UK, 1996), pp. 1–8.
[11] N. Kanedera, T. Arai, H. Hermansky, and M. Pavel, ''On the Importance of Various Modulation Frequencies for Speech Recognition,'' in *Proceedings of the 5th European Conference on Speech Communication and Technology*, Greece, Vol. 3, pp. 1079–1082 (1997).

Center frequency modulation detection for harmonic complexes resembling vowel formants and its interference by off-frequency maskers

J. Lyzenga[a] and R. P. Carlyon
MRC Cognition and Brain Sciences Unit, 15 Chaucer Road, Cambridge CB2 2EF, United Kingdom

(Received 13 April 1998; revised 30 December 1998; accepted 22 February 1999)

Vowels are characterized by peaks in their spectral envelopes: the formants. To gain insight into the perception of speech as well as into the basic abilities of the ear, sensitivity to modulations in the positions of these formants is investigated. Frequency modulation detection thresholds (FMTs) were measured for the center frequency of formantlike harmonic complexes in the absence and in the presence of simultaneous off-frequency formants (maskers). Both the signals and the maskers were harmonic complexes which were band-pass filtered with a triangular spectral envelope, on a log-log scale, into either a LOW (near 500 Hz), a MID (near 1500 Hz), or a HIGH region (near 3000 Hz). They had a duration of 250 ms, and either an 80- or a 240-Hz fundamental. The modulation rate was 5 Hz for the signals and 10 Hz for the maskers. A pink noise background was presented continuously. In a first experiment no maskers were used. The measured FMTs were roughly two times larger than previously reported just-noticeable differences for formant frequency. In a second experiment, no significant differences were found between the FMTs in the absence of maskers and those in the presence of stationary (i.e., nonfrequency modulated) maskers. However, under many conditions the FMTs were increased by the presence of simultaneous modulated maskers. These results indicate that frequency modulation detection interference (FMDI) can exist for formantlike complex tones. The FMDI data could be divided into two groups. For stimuli characterized by a steep (200-dB/oct) slope, it was found that the size of the FMDI depended on which cues were used for detecting the signal and masker modulations. For stimuli with shallow (50-dB/oct) slopes, the FMDI was reduced when the signal and the masker had widely differing fundamentals, implying that the fundamental information is extracted before the interference occurs. [S0001-4966(99)04805-5]

PACS numbers: 43.66.Mk, 43.66.Fe, 43.66.Dc, 43.71.Ed [RVS]

INTRODUCTION

An important aspect of vowels is the presence of a number of peaks in their spectral envelopes; the formants. The locations of the first two or three formants classify the vowel. However, the locations (or frequencies) of one or more formants may change during pronunciation of a vowel. For example, the second and third formant of the /ʊ/ in ''put'' can shift down by as much as 400 Hz from 1500 and 2300 Hz, respectively (Fletcher, 1953). Such formant changes may also convey information about the bordering consonants (e.g., Fletcher, 1953), and occur in diphthongs (e.g., the /eɪ/ and /aʊ/ as in ''hay'' and ''how,'' respectively). Both for gaining insight into speech recognition, and for researching the basic abilities of the ear, it is interesting to investigate the sensitivity for dynamic changes in the positions, or the center frequencies, of formants. We used a task in which normal-hearing subjects had to detect a sinusoidal modulation in the center frequency of a synthetic formant that had a fixed fundamental (F_0). These formants were presented either in isolation, or in the presence of other interfering formants which were either stationary or modulated.

A number of studies have investigated sensitivity for differences in formant frequency (e.g., Mermelstein, 1978; Hawks, 1994; Kewley-Port and Watson, 1994; Lyzenga and Horst, 1995, 1997, 1998), for stimuli consisting of one or more formants, in which either a single formant was changed or two or more formants were changed simultaneously (single versus multiple formant changes). Various mechanisms have been suggested to explain the recorded just-notable differences (jnd's) for single and multiple formant changes. Under most conditions the results of these studies could be accurately described using ''place'' models, based on assumed patterns of stimulus excitation along the length of the basilar membrane, combined with summation rules for multiple formant changes. Under some ''special'' conditions listeners used temporal cues arising from the interaction of two or more harmonics; these included beats and differences in amplitude-modulation depth (Lyzenga and Horst, 1997, 1998). One motivation for the present study was to determine whether listeners can use these temporal cues when the formants are changing dynamically. Modulation masking data (Strickland and Viemeister, 1996) show hardly any interference from maskers at modulation rates more than a factor of 8 away from that of the signal, and, so, modulation masking is not expected to play a role here. However, since sensitivity for detection of modulations is much larger around a 5-Hz rate than for higher rates such as 80 or 240 Hz (Viemeister, 1979), listeners may not be using the dynamic changes in the fast amplitude modulations (AM) in the wave-

[a]Electronic mail: johannes.lyzenga@usa.net

forms of the stimuli (at the rate of F_0), which are generated by the slow modulations of the formant frequencies (FM), as a cue.

In order to study the detection mechanisms involved, we varied such parameters as spectral slope, fundamental, center frequency region, and whether the formant frequency fell at a harmonic or between two harmonics. Lyzenga and Horst (1995, 1997) found evidence of temporal mechanisms for center frequency discrimination for isolated formants, which disappeared when a stationary off-frequency formant was added during stimulus presentation. It is interesting to see whether something similar can be observed for center frequency modulation detection, which uses dynamic rather than static stimuli. Such an effect should then appear as a difference between the results without any maskers present and those with stationary maskers.

All stimuli were harmonic complexes. To shape them like formants, they were band-pass filtered into either a LOW, a MID, or a HIGH region. These three regions were chosen to represent the first, second, and third formant regions of speech (Peterson and Barney, 1952), and were well separated in frequency to reduce mutual influence of the formants at the level of the cochlea. With the choice of two widely differing fundamentals (80 and 240 Hz) we introduced the spectral resolvability of stimulus partials as an experimental parameter to investigate whether the cues used for center frequency modulation detection are the same as those for pure-tone FM, and whether two different mechanisms might exist for stimuli with resolved and unresolved partials.

We measured listeners' ability to detect a modulation in the center frequency of formants. Such formant modulations are reflected in combined amplitude modulations of the harmonics of the formant, while their frequencies are fixed. A number of investigations (e.g., Yost and Sheft, 1989; Yost *et al.*, 1989; Moore *et al.*, 1991; Hall and Grose, 1991; Moore and Shailer, 1992; Bacon and Konrad, 1993; Bacon and Opie, 1994; Mendoza *et al.*, 1995) have shown that detecting amplitude or frequency modulation of a tone can be impaired by presenting another modulated tone at a remote frequency. This effect is called modulation detection interference (MDI), or more specifically FMDI for frequency modulation (studied for pure tones by, e.g., Moore *et al.*, 1991; Carlyon, 1994). MDI and FMDI are considered to be across-channel effects. One of the topics addressed in this paper is whether FMDI can also be observed for a modulation of the center frequency of complex tones resembling vowel formants. If so, this could have consequences for speech perception. It might then be harder to detect frequency changes in a formant when formants from either the same or competing voices are changing simultaneously. Therefore, we performed our measurements in the absence and in the presence of simultaneous competing formants that were either stationary or modulated.

An important advantage of using complex tones rather than sinusoids is that it allows us to determine whether FMDI can exist across sources with a different F_0. To do this, we compared FMDI for conditions where the fundamentals of the targets (signals) and maskers were the same and where they differed widely. The answer to this question might reveal whether the mechanism underlying FMDI receive input from those that extract the fundamental information, i.e., whether FMDI occurs at a later or an earlier stage along the auditory pathway than F_0 extraction.

To maximize possible MDI effects, we used a low (5 Hz) modulation rate (Yost *et al.*, 1989; Bacon and Konrad, 1993) for the signals (note that for a 5-Hz rate, the 200-ms steady-state portion of the stimuli contains just a single modulation cycle). The maskers had a 10-Hz modulation rate. They were all given roughly equally detectable modulation ranges. These modulation ranges were rather restricted to make sure that the frequency excursions of the formants would not be much larger than occur naturally. Large excursions give rise to very ''unnatural'' modulation characteristics. To avoid artifacts from such effects we limited the masker modulation range, even though such a restriction limits the amount of interference (Bacon and Konrad, 1993).

I. STIMULI AND METHODS

A. Stimuli

Two experiments were carried out using bandlimited harmonic complexes as stimuli. Stimulus parameters were: the fundamental, the spectral slope, the center frequency range, and the position of the center frequency relative to the harmonics. The subjects' task was detection of a modulation of the center frequency of the stimuli. In experiment 1 the stimuli were presented in isolation, whereas in experiment 2 they were presented in combinations, in which one stimulus was the signal and one or two others acted as simultaneous maskers that were either stationary or modulated at a fixed FM range.

All stimuli were harmonic tones which were band-pass filtered with a triangular spectral envelope, on a log-log scale, into either a LOW (near 500 Hz), a MID (near 1500 Hz), or a HIGH region (near 3000 Hz). The experiments were performed with both 50 and 200 dB/oct slopes for the triangular filter. Dependent on the experimental conditions, the stimuli were used as signals or maskers. Signals and maskers always had the same slope. The fundamental of the stimuli was either 80 or 240 Hz. The center frequency was either located at a harmonic or in the middle between two harmonics, denoted in the result figures as /|\ and /‖\, respectively.

The stimulus duration was 250 ms (including 25-ms raised-cosine ramps). The center frequency of the triangular filter was modulated at a 5-Hz rate for the signals, so their steady-state portion contained a single modulation cycle. A 10-Hz modulation rate was used for the maskers; these stimuli contained two modulation cycles. A test revealed very similar, though slightly larger, FMDI effects for the 10-Hz modulation rate of the maskers as for a 5-Hz rate. This is probably because adding an extra modulation cycle makes the modulation clearer (Lee and Bacon, 1997), while a factor of 2 difference in modulation rate somewhat reduces the MDI (Yost *et al.*, 1989; Moore *et al.*, 1991; Moore and Shailer, 1992; Bacon and Opie, 1994; Strickland and Viemeister, 1996). We gave all maskers roughly equally detect-

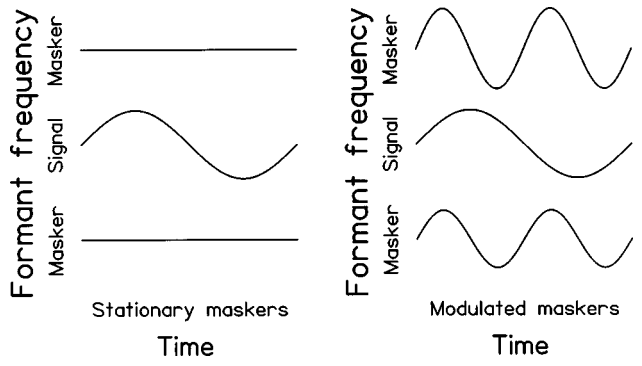

FIG. 1. Examples of the relation between signal and masker frequencies for a signal with two stationary maskers (left) and two modulated maskers (right).

able modulations, corresponding to three times the detection threshold (at $d'=1$). The FM applied to all stimuli (both signals and maskers) had a starting phase of 0 degrees. Figure 1 shows two examples of the relations between signals and maskers as functions of time.

The stimulus waveforms were computed digitally off-line with 16-bit resolution, and were stored on disk. Each stimulus was generated by calculating its (modulated) spectral envelope as a function of time, after which all sinusoidal frequency components were added to the stimulus with their thus calculated time-varying amplitudes. In this way the frequency modulation of the formant resulted in combined amplitude modulations of the components, where these modulations were in anti-phase for components to the lower-and the higher-frequency sides of the formant. The actual frequencies of these components were fixed. All components were added in sine phase. In the spectral slopes, they were included down to a level of at least 50 dB below the largest component. Figure 2 shows all the spectra of the unmodulated (reference) stimuli with a slope of 200 dB/oct. Figure 3 shows four examples of waveforms; the upper and lower traces of each panel contain unmodulated and modulated waveforms, respectively.

A set of stimuli, needed for the determination of one frequency modulation detection threshold (FMT), consisted of a reference tone with center frequency F_C and 23 targets with an increasingly strong modulated center frequency. The target modulation range ranged from 0.0125% to 25.6% in 22 steps of a factor $\sqrt{2}$, giving a range with a small step size from clearly audible modulations to well below detection threshold.

A continuous pink noise was present at a spectrum level of 0 dB (dB SPL/Hz) at 1 kHz. For each subject we measured the detection thresholds of all stimuli both in quiet and in the pink noise background. Signals and maskers were all presented at 30 dB above their thresholds in the pink noise background. On average, these stimulus presentation levels corresponded to sensation levels between 46 and 48 dB above the threshold in quiet for all four subjects.

The signals were in one of the three regions, and the maskers were either to the lower-frequency side, the higher-frequency side, or to both sides. Three different types of maskers were used: stationary, modulated while having the same fundamental as the signal, and modulated while having

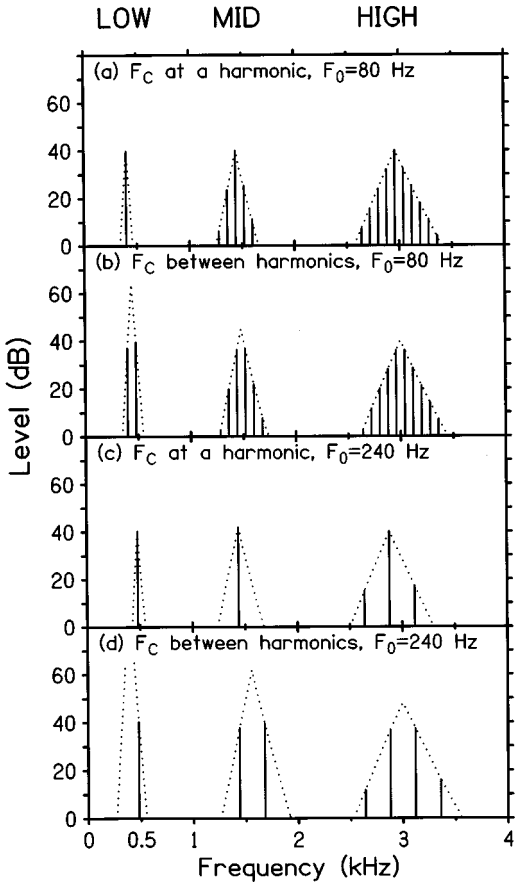

FIG. 2. Examples of stimulus spectra. The dotted lines represent the spectral envelopes. Each panels shows stimuli in the LOW, MID, and HIGH regions. In panels (a) and (b) the stimuli have an 80-Hz fundamental and in panels (c) and (d) the fundamental is 240 Hz. In panels (a) and (c) the center frequencies coincide with a harmonic and in panels (b) and (d) they are in the middle between two harmonics.

a different fundamental. In the conditions with maskers present we inserted narrow-band noises between the signal and the maskers. The center frequencies of these noise bands were 850 and 2150 Hz, and their spectrum levels were set 10 dB above the pink noise background. Their bandwidths (200 Hz for the low-frequency noise band and 400 Hz for the high-frequency noise band) were roughly equal to the critical bandwidth at their center frequencies (Scharf, 1970). These noise bands were added to mask any interference effects in the slopes of the signals and the maskers. A second strategy to prevent interference effects from simultaneous presentation of adjacent formants was to have their fundamentals at an integer multiple of each other. In this way the occurrence of beating by closely spaced components (each belonging to a different formant) could be avoided.

Using the resolvability criteria of Shackleton and Carlyon (1994) the stimuli can be classified as follows: In the LOW region, the components of all complexes were well resolvable by the peripheral auditory system, whereas in the MID region only complexes with the F_0 of 240 Hz were well resolved, and in the HIGH region no complexes were well resolved (though the harmonics of the 240-Hz fundamental are in the gray region between resolved and unresolved, having 2.5 to 2.8 components within the 10-dB bandwidth of the auditory filter as specified by Glasberg and Moore, 1990).

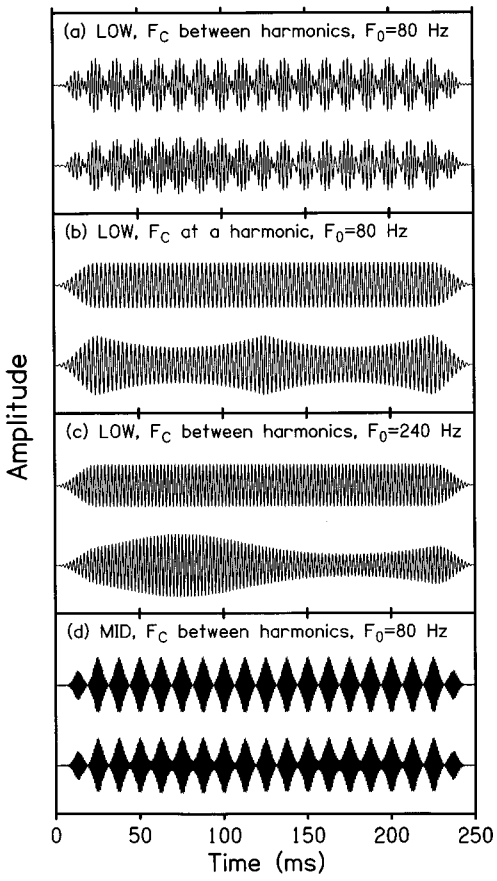

FIG. 3. Four examples of waveforms of formants. The upper trace of each panel contains the unmodulated waveform, the lower trace contains the waveform modulated at approximately two times detection threshold. The corresponding spectra for waveforms in panels (a)–(d) can be found in Fig. 2 as LOW of panel (b), LOW of panel (a), LOW of panel (d), and MID of panel (b), respectively. In comparison with the unmodulated waveforms, the modulated waveform in panel (a) shows an FM nature, those in panels (b) and (c) show a pure AM nature, and the one in panel (d) only differs from the unmodulated waveform near the minima of the temporal envelope (which is associated with a beating cue).

In the experiments, the stimuli were retrieved from disk by a PC and converted to analog signals using a 16-bit DAC (CED 1401 plus) at a sample rate of 40 kHz. The waveforms were low-pass filtered at 17.2 kHz (3-dB-down point, VBF/25.01, slope=100 dB/oct). Attenuation and mixing was performed by computer-controlled TDT attenuators and mixers. The noise bands interspersed between the masker and signal frequency regions were generated using white noises (TDT WG1), which were low-pass filtered to half the desired bandwidth (Kemo VBF/25.03, slope=48 dB/oct), and subsequently multiplied with a sinusoid of the appropriate center frequency using TDT four-quadrant multipliers. All undesired products of the multiplication were well below the pink noise floor. Stimuli were presented monotically through the right earpiece of Sennheiser HD414 headphones. They were checked using an HP 3561 A spectrum analyzer.

B. Procedure

Using an adaptive procedure, FMTs for the center frequencies of synthetic formants were measured for normal-hearing subjects. We used a three-interval, three-alternative forced-choice paradigm (3I, 3AFC), in which two of three tone intervals contained the stationary reference formant and the remaining interval contained the sound with the modulated formant (the target). When present, the interfering sounds (the maskers) were presented in all three tone intervals. Immediate feedback was provided in the soundproof booth. The 3I, 3AFC method was chosen to allow subjects to use any cue they could find. The silent interval between the three stimuli was 400 ms.

All measurements were performed under computer control. This included experimental timing and the collection of responses. Each FMT estimation was started with the maximum center-frequency modulation of 25.6% for the target tones. This guaranteed starting at a modulation range that was clearly audible for all subjects. After four correct responses, the modulation range of the target was decreased by a factor of $\sqrt{2}$. It was also decreased after one incorrect combined with five correct responses, or after two incorrect combined with six correct responses. The combination of three incorrect and six correct responses led to a test repetition at the same modulation range. After four incorrect responses, the modulation range was increased by a factor of $\sqrt{2}$. The trials were repeated until one of these conditions was met, after which the modulation range was adapted accordingly and the next set of trials performed. These decision rules were introduced, and described in detail, by Lyzenga and Horst (1995). The resulting procedure converges at 63% correct responses, which corresponds to a d' of 1 for the 3I, 3AFC paradigm. Data were collected until the direction of the modulation range adaptation was reversed six times, or after three consecutive test repetitions at the same modulation range. On average, one FMT measurement required about 85 trials.

Estimates of the FMTs were made after the each set of conditions was measured three times (making 200 to 300 trials near threshold), in a pseudorandom order. After these three series, the scores for each stimulus were checked for consistency and, where the thresholds showed a spread greater than a factor of 2, one or two additional estimations were made. The FMTs for a small proportion (less than 0.5%) of runs were more than a factor of 4 away from the others and were discarded. First all the stimuli of experiment 1 were presented to the subjects, after which the stimuli for both conditions of experiment 2 (stationary and modulated maskers) were presented in alternating batches. For each subject, the percent correct $p(c)$ as a function of the modulation range was estimated by averaging the scores for each target. These psychometric functions were fitted to the theoretical expectations of $p(c)$ as a function of d' from detection theory to scale the modulation range relative to d'. This results in a threshold that represents the modulation range that corresponds to a d' of 1, which coincides with the range where most of the data were collected. The standard deviation of the individual FMTs was found to be smaller than 30% (between a factor of 1.2 and 1.3). When calculating d' we assumed that subjects were not biased towards one of the three signal intervals in their answers. In our measurements, we found for the incorrect answers that 38% occurred for the first, 33% for the second, and 29% for the third interval

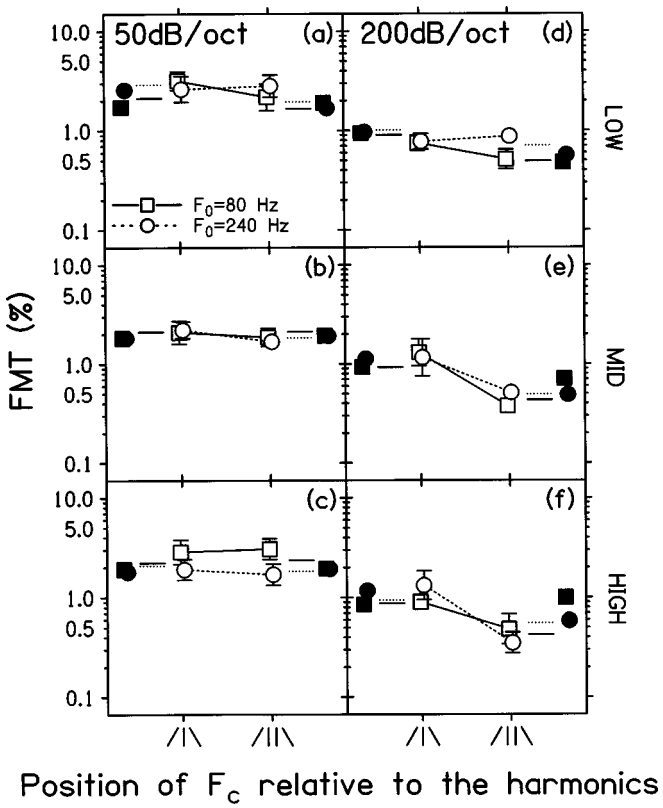

FIG. 4. The open symbols show the FMTs for stimuli without any maskers present. The squares and the circles denote the 80- and the 240-Hz fundamental, respectively. The left and right columns show the data for the 50- and the 200-dB/oct slopes, respectively. From top to bottom the data for the frequency regions LOW, MID, and HIGH are displayed. The short lines at the sides of the panels give the expectations of the hybrid model, and the solid symbols give the expectations the alternative version of this model (see text).

(instead of 33% for all three intervals). This showed that the subjects were slightly biased towards the first interval. This minor effect was ignored in the calculations.

C. Subjects

Four normal-hearing subjects participated for the conditions without maskers, and for those with two maskers. For the conditions with a single masker three of the original group of subjects participated. One subject (the first author) was highly experienced in the task; the others were trained before starting data collection. Nevertheless, two subjects showed some training effects for 2 of the 24 stimuli. To eliminate these training effects, the earlier conditions were rerun for these two subjects at the end of the measurement series, discarding the old runs. Including the outlying runs discussed above, fewer than 1% of the estimations were discarded.

II. EXPERIMENT 1. NO MASKERS

In this experiment FMTs were measured for the stimuli in all three frequency regions. The open symbols in Fig. 4 show the FMTs, without any maskers present, averaged across four subjects. The results for the LOW, MID, and HIGH region are displayed on the first, second, and third rows, respectively. The left column contains results for the shallow slope (50 dB/oct), and the right one for the steep slope (200 dB/oct). The symbols /|\ and /||\ correspond to formant positions at a harmonic and between two harmonics, respectively. The open squares and circles show the FMTs for the 80- and the 240-Hz F_0. The FMTs are roughly a factor of 2 larger than have been obtained for jnd's in center frequency for comparable stimuli. For example, the present FMTs for the LOW region and the 50-dB/oct slope [panel (a)] are between 2% and 3%, while the jnd's of Lyzenga and Horst (1997) for the first formant ($F_C \approx 500$ Hz) and equal slope are between 1% and 2%. Likewise for the MID and the HIGH regions, the present FMTs for the 80-Hz fundamental and the 200-dB/oct slope [squares in panels (e) and (f)] range from 0.4% to 1.4%, while the jnd's of Lyzenga and Horst for the second formant ($F_C \approx 2000$ Hz), equal slope, and a 100-Hz fundamental range from 0.2% to 0.6%. In agreement with the jnd's, the FMTs are smaller for the steep (right column) than for the shallow slope (left column), and, for stimuli with unresolved patrials [panels (e) and (f)], they are smaller for center frequencies between two harmonics compared to those at a harmonic.

For comparison, the predictions of a hybrid model are also shown in Fig. 4, by means of the short line segments at the sides of each panel. The solid and the dotted line segments represent the expected jnd's for the 80- and the 240-Hz fundamental, respectively. This hybrid model encompasses three underlying models, which are similar to those that were used by Lyzenga and Horst (1997) to account for formant frequency jnds. These three models will be described only briefly here, with a more detailed description being provided in the Appendix. In generating the combined d' values, we assumed that d' is proportional to the modulation range (see Sec. III C), and that listeners add them as independent variables (square root of sum of squares).

The first model in the combination is a modified place model in which hypothetical excitation patterns for two sounds are compared, and when these patterns differ by more than a certain threshold value, the two sounds are considered to be perceptually discriminable. It was developed to predict jnd's, and it was slightly adapted for use with the present modulation detection task. The most important adaptations were the introduction of two ''looks'' at each stimulus and an increase in threshold value. The second model is based on the perception of amplitude-modulation depth differences. For this model we assumed that subjects compare the slow amplitude modulations of the targets of each trial with the absence of any slow AM in the reference tones [e.g., Fig. 3, panels (b) and (c)]. In this model the detection of AM in the temporal envelopes of complex stimuli is related to that for pure tones by filtering the complex stimuli with a hypothetical auditory filter (Patterson and Moore, 1986), and comparing the resulting modulation depths in the auditory channels to AM detection thresholds for pure tones. The present stimuli often showed fast amplitude modulations at the rate of the fundamental (80 or 240 Hz), which were disregarded in the AM detection model. They were used in the third model, based on the detection of within-channel interactions of components. This model assumes that two sounds are perceptually discriminable when (after auditory filtering) one

sound does, and the other does not, show clear zero crossings in the temporal envelopes of the stimuli [e.g., Fig. 3, panel (d)]. It will be referred to as the ''beating detector'' model.

The thresholds used in the three models underlying this hybrid model were chosen to produce least-squared errors between predictions and data (see the Appendix for these threshold values). The output of each model was divided by its thresholds to generate predicted d' values, after which these d' values were combined and the combined d' was compared with a threshold of 1. The expectations of this hybrid model (the line segments) show very good correspondence with the FMTs under all conditions: all predictions are within a factor of 1.6 of the FMTs. The sum of the squared relative errors is 1.18, summed over 24 stimuli. The least accurate prediction occurs for the stimulus with a 200-dB/oct slope, a 240-Hz F_0, and a center frequency between two unresolved harmonics [lower right corner of panel (f)]. For this stimulus a within-channel beating cue might have played a role in the modulation detection, but the present beating detector did not produce a sizable d' value. It was more successful for similar stimuli with a lower F_0 (see below).

Expectations of an alternative version of the hybrid model are shown by the solid symbols at the sides of the panels. This model combines the aforementioned modified place model with an AM detection model introduced by Strickland and Viemeister (1996) to describe tuning of modulation masking for broadband AM noises. In short, this model consists of a bandpass filter (which we chose wide enough to pass all stimuli without attenuation), followed by a half-wave rectifier and a single-pole lowpass filter, after which five different decision statistics are calculated over the central 200 ms of the stimulus from the thus-obtained temporal envelope. These are the standard deviation of the envelope, its fourth moment, its crest factor, the ratio of its maximum and minimum, and the average magnitude of its slope. We found that predictions generated using the crest factor (in combination with a cutoff frequency of 150 Hz for the low-pass filter) approximated our FMTs better than the other four statistics. For clarity, only these predictions were included in Fig. 4.

When choosing the thresholds of the two models underlying the alternative hybrid model to produce least squared errors, the sum of the squared relative errors (summed over 24 stimuli) is 2.58. This is considerably larger than found for the original version of the model. The major deviations of the alternative model are found for stimuli with a center frequency between two unresolved harmonics [right side in panel (f) and right square in panel (e)]. These are stimuli for which within-channel (beating) cues are likely to play a role. When excluding these stimuli from the sum of the squared errors and again finding its minimum, the fit for the remaining 21 points could be improved considerably. These predictions are shown in Fig. 4 (solid symbols). They show good correspondence with the data except for the described stimuli with possible within-channel cues.

Since Fig. 4 only shows predictions of combined models, it does not contain information about which of the underlying models was the most influential one under each condition. This information is given in Table I. It shows which underlying model in the original hybrid model provided the largest contribution to each combined d'. For one stimulus both the place and the AM detection model contributed in approximately equal amounts (with d' values of 0.72 and 0.69, respectively). This is indicated by the code ''C.''

TABLE I. Cues used for the signals: P: place model cue; A: AM detection cue; B: beating cue. The code C stands for combined place and AM cues, such entries signify d' scores that were within 10% of each other. The panel labels correspond with those in Fig. 4. Cues used for the maskers are given between brackets. They can be found at the corresponding positions in the panel above (lower-frequency masker) or below (higher-frequency masker) that of the signal. For all modulated maskers, the center frequency coincided with a harmonic, so only these cues are given.

		$G=50$ dB/oct		$G=200$ dB/oct	
Region	F_0	$F_C=/\backslash$	$F_C=/\|\|\backslash$	$F_C=/\backslash$	$F_C=/\|\|\backslash$
LOW	80	P (P)	P [a]	A (A)	P [d]
	240	C (P)	P	A (A)	A
MID	80	P (P)	P [b]	A (C)	B [e]
	240	P (P)	P	A (A)	P
HIGH	80	P (P)	P [c]	A (P)	B [f]
	240	P (P)	P	A (C)	P

When examining the cues used for modulation detection in Table I, we find mainly place model cues for the 50-dB/oct slope (left column). These stimuli either contain the fundamental or they contain four or more harmonics. Those with unresolved partials show amplitude fluctuations at the rate of the fundamental. So, these stimuli contain information about the fundamental in the spectral or in the temporal domain. A single exception is found in the lower left corner of panel (a) of Table I, where the entry is C. This stimulus mainly consists of one large central component. All other harmonics are 30 dB or more down from the central one, both in reference and in the targets near threshold, so they are masked by the pink noise background. When modulating the center frequency of this stimuli with 5 Hz, the result is a 10-Hz amplitude modulation of the main central component [see Fig. 3, panel (b)]. Therefore, it is very likely that an AM detection cue also played a role for this stimulus.

For the 200-dB/oct slope, a more complex pattern is observed. For stimuli with a center frequency coinciding with a harmonic, AM cues are the more important ones. All these stimuli mainly consist of one large central component with all remaining harmonics strongly attenuated. From top to bottom in this column of Table I, the largest remaining harmonics are attenuated by 53, 117, 12, 44, 8, and 23 dB. So, these stimuli show a modulation behavior similar to that of the AM stimulus described in the previous paragraph. (Note that for the stimuli with the smaller attenuation values the place model cue gains importance for the large FM range of the maskers.) For stimuli with a center frequency between harmonics a range of different cues emerge. An AM cue is found in panel (d) for a 240-Hz fundamental and a center frequency between harmonics (lower right corner). Here the stimulus consists of one component in the slope of the spectral envelope. For this stimulus, the 5-Hz center frequency modulation results in a 5-Hz amplitude modulation of the main component [see Fig. 3, panel (c)]. For the stimuli with

unresolved partials [panel (f) and upper row of panel (e)], we find beating cues for the 80-Hz fundamental, whereas a place model cue is the more important one for the 240 Hz F_0. These stimuli have two large unresolved components near the center of the stimuli, so within-channel cues may well play a role here. An example of such a stimulus is given in panel (d) of Fig. 3.

In summary, we need a hybrid model to describe the FMTs, which is in accordance with the findings of Lyzenga and Horst (1997) for formant frequency jnds. Table I gives an overview of the cues which, according to the hybrid model, were used to detect FM on each of the synthetic formants used in the experiments. For the shallow slope a place cue is used in all except one condition, whereas for the steep slope we predominantly find temporal cues.

III. EXPERIMENT 2. SIMULTANEOUS MASKERS

A. Stationary maskers

In this experiment the effect on the FMT of simultaneous presentation of stationary maskers was determined. The individual FMDI was calculated for each listener as the FMTs for signals with stationary maskers divided by those for signals without maskers. In this and all following experiments, the mean FMDIs were evaluated as the geometrical mean of the individual FMDIs. These means are shown in Fig. 5. The error bars indicate the standard deviations of the means. Three subjects participated for the lower-and higher-frequency maskers [panels (a) to (h)], and four for the conditions with both maskers [panels (i) and (j)].

Figure 5 shows that, in all conditions, the unmodulated maskers have little or no effect. On average, the increase in the FMTs when adding stationary maskers with a center frequency at a harmonic (open symbols) is only 1%, and for those with a center frequency between two harmonics (filled symbols) the increase is just 2%. A paired *t*-test on the logarithmic transform of all individual FMTs showed that the mean increases were far from significant for the both the former ($df=127$, $t=-0.38$, $p=0.71$) and the latter masker type ($df=127$, $t=-1.20$, $p=0.23$). So, there are no differences between the FMTs in the absence of maskers and those in the presence of stationary (i.e., nonfrequency modulated) maskers. For the modulated masker conditions (see Secs. III B and III C), only maskers with center frequencies coinciding with a harmonic were used.

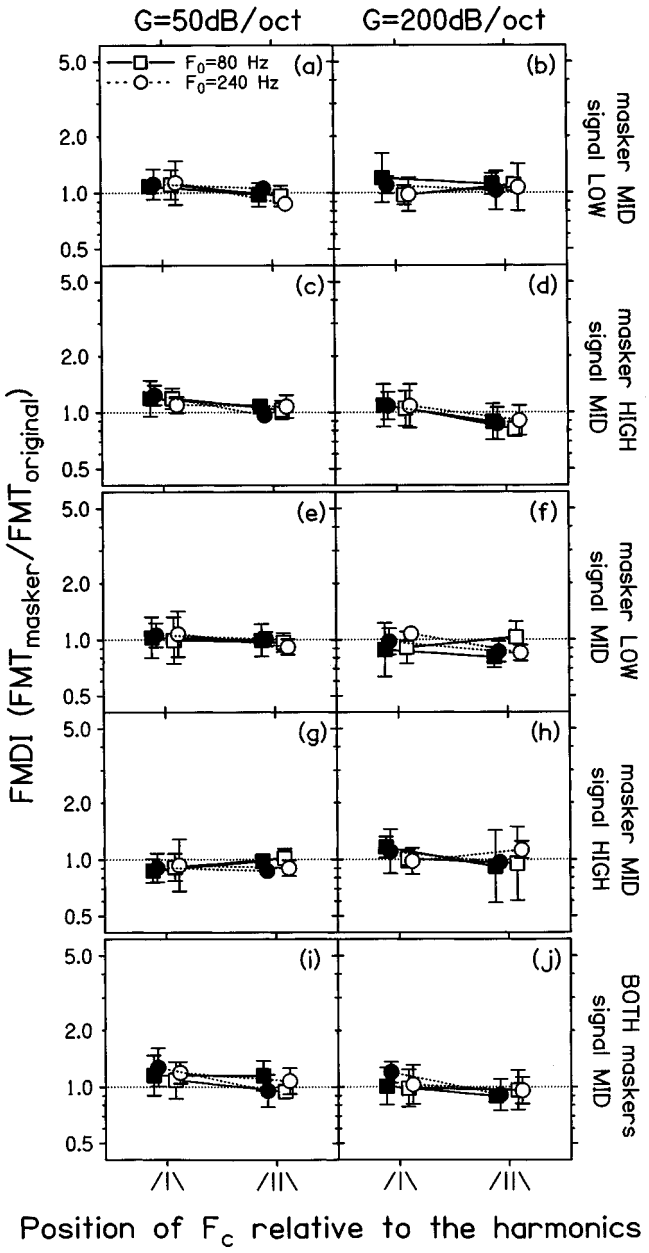

FIG. 5. Mean FMDI for stationary maskers located either to the higher-frequency side [panels (a)–(d)], to the lower-frequency side [panels (e)–(h)], or to both sides [panels (i) and (j)]. The frequency regions of signals and maskers are indicated on the right of each row. The left column shows the data for the 50-dB/oct slope, and the right one for the 200-dB/oct slope. The squares and the circles display data for the 80- and 240-Hz fundamental, respectively. The open and solid symbols indicate maskers with center frequencies at a harmonic and between two harmonics, respectively.

B. Two modulated maskers

Figure 6 shows the mean FMDI for four subjects for signals in the MID region presented simultaneously with modulated maskers in both the LOW and the HIGH regions. The left and right columns show the data for the 50- and 200-dB/oct slopes, respectively, with the upper and lower rows corresponding to signal fundamentals of 240 and 80 Hz. The open symbols refer to signals that were accompanied by maskers on the same fundamental (same-F_0 condition), and the filled symbols display the data for maskers with different fundamentals than the signals (different-F_0 condition). The FMDI is expressed as the FMT for the modulated maskers divided by that for the stationary maskers.

For the signals with the 50-dB/oct slope (left column), the FMTs show a marked increase in the presence of modulated maskers. This increase is larger when the maskers have the same fundamental as the signal (factor of 1.72) than when they have a different fundamental (factor of 1.38). To assess the significance of this effect, a three-way repeated measures ANOVA was performed on the FMDI ratios shown in the left-hand column of Fig. 6, with factors corresponding to formant position, signal F_0, and masker/signal F_0 simi-

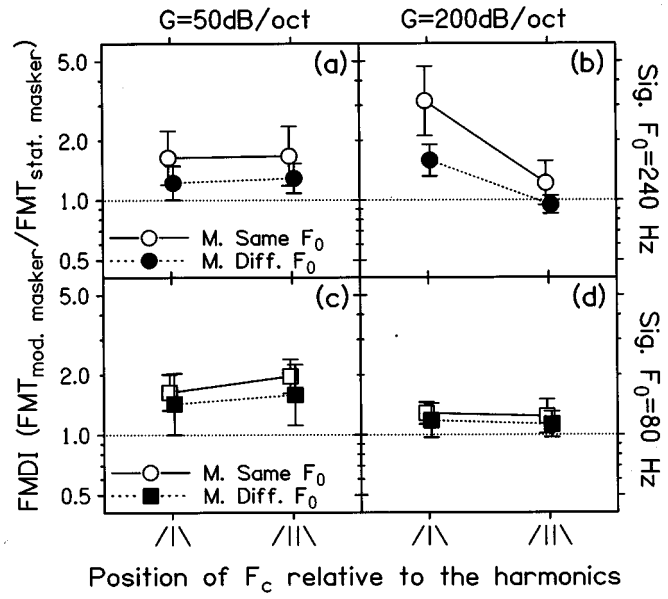

FIG. 6. Mean FMDI for signals in the MID region with modulated maskers to both lower- and higher-frequency sides. The error bars indicate the standard deviations of the means. The FMDI is expressed relative to the FMT obtained with an unmodulated masker with the same F_0 as the signal. The left column shows the data for the 50-dB/oct slope, and the right one for the 200-dB/oct slope. The squares and the circles display data for the 80- and 240-Hz fundamental, respectively. The open and filled symbols represent maskers with a same and with a different fundamental than the signals, respectively.

larity. This revealed significant effects for the similarity of masker and signal fundamentals [$F(1,3)=28.4$, $p<0.02$] and the signal F_0 [$F(1,3)=17.3$, $p<0.03$], but not for the formant position. On average, FMDI for a signal F_0 of 80 Hz is slightly larger than for the 240-Hz fundamental (1.71 versus 1.50, respectively). So, for the 50-dB/oct slope we find clear FMDI effects for modulated maskers, which are significantly larger for maskers with the same fundamental as the signal than for those with a different F_0.

For the signals with the 200-dB/oct slope (right column), the FMDI ratios are also above unity in many conditions, and there is some indication that thresholds are higher in the same-F_0 condition than in the different-F_0 condition. However, a three-way repeated measures ANOVA (formant position×signal F_0×masker/signal F_0 similarity) revealed that this effect of masker/signal F_0 similarity just failed to reach significance [$F(1,3)=9.54$, $p=0.054$]. Only for the position of the formants relative to the harmonics a significant main effect was found [$F(1,3)=19.33$, $p<0.03$]. This effect was due mainly to the large FMDIs observed at 240 Hz when the formants were centered on a harmonic. This condition also showed the largest effect of F_0 similarity, and, unfortunately, complicates interpretation of that effect, because the signal ''formant'' is, in fact, one of the amplitude-modulated pure tones described in Sec. II. It is therefore highly unlikely that for this stimulus the effect of F_0 similarity arises from a processing of fundamental frequency information *per se*. An alternative explanation might be found in the nature of the cues used for detecting the modulations of the signals and maskers. This will be examined in more detail in the next section, where single rather than double maskers are used, and where the influence of signal and masker cues can be studied more directly. The effect of F_0 similarity was assessed for the remaining combinations of formant position and signal F_0 by a two-way ANOVA in which these three conditions were treated as different levels of a single factor, with the other factor being the similarity between the masker and signal fundamentals. This revealed no significant effects of either the three formant/F_0 conditions, or the masker/signal F_0 similarity.

To summarize, the addition of two modulated maskers often increases FMTs, and this effect is greatest when the maskers share the same F_0 as the signal. This effect of F_0 similarity occurs mainly for stimuli with shallow formant slopes, most of which have sufficient harmonics to convey F_0 information. However, an effect of F_0 similarity can sometimes be seen with stimuli whose F_0 is unlikely to have been processed by the auditory system.

C. Single modulated maskers

Figures 7 and 8 show the mean FMDI for three subjects for signals in all three frequency regions with a single modulated masker, located either to the higher- (upper four panels) or to the lower-frequency side (lower four panels). The signal and masker regions are indicated on the right of the figures. Figure 7 shows the data for signals with the 240-Hz fundamental, and Fig. 8 for the 80-Hz F_0. The fundamentals of the maskers were either the same (open symbols) or different (filled symbols) than those of the signals. Below all data pairs for the same- and different-F_0 conditions, the cues that we proposed for the detection of FM imposed on isolated signals (left) and maskers (right), as given in Table I, are indicated separated by a slash. It is worth recalling that these cues also correspond roughly to the number of components within 20 dB of the peak of each stimulus, with an AM cue being used when there is a single component, and a place model accounting for detection when there are two or more components. Alternatively, a within-channel beating cue comes into play for those formants that are unresolved and have two approximately equally large central components. When describing the various effects that can be seen in the data, we will refer to the outcome of a five-way ANOVA applied to the entire data set (four combinations of masker/signal frequency region×masker/signal F_0 similarity (same versus different)×two slopes×two signal fundamentals ×two formant positions).

A preliminary inspection of Figs. 7 and 8 reveals that, in the majority of cases, the FMDI is greater when the masker has the same fundamental as the signal (open symbols) than when the masker and signal fundamentals are different (filled symbols). This was reflected by a significant main effect in the ANOVA [$F(1,2)=84.4$, $p<0.02$], and provides evidence in support of the idea that processes that extract F_0 information from signals and maskers affect the FMDI mechanism. A degree of caution is, however, required when interpreting this finding, because there are a number of conditions where it is unlikely that there is any processing of F_0 *per se*, yet where FMDI is greater when the masker and signal fundamentals are similar than when they are different. An example of this comes from the right-hand points in

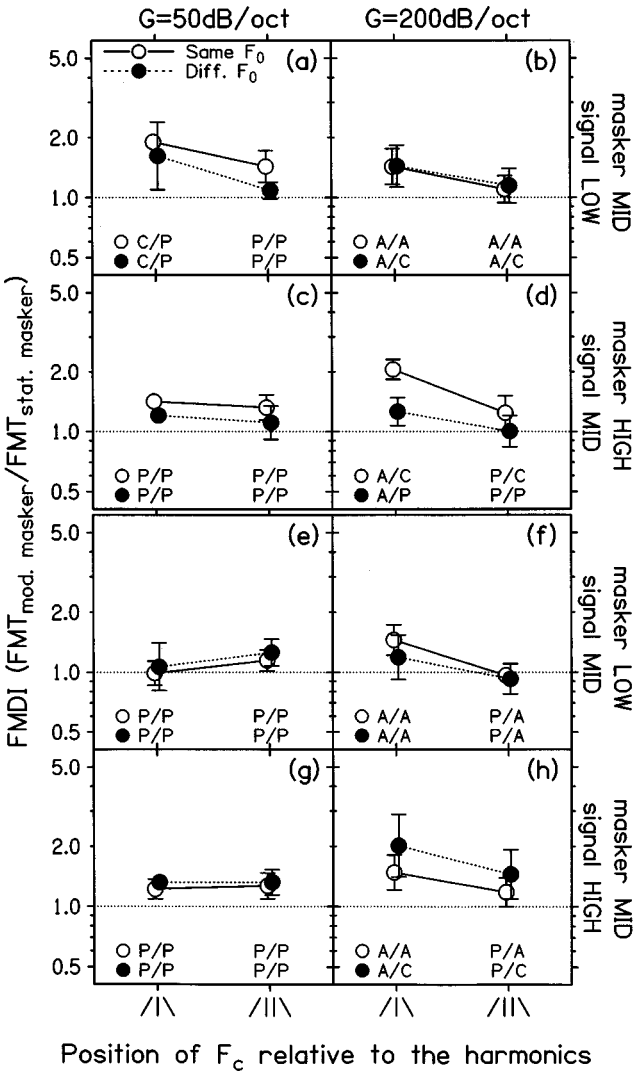

FIG. 7. Mean FMDI for signals with a 240-Hz fundamental and with single modulated maskers. The error bars indicate the standard deviations of the means. The FMDI is expressed relative to the FMT obtained with an unmodulated masker with the same F_0 as the signal. The format of this figure is the same as that of the upper eight panels of Fig. 5. The meaning of the symbols is the same as in Fig. 6. Below each pair of symbols, a code (see Table I) indicates the cues associated with signals and maskers, where the code C is used for combined A and P cues.

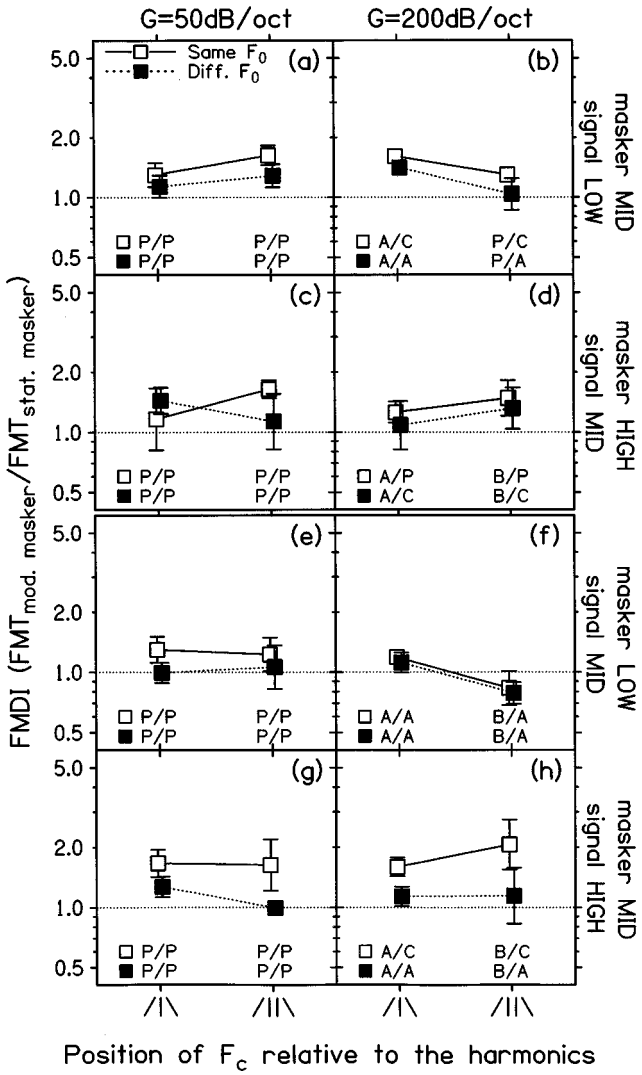

FIG. 8. Mean FMDI for signals with an 80-Hz fundamental and with single modulated maskers. The format of this figure is the same as that of Fig. 7.

panel (h) of Fig. 7, where changing the masker F_0 from 80 (filled circle) to 240 Hz (open circle) results in the masker being dominated by a single component, and its FM being detected by the AM of that component (as indicated in the legends underneath those two points). Indeed, Table II, which gives the frequencies of occurrence of FMDI effects for all cue combinations, shows that we rarely find FMDI effects for cases where the detection of FM imposed on the masker is detected by virtue of the resulting AM, and where that on the signal is consistent with a ''place'' or ''beating'' model (lower entries in left-hand column). In order to determine whether similarity of masker and signal fundamentals affected FMDI independently of these cue changes, we analyzed separately the 15 pairs of conditions (masker F_0 same or different to signal) in which detection of FM imposed on both the masker and signal was consistent with a place model. These conditions are identified in Figs. 7 and 8 by the label ''P/P'' for both the same-F_0 (open symbols) and different-F_0 (filled symbols) conditions. A two-way ANOVA (condition×masker/signal F_0 similarity) on the logarithmic transform of the FMTs revealed a large main effect of masker F_0 relative to signal F_0 [$F(1,2)=104.9$, $p<0.01$], indicating that, although cue changes can mediate the effect of ''F_0 similarity'' on FMDI, this effect persists even when no such cue changes take place.

Under the remaining conditions of Figs. 7 and 8, most

TABLE II. Frequencies of the occurrence of FMDI for signal/masker cue combinations. Entries give the number of occurrences of FMDI and of signal/masker cue combinations separated by a slash. FMDI was considered to be present when the ratio between the FMTs was larger than both its standard deviation and a factor of 1.2. The code C signifies combined A and P cues. Occurrences of C/P have not been included.

Cues for signals	Cues for maskers		
	A	P	C
A	4/9	2/2	5/7
P	1/4	19/31	3/3
B	0/3	1/1	2/2

maskers have a change in associated cues with changing fundamental. For this group FMDI is smaller for maskers associated with an AM detection cue than for those for which a place-model cue plays a role. Inspecting the figures we can see that this is true for all conditions except for panel (d) of Fig. 7. For these signals, the masker used under the same-F_0 condition is the previously described AM tone whose harmonics next to the central one are down by 23 dB [HIGH region, $G=200$ dB/oct, $F_0=240$ Hz, left circle in panel (f), Fig. 4]. However, for the large modulation range of the maskers, these side harmonics increase considerably in level, one after the other, and this effect is large enough to affect the perceived formant frequency of the tone. This produced FM in addition to a strong AM, a combination of characteristics which may be responsible for the large amount of interference produced by this stimulus (in accordance, the hybrid model predicts an unusually large d' for this masker).

The ANOVA performed on the entire data set also revealed an effect of masker/signal frequency region [$F(3,6)=7.3$, $p<0.02$]. Inspection of the FMDI for each combination of frequency regions, averaged across the other factors, revealed that this was due to the FMDI being generally lower with the masker in the LOW region and the signal in the MID region (third row of each figure) than in the other three conditions. This may partly reflect the fact that, for this combination of masker and signal regions, the masker FM was often detected from the resulting AM, whereas that of the signal was consistent with either a place [both panels (e) and the two rightmost points of Fig. 7, panel (f)] or beating [right of Fig. 8, panel (f)] model. As discussed above and shown in Table II, this combination of cues rarely results in substantial FMDI. In contrast, FMDI is often quite large when both the signal and masker FM are detected from the resulting AM: In other words, a single AM tone hardly interferes with the detection of FM on a complex tone, but it does so for the detection of AM on another AM tone. A slightly different pattern of interference was reported for detection of increases in AM depth and FM range of pure tones by Moore *et al.* (1991). They found much larger interference for AM sinusoids than for FM sinusoids, and the modulation type of the maskers (AM and FM) did not greatly affect MDI.

The susceptibility of amplitude-modulated signals to FMDI might also account for a two-way interaction[1] obtained between spectral slope and formant position [$F(1,2)=25.4$, $p<0.05$]. This interaction is reflected in the fact that, at a slope of 200 dB/oct, FMDI was often greater for a formant centered on a harmonic (/|\) than for one centered between two harmonics (/||\), whereas no such trend occurred at the shallower slope. Inspection of the cues shown in Figs. 7 and 8 shows that at 200 dB/oct (right-hand column), the /|\ signal was often an AM tone whereas the /||\ stimulus was not.

A final topic of interest is whether the size of the FMDI is greater for maskers occupying frequency regions above or below that of the signal. For example, for signals in the MID region we found very little FMDI for LOW maskers but substantial FMDI for HIGH maskers (third and second rows of Figs. 7 and 8, respectively). Such an asymmetry for the side to which a masker is located relative to the same signal has been reported for AM tones by Yost and Sheft (1989), Bacon and Moore (1993), Bacon and Konrad (1993), and Bacon *et al.* (1995). However, this side-of-masker issue can best be approached by considering those pairs of conditions in which the stimuli are identical except for the roles of the masker and signal being reversed.[2] Two such comparisons can be made, in which the signal and masker are in the LOW and MID regions and vice versa (first versus third rows of Figs. 7 and 8), and where they are in the MID and HIGH regions (second versus fourth rows). For each of these comparisons one can only consider the cases where the signal formants were centered on a harmonic (as this was always the case for the maskers). For the LOW/MID combination we performed a four-way ANOVA on the two possible assignments of masker and signal regions, the two spectral slopes, the signal F_0, and the masker/signal F_0 similarity. This revealed no main effect of which region was chosen to be the signal. A similar finding was obtained for the MID and HIGH regions, though here main effects were found for the signal F_0 [$F(1,2)=115.6$, $p<0.01$] and for the masker/signal F_0 similarity [$F(1,2)=63.2$, $p<0.02$]. Overall, the lack of an effect of masker/signal role is broadly consistent with the results of Yost *et al.* (1989) who found no substantial effects of relative frequency region on MDI for 1- and 4-kHz AM pure tones. Therefore, the present asymmetry between the second and third rows of Figs. 7 and 8 seems to be an effect of the cues associated with maskers and signals (as argued previously), rather than of the side at which the masker is located.

IV. GENERAL DISCUSSION

A. The FMTs in absence of a masker

The FMTs can be understood from a hybrid model, in which the nature of the cue used varies across three classes of stimuli. For stimuli with the shallow slope (50 dB/oct), the modified place model provided a good description of most data. For those with the steeper 200-dB/oct slope three different models were needed to explain the data. When the center frequency coincided with a harmonic, a model based on AM detection provided a good description of the data. For a few of the remaining conditions where stimuli had unresolved components, we found very small FMTs. Here neither the place model nor the AM detection model were able to provide a good description. Under such conditions it is likely that within-channel cues played a role, so the discrimination may well have been based on a temporal mechanism. We applied a ''beating detector'' model, which was found to be reasonably successful, at least for stimuli with an F_0 of 80 Hz.

The FMTs in the absence of maskers were roughly a factor of 2 larger than formant frequency jnd's. However, the present stimuli contain only a single modulation cycle. For longer stimulus duration the FMTs are likely to decrease until about four modulation cycles are present (Lee and Bacon, 1997). This would probably bring the FMTs much closer to the jnd's. For the place model this would mean that a lower threshold value would be required (from 7 to roughly 3 dB, see the Appendix). Such a lower threshold value would

then be in closer agreement with the 2-dB value used by Lyzenga and Horst (1997). An analogous modification can be made to the AM model. We used threshold values of 45% for a 5-Hz rate and 25% for a 10-Hz rate (see the Appendix), which are larger than those (between 10% and 20% for small initial modulation depths) found by Lyzenga and Horst (1997). So, a decrease in these thresholds would bring them in closer agreement with those used for formant-discrimination jnd's.

Furthermore, Lyzenga and Horst (1995, 1997) found good correspondence between modulation-depth differences and the center frequency jnd for stimuli with a triangular spectral envelope, unresolved partials, and a center frequency coinciding with a harmonic. Under a number of these conditions the predictions of their place-model predictions also showed good correspondence, giving an area of overlap where both models functioned reasonably well. Correspondence was generally worse for center frequencies between harmonics (where they used a beating detector). The present results for the MID and the HIGH regions are in good agreement with these findings. Therefore we can conclude that for the sensitivity to changes in formant frequency, the interpretations in terms of the present models does not depend on whether these changes are ''static'' or ''dynamic'' (jnd versus FMT).

The formant modulations of the present stimuli reflect the combined amplitude modulations of the components in the low- and the high-frequency flanks of the spectral envelope, where the modulations of these two groups of components are in antiphase. This mechanism carries some resemblance to the FM-induced AM discussed by Plack and Carlyon (1994). They modulated the fundamentals of complex tones and argued that this can produce amplitude modulations within separate auditory filters as the components move through their pass band. For the present stimuli the components are fixed, but the spectral envelope is moving, which directly amplitude modulates the components. This explains the success of the amplitude-modulation detection model for stimuli with only one major component. For stimuli with more than one large component, the mechanism of the place model is simply the detection of the level variations, which might explain the success of this model for the shallow spectral slope. For such stimuli, the locus of the excitation pattern changes its position over time, which closely resembles the ''second FM-encoding mechanism'' as proposed by Edwards and Viemeister (1994). They measured discrimination of pure-tone FM from AM, and found that the mechanisms for encoding these two types of modulation were very similar for small modulation depths and highly dissimilar for large modulation depths. For large modulation depths, a second FM-encoding mechanism started to operate, which was highly independent from the AM-encoding mechanism. They argued that this second mechanism was a place mechanism based on the dynamic changes in the locus of the excitation pattern. The competition between the place and AM-detection models, as proposed in the present study, assumes an intrinsic independence between these two mechanisms, which is in agreement with the findings of Edwards and Viemeister.

For all stimuli with several components, two modulation rates were present in the waveforms; a slow one caused by the 5-Hz frequency modulation, and a fast one at a rate equal to F_0. For stimuli that were likely to give rise to within-channel cues, we applied the beating-detector model. These stimuli all had two unresolved central components of similar size which were beating at the (fast) rate of the fundamental. As the center frequency moved, the relative amplitudes of these two components changed, producing a change in the depth of the beating. So, here it seems likely that the FM was detected from a slow variation in the depth of a faster amplitude modulation produced by the interaction of unresolved components.

B. Stationary simultaneous maskers

We did not find any interference of frequency modulation detection when the stimuli were presented simultaneously with stationary maskers and the narrow-band noises that were inserted between the signal and the maskers. This indicates that either there were no interactions at the level of the cochlea between signals and maskers and between signals and noise bands, or these interactions did not interfere with the modulation detection. This observation is in agreement with the models used to describe the FMTs. All three models concentrate on a region around the spectral peak of the stimuli. For the AM detection model and the beating detector this is obvious. In the place model this is caused by a modification of the model that was originally made in order to apply it to experiments with roving stimulus levels. The modified place model adds the absolute values of the level differences in both flanks of the excitation. This strategy generally produces the largest effective excitation differences near the top of the excitation, limiting the operation of the model to a region close to the center frequency of the stimuli.

Moore and Sek (1994) proposed a multichannel excitation-pattern model for the detection of combined AM and FM, in which the excitation changes in all channels with a positive signal-to-noise ratio were taken into account, instead of just two channels as is the case in the present model. Therefore, in the model proposed by Moore and Sek, addition of the noise bands and the stationary maskers can be expected to increase the predicted thresholds. Using the present place and AM detection models we found no marked increases in the expectations for stationary maskers (the average increase equaled a ratio of 1.01), which seems in good agreement with our findings and contrary to the model of Moore and Sek. For pure-tone AM, Bacon *et al.* (1995) found an interference effect of adding stationary maskers. Since we found no FMDI for stationary maskers, this is in contrast with our data. Bacon *et al.* concluded that interference via spread of excitation is only a secondary effect in MDI. In the present place model the two channels that show the largest excitation differences in both flanks of the stimulus lie well away from the noise bands, and the presence of noise bands and stationary maskers does not greatly affect the predicted FMTs. Therefore, it seems safe to conclude for the present stimuli that spread of excitation plays no role in FMDI.

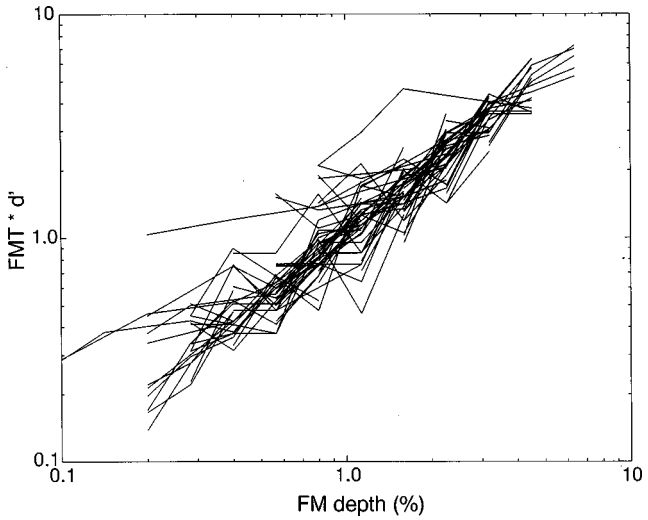

FIG. 9. Double logarithmic plot of the recorded d' values as a function of the modulation range for all subjects and conditions. To prevent jumps in the graph, the plotted d' values have been multiplied by the FMT which lowers the lines for small FMTs and raises those for large FMTs, but does not change their slopes.

C. Modulated simultaneous maskers

Before comparing the amount of FMDI across different conditions it is useful to have some information concerning the slopes of the psychometric functions. This is because the effect on sensitivity (d') of a given threshold change produced by a masker will depend on the slope of the underlying psychometric function, and changes in that slope across conditions could then distort comparisons of the masker effects. In order to obtain such information we derived the underlying psychometric functions for each condition using the method described in Sec. I C. Figure 9 shows the psychometric functions ($\log d'$ versus log FM range) for each condition, with the d' values for each curve multiplied by the FMT (corresponding $d'=1$) for that condition. This correction with the value of the FMT lowers the d' versus modulation-depth lines for small, and raises those for large FMTs, without altering the original slope of these lines. The resulting collection of overlaid FMTs shows an overall slope of one. If the correction had been made with the square or the square root of the FMT, the graph would have shown a zigzag nature. The uniform slope observed here indicates that d' is roughly proportional to FM range over the range of conditions studied here. This result differs from that obtained for the FM of pure tones, for which d' is proportional to the square of the modulation range (Moore and Sek, 1992). It shows that a given proportional change in FMT, produced by a modulated masker, reflects approximately the same proportional change in d' in all conditions.

We found FMDI for single modulated maskers under most of the conditions. Redoing the modeling for the place and AM detection models with modulated maskers reveals no increases in the expected FMTs (the average increase equaled a ratio of 1.01, with a maximum of 1.03). This is due to the auditory filtering taking place as the initial stage of these models. Because of this filtering the interferers are strongly attenuated and, therefore, do not interfere with the processing of the target stimuli. The alternative version of the AM detection model (after Strickland and Viemeister, 1996) is not successful either. This model predicts very large interference effects when adding stationary maskers and no further increases (often even decreases) in the FMTs when modulating the maskers. This is in sharp contrast with our data. Strickland and Viemeister (1997) argued that great care should be taken when applying this model to complex tones (AM and QFM tones). They added a stage of initial peripheral (auditory) filtering to the model to explain data for AM noise bands with varying bandwidths. Addition of such a peripheral filtering stage hardly affected predicted FMTs for the present stimuli (in the absence of maskers). However, because of the argument concerning such initial filtering given above, this version of the model was found to predict no FMDI at all. So, the present FMDI cannot be explained using the peripheral and single modulation channel models discussed here. A model with more than one channel for the processing of frequency modulation, such as the model introduced for AM stimuli by Dau *et al.* (1997a, b), might be more successful in explaining the present FMDI effects.

The conditions under which we found FMDI were split into two different groups; one group in which a place-model cue was associated with both signals and maskers, and one where this was not the case. The conditions with double place-model cues are mainly found for the 50-dB/oct slope in Figs. 7 and 8, with a single exception on the left in panel (a) of Fig. 7 where the signal is an AM pure-tone and does not convey any information about the fundamental. For the remaining conditions, FMDI is larger for maskers with the same fundamental as the signals than for those with a different F_0. The stimuli in this group have sufficient components (four or more) to convey F_0 information, or, as is the case for the signal on the right side of panel (a), Fig. 8, they contain the F_0. So, for this group of conditions we find a clear effect of common harmonicity on the FMDI.

As discussed in Sec. III C, detection of FM on a signal formant using a ''place'' cue was more disrupted by a masker with a same than with a different F_0. We interpret this finding as evidence that the mechanism (Meddis and O'Mard, 1997) or mechanisms (Carlyon, 1998; Shackleton and Carlyon, 1994) which extract F_0 provide an input to that responsible for FMDI. An alternative explanation is that the FMDI mechanism is sensitive to some aspect of the maskers and signals which covaries with the similarity of their fundamentals. For example, when the masker is in the MID region and the signal is in the HIGH region, and both have an F_0 of 80 Hz [open symbols, panel (g) of Fig. 8], then the harmonics of both complexes are unresolved by the peripheral auditory system. This will result in the outputs of auditory filters responding to the signal, and those responding to the masker, to both show a modulation at a rate of 80 Hz, a similarity which will be absent when the masker F_0 is changed to 240 Hz (filled symbols). It is possible that the similarity in modulation when the masker and signal F_0 were similar somehow increased the amount of interference for reasons that were intrinsic to the FMDI mechanism. We think it unlikely that a similarity in a fast (80 Hz) rate of temporal fluctuation would interfere with the detection of

slow (5 Hz) changes in the place of excitation. It seems even less likely that it could account for the effect of F_0 similarity in conditions where, even when the fundamentals of the signal and masker are identical, the two formants differ markedly in their ''resolvability'' and therefore in the form of the auditory filter responses to them [panel (c), Fig. 7, and panels (a) and (e), Fig. 8; resolvability as defined by Shackleton and Carlyon, 1994]. Rather, a more parsimonious and more convincing explanation is that stimuli with widely differing fundamentals are segregated by a separate mechanism or mechanisms, and that this segregation reduces their mutual interference at the stage of processing which is normally responsible for FMDI.[3] In summary, for stimuli that convey F_0 information, common harmonicity gives rise to larger interference. This implies that the interference mechanism receives input from F_0 extraction mechanisms.

V. CONCLUSIONS

The FMTs can be understood from a hybrid model, the nature of which depends on the stimuli, but not on whether the task was dynamic or static (FM detection versus frequency discrimination). For signals with a shallow slope the data are well described by a place model, and for signals that were in essence just amplitude-modulated pure tones a model based on amplitude-modulation detection provided a good description of the data. The smallest FMTs occurred for signals with two large unresolved components at either side of the center frequency, for which a beating cue was present.

No significant differences were found between the FMTs in the absence of maskers and those in the presence of simultaneous and stationary off-frequency maskers. So, FM detection was impaired neither by restricting the frequency range of the signals, nor by the presence of unmodulated maskers.

The FM detection was impaired when modulated maskers were presented simultaneously with the signals. This interference showed an effect of masker F_0 which could often, but not always, be associated with a change in the cue used for the detection of the masker modulation, which accompanied a change in its F_0. For a group in which a place-model cue was associated with both signals and maskers, we still found significantly larger FMTs for maskers with the same fundamental as the signals than for those with a different one. This effect of common harmonicity on FMDI is consistent with interference effects taking place after F_0 extraction, and supports the notion that perceptual grouping is involved in MDI effects.

ACKNOWLEDGMENTS

This research was funded by the Wellcome Trust. The authors would like to thank Christophe Micheyl for his help with the statistics and Brian Strope and Walt Jesteadt for their helpful comments on an earlier version of this paper.

APPENDIX: MODEL DESCRIPTIONS

1. The modified place model

A detailed description of the modified place model is given by Lyzenga and Horst (1997). In short, the model consists of a linear filter bank followed by a detector of level differences. The filter bank consists of 3400 Roex (Rounded exponential) filters with a Q of 5 (Patterson and Moore, 1986). The spacing of the center frequencies of these filters is logarithmic above, and linear below, 800 Hz. To form an excitation pattern, the outputs of the filters of all channels are squared, integrated over the stimulus duration, and converted to a level in dB. As a representation of the absolute threshold, a noise floor with a power of 1 (i.e., a level of 0 dB) is added to the output power of each filter before it is converted to dB. A level difference detector compares the excitation patterns for two tones. This detector ignores overall-level cues: the excitation levels of the presented tones are roughly equalized (by matching their overall levels), after which the maximum positive excitation difference and the absolute value of the largest negative difference are summed, and last, this sum is compared with a detection threshold. This model was developed for use in frequency discrimination experiments, and was applied to the present FMTs by assuming that subjects can detect modulation as soon as they can perceive a difference between two well-chosen ''looks'' at a stimulus. These looks were chosen at the maximum positive and negative center frequency excursion of the (single) modulation cycle of the stimulus. However, the duration of these looks (i.e., the time the frequency excursions are near their maximum) is much shorter than the total stimulus duration. Since frequency discrimination deteriorates for short stimulus duration (Moore, 1973), we expected to need a larger detection threshold than in the original settings of the model. We found we needed an increase of about a factor of 3, which is roughly in agreement with the increase in the data between the frequency discrimination task (jnd's) and the modulation detection task (FMTs). In the original model a 2-dB detection threshold was used. For the present task we found that a 7-dB threshold produced the smallest errors with the data when this model formed part of the hybrid model (on its own the optimal threshold would have been 5.5 dB).

2. The amplitude-modulation detection model

The first stage of the amplitude-modulation detection model was the same Roex filterbank of the modified place model. In the channel located at the center frequency of the stimulus and those at the positions of the two largest components we calculated the temporal envelope of the filtered stimuli using the Hilbert transform. For the rates of 5 and 10 Hz, we calculated the modulation depths from the Fourier transform of the envelopes. The AM was considered to be detectable when one of the thus found modulation depths was larger than a threshold value. To account for the fact that either just one or two cycles were present in the stimuli, we used different thresholds for the 5- and the 10-Hz modulation rates. The expected FMT was determined with the described algorithm by finding the smallest center frequency modula-

tion range of the target that gave rise to an AM depth equal to the corresponding threshold. For all but one stimuli we found the largest modulation depths in one of the channels at the frequency of the largest components. For the remaining stimulus (which had unresolved partials), the channel at the center frequency of the stimulus gave the largest modulation depth [the open square on the right of panel (f), Fig. 4]. When applying the AM detection model in the hybrid model, the optimal threshold values for the 5- and the 10-Hz modulation rates were found to be 45% and 25%, respectively. These values are in good agreement with thresholds found by Lee and Bacon (1997). For a 10-Hz rate and a 200-ms stimulus duration they found a threshold of 30%. Viemeister (1979) found similar but slightly smaller values. In the ''gated carrier'' condition of Viemeister, stimuli had a total duration of 250 ms. For 4-, 8-, and 16-Hz rates he found detection thresholds for m of approximately 0.2, 0.11, and 0.10, respectively. Interpolating between these values for rates of 5 and 10 Hz, we would find m-values of 0.18 and 0.11, which would correspond to depths of 30% and 20%, respectively.

3. The beating detector

A detailed description of the beating detector model is given as the ''temporal model'' by Lyzenga and Horst (1997). As with the AM detection model, it is based on changes in the temporal envelope of the stimuli. However, the limiting case for the AM detection model is a 100% modulation depth, whereas within-channel beating represents a depth of 200%. For such a depth the envelope does not touch down to zero at a shallow angle, but it cuts through zero at a steep angle, producing a sharp turning in its absolute value [see Fig. 3, panel (d)]. Therefore, the beating detector is based on the sharpness of the zero crossings in the temporal envelope. This sharpness depends strongly on the relative levels of the unresolved partials of a stimulus. So, for the present stimuli with unresolved components, the 5-Hz center frequency modulation may produce a cue in fluctuations of roughness or beating. In short the model works as follows: the stimuli are filtered with a simulated auditory filter bank consisting of Roex filters with a Q of 5, and an exponential-phase relation as shown in Fig. 8 of Lyzenga and Horst (1997). In the channel at the center frequency of the stimulus, the Hilbert transform is used to calculate the temporal envelope, after which its second-order derivative is calculated. When sharp zero crossings are present in the temporal envelope, peaks can be found in the second-order derivative of the reference tone. When a large peak is present, the center frequency modulation range is located for which this peak is reduced to a certain fraction of its original value. The corresponding modulation range is then taken as the expected FMT. This model has been adapted for application in the present study, where the sharpness of the zero crossings in the stimuli is a quantity that changes over time. It now uses the average sharpness of the zero crossings (i.e., the average peak values in the second-order derivative). The optimal threshold was found to be a reduction of the average peak to 15% of its original value (a 33% threshold used by Lyzenga and Horst, 1997).

[1]Various higher-order interactions were also significant but are omitted from the discussion in the interests of brevity and clarity. These were: region $\times F_0$ similarity$\times$signal F_0 ($p<0.02$), region$\times$slope$\times$formant position ($p<0.02$), F_0 similarity$\times$signal $F_0\times$formant position ($p<0.03$), region $\times F_0$ similarity$\times$slope$\times$signal F_0 ($p<0.01$), region$\times F_0$ similarity$\times$slope $\times$formant position ($p<0.05$), region$\times$slope$\times$signal $F_0\times$formant position ($p<0.03$).

[2]In the present study, the modulation rates differ for signals and maskers, as signals are modulated with a 5-Hz rate, and maskers with a 10-Hz rate. However, in a preliminary study (as mentioned in Sec. I A) we found that these modulation rates had only a minor effect on FMDI.

[3]Note that this explanation implies that, although listeners are very poor at detecting moderate differences between the fundamentals of resolved and unresolved groups of harmonics (Carlyon and Shackleton, 1994), they are able to detect the threefold differences used here.

Bacon, S. P., and Konrad, D. L. (**1993**). ''Modulation detection interference under conditions favoring within- or across-channel processing,'' J. Acoust. Soc. Am. **93**, 1012–1022.

Bacon, S. P., and Moore, B. C. J. (**1993**). ''Modulation detection interference, some special effects,'' J. Acoust. Soc. Am. **93**, 3442–3453.

Bacon, S. P., and Opie, J. M. (**1994**). ''Monotic and dichotic modulation detection interference in practiced and unpracticed subjects,'' J. Acoust. Soc. Am. **95**, 2637–2641.

Bacon, S. P., Moore, B. C. J., Shailer, M. J., and Jorasz, U. (**1995**). ''Effects of combining maskers in modulation detection interference,'' J. Acoust. Soc. Am. **97**, 1847–1853.

Carlyon, R. P. (**1994**). ''Further evidence against an across-frequency mechanism specific to the detection of frequency modulation (FM) incoherence between resolved frequency components,'' J. Acoust. Soc. Am. **95**, 949–961.

Carlyon, R. P. (**1998**). ''Comments on 'A unitary model of pitch perception' [J. Acoust. Soc. Am. **102**, 1811–1820],'' J. Acoust. Soc. Am. **104**, 1118–1121.

Carlyon, R. P., and Shackleton, T. M. (**1994**). ''Comparing the fundamental frequencies of resolved and unresolved harmonics: Evidence for two pitch mechanisms?,'' J. Acoust. Soc. Am. **95**, 3541–3554.

Dau, T., Kollmeier, B., and Kohlrausch, A. (**1997a**). ''Modeling auditory processing of amplitude modulation. I. Detection and masking with narrow-band carriers,'' J. Acoust. Soc. Am. **102**, 2892–2905.

Dau, T., Kollmeier, B., and Kohlrausch, A. (**1997b**). ''Modeling auditory processing of amplitude modulation. II. Spectral and temporal integration,'' J. Acoust. Soc. Am. **102**, 2906–2919.

Edwards, B. W., and Viemeister, N. F. (**1994**). ''Frequency modulation versus amplitude modulation discrimination: Evidence for a second frequency modulation encoding mechanism,'' J. Acoust. Soc. Am. **96**, 733–740.

Fletcher, H. (**1953**). *Speech and Hearing in Communication*. The ASA Edition, 1995, edited by J. B. Allen (ASA, New York), pp. 60–61.

Glasberg, B. R., and Moore, B. C. J. (1990) ''Derivation of auditory filter shapes from notched-noise data,'' J. Speech Hear. Res. **47**, 103–138.

Hall, W. H., and Grose, J. H. (**1991**). ''Some effects of auditory grouping factors on modulation detection interference (MDI),'' J. Acoust. Soc. Am. **90**, 3028–3035.

Hawks, J. W. (**1994**). ''Difference limens for formant patterns of vowel sounds,'' J. Acoust. Soc. Am. **95**, 1074–1084.

Kewley-Port, D., and Watson, C. S. (**1994**). ''Formant-frequency discrimination for isolated English vowels,'' J. Acoust. Soc. Am. **95**, 485–496.

Lee, J., and Bacon, S. P. (**1997**). ''Amplitude modulation depth discrimination of a sinusoidal carrier: Effect of stimulus duration,'' J. Acoust. Soc. Am. **101**, 3688–3693.

Lyzenga, J., and Horst, J. W. (**1995**). ''Frequency discrimination of band-limited harmonic complexes related to vowel formants,'' J. Acoust. Soc. Am. **98**, 1943–1955.

Lyzenga, J., and Horst, J. W. (**1997**). ''Frequency discrimination of stylized synthetic vowels with a single formant,'' J. Acoust. Soc. Am. **102**, 1755–1767.

Lyzenga, J., and Horst, J. W. (**1998**). ''Frequency discrimination of stylized synthetic vowels with two formants,'' J. Acoust. Soc. Am. **104**, 2956–2966.

Meddis, R., and O'Mard, L. (**1997**). ''A unitary model of pitch perception,'' J. Acoust. Soc. Am. **102**, 1811–1820.

Mendoza, L., Hall, W. H., and Grose, J. H. (**1995**). ''Within- and across-channel processes in modulation detection interference,'' J. Acoust. Soc. Am. **97**, 3072–3079.
Mermelstein, P. (**1978**). ''Difference limens for formant frequencies of steady-state and consonant-bound vowels,'' J. Acoust. Soc. Am. **63**, 572–580.
Moore, B. C. J. (**1973**). ''Frequency difference limens for short-duration tones,'' J. Acoust. Soc. Am. **54**, 610–619.
Moore, B. C. J., and Sek, A. (**1992**). ''Detection of combined frequency and amplitude modulation,'' J. Acoust. Soc. Am. **92**, 3119–3131.
Moore, B. C. J., and Shailer, M. J. (**1992**). ''Modulation discrimination interference and auditory grouping,'' Philos. Trans. R. Soc. London, Ser. B **336**, 339–346.
Moore, B. C. J., and Sek, A. (**1994**). ''Effects of carrier frequency and background noise on the detection of mixed modulation,'' J. Acoust. Soc. Am. **96**, 741–751.
Moore, B. C. J., Glasberg, B. R., Gaunt, T., and Child, T. (**1991**). ''Across-channel masking of changes in modulation depth for amplitude- and frequency-modulated signals,'' Q. J. Exp. Psychol. **43A**, 327–347.
Patterson, R. D., and Moore, B. C. J. (**1986**). ''Auditory filters and excitation patterns as representations of frequency resolution,'' in *Frequency Selectivity in Hearing*, edited by B. C. J. Moore (Academic, London), pp. 123–177.
Peterson, G. E., and Barney, H. L. (**1952**). ''Control methods used in a study of the vowels,'' J. Acoust. Soc. Am. **24**, 175–184.
Plack, C. J., and Carlyon, R. P. (**1994**). ''The detection of differences in the depth of frequency modulation,'' J. Acoust. Soc. Am. **96**, 115–125.
Scharf, B. (**1970**). ''Critical bands,'' in *Foundation of Modern Auditory theory*, edited by J. V. Tobias (Academic, New York), Vol. 1, pp. 159–202.
Shackleton, T. M., and Carlyon, R. P. (**1994**). ''The role of resolved and unresolved harmonics in pitch perception and frequency modulation discrimination,'' J. Acoust. Soc. Am. **95**, 3529–3540.
Strickland, E. A., and Viemeister, N. F. (**1996**). ''Cues for discrimination of envelopes,'' J. Acoust. Soc. Am. **99**, 3638–3646.
Strickland, E. A., and Viemeister, N. F. (**1997**). ''The effects of frequency region and bandwidth on the temporal modulation transfer function,'' J. Acoust. Soc. Am. **102**, 1799–1810.
Yost, W. A., and Sheft, S. (**1989**). ''Across-critical-band processing of amplitude-modulated tones,'' J. Acoust. Soc. Am. **85**, 848–857.
Yost, W. A., Sheft, S., and Opie, J. (**1989**). ''Modulation interference in detection and discrimination of amplitude modulation,'' J. Acoust. Soc. Am. **86**, 2138–2147.
Viemeister, N. F. (**1979**). ''Temporal modulation transfer functions based upon modulation thresholds,'' J. Acoust. Soc. Am. **66**, 1364–1380.

A binaural analog of gap detection

Michael A. Akeroyd[a] and A. Quentin Summerfield
MRC Institute of Hearing Research, University Park, Nottingham NG7 2RD, United Kingdom

(Received 6 March 1997; revised 29 September 1998; accepted 18 February 1999)

The temporal resolution of the binaural auditory system was measured using a binaural analog of gap detection. A binaural ''gap'' was defined as a burst of interaurally uncorrelated noise (*Nu*) placed between two bursts of interaurally correlated noise ($N0$). The *Nu* burst creates a dip in the output of a binaural temporal window integrating interaural correlation, analogous to the dip created by a silent gap in the output of a monaural temporal window integrating intensity. The equivalent rectangular duration (ERD) of the binaural window was used as an index of binaural temporal resolution. In order to derive the ERD, both the shortest-detectable binaural gap and the jnd for a reduction in interaural correlation from unity were measured. In experiment 1, binaural-gap thresholds were measured using narrow-band noise carriers as a function of center frequency from 250 to 2000 Hz (fixed 100-Hz bandwidth) and as a function of lower-cutoff frequency from 100 to 400 Hz (fixed 500-Hz upper-cutoff frequency). Binaural-gap thresholds (1) increased significantly with increasing frequency in both tasks, and (2) at frequencies below 500 Hz, were shorter than corresponding silent-gap thresholds measured with the same $N0$ noises. In experiment 2, interaural-correlation jnd's were measured for the same conditions. The jnd's also increased significantly with increasing frequency. The results were analyzed using a temporal window integrating the output of a computational model of binaural processing. The ERD of the window varied widely across listeners, with a mean value of 140 ms, and did not significantly depend on frequency. This duration is about an order of magnitude longer than the ERD of the monaural temporal window and is, therefore, consistent with ''binaural sluggishness.'' © *1999 Acoustical Society of America.* [S0001-4966(99)04605-6]

PACS numbers: 43.66.Pn, 43.66.Mk, 43.66.Ba [RHD]

INTRODUCTION

An important step in describing the performance of the human auditory system is to measure its temporal response to time-varying changes in acoustic parameters. Previous research has indicated that the binaural response to changes in interaural time delay or interaural correlation is more gradual than the monaural response to changes in intensity. The results can be understood by assuming that the changes are detected at the output of a smoothing device or temporal ''window.'' We report below a method for measuring the temporal response of the binaural auditory system. It is based on a temporal-window analysis of a binaural analog of gap detection.

The measurement of the shortest silent gap which listeners can detect in a sound is one of a number of methods for assessing the monaural auditory response to changes in intensity (e.g., Plomp, 1964; Penner, 1975; Moore *et al.*, 1993; Snell *et al.*, 1994). Others include detection of masked signals (e.g., Moore *et al.*, 1988), detection of amplitude modulation (e.g., Viemeister, 1979; Akeroyd and Patterson, 1997), and discrimination of time-reversed stimuli (e.g., Ronken, 1970; Akeroyd and Patterson, 1995); see also the reviews by Viemeister and Plack (1993) and Eddins and Green (1995). The results show that the auditory system does not respond abruptly to an abrupt change in intensity; instead, it responds gradually, as though the change in the internal representation of intensity were smoothed. This process can be modeled by convolving the stimulus with a temporal window, often implemented as a leaky integrator. Listeners' decisions are then based on the resulting smoothed waveform (e.g., Plomp, 1964; Jeffress, 1967; Penner, 1975; Viemeister, 1979; Moore *et al.*, 1988). The temporal resolution of the system is measured by the effective duration of the window or leaky integrator: the longer the duration, the worse the temporal resolution.

The action of the window is illustrated in Fig. 1, which shows a noise with a central, silent gap, and the corresponding output of the window. The window smoothes the gap into a dip. The depth of the dip depends upon the durations of both the gap and the window: the shorter the window or the longer the gap, the greater the depth of the dip. The detectability of the gap is determined by the detectability of the dip, so that performance is limited in part by intensity resolution (Penner, 1975; Green, 1985; Buus and Florentine, 1985). Thus, the duration of the shortest-detectable gap is determined both by intensity resolution and by the duration of the window.

Several experimental methods have been employed to measure the auditory response to time-varying changes in binaural parameters. In one class of methods, the task is to detect changes in interaural configuration; for example, to detect the modulation of interaural time differences, interaural intensity differences, or interaural correlation (Blauert, 1972; Grantham and Wightman, 1978; Grantham, 1982, 1984; Bernstein and Trahiotis, 1992). In a second class of methods, the task is to detect a signal in the presence of a

[a]Electronic mail: michael.akeroyd@ihr.mrc.ac.uk

 0001-4966/99/105(5)/2807/14/$15.00

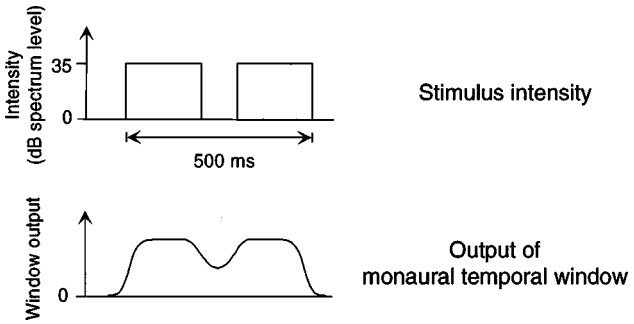

FIG. 1. Schematic illustration of the output of the monaural temporal window for a silent-gap stimulus.

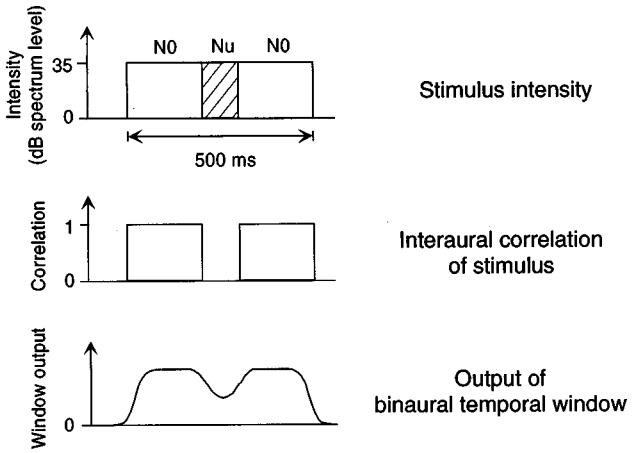

FIG. 2. Schematic illustration of the output of the binaural temporal window for a binaural-gap stimulus.

masker whose interaural configuration varies with time. Detection has been measured as a function of masker duration (e.g., McFadden, 1966; Robinson and Trahiotis, 1972; Trahiotis *et al.*, 1972; Kohlrausch, 1986), of masker envelope (Grantham and Wightman, 1978, 1979; Holube *et al.*, 1998), and of signal envelope (Grantham and Luethke, 1988), as well as under conditions of forward or backward masking (Lakey, 1976; Yost and Walton, 1977; Yost, 1985; Kollmeier and Gilkey, 1990; Gilkey *et al.*, 1990; Yama, 1992; Holube *et al.*, 1998), and of combined forward-and-backward masking (Shackleton and Bowsher, 1989; Culling and Summerfield, 1998).

These experiments have shown that the binaural auditory system is unable to respond abruptly to an abrupt change in interaural timing or correlation. Instead, the system responds gradually, as though the interaural change were smoothed; moreover, when compared with the monaural response to a change in intensity, the binaural response is more gradual. This effect was termed ''binaural sluggishness'' by Grantham and Wightman (1978), and later described by Grantham (1995, p. 307) as ''the relative difficulty subjects have in detecting or discriminating dynamic changes in interaural differences.'' One demonstration of binaural sluggishness was reported by Kollmeier and Gilkey (1990), who measured the detectability of a brief 500-Hz signal simultaneously masked by a broadband noise. The signal was placed after an abrupt change in either the interaural correlation or intensity of the masker. In both conditions, the detectability of the signal improved as the separation between it and the abrupt change increased, but the rate of improvement was significantly more gradual in the binaural condition than in the monaural condition.

Just like the monaural temporal response, the binaural temporal response has been modeled as the running convolution of a window with the stimulus. Binaural sluggishness is then reflected in the binaural window being longer than the corresponding monaural window. For example, at a signal frequency of 500 Hz and a masker spectrum level of 50 dB SPL, Moore *et al.* (1988) measured a monaural window with an equivalent rectangular duration (ERD) of 27 ms.[1] At the same frequency and masker intensity and using an analogous method, Culling and Summerfield (1998) measured a binaural window with an ERD of 97 ms.

Culling and Summerfield (1998) assumed that the binaural window generated a weighted running average of interaural correlation (cf. Grantham and Wightman, 1979; Grantham, 1982; Kollmeier and Gilkey, 1990; Holube *et al.*, 1998). The interaural correlation of a stimulus is the correlation between the waveform presented to the left ear and the waveform presented to the right ear after one waveform has been time shifted to maximize the correlation (Grantham, 1995). If the two waveforms of a noise stimulus are identical, then the noise (denoted ''*N*0,'' because the interaural phase difference is 0 radians) has an interaural correlation of unity, but if the two waveforms are statistically independent, then the noise (denoted ''*Nu*,'' because the noise is uncorrelated) has an interaural correlation of zero. The apparent width of the intracranial image of the stimulus depends upon its interaural correlation: an *N*0 stimulus is perceived as compact and at the center of the head, whereas an *Nu* stimulus is perceived as diffuse, across the head (Gabriel and Colburn, 1981; Grantham, 1995).

In the present method, a ''gap'' in interaural correlation is created by placing an *Nu* burst between two *N*0 bursts. The interaural correlation thus varies from 1 to 0 and back to 1 (Fig. 2). The listener's task is to detect the gap. By analogy with monaural gap detection, the shortest binaural gap that can be detected could be one measure of the temporal response of the binaural system to changes in interaural correlation. We define the temporal *resolution* of the system, however, to be measured by the ERD of the binaural temporal window. It can be calculated from the binaural-gap thresholds, provided that the just-noticeable-difference (jnd) for interaural correlation is known. The binaural gap is smoothed by the window into a dip in its output, shallower in depth than the original gap but broader in time (Fig. 2). If it is assumed that the detectability of the binaural gap is limited by the detectability of the dip, then performance in the binaural-gap detection task must be limited both by the jnd for departures in interaural correlation from unity and by the characteristics of the window.

In consequence, the temporal-window theory predicts that the binaural-gap threshold is only indirectly related to temporal resolution. If measurements of the binaural-gap threshold and the jnd are used to estimate the ERD of the binaural window, then it is expected that the resulting values

should be similar to those measured by other methods (e.g., Culling and Summerfield, 1998). One motivation for the present experiments was to confirm this expectation.

A particular reason for using the binaural-gap task is its conceptual simplicity, in contrast with some tasks used previously in studies of binaural temporal resolution. For example, in Culling and Summerfield's (1998) method, listeners had to detect a brief tonal signal that was presented, interaurally out-of-phase, against a masker noise whose interaural correlation varied from 0.0 (*Nu*) to 1.0 ($N0$) to 0.0 (*Nu*). A two-interval paradigm was used, with the noise presented in both intervals but the signal presented in only one interval. This detection task is a difficult one, since the signal generates a small change in interaural correlation amidst the large changes—in *both* intervals—in interaural correlation due to the masker. In contrast, in the binaural-gap method there is only one change—the binaural gap itself—present in either interval.

A further motivation for the present experiments was to examine the dependency of binaural temporal resolution on frequency, for the reasons explained below.

A. The effect of frequency on binaural temporal resolution

Three previous studies have compared binaural temporal resolution across frequency (Grantham and Wightman, 1979; Grantham, 1982; Culling and Summerfield, 1998). All three showed that temporal resolution depends upon frequency—with temporal resolution generally being worst at the lowest frequency tested—but the detailed pattern of the results varies across studies.

Grantham and Wightman (1979) measured the binaural detection of a brief $S\pi$ signal, at 250, 500, or 1000 Hz, masked by a narrow-band (0.6-octave) noise whose interaural correlation was sinusoidally modulated between 1.0 and -1.0. Their measure of temporal resolution was the time constant of an exponential-shaped window, calculated from the binaural unmasking at the instant when the noise had an interaural correlation of 1.0. They reported that the mean time constant at 250 Hz (170 ms) was consistently longer than that at 500 Hz (74 ms) for all three listeners tested. The mean time constant at 1000 Hz was 130 ms but, because the values were inconsistent amongst listeners, Grantham and Wightman did not draw any conclusions as to the size of the time constant at 1000 Hz in comparison to 500 Hz.

Grantham (1982) measured the detection of sinusoidal modulations in the interaural correlation of a narrow-band (0.4-octave) noise centered on 500, 1000, 2000, or 4000 Hz. He did not report quantitative measures of temporal resolution, but its dependence on frequency can be estimated by comparing the rate-of-change of performance with modulation frequency at the different center frequencies. The rate-of-change was steeper at 500 Hz than at the higher frequencies, indicating that binaural temporal resolution was worse at 500 Hz than at the higher frequencies.

Culling and Summerfield (1998) measured the binaural detection of a brief $S\pi$ tone, at 125, 250, 500, or 1000 Hz, placed in the center of a broadband masker noise constructed by inserting an $N0$ burst between two *Nu* bursts. Their measure of temporal resolution was the ERD of a Gaussian-shaped temporal window, calculated from the rate-of-change of binaural unmasking with the duration of the $N0$ burst. They reported that the ERD was longest at 250 Hz (160 ms), being shorter at both 500 Hz (110 ms) and 1000 Hz (86 ms). The results were inconclusive at 125 Hz: the ERD was 130 ms, but only two of the three listeners completed the threshold measurements.

B. Experimental conditions

Although the results of the three studies discussed above are not fully consistent, they generate the hypothesis that binaural temporal resolution improves as frequency increases. This hypothesis is tested in this paper by measuring temporal resolution at center frequencies ranging from 250 Hz to 2 kHz using noise carriers with a fixed bandwidth of 100 Hz. These conditions are referred to as ''center frequency'' (CF) conditions.

A further set of conditions was included in which temporal resolution was measured using noise carriers below 500 Hz with a range of bandwidths. These conditions were included for two reasons. First, at 250 Hz in the center-frequency conditions, the mean binaural gap threshold was found to be shorter than the minimal detectable silent gap in an $N0$ noise. We wanted to check that this result would replicate. Second, we wanted to establish whether the binaural-gap task or the jnd task generated any evidence of ''nonoptimal'' analysis of the sort identified by Gabriel and Colburn (1981) and Jain *et al.* (1991). Their studies demonstrated that jnd's for a departure of interaural correlation from unity could be smaller for narrow-band noises than for broadband noises embracing the frequency range of the narrow-band noises. This result implies that listeners may fail to attend to the frequency region in a broadband signal where jnd's are smallest, or may base decisions after aggregating evidence over frequency regions where interaural correlation is represented with differing degrees of precision. We examined this idea by establishing whether performance with a broadband stimulus was poorer than the best performance achieved with a narrow range of frequencies contained in the broadband stimulus.

In summary, experiment 1 measured the shortest binaural gap that listeners could detect in noises of different center frequency or bandwidth. Experiment 2 measured the jnd for departures of interaural correlation from unity for the same listeners and at the same center frequencies and bandwidths. In Sec. III, the ERD of the binaural window is derived using two related models of binaural processing.

I. EXPERIMENT 1: BINAURAL-GAP THRESHOLDS

Listeners were required to detect an *Nu* segment introduced into a burst of $N0$ noise (Fig. 2). Both the *Nu* segment and the $N0$ burst had identical levels and spectral characteristics. The *Nu* segment can be detected only from binaural cues, and so it is termed a ''binaural gap.'' In a control task, listeners were required to detect a silent gap introduced into an $N0$ burst (Fig. 1). Although this stimulus was presented diotically, the silent gap need not be detected using binaural

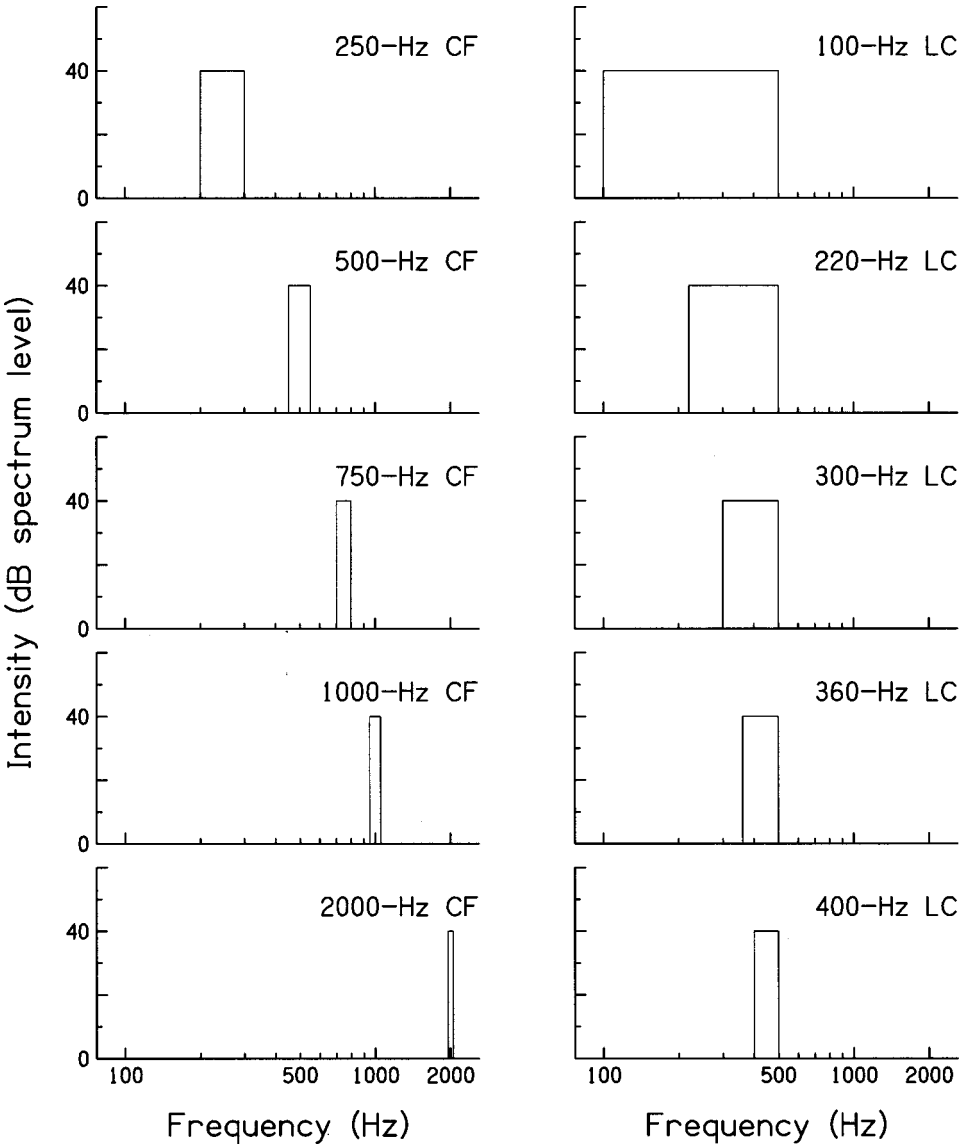

FIG. 3. Schematic illustration of the CF conditions (left column) and LC conditions (right column).

cues, and so is termed a ''monaural gap.'' In both tasks, the experimental measure was the duration of the shortest-detectable gap.

In a first test of the effect of frequency on binaural temporal resolution, the center frequency of a narrow-band noise was increased from 250 to 2000 Hz, using a constant absolute bandwidth of 100 Hz [center frequency (CF) conditions: Fig. 3, left column]. In a second test, the lower-cutoff frequency of a narrow-band noise was raised from 100 to 400 Hz, while keeping the upper-cutoff frequency fixed at 500 Hz [''lower cutoff'' (LC) conditions: Fig. 3, right column]. Consequently, in both tests the center frequency of the stimuli was varied. Note that there was an associated change in the bandwidth of the stimuli in the second test.

A. Method

The stimuli were bandpass Gaussian noises constructed digitally at a sampling rate of 20 kHz with 16-bit amplitude quantization. The binaural-gap stimuli were constructed by replacing the central part of an $N0$ noise with the central part of an *Nu* noise. The silent-gap stimuli were constructed by replacing the central part of an $N0$ noise with silence. Each noise was chosen at random from a set of 200 $N0$ and 200 *Nu* noises, generated using the Box–Muller algorithm (Press *et al.*, 1992). A new set was generated for each day of testing. The onset and offset of the silent gap were rectangular. All the stimuli had an overall duration of 500 ms, including 20-ms raised-cosine amplitude envelopes applied digitally to the onset and the offset. The stimuli were converted to analog by a Loughborough Sound Images digital-to-analog converter (AM/D16DS), passed through a custom-built attenuator and an amplifier, and presented to listeners over both channels of a Sennheiser HD-414 headset. Listeners sat in a double-walled sound booth. The stimuli were presented at a spectrum level of 40 dB SPL.

In the CF conditions, the stimuli had a fixed bandwidth of 100 Hz and a center frequency of either 250, 500, 750, 1000, or 2000 Hz (Fig. 3, left column). In the LC conditions, the stimuli had a fixed upper-cutoff frequency of 500 Hz and a bandwidth of either 100, 140, 200, 280, or 400 Hz; thus, the lower-cutoff frequency was either 400, 360, 300, 220, or 100 Hz (Fig. 3, right column). The stimuli were filtered with a 296-point digital bandpass filter approximating a rectangu-

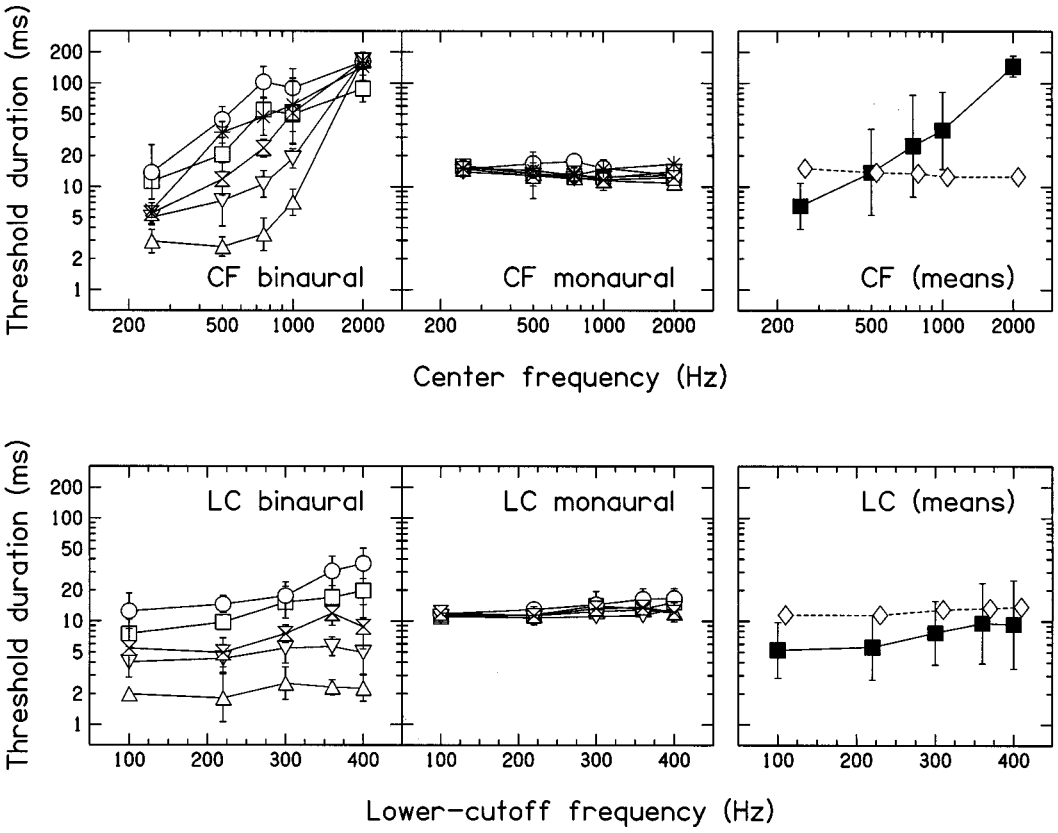

FIG. 4. Results of experiment 1: binaural-gap thresholds (left column) and monaural-gap thresholds (middle column), for the CF conditions (top row) and LC conditions (bottom row). The left and middle columns show results for individual listeners: A (squares), B (circles), C (upward-pointing triangles), D (downward-pointing triangles), E (double triangles), and F (asterisks). The error bars show the within-listener standard deviations. The right column shows the mean binaural-gap thresholds (solid squares) and mean monaural-gap thresholds (diamonds), averaged across listener. The error bars show the across-listener standard deviations.

lar frequency response; the filter attenuation was about 10 dB at frequencies 50 Hz away from the −3-dB cutoff frequencies and about 50 dB at frequencies 150 Hz away. Since each stimulus was filtered after any binaural or monaural gap was introduced, there were no spectral artefacts due to energy splatter outside the passband. Pilot tests confirmed that the binaural-gap task could not be performed monaurally.

Gap thresholds were measured using a two-interval, two-alternative forced-choice task and a three-down, one-up adaptive method, estimating the 79.4%-point on the psychometric function (Levitt, 1971). The gap duration was decreased by a factor of 2 per adaptive step until the first incorrect response; subsequently, the gap duration was increased or decreased by a factor of 1.414 per adaptive step. The initial gap durations were 200 ms (binaural task) and 50 ms (monaural task). Each adaptive staircase continued for 15 reversals. The midpoints of the 6 up-reversal/down-reversal pairs defined by the last 12 reversals were measured. Their geometric mean was defined as the gap threshold. Correct/incorrect feedback was provided visually. Stimulus timing and presentation, together with response collection and feedback, were controlled by a Dell 486 personal computer. Each threshold was the average of five adaptive runs. Two criteria were used to reject unreliable gap thresholds. First, runs were rejected, and replaced by an extra run, if the standard deviation of the six mid-run estimates was larger than 1.5 adaptive steps. Approximately 14% of the binaural adaptive runs and 0.5% of the monaural adaptive runs were affected in this way. Second, approximately 1% of the monaural adaptive runs were terminated because listeners were unable to detect reliably the longest gap tested (200 ms); these runs were marked with a threshold value of 200 ms.

Six listeners participated. Listener A was the first author. The remaining listeners were paid for their participation. Five of the six listeners had audiometric thresholds within normal limits at octave frequencies from 250 to 4000 Hz inclusive; listener B had a hearing level at 500 Hz of 30 dB in the left ear and 20 dB in the right ear. All listeners participated in at least 60 practice adaptive runs before the data reported below were collected. Listener F participated in the CF conditions but not the LC conditions.

B. Results

The results are shown in Fig. 4. The left and middle columns show the individual binaural-gap thresholds (left) and monaural-gap thresholds (middle). The two rows show the CF conditions (top) and LC conditions (bottom). The right column shows the across-listener mean thresholds.

In the CF conditions, the mean binaural-gap threshold increased from 6.5 to 35 ms as the center frequency was increased from 250 to 1000 Hz [$F(4,20)=25.2$, $p<0.001$]. Performance was worst at 2000 Hz. Monaural-gap thresholds did not change significantly as the center frequency was in-

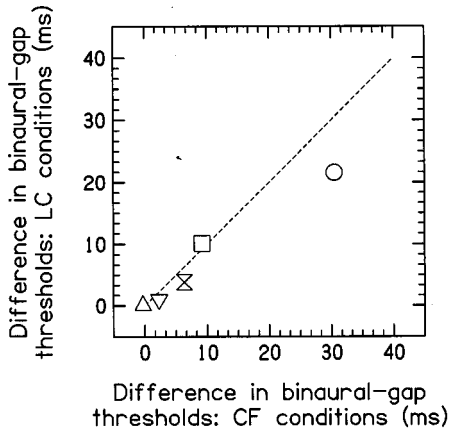

FIG. 5. Comparison of the change in binaural-gap thresholds across conditions. The difference in threshold between the 100-Hz and 400-Hz low-pass-cutoff frequency (LC) conditions is plotted as a function of the difference in threshold between the 250-Hz and 500-Hz center-frequency (CF) conditions. Each data point shows the comparison for one listener using the same symbols as in Fig. 4. The dashed line shows a 1:1 relationship between the differences.

creased: the mean thresholds at 250 and 2000 Hz were, respectively, 15.1 and 12.6 ms [$F(4,20)=2.45$, $p=0.08$].

In the LC conditions, the mean binaural-gap threshold increased from 5.3 to 9.3 ms as the lower-cutoff frequency was raised from 100 to 400 Hz [$F(4,16)=10.1$, $p<0.001$]. The monaural-gap thresholds showed a similar effect, with the mean thresholds increasing from 12 to 14 ms [$F(4,16)=7.12$, $p=0.002$].

C. Discussion

Binaural-gap thresholds have not been measured previously, and so there are no existing results with which to the compare the present data. Monaural gap thresholds have been measured in many studies, with which the present results are compatible. For example, Eddins *et al.* (1992) reported gap thresholds of approximately 20 ms for 100-Hz bandwidth stimuli centered at 600 and 2200 Hz.

The binaural-gap thresholds were not significantly worse in the 220-Hz LC condition (i.e., a 220–500-Hz bandpass noise) than in the closest-matched CF condition, 250 Hz (i.e., a 200–300-Hz bandpass noise): the mean values were, respectively, 6.5 and 5.6 ms [$t(4)=1.6$, $p>0.1$]. This result suggests that in the LC conditions, listeners were able to attend to the frequency region permitting the best performance—the lowest frequencies—without interference from higher frequencies. Figure 5 shows that the threshold change as the center frequency was increased from 250 to 500 Hz was similar to the threshold change as the lower-cutoff frequency was raised from 220 to 400 Hz [$r=0.98$, $t(3)=8.2$, $p=0.004$]. Together, the results imply that the change in performance across the LC conditions is probably due to the change in frequency instead of the associated change in bandwidth.

Individual differences in gap thresholds were appreciable in the binaural tasks, but negligible in the monaural tasks. The differences were quantified as the coefficient-of-variation: the across-listener standard deviation divided by the across-listener mean. The mean values for the binaural tasks were 0.83 (CF conditions) and 0.76 (LC conditions), compared with values for the monaural tasks of 0.11 (CF conditions) and 0.12 (LC conditions). Listeners were, however, consistent across binaural tasks, in that those who performed well in the CF conditions also performed well in the LC conditions.

In the CF conditions, the binaural-gap thresholds were smaller than the monaural-gap thresholds at frequencies below 500 Hz. This result was replicated in the LC conditions. Thus, at low frequencies, the results apparently run counter to the idea that the binaural system is sluggish relative to the monaural system. As mentioned in the Introduction, however, binaural sluggishness should be reflected in the relative temporal acuities; i.e., the relative durations of the monaural and binaural temporal windows. The aim of experiment 2 was to measure the jnd for interaural correlation so that the ERD of the binaural temporal window could be calculated.

II. EXPERIMENT 2: INTERAURAL-CORRELATION JND

A. Method

In experiment 2, we measured the jnd for a reduction in interaural correlation from unity for the same listeners and conditions of center frequency and bandwidth as in experiment 1 (cf. Pollack and Trittipoe, 1959a, b; Gabriel and Colburn, 1981; Koehnke *et al.*, 1986; Jain *et al.*, 1991; Gabriel *et al.*, 1992; Koehnke *et al.*, 1995).

The stimuli were bandpass noises of 500-ms duration, with a fixed value of the interaural correlation ρ. They were generated using a digital implementation of Licklider and Dzendolet's (1948) three-noise method (see also Jeffress and Robinson, 1962). The left channel of each stimulus was made by adding one noise to a second noise in a power ratio of $(\rho):(1-\rho)$. The right channel of each stimulus was made by adding the first noise to a third noise in a power ratio of $(\rho):(1-\rho)$. Each noise was chosen, at random without replacement, from a set of 400 noises, digitally generated using the Box–Muller algorithm at a sampling rate of 20 kHz (Press *et al.*, 1992). A new set was generated for each day of testing. The overall levels of the left and right channels were the same. The remainder of the apparatus and the stimulus parameters were the same as those in experiment 1.

Jnd's were measured using a two-interval, two-alternative forced-choice task and a three-down, one-up adaptive method, estimating the 79.4%-point on the psychometric function (Levitt, 1971). The adaptive steps were defined on a dB scale of equivalent signal-to-noise ratio for an $S\pi$ signal placed in an $N0$ masker (Durlach *et al.*, 1986)

$$\text{equivalent signal to noise ratio in dB} = \text{SNR} = 10\log\frac{\Delta\rho}{2-\Delta\rho}, \tag{1}$$

$$\therefore \text{ change in interaural correlation} = \Delta\rho = 2\left(\frac{10^{\text{SNR}/10}}{1+10^{\text{SNR}/10}}\right). \tag{2}$$

The adaptive procedure started at an SNR of -10 dB, corresponding to an interaural correlation of 0.818 and therefore

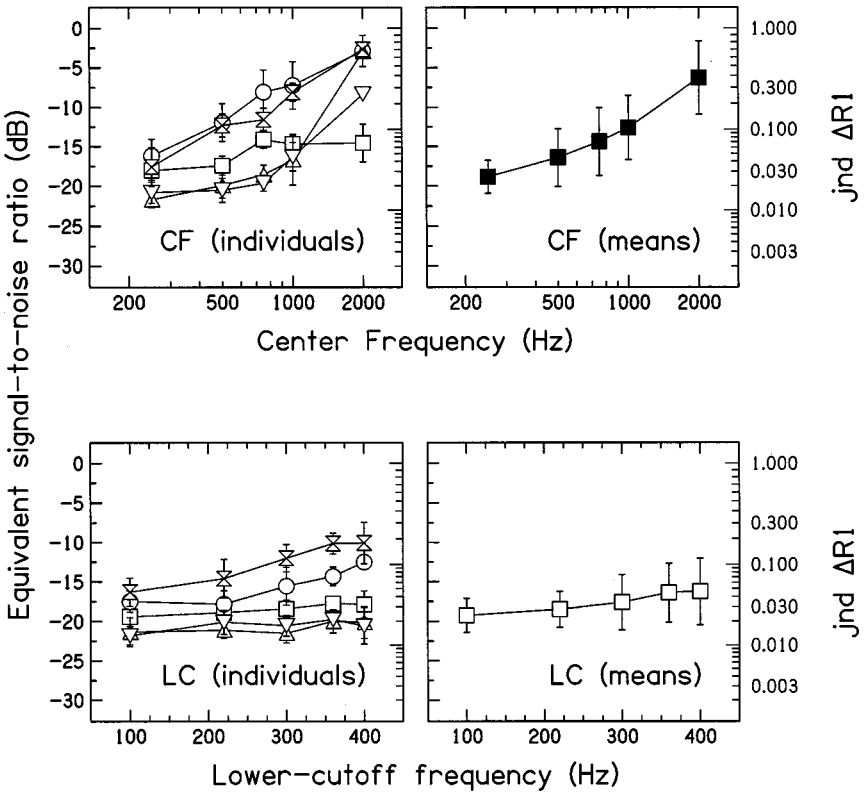

FIG. 6. Results of experiment 2: interaural-correlation jnd's for the CF conditions (top row) and LC conditions (middle row). The left column shows the individual results using the same symbols as in Fig. 4. The error bars show the within-listener standard deviations. The right column shows the mean jnd's. The error bars show the across-listener standard deviations.

a $\Delta\rho$ of 0.182. Each adaptive step before the first reversal was equal to a change in SNR of 4 dB, and each adaptive step after the first reversal was equal to a change in SNR of 2 dB. Each adaptive staircase continued for 15 reversals. The jnd was defined as the mean of the midpoints of the 6 up-reversal/down-reversal pairs defined by the last 12 reversals.

Each jnd is the average of five adaptive runs. Runs were rejected, and replaced with a new run, if the standard deviation of the six mid-run estimates was larger than 3 dB. Approximately 12% of the adaptive runs were rejected in this way. Listeners A–E participated.

B. Results

The results are shown in Fig. 6. The jnd's from individual listeners are plotted in the left column for the CF conditions (top row) and LC conditions (bottom row). The across-listener mean jnd's are plotted in the right column.

In the CF conditions, the mean jnd increased from 0.026 to 0.38 as the center frequency was increased from 250 to 2000 Hz [$F(4,16)=15.6$, $p<0.001$]. In the LC conditions, the mean jnd increased from 0.023 to 0.047 as the lower-cutoff frequency was raised from 100 to 400 Hz [$F(4,16)=6.27$, $p=0.003$].

C. Discussion

The jnd was smallest at lower frequencies. This trend has been observed before in studies using 1/3-octave-wide noises (Koehnke *et al.*, 1986, 1995; Gabriel *et al.*, 1992). Koehnke *et al.* (1986) tested performance at 500 and 4000 Hz, and reported that the jnd increased from 0.02 at 500 Hz to 0.09 at 4000 Hz. Koehnke *et al.* (1995) reported jnd's of approximately 0.01 and 0.05 for the same pair of frequencies. Gabriel *et al.* (1992) tested performance at 250, 500, 1000, 2000, and 4000 Hz in two listeners, and reported that the jnd increased from approximately 0.01 at 500 Hz to approximately 0.03 at 2000 Hz. The latter value is considerably smaller than the present value (0.38), although for the best listener the jnd was 0.07. This difference may be due to the difference in stimuli bandwidths (1/3-octave versus 100 Hz). It may also be due to individual differences amongst listeners, in that the range in measurements of the jnd can be considerable: Koehnke *et al.* (1986) reported ranges of 0.006–0.075 at 500 Hz and 0.014–0.394 at 4000 Hz.

Gabriel *et al.* (1992) also found that the jnd at 500 Hz was smaller than the jnd at 250 Hz. We observed the opposite result with both the CF and LC conditions. In the CF conditions, the jnd increased from 0.026 to 0.046 as the frequency was increased from 250 to 500 Hz. In the most-closely matched LC conditions, the jnd increased from 0.028 to 0.047 as the lower-cutoff frequency was raised from 220 to 400 Hz. Since the jnd's were not significantly worse in the 220-Hz LC condition than in the 250-Hz CF condition [$t(4)=0.43$, $p>0.1$], the change in performance in the LC conditions is probably due to the change in frequency rather than the associated change in bandwidth. This result is analogous to that found for the binaural-gap thresholds (Sec. I C), and, as there, indicates that listeners were able to attend to the frequency region permitting best performance. Furthermore, Fig. 7 shows that if a large change in jnd was observed for a listener as the center frequency was increased from 250 to 500 Hz, then in general, a large change was also observed in the same listener as the lower-cutoff frequency was raised from 220 to 400 Hz [$r=0.94$, $t(3)=4.8$, $p=0.02$] (cf. Fig. 5).

The coefficients-of-variation for the CF and LC condi-

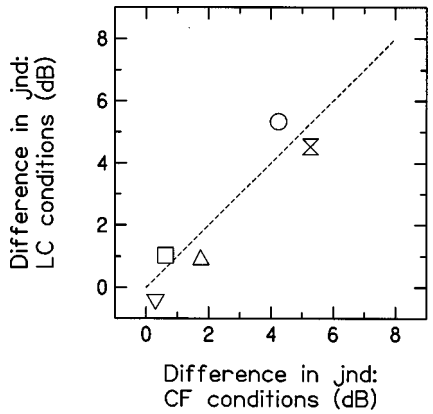

FIG. 7. Comparison of the change in jnd across conditions. The difference in jnd between the 100-Hz and 400-Hz low-pass-cutoff frequency (LC) conditions is plotted as a function of the difference in thresholds between the 250-Hz and 500-Hz center-frequency (CF) conditions. Each data point shows the comparison for one listener using the same symbols as in Fig. 4. The dashed line shows a 1:1 relationship between the differences.

tions were, respectively, 0.80 and 0.83. These values are similar to those obtained for the binaural-gap thresholds (Sec. I C), indicating that the individual differences in jnd's were approximately equal to those in binaural-gap thresholds. The listeners did, however, perform consistently in both tasks, in that those who performed well in the CF conditions also performed well in the LC conditions.

The purpose for measuring the jnd for interaural correlation was to allow the calculation of the ERD of the binaural temporal window. Both the binaural-gap threshold and the jnd for interaural correlation depend on frequency. Visually, the dependencies are similar (compare the left columns of Figs. 4 and 6). For the CF conditions, the correlation between the two measures was 0.94 [$t(23)=7.7$, $p<0.001$], although for the LC conditions, it was only 0.33 [$t(23)=1.67$, $p>0.1$]. This correspondence suggests that the ERD of the window may be independent of frequency, in that the dependence of binaural-gap threshold on frequency may be due to the dependence of jnd on frequency. This hypothesis is tested in the next section.

III. THE ERD OF THE BINAURAL TEMPORAL WINDOW

The ERD of the window was calculated using two related models (Fig. 8). The first model adopted the approach of Grantham and Wightman (1979), Kollmeier and Gilkey (1990), and Culling and Summerfield (1998), measuring interaural correlation directly on a stimulus waveform (''ρ_w'' model). The second model simulated the effects of spectral filtering, mechanical-to-neural transduction, and the progressive loss of phase-locking at high frequencies, measuring the internal interaural correlation of a stimulus (''ρ_I'' model).

In both models, the shape of the window must be assumed. We chose a Gaussian shape, following the comparison of exponential, rounded-exponential, and Gaussian shapes reported by Culling and Summerfield (1998). They

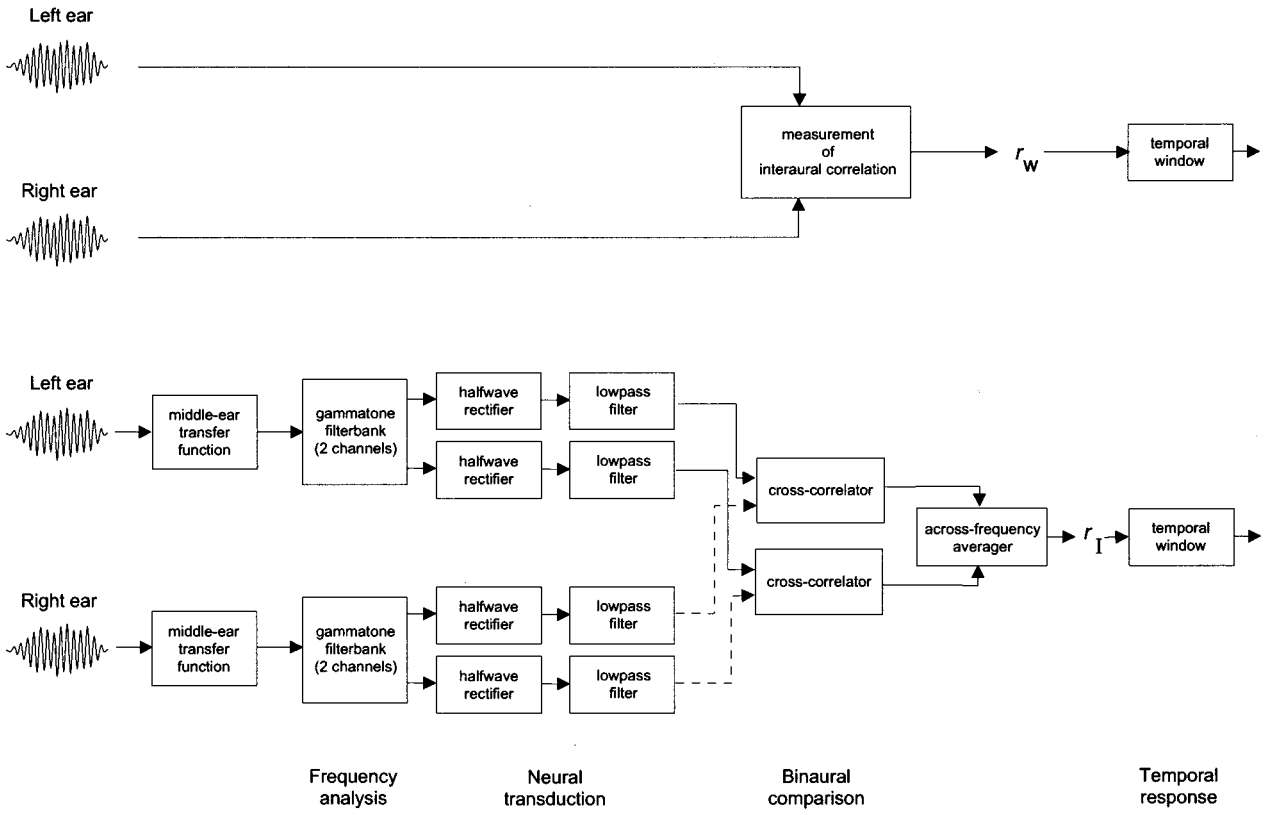

FIG. 8. Block diagrams of the ρ_w model (top panel) and the ρ_I model (bottom panel). A two-channel ρ_I model is illustrated. The number of channels used depended upon the bandwidth of the stimuli, varying between 1 and 8.

observed a slight temporal asymmetry of the window, with the duration of the forward lobe being approximately 3/5 of the duration of the backward lobe. The degree of asymmetry, however, varied considerably amongst listeners. For this reason, and also for analytic simplicity, we assumed that the window is symmetric.

A. The ρ_w model

1. Method

The ρ_w model assumes that a binaural gap is detected if the change in the output of the temporal window exceeds the jnd for a reduction in interaural correlation. The window is a Gaussian of ERD D and with a limitation on the dynamic range r (fixed at 0.000 001; i.e., -60 dB)

$$w(\tau)=(1-r)e^{(-\pi\tau^2)/D^2}+r, \tag{3}$$

where τ is time relative to the center of the window. The window generates a weighted running average of the instantaneous interaural correlation, $\rho_w(t)$, of the binaural stimulus. Its output $y(t)$ is given by

$$y(t)=\int_{-\infty}^{\infty} w(\tau)\rho_w(t-\tau)d\tau. \tag{4}$$

The value of ρ_w is, by definition, equal to 1.0 and 0.0, respectively, for $N0$ and Nu bursts. Its value for a $N0-Nu-N0$ binaural-gap stimulus changes from 1.0 to 0.0 and then to 1.0

$$\rho_w(t)=\begin{cases} 1 & -250\leqslant t<-\Delta t/2, \\ 0 & -\Delta t/2\leqslant t<\Delta t/2, \\ 1 & \Delta t/2\leqslant t<250, \end{cases} \tag{5}$$

where Δt is the duration of the Nu burst in milliseconds and the overall duration of the stimulus is 500 ms. The window smoothes this ''gap'' in ρ_w into a dip in its output. The size of the dip is defined as the window output as the center of the Nu burst measured relative to the window output for a static $N0$ burst

$$\text{size of dip}=\frac{\int_{-250}^{250} w(\tau)d\tau-\int_{-250}^{250} w(\tau)\rho_w(t-\tau)d\tau}{\int_{-250}^{250} w(\tau)d\tau}. \tag{6}$$

The detectability of the Nu burst is determined by the detectability of this dip. In particular, at binaural-gap threshold the size of the dip is assumed to be equal to the interaural-correlation jnd.

For each experimental combination of listener and stimulus condition, the ERD was found using Eqs. (4) and (6). In order to obtain an estimate of its experimental error, the process was repeated 1000 times, using binaural-gap thresholds and jnd's selected from Gaussian distributions based on the means and standard deviations equal to those measured experimentally for that combination of listener and stimulus condition.

2. Results

The results are shown in Fig. 9, for the CF conditions (top row) and LC conditions (bottom row). The individual ERDs are plotted in the left column. A minority of ERD estimates has been omitted because the model did not return a value (see below). The across-listener mean ERDs are plotted in the right column.

The binaural ERD did not depend significantly upon either CF condition or LC condition [respectively, $F(3,9)=0.47$; $p>0.1$, and $F(4,12)=0.053$, $p>0.1$]. The mean ERD, averaged across all conditions, was 210 ms.

3. Discussion

A mean ERD of 210 ms for the binaural temporal window is eight times longer than the ERD of the monaural window reported by Moore *et al.* (1988; Table AII; a subset of their measurements is plotted in the top-right panel of Fig. 9 as diamonds).[2] The results are therefore consistent with the effect of binaural sluggishness, validating the temporal-window analysis of the binaural-gap thresholds.

The ERD was independent of frequency, even though both experimental measures showed a significant dependency on frequency. This result differs from the previous measurements of the effect of frequency upon temporal resolution reviewed in the Introduction, which, in general, showed temporal resolution to improve as frequency is increased from 250 Hz (Grantham and Wightman, 1979; Grantham, 1982; Culling and Summerfield, 1998). Furthermore, the present ERD was generally longer than those measured previously. For example, at 500 Hz the mean ERD was 200 ms whereas Culling and Summerfield (1998) reported a value of 120 ms for the same frequency and spectrum level (40 dB SPL), although the large individual differences amongst listeners reduce the force of this comparison. One reason for developing the ρ_1 model was to attempt to resolve these two inconsistencies.

A number of ERD estimates are missing from Fig. 9. Five estimates—from the 2000-Hz CF condition—are missing because either the binaural-gap threshold or the jnd were within one adaptive step of the upper limits of the adaptive procedures (respectively, 200 ms or 1.0), and so the measurements may not be reliable. Six other estimates—all from listener A—are missing because the model could not calculate a value for the ERD. This problem is illustrated in Fig. 10. The lines show the relationship between the binaural-gap threshold (ordinate), the jnd (abscissa), and the ERD (parameter). The ERD was varied from 32 to 4096 ms in factors of 2. The lines converge as the ERD is increased above 1024 ms, and it is expected that the line for an ERD of infinity would be almost indistinguishable from the 2048-ms and 4096-ms lines. The symbols plot the individual experimental results. Although the majority is clustered near the 128-ms and 256-ms ERD lines, six are above the 1024-ms ERD line. These represent combinations of binaural-gap threshold and jnd which are incompatible with the model: either the binaural-gap threshold was too long for the corresponding jnd or the jnd was too small for the corresponding binaural-gap threshold. A second reason for developing the ρ_1 model was to overcome this problem.

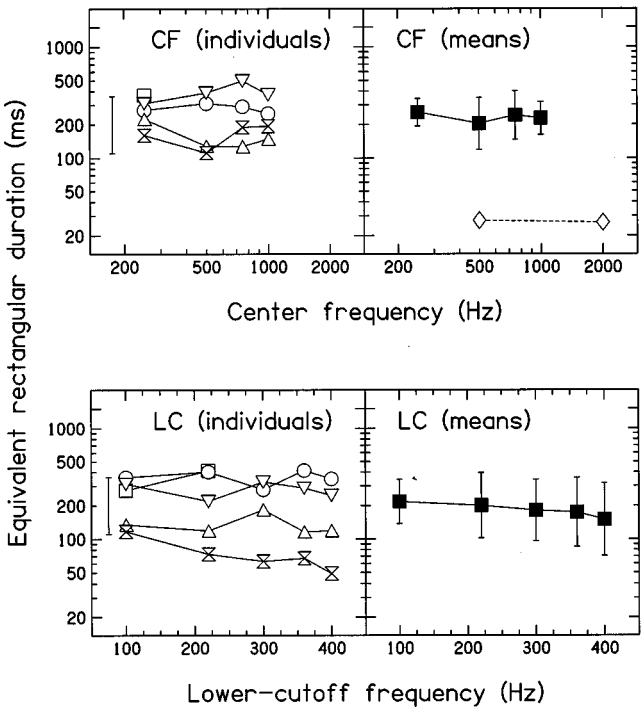

FIG. 9. Equivalent-rectangular durations (ERDs) of the binaural window calculated using the ρ_w model, for the CF conditions (top row) and LC conditions. The left column shows the individual results using the same symbols as in Fig. 4. The vertical lines at the far left show representative within-listener standard deviations of the ERDs. The right column shows the mean ERDs (solid squares). The error bars show the across-listener standard deviations. Monaural ERDs from Moore *et al.* (1988, Table AII) are also plotted (open diamonds).

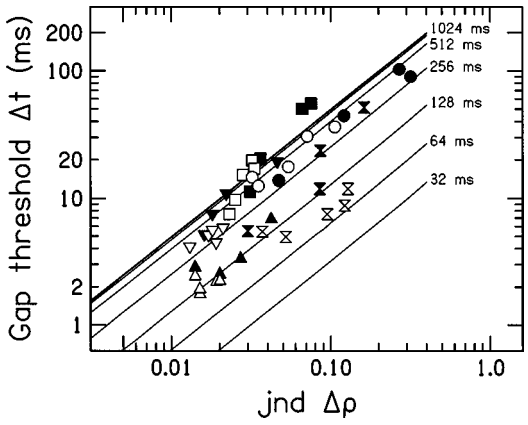

FIG. 10. The relationship between the jnd $\Delta\rho$ and the binaural-gap threshold Δt calculated using the ρ_w model. Each curve shows the relationship for a separate ERD: from bottom to top, 32, 64, 128, 256, 512, 1024, 2048, and 4096 ms. Note that the 2048 and 4096 ms curves lie on top of the 1024-ms curve. The data points show the individual experimental measurements for the CF conditions (solid symbols) and LC conditions (open symbols), using the same symbols as in Fig. 4. The 2000-Hz CF results are excluded, as explained in Sec. III A 3.

B. The ρ_I model

1. Method

The ρ_I model assumes that the binaural temporal window generates a running average of the instantaneous internal interaural correlation, $\rho_I(t)$, of the binaural stimulus. The method of calculating the ERD of the window is based on Eqs. (3)–(6) and is therefore identical to that used with the ρ_w model. The only exception is that all values of waveform interaural correlation ρ_w used in the calculations—both the value for an *Nu* burst and the value of the jnd—are transformed into values of internal interaural correlation ρ_I before the calculations are begun. A computational model of peripheral auditory processing is used to calculate the transformation. The model only includes auditory filters maximally excited by the stimulus. Since the bandwidth of the experimental stimuli varied, the number of frequency channels used in the model is varied accordingly. We describe first the single-channel model used for the CF conditions and then the multichannel model used for the LC conditions.

In the single-channel model, $\rho_I(t)$ is defined as the instantaneous output of a binaural analyzer which measures the instantaneous crossproduct of the output $L(t)$ of a single-frequency channel at the left ear with the output $R(t)$ of the corresponding frequency channel at the right ear, normalized by the mean energy:[3]

$$\rho_I(t) = \frac{L(t)R(t)}{0.5(L(t)^2 + R(t)^2)}. \tag{7}$$

The output of the frequency channel is a first-order approximation to the probability of spike discharge in a cochlear-nerve fiber. It is modeled as a gammatone filter followed by a half-wave rectifier and a first-order low-pass filter. A band-pass filter placed before the gammatone filter models the transfer function of the middle ear (Lutman and Martin, 1979). The frequency of the gammatone filter is equal to the center frequency of the CF condition. Its equivalent rectangular bandwidth (ERB) increases with frequency (Glasberg and Moore, 1990, Eq. (3); Patterson *et al.*, 1995). The half-wave rectifier reflects the fact that the inner-hair cells respond only to one direction of the movement of the organ of Corti (Rose *et al.*, 1971). The low-pass filter, with a −3-dB cutoff frequency of 800 Hz (Lindemann, 1986), models the reduction in phase locking at high center frequencies.

The ρ_w–ρ_I transformation is the second-order polynomial which best fits a set of measured values of ρ_I. The measurements were made at values of ρ_w from 0.00 to 1.00, in steps of 0.10 from 0.0 to 0.90, and in steps of 0.02 from 0.92 to 1.0. Each was based on the output of the binaural analyzer averaged across 250 independent examples of a 500-ms Gaussian noise. Individual ρ_w–ρ_I transformations are used for each CF condition (Fig. 11). The values of ρ_I for an *Nu* burst are equal to the *y*-axis intercept of the transformations: they increase with frequency, being 0.35, 0.40, 0.46, 0.52, and 0.67 for center frequencies of 250, 500, 750, 1000, and 2000 Hz. The value of ρ_I for an *N*0 burst is always equal to 1.0.[4]

In the multichannel model, several frequency channels were included, spaced at 1-ERB intervals across the nominal passband of each LC condition. The numbers of frequency channels were 2, 2, 3, 5, and 8 for the lower-cutoff frequencies of, respectively, 400, 360, 300, 220, and 100 Hz. Each frequency channel used the appropriate gammatone filter and had its own, independent, binaural analyzer. The outputs of each binaural analyzer were integrated across frequency to give a mean value of ρ_I (Fig. 8). Individual ρ_w–ρ_I transformations were again used for each condition. The transforma-

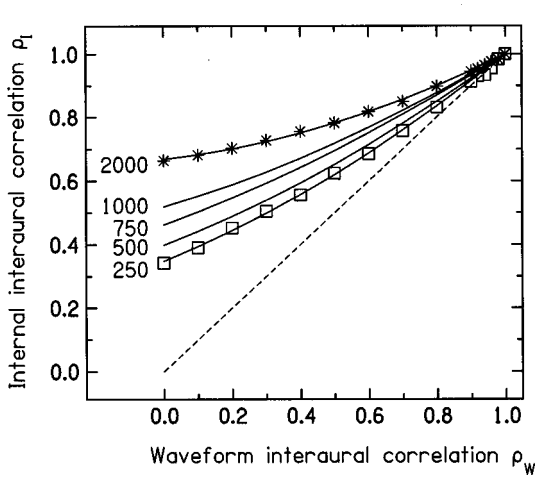

FIG. 11. The curves plot the ρ_I–ρ_w transformations for each of the five CF conditions (indicated in Hz). The symbols show the measured values for the 250-Hz (squares) and 2000-Hz (asterisks) conditions. The dashed line shows $\rho_I = \rho_w$.

tions were of the same form as those illustrated in Fig. 11, but differed in the values of ρ_I for an *Nu* stimulus. The values decreased marginally with reducing lower-cutoff frequency, being 0.39, 0.39, 0.39, 0.38, and 0.38 for lower-cutoff frequencies of 400, 360, 300, 220, and 100 Hz, respectively.

2. Results and discussion

The results are shown in Fig. 12. The format is the same as used in Fig. 9, with the addition that the mean ρ_w ERDs are also plotted (asterisks). As with the ρ_w model, the ERD

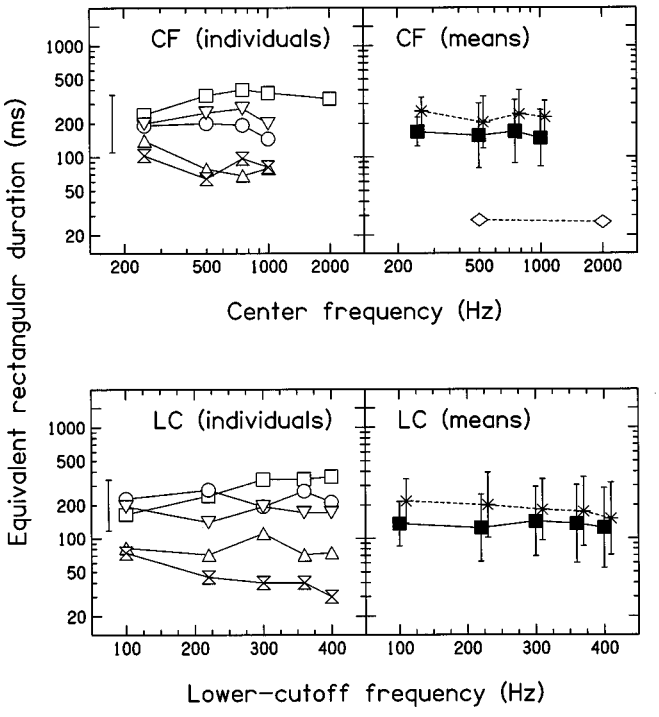

FIG. 12. Equivalent-rectangular durations (ERDs) of the binaural window calculated using the ρ_I model, for the CF conditions (top row) and LC conditions (bottom row). The format is the same as Fig. 9. In addition the mean ERDs from Fig. 12 are plotted in the right column (asterisks).

did not depend significantly upon either CF or LC condition [respectively, $F(3,12) = 0.57$, $p > 0.1$, and $F(4,16) = 0.11$, $p > 0.1$]. The mean ERD, averaged across all conditions, was 140 ms.

This value was considerably shorter than the ERD derived by the ρ_w model (210 ms), but is still consistent with the effect of binaural sluggishness. The ρ_I ERDs were shorter than the ρ_w ERDs for both stimulus conditions [CF: $F(1,3) = 22.7$; $p < 0.05$; LC: $F(1,3) = 10.6$, $p < 0.02$]. A second result was that all of the ρ_I ERDs were finite. The six individual conditions which were incompatible with the ρ_w model gave ρ_I ERDs between 200 and 400 ms.

C. Comparison of the two models

The ERDs calculated using the ρ_I model were significantly shorter than those calculated using the ρ_w model, by a factor of approximately 1.4. We attribute the difference in ERDs to the computational simulation of peripheral auditory processing, and in particular to the half-wave rectifier. Since its output can only contain positive half-cycles, the internal interaural correlation for an *Nu* burst must always be larger than zero, even though the interaural correlation of the left and right waveforms is zero. This effect leads to a corresponding change in the depth of the binaural gap defined by the *Nu* burst. In the ρ_w model, the gap's depth is 1.0, because the interaural correlations for *N*0 and *Nu* bursts are, respectively, 1.0 and 0.0. In the ρ_I model, the gap's depth depends upon the condition, but for the 500-Hz CF condition it is 0.60, because the interaural correlations are, respectively, 1.0 and 0.40 (the latter value is the *y*-intercept of the ρ_w–ρ_I transformations shown in Fig. 11). This reduction in depth leads to corresponding reductions in, first, the size of the dip in the output of the window and, second, the amount of smoothing required to reduce the dip to the size of the interaural-correlation jnd. A reduction in temporal smoothing corresponds to a decrease in window ERD, and so the ERDs calculated using the ρ_I model are shorter than the ERDs calculated using the ρ_w model.

The ρ_w model's direct access to the interaural correlation of the stimulus waveforms, without any intervening auditory filtering or neural transduction, is one reason for rejecting it in favor of the ρ_I model. Two other reasons are that the ERDs calculated with the ρ_w model, in general, differed more from previous measurements, and, for a subset of listeners and conditions, the ρ_w model was unable to calculate an ERD. We therefore prefer the ρ_I model.

IV. GENERAL DISCUSSION

The experiments and models reported in this paper tested a temporal-window theory of binaural temporal resolution. The results validated the theory, in that only the ERD of the binaural window–but not the binaural-gap threshold—was consistent with the effect of binaural sluggishness. For example, at 500 Hz the window ERD was 160 ms, considerably longer than both the monaural window (27 ms; Moore *et al.*, 1988) and the binaural-gap threshold (14 ms; Fig. 4).

This result indicates that temporal resolution should be measured indirectly as a temporal window rather than directly as a gap threshold.

A. The effect of frequency on binaural temporal resolution

We chose the experimental conditions in order to test if the binaural-gap task was sensitive to the dependence of binaural temporal resolution upon frequency. Three previous studies have measured this dependence (Grantham and Wightman, 1979; Grantham, 1982; Culling and Summerfield, 1998). They showed that the temporal resolution depends upon frequency, worst around 250 Hz and progressively better at higher or lower frequencies. In neither of our tests did we observe any significant effect of frequency. We did observe an effect on the binaural-gap thresholds themselves—they were smaller at lower frequencies—but the temporal-window theory showed that this effect was due to the across-frequency variation in the interaural-correlation jnd instead of any variation in the ERD.

The present results show that, in general, binaural temporal resolution does not vary with frequency. There are large individual differences amongst listeners, however: some listeners show evidence of an improvement in temporal resolution with frequency, while others show a worsening. The inconsistencies in previous results may reflect large individual differences, since those experiments have generally tested small numbers of listeners.

B. Multiple looks?

The present ERDs were close to previous estimates of the ERD of the binaural window, but were generally longer. Two other studies have calculated the ERD of Gaussian-shaped windows similar to those used here, reporting values of 84 ms (Kollmeier and Gilkey, 1990) and 120 ms (Culling and Summerfield, 1998) for a frequency of 500 Hz. At this frequency, we estimated a mean ERD of 160 ms using the ρ_I model, a factor of 1.3–1.9 larger. A possible explanation is that the ρ_I model excludes an analysis of multiple looks. In order to calculate the ERDs, we assumed that the size of the change in window output due to a just-detectable binaural gap was equal to the measured value of the interaural-correlation jnd. The assumption may not be valid, in that the measured jnd could be smaller than the change in window output. This effect would occur if listeners used a multiple-looks strategy to improve their performance in the jnd task, which may have occurred because the jnd-task stimuli were longer (at 500 ms) than most of the ERDs. For example, if two looks were possible, then the jnd would be smaller than the change in window output by a d' factor of 1.414. This value corresponds to a decrease of approximately 2 dB, when expressed as equivalent signal-to-noise ratio, or a factor of 1.5, when expressed as a correlation (Koehnke *et al.*, 1986). Inspection of Fig. 10 shows that this change in jnd leads to an increase in window ERD by a factor of approximately 1.5. In consequence, if listeners had used a two-look strategy, then the calculated ERD would be longer, by a factor of 1.5, than the true ERD. The similarity of this value to the difference between previous measurements of the ERD and those here suggests that the listeners may have used this strategy.

C. Individual differences

Although individual differences amongst the listeners are apparent in the ERDs, they were smaller than in either set of experimental data. The coefficient-of-variation quantifies these differences: the larger it is, the larger the individual differences. For the ρ_I-model, its mean value, averaged across all conditions, was 0.60, whereas for the binaural-gap threshold and for the interaural-correlation jnd, its mean values were, respectively, 0.80 and 0.81. In consequence, some of the individual differences in the experimental measurements are due to individual variations in binaural temporal resolution. Furthermore, since the coefficient-of-variation was far smaller in the monaural gap-detection task—a mean value of 0.11—the individual differences are primarily in binaural processing instead of any generic, ''overall,'' temporal processing.

V. SUMMARY

A binaural analog to gap detection was reported. A binaural gap is defined as an *Nu* burst placed between two *N*0 bursts. The binaural-gap threshold, in conjunction with the just-noticeable decrease in interaural correlation from a reference value of unity, was used to estimate the duration of the binaural temporal window.

(1) For a 100-Hz-wide noise, the binaural-gap threshold depends upon frequency. It ranges from 6 ms at 250 Hz to more than 100 ms at 2000 Hz. Below 500 Hz, it is shorter than the corresponding silent-gap threshold.
(2) For a 100-Hz-wide noise, the jnd for a reduction in interaural correlation from unity also depends upon frequency. It ranges from 0.03 at 250 Hz to more than 0.4 at 2000 Hz.
(3) The equivalent-rectangular duration (ERD) of the binaural temporal window is independent of frequency. The mean ERD is 140 ms. This value is almost an order of magnitude larger than the ERD of the monaural temporal window. It therefore reflects binaural sluggishness.
(4) The ERD is significantly longer when calculated using a model which excludes peripheral filtering, mechanical-to-neural transduction, and the loss of phase-locking at high frequencies.
(5) Individual differences amongst listeners are large. They are smaller when measured as ERDs than when measured as either binaural-gap thresholds or jnd's. Nonetheless, ERDs ranged across listeners from 50 ms to more than 300 ms.

ACKNOWLEDGMENTS

We thank John Culling, David McAlpine, Andrew Oxenham, Trevor Shackleton, Toby Dye (Associate Editor), and two anonymous reviewers for their helpful comments on previous versions of this paper.

[1]The equivalent rectangular duration of a window is the duration of a rectangular window with the same integral and maximum value (Moore *et al.*, 1988; Kollmeier and Gilkey, 1990, footnote 2). The reported window durations are the ERDs of Gaussian (T_p, r) windows. The reader of Moore *et al.* (1988) should note that there is an error in the published values of the ERDs of their Gaussian (T_p, r) and the Gaussian (T_p, w, T_s) windows. The correct values are equal to the reported values multiplied by $\sqrt{\pi}$.

[2]We were unable to calculate the duration of the monaural temporal window from the monaural gap thresholds using a similar, but monaural, model because we did not measure the jnd for differences in intensity. Nevertheless, since the monaural gap thresholds measured in experiment 1 were highly consistent amongst listeners and were close, although slightly smaller than, those measured previously for similar stimuli (e.g., Eddins *et al.*, 1992), we expected that the monaural-window durations would be similar to those reported before. Consequently, we used Moore *et al.*'s (1988) values of the duration of the monaural temporal window for the comparisons of monaural and binaural temporal resolution.

[3]If either $L(t)$ or $R(t)$ is equal to zero, then $\rho_1(t)$ is assumed to be zero.

[4]The second-order polynomial was constrained so that ρ_1 equaled 1.0 if ρ_w also equaled 1.0.

Akeroyd, M. A., and Patterson, R. D. (**1995**). ''Discrimination of wideband noises modulated by a temporally asymmetric function,'' J. Acoust. Soc. Am. **98**, 2466–2474.

Akeroyd, M. A., and Patterson, R. D. (**1997**). ''A comparison of detection and discrimination of temporal asymmetry in amplitude modulation,'' J. Acoust. Soc. Am. **101**, 430–439.

Bernstein, L. R., and Trahiotis, C. (**1992**). ''Detection of antiphasic sinusoids added to the envelopes of high-frequency bands of noise,'' Hearing Res. **62**, 157–165.

Blauert, J. (**1972**). ''On the lag of lateralization caused by interaural time and intensity differences,'' Audiology **11**, 265–270.

Buus S., and Florentine, M. (**1985**). ''Gap detection in normal and impaired listeners: The effect of level and frequency,'' in *Time Resolution in Auditory Systems*, edited by A. Michelson (Springer, Berlin).

Culling, J. C., and Summerfield, Q. (**1988**). ''Measurements of the binaural temporal window using a detection task,'' J. Acoust. Soc. Am. **103**, 3540–3553.

Durlach, N. I., Gabriel, K. J., Colburn, H. S., and Trahiotis, C. (**1986**). ''Interaural correlation discrimination: II. Relation to binaural unmasking,'' J. Acoust. Soc. Am. **79**, 1548–1557.

Eddins, D. A., and Green, D. M. (**1995**). ''Temporal integration and temporal resolution,'' in *Hearing*, edited by B. C. J. Moore (Academic, London).

Eddins, D. A., Hall, J. W., and Grose, J. H. (**1992**). ''The detection of temporal gaps as a function of frequency and absolute noise bandwidth,'' J. Acoust. Soc. Am. **91**, 1069–1077.

Gabriel, K. J., and Colburn, H. S. (**1981**). ''Interaural correlation discrimination: I. Bandwidth and level dependence,'' J. Acoust. Soc. Am. **69**, 1394–1401.

Gabriel, K. J., Koehnke, J., and Colburn, H. S. (**1992**). ''Frequency dependence of binaural performance in listeners with impaired binaural hearing,'' J. Acoust. Soc. Am. **91**, 336–347.

Gilkey, R. H., Simpson, B. D., and Weisenberger, J. M. (**1990**). ''Masker fringe and binaural detection,'' J. Acoust. Soc. Am. **88**, 1323–1332.

Glasberg, B. R., and Moore, B. C. J. (**1990**). ''Derivation of auditory filter shapes from notched-noise data,'' Hearing Res. **47**, 103–138.

Grantham, D. W. (**1982**). ''Detectability of time-varying interaural correlation in narrow-band noise stimuli,'' J. Acoust. Soc. Am. **72**, 1178–1184.

Grantham, D. W. (**1984**). ''Discrimination of dynamic interaural intensity differences,'' J. Acoust. Soc. Am. **76**, 71–76.

Grantham, D. W. (**1995**). ''Spatial hearing and related phenomena,'' in *Hearing*, edited by B. C. J. Moore (Academic, London).

Grantham, D. W., and Wightman, F. L. (**1978**). ''Detectability of varying interaural temporal difference,'' J. Acoust. Soc. Am. **63**, 511–523.

Grantham, D. W., and Wightman, F. L. (**1979**). ''Detectability of a pulsed tone in the presence of a masker with time-varying interaural correlation,'' J. Acoust. Soc. Am. **65**, 1509–1517.

Grantham, D. W., and Luethke, L. E. (**1988**). ''Detectability of tonal signals with changing interaural phase differences in noise,'' J. Acoust. Soc. Am. **83**, 1117–1123.

Green, D. M. (**1985**). ''Temporal factors in psychoacoustics,'' in *Time Resolution in Auditory Systems*, edited by A. Michelson (Springer, Berlin).

Holube, I., Kinkel, M., and Kollmeier, B. (**1998**). ''Binaural and monaural auditory filter bandwidths and time constants in probe-tone detection experiments,'' J. Acoust. Soc. Am. **104**, 2412–2425.

Jain, M., Gallagher, D. T., Koehnke, J., and Colburn, H. S. (**1991**). ''Fringed correlation discrimination and binaural detection,'' J. Acoust. Soc. Am. **90**, 1918–1926.

Jeffress, L. A. (**1967**). ''Stimulus-oriented approach to detection reexamined,'' J. Acoust. Soc. Am. **41**, 480–488.

Jeffress, L. A., and Robinson, D. E. (**1962**). ''Formulas for the coefficient of interaural correlation for noise,'' J. Acoust. Soc. Am. **34**, 1658–1659.

Koehnke, J., Colburn, H. S., and Durlach, N. I. (**1986**). ''Performance in several binaural-interaction experiments,'' J. Acoust. Soc. Am. **79**, 1558–1562.

Koehnke, J., Culotta, C. P., Hawley, M. L., and Colburn, H. S. (**1995**). ''Effects of reference interaural time and intensity differences on binaural performance in listeners with normal and impaired hearing,'' Ear Hear. **16**, 331–353.

Kohlrausch, A. (**1986**). ''The influence of signal duration, signal frequency, and masker duration on binaural masking-level differences,'' Hearing Res. **23**, 267–273.

Kollmeier, B., and Gilkey, R. H. (**1990**). ''Binaural forward and backward masking: Evidence for sluggishness in binaural detection,'' J. Acoust. Soc. Am. **87**, 1709–1719.

Lakey, J. R. (**1976**). ''Temporal masking-level differences: The effect of masker duration,'' J. Acoust. Soc. Am. **59**, 1434–1442.

Levitt, H. L. (**1971**). ''Transformed up–down methods in psychophysics,'' J. Acoust. Soc. Am. **49**, 467–477.

Licklider, J. C. R., and Dzendolet, E. (**1948**). ''Oscillographic scatterplots illustrating various degrees of correlation,'' Science **107**, 121–124.

Lindemann, W. (**1986**). ''Extension of a binaural cross-correlation model by contralateral inhibition. I. Simulation of lateralization for stationary signals,'' J. Acoust. Soc. Am. **80**, 1608–1622.

Lutman, M. E., and Martin, A. M. (**1979**). ''Development of an electroacoustic analogue model of the middle ear and acoustic reflex,'' J. Sound Vib. **64**, 133–157.

McFadden, D. (**1966**). ''Masking-level differences with continuous and with burst masking noise,'' J. Acoust. Soc. Am. **40**, 1414–1419.

Moore, B. C. J., Glasberg, B. R., Plack, C. J., and Biswas, A. K. (**1988**). ''The shape of the ear's temporal window,'' J. Acoust. Soc. Am. **83**, 1102–1116.

Moore, B. C. J., Peters, R. W., and Glasberg, B. R. (**1993**). ''Detection of temporal gaps in sinusoids: Effects of frequency and level,'' J. Acoust. Soc. Am. **93**, 1563–1570.

Patterson, R. D., Allerhand, M. H., and Giguère, C. (**1995**). ''Time-domain modeling of peripheral auditory processing: A model architecture and a software platform,'' J. Acoust. Soc. Am. **98**, 1890–1894.

Penner, M. J. (**1975**). ''Persistence and integration: Two consequences of a sliding integrators,'' Percept. Psychophys. **18**, 114–120 (erratum: Percept. Psychophys. **19**, 469–470).

Plomp, R. (**1964**). ''Rate of decay of auditory sensation,'' J. Acoust. Soc. Am. **36**, 277–282.

Pollack, I., and Trittipoe, W. J. (**1959a**). ''Binaural listening and interaural noise cross correlation,'' J. Acoust. Soc. Am. **31**, 1250–1252.

Pollack, I., and Trittipoe, W. J. (**1959b**). ''Interaural noise correlations: Examination of variables,'' J. Acoust. Soc. Am. **31**, 1616–1618.

Press, W. H., Flannery, B. P., Teukolsky, S. A., and Vetterling, W. T. (**1992**). *Numerical Recipes: The Art of Scientific Computing* (Cambridge University Press, Cambridge).

Robinson, D. E., and Trahiotis, C. (**1972**). ''Effects of signal duration and masker duration on detectability under diotic and dichotic listening situations,'' Percept. Psychophys. **12**, 333–334.

Ronken, D. A. (**1970**). ''Monaural detection of a phase difference between clicks,'' J. Acoust. Soc. Am. **47**, 1091–1099.

Rose, J. E., Hind, J. E., Anderson, D. J., and Brugge, J. F. (**1971**). ''Some effects of stimulus intensity on response of auditory nerve fibers in the squirrel monkey,'' J. Neurophysiol. **34**, 685–699.

Shackleton, T. M., and Bowsher, J. M. (**1989**). ''Binaural effects of the temporal variation of a masking noise upon the detection thresholds of tone pulses,'' Acustica **69**, 218–225.

Snell, K. B., Ison, J. R., and Frisina, D. R. (**1994**). ''The effects of signal frequency and absolute bandwidth on gap detection in noise,'' J. Acoust. Soc. Am. **96**, 1458–1464.

Trahiotis, C., Dolan, T. R., and Miller, T. H. (**1972**). ''Effect of backward masker fringe on the detectability of pulsed diotic and dichotic tonal signals,'' Percept. Psychophys. **12**, 335–338.

Viemeister, N. F. (**1979**). ''Temporal modulation transfer functions based upon modulation thresholds,'' J. Acoust. Soc. Am. **66**, 1364–1380.
Viemeister, N. F., and Plack, C. J. (**1993**). ''Time analysis,'' in *Human Psychophysics*, edited by W. A. Yost, A. N. Popper, and R. R. Fay (Springer, New York).
Yama, M. F. (**1992**). ''Effects of temporal separation and masker level on binaural analysis in forward masking,'' J. Acoust. Soc. Am. **91**, 327–335.
Yost, W. A. (**1985**). ''Prior stimulation and the masking-level difference,'' J. Acoust. Soc. Am. **78**, 901–907.
Yost, W. A., and Walton, J. (**1977**). ''Hierarchy of masking-level differences obtained for temporal masking,'' J. Acoust. Soc. Am. **61**, 1376–1379.

Sensitivity of human subjects to head-related transfer-function phase spectra

Abhijit Kulkarni,[a] S. K. Isabelle,[b] and H. S. Colburn
Hearing Research Center and Department of Biomedical Engineering, Boston University, 44 Cummington Street, Boston, Massachusetts 02215

(Received 13 July 1997; revised 28 January 1999; accepted 19 February 1999)

Head-related transfer functions (HRTFs) for human subjects in anechoic space were modeled with modified phase spectra, including minimum-phase-plus-delay, linear-phase, and reversed-phase-plus-delay functions. The overall (wide-band) interaural time delay (ITD) for the modeled HRTFs was made consistent with that of the empirical HRTFs by setting the position-dependent, frequency-independent delay in the HRTF for the lagging ear. Signal analysis of the minimum-phase-plus-delay reconstructions indicated that model HRTFs deviate from empirical HRTF measurements maximally for contralateral azimuths and low elevations. Subjects assessed the perceptual validity of the model HRTFs in a four-interval, two-alternative, forced-choice discrimination paradigm. Results indicate that monaural discrimination performance of subjects was at chance for all three types of HRTF models. Binaural discrimination performance was at chance for the linear-phase HRTFs, was above chance for some locations for the minimum-phase-plus-delay HRTFs, and was above chance for all tested locations for the reversed-phase-plus-delay HRTFs. An analysis of low-frequency timing information showed that all of these results are consistent with efficient use of interaural time differences in the low-frequency components of the stimulus waveforms. It is concluded that listeners are insensitive to HRTF phase spectra as long as the overall ITD of the low-frequency components does not provide a reliable cue. In particular, the minimum-phase-plus-delay approximation to the HRTF phase spectrum is an adequate approximation as long as the low-frequency ITD is appropriate. These results and conclusions are all limited to the anechoic case when the HRTFs correspond to brief impulse responses limited to a few milliseconds.
[S0001-4966(99)04505-1]

PACS numbers: 43.66.Pn, 43.66.Qp, 43.64.Ha [RHD]

INTRODUCTION

The head-related transfer function (HRTF) is the direction-dependent acoustical transfer function from a sound source to a listener's eardrum. This function, which encodes the acoustical cues involved in sound localization, is believed to be the major determinant of perceived source location. The exact nature of the localization cues encoded by the transfer function has been an active area of research. It is now generally believed that the interaural time difference (ITD) embodied by the interaural phase of the HRTFs is the principal determinant of source azimuth. Also, cues obtained from the spectral shape of the transfer function are considered to be the major determinants of source elevation (Middlebrooks and Green, 1991).

HRTFs, obtained from impulse responses in a listener's ear canal for different sound-source locations, have been used to implement virtual auditory displays (e.g., Wightman and Kistler, 1989a, b). These implementations involve the convolution of a sound stream with the measured impulse responses appropriate for a desired location and the presentation of the result to a listener over headphones. To the extent that the HRTFs have been accurately measured, based on the principle that acoustically equivalent stimuli would be perceived equivalently, stimuli processed in this manner should yield the perception of a real sound source that is localized in space at the position from which the HRTFs were measured. Such observations have been reported in literature (e.g., Wightman and Kistler, 1989b) and the use of virtual stimuli is becoming increasingly popular in both auditory psychophysical experiments (e.g, Wightman and Kistler, 1992) and experiments involving physiological preparations (e.g., Brugge *et al.*, 1994). With the advent of specialized digital hardware, starting with the Convolvotron from Crystal River Engineering (cf. Wenzel, 1992), sound stimuli processed through HRTFs are also being used in Virtual-Reality (VR) applications.

The HRTF is a complex-valued function of frequency; that is, at each frequency it represents both the the magnitude and phase shifts in the transformation of the sound-pressure waveform from source to eardrum. Most speculation of source-position coding by the HRTF has been generally restricted to analysis of features in the magnitude spectra of the HRTF, typically associating peaks and valleys in the spectra from a given position with localization judgments (e.g., Blauert, 1983; Butler and Belendiuk, 1977; Middlebrooks, 1992). Reports on the analysis of HRTF phase as it relates to source localization are sparse, with only a few relevant ex-

[a]Current address: Bose Corporation, MS 15D, The Mountain, Framingham, MA 01701.
[b]Current address: Signal Detection Lab, 437A Fawcet Hall, 3640 Col. Glenn Highway, Wright State University, Dayton, OH 45435.

periments. Wightman and Kistler (1992), in a recent study that systematically varied the phase and amplitude spectra in different frequency bands, demonstrated the dominant role of low-frequency interaural time information in judgments of azimuth. Among several interesting conclusions, it was shown that if low-frequency phase information was appropriately conveyed in the HRTF, randomizing the phase spectra in higher-frequency bands did not affect localization performance by subjects. In a different study, involving the modeling of the HRTFs using principal components analysis, Kistler and Wightman (1992) used a simplifying assumption for HRTF phase in constructing virtual stimuli, and reported localization performance by subjects comparable to that achieved using free-field stimuli. The specific model employed by Kistler and Wightman (1992) assumes that the measured HRTF is a minimum-phase sequence and assumes interaural time delay for a given position to be frequency independent. Previously, based on analysis of HRTFs measured from human subjects, Mehrgardt and Mellert (1977) had reported that HRTFs are very nearly minimum-phase sequences up to 10 kHz. Their study, however, did not offer any psychophysical validation.

The overall goal of this study was to investigate the sensitivity of human listeners to HRTF phase spectra for anechoic stimuli, subject to the constraint that the overall (wide-band), empirically measured interaural time delay (ITD) is maintained. (For each source position, the overall ITD is the delay corresponding to the maximum of the cross-correlation function of the left- and right-ear impulse responses.) The HRTF is represented by $H(e^{J\omega})$, the Fourier transform of the discrete-time impulse response for a source at a given location. This transfer function is generally characterized in terms of its magnitude spectrum $|H(e^{J\omega})|$ and its phase spectrum $\arg[H(e^{J\omega})]$. Attention is restricted to systems that are stable and causal. In this case $H(e^{J\omega})$ can be expressed as

$$H(e^{J\omega}) = H_{\min}(e^{J\omega}) H_{\mathrm{ap}}(e^{J\omega}), \tag{1}$$

where $H_{\min}(e^{J\omega})$ is a *minimum-phase* function and $H_{\mathrm{ap}}(e^{J\omega})$ is an *all-pass* function (Oppenheim and Schafer, 1989). Since the all-pass transfer function has a magnitude spectrum equal to unity for all values of ω and since, as we discuss below, the phase spectrum of the minimum-phase transfer function is completely determined by its *log*-magnitude spectrum, there are generally an infinite number of phase spectra that are compatible with a given magnitude spectrum, corresponding to the infinite number of possible all-pass transfer functions. This paper evaluates the sensitivity of the human auditory system to the phase spectrum when the magnitude spectrum is maintained equal to the original, measured magnitude spectrum. We consider three distinct cases, which are referred to as the minimum-phase-plus-delay case, the linear-phase case, and the reversed-phase-plus-delay case. In all cases, the interaural time delay for the overall transfer function, defined as the value of delay that maximizes the cross-correlation function of the left and right impulse responses for the given location, is maintained at the actual value by adding an appropriate delay to the left or right calculated response.

The minimum-phase-plus-delay case, which is the primary focus of the analysis and experiments, uses $H_{\min}(e^{J\omega})$ as defined above with a simple delay (i.e., a linear-phase function) added to maintain the interaural time delay at the value determined by the measured HRTFs. Thus $H_{\mathrm{ap}}(e^{J\omega})$ is just a pure delay $[H_{\mathrm{ap}}(e^{J\omega}) = e^{-J\omega\tau_{\mathrm{ap}}}]$, where the pure delay τ_{ap} is chosen to make the overall interaural time delay match the measured interaural time delay τ_e.

The linear-phase case, which has been used by McKinley and colleagues (e.g., McKinley and Ericson, 1997) in virtual-sound-field experiments, adds the measured interaural time delay τ_e to a zero-phase transfer function with the measured magnitude spectrum (corresponding to an impulse response that is symmetric around zero time and shifted to maintain causality), which implies a phase spectrum for the resulting transfer function that is a linear function of ω. This case incorporates the simplest phase spectrum compatible with the empirical ITD τ_e.

The reversed-phase-plus-delay case, which is chosen as an extreme variation in the fine structure of the phase spectrum while still maintaining the correct interaural time delay, corresponds to choosing a phase spectrum (before overall delay compensation) that has the opposite sign at each frequency than the empirical phase spectrum. This case corresponds to an impulse response that is reversed in time for each ear and then shifted to maintain the ITD.

The paper is organized in terms of these various phase models. In Sec. I, the minimum-phase-plus-delay model for the HRTF is described in more detail and compared to the measured HRTF. In Sec. II, experiments are reported in which human listeners tried to discriminate between the minimum-phase-plus-delay model HRTFs and the measured HRTFs for various situations. In Sec. III, similar experiments involving the linear-phase and reversed-phase-plus-delay cases are presented. The last section describes our conclusions.

I. MINIMUM-PHASE-PLUS-DELAY MODEL FOR HRTFs

A. Minimum-phase systems

A minimum-phase function is defined to be one whose *log*-magnitude spectrum and phase spectrum are Hilbert transforms of each other (Oppenheim and Schafer, 1989). More generally, a minimum-phase system is one for which the Fourier transform of the system impulse response is a minimum-phase function, and the impulse response of a minimum-phase system is called a minimum-phase impulse response or a minimum-phase sequence.

An all-pass transfer function is one in which the magnitude spectrum is constant for all frequencies ω. For our purposes, we assume that the constant is unity since any scale factor is incorporated into $H_{\min}(e^{J\omega})$ in Eq. (1). An all-pass system function thus passes all of the frequency components of its input with magnitude gain of unity. A pure time delay is an example of an all-pass system, albeit a special one such that there is no phase distortion and the waveform shape is preserved. More typical all-pass system functions are products of factors having the general form

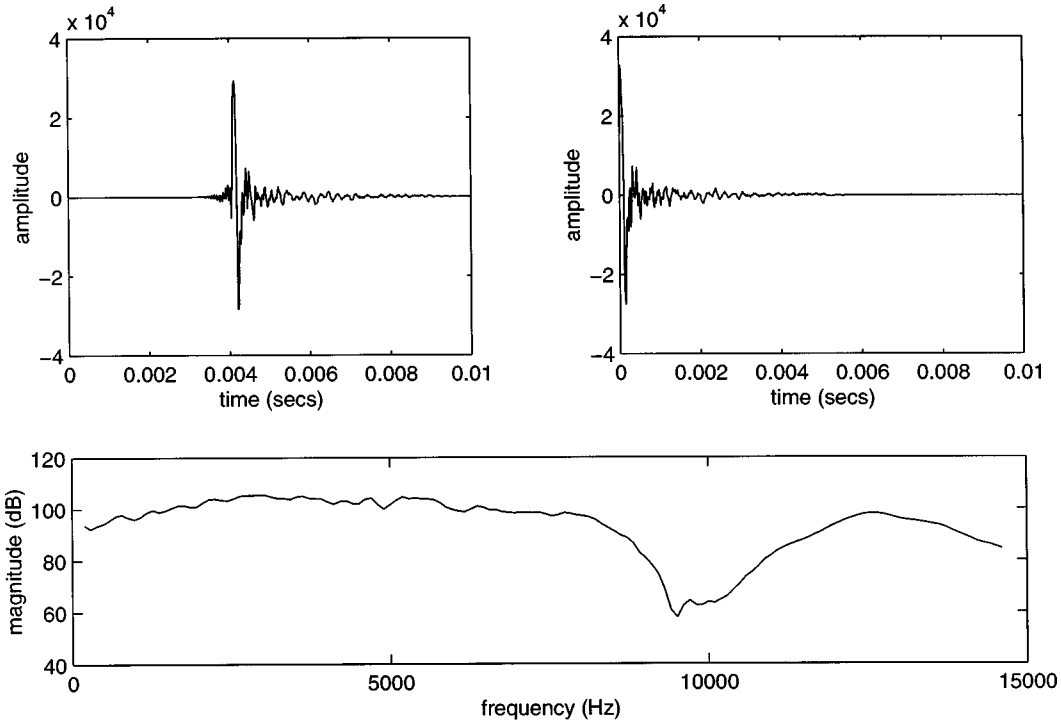

FIG. 1. Representative HRTF impulse response measured from a human listener in anechoic space (top-left panel) and its minimum-phase reconstruction (top-right panel). The magnitude spectrum for both impulse responses is identical and is shown in the bottom panel, plotted versus the frequency in Hz. Recall that this f is related to the ω in the discrete-time Fourier transform by $\omega = 2\pi f/f_s$, where f_s is the sampling frequency in Hz. (The sampling frequency was 50 kHz for the data shown here.)

$$H_{\text{ap}}(e^{J\omega}) = \frac{1 - a^* e^{J\omega}}{e^{J\omega} - a}, \tag{2}$$

where a and a^* are complex conjugates. It is easy to confirm that $|H_{\text{ap}}(e^{J\omega})| = 1$ for all ω in this case.

Minimum-phase and all-pass systems are usually described in terms of the more general z-transform representation of the system function (Oppenheim and Schafer, 1989). (The Fourier transform is equal to the z-transform evaluated for $z = e^{J\omega}$.) For the brief comments here, we restrict attention to z-transforms of rational transfer functions, which can be represented as ratios of polynomials in z and can be characterized by the locations of their poles (roots of the denominator polynomial) and zeros (roots of the numerator polynomial). In terms of poles and zeros, a stable and causal system must have all its poles inside the unit circle (where $|z| = 1$ and thus $z = J\omega$), but stability and causality place no restriction on the position of zeros. A minimum-phase system is a stable and causal system whose zeros (as well as poles) are all inside the unit circle. The zeros of the complete system function $H(z)$ that are not within the unit circle can be accounted for by an associated all-pass transfer function as in Eq. (1). Since an all-pass system must be comprised of conjugate-reciprocal poles and zeros, each of the zeros outside the unit circle must be matched by a conjugate-reciprocal pole within the unit circle (which is itself canceled by a zero of the minimum-phase function). Hence, in the z-transform version of Eq. (1) $[H(z) = H_{\text{min}}(z)H_{\text{ap}}(z)]$, $H_{\text{min}}(z)$ comprises the poles and zeros of $H(z)$ that lie inside the unit circle and additional zeros that are conjugate reciprocals of the zeros of $H(z)$ that lie outside the unit circle. The zeros of $H(z)$ which lie outside the unit circle, together with the poles needed to cancel the reflected conjugate-reciprocal zeros in $H_{\text{min}}(z)$, constitute $H_{\text{ap}}(z)$.

B. Computation of minimum-phase HRTF sequences

In this section, the minimum-phase-plus-delay model of the HRTF is described in the spirit of Mehrgardt and Mellert (1977) and Kistler and Wightman (1992).

The HRTF $H(e^{J\omega})$, which is the Fourier transform of the measured impulse response at the eardrum from a given source location, can be written as

$$H(e^{J\omega}) = |H(e^{J\omega})| e^{J\phi_{\text{min}}(\omega)} \times e^{J\phi_{\text{ap}}(\omega)}, \tag{3}$$

where $\phi_{\text{min}}(\omega)$ is the minimum-phase function corresponding to the magnitude spectrum $|H(e^{J\omega})|$ and $\phi_{\text{ap}}(\omega)$ is the residual all-pass phase function. Comparison of Eq. (1) and Eq. (3) yields

$$H_{\text{min}}(e^{J\omega}) = |H(e^{J\omega})| e^{J\phi_{\text{min}}(\omega)} \tag{4}$$

and

$$H_{\text{ap}}(e^{J\omega}) = e^{J\phi_{\text{ap}}(\omega)}. \tag{5}$$

The phase component $\phi_{\text{min}}(\omega)$ is related to the log-magnitude spectrum by the Hilbert transform (Oppenheim and Schafer, 1989). An empirical HRTF impulse response and its associated minimum-phase impulse response are shown in the upper two panels of Fig. 1. The common magnitude spectrum for the two responses is shown in the bottom panel of the figure (plotted in terms of the actual frequency, which is determined by the sampling frequency of the

discrete-time sequence). Note that the minimum-phase sequence is not merely the empirical impulse response shifted; significant differences between the two sequences may be observed on close inspection.

For the minimum-phase model of HRTFs, the all-pass phase function $\phi_{ap}(\omega)$ in Eq. (5) is modeled as a linear-phase term (i.e., a constant group delay); specifically,

$$H_{ap}(e^{J\omega}) = e^{-J\omega\tau_{ap}}, \tag{6}$$

where τ_{ap} is a position-dependent and frequency-independent delay. Thus the model impulse response is the time-shifted minimum-phase response, and the complete model of the HRTF $H(e^{J\omega})$ is determined by $|H(e^{J\omega})|$, with its associated minimum-phase function, and a single value of delay τ_{ap}. In order to synthesize binaural stimuli using minimum-phase constructed HRTFs, this delay is pre-computed and introduced in the waveform to the lagging ear to obtain appropriate overall interaural time differences.

This overall ITD between the approximated HRTFs should be consistent with the overall ITD obtained from the empirical HRTFs. An estimate of the overall empirical ITD for a given position, τ_e, may be obtained by computing the delay corresponding to the maximum in the cross-correlation function for the appropriate pair of left- and right-ear HRTFs. Or, equivalently, the mean group delay measured at each ear may be subtracted to obtain the estimate. Either computation estimates a delay embodying the contribution of the linear delays associated with both the minimum-phase and the all-pass components of the HRTF. Therefore, the linear delay arising from the minimum-phase components of the HRTFs needs to be calculated separately, and subtracted from the overall ITD to obtain the all-pass delay of interest. The linear-delay term associated with the minimum-phase component of the HRTFs has been ignored in previous studies (Kistler and Wightman, 1991) and we emphasize its importance in introducing an accurate estimate of overall ITD in the minimum-phase-plus-delay representation of HRTFs.

For the results shown here, delays are calculated from the cross-correlation functions for original and minimum-phase modeled HRTFs, by determining the time delay argument which maximize each of the functions. The cross-correlation functions were computed as the inverse Fourier transforms of the cross spectra:

$$\tau_e = \underset{\tau}{\arg\max}\ \mathcal{F}^{-1}[H_l(e^{J\omega})H_r^*(e^{J\omega})],$$
$$\tau_m = \underset{\tau}{\arg\max}\ \mathcal{F}^{-1}[H_{\min,l}(e^{J\omega})H_{\min,r}^*(e^{J\omega})], \tag{7}$$

where $H_l(e^{J\omega})$ and $H_r(e^{J\omega})$ are the left- and right-ear HRTFs for a given position and $H_{\min,l}(e^{J\omega})$ and $H_{\min,r}(e^{J\omega})$ are the left- and right-ear minimum-phase HRTFs for the same position. The appropriate all-pass delay is then given by

$$\tau_{ap} = \tau_e - \tau_m, \tag{8}$$

which is implemented as a positive delay and is applied to the appropriate ear signal to make the overall interaural delay appropriate.

C. HRTF data

HRTFs measured from two human subjects and from the KEMAR acoustical mannequin were analyzed. The human HRTF measurements were obtained from Dr. Fred Wightman at the University of Wisconsin. One data set corresponds to that from subject SDO in a previously published study (Wightman and Kistler, 1989a). The other data set (SOW), also obtained at the facility at the University of Wisconsin, is from one of the authors in this study (AK). HRTFs from the KEMAR mannequin were measured at the anechoic chamber at MIT (Kulkarni, 1993).

The SDO data set consists of 144 measurements from various source locations. Specifically, there are 6 elevation measurements (every 18 degrees from $+54$ to -36 degrees) at each of 24 azimuths (every 15 degrees starting a position directly behind the listener). The resulting impulse responses are 512-tap FIR filters at a sampling rate of 50 kHz. Details of the measurement protocol have been reported in Wightman and Kistler (1989a). The SOW data set consists of 505 measurements. There are 14 elevation measurements (every 10 degrees from $+80$ to -50 degrees) at each of 36 azimuths (every 10 degrees starting from a position directly behind the listener), plus a measurement from directly above ($+90$ degrees). The resulting impulse responses are 512-tap FIR filters measured at a sampling rate of 100 kHz. For the purposes of this study we downsampled these data, giving an equivalent 256-tap filter at 50 kHz and zero padded it to 512 taps. Data from the KEMAR mannequin correspond to 360 measurements obtained at a resolution of every 1 degree in the azimuthal plane starting from a position directly behind. The KEMAR impulse responses were measured using Golay code (Foster, 1986; Golay, 1961) techniques and resulted in 512-tap filters at a 50-kHz sample rate.

D. Methods

By construction, both the original measurements and the minimum-phase-plus-delay model impulse responses have the same magnitude spectra. To address the issue whether or not the original measurements are delayed minimum-phase sequences, we computed a measure of similarity between original and reconstructed impulse responses based on the normalized cross-correlation function $\rho_{xy}(n)$ for the waveforms. For two zero-mean, finite-energy, causal signals $x(k)$ and $y(k)$, this function is defined as:

$$\rho_{xy}(n) = \frac{\Sigma_{k=0}^{N} x(k)y(k+n)}{\sqrt{\Sigma_{k=0}^{N} x^2(k)\Sigma_{k=0}^{N} y^2(k)}}, \tag{9}$$

where N is large enough that both $x(k)$ and $y(k)$ are zero outside of the interval $[0,N]$. The formal index of similarity (or coherence) between two waveforms is defined as

$$c = \max_{n} |\rho_{xy}(n)|, \tag{10}$$

and any two waveforms for which $c=1$ will be called coherent. With this definition, two waveforms are coherent if they are identical, if they differ from each other by a frequency-independent amplitude factor or/and if they differ by a frequency-independent time delay. Departure of c from unity is a quantitative measure of the degree to which empirically measured HRTF sequences deviate from minimum-phase-plus-delay.

Phase spectra from empirical HRTF measurements were also analyzed to estimate the extent to which they fitted the description of a minimum-phase phase function and a constant frequency-independent delay term. Monaural all-pass phase functions were obtained from the empirical measurements by subtracting minimum-phase phase functions from empirical phase functions at each ear and deriving best-fit straight lines (in the least-squares sense) for the residual phase functions. The negative of the slope of the fitted line is the best least-squares estimate of the constant all-pass delay term in an HRTF phase function and the error in the fit is a measure of the departure from our minimum-phase-plus-delay assumption. The root-mean-square (rms) error in the straight line fits to the residual phase functions were calculated to obtain a quantitative measure of the mismatch. If the residual-phase function is denoted by $\phi_{\text{res}}(\omega)$ and the slope of the best-fitting straight line by τ_{est}, the rms error in the fit is expressed by the relation

$$\epsilon_{\text{rms}}=\frac{1}{\sqrt{\pi}}\left(\int_0^{\pi}(\phi_{\text{res}}(\omega)-\omega\tau_{\text{est}})^2\,d\omega\right)^{1/2}, \tag{11}$$

where the integral is computed over the frequency region of interest (π denoting the Nyquist frequency). Note that this is equivalent to, but simpler than, computing the rms deviation of the minimum-phase model phase function from the actual phase function.

A similar error analysis was carried out for interaural phase spectra arising from empirical HRTFs compared with those arising from the best minimum-phase-plus-delay HRTFs. For each HRTF pair, the interaural-phase spectra obtained from minimum-phase reconstructions of the originals were subtracted from the original HRTF phase spectra. The rms error in the best-fitting linear function for the interaural-phase spectra was calculated as above. The equation describing the interaural-phase rms error is identical in form to Eq. (11), where $\phi_{\text{res}}(\omega)$ would denote the empirically obtained interaural all-pass phase function and τ_{est} would be the slope of the best-fitting straight line.

Finally, we calculated the ITD for the minimum-phase response with no added delay, which is the value of τ_m as defined in Eq. (8) above.

E. Results and discussion

Because the total number of HRTFs analyzed is large (144 pairs of SDO functions, 505 pairs of SOW functions, and 360 pairs of KEMAR functions), we describe the results in terms of the summary measures described above. Specific details are presented for only a few representative cases. Also, results are presented only for the SDO and SOW data sets. The KEMAR data, which were restricted to the horizontal plane, were compatible with the presented results and are not shown here.

Coherence index values calculated for the SDO and SOW data sets are presented in Fig. 2. The graphs show values of the coherence index along the ordinate for different HRTF positions indexed along the abscissa. Recall that an index of 1 indicates complete coherence between waveforms. The top two panels are data for the SDO data set (left and right ear, respectively) while the bottom two panels are for the SOW data. Most positions for both data sets show a high coherence index. For the 144 HRTFs tested from the SDO data set, 92% of the left-ear HRTFs and 75% of the right-ear HRTFs match minimum-phase reconstructions with a coherence index greater than 0.9. This also indicates that the population of HRTFs at the left ear are better approximated by minimum-phase function than HRTFs measured at the right ear. Such an asymmetry is not observed in 505 HRTFs from the SOW data set, for which 96% of the left-ear HRTFs and 97% of the right-ear HRTFs have a coherence index greater than 0.9. The values of the coherence indices also indicate that the SOW data set was better approximated by a minimum-phase sequence than the SDO set. The lower coherence values generally correspond to low elevations and contralateral azimuths (not shown).

The root-mean-square error ϵ_{rms} defined in Eq. (11) is presented in Fig. 3 for the SDO (top panels) and SOW (bottom panels) data sets as a function of source position. There appears to be a systematic variation of the error as a function of source position observable for both data sets. The error is observed to be maximum at lower elevations for azimuths where the ear is shadowed from the source. The error at high elevations, however, has a low (and roughly constant) value at all source azimuths. This result leads to the conclusion that the all-pass component of HRTF phase is most poorly fit by the linear-phase assumption for source positions where the sound signal to the ear is complicated due to interactions with the head and torso. Sound reaching the shadowed ear from a low elevation is most likely to be influenced by phenomena of diffraction and scattering by the head and torso (Kuhn, 1977); correspondingly, the HRTF from these positions has the worst approximation to the minimum-phase model. The sound path to both ears from high elevations is more direct for all azimuths, having only to bend over the top of the head to reach either ear, and the HRTF phase for these positions is best approximated by the minimum-phase model.

It was suggested to us (Zweig, 1996) that the departure of HRTF phase spectra from the model of a minimum-phase function plus a frequency-independent delay might be due to errors in measurement. With this concern in mind, one might hypothesize that the residual phase function may be larger in value at frequencies where the signal-to-noise ratio (SNR) in the measurement was lower (notches) compared to regions of high SNR (peaks). We confirmed that this was not the case by calculating the difference in the phases for the minimum-phase-plus-delay model and the empirical measurements and comparing this difference with the level of the HRTF magnitude spectrum, both as a function of frequency. A repre-

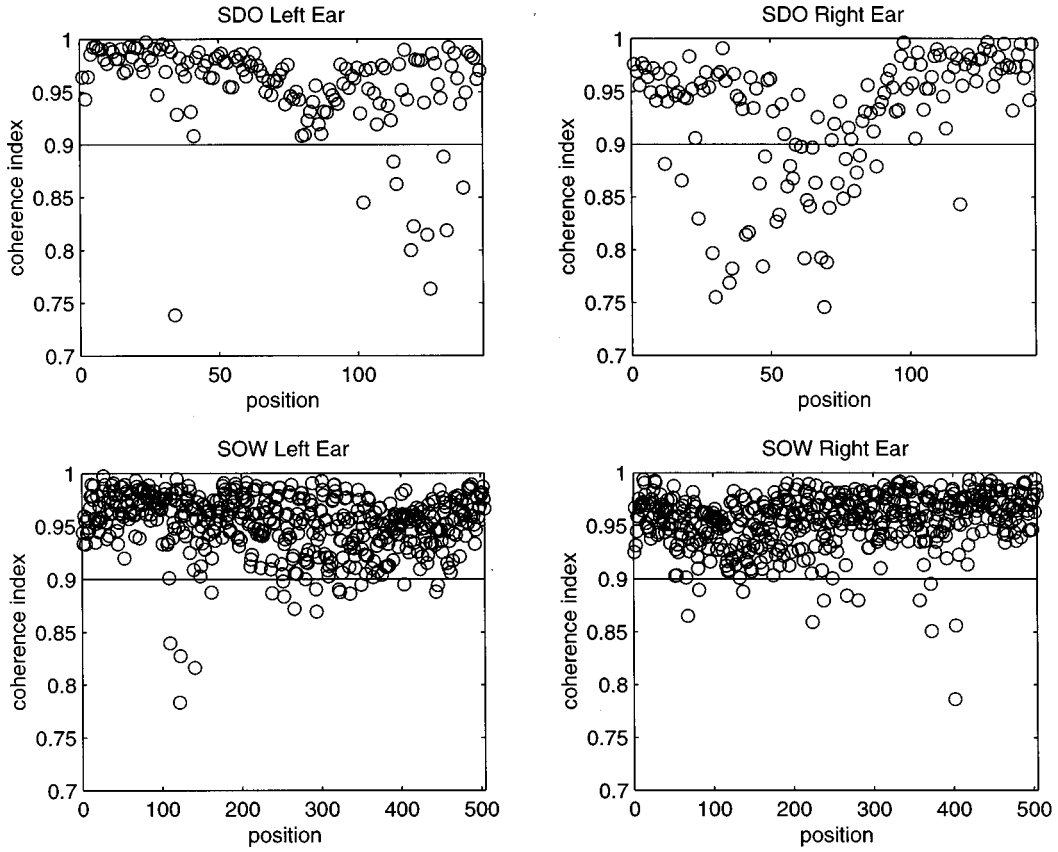

FIG. 2. Coherence index values calculated for the SDO (top panel) and SOW (bottom panel) HRTF data sets. Results corresponding to left- and right-ear measurements are displayed in the left and right panel, respectively, for each data set. The coherence index is displayed along the ordinate with HRTF positions being indexed (arbitrarily) along the abscissa. See text for details of the HRTF data.

sentative phase-error function is shown in Fig. 4 along with the magnitude spectrum. It may be noted that the size of the phase difference has no apparent relation to the HRTF magnitude spectrum level (and hence no relation to the apparent signal-to-noise ratio). We conclude that the phase differences result from the complex, frequency-dependent, diffraction and scattering of sound waves around the head and torso and do not reflect imperfections in the measurement.[1]

The rms error in interaural phase, due to modeling the monaural phase at the two ears for a given position as a combination of a minimum-phase term and a linear-phase all-pass term, followed the patterns observed in the monaural phase spectra (Fig. 3). The error was greatest at low elevations for azimuths where either ear is maximally shadowed from the source. This result can be inferred from Fig. 3 and is hence not plotted. We note that it is difficult to interpret the rms error as a perceptual metric because it collapses the error across frequency into a single numerical quantity. However, it is a useful signal analysis measure that describes the departure of the measured HRTF impulse responses from the theoretical description of a minimum-phase-plus-delay sequence. The perceptual consequences of such a departure are addressed in Sec. II below.

The estimated delay τ_m between the minimum-phase sequences, calculated [using Eq. (7)] from the left and right HRTF magnitudes, is plotted in Fig. 5 for each position for the SDO and SOW data sets. This delay varies systematically with source azimuth, having a peak values of approximately 100 μs at positions close to $\pm$90 degrees. The delay is also larger at the lower elevations at these azimuths. At these positions, the distances from the source to the two ears are most different. Because the corresponding transformations to each ear are maximally different at these positions, the contribution of τ_m is maximal in these regions. Note that because the value of τ_m is larger than the detectable increment in ITD at several locations, the compensation in Eq. (8) is expected to be perceptually important.

II. PSYCHOPHYSICAL ANALYSIS OF MINIMUM-PHASE MODEL

The minimum-phase-plus-delay model for HRTF phase spectra was examined in a series of psychophysical experiments. All experiments employed the discrimination paradigm which is described in the following sections. Conditions specific to each experiment are discussed in the individual sections.

A. Methods

Subjects were tested in a four-interval two-alternative forced-choice (4I-2AFC) discrimination paradigm. Subjects were presented with four sounds processed through empirical and minimum-phase-plus-delay model HRTFs. Stimuli in three intervals of a set of four were processed through the

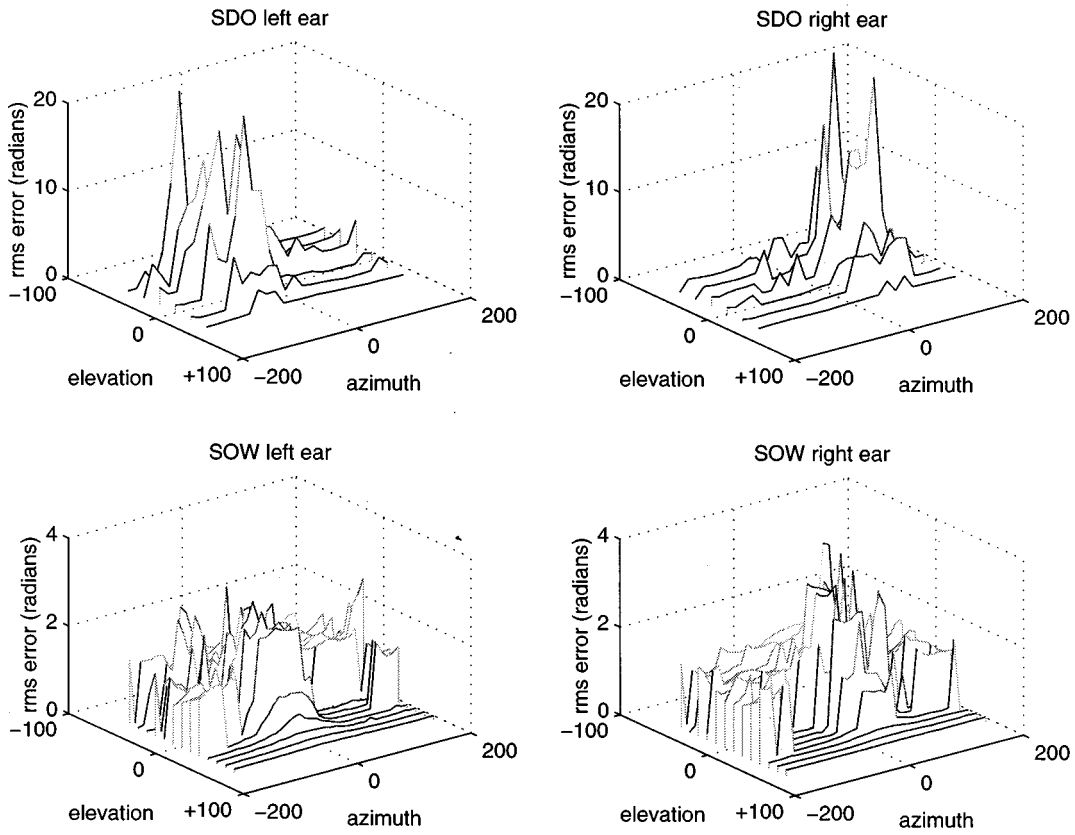

FIG. 3. The root-mean-square (rms) error in modeling the HRTF phase as a combination of a minimum-phase term and a linear-phase all-pass term. Results for the SDO data and SOW data are shown in the top and bottom panel, respectively, and results for the left- and right-ear measurements of each data set are shown in the left and right panel, respectively. The rms error in radians is displayed along the *y*-axis as a function of source location.

empirically measured HRTFs for the position of interest. The stimulus in either the second or the third interval of a set (determined randomly for each set) was processed through the model HRTFs. The task entailed subjects to pick this odd interval from the set of four.

The standard stimulus was a 500-ms burst of noise (50-ms cosine-squared onset/offset ramps) presented at a comfortable listening level, about 65 dB SPL. The interstimulus interval was 500 ms. Listening was conducted in a sound-attenuated booth using headphones (Sony, MDR V6) with no compensation. The generation of the noise waveform (random noise generator or precomputed noise waveform) depended on the specific experiment.

Both monaural and binaural experiments were conducted. For monaural conditions, the signal to one ear was disconnected (left-ear monaural and right-ear monaural). In the binaural synthesis of minimum-phase HRTFs, appropriate interaural delays calculated from Eq. (8) were computed for the position of interest. The delay appropriate for the position of interest was then introduced in the minimum-phase signal to the lagging ear.

The sound waveforms were presented to listeners via the Convolvotron audio display system marketed by Crystal River Engineering, CA. The Convolvotron, which is housed in an IBM-PC-compatible host computer, is a specialized digital-signal-processing device optimized for performing real-time convolutions. It presents over headphones, the composite binaural signal derived from simultaneously convolving up to four sound sources with an equal number of HRTF pairs. For the purposes of this experiment, a single channel of source input corresponding to the noise stimulus was specified. For each presentation interval, an HRTF pair was moved from a file on the IBM PC hard-drive onto the memory of the Convolvotron, which then performed the convolutions.

B. Subjects

Four subjects (two males and two females) participated as volunteers in the experiment; their ages were between 20 and 30. Subjects S2 and S1 are the first and second authors, respectively. All four subjects had normal hearing (as indicated by their pure tone audiograms) and had several hours of listening experience, having previously participated in similar auditory experiments.

C. Experiment I: Random-token random-position condition

1. Stimulus

The noise samples used in this experiment were derived from a random-noise generator (Grason-Stadler, Model

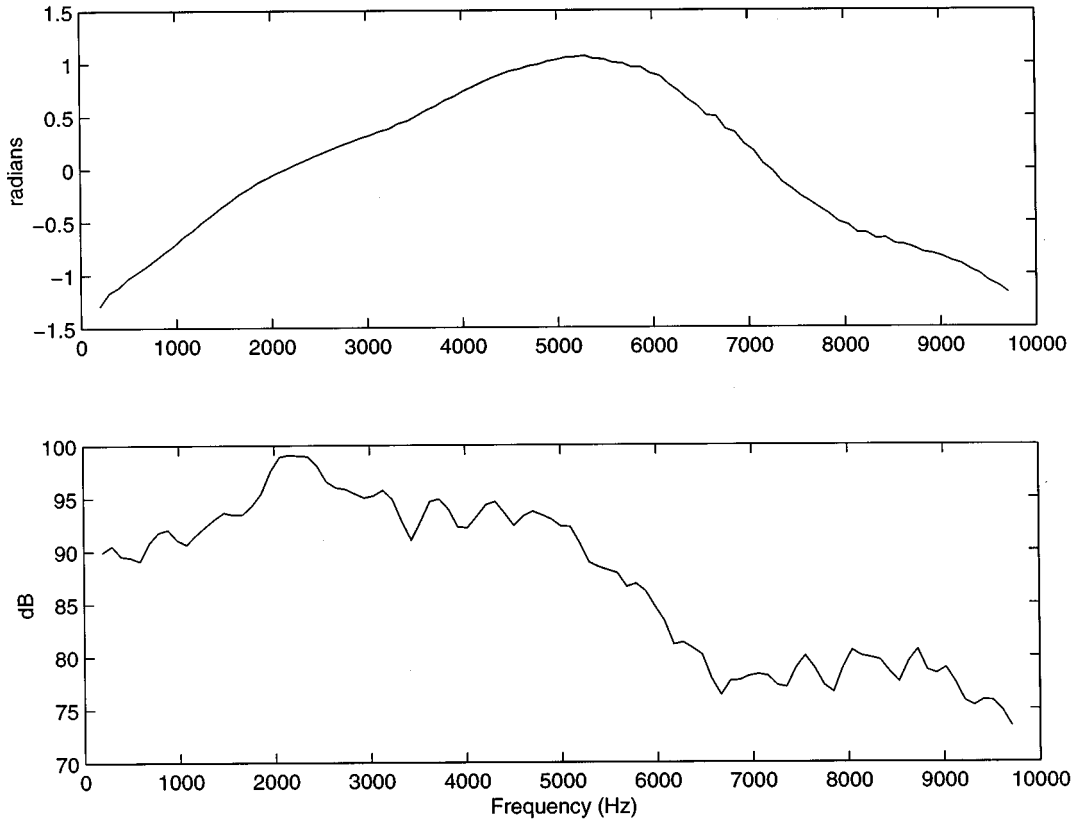

FIG. 4. The residual phase function for a representative HRTF (top panel) and its corresponding magnitude spectrum (bottom panel).

1382). Each interval consisted of a fresh noise token which was gated on and off using an electronic switch (Wilsonix, Model BSIT).

The HRTFs used were those from the SDO data set. All HRTFs in the set (corresponding to 144 positions) were tested using the 4I-2AFC procedure. Each position was tested 10 times, ordered randomly in sets of 30. Both monaural (left and right ear) and binaural conditions were tested.

2. Results and discussion

The results averaged over all 144 positions tested, for the two monaural conditions and the binaural condition, are presented for the four subjects in Fig. 6. Each average has been computed from a total of 1440 data points. The region bounding chance performance for a significance level $\alpha=0.05$ is indicated on the graph. Data for subject performance at individual positions were noisy (only ten trials per position) and are not presented. Although there were positions where subjects had perfect scores (out of ten trials), positions where subjects had chance performance, and positions with intermediate levels of performance, positions with high and low percent correct varied over subjects and there was no common trend. Also, in order to determine if any specific region in space yielded more errors for some subjects than others, we analyzed the data in sectors of 45-degree azimuths. No spatial dependence was observed for any of the subjects.

In Fig. 6, note that most subjects are operating near chance in both the binaural and the two monaural conditions. This is consistent with the subjective reports from all subjects, that the task was frustrating and difficult and that they felt they needed to guess on most trials. Given the high values of the coherence index analyzed in the first part of this study (Fig. 2), these results are not surprising. This result is also consistent with a previous study utilizing minimum-phase HRTF model constructions by Kistler and Wightman (1992). In that study, in an absolute judgment task, subjects were able to localize stimuli comparably with empirical HRTFs and model minimum-phase-plus-delay HRTFs.

This experiment served as a pilot study to investigate the sensitivity of listeners to HRTF phase spectra. As noted before, the large number of positions tested resulted in a small number of trials for each source position and the data were noisy. A subset of four locations corresponding to 0-, 90-, 180-, and −90-degree azimuths in the horizontal plane (where 0 is straight ahead) was chosen for more detailed experimentation. For each subject, these positions covered the range of subject performance from chance to perfect scores in experiment I.

D. Experiment II: Random-token, fixed-position condition

1. Stimulus

The noise samples used in this experiment were again obtained from the random-noise generator. The source posi-

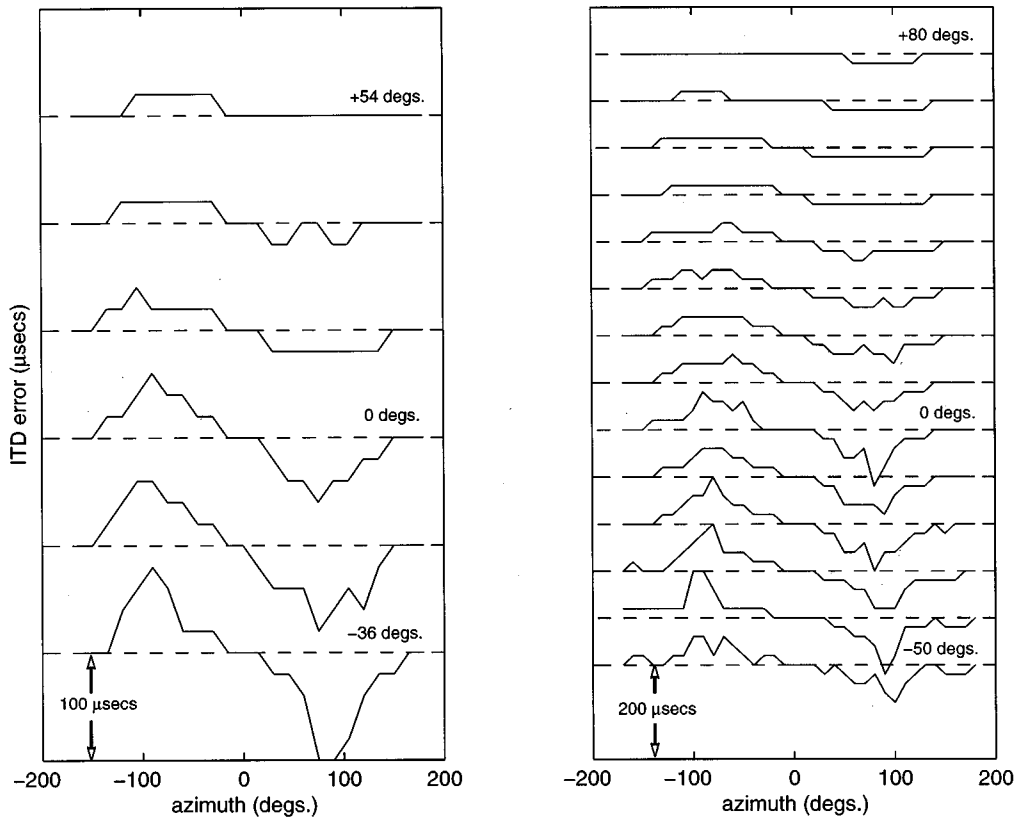

FIG. 5. Interaural delay τ_m computed from the minimum-phase impulse responses, which were calculated from the magnitudes of the empirical left- and right-ear HRTFs. Results for the SDO and SOW data are presented in the left and right panels, respectively. In each panel, the delay τ_m in μs is displayed along the ordinate as a function of source location. See text for details.

tions tested, however, were restricted to four positions in the horizontal plane at azimuths of 0, 90, 180, and −90 degrees (where 0 is straight ahead). The position and listening condition (monaural left, monaural right, and binaural) were fixed for each 50-trial run of the experiment. A total of 100 responses for each position, for each of the binaural and the two monaural conditions were collected for each subject.

2. Results and discussion

The results for the left and right monaural condition and the binaural condition are shown in Fig. 7. The confidence bounds for chance performance at a significance level $\alpha=0.05$ is indicated on the graphs as the region bounded by the two horizontal lines.

Note that, with the exception of subject S1 at the 90-degree position in the binaural condition and subject S3 at the 0-degree position in the right-ear monaural condition, all subjects have performance within the chance bounds. The greater-than-chance performance by subject S3 in the right-ear monaural condition might also reflect on the right-ear monaural-condition ensemble performance in experiment I (Fig. 6), which is significantly better than chance at the 0.05

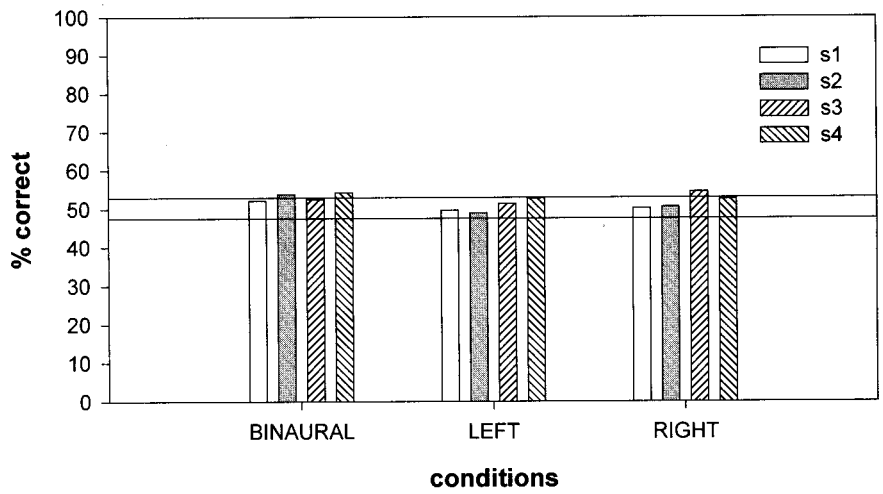

FIG. 6. Performance of subjects in the 4I-2AFC task testing the discriminability of empirical HRTF measurements from the SDO data set from corresponding minimum-phase reconstructions of the data. The percent-correct performance averaged over all 144 positions tested is displayed for the binaural and (left and right ear) monaural conditions described in the text. The 95% confidence region ($\alpha=0.05$) corresponding to chance performance (50% correct) is depicted by the region bounded by the two horizontal lines on the graph.

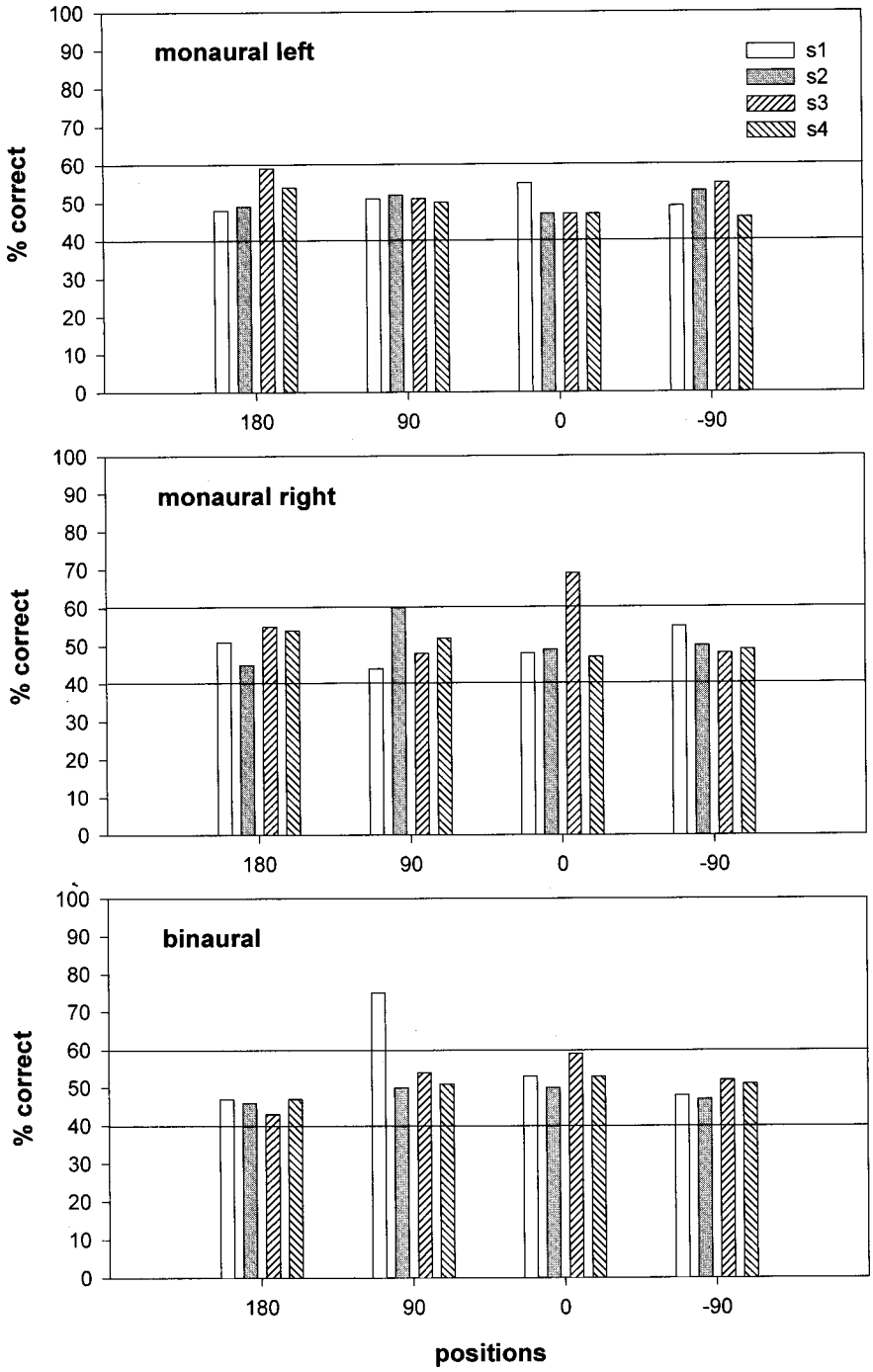

FIG. 7. Discrimination performance of subjects with minimum-phase HRTFs in the left-ear monaural condition (top panel), right-ear monaural condition (middle panel), and binaural condition (bottom panel) at four locations (180, ±90, and 0 degrees). A fixed position was tested in each session of the experiment and the stimulus was a noise token which was chosen randomly for each presentation of the experiment. Performance for each location and each subject is shown as percent-correct and the 95% confidence region (α=0.05) corresponding to chance performance (50% correct) is depicted by the region bounded by the two horizontal lines on the graph.

significance level. Note from Fig. 2 that the coherence index for the SDO HRTF data set is lower for the right ear. In fact, for the 0-degree position, the coherence index for the right ear is 0.84, whereas it is greater than 0.9 for the other HRTFs tested in this condition. The reduced coherence on the right ear is consistent with the above-chance monaural discriminability of subject S3 for the right ear.

The binaural discrimination capability of subject S1 at 90 degrees is consistent with reports from this subject of a position cue at that location. Subject S1 also reported that it was difficult to utilize this cue consistently. Additional testing of subject S1 for the 90-degree binaural condition yielded results nearly identical to those presented in Fig. 7.

E. Experiment III: Fixed-token fixed-position condition

1. Stimulus

A single noise token was used for every trial of this experiment. This token was digitally constructed using an inverse FFT procedure by choosing random-amplitude (Rayleigh distributed) and random-phase (uniformly distributed) spectra for a bandwidth of 20 kHz. The cosine-squared onset and offset ramps were applied to the token, which was stored on a Loughborough C-25 card and input to the Convolvotron as a sound source via the D/A converter on the card. The positions tested were again restricted to 180, 90, 0, and −90

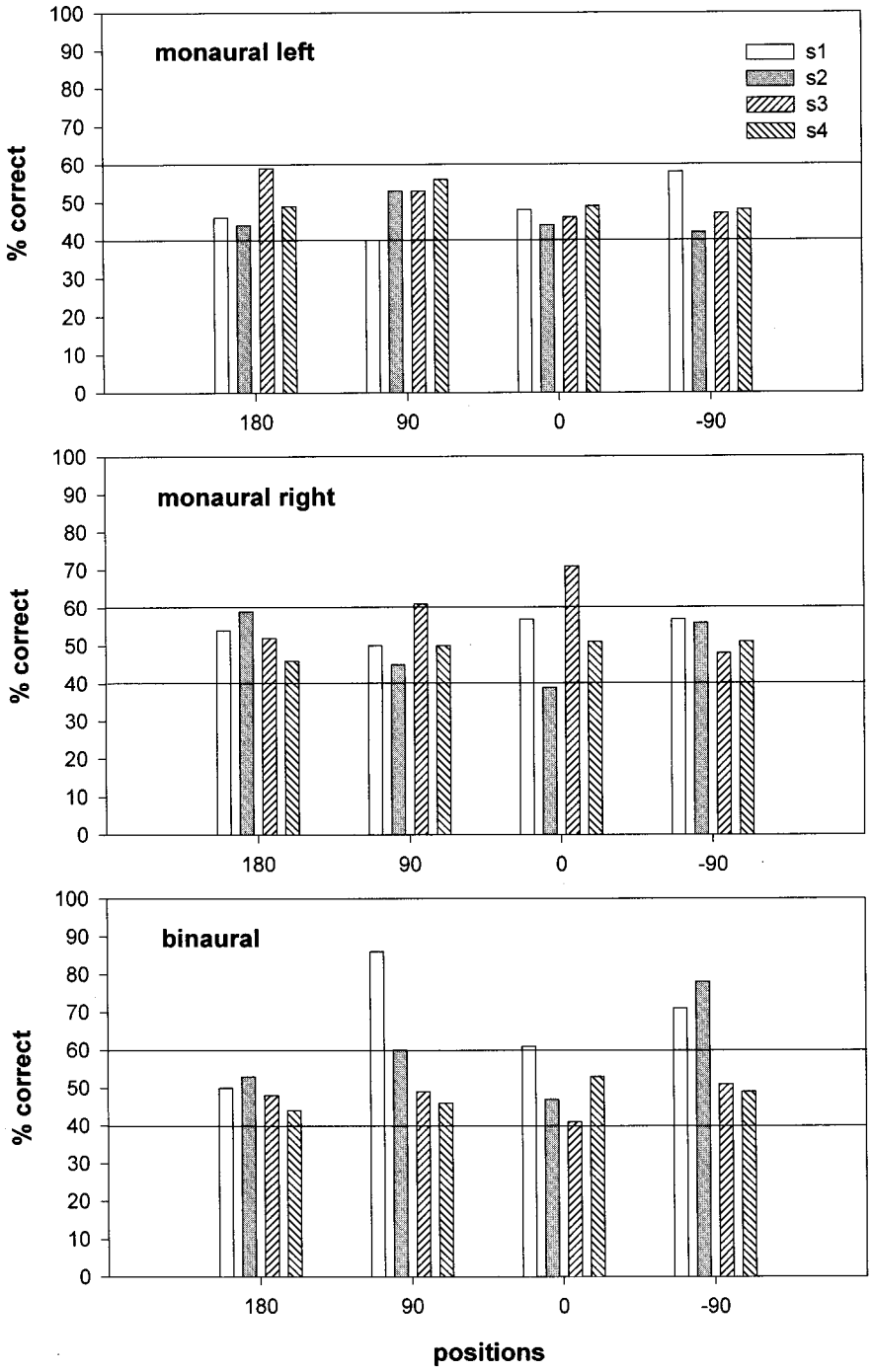

FIG. 8. Discrimination performance of subjects for the fixed-position, fixed-token condition with minimum-phase-plus-delay HRTFs in the left-ear monaural condition (top panel), right-ear monaural condition (middle panel), and binaural condition (bottom panel) at four locations (180, ±90, 0 degrees). (See text for details.) Performance for each location and each subject is shown as percent correct and the 95% confidence region (α=0.05) corresponding to chance performance (50% correct) is depicted by the region bounded by the two horizontal lines on the graph.

degrees and fixed for each 50-trials run as in experiment II. A total of 100 subject responses were measured for each condition examined.

2. Results and discussion

The results for the two monaural conditions (left and right ear) and the binaural condition are shown in Fig. 8. As with the previous results, the confidence region bounding chance performance at a significance level of α=0.05 is indicated on the graph by the two horizontal lines.

The monaural performance appears to be unaffected by freezing the token. The left ear again shows chance performance for all subjects, and for the right ear, subject S3 continues to have performance which is significantly better than chance at the 0-degree position as in the previous experiment. Also for the same subject, performance at 90 degrees also reaches significance above chance, although only marginally so.

For the binaural condition, two subjects (S1 and S2) have a better than chance performance at the ±90-degree positions. In the previous condition where only subject S1 had better than chance performance at 90 degrees. The cue reported by both subjects was position, which was again reported to be perceived sporadically during a run. In fact, both subjects reported that the cue was usually present, although it was easy to ''lose it'' for several trials at a time. This is consistent with the fact that despite running repeated addi-

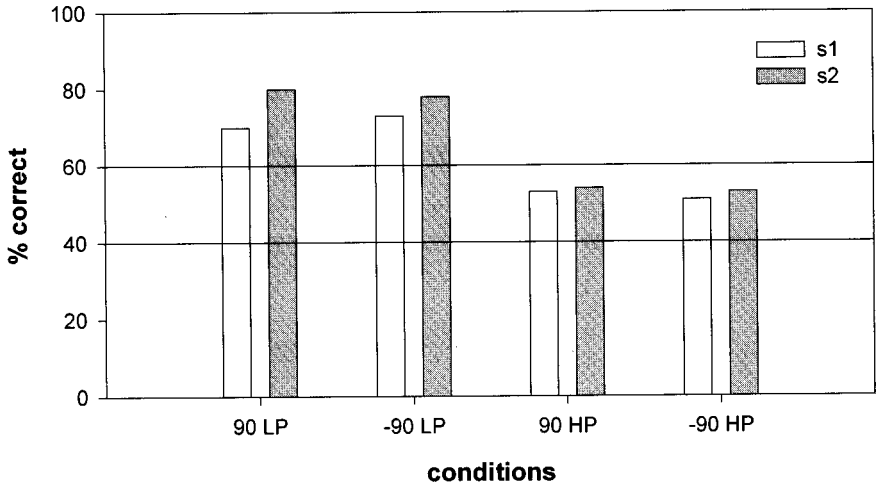

FIG. 9. Discrimination performance of two subjects (S2 and S1) for the ±90-degree positions using 2-kHz low-pass and 2-kHz high-pass stimuli. The position tested was fixed for each session and a frozen-noise token was used for each condition. Performance for each location and each subject is shown as percent correct and the 95% confidence region (α=0.05) corresponding to chance performance (50% correct) is depicted by the region bounded by the two horizontal lines on the graph.

tional trials, the performance statistics did not change for either subject.

F. Experiment IV: Fixed-token, fixed-position, low-pass and high-pass stimulus conditions

This experiment was conducted to analyze the binaural performance of subject S1 and S2 in the previous condition for the ±90-degree positions. Only subjects S1 and S2 participated in this condition which was restricted to the binaural testing of the ±90-degree positions.

1. Stimulus

Two new noise tokens were created digitally using the same techniques as in experiment III. One token was created to have a 2-kHz low-pass characteristic (with no signal energy in the stop-band and random amplitude and phase spectra in the pass band). This is called the LP condition. The other token was created to have a 2-kHz high-pass characteristic (with no signal energy in the stop band and random amplitude and phase spectra in the pass band). This is called the HP condition. The 50-ms cosine-squared onset offset ramps were imposed on the noise waveforms as before and they were stored on the Loughborough C25 board for input to the Convolvotron via the D/A converter on the card. As in the previous experiment, the token was frozen and the position was fixed to either ±90 degrees for a given run.

2. Results and discussion

Results for subjects S1 and S2 in the LP and HP conditions are shown in Fig. 9. The performance is averaged from a total of 100 trials for each condition, per subject.

The results for the LP condition for both subjects show a performance comparable to that seen for the ±90-degree positions in experiment III (Fig. 8). Chance performance is observed for the HP condition for both subjects. This result is consistent with the reported use of a position cue by both subjects. Because such a cue would be possibly encoded by the low frequencies, results in the LP conditions are consistent with the results using a full-band noise token. However, when the low frequencies are eliminated from the stimulus in the HP condition, the absence of a position cue results in chance performance. Both subjects reported the absence of the cue in the HP condition. In spite of the reported presence of the cue in the LP condition, as before with the full-band noise token, the cue was only sporadically perceived and subject performance did not improve despite repeated testing.

In order to analyze the presence of the low-frequency position cue, the ITDs resulting from the minimum-phase-plus-delay HRTFs and the empirical HRTFs were examined for the four positions of interest (180, 90, 0, and −90 degrees). The ITD was computed as a function of frequency f using the equations

$$\tau_e(f) = \frac{\phi^l(\omega) - \phi^r(\omega)}{2\pi f}, \qquad \tau_m(f) = \frac{\phi^l_{\min}(\omega) - \phi^r_{\min}(\omega)}{2\pi f}, \tag{12}$$

where $\phi^l(\omega)$ and $\phi^r(\omega)$ are the empirical phase functions for the left and right ear and $\phi^l_{\min}(\omega)$ and $\phi^r_{\min}(\omega)$ are the corresponding minimum-phase-plus-delay functions. As above, $\omega = 2\pi f/f_s$ where f_s is the sampling frequency of the discrete-time sequence and f is the actual frequency. The empirical-phase and minimum-phase-plus-delay ITD functions are denoted by $\tau_e(f)$ and $\tau_m(f)$.

The ITD functions measured for the empirical-phase and model HRTFs are shown in Fig. 10 for the four positions. For the 180- and 0-degree positions, the differences in the empirical and model ITD functions are always less than 10 μs and are not expected to be perceptually relevant. This is consistent with the chance performance for all subjects in all conditions for these positions. However, for the ±90-degree positions, the differences are larger in the low-frequency region, presumably large enough to be be perceived by the auditory system. This is consistent with the reported usage of the position cue by subjects S1 and S2 for these positions for the LP condition (and consistent with chance performance observed in the HP condition for the same subjects). Finally, we note that the ITD cue at the ±90 degree positions is consistent across frequency so that the average ITD across the low-frequency region is also large.

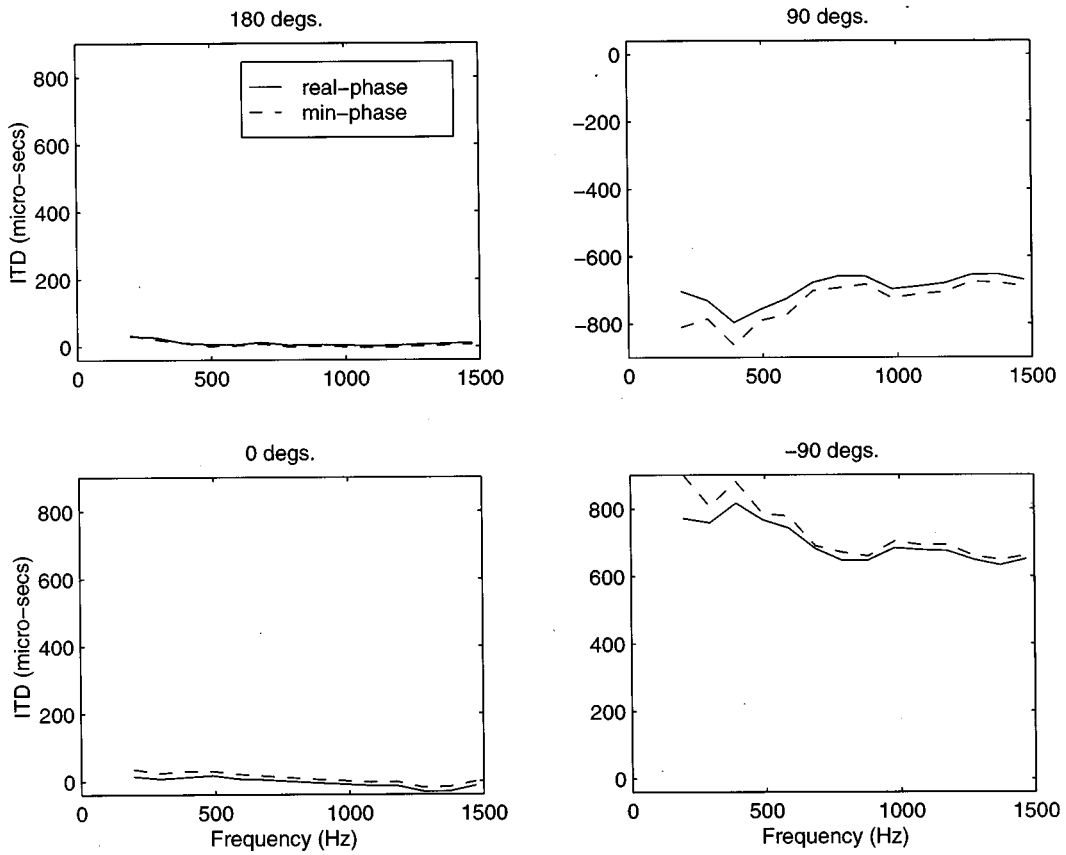

FIG. 10. The ITD functions computed from the empirical HRTF phase spectra [$\tau_e(f)$, solid line] and minimum-phase-plus-delay reconstructed HRTF phase-spectra [$\tau_m(f)$, dashed line] for the four locations tested in the psychophysical experiment.

The ITD results obtained above are from the steady-state phase functions of the HRTFs. We also computed the ITDs for the actual stimuli (a noise token convolved with the HRTFs) using a more physiological model of ITD extraction. The frozen-noise token used in experiment III was convolved with empirical and model HRTFs for each of the four positions. The resulting stimuli, which correspond to the sound waveforms presented to subjects during the psychophysical experiment, were processed through a simple computational model of the auditory periphery followed by a short-time cross correlator. The peripheral model consisted of a bank of critical band filters (Patterson *et al.*, 1992), each followed by a half-wave rectifier. The signals in common frequency channels from the left and right input were sliced in time using overlapping segments (50% overlap) of a Hanning window having a duration $T=10$ ms and processed by a running cross correlation. The output from the cross correlator with internal delay τ at time t_i is

$$\phi_i(f,\tau)=\phi(f,t_i,\tau)=p(\tau)\sum_{k=0}^{T/\delta t} l(f,t_i-k\,\delta t)r(f,t_i-k\,\delta t-\tau), \tag{13}$$

where δt is the sampling interval given by the inverse of the 50-kHz sampling rate ($\delta t=20\ \mu$s), $l(f,t)$ and $r(f,t)$ are the inputs to the cross correlator having a center frequency f, and $p(\tau)$ is a central weighting function applied to emphasize the contribution of ITDs near zero (cf. Colburn, 1977).

For each frequency f, the internal delay τ_f^i corresponding to the peak in the cross-correlation function for the ith slice was taken as the estimate of the interaural delay in that interval. Hence, if the cross-correlation function for each frequency f and time slice i is expressed as $\phi_i(f,\tau)$, then τ_f^i is expressed as

$$\tau_f^i=\overset{\max}{\tau}\ \phi_i(f,\tau). \tag{14}$$

The ITD for each frequency was then estimated as the mean value of τ_f^i over the N time segments; that is,

$$\tau_f=\frac{1}{N}\sum_{i=1}^{N}\tau_f^i. \tag{15}$$

Results showing the values of τ_f for the empirical HRTFs and minimum-phase-plus-delay HRTFs for the four positions are plotted in Fig. 11. [Incidentally, we noted that the variability of τ_f^i over i (i.e., over the time slices) was very small.] Substantial discrepancies between the minimum-phase-plus-delay and empirical-phase stimuli at the low-frequency regions for the $\pm$90-degree locations can be noted, as in the steady-state phase analysis. Moreover, these discrepancies are again consistent across frequency, and the position cue noted by subjects S1 and S2 at these positions is hence predictable. [Since the empirical ITDs are greater at low frequencies than high frequencies on the sides (Kuhn,

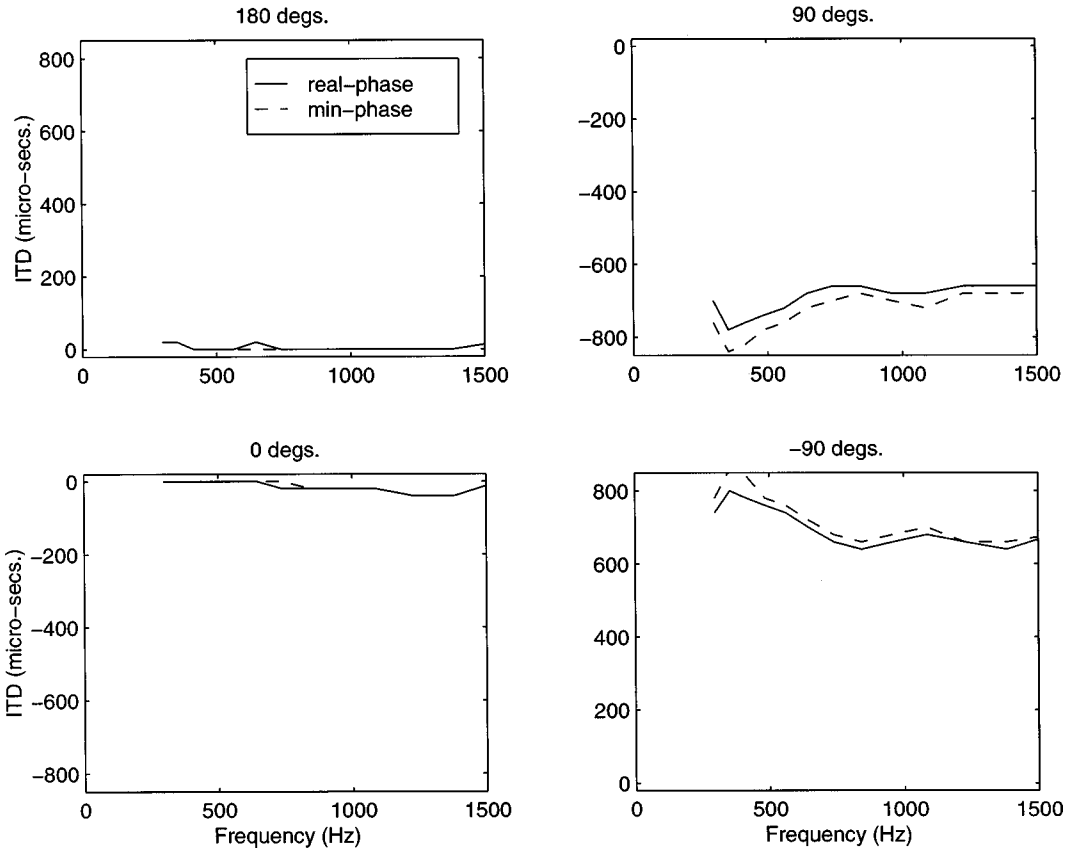

FIG. 11. ITD computed from an interaural processing model consisting of a short-term, running, cross correlation of critical-band filtered and rectified stimulus inputs. The ITD is estimated as the delay for which the cross-correlation function reaches the maximum. (See text.) ITD spectra computed from empirical-phase and model minimum-phase virtual stimuli delivered to the listener's ears are presented in each panel for the four locations tested in the psychophysical experiment.

1977) and since a frequency-independent delay was used in the minimum-phase-plus-delay model, the observed mean errors for low frequencies are to be expected.]

III. LINEAR-PHASE AND REVERSED-PHASE-PLUS-DELAY MODELS

In the final part of the study, two additional models of the HRTF phase spectrum were explored. In the first model, the HRTF phase is approximated as a linear function. The linear-phase slope (corresponding to the delay of the zero-phase impulse response) was computed so that the HRTFs would be causal. These HRTFs are called linear-phase HRTFs. In this model, the ITD function defined in Sec. II F has a frequency-independent (but position-dependent) value, and this constant ITD was chosen to equal the overall ITD in the empirical HRTF measurements. In the second model, the HRTF phase was based on the negative of the empirical phase function with a linear-phase (pure delay) added. These HRTFs are called reversed-phase-plus-delay HRTFs. The added delay was computed to equate the overall ITD in the model HRTFs with that in the empirical HRTFs. Results are presented below for the monaural and binaural discriminability of both model HRTFs from empirical HRTFs.

A. Linear-phase and reversed-phase-plus-delay HRTFs

A linear-phase HRTF representation is based on the zero-phase HRTF which may be obtained by combining the HRTF magnitude spectra with a zero-phase spectrum. By taking an inverse-Fourier transform of this combination, the impulse response of the zero-phase filter can be obtained. This filter is symmetric about the zeroth time lag and is not causal. By shifting the filter samples by half the number of filter taps, one obtains a linear-phase filter which is causal and symmetric about the center tap of the filter. The phase of this filter is a linear function of frequency.

A reversed-phase-plus-delay HRTF is obtained by time reversing the filter coefficients of an empirically obtained filter, then shifting them to equate delays. In the frequency domain, this corresponds to taking the complex conjugate of the Fourier transform of the empirical filter and then shifting in time by a delay equaling the number of coefficients in the filter to ensure causality.

B. Psychophysical testing of models

The goal of psychophysical experiments V and VI was to measure the discriminability of linear-phase and reversed-phase-plus-delay HRTFs from empirical HRTFs. The psychophysical paradigm and methods employed for these tests

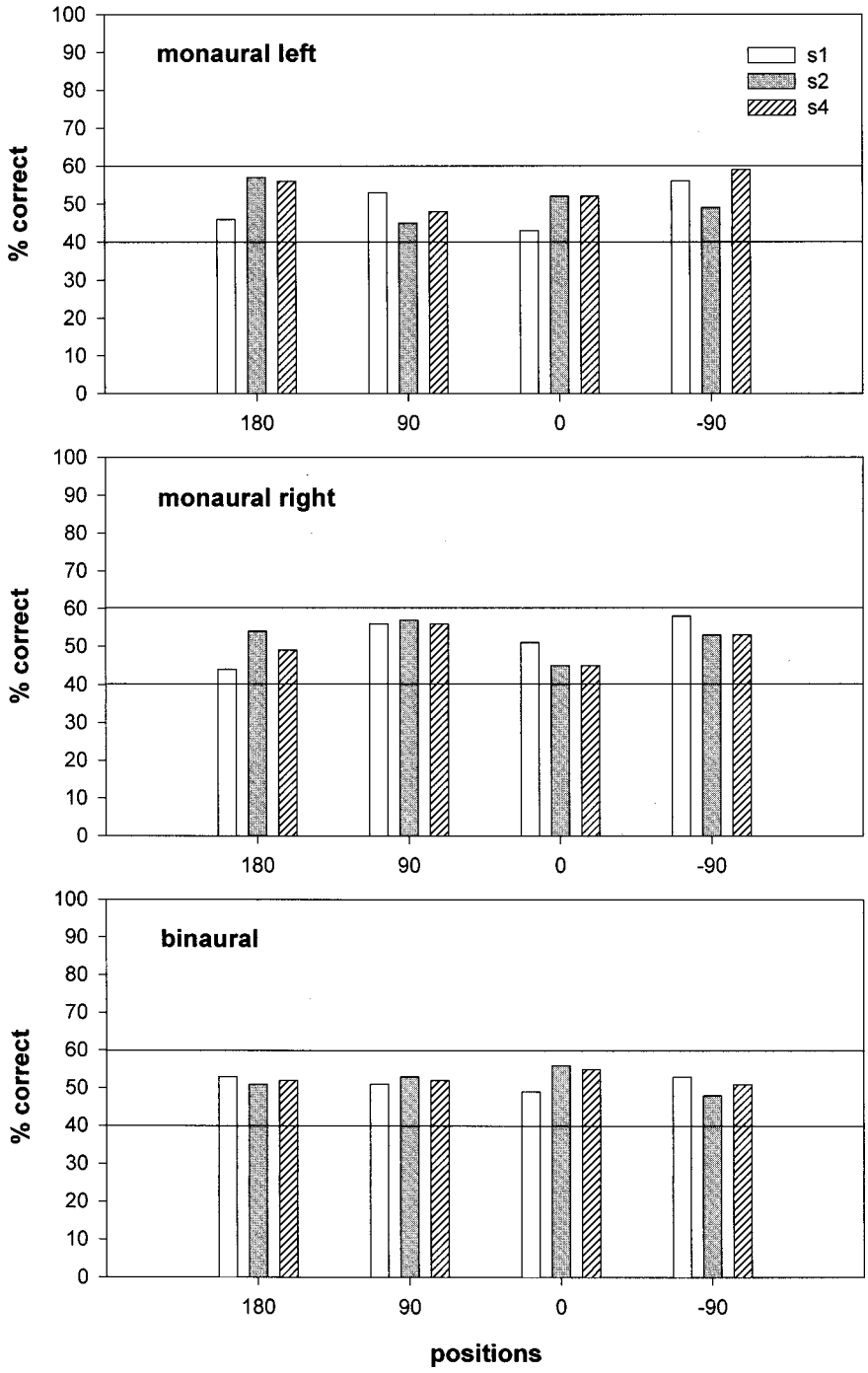

FIG. 12. Discrimination performance of subjects with linear-phase HRTFs in the left-ear monaural condition (top panel), right-ear monaural condition (middle panel), and binaural condition (bottom panel) at four locations (180, ±90, 0 degrees). A fixed position was tested in each session of the experiment and the stimulus was a frozen-noise token. See text for details. Performance for each location and each subject is shown as percent correct and the 95% confidence region (α=0.05) corresponding to chance performance (50% correct) is depicted by the region bounded by the two horizontal lines on the graph.

were the same as those used in Sec. II E. The same four source positions (180, +90, 0, −90), three of the same subjects, and the same fixed token of noise were used.

C. Results

1. Subjective results

All subjects reported the absence of any cue in all the monaural conditions tested in this study. Even in the absence of stimulus token variability, subjects were unable to determine any discriminable attribute between model HRTF stimuli and empirical HRTF stimuli.

In the linear-phase binaural condition, all subjects reported no differences between the model HRTFs and empirical HRTFs at all locations. In the reversed-phase binaural condition, all subjects reported perceiving a position cue at each of the four locations. However, this cue, which was most potent for the position in front, was subtle and subjects found it hard to use consistently.

2. Objective results

The monaural and binaural discrimination performance of the four subjects for the linear-phase HRTF condition (experiment V) is presented in Fig. 12. Performance in the reversed-phase-plus-delay condition (experiment VI) is presented in Fig. 13. Percent-correct shown was computed from a total of 100 trials for each point. The two solid lines on

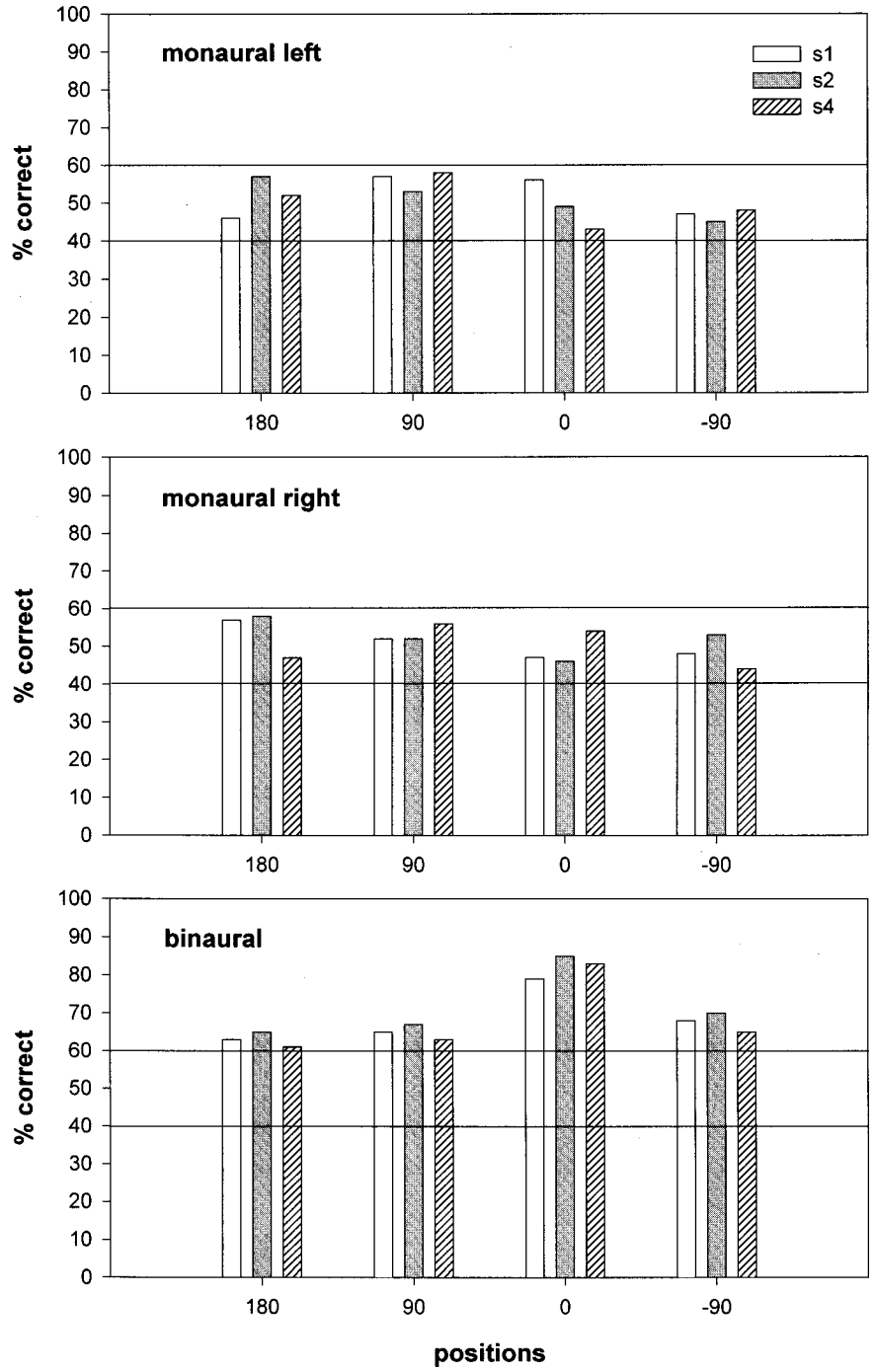

FIG. 13. Discrimination performance of subjects with reversed-phase-plus-delay HRTFs in the left-ear monaural condition (top panel), right-ear monaural condition (middle panel), and binaural condition (bottom panel) at four locations (180, ±90, 0 degrees). A fixed position was tested in each session of the experiment and the stimulus was a frozen noise token. See text for details. Performance for each location and each subject is shown as percent correct and the 95% confidence region (α=0.05) corresponding to chance performance (50% correct) is depicted by the region bounded by the two horizontal lines on the graph.

each graph indicate the confidence bounds for chance performance at a 95% level. Note that, for the linear-phase condition, subject performance is near chance for both the monaural and binaural conditions at all positions. In the reversed-phase conditions, monaural performance is again at chance for all the positions, but binaural performance is better than expected from chance at all positions. More specifically, binaural performance is better for all subjects at the front location (85% average) and back locations (80% average) than the positions to the left (63% average) and right (61% average). Results shown in Figs. 12 and 13 are extremely stable and repeatable; subjects S1 and S2 were tested on several additional runs and results nearly identical to those reported were obtained.

3. Discussion of experiments V and VI

The ITD functions as defined in Eq. (12) for the empirical, linear-phase, and reversed-phase-plus-delay HRTFs are shown in the four panels of Fig. 14 for the four source positions. Note that for all positions, the linear-phase ITD function is approximately independent of frequency and has a value equal to the overall empirical ITD τ_e for that position. Note also that the difference between the reversed-phase-plus-delay ITD function and the linear-phase ITD value at each frequency is equal and opposite in sign to the corresponding difference for the empirical ITD function.

We also computed the ITD functions available to subjects in the actual noise waveforms that were presented to the

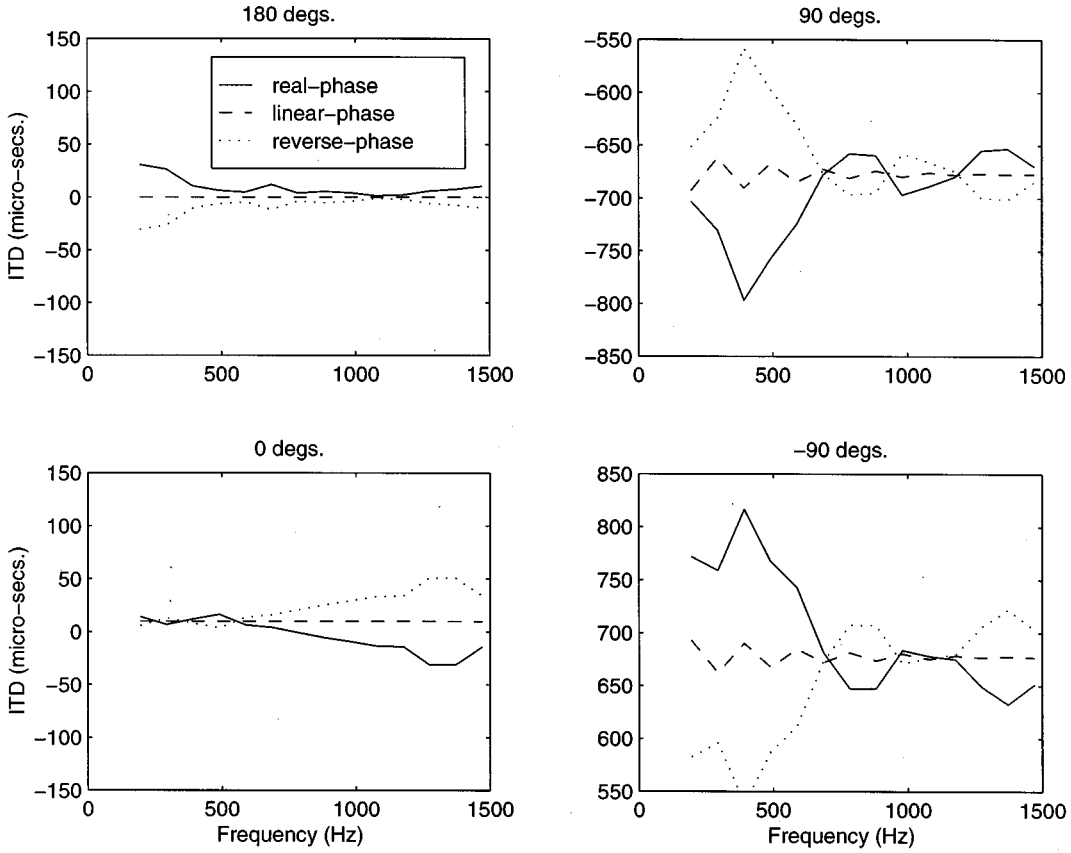

FIG. 14. ITD functions computed from empirical-phase, linear-phase, and reversed-phase-plus-delay model HRTFs for the four positions tested in the psychophysical experiment.

subject's left and right ears, computed using the interaural time model described at the end of Sec. II [cf. Eqs. (13)–(15)]. Specifically, the mean ITD across the time slices for each frequency channel was computed according to Eqs. (14) and (15) for the empirical-phase, linear-phase, and reversed-phase-plus-delay. These values are shown in the four panels of Fig. 15 for the four positions of interest along with the results shown above for the minimum-phase-plus-delay model for the same locations. Note that the ITD computed with this model scheme compares very well with the steady-state values computed directly from the HRTFs and shown in Fig. 14. We also computed the mean ITD across frequency, for frequencies less than 2000 Hz, for the empirically measured and the three modeled phase functions. These values are shown in Table I. Note that the mean minimum-phase ITD deviates substantially from the empirical ITD for the ± 90-degree positions, the mean linear-phase ITD is closer to the empirical ITD for all locations, and the reversed-phase ITD is also substantially different from the empirical ITD at each of the four locations.

IV. OVERALL DISCUSSION

A. Implications for human psychophysics

The physical nature of the process by which sound propagates from a sound source to the two ears introduces complicated features in the received phase spectra. The psychophysical experiments described above were designed to determine the sensitivity of human subjects to attributes of the phase spectra. In this section, results from all six psychophysical experiments are discussed together.

When listening monaurally, subjects exhibited very poor sensitivity to the phase spectra of the transfer functions. Even when the HRTF filter response is reversed in time (experiment VI), subjects were unable to distinguish this response from the empirical HRTF responses. Only one subject (S3) in experiments II and III obtained performance significantly better than chance and only for one condition. She consistently obtained 70% correct with her right ear alone for HRTFs corresponding to a source straight ahead in distinguishing minimum-phase-plus-delay HRTFs from empirical HRTFs. (She was unable to distinguish these with the left ear or binaurally.) This exceptional subject's performance is not understood. More generally, subjects showed no sensitivity to the monaural phase spectra. This lack of monaural phase sensitivity is consistent with a previous study by Green (1971) who found no monaural temporal sensitivity for stimulus durations less than 2 ms. Note that the anechoic HRTFs used in our study were measured in anechoic space and are hence of a short duration (less than a few ms). Thus based on Green's earlier result, the lack of monaural temporal sensitivity to our anechoic stimuli is not surprising.

When listening binaurally, subjects' abilities in distin-

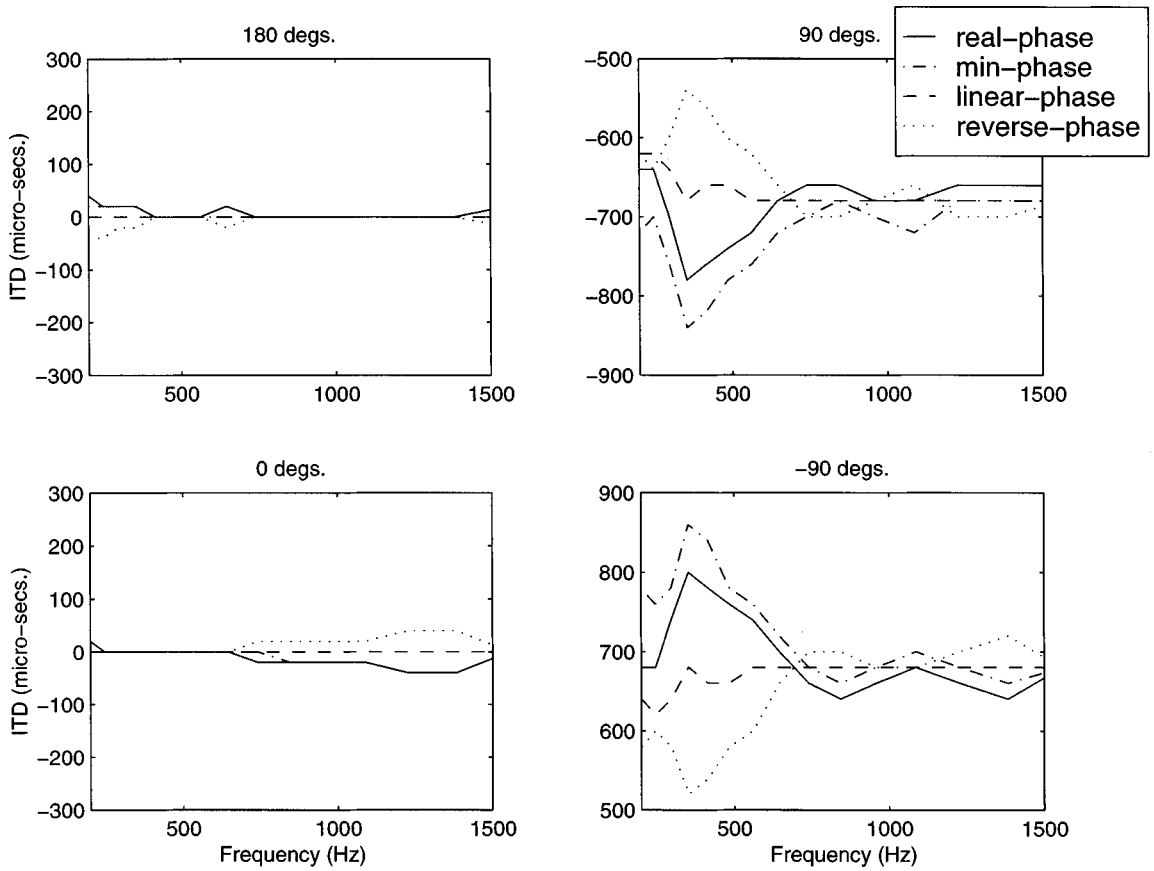

FIG. 15. ITD functions computed from the interaural processing scheme incorporating a short-term, running, cross correlation of critical-band filtered stimulus inputs. ITD spectra computed from minimum-phase-plus-delay, linear-phase, and reversed-phase-plus-delay model HRTFs are presented along with empirically based functions in each panel for the four locations tested in the psychophysical experiment. (See text.)

guishing model HRTFs with phase spectra that differed from the empirical phase spectra depended on conditions. In all experiments, the magnitude spectra and the overall (wideband) ITD were matched to the empirical value and, in the most definitive experiments, both the source position and the noise token were fixed throughout a run. When the linear-phase model HRTFs were used, subjects were unable to distinguish model and empirical phase spectra. When the minimum-phase-plus-delay model HRTFs were used, some subjects were able to distinguish model and empirical phase spectra at some locations (on the sides). When the reversed-phase-plus-delay model HRTFs were used, subjects were consistently able to distinguish model from empirical phase spectra. Supplemental experiments suggested that the useful information was being carried by the low-frequency components of the stimuli.

TABLE I. Mean ITD computed for the four HRTF conditions from a computational model involving a running, short-term cross correlation of critical-band filtered stimuli. For each location, the average ITD for frequencies below 2 kHz for each HRTF condition is presented. HRTFs of subject SDO were used for this analysis. See text for details.

	Mean ITD (across frequency) in μs			
Angle	Emp. phase	Min. phase	Lin. phase	Rev. phase
0 degs	9	6	0	−10
90 degs	−688	−729	−666	−644
180 degs	−10	−8	0	10
−90 degs	700	745	688	634

In order to analyze available interaural timing information, we calculated the ITD frequency function for the binaural stimulus conditions, for the empirical stimuli and for the three model stimuli. The ITD frequency functions essentially reflect the interaural-phase delay as a function of frequency, although an interaural time processor based on cross-correlation functions of outputs from a simple peripheral model provides similar information. All of the results shown here are consistent with the assumptions that the auditory system extracts an overall ITD from the low-frequency components of the stimulus and that two stimuli with the same overall mean ITD in the low-frequency components are predicted to be perceived equivalently, independent of the details of the ITD function. We consider the three phase models in order of simplicity of the results. First, stimuli with an ITD function having a natural frequency dependence were indiscriminable from stimuli with a constant ITD function (corresponding to the linear-phase model). Note from Table I that the mean low-frequency ITDs for empirical-phase stimuli and for linear-phase stimuli differ by at most 20 μs (for all source positions considered). This value is less than the ITD jnd with broadband stimuli at these reference ITDs that is generally reported in literature (e.g., Durlach and Colburn, 1978) for well-practiced listeners. Consistent with these data, subject performance was at

chance when distinguishing between empirical-phase and linear-phase stimuli. Second, the mean ITD computed from reversed-phase HRTFs (and shown Table I) is significantly different from the ITD computed from the empirical-phase HRTFs (by more than three times 20 μs). Consistently, all subjects reported a position cue in the reversed-phase conditions and subject performance exceeds chance in this case. In fact, the ITD differs maximally at the $\pm$90-degree positions, which is consistent with the higher performance of subjects at these positions. Third, consider the minimum-phase-plus-delay model. In this case, performance depended on the position of the virtual source: performance was above chance for the $\pm$90 degree locations and at chance for the 0-degree and 180-degree locations. The ITD from the minimum-phase-plus-delay model and the empirical ITD for the $\pm$90 degree locations, calculated according to the cross-correlation mechanism described above, are shown in Fig. 15 as functions of frequency. Although the minimum-phase-plus-delay fit to the empirical ITD is closer than the linear-phase fit for some frequencies (around 300 Hz), the linear-phase fit is closer on the average over the range of frequency up to 2000 Hz. The mean error in ITD across low frequencies is given in Table I. It can be seen that the mean minimum-phase ITD at these positions is different from the mean empirical-phase ITD by about 40 μs, which is close to the best ITD jnd reported in literature at these positions (Koehnke *et al.*, 1995). The two subjects, who are very experienced with binaural hearing experiments, reported utilizing a position cue and correspondingly performed above chance at these locations.

We conclude that the phase spectrum is relatively unimportant for anechoic HRTFs as long as the mean ITD for low-frequency components is correct. In the experiments reported here the wide-band ITD was equated in all cases. This match was adequate for the linear-phase model and for some positions with the minimum-phase-plus-delay model, but led to significant differences in the low-frequency ITDs for some positions with the minimum-phase-plus-delay model and all positions tested for the reversed-phase-plus-delay model. It is important to note that the experiments reported here are an extreme test in the sense that the context was ideal for making distinctions. There was no stimulus variability, there was no location variability, and the paired-comparison test used, a two-cue, two-interval forced-choice paradigm, is generally regarded as giving the listener the best circumstances to make distinctions.

Finally, we emphasize again that we have found no reason for concern about the adequacy of minimum-phase-plus-delay or linear-phase (pure delay) models of HRTFs when stimuli and directions are variable. Thus we believe that results of previous studies of localization (e.g., Wightman and Kistler, 1989a, b) would not be affected by using one of these models.

B. Implications for virtual acoustic stimuli

The results of the phase study have, at least, the following implications for virtual acoustical display research and implementation. First, HRTF models only need to fit the magnitude spectra of HRTFs. An overall frequency-independent ITD in addition to the accompanying minimum-phase phase function provides a perceptually adequate description of the ITD for a given position. However, an overall ITD computed from the empirical measurements over the entire spectrum can still lead to consistent discrepancies (across frequency) in the low frequencies of the minimum-phase-plus-delay model ITD spectrum. We propose that these discrepancies, which can be perceptually salient, can be minimized by making the overall low-frequency ITD in the model HRTFs to be the same as the overall low-frequency ITD in the empirical HRTFs. Note that the minimum-phase-plus-delay assumption reduces the modeling problem to fitting a real-valued function rather than fitting a complex-valued HRTF. Note also that minimum-phase HRTFs are the shortest of all FIR filter implementations. Thus the memory demands of virtual displays are least for minimum-phase model HRTFs. Modeling studies (Kistler and Wightman, 1992; Kulkarni and Colburn, 1995a, b; Blommer and Wakefield, 1994) have exploited the minimum-phase assumption to achieve low-dimensional HRTF representations. Psychophysical studies using the minimum-phase-plus-delay model with magnitude spectra that are only approximate indicate that the minimum-phase-plus-delay model is adequate for these cases as well (Kistler and Wightman, 1992; Kulkarni and Colburn, 1995a, b, 1998).

Second, the results of this study only apply to anechoic spaces. HRTF measurements in reverberant spaces include the effect of the environment on the transmission of sound in addition to the directional features of the head and pinna. The time structure of these reflections has an important contribution to our perceptions in these spaces. It would therefore be incorrect to conclude that the HRTF impulse response in a reverberant environment can be simplified to be a minimum-phase function. We suggest, however, that the individual discrete reflections constituting this impulse response can individually be approximated as minimum-phase functions.

Third, the results of this study are important with regard to the spatial interpolation of virtual space which is an important issue for all current virtual space implementations. Linear-phase HRTFs are artifact free in this regard and minimum-phase-plus-delay HRTFs result in artifacts that are small enough to be perceptually irrelevant (Tollin, 1995). This is in contrast to empirical HRTFs, which have perceptually significant artifacts associated with regards to the spatial interpolation operation (Kulkarni and Colburn, 1993; Wenzel and Foster, 1993).

V. CONCLUSIONS

In terms of hearing sensitivity, the following conclusions can be drawn from the studies reported here. It is important to keep in mind that the experiments and conclusions are all restricted to HRTFs for anechoic space. Further study is required to evaluate the attributes of the phase spectra of HRTFs that are important for characterizing reverberant spaces.

(1) The variation of the phase spectrum is not perceptually significant monaurally.
(2) Listeners are insensitive to the details of the interaural phase spectrum as long as the interaural time delay of the combined low-frequency part of the waveform is maintained.
(3) The phase-spectrum of empirically measured HRTFs, in particular the deviation about some mean frequency-independent time delay, is adequately described by a minimum-phase function for most positions.

ACKNOWLEDGMENTS

This work was supported by National Institutes of Health, NIDCD Grant No. RO1 DC00100.

[1]To test further the sensitivity to measurement error, the transfer function of the KEMAR mannequin ear canal was measured and compared to the minimum-phase-plus-delay model. The measurement was performed by delivering a Golay-code stimulus (Kulkarni, 1993) at the ear canal entrance via a Etymotic ER-2 tubephone (without the earplugs). We hypothesized that because of the simplicity of the acoustic path in the earcanal, which does not support multiple modes of transmission (Siebert, 1970), the measured impulse response should be be a minimum-phase function plus a delay. The coherence index between the measured impulse response and the minimum-phase-plus-delay impulse response was 0.99, suggesting that the measurement was very nearly minimum phase and that measurement error was not responsible for the departure of the HRTF spectra from the minimum-phase assumption. However, since there is a theoretical basis for expecting the HRTFs to be minimum-phase-plus-delay functions (Zweig, 1996), we believe that this issue merits further study.

Blauert, J. (**1997**). *Spatial Hearing: The Psychophysics of Human Sound Localization* (MIT Press, Cambridge).

Blommer, M. A., and Wakefield, G. H. (**1994**). ''On the design of pole-zero approximations using a logarithmic error measure,'' IEEE Trans. Signal Process. **42**, 3245–3248.

Brugge, J. F., Reale, R. A., Hind, J. E., Chan, J. C. K., Musicant, A. D., and Poon, P. W. F. (**1994**). ''Simulation of free-field sound sources and its application to studies of cortical mechanisms of sound localization in the cat,'' Hearing Res. **73**, 67–84.

Butler, R. A., and Belendiuk, K. (**1977**). ''Spectral cues utilized in the localization of sound in the median plane,'' J. Acoust. Soc. Am. **61**, 1264–1269.

Colburn, H. S. (**1977**). ''Theory of binaural interaction based on auditory nerve data. II. Detection of tones in noise,'' J. Acoust. Soc. Am. **61**, 525–533.

Durlach, N. I., and Colburn, H. S. (**1978**). ''Binaural phenomenon,'' in *Handbook of Perception, Vol. 4*, edited by E. C. Carterette and M. P. Friedman (Academic, New York), pp. 365–466.

Foster, S. (**1986**). ''Impulse response measurement using Golay codes,'' in *IEEE Conference on Acoustics, Speech, and Signal Processing, Vol. 2* (IEEE, New York), pp. 929–932.

Golay, M. J. (**1961**). ''Complementary series,'' IRE Trans. Inf. Theory **7**, 82–87.

Green, D. M. (**1971**). ''Temporal auditory acuity,'' Psychol. Rev. **78**, 540–551.

Kistler, D. J., and Wightman, F. L. (**1992**). ''A model of head-related transfer functions based on principal components analysis and minimum-phase reconstruction,'' J. Acoust. Soc. Am. **91**, 1637–1647.

Koehnke, J., Culotta, C. P., Hawley, M. L., and Colburn, H. S. (**1995**). ''Effects of reference interaural time and intensity differences on binaural performance in listeners with normal and impaired hearing,'' Ear Hear. **16**, 331–353.

Kuhn, G. (**1977**). ''Model for the interaural time differences in the azimuthal plane,'' J. Acoust. Soc. Am. **62**, 157–167.

Kulkarni, A. (**1993**). ''Auditory imaging a virtual acoustical environment,'' Masters Thesis, Boston University.

Kulkarni, A., and Colburn, H. S. (**1993**). ''Evaluation of a linear interpolation scheme for approximating head-related transfer functions,'' J. Acoust. Soc. Am. **93**, 2350.

Kulkarni, A., and Colburn, H. S. (**1995a**). ''Infinite-impulse-response models of the head-related-transfer-function,'' J. Acoust. Soc. Am. **97**, 3278.

Kulkarni, A., and Colburn, H. S. (**1995b**). ''Efficient finite-impulse-response models of the head-related-transfer-function,'' J. Acoust. Soc. Am. **97**, 3278.

Kulkarni, A., and Colburn, H. S. (**1998**). Nature (London) **396**, 747–749.

McKinley, R. L., and Ericson, M. A. (**1977**). ''Flight demonstration of a 3-D audio display,'' in *Binaural and Spatial Hearing in Real and Virtual Environments*, edited by R. H. Gilkey and T. A. Anderson (Erlbaum, Mahwah, NJ), pp. 683–699.

Mehrgardt, S., and Mellert, V. (**1977**). ''Transformation characteristics of the external human ear,'' J. Acoust. Soc. Am. **61**, 1567–1576.

Middlebrooks, J. C., and Green, D. M. (**1991**). ''Sound localization by human listeners,'' Annu. Rev. Psychol. **42**, 135–159.

Middlebrooks, J. C. (**1992**). ''Narrow-band sound localization related to external ear acoustics,'' J. Acoust. Soc. Am. **92**, 2607–2624.

Oppenheim, A. V., and Schafer, R. W. (**1989**). *Discrete-Time Signal Processing* (Prentice-Hall, Englewood Cliffs, NJ).

Patterson, R. D., Robinson, K., McKeown, D., Zhang, C., and Allerhand, M. H. (**1992**). ''Complex sounds and auditory images,'' in *Auditory Physiology and Perception*, edited by Y. Cazals, L. Demany, and K. Horner (Oxford Pergamon, New York), pp. 429–446.

Siebert, W. M. (**1970**). ''Simple model of the impedance matching properties of the external ear,'' Research Laboratory of Electronics QPR, No. 96 (MIT, Cambridge, MA).

Tollin, D. J. (**1995**). ''Analysis of linear interpolation reconstructions of human head-related-transfer functions,'' B.S. Thesis, Biomedical Engineering Department, Boston University, May 1995.

Wenzel, E. M. (**1992**). ''Localization in virtual acoustic displays,'' Presence: Teleoperators and Virtual Environments, **1**, 80–107.

Wenzel, E. M., and Foster, S. H. (**1993**). ''Perceptual consequences of interpolating head-related transfer functions during spatial synthesis,'' Proceedings of the ASSP (IEEE) Workshop on Applications of Signal Processing to Audio and Acoustics, New Paltz, NY, Oct. 17–20. Environments, Vol. 1, pp. 80–107.

Wightman, F. L., and Kistler, D. J. (**1989a**). ''Headphone stimulation of free-field listening I: Stimulus synthesis,'' J. Acoust. Soc. Am. **85**, 858–867.

Wightman, F. L., and Kistler, D. J. (**1989b**). ''Headphone stimulation of free-field listening II: Psychophysical validation,'' J. Acoust. Soc. Am. **85**, 868–878.

Wightman, F. L., and Kistler, D. J. (**1992**). ''The dominant role of low-frequency interaural time differences in sound localization,'' J. Acoust. Soc. Am. **91**, 1648–1661.

Zweig, G. (**1996**). Personal communication.

Resolution of front–back ambiguity in spatial hearing by listener and source movement

Frederic L. Wightman
Department of Psychology and Waisman Center, University of Wisconsin—Madison, Madison, Wisconsin 53705

Doris J. Kistler
Waisman Center, University of Wisconsin—Madison, Madison, Wisconsin 53705

(Received 29 January 1998; revised 20 May 1998; accepted 19 February 1999)

Normally, the apparent position of a sound source corresponds closely to its actual position. However, in some experimental situations listeners make large errors, such as indicating that a source in the frontal hemifield appears to be in the rear hemifield, or vice versa. These front–back confusions are thought to be a result of the inherent ambiguity of the primary interaural difference cues, interaural time difference (ITD) in particular. A given ITD could have been produced by a sound source anywhere on the so-called ''cone of confusion.'' More than 50 years ago Wallach [J. Exp. Psychol. **27**, 339–368 (1940)] argued that small head movements could provide the information necessary to resolve the ambiguity. The direction of the change in ITD that accompanies a head rotation is an unambiguous indicator of the proper hemifield. The experiments reported here are a modern test of Wallach's hypothesis. Listeners indicated the apparent positions of real and virtual sound sources in conditions in which head movements were either restricted or encouraged. The front–back confusions made in the restricted condition nearly disappeared in the condition in which head movements were encouraged. In a second experiment head movements were restricted, but the sound source was moved, either by the experimenter or by the listener. Only when the listener moved the sound source did front–back confusions disappear. The results clearly support Wallach's hypothesis and suggest further that head movements are not required to produce the dynamic cues needed to resolve front–back ambiguity.
[S0001-4966(99)05005-5]

PACS numbers: 43.66.Qp, 43.66.Pn, 43.66.Yw [DWG]

INTRODUCTION

The cornerstone of psychoacoustics is complete and precise stimulus control. Without it few meaningful conclusions can be drawn about the relationships between stimuli and the perceptions associated with them. Unfortunately, complete stimulus control is typically achievable only in an artificial laboratory environment. In the case of research on spatial hearing, for example, experiments are often carried out in a soundproof anechoic chamber. The listener is deprived of visual cues and required to remain motionless while single abstract stimuli are presented. In everyday life most listeners hear multiple sources, echoes, and other environmental effects, and they are free to move around in the environment. Whether or not these differences between the laboratory and everyday life limit the generalizability of the laboratory results is a matter of debate.

There are at least two potentially troublesome consequences of conducting spatial hearing research in artificial environments. First, effects which are important in everyday sound localization may be minimized or masked in a laboratory environment. For example, the accuracy of sound localization, expressed in terms of the correspondence between the actual source position and the apparent position, is almost certainly better in the absence of room reflections or the interference created by other sources than in everyday life (Hartmann, 1983; Rakerd and Hartmann, 1985). This is of little concern if our interest is in the limits of our auditory spatial resolving power. However, it may be that listeners adopt localization strategies that differ depending on whether reflections are missing or present. If so, results from laboratory studies may not be generalizable. Second, the austere acoustical environment of the laboratory may exaggerate certain sound localization behaviors that are rarely observed in everyday life. An example of this is a front–back confusion, a kind of localization error in which a listener indicates an apparent source position in the wrong hemifield. The focus of the research reported in this article is on this second problem, particularly front–back confusions and the strategies listeners might use in everyday life to avoid them.

A front–back confusion is said to have occurred when a listener indicates an apparent source position in the rear hemifield when the actual source is in front. Thus, a source might be presented in the horizontal plane at an azimuth of 30 degrees (which is in the frontal hemifield) and the listener might indicate its apparent position as 150 degrees (in the rear hemifield). Back–front confusions also occur, but for convenience we usually refer to either kind as ''front–back'' confusions. In many laboratory situations the frequency of front–back confusions is high, with the data from some listeners suggesting a confusion rate as great as 50% (Wenzel *et al.*, 1993). Experiments in which listeners localize virtual sources often produce higher front–back confusion rates than those involving localization of real sources (Wightman and

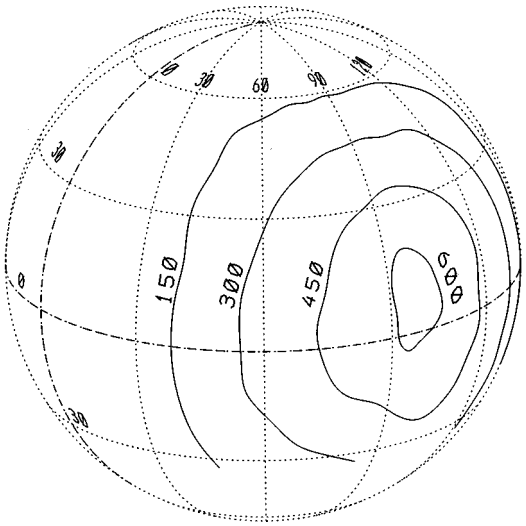

FIG. 1. Contours of constant ITD (in μs) displayed on a globe. The ITDs were estimated from the HRTF measurements of a single listener. Smooth contours were derived from cubic spline fits to the ITD estimates. The listener is facing 0 degrees longitude and the listener's ears are centered at 0 degrees latitude.

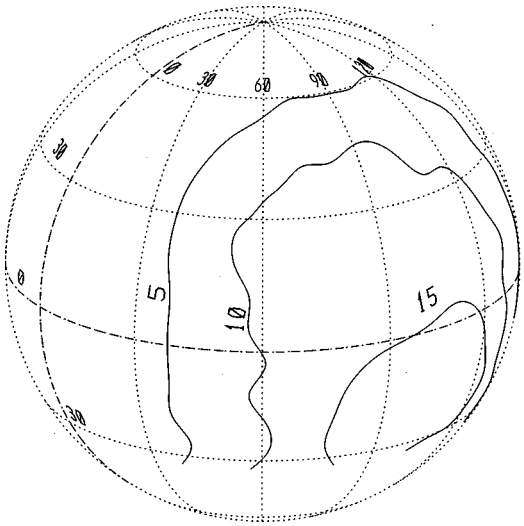

FIG. 2. Contours of constant interaural level difference (ILD, in dB) obtained by subtracting the overall level of the right ear HRTFs (0 Hz to 14 kHz, in dB) from the overall level in the left ear HRTFs.

Kistler, 1989b; Oldfield and Parker, 1984; Makous and Middlebrooks, 1990; Bronkhorst, 1995). There are large individual differences. Some listeners make a large number of front–back confusions and others almost none. Also, about half of the listeners who make confusions make mostly front–back confusions and about half make mostly back–front confusions (Wenzel *et al.*, 1993). While there are no data of which we are aware on the frequency of front–back confusions in everyday life, it is difficult to accept the possibility that the rate is nearly as high as has been demonstrated in the laboratory.

To the extent that the apparent position of a sound source depends on acoustical cues derived from interaural differences, front–back confusions are expected. Figure 1 shows contours of constant difference in time-of-arrival of a sound at the two ears (interaural time difference, or ITD) as a function of the azimuth and elevation of a sound source. Note that for any azimuth in front (azimuths between 0 and 90 degrees) there exists an azimuth in the rear (azimuths between 90 to 180 degrees) that produces the same ITD. Thus, if apparent position were determined only by ITD, source positions in the front and rear would be confused. The contours of constant ITD on Fig. 1 indicate the locus of source positions which produce the same ITD, and thus the locus of source positions which would be confused if ITD were the only cue. Figure 2 shows the difference in stimulus level at the two ears (interaural level difference, or ILD) as a function of the azimuth and elevation of the source. Note that ILD is also an ambiguous cue to source position, since it assumes a particular value not for a single source position but for an entire locus of source positions.

It was suggested more than half a century ago that head movements can provide the information necessary to resolve front–back ambiguities. If a source is off to the side in front and the listener orients toward it, both ILD and ITD decrease. If the source had been in the rear and the listener had made the same head movement, both ILD and ITD would have increased. Thus, the direction of change of ILD and/or ITD could be used to resolve a front-back confusion. Wallach (1940) was perhaps the first to articulate the details of this hypothesis, and both Young (1931) and Wallach (1939, 1940) offered convincing empirical evidence of the connection between head movements and front–back confusions. In Young's experiments (1931), listeners localized repeated clicks presented through sealed rubber tubes connecting ear trumpets to the ear canals. The ear trumpets were immobile, thus preventing the listener's head movements from causing the usual changes in interaural stimulus parameters. The clicks were presented from a number of directions relative to the trumpets, but all apparent source positions were in the rear, suggesting that with head movement cues removed, front–back confusions appeared. Wallach (1939, 1940) assessed the role of head movements by creating an ingenious switching arrangement whereby the rotational position of a listener's head controlled the direction of the sound source in relation to the listener. Sources were arranged in an arc around the listener, with the position of the listener's head determining which source was active at any given time. By switching from one source to another as the listener's head rotated, Wallach was able to simulate the interaural consequences of a stationary rear source by moving a frontal source through twice the angle of the head movement. Listeners' localization judgments from conditions in which they moved their own heads confirmed the success of the simulation. In addition, Wallach's data (1940) suggested that actual movement of the head was not necessary for the cues to be salient. In one condition Wallach rotated the listener's chair, while the listener was seated and immobile. This produced the same illusion, suggesting that proprioceptive feedback from the neck musculature was not important for extracting the movement information. In another condition Wallach induced an *illusory* perception of self movement (by rotating a screen around the seated listener) and found the same illusion of a rear source occurred if a frontal source were rotated in the opposite direction at double the

angular rate of the visual field, even though the listener was not moved at all. This latter result rules out contributions from both neck muscles and the vestibular system.

Other research on the role of head movements generally confirms Wallach's (1939, 1940) and Young's (1931) findings. For example, Pollack and Rose (1967) report higher accuracy in horizontal plane localization when a long-duration noise burst stimulus is presented during a head movement than when the same stimulus is presented with the head not moving. Thurlow and Runge (1967) induced a listener's head movements with a mechanical apparatus during a localization task and report that a substantial decrease in the frequency of front–back confusions accompanies a rotational movement, while there is only a modest decrease with pivot (head tilt) movements. Finally, Bronkhorst (1995) reports that front–back confusion rate is low when listeners orient their heads toward a long-duration sound source but high when listeners localize a short-duration stimulus without head movement.

Recent research reported by Perrett and Noble (1997a, b) provides additional and more comprehensive tests of Wallach's hypotheses. In one set of experiments, Perrett and Noble (1997a) measured the accuracy with which listeners could localize the source of a 2-kHz low-pass filtered noise burst, both with and without head movement. Sources were positioned on the horizontal and median vertical planes, and listeners indicated the apparent source position with a laser pointer attached to a headband. In a head-motionless condition listeners made large numbers of front–back confusions, not a surprising result given that the spectral cues normally provided by the pinnae had been removed by the low-pass filtering. When listeners were instructed to move their heads naturally or to make a single 45° head rotation during stimulus presentations, front–back confusions nearly disappeared, in agreement with Wallach's predictions. In the second set of experiments, Perrett and Noble (1997b) tested Wallach's hypothesis that elevation perception would also be more accurate with head movements. This hypothesis suggests that listeners could use the rate at which the interaural cues changed with head rotation as an indicator of source elevation (interaural cues change less rapidly with a source at higher elevations). Listeners localized noise bursts produced by loudspeakers positioned on the vertical median and lateral vertical planes. As long as the noise bursts contained low-frequency energy, elevation was more accurately reported with head rotation than without, even when pinna cues were distorted. This result offers convincing support for Wallach's hypothesis about the use of dynamic cues for elevation perception. In both sets of experiments Perrett and Noble (1997a, b) report substantial individual differences.

The research reported in this article attempts to extend and elaborate the earlier studies. In particular, we pursue Wallach's observation that actual listener movement is not required for the role of dynamic cues to be important. We highlight the issue of individual differences by selecting as listeners both those individuals who, in normal experimental conditions, make large numbers of front–back confusions and those who make very few. The experiments capitalize on the availability of modern technology by using virtual sources (Wightman and Kistler, 1989a b, 1992, 1997b) with which precise stimulus control is straightforward. Two experiments are reported.[1] In the first, listeners judge the apparent positions of real or virtual sources in one of three head movement conditions: (1) listeners are instructed not to make head movements (both real and virtual sources); (2) listeners are encouraged to make whatever movements they feel might help them to localize the sources (both real and virtual sources); (3) listeners are instructed to make orienting movements toward the apparent position of the source (virtual sources only). This first experiment is intended as further confirmation of Wallach's (and others') hypotheses about the utility of head movement cues. The second experiment asks listeners to judge the apparent starting position of a moving source. Head movements are discouraged in the second experiment. In one condition the source is moved by the experimenter and in another condition the listener moves the source. The second experiment is intended as a further exploration of Wallach's suggestion that actual head movement is not required to resolve front–back ambiguity.

I. GENERAL METHOD

A. Listeners

A total of eight individuals served as paid volunteers in the experiments. Not all listeners participated in all experiments, but no fewer than four listeners participated in any one experiment. Three listeners participated in all experiments. The listeners were college students with normal hearing, as verified by standard clinical audiometry, with ear canals free of wax, and with no history of hearing problems.

B. Stimuli

The stimulus for all experiments was a burst of white Gaussian noise, generated independently for each trial, the duration of which was either 2.5 or 1 s depending on condition. In real source conditions the noise burst was presented at roughly 70 dB SPL from 1 of 15 small, digitally equalized loudspeakers (Radio Shack Minimus 3.5) mounted with 10-degree spacing on a vertical semicircular arc in an anechoic chamber. The listener's head was at the center of the arc, 1.4 m from the loudspeakers. The arc could be rotated around the listener, thus permitting source locations at any azimuth and at 10-degree intervals of elevation (from 90 degrees, directly overhead, to −50 degrees below the horizontal plane). Between trials the arc was repositioned by an assistant who remained in the chamber during testing.

Virtual sources, which were presented over headphones to listeners seated in a double-walled sound room, were synthesized by convolving the noise burst, at a 50-kHz/channel sample rate in real time, with the impulse response of a FIR digital filter. The filter characteristics were derived from minimum-phase versions (Kistler and Wightman, 1992) of the listener's own head-related transfer functions (HRTFs), which are the transfer functions from the desired point in the anechoic chamber to the listener's two eardrums. The digital filter also incorporated compensation for the response of the headphone (Sennheiser HD430) measured on the listener's ears. Details of the synthesis procedures can be found in

Wightman and Kistler (1989a). The current procedures for measuring the HRTFs are similar in concept to those described by Wightman and Kistler (1989a), and the interested reader is referred there for more detail. A 0.95-mm flexible silicone probe tube was inserted in the ear canal so that the tip was very close to the listener's eardrum. A wideband periodic noise test stimulus was then presented from a loudspeaker. The position of the probe relative to the eardrum was determined with an adaptive acoustical procedure which searched for the pressure node caused by interference between incoming and reflected sound waves. A microphone (Etymotic ER7-C) connected to the probe tube recorded the response to the test stimulus and a computer averaged the responses to multiple periods to improve signal-to-noise ratio. The HRTFs were measured simultaneously from both ears at 505 source positions (at 10-degree azimuth intervals all around the listener and at 10-degree elevation intervals from -50 to $+90$ degrees relative to the horizontal plane) during a single 30-min session.

In those conditions in which head tracking was required, the listener's head orientation was measured by a Polhemus (Isotrack or Fastrack) magnetic tracker, which was interfaced either to a Crystal River Convolvotron (experiment 1) or to a Tucker-Davis Power-Dac system (experiment 2). The tracker's receiver was mounted on a small plastic headband worn by the listener and the source was mounted no more than 50 cm from the listener's head. In the head movement conditions of experiment 1, the tracker's reports of head orientation (25–30/s) were routed to PC software which updated the HRTFs used to synthesize the virtual sources in order to simulate a stationary external source. Since HRTFs were measured at 10-degree intervals of azimuth and elevation, interpolation was required to simulate a motionless source during head movement. Bilinear interpolation[2] of the nearest four measured HRTFs was found to produce effective simulations. Informal conversations with the listeners suggested that even during very rapid head movements, there was no ''jerkiness'' or ''sluggishness'' of the synthesis system, and virtual images were stable and externalized.

C. Procedure

The experiments required listeners to judge the apparent direction and distance of both real and virtual sources. They did this by giving verbal reports of apparent azimuth, elevation, and distance (Wightman and Kistler, 1989b, 1992, 1997a, b; Kistler and Wightman, 1992). The listeners were instructed in how to use the coordinate system (a standard spherical, or ''world'' coordinate system) during a single 30-min training session conducted outside the anechoic chamber in which the listeners were tested. Next listeners completed two 2-h sessions of practice trials with real sources. These blocks of trials were identical to the test blocks except that the data were not included in the final analysis. In both practice and test blocks there was no feedback regarding actual or intended source position, and listeners were blindfolded except in the one condition in which the listeners used a keyboard to control the source position.

A typical 2-h session consisted of about four blocks of trials interspersed with breaks. In the virtual source conditions, each block of trials included 156 stimulus presentations with directions chosen to form a representative subset of the 505 directions from which HRTFs had been measured. In the real source conditions, there were 72 stimulus presentations in each block of trials. The 72 source directions were a representative selection of the 156 positions tested in the virtual source conditions. Fewer presentations were possible with real sources since some time was required to move the speaker arc between trials. In each of the experiments, the apparent positions of the 72 real sources were judged approximately four times each by each listener, and the apparent positions of the 156 virtual sources were also judged approximately four times each.

D. Data analysis

Because of the fact that in our experiments the distributions of apparent position judgments are frequently multimodal, we do not compute measures of central tendency or dispersion. Instead, we display raw data and develop interpretations based on visual inspection of those data displays. Moreover, since individual differences are often large, the data from each listener are considered separately.

The azimuth and elevation reports are displayed in a three-pole coordinate system, first described by Kistler and Wightman (1992). The azimuth and elevation coordinates are transformed into right–left, front–back, and up–down angles. The right–left angle is the angle subtended by the judgment vector and the median plane, and the front–back angle is the angle subtended by the judgment vector and the lateral vertical plane (vertical plane that includes the interaural axis). The up–down angle is the same as the elevation angle in the response. All three angles are plotted in separate graphs. Thus, a given response appears in all three plots. The main advantage of the three-pole plots for our purposes here is that front–back confusions, which appear only in the front–back panels of the data displays, are readily identified. Prior to graphing the data points are ''jittered'' slightly by adding a uniform random deviate (± 2.5 degrees) to the coordinates to eliminate the overlap resulting from duplicate responses to a given target (Cleveland, 1985). Figure 3 demonstrates the variability that results from the jittering technique when the positions of all sources are reported with no error. Figure 3 also shows the data from a listener judging the apparent positions of virtual wideband noise sources. To facilitate comparisons across conditions, the data are summarized by computing the correlation (Pearson) between target and judgment coordinates for each of the three dimensions, separately for each listener.

The right–left component of the judgments was nearly the same as that shown in Fig. 3 for all listeners in all conditions of the experiments reported in this article (correlations ranged from 0.87 to 0.98 with a median of 0.96). In other words, the right–left dimension was perceived reasonably accurately in all cases, and no stimulus manipulation seemed to affect that perception. For this reason, and to conserve space, no additional right–left data are shown.

The listeners also reported apparent distance, but a detailed analysis of the distance data is not presented. All reports indicated externalized sound images (no estimates were

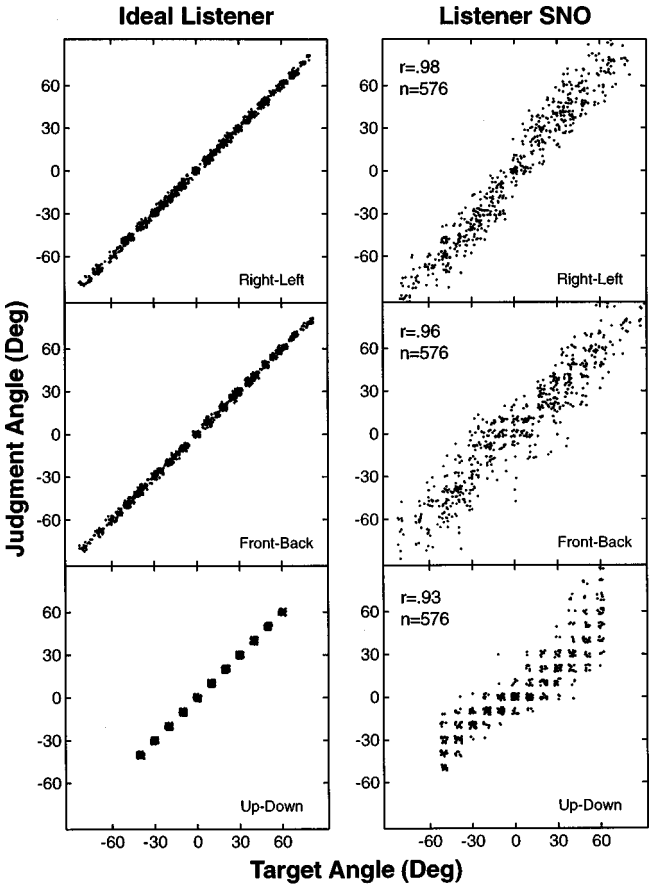

FIG. 3. Scatterplots of judged and target directions represented in terms of three angles, right–left, front–back, and up–down, for an ''ideal'' localizer and for listener SNO. The locations of the 576 data points plotted in each panel were ''jittered'' (see text) to minimize overlap.

smaller than 30 cm). Average distance estimates obtained for each listener in each condition ranged from 1 to 2 m with individual standard deviations of about 1 cm. None of the experimental manipulations had an effect on the distance reports (e.g., head movements did not cause an increase in apparent distance), so we view the distance data as relatively uninformative.

II. EXPERIMENT 1: THE ROLE OF HEAD MOVEMENT

A. Methods

This experiment included three conditions: ''restricted'' in which listeners were encouraged to keep their heads stationary; ''freestyle'' in which head movement to aid localization was encouraged; and ''compulsory'' in which listeners were instructed to orient (point the nose) toward the source on each trial. The restricted and freestyle conditions were tested with both real and virtual sources. In the restricted condition head position was monitored, but the stimulus position was not coupled to head position. In this condition, trials on which head movements were greater than 3 degrees in either azimuth, elevation, or tilt parameters were discarded. Examination of the movement records suggests that listeners were reasonably compliant with the various head movement instructions.

B. Results

1. Analysis of apparent position judgments

Seven listeners were tested in the three conditions of this experiment. Figure 4 shows the front–back and up–down components of the judgments to the real sources in both restricted and freestyle conditions. Figure 5 shows comparable data from the conditions in which virtual sources were presented. All the data contributed by each listener are shown. However, some listeners contributed more data than others. The target–judgment correlations are displayed in the upper left corner of each panel, and the number of judgments contributed by each listener is also indicated in the upper left corner of each panel.

The restricted condition in which stimuli were presented from real sources is much like a traditional localization condition. Blindfolded and motionless listeners indicate the apparent positions of sound images produced by loudspeakers in an anechoic chamber. Thus, results from this condition constitute a control, against which results from other experiments and the other conditions of this experiment can be contrasted. Note that, in this condition, three of the seven listeners (SMQ, SMW, and SNF) make substantial numbers of front–back confusions, revealed by responses well off the major diagonal in the front–back panels of Fig. 4. Two of the listeners (SNJ and SMU) participated in all conditions of both experiments and made very few front–back confusions in any condition.

A comparison of the response patterns from the real-source (Fig. 4) and virtual-source (Fig. 5) conditions reveals the adequacy of the virtual-source synthesis techniques, in much the same way as was shown previously (Wightman and Kistler, 1989b). The virtual source data in Fig. 5 are consistent with the typical finding that the rate of front–back confusions is often higher with virtual sources, even when those sources are synthesized from listeners' own HRTFs. However, some of the listeners who rarely make front–back confusions with real sources (SNJ and SMU) make very few with virtual sources as well. Note also that the patterns of responses in the up–down dimension are the same with real and virtual sources.

Figures 4 and 5 also show the apparent position data from the freestyle conditions, in which head movements were encouraged. Three points can be made. The first is that with real sources no listener made more than a few front–back confusions. This is entirely consistent with results from other experiments in which listeners were encouraged to move their heads (e.g., Bronkhorst, 1995; Perrett and Noble, 1997a) and supports Wallach's (1939, 1940) arguments that head movements can provide information for resolving front-back ambiguities. The second point is that with virtual sources front–back confusions appear to be nearly, but not completely, eliminated in the freestyle condition. Note that listeners SNY and SMW, who made large numbers of front–back confusions in the restricted conditions, still make some confusions in the freestyle virtual source condition, although the rate is much reduced. One difference between the movement cues provided by real and virtual sources is that the cues are slightly delayed in the virtual source conditions.

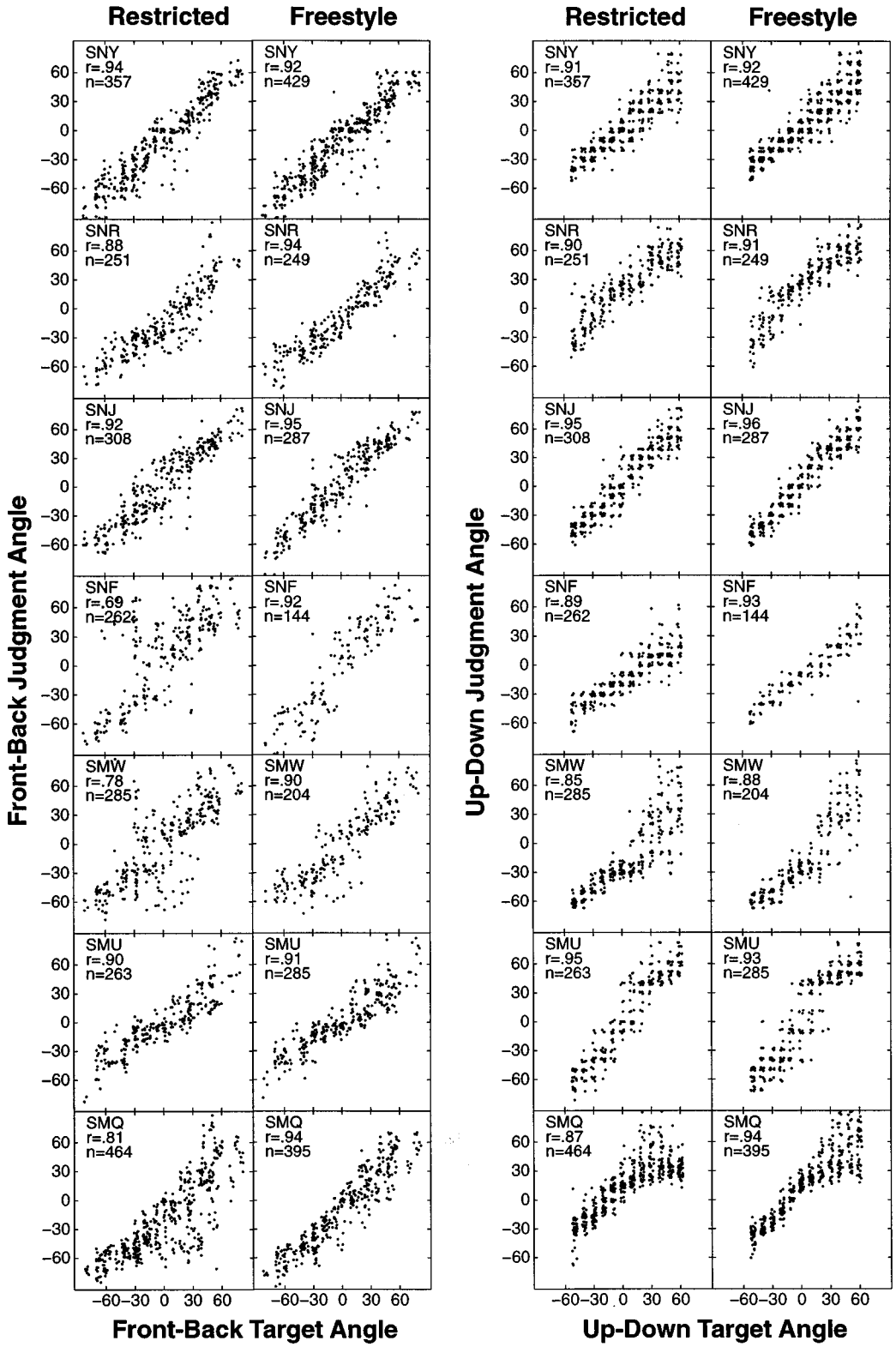

FIG. 4. Scatterplots of judged direction versus target direction from all seven listeners in both the restricted and freestyle real source conditions of experiment 1. The front–back components of the judgments to real sources are shown at the left and the up–down components are shown at the right. Correlations (Pearson) between judged and target directions and the number of judgments are given in the upper left corner of each panel.

There are inescapable delays, on the order of tens of milliseconds, between a head movement and the resultant HRTF updating that would cause the source position cues (ITD, for example) to lag the actual head position. It is possible that this lag interfered with listeners' ability to extract the necessary information to resolve all ambiguities. Nevertheless, the main finding is clear: front–back ambiguities can be resolved by listener-initiated head movements. A third point is that the patterns of listener judgments on the up–down dimension are the same in the restricted and freestyle conditions.

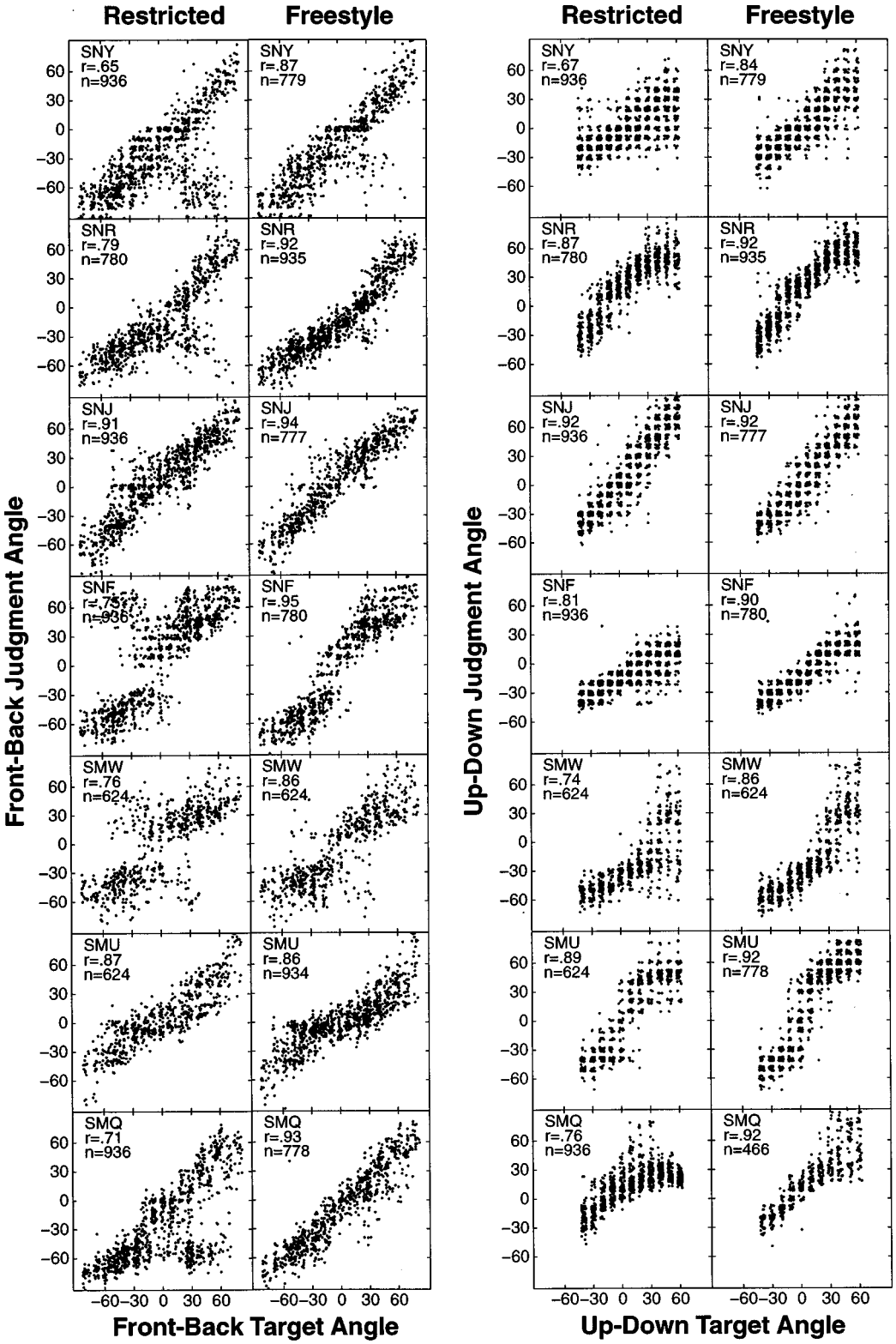

FIG. 5. Same as Fig. 4, but the data are from the virtual source conditions.

Although the Freestyle conditions encouraged listeners to use head movements, there was no control over the type of head movements chosen by the listeners (cf. Perrett and Noble, 1997a, b). Any movement which included a rotation around the vertical axis through the head would provide the necessary cues for resolving front–back ambiguities (Wallach, 1940). However, since some listeners still made a number of front–back confusions in the virtual source conditions (e.g., SNY and SMW), the head movements made by those listeners may have been inadequate in some way. The compulsory movement condition, which asked listeners to orient toward the source, was included in part as a control over the type of head movements made by the listeners. In this condition, only virtual sources were presented. Figure 6

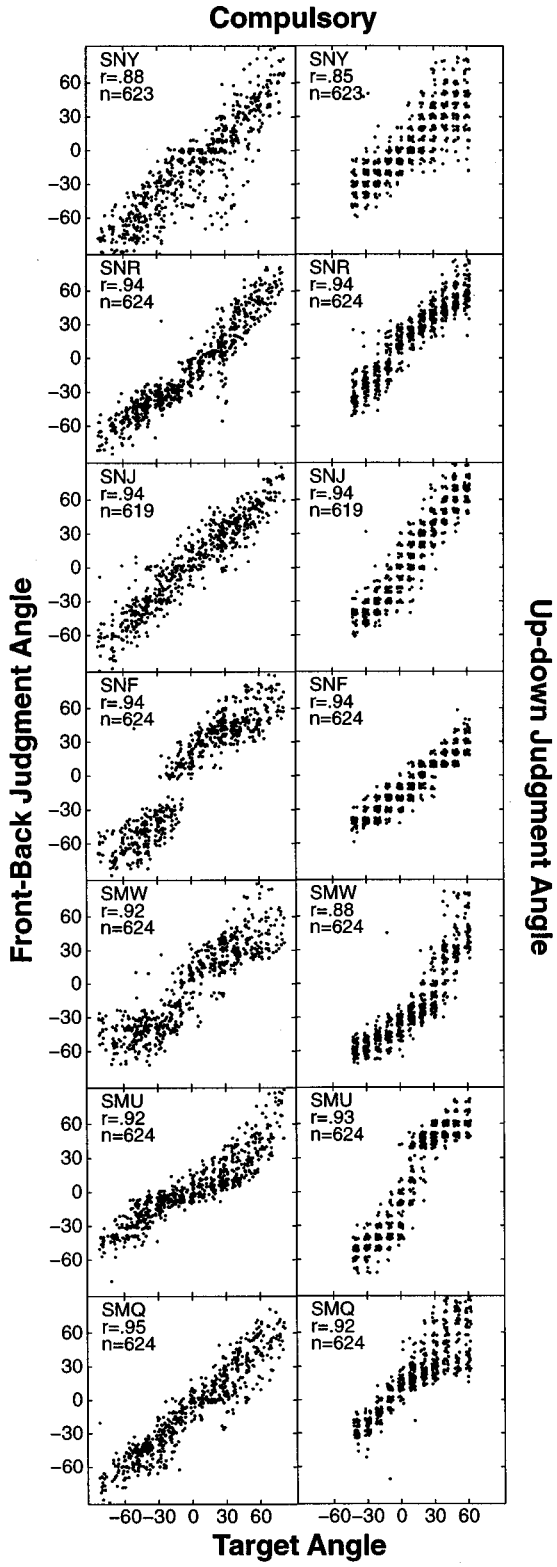

FIG. 6. Same as Fig. 4, but the data are from the virtual source compulsory head movement conditions, and the front–back components of the judgments are in the left column and the up–down components are in the right column.

shows apparent position judgments in the compulsory condition. Note that for all but one listener (SNY), front–back confusions are almost completely eliminated in this condition. Target–judgment correlations in the front–back dimension exceeded 0.92 for six of the seven listeners in this condition. The pattern of judgments in the compulsory movement condition is nearly identical to that in the freestyle real source condition. Thus, it appears that, with some coaching, listeners can make the type of head movement required for resolution of nearly all front–back ambiguities, with virtual sources as well as with real sources.

There is both theoretical (Wallach, 1940) and empirical (Thurlow *et al.*, 1967; Perrett and Noble, 1997b) support for the suggestion that head movements may also provide important information for perception of source elevation. Elevation (up–down) confusions are also expected, given the ambiguity of ITD and ILD cues (see Figs. 1 and 2), but there are relatively few reports of their presence in studies of sound localization (e.g., Wenzel *et al.*, 1993; Bronkhorst, 1995). The results shown here (Figs. 4–6) suggest that head movements are relatively unimportant for the perception of the elevation of wideband sources. Not only is there no difference in the patterns of elevation judgments between the restricted condition and the two movement conditions, but it is also the case that those listeners who demonstrate rather poor elevation perception (e.g., SMW and SNY), especially in the restricted virtual source condition, show only a modest improvement in the movement conditions. One listener (SMW) produced a pattern of elevation judgments with virtual stimuli (Fig. 5) that was suggestive of up–down confusions (target elevation high, judgment low), and this pattern changed when head movement was encouraged such that the confusions appeared to have been eliminated (see especially Fig. 6). However, such an effect was not observed in the data from any of the other listeners. It should be noted that our results are for wideband sources only. Perrett and Noble (1997b) found elevation perception to be improved by head movements, especially if high frequencies were eliminated from the stimuli. However, in their experiments the sound sources were positioned only on the median and lateral vertical planes, and the effect of head movement on elevation accuracy was large only for low-pass sources on the median plane. Our data include judgments at many more source positions, most of which are not on either of the planes studied by Perrett and Noble (1997b). Thus, it is possible that the elevation improvements reported by Perrett and Noble (1997b) are masked in our data, either because we used broadband stimuli or because we studied a wider range of source positions.

2. Analysis of head movement trajectories

In all but the restricted virtual source condition of this experiment, the orientation of the listener's head was continuously monitored during each trial. Thus, from stimulus presentation to listener response a record (25–30 reports/second) was kept of head azimuth (yaw), elevation (pitch), and tilt (roll). These data were examined to address a number of questions. The first was compliance in the restricted real source condition. Recall that trials were excluded if any one of the three head orientation parameters changed more than 3 degrees during a trial. For all listeners this meant than some trials were excluded. However, the percent of trials excluded differed considerably from listener to listener. Table I lists

TABLE I. Percent of trials in the real source restricted condition on which each listener's head movement was 3 degrees or greater in azimuth, elevation, or tilt. Trials were excluded if movement in any of the three directions exceeded 3 degrees. The percent of trials excluded is in the rightmost column.

Listener	Azimuth	Elevation	Tilt	Trials excluded
SMQ	0.00	0.21	0.00	0.21
SMU	4.86	6.25	2.08	8.68
SMW	0.00	1.04	0.00	1.04
SNF	4.51	4.86	1.39	8.68
SNJ	5.56	11.11	5.56	14.44
SNR	20.28	23.06	15.00	30.28
SNY	12.50	10.19	3.94	17.13

the percent of trials excluded for each listener. Note that all but one listener could be considered reasonably compliant.

The second issue addressed by analysis of the head movement trajectories is the extent and nature of head movement in conditions in which it was encouraged (the freestyle and compulsory conditions). A thorough visual examination of plotted trajectories from all listeners reveals a number of interesting features. First, head movement trajectories were highly idiosyncratic. Second, there was no obvious difference in the trajectories from freestyle and compulsory conditions, and no difference that depended on whether listeners were localizing real or virtual sources. It appeared to be the case that most listeners in the freestyle condition adopted an orienting strategy, and that movement in the compulsory condition was only somewhat more extensive, not different in style. Third, only listeners who demonstrated a substantial number of front–back confusions made large head movements in the freestyle condition. This is perhaps the most interesting result from our visual analysis of head movement trajectories. It implies that listeners may have been aware of the fact that they made front–back confusions (in spite of the fact that there was no feedback regarding the actual source position) and used head movements explicitly to resolve the ambiguity that led to those confusions. Informal questioning of listeners who did not make large head movements elicited comments such as, ''I don't need to move my head, and it doesn't help when I do.''

Figure 7 shows sample head movement trajectories from one listener in the virtual source conditions. This listener (SMQ) made a large number of front–back confusions in the restricted condition (Figs. 4 and 5). Trajectories recorded from four representative trials are shown, with separate tracks for freestyle and compulsory conditions. The virtual target position is indicated, as well as the centroid of that listener's confusions to the same target in the restricted condition, and the apparent position judgment on the trial shown. For this listener, in either the freestyle or compulsory condition, the movement trajectories suggest an initial orientation toward the confused location, with later movement toward the actual location. Such a suggestive movement pattern was not produced by all listeners.

Figure 8 shows sample movement trajectories from a listener who does not make many front–back confusions (SNJ). Note that in the freestyle condition there was essentially no head movement, on each of the trials shown. This is

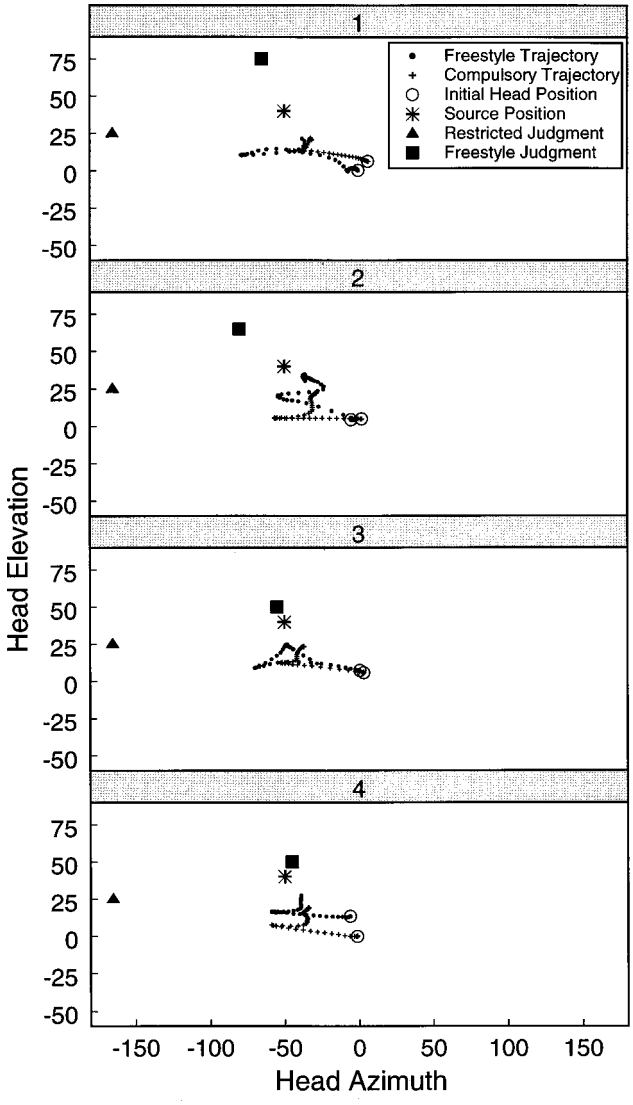

FIG. 7. Head movement trajectories from four trials in which the listener (SMQ) judged the apparent position of the same virtual source. Trajectories are shown from both the freestyle and compulsory conditions. The nominal target position is indicated by the* symbol, the centroid of the listener's judgments to the same stimulus in the restricted condition is indicated by ▲, and the judgment for the freestyle trial is indicated by ■. The head orientation at the start of the trial is indicated by the circles. The dots (freestyle) and pluses (compulsory) indicate head trajectory sampled at equally spaced time intervals.

a typical pattern of head movements for those listeners who do not make front–back confusions. Apparently, through long experience these listeners become aware of their ability to resolve front from rear sound source locations without head movements, and they simply do not make them unless required by the task (the compulsory condition). Differences in the acoustical cues available to these listeners and those who make large numbers of front–back confusions could not be revealed by a detailed analysis of the HRTFs.

III. EXPERIMENT 2: THE ROLE OF SOURCE MOVEMENT

A. Methods

In the first condition of this experiment the listener's task was to judge the apparent starting position of a virtual

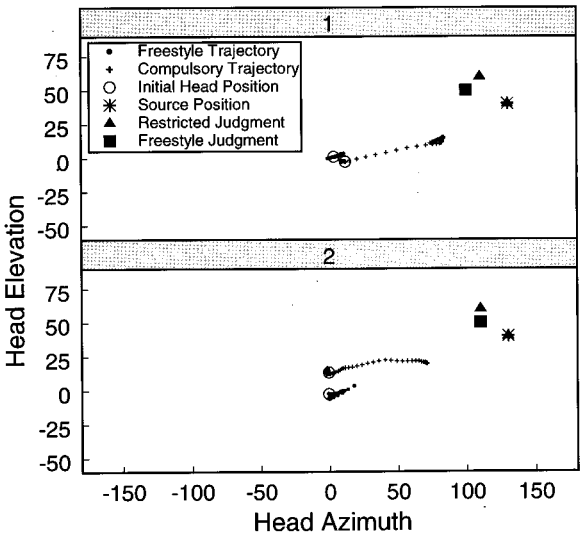

FIG. 8. Same as Fig. 7, but data are from a listener (SNJ) who does not make front–back confusions. Note that in the freestyle condition the head is moved very little during a trial. In the compulsory condition the listener clearly oriented toward the source, but never fully rotated the head to the source direction, probably because it was in the rear hemifield. Trajectories from only two trials are shown.

stimulus that moved 40 degrees in azimuth during its 1-s duration, clockwise or counterclockwise, determined randomly and not revealed to the listeners. Listeners were instructed not to follow the apparent movement with their eyes and to hold the head motionless during the stimulus presentation. In a pilot experiment listeners judged starting and ending position in separate trial blocks. Since there were no apparent differences between the two sets of data, the current experiment asked for judgments of starting position only.

In the second condition, listeners were allowed to ''explore'' the virtual auditory space, not by moving their heads (which had no effect since the tracker was not coupled to the stimulus synthesis software in this experiment) but by moving the stimulus itself. The 2.5-s stimulus was repeated continuously. Listeners were encouraged to change the position of the virtual source by depressing the ''arrow'' keys on a PC keyboard. Azimuth was controlled by the ''right'' or ''left'' keys and elevation by the ''up'' and ''down'' keys. The fact that pressing the ''right'' key moved the stimulus in a clockwise direction around the head and pressing the ''left'' key moved it counter-clockwise was carefully explained to each listener. A single keypress moved the source 5 degrees. Once the listener was ready to make a response, the ''enter'' key was depressed, and the stimulus was returned to the starting position, terminating 250 ms later. The listener was instructed to judge the apparent starting position. There were no constraints on the extent of movement or the duration of exploration permitted of the listener. However, listeners were encouraged not to move their heads during the exploration.

B. Results

Seven listeners were tested in the first condition of this experiment, in which the source was moved by the experimenter during a trial. Six of the seven listeners had previously participated in experiment 1. Figure 9 shows the judgments of the apparent position of the starting position of a moving sound source from all seven listeners.

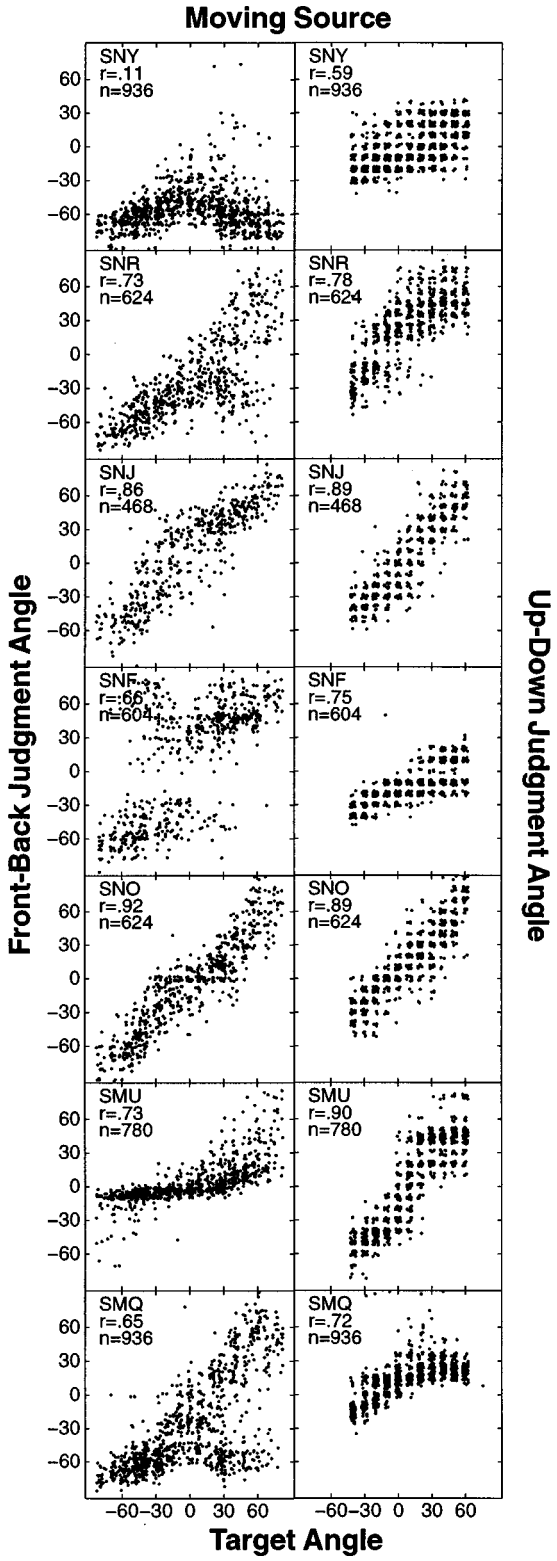

FIG. 9. Same as Fig. 6, but the data are from the condition (''Moving Source'') in which the virtual source was moved by the experimenter during a trial.

The main result from this condition is that movement of the sound source had no positive effect on the front–back

components of the apparent position judgments. Comparison of the data in Fig. 5 (and Fig. 3 for listener SNO), which are from a comparable condition involving stationary sources, with the data in Fig. 9 reveals that those listeners who make front–back confusions with stationary sources appear to make at least as many confusions with moving sources. In fact, one listener, SNY, made more confusions in this condition. Those listeners who make very few front–back confusions with stationary sources (SNO and SNJ) demonstrate the same ability to resolve ambiguities with moving sources. All listeners performed somewhat more poorly in this condition (lower correlations), and one listener (SMU) appeared to have considerable difficulty with the task. Thus, it appears at the very least that source movement alone cannot provide the information needed to resolve front–back ambiguities. This result would come as no surprise to Wallach (1940), since his theory requires the listener to know the direction of movement, either through purposeful movement of the head or by some other means. The latter possibility is tested in the second condition of this experiment, which allowed listeners to move the source, but without accompanying head or body movement (or perceived body movement, as in Wallach's 1940 experiment).

Four listeners were tested in the second condition, which encouraged listeners to ''explore'' the auditory space by moving the position of the virtual sound source with hand controls. The mean exploration times were 17.1 s (SMQ), 20.6 s (SNF), 17.2 s (SNR), and 40.4 s (SNO). Figure 10 shows the apparent position data from all four listeners in this ''exploration'' condition. Note that three of the four listeners produce very few front–back confusions in this condition. Two of these (SMQ and SNF) had shown a large number of front–back confusions in the restricted conditions of experiment 1 (Figs. 4 and 5) and in the first condition of experiment 2 (Fig. 9). For both of these listeners head movements greatly reduced the rate of front–back confusions (Figs. 4–6). The data from the fourth listener (SNR) are puzzling. Although this listener did make front–back confusions in the restricted conditions of experiment 1 and although those confusions appear to have been eliminated by head movements in both the freestyle and compulsory conditions of that experiment, self-initiated source movement for this listener does not appear to be effective for resolving ambiguities. Perhaps this listener never fully appreciated the association between ''right'' or ''left'' key presses and the resultant clockwise or counter-clockwise source movements. Individual differences such as these are not uncommon in research on spatial hearing and are a source of both frustration and inspiration.

The data in Fig. 10 suggest that head movements are not necessary to resolve front–back ambiguities and that source movement cues are adequate, so long as the listener knows the direction of movement. Such knowledge is presumed to be available in this condition since the listener is initiating and controling the movement. It is important to emphasize here that this condition involves virtual sound source only. In real auditory space listeners would rarely enjoy an equivalent form of control over the direction of movement of a sound source. Thus, it is not clear how the results from this experiment might generalize to real auditory space.

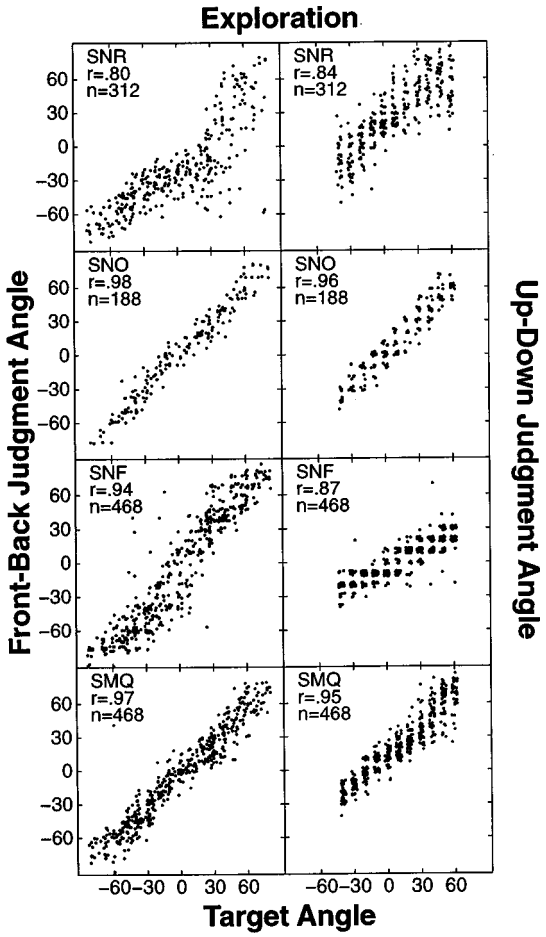

FIG. 10. Same as Fig. 9, but the data are from the condition (''Exploration'') in which the listeners controlled the direction and extent of movement of the virtual source with a PC keyboard.

IV. DISCUSSION AND CONCLUSIONS

The results of the experiments reported in this article are in complete agreement with Wallach's hypotheses about the role of dynamic cues in resolving localization ambiguities that arise because of the symmetry of interaural differences. Experiment 1 evaluated the role of head movements in providing the dynamic cues and showed that natural, self-initiated head movements afford even those listeners who make large numbers of confusions with virtual sources the information needed to reduce the frequency of those confusions. The results of experiment 2 suggest that in order for dynamic cues to be informative about source position they should be under the listener's control. Front-back confusions are not reduced with source movement alone (first condition of experiment 2). Moreover, also in agreement with Wallach (1940), the result of the second condition of experiment 2 suggests that the dynamic cues required for disambiguating front and rear source positions do not need to have been produced by movement of the listener. It appears that if the listener is aware of the direction of movement, the necessary information can be extracted. It should be noted that Wallach's hypothesis also predicts up–down confusions (in

fact, it predicts confusions all along the ''cone of confusion''), which have been reported is other studies (Wenzel *et al.*, 1993). However, in our experiments here, there was relatively little evidence for up–down confusions, even among those listeners who produced large numbers of front–back confusions. Only one of our listeners (SMW in Fig. 5) produced up–down confusions, and these were essentially eliminated with head movements (Fig. 6). The relative frequencies of front–back and up–down confusions may indicate that spectral cues are more useful for disambiguating up and down than they are for disambiguating front and back. Consistent with this view is the observation that elevation changes are sometimes accompanied by systematic changes in the center frequency of a prominent spectral notch in the HRTF, but front–back differences are indicated simply by gain differences in the 4–6-kHz region (Wightman and Kistler, 1997a, Fig. 12).

Our results are consistent with those from several other studies of sound localization in which head movements were a factor (e.g., Bronkhorst, 1995; Pollack and Rose, 1967; Thurlow and Runge, 1967). They are also consistent with the results of the recent Perrett and Noble (1997a, b) studies. Although all of these studies focused on slightly different aspects of the problem of front–back confusions, they all report that localization error is reduced by head movements and this is certainly consistent with our findings. It is of some interest that in the Thurlow and Runge study, the head movements were controlled by the experimenters and not initiated by the listeners. Nevertheless, localization performance improved markedly when head movements were made.

A noteworthy feature of the data from the experiments described in this article is large individual differences (see also Perrett and Noble, 1997a, b). Some listeners make very few front–back confusions, while for others the rate of front–back confusions is high. Either the available acoustical information is very different from one listener to the next or the way the information is extracted and processed differs widely. Although we have not carried out a systematic study as yet, our efforts to uncover an acoustical basis for the individual differences in rates of front–back confusions have been totally unsuccessful. The HRTFs, in which the spectral cues that might be used to resolve front–back ambiguities are encoded, appear to be no less rich in spectral detail in those who make front–back confusions than in those who do not. Given the presence of large individual differences in performance on tasks involving spectral pattern discrimination (Green, 1988), one might speculate that listeners who do not make front–back confusions might also be those who would demonstrate superior performance on spectral pattern discrimination tasks.

Another kind of individual difference relates to the fact that some listeners who do not make front–back confusions with real sources (even when head movements are restricted) do make them with virtual sources (e.g., SNR and SNY in Fig. 5). This may represent a manifestation of the familiar observation that with virtual sources the rate of front–back confusions (and errors in general) is higher than with real sources (Bronkhorst, 1995; Wightman and Kistler, 1989b). However, for most of our listeners there is no apparent performance difference, in error rate generally or front–back confusion rate specifically, between virtual and real conditions. Whether these individual differences represent differences in the fidelity of the virtual sources between listeners or the influence of some other factor is unknown. The ease of measuring HRTFs clearly varies between listeners, especially in our ability to position the probe microphone in a stable way. The validity of the synthesis procedure depends critically on stable microphone positioning. It is also possible that with real sources the small head movements that all listeners make, even when such movements are discouraged, provide useful information to some listeners. Those same head movements made with virtual sources would provide unnatural cues as a result of the combined head and source movement, unless virtual source synthesis was modified during head movement to simulate a stationary external source. In our restricted condition head movement was not coupled to virtual source synthesis.

There are obvious practical applications for the virtual source synthesis techniques described here and elsewhere [see Wenzel (1992) for a discussion of such applications]. The results of the experiments reported in this article have significant implications for some of these applications. First, the results strongly suggest that for any application in which front–back confusions could not be tolerated (e.g., air traffic control), production of the virtual sources should be coupled to the position of the operator's head. While presentation of correlated visual cues may reduce the rate of front–back confusions, this would only be expected for targets in the visual field, and many of the most important applications for virtual auditory sources are in situations in which the targets are outside the visual field. Second, in agreement with Toole (1970), we would argue that the dynamic cues provided by head movements are not required for externalization of a virtual source. While externalization was not a focus of our experiments, the distance estimates we routinely collected indicate externalized images for all listeners in all conditions. Thus, suggestions by some (e.g., Durlach *et al.*, 1992) that failures to externalize virtual sources are a result of lack of head movement cues should be interpreted with some caution.

Whether or not dynamic cues can be used to resolve all of the confusions that occur with virtual sources is an open question. It is well established that an increase in confusion rate accompanies many different kinds of degradation of the virtual sources, such as the use of nonindividualized HRTFs in synthesis (Bronkhorst, 1995; Wenzel *et al.*, 1993) or the use of low-order approximations of the HRTFs (Kistler and Wightman, 1992). The advantage of head coupling in these situations is a topic of future study.

ACKNOWLEDGMENTS

The authors gratefully acknowledge the assistance of Pavel Zahorik, Shelly Godar, Tonya Rasmussen, and Douglas Swiggum in the technical phases of the work and the very helpful editorial comments of Erno Langendijk, Robert Lutfi, Ewan Macpherson, and Pavel Zahorik. Financial sup-

port was provided by NASA (Cooperative Agreement No. NCC2-542) and the NIH-NIDCD (DC00116).

[1]All of the data gathered during the experiments described in this article are available in electronic form as an E-PAPS supplement. The data set includes trial-by-trial apparent position judgments from all of the psychophysical experiments, all of the sampled head-trajectory data from experiment 1, and the listener-controlled source position data from experiment 2. See AIP Document No. E-PAPS: E-JASMAN-105-050905 for a description of the available files. E-PAPS document files can be retrieved free of charge from the AIP FTP server (http://www.aip.org/epaps/epaps.html) or from ftp.aip.org in the directory /epaps/. For further information, E-mail: paps@aip.org or Fax: 516-576-2223.

[2]As used here bilinear interpolation defines the HRTF at the target location as a weighted sum of the four nearest HRTFs. The computation can be understood by imagining the desired target location inside the ''rectangle'' formed by the four nearest locations on the 10-degree azimuth/elevation grid at which HRTFs had been measured (call this the ''large'' rectangle). Vertical and horizontal lines through the target location divide this rectangle into four small rectangles. The weight for the HRTF at any corner of the large rectangle is given by the ratio of the area of the small rectangle farthest away from that corner to the total area of the large rectangle. Thus, the weight given to the HRTF at the NE corner is given by the ratio of the area of the SW small rectangle to the total area of the large rectangle.

Bronkhorst, A. W. (**1995**). ''Localization of real and virtual sound sources,'' J. Acoust. Soc. Am. **98**, 2542–2553.

Cleveland, W. S. (**1985**). *The Elements of Graphing Data* (Wadsworth, Monterey, CA), pp. 161–162.

Durlach, N. I., Rigopulos, A., Pang, X. D., Woods, W. S., Kulkarni, A., Colburn, H. S., and Wenzel, E. M. (**1992**). ''On the externalization of auditory images,'' Presence **1**, 251–257.

Green, D. M. (**1988**). *Profile Analysis* (Oxford U.P., New York), pp. 93–96.

Hartmann, W. M. (**1983**). ''Localization of sound in rooms,'' J. Acoust. Soc. Am. **74**, 1380–1391.

Kistler, D. J., and Wightman, F. L. (**1992**). ''A model of head-related transfer functions based on principal components analysis and minimum-phase reconstruction,'' J. Acoust. Soc. Am. **91**, 1637–1647.

Makous, J. C., and Middlebrooks, J. C. (**1990**). ''Two-dimensional sound localization by human listeners,'' J. Acoust. Soc. Am. **87**, 2188–2200.

Oldfield, S. R., and Parker, S. P. A. (**1984**). ''Acuity of sound localization: A topography of auditory space. I. Normal hearing conditions,'' Percept. **13**, 581–600.

Perrett, S., and Noble, W. (**1997a**). ''The contribution of head motion cues to localization of low-pass noise,'' Percept. Psychophys. **59**, 1018–1026.

Perrett, S., and Noble, W. (**1997b**). ''The effect of head rotations on vertical plane sound localization,'' J. Acoust. Soc. Am. **102**, 2325–2332.

Pollack, I., and Rose, M. (**1967**). ''Effects of head movements on the localization of sounds in the equatorial plane,'' Percept. Psychophys. **2**, 591–596.

Rakerd, B., and Hartmann, W. M. (**1985**). ''Localization of sound in rooms, II: The effects of a single reflecting surface,'' J. Acoust. Soc. Am. **78**, 524–533.

Thurlow, W. R., and Runge, P. S. (**1967**). ''Effect of induced head movements on localization of direction of sounds,'' J. Acoust. Soc. Am. **42**, 480–488.

Toole, F. W. (**1970**). ''In-head localization of acoustic images,'' J. Acoust. Soc. Am. **48**, 943–949.

Wallach, H. (**1939**). ''On sound localization,'' J. Acoust. Soc. Am. **10**, 270–274.

Wallach, H. (**1940**). ''The role of head movements and vestibular and visual cues in sound localization,'' J. Exp. Psychol. **27**, 339–368.

Wenzel, E. M. (**1992**). ''Localization in virtual acoustic displays,'' Presence **1**, 80–107.

Wenzel, E. M., Arruda, M., Kistler, D. J., and Wightman, F. L. (**1993**). ''Localization using nonindividualized head-related transfer functions,'' J. Acoust. Soc. Am. **94**, 111–123.

Wightman, F. L., and Kistler, D. J. (**1989a**). ''Headphone simulation of free-field listening I: Stimulus synthesis,'' J. Acoust. Soc. Am. **85**, 858–867.

Wightman, F. L., and Kistler, D. J. (**1989b**). ''Headphone simulation of free-field listening II: Psychophysical validation,'' J. Acoust. Soc. Am. **85**, 868–878.

Wightman, F. L., and Kistler, D. J. (**1992**). ''The dominant role of low-frequency interaural time differences in sound localization,'' J. Acoust. Soc. Am. **91**, 1648–1661.

Wightman, F. L., and Kistler, D. J. (**1997a**). ''Factors affecting the relative salience of sound localization cues,'' in Binaural and Spatial Hearing, edited by R. Gilkey and T. Anderson (Erlbaum, Mawah, NJ), pp. 1–23.

Wightman, F. L., and Kistler, D. J. (**1997b**). ''Monaural sound localization revisited,'' J. Acoust. Soc. Am. **101**, 1050–1063.

Young, P. T. (**1931**). ''The role of head movements in auditory localization,'' J. Exp. Psychol. **14**, 95–124.

Articulatory tradeoffs reduce acoustic variability during American English /r/ production

Frank H. Guenther[a)]
Department of Cognitive and Neural Systems, Boston University, Boston, Massachusetts 02215 and Research Laboratory of Electronics, Massachusetts Institute of Technology, Cambridge, Massachusetts 02139

Carol Y. Espy-Wilson
Department of Electrical and Computer Engineering, Boston University, Boston, Massachusetts 02215 and Research Laboratory of Electronics, Massachusetts Institute of Technology, Cambridge, Massachusetts 02139

Suzanne E. Boyce
Department of Communication Sciences and Disorders, University of Cincinnati, Cincinnati, Ohio and Research Laboratory of Electronics, Massachusetts Institute of Technology, Cambridge, Massachusetts 02139

Melanie L. Matthies
Department of Communication Disorders, Boston University, Boston, Massachusetts 02215 and Research Laboratory of Electronics, Massachusetts Institute of Technology, Cambridge, Massachusetts 02139

Majid Zandipour
Research Laboratory of Electronics, Massachusetts Institute of Technology, Cambridge, Massachusetts 02139 and Department of Cognitive and Neural Systems, Boston University, Boston, Massachusetts 02215

Joseph S. Perkell
Research Laboratory of Electronics, Massachusetts Institute of Technology, Cambridge, Massachusetts 02139 and Department of Brain and Cognitive Sciences, Massachusetts Institute of Technology, Cambridge, Massachusetts 02139

(Received 30 December 1997; revised 8 September 1998; accepted 25 January 1999)

The American English phoneme /r/ has long been associated with large amounts of articulatory variability during production. This paper investigates the hypothesis that the articulatory variations used by a speaker to produce /r/ in different contexts exhibit systematic tradeoffs, or articulatory trading relations, that act to maintain a relatively stable acoustic signal despite the large variations in vocal tract shape. Acoustic and articulatory recordings were collected from seven speakers producing /r/ in five phonetic contexts. For every speaker, the different articulator configurations used to produce /r/ in the different phonetic contexts showed systematic tradeoffs, as evidenced by significant correlations between the positions of transducers mounted on the tongue. Analysis of acoustic and articulatory variabilities revealed that these tradeoffs act to reduce acoustic variability, thus allowing relatively large contextual variations in vocal tract shape for /r/ without seriously degrading the primary acoustic cue. Furthermore, some subjects appeared to use completely different articulatory gestures to produce /r/ in different phonetic contexts. When viewed in light of current models of speech movement control, these results appear to favor models that utilize an acoustic or auditory target for each phoneme over models that utilize a vocal tract shape target for each phoneme. [S0001-4966(99)00205-2]

PACS numbers: 43.70.Aj, 43.70.Bk [AL]

INTRODUCTION

The American English phoneme /r/ has long been associated with relatively large amounts of articulatory variability (Alwan *et al.*, 1997; Delattre and Freeman, 1968; Espy-Wilson and Boyce, 1994; Hagiwara, 1994, 1995; Ong and Stone, 1998; Westbury *et al.*, 1995, 1998). In fact, the endpoints of the articulatory continuum for /r/ can be analyzed as functionally different articulator configurations that use different primary articulators (tongue tip versus tongue dorsum). These endpoints have been characterized in the literature as ''bunched'' (using the tongue dorsum) and ''retroflexed'' (using the tongue blade/tip). Often, the same speaker will use different types of /r/ in different productions, e.g., in different phonetic contexts. At the same time, the primary acoustic cue for /r/ is relatively simple and stable: a deep dip in the trajectory of the third spectral energy peak of the acoustic waveform, or third formant frequency ($F3$) (Boyce and Espy-Wilson, 1997; Delattre and Freeman, 1968; Westbury *et al.*, 1995, 1998). Furthermore, no consistent acoustic

[a)]Address correspondence to: Prof. Frank H. Guenther, Boston University, Center for Adaptive Systems and Department of Cognitive and Neural Systems, 677 Beacon Street, Boston, MA 02215, Fax number: (617) 353-7755, Electronic mail: guenther@cns.bu.edu

difference between bunched and retroflexed /r/'s has been discovered.

How is it that a speaker can produce perceptually acceptable /r/'s despite using such variable vocal tract shapes? One possible answer to this question is that the variations in vocal tract shape for /r/ are not haphazard, but are instead systematically related in a way that maintains a relatively stable acoustic signal across productions despite large variations in vocal tract shape across productions. In other words, the different vocal tract shapes used to produce /r/ by a particular subject might involve articulatory tradeoffs, or *trading relations*. The concept of articulatory trading relations is illustrated by the following example. Assume that narrowing either of two constrictions at different locations along the vocal tract (call them location 1 and location 2) has the same effect on an important acoustic cue for a phoneme. Assume further that narrowing either constriction causes a reduction in $F3$. In such a case, one could use different combinations of the two constrictions to achieve the same acoustic effect. For example, to achieve a particular value of $F3$, one might form a very narrow constriction at location 1 and a less narrow constriction at location 2, or one might alternatively form a very narrow constriction at location 2 and a less narrow constriction at location 1. If a speaker used one of these options in one phonetic context and the other option in a second phonetic context, a negative covariance between the sizes of these two constrictions would be seen across phonetic contexts.

The primary purpose of the current study is to investigate the issue of whether the various vocal tract shapes used by an individual to produce /r/ in different phonetic contexts exhibit articulatory trading relations that act to maintain a relatively stable acoustic signal. As discussed at the end of this article, this issue has important implications for theories of speech motor control and speech production. Largely for this reason, several recent experiments have investigated the trading relations issue for phonemes other than /r/ (e.g., de Jong, 1997; Perkell *et al.*, 1993, 1994; Savariaux *et al.*, 1995a), but the results have not been uniform across subjects: Although most subjects exhibit expected articulatory trading relations, some others do not. A possible reason for this ambiguity is that these studies have primarily concentrated on one hypothesized trading relationship, and subjects who do not exhibit this trading relation may exhibit other, unanalyzed trading relations that act to reduce acoustic variability. For example, Perkell *et al.* (1993) investigated an hypothesized trading relation between lip rounding and tongue body raising for the vowel /u/. Three of four subjects showed weak trading relations, but the fourth subject showed the opposite pattern. This fourth subject may have been using other trading relations that overrode the effect of the lip rounding/tongue body raising relationship. In the current study, we employ analysis procedures that allow us to assess the combined effects of multiple articulatory covariances on the variability of the acoustic signal. Furthermore, American English /r/ was chosen[1] because the large amount of articulatory variability associated with /r/ productions should make it easier to detect trading relations if they are present.

I. METHODS

A. Data collection

An electromagnetic midsagittal articulometer (EMMA) system (Perkell *et al.*, 1992) was used to track the movements of six small (5 mm long×2.5 mm diameter) transducer coils. The coils were attached in the midsagittal plane to the tongue (three coils), lips (two coils), and lower incisor (one coil) with bio-compatible adhesive. Transducers were also placed on the upper incisor and the bridge of the nose, for defining a coordinate system with a maxillary frame of reference. A directional microphone was suspended 14 in. from the subject's mouth and the acoustic signal was recorded simulatenously with the EMMA signals. Standard EMMA calibration protocols were completed prior to each experiment (cf. Perkell *et al.*, 1992 for details). The current study focused on the positions of the three tongue transducers, which were located approximately 1, 2.5, and 5 cm back from the tongue tip (with the tongue in a neutral configuration).

The seven subjects were young adults, two females (subjects 2 and 3) and five males. They had no history of speech, language, or hearing deficits or pronounced regional dialects. Each of the seven subjects produced 4–6 repetitions of the carrier phrase ''Say ____ for me'' for each of the five test utterances; /warav/, /wabrav/, /wadrav/, /wagrav/, and /wavrav/. The articulatory and acoustic data from these utterances were time aligned to allow direct comparison between the two data types.

B. *F3* extraction and alignment

The minimum measured $F3$ value during /r/ production, which can be thought of as the acoustic ''center'' of /r/, served as a landmark for time alignment of the data across utterances for each speaker. Formant tracks were computed for all utterances using the ESPS/WAVES formant tracker and a 51.2-ms window and 3.2-ms frame rate. The $F3$ minimum was detected using an automatic procedure that first identified all sonorant regions, then located the point of minimal $F3$ from the relevant sonorant regions. $F3$ values and transducer positions within a 140-ms time window centered at the $F3$ minimum were extracted. Extracted $F3$ traces for some utterances were corrupted due to technical difficulties in automatically tracking low-amplitude and low-frequency values of $F3$ after stop consonants. Therefore, utterances whose $F3$ tracks changed by more than 200 Hz in a 3.2-ms time step were eliminated from the study, leaving 12 to 27 analyzed utterances per subject. After this elimination process, the tongue shapes at the $F3$ minimum of the remaining utterances were visually inspected, and two additional utterances (one each for subjects 1 and 4) were identified as having articulations that were incorrectly labeled as /r/ by the automatic extraction process. These two utterances were also eliminated from the study.

C. Effects of vocal tract shape parameters on *F3*

The vocal tract shape for /r/ involves a palatal constriction formed by the tongue in the anterior third of the tract.

Roughly speaking, the third formant frequency ($F3$) of /r/ is the resonance resulting from the cavities anterior to the palatal constriction (e.g., Alwan *et al.*, 1997; Espy-Wilson *et al.*, 1997; Stevens, 1998). This part of the vocal tract consists of an acoustic compliance due to a large front cavity volume and two parallel acoustic masses due to natural tapering by the teeth/lips and the palatal constriction behind the front cavity. The resulting resonance is inversely proportional to the product of the total acoustic mass and the acoustic compliance. Because it is difficult to accurately infer lip aperture from EMMA data, we focus on the effects of the acoustic mass due to the size and location of the palatal constriction. From these considerations, we conclude that the frequency of $F3$ can be decreased by tongue movements that lengthen the front cavity (thereby increasing the acoustic compliance of the front cavity), lengthen the constriction (thereby increasing the acoustic mass of the constriction behind the front cavity), or decrease the area of the constriction (thereby increasing the acoustic mass of the constriction).[2]

The predicted effects of these movements on $F3$ were confirmed using vocal tract area functions derived from structural MRI scans of a speaker producing /r/.[3] Two area functions were derived: one representing a ''bunched'' /r/ configuration, and one representing a ''retroflexed'' /r/ configuration. Three manipulations were carried out on each area function to test the effects on $F3$ predicted from acoustic theory: (i) the palatal constriction was extended backward by narrowing the vocal tract area immediately behind the constriction; (ii) the front cavity was lengthened by displacing the palatal constriction backward; and (iii) the vocal tract area at the palatal constriction was decreased. For all three manipulations, an acoustic signal was synthesized (using S. Maeda's VTCALCS program; Maeda, 1990) and compared to the signal synthesized from the original area function. Each manipulation resulted in a lower $F3$ in both the bunched and retroflexed /r/ cases, as expected from the acoustic theory analysis.

Because all three manipulations act to lower $F3$, subjects could maintain a relatively stable $F3$ despite vocal tract shape variations across contexts if these variations involved tradeoffs between the different manipulations. When looking at the different vocal tract shapes for /r/ across contexts, these tradeoffs would be manifested by correlations between constriction length, front cavity length, and constriction area. Specifically, the following three correlations would be expected to aid in maintaining a relatively stable $F3$ across utterances while allowing variations in vocal tract shape:

(1) a negative correlation between constriction length and front cavity length, since increases in constriction length and front cavity length both act to reduce $F3$;
(2) a positive correlation between constriction length and constriction area, since increases in constriction length reduce $F3$ and decreases in constriction area reduce $F3$; and
(3) a positive correlation between front cavity length and constriction area, since increases in front cavity length reduce $F3$ and decreases in constriction area reduce $F3$.

D. Predicted articulatory covariances

To determine whether a subject uses any of the three trading relations hypothesized above, we must first describe the trading relations in terms of the x and y coordinates of the tongue transducers. For tongue configurations during /r/ production, a forward movement of the tongue front transducer generally corresponds to a shortening of the front cavity, an upward movement of the tongue front transducer generally corresponds to a decrease in the area of the palatal constriction for /r/, and, since the point of maximal constriction for /r/ is typically anterior to the tongue back transducer, an upward movement of the tongue back transducer generally corresponds to a lengthening of the palatal constriction and possibly a decrease in the area of the constriction. When determining the signs of the transducer coordinate correlations corresponding to the trading relations delineated above, we must take into account that increasing values of the tongue front horizontal position correspond to decreases in front cavity length, and increasing values of the tongue front vertical position correspond to decreases in constriction area. From these considerations, we can surmise that the three trading relation strategies described above should be evidenced by the following articulatory correlations:

(1) a positive correlation between tongue back height and tongue front horizontal position;
(2) a negative correlation between tongue back height and tongue front height; and
(3) a positive correlation between tongue front horizontal position and tongue front height.

Note that the use of all three trading relations by a single subject is unlikely given that they impose competing constraints; i.e., if tongue back height and tongue front horizontal position are positively correlated as in relation (1), and tongue front horizontal position and tongue front height are positively correlated as in relation (3), it is very likely that tongue back height and tongue front height will also be positively correlated, thus violating relation (2).

E. Analysis of articulatory and acoustic variances

To quantify the combined effects of articulatory covariances on $F3$ variability, an analysis was performed using both acoustic and articulatory data to estimate $F3$ variance as a function of articulatory variances. The relationship between transducer coordinates and $F3$ during /r/ can be written for each speaker as follows:

$$F3 = A_0 + \sum_{i=1}^{N} A_i c_i + E, \tag{1}$$

where the A_i are constants, the c_i are the transducer coordinates, N is the number of transducer coordinates considered in the analysis, and E is a residual term that accounts for the effects on $F3$ due to all other sources, including articulators not included in the analysis, measurement errors, and nonlinearities in the relationship between $F3$ and the transducer coordinates. The equation relating $F3$ variance to articulatory variances at each point in time is then:

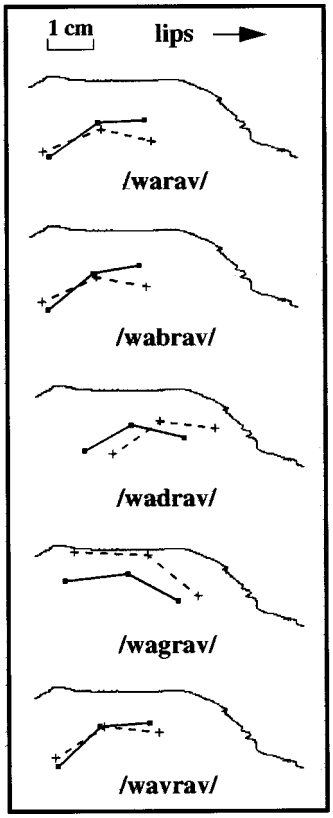

FIG. 1. Sample lingual articulations used by subject 1 to produce /r/ in the five phonetic contexts. For each context, two schematized tongues shapes and a palatal trace are shown. Each tongue shape schematic was formed by connecting the three tongue transducers with straight lines. The tongue shape at the $F3$ minimum for /r/ is drawn with solid lines. The tongue shape 70 ms prior to the $F3$ minimum is drawn with dashed lines.

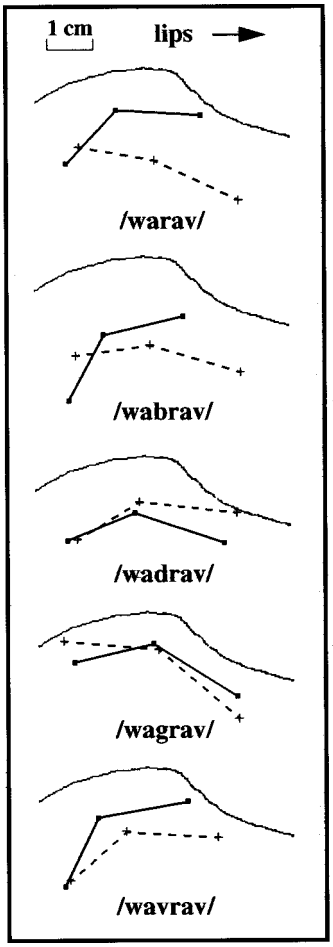

FIG. 2. Sample lingual articulations used by subject 2 to produce /r/ in the five phonetic contexts. For each context, two schematized tongues shapes and a palatal trace are shown. Each tongue shape schematic was formed by connecting the three tongue transducers with straight lines. The tongue shape at the $F3$ minimum for /r/ is drawn with solid lines. The tongue shape 70 ms prior to the $F3$ minimum is drawn with dashed lines.

$$\mathrm{Var}(F3)=\sum_i A_i^2\,\mathrm{Var}(c_i)+\mathrm{Var}(E)+2\sum_{i<j}\sum A_iA_j\,\mathrm{Cov}(c_i,c_j)+2\sum_i A_i\,\mathrm{Cov}(c_i,E). \quad (2)$$

To determine the effects of articulatory covariances on $F3$ variability, we can compare the variance estimate of Eq. (2) to the following variance estimate that excludes the covariances between the analyzed transducer coordinates:

$$\mathrm{Var}(F3)=\sum_i A_i^2\,\mathrm{Var}(c_i)+\mathrm{Var}(E)+2\sum_i A_i\,\mathrm{Cov}(c_i,E). \quad (3)$$

If the $F3$ variance estimate in the absence of articulatory covariances [Eq. (3)] is significantly larger than the variance estimate including the articulatory covariances [Eq. (2)], we conclude that the primary effect of the articulatory covariances is a reduction in the variance of $F3$.

Strictly speaking, a comparison of the $F3$ variance estimates in Eqs. (2) and (3) tells us only about the effects of the covariances of the *linear* component of each transducer's relation to $F3$. However, the relationship between $F3$ and transducer coordinates should be linear near a particular configuration of the vocal tract, since $F3$ is presumably a continuous nonlinear function of the vocal tract area function, and such functions are locally linear. One would further expect that the relationship is still approximately linear for the relatively limited range of vocal tract configurations utilized by a particular subject for /r/. The linear approximations reported below captured approximately 80% of the variance when using only three pellet coordinates, providing support for the assertion that the primary effect of articulatory covariances on $F3$ variance can be captured by considering only the linear component of each transducer's relationship to $F3$. Furthermore, the sign (positive or negative) of an articulatory covariance's contribution to $F3$ variance depends only on the sign of the corresponding A_i terms, and we are primarily interested in the sign of the combined effects of articulatory covariances on $F3$ variance. The expected signs of the A_i for tongue back height, tongue front horizontal position, and tongue front height can be deduced from acoustic theory considerations (Secs. I C and I D). A_i values were estimated for each subject using multiple linear regression on the acoustic and articulatory data. As discussed in Sec. II D, all

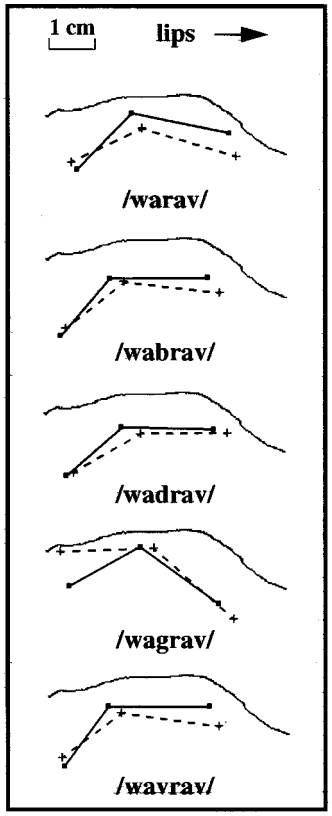

FIG. 3. Sample lingual articulations used by subject 3 to produce /r/ in the five phonetic contexts. For each context, two schematized tongues shapes and a palatal trace are shown. Each tongue shape schematic was formed by connecting the three tongue transducers with straight lines. The tongue shape at the $F3$ minimum for /r/ is drawn with solid lines. The tongue shape 70 ms prior to the $F3$ minimum is drawn with dashed lines.

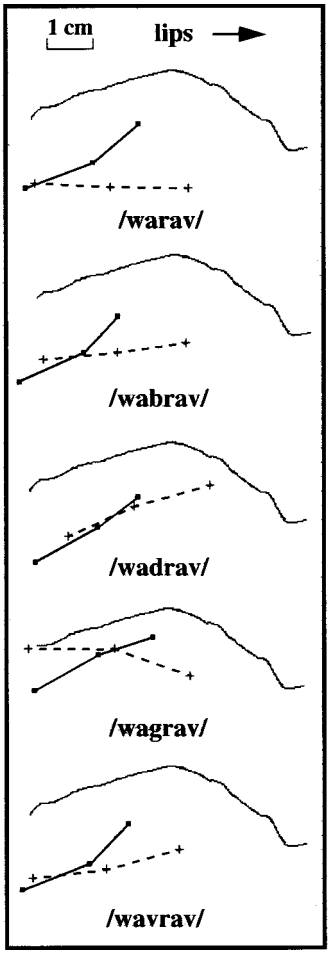

FIG. 4. Sample lingual articulations used by subject 4 to produce /r/ in the five phonetic contexts. For each context, two schematized tongues shapes and a palatal trace are shown. Each tongue shape schematic was formed by connecting the three tongue transducers with straight lines. The tongue shape at the $F3$ minimum for /r/ is drawn with solid lines. The tongue shape 70 ms prior to the $F3$ minimum is drawn with dashed lines.

21 estimated A_i values (three values for each of seven subjects) were of the sign expected from these acoustic theory considerations.

II. RESULTS

A. Temporal progression of tongue shapes

Figures 1–7 show sample lingual articulations used to produce /r/ in the five contexts by the seven subjects. For each context, two schematized tongue shapes and a palatal trace[4] are shown. The tongue shape schematics were formed by connecting the three tongue transducers with straight lines. The solid tongue shape corresponds to the point in time at which $F3$ reached its minimum value. The tongue shape 70 ms prior to the $F3$ minimum is indicated by dashed lines. The movement of the tongue can thus be roughly characterized as a transition from the dashed tongue shape to the solid tongue shape. This movement corresponds to the articulation toward the ''acoustic center'' of /r/; i.e., the portion of the movement up to the point in time of the $F3$ minimum.

Inspection of the lingual articulations for some subjects suggests that these subjects utilize different articulatory gestures, aimed at different vocal tract shapes, to produce /r/ in different phonetic contexts. For example, the backward movement of the tongue, with a slight downward movement of the tongue blade, used by subject 1 to produce the /r/ in /wadrav/ does not appear to be aimed at the same vocal tract shape for /r/ as the upward movements of the tongue blade used by the same subject to produce /r/ in the /warav/, /wabrav/, and /wavrav/ contexts (Fig. 1). Similarly, the downward movement of the tongue blade used by subject 2 to produce the /r/ in /wadrav/ does not appear to be aimed at the same vocal tract shape as the upward movements of the tongue blade used by the same subject to produce /r/ in /warav/, /wabrav/, or /wavrav/ (see Fig. 2). Additional examples of this phenomenon can be seen in Figs. 1–7. The possible relevance of these observations to theories of speech motor control will be addressed in Sec. III.

B. Tongue shapes at acoustic center of /r/

Figure 8 shows tongue configurations at the $F3$ minimum of /r/ for each of the seven speakers. For each utterance, the three tongue transducer positions are connected by a straight line. The tongue configurations for all repetitions in all phonetic contexts are superimposed for each speaker. Thus the fact that different numbers of utterances were analyzed for different subjects and contexts is reflected in this figure. As previously reported elsewhere (e.g., Delattre and Freeman, 1968; Hagiwara, 1994, 1995; Ong and Stone,

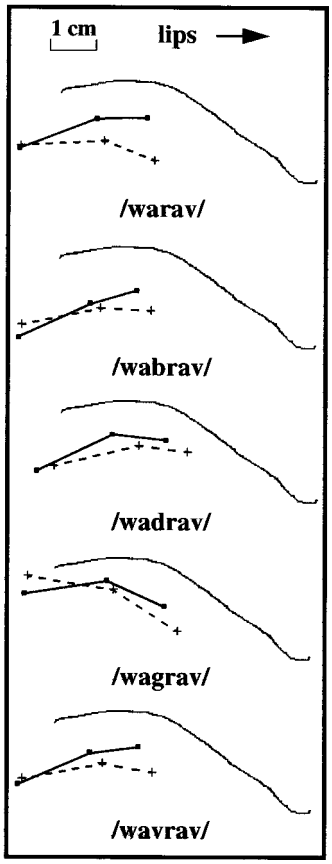

FIG. 5. Sample lingual articulations used by subject 5 to produce /r/ in the five phonetic contexts. For each context, two schematized tongues shapes and a palatal trace are shown. Each tongue shape schematic was formed by connecting the three tongue transducers with straight lines. The tongue shape at the $F3$ minimum for /r/ is drawn with solid lines. The tongue shape 70 ms prior to the $F3$ minimum is drawn with dashed lines.

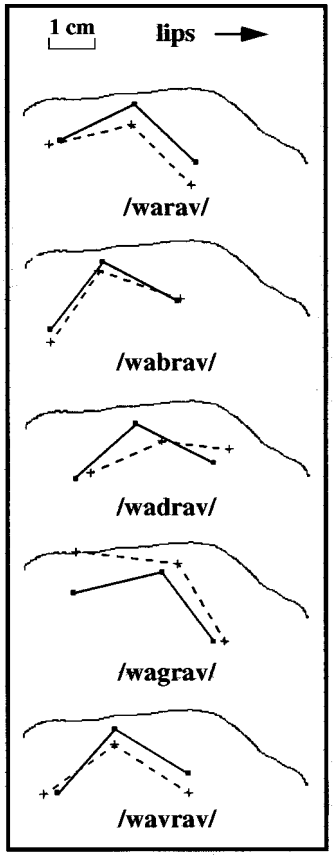

FIG. 6. Sample lingual articulations used by subject 6 to produce /r/ in the five phonetic contexts. For each context, two schematized tongues shapes and a palatal trace are shown. Each tongue shape schematic was formed by connecting the three tongue transducers with straight lines. The tongue shape at the $F3$ minimum for /r/ is drawn with solid lines. The tongue shape 70 ms prior to the $F3$ minimum is drawn with dashed lines.

1998; Westbury *et al.*, 1995), a wide range of tongue shapes is seen both within and across subjects. Also of note is the fact that, although most subjects seem to use an approximate continuum of tongue shapes (e.g., S2, S3, S6, S7), others show a more bimodal distribution of tongue shapes (e.g., S4, S5). Finally, the tongue shapes across subjects appear to form an approximate continuum between a bunched configuration (e.g., S6) and a retroflexed configuration (e.g., S4). A more detailed indication of the effects of the different phonetic contexts on the tongue shapes for /r/ can be gained from Fig. 9, which shows the average tongue shapes used by each subject in each phonetic context, coded by phonetic context. Figures 10–16 show the corresponding average $F3$ traces, starting from the point of the $F3$ minimum for /r/ and continuing for 70 ms, for each speaker coded by phonetic context. With the exception of the /wadrav/ productions of subject 2, which had considerably higher values of $F3$ than the other utterances for that subject, the subjects showed minimum $F3$ values well below 2000 Hz in all contexts, as expected from earlier studies of /r/ production.

Figure 17 shows the midsagittal palatal outline (thick solid line) and mean tongue shapes at the time of the $F3$ minimum for /r/ for each of the seven subjects. For each subject, mean configurations from two phonetic contexts (solid and dashed lines) are shown to illustrate the range of tongue shapes used by that subject. Tongue outlines were created by connecting the average positions of the three tongue transducers for a given utterance with a smooth curve to roughly approximate tongue shape.[5] A line was then extended downward from the tongue front transducer position, then forward to the lower incisor transducer position, to provide a rough estimate of the relative size of the front cavity across contexts.[6] Also shown in the upper left corner of this figure are two superimposed, highly schematic vocal tract outlines that illustrate trading relations for maintaining a relatively stable $F3$. The effect on $F3$ of the longer front cavity of the dashed outline, which can be roughly characterized as a retroflexed /r/, is counteracted by the effects of the longer and slightly narrower constriction of the solid outline, which can be roughly characterized as a bunched /r/. Similarly, the vocal tract outlines for all subjects indicate that shorter front cavity lengths are accompanied by a compensating increase in constriction length and/or decrease in the constriction area. Furthermore, the tongue shapes during /wagrav/ (solid lines) are generally much closer in shape to tongue shapes for /g/ than are the /r/ shapes for /wabrav/ or /warav/ (dashed lines), suggesting that subjects utilize /r/ configurations that are reached relatively easily in the current phonetic context.

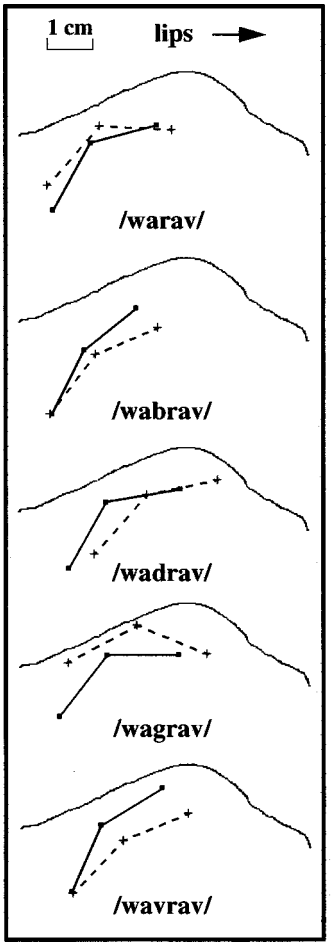

FIG. 7. Sample lingual articulations used by subject 7 to produce /r/ in the five phonetic contexts. For each context, two schematized tongues shapes and a palatal trace are shown. Each tongue shape schematic was formed by connecting the three tongue transducers with straight lines. The tongue shape at the $F3$ minimum for /r/ is drawn with solid lines. The tongue shape 70 ms prior to the $F3$ minimum is drawn with dashed lines.

C. Articulatory trading relations

For each subject, Pearson correlation coefficients corresponding to the predicted covariances described in Sec. I D were estimated across utterances at the point of $F3$ minimum and are listed in Table I. All subjects showed a significant positive correlation between tongue back height (TBY in Table I) and tongue front horizontal position (TFX), indicative of a trading relation between constriction length and front cavity length. Six of seven subjects also showed a second strong trading relation: five subjects showed a trading relation between constriction length and constriction area as evidenced by a negative correlation between TBY and tongue front height (TFY), and one subject showed a trading relation between front cavity length and constriction area as evidenced by a positive correlation between TFX and TFY. One subject (subject 7) showed only very weak correlations other than the strong trading relation between tongue back height and tongue front horizontal position.

D. Analysis of acoustic and articulatory variabilities

The results in Sec. II C indicate that most subjects exhibited two of three hypothesized articulatory trading relationships that act to reduce acoustic variability. Furthermore, as described in Sec. I D, it is unlikely or impossible for a subject to utilize all three trading relations because they counteract one another. However, it is still possible that the

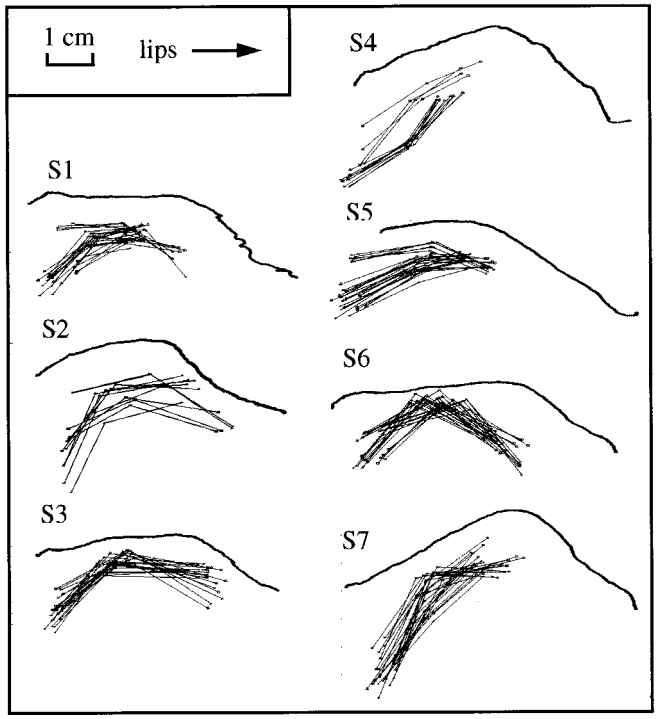

FIG. 8. Tongue configurations at the $F3$ minimum of /r/ for each of the seven speakers. For each utterance, the three tongue transducer positions are connected by straight lines. The tongue configurations for all repetitions in all phonetic contexts are superimposed for each speaker.

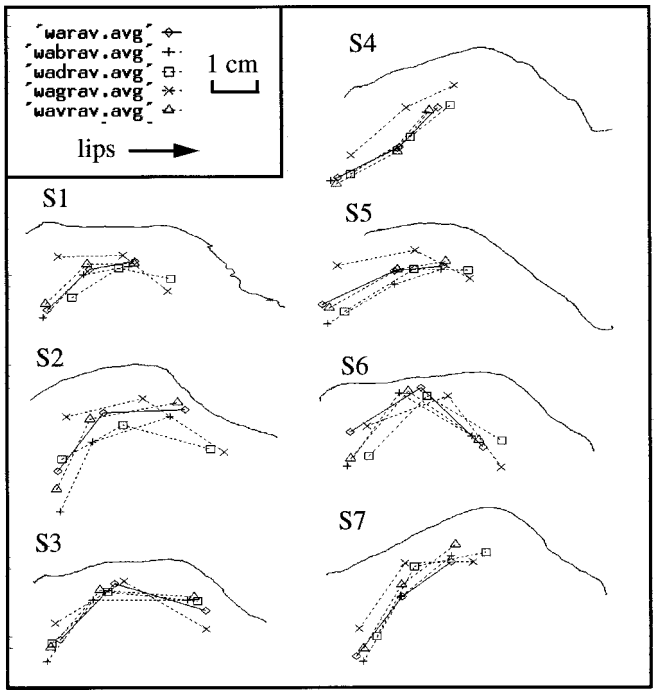

FIG. 9. Averaged tongue configurations at the $F3$ minimum of /r/ for each of the seven speakers. The averaged positions of the three tongue transducer positions for each of the five phonetic contexts are connected by straight lines.

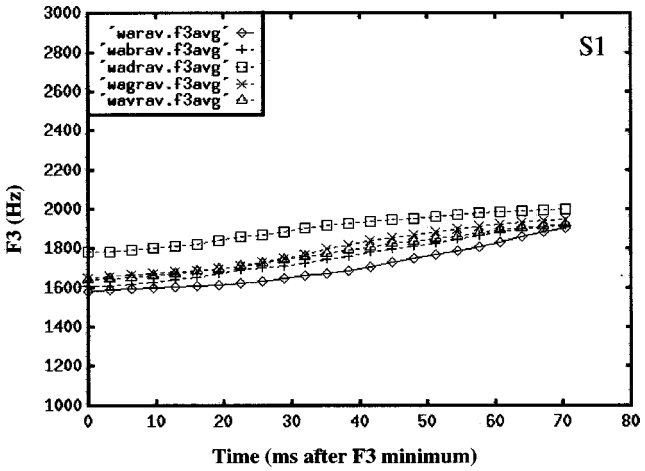

FIG. 10. Averaged $F3$ values for /r/ in the five phonetic contexts for subject 1. For each context, the averaged $F3$ is plotted as a function of time starting from the $F3$ minimum.

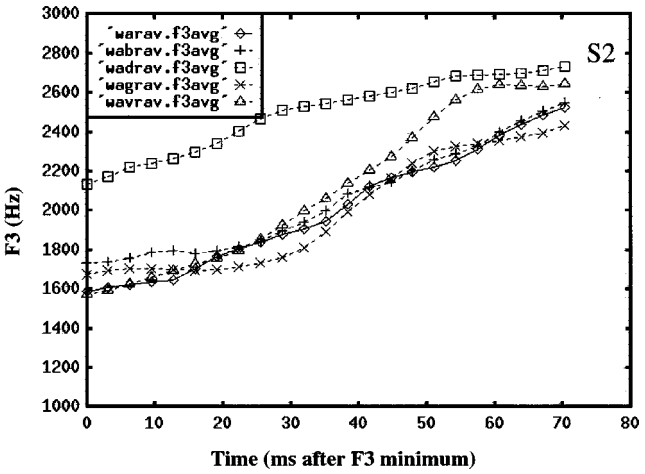

FIG. 11. Averaged $F3$ values for /r/ in the five phonetic contexts for subject 2. For each context, the averaged $F3$ is plotted as a function of time starting from the $F3$ minimum.

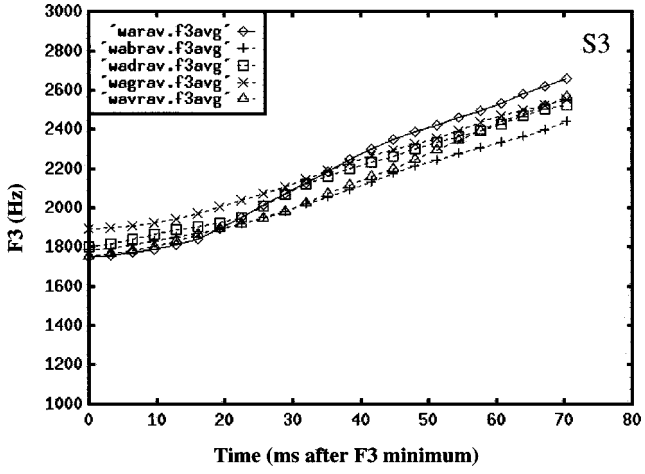

FIG. 12. Averaged $F3$ values for /r/ in the five phonetic contexts for subject 3. For each context, the averaged $F3$ is plotted as a function of time starting from the $F3$ minimum.

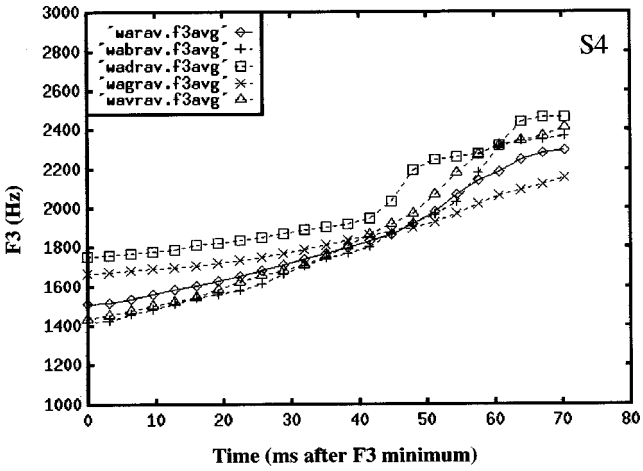

FIG. 13. Averaged $F3$ values for /r/ in the five phonetic contexts for subject 4. For each context, the averaged $F3$ is plotted as a function of time starting from the $F3$ minimum.

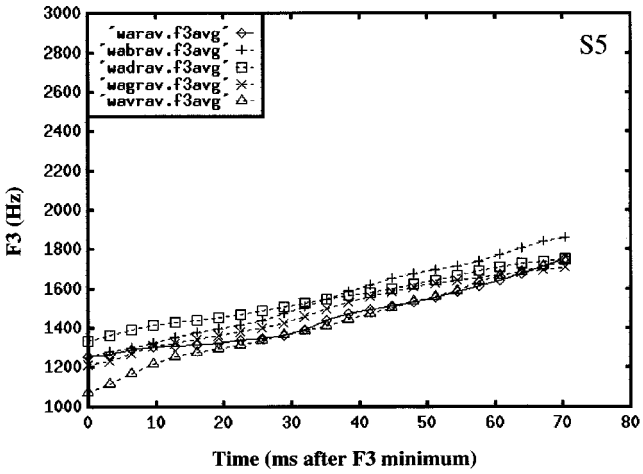

FIG. 14. Averaged $F3$ values for /r/ in the five phonetic contexts for subject 5. For each context, the averaged $F3$ is plotted as a function of time starting from the $F3$ minimum.

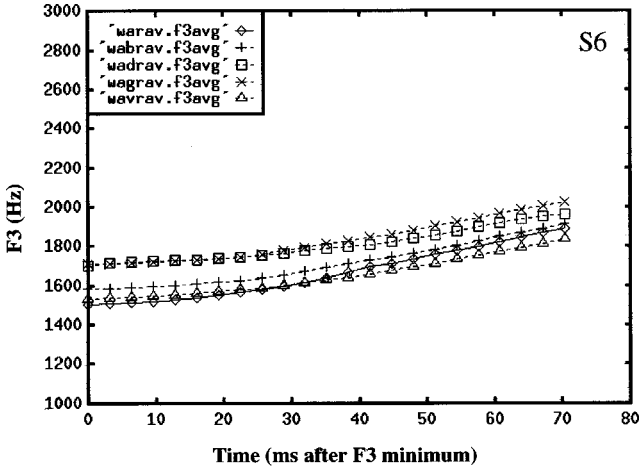

FIG. 15. Averaged $F3$ values for /r/ in the five phonetic contexts for subject 6. For each context, the averaged $F3$ is plotted as a function of time starting from the $F3$ minimum.

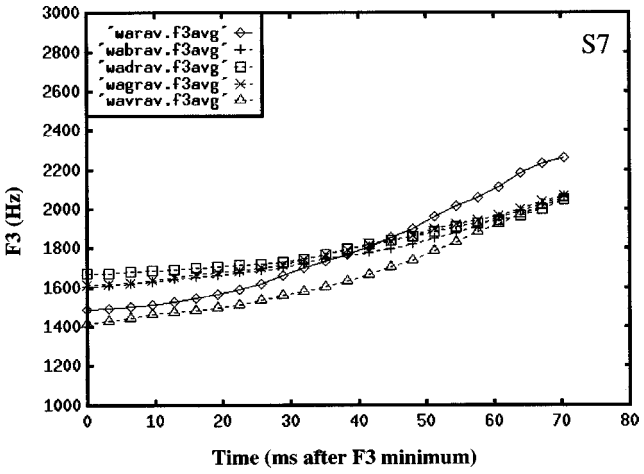

FIG. 16. Averaged $F3$ values for /r/ in the five phonetic contexts for subject 7. For each context, the averaged $F3$ is plotted as a function of time starting from the $F3$ minimum.

significant correlations that violate the trading relations could effectively ''override'' the beneficial articulatory tradeoffs, potentially nullifying or even reversing the effect of the utilized trading relations on acoustic variability. It is therefore necessary to estimate the net effect of all three articulatory covariances, as outlined in Sec. I E.

$F3$ variance estimates with and without covariance terms [Eqs. (2) and (3), respectively] were calculated using the tongue back height, tongue front horizontal position, and tongue front height transducer coordinates. The corresponding $F3$ standard deviations were then averaged across subjects. The A_i values for each speaker were estimated using multiple linear regression across utterances and time bins and are provided in Table II; the value of E for a particular time bin was simply the residual of the regression in that time bin. R^2 values for the $F3$ fit (without the residual term) ranged from 0.75 to 0.87 for the different subjects, with an average R^2 of 0.79. If covariances are high and the actual effect of an articulator's position on $F3$ is very low, regression analysis can possibly result in estimates of transducer contributions that have the wrong sign, which could in turn cause some articulatory covariances to decrease estimated $F3$ variability when in reality they increase or have no significant effect on $F3$ variability. The fact that none of the transducer contribution estimates produced by the regression were of the opposite sign as expected from acoustic theory considerations and the MRI-based area function analysis indicates that this potential problem did not affect our results.

$F3$ standard deviation estimates with and without covariance terms are shown in Fig. 18 as a function of time starting at the $F3$ minimum for /r/, averaged across subjects. (Standard deviations were plotted in place of variances to produce values whose units are Hz.) Also plotted is the standard deviation obtained from measured values of $F3$. When articulatory covariances are included, the $F3$ standard deviation estimate is equal to the measured $F3$ standard deviation; this is as expected because of the inclusion of the residual term in the variance estimate calculations. The solid line in the figure thus represents both the measured $F3$ standard deviation and the estimated $F3$ standard deviation including

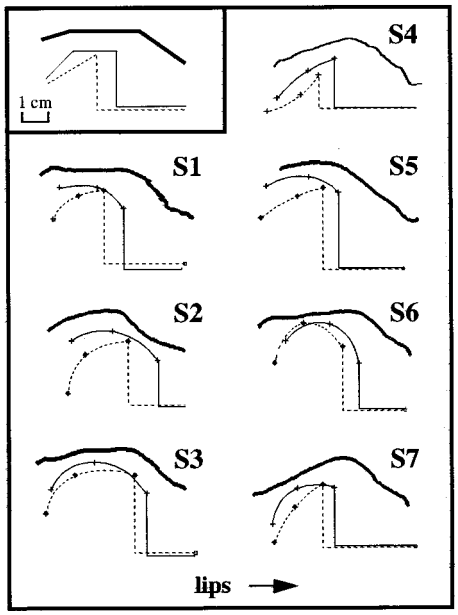

FIG. 17. Trading relations during /r/ production. The upper left corner shows two superimposed, highly schematized vocal tract outlines (dashed and solid lines) illustrating trading relations between front cavity length and palatal constriction length and area. Also shown are vocal tract outlines that illustrate the range of tongue shapes used by each of the seven subjects to produce /r/ in different phonetic contexts. Thin solid lines correspond to the tongue shapes for /r/ in /wagrav/ (averaged across repetitions), and dashed lines correspond to the /r/ in /wabrav/ or /warav/, depending on the subject. Thick solid lines indicate palatal outlines. Each outline is formed by connecting the three tongue transducer positions with a smooth curve, then projecting downward and forward from the frontmost tongue tongue transducer to the lower incisor transducer. All seven subjects show tradeoffs between the front cavity length and the constriction length and/or area when producing /r/ in the two different contexts.

TABLE I. Articulator correlation coefficients. Significant correlations that are consistent with hypothesized trading relations are shown in boldface. TBY=tongue back height; TFX=tongue front horizontal position; TTY =tongue front height.

Subject	TBY-TFX	TBY-TFY	TFX-TFY
1	**0.74**[a]	**−0.75**[a]	−0.75[a]
2	**0.92**[a]	**−0.69**[a]	−0.88[a]
3	**0.77**[a]	**−0.74**[a]	−0.46
4	**0.91**[a]	0.89[a]	**0.82**[a]
5	**0.64**[a]	**−0.49**[a]	−0.57[a]
6	**0.55**[a]	**−0.81**[a]	−0.60[a]
7	**0.84**[a]	0.05	0.06

[a]Statistically significant ($p<0.01$).

TABLE II. Regression coefficients indicating the relationship between transducer coordinates and $F3$. Units are Hz/mm.

Subject	A_1 (TBY)	A_2 (TTX)	A_3 (TTY)
1	−28.25	15.20	−35.61
2	−81.13	92.77	−35.25
3	−12.28	25.93	−51.50
4	−36.83	77.34	−36.55
5	−24.04	21.44	−30.49
6	−21.68	10.99	−30.95
7	−46.29	33.71	−31.87

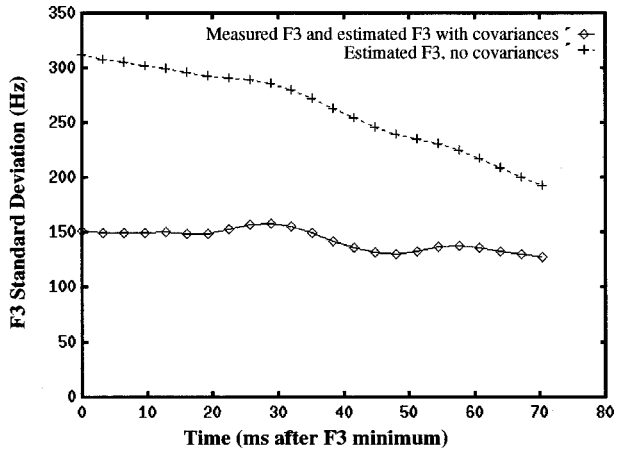

FIG. 18. Comparison of the measured $F3$ standard deviation with estimates of $F3$ standard deviation derived from articulator transducer positions, averaged across subjects. Removal of the articulatory covariance terms results in a much higher estimate of $F3$ standard deviation, indicating that articulatory covariances greatly reduce acoustic variation.

the covariance terms. When articulatory covariances are removed from the estimates, the estimated $F3$ standard deviation increases substantially. The dashed line in Fig. 18 represents estimated $F3$ standard deviation without covariances using the three tongue transducer coordinates. According to this estimate, then, $F3$ standard deviation would be 105% higher at the acoustic center of /r/ if the articulatory tradeoffs had not been present.

The increase in the $F3$ variance estimate without covariances is seen at the $F3$ minimum for all subjects. This observation suggests that ambiguous results from previous studies may have been at least partly due to analyzing only one articulatory tradeoff at a time, since in our study no subject exhibited all three hypothesized trading relations, but all subjects showed a net decrease in acoustic variability due to the *combined* effects of the articulatory covariances. Assume, for example, that the data listed in each column of Table I were the result of an independent research study. Researchers investigating the trading relation in column 2 (in which five of seven subjects used the trading relation) would sharply disagree with researchers investigating the trading relation in column 3 (in which only one of seven subjects used the trading relation) as to whether or not trading relations are reliably exhibited, and both sets of researchers would report ambiguous results since in neither case do all subjects behave in the same way. A much clearer picture has emerged from the current study due to the analysis of the combined effects of the articulatory covariances.

Also evident in Fig. 18 is a steady decrease with time of the effects of the covariance terms on $F3$ as the /r/ transitions into the following /a/. This decrease, evident in six of the seven subjects, is suggestive of a decrease in the use of trading relations as vocal tract shape differences across utterances (due to the different phonemes preceding /r/ in different utterances) diminish.

III. DISCUSSION

The results of this study indicate that the widely varying tongue shapes used by each subject to produce /r/ in different phonetic contexts exhibit systematic articulatory tradeoffs that act to reduce acoustic variability across contexts despite the large variations in vocal tract shape. The first piece of evidence arises from inspection of the tongue shape extremes for each subject (i.e., the averaged tongue shapes from the two phonetic contexts whose averaged tongue shapes differed the most), which show clear tradeoffs between the length of the front cavity and the length and/or area of the palatal constriction (Fig. 17). An acoustic theory analysis of the effects of these aspects of vocal tract shape on $F3$ indicates that the systematic tradeoffs would be expected to reduce acoustic variability across contexts. Analysis of articulatory covariances indicates that most speakers exhibit two of three articulatory trading relationships that were hypothesized based on acoustic properties of the vocal tract (Sec. II C). Furthermore, the use of all three trading relationships is very unlikely if not impossible given that they counteract each other. Finally, analysis of the combined effects of these articulatory covariances indicates that they strongly influence $F3$ variability across contexts, effectively cutting $F3$ standard deviation in half compared to what it would have been without the articulatory covariances (Sec. II D; Fig. 18).

Unlike earlier trading relations studies that reported mixed results across subjects (e.g., de Jong, 1997; Perkell *et al.*, 1993, 1994; Savariaux *et al.*, 1995a), the reduction of $F3$ variability due to articulatory covariances was seen at the acoustic center of /r/ for all seven subjects in the current study. We believe that the following factors contributed to this difference. First, the current study investigated a phoneme known to exhibit a large amount of articulatory variability across contexts. Such a sound would be expected to exhibit stronger trading relations due to the larger overall articulatory variability. Second, the current study investigated the combined effects of multiple articulatory covariances. Although the combined effect of articulatory covariances was a reduction of $F3$ variability in all seven subjects according to the analysis of Sec. II D, different subjects used different combinations of the individual articulatory trading relations (Table I). It is therefore not surprising that in earlier studies, which investigated articulatory covariances individually, some subjects did not use an hypothesized trading relationship. The results of the current report suggest that these subjects may well have used other, unanalyzed trading relations that reduced acoustic variability.

The issue of articulatory trading relations in speech production is relevant to current theories concerning the control of speech movements. Roughly speaking, computational models of speech motor control can be classified according to the type of phonemic ''targets'' that they use to command movements of the speech articulators. One type of computational model, exemplified by the task-dynamic model of Saltzman and Munhall (1989), utilizes a target for each phoneme that specifies important aspects of the shape of the vocal tract for that phoneme. This ''vocal tract shape target'' view is closely related to theories of speech perception and production in which the articulatory gesture serves as the basic unit of speech. These include the motor theory of speech perception (Liberman and Mattingly, 1985; Liberman *et al.*, 1967), the direct realist theory of speech perception (Fowler, 1986, 1996), and the linguistic-gestural theory of

phonology (Browman and Goldstein, 1990a,b). A second type of computational model, exemplified by the DIVA model of speech acquisition and production (Guenther, 1995; Guenther *et al.*, 1998), utilizes only an acoustic or auditory target for each phoneme, with no explicit vocal tract shape target. These models may use different shapes of the vocal tract to produce the same acoustic signal for a phoneme depending on things like phonetic context. Theories related to this ''auditory target'' view have been posited by various researchers (for some recent examples, see Johnson *et al.*, 1993; Perkell *et al.*, 1993, 1995, 1997; Savariaux *et al.*, 1995a,b) and many of the roots for this line of thinking can be traced to the influential work of Jakobson *et al.* (1951).

A major difference between the auditory target and vocal tract shape target computational model classes is that the former explicitly predict the existence of articulatory trading relations when producing the same phoneme in different contexts, whereas the latter do not. Because the current results show the existence of trading relations in all seven subjects, they appear to favor acoustic target models over vocal tract shape target models. A potential reason for the use of articulatory tradeoffs is that they can reduce the amount of effort required to move the articulators through a set of acoustic targets. For example, the tongue shapes for /r/ in /wagrav/ were generally closer to the tongue shapes for /g/ than the tongue shapes for /r/ in other contexts, suggesting that, to a first approximation, subjects moved to the closest vocal tract shape that could be used to produce the appropriate sound in the prevailing phonetic context. The acoustic target control scheme used by the DIVA model has this property.

It is possible, however, that the trading relations found in the current study are artifactual, rather than the result of a movement control process that is making use of them to minimize effort while maintaining an acceptable acoustic signal. For example, one might imagine that the tongue shape variations simply reflect a controller that undershoots the vocal tract shape target for /r/ (thus maintaining some aspects of the vocal tract shape from the preceding phoneme at the point of $F3$ minimum), rather than one that purposefully utilizes a different vocal tract shape for /r/ in different contexts because it ''knows'' how to use different shapes to achieve the same acoustic/auditory result in different contexts. However, the fact that some subjects appear to use articulatory gestures toward different vocal tract shapes to produce /r/ in different contexts argues against an ''artifact'' interpretation. For example, the backward movement of the tongue, with a slight downward movement of the tongue blade, used by subject 1 to produce the /r/ in /wadrav/ does not appear to be a truncated movement aimed at the same vocal tract shape for /r/ as the upward movements of the tongue blade used by the same subject to produce /r/ in the /warav/, /wabrav/, and /wavrav/ contexts (see Fig. 1). Instead, it appears that the /r/ gesture in /wadrav/ is toward a different vocal tract shape that nonetheless suffices for /r/. (See Sec. II and Figs. 1–7 for further examples.) Further research into this issue will be carried out in a subsequent modeling study that will address other possible explanations for the trading relations found in the current study.

ACKNOWLEDGMENTS

We thank Ken Stevens, Harlan Lane, Dan Bullock, and John Ingram for their help and comments, Shinji Maeda for the VTCALCS program, Abeer Alwan and colleagues for the MRI data, and John Westbury and Anders Löfqvist for constructive reviews of an earlier draft of this paper. Supported by NIDCD Grants Nos. 1R29-DC02852 to Frank Guenther, 5R01-DC01925-04 to Joseph Perkell, and 1R03-C2576-01 to Suzanne Boyce, and NSF Grant No. IRI-9310518 to Carol Espy-Wilson. Frank Guenther is also supported by the Alfred P. Sloan Foundation.

[1]In the International Phonetic Alphabet, this phoneme is indicated by the symbol /ɹ/. We use the symbol /r/ here because it is more widely recognized and is unambiguous with regard to American English.

[2]Although the direction of the effect on $F3$ for all of these vocal tract shape manipulations should be the same, the magnitude of the effect on $F3$ will be different for each manipulation. We account for this by including the magnitudes of the effects when analyzing the combined acoustic effect of these movements; this is done through the A_i terms in Eqs. (1)–(3) below.

[3]The vocal tract area functions were provided by Abeer Alwan and colleagues from the Electrical Engineering Department at the University of California, Los Angeles.

[4]The palatal traces for subjects 2 and 4 were slightly misaligned relative to the tongue transducer data. To correct for this, the palatal trace for these subjects have been raised approximately 3 mm relative to the tongue transducer positions in all figures.

[5]Because any form of curve through the three tongue transducer points would represent only a rough approximation to the actual tongue shape, the curves in Fig. 17 were simply hand-drawn using computer drawing software.

[6]The lower incisor location was not available for subject 2, so the vocal tract outlines for this subject in Fig. 17 are based on a lower incisor position estimated from the lower lip position.

Alwan, A., Narayanan, S., and Haker, K. (**1997**). ''Toward articulatory-acoustic models for liquid approximants based on MRI and EPG data. Part II. The rhotics,'' J. Acoust. Soc. Am. **101**, 1078–1089.

Boyce, S., and Espy-Wilson, C. Y. (**1997**). ''Coarticulatory stability in American English /r/,'' J. Acoust. Soc. Am. **101**, 3741–3753.

Browman, C., and Goldstein, L. (**1990a**). ''Tiers in articulatory phonology, with some implications for casual speech,'' in *Papers in laboratory phonology. I: Between the grammar and physics of speech*, edited by J. Kingston and M. E. Beckman (Cambridge University Press, Cambridge, UK), pp. 341–376.

Browman, C., and Goldstein, L. (**1990b**). ''Gestural specification using dynamically-defined articulatory structures,'' J. Phonetics **18**, 299–320.

De Jong, K. J. (**1997**). ''Labiovelar compensation in back vowels,'' J. Acoust. Soc. Am. **101**, 2221–2233.

Delattre, P., Freeman, D. C. (**1968**). ''A dialect study of American r's by x-ray motion picture,'' Linguistics **44**, 29–68.

Espy-Wilson, C. Y., and Boyce, S. E. (**1994**). ''Acoustic differences between ''bunched'' and ''retroflex'' variants of American English /r/,'' J. Acoust. Soc. Am. **95**, 2823.

Espy-Wilson, C. Y., Narayanan, S., Boyce, S. E., and Alwan, A. (**1997**). ''Acoustic modeling of American English /r/,'' *Proceedings of Eurospeech*, September 1997, Rhodes, Greece (ESCA, Grenoble, France), Vol. 1, pp. 393–396.

Fowler, C. A. (**1986**). ''An event approach to the study of speech perception from a direct-realist perspective,'' J. Phonetics **14**, 3–28.

Fowler, C. A. (**1996**). ''Listeners do hear sounds, not tongues,'' J. Acoust. Soc. Am. **99**, 1730–1740.

Guenther, F. H. (**1995**). ''A modeling framework for speech motor development and kinematic articulator control,'' *Proceedings of the XIIIth International Conference of Phonetic Sciences* (KTH and Stockholm University, Stockholm, Sweden), Vol. 2, pp. 92–99.

Guenther, F. H., Hampson, M., and Johnson, D. (**1998**). ''A theoretical investigation of reference frames for the planning of speech movements,'' Psychol. Rev. **105**, 611–633.

Hagiwara, R. (**1994**). ''Three types of American /r/,'' UCLA Working Papers in Phonetics **88**, 63–90.
Hagiwara, R. (**1995**). ''Acoustic realizations of American /r/ as produced by women and men,'' UCLA Working Papers in Phonetics **90**, 1–187.
Jakobson, R., Fant, G., and Halle, M. (**1951**). *Preliminaries to speech analysis: The distinctive features and their correlates* (MIT Press, Cambridge, MA).
Johnson, K., Ladefoged, P., and Lindau, M. (**1993**). ''Individual differencs in vowel production,'' J. Acoust. Soc. Am. **94**, 701–714.
Liberman, A. M., Cooper, F. S., Shankweiler, D. P., and Studdert-Kennedy, M. (**1967**). ''Perception of the speech code,'' Psychol. Rev. **74**, 431–461.
Liberman, A. M., and Mattingly, I. G. (**1985**). ''The motor theory of speech revisited,'' Cognition **21**, 1–36.
Maeda, S. (**1990**). ''Compensatory articulation during speech: Evidence from the analysis and synthesis of vocal tract shapes using an articulatory model,'' in *Speech Production and Speech Modeling*, edited by W. J. Hardcastle and A. Marchal (Kluwer Academic, Boston), pp. 131–149.
Ong, D., and Stone, M. (**1998**). ''Three-dimensional vocal tract shapes in /r/ and /l/: A study of MRI, ultrasound, electropalatography, and acoustics,'' Phonoscope **1**, 1–13.
Perkell, J., Cohen, M., Svirsky, M., Matthies, M., Garabieta, I., and Jackson, M. (**1992**). ''Electromagnetic midsagittal articulometer (EMMA) systems for transducing speech articulatory movements,'' J. Acoust. Soc. Am. **92**, 3078–3096.
Perkell, J. S., Matthies, M. L., Lane, H., Guenther, F. H., Wilhelms-Tricarico, R., Wozniak, J., and Guiod, P. (**1997**). ''Speech motor control: Acoustic segmental goals, saturation effects, auditory feedback and internal models,'' Speech Commun. **22**, 227–250.
Perkell, J. S., Matthies, M. L., and Svirsky, M. A. (**1994**). ''Articulatory evidence for acoustic goals for consonants,'' J. Acoust. Soc. Am. **96**, 3326.
Perkell, J. S., Matthies, M. L., Svirsky, M. A., and Jordan, M. I. (**1993**). ''Trading relations between tongue-body raising and lip rounding in production of the vowel [u]: A pilot ''motor equivalence'' study,'' J. Acoust. Soc. Am. **93**, 2948–2961.
Perkell, J. S., Matthies, M. L., Svirsky, M. A., and Jordan, M. I. (**1995**). ''Goal-based speech motor control: A theoretical framework and some preliminary data,'' J. Phonetics **23**, 23–35.
Saltzman, E. L., and Munhall, K. G. (**1989**). ''A dynamical approach to gestural patterning in speech production,'' Ecological Psychol. **1**, 333–382.
Savariaux, C., Perrier, P., and Orliaguet, J. P. (**1995a**). ''Compensation strategies for the perturbation of the rounded vowel [u] using a lip tube: A study of the control space in speech production,'' J. Acoust. Soc. Am. **98**, 2428–2442.
Savariaux, C., Perrier, P., and Schwartz, J. L. (**1995b**). ''Perceptual analysis of compensatory strategies in the production of the French rounded vowel [u] perturbed by a lip tube,'' in *Proceedings of the XIIIth International Congress of Phonetic Sciences* (KTH and Stockholm University, Stockholm, Sweden), Vol. 3, pp. 584–587.
Stevens, K. (**1998**). *Acoustic Phonetics* (MIT Press, Cambridge, MA).
Westbury, J. R., Hashi, M., and Lindstrom, M. J. (**1995**). ''Differences among speakers in articulation of American English /r/: An x-ray microbeam study,'' *Proceedings of the XIIIth International Conference of Phonetic Sciences* (KTH and Stockholm University, Stockholm, Sweden), Vol. 4, pp. 50–57.
Westbury, J. R., Hashi, M., and Lindstrom, M. J. (**1998**). ''Differences among speakers in lingual articulation of American English /ɹ/,'' Speech Commun. **26**, 203–226.

Perturbation-free measurement of the harmonics-to-noise ratio in voice signals using pitch synchronous harmonic analysis

Peter J. Murphy
Department of Physics, Royal College of Surgeons in Ireland, 123 St. Stephen's Green, Dublin 2, Ireland

(Received 18 February 1998; revised 8 January 1999; accepted 26 January 1999)

The measurement of the harmonics-to-noise ratio (HNR) in speech signals gives an indication of the aperiodicity of the speech waveform. This may be due to the presence of jitter, shimmer, additive noise, waveshape change, or some unknown combination of these factors. In order to estimate the HNR as a measure of the additive noise component only, the contaminating effects of the other contributory components must first be removed. A pitch synchronous harmonic analysis is proposed to overcome this problem. The procedure takes advantage of the time scale compression–frequency expansion property of the Fourier series in order to eliminate jitter and shimmer. Successive spectra are added by harmonic number as opposed to frequency location, and perturbation is removed due to the fact that the relative heights of the harmonic components remain the same for scaled signals. The technique is examined on synthetically generated voice signals. A discussion of the results is given in terms of human voice signals, characterization of jitter, vocal tract filtering effects, perturbation mechanisms, nonlinear dynamics, and the possibility of developing the method for use with inverse filtering strategies. [S0001-4966(99)01305-3]

PACS numbers: 43.70.Dn, 43.70.Gr [AL]

INTRODUCTION

An initial attempt to quantify the noise level in pathological voices using acoustic analysis was proposed by Yanagihara (1967) three decades ago. The method was based on the visual inspection of narrow-band speech spectrograms, where a four-point rating scale of the noise level (in the spectrogram) was correlated with hoarseness ratings as assessed by three listeners. A positive correlation of 0.65 at the 0.01 significance level was found between the spectrographic type and the judge-perceived degree of hoarseness. Yanagihara went on to say that ''study on the cycle to cycle spectrum change with hoarseness with the use of wide band filter settings will provide additional information on noise components and harmonic changes.'' (p. 540). Rontal *et al.* (1975) reported favorably on the use of broadband spectrograms and cited several advantages in using spectrography, such as the ability to keep a permanent record and the capacity to analyze continuous speech. A thorough and up to date exposition on the clinical use of speech spectrography can be found in Baken and Daniloff (1991). Although the spectrograph remains an extremely useful clinical tool, it is not without disadvantages. Among these are that the method is a visual comparison and, in that sense, still subjective, and some training or at least familiarity is required to be able to read the spectrographic images effectively and hence make useful diagnoses. Other potential drawbacks are cited in Klatt (1982).

Many possible solutions have been put forward in an attempt to automate the spectrographic procedure, thereby removing the inherent subjectivity (and time consumption) of the visual approach. Indices such as the HNR and the SNR (harmonics-to-noise and signal-to-noise ratios) calculated from such diverse methodologies as spectral (Kitajima, 1981; Klingholtz and Martin, 1985; Kasuya *et al.*, 1986a; Kasuya and Endo, 1995; Kojima *et al.*, 1980; Muta *et al.*, 1988; Hiraoka *et al.*, 1984; Qi *et al.*, 1995; Michaelis *et al.*, 1997), cepstral (Koike and Kohda, 1991; de Krom, 1993; Hillenbrand, 1994; Qi and Hillman, 1997) and time domain (Yumoto *et al.*, 1982; Kasuya, 1986; Kasuya and Ando, 1991; Imaizumi, 1986; Klatt and Klatt, 1990; Hillenbrand *et al.*, 1994; Qi, 1992; Ladefoged and Antonanzas-Barroso, 1985) analysis have been investigated.

Despite this widespread investigation into harmonics-to-noise ratios in pathological voices, all of the above-mentioned approaches, with the exception of the Ladefoged and Antonanzas-Barroso (1986), Qi (1992), Qi *et al.* (1995), Klingholtz and Martin (1985), and Michaelis *et al.* (1997) methods, give HNRs that are dependent on jitter and shimmer as well as additive noise, i.e., the HNR values obtained from these procedures reflect the aperiodicity in the waveform but they supply a nonspecific index. However, HNR, when supplied in popularly available commercial software packages, is presented as an independent parameter, separate from jitter and shimmer, i.e., as if it was representative of a random noise component such as aspiration noise. Many researchers have commented on this problem; for example, de Krom (1993) states ''...HNR integrates several aspects of the acoustic stability of the signal. As such, HNR may be a useful parameter in the analysis of voice quality, although it cannot be directly interpreted in terms of the underlying glottal events or perceptual characteristics.'' (p. 254). Hillenbrand (1987), in a comprehensive assessment of not only this problem but of the related problems of extracting jitter and shimmer in the presence of additive noise (as well as each other), similarly concludes that care must be taken when interpreting these indices as independent parameters.

Methods to overcome the problem of having jitter and shimmer sensitive HNRs have primarily focused on time-domain strategies. The most commonly used time-domain technique has been the Yumoto *et al.* (1982) technique,

which obtains harmonics-to-noise ratio based on the traditional HNR calculation where the square of the average wavelet[1] equals energy and the average of the variance (i.e., the sum of the squares of the differences between the average wavelet and the other wavelets) equals noise. The problem is that jitter contributes to the noise estimate because the maximum period is taken in the averaging. Modification of this approach has formed the basis of several innovative attempts at providing jitter-free HNRs—Hillenbrand (1987) investigated using the minimum period for averaging.[2] Ladefoged and Antonanzas-Barroso investigated using 75 percent of each period and hopping the period until maximum overlap between successive wavelets occurred, thereby minimizing the jitter contribution to the HNR. It is noted that this may provide a useful strategy in certain cases, but for the radiated speech waveform, such an approach can never guarantee a completely jitter-free measurement of the HNR. Qi has applied the temporal matching, word recognition schemes of dynamic programming (DP) (Qi, 1992) and unconstrained dynamic programming (UDP) (Qi *et al.*, 1995) to this problem. A procedure, termed zero-phase transformation (ZPT) (of successive signal periods) was also investigated by this author (Qi *et al.*, 1995). Although these methods have been shown to provide jitter-free HNRs, they may also remove random variations in the waveform accidentally. As stated by Qi (1992), ''It should be pointed out that the time normalization of the wavelets using DTW (dynamic time warping) will remove indiscriminately all possible variations of wavelets due to temporal differences, even if the temporal differences are due to additive noise.'' (p. 2575). Therefore, optimum time alignment (DP and UDP) may be susceptible to overestimating HNR. Furthermore, it is computationally expensive. As will be shown shortly, the main problem with any of these approaches, with the exception of the Michaelis *et al.* (1997) technique, is that they attack the problem of defining source variability through examining the output waveform.

Klingholtz and Martin (1985) have taken the alternative approach of correlating the HNR with respect to jitter and additive noise separately. Therefore, if the value for jitter is known, the corresponding HNR value can be directly determined. If the HNR value is less than that assigned to that value, then the remainder can be assumed to be the actual additive random noise component. Several problems exist with this approach when applied to human voice signals. As stated by Hillenbrand (1987), ''adding increasing amounts of noise to an otherwise perfectly periodic voice signal resulted not only in decreases in HNR values, but also substantial increases in measured values of pitch and amplitude perturbation.'' (p. 458). Therefore, in the presence of noise, jitter values are inflated and therefore, the jitter correlation with HNR will be offset. As stated previously, the aim of obtaining jitter- and shimmer-free HNRs is to acquire greater specificity in determining the speech signal with continued specificity possibly providing information regarding flow dynamics. However, the Klingholtz and Martin (1985) study, although in theory capable of specifying perturbation-free HNRs, does not allow for such continued development. Similar comments can be made regarding the Michaelis *et al.* (1997) technique. This approach, which is based on the use of the inverse-filtered residual (or error) signal, suffers from the same problems reported by Kasuya *et al.* (1986b) about the approach of Davis (1976) who similarly used the residual signal, i.e., unlike the flow waveform (see, for example, Holmberg *et al.* (1988), for data on normal voice types, and Hillman *et al.* (1989) for data on pathological voice types), it is not physically realizable and cannot be explained in terms of glottal attributes.

Another problem common to all approaches, except for the studies of Qi (1992), Qi *et al.* (1995), and Hillenbrand (1988), is that they do not provide accurate quantification of the harmonics-to-noise ratio, even when synthesis data have been used. The methods show the general trend of HNR decreasing with increasing noise levels as opposed to accurate quantification. Furthermore, the HNR consists of a numerator (harmonic energy) and a denominator (noise energy) and hence the ratio by itself does not give absolute information regarding either the noise level or the signal strength.[3] A low HNR may indicate moderate signal strength in the presence of a strong contaminating noise signal, or it may indicate a low amplitude signal in the presence of moderate noise levels. Therefore, specification of the noise or harmonic energy in conjunction with the HNR is required for a more complete description. In addition, the use of the averaged signal has proven superior to the use of noise-contaminated estimates (Cranen and Boves, 1987), and the extraction of the noise component gives important information relevant to the temporal distribution of noise (Imaizumi, 1986).

Therefore, given the limitations of the above-mentioned direct and indirect approaches, new methods for determining perturbation-free HNRs are required. The purpose of the present investigation is to devise a method that gives an HNR where the noise is representative of the additive random noise component in voice signals. This ongoing extraction of greater specificity from acoustic measures may help to provide more precise information regarding glottal flow dynamics and hence, tentatively, vocal fold vibration. Before detailing the method, it is instructive to give operational definitions of aperiodicity, noise, and perturbation.

A. Definition of aperiodicity and noise

The terms ''aperiodic,'' ''noise,'' and ''perturbation'' can all be equally applied in describing waveform irregularities, no matter what the source of these irregularities may be. However, terms that facilitate greater specificity are required for discussing the nature of these irregularities. Despite the substantial amount of work into HNRs in voice signals in the vocal pathology literature, a clear definition of what is meant by noise has been conspicuous by its absence. An operational definition generally given or more often implied is that noise constitutes the *nonharmonic energy* found in the speech signal. Thus, a perfectly periodic waveform exhibits an infinite harmonics-to-noise ratio. In contrast, the waveforms from real human voices will always vary to a certain extent, due to effects such as flutter or tremor, and therefore contain noise energy with harmonics-to-noise ratios in the

15-to-30-dB range being typical (somewhat dependent on ratio type and methodology). Furthermore, jitter and shimmer contribute to a reduction in measured HNRs because, by this definition, they are properly labeled noise components. Consequently, for an overall measurement of noise according to the above definition, all perturbation parameters should be included.

However, the present investigation is concerned with obtaining greater specificity from the waveform analysis, and in this respect, it is required to differentiate, if possible, the different origins of the noise. For this reason, the term aperiodic is used to denote any of the multivariate deviations from perfect periodicity that may exist and the term noise is attributed a more narrow meaning as detailed below.

For the immediate purposes of the present investigation, four distinct sources of deviation from perfect periodicity can be considered to exist.

(1) Variation in period of the waveform from cycle to cycle (jitter).
(2) Variation in amplitude of the waveform from cycle to cycle (shimmer).
(3) (Additive) noise.
(4) Waveshape change.

Number 3 refers to the turbulent flow produced at the glottis during phonation, perhaps due to lack of, or incomplete, closure, or due to the presence of mass lesions of the vocal folds. Investigations into the origin of turbulent flow and its acoustic manifestation (Dowling and Ffowcs Williams, 1982) have been conducted in relation to voiced fricatives (Stevens, 1971; Shadle, 1985), vocal fold pathologies (see, for example, Isshiki *et al.*, 1978; Hillman *et al.*, 1983) and glottal geometries (Scherer and Guo, 1991). For synthesis purposes, glottal noise is generally modeled as random, mean zero, Gaussian noise. This may occur predominately at peak flow, at closure, or it can be a continuous random distribution existing during both the open and closed phases of the glottal cycle. Imaizumi (1988) describes the two former manifestations in pathological speakers. These conditions may be explained in part by a consideration of phonation theory and the conditions for turbulence as dictated by the Reynolds number, but further studies are required.

Aperiodicity can also occur due to specific changes within the vibratory pattern from cycle to cycle which are not due to shimmer or jitter but due to a change in the shape of the glottal waveform (number 4 above). Study of this latter characteristic requires precise knowledge of the flow waveform, i.e., measurement of open quotient (open time divided by period), closing quotient (closed time divided by period), speed quotient (open time divided by closed time), etc. Organic pathologies resulting from hyperfunctional voice use provide examples of where adductory bias or decreased closing quotient may occur (Hillman *et al.*, 1989). Though this study provides an example of a waveshape change with respect to normal, the parameter of primary interest in the present investigation is the variation in waveshape over many cycles.

It should be pointed out that, in theory at least, a periodic signal can also show considerable deviation from expected ''normality'' i.e., the waveshape could be quite atypical, yet consistent from period to period (cf. normal, breathy, pressed, Alku and Vilkman, 1996). This point is clearly stated in Hiraoka's harmonic intensity analysis, where the amplitude of the fundamental is removed from the calculation of the harmonic frequencies. Conversely, a situation in which the period markers are fixed for each cycle but the waveform behaves very erratically between the period markers is also feasible. Spasmodic dysphonia is an example of a waveform containing irregular, unrelated waveshapes of similar period, albeit not changing on a period-by-period basis (Aronson, 1990).

For completeness, it should be stated that the aperiodicities listed above cover what may be termed ''periodwise'' periodic phenomena, i.e., the analysis covers a system that is expected to to be periodic on a period-by-period basis, but aperiodicities are introduced during each period. This does not include the quasiperiodic phenomena that may result from asynchronous coupled oscillators or from nonlinear dynamical systems. These phenomena are analyzed using the methods of nonlinear dynamics (Titze *et al.*, 1993). The degree to which aperiodicities in voice signals result from chaotic behavior or from behavior describable by traditional signal processing strategies is unknown. A preliminary estimate is given in Herzel *et al.* (1994) where 25% of the pathological voice samples show signs of underlying chaotic oscillation.

B. Definition of perturbation

As stated above, perturbation can be broadly defined as the variation from perfect periodicity of the waveform from cycle to cycle. However, as in the case for the definition of noise, it is convenient in the present discussion to restrict this term to specify number one and two in the definition of aperiodicity, i.e., jitter (pitch perturbation) and shimmer (amplitude perturbation). In defining jitter and shimmer, the descriptions are given in terms of the glottal flow waveform (as opposed to the fundamental frequency, the differentiated flow, or the radiated speech waveform). Jitter can be defined in general terms as the variation in the period of the waveform from period to period. Scaled jitter is the variation in the period of the waveform from period to period such that $f(t)=1/f(k)\times f(t')$ where $(t'=k\times t)$. Holmes (1973) and Rosenberg (1971), for example, have used scaled jitter in order to provide improved speech synthesis.

Shimmer is broadly defined as the variation in amplitude of the waveform from period to period. For the glottal flow waveform, using statistical arguments it can be shown (Hillenbrand, 1987) that the same shimmer levels will result regardless of whether peak or root-mean-square intensity in a glottal cycle is used to calculate the amplitude of the waveform. However, from this definition it is obvious that shimmer levels will be very sensitive to additive noise. Hillenbrand (1987) states that ''the effect of additive noise on measures of amplitude perturbation is disturbing since it is generally assumed—implicitly if not explicitly—that shimmer measurements reflect variability in the amplitude of the glottal source'' (p. 451). In fact, Qi *et al.* (1995) use the term amplitude perturbation (shimmer) to include any varia-

tion in amplitude (i.e., including additive noise) of the glottal source. This, however, leads to a redundancy in a variable exclusively defined for measuring the variation in the amplitude of the glottal flow waveform (exclusive of additive noise). Therefore, the definition of shimmer is altered in order to differentiate its presence from that of additive noise by imposing the constraint that the amplitude variation between corresponding points of two consecutive cycles must differ by a multiplicative factor.

I. METHOD

In an attempt to overcome the influence of jitter and shimmer on the harmonics-to-noise ratio, and with a view to obtaining spectral measures on a period-by-period basis in order to obtain greater specificity from the acoustic analysis, the following novel technique is implemented. A periodic wavetrain of glottal flow pulses with period T contaminated with additive noise is considered and the wavetrain is analysed on a period-by-period basis. The Fourier series[4] coefficients a_k and b_k are calculated via Eqs. (2) and (3) for the period in question, from which the harmonic amplitude is determined via Eq. (4).

$$s(t)=\frac{a_0}{2}+\sum_{k=1}^{\infty}\left(a_k\cos\left(\frac{2k\Pi t}{T}\right)+b_k\sin\left(\frac{2k\Pi t}{T}\right)\right), \quad (1)$$

where

$$a_k=\frac{2}{T}\int_0^T s(t)\cos\left(\frac{2k\Pi t}{T}\right)dt, \quad (2)$$

and

$$b_k=\frac{2}{T}\int_0^T s(t)\sin\left(\frac{2k\Pi t}{T}\right)dt, \quad (3)$$

t=time, T=periodic time, a_0=mean value of waveform.

$$h_k=(a_k^2+b_k^2)^{1/2}. \quad (4)$$

In taking the ''series'' viewpoint, the noise-contaminated wavelet is considered to be one of an infinite train of identical wavelets,[5] i.e., the noise is counted into the signal harmonics. The Fourier series is then taken for the next period and the analysis is continued in this fashion for the complete waveform. If the waveform is truly periodic, comparison between adjacent periods (i.e., Fourier series coefficients) should indicate equality. However, because additive noise is present, the series coefficients will differ. A typical HNR calculation can now be implemented, e.g., the Yumoto *et al.* technique with the series coefficients replacing the time-domain signal amplitudes. In order to obtain the harmonics-to-noise ratio, the pitch-synchronous Fourier coefficients are averaged and the averaged coefficients are then subtracted from the individual pitch-synchronous coefficients in order to obtain the spectral noise estimate and hence the HNR.

$$\mathrm{HNR}=10\times\log_{10}\left[\frac{M\times\Sigma_i^L(a_{iAV})^2+(b_{iAV})^2}{\Sigma_i^L\Sigma_j^M(a_{ij}-a_{iAV})^2+(b_{ij}-b_{iAV})^2}\right]. \quad (5)$$

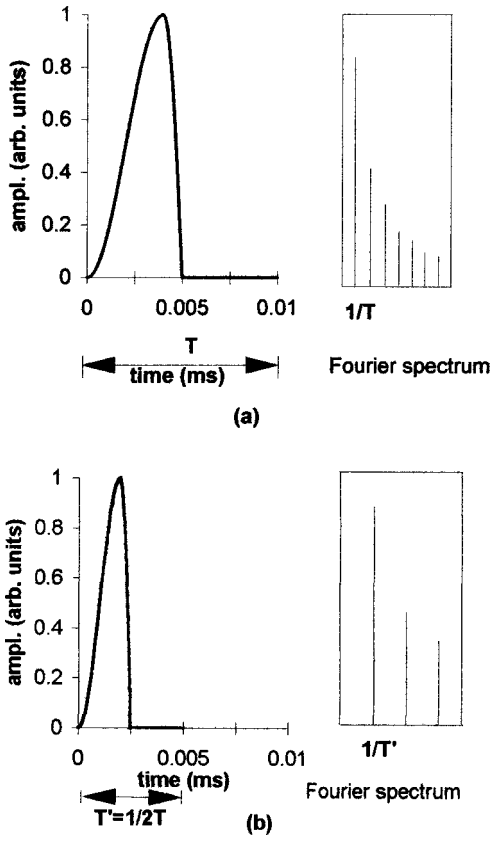

FIG. 1. Glottal flow waveforms with periods of (a) 10 ms, and (b) 5 ms with corresponding Fourier coefficients (absolute magnitude values) shown in captions. [(a) $n\times100$ Hz and (b) $n\times200$ Hz.]

$a_{ij}=i$th cosine of jth spectrum and $b_{ij}=i$th sine of jth spectrum, M=total number of spectra, L=total number of harmonics, where

$$a_{i\mathrm{AV}}=\sum_j^M a_{ij} \quad \text{and} \quad b_{i\mathrm{AV}}=\sum_j^M b_{ij}. \quad (6)$$

The Fourier coefficients are averaged as opposed to the harmonic amplitudes or energies because otherwise, when the noise is greater than the harmonic levels (the higher harmonics for the flow pulse), the noise contributions will not sum to zero as required, giving rise to overestimates of the HNR.

A periodic wavetrain of glottal flow pulses contaminated with jitter is now considered. In applying the Fourier series, any periodic waveform[6] can be represented as the sum of sine and cosine terms [Eq. (1)] and it can be seen [Eqs. (2) and (3)] that any two waveshapes that are identical in every respect excepting period length (T) will have Fourier coefficients that bear the same relationship to each other, spaced at an integer number times the inverse of their period. Compression in the time domain results in frequency domain expansion and vice versa. This ''time compression–frequency expansion'' property [Eq. (7)] of the Fourier series is illustrated for glottal flow waveforms of 10 ms and 5 ms in Fig. 1(a) and (b) with Fourier spectra captions shown in the right-hand side of the figure.

$$s(t)=F(f), \quad s(kt)=F\left(\frac{f}{k}\right), \tag{7}$$

where f = frequency, k = scaling parameter, F = Fourier series coefficient, and t = discrete time.

A comparison of harmonic amplitudes for two identical wavelets differing only in period (i.e., wavelets that are scaled versions of each other with no amplitude difference between corresponding points in consecutive cycles) should indicate that the Fourier coefficients are equal, i.e.,

$$\begin{aligned} a_n(1/T)-a_n(1/T')&=0,\\ b_n(1/T)-b_n(1/T')&=0, \end{aligned} \tag{8}$$

where $a_n = n$th cosine amplitude and $b_n = n$th sine amplitude.

Now applying Eq. (5) to a wavetrain contaminated with both additive noise and jitter, it can be seen that the algorithm provides a jitter-free HNR. In this manner, waveforms are compared by harmonic number as opposed to the more usual comparison between ''same frequency'' location.

A periodic wavetrain of glottal flow pulses contaminated with shimmer is considered next. First, the method [Eq. (5)] represents the effect of shimmer on HNR accurately, i.e., if $g(t)$ $(0\text{ to }T)=c\times g(t')$ $(T\text{ to }2T)$, where t' is equal to $t+T$ and c is a constant, then $a_k(t)=c\times a_k(t')$ and $b_k(t)=c\times b_k(t')$ [where $g(t)$ is the flow waveform and a_k and b_k are the Fourier coefficients]. Shimmer is therefore conveniently removed through pitch-synchronous amplitude normalization (in either domain). However, considering the multivariate case, the normalization in the time domain is problematic due to the presence of additive noise. This is not the case in the frequency domain, as the noise is spread equally over all frequencies while most of the signal energy is present within the first few harmonics. Therefore, frequency-domain normalization is much less sensitive to additive noise than time-domain normalization. This seemingly trivial difference is in fact a very important advantage of the frequency-domain analysis over any time-domain counterparts.

In considering the ''all in'' aperiodicities of jitter, shimmer, additive noise, and waveshape change, if the denominator in Eq. (5) is not equal to zero, then either a waveshape change has occurred or additive noise is present in the signal, i.e., Eq. (5) provides a jitter- and shimmer-free harmonics-to-noise ratio (waveshape changes are dealt with in the Discussion section). A slight modification of the equation gives the harmonics-to-noise ratio based on the difference in consecutive spectra. Obtaining the spectrum pitch synchronously opens up the possibility of taking a variety of spectral measurements specifically related to glottal flow characteristics and perturbations. The total harmonic, average percentage amplitude perturbation, THAPAP, is defined as

$$\text{THAPAP}=\left[\sum_{i}^{L}\sum_{j}^{M-1}\frac{|a_{ij}-a_{i\text{AV}}|}{a_{i\text{AV}}}+\frac{|b_{ij}-b_{i\text{AV}}|}{b_{i\text{AV}}}\right]. \tag{9}$$

Substituting dB values for the Fourier coefficients in the numerator of Eq. (9) and removing the denominator gives the total harmonic shimmer index. Other indices such as average percentage amplitude perturbation for 1st harmonic (APAP), distortion factor (amplitude of $f0$ divided by total signal amplitude), H_1-H_2 (ratio of amplitude of first harmonic to that of the second) and H_1-A_3 (amplitude of the first harmonic to that of the first formant frequency) can also be conveniently extracted (the latter being taken from the output waveform). Explanations of the physiological correlates of these later two indices are found in Hanson (1997). It is preferable to extract indices such as H_1-H_2 from pitch-synchronous spectra, at least for pathological voice samples, so that perturbation does not offset the spectral content of the wavelets. Averaging the pitch-synchronous indices will then remove the additive noise contamination. Furthermore, at least for glottal flow correlations, it may be preferable to use the Fourier coefficients as opposed to the harmonic energies, as the glottal waveshape is phase sensitive.

The important deviation that is introduced when analyzing the radiated speech waveform is now considered. This occurs as a result of adding by harmonic number as opposed to exact frequency location. The problem is due to the vocal tract filtering action. If the technique had been developed using the resonated and radiated speech waveform, and wavelets were considered to be the same in every respect except period, we would have been dealing with waveforms that are impossible to realize in practice.[7] The fundamental frequency, $f0=1/T$, governs the harmonic source spectrum frequency locations. The amplitudes of these harmonics are modified on passing through the vocal tract filter. For the output waveform, therefore, two cycles cannot be the same in every respect except for a period difference as they receive different resonant contributions. It is assumed that the vocal tract resonance configuration is exactly the same in each case. In the frequency domain, it can be seen that the slight offset in harmonic structure leads to a slightly different resonance contribution to the harmonic output spectrum. Therefore, jitter is effectively turned into ''harmonic shimmer.'' It is interesting to note that jitter cannot exist independently of shimmer for the radiated speech waveform. This fact has also been noted by Hillenbrand (1988), while examining the effect of aperiodicities on the perception of vocal qualities. He also examined a second shimmer contribution which was due to the overlay of energy found due to the convolution sum of vocal tract impulse response and glottal pulse not being completely damped before the next period of excitation. Through comparison of typical jitter values for normal (0%–1%) (and pathological) voices with the resonant bandwidths for the first five formants, the magnitude of the shimmer component can be estimated. The relationship between the location of the fundamental and formant locations must also be taken into consideration. A correction scheme could then be developed based on a correlation between jitter, for a given $f0$ and the resultant harmonic shimmer. However, taking all of these parameters into consideration, it can be seen that the method is too unpredictable and that any approach developed to remove shimmer and jitter from the output waveform is likely to be contaminated, to some extent, from the filtering action of the vocal tract.

A more practical and potentially more useful approach is to use inverse filtering. Rosenberg (1971) obtained excellent results for inverse filtering based on pitch-synchronous spec-

tral analysis. The analytical expression for the glottal flow waveform [Eq. (11)] is derived from Rosenberg's observations of inverse filtered data. The method as introduced by Mathews *et al.* (1961), who state that ''the contributions from the vocal tract and glottal source can be uniquely separated and examined,'' (p. 667), is to first estimate the model parameters defined by $H(f_p)=R(f_p)V(f_p)G(f_p)$, where R, V, and G indicate frequency representations of radiation at the lips, the vocal tract, and glottal waveform, respectively (for the pth period). Values are computed for $H(f_p)$ and matched to the spectrum of the waveform $[Xn(f_p)]$ under investigation. The parameters are then adjusted so as to minimize the error criterion $[Xn(f_p)-H(f_p)]$. The spectrum of the glottal pulse waveform is then computed according to

$$G(k)=\frac{X_n(e^{j(2\Pi/Np)k})}{R(e^{j(2\Pi/Np)k})V(e^{j(2\Pi/Np)k})}, \quad 0\leqslant k\leqslant N_p-1, \tag{10}$$

where N_p is the number of samples in the pth period.

This result is important for the present development in that the two approaches can be combined, first obtaining the glottal frequency spectra $[G(k)_p]$ according to Eq. (10) and therefore removing the effects of the filtering action of the vocal tract, and then applying HNR [Eq. (5)]. It is a convenient arrangement in that the same analysis techniques are used. Also, of course, the inverse filtering not only eliminates the effects of the formant frequencies on HNR but also supplies the glottal spectrum (and pulse, if required).

II. ANALYSIS

A. Synthetic speech signals

The vowel /a/ is synthesized using an implementation of the discrete time model for speech production (Rabiner and Schafer, 1978) with the Rosenberg glottal flow pulse [Eq. (11)] used as the source function.

$$\begin{aligned} g_r(n)&=1/2[1-\cos(\Pi n/N_1)] \quad 0\leqslant n\leqslant N_1 \\ &=\cos(\Pi(n-N_1)/2N_2) \quad N_1<n\leqslant N_1+N_2 \\ &=0 \quad \text{otherwise.} \end{aligned} \tag{11}$$

A sequence of Rosenberg glottal pulses is used as input into a delay line digital filter, where the filter coefficients are obtained based on area function data for the Russian vowel a as given by Fant (1970) and a reflection coefficient at the lip end of 0.71. Radiation at the lips is modeled by the first-order difference equation $R(z)=(1-z^{-1})$. Figure 2 shows a few cycles of a 110-Hz waveform for the vowel a resulting from the digital realization. A sampling frequency of 10 kHz is used in the synthesis.

Aperiodicity is introduced into the waveform by altering the source function. Random shimmer is introduced by adding a random variable gain factor (of a given s.d. ranging from 1% to 32%) to the amplitude of the pitch period impulse train prior to convolution with the glottal pulse. The pitch period is multiplied by a random number generator of given variance in order to provide the required amount of random jitter (1% to 6% s.d.). Random additive noise is introduced by multiplying the glottal pulse by a random noise

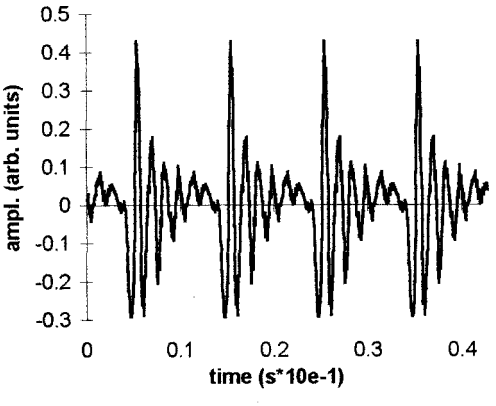

FIG. 2. Synthesized waveform (110 Hz) for the vowel /a/ produced from the digital realization of the discrete time model of speech production.

generator arranged to give signal dependent additive noise of a user-specified variance (s.d. 1% to 32%). The list of synthesis data is given in Table I. Further signals are also created for three levels of additive noise for frequencies beginning at 80 Hz and increasing in six, approximately equispaced steps of 60 Hz up to 350 Hz. The source signals are also produced at 40-kHz sampling at the six fundamental frequencies for each of the aperiodicties. These signals are not used to excite the filter function as this is designed to filter signals sampled at 10 kHz [see Cox *et al.* (1989) for an explanation of and solution to this problem].

B. Results

The number of periods ''n'' used in the calculation of the HNR using the present method, termed pitch-synchronous harmonic analysis (PSHA) is examined in Fig. 3. The HNR approaches the true HNR very quickly. In order to investigate the improvement in HNR obtained using the new approach (PSHA) over other methods, two standard, Fourier-based HNR algorithms are implemented. These are the Kojima *et al.* (1980) technique and a modified Hiraoka *et al.* (1984) analysis, similar to the Childers and Lee (1991) realization of this approach. Figure 4 shows the harmonics-to-noise ratio plotted with respect to $f0$ for the six levels of additive noise for each of the algorithms. Each method shows an $f0$ invariant characteristic and the noise levels are

TABLE I. List of synthesis data produced at 80, 110, 160, 220, 290, and 350 Hz for source signals sampled at 40 kHz and for 110-Hz filtered signals sampled at 10 kHz. [Filtered signals were also produced at the six fundamental frequencies for three levels of additive noise (4%, 8%, and 16% s.d.).]

Random jitter (s.d. %)	Additive noise (s.d. %)	Random shimmer (s.d. %)
1	1	1
2	2	2
3	4	4
4	8	8
5	16	16
6	32	32

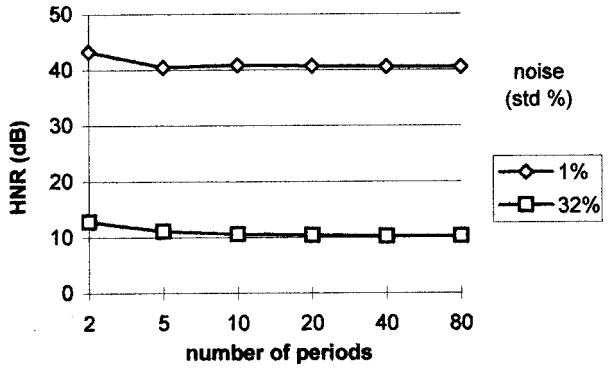

FIG. 3. HNR vs number of periods (n) used in the analysis for 1% and 32% random additive noise.

reflected at each fundamental frequency, showing approximately equi-spaced increments in HNR for decreases in noise level.

The three algorithms are next tested against the perturbation parameters. The HNR is plotted against shimmer in Fig. 5. Part (a) PSHA with and (b) without normalization, (c) Kojima *et al.* and (d) modified Hiraoka *et al.* Shimmer is completely eliminated by normalizing the waveform prior to obtaining the PSHA spectral estimates, and hence gives an infinite harmonics-to-noise ratio.

The variation of the HNR with jitter is examined in Fig. 6. For the Kojima *et al.* (b) and modified Hiraoka *et al.* (c) techniques, the HNRs are jitter- and shimmer sensitive, whereas the PSHA technique (a) is relatively jitter insensitivite. In the worst case (350 Hz–6% s.d.), the HNR is still 12 dB higher than the highest HNR corresponding to the lowest noise level [compare Fig. 4(a) with Fig. 6(a)].

The variation of the HNR for the perturbation parameters of the radiated speech waveforms are shown in Fig. 7. Both the Kojima *et al.* (b) and modified Hiraoka *et al.* (c) techniques are sensitive to jitter and shimmer as expected. PSHA (without normalization) (a) shows a reduced sensitivity to jitter; however, the effects of this perturbation parameter are not entirely eliminated. For the worst cases of jitter, the (PSHA-based) HNR is still above 20 dB, whereas the ratio has reached this index at ~2% s.d. random additive noise. The effects of jitter on the index have not been totally eliminated due to the filtering action of the vocal tract referred to in the previous section. All methods reflect the general trend of reduced HNR with either increased additive noise or increased shimmer. Figure 8 shows the variation of the harmonics-to-noise ratio with $f0$ for the three methods for the radiated speech waveform. For each method, the HNR increases with fundamental frequency.

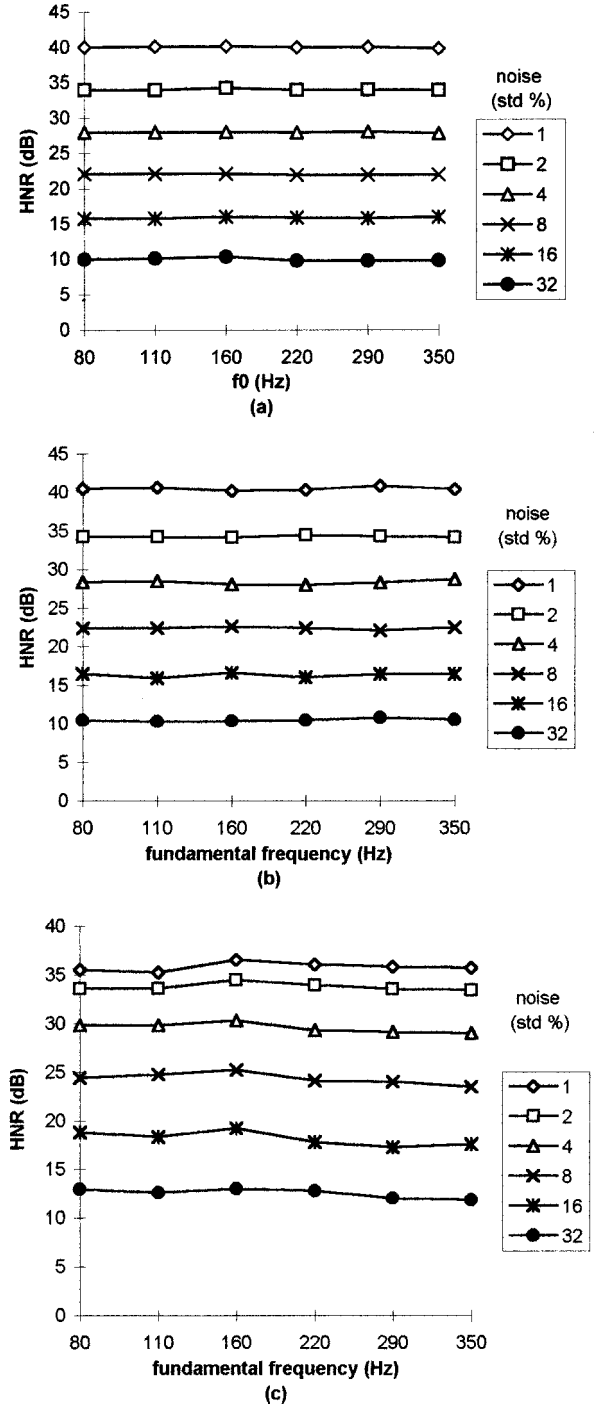

FIG. 4. HNR plotted against additive noise for the glottal flow waveform, where HNR was evaluated using (a) pitch-synchronous harmonic analysis (PSHA), (b) the Kojima *et al.* technique, and (c) the modified Hiraoka *et al.* analysis.

III. DISCUSSION

A discussion of the graphs in the results section follows.

A. Number of periods for use in determining the average Fourier series coefficients in the pitch-synchronous HNR calculation

A preliminary consideration for the PSHA algorithm is the choice of the number of periods n to use in the analysis. A variety of lengths of speech data is used in the list of HNR methods cited in the introduction. However, many of these analysis lengths are not directly comparable, as the methods are not pitch synchronous. The time-domain methods are comparable. Yumoto *et al.* (1982) use 50 periods in the analysis, stating that ''when one averages a sufficiently large number ... the noise component is cancelled.'' (p. 1545). The Qi refinement (Qi, 1992) of this method uses 20 periods in the analysis. The Ladefoged and Antonansos-Barrosso (1985) method uses 100 ms for both male and female voice samples. None of these reports tests the variation of the HNR

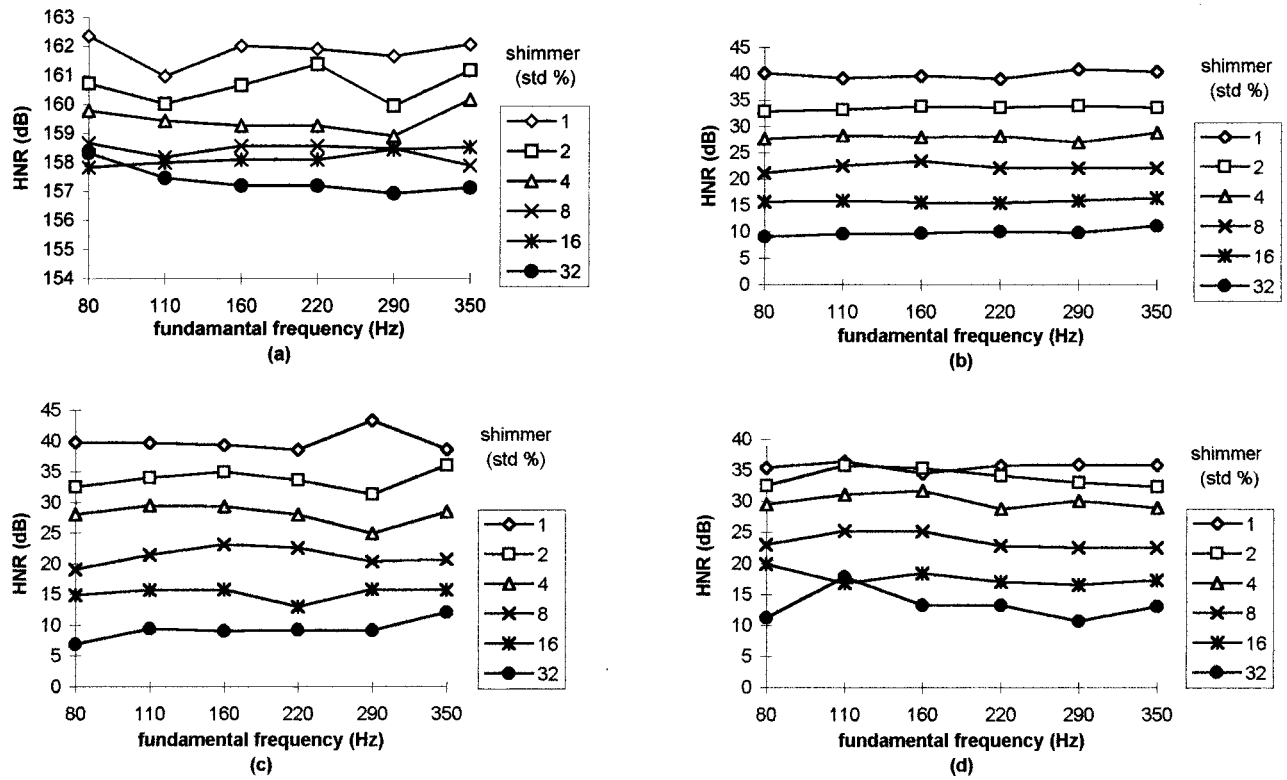

FIG. 5. HNR plotted against shimmer for the glottal flow waveform, where HNR was evaluated using (a) pitch-synchronous harmonic analysis (PSHA—normalized), (b) PSHA (without normalization), (c) the Kojima *et al.* technique, and (d) modified Hiraoka *et al.* analysis.

against the number of analysis periods. However, examination of a somewhat related issue, namely, the determination of the number of analysis periods for the precise quantification of jitter, has been investigated. Deem *et al.* (1989) report, in agreement with Titze *et al.* (1989), that reliable estimation requires ''at least forty cycles sample duration when measuring jitter in normal speakers. Whether or not this is the case in some or all pathological speakers is uncertain.'' (p. 694).

Figure 3 shows the HNR plotted for n varying from two to 80 periods for two levels of noise (1% and 32% s.d.). A good approximation to the actual HNR is obtained at each noise level for as little as two periods used in the averaging. By five periods, the HNRs have approached the true HNRs at each level of noise and remain at these values as n increases to 80 periods. For truly random processes, a longer observation time where the signal average approaches the true mean, and the estimated variance approaches the true variance, seems merited. However, in anticipation of nonstationarity (as in connected speech), a shorter observation interval may be more applicable. The fast convergence of the measured HNR to the true HNR shows promise for the method for use on connected speech. The number of analysis periods for accurate HNR estimation is considerably less than that required for accurate jitter estimation. This is perhaps because jitter is a difference measurement (even when waveform matching is used to extract the period), whereas the amplitude at each point in the wavelets goes into the calculation of the HNR.

B. HNR vs *f*0 (noise)

The use of synthetic speech signals, where known amounts of noise are added to the speech signal, enable a method of testing the HNR algorithms in a quantitative manner. Despite the long list of analysis techniques used to determine HNR, except for the methodological study of Hillenbrand (1987) and the studies of Qi and his co-workers, the effectiveness of a new algorithm has been inferred only in terms of general trends, i.e., the harmonics-to-noise ratio of the signal decreases as the noise level increases.

Figure 4(a) shows accurate correlation between the PSHA-(normalized) derived HNR values and noise levels for a broad range of fundamental frequencies to be expected in phonation (80 to 350 Hz). The Kojima *et al.* technique also reflects the noise levels acurately. For PSHA, the measurement is within 0.5 dB, and for the Kojima *et al.* technique, the method is within 1 dB. The modified Hiraoka *et al.* technique overestimates the HNR at low levels of noise and underestimates the HNR at higher noise levels. Therefore, in the absence of other signal aperiodicities, the PSHA and the modified Kojima *et al.* techniques indicate the HNRs accurately, with the Hiraoka *et al.* method showing reasonable correlation for a narrower noise range.

C. HNR vs *f*0 (shimmer) (Fig. 5)

Both the PSHA (without normalization) and Kojima *et al.* techniques reflect the influence of shimmer on the HNR reasonably accurately. The modified Hiraoka *et al.* analysis is less accurate but still shows the general trend. The

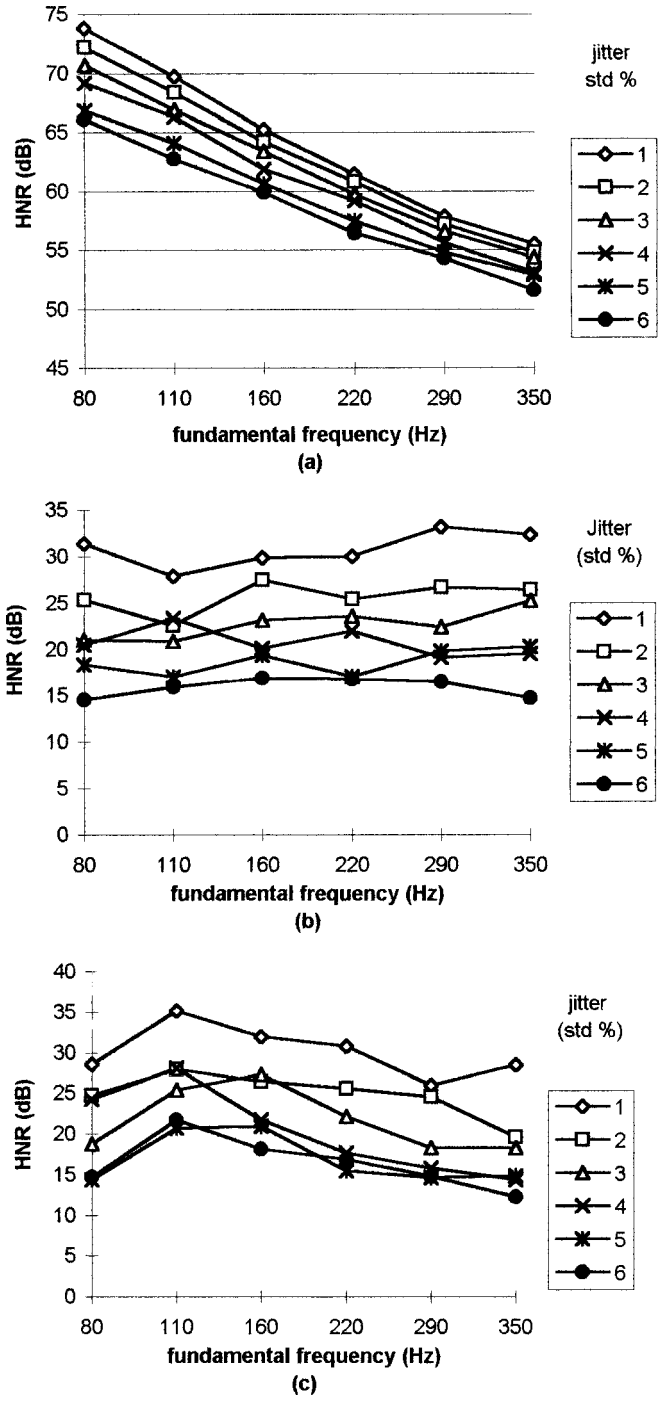

FIG. 6. HNR plotted against jitter for the glottal flow waveform, where HNR was evaluated using (a) pitch-synchronous harmonic analysis (PSHA), (b) the Kojima *et al.* technique, and (c) the modified Hiraoka *et al.* analysis.

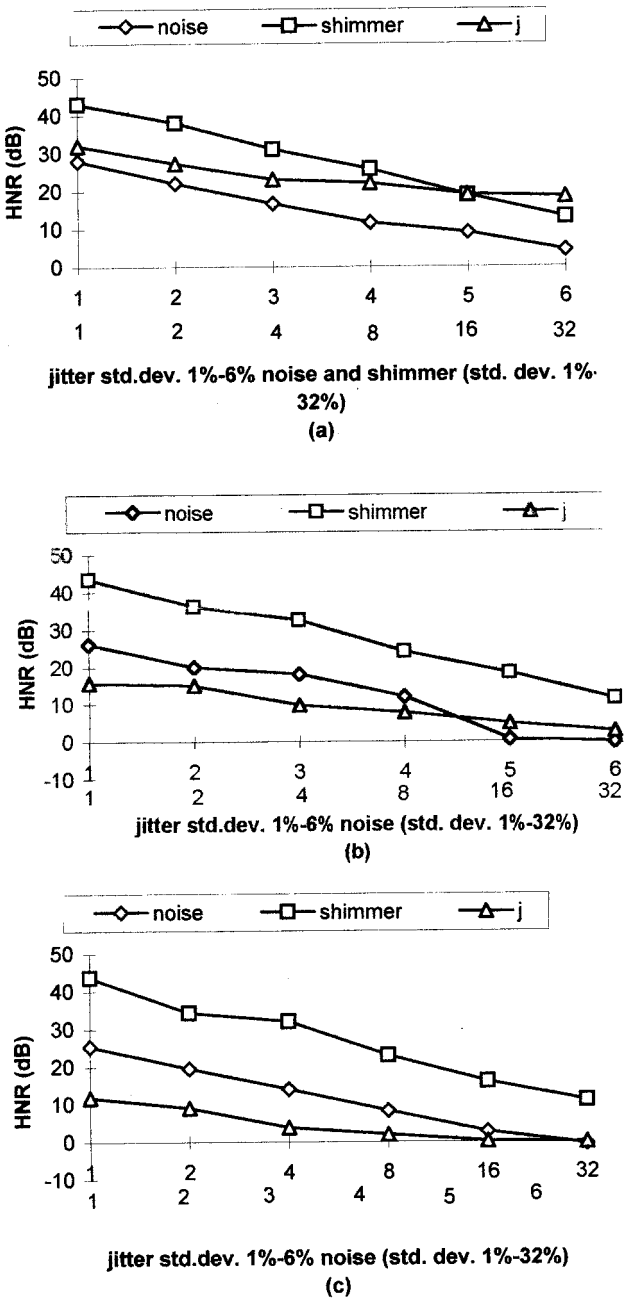

FIG. 7. HNR plotted against three perturbation measures of additive noise, random jitter, and shimmer for the output radiated speech waveform (at 110 Hz), where HNR was evaluated using (a) pitch-synchronous harmonic analysis (PSHA), (b) the Kojima *et al.* technique, and (c) the modified Hiraoka *et al.* analysis.

normalized PSHA algorithm is insensitive to shimmer as required. This gives an essentially infinite HNR (155–165 dB). An important point is that the normalized PSHA approach gives accurate HNR values for additive noise levels. This normalization is carried out in the frequency domain. As stated in Sec. I, this is an important advantage of a frequency-domain algorithm over a time-domain equivalent. Although the method is not examined on what Hillenbrand (1988) referred to as multivariate data, the approach is developed in anticipation of such signals, i.e., if jitter, shimmer, and additive noise are all present, the technique will be largely insensitive to the former two and would reflect the additive noise component as required.

D. HNR vs *f*0 (jitter) (Fig. 6)

The greatest influence of jitter on the HNR (6% s.d. at 350 Hz) for the PSHA technique still gives an HNR that is 12 dB larger than the highest HNR value for the smallest amount of additive noise. Therefore, the influence of jitter on the index can, for all practical purposes, be considered to be removed although it is not completely eliminated. However, upsampling the periods to an equal length would remove the remaining jitter sensitivity with upsampling to an integer

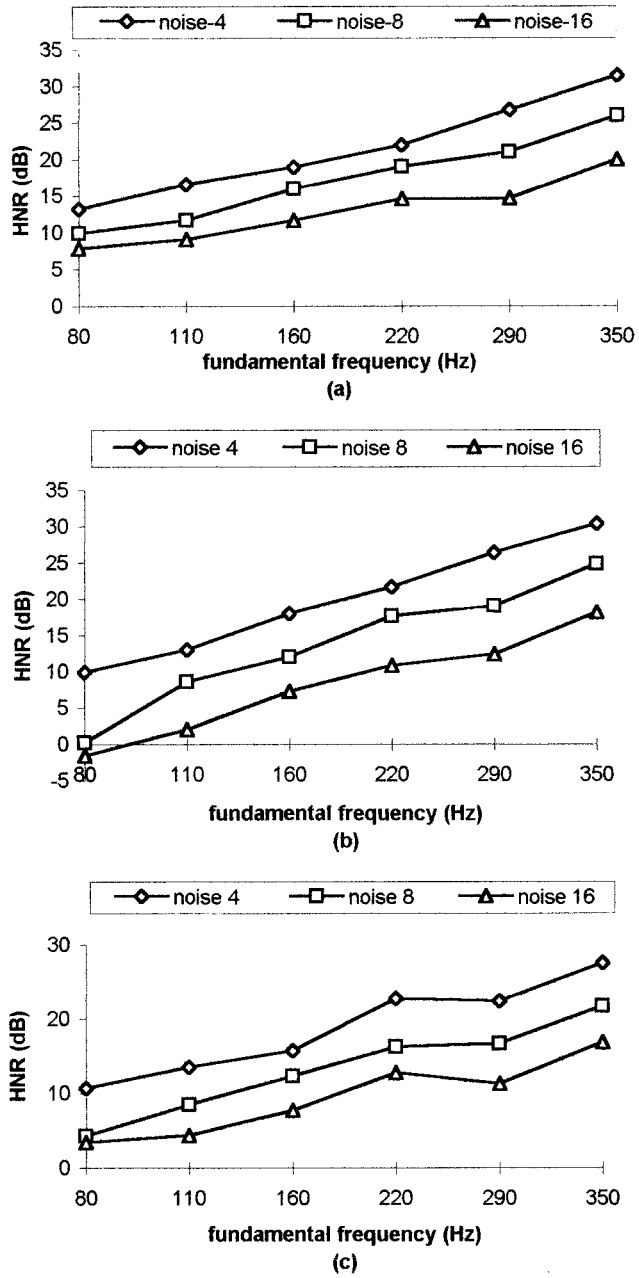

FIG. 8. HNR plotted against fundamental frequency ($f0$) for three levels of additive noise, where HNR was evaluated using (a) pitch-synchronous harmonic analysis (PSHA), (b) the Kojima *et al.* technique, and (c) the modified Hiraoka *et al.* analysis.

power of 2, providing a more efficient algorithm. The other two methods are jitter sensitive as expected, with jitter reducing the HNR from between 30 dB (1% jitter) to 15 dB (6% jitter) for each method.

E. HNR versus aperiodicities for the radiated speech waveform (Fig. 7)

The influence on the HNR of shimmer is reflected at the same levels as it is for the source (40 to 10 dB for 1% to 32% s.d. shimmer) for each method (PSHA without normalization). The effect of vocal tract filtering and radiation has not affected the influence of shimmer on the HNR, and therefore this is a situation where a measurement on the output waveform reflects source variability. In contrast, the HNR is different for the radiated waveform and the source waveform for equal noise levels added to the source. This is because of the influence of the formants on the levels of noise. However, the trend of equal increments in noise having corresponding decrements in the HNR is reflected for each method. Radiated jittered signals have a larger effect on the HNR as opposed to jittered source signals because of the many secondary effects of vocal tract filtering on jitter.

The trend of reduced sensitivity to jitter for the PSHA technique in comparison to the Kojima *et al.* and the Hiraoka *et al.* methods is encouraging (Fig. 7). However, a word of caution about using the PSHA technique (or any other algorithm) on the radiated speech waveform is merited. In the present investigation, jitter is only tested at a single value of fundamental frequency (110 Hz) for the radiated speech waveform. A jitter value of 2% is taken by way of illustration; at 100 Hz, $\Delta T = 0.2$ ms, while at 200 Hz, $\Delta T = 0.1$ ms. Because jitter is a time–frequency invariant measurement, as indicated by Eq. (12), for a given percentage jitter value the variation in fundamental frequency

$$\frac{\Delta f0}{f0} = \frac{\Delta T}{T}, \tag{12}$$

increases with fundamental frequency. For the example values given, the ΔTs correspond to $\Delta f0$s of 2 and 4 Hz for the 100 and 200 Hz signals, respectively. The variation in frequency introduced by the jitter component doubles for each successive harmonic doubling, giving a jitter value of 4 Hz for the 100 Hz signal and a jitter value of 8 Hz for the 200 Hz signal. The density of harmonics will be double for the 100 Hz signal and at a given frequency location where the 100 and 200 Hz signals' harmonics coincide (e.g., 200 Hz, first harmonic for the 200 Hz signal and second harmonic for the 100 Hz signal), the harmonic amplitudes will differ. Therefore, radiated waveforms with equal percentage jitter values at different fundamental frequencies will have different influences on HNR reduction. There are two further complicating factors:

(1) The relationship between harmonic locations and format peaks varies with $f0$.
(2) The overlay of energy into adjacent cycles due to the impulse response of the vocal tract has an $f0$ dependence, increasing with $f0$ increases.

The overflow of energy from adjacent cycles is tested by putting an impulse into the vocal tract filter to investigate the impulse response of the filter (v). The response still has energy contributions into the next period. The temporal extent of a filtered ''period'' depends on the convolution sum ($v*g$), where ''g'' is the glottal flow waveform. In the present synthesis, ''v'' is the dominant term (temporally) with increased periods having larger overlay, but the overriding criterion for determining the magnitude of the overlay was the proximity of the pitch periods. For jittered signals, the overlay will differ from period to period, introducing increased aperiodicity into the waveform and hence reduced HNR.

Therefore, several $f0$-dependent factors have an influence on HNR and a rather complicated $f0$ correction scheme is required. Hence, use of the PSHA method with the output waveform is not recommended. Furthermore, throughout all discussions, source/filter separability has been assumed, whereas in dealing with pathological voice types, this assumption is expected to be more severely tested, e.g., varying open times during a glottal cycle and hence a varying nonlinear filtering (however, see Hanson (1997) for a negligible effect reported for this hypothesis).

F. Variation of harmonics-to-noise ratio with fundamental frequency for the radiated speech waveforms

One of the most striking features of the graphs in the Results section is the variation of the harmonics-to-noise ratio with fundamental frequency ($f0$). All methods show this trend of increased HNR with $f0$ (Fig. 8). In the pitch-synchronous harmonic analysis technique implemented by Muta *et al.* (1988), a similar $f0$ trend is also noticed. The variation is simply attributed to the type of synthesis used. In a report which determined the harmonics-to-noise ratio using the cepstrum technique, de Krom (1993) also observes the same variation of the HNR with fundamental frequency, i.e., HNR increased as $f0$ increased. However, no satisfactory explanation of this trend has been proposed.

Some possible causes for this trend include bandwidth considerations,[8] statistical arguments (differing number of sample points for differing period lengths), or the type of synthesis. The first two postulates can be immediately disregarded as there is no variation in the HNR with $f0$ for the source signals. Examination of the spectra for s.d. 4% additive noise for the 80-, 160-, and 350-Hz source signals (Fig. 9) helps provide the answer for the observed $f0$ trend. The basis behind this occurrence is examined in the Method section, where ''scaled jitter'' is investigated. The source signals with different fundamental frequencies can be viewed as scaled versions of each other, and therefore their relative harmonic strengths are equal. The first 14 harmonics for the 80-Hz file have occurred by 1120 Hz, whereas the first 14 harmonics for the 350-Hz file span the complete frequency range up to 5000 Hz (some alias contributions are expected here also). In one sense, therefore, it can be inferred that the HNR variation is due to the synthesis. However, it is due to the difference in the distribution of harmonics over a set frequency range as opposed to any peculiarities due to the digital implementation of vocal tract filtering, i.e., it is a real voice issue.

In consideration of the HNR versus $f0$ trend reported for the synthetic voice signals in the present study (and in other studies), if an HNR calculation is applied to a data set of human voice signals, then an $f0$ correction scheme is also required. However, HNRs have shown good differentiability between patient and normal data sets without any $f0$ correction factor (see, for example, Yumoto *et al.*, 1982; Kojima *et al.*, 1980). Three considerations might mitigate against this trend (and hence need for an $f0$ correction factor) in human voice signals. First, formant frequency locations for female speakers are on average 25% higher, second, breathiness (and hence increased spectral tilt) is a common characteristic of female voice (Hanson, 1997), and third, the perception of roughness has a psychoacoustic dependency on frequency, increasing as fundamental frequency decreases (Zwicker and Fastl, 1990). Therefore, although the Yumoto *et al.* and Kojima *et al.* techniques have ignored the HNR vs $f0$ trend introduced as a result of the speech production process, the need for a correction scheme is offset, in part, due to a speech-perception phenomenon. Although this is fortuitous for the correlation of the HNR and roughness (at least for males), for accurate quantification the processes of speech production and auditory response must be accounted for within the algorithmic analysis. Martin *et al.* (1995), noting that the HNR (Yumoto *et al.*) correlates better for perceptually rated roughness scores (73% of which were for male speakers) than for breathiness scores (80% female), postulate that this may be because the HNR is more effective at lower frequencies (as shown above). They also point out that in the studies of Yumoto *et al.* and Kojima *et al.*, there is, in fact, a two to one ratio in favor of male subjects.

The observed trend also has implications for bandwidth

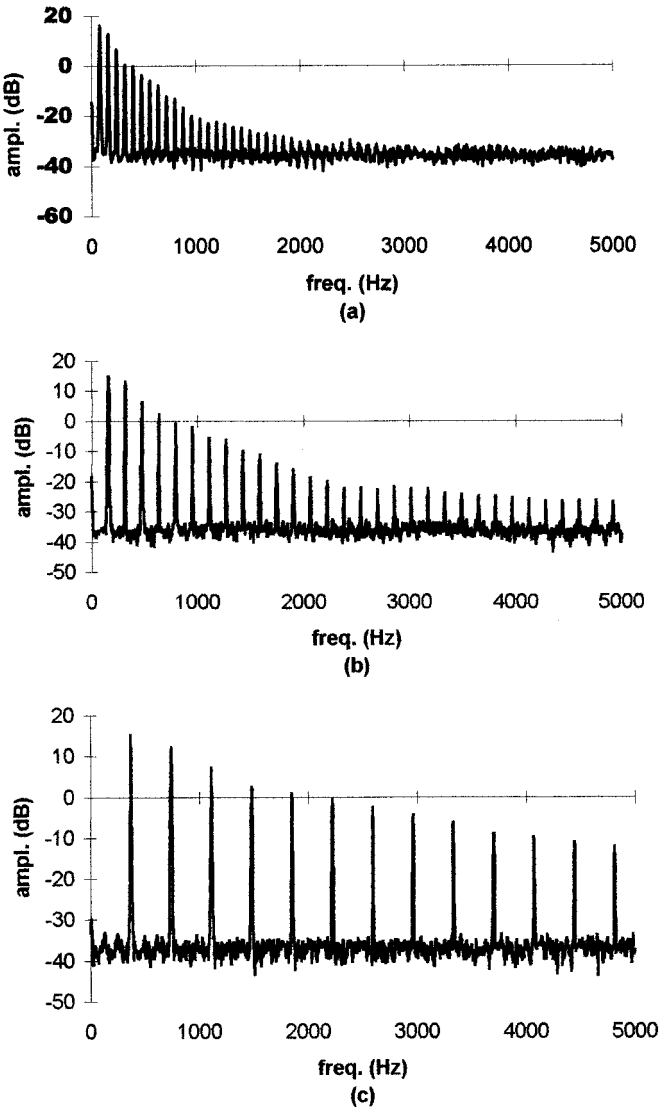

FIG. 9. Spectra (modified Hiraoka *et al.* analysis) of glottal source data for (a) 80-Hz, (b) 160-Hz, and (c) 350-Hz signals with s.d. 4% additive noise.

considerations in inverse filtering studies. Referring again to Fig. 9, to capture the same information for the 350-Hz signal as the 80-Hz signal requires the same ratio of sampling frequency to signal bandwidth. Inverse filtering strategies have reported more accurate results for low-pitched males than for female voices (Rosenberg, 1971; Alku and Vilkman, 1994). It is acknowledged that there may be other contributing factors to this phenomenon.

G. Jitter characterization

In order for any HNR algorithm to provide truly jitter-free HNRs, accurate determination of the jittered signal is essential. Characterization of jitter involves:

(1) The specification of an overall or global value.
(2) The specification of the temporal occurrence, including slow and fast trends.
(3) A description of the nature of the waveshape change.

In the present synthesis, the variation is random (point 2) of a user-specified amount (point 1), and the waveforms within consecutive periods are scaled versions of each other (point 3). Scaled jitter has been reported in the literature; for example, Monsen and Engebretson (1977) reported that in declarative (falling $f0$) intonation the periods are essentially scaled version of each other (more recent studies of source variations in connected speech can be found in Lofqvist and McGowan, 1991, or Gobl, 1988). Therefore, although this fact is not directly related to voice pathology, it can be inferred that the underlying physiology of voice production enables scaled jitter to occur and therefore it is a valid component for synthesis.

As a consequence of this rather uncomplicated jitter variation (random scaling), it is expected that this element should not be too difficult to remove (from the source waveform) and therefore, the result of Fig. 6 is not unexpected, i.e., the method is practically jitter insensitive. The result is encouraging, but even in this simulation, which must be conceded to be the least demanding of all possible tests for the algorithm, the method shows some slight variation with $f0$ and jitter. However, upsampling should almost entirely eliminate this variation.

Several possibilities exist for period changes other than simply scaling the wavelets. The changes most likely to occur in reality for pathological voice types are largely unknown (e.g., a period variation may typically include a waveshape change or vice versa) and are likely to be dependent on the pathology or disorder under investigation. For example, closure events might occur in quite a random fashion, i.e., the open phase remains exactly the same but the closed phase is either elongated or truncated with respect to normal. Monsen and Engebretson (1977) have shown this period variation to occur during interrogative (rising) intonation, which again is of interest to the present investigation in that it provides evidence that closed-phase alteration is a physiologically plausible manner of $f0$ variation. Ladefoged and Antonanzas-Barroso (1985), in attempting to provide a jitter-free index representing the random noise components associated with breathiness, proposed to use ''only part of a cycle and compare it with the corresponding part of the next cycle,'' (p. 82). This technique seems applicable for use on glottal waveforms with differing closed phases, although for use on the output radiated speech waveform the filtering effects will also be present. The spectral consequence of changing the closed phase is to change the relative height of the harmonics. However, the spectral envelope remains the same, and therefore ''zero-padding'' the periods until they are of equal length will regain the relative ''harmonic'' strengths. The period may also change due to a change in adductory or abductory function. Other possible mechanisms are found in cases involving vocal pathology where the presence of vocal fold nodules or mass lesions give rise to aperiodicities including turbulent flow. It is of considerable interest to spectrally characterize these conditions.

List 1–7 provides the basis for a possible algorithm for investigating glottal flow waveform aperiodicities.

(1) If $|h_{ij}-h_{i\mathrm{av}}|$ in Eq. (9) gives a value of 0, then there is no additive noise present in the signal, no change in open quotient (OQ—open time to total time in one period of oscillation), and no change in waveshape.
(2) If $|h_{ij}-h_{i\mathrm{av}}|$ is not equal to 0, then (a) additive noise, (b) OQ change, or (c) waveshape change is present.
(3) Check for (b) spectral envelope may be the same, therefore zero pad to make periods equal and calculate $|h_{izc}-h_{\mathrm{avzc}}|$, where h_{izc} is the ith harmonic for the spectrum derived from the zero padded waveform.
(4) If noise$\neq 0$, then
(5) (a) or (c).
(6) (a) The mean of $|h_{ij}-h_{i\mathrm{av}}|$ over ''j'' is constant for all ''i'' i.e., white noise is present.
(7) Check for (c) abduction (look for lower f changes), adduction (tilt—look for higher f changes).

As combinations of the above aperiodicities are considered within a single glottal period, e.g., a scaled open phase with a different closed phase for the jth wavelet (as compared to the previous or averaged wavelet), the use of subperiod spectra (or their time-domain counterparts) is required in order to compare different parts of the wavelets. For testing a proposed algorithm (list 1–7), there are obvious advantages for using synthesis data in that there is a strict control on the variables, a situation that is always absent in reality, even for ''normal'' voice. The disadvantage is that these situations may, in fact, not be physically realizable. Independent model parameters may not behave in an unconstrained manner in practical situations. Gauffin and Sundberg (1989) made a similar comment when studying the flow glottograms of singers and nonsingers: ''As the Fant model (Fant, Liljencrants, and Lin, 1985) is theoretical, it will consider cases, regardless of whether or not they occur in reality. In our material, on the other hand, we have included only normal or trained voices. In pathological voices, glottogram characteristics may be combined in other ways,'' (p. 562). This comment underlines the importance of studies that examine the flow waveform characteristics of speakers with voice disorders (see, for example, Hillman *et al.*, 1989).

H. Aperiodicity mechanisms

An understanding of the underlying causes of aperiodicities in voice signals and of how these factors alter the waveshape and/or period of the waveform is important for the development of strategies that attempt to reveal the inverse, i.e., deduce physiological inferences from the acoustic signal. In consideration of the fact that the flow waveform, as measured in inverse filtering studies, is the acoustic result of a complex interaction between aerodynamical, fluid dynamical, biomechanical, neurological, and acoustic factors, and furthermore, that to maintain self-sustained oscillation[9] requires simply that gain must be at least equal to the losses over the periods of vocal fold vibration in question, it can be seen that the possibilities for waveform perturbation are manifold. In opposition to these period/waveshape altering parameters are the constancy-seeking properties of the system, including the natural frequencies as determined by the mass, tension, and length of the folds and entrainment between normal modes of vibration (Titze, 1980). In addition, the intrinsic and extrinsic laryngeal muscles and the respiratory system act to regulate the fundamental frequency. Therefore, studies that relate flow waveform characteristics to other physiological data (Holmberg *et al.*, 1995; Hertegard and Gauffin, 1996), studies that model glottal dynamics (Titze, 1984; Childers *et al.*, 1986; Cranen, 1991), and studies that attempt to model voice-source production in a physiologically (Titze, 1991; Farley, 1996) and neurologically (Titze, 1996) motivated manner, are of paramount importance if the inverse problem of relating acoustics to physiology is to be realized.

The present analysis is an attempt to characterize aperiodicities and to remove the effect of these aperiodicities on the HNR in voice signals, from what might be termed a signal speech processing viewpoint; an underlying assumption is made that there exists a quasiperiodic process where the periods under consideration are well-defined entities. However, other sources of aperiodicities present themselves when considering the underlying physical processes. In considering the vocal folds as a mechanical system, many possibilities for aperiodicity arise in which the period of oscillation becomes a less well-defined entity, e.g., the underdamped or overdamped motion of a mass, spring, damper system (Dejonckere and Lebacq, 1984), or the resultant beat frequencies characteristic of asymmetrical vocal folds (Ishizaka and Isshiki, 1976; Wong *et al.*, 1991). This type of phenomena, and more, have recently been described in the rich vocabulary of chaos theory (Fletcher, 1996; Herzel *et al.*, 1994; Titze *et al.*, 1993). The waveforms resulting from such nonlinear system behavior have been illustrated with real voice data, and the processes have been replicated using a variety of models varying in complexity (Steinecke and Herzel, 1995; Berry *et al.*, 1994), in order to suggest the underlying causative mechanisms. In a study of nonlinear phenomena in pathological voice types, approximately a quarter of cases exhibiting aperiodicity in their waveforms was found to be related to underlying system nonlinearities (Herzel *et al.*, 1994). Therefore nonlinear/chaotic phenomena may be considered another subclass of aperiodicity (i.e., a fifth point added to the definition of aperiodicity in the introduction section). The perturbation-free HNR algorithm must be capable of detecting these different sources of aperiodicity and eliminating their influence on the HNR. Quantification of these phenomena require more long-term methods of analysis, either through methods of nonlinear dynamics (Behrman and Baken, 1997) or through more traditional signal processing approaches (Imaizumi, 1986). The extent to which the variation in the variance of the PSHA technique will reveal waveforms resulting from chaotic processes remains to be seen.

IV. CONCLUSION AND FUTURE WORK

A new method for determining the HNR in speech signals, independent of jitter and shimmer, is proposed and tested on a set of synthetic voice signals. The method, termed pitch-synchronous harmonic analysis (PSHA), is shown to provide jitter and shimmer free HNRs for the glottal source signals, whereas jitter and shimmer still contribute to the HNR for the radiated speech waveform. Many secondary aperiodicities are shown to occur in the wavelets of radiated speech waveforms which result from the vocal tract filtering of aperiodic source signals. Therefore, it is recommended to use the PSHA method (or any other method that aims to provide a perturbation-free measurement of the HNR) solely on inverse-filtered or other source-related data.

Although the complications that arise due to vocal tract filtering are removed by inverse filtering, this puts all the demands on the inverse-filtering technique to provide a reliable source function while retaining the additive noise component. However, there are still many unresolved issues connected with inverse filtering aside from the practical difficulties of estimating the formant frequencies and bandwidths, and measuring the phase accurately down to the lowest frequencies, e.g., what is to be attributed to the source and what is to be attributed to the filter, or whether a constant filtering function is justified. It is also noted that in a pitch-synchronous inverse filtering strategy, the effect of the filtering has not diminished entirely within a single period, and overlay is still present in adjacent periods. There are also further questions to be answered in relating the inverse-filtered glottal flow to glottal parameters (see, for example, Davies *et al.*, 1993, for a discussion regarding the interpretation of the inverse filtered waveform).

To address some of the above questions further, studies will look at how inverse filtering techniques perform on synthesis data—e.g., given a radiated waveform which is synthesized with a glottal flow waveform of ''*x*'' % s.d. random noise, it is of interest to check how much noise is returned on inverse filtering. It is similarly interesting to investigate how inverse-filtering techniques cope with the irregular overlay of energy introduced by jitter. Although a method of successive approximations of inverse filtering is suggested in the method section, such an approach is bound to be problematic for accurate inverse filtering as it is dependent on model assumptions for the source and filter which inherently limit the accuracy of the method. Approaches such as the two-channel (glottal flow waveform and electroglottogram) method of Krishnamurty and Childers (1986), where accurate determination of the pitch period and closed phase are

determined, are more suited to the present goal. The PSHA algorithm can then be tested directly on the electroglottogram and simultaneously on the inverse filtered flow signal. However, given that there is limited knowledge regarding the system function, more radical approaches to inverse filtering that supply more system information may be required for high accuracy inverse filtering.

In order to test any algorithm in an objective manner, the use of synthesis data (or simulated data produced from vocal-fold modeling studies) is essential. Therefore, analytical functions that represent the features found in the flow waveforms or spectra of pathological voice types are required. This requires a closer characterization of aperiodicities than has been reported to date. Acoustic indices such as the HNR have displayed an ability to separate patient and normal data sets (Yumoto *et al.*, 1982; Kojima *et al.*, 1980). It is now expedient to refine these indices, using improved physiological and perceptual correlations, in order to provide differential diagnoses. Pertinent data should be collected regarding specific disorders and pathologies. This data should include indices that are disorder specific as opposed to using vague or catchall criteria that may give rise to excessive, nonindependent data which are difficult to interpret and hence are of questionable value in voice quality assessment and/or clinical practice. There is a lack of such disorder-specific data because the techniques available to researchers have been limited. Comprehensive assessments have been made despite the limited measurement instrumentation available (e.g., Martin *et al.*, 1995). However, the difficulty in interpreting the results of this study reflects the nonindependence of the indices used and the fact that fundamental considerations in both the production and perception of speech are overlooked in the algorithms presently available in commercial voice quality assessment systems.

Primary aims of the present investigation are to provide a solid framework for the development of a perturbation-free HNR measurement, and for the quantification of voice aperiodicities in general. These goals form part of a larger study which aims to extract greater specificity from the acoustic analyses. Therefore, other measurements taken from the glottal-flow spectrum to infer glottal characteristics are considered. The potential usefulness of the source spectrum for investigating glottal dynamics might be queried, however. For studying energy losses in the vocal tract and radiation impedance at the mouth opening, the frequency domain has obvious advantages over time-domain analyses. However, in studying glottal dynamics, changes that occur within a single glottal period, at specific temporal instances, are the factors that are of interest. A possible advantage of frequency-domain modeling is that the strict phase sensitivity of the recording is no longer required (although phase is required for the PSHA algorithm). Another advantage is that it avoids the need for detecting microtemporal events (e.g., point of closure, if any) within the glottal cycle (Alku *et al.*, 1997). Also, for studying perceptual assessments of changing glottal-flow parameters, the use of the glottal spectrum may be of use, although the phase spectrum may also be of interest (Flanagan, 1958). Ladefoged *et al.* (1988) found using the glottal spectrum preferable to using the flow waveform for describing linguistic contrasts because the former was found to be less seriously affected by small errors in removing the formants. Recent work has aimed to describe glottal characteristics in terms of the spectrum (Fant and Lin, 1988; Ananthapadmanabha, 1984; Alku *et al.*, 1997; Childers and Lee, 1991). It may be possible to further develop these strategies in order to investigate how much specific time events impact on certain harmonic locations. Another interesting aspect of frequency-domain analysis is that it can differentiate between a narrow-band signal embedded in broadband noise more effectively than a time-domain analysis. Since the flow waveform has a falloff of approximately -12 dB per octave, the first few harmonics contain most of the energy, while noise, if random, is spread over all frequencies. This fact is put to use in the normalization of the PSHA algorithm. Further development of these strategies, such as inverse Fourier transform of a ''cleaned up'' frequency-domain signal back into the time domain, may provide a useful method for removing noise in glottal flow waveforms.

Finally, the short-term performance of the PSHA HNR algorithm is encouraging as it implies that the method may be of use in connected speech to give time-varying estimates of the HNR. This is advantageous as some dysphonias only show up intermittently and may be missed in rehearsed sustained phonations and furthermore, perturbation levels have been found to be higher in connected speech, e.g., increase in jitter levels has been reported for connected speech as opposed to sustained vowels (Baken and Orlikoff, 1986).

In conclusion, more specific indices, such as the perturbation-free HNR, are required for accurate voice-quality assessment. The further development of such strategies, in conjunction with examining more physiologically based measurements, form the basis for future research which should lead to the development of more reliable HNRs and to a better quantification of glottal flow dynamics in normal and dysphonic speakers.

ACKNOWLEDGMENT

This work was supported in part by a Health Research Board grant (No. 01-95).

[1]The term wavelet refers to the amplitude of the waveform as a function of time (or space) within a period.

[2]Pilot studies carried out by the present author found the median period resulted in the least jitter-sensitive ratio.

[3]HNR has this property in common with many other quantitative voice indices such as open quotient (ratio between open time in a period and period length), efficiency (ratio between acoustic power and aerodynamic power), spectral tilt, or relative harmonic levels (H_1-H_2).

[4]This approach is in agreement with the more commonly used Fourier transform implementation of spectral estimation, whose frequency resolution increases with increasing window length. The increased window length in this instance, through repetition and concatenation of the analysis period, provides more identical waveforms in the analysis frame. The spectral consequence of this is to provide more spectral estimates, i.e., increased frequency resolution, but because the waveform is repetitive, the extra spectral estimates are simply zero. The mainlobe width of the convolving window function decreases and in the limit as the repetitive waveform approaches infinity, the convolved spectral harmonic estimates approach the Fourier series coefficients. This development is useful for showing the equivalence of each approach, but it should also be mentioned that the Fourier transform cannot be evaluated for a waveform of infinite extent.

[5]This is consistent with the source functions used in models of speech pro-

duction (Rabiner and Schafer, 1978), which infer that a period of the voiced source is taken from a periodic waveform $g_r(n)$ as given by

$$g_r(n)=\sum_{m=-\infty}^{m=+\infty} g(n+mN_p),$$

$g_r(n)$=glottal pulse,

N_p=period length (in sample numbers).

[6]Which satisfies the following criteria known as the Dirichlet conditions; the function must have a finite number of discontinuities within a period, a finite number of minima and maxima in the region of any point, and must be absolutely integrable within a period (as is the case for all glottal-flow waveforms).

[7]Scaled radiated waveforms can be produced (e.g., taking the simple approximate analytical functions described by Klingholtz and Martin (1985), and Hanson (1997) and changing t to t'). However, in scaling the radiated waveform, the source function must have been altered in a highly nonlinear fashion.

[8]Of basic concern in spectral analysis is the resolution required for a certain measurement. Depending on resolution, different characteristics of a signal are revealed. Obvious examples of this in speech analysis are the narrowband and broadband spectrograms, the former resolving the harmonic frequencies and the latter showing more gross characteristics, i.e., the formant trace. Due to the coherent addition of the discrete Fourier transform, it is the 6-dB bandwidths that determine spectral resolution, as opposed to the 3-dB criterion of classical signal analysis (Harris, 1978). Two factors determine whether two, equal-strength signals spaced at given frequency locations will be resolved:
(1) the difference in frequency between the signals, and
(2) the bandwidth of the Fourier estimates.
Increased fundamental frequency therefore produces greater separation between the harmonic locations.

[9]Self-sustained oscillation—''self'' in the present discussion refers to to the complete voice production system, including sub- and supra-glottal components in order to give the most flexible definition of self-sustained oscillation and hence the most perturbation sensitive definition.

Alku, P., and Vilkman, E. (**1994**). ''Effects of bandwidth on glottal airflow waveforms estimated by inverse filtering,'' J. Acoust. Soc. Am. **98**, 763–767.

Alku, P., and Vilkman, E. (**1996**). ''A comparison of glottal voice source quantification parameters in breathy, normal and pressed phonation of female and male speakers,'' Folia Phoniatr. **48**, 240–254.

Alku, P., Strik, H., and Vilkman, E. (**1997**). ''Parabolic spectral parameter-A new method for quantification of the glottal flow,'' Speech Commun. **22**, 67–79.

Ananthapadmanabha, T. V. (**1984**). ''Acoustic analysis of voice source dynamics,'' Speech Trans. Lab. Quarterly. Prog. Stat. Rep. 2-3, Royal Institute of Technology, Stockholm, Sweden, pp. 1–24.

Aronson, A. E. (**1990**). *Clinical Voice Disorders* (Thieme, New York).

Baken, R. J., and Orlikoff, R. (**1986**). Perturbation of vocal fundamental frequency during voiced fricatives. Presentation at the International Conference on Voice, Kurume, Japan.

Baken, R. J., and Daniloff, R. G. (**1991**). *Readings in Clinical Spectrography of Speech* (Singular Publishing Group, San Diego).

Behrman, A., and Baken, R. J. (**1997**). ''Correlation dimension of electrographic data from healthy and pathologic subjects,'' J. Acoust. Soc. Am. **102**, 2371–2379.

Berry, D. A., Herzel, H., Titze, I. R., and Krischer, K. (**1994**). ''Interpretations of biomechanical simulations of normal and chaotic vold fold oscillations with empirical eigenfunctions,'' J. Acoust. Soc. Am. **95**, 3595–3604.

Childers, D. G., and Lee, C. K. (**1991**). ''Vocal quality factors: Analysis, synthesis and perception,'' J. Acoust. Soc. Am. **90**, 2390–2410.

Childers, D. G., Hicks, D. M., Moore, G. P., and Alsakya, Y. A. (**1986**). ''A model for vocal fold vibratory motion, contact area, and the electroglottogram,'' J. Acoust. Soc. Am. **80**, 1309–1320.

Cox, N. B., Ito, M. R., and Morrison, M. D. (**1989**). ''Technical considerations in computation of spectral harmonics-to-noise ratios for sustained vowels,'' J. Speech Hear. Res. **32**, 203–218.

Cranen, B., and Boves, L. (**1987**). ''On subglottal formant analysis,'' J. Acoust. Soc. Am. **81**, 734–746.

Cranen, B. (**1991**). ''Simultaneous modeling of EGG, PGG, and glottal flow,'' *in Vocal Fold Physiology: Acoustic, Perceptual and Physiological Aspects of Voice Mechanisms*, edited by Jan Gauffin and Britta Hammarberg (Singular Publishing Group, San Diego), pp. 57–64.

Davies, P. O. A. L., McGowan, R. S., and Shadle, C. (**1993**). ''Practical flow duct acoustics applied to the vocal tract,'' in *Vocal Fold Physiology: Frontiers in Basic Science*, edited by Ingo R. Titze (Singular Publishing Group, San Diego), pp. 93–142.

Davis, S. B. (**1976**). ''Computer evaluation of laryngeal pathology based on inverse filtering of speech,'' Speech Communication Research Laboratory, Santa Barbara, California, Monograph 13.

Deem, J. F., Manning, W. H., Knack, J. V., and Matesich, J. S. (**1989**). ''The automatic extraction of pitch perturbation using microcomputers: some methodological considerations,'' J. Speech Hear. Res. **32**, 689–697.

Dejonckere, P. H., and Lebacq, J. (**1984**). ''Damping coefficient of oscillating vocal folds in relation with pitch perturbations,'' Speech Commun. **3**, 89–92.

de Krom, G. (**1993**). ''A cepstrum based technique for determining a harmonics-to-noise ratio in speech signals,'' J. Speech Hear. Res. **36**, 254–266.

Dowling, A. P., and Ffowcs Williams, J. E. (**1982**). *Sound and Sources of Sound* (Ellis Horwood, England).

Fant, G. (**1970**). *Acoustic Theory of Speech Production* (Mouton, The Hague).

Fant, G., Liljencrants, J., and Lin, Q. (**1985**). A four parameter model of glottal flow. Speech Trans. Lab. Quarterly Prog. Stat. Report No. 4, Royal Institute of Technology, Stockholm, Sweden, pp. 1–13.

Fant, G., and Lin, Q. (**1988**). ''Frequency domain interpretation and derivation of glottal flow parameters,'' Speech Trans. Lab. Quarterly Prog. Stat. Report No. 2–3, Royal Institute of Technology, Stockholm, Sweden, pp. 1–21.

Farley, G. R. (**1996**). ''A biomechanical laryngeal model of voice $f0$ control and glottal width control,'' J. Acoust. Soc. Am. **100**, 3794–3812.

Flanagan, J. L. (**1958**). ''Some properties of the glottal sound source,'' J. Speech Hear. Res. **1**, 99–111.

Fletcher, N. H. (**1996**). ''Nonlinearity, Complexity and Control in Vocal Systems,'' in *Vocal Fold Physiology: Controling Complexity and Chaos*, edited by Pamela J. Davis and Neville H. Fletcher (Singular Publishing Group, San Diego), pp. 3–16.

Gauffin, J., and Sundberg, J. (**1989**). ''Spectral correlates of glottal voice source waveform characteristics,'' J. Speech Hear. Res. **32**, 556–565.

Gobl, C. (**1988**). ''Voice source dynamics in connected speech,'' Speech Trans. Lab. Quarterly Prog. Stat. Report No. 1, Royal Institute of Technology, Stockholm, Sweden, pp. 123–159.

Hanson, H. M. (**1997**). ''Glottal characteristics of female speakers; Acoustic correlates,'' J. Acoust. Soc. Am. **101**, 466–481.

Harris, F. J. (**1978**). ''On the use of windows for harmonic analysis with the discrete Fourier transform,'' Proc. IEEE **66**, 51–142.

Hertegard, S., and Gauffin, J. (**1995**). ''Glottal area and vibratory patterns studied with simultaneous stroboscopy, flow glottography, and electroglottography,'' J. Speech Hear. Res. **38**, 85–100.

Herzel, H., Berry, D., Titze, I. R., and Saleh, M. (**1994**). ''Analysis of vocal disorders with methods from non-linear dynamics,'' J. Speech Hear. Res. **37**, 1008–1019.

Hillenbrand, J. (**1987**). ''A methodological study of perturbation and additive noise in synthetically generated voice signals,'' J. Speech Hear. Res. **30**, 448–461.

Hillenbrand, J. (**1988**). ''Perception of aperiodicities in synthetically generated voice signals,'' J. Acoust. Soc. Am. **83**, 2361–2371.

Hillenbrand, J., Cleveland, R. A., and Erickson, R. L. (**1994**). ''Acoustical correlates of breathy vocal quality,'' J. Speech Hear. Res. **37**, 769–778.

Hillman, R. E., Oesterle, E., and Feth, L. L. (**1983**). ''Characteristics of the glottal turbulent noise source,'' J. Acoust. Soc. Am. **74**, 691–694.

Hillman, R. E., Holmberg, E. B., Perkell, J. S., Walsh, M., and Vaughan, C. (**1989**). ''Objective assessment of vocal hyperfunction: An experimental framework and initial results,'' J. Speech Hear. Res. **32**, 373–392.

Hiraoka, N., Kitazoe, Y., Ueta, H., Tanaka, S., and Tanabe, M. (**1984**). ''Harmonic intensity analysis of normal and hoarse voices,'' J. Acoust. Soc. Am. **76**, 1648–1651.

Holmberg, E. B., Hillman, R. E., and Perkell, J. S. (**1988**). ''Glottal airflow and transglottal air pressure measurements for male and female speakers in soft, normal, and loud voice,'' J. Acoust. Soc. Am. **84**, 511–529.

Holmberg, E. B., Hillman, R. E., Perkell, J. S., Guiod, P. C., and Goldman, S. L. (**1995**). ''Comparisons among aerodynamic, electroglottographic, and acoustic spectral measures of female voice,'' J. Speech Hear. Res. **38**, 1212–1223.

Holmes, J. N. (**1973**). ''The influence of glottal waveform in the naturalness of speech from a parallel formant synthesizer,'' IEEE Trans. Audio Electroacoust. **AU-21**, 298–305.
Imaizumi, S. (**1986**). ''Acoustic measurement of pathological voice qualities for medical purposes,'' ICASSP, Tokyo, IEEE, pp. 677–680.
Imaizumi, S. (**1988**). ''A preliminary study on the generation of pathological voice types,'' in *Vocal Fold Physiology: Voice Production, Mechanisms and Functions*, edited by Osamu Fujimura (Raven, New York), pp. 249–258.
Ishizaka, K., and Isshiki, N. (**1976**). ''Computer simulation of pathological vocal-cord vibration,'' J. Acoust. Soc. Am. **60**, 1193–1198.
Isshiki, N., Kitajima, K., Kojima, H., and Harita, Y. (**1978**). ''Turbulent noise in dysphonia,'' Folia Phoniatr. **30**, 214–224.
Kasuya, Y. (**1986**). ''An adaptive comb filtering method as applied to acoustic analysis of pathological voice,'' ICASSP Tokyo, IEEE, pp. 669–672.
Kasuya, H., Ogawa, S., Mashima, K., and Ebihara, S. (**1986a**). ''Normalized noise energy as an acoustic measure to evaluate pathologic voice,'' J. Acoust. Soc. Am. **80**, 1329–1334.
Kasuya, H., Ogawa, S., and Kikuchi, Y. (**1986b**). ''An acoustic analysis of pathological voice and it's application to the evaluation of laryngeal pathology,'' Speech Commun. **5**, 171–181.
Kasuya, H., and Ando, Y. (**1991**). ''Analysis, synthesis and perception of breathy voice,'' in *Vocal Fold Physiology: Acoustic, Perceptual and Physiologic Aspects of Voice Mechanisms*, edited by Jan Gauffin and Britta Hammarberg (Singular Publishing Group, San Diego), pp. 251–258.
Kasuya, H., and Endo, Y. (**1995**). ''Acoustic analysis, conversion, and synthesis of the pathological voice,'' in *Vocal Fold Physiology: Voice Quality Control*, edited by Osamu Fujimura and Minoru Hirano (Singular Publishing Group, San Diego), pp. 305–320.
Kitajima, K. (**1981**). ''Quantitative evaluation of the noise level in the pathologic voice,'' Folia Phoniatr. **33**, 115–124.
Klatt, D. H. (**1982**). ''Speech processing strategies based on auditory models,'' in *The Representation of Speech in the Peripheral Auditory System*, edited by R. Carlson and B. Granstrom (Elsevier Biomedical, Amsterdam).
Klatt, D. H., and Klatt, L. C. (**1990**). ''Analysis, synthesis and perception of voice quality variations amoung female and male talkers,'' J. Acoust. Soc. Am. **87**, 820–857.
Klingholtz, M., and Martin, F. (**1985**). ''Quantitative spectral evaluation of shimmer and jitter,'' J. Speech Hear. Res. **28**, 169–174.
Koike, Y., and Kohda, J. (**1991**). ''The effect of vocal fold surgery on the speech cepstrum,'' in *Vocal Fold Physiology: Acoustic, Perceptual and Physiologic Aspects of Voice Mechanisms*, edited by Jan Gauffin and Britta Hammarberg (Singular Publishing Group, San Diego), pp. 259–264.
Kojima, H., Gould, W. J., Lambiase, A., and Isshiki, N. (**1980**). ''Computer analysis of hoarseness,'' Acta Oto-Laryngol. **89**, 547–554.
Krishnamurty, A. K., and Childers, D. G. (**1986**). ''Two-channel speech analysis,'' IEEE Trans. Acoust., Speech, Signal Process. **34**, 730–743.
Ladefoged, P., and Antonanzas-Barroso, N. (**1985**). ''Computer measures of breathy voice quality,'' UCLA Working Papers in Phonetics **61**, 79–86.
Ladefoged, P., Maddieson, I., and Jackson, M. (**1988**). ''Investigating phonation types in different languages,'' in *Vocal Fold Physiology: Voice Production, Mechanisms and Functions*, edited by Osamu Fujimura (Raven, New York), pp. 297–318.
Lofqvist A., and McGowan, R. S. (**1991**). ''Voice source variations in running speech,'' in *Vocal Fold Physiology: Acoustic, Perceptual, and Physiological Aspects of Voice Mechanisms*, edited by Jan Gauffin and Britta Hammarberg (Singular Publishing Group, San Diego), pp. 113–120.
Martin, D., Fitch, J., and Wolfe, V. (**1995**). ''Pathological voice type and the acoustic prediction of severity,'' J. Speech Hear. Res. **38**, 765–771.
Mathews, M. V., Miller, J. E., and David, Jr, E. E. (**1961**). ''Pitch synchronous analysis of voiced sounds,'' J. Acoust. Soc. Am. **33**, 179–186.
Michaelis, D., Gramss, T., and Strube, H. W. (**1997**). ''Glottal to noise excitation ratio-a new measure for describing pathological voices,'' Acust. Acta Acust. **83**, 700–706.
Monsen, R. B., and Engebretson, A. M. (**1977**). ''Study of variation in the male and female glottal wave,'' J. Acoust. Soc. Am. **62**, 981–993.
Muta, H., Baer, T., Wagatsuma, K., Muraoka, T., and Fukuda, H. (**1988**). ''A pitch synchronous analysis of hoarseness in running speech,'' J. Acoust. Soc. Am. **84**, 1292–1301.
Qi, Y. (**1992**). ''Time normalization in voice analysis,'' J. Acoust. Soc. Am. **92**, 1569–1576.
Qi, Y., Weinberg, B., Bi, N., and Hess, W. J. (**1995**). ''Minimizing the effect of period determination on the computation of amplitude perturbation in voice,'' J. Acoust. Soc. Am. **97**, 2525–2532.
Qi, Y., and Hillman, R. E. (**1997**). ''Temporal and spectral estimations of harmonics-to-noise ratio in human voice signals,'' J. Acoust. Soc. Am. **102**, 537–543.
Rabiner, L., and Schafer, R. (**1978**). *Digital Processing of Speech Signals* (Prentice-Hall, Englewood Cliffs, NJ).
Rontal, E., Rontal, M., and Rolnick, M. I. (**1975**). ''Objective evaluation of vocal pathology using voice spectrography,'' Ann. Otol. **84**, 662–671.
Rosenberg, A. E. (**1971**). ''Effect of glottal pulse shape on the quality of natural vowels,'' J. Acoust. Soc. Am. **84**, 583–588.
Scherer, R. C., and Guo, C. G. (**1991**). ''Generalised translaryngeal pressure coefficient for a wide range of laryngeal configurations,'' in *Vocal Fold Physiology: Acoustic Perceptual and Physiologic Aspects of Voice Mechanisms*, edited by Jan Gauffin and Britta Hammarberg (Singular Publishing Group, San Diego), pp. 83–90.
Shadle, C. H. (**1995**). ''Modelling the noise source in voiced fricatives,'' in *Proceedings of the 15th International Conference on Acoustics*, Trondheim, Norway, June 1995, Vol. 3, pp. 145–148.
Steinecke, I., and Herzel, H. (**1995**). ''Bifurcations in an asymmetric vocal-fold model,'' J. Acoust. Soc. Am. **97**, 1874–1884.
Stevens, K. N. (**1971**). ''Airflow and turbulent noise for fricative and stop consonants,'' J. Acoust. Soc. Am. **50**, 1180–1192.
Titze, I. R. (**1980**). ''Comments on the myoelastic-aerodynamic theory of phonation,'' J. Speech Hear. Res. **23**(3), 495–510.
Titze, I. R. (**1984**). ''Parameterization of the glottal area, glottal flow, and vocal fold contact area,'' J. Acoust. Soc. Am. **75**, 570–580.
Titze, I. R. (**1991**). ''Mechanisms underlying the control of fundamental frequency,'' in *Vocal Fold Physiology: Acoustic, Perceptual and Physiologic Aspects of Voice Mechanisms*, edited by Jan Gauffin and Britta Hammarberg (Singular Publishing Group, San Diego), pp. 129–138.
Titze, I. R. (**1996**). ''Coupling of neural and mechanical oscillators in control of pitch, vibrato, and tremor,'' in *Vocal Fold Physiology: Controlling Complexity and Chaos*, edited by Pamela J. Davis and Neville H. Fletcher (Singular Publishing Group, San Diego), pp. 47–62.
Titze, I. R., Horii, Y., and Scherer, R. (**1989**). ''Some technical considerations in voice perturbation measurements,'' J. Speech Hear. Res. **30**, 252–260.
Titze, I. R., Baken, R., and Herzel, H. (**1993**). ''Evidence of chaos in vocal fold vibration,'' in *Vocal Fold Physiology: Frontiers in Basic Science*, edited by Ingo R. Titze (Singular Publishing Group, San Diego), pp. 143–188.
Wong, D., Ito, M. R., Cox, N. B., and Titze, I. R. (**1991**). ''Observations of perturbation in a lumped-element model of the vocal folds with application to some pathological cases,'' J. Acoust. Soc. Am. **89**, 383–394.
Yanaghihara, N. (**1967**). ''Significance of harmonic changes and noise components in hoarseness,'' J. Speech Hear. Res. **10**, 531–541.
Yumoto, E., Gould, W. J., and Baer, T. (**1982**). ''Harmonics-to-noise ratio as an index of the degree of hoarseness,'' J. Acoust. Soc. Am. **71**, 1544–1549.
Zwicker, E., and Fastl, H. (**1990**). *Psychoacoustics* (Springer, Berlin).

Influences of pellet markers on speech production behavior: Acoustical and perceptual measures

Gary Weismer and Kate Bunton
Department of Communicative Disorders, Waisman Center, 1500 Highland Avenue, University of Wisconsin-Madison, Madison, Wisconsin 53705-2280

(Received 7 December 1998; accepted for publication 12 February 1999)

Peri- and intraoral devices are often used to obtain measurements concerning articulator motions and placements. Surprisingly, there are few formal evaluations of the potential influence of these devices on speech production behavior. In particular, the potential effects of lingual pellets or coils used in x-ray or electromagnetic studies of tongue motion have never been evaluated formally, even though a large x-ray database exists and electromagnetic systems are commercially available. The x-ray microbeam database [Westbury, J. ''X-ray Microbeam Speech Production Database User's Handbook, version 1'' (1994)] includes several utterances produced with pellets-off and -on, which allowed us to evaluate effects of pellets for the utterance, *She had your dark suit in greasy wash water all year*, using acoustic and perceptual measures. Overall, there were no acoustic or perceptual measures that showed consistent effects of pellets across speakers, but certain effects were consistent either within a given speaker or in direction across a subgroup of the speakers. The results are discussed in terms of the general goodness of the assumption that point parameterization of lingual motion does not interfere with normal articulatory behaviors. A brief screening procedure is suggested to protect articulatory kinematic experiments from those individuals who may show consistent effects of having devices placed on perioral structures. © *1999 Acoustical Society of America.* [S0001-4966(99)04005-9]

PACS numbers: 43.70.Gr, 43.70.Jt, 43.71.Gv [AL]

INTRODUCTION

Research on speech production has always relied on perioral or intraoral devices to provide information on the movements of articulators, forces exerted by articulatory structures, or to record patterns of contact between mobile articulatory structures and fixed vocal tract boundaries. Similarly, intraoral devices have been used to measure air pressures within the vocal tract, and in the case of bite blocks and transient loads to alter the normal setting and/or movement of vocal tract structures to determine effects on articulatory behavior and vocal tract acoustic output.

It is axiomatic in scientific activity that the process of observation may change the phenomenon being observed (e.g., Reichenbach, 1973), thereby requiring some understanding of the interaction between the presence of instruments and the measures being taken. It is therefore somewhat surprising to find little formal assessment of the potential effects of perioral and intraoral devices on speech production behavior. An exception to this has been the several attempts to determine the influence of pseudopalates on speech production behavior. For example, Hamlet and Stone (1976, 1978; Hamlet, 1985) showed that several temporal aspects of speech production change gradually from the time speakers first insert a pseudopalate for chronic adaptation to a point in time some two weeks later. Reports of chronic effects on articulatory timing of sibilants due to dental prostheses can be found in the literature (Hamlet *et al.,* 1979; Ichikawa *et al.,* 1995). Some of the articulatory changes induced by the presence of a pseudopalate are fairly easy to demonstrate via acoustic and perceptual analyses (see McFarland *et al.*, 1996). The demonstrated influence of the pseudopalates on articulatory behavior makes it difficult to evaluate the generalizability of findings from electropalatographic studies of speech production phenomena such as coarticulation and assimilative processes (e.g., Butcher, 1989; Recasens *et al.*, 1993; Wright and Kerswill, 1989) when the studies contain no formal assessment of the effect of the device on the measurements of interest.

Bite blocks constitute a somewhat different interaction between the intraoral modification and the observables, because in many such studies the intraoral modification is *meant* to change aspects of articulatory behavior. The classic bite block study produces a demonstration of nearly identical vowel formant frequencies for unblocked and blocked conditions (Gay *et al.*, 1981). This demonstration has been taken to show the capacity of the speech motor control system to compute and produce the correct area function for an intended vowel, even in the face of different vocal tract postures. However, not all studies have demonstrated this immediate compensation of the vocal tract area function to the presence of a bite block (e.g., McFarland and Baum, 1995), indicating another example of interference with normal articulatory behavior by an intraoral device (see also Baum and McFarland, 1997; Savariaux *et al.*, 1995). In the few studies wherein measures such as segment durations and formant transition characteristics (e.g., frequency range and duration) are compared across normal and bite-block conditions, there is evidence of a bite-block effect (Smith, 1987; Mulligan, 1986). Flege *et al.* (1988), in a palatography study, also showed effects of a bite block on obstruent and vocalic spectra. This study is interesting because the demonstrated acoustic effects were not necessarily associated with perceptual effects (see Sec. III).

Transient loads applied during speech to the lips and jaw have been used to study various aspects of articulatory coor-

dination (Abbs and Gracco, 1984; Folkins and Abbs, 1985; Gracco and Abbs, 1988; Kelso *et al.*, 1984; Shaiman, 1989; Munhall *et al.*, 1994), but only Munhall *et al.* (1994) have examined the effect of these loads on selected aspects of speech timing; loads applied to the lower lip had a clear effect on stop closure durations and voice-onset times, but no formal perceptual measures were obtained. In other studies, the evaluation of a load's effect on vocal tract output, which is fairly critical for the interpretation of the articulatory response in terms of automatic neural pathways serving the articulatory mechanism (i.e., as compared to an interpretation of conscious compensatory adjustments to the transient load), is typically by experimenter's report: ''. . . despite some sizable movement perturbations... the intended speech motor objective was not disrupted in a discernible way (i.e., a listener could not distinguish acoustic speech patterns for loaded trials from those produced during normal, unloaded trials)'' (Abbs *et al.*, 1984, p. 204). The lesson from the available studies on pseudopalates and bite blocks would seem to suggest that formal evaluation of the effect of transient loads on vocal tract output and/or the perception of that output should be undertaken before using the technique as a window to normal articulatory processes.

One approach to speech production research that requires this kind of evaluation is the point parameterization of articulatory movement. A review of the literature suggests that, of the many studies in which pellets or electromagnetic transducers have been placed on the articulators, and especially the tongue (e.g., Kent, 1972; Kent and Moll, 1972; Perkell and Nelson, 1985; Perkell and Cohen, 1989; and see review in Perkell, 1997), none has included a formal comparison of speech production behavior with and without the intraoral devices in place. There are, however, indirect data that suggest little impact of tongue pellets on the formant frequencies of vowels. Perkell and Nelson (1985) reported vowel formant frequencies for two speakers from the Tokyo x-ray microbeam data set that are quite consistent with values reported in studies wherein speech acoustic recordings were made in the absence of any intraoral device (e.g., Peterson and Barney, 1952; Hillenbrand *et al.*, 1995). Obviously it would be useful to have such acoustic comparisons between intraoral device *versus* no intraoral device for the same speakers, producing utterances common to both conditions. Moreover, a logical hypothesis is that the articulation of sounds such as fricatives may be more susceptible than vowels to the presence of intraoral devices such as pellets or coils; there are no data in the literature, even of the indirect kind, bearing on this issue.

The purpose of the present study was to obtain formal comparisons of vocal tract output and listener judgments for utterances produced with and without pellets attached to the tongue and other articulators. This kind of comparison is important for several reasons. First, the extensive x-ray microbeam database collected at the University of Wisconsin-Madison (Westbury, 1994) will be subject to analyses for the next several years, making it necessary to interpret findings relative to possible disruptions of typical articulatory processes by the presence of pellets on articulatory structures. Second, point-parameterized observations of articulatory (and especially the tongue) motion are becoming accessible to a large pool of scientists with the advent of commercially available, relatively inexpensive (compared to the x-ray microbeam) electromagnetic tracking systems (e.g., see Tuller and Kelso, 1990). The constraints, if any, on interpretation of such point-parameterized data introduced by the process of observation should be carefully documented.

The speech sample protocol for the x-ray microbeam database project (Westbury, 1994) includes a series of utterances recorded under conditions identical to those in the main experiment, except without the pellets in place. This series of utterances, which was recorded prior to the attachment of the pellets and collection of x-ray microbeam data, represent a subset of the utterances forming the kinematic database. This allowed for a direct comparison, at the acoustic and perceptual levels of analysis, of speech production behavior with and without the pellets in place.

I. METHOD

A. Subjects

Acoustic data used in the present study were collected as part of the x-ray microbeam database project at the University of Wisconsin-Madison. The data base consists of 57 subjects who produced a common speech sample. Subjects passed a pure tone hearing screening and had no self-reported history of neuromotor or articulation disorders. Most subjects spoke an Upper Midwest dialect of American English. In the present report, analysis was completed for 21 subjects (11 males, 10 females). No special criteria were used to select these subjects from the total of 57, other than attaining gender balance. Age range for the subjects was 18.33 to 36.02 years (mean 22.56 years).

B. Speech sample and pellet array

A sample of 19 tasks from the full task inventory, recorded prior to pellet placement but under identical conditions (e.g., with the subject seated in the experimental chair and with speech samples presented in exactly the same way as in the main experiment) was obtained for comparative purposes and to familiarize subjects with the tasks and experimental conditions. The subset included isolated vowels, single words, and several sentences. For the present study the sentence *She had your dark suit in greasy wash water all year* was analyzed. The sentence was useful because it contained a variety of segment types, including one exemplar each of the four corner vowels /i/ (in *she*), /æ/ (in *had*), /u/ (in *suit*), and /ɑ/ (in *wash*). This allowed a direct comparison across conditions (pellets-on vs pellets-off) of the acoustic (and by inference, articulatory) working space for vowels. The sentence was produced three times by each subject prior to pellet placement and five times during the full task inventory with the pellets in place. The five repetitions of theutterances with pellets-on were distributed throughout the entire x-ray microbeam protocol; the sequence of the entire protocol, and hence the repetitions of interest, was the same for all speakers.

The typical array for the collection of kinematic data included a total of 11 pellets, 4 of which were on the tongue,

2 on the mandible, 2 on the lips, 2 on the nose, and 1 on the buccal surface of the maxillary incisors. The four lingual pellets, the effects of which are of primary interest here, were glued to the tongue such that the most anterior pellet was placed approximately 10 millimeters (mm) posterior to the lingual apex, and the most posterior pellet approximately 60 mm from the lingual apex. The middle two pellets were then placed at approximately equal intervals between the most anterior and posterior pellets, creating three inter-pellet distances of roughly equal length from front to back (additional details can be found in Westbury, 1994).

C. Data collection

The sound pressure wave was recorded with a directional microphone (SHURE SM81 Condenser) placed at mouth level. The microphone signal was fed into a 15-bit-resolution A/D converter programmed to sample at 21 739 times per second and to store the resulting digital stream synchronously with pellet position histories on SMD computer disks. Prior to digital conversion, an anti-aliasing filter (-3 dB at 7500) was applied to the microphone signal. For two subjects (JW7 and JW8) recorded early in database collection, recordings were made at 16 129 samples/s. Further details regarding recording procedures can be found in Westbury (1994).

D. Acoustic measures

The acoustic variables were chosen to sample a range of measures used extensively in the literature (e.g., segment durations and vowel formant frequencies), and to reflect articulatory behaviors that may on logical analysis be likely candidates for disruption by the pellets (e.g., formant trajectory measures and spectral moments for fricatives). Acoustic analyses for the present study were completed using Cspeech (Milenkovic, 1994). To measure segment duration a combined digital spectrogram/waveform display was used. Most segment durations were measured according to conventional criteria in the literature (Umeda, 1975, 1977; Crystal and House, 1988a, b, c), but in some cases several phonetic segments were combined as a single measured interval because of the absence of reliable boundaries. Examples of the latter include /yɔr/ (in *your*), /ri/ (in *greasy*), and /ɔlyir/ (in *all year*).

LPC formant analysis was used to generate $F1$-$F2$-$F3$ data for each of the corner vowels noted above. The automatic formant tracking option in CSpeech yielded formant trajectories that were superimposed on the digital spectrogram. Formant tracks were individually inspected and manually corrected for tracking errors. These tracks were generated from data files containing frequency values sampled at 5-ms intervals. $F1$-$F2$-$F3$ frequency values at the temporal midpoint of each vowel were recorded from these output files, and served as the vowel target values.

Consonant spectra for the /ʃ/ in *she* and *wash* and the /s/ in *suit* and *greasy* were measured by computing spectral moments (Forrest *et al.*, 1988) from a 50-ms segment taken from the midpoint of each fricative. Moments were computed for consecutive 20-ms windows stepped at 10-ms increments throughout this middle 50-ms interval and then averaged across the analyzed windows. The moments were compared across conditions to evaluate the influence of pellets on fricative production.

E. Perceptual measures

An audiotape, including 8 repetitions (3 with pellets-off, 5 with pellets-on) of the utterance for each of the 21 subjects, was prepared for perceptual tests. The tape consisted of 167 randomly sequenced repetitions of the utterance with a 6-s pause between each item; one token was omitted from this sequence because the original recording was cut off before the end of the utterance. Ten listeners who had worked with data from the x-ray microbeam project were selected to make a series of judgments about the recorded utterances. It was reasoned that listeners who were familiar with the database would be more sensitive to the potential effects of pellets on articulatory structures because of their familiarity with both the speakers and task materials. Listeners sat individually in a sound proof booth and heard the tape twice at a comfortable listening level. During one presentation the listeners were asked to make the simple, dichotomous judgment about whether the speaker had pellets-on or -off. Instructions for this task were as follows: ''You will hear a series of speakers repeat the sentence, *She had your dark suit in greasy wash water all year*; Please listen carefully and decide if you think the speaker has pellets-on, or pellets-off, then circle the appropriate selection next to the utterance number.'' During the other presentation, listeners were asked to scale the articulatory precision of each utterance using a free-modulus variation of the method of magnitude estimation. No standard was presented, and the experimenter prescribed no standard scale value; instead listeners were instructed to select the number he or she found appropriate for the first and every subsequent repetition of the utterance. For the present experiment, the listeners were told that ''articulatory precision is defined as the clear articulation of both vowels and consonants: The most precise articulation is that in which the consonants and vowels appear to be 'perfectly' articulated, and the least precise articulation is that in which the consonants and vowels are clearly distorted and perceived as 'sloppy.' '' Listeners were told to assign low numbers to the 'sloppy' end of the scale and high numbers to the precise end of the scale. A procedure described by Engen (1971) was used to eliminate inter- and intra-listener variance in the data cause by differing choice of moduli. This procedure provided an exponent of the function with invariant individual slopes as well as an average of the individual intercepts. The order of listening tasks was controlled across subjects to eliminate any biases.

II. RESULTS

A. Segment durations

Mean segment durations for the two speaking conditions (pellets-on and pellets-off) are presented in Appendix A for individual speakers. Data averaged across the speakers and repetitions are presented in Fig. 1. Data for the final segment (/ɔlyir/) are not included in the chart for scaling reasons. This figure shows that for 17 of the 24 segments slightly longer

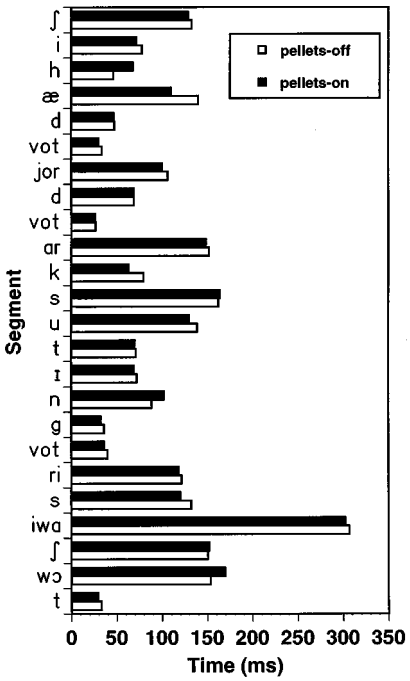

FIG. 1. Group mean segment durations, shown by speaking condition (unfilled bars=pellets-off, filled bars=pellets-on.

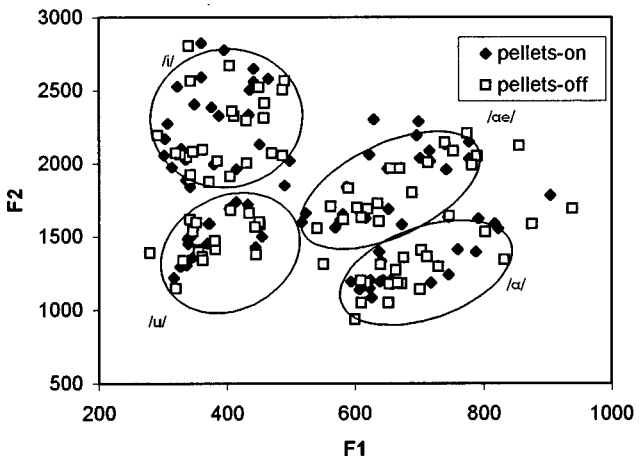

FIG. 2. $F1$-$F2$ plot for pellets-off (unfilled boxes) and pellets-on (filled diamonds). Each plotted point represents a mean for a single subject; sigma ellipses are shown for each vowel category.

durations were produced in the pellets-off condition. Statistically significant differences were found between conditions for several individual segments, most frequently in the /h/ and /æ/ segments in *had* and /ɪ/ and /n/ in the word *in*; these occurred for no more than half the speakers, with the magnitude of the effect ranging between 4 and 57 ms. The segment duration effects for the word *in* were typically in the 20–30 ms range. The direction of these significant effects, however, was not consistent between conditions.

B. Formant frequencies and trajectories

The average formant frequencies ($F1, F2, F3$) are reported by speaker gender group for each vowel and condition in Table I; average data for individual speakers, vowel, and condition are reported in Appendix B. Between-conditions differences in formant frequencies of 75, 150, and 200 Hz for $F1$, $F2$, and $F3$, respectively, are bolded in Appendix B. These difference values were chosen based on considerations of typical measurement error for formant values (e.g., Lindblom, 1962; Monsen and Engebretson, 1983) and difference limen data for formant frequencies (e.g., Kewley-Port and Watson, 1994). Part of the data from Appendix B is shown in Fig. 2 as an $F1$-$F2$ plot where it can be seen that, taken as a whole, the distributions of coordinates appear to be roughly similar for the pellets-on and pellets-off conditions. Among the male speakers, 1 (JW07) of the 11 speakers had very large formant frequency differences between the conditions. Most of the other differences for the male speakers that met the 150-Hz criterion for $F2$ showed lower values in the pellets-on condition.

Among the female speakers there were six $F1$ comparisons (derived from four of the ten speakers) that met the 75-Hz criterion, and all but one (JW16, /a/) involved a higher $F1$ in the pellets-on condition. Seven $F2$ comparisons (derived from five of the ten speakers) met the 150-Hz criterion for the female speakers, and six of these were consistent with the pattern seen for the males of lower $F2$'s in the pellets-on condition.

There was no obvious pattern for any of these between condition differences to favor a specific vowel, for either gender. Although the direction of the $F2$ effect is very consistent across speakers, the articulatory interpretation is not straightforward. The lowering of $F2$ with pellets-on may suggest a less fronted tongue for /i/ and /æ/ (four effects for males, two for females), but the lowering for /u/ (two effects for males, one for females) is more difficult to interpret. One possibility for /u/ is that the tongue does not move as far back and up in the pellets-on condition as it does with pellets-off, which induces an over compensating lip-rounding gesture (see Perkell *et al.*, 1993). The lip rounding

TABLE I. Mean target formant frequency values for male and female groups across speaking conditions.

		/i/			/ae/			/u/			/a/		
	Pellets	$F1$	$F2$	$F3$	$F1$	$F2$	$F3$	$F1$	$F2$	$F3$	$F1$	$F2$	$F3$
Males-mean	off	339	2087	2729	601	1706	2482	358	1476	2278	647	1242	2345
SD	off	41	198	285	70	163	274	49	213	232	61	135	282
Males-mean	on	351	1991	2589	585	1663	2374	344	1412	2205	631	1168	2272
SD	on	38	145	162	55	79	143	27	133	92	37	117	174
Females-mean	off	391	2553	3098	701	2100	2891	431	1814	2726	765	1543	2581
SD	off	44	155	154	49	117	142	31	278	134	62	240	45
Females-mean	on	425	2503	2987	742	2032	2752	436	1784	2699	772	1435	2493
SD	on	51	150	144	58	108	145	30	275	132	82	164	107

would produce lower $F2$'s in the pellets-on condition. The same explanations may account for the lower $F2$'s for /a/ (three effects for males, three for females) in the pellets-on condition.

The articulatory interpretation of the $F1$ effects in female speakers, where the $F1$ was higher in the pellets-on condition for five of the six cases meeting the 75-Hz criterion, is most likely a more open jaw. This adjustment would move the lingual pellets away from the hard tissue boundaries of the vocal tract. For males, only one $F1$ effect was produced by a speaker other than JW07 (JW41, /i/), and it also involved a higher $F1$ in the pellets-on condition. The remaining $F1$ effects were produced by JW07, who consistently produced *lower* values of $F1$ in the pellets-on condition.

The magnitude of between-conditions differences are certainly not large for the group comparisons reported in Table I, and this would follow from the relatively small proportion of large effects described above for the individual subject comparisons. The consistency of these relatively few individual-subject effects, however, is mirrored in the group means, where all four vowel comparisons for the female speakers show higher $F1$ in the pellets-on condition, and all comparisons for $F2$ show lower values in the pellets-on condition.

Vowel formant trajectories, either of the CV or VCV type, were plotted for the speakers who showed differences in target frequencies for any of the four vowel segments. The formant plots for all vowels and subjects plotted showed no remarkable differences in shape and slope. An example of a trajectory with between-conditions differences only in target frequency is shown in Fig. 3 for a male speaker (JW07). Similar vowel trajectory plots were made for the subjects who showed significant changes in segment duration related to speaking condition. These plots showed differences only in timing of the trajectories (Fig. 4); target frequency, shape, and slope remained unchanged. Additional trajectory plots were completed based on differences found in consonant spectra analysis (see below); plots of /iwɑ/ from *greasy wash* were completed for 11 speakers. It was reasoned that significant changes in fricative spectra might reflect differences in neighboring vowel trajectories; however, no trajectory differences were noted between the pellets-on and pellets-off repetitions of this segment.

C. Consonant spectra

A complete table of the spectral moments for each speaker can be found in Appendix C. No general patterns that distinguish pellets-on *versus* pellets-off emerge from these data, but there is at least one noteworthy trend for the mean (i.e., the first moment). Average values for the first spectral moment of the /s/ frication in *suit* and *greasy* and the /ʃ/ frication in *she* and *wash* are reported for the two conditions in Table II. Using a minimum difference of at least 1.0 kHz between conditions as significant, 18 of the complete set of 84 pellets- on vs pellets-off comparisons (4 fricatives×21 subjects) are significant; moreover, 13 of these comparisons are for either the /s/ in *suit* or *greasy*, and among these 12 have the higher mean in the pellets-on condition (for /ʃ/, 3 of the 4 comparisons meeting the criterion—all for men—also showed a higher mean in the pellets-on condition). This would suggest a tendency among speakers to create the vocal tract constriction for /s/ (or /ʃ/) somewhat more forward with the pellets-on, as compared to off; it is also possible that the higher means in the pellets-on condition reflect greater overall effort in utterance production, with higher flows through the fricative constriction and consequently greater energy in the higher frequencies of the source spectrum (Shadle, 1990). A final possibility is that the pellets act like obstacles in the path of the flow, increasing the high frequency energy in the turbulent source and thus contributing to first spectral moment differences between the pellets-on versus pellets-off condition.

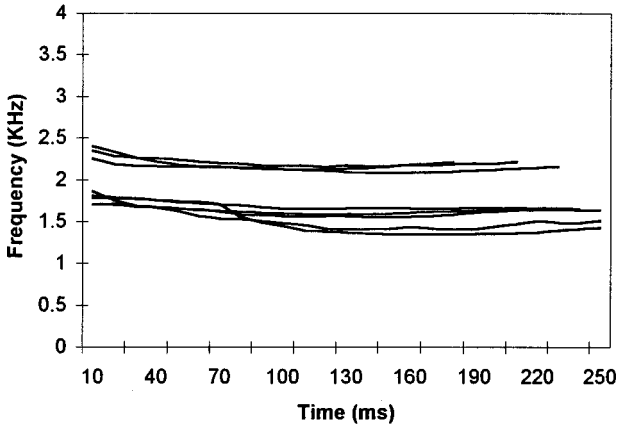

FIG. 3. $F2$ formant trajectories for /æ/, produced by subject JW07; the higher group of three trajectories are for the pellets-off repetitions, the lower group of five trajectories are for the pellets-on repetitions.

D. Perceptual judgments

1. Dichotomous judgments

The results from the dichotomous judgments are summarized in Figs. 5 and 6 for pellets-off and -on, respectively. For judgments of either 'pellets-off' or 'pellets-on,' when at least 80% inter-listener agreement was used as a criterion of consistency only 53 of the 167 tokens were judged consistently; the remaining 115 utterances were judged uniformly

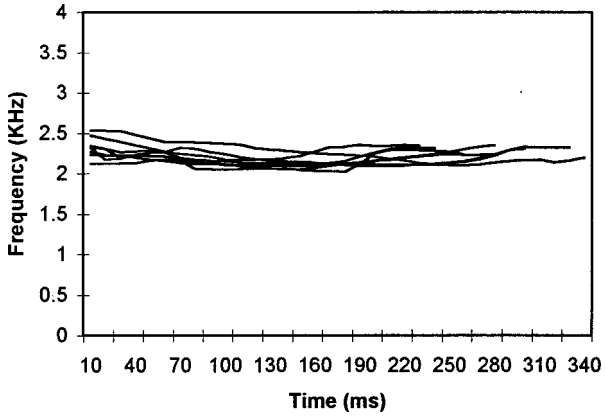

FIG. 4. $F2$ format trajectories for /æ/, produced by subject JW18; the trajectories for both conditions are superimposed, with some between-conditions differences in overall duration.

TABLE II. Mean Moment values for the fricatives across speaking conditions.

Male speakers	Pellet	JW07	JW08	JW11	JW12	JW18	JW19	JW28	JW32	JW40	JW41	JW43
SHE	off	3.49	3.313	4.062	3.159	3.224	4.654	3.575	3.775	3.452	3.799	3.105
	on	5.208	3.229	3.834	3.916	3.481	3.893	3.591	3.709	3.105	3.430	2.94
SUIT	off	5.377	5.569	6.366	4.091	5.170	5.941	4.77	5.94	5.539	5.452	5.32
	on	7.225	5.695	7.672	7.867	7.44	8.515	6.355	6.958	7.424	4.509	4.86
GREASY	off	5.229	5.749	5.96	4.441	5.153	6.044	5.126	6.182	5.352	5.864	5.77
	on	6.81	5.3	6.232	3.137	5.29	6.043	6.284	5.479	5.559	7.329	5.382
WASH	off	3.415	4.23	3.906	2.807	3.196	4.651	3.984	4.022	2.725	3.595	2.868
	on	4.697	3.926	4.203	4.35	3.894	3.875	3.546	4.16	2.672	3.693	2.704
Female speakers	**Pellet**	**JW14**	**JW16**	**JW27**	**JW29**	**JW31**	**JW36**	**JW37**	**JW48**	**JW50**	**JW52**	
SHE	off	3.944	4.503	4.110	4.222	4.935	4.914	4.271	4.523	3.982	3.795	
	on	4.067	4.184	4.448	4.155	4.787	4.799	4.334	5.19	3.92	3.663	
SUIT	off	7.311	6.604	6.553	6.588	6.68	7.357	5.954	5.421	7.398	5.385	
	on	7.225	5.695	7.672	7.867	7.44	8.515	6.355	6.958	7.424	4.509	
GREASY	off	7.652	7.006	6.613	7.58	7.188	6.556	6.639	5.916	7.224	4.995	
	on	7.414	6.581	7.83	7.74	7.485	8.090	7.003	7.568	7.557	5.321	
WASH	off	3.626	4.543	4.108	3.918	4.711	4.122	4.191	3.733	3.977	4.43	
	on	3.073	3.731	4.09	3.52	3.939	4.107	3.138	3.944	4.15	3.458	

by the 10 listeners less than 60% of the time. There were 5 speakers (3 males and 2 females) of the original 21 speakers for whom no repetitions met the criterion of 80% agreement. These speakers are not included in Figs. 5 and 6.

Figure 5 shows for each speaker (excepting the five noted above) the percentage of pellets-off utterances that were judged consistently. Unfilled bars show utterances that were judged correctly (i.e., utterances with 'pellets-off' judged consistently [8 of 10 judges] as 'off'), and filled bars show utterances that were judged incorrectly (i.e., utterances with 'pellets-off' judged consistently as 'on'). Of the 28 utterances displayed in this figure, 22 were judged accurately (i.e., as having the pellets-off) and 6 were judged incorrectly (i.e., as having the pellets-on when they were off). For example, of the three utterances produced with pellets-off by subject JW12, one was not judged consistently, one was judged consistently and correctly, and the other was judged consistently yet incorrectly. JW40 had all three of his pellets-off utterances judged consistently, but incorrectly. JW27 and JW37 have the opposite situation, where all of their pellets-off utterances were judged correctly.

The percentage of pellets-on utterances that were judged consistently is shown in Fig. 6. As in the case of the pellets-off utterances, the majority of consistently identified pellets-on utterances were correct judgments (21 correct, 4 incorrect). No subject had all pellets-on utterances judged consistently. In general, there were proportionately fewer

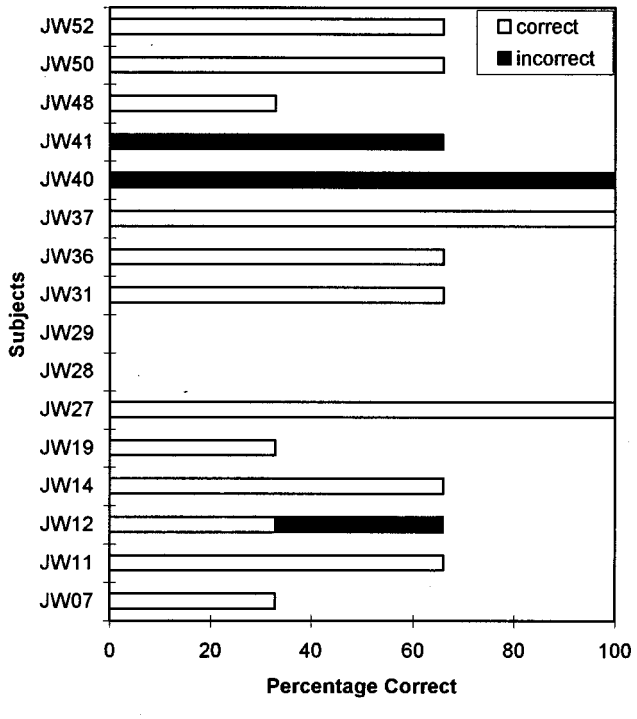

FIG. 5. Percentage of pellets-off utterances identified consistently (at least eight of ten listeners in agreement), shown by individual speakers; five speakers are not shown because none of their pellets-off utterances were identified consistently by the criterion. Correctly identified utterances are shown by unfilled bars, incorrectly identified utterances by filled bars.

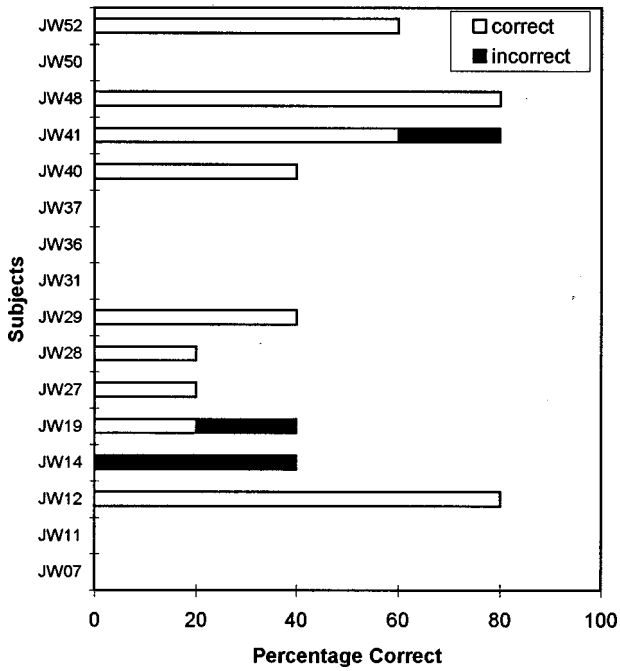

FIG. 6. Percentage of pellets-on utterances identified consistently (at least eight of ten listeners in agreement), shown by individual speakers; five speakers are not shown because none of their pellets-on utterances were identified consistently by the criterion. Correctly identified utterances are shown by unfilled bars, incorrectly identified utterances by filled bars.

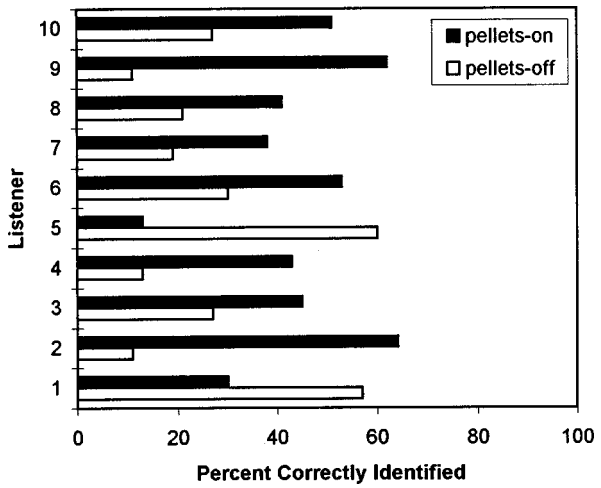

FIG. 7. Percentage of utterances identified correctly by each listener. Pellets-off utterance are shown as unfilled bars, pellets-on utterances as filled bars.

pellets-on utterances (25 of 104 utterances) judged consistently as compared to the pellets-off judgments shown in Fig. 5 (28 of 63 utterances).

Figure 7 shows the percentage of correctly identified utterances for each of the ten listeners broken down by pellets-on versus pellets-off. In this figure, there are no *a priori* criteria of consistency and the percentages are based on an item-by-item count. Eight of the ten listeners were more successful in the identification of pellets-on utterances, as compared to pellets-off utterances. Across listeners, 44% of the pellets-on utterances were identified correctly, and 28% of the pellets-off utterances were identified correctly.

2. Articulatory precision

Mean articulatory precision ratings for each subject in both speaking conditions were calculated. One-way ANOVA was used to test whether the mean ratings for each of the eight utterances (three off/five on) differed for any single speaker ($\alpha = 0.05$). Results of the omnibus tests were not significant for any speakers. These findings were interesting given that roughly 35% of the utterances were identified consistently in the dichotomous listening task. Based on acoustic measures completed for this group of subjects, it might have been expected that subjects who showed differences in either timing or consonant spectra across speaking conditions would receive lower articulatory precision ratings; this was not the case, as no between-conditions differences were found.

III. DISCUSSION

There are a large number of studies in the literature on speech production that are based on point-parameterized estimates of articulatory motion. The findings from many of these studies are often used to address certain theoretical issues, many of which are associated with temporal and spatial aspects of articulatory behavior. It is likely that the volume of published point-parameterized data, especially from the tongue, will increase in the next few years as a result of commercially available, electromagnetic systems for collecting and analyzing such data, and the existence of at least one public database of point-parameterized articulatory motion (Westbury, 1994). It seems important to know how the presence of the point markers might affect articulatory behavior, and how the interpretation of such data might be constrained by such effects.

In the present study, we selected acoustic and perceptual measures to evaluate the possibility of such effects. The findings for each of these measures will be discussed in turn.

A. Temporal measures

Measures of segment durations revealed some between-conditions differences for individual subjects, but generally there was little consistency across subjects with respect to the direction of these effects. To the extent that segment durations reflect variation in speaking rate, it seems safe to conclude from the present findings that the presence of pellets on the articulators had little effect on global speech timing. And, there was no evidence of consistent segment-level effects for specific sound types, such as fricatives.

B. Formant frequencies

Although the $F1$-$F2$ plot (Fig. 2) showed a great deal of between-conditions overlap in the coordinate points, there were some subtle group trends and some interesting patterns in the individual subject data. Using frequency-difference criteria based on measurement error and difference limens for formant frequencies, 6 of the 40 $F1$ comparisons exceeded 75 Hz for individual female subjects (Appendix B), all of which involved a higher $F1$ with the pellets-on, as compared to off. For $F2$ 11 of the 44 individual-subject comparisons for males and 7 of the 40 individual subject comparisons for females met the criterion of a 150-Hz difference; in 16 of these comparisons, the $F2$ value was lower with the pellets-on. Thus when formant frequency differences were observed across multiple subjects, they had a strong tendency to be consistent in direction. The $F1$ effect in females seems to reflect a greater mouth opening with the pellets-on, and the $F2$ effect in both males and females is most likely the result of a more retracted tongue. Both effects seem to be amenable to a common sense interpretation of how a speaker might react to the presence of pellets on articulatory structures, and especially on the tongue. Specifically, the effects seem to reflect an articulatory adjustment to avoid making contact between a pellet (or pellets) and the bony upper and anterior boundary of the vocal tract. The more open mouth (the $F1$ effect) would keep the anterior pellets away from the hard palate, and a more retracted tongue (the $F2$ effect) would pull the anterior pellet away from the inferiorly protruding alveolar ridge. Whereas these appear to be reasonable interpretations of these patterns, the data of one subject (JW07) consistently showed the opposite trend for $F1$, with lower values in the pellets-on condition, indicating a more closed vocal tract. Why this subject would have brought the pellets closer to the upper boundary of the vocal tract is not clear.

The fact that there was a relatively small proportion of cases in which these effects were observed indicates a differential rate of adaptation or tolerance across subjects to the presence of pellets, but the relative consistency of the effect

direction (excepting JW07), when it occurred, suggests a common response when the adaptation or tolerance was incomplete. All speakers were given a short period of preexperiment talking time after the pellets were attached to the articulatory structures, but it is impossible to know if the effects would disappear with a more extended adaptation period. A sampling of some older (Gay, 1974; Nearey, 1978; Wood, 1979) and more recent (Perkell and Nelson, 1985; Perkell and Cohen, 1989) studies in which point-parameterized articulatory positions for vowel production are reported reveals little information on the time period between attachment of pellets and collection of data. It is certainly possible, then, that some of the tongue positions and formant frequencies reported in the studies cited here (and in others) reflect an articulatory adjustment to the presence of the pellets. It is also fairly clear that in experiments of this type (e.g., Flege *et al.*, 1988; Savariaux *et al.*, 1995; and the present one) there is a good deal of intersubject variability in reaction to the presence of an intra- or perioral device.

C. Fricative articulation

Spectral moments analysis failed to reveal a pervasive effect of pellets on fricative articulation. As noted in the Introduction, fricatives would seem to be the most rigorous test of the effects of pellets on articulatory behavior. The absence of frequent effects would seem to be a strong endorsement of the notion that point parameterization of lingual motion does not interfere, at least in any pervasive way, with production of the lingual fricatives studied here.

Approximately 20% of the possible comparisons (17/84) for the moments did show a between-conditions effect, and in the great majority of these cases (15/17) there was a higher mean in the pellets-on condition. Thus even though the effects were relatively infrequent, they were systematic when they occurred. Among the potential interpretations of these effects, two would seem to have important consequences for studies of fricative articulation. The first spectral moment could have been increased in the pellets-on condition by either a more forward point of constriction or a deepening of the midline lingual groove (Fant, 1960), either of which would be a distortion of typical articulatory patterns for fricatives. The present data do not permit a clear choice between these two adjustments, but the more forward point of constriction seems counterintuitive because it would probably create greater contact between at least the frontmost pellet (and, perhaps, the pellet immediately posterior) and the bony roof of the vocal tract. As in the case of vowel effects, discussed above, a more natural articulatory response would seem to be one in which the pellets were moved away from contact with bony structures. A deeper lingual groove would accomplish this, and may be the more reasonable interpretation of the systematic effects for the first moments of /s/ and /ʃ/.

The increase in the value of the first moment could also have occurred in the absence of the kind of lingual adjustments described above, and therefore may not reflect distortions of typical fricative articulation. For example, the first moment could increase as a result of increased high frequency energy due to greater subglottal pressure (and hence trans-constriction flows) or from higher frequency source energy associated with interruption of laminar flow streams by the pellets (see Shadle, 1990). The acoustic effects resulting from either or both of these mechanisms would be more like epiphenomena of the presence of pellets, rather than true articulatory effects.

D. Perceptual findings

Listeners were not able to make reliable identifications of utterances spoken with pellets-on vs pellets-off, nor could they scale articulatory precision differentially across conditions. Even when listeners were consistent among themselves, they were as likely to be correct as incorrect in making the simple dichotomous judgment of 'on' vs 'off.' The listeners' poor performance extended to speakers for whom consistent acoustic differences between pellets-on and pellets-off had been demonstrated. For example, JW07 had very dramatic acoustic differences between conditions for vowels (Appendix B) and fricatives (Appendix C), but his utterances could not be identified reliably as being produced with or without pellets, and were not distinguished by scalings of articulatory precision. This particular case, as well as that of several other subjects who had between-conditions acoustic effects that did not translate to consistent perceptual effects, raises an important caveat about the use of either formal or informal perceptual measures in experiments using point parameterization of articulatory motions. This finding is consistent with the report of Flege *et al.* (1988), who found that reliable acoustic effects produced by a bite block did not translate to reliable perceptual judgments of the presence versus absence of the block during utterance production.

As noted in the Introduction, the typical experiment using point parameterization of articulatory motion or any type of perioral or intraoral measurement device, relies on informal listening and a subject's own report for evidence that the markers or devices are not interfering with normal speech production. Many of these same studies employ a small number of speakers because of the technical challenge of collecting and analyzing a large amount of complex data which often exist in multiple streams and are not amenable to fully-automated processing. The use of small numbers of subjects in these experiments is understandable, but a subject such as JW07 exposes a potential danger for a speech production experiment in which a few subjects are used to test a model's prediction, or the validity of a theoretical axiom. If JW07 was one of the few speakers in such an experiment (or, for example, JW27 and JW36 in experiments dealing with /s/ articulation: see Table II; or JW31 and JW41 in experiments dealing with vowel articulation: see Appendix B), the articulatory behavior observed in the experiment would very possibly be different from the speaker's 'normal' articulatory behavior, and thus not be a fair test of the model or theory. The present results suggest that even formal, apparently simple perceptual tests may not identify these speakers. It is possible, of course, that a more sensitive perceptual test of a segment's vulnerability to the presence of pellets may have revealed listeners' ability to make reliable identifications of

speaking condition. For example, listeners might have been able to identify the pellets-on vs pellets-off conditions if only presented with excised /s/ or /ʃ/ waveforms (but see Flege *et al.*, 1988); we chose not to do this in our experiment because we were interested in formal perceptual judgments similar to the informal evaluations found most frequently in the literature and used for our own x-ray microbeam database.

If formal perceptual judgments may miss those subjects who are affected by the presence of pellets, what options exist for eliminating speakers who are likely to adjust their typical articulatory behavior when pellets, coils, or other devices are placed on their oral structures? We would suggest a fairly simple screening protocol to eliminate potential subjects who show large effects due to the placement of pellets-on the articulators. The protocol should consist of a small group of utterances produced first with no pellets attached to the articulators, and then with the pellets attached. The speech sample should include lingual fricatives as well as high vowels, and speech acoustic measures such as those used in the present investigation should be used to evaluate a potential subject's speech production sensitivity to the presence of pellets on articulatory structures in general, but especially on the tongue. The criteria for rejecting a potential subject for participation in an experiment obviously will depend on the purposes of the experiment and the hypothesis under evaluation; the criteria used in the present experiment, especially in the case of fricative spectra, may actually be overly liberal for certain experimental questions. Whereas it is possible that formal adaptation periods could be built into articulatory kinematics experiments as a way to circumvent such a screening protocol, the small number of speakers who do show acoustic effects in the present experiment argue for the screening as a more efficient and rigorous approach to the problem. Formal adaptation periods could not ensure the elimination of effects in the absence of some analytical demonstration of complete adaptation. Finally, the use of perceptual evaluation of 'normal' speech with pellets or coils in place does not seem to be an acceptable way to validate the absence of unwanted influences from the markers. Many of the perceptual evaluations in the present experiment were 'normal' for specific subjects who showed large acoustic effects of the pellets. This finding suggests that acoustic measures are the preferred indices of a subject's ability to produce typical articulatory behavior with pellets or coils attached to the tongue.

ACKNOWLEDGMENTS

The work reported here was supported by NIH Award Nos. DC000820 and DC00319. Portions of the results were reported previously in 1996 at the 3rd Joint Meeting of the Acoustical Society of America and the Acoustical Society of Japan. We would like to thank Anders Löfqvist and two anonymous reviewers for comments on an earlier version of the manuscript. Requests for reprints should be directed to weismer@waisman.wisc.edu or bunton@waisman.wisc.edu.

APPENDIX A

Segment durations for individual subjects across speaking conditions.

Subject Pellets	Segment 1 /ʃ/	Segment 2 /i/	Segment 3 /h/	Segment 4 /æ/	Segment 5 /d/	Segment 6 vot	Segment 7 /ɔ/	Segment 8 /d/	Segment 9 vot	Segment 10 /ar/	Segment 11 /k/	Segment 12 /s/	Segment 13 /u/	Segment 14 /t/
7 off	129.67	84.67	42.00	157.67	66.67	46.00	163.00	68.67	17.33	201.00	82.67	130.67	179.00	63.67
7 on	119.40	88.60	48.20	125.20	51.80	30.20	121.00	63.40	17.20	165.80	77.00	111.80	153.80	56.20
8 off	130.67	90.00	23.67	174.00	58.33	29.00	111.33	91.00	22.33	175.67	97.33	189.00	162.67	49.33
8 on	134.40	76.80	61.20	120.20	53.00	31.20	99.00	60.20	28.00	158.40	50.00	181.20	141.60	45.00
11 off	138.00	67.00	18.67	137.33	64.00	26.33	90.00	84.33	19.67	158.67	77.67	141.00	133.00	53.67
11 on	133.00	46.20	59.60	100.20	49.80	31.20	82.20	58.60	28.00	174.20	75.60	145.20	112.20	55.80
12 off	170.67	113.33	25.00	181.67	39.00	27.00	162.00	55.33	18.33	152.67	69.33	166.67	121.67	59.67
12 on	178.80	141.80	53.00	157.60	52.20	25.60	114.80	63.20	30.20	135.20	60.00	185.20	127.80	42.40
14 off	127.33	77.67	32.00	152.67	63.33	37.33	80.33	50.67	16.00	135.67	80.33	119.67	122.00	36.33
14 on	117.40	63.00	61.20	119.60	51.40	43.20	66.60	52.40	13.80	149.40	47.00	149.20	119.00	27.00
16 off	137.67	105.00	31.33	167.33	56.33	24.00	116.67	93.00	20.00	159.33	97.67	163.00	146.33	84.67
16 on	118.20	97.20	62.80	128.60	48.20	32.00	101.80	72.60	21.40	155.20	87.60	168.60	144.00	71.60
18 off	179.50	81.50	40.50	185.00	22.00	43.50	168.50	43.00	49.00	138.00	85.00	189.00	163.00	52.50
18 on	151.75	72.50	77.50	108.00	33.75	33.25	124.50	62.00	32.50	132.00	77.75	180.75	167.25	55.50
19 off	136.33	92.33	25.33	133.00	37.67	23.33	109.00	65.00	23.33	139.33	63.67	169.33	135.67	37.67
19 on	138.40	95.60	69.40	115.20	47.40	25.80	94.40	82.80	21.20	141.60	54.40	172.60	129.80	44.60
36 off	142.00	75.00	19.67	194.67	30.50	12.50	147.00	71.00	14.67	175.67	76.00	167.00	186.67	25.67
36 on	124.20	93.60	66.40	122.40	15.00	21.40	143.40	62.80	34.60	162.40	69.20	138.60	146.40	26.20
37 off	115.33	63.67	16.00	136.00	25.00	24.67	90.67	76.67	15.00	153.67	64.67	154.33	135.67	65.33
37 on	118.40	61.60	50.20	123.20	26.00	20.00	88.60	67.40	13.40	146.60	56.00	141.80	119.80	50.20
48 off	129.33	85.67	29.00	190.33	48.67	29.67	94.33	61.00	19.67	181.33	80.33	157.33	147.00	49.33
48 on	139.00	82.60	62.40	173.00	39.20	27.00	109.80	64.60	17.00	170.60	72.60	176.80	146.20	19.20
27 off	127.67	66.00	77.33	77.33	44.67	40.67	95.67	53.00	20.33	156.33	64.00	178.67	123.67	68.00
27 on	130.40	66.00	86.00	83.80	55.60	26.60	124.80	59.40	18.60	151.60	53.00	204.40	117.80	54.60
28 off	144.33	89.33	82.67	137.67	75.33	38.33	64.33	82.00	16.67	133.00	75.33	161.67	118.00	84.33
28 on	138.20	92.60	69.20	129.00	71.60	20.80	81.60	85.80	17.60	155.20	67.00	161.60	136.40	57.40
29 off	128.00	47.33	65.33	142.67	41.00	37.33	84.33	86.67	14.33	151.33	72.33	171.00	156.33	75.00
29 on	129.20	57.80	70.80	116.20	37.80	23.40	98.40	74.80	14.00	146.80	84.00	157.60	171.20	87.20

(*Continued.*)

Subject Pellets	Segment 1 /ʃ/	Segment 2 /i/	Segment 3 /h/	Segment 4 /æ/	Segment 5 /d/	Segment 6 vot	Segment 7 /ɔ/	Segment 8 /d/	Segment 9 vot	Segment 10 /ar/	Segment 11 /k/	Segment 12 /s/	Segment 13 /u/	Segment 14 /t/
31 off	122.33	70.00	70.67	108.00	44.33	13.00	127.33	85.67	19.00	171.00	70.33	161.00	152.00	68.33
31 on	132.00	70.00	73.00	115.00	48.00	15.00	135.00	92.00	21.00	165.00	68.00	153.00	146.00	63.00
32 off	138.33	57.67	64.33	99.67	49.67	35.67	125.33	95.67	13.00	144.33	44.67	200.60	134.00	109.67
32 on	160.20	62.40	61.60	82.20	43.20	35.20	103.80	131.80	15.60	139.00	53.80	154.00	135.40	90.80
40 off	108.00	67.67	81.33	94.67	34.33		123.33	68.67	18.33	164.67	64.67	166.67	120.67	87.67
40 on	126.60	62.00	60.40	96.80	37.00	16.00	124.60	53.80	20.20	158.60	62.20	143.80	91.40	42.20
41 off	108.00	52.00	46.67	50.00	40.67	23.00	49.33	95.33	18.33	122.00	47.33	154.33	103.00	53.00
41 on	128.25	49.25	50.25	34.25	55.50	18.25	75.25	90.50	21.25	128.50	45.75	162.50	133.75	42.00
43 off	144.67	78.33	62.67	123.00	54.67	40.67	79.67	75.00	22.67	145.33	71.33	211.67	142.67	63.00
43 on	128.00	85.40	75.40	138.80	52.40	37.40	112.60	78.00	17.60	148.40	65.60	204.40	167.80	60.00
50 off	101.33	67.00	68.33	121.67	52.33	16.67	89.00	54.67	10.67	151.33	66.67	156.33	118.33	65.00
50 on	122.20	54.20	82.40	102.80	56.80	22.60	79.00	54.60	15.00	140.40	64.40	148.20	102.60	57.20
52 off	133.67	78.67	68.00	131.33	50.33	16.50	131.00	67.33	12.33	173.67	77.67	178.33	144.67	47.67
52 on	130.50	48.50	56.75	103.75	33.25	15.00	105.75	73.00	15.00	160.00	72.00	165.00	119.00	22.00

(*Continued.*)

Segment 15 /i/	Segment 16 /n/	Segment 17 /g/	Segment 18 vot	Segment 19 /ri/	Segment 20 /s/	Segment 21 /iwa/	Segment 22 /ʃ/	Segment 23 /w9/	Segment 24 /t/	Segment 25 /ɔ/yir/
91.33	133.00	30.00	41.33	131.00	110.67	367.67	140.00	187.00	23.33	860.33
90.20	89.20	28.80	28.80	126.60	109.20	325.00	122.60	193.00	29.00	797.20
125.00	69.00	33.67	34.67	119.67	121.00	327.67	150.67	223.33	22.67	862.67
53.20	136.20	35.40	27.20	117.80	110.00	303.20	153.60	194.60	32.20	862.00
84.67	112.00	33.00	25.00	122.00	130.33	285.33	137.33	140.67	22.33	788.00
55.20	123.60	47.60	34.00	109.40	125.20	308.00	146.80	150.00	21.20	750.60
92.67	87.33	21.00	45.67	123.33	114.33	320.33	133.00	172.00	19.67	658.00
31.20	159.00	13.60	28.00	125.00	115.40	299.40	134.20	159.20	30.20	650.80
55.00	136.33	35.00	27.00	115.67	125.67	335.33	146.00	166.00	19.00	744.33
48.40	124.40	34.00	32.20	125.20	107.60	317.20	138.20	159.40	17.80	743.80
59.00	86.67	30.67	30.00	145.00	105.33	351.67	124.33	150.00	22.67	844.00
79.00	121.40	28.00	30.40	158.40	126.40	360.60	149.40	175.40	25.20	804.60
37.50	96.50	34.50	48.00	98.50	138.00	328.50	197.00	158.50	24.00	806.00
81.33	92.00	36.50	47.25	116.00	124.25	334.50	173.50	168.00	23.75	727.25
51.00	66.33	43.67	51.00	105.00	122.33	271.00	149.00	139.33	18.00	577.00
32.00	96.00	45.80	44.20	115.60	126.20	282.00	150.80	146.80	20.00	673.80
63.67	111.67	30.67	28.33	143.00	102.33	329.33	126.00	174.33	18.00	724.67
92.60	83.60	23.00	24.20	152.60	112.00	336.80	109.20	199.20	23.20	697.80
54.33	76.67	23.00	33.00	96.33	106.33	251.67	128.33	122.67	11.33	602.00
50.20	67.60	32.50	31.60	107.80	121.40	274.20	139.20	147.80	11.60	651.40
81.00	69.00	32.67	30.00	141.00	131.33	332.33	146.67	170.67	15.67	676.33
66.20	112.40	21.40	25.20	148.00	141.00	367.00	147.20	180.00	14.40	752.80
45.33	77.00	29.00	50.33	96.33	145.33	316.33	152.00	146.33	38.33	814.67
55.20	99.60	26.40	38.00	101.40	152.80	313.60	168.40	140.00	31.40	801.80
95.67	118.00	38.33	31.00	146.67	136.00	348.00	177.00	153.33	29.67	655.00
66.40	101.60	39.00	41.60	129.40	132.40	312.80	166.00	160.20	36.80	696.40
52.67	74.00	26.00	34.33	114.67	143.00	281.00	167.67	151.67	20.00	715.00
87.60	90.80	24.00	25.20	113.80	139.80	271.20	159.40	149.80	19.40	738.60
59.67	74.00	47.67	23.33	147.33	134.67	269.00	154.67	161.00	26.33	734.33
55.00	70.00	48.00	25.00	148.00	135.00	280.00	142.67	152.00	32.00	730.00
79.67	99.67	50.67	36.00	86.67	135.00	308.33	142.67	129.00	19.67	655.00
77.00	54.40	28.40	28.80	91.80	127.60	307.80	224.60	126.60	22.20	663.60
76.00	106.00	23.00	31.00	125.67	141.33	287.00	136.33	157.00	23.00	652.33
83.75	109.50	32.60	33.60	121.80	146.20	290.80	154.60	211.60	28.00	679.40
61.33	57.00	40.33	37.67	89.33	121.00	283.67	119.00	138.67	21.33	592.67
40.75	90.50	29.25	45.50	115.50	108.25	283.00	130.50	121.25	22.75	572.50
80.00	125.67	40.67	41.00	115.67	125.00	390.33	207.00	154.00	20.00	684.33
82.20	97.40	37.60	39.60	117.40	122.20	337.20	186.40	154.20	21.20	708.80
55.00	73.67	39.67	27.67	100.67	118.33	260.67	174.00	132.00	23.33	623.67
65.00	84.00	17.20	19.40	108.80	122.20	295.40	170.40	127.80	24.60	630.40
88.00	104.00	39.00	32.00	139.67	121.67	350.67	124.33	199.00	21.33	708.00
70.25	100.25	19.75	29.25	128.50	119.75	342.25	132.50	189.50	19.75	709.50

APPENDIX B

Mean formant values for the four vowels in 'pellets-off' and 'pellets-on' conditions, male speakers.

		/i/			/ae/			/u/			/ɛ̈/		
		*F*1	*F*2	*F*3	*F*1	*F*2	*F*3	*F*1	*F*2	*F*3	*F*1	*F*2	*F*3
JW07	off	442	**2561**	**3515**	**777**	**2146**	**3209**	**498**	**2018**	**2910**	**823**	**1554**	**3079**
	on	372	**1874**	**2509**	**582**	**1616**	**2359**	**347**	**1534**	**2191**	**618**	**1185**	**2264**
JW08	off	328	2100	**2619**	652	1686	2422	338	1487	2222	641	1333	2318
	on	337	2042	**2446**	635	1724	2399	355	1410	2186	664	1271	2378
JW11	off	342	2076	2774	581	1654	2460	373	**1590**	2293	624	**1205**	1945
	on	362	2092	2674	610	1687	2313	356	**1395**	2318	652	**1048**	1964
JW12	off	314	1975	2776	606	1676	2497	339	1451	2244	638	1397	2308
	on	327	2061	2764	620	1686	2500	361	1361	2156	640	1307	2294
JW18	off	307	**2274**	2658	608	1694	2501	369	1455	2381	623	1149	2536
	on	347	**2079**	2462	603	1696	2467	382	1414	2328	654	1176	2625
JW19	off	303	2169	2645	587	1840	2636	343	1497	2319	639	1192	2275
	on	291	2193	2736	590	1829	2567	342	1618	2314	609	1200	2133
JW41	off	**342**	**1840**	2492	517	1598	**2420**	327	1296	2031	607	**1139**	2303
	on	**435**	**1660**	2359	444	1565	**2027**	279	1391	2067	600	**935**	2172
JW32	off	380	1996	2615	523	1662	2167	337	1306	2153	656	1205	2279
	on	385	2015	2714	562	1705	2289	331	1335	2113	673	1179	2279
JW40	off	336	1888	2483	569	1563	2375	347	1560	2241	594	1195	2238
	on	342	1891	2495	541	1557	2330	352	1595	2292	551	1313	2261
JW28	off	301	2056	2860	577	1614	2401	317	1220	2124	626	1084	2151
	on	320	2068	2851	610	1631	2404	320	1146	2129	610	1047	2170
JW43	off	335	2027	2585	617	1628	**2215**	346	1360	2135	644	1204	2368
	on	343	1921	2468	638	1602	**2460**	362	1338	2164	667	1185	2448

Mean formant values for the four vowels in 'pellets-off' and 'pellets-on' conditions, female speakers.

		/i/			/ae/			/u/			/a/		
		*F*1	*F*2	*F*3	*F*1	*F*2	*F*3	*F*1	*F*2	*F*3	*F*1	*F*2	*F*3
JW14	off	322	2525	3030	622	2061	2676	371	1589	2706	746	1241	**2583**
	on	343	2564	3041	655	1965	2539	381	1471	2722	730	1296	**2296**
JW16	off	436	2502	3130	696	2193	3033	414	**1737**	2516	**792**	**1622**	2611
	on	459	2410	3020	740	2141	2887	405	**1910**	2649	**676**	**1356**	2499
JW36	off	465	2580	**3382**	**699**	2286	3000	451	2132	2808	**745**	1632	2586
	on	490	2564	**2990**	**774**	2205	2891	470	2070	2710	**875**	1586	2432
JW37	off	396	2777	3272	777	2034	3042	434	2333	2851	817	1588	2692
	on	404	2669	3076	790	2048	3036	430	2294	2819	803	1531	2626
JW48	off	442	2647	3113	740	2130	**2996**	445	1430	2830	701	**2036**	2584
	on	450	2521	3020	753	2082	**2765**	446	1377	2828	747	**1641**	2454
JW52	off	**360**	**2591**	2818	651	1966	**2866**	455	1501	2519	718	1188	2558
	on	**458**	**2310**	2680	670	1965	**2627**	452	1582	2572	701	1138	2661
JW29	off	387	2327	3103	742	1957	2747	433	1722	2674	788	1396	2548
	on	411	2324	2905	782	1990	2692	451	1599	2587	832	1342	2503
JW27	off	**349**	2403	3026	**716**	2085	2776	415	1961	2779	673	**1583**	2578
	on	**487**	2503	3042	**855**	2119	2794	431	2002	2611	704	**1405**	2599
JW31	off	360	2824	3210	629	**2299**	**3075**	490	**2052**	2942	903	1783	2593
	on	340	2805	3253	689	**1800**	**2620**	487	**1850**	2971	938	1692	2475
JW50	off	376	2383	2950	717	2017	2763	404	1693	2643	760	1415	2520
	on	408	2356	2845	714	2007	2670	406	1682	2524	712	1364	2381

APPENDIX C

Mean values for the first four moments (mean (1), standard deviation (2), skewness (3), and kurtosis (4)) for individual speakers and speaking condition (pellets-off versus pellets-on).

Male speakers Pellets-off	Moment	JW07	JW08	JW11	JW12	JW18	JW19	JW28	JW32	JW40	JW41	JW43
SHE	1	5.21	3.23	3.83	3.92	3.48	3.89	3.59	3.71	3.11	3.43	2.94
	2	1.91	1.06	1.27	1.48	1.14	0.98	1.31	1.26	0.64	1.00	0.85
	3	1.34	2.64	2.01	1.63	2.47	2.62	2.37	2.14	5.08	1.87	3.70
	4	1.11	7.93	4.19	2.00	7.03	10.92	5.99	4.67	40.80	4.51	17.90
SUIT	1	7.23	5.24	6.06	4.63	5.14	4.93	6.20	5.51	5.98	7.11	4.86
	2	1.76	1.39	1.64	1.62	1.50	1.11	1.35	1.73	1.53	1.29	0.88
	3	0.66	0.90	0.18	1.22	1.47	2.11	0.49	0.84	−0.15	−1.40	3.47
	4	−0.20	−0.41	−0.96	0.26	1.65	5.80	−0.27	−0.23	−0.14	2.29	20.05
GREASY	1	6.81	5.30	6.23	3.14	5.29	6.04	6.28	5.48	5.56	7.33	5.38
	2	1.59	1.15	1.83	1.44	1.51	1.48	1.27	1.71	1.52	1.27	1.27
	3	0.61	0.85	0.18	2.35	0.89	0.51	0.37	0.90	0.00	−0.58	1.57
	4	0.83	0.44	−1.08	6.06	0.84	0.20	−0.24	−0.02	−0.13	0.79	3.63
WASH	1	4.70	3.93	4.20	4.35	3.89	3.88	3.55	4.16	2.67	3.69	2.70
	2	2.68	1.74	1.96	1.40	2.28	1.40	1.91	2.14	0.74	1.68	0.91
	3	1.02	1.31	0.99	1.48	1.37	2.01	1.46	0.60	4.55	0.91	3.83
	4	−0.27	2.18	0.09	2.39	1.04	4.93	1.38	−0.44	29.81	0.54	18.70

Female speakers Pellets-off	Moment	JW14	JW16	JW27	JW29	JW31	JW36	JW37	JW48	JW50	JW52
SHE	1	4.07	4.18	4.45	4.16	4.79	4.80	4.33	5.19	3.92	3.66
	2	1.07	1.15	1.11	0.94	1.17	1.24	0.82	1.62	1.07	0.97
	3	2.04	1.56	2.20	2.16	1.16	1.84	1.89	1.06	1.52	1.33
	4	5.34	2.68	5.75	6.34	1.76	4.06	7.79	0.22	3.15	1.86
SUIT	1	7.23	5.70	7.67	7.87	7.44	8.52	6.36	6.96	7.42	4.51
	2	1.42	1.55	0.89	1.35	1.69	0.84	1.45	1.36	1.16	0.91
	3	−0.21	1.01	−0.99	−0.98	−0.07	−1.33	0.38	−0.23	0.01	1.73
	4	−0.28	0.86	4.71	1.09	0.09	6.47	0.30	1.26	1.10	3.68
GREASY	1	7.41	6.58	7.83	7.74	7.49	8.09	7.00	7.57	7.56	5.32
	2	1.15	1.19	0.86	1.22	1.59	0.88	1.68	1.43	1.16	1.10
	3	−1.06	0.13	−1.14	−1.08	−0.55	−1.87	0.11	−0.73	−0.30	0.68
	4	4.77	4.18	5.41	3.39	0.83	13.63	−0.39	1.13	1.46	0.90
WASH	1	3.07	3.73	4.09	3.52	3.94	4.11	3.14	3.94	4.15	3.46
	2	1.20	1.49	1.39	1.43	1.12	1.52	1.15	1.41	1.39	1.25
	3	2.01	1.72	2.22	1.99	2.67	2.33	1.96	2.30	1.10	1.69
	4	5.19	3.18	4.83	5.16	8.66	7.24	6.76	5.51	1.49	2.28

Abbs, J. H., and Gracco, V. L. (**1984**). ''Control of complex motor gestures: Orofacial muscle responses to load perturbation of the lip during speech,'' J. Neurophysiol. **51**, 705–723.

Abbs, J. H., Gracco, V. L., and Cole, K. J. (**1984**). ''Control of multimovement coordination: Sensorimotor mechanisms in speech motor programming,'' J. Motor Behavior **16**, 195–231.

Baum, S., and McFarland, D. (**1997**). ''The development of speech adaptation to an artificial palate,'' J. Acoust. Soc. Am. **102**, 2353–2359.

Butcher, A. (**1989**). ''Measuring coarticulation and variability in tongue contact patterns,'' Clin. Linguistics Phon. **3**, 39–47.

Crystal, T., and House, A. (**1988a**). ''Segmental durations in connected-speech signals: Current results,'' J. Acoust. Soc. Am. **83**, 1553–1573.

Crystal, T., and House, A. (**1988b**). ''The duration of American English vowels: An overview,'' J. Phonetics **16**, 263–284.

Crystal, T., and House, A. (**1988c**). ''The duration of American English stop consonants: An overview,'' J. Phonetics **16**, 285–294.

Engen, T. (**1971**). ''Psychophysics. II. Scaling Methods,'' in *Woodworth and Schlossberg's Experimental Psychology*, edited by J. W. Kling and L. Riggs (Holt, Rinehart, and Winston, New York), pp. 47–86.

Fant, G. (**1960**). *Acoustic Theory of Speech Production* (Mouton, The Hague).

Flege, J. E., Fletcher, S. G., and Homiedan, A. (**1988**). ''Compensating for a bite block in /s/ and /t/ production: Palatographic, acoustic, and perceptual data,'' J. Acoust. Soc. Am. **83**, 212–228.

Folkins, J. W., and Abbs, J. H. (**1985**). ''Lip and jaw motor control during speech: Responses to resistive loading of the jaw,'' J. Speech Hear. Res. **18**, 207–220.

Forrest, K., Weismer, G., Milenkovic, P., and Dougall, R. (**1988**). ''Statistical analysis of word-initial voiceless obstruents: Preliminary data,'' J. Acoust. Soc. Am. **84**, 115–123.

Gay, T. (**1974**). ''A cinefluorographic study of vowel production,'' J. Phonetics **2**, 255–266.

Gay, T., Lindblom, B., and Lubker, J. (**1981**). ''Production of bite-block vowels: Acoustic evidence by selective compensation,'' J. Acoust. Soc. Am. **69**, 802–810.

Gracco, V. L., and Abbs, J. H. (**1988**). ''Central patterning of speech movements,'' Exp. Brain Res. **65**, 156–166.

Hamlet, S. L. (**1985**). ''Speech adaptation: An aerodynamic study of adults with a childhood history of articulation defects,'' J. Prosthet. Dent. **53**, 553–557.

Hamlet, S. L., and Stone, M. (**1976**). ''Compensatory vowel characteristics resulting from the presence of different types of dental prostheses,'' J. Phonetics **4**, 199–218.

Hamlet, S. L., and Stone, M. (**1978**). ''Compensatory alveolar consonant production induced by wearing a dental prosthesis,'' J. Phonetics **6**, 227–248.

Hamlet, S. L., Cullison, B. L., and Stone, M. (**1979**). ''Physiological control of sibilant duration: Insights afforded by speech compensation to dental prosthesis,'' J. Acoust. Soc. Am. **65**, 1276.

Hillenbrand, J., Getty, L., Clark, M., and Wheeler, K. (**1995**). ''Acoustic

characteristics of American English vowels,'' J. Acoust. Soc. Am. **97**, 3099–3111.
Ichikawa, T., Komoda, J., Horiuchi, M., and Matsumoto, N. (**1995**). ''Influence of alterations in the oral environment on speech production,'' J. Oral Rehab. **22**, 295–299.
Kelso, J. A. S., Tuller, B., Vatikiotis-Bateson, E., and Fowler, C. A. (**1984**). ''Functionally specific articulatory cooperation following jaw perturbations during speech: Evidence for coordinative structures,'' J. Exp. Psychol. **10**, 812–832.
Kent, R. (**1972**). ''Some considerations in the cinefluorographic analysis of tongue movements during speech,'' Phonetica **26**, 16–32.
Kent, R., and Moll, K. (**1972**). ''Cinefluorographic analyses of selected lingual consonants,'' J. Speech Hear. Res. **15**, 453–473.
Kewley-Port, D., and Watson, C. S. (**1994**). ''Formant frequency discrimination for isolated English vowels,'' J. Acoust. Soc. Am. **95**, 485–496.
Lindblom, B. (**1962**). ''Accuracy and limitations of sona-graphic measurements,'' Proceedings of the 4th International Congress of Phonetic Sciences, Helsinki 1961 (Mouton, The Hague).
McFarland, D. H., and Baum, S. R. (**1995**). ''Incomplete compensation to articulatory perturbation,'' J. Acoust. Soc. Am. **97**, 1865–1873.
McFarland, D. H., Baum, S. R., and Chabot, C. (**1996**). ''Speech compensation to structural modifications of the oral cavity,'' J. Acoust. Soc. Am. **100**, 1093–1104.
Milenkovic, P. (**1994**). *Cspeech Version 4.0* (Computer Program), University of Wisconsin-Madison.
Monsen, R., and Engebretson, A. (**1983**). ''The accuracy of formant frequency measurements: A comparison of spectrographic analysis and linear prediction,'' J. Speech Hear. Res. **26**, 89–97.
Mulligan, M. (**1986**). ''Acoustical and perceptual characteristics of bite-block speech in eight adult males,'' Unpublished Masters Thesis. University of Wisconsin-Madison.
Munhall, K. G., Löfqvist, A., and Kelso, J. A. S. (**1994**). ''Lip-larynx coordination in speech: Effects of mechanical perturbation to the lower lip,'' J. Acoust. Soc. Am. **95**, 3605–3616.
Nearey, T. (**1978**). *Phonetic Feature Systems for Vowels* (Indiana University Linguistics Club, Bloomington, IN).
Perkell, J. S. (**1997**). ''Articulatory processes,'' in *The Handbook of Phonetic Sciences*, edited by W. J. Hardcastle and J. Laver (Cambridge University Press, Oxford), pp. 333–370.
Perkell, J. S., and Cohen, M. H. (**1989**). ''An indirect test of the quantal nature of speech in the production of the vowels /i/, /a/, and /u/,'' J. Phonetics **17**, 123–133.
Perkell, J. S., and Nelson, W. L. (**1985**). ''Variability in production of the vowels /i/ and /u/,'' J. Acoust. Soc. Am. **77**, 1889–1895.
Perkell, J. S., Matthies, M. L., Svirsky, M. A., and Jordan, M. I. (**1993**). ''Trading relations between tongue body raising and lip rounding in the production of the vowel /u/: A pilot motor equivalence study,'' J. Acoust. Soc. Am. **93**, 2948–2961.
Peterson, G., and Barney, H. (**1952**). ''Control methods used in a study of the vowels,'' J. Acoust. Soc. Am. **24**, 175–184.
Recasens, D., Farnetani, E., Fontdevila, J., and Pallares, M. (**1993**). ''An electropalatographic study of alveolar and palatal consonants in Catalan and Italian,'' Lang. Speech **36**, 213–234.
Reichenbach, H. (**1973**). *The Rise of Scientific Philosophy* (University of California Press, Berkeley, CA).
Savariaux, C., Perrier, P., and Orliaguet, J. P. (**1995**). ''Compensation strategies for the perturbation of the rounded vowel /u/ using a lip tube: A study of the control space in speech production,'' J. Acoust. Soc. Am. **98**, 2428–2442.
Shadle, C. H. (**1990**). ''Articulatory-acoustic relationships in fricative consonants,'' in *Speech Production and Speech Modeling*, edited by W. J. Hardcastle and A. Marchal (Kluwer Academic, Dordrecht), pp. 187–209.
Shaiman, S. (**1989**). ''Kinematic and electromyographic responses to perturbation of the jaw,'' J. Acoust. Soc. Am. **86**, 78–87.
Smith, B. (**1987**). ''Effects of bite block speech on intrinsic segment duration,'' Phonetica **44**, 65–75.
Tuller, B., and Kelso, J. (**1990**). ''An evaluation of an alternating magnetic field device for monitoring tongue movements,'' J. Acoust. Soc. Am. **88**, 674–679.
Umeda, N. (**1975**). ''Vowel duration in American English,'' J. Acoust. Soc. Am. **58**, 434–445.
Umeda, N. (**1977**). ''Consonant duration in American English,'' J. Acoust. Soc. Am. **61**, 846–858.
Westbury, J. (**1994**). *X-ray Microbeam Speech Production Database User's Handbook, Version 1* (University of Wisconsin-Madison).
Wood, S. (**1979**). ''A radiographic analysis of constriction locations for vowels,'' J. Phonetics **7**, 25–43.
Wright, S., and Kerswill, P. (**1989**). ''Electropalatography in the analysis of connected speech processes,'' Clin. Linguistics Phon. **3**, 49–57.

Measuring the threshold for speech reception by adaptive variation of the signal bandwidth. I. Normal-hearing listeners

Ingrid M. Noordhoek, Tammo Houtgast, and Joost M. Festen
Department of Otolaryngology, University Hospital VU, P.O. Box 7057, 1007 MB Amsterdam, The Netherlands

(Received 21 January 1998; accepted for publication 8 February 1999)

An adaptive test has been developed to determine the minimum bandwidth of speech that a listener needs to reach 50% intelligibility. Measuring this speech-reception *bandwidth* threshold (SR*B*T), in addition to the more common speech-reception threshold (SRT) in noise, may be useful in investigating the factors underlying impaired suprathreshold speech perception. Speech was bandpass filtered (center frequency: 1 kHz) and complementary bandstop filtered noise was added. To obtain reference values, the SR*B*T was measured in 12 normal-hearing listeners at four sound-pressure levels, in combination with three overall spectral tilts. Plotting SR*B*T as a function of sound-pressure level resulted in U-shaped curves. The most narrow SR*B*T (1.4 octave) was obtained at an A-weighted sound-pressure level of 55 dB. The required bandwidth increases with increasing level, probably due to upward spread of masking. At a lower level (40 dBA) listeners also need a broader band, because parts of the speech signal will be below threshold. The SII (Speech Intelligibility Index) model reasonably predicts the data, although it seems to underestimate upward spread of masking. © *1999 Acoustical Society of America.* [S0001-4966(99)02305-X]

PACS numbers: 43.71.Es [WS]

INTRODUCTION

Sensorineural hearing loss not only reduces the sensitivity for soft sounds, but often decreases the ability to understand speech presented well above the hearing threshold. The difficulties hearing-impaired listeners encounter in understanding suprathreshold speech become especially clear when speech is in some way distorted or masked. In everyday situations, ambient noise is the most frequent disturbing factor. Plomp and Mimpen (1979) developed an adaptive test for accurately measuring the speech-reception threshold (SRT) for sentences in noise. The SRT is defined as the signal-to-noise ratio required for 50% intelligibility, with the noise spectrum shaped according to the long-term speech spectrum. Hearing-impaired listeners often need higher signal-to-noise ratios than normal-hearing listeners to correctly understand 50% of the sentences. The increase of the signal-to-noise ratio required for speech understanding is denoted as hearing loss for speech in noise (Plomp, 1978).

Various efforts have been made to relate hearing loss for speech in noise to a deterioration of specific auditory functions, but they did not lead to a clear picture. Festen and Plomp (1983) investigated the relations between the pure-tone audiogram, frequency resolution, temporal resolution, and speech reception in noise for 22 sensorineural hearing-impaired listeners with moderate losses. All tests concerning frequency resolution and temporal resolution were performed at 1 kHz. Hearing loss for speech in noise was related to various measures of frequency resolution at 1 kHz (correlation coefficients from 0.49 to 0.63). No significant correlations were found between hearing loss for speech in noise and temporal resolution or the audiogram. Glasberg and Moore (1989) found a relation ($R=0.56$) between the SRT in noise and the audiogram for 15 subjects with moderate cochlear hearing loss, but correlations were higher with various measures of both frequency resolution and temporal resolution at 0.5, 1, and 2 kHz (correlation coefficients from 0.59 to 0.68). Van Rooij and Plomp (1990) found significant correlations between the SRT in noise and pure-tone thresholds for 72 elderly subjects. In contrast to the previous studies, frequency resolution and temporal resolution at 0.8 and 2.4 kHz could not account for an additional part of the variance. Smoorenburg (1992) showed that the pure-tone average at 2 and 4 kHz is an adequate predictor for the SRT in noise in 200 individuals with noise-induced hearing loss ($R=0.72$). This prediction could not be improved by taking into account two measures of frequency resolution: the critical ratio at 0.25 and 0.5 kHz for low-frequency noise (cutoff frequency of about 0.7 kHz) and the slope of its upward spread of masking.

In very general terms, one may identify two main factors underlying a listener's hearing loss for speech in noise: (1) a reduction of the effective frequency range (for instance in case of a high-frequency loss), and/or (2) a deterioration in suprathreshold sound processing. Only in the latter case, one would expect a correlation between SRT and specific auditory functions like frequency resolution and temporal resolution.

For understanding speech, a broad frequency region from about 125 to 8000 Hz is important. Therefore, correlations between the ability to understand wide-band speech and auditory functions at a specific frequency may be small or absent. In order to find clear correlations between speech understanding and auditory functions at a specific frequency, it is more relevant to consider only a limited frequency range of the speech, in which the full dynamic range of the speech is above the hearing threshold.

In the present study, an adaptive test was developed that may be helpful in investigating the factors that cause reduced

intelligibility of suprathreshold speech. This test determines the minimum speech bandwidth around 1 kHz required for 50% intelligibility (Speech-Reception *Bandwidth* Threshold or SR*B*T). To obtain reference SR*B*T values, the SR*B*T for normal-hearing listeners was determined.

If a hearing-impaired listener cannot reach 50% intelligibility with the same frequency region as a normal-hearing listener, then (1) this frequency region does not operate as well as for the normal-hearing listener, and (2) the hearing-impaired listener will have a wider-than-normal SR*B*T. Thus the cause for a wider-than-normal SR*B*T must be due to changes in the auditory system in the 1-kHz frequency region. Consequently, correlations between auditory functions at 1 kHz and the SR*B*T are more obvious than correlations between auditory functions at some frequency and the wide-band SRT in noise.

The SR*B*T test may be incorporated in a test battery in which, for a group of hearing-impaired listeners, several auditory functions are measured at 1 kHz. A strong correlation between a specific auditory function at 1 kHz (e.g., frequency resolution, temporal resolution, or intensity discrimination) and the SR*B*T would suggest that the deterioration of this auditory function underlies the impaired ability to understand suprathreshold speech.

The frequency region that is most important for understanding speech is centered at 2 kHz (Pavlovic, 1987). However, 1 kHz was chosen as a center frequency for the speech filter in the SR*B*T test, because this test is intended to be presented to hearing-impaired listeners with the full relevant dynamic range of the speech above their hearing threshold. The dynamic range of the speech that is relevant for intelligibility is best approximated as 30 dB (Steeneken and Houtgast, 1980). If the dynamic range (the difference between uncomfortable loudness level and hearing threshold) of a hearing-impaired listener is smaller than 30 dB in the frequency region involved in the SR*B*T test, presenting the full relevant dynamic range of the speech above hearing threshold is not possible. For many hearing-impaired listeners a small dynamic range is typically found in the high-frequency region. Therefore, a somewhat lower frequency, 1 kHz, was chosen as center frequency of the speech filter in the SR*B*T test. With this center frequency, the speech is still presented in a frequency region that contributes significantly to intelligibility. For instance, in a speech band of 1 octave, 26% of the relevant speech information is present when it is centered at 2 kHz, and 24% when it is centered at 1 kHz (Pavloic, 1987).

In the SR*B*T test, a similar adaptive procedure as with the SRT test was followed, except that now the bandwidth of the sentences was changed in the up–down procedure. Complementary bandstop-filtered noise was added to the speech to limit the frequency region contributing to intelligibility as much as possible.

The SR*B*T was measured for 12 normal-hearing listeners at four sound-pressure levels (SPLs). We also investigated the effect of imposing a spectral tilt of -6 or -12 dB/octave. This is of interest for comparing the performance of hearing-impaired listeners with a sloping audiogram to results of the normal-hearing listeners.

The SR*B*T can be expressed in SII (Speech Intelligibility Index) values. The effectiveness of the SII model in predicting the SR*B*T of normal-hearing listeners for the various conditions was examined. If the SII model is consistent with the results of the normal-hearing listeners, the model will yield fixed intelligibility indices at the threshold. In that case, the model can be used in future experiments as a framework to predict the baseline SR*B*T of individual hearing-impaired listeners, given the speech spectrum, the noise spectrum, and the audiogram. The rationale is that the deviation of the actual performance from the SII model predictions can be used to ''quantify'' the degree of deterioration in suprathreshold speech processing of hearing-impaired listeners.

In the SR*B*T experiments, narrow-band speech is presented to the listeners. To investigate whether the SII at 50% intelligibility for narrow-band speech is equal to the SII at 50% intelligibility for wide-band speech, the standard SRT in noise (Plomp and Mimpen, 1979) was also measured. Additionally, 50% intelligibility thresholds for two intermediate conditions were measured: the SRT for a $2\frac{1}{2}$-octave band of speech, and the SR*B*T at a signal-to-noise ratio of 0 dB.

I. SPEECH INTELLIGIBILITY INDEX

The Speech Intelligibility Index (SII) is a physical measure that is highly correlated with the intelligibility of speech under a variety of adverse listening conditions, such as noise masking, filtering, and reverberation (ANSI, 1997). It is a major revision of the Articulation Index (ANSI, 1969). The SII can be represented by the equation

$$\mathrm{SII}=\sum_{i=1}^{n} I_i A_i , \tag{1}$$

where n is the number of frequency bands used in the calculations. The band-importance function I_i reflects the importance of frequency band i to speech intelligibility. The band-audibility function A_i is equal to the effective proportion of the speech dynamic range within band i that contributes to intelligibility. Input variables of the SII model are the speech spectrum, the noise spectrum, and the hearing threshold.

The SII may be interpreted as a proportion of the total speech information available to the listener. When the SII is maximal (1.0), all speech information is available to the listener. The lowest value of the SII (0.0) signifies that no speech information is available.

In this study speech-reception thresholds as well as speech-reception *bandwidth* thresholds were measured. At these thresholds 50% of the sentences are intelligible for the listeners. Therefore, equal SIIs are expected at these thresholds.

II. METHOD

A. Materials and design

The speech material consisted of 16 lists of 13 everyday Dutch sentences (8 or 9 syllables). Eight lists were pronounced by a female speaker and eight lists by a male speaker (Plomp and Mimpen, 1979; Smoorenburg, 1992). For masking, a Gaussian noise was used, shaped according

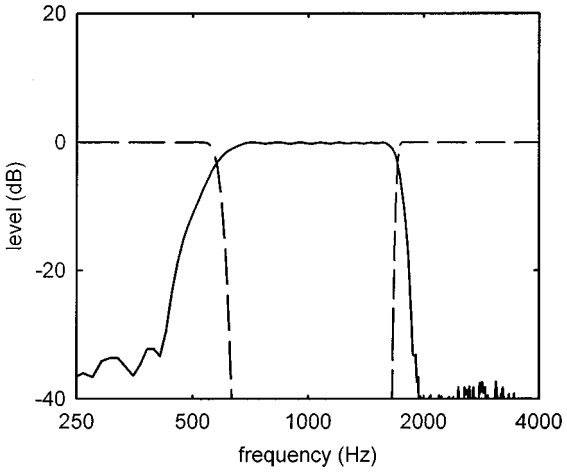

FIG. 1. Example of one combination of filters, used for filtering the speech (solid line) and noise (dashed lines) in the SR*B*T experiment.

to the long-term average spectrum of the sentences. The shape of the long-term average spectrum was determined separately for the two speakers. Both the speech and the noise were digitized at a sampling rate of 15 625 Hz with 16-bit resolution.

The experiment consisted of two parts. In the first part the SR*B*T was measured at various sound-pressure levels and imposed spectral tilts. In the second part the combined effect of noise and bandwidth reduction was investigated.

Twelve lists of sentences were used in the first part of the experiment and four lists in the second part. The lists were presented in a fixed order. To avoid order and list effects, the presentation order of the conditions was counterbalanced over the listeners according to a Latin square, 12×12 for the first part and 4×4 for the second part of the experiment. With 12 subjects, each sequence was presented to 1 subject in the first part and to 3 subjects in the second part of the experiment.

In the SR*B*T experiments, the bandwidth of the speech signal was varied. The speech was bandpass filtered with a fixed center frequency of 1 kHz. The bandpass filters were finite impulse response filters, designed by windowing, with 256 coefficients. This allowed on-line processing of the speech.

Bandstop noise was added to the speech (Fig. 1) to mask speech components below and above the cutoff frequencies of the bandpass filter, and to restrict spread of excitation of the speech. Although spread of excitation in the auditory system does not provide new information, the speech could spread to a frequency region in which the integrity of the auditory system is better than in the frequency region aimed at. The bandstop noise spectrum was complementary to the speech passband. The noise was filtered off line, using finite impulse response filters with 1024 coefficients. The level and spectrum of the flanking noise were equal to the long-term average of the speech. Therefore, the SPL of the total signal (speech plus noise) remained constant, independent of the speech bandwidth.

In the first part of the experiment the SR*B*T was measured in 12 conditions: 4 A-weighted SPLs (40, 55, 70, and 85 dB) each at 3 imposed spectral tilts (0, -6, and -12 dB/octave). The tilt was imposed on the total signal, i.e., the bandpass-filtered speech and the bandstop-filtered noise. The sound-pressure level was defined as the level of the signal before application of the spectral tilt. The spectral tilt of -6 dB/octave was obtained by low-pass filtering the signal with a cutoff frequency of 250 Hz. The filter of -12 dB/octave had a cutoff frequency of 500 Hz. After this low-pass filtering, the signal was amplified by 12 dB to obtain a fixed spectrum level at the 1-kHz center frequency of the speech band for the three spectral tilts.

In the second part of the experiment four measurements were performed at an A-weighted level of 70 dB: (1) the SR*B*T as in the first part of the experiment; (2) the SR*B*T in broadband speech-shaped noise, with a signal-to-noise ratio of 0 dB in the speech passband; (3) the SRT with a $2\frac{1}{2}$-octave band of speech (center frequency: 1 kHz) in broadband speech-shaped noise; and (4) the standard SRT in noise.

B. Listeners

Twelve normal-hearing listeners, ranging in age from 19 to 34 years, participated in the experiment. The pure-tone air-conduction thresholds in the tested ear did not exceed 15 dB HL at octave frequencies from 125 to 8000 Hz.

C. Test procedure

In the SRT experiment, the level of the sentences was changed according to an adaptive procedure (Plomp and Mimpen, 1979). The first sentence of a list was presented at a signal-to-noise ratio of -8 dB. This sentence was repeated, each time at a 4-dB higher level, until the listener could correctly reproduce the sentence. The subsequent 12 sentences were then presented only once, using an up–down procedure with a step size of 2 dB. The SRT was defined as the average signal-to-noise ratio of sentences 5 to 14. Sentence 14 was not actually presented, but its signal-to-noise ratio was known from the response to sentence 13. The A-weighted level of the masking noise was fixed at 70 dB.

In the SR*B*T test, a procedure comparable with the SRT test was followed, except that now the bandwidth of the speech signal was changed adaptively. In an adaptive up–down procedure, the step size is very important. If the step size is too large, the error variance of the threshold estimate will be large. If the step size is too small, many observations are wasted in converging on the threshold (Levitt, 1971). In the SRT experiment, the slope of the intelligibility score as a function of level is about 20%/dB over the middle range (Plomp and Mimpen, 1979). This corresponds to 40% in intelligibility score per step in the adaptive procedure. To find an equivalent step size for the SR*B*T procedure, a pilot experiment was performed with ten normal-hearing listeners in which speech intelligibility (percentage-correct score for sentences) was measured in ten conditions of bandwidth reduction. The ten bandwidths were equidistant on a logarithmic frequency axis. Near the 50% intelligibility score, a widening of the speech band (in Hz) by a factor 1.37 appeared to give about the same increase in intelligibility as a 2-dB increment of the signal-to-noise ratio in the SRT procedure.

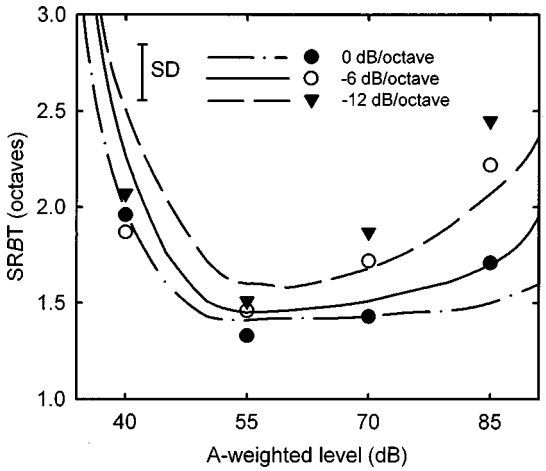

FIG. 2. Mean speech-reception *bandwidth* threshold for 12 normal-hearing listeners (symbols) and predictions by the SII model (curves) as a function of A-weighted sound-pressure level, with spectral tilt as a parameter. The vertical bar represents the inter-individual standard deviation. Prediction from the SII model deviate substantially from the data at 85 dBA.

Hence, we chose a step size in the SR*B*T procedure corresponding to multiplication or division of the bandwidth (in Hz) by a factor 1.37.

In the SR*B*T procedure, the first sentence in a list was presented initially at a 600-Hz bandwidth. This sentence was repeated each time with the bandwidth multiplied by $(1.37)^2$ (a double step), until the listener could correctly reproduce the sentence. The other sentences in a list were presented only once. If a sentence was repeated correctly, the bandwidth for the next sentence was divided by 1.37. If a sentence was not repeated correctly, the bandwidth for the next sentence was multiplied by 1.37. The SR*B*T was defined as the geometric mean of the bandwidth of sentences 5 to 14.

The stimuli were presented monaurally through headphones (Sony MDR-CD999) in a soundproof room. Before the experiment, a list of 13 sentences was presented, to familiarize the listeners with the procedure. During this familiarization, an SR*B*T test was performed at an A-weighted SPL of 70 dB and a spectral tilt of -6 dB/octave.

D. SII calculations

The SII was calculated following the 1/3-octave band procedure of ANSI (1997). For free-field listening, the SII calculation procedure is based on the SPLs of speech and noise measured in absence of the listener at the position of the listener's head. For other listening situations, the SPLs need to be transformed to equivalent SPLs that would have been measured at the listener's position in a free field, while producing the same SPL at the eardrum of the listener as under the actual circumstances.

In this study, the SPLs of the speech and noise were measured in 1/3-octave bands with the headphone (Sony MDR-CD999) on a Brüel & Kjær type 4152 artificial ear with a flat-plate coupler. These SPLs need to be transformed to equivalent free-field levels. The appropriate ''artificial-ear-to-free-field transfer function'' was calculated, considering that at threshold the SPL at the eardrum will be the same for both free-field and headphone measurements.

For this purpose, absolute thresholds were measured with ten normal-hearing listeners at octave frequencies from 250 to 4000 Hz through headphones. In designing the appropriate transform, a revised free-field hearing threshold was used, because research by Killion (1978) and Berger (1981) suggests that ISO R226 (1961) is in error at low frequencies. The ''artificial-ear-to-free-field transfer function'' was calculated as the difference between the free-field hearing threshold (corrected by a ''monaural disadvantage'' of 2 dB) and the average threshold for the normal-hearing subjects listening through headphones. The free-field hearing threshold used in this calculation is identical to ISO (1961) at 500 Hz and above, whereas from 400 Hz downwards to 100 Hz the SPLs are between 1 and 8 dB higher.

With the ''artificial-ear-to-free-field transfer function'' SPLs of speech and noise, measured on the artificial ear, were transformed to equivalent free-field levels. These free-field SPLs were next converted to spectrum levels, contained within a band 1 Hz wide, as required by the SII procedure.

III. RESULTS

The mean SR*B*T (in octaves) for four sound-pressure levels and three spectral tilts is presented by the symbols in Fig. 2. The lines in this figure represent SII predictions, and will be discussed in Sec. IV B. Because the inter-individual standard deviation did not significantly differ over the 12 conditions, the mean standard deviation (0.29 octave) is given only once, in the upper-left corner. The most narrow SR*B*T (1.33 octave) is obtained at 55 dBA for the spectral tilt of 0 dB/octave. Between 55 and 85 dBA, the SR*B*T increases with increasing SPL and steepening spectral tilt. The widest SR*B*T (2.45 octave) is found at 85 dBA and a tilt of -12 dB/octave. At 40 dBA the SR*B*T is on average about 0.5 octave wider than at 55 dBA.

To evaluate the effects of level and tilt, a two-factor analysis of variance for a Latin Square design with repeated measures on both factors was performed (Neter *et al.*, 1990). The effect of level was significant $[F(3,110)=52,\ p<0.001]$ as was the effect of tilt $[F(2,110)=24,\ p<0.001]$ and the interaction $[F(6,110)=3.8,\ p<0.01]$. Pairwise comparisons of the mean scores with the Tukey HSD test (Hays, 1988) showed that listeners need a significant wider SR*B*T than the most narrow SR*B*T (at the tilt of 0 dB/octave and 55 dBA) in eight conditions ($p<0.05$): all spectral tilts at 40 and 85 dBA, and the tilts of -6 and -12 dB/octave at 70 dBA.

In each SR*B*T measurement, 13 sentences were presented at various bandwidths around the SR*B*T. The response on each sentence (correct or incorrect) is known. From these data, the proportion of correctly repeated sentences as a function of bandwidth can be calculated. The first sentence of each list is excluded from the calculation, because this sentence was presented more than once to each listener. To calculate one psychometric function from all 1728 responses (12 sentences$\times$12 listeners$\times$12 conditions), the bandwidth of each presented sentence is converted to a relative bandwidth (RB) by scaling the actual bandwidth relative to the corresponding SR*B*T for that condition and listener:

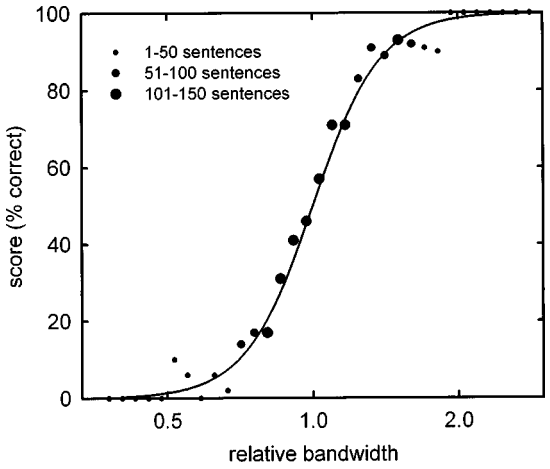

FIG. 3. Mean percentage-correct score for sentences as a function of the bandwidth relative to the SR*B*T, based on 1728 responses (12 sentences×12 listeners×12 conditions).

$$RB = \frac{\text{bandwidth (in Hz)}}{\text{SR}B\text{T (in Hz)}}. \tag{2}$$

Next, the percentage-correct score as a function of this relative bandwidth is calculated (Fig. 3). A logistic function is fitted to the data using the maximum-likelihood method. The obtained function can be written as

$$\text{score} = \frac{100}{RB^{-6.17}+1}. \tag{3}$$

By definition, a relative bandwidth of 1 corresponds to 50% intelligibility. At a relative bandwidth of 0.7, only 10% of the sentences are reproduced correctly by the listeners. At a relative bandwidth of 1.4, the number of correctly repeated sentences reaches almost 90%.

Over the middle range, the slope of the psychometric function is about 40% in intelligibility score per 2-dB step in the SRT procedure. In the steepest section of Fig. 3, the chosen step size (multiplication of the bandwidth by 1.37) appears to result in a slightly steeper slope of about 50% in intelligibility score per step.

The means and standard deviations of the two SR*B*T and two SRT values, which were measured in the second part of the experiment are presented in Table I. These conditions represent combinations of noise addition and bandwidth reduction that all lead to a 50% intelligibility. As expected, as the signal-to-noise ratio decreases listeners need a broader band of speech to understand 50% of the sentences.

The SR*B*T at the level of 70 dBA was measured in both parts of the experiment, with the same listeners. The average SR*B*T was 1.43 octave in the first part of the experiment and 1.41 octave in the second part. A *t* test for matched samples revealed no significant learning effect ($p<0.05$). Therefore, the standard deviation of individual SR*B*T values could be calculated. This standard deviation, which represents a reliability measure of the test, is 0.15 octave.

TABLE I. Four combinations of noise addition and bandwidth reduction leading to 50% intelligibility, and the corresponding modified speech intelligibility indices. Standard deviations are given between parentheses.

Condition	SRT (dB S/N ratio)	SR*B*T (octaves)	SII
no noise		1.41 (0.15)	0.319 (0.052)
$2\frac{1}{2}$-octave band	4.2 (2.2)		0.366 (0.054)
0 dB S/N ratio		3.39 (0.50)	0.341 (0.037)
no band-limiting	−3.8 (1.1)		0.324 (0.036)

IV. DISCUSSION

A. Effect of level and tilt on the SR*B*T

The SR*B*T appears to vary considerably as a function of presentation level and spectral tilt and is, in this respect, far less robust than the SRT in noise. Qualitatively, this may be understood as a result of the spectral configuration of the stimulus in the SR*B*T experiment, i.e., a central spectral region of (physically) unmasked speech flanked by two noise bands. This configuration is vulnerable for the effect of upward spread of masking, which is expected to increase with level and negative spectral tilt. The increased SR*B*T for the 40-dBA condition probably reflects that the lower part of the relevant dynamic range of speech in the unmasked central stimulus region already falls below the hearing threshold. The stimulus configuration in the SRT test, with a low speech-to-noise ratio over the whole spectral range, is much less sensitive to these effects.

Usually, for the SRT in noise a threshold is obtained which is independent of sound-pressure level, but Smoorenburg (1992) reported that the SRT as a function of noise level increases 1.4 dB between 50 and 80 dBA for normal-hearing listeners. Probably, this was also caused by upward spread of masking. Van Dijkhuizen *et al.* (1987) investigated the effect of various spectral tilts on the SRT in noise, at an SPL of 80 dB. They concluded that spectral tilts from about −7 up to +10 dB/octave do not affect the SRT in noise. At the spectral tilt of −12 dB/octave the SRT was about 6 dB higher than without tilt. This was partially explained by upward spread of masking.

B. Predictions by the SII model

For a more quantitative approach to interpret the present data, the SII calculation model was applied, which includes the effects of upward spread of masking and speech audibility. The SII was calculated for the 12 SR*B*T values measured in the first part of the experiment. At these speech-reception *bandwidth* thresholds, 50% of the sentences are intelligible for the listeners. Consequently, equal speech intelligibility indices are expected at these thresholds.

The curves in Fig. 2 connect SR*B*T values with an SII of 0.33. This value corresponds to the SII for the average SR*B*T in the 70-dBA condition without spectral tilt. This SII was used as a reference for the 11 other SR*B*T values, because in the 70-dBA condition without spectral tilt all speech is well above hearing threshold and the SR*B*T is not wider due to upward spread of masking. Thus the SII in the 70-dBA condition without spectral tilt is essentially insensitive for small errors in the input variables of the SII model (spectrum levels of speech and noise, and hearing threshold).

The observed increase in SR*B*T at 40 dBA is consistent with the predictions by the SII model. The predicted SR*B*T

increases as the presentation level decreases below 55 dBA, because part of the 30-dB dynamic range of the speech falls below hearing threshold. For levels between 55 and 85 dB, both observed and SII predicted SR*B*T increase with increasing SPL and steepening spectral tilt. The increase in the predicted SR*B*T is due to the estimated effect of upward spread of masking. At 85 dBA, the model also predicts some level distortion (i.e., the decrease of intelligibility because of a high presentation level). However, the amount of distortion is so small that the influence on the predicted SR*B*T is negligible.

The observed SR*B*T increases faster than the predicted one between 55 and 85 dBA. This suggests that the SII model underestimates the effect of upward spread of masking of the low-frequency noise band. The exact way in which the upward spread of masking is accounted for by the model greatly influences the calculated SII for the present conditions. This holds especially for those conditions with the high SPLs and the negative spectral tilt. The SPL of the low-frequency noise was higher than the SPL of the speech in the frequency region around 1 kHz, especially in the conditions with a spectral tilt of -6 or -12 dB/octave (but also without spectral tilt), because the noise was obtained by bandstop filtering the speech-shaped noise. Furthermore, no external noise is present in the frequency region around 1 kHz, so when the upward spread of masking reaches the lower limit of the dynamic range of the speech, it already starts to affect speech intelligibility.

A possible explanation for the discrepancy between our data and the predictions by the SII model is that the slope of the masking curve in the SII model may be too steep for low-frequency maskers. In the SII model, the slope of the upward spread of masking in dB/octave (C_i) due to frequency band i is calculated as

$$C_i = -80 + 0.6 \cdot BL_i, \tag{4}$$

where BL_i is the SPL of frequency band i. This procedure is based on the 1/3-octave spread of masking protocol discussed in Ludvigsen (1985), who deduced this relation from the masking curves of Zwicker (1963) with masker frequencies of 650, 1000, and 2000 Hz. In the SII model, the slope of the masking curve does not depend on masker frequency. However, below 500 Hz the relative bandwidth of the auditory filter increases with decreasing center frequency (Moore, 1986). Thus for frequencies below 500 Hz, the slope of the masking curve may be expected to decrease with decreasing center frequency. This effect is not accounted for by the SII model.

C. Modified SII model

The present SII model cannot accurately predict the SR*B*T of the normal-hearing listeners in the various conditions of this experiment, making it unfit to predict the SR*B*T in future experiments with hearing-impaired listeners. We tried to modify the SII model in order to find a better correspondence with the SR*B*T measurements.

In the AI model (ANSI, 1969) the calculation of the upward spread of masking is frequency dependent. Therefore, the masking spectrum was recalculated using the spread-of-masking algorithm from the old ANSI S3.5 standard. However, this did not lead to better predictions. At 70 dBA, the observed increase in SR*B*T when the spectral tilt becomes more negative is not predicted by the SII model with the old ANSI S3.5 spread-of-masking algorithm, while this increase is predicted by the unmodified SII model. For the negative spectral tilts at 85 dBA, the SII model with the old ANSI S3.5 spread-of-masking algorithm predicts SR*B*T values that are about the same amount too high as the predictions by the unmodified SII model are too low.

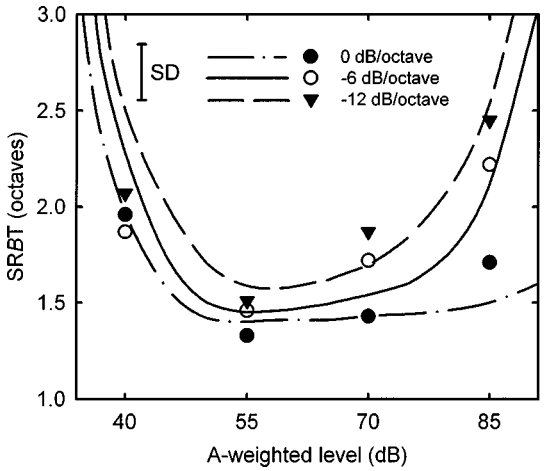

FIG. 4. Mean speech-reception *bandwidth* threshold for 12 normal-hearing listeners (symbols) and predictions by a modified SII model (curves) as a function of A-weighted sound-pressure level, with spectral tilt as a parameter. The vertical bar represents the inter-individual standard deviation. For all presentation levels the SII predictions are in good agreement with the data.

In a second attempt to obtain a better correspondence between the 12 SR*B*T measurements in the first part of the experiments and the SII model, shallower slopes of the masking curves were used for frequencies below 500 Hz. The slope of the masking curve (in dB/octave) was chosen to decrease linearly with center frequency below 500 Hz. Thus for 1/3-octave bands with masker frequencies greater or equal to 500 Hz (i.e., $i \geqslant 6$), the slope of the masking curve was calculated according to Eq. (4); and for 1/3-octave bands with center frequencies below 500 Hz (i.e., $i < 6$) according to

$$C_i = [1 - (6 - i) \cdot \alpha] \cdot [-80 + 0.6 \cdot BL_i]. \tag{5}$$

The parameter α was varied on a *post hoc* basis. The differences between the 12 SIIs were minimized for $\alpha = 0.08$.

Only rarely has the masking pattern of narrow noise bands below 500 Hz been measured. Maiwald (1967) measured the masking pattern of a narrow-band noise with a center frequency of 250 Hz and an SPL of 60 dB. The slope of the masking curve was about -30 dB/octave. Combination of Eq. (5) with $i = 3$ and $\alpha = 0.08$ results in a slope of -33 dB/octave, so the value of 0.08 seems reasonable.

With the inclusion of Eq. (5) in the SII model, the differences among the 12 SIIs were decreased. Figure 4 again shows the SR*B*T measurements (symbols), but now with the predictions by the modified SII model (lines). The equal SII contours (SII of 0.33) in Fig. 4 correspond better to the SR*B*T measurements than the curves in Fig. 2. The 40-dBA

conditions with a spectral tilt of −6 or −12 dB/octave provided the only significant differences between measured and calculated SR*B*T (*t* test, $p<0.05$). The cause may be a small deviation of the SPL or hearing threshold in the calculations from its actual value. The calculated SR*B*T increased very fast with decreasing SPL in the region around 40 dBA. Consequently, a small deviation of the SPL or hearing threshold results in a large change in SR*B*T.

The four conditions in Table I are combinations of noise addition and bandwidth reduction that all lead to a 50% intelligibility. Therefore, equal speech intelligibility indices are expected for these for conditions. The exact way in which the upward spread of masking is calculated in the SII model had a negligible effect on the SII for these four conditions. The average and standard deviation of the individual modified SII is given in the last column of Table I. An analysis of variance for a Latin Square design with repeated measures showed a significant effect of condition on the speech intelligibility index [$F(3,30)=4.55$, $p<0.05$]. Pairwise comparisons of the mean scores with the Tukey HSD test (Hays, 1988) showed that the SII in the $2\frac{1}{2}$-octave-band condition was significantly higher ($p<0.05$) than in the no-noise and no-bandlimiting conditions. So far, we have no explanation for this finding.

D. Reference SR*B*T values

The SR*B*T test is meant as a tool for studying impairment of suprathreshold speech processing in hearing-impaired listeners. The aim of this experiment was to obtain reference SR*B*T values as a framework for interpreting future results with hearing-impaired listeners. It appeared that for normal-hearing listeners, four conditions in our experiment were optimal for the SR*B*T measurement (i.e., no influence of upward spread of masking or the hearing threshold): the three spectral tilts at the SPL of 55 dBA, and no spectral tilt at the SPL of 70 dBA. In these conditions, the SR*B*T is about 1.4 octave (i.e., a frequency band from 600 Hz to 1600 Hz).

Various frequency bands contribute different amounts to intelligibility. Therefore, the bandwidth required to understand 50% of the speech is frequency dependent. As mentioned in the Introduction, the frequency region that is most important for understanding speech is centered at 2 kHz. Thus if 2 kHz had been chosen as center frequency, probably a smaller SR*B*T would have been measured. According to the SII model, the importance of the frequency region from 600 to 1600 Hz, relative to the total frequency region relevant for speech intelligibility, is 33%. A frequency band centered at 2 kHz, with the same relative importance has a width of 1.2 octave (1.3 kHz–3.0 kHz). Therefore, if the experiment had been carried out with a center frequency of 2 kHz, instead of 1 kHz, presumably an SR*B*T of about 1.2 octave, instead of 1.4 octave, would have been measured.

If the SR*B*T is measured in a condition in which there is essentially no influence of upward spread of masking or the hearing threshold, and 1 kHz is chosen as center frequency, the appropriate reference value is 1.4 octave. Reference values for the other conditions reflect the effects of upward spread of masking and/or of proportions of the speech signal falling below the hearing threshold. For these conditions, results for normal-hearing listeners are consistent with the modified SII model.

V. CONCLUSIONS

An adaptive test has been developed for measuring the minimum bandwidth of speech, with a center frequency of 1 kHz, required for 50% intelligibility (speech-reception *bandwidth* threshold or SR*B*T). The performance of normal-hearing listeners on the SR*B*T test was measured. Normal-hearing listeners need a speech band of about 1.4 octave (i.e., 600–1600 Hz) to understand everyday sentences at an A-weighted SPL of 55 dB. The required minimum bandwidth increases with increasing level, due to upward spread of masking. At lower SPLs, the listeners also need a broader bandwidth to understand the sentences, because parts of the speech will fall below the hearing threshold.

The SII model appears to underestimate the amount of upward spread of masking produced by the low-frequency noise in the SR*B*T measurements. Using shallower slopes of the masking curves for frequencies below 500 Hz, a better correspondence between the measurements and the SII model was obtained.

ACKNOWLEDGMENT

This research was supported by the Foundation ''Heinsius-Houbolt Fonds,'' The Netherlands.

ANSI (**1969**). ANSI S3.5-1969, ''American national standard methods for the calculation of the articulation index'' (American National Standards Institute, New York).

ANSI (**1997**). ANSI S3.5-1997, ''American national standard methods for calculation of the speech intelligibility index'' (American National Standards Institute, New York).

Berger, E. H. (**1981**). ''Re-examination of the low-frequency (50–1000 Hz) normal threshold of hearing in free and diffuse sound fields,'' J. Acoust. Soc. Am. **70**, 1635–1645.

Festen, J. M., and Plomp, R. (**1983**). ''Relations between auditory functions in impaired hearing,'' J. Acoust. Soc. Am. **73**, 652–662.

Glasberg, B. R., and Moore, B. C. (**1989**). ''Psychoacoustic abilities of subjects with unilateral and bilateral cochlear hearing impairments and their relationship to the ability to understand speech,'' Scand. Audiol. Suppl. **32**, 1–25.

Hays, W. L. (**1988**). *Statistics*, 4th ed. (Holt, Rinehart, and Winston, New York).

International Organization for Standardization (**1961**). ISO R226-1961, ''Normal equal-loudness contours for pure tones and normal threshold of hearing under free field listening conditions'' (available from American National Standards Institute, New York).

Killion, M. C. (**1978**). ''Revised estimate of minimum audible pressure: Where is the ''missing 6 dB''?,'' J. Acoust. Soc. Am. **63**, 1501–1508.

Levitt, H. (**1971**). ''Transformed up–down methods in psychoacoustics,'' J. Acoust. Soc. Am. **49**, 467–477.

Ludvigsen, C. (**1985**). ''Relations among some psychoacoustic parameters in normal and cochlearly impaired listeners,'' J. Acoust. Soc. Am. **78**, 1271–1280.

Maiwald, D. (**1967**). ''Beziehungen zwischen Schallspektrum, Mithörschwelle und der Erregung des Gehörs,'' Acustica **18**, 69–80.

Moore, B. C. J. (**1986**). *Frequency Selectivity in Hearing* (Academic, London).

Neter, J., Wasserman W., and Kutner M. H. (**1990**). *Applied Linear Statistical Models*, 3rd ed. (IRWIN, Homewood, IL; Boston, MA).

Pavlovic, C. V. (**1987**). ''Derivation of primary parameters and procedures for use in speech intelligibility predictions,'' J. Acoust. Soc. Am. **82**, 413–422.

Plomp, R. (**1978**). ''Auditory handicap of hearing impairment and the limited benefit of hearing aids,'' J. Acoust. Soc. Am. **63**, 533–549.
Plomp, R., and Mimpen, A. M. (**1979**). ''Improving the reliability of testing the Speech Reception Threshold for sentences,'' Audiology **18**, 43–52.
Smoorenburg, G. F. (**1992**). ''Speech reception in quiet and in noisy conditions by individuals with noise-induced hearing loss in relation to their tone audiogram,'' J. Acoust. Soc. Am. **91**, 421–437.
Steeneken, H. J. M., and Houtgast, T. (**1980**). ''A physical method for measuring speech-transmission quality,'' J. Acoust. Soc. Am. **67**, 318–326.
Van Dijkhuizen, J. N., Anema, P. C., and Plomp, R. (**1987**). ''The effect of varying the slope of the amplitude-frequency response on the masked speech-reception threshold of sentences,'' J. Acoust. Soc. Am. **81**, 465–469.
Van Rooij, J. C. G. M., and Plomp, R. (**1990**). ''Auditive and cognitive factors in speech perception by elderly listeners. II: Multivariate analyses,'' J. Acoust. Soc. Am. **88**, 2611–2624.
Zwicker, E. (**1963**). ''Über die Lautheit von ungedrosselten und gedrosselten Schallen,'' Acustica **13**, 194–211.

Compression and expansion of the temporal envelope: Evaluation of speech intelligibility and sound quality

Ronald A. van Buuren,[a] Joost M. Festen, and Tammo Houtgast
University Hospital VU, P.O. Box 7057, 1007 MB Amsterdam, The Netherlands

(Received 30 April 1996; accepted for publication 8 February 1999)

Sensorineural hearing loss is accompanied by loudness recruitment, a steeper-than-normal rise of perceived loudness with presentation level. To compensate for this abnormality, amplitude compression is often applied (e.g., in a hearing aid). Alternatively, since speech intelligibility has been modeled as the perception of fast energy fluctuations, enlarging these (by means of *expansion*) may improve speech intelligibility. Still, even if these signal-processing techniques prove useful in terms of speech intelligibility, practical application might be hindered by unacceptably low sound quality. Therefore, both speech intelligibility and sound quality were evaluated for syllabic compression and expansion of the temporal envelope. Speech intelligibility was evaluated with an adaptive procedure, based on short everyday sentences either in noise or with a competing speaker. Sound quality was measured by means of a rating-scale procedure, for both speech and music. In a systematic setup, both the ratio of compression or expansion and the number of independent processing bands were varied. Individual hearing thresholds were compensated for by a listener-specific filter and amplification. Both listeners with normal hearing and listeners with sensorineural hearing impairment participated as paid volunteers. The results show that, on average, both compression and expansion fail to show better speech intelligibility or sound quality than linear amplification. [S0001-4966(99)02605-3]

PACS numbers: 43.71.Ky [WS]

INTRODUCTION

In many of today's hearing aids, some type of nonlinear amplification is employed. In practically all cases, amplification is linear up to a certain input level (the *knee point*), above which the input is amplified by a level-dependent amount. An extreme case of nonlinear amplification is clipping, where the knee point equals the maximum output level. But in many other applications of nonlinear amplification, the aim is to compensate for the narrower dynamic range of listeners with sensorineural hearing impairment.

According to Caraway and Carhart (1967), nonlinear amplification has been applied in hearing aids since about 1936, but these applications were essentially output limiters. At the time they wrote their paper, there were no commercially available hearing aids ''with compression functioning over all or at least a substantial part of the operating range'' (p. 1426). They tested speech intelligibility after processing their material with a three-band compressor circuit, in which compression ratios of 2 and 3 were applied to the input signals. The tests were all performed at low sensation levels (up to 24 dB SL) without any masking signals. They found small advantages for nonlinear processing in their group with normal hearing (on the order of 15% spondee identification) but smaller (and hardly significant) advantages for their three groups with hearing impairments. This led them to the conclusion that ''the aberrations in the loudness function brought about by recruitment do not make the auditor more capable of abstracting information from compressed speech than from uncompressed speech'' (p. 1432).

Villchur (1973), however, reported significant improvements in speech intelligibility for six listeners with sensorineural hearing losses, using a system which applied compression in two independent frequency bands with (individually adapted) compression ratios between 2 and 3. Besides improved intelligibility for CVCs, he found that his six listeners preferred the compressed speech to the unprocessed condition. The problem, however, in interpreting Villchur's results is that he only considered the *combination* of compression and frequency shaping, and compared it to linear amplification *without* frequency shaping. Villchur supports this choice by noting that the listeners would simply not have tolerated frequency shaping without compression, since it will amplify high-frequency noises into the discomfort region.

The results of the authors mentioned above can be seen as representative of many others, in that the evaluation of speech intelligibility for compression processing has produced varying results over time. Lippman *et al.* (1981) found compression to generally result in slightly reduced speech intelligibility when compared to linear amplification; compression was superior only when the speech material contained significant level variations or when the input level was low. Náběl ek (1983) tested a wide variety of compression ratios and attack/release times, in combination with reverberation, noise masking, and peak clipping. Overall, he concluded that compression is advantageous to speech intelligibility only for certain compression settings (values of ratio, attack/release times) and at larger S/N ratios. Walker *et al.* (1984) compared linear amplification to a combination of compression and expansion (compression above the knee point, and expansion below it), in a system with six indepen-

[a]Present address: Blesgraaf bureau voor bouwen & milieu bv, Treubstraat 15c, NL-2288 EG Rijswijk, The Netherlands.

dent frequency bands. Their results are ''mainly negative'' (as they put it), since positive effects of their processing on nonsense syllable intelligibility were found only for some listeners in specific listening conditions. Bustamante and Braida (1987) tested various compression algorithms and linear amplification; at best, the compression conditions resulted in speech-intelligibility scores comparable to the condition with linear amplification, although compression processing maintained its score over a greater range of input levels. Levitt and Neuman (1991) also found that none of their principal-component compression algorithms performed better than linear amplification, except (obviously) for the lowest input level (55 dB SPL) in their experiments, where the fixed amount of linear amplification was insufficient. Maré *et al.* (1992) compared three different compression curves to linear amplification. Their results show that, for listeners with normal and with sensorineurally impaired hearing, effects of compression on speech intelligibility in noise are comparable. Advantages of the compression conditions over linear amplification were maximally 9% (considering initial and final consonants only) for the listeners with hearing impairment. Additionally, a sentence-intelligibility test (according to Plomp and Mimpen, 1979), which estimates the S/N ratio for 50% performance, was used. It showed that the most advantageous compression condition results in an average S/N ratio of only 0.4 dB below the value for linear amplification, indicating that speech intelligibility is only marginally easier in the compression condition.

Verschuure *et al.* (1994) evaluated the effects of frequency shaping and compression on speech intelligibility by listeners with impaired hearing. Their one-band compression system provided a maximum gain of about 7% in CVC intelligibility, compared to linear processing, but only for some compression factors. Yund and Buckles (1995a,b) evaluated a compression system in which the compression ratio in each frequency band was fitted individually, based on each listener's threshold. In this way, their compression ratios ranged from 1 to 7; attack and release times were short (on the order of 4 ms). They carried out nonsense-syllable tests in quiet and at S/N ratios from -5 to 15 dB. In one study (Yund and Buckles, 1995a), where compression configurations were compared, they found maximum performance in noise for 8- and 16-band systems, although the increase in intelligibility with respect to a 4-band system (which gave the lowest correct scores at each S/N ratio) was always smaller than 10%. In the second study (Yund and Buckles, 1995b), where linear amplification (with and without frequency shaping) was compared to the 8-band compression system from their first study, they found increasing advantages from the compression system with decreasing S/N ratio; as in the first study, intelligibility gains with respect to the linear-amplification system were small (below 10%).

For listeners with normal hearing, syllabic amplitude compression is not expected to have any beneficial effect on speech intelligibility at all. This is in accordance with views that have led to the Modulation Transfer Function (MTF) concept, upon which the Speech Transmission Index (STI) is based. According to Houtgast and Steeneken (1985), temporal intensity modulations in relevant frequency bands are the actual carriers of speech information. Several well-known disturbances of speech communication (e.g., interfering noise, reverberation) can elegantly be described in terms of a reduction of the modulation depth in some or all of the frequency bands. For speech-intelligibility experiments in various signal-processing conditions (e.g., reverberation, peak clipping, automatic gain control), Steeneken and Houtgast (1980) found a good correlation between word scores and the STI, thus confirming the importance of intensity modulations for speech intelligibility. The STI will predict *reduced* intelligibility for listeners with normal hearing when syllabic amplitude compression is applied, since all level variations (including intensity modulations) are reduced. It is interesting to see whether the ''opposite'' operation, syllabic amplitude *expansion* (i.e., enlarging intensity modulations), will *enhance* speech intelligibility, because at least for listeners with normal hearing, the STI so predicts.

Apart from speech intelligibility, sound quality will also be affected by compression and expansion. Agreeable sound quality is very important for the successful implementation of any signal processing scheme in a hearing aid; poor sound quality is likely to prevent any hearing aid from being accepted by listeners with hearing impairment. As opposed to analyses of speech intelligibility, sound quality has not been evaluated very often for amplitude compression and expansion; we will mention three examples known to us. Byrne and Walker (1982) evaluated their system, in which compression and expansion were combined, for sound quality as well (for speech intelligibility see Walker *et al.*, 1984). Their three listeners gave paired-comparison judgments of intelligibility, pleasantness, and naturalness of linearly versus nonlinearly processed speech at three SPLs, in quiet and in noise. The vast majority of preferred conditions were those that had been processed linearly, although one of the three listeners, when judging pleasantness of speech in noise, preferred the nonlinear processing at all SPLs.

Neuman *et al.* (1994) asked 20 listeners with sensorineural hearing impairment to give paired-comparison judgments of sound quality for speech in three types of noise, processed by six compression algorithms (attack time: 5 ms; release time: 200 ms) varying only in compression ratio. The results showed a monotonically decreasing preference score for increasing compression ratios, with linear amplification being preferred about 70% of the trials, and the highest compression ratio (10) only about 25%. Differences between linear amplification and compression ratios of 1.5 and 2 were not statistically significant. In a more recent paper (Neuman *et al.*, 1998), rating-scale experiments were reported for several compression conditions. The results show that with compression ratios of 5 and 10, ratings of clarity, pleasantness, and overall impression are significantly lower than with either linear amplification or with compression ratios of 1.5 or 2. In other words, from the limited experimental results available for sound quality, one can deduce that nonlinear processing may not be preferred strongly to linear amplification.

For the experiments reported in this paper, we tested 26 listeners with sensorineural hearing loss, as well as 26 listen-

ers with normal hearing. We measured speech intelligibility and sound quality for several conditions with syllabic compression and expansion, for which the number of independent frequency bands and the compression (or expansion) ratio were varied systematically. Speech intelligibility was measured in steady-state noise and with a single competing speaker, using short everyday sentences. Sound quality was evaluated for speech in quiet and for four fragments of music, using a rating-scale procedure. Because the signal processing was carried out off-line, we were able to create a system *without* time delays. Therefore, the amplification was optimally matched to the actual input envelope level at each time sample, instead of slightly lagging behind (as in most practical implementations of compression).

I. GENERAL METHOD

A. Equipment and listeners

Twenty-six listeners with sensorineural hearing loss were selected from the files of the University Hospital's Audiology Center. The pure-tone hearing losses at the test ears, averaged for 0.5, 1, and 2 kHz, ranged from 10.0 to 60.0 dB HL (*re*: ISO, 1975). The losses in all these ears can be classified as *sloping* to various degrees. As an estimate for the overall slope of the audiogram (from 0.25 to 8.0 kHz), we computed straight-line approximations to the thresholds by means of linear regression analyses. Four ears showed essentially flat losses (slope between -5 and 5 dB/oct); in nine ears, slopes were moderate (between 5 and 10 dB/oct); in ten ears, slopes were steep (between 10 and 15 dB/oct); and in three ears, the slopes were extremely steep (above 15 dB/oct). In quiet, these listeners could reach at least 70% intelligibility for monosyllables and they were free of persistent tinnitus; age ranged from 25 to 75 years, with an average of 58 years. Twenty-six listeners with normal hearing participated in the experiments; in this group, age ranged from 17 to 28 years, with an average of 22 years. For these listeners, the threshold of hearing was maximally 15 dB HL at any test frequency between 0.125 and 8.0 kHz.

The experiments were carried out in a double-walled, sound-proof booth. All test signals were presented monaurally, without masking of the contralateral ear. If the two ears had equal thresholds (e.g., for all listeners with normal hearing), we presented the tests to the preferred ear; otherwise, the better ear was selected. Off-line signal processing was carried out on a Tucker-Davis AP2 (with an AT&T DSP32C). We used a PC-hosted Digital Signal Processor board (OROS ''AU21,'' featuring Texas Instruments' TMS 320C25) with a 16-bits single-channel D/A converter, to generate the experimental stimuli. The stimuli were presented to the listeners through Sony MDR-CD999 circumaural headphones. The experiments took about $2\frac{1}{2}$ h per listener, including breaks.

B. Determination of dynamic range

At the beginning of the experimental session, each listener completed a test in which the dynamic range was measured. The frequency range of interest was from 0.1 to 6.4 kHz, in which we defined 16 adjacent frequency bands with logarithmically equal widths. For each of these bands, the threshold and uncomfortable loudness (UCL) levels were determined. The stimuli were 16 noise bands, each corresponding to a frequency band in the range from 0.1 to 6.4 kHz, and an individually shaped wide-band noise (see below) in the second stage of the UCL determination.

The measurement of the threshold level, for each of the frequency bands, consisted of repeated presentation (repetition frequency: 2.4 Hz; stimulus duration: 310 ms; rise/fall times: 10 ms) of the noise band of interest. The listener was instructed to push the space bar of a PC keyboard as long as the noise burst was audible (upon which the level was decreased), and to release it as soon as the noise had become inaudible (whereafter the level was increased again). Starting at a clearly audible level, the noise was attenuated by 2 dB at each presentation, until the noise first became inaudible. After the listener had released the space bar, the level was increased in 1-dB steps until the spacebar was pressed again. Then, the level was decreased again (in 1-dB steps) until the space bar was released, and so on, until 11 reversals had been registered. At that point, the measurement was terminated and the threshold level was computed by averaging the 10 last turnpoint levels.

UCL levels were measured only for the odd-numbered frequency bands, plus band 16, to restrict fatigue; the UCL levels for the nonmeasured bands were interpolated from the results of the two adjacent bands. We urged our listeners to react as soon as they considered the stimulus uncomfortably loud, rather than using pain sensation as a criterion. For each of the measured frequency bands, a noise burst was presented repeatedly (burst duration: 310 ms; rise/fall times: 10 ms; repetition frequency: 1.4 Hz). At each next presentation, its level was increased by 3 dB, until the listener pushed the space bar (indicating that the noise had become too loud). At that point, the level was decreased by a random amount between 21 and 31 dB, and the procedure was run again. After six ''too loud'' reactions, the measurement was terminated and the UCL level was computed by averaging the six levels at which the space bar had been pressed. In succession to the nine narrow-band UCL measurements, we shaped a wide-band noise such that its frequency spectrum equaled the combined results of the narrow-band stimuli. This noise (duration: 3.7 s, representative for the duration of a sentence-in-noise in the speech-intelligibility test) was then used as a stimulus in a second UCL determination, since a wide-band stimulus will generally be considered uncomfortably loud at lower narrow-band levels (because of loudness summation; see for example Zwicker and Scharf, 1965). The wide-band stimulus was presented repeatedly at increasing levels; after each presentation, the listener had to indicate whether or not the stimulus had been too loud. If not, the level was increased and the stimulus was presented again; otherwise, the last presentation level was taken as the UCL that was used in the computation of the reference frequency spectrum (see below).

The results of the dynamic-range experiments are displayed in Fig. 1. In the group with impaired hearing, the average threshold levels are higher in comparison to the group with normal hearing at all frequencies. The difference

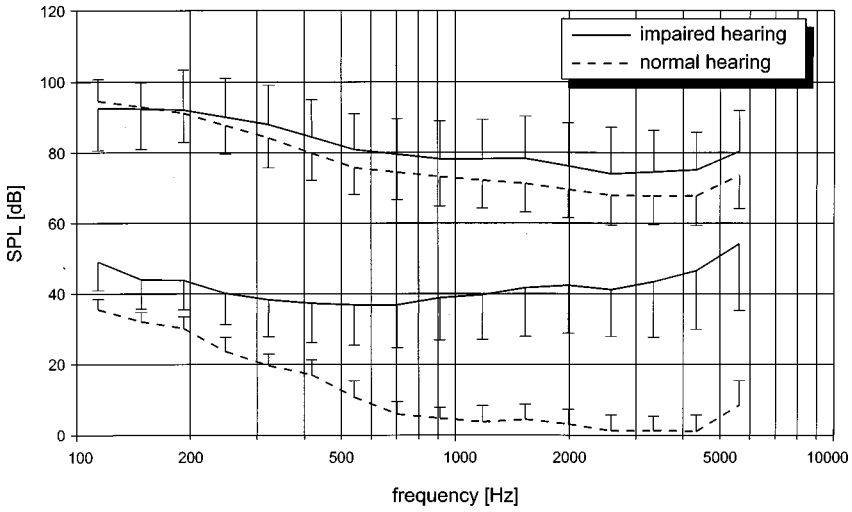

FIG. 1. Average dynamic ranges of both listener groups. All levels are for noise bands centered at the frequencies indicated. Upper curves denote the UCL levels; lower curves are for the threshold levels. Vertical bars are the standard deviations (shown in only one direction) corresponding to the curve they are connected to.

ranges from 13.6 dB at 114 Hz to 45.7 dB at 5620 Hz (both frequencies are at the center of a noise band). The average UCL levels are less different; here, differences range from −2.0 dB at 114 Hz to maximally 7.3 dB at 4334 Hz. An ANOVA of the UCL data reveals that this difference is not significant [$F(1,50)=3.49$; $p=0.068$] at the 5% level. As a result of the UCL determination with the shaped wide-band noise, the UCL levels drawn in Fig. 1 are lower than the narrow-band results. In the group with hearing impairment, this shift is 26.8 dB, on average; the corresponding value for the group with normal hearing is 30.7 dB.

C. Signal processing

In the frequency range from 0.1 to 6.4 kHz, we performed bandfiltering, envelope detection, envelope compression/expansion, and resynthesis of speech in noise (see Fig. 2).

Since our processing was clearly nonlinear, and since we were interested in critical S/N ratios at the input of an imaginary hearing aid, we summed speech and masker signals *before* processing. The masker was at a fixed level, and the S/N ratio was varied by changing the level of the speech. After the addition of speech and masker, the signal was always divided into 16 frequency bands by means of a bank of elliptical bandpass filters. The filters corresponded to the 16 frequency bands in the dynamic-range experiments. These filters were applied twice; once to the wide-band signal, and once again to the filtered, *time-reversed* signal, to remove any phase shifts introduced in the first pass. In the range of about −3 down to −30 dB of a filter band's frequency response, the resulting slopes were about 96 dB/oct. Depending on the experimental condition, the number of independent processing bands was 16, 4, or 1; in the case of 4 or 1 processing bands, the 16 bands were combined (by summation) into the desired number of processing bands. In the 4-band case, the bands crossed over at 283, 800, and 2263 Hz. Next, the signal was fed to an envelope detector, comprising a Hilbert transformer (the envelope was defined as the magnitude of the *analytic* signal; see Rabiner and Gold, 1975) and a 32-Hz low-pass filter (to prevent higher-frequency envelope components, such as the pitch, from controlling the processing). The low-pass filter, like the bandpass filters, was applied twice, effecting a system without phase shifts. The resulting envelope signal was processed (i.e., compressed or expanded) and then divided, sample by sample, by the original envelope, resulting in a multiplication factor for each sample in the band signal. Finally, these multiplication factors were applied to the band signal and the resulting signal was scaled such that its rms level equaled the input rms level. For conditions with more than one independent processing band, there was of course a final summation.

The expansion and compression of the low-pass-filtered temporal envelope were carried out on a logarithmic amplitude scale (see Fig. 3). The expansion/compression factor determines by how much a 1-dB change in input level is expanded/reduced. In the case of compression, only envelope

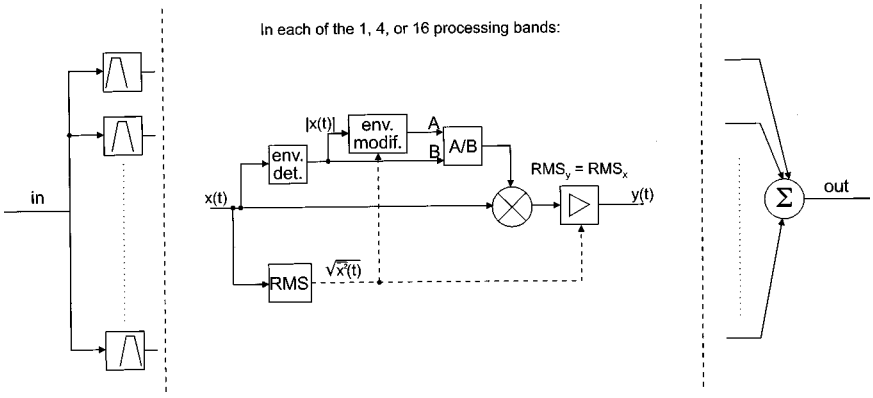

FIG. 2. Flow diagram of signal processing. Left: filter bank; center: nonlinear processing (dashed lines indicate the use of the signal's average level, not the time-varying level); right: summation of processed bands.

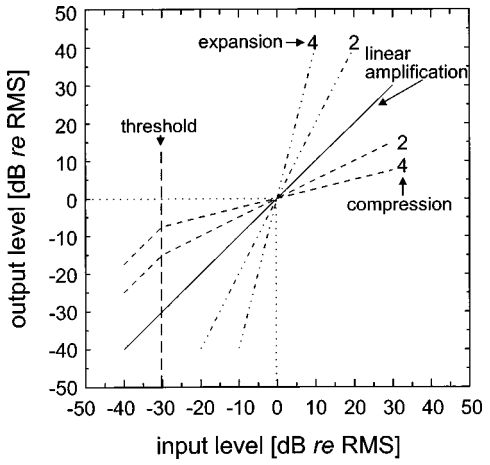

FIG. 3. Output level as a function of input level for each of the compression/expansion conditions.

levels down to 30 dB below rms (the compressor's ''knee point'') were compressed; lower envelope levels were linearly amplified.

Because expansion of the temporal envelope will increase the crest factor (the ratio of maximum amplitude and rms level), all signals were digitally attenuated by 12.0 dB prior to processing; this attenuation was compensated for by analog amplification. The processing could not be accomplished in real time and was carried out off-line, before an experimental session. Computation of the stimuli took about 21 h for each listener.

During the experiments, all signals were filtered such that the spectrum of the steady-state noise, expressed in band levels, was halfway between the threshold and UCL levels;

$$spec_B = \frac{thr_B + ucl_B}{2} \quad (B = 1,...,16),$$

where $spec_B$=level of the target spectrum in dB SPL at band B; thr_B=threshold level at band B; ucl_B=uncomfortable loudness level at band B.

This on-line filtering was achieved by means of a 256-tap Finite Impulse Response (FIR) filter, that was computed individually from the speech spectrum and the listener's threshold and UCL data. Because the rms level is restored to its original value after processing (see Fig. 2), the average frequency spectrum of the processed speech was the same in all processing conditions.

The speech-intelligibility experiments were carried out for 26 signal-processing conditions. The number of processing bands was 1, 4, or 16; there were four compression ratios (0.25, 0.50, 2.0, and 4.0, with ratios below 1.0 for expansion), and there was of course linear amplification. This adds up to a total of 13 conditions, each of which was evaluated with the 2 maskers (steady-state noise and a competing speaker). Linear amplification was realized by processing the speech in one band (i.e., before envelope manipulation, all 16 filter bands were summed) with compression factor 1.0; in other words, this condition has undergone the same filtering as all other conditions.

For the sound-quality experiments, we did not use any masker signals; in the speech-intelligibility experiments, they merely served as a means of achieving a fixed intelligibility score (50%) for all conditions. Because the sound-quality ratings were done for speech and music in *quiet*, there were only thirteen conditions in those experiments.

D. Tests of statistical significance

All data were analyzed by means of nonparametric statistical tests, because the prime assumption for using parametric tests (i.e., a normally distributed data set) was not met. For the evaluation of overall effects, we used a Friedman ANOVA. When the result of this test was significant, each of the conditions was compared to the linear-amplification condition by means of a Wilcoxon Matched-Pairs Signed-Ranks test. Because there were 12 other conditions, a 5% error rate for the whole set of comparisons requires a significance level of 0.0042 (5% divided by 12) or less for each of the individual comparisons (this procedure is known as the Bonferroni approach for multiple comparisons; see, for example, Altman, 1992). The results of these comparisons turned out such (in almost all figures) that we were able to separate conditions that were significantly different from linear amplification from those that were not, by means of a horizontal dashed line. In only one case (Fig. 6, see below), the dashed line crosses two data points of which one is and the other is not significantly different from linear amplification.

II. SPEECH INTELLIGIBILITY

A. Method

Speech intelligibility was evaluated by means of a sentence test (Plomp and Mimpen, 1979) in which short, everyday Dutch sentences are presented in a noise background at S/N ratios that are chosen according to a simple up–down procedure. This procedure converges to a S/N ratio at which 50% of the sentences is correctly reproduced, which is defined as the Speech Reception Threshold (SRT) in noise. For each of our experimental conditions, the SRT was determined with a list of ten sentences; the first three sentences in a list were used to obtain an initial estimate of the SRT, while the S/N ratios specified after the remaining seven sentences were averaged to produce the SRT for the condition. Starting at a low S/N ratio (−10 dB in steady-state noise, and −20 dB in a competing speaker), the first sentence was presented as often as necessary, increasing the S/N ratio by 4 dB on each presentation. This was continued until the sentence was reproduced correctly. For subsequent sentences, the S/N ratio was 2 dB lower after a correct response, and 2 dB higher after an incorrect response. Listeners were urged to reproduce the sentences as accurately as they could; at the same time, we encouraged them to guess those words they could not extract.

We used speech from a female and a male speaker in our speech-intelligibility experiments. The test would always start with speech from 1 speaker, masked by a spectrally matched steady-state noise for all 13 conditions. After this, speech from the other speaker was presented, but now

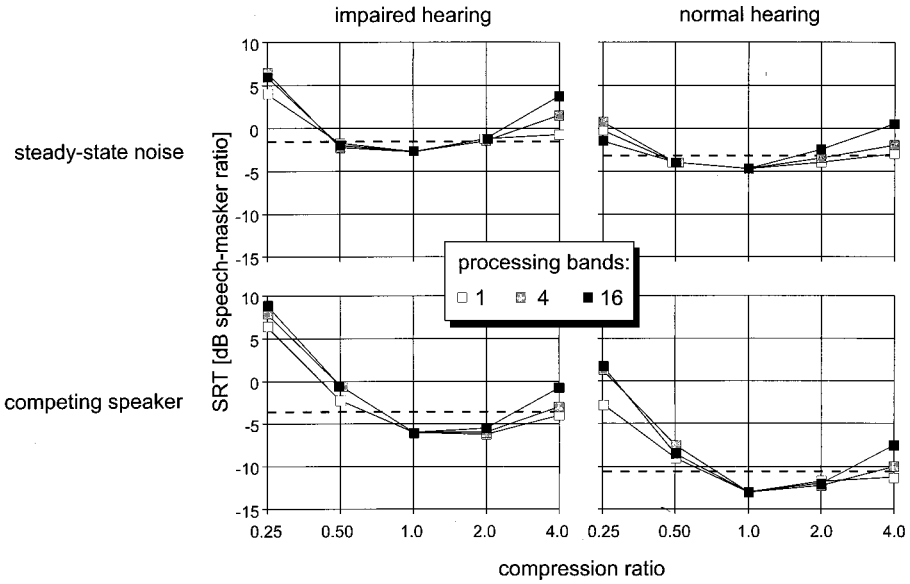

FIG. 4. Median SRTs, in steady-state noise (upper panels) and in the presence of a competing speaker (lower panels), as a function of compression ratio (ratios below 1.0 indicate *expansion*). The left panels are for the listeners with hearing impairment; the right panels are for the listeners with normal hearing. Dashed lines indicate the level *above* which conditions differ significantly from linear amplification.

masked by the speech from the first speaker. The masker signals for the second speaker were chosen randomly from the speech set of the first speaker. Half of the listeners first heard the female speaker; the other half first listened to the male speaker. The order of the sentences within one speaker was identical for all listeners; to prevent order and list effects from systematically influencing the results, we balanced the signal processing conditions over the sentence lists.

B. Results and discussion

Figure 4 shows the median SRTs for both listener groups and the two masker types. From these graphs, it is immediately clear that none of the conditions provides a significant improvement over linear amplification. Only one condition produces a slightly lower median SRT (i.e., better speech intelligibility) in comparison to linear amplification, i.e., compression by a factor of 2.0 in 1 band with a competing speaker. This small (and statistically nonsignificant) advantage of -0.25 dB occurs only for the listeners with hearing impairment.

Statistical analyses (Friedman's ANOVA) showed that the main effect of compression/expansion was highly significant in all four situations [listeners with normal hearing: steady-state noise, $\chi^2(12)=165.4$; competing speaker, $\chi^2(12)=218.8$; listeners with impaired hearing: steady-state noise, $\chi^2(12)=204.0$; competing speaker, $\chi^2(12)=234.4$; in all cases, $p<5\times10^{-5}$]. In order to discriminate between linear amplification and the conditions with compression or expansion, pairwise comparisons were performed. The results of these analyses have been incorporated in Fig. 4: those medians that lie above the dashed line in a panel differ significantly from the corresponding condition with linear amplification (see Sec. I D).

From Fig. 4, it can be seen that the listeners with impaired hearing, compared to those with normal hearing, always need a higher S/N ratio for 50% intelligibility. This observation was confirmed by a series of Mann–Whitney tests, that reported 24 out of 26 conditions to result in significantly higher SRTs for the listeners with hearing impairment (the exceptions are, in the case of steady-state noise, for a compression ratio of 2.0 in either 4 or 16 independent bands). In the case of linear amplification, the difference between the medians is 2.0 dB with steady-state noise; for a competing speaker, it amounts to 7.0 dB. For all other conditions the difference is of roughly the same order as in the corresponding condition with linear amplification, except for the 0.25 compression factor (i.e., expansion with a factor of 4.0) with steady-state noise, where it rises to as much as 7.5 dB in the 16-band condition.

The intelligibility of speech suffers more from expansion in the case of a competing speaker, as compared to the steady-state noise masker. Comparing the speech-intelligibility results for the two masker types, it turns out that the effects of compression are comparable to a certain degree; for both listener groups, differences in SRT (between masker conditions) are less than 2 dB. The results for the expansion conditions show a difference between the masker types of up to 6 dB for the listeners with hearing impairment and of maximally 11 dB for the listeners with normal hearing.

C. Analysis of individual results

So far, we have concentrated on group averages. But even though our data show that compression or expansion is not beneficial to speech intelligibility at the group level, individual listeners may have experienced benefit from certain types of nonlinear processing. To analyze whether this in fact occurred, we will now zoom in on the speech-intelligibility results from the group with hearing impairment, since they are the only real candidates for the practical application of nonlinear amplification. The analysis consists of comparisons of individual SRT values, with their larger error margin not compensated for by taking many listeners together; therefore, the results presented here should be interpreted with some caution. For the group with hearing impairment, there are five conditions with steady-state noise in which not a single listener achieved better speech intelligibility than with linear amplification (viz. expansion with a

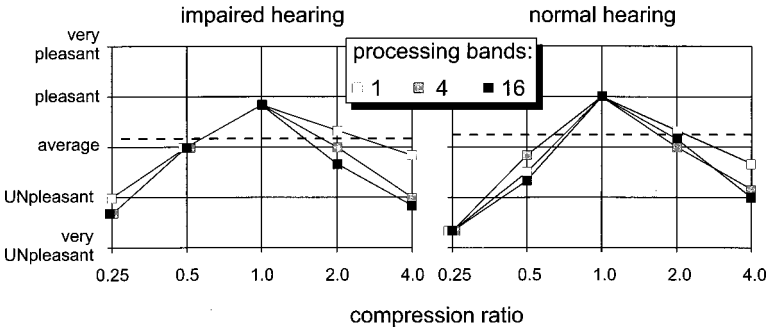

FIG. 5. Median pleasantness judgments for speech. Overlapping symbols have been offset horizontally. The left panel is for the listeners with hearing impairment; the right panel is for the listeners with normal hearing. Dashed lines indicate the level *below* which conditions differ significantly from linear amplification.

factor of 4.0 in all three bandwidth variants, and compression with a factor of 4.0 in 4 and 16 independent bands). For the remaining conditions with steady-state noise, at most nine listeners do better with nonlinear processing (viz. expansion with a factor of 2.0); their SRTs were lower than in the case of linear amplification by an average 1.2 dB. The competing-speaker conditions showed a slightly different result. Here, there were four conditions where not a single listener achieved better speech intelligibility than with linear amplification (viz. expansion with a factor of 4.0 in all three bandwidth variants, and expansion with a factor of 2.0 in 16 independent bands). At most 14 listeners (some of which were in the abovementioned group of 9 as well) did achieve better results in nonlinear-processing conditions; for compression with a factor of 2.0 in either 1 or 4 independent bands, their SRTs are lower than for linear amplification by 2.2 or 2.6 dB, respectively.

III. SOUND-QUALITY RATINGS

A. Method

For two types of stimulus, speech and music (both in quiet), sound quality was judged in rating-scale experiments. These stimuli had been processed off-line according to the same scheme as for the speech-intelligibility experiments. During the experiments, the same frequency shaping as in the speech-intelligibility experiments was applied to both speech and music. Since we were not interested in the effect of masker signals, there were only 13 conditions in this experiment. The presentation order of the conditions was balanced over the listeners to prevent order effects from having a systematic influence; this sequence was repeated three times to improve reliability. After having listened to a stimulus, the listener had to judge the sound quality by pressing one out of five keys, labeled with the Dutch equivalents (including capitalization) of ''very UNpleasant,'' ''UNpleasant,'' ''average,'' ''pleasant,'' and ''very pleasant.'' In order to familiarize the listener with the experimental task, and to give an idea of the range of conditions for the stimulus under test, ten judgments were carried out prior to the start of each judgment session.

1. Speech

Five sentences from the speech set by the female speaker were used as stimuli for the speech judgment. To prevent processing artifacts (i.e., zero input envelope), spectrally matched noise was added, at a S/N ratio of −30 dB, prior to processing. Since all relevant information in the speech signal was well above this level, this was not considered a problem. Additionally, it effectively masked the background noise of the analog source tape. In the experiment, the five sentences were always presented in fixed order, returning to the first sentence after having judged the fifth. Because there were 13 conditions, each condition was judged 3 times with different sentences.

2. Music

Four different fragments of music were judged in four judgment sessions (i.e., one session per fragment). The music fragments were taken from the following compositions: (i) ''Opzij'' by Herman van Veen (German flute, piano, and voice); (ii) ''Te Deum'' by M.A. Charpentier (trumpet and orchestra); (iii) ''Drive'' by The Cars (drums, synthesizer, and voice); and (iv) ''Mazurka in C,'' op. 56 no. 2 by F. Chopin (piano). The average length of the fragments was 3.8 s and they were cut from Compact-Disc tracks after resampling at 15 625 Hz. To prevent processing artifacts because of a zero input envelope, the input envelope was set to a constant value (of at least 80 dB below the rms of the band, which was possible because of the very low background noise level) whenever it was below that value.

B. Results and discussion

For the purpose of statistical analyses, each rating-scale item was assigned an integer value from −2 (''very UNpleasant'') to 2 (''very pleasant''); after averaging the trials, these values were analyzed.

1. Speech

Figure 5 shows median values for the sound-quality judgments of speech. The general trend is the same for both listener groups; the more the envelope is compressed or expanded, the worse the sound quality. The overall effect of processing condition is highly significant in both listener groups [impaired hearing: $\chi^2(12)=195.7$, normal hearing: $\chi^2(12)=207.6$; in both cases, $p<5\times10^{-5}$]. Further analysis showed that the only condition for which the judgment is *not* significantly lower than in the case of linear amplification, is compression with a factor of 2.0 in one frequency band. Therefore, it is the only condition which lies above the dashed lines in Fig. 5 (which separate the significantly dif-

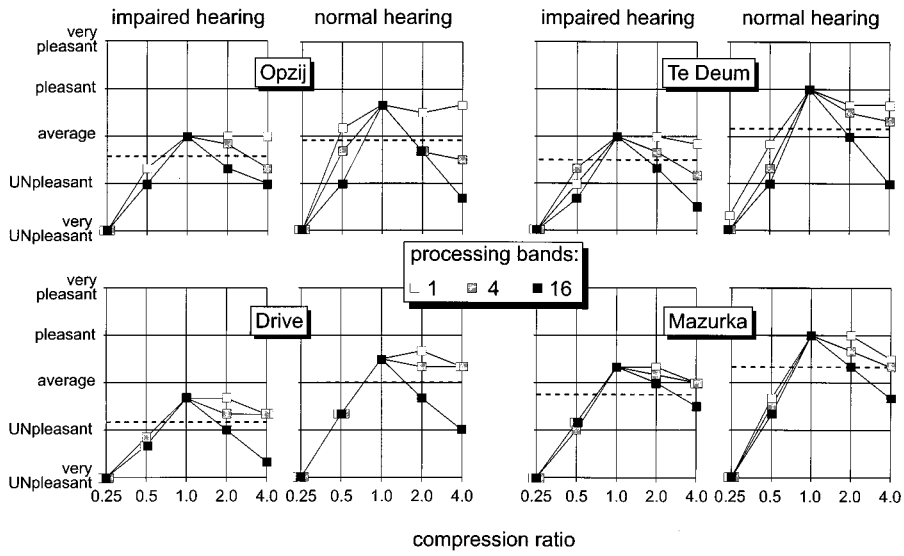

FIG. 6. Median pleasantness judgments for music for each of the four fragments. Overlapping symbols have been offset horizontally. The left panels are for the listeners with hearing impairment; the right panels are for the listeners with normal hearing. Dashed lines indicate the level *below* which conditions differ significantly from linear amplification.

ferent conditions from those not statistically distinguishable from linear amplification). This result is identical for the two listener groups; from a comparison of the two panels in Fig. 5, one would conclude that the data from the two listener groups are in good agreement.

2. Music

For each of the four fragments, median judgments are depicted in Fig. 6, with the listener groups side-by-side for easy comparison. Just like in the results from the speech judgments, the general pattern is the same in both listener groups, in the sense that the *differences* between processing conditions are of the same sign and of (roughly) the same order of magnitude. But it is also evident that the listeners with hearing impairment are generally ''less positive'' in their judgments; for all fragments, the data points from the listeners with hearing impairment are at lower-or-equal levels than those from the listeners with normal hearing, except for two conditions of the ''Opzij'' fragment.

The effect of processing condition was highly significant for both listener groups and all fragments [group with impaired hearing: ''Opzij,'' $\chi^2(12)=170.0$; ''Te Deum,'' $\chi^2(12)=213.0$; ''Drive,'' $\chi^2(12)=183.0$; ''Mazurka,'' $\chi^2(12)=195.4$; group with normal hearing: ''Opzij,'' $\chi^2(12)=193.9$; ''Te Deum,'' $\chi^2(12)=197.9$; ''Drive,'' $\chi^2(12)=195.8$; ''Mazurka,'' $\chi^2(12)=210.1$; in all cases, $p<5\times10^{-5}$]. The dashed lines in Fig. 6 indicate the level below which conditions are significantly different from linear amplification. In the lower right panel (''Mazurka,'' normal hearing) there are two conditions of which one (compression with a ratio of 4.0 in 4 bands) is significantly different from linear amplification, and another (compression with a ratio of 2.0 in 16 bands) is *not*, although the medians are exactly the same (0.33). This may be understood by noting that the graphs show median values, whilst the statistical test compares the entire data sets.

Wide-band compression (i.e., a single processing band) with a factor of 2.0 never caused a significant degradation of sound quality. This may be caused by the relative ''gentleness'' of wide-band compression, since only overall level variations are reduced, while the relative levels of sounds at different frequencies are preserved. In both listener groups, the conditions in which expansion was applied tended to be judged less pleasant than those with compression. Also, the appreciation of expansion seems to be less dependent on the number of independent processing bands than in the case of compression (where an increase in the number of independent bands results in lower appreciation). However, this is partly caused by the floor effect inherent to the experimental setup. In the case of expansion with a factor of 4.0, the median judgments are (in seven of the eight panels) at the negative extreme of the rating scale for all processing band variants. This does not imply that those conditions are equally unpleasant to the listeners; had the rating scale been extended further into the negative, then the listeners might have used those points to discriminate among the conditions.

IV. GENERAL DISCUSSION

The narrow dynamic range in sensorineurally impaired ears is accompanied by a steeper-than-normal growth of perceived loudness (e.g., Hellman and Meiselman, 1990). Intrinsically, it has been supposed that external compensation of this abnormality by means of a compressing amplifier would, to a substantial degree, restore speech intelligibility to normal levels. This does not necessarily follow, however. First, it might be revealing to measure just-noticeable differences (jnd's) for SPL in listeners with sensorineural hearing impairment, to check whether the steeper growth of loudness is indeed accompanied by increased sensitivity for level *differences* (such as those occurring in modulated signals). If *smaller* jnd's are found, then there is reason to expect that compression of the input to the impaired ear will restore normal loudness and speech perception. Zwislocki and Jordan (1986) measured intensity jnd's in both normal and sensorineurally impaired ears. They found that the jnd's were essentially *equal* for the two groups. Comparable results have been reported by Buus *et al.* (1995), who found differ-

ence limens for level to be normal for some but *enlarged* in other listeners from a group with predominantly sensorineural hearing impairment.

Second, since speech intelligibility is based on the perception of *rapid* energy fluctuations (i.e., modulations of the temporal energy envelope), it is of interest to test the *temporal* acuity of the sensorineurally impaired ear. Results from such experiments have been equivocal. For example, Moore *et al.* (1992) measured the modulation detection threshold for a sinusoidally modulated noise band in normal and sensorineurally impaired ears; they did not find significant differences between the results from normal and impaired ears, both at equal sound-pressure levels (SPLs) and at equal sensation levels (SLs). On a similar modulation detection task, but using a *wide-band* noise stimulus, Bacon and Gleitman (1992) found that at the lowest SL at which they tested both of their listener groups, performance of the listeners with hearing impairment tended to be slightly *better* than that of the listeners with normal hearing. This difference disappeared or was even reversed at higher SLs. The authors stress the importance of using wide-band stimuli for demonstrating such effects; further, they suggest that the magnitude of the hearing loss or the exact etiology can be decisive for temporal acuity of the impaired ear (see also Florentine and Buus, 1984). Experiments by Moore and Glasberg (1988) showed that, for the detection of temporal gaps in *sinusoids*, impaired ears often perform better than normal ears at equal SL, while performance is similar at equal SPL. The listeners with hearing impairment showed worse performance than those with normal hearing when temporal gaps in *noise bands* were to be detected. This difference was explained from the intrinsic level variations (modulations) that are present in noise bands. In combination with loudness recruitment (which may enlarge level variations), these modulations may be mistaken for the deterministic gap that is to be detected.

The experiments referenced above do not show a very distinct difference between listeners with normal hearing and listeners with hearing impairment. This parallels our results in the sense that the effects of most of the processing conditions were of roughly the same order of magnitude in both listener groups. Furthermore, neither compression nor expansion were beneficial to either speech intelligibility or sound quality.

The fact that the present data do not show improved speech intelligibility with compression for listeners with sensorineural hearing impairment should be taken for an indication that their abnormal loudness growth is *not* accompanied by an enhanced ability to resolve (compressed) modulations. In other words, the concept of compensating loudness recruitment, which assumes that a steeper loudness growth implies an improved level discrimination, does not seem to be supported by the present experiments either. Plomp (1994) stated that recruitment is not a characteristic of the sensorineurally impaired ear only. He refers to measurements by Hellman and Zwislocki (1964) of the loudness of pure tones in noise-masked normal ears, where recruitmentlike curves were found. Recruitment, according to Plomp, ''reduces the interaction between sounds,'' and therefore ''should be considered positively, not to be destroyed by compression'' (p. 7). In a discussion paper on the effects of amplitude compression on speech intelligibility, Plomp (1988) argued that besides deleterious effects on temporal modulations, spectral contrasts would also be affected by multichannel syllabic amplitude compression. These effects will be greater as the number of independent frequency bands or the compression ratio increases, leading to a completely stationary frequency spectrum in the extreme case of a very large number of narrow frequency bands, in which high compression ratios are applied. Plomp notes that the loss of spectral contrasts is a problem for listeners with hearing impairment, because their frequency resolution is generally *poorer* than for listeners with normal hearing.

The fact that the expansion of level variations does not improve speech intelligibility for either listener group also indicates that the concept of modulations as the basic carriers of information has its limits. At the basis of the Speech Transmission Index (STI, e.g., Houtgast and Steeneken, 1985) is a weighted sum of seven Modulation Transfer Functions (MTFs), each of which specifies how modulations in an octave-wide frequency band (center frequencies from 125 Hz to 8 kHz) are affected by transmission or, such as in our case, signal processing. Since the expansion we carried out enlarges the amplitude fluctuations of the temporal envelope, it seems obvious that the resulting MTFs and also the STI will be larger than for linear amplification. This was verified by applying our signal processing to a special STI test signal in noise and subsequently computing STI values. However, our results (see Fig. 4) show the opposite for all expansion conditions, except those with steady-state noise and expansion with a factor of 2 (where the decrease of intelligibility is statistically nonsignificant). The STI, however, was never designed for expansion conditions like those applied in the present experiments. As stated before, it is a good predictor of speech intelligibility in practical situations with noise, reverberation, AGC, or peak clipping. The fact that the effects of certain types of nonlinear processing on speech intelligibility cannot be predicted accurately with the STI has also been found by Drullman *et al.* (1994), although their results show only small errors in the magnitude of the STI, and by Hohmann and Kollmeier (1995). In our case, the prediction from the STI is in the wrong direction for the expansion conditions. An explanation for this prediction error may lie in the nature of the modulations as they appear in the summed speech and noise that we used in the intelligibility experiments. Both speech and noise contain modulations, of which those in the noise cause part of the reduction of intelligibility (the other part being associated with the fine structure of the noise; see Drullman, 1995). By enlarging the modulations in the summed signal, both the information-carrying modulations (speech) and the disturbing modulations (noise) are enhanced. Therefore, one cannot guarantee that speech intelligibility in noise will be improved by expansion. Another effect of expansion is that weak components in the speech signal will be made even weaker. Because of temporal masking, these sounds may now be masked, whilst they were not in conditions with linear amplification. The result of this masking may be that the num-

ber of useful cues for speech intelligibility decreases, resulting in lower scores.

We did not use a frequency-dependent compression ratio in our experiments. Since recruitment is most notable at those frequencies where the hearing loss is most severe, it might have been feasible to adapt the compression ratio to the available dynamic range. Although we did not implement this in our experiments, our data may allow some insight into the success of adapting the compression ratio to the residual dynamic range. The idea here is that since the majority of our listeners with hearing impairment had a sloping loss, recruitment was more pronounced at the higher frequencies. At these frequencies, a higher compression ratio would be needed for optimal compensation. If this were true, then one would expect speech that was processed with a certain compression ratio to yield better intelligibility for some losses (i.e., for some listeners), but not for others, depending on how well the residual dynamic range matches the level variations that result after compressing the speech. To examine whether this was actually the case in our data, we investigated the relationship between high-frequency hearing loss (i.e., the pure-tone average for 2.0, 4.0, and 8.0 kHz, which ranged from 15 to 78 dB HL) and speech intelligibility for the compression conditions. In our data, we could *not* identify distinct maxima for speech intelligibility, for the range of hearing losses present in our listener group. This is not encouraging for the actual implementation of frequency-dependent compression ratios; it serves as an indication that the problems of listeners with hearing impairment are more complicated than to be fully compensated by syllabic amplitude compression.

In the case of expansion, the intelligibility of speech appears to suffer more for a competing-speech masker than for a steady-state noise masker. This difference may be understood by noting that (a) the greater modulations in the masking speaker may become more effective temporal maskers because of their increase in level and (b) because below-rms modulations will get a lower average level and may therefore be masked by modulations in the speech masker, where they were not in the case of a steady-state noise masker. Our results indicate that the increased modulations of the target speech do not compensate for the increased modulations (and the associated temporal masking) in the speech masker. Another interesting question is whether the ''opposite'' processing (compression) produces the opposite result, i.e., better speech intelligibility for the competing-speech masker than for the steady-state noise masker. This cannot be concluded from our results, given the magnitude of this difference (less than 2 dB for both listener groups). Although it seems evident that temporal masking is reduced by compression, this does not necessarily imply that speech intelligibility is enhanced; for example, the reduced temporal masking may be counterbalanced by a less successful extraction of information from the compressed information-carrying modulations in the target speech.

The results of the sound-quality ratings are in accordance with those from the speech-intelligibility experiments, in the sense that linear amplification was always judged to be among the most pleasant conditions. Byrne and Walker (1982), who compared a linear amplifier to a nonlinear-amplification system in which compression and expansion were *combined*, report comparable results at this point. We found that, for compression, a greater number of processing bands was generally associated with poorer sound quality. This is similar to what we found in the speech-intelligibility experiments, where a greater number of independent processing bands causes a degradation of intelligibility. Also, increasing the compression ratio caused sound quality to be degraded. This is similar to the findings of the paired-comparison experiments by Neuman *et al.* (1994). They reported that small compression ratios (i.e., maximally 2) did not cause a significant degradation of sound quality, while linear amplification was preferred in most of the comparisons.

Our data show that compression or expansion is not beneficial to speech intelligibility at the group level. Depending on the exact processing parameters, individual listeners do experience benefit from nonlinear processing. An analysis of our data showed that, for the group with hearing impairment, there are 5 (out of 12) conditions with steady-state noise in which not a single listener achieved better speech intelligibility than with linear amplification. For the remaining seven conditions with steady-state noise, at most nine listeners do better with nonlinear processing. The competing-speaker conditions showed a slightly different result. Here, there were 4 (out of 12) conditions where not a single listener achieved better speech intelligibility than with linear amplification. At most 14 listeners did achieve better results in the remaining 8 competing-speaker conditions.

These results raise an additional dilemma: in steady-state noise, one nonlinear amplification strategy provided benefit to some listeners, whilst in a situation with a single competing speaker, another type of nonlinear amplification was of help to the same listeners. If possible at all in a practical hearing aid, and if the modest improvements in SRT are of practical interest (considering the limited reliability of this analysis), this calls for a very advanced signal analysis prior to processing. But a uniform solution for all listeners with sensorineural hearing impairment cannot, at present, be derived from our results.

A positive aspect of the experimental results reported here is that there are processing conditions (e.g., wide-band compression with a factor of 2.0) in which both speech intelligibility and sound quality hardly suffer, as compared to linear amplification. Should the decrements in performance be counterbalanced by enhanced comfort, for example because the listener will not any longer have to manually change the amplification in situations with large loudness variations, then nonlinear processing of the type tested in our experiments may be considered for practical application.

V. CONCLUSIONS

(1) Neither compression nor expansion, for the variants tested, provide a consistent improvement for speech intelligibility or sound quality relative to linear amplification.
(2) Given the measured effect of expansion on speech intelligibility, the STI (in its present form) should not be used

for predictions of speech intelligibility in conditions with such signal processing.

ACKNOWLEDGMENTS

This research was financially supported by Philips Hearing Instruments. We would like to thank Rick Aretz and Theo S. Kapteyn, of the University Hospital's Audiology Center, for their kind assistance in selecting the listeners with hearing loss. Rob Drullman and Jan Verhave, of TNO Human Factors Research Institute, Soesterberg, are acknowledged for performing STI computations. Finally, we thank two anonymous reviewers who helped us improve the paper's quality.

Altman, D. G. (**1992**). *Practical Statistics for Medical Research*, 2nd ed. (Chapman & Hall, London).

Bacon, S. P., and Gleitman, R. M. (**1992**). ''Modulation detection in subjects with relatively flat hearing losses,'' J. Speech Hear. Res. **35**, 642–653.

Bustamante, D. K. and Braida, L. D. (**1987**) ''Principal-component amplitude compression for the hearing impaired,'' J. Acoust. Soc. Am. **82**, 1227–1242.

Buus, S., Florentine, M., and Zwicker, T. (**1995**). ''Psychometric functions for level discrimination in cochlearly impaired and normal listeners with equivalent-threshold masking,'' J. Acoust. Soc. Am. **98**, 853–861.

Byrne, D., and Walker, G. (**1982**). ''The effects of multichannel compression and expansion on perceived quality of speech,'' Aust. J. Audiol. **4**, 1–8.

Caraway, B. J., and Carhart, R. (**1967**). ''Influence of compressor action on speech intelligibility,'' J. Acoust. Soc. Am. **41**, 1424–1433.

Drullman, R., Festen, J. M., and Plomp, R. (**1994**). ''Effect of temporal envelope smearing on speech reception,'' J. Acoust. Soc. Am. **95**, 1053–1064.

Drullman, R. (**1995**). ''Temporal envelope and fine structure cues for speech intelligibility,'' J. Acoust. Soc. Am. **97**, 585–592.

Florentine, M., and Buus, S. (**1984**). ''Temporal gap detection in sensorineural and simulated hearing impairment,'' J. Speech Hear. Res. **27**, 449–455.

Hellman, R. P., and Meiselman, C. H. (**1990**). ''Loudness relations for individuals and groups in normal and impaired hearing,'' J. Acoust. Soc. Am. **88**, 2596–2606.

Hellman, R. P., and Zwislocki, J. (**1964**). ''Loudness function of a 1000-cps tone in the presence of a masking noise,'' J. Acoust. Soc. Am. **36**, 1618–1627.

Hohmann, V., and Kollmeier, B. (**1995**). ''The effect of multichannel dynamic compression on speech intelligibility,'' J. Acoust. Soc. Am. **97**, 1191–1195.

Houtgast, T., and Steeneken, H. J. M. (**1985**). ''A review of the MTF concept in room acoustics and its use for estimating speech intelligibility in auditoria,'' J. Acoust. Soc. Am. **77**, 1069–1077.

Levitt H., and Neuman A. C. (**1991**) ''Evaluation of orthogonal polynomial compression,'' J. Acoust. Soc. Am. **90**, 241–252.

Lippman, R. P., Braida, L. D., and Durlach, N. I. (**1981**). ''Study of multichannel amplitude compression and linear amplification for persons with sensorineural hearing loss,'' J. Acoust. Soc. Am. **69**, 524–534.

Maré, M. J., Dreschler, W. A., and Verschuure, H. (**1992**). ''The effects of input-output configuration in syllabic compression on speech perception,'' J. Speech Hear. Res. **35**, 675–685.

Moore, B. C. J., and Glasberg, B. R. (**1988**). ''Gap detection with sinusoids and noise in normal, impaired, and electrically stimulated ears,'' J. Acoust. Soc. Am. **83**, 1093–1101.

Moore, B. C. J., Shailer, M. J., and Schooneveldt, G. P. (**1992**). ''Temporal modulation transfer functions for band-limited noise in subjects with cochlear hearing loss,'' Br. J. Audiol. **26**, 229–237.

Náběl̆ek, I. V. (**1983**). ''Performance of hearing-impaired listeners under various types of amplitude compression,'' J. Acoust. Soc. Am. **74**, 776–791.

Neuman, A. C., Bakke, M. H., Hellman, S., and Levitt, H. (**1994**). ''Effect of compression ratio in a slow-acting compression hearing aid: Paired-comparison judgments of quality,'' J. Acoust. Soc. Am. **96**, 1471–1478.

Neuman, A. C., Bakke, M. H., Mackersie, C., Hellman, S., and Levitt, H. (**1998**). ''The effect of compression ratio and release time on the categorical rating of sound quality,'' J. Acoust. Soc. Am. **103**, 2273–2281.

Plomp, R. (**1988**). ''The negative effect of amplitude compression in multichannel hearing aids in the light of the modulation-transfer function,'' J. Acoust. Soc. Am. **83**, 2322–2327.

Plomp, R. (**1994**). ''Noise, amplification, and compression: Considerations of three main issues in hearing aid design,'' Ear Hear. **15**, 2–12.

Plomp, R., and Mimpen, M. (**1979**). ''Improving the reliability of testing the speech reception threshold for sentences,'' Audiology **18**, 43–52.

Rabiner, L. R., and Gold, B. (**1975**). *Theory and Application of Digital Signal Processing* (Prentice-Hall, Inc., Englewood Cliffs, NJ).

Steeneken, H. J. M., and Houtgast, T. (**1980**). ''A physical method for measuring speech-transmission quality,'' J. Acoust. Soc. Am. **67**, 318–326.

Verschuure, H., Prinsen, T. T., and Dreschler, W. A. (**1994**). ''The effects of syllabic compression and frequency shaping on speech intelligibility in hearing impaired people,'' Ear Hear. **15**, 13–21.

Villchur, E. (**1973**). ''Signal processing to improve speech intelligibility in perceptive deafness,'' J. Acoust. Soc. Am. **53**, 1646–1657.

Walker, G., Byrne, D., and Dillon, H. (**1984**). ''The effects of multichannel compression/expansion on the intelligibility of nonsense syllables in noise,'' J. Acoust. Soc. Am. **76**, 746–757.

Yund, E. W., and Buckles, K. M. (**1995a**). ''Multichannel compression hearing aids: Effect of number of channels on speech discrimination in noise,'' J. Acoust. Soc. Am. **97**, 1206–1223.

Yund, E. W., and Buckles, K. M. (**1995b**). ''Enhanced speech perception at low signal-to-noise ratios with multichannel compression hearing aids,'' J. Acoust. Soc. Am. **97**, 1224–1240.

Zwicker, E., and Scharf, B. (**1965**). ''A model of loudness summation,'' Psychol. Rev. **72**, 3–26.

Zwislocki, J. J., and Jordan, H. N. (**1986**). ''On the relations of intensity jnd's to loudness and neural noise,'' J. Acoust. Soc. Am. **79**, 772–780.

Time-delay estimation of reverberated speech exploiting harmonic structure

Michael S. Brandstein[a)]
Division of Engineering and Applied Sciences, Harvard University, Cambridge, Massachusetts 02138

(Received 20 December 1997; accepted for publication 28 January 1999)

The relative time delay associated with a speech signal received at a pair of spatially separated microphones is a key component in talker localization and microphone array beamforming procedures. The traditional method for estimating this parameter utilizes the generalized cross correlation (GCC), the performance of which is compromised by the presence of room reverberations and background noise. Typically, the GCC filtering criteria used are either focused on the signal degradations due to additive noise or those due exclusively to multipath channel effects. There has been relatively little success at applying GCC weighting schemes which are robust to both of these conditions. This paper details an alternative approach which attempts to employ a signal-dependent criterion, namely, the estimated periodicity of the speech signal, to design a GCC filter appropriate for the combination of noise and multipath distortions. Simulations are performed across a range of room conditions to illustrate the utility of the proposed time-delay estimation method relative to conventional GCC filtering approaches. © *1999 Acoustical Society of America.* [S0001-4966(99)01605-7]

PACS numbers: 43.72.Ew [JH]

INTRODUCTION

The accurate estimation of the relative time delay associated with a speech signal received by a pair of microphones is essential for source localization and any subsequent multichannel speech enhancement procedures. The two major sources of signal degradation which complicate this estimation problem are environmental background noise and channel multipath due to room reverberations. The noise-alone case has been addressed at length and is well understood. Assuming uncorrelated, stationary Gaussian signal and noise sources with known statistics and no multipath, the maximum likelihood (ML) time-delay estimate is derived from an SN-ratio-weighted version of the generalized cross-correlation (GCC) function.[1] An ML-type weighting appropriate for nonstationary speech sources was presented in Ref. 2 and applied successfully to speech-source localization in low-multipath environments.[3] However, once room reverberations rise above minimal levels, these methods begin to exhibit dramatic performance degradations and become unreliable.[4,5] A basic approach to dealing with multipath channel distortions in this context has been to make the GCC function more robust by deemphasizing the frequency-dependent weightings. The phase transform (PHAT)[1] is one extreme of this procedure which has received considerable attention recently as the basis of speech-source localization systems.[6–8] By placing equal emphasis on each component of the cross-spectrum phase, the resulting peak in the PHAT GCC function corresponds to the dominant delay in the reverberated signal. While effective at reducing some of the degradations due to multipath, the phase transform accentuates components of the spectrum with poor SN ratios and has the potential to provide poor results, particularly under low reverberation, high-noise conditions.

The ML-weighting and phase transform are designed to be responsive to specific signal degradations, additive noise, and multipath, respectively. Subsequently, each suffers performance shortcomings in the presence of the other form of distortion; the phase transform makes no accounting for SN ratio conditions while the ML-weighting is overly susceptible to enclosure acoustics. It would be of considerable advantage to develop a GCC weighting strategy which possesses the desirable features of each of these approaches while diminishing their less favorable characteristics. Additionally, these cross-correlation-based estimation schemes do not make any effort to exploit features associated with the content of the signals themselves, particularly the signal periodicity associated with voiced speech. The time-delay estimation procedure detailed below is designed with these goals in mind. By utilizing a speech-specific criterion in the design of the GCC weighting function, the proposed method achieves a robustness to background noise on par with the ML method and a degree of insensitivity to multipath conditions similar to that of the PHAT.

The following section overviews the GCC structure. Section II details the proposed time-delay estimator while Sec. III presents the results of simulations validating its utility. The paper concludes with some discussion in Sec. IV.

I. THE GENERALIZED CROSS CORRELATOR

The signals received at the two microphones, $x_1(t)$ and $x_2(t)$, may be modeled as:

$$x_1(t) = h_1(t) * s(t) + n_1(t), \quad 0 \leqslant t \leqslant T$$

$$x_2(t) = h_2(t) * s(t-\tau) + n_2(t),$$

where τ is the relative signal delay of interest, $h_1(t)$ and $h_2(t)$ represent the impulse responses of the reverberant channels, $s(t)$ is the speech signal, $n_1(t)$ and $n_2(t)$ corre-

a)Electronic mail: msb@hrl.harvard.edu

spond to uncorrelated noise, and $*$ denotes linear convolution.

The generalized cross-correlation function for a given time-lag, $R_{x_1x_2}(\tau)$, is calculated as the inverse Fourier transform of the received signal cross spectrum, $X_1(\omega)X_2'(\omega)$, scaled by a weighting function, $W(\omega)$

$$R_{x_1x_2}(\tau)=\int_{-\infty}^{\infty} W(\omega)X_1(\omega)X_2'(\omega)e^{j\omega\tau}d\omega. \tag{1}$$

The delay estimate, $\hat{\tau}$, corresponds to the lag value which maximizes $R_{x_1x_2}(\tau)$. Typically, a parabolic fit is performed about the peak in $R_{x_1x_2}(\tau)$ to achieve subsample resolution.

The ML-weighting function, $W_{\mathrm{ML}}(\omega)$, is derived from magnitude squared signal coherence and is used to emphasize specific frequencies deemed advantageous based upon signal-to-noise considerations alone. In practice, the required coherence function is unavailable *a priori* and must be estimated from the given data. This is typically done via a temporal averaging technique, such as in Ref. 9. This process can prove to be problematic for any nonstationary signal and is addressed specifically for speech applications in Ref. 2 where a single-frame, ML-type weighting approximation, $\hat{W}_{\mathrm{ML}}$, is advocated. The approximated ML weighting, which will be used in the simulations to follow, is roughly equivalent to the SN ratio evaluated from a single frame of observed data and given by

$$\hat{W}_{\mathrm{ML}}(\omega)=\frac{|X_1(\omega)||X_2(\omega)|}{|N_1(\omega)|^2|X_2(\omega)|^2+|N_2(\omega)|^2|X_1(\omega)|^2}.$$

The noise power spectra, $|N_1(\omega)|^2$ and $|N_2(\omega)|^2$, are assumed to be available or estimable during silence intervals.

The phase transform employs the weighting function

$$W_{\mathrm{PHAT}}(\omega)=|X_1(\omega)X_2'(\omega)|^{-1}, \tag{2}$$

to eliminate the influence of the spectral magnitudes and produce a GCC function dependent entirely on the phase of the cross spectrum.

A number of other suboptimal GCC weighting functions derived from frequency-dependent SN ratio conditions are available.[1] These represent various compromises between the two extremes of SN ratio dependence inherent in the ML and PHAT weightings. While generally considered more robust than the ML weighting, for the simulations performed in this paper none of these alternative schemes performed better than the ML weighting in the noise-only case nor achieved results superior to the PHAT weighting in the presence of reverberations. For these reasons, only the ML and PHAT results will be presented.

II. A PITCH-BASED TIME-DELAY ESTIMATOR

The proposed estimation scheme is based upon the rationale that given a segment of voiced speech, those portions of the signal spectrum which exhibit a distinctly periodic nature have been less influenced by the deleterious effects of noise and reverberation. Accordingly, these spectral regions should receive appropriate emphasis in the form of an inflated weighting value in calculation of the GCC function. A necessary prerequisite for such a scheme is the means to define and estimate the degree of signal periodicity associated with specific frequency bands. The criterion, to be detailed below, is derived from the frequency-dependent fit error associated with the observed signal spectrum and the synthetic spectrum of a periodic signal.

Consider the multiband excitation (MBE) speech model[10,11] developed in the context of speech compression. The MBE model generates the excitation spectrum as a function of a fundamental frequency, ω_0, and harmonic-dependent voiced/unvoiced mixtures. Specifically, the speech spectrum, $X(\omega)$, is modeled as the product of a spectral envelope, $H(\omega)$, and an excitation spectrum, $E(\omega)$. The fundamental frequency, spectral envelope parameters, and voicing mixture values are estimated via minimization of the error criterion

$$\varepsilon=\frac{1}{2\pi}\int_{-\pi}^{\pi}|X(\omega)-H(\omega)E(\omega)|^2d\omega. \tag{3}$$

This nonlinear optimization problem may be decoupled efficiently by noting that for a given fundamental frequency, the spectral envelope parameters which minimize the error are found through a set of uncoupled linear equations. The excitation is first assumed to be periodic with fundamental frequency ω_0, and thus $E(\omega)$ corresponds to the spectrum of a windowed periodic impulse train

$$E(\omega,\omega_0)=\sum_{m=-M}^{M} W(\omega-m\omega_0), \tag{4}$$

where $W(\omega)$ is the Fourier transform of the analysis window and M is the total number of harmonics ($M=\lfloor\pi/\omega_0\rfloor$). The spectrum is divided into frequency bands centered about the harmonics of the fundamental frequency. The error associated with the mth harmonic, $\varepsilon_m(\omega_0)$, may then be well approximated by

$$\varepsilon_m(\omega_0)=\frac{1}{2\pi}\int_{a_m}^{b_m}|X(\omega)-A_mW(\omega-m\omega_0)|^2d\omega, \tag{5}$$

where the interval $[a_m,b_m]$ is the frequency region centered on the mth harmonic of the fundamental, and A_m is the complex spectral amplitude (assumed constant) for that harmonic. The error, $\varepsilon_m(\omega_0)$, may be shown to be minimized by

$$A_m=\int_{a_m}^{b_m}X(\omega)W'(\omega)d\omega \Big/ \int_{a_m}^{b_m}|W(\omega)|^2d\omega. \tag{6}$$

The error criterion in (3) for a given fundamental frequency may then be computed as

$$\varepsilon(\omega_0)=\sum_m \varepsilon_m(\omega_0), \tag{7}$$

where $\varepsilon_m(\omega_0)$ from (5) is evaluated with the optimal value of A_m found from (6). The above summation may be limited to a subset of the harmonics and may include appropriate weighting terms to emphasize particular spectral regions. By calculating the error function in (7) versus all fundamental frequencies of interest, a global minimum can be found, producing the estimate $\hat{\omega}_0$. To effectively model the spectrum of the higher harmonics, a fundamental-frequency resolution

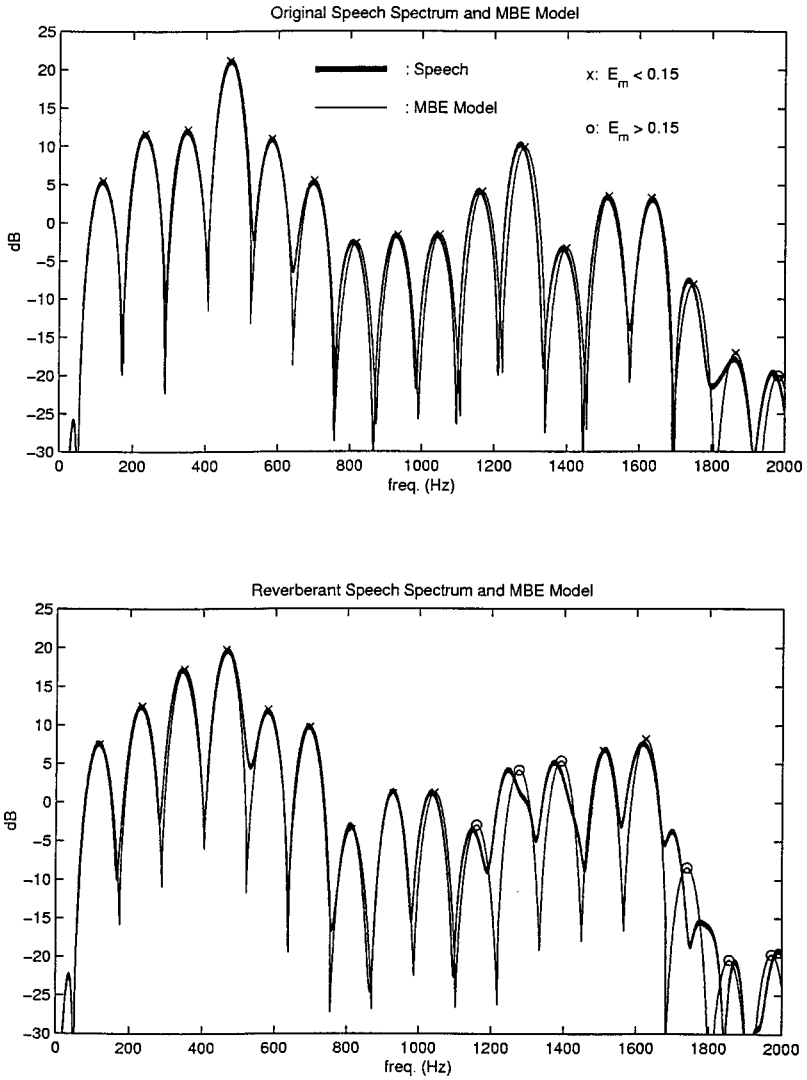

FIG. 1. Illustration of the MBE model estimates for two segments of voiced speech. The top graph plots the spectrum of a clean speech segment and its MBE estimate. The lower graph plots the spectrum of the same segment produced in a reverberant environment along with its MBE estimate.

of less than 1 Hz is typically required. In practice, this exhaustive procedure may be computationally prohibitive. A more efficient approach is to evaluate a coarse, integer pitch estimate via a traditional time-domain pitch estimation procedure and then use the above frequency-domain analysis to refine the fundamental-frequency estimate.

Once a fundamental-frequency estimate has been found, the voiced/unvoiced mixture associated with each harmonic is evaluated by examining how well the periodic excitation matches the observed spectral region. This is achieved by calculating the normalized error associated with the *m*th harmonic from

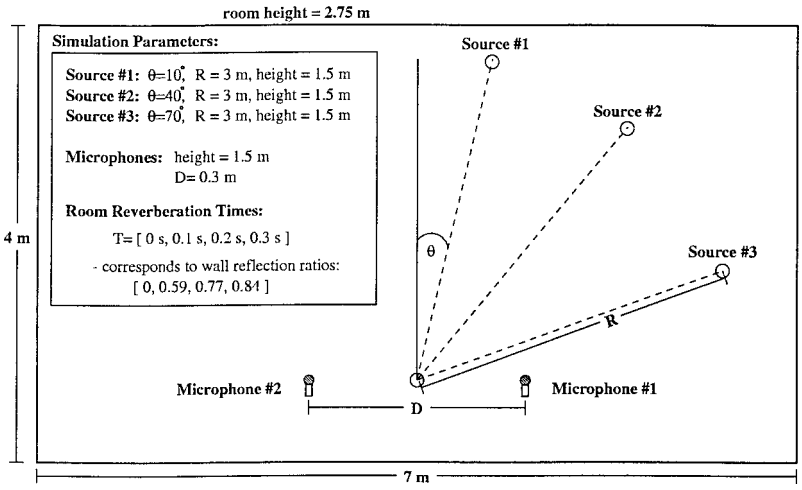

FIG. 2. Overhead view of the room setup and simulation parameters.

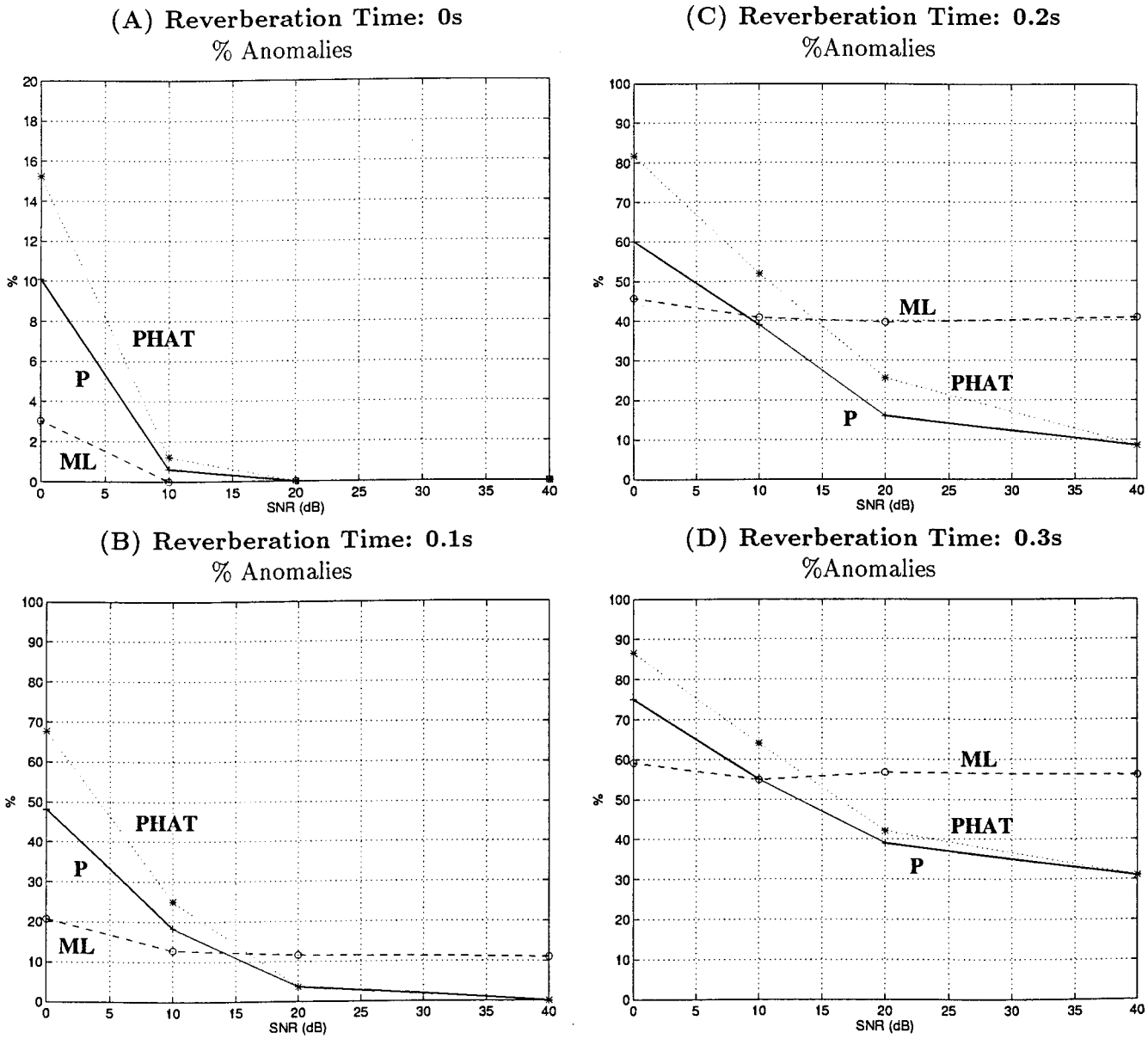

FIG. 3. Time-delay estimator simulation results: percent anomaly trial statistics for source location #2.

$$E_m = \varepsilon_m(\hat{\omega}_0) \Big/ \frac{1}{2\pi}\int_{a_m}^{b_m} |X(\omega)|^2 d\omega. \tag{8}$$

A low value for $E_m(\approx 0)$ indicates a strongly voiced harmonic interval, while a high value (≈ 1) is indicative of a spectral region dominated by noise or nonperiodic activity.

Figure 1 illustrates the MBE model estimates for two segments of voiced speech. The top graph plots the spectra (0 to 2 kHz) of a clean signal in bold, and its MBE approximation as a thin line. The MBE spectrum is assumed to be entirely periodic. Harmonic regions with voicing mixture errors below 0.15 are indicated by an ''×,'' while those above 0.15 are denoted by an ''○.'' Due to the periodic nature of the original speech segment, the MBE model closely tracks the signal spectrum, producing low mixture values. The lower graph illustrates the spectra achieved for the same segment of speech corrupted by room reverberations. Here, the periodic signal assumption is less appropriate as witnessed through inflated voiced/unvoiced mixture values for several of the harmonic regions.

For the MBE vocoder, these speech parameters (fundamental frequency, spectral amplitudes, and voiced/unvoiced mixture values) are used as a means of effectively parameterizing the speech segment for an efficient representation in speech-coding applications. Here, the voiced/unvoiced mixture errors in (8) will be utilized to evaluate the periodicity associated with spectral regions of each of the received signals, $X_1(\omega)$ and $X_2(\omega)$. Accordingly, the above parameter-estimation procedure is extended in a straightforward fashion to accommodate two signals. The fundamental frequency is jointly estimated by minimization of (7) summed over both channels. The pairs of harmonic voicing mixture errors, E_{m1} and E_{m2}, are then utilized to derive a weighting function for use with the GCC function in (1). A proposed weighting scheme is of the form

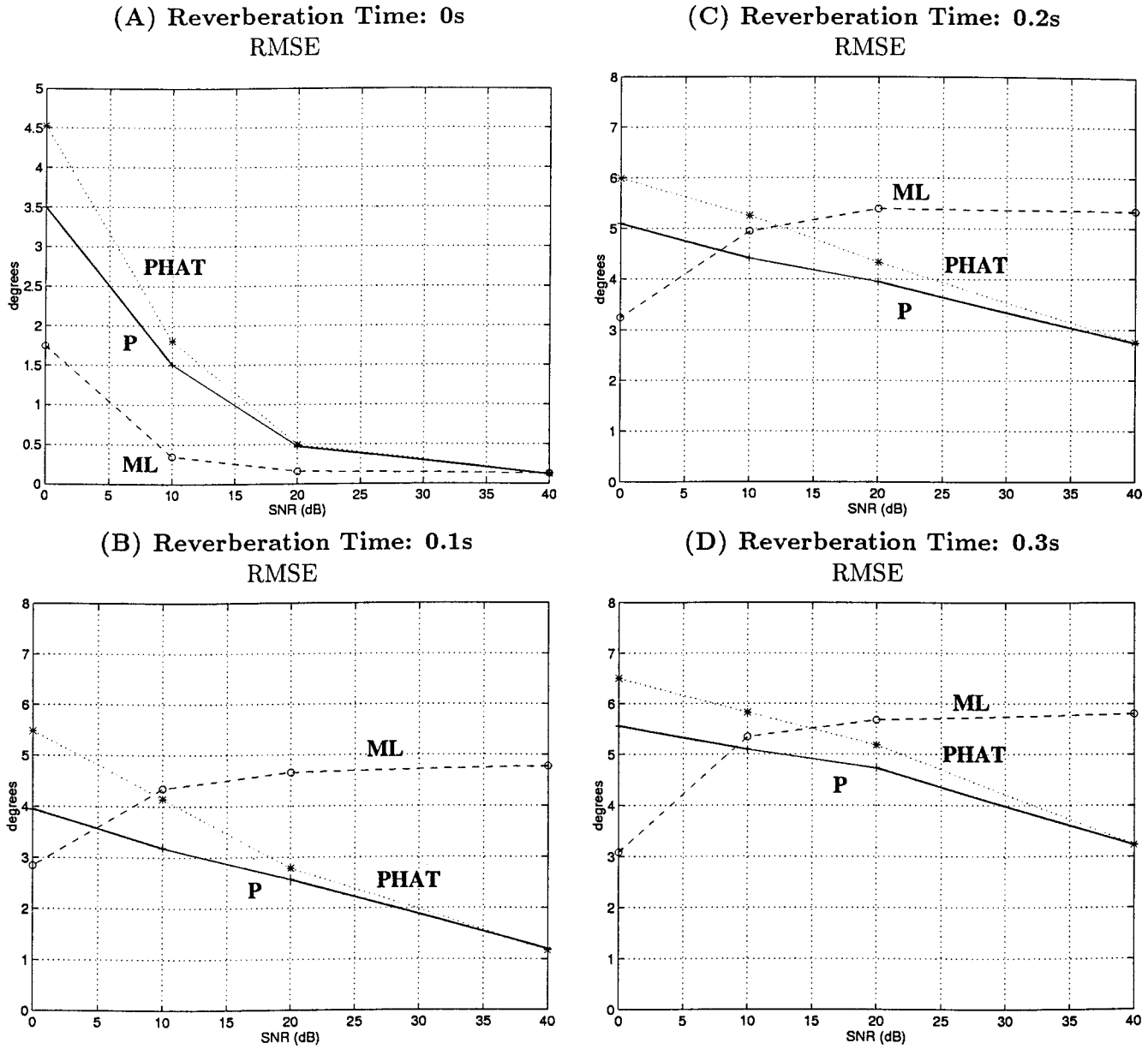

FIG. 4. Time-delay estimator simulation results: rms error trial statistics for source location #2.

$$W_P(\omega)=\frac{(1-\max\{E_{m1},E_{m2}\})^{\gamma}}{|X_1(\omega)X_2'(\omega)|},$$

$$\omega\in[(m-1/2)\hat{\omega}_0,(m+1/2)\hat{\omega}_0]. \tag{9}$$

This heuristically derived expression represents a frequency-dependent version of the phase transform, the distinction being that the spectral intervals for which both channels exhibit a strong voicing characterization will be emphasized over those which are more noise-like or mutually inconsistent. Based upon limited experimentation, a value of γ between 1 and 2 is effective.

III. EXPERIMENTAL ANALYSIS

The relative performance of the time-delay estimators was evaluated through a series of Monte Carlo trials in a simulated (4×7×2.75 m) rectangular room (illustrated in Fig. 2) with plane reflective surfaces and uniform, frequency-independent reflection coefficients. Room impulse responses were generated with the image model technique[12] using intrasample interpolation,[13] up to sixth-order reflections, and cardioid microphone patterns. Room reverberation times, T, ranged from 0 to 0.3 s. The corresponding reflection ratio, β, used by the image model, was calculated via Eyring's formula[14]

$$\beta=\exp(-13.82/[c(L_x^{-1}+L_y^{-1}+L_z^{-1})T]),$$

where L_x, L_y, and L_z are the room dimensions and c is the speed of sound in air (≈342 m/s). Three different source locations were considered corresponding to small, moderate, and large bearing angles relative to the microphone pair. Details of the simulation parameters are listed in Fig. 2.

For each combination of parameters, 165 segments of 20-kHz sampled voiced speech were convolved with the appropriate channel impulse response. White, zero-mean, Gaussian noise was added to the segments which were then

truncated to 45-ms analysis frames using a Hanning window. Signal-to-noise ratios were varied from 0 to 40 dB.

The GCC-based time-delay estimators were calculated from discrete-time versions of (1) through conventional processing techniques. A sampled version of the GCC function was computed with the FFT and the integer sample delay corresponding to the maximum of the GCC function was found. In practice, the domain of potential time delays was limited to possible values given the microphone separation. This coarse delay estimate was refined through quadratic interpolation.

Three different GCC-based time-delay estimators were evaluated: the ML-weighting (ML), the phase transform (PHAT), and the proposed pitch-based weighting scheme (P). Bias, variance, root-mean-square (rms) error, and % anomaly statistics were calculated over the ensemble of speech segments with each of the source locations, reverberation times, and SN ratio conditions. However, in the interest of brevity (and clarity), only the % anomaly and rms error statistics obtained for source #2 are presented. The % anomaly figures represent the percentage of estimates outside a 10 deg absolute error threshold. The rms error value incorporates the tradeoff between bias and variance into a single statistic. It was calculated using

$$\text{rms error} = \sqrt{\text{bias}^2 + \text{variance}}$$

of the nonanomalous time delays and then converted to a direction of arrival (DOA) in degrees. The plots in Figs. 3 and 4 represent the % anomaly and rms error-scores achieved for the three estimators as a function of SN ratio and reverberation time. The general results observed here are consistent with those obtained with the other source locations and statistical measures. In the noise-only case, plot (A), each of the estimators performs well at the high SN ratio levels. As expected, the ML estimator exhibits the best performance as the SN ratio level is decreased. The proposed estimator achieves results superior to those of the phase transform estimator. This illustrates the harmonic-dependent weighting function's ability to favorably emphasize regions of high SN ratio, though not to the degree achieved by the ML-weighting. Once channel multipath is included in the simulation environment, plots (B)–(D), several trends become clear. The ML estimator exhibits anomaly statistics that are relatively independent of SN ratio and increase with the reverberation time. The shortcomings of the SN ratio-only weighting in a reverberant environment are made clear from these plots. At the high-SN ratio levels, both the proposed and the phase transform estimators easily outperform their ML counterpart. While the two show nearly identical values in the lowest noise cases, the phase transform estimator is clearly more susceptible to the effects of increased noise. The proposed weighting scheme degrades more gracefully, achieving the best results of the three estimators at all but the lowest SN ratio conditions.

IV. DISCUSSION

As the preceding set of simulations illustrates, by emphasizing those spectral regions exhibiting a periodic structure, it is possible to achieve a GCC-based time-delay estimator that exhibits a degree of robustness to both additive noise and multipath conditions. The proposed weighting scheme outperforms the popular phase transform estimator, particularly under noisy conditions, and is significantly less susceptible to the effects of reverberation when compared to the ML-weighted estimator.

By exploiting known features of the signal of interest, in this case the periodicity of voiced speech, it is possible to achieve enhanced time-delay estimation performance. A logical extension to this approach would be to incorporate a more sophisticated model of the speech content (e.g., all-pole structure) into the estimation procedure. Also, while it is not considered here, this pitch-based approach would be attractive to the problem of multisource time-delay estimation. This could be achieved through the appropriate utilization of several simultaneous fundamental-frequency estimates, each corresponding to a specific source.

ACKNOWLEDGMENTS

Portions of this work have appeared in the 1997 IEEE ASSP Workshop on Applications of Signal Processing to Audio and Acoustics. The author wishes to thank the anonymous reviewers for their helpful suggestions.

[1] C. H. Knapp and G. C. Carter, ''The generalized correlation method for estimation of time delay,'' IEEE Trans. Acoust., Speech, Signal Process. **ASSP-24**(4), 320–327 (1976).
[2] M. Brandstein, J. Adcock, and H. Silverman, ''A practical time-delay estimator for localizing speech sources with a microphone array,'' Comput. Speech Lang. **9**, 153–169 (1995).
[3] M. Brandstein and H. Silverman, ''A practical methodology for speech source localization with microphone arrays,'' Comput. Speech Lang. **11**(2), 91–126 (1997).
[4] S. Bédard, B. Champagne, and A. Stéphenne, ''Effects of room reverberation on time-delay estimation performance,'' in *Proceedings of ICASSP 94*, pp. II-261–II-264 (IEEE, New York, 1994).
[5] M. Brandstein and H. Silverman, ''A robust method for speech signal time-delay estimation in reverberant rooms,'' in *Proceedings of ICASSP 97*, pp. 375–378, Munich, Germany, 20–24 April 1997 (IEEE, New York).
[6] M. Omologo and P. Svaizer, ''Use of the crosspower-spectrum phase in acoustic event localization,'' IEEE Trans. Speech Audio Process. **5**(3), 288–292 (1997).
[7] H. Wang and P. Chu, ''Voice source localization for automatic camera pointing system in videocenferencing,'' in *Proceedings of ICASSP 97*, pp. 187–190, Munich, Germany, 20–24 April 1997 (IEEE, New York).
[8] P. Svaizer, M. Matassoni, and M. Omologo, ''Acoustic source location in a three-dimensional space using crosspower spectrum phase,'' in *Proceedings of ICASSP 97*, pp. 231–234, Munich, Germany, 20–24 April 1997 (IEEE, New York).
[9] G. C. Carter, C. H. Knapp, and A. H. Nuttall, ''Estimation of the magnitude-squared coherence function via overlapped fast Fourier transform processing,'' IEEE Trans. Audio Electroacoust. **AU-21**(4), 337–344 (1973).
[10] D. Griffin and J. Lim, ''Multiband excitation vocoder,'' IEEE Trans. Acoust., Speech, Signal Process. **36**(8), 1223–1235 (1988).
[11] M. Brandstein, J. Hardwick, and J. Lim, ''The multi-band excitation speech coder,'' in *Advances in Speech Coding*, edited by B. S. Atal, V. Cuperman, and A. Gersho (Kluwer Academic, Norwell, MA, 1991).
[12] J. B. Allen and D. A. Berkley, ''Image method for efficiently simulating small room acoustics,'' J. Acoust. Soc. Am. **65**, 943–950 (1979).
[13] P. M. Peterson, ''Simulating the response of multiple microphones to a single acoustic source in a reverberant room,'' J. Acoust. Soc. Am. **80**, 1527–1529 (1986).
[14] H. Kuttruff, *Room Acoustics*, 3rd ed. (Elsevier, London, 1991).

An acoustical study of sound production in biphonic singing, Xöömij

Seiji Adachi[a)]
ATR Human Information Processing Research Laboratories, 2-2 Hikaridai, Seika, Kyoto 619-02, Japan

Masashi Yamada
Department of Musicology, Osaka University of Arts, Higashiyama, Kanan, Osaka 585, Japan

(Received 8 December 1997; revised 6 January 1999; accepted 19 January 1999)

A theory that the high melody pitch of biphonic singing, Xöömij, is produced by the pipe resonance of the rear cavity in the vocal tract is proposed. The front cavity resonance is not critical to the production of the melody pitch. This theory is derived from acoustic investigations on several three-dimensional shapes of a Xöömij singer's vocal tract measured by magnetic resonance imaging. Four different shapes of the vocal tract are examined, with which the melody pitches of F6, G6, A6, and C7 are sung, along with the F3 drone of a specific pressed voice. The second formant frequency calculated from each tract shape is close to the melody pitch within an error of 36 cents. Sounds are synthesized by convolving a glottal source waveform provided by the Rosenberg model with transfer functions calculated from the vocal tract shapes. Two pitches are found to be successfully perceived when the synthesized sounds are listened to. In a frequency range below 2 kHz, their spectra have a strong resemblance to those of the sounds actually sung. The synthesized sounds, however, fail to replicate the harmonic clustering at 4–5 kHz observed in the actual sounds. This is speculated to originate from the glottal source specific to the ''pressed'' timbre of the drone.
 [S0001-4966(99)00305-7]

PACS numbers: 43.75.Rs, 43.70.Aj [WJS]

INTRODUCTION

Biphonic singing, also known as throat-singing, is a vocal technique found in Central Asian cultures, by which one singer produces two voices with different pitches simultaneously. When listening to the performance, a high melody pitch can be perceived along with a low drone pitch. Xöömij, also transliterated variously as Khoomei, Xoomii, etc., is the name used in Mongolia and Tuva to describe this technique. In other regions, it may have other names. In this paper, we use Xöömij as the general term indicating all biphonic singing.

Up until now, two major theories have been proposed on the production of the two pitches by Xöömij singing: (1) The ''double-source'' theory,[1] which asserts the existence of a second sound source such as a whistlelike mechanism formed by the narrowing of the false vocal folds in addition to the true vocal fold vibration; and (2) the ''resonance'' theory,[2] which asserts that only a glottal sound source exists, but that a higher harmonic component is so emphasized by an extreme resonance of the vocal tract that it is segregated from the other components and heard as another pitch. The fact that the melody pitches producible by the singer are limited to the harmonic series of the drone supports the resonance theory. This has also been confirmed by a spectrum analysis of recorded Xöömij singing.[3] The resonance theory is thus currently considered to be consistent with the observations.

If the resonance theory is correct, the next question is: Which part of the vocal tract causes such an extreme resonance? Generally in biphonic singing, the singer divides his vocal tract into two cavities connected by a narrow opening using his tongue. Trân and Guillou[2] infer that both of the cavities contribute to the resonance producing the melody pitch. This is, however, just an inference from introspections of Trân as an amateur Xöömij singer and from their own spectrum analysis.

To answer the question posed above and to further test the resonance theory, the following procedures were performed: (1) measure the vocal tract shape while singing Xöömij; (2) examine the acoustical characteristics of the tract; and (3) synthesize sounds which can actually be perceived as two separate pitches by the listener. Following preliminary investigations,[4–7] this research verifies the resonance theory. We further propose a theory stating that the resonance of the rear cavity, that is from the glottis to the narrowing of the tongue, produces the Xöömij melody pitch. The resonance of the front cavity, that is from the articulation by the tongue to the mouth exit, is not critical to the production of the melody pitch.

I. VOCAL TRACT MEASUREMENT BY MRI

A method of measuring three-dimensional (3-D) shapes of the vocal tract using magnetic resonance imaging (MRI) is rapidly becoming established.[8] This method has an advantage in that it is noninvasive and is capable of obtaining tomographic images in any direction. It also poses no known danger to the human subject being imaged. The main disadvantage of using this method is that the scanning time for

[a)]Present address: Faculty of Information Science and Technology, Aichi Prefectural University, Nagakute, Aichi, 480-1198 Japan. Electronic mail: adachi@ist.aichi-pu.ac.jp

TABLE I. Measured frequencies (Hz) of the drone and the melody pitches of Xöömij tones, and of monophonic singing voices.

	Xöömij tones				Monophonic tones	
	F6	G6	A6	C7	Pressed	Normal
Drone	168.6	170.4	169.2	169.8	166.0	165.0
Melody	1349	1530	1698	2042	···	···

acquiring an image is a few tens of seconds to several minutes. Fortunately, this does not become a serious problem for the purpose of measuring stationary vocal tract shapes while long tones such as in Xöömij are being sung.

In our measurement, one male subject (S.K.), who is able to sing various Xöömij tones with a high degree of stability, was employed. He was instructed to produce four different Xöömij tones for measurement purposes. These tones have the same drone pitch of F3 and their melody pitches are F6, G6, A6, and C7. For comparison, measurements were also made for two ordinary monophonic tones of the vowel /ɑ/ sung by the same subject: One was phonated with a pressed voice as if producing the drone of Xöömij, and the other was phonated normally. No audio signal indicating the pitch was presented to the subject. All of the Xöömij and monophonic tones were sung at his own pitch, which was about 50 cents lower than the standard pitch of A4=440 Hz. Although intense scan noise was generated from the MRI equipment, the subject did not wear ear plugs. During the imaging process, we also recorded the singing tones. Note that these are not fit for the spectrum analysis, because of interference with the scan noise, but are sufficient for pitch detection. The detected sound frequencies of the melody and drone pitches of the Xöömij tones, and those of the monophonic tones are shown in Table I.

The equipment used for the measurements was a Shimazu Magnetic Resonance Tomograph SMT-100GUX (static magnetic field density of 1.0 T) with an anterior neck coil. For each image production, 33 axial slices from the glottis to the palate were taken. The major scanning parameters were a repetition time of 1010 ms, an echo time of 15 ms, and a slice thickness of 4 mm. There was no gap for imaging between slices. Each slice had a size of 258.1 mm $\times$258.1 mm and a pixel matrix of 256$\times$256. It took 153 s for one image acquisition. During the image scanning the subject was instructed to continue singing except for brief times (allowed for breathing). No pause in the scanning was taken while acquiring one image.

The 33 axial slices for each imaging sequence were interpolated by volume rendering software (VoxelView) to reconstruct the 3-D data. Two-dimensional slices in any (not necessarily the axial) direction can be reproduced from this data. Figure 1 shows the mid-sagittal slices of the vocal tracts for the four Xöömij tones and the two monophonic tones. We can see in Fig. 1(a)–(d) that the singer narrows his vocal tract by using the tongue tip and the palate to produce the Xöömij tones. The tract is, therefore, divided into two cavities. We call the one from the glottis to the narrowing the ''rear cavity,'' and the other from the narrowing to the mouth exit the ''front cavity.'' Note that the tongue tip moves toward the rear as the melody pitch is raised from F6 to C7. No such narrowing is found in the vocal tract shapes for the monophonic tones, regardless of the voice timbre [Fig. 1(e) and (f)].

The superimposed lines on each vocal tract in Fig. 1 show the upper boundary, lower boundary, and the mid-line of the tract. Line segments with a constant interval of 5.162 mm are also drawn perpendicular to the midline. The boundaries were estimated by hand first, and the mid-line was then extracted by the same algorithm used in Ref. 9. According to the positions and the angles of the line segments, cross-sectional slices were reproduced from the 3-D image data. Each slice was then analyzed to measure the area of the vocal tract at the position where that slice came from.

Figure 2 depicts the area functions, which indicate the cross-sectional areas as functions of the distance from the glottis along the mid-line, for all of the vocal tract shapes we measured for the Xöömij and monophonic tones. Table II lists numerical data for the area functions.

II. TRANSFER FUNCTIONS

The acoustic model employed in this paper is described in the Appendix. This model assumes the transmission of a one-dimensional wave along the axis of the vocal tract. To construct the model, we modified a model for calculating the input impedance of brass instruments, developed by Caussé *et al.*[10] The original model includes visco-thermal loss, i.e., loss due to the friction and thermal exchange between the air and the wall of the acoustic tube concerned, and loss due to the radiation from the exit. In our model, the same visco-thermal loss is considered. The radiation from the mouth is modeled by that from a piston with an infinite baffle. In addition to the losses above, our model includes the yielding wall effect[11] and loss due to the incomplete glottal closure.

Calculated volume velocity transfer functions for the Xöömij tones are depicted by solid lines in Fig. 3(a)–(d). The first and the second formant frequencies, and their bandwidths are listed in Table III(a). Note that the second formant frequencies for the F6, G6, A6, and C7 vocal tract shapes are 1356, 1562, 1692, and 2066 Hz, respectively. These values are close to the sound frequencies of melody pitches of recorded F6, G6, A6, and C7 Xöömij tones within an error of 36 cents. This implies that the melody pitch is produced by the resonance corresponding to the second formant. Transfer functions for the monophonic tones are depicted in Fig. 3(e) and (f). Their formant structures, especially the relations between the first and the second formant frequencies, are those typically observed in the phonation of the vowel /ɑ/.

To examine how the rear and front cavities of vocal tract shapes for Xöömij tones contribute to the resonance, we calculated the transfer functions of tract shapes whose front cavity had been removed, i.e., having only the rear cavity and the narrowing by the tongue. Data regarded as the ends of narrowing are underlined in Table II. Transfer functions without the front cavity are plotted by dashed lines in Fig. 3(a)–(d). We can see that the transfer functions without the front cavity have smaller magnitudes in the range of 2–3 kHz. This is because of the lack of the front cavity resonance, which should be in the same range and has a very

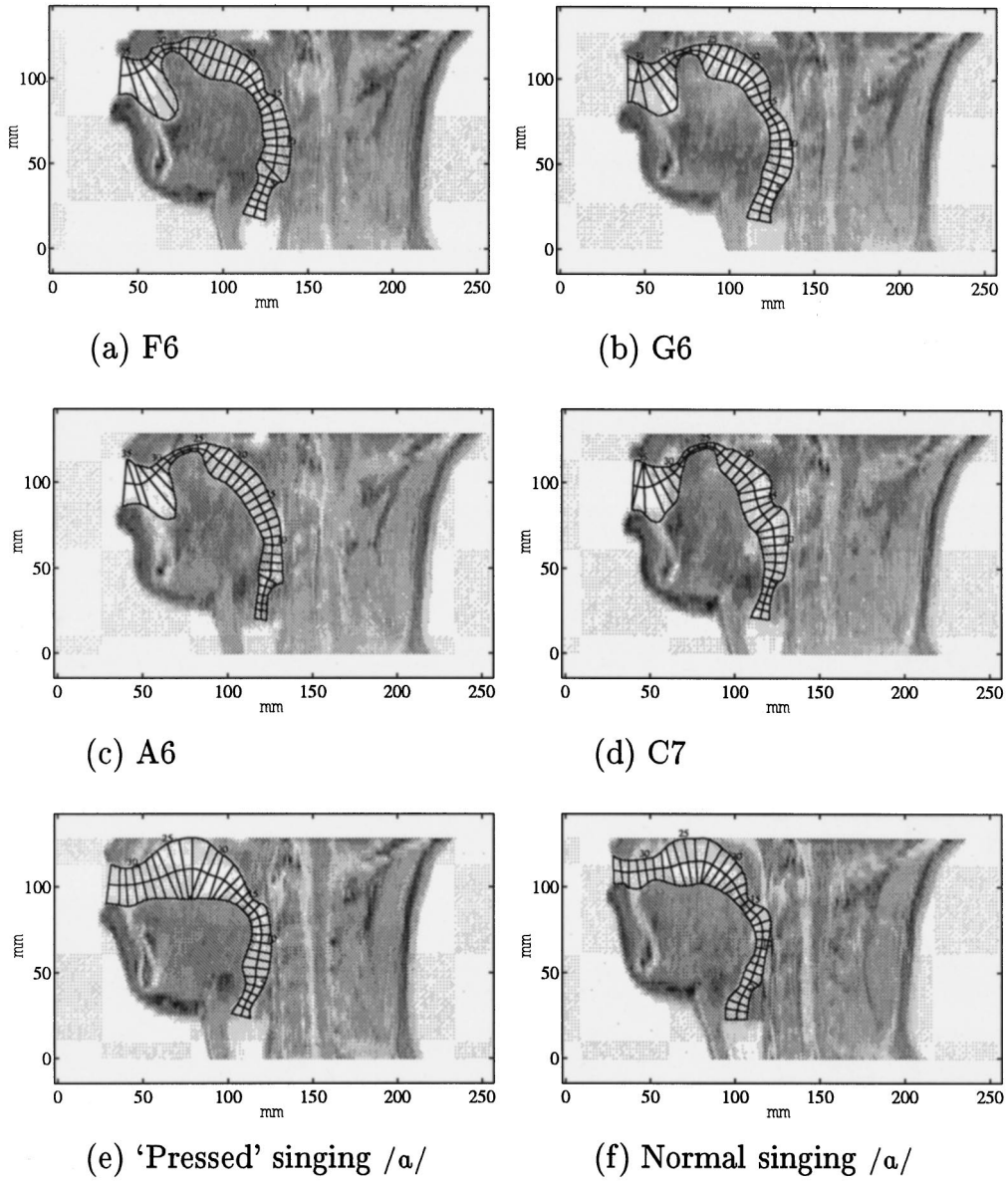

FIG. 1. Mid-sagittal slices of the vocal tract during the singing of various Xöömij [(a)–(d)] and monophonic [(e) and (f)] tones. Each slice is reproduced from a 3-D image obtained by MRI measurement. All of the Xöömij tones have the same drone pitch of F3. Their melody pitches are (a) F6, (b) G6, (c) A6, and (d) C7, respectively. The ordinary monophonic tones of the vowel /ɑ/, whose pitch is F3, were sung with a pressed voice in (e), and normally in (f).

large bandwidth. Small humps of the plots by the solid lines in Fig. 3(b) and (c), which are visible between the second and third formants, are evidence of this resonance.

In Table III(b), the first and the second formant frequencies, and their bandwidths of the transfer functions without the front cavity are listed. We find that the frequencies are hardly changed by the removal of the front cavity. This suggests that the fundamental formant structure is determined by the rear cavity resonance, and that the effect of the front cavity resonance on the structure is small. The second formant producing the Xöömij melody pitch can, therefore, be directly associated with the rear cavity resonance. The front cavity may assist the melody pitch by enhancing the magnitude of the formant peak. This effect becomes apparent for the C7 tone, whose melody pitch is closer to the 2–3 kHz range than the other tones. It will, however, be found in the next section that the enhancement is not critical to the production of the melody pitch.

To further investigate the relation between formants and resonance modes of the rear cavity, we utilized a method by which ''craftsmen'' often adjust the resonance frequencies of wind instruments, that is, we changed the original tract shape locally to see how the formant frequencies would be perturbed by the change. By reducing the cross-sectional area at several places in the vocal tract, the first and the second formant frequencies were calculated. The main observations were: The first formant frequency is not perturbed very much except for a reduction near the narrowing portion of the tract, whereas the second formant frequency is considerably decreased by reductions in the vicinity of data 12 to 16. The observations suggest that the Helmholtz resonance mode, which has no pressure node in the cavity, causes the first formant, and that the pipe resonance mode, which has one pressure node, causes the second formant. Consequently, we conclude that the pipe resonance mode of the rear cavity produces the Xöömij melody pitch.

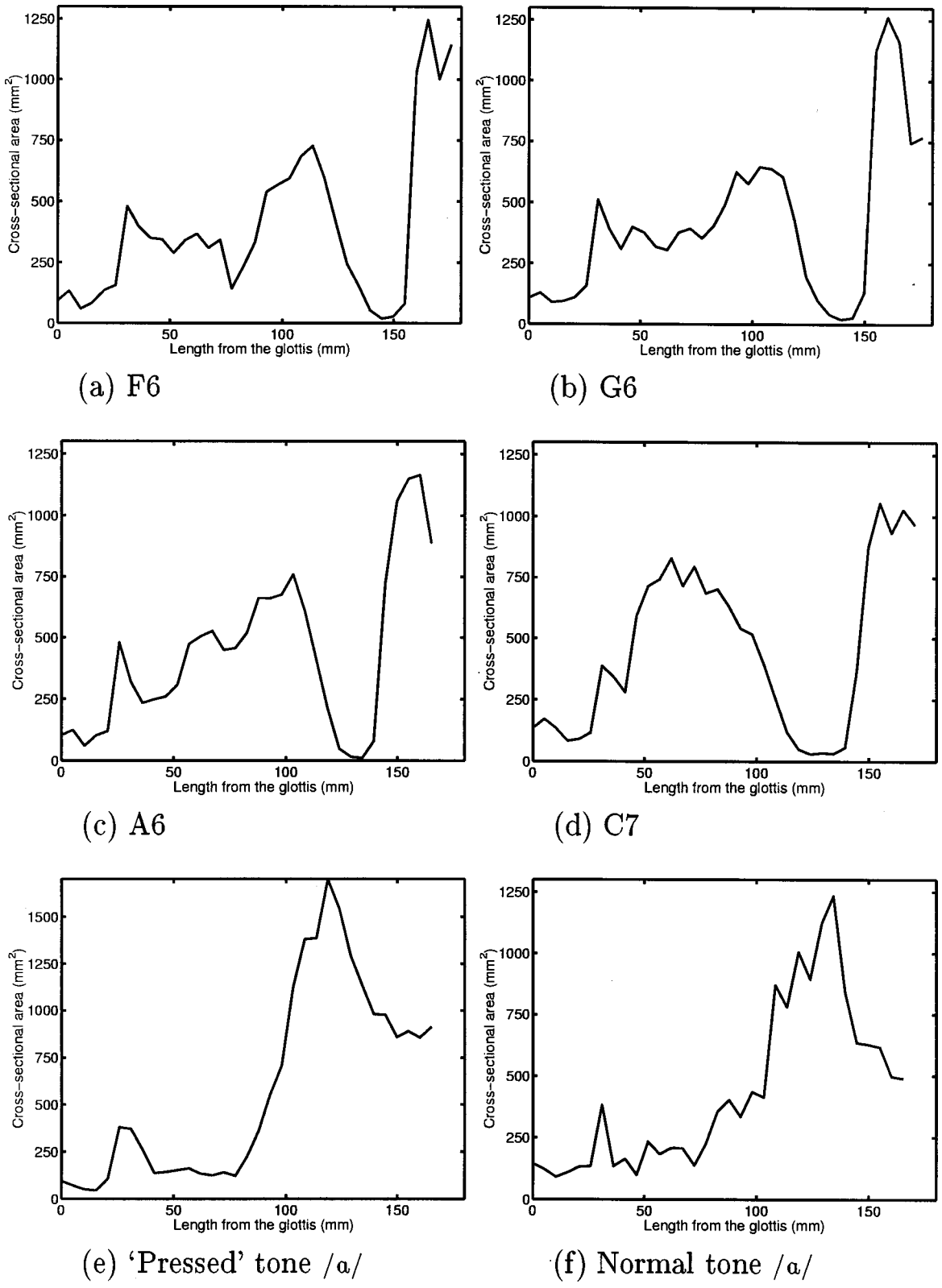

FIG. 2. Area functions of vocal tract shapes for Xöömij [(a)–(d)] and monophonic [(e) and (f)] tones.

III. SOUND SYNTHESIS

Let us investigate whether tones having two pitches can actually be reproduced by the transfer functions for the Xöömij tones obtained in the previous section. To this end, we synthesized tones using the acoustic tube model.

In this synthesis method, a glottal flow waveform is convolved with the transmission impulse response of the vocal tract, which is the inverse Fourier transformation of the pressure-to-velocity transfer function. Here we assume that the Rosenberg model,[12] capable of providing the glottal flow for various qualities of normal speech, can also be applied to

TABLE II. Equal interval (5.162 mm) area functions of vocal tract shapes for the Xöömij and monophonic tones. The data are listed in mm^2, and numbered from the input end to the mouth exit.

Data	F6	G6	A6	C7	Press	Norm
1	93	108	103	134	94	146
2	133	129	124	172	72	123
3	59	90	60	135	51	92
4	84	94	102	83	45	110
5	135	110	120	90	106	133
6	156	157	480	116	380	135
7	481	512	319	388	371	383
8	397	392	234	344	262	135
9	351	310	249	281	138	165
10	345	401	260	593	143	100
11	289	378	309	714	153	234
12	342	320	474	743	162	184
13	368	306	505	828	134	209
14	310	378	527	715	125	207
15	343	395	449	794	141	139
16	142	355	457	685	123	225
17	232	404	520	702	224	356
18	332	493	662	631	359	404
19	540	626	661	541	553	335
20	569	578	676	517	706	436
21	595	646	759	395	1127	414
22	684	639	612	256	1381	870
23	727	606	411	119	1386	780
24	598	429	211	50	1699	1005
25	418	196	49	30	1542	894
26	243	97	16	35	1289	1124
27	154	41	11	32	1133	1234
28	53	20	79	57	980	843
29	19	27	724	368	975	635
30	27	130	1059	875	859	628
31	80	1126	1149	1056	889	617
32	1030	1263	1165	931	856	498
33	1246	1160	887	1028	912	490
34	1001	744		966		
35	1143	767				

Xöömij singing. The glottal volume flow $U_g(t)$ for one oscillation period T is modeled by

$$U_g(t)=\begin{cases} \frac{1}{2}[1-\cos(\pi t/T_p)] & (0\leqslant t\leqslant T_p) \\ \cos(\pi(t-T_p)/2T_n) & (T_p\leqslant t\leqslant T_s), \\ 0 & \text{otherwise} \end{cases} \tag{1}$$

where T_p is the time for increasing the flow, and T_n is the time for decreasing the flow. The duty period T_s is the sum of T_p and T_n.

Figure 4(a) depicts an example ($T_s/T=0.4$ and $T_p/T_n=3.0$) of the modeled waveforms. To mimic the characteristic ''pressed'' timbre of the drone of Xöömij, we adjusted the parameter ratios as $T_s/T=0.2$ and $T_p/T_n=3.0$. As a result, $U_g(t)$ contains rich harmonics as shown in Fig. 4(b). The oscillation period T was set to the inverse of the fundamental frequency of the drone pitch.

Four synthesized Xöömij tones of 4.0-s duration, and of 48-kHz sampling, were produced from the F6, G6, A6, and C7 transfer functions. The spectra of these tones are presented in Fig. 5(a)–(d). The dashed lines drawn in the same figure are spectrum envelopes estimated by linear prediction (LP). To do the estimation, the tones of the 48-kHz sampling were down sampled to 12 kHz, and the number of LP coefficients was set to 20.

The fundamental frequencies and the formant data estimated from the synthesized tones are listed in Table IV(a). We find that the estimated formant frequencies are different from the formant frequencies directly derived from the transfer functions listed in Table III. The estimation errors of the first formant frequencies (F_1) of F6, G6, A6, and C7 tones are -108.7, -60.7, 120.9, and 62.3 cents, respectively. Those of the second formant frequencies (F_2) of F6, G6, A6, and C7 tones are -5.1, -37.0, 2.0, and -27.9 cents, respectively. By a simple test of listening to these synthesized tones, we could confirm that the same melody pitches heard when listening to the actual Xöömij tones are able to successfully be perceived in addition to the F3 drone.[13]

Using the same parameters of $T_s/T=0.2$ and $T_p/T_n=3.0$, a pressed monophonic tone was synthesized from the transfer function shown in Fig. 3(e). A normal monophonic tone was also synthesized from the transfer function shown in Fig. 3(f) with $T_s/T=0.4$ and $T_p/T_n=3.0$. The spectra of these synthesized monophonic tones (solid lines) and the envelopes (dashed lines) are depicted in Fig. 5(e) and (f). A simple listening test confirmed that these tones are able to be heard as phonations of the vowel of /ɑ/, but that their timbres differ slightly.[13]

We also synthesized tones from transfer functions calculated without the front cavity. Their spectra (solid lines) and the spectrum envelopes (dashed lines) are depicted in Fig. 6. The fundamental frequencies and the formant data are listed in Table IV(b).

The magnitudes of the second formants generally decrease due to the lack of the front cavity resonance. A simple listening test, however, showed that the melody pitches of all the tones (F6, G6, A6, and C7) are able to still be heard in addition to the drone. Consequently, we conclude that the melody pitch of the Xöömij tone is produced by the rear cavity resonance. The front cavity resonance may enhance the sensation of the melody pitch somehow, but this effect is not critical to the production of the pitch. A remaining issue is to quantitatively analyze to what extent the front cavity contributes to the sensation. In this case, a psychoacoustic experiment will probably be needed. This is, however, out of the scope of this paper.

The synthesized tones can be compared with tones actually sung by the same subject, S.K. The spectra (solid lines) and the estimated envelopes (dashed lines) of the Xöömij and monophonic tones are shown in Fig. 7. These were recorded separately from the MRI measurement, since the intense scan noise from the magnet interfered with the recording acceptable for spectrum analysis. The recording was done in an anechoic room, with a B&K 4003 microphone connected to a SONY DTC-A8 DAT recorder. The sampling rate was 48 kHz. During the recording, S.K. was in a supine position as he was in the MRI experiment.

In the frequency range up to around 2 kHz, where the first and the second formants appear, the spectra of the synthesized and recorded Xöömij tones for each pitch have a strong resemblance. In particular, the harmonic components

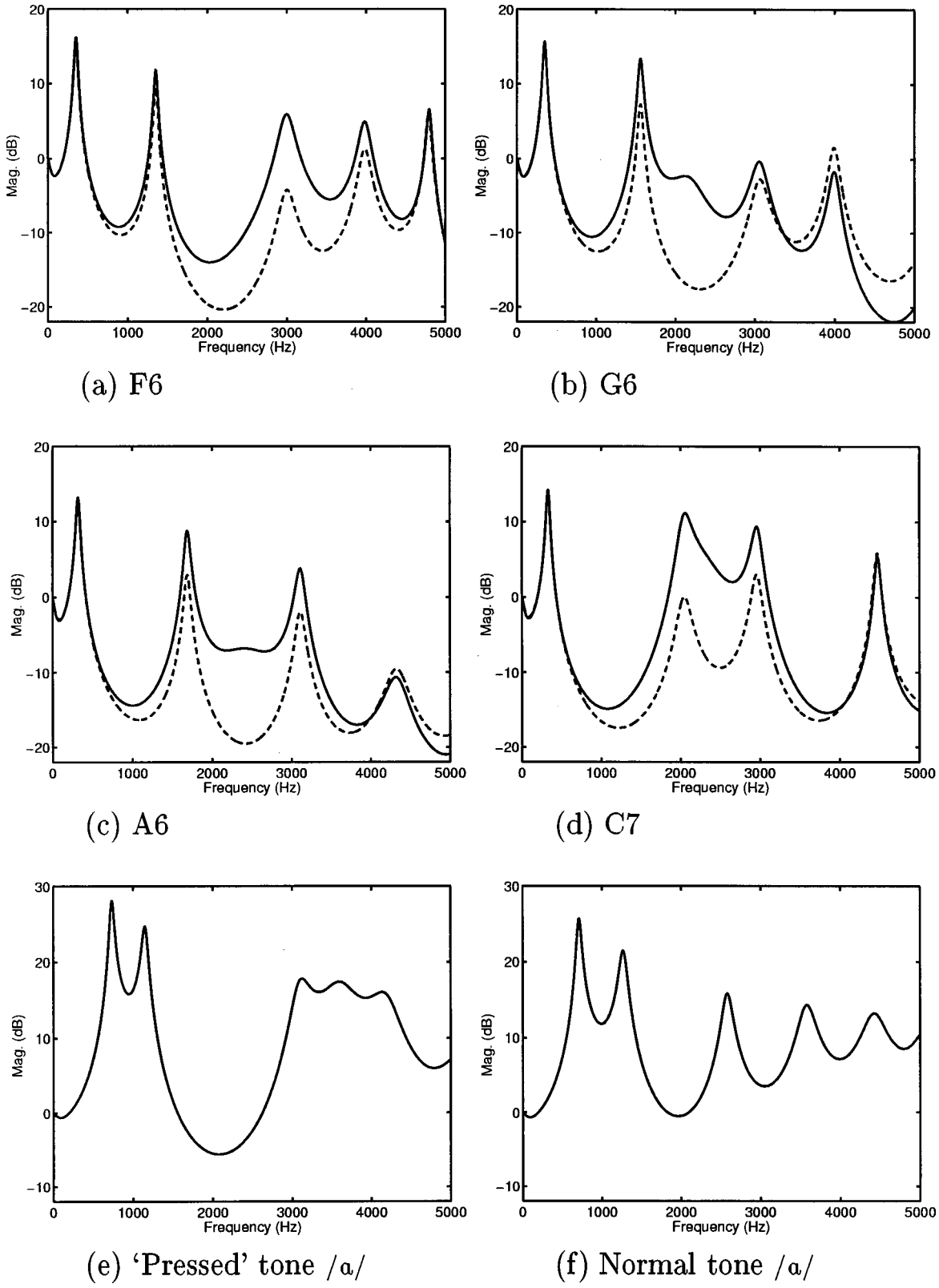

FIG. 3. Transfer functions of vocal tract shapes for Xöömij [(a)–(d)] and monophonic [(e) and (f)] tones. The solid lines denote those of entire vocal tract shapes. The dashed lines in (a)–(d) represent those of vocal tract shapes without the front cavity, i.e., having only the rear cavity and the narrowing by the tongue.

having the largest magnitudes in the second formant of the synthesized and recorded Xöömij tones are the same: the 8th, 9th, 10th, and 12th harmonics for the F6, G6, A6, and C7 Xöömij tones, respectively. It is these harmonic components that are segregated from the others and that can each be perceived as the melody pitch.

More minute observations can be made by comparing the formant data estimated from the synthesized tones listed

TABLE III. First and second formant frequencies (F_1,F_2), and their bandwidths (BW_1,BW_2) of transfer functions calculated for (a) Xöömij and monophonic vocal tract shapes, plus (b) Xöömij tract shapes without the front cavity. These are listed in Hz.

	Xöömij				Monophonic singing	
(a)	F6	G6	A6	C7	Pressed	Normal
F_1	358.3	353.7	324.8	333.0	738.3	714.5
BW_1	42.8	44.0	48.0	45.3	57.4	63.4
F_2	1356	1562	1692	2066	1151	1271
BW_2	48.0	64.8	78.4	233.4	78.6	103.3

	Xöömij, No front cavity			
(b)	F6	G6	A6	C7
F_1	355.0	353.7	323.3	333.1
BW_1	42.4	43.8	47.6	44.8
F_2	1355	1563	1690	2052
BW_2	47.8	63.0	77.3	182.4

in Table IV(a) with the data estimated from the recording tones listed in Table V. The F_1 differences between the synthesized and recorded tones of F6, G6, A6, and C7 are 4.1, 10.6, −13.0, and −54.0 cents, respectively. The F_2 differences for the F6, G6, A6, and C7 tones are −21.9, −36.6, −9.2, and −46.6 cents, respectively. These are acceptable values, because they are comparable with the estimation errors between the formant frequencies derived from the transfer functions and those estimated from the synthesized tones. On the other hand, the bandwidths estimated from the synthesized and recorded tones are roughly of the same order. In particular, a common tendency is observed for the second formant bandwidth (BW_2) to become larger as the melody pitch is increased. These observations provide general support for the parameters of the acoustic model we set for the calculations.

In the higher frequency range above 2 kHz, however, the spectra do not have a strong resemblance. The recorded Xöömij tones have less energy in the 2–4 kHz frequency range, and, in contrast, show a clustering of the harmonics in the range of 4–5 kHz. For the synthesized Xöömij tones, no such harmonic structures are found. Their spectra show smooth reductions of the harmonic levels due to the character of the glottal waveform, except for some modulation due to the formant structure. The spectrum difference in this frequency range is one of the reasons why the timbre of synthesized Xöömij tones is artificial and different from that of recorded tones.

The energy suppression at 2–4 kHz may be due to zeros in the transfer function. These are generally produced by cross-modes of propagation in the side branches of the vocal tract. The possible branches are the piriform fossa,[14] which is a pair of bilateral cavities in the hypopharynx, and the large volume under the tongue surface in the front cavity. Because we omitted the piriform fossa, and assumed no cross-mode propagation in the front cavity, this effect did not appear in the spectra of the synthesized tones.

Let us find the cause of the harmonic clustering in the range of 4–5 kHz. A similar clustering can be found in the recorded pressed monophonic tone [Fig. 6(e)]. On the other hand, no such clustering can be observed in the recorded normal monophonic tone [Fig. 6(f)]. It is therefore probable that the energy concentration at 4–5 kHz found in the Xöömij and pressed monophonic tones is due to the glottal flow waveform characterizing the ''pressed'' timbre, rather than due to the resonance characteristics of the vocal tract.

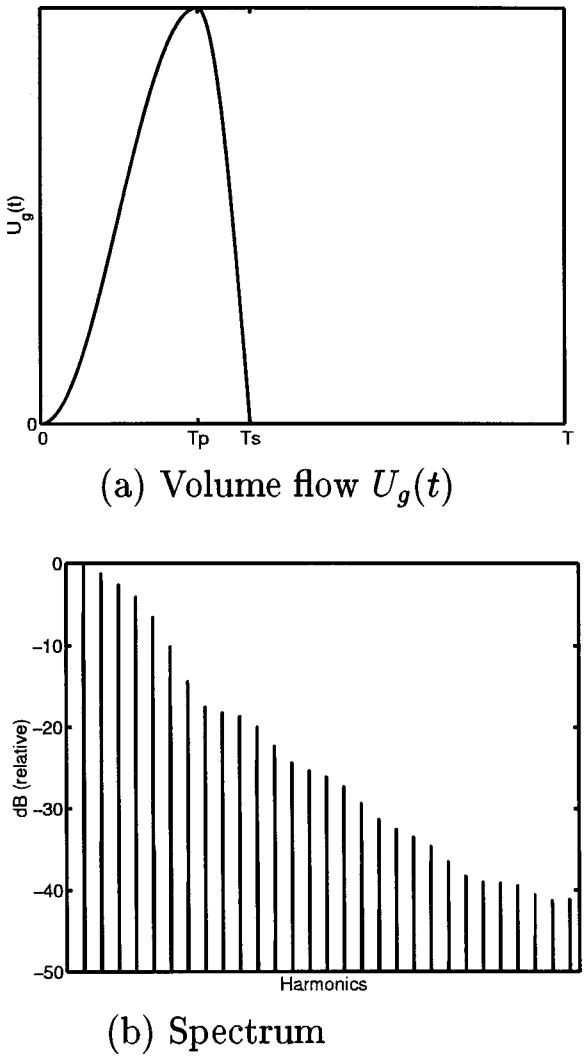

FIG. 4. A glottal flow waveform (a) and a sound spectrum (b) assumed by the Rosenberg source model. The parameters are $T_s/T=0.4$ and $T_p/T_n=3.0$ in (a), and $T_s/T=0.2$ and $T_p/T_n=3.0$ in (b).

The above comparison between the pressed and normal tones leads us to speculate as to the reason why the reproduction of the sound spectra of the Xöömij tones failed in the high frequency range. This is probably because the glottal waveform for Xöömij singing has spectral peaks in a specific frequency range, which cannot be provided by the Rosenberg glottal source model. We believe that future studies should contain refinements of the source modeling to obtain a better agreement of the spectrum in the high frequency range. To estimate the actual glottal waveform for Xöömij singing, an inverse filtering method may be useful, such as the two-pass method[15] used to clarify the relation between the voice quality and the vocal fold vibratory pattern. A dynamical model of the vocal fold vibration, such as the two-mass model,[16] may also be helpful in seeing how the glottal waveform is

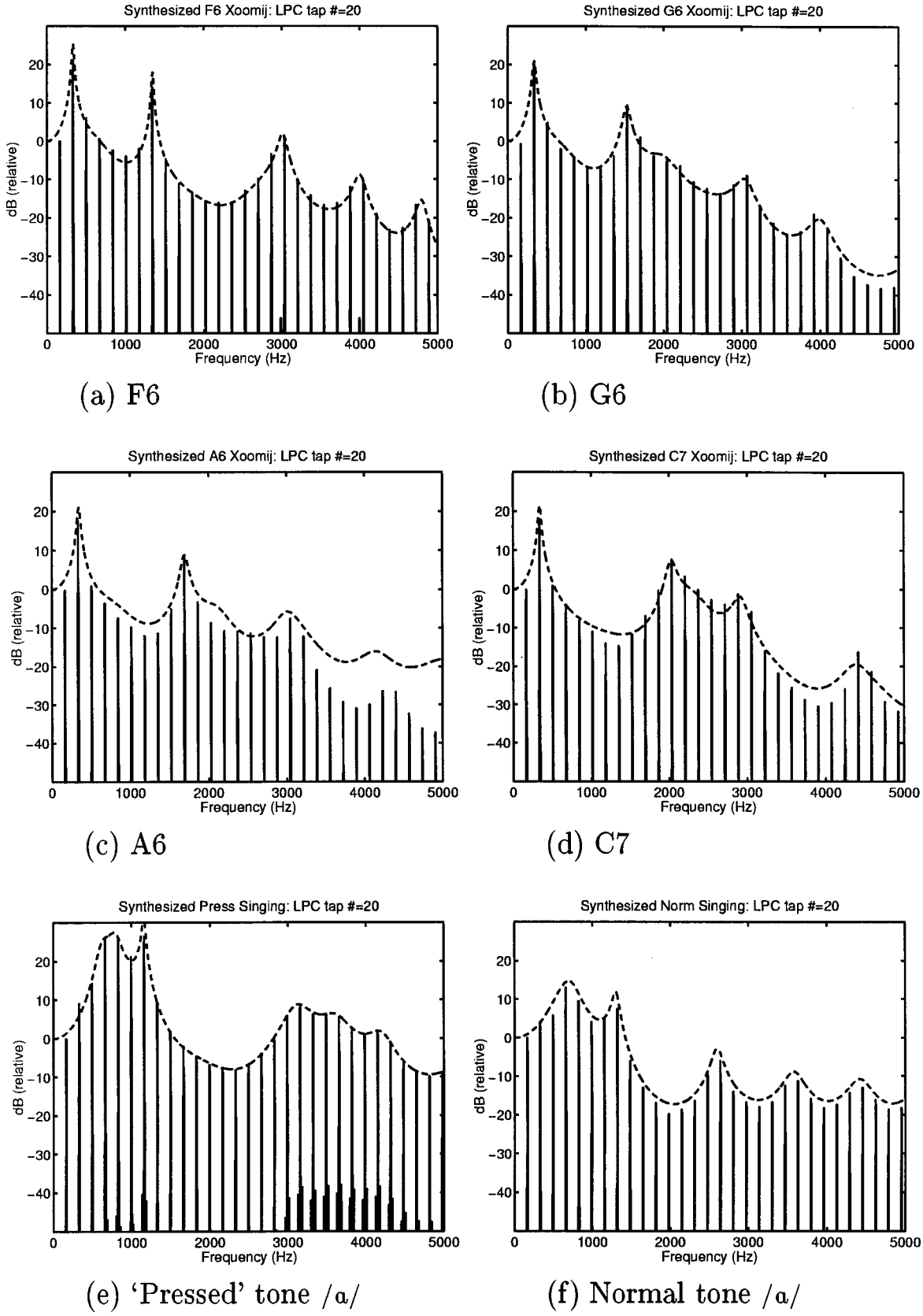

FIG. 5. Sound spectra of Xöömij [(a)–(d)] and monophonic [(e) and (f)] tones synthesized by the acoustic tube model. The 8th harmonic in (a), the 9th in (b), the 10th in (c), and the 12th in (d) are enhanced by the second formant resonances. These can each be heard as the melody pitch separated from the others composing a complex tone of the drone pitch.

TABLE IV. Fundamental frequencies (F_0), first and second formant frequencies (F_1,F_2), and their bandwidths (BW_1,BW_2) of (a) synthesized Xöömij and monophonic tones, plus (b) Xöömij tones synthesized without the front cavity. These are listed in Hz.

	Xöömij tones				Monophonic tones	
(a)	F6	G6	A6	C7	Pressed	Normal
F_0	168.6	170.4	169.2	169.8	166.0	165.0
F_1	336.5	341.5	348.3	345.2	778.1	696.9
BW_1	25.8	42.7	39.7	35.5	253.1	257.7
F_2	1352	1529	1694	2033	1159	1301
BW_2	25.1	93.8	88.7	135.3	41.2	93.5

	Xöömij tones, No front cavity			
(b)	F6	G6	A6	C7
F_0	168.6	170.4	169.2	169.8
F_1	336.6	346.8	336.9	345.1
BW_1	24.9	41.9	40.7	37.3
F_2	1354	1529	1702	2029
BW_2	26.5	137.0	74.9	169.4

affected by the acoustic response of the vocal tract for Xöömij singing.

IV. CONCLUSION

To examine the sound production of biphonic singing, Xöömij, we measured 3-D shapes of the vocal tract, while our subject sang, using the MRI method. Transfer functions were calculated from the measured vocal tract shapes. It was found that the second formant frequency of each tract shape was close to the fundamental frequency of the melody pitch within an error of 36 cents. Tones were also reproduced from the transfer functions by synthesis based on the acoustic tube model. Two pitches could successfully be perceived when the synthesized sounds were listened to. In conclusion, we proposed a theory stating that the high melody pitch is produced by the pipe resonance of the rear cavity in the vocal tract.

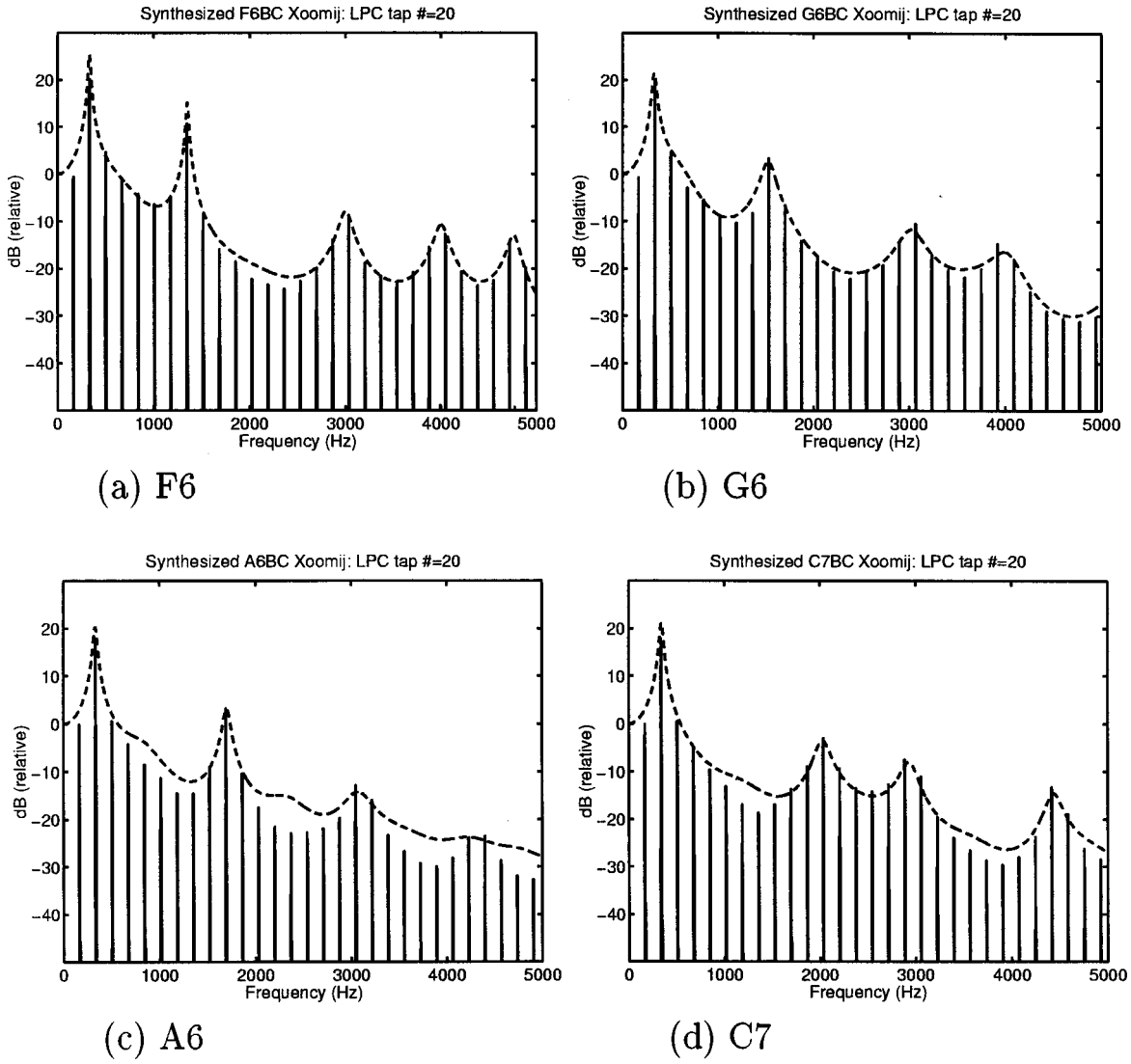

FIG. 6. Sound spectra of Xöömij tones synthesized from vocal tract shapes without the front cavity. The same harmonic component in each of (a)–(d) as in Fig. 5 are enhanced by the second formant resonances. Although the magnitudes of the components are reduced due to the lack of the front cavity resonance, each of these is still heard as the melody pitch.

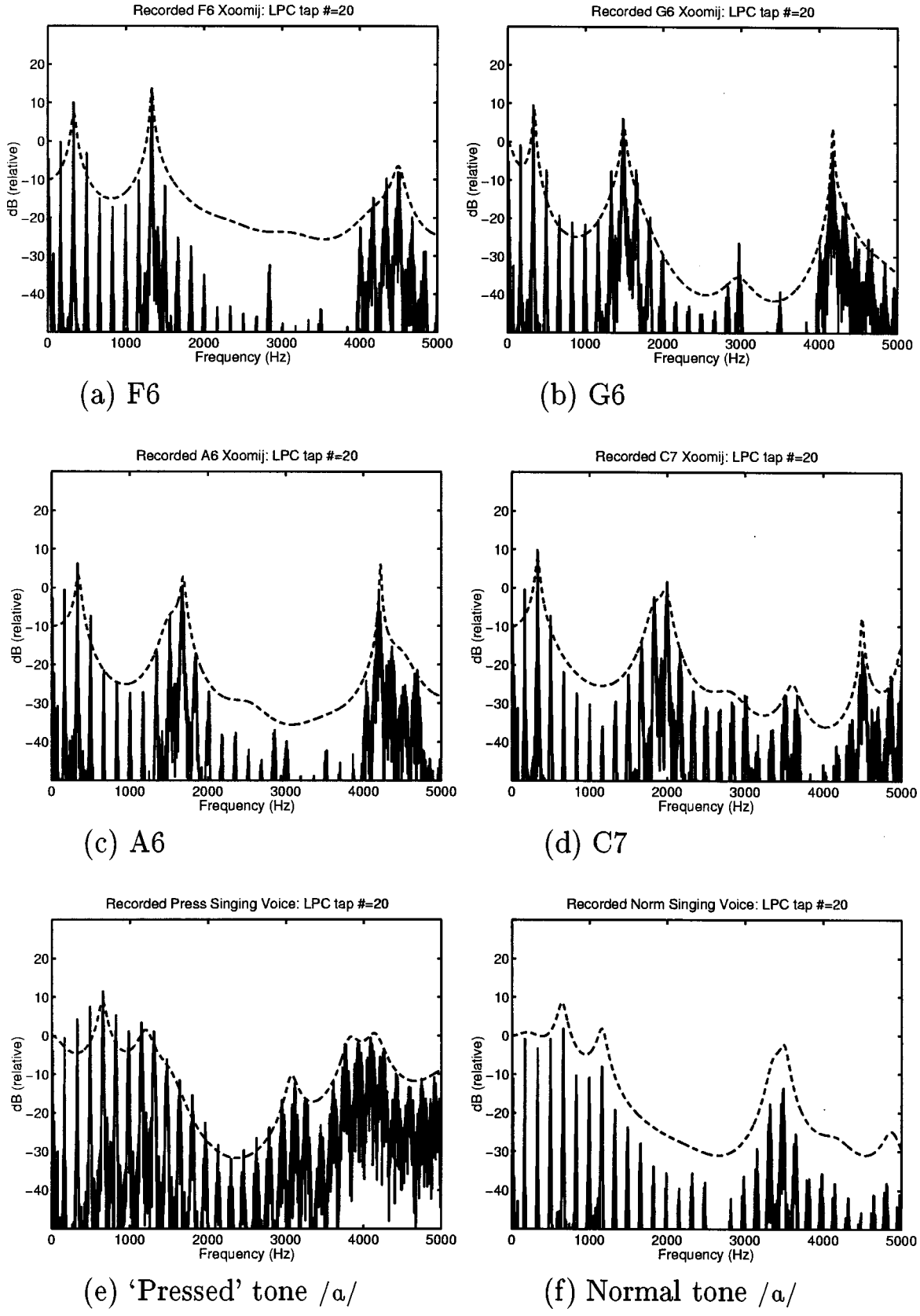

FIG. 7. Sound spectra of Xöömij [(a)–(d)] and monophonic [(e) and (f)] tones actually produced by the subject singer. The largest harmonic components in the second formant are the 8th, 9th, 10th, and 12th in (a), (b), (c), and (d), respectively. Clustering of the harmonics at 4–5 kHz is found for the Xöömij [(a)–(d)] tones and the monophonic pressed [(e)] tone. No such clustering is found for the monophonic normal [(f)] tone.

TABLE V. F_0, F_1, F_2, BW_1, and BW_2 of recorded Xöömij and monophonic tones. Listed in Hz.

	Xöömij tones				Monophonic tones	
	F6	G6	A6	C7	Pressed	Normal
F_0	167.8	167.4	168.7	167.8	164.7	166.7
F_1	337.3	343.6	345.7	334.6	652.0	645.6
BW_1	54.5	27.0	57.7	48.9	90.4	106.2
F_2	1335	1497	1685	1979	1200	1158
BW_2	30.2	54.0	53.8	179.9	194.2	114.3

This research clarifies the nature of the production mechanism of Xöömij, and this finding is verified through the synthesis of sounds actually having two pitches. It should be noted, however, that the synthesis was not at such a level that the timbre of the sound could be completely reproduced, and therefore, future studies should focus on the modeling of the glottal source.

The psycho-acoustical aspect of why a harmonic component emphasized by an extreme resonance of the vocal tract is segregated by the auditory system is another issue. Reference 17 addresses this problem.

ACKNOWLEDGMENTS

The authors are grateful to Yasuhiro Shimada and Ichiro Fujimoto of Takanohara Chuo Hospital for their helpful collaboration in the MRI measurements, to Shinobu Masaki for his useful suggestions on the image processing, to Jianwu Dang for his valuable discussions on the calculated transfer functions, and to Shinji Maeda of CNRS for letting the authors realize the importance of the glottal impedance.

APPENDIX: ACOUSTIC MODEL

Wave propagation in the vocal tract

We use the same values for the air constants as used in Ref. 10. Some of them are dependent on the air temperature T. In this paper, we set $T=25$ degrees Celsius for the vocal tract. The values of the constants are:

Speed of sound, $c=331.45(1+0.0018T)$ m/s.
Air density, $\rho=1.2929(1-0.0037\mathrm{T})$ kg/m^3.
Viscosity coefficient,
$\mu=1.708\times10^{-5}(1+0.0029T)$ kg/(s·m).
Thermal conductivity,
$d=5.77\times10^{-3}(1+0.0033T)$ cal/(m·s·°C).
Specific heat at constant pressure, $C_p=240$ cal/kg·°C.
Specific heat ratio, $\gamma=C_p/C_v=1.402$.

The yielding wall of the vocal tract can be modeled as a damped spring-mass system.[11] Three parameters characterizing the mechanical property of the vocal tract wall are:

Lowest angular resonance frequency of the tract when closed at both ends, $\omega_0=406/\pi$ rad/s, which is inversely proportional to the square root of the wall mass per unit length.
Ratio of the wall resistance to the mass,
$a=130\pi$ rad/s.
Squared angular frequency of the mechanical resonance, $b=(30\pi)^2$ (rad/s)^2.

The following symbols are also defined:

Angular frequency, ω rad/s.
Pipe radius, γ.
Ratio of the pipe radius to the viscous boundary layer thickness, $r_v=r\sqrt{\omega\rho/\mu}$.
Ratio of the pipe radius to the thermal boundary layer thickness, $r_t=r\sqrt{\omega\rho C_p/\lambda}$.

The vocal tract can be considered as a succession of finite elements, each of which is a truncated cone. In each element, pressure $p(x)$ and particle velocity $u(x)$ satisfy the following one-dimensional wave equations:

$$\frac{\partial p}{\partial x}(x)=-Z_v u(x), \tag{A1}$$

$$\frac{\partial u}{\partial x}(x)=-(Y_t+Y_w)p(x)-\frac{2}{x}u(x), \tag{A2}$$

where x is the distance along the axis from the apex of the cone, Z_v is the series impedance per unit length including the viscous effect, Y_t is the shunt admittance per unit length including the thermal exchange, and Y_w is the shunt admittance per unit length due to the yielding wall. These are assumed to be constant over the length of the truncated cone, and modeled by

$$Z_v=i\omega\rho\left(1+\frac{2}{r_v}(1-i)-\frac{3i}{r_v^2}\right), \tag{A3}$$

$$Y_t=\frac{i\omega}{\rho c^2}\left[1+(\gamma-1)\left(\frac{\sqrt{2}}{r_t}(1-i)+\frac{i}{r_t^2}\right)\right], \tag{A4}$$

$$Y_w=\frac{i\omega}{\rho c^2}\,\frac{\omega_0^2}{b+i\omega a-\omega^2}, \tag{A5}$$

respectively. To calculate r_v and r_t in Eqs. (A3) and (A4), the pipe radius r is regarded as the arithmetic mean of the radii of the two ends. The propagation constant Γ and the wave impedance ζ become

$$\Gamma=\sqrt{Z_v(Y_t+Y_w)}, \tag{A6}$$

$$\zeta=\sqrt{\frac{Y_t+Y_w}{Z_v}}, \tag{A7}$$

respectively. Integrating Eqs. (A1) and (A2) from one end at x_1 to the other at x_2, we have the following transmission matrix equation:

$$\begin{bmatrix}p_2\\u_2\end{bmatrix}=L^{-1}(x_2)ML(x_1)\begin{bmatrix}p_1\\u_1\end{bmatrix}, \tag{A8}$$

where

$$L(x)=\begin{bmatrix}x & 0\\ -\dfrac{1}{Z_v} & x\end{bmatrix}, \tag{A9}$$

$$M=\begin{bmatrix} \cosh\Gamma(x_1-x_2) & \zeta\sinh\Gamma(x_1-x_2) \\ \frac{1}{\zeta}\sinh\Gamma(x_1-x_2) & \cosh\Gamma(x_1-x_2) \end{bmatrix}. \quad \text{(A10)}$$

Multiplying the transmission matrices of all elements, we have an equation relating pressure p_{in} and particle velocity u_{in} at the input end of the vocal tract with pressure p_{out} and particle velocity u_{out} at the output end as follows:

$$\begin{bmatrix} p_{\text{in}} \\ u_{\text{in}} \end{bmatrix}=\hat{M}\begin{bmatrix} p_{\text{out}} \\ u_{\text{out}} \end{bmatrix}, \quad \text{(A11)}$$

where

$$\hat{M}=\prod_{\text{all elements}} L^{-1}ML\equiv\begin{bmatrix} m_{11} & m_{12} \\ m_{21} & m_{22} \end{bmatrix}. \quad \text{(A12)}$$

The input and output volume velocities are defined by

$$U_{\text{in}}=A_{\text{in}}u_{\text{in}}, \quad U_{\text{out}}=A_{\text{out}}u_{\text{out}}, \quad \text{(A13)}$$

respectively, where A_{in} and A_{out} are the areas of the input and output ends, respectively.

Radiation load

The radiation at the output end, i.e., the mouth, can be modeled by the radiation from a round piston head surrounded by an infinite baffle. In the low frequency range up to a few kHz, where the wavelength is sufficiently larger than the length characterizing the size of the mouth, the radiation impedance Z_r is approximated by a lumped acoustic resistance R_r and an inductance L_r (Ref. 18) as follows:

$$Z_r\equiv\frac{p_{\text{out}}}{U_{\text{out}}}=\frac{\zeta}{A_{\text{out}}}\frac{i\omega R_rL_r}{R_r+i\omega L_r}, \quad \text{(A14)}$$

where

$$R_r=\frac{128}{9\pi^2}, \quad L_r=\frac{8\sqrt{A_{\text{out}}}}{3\pi^{3/2}c}. \quad \text{(A15)}$$

By substituting Eqs. (A13) and (A14) into Eq. (A11), the volume velocity transfer function, pressure-to-velocity transfer function and input impedance of the vocal tract become

$$T_U\equiv\frac{U_{\text{out}}}{U_{\text{in}}}=\frac{A_{\text{out}}}{A_{\text{in}}}\frac{1}{m_{21}Z_rA_{\text{out}}+m_{22}}, \quad \text{(A16)}$$

$$T_{p/U}\equiv\frac{p_{\text{out}}}{U_{\text{in}}}=\frac{A_{\text{out}}}{A_{\text{in}}}\frac{Z_r}{m_{21}Z_rA_{\text{out}}+m_{22}}, \quad \text{(A17)}$$

$$Z_{\text{in}}\equiv\frac{p_{\text{in}}}{U_{\text{in}}}=\frac{1}{A_{\text{in}}}\frac{m_{11}Z_rA_{\text{out}}+m_{12}}{m_{21}Z_rA_{\text{out}}+m_{22}}, \quad \text{(A18)}$$

respectively.

Glottal impedance

In voice synthesis based on the acoustic tube model, a glottal volume velocity U_g is provided by a source model, e.g., the Rosenberg model. In a physical sense, U_g is a flow generated by a constant subglottal pressure p_0 when the supraglottal pressure is zero. Bernoulli's law yields

$$U_g=\sqrt{\frac{2p_0}{\rho}}A_g, \quad \text{(A19)}$$

where A_g is the glottal area made by the vocal folds. Note here that U_g is different from volume velocity U_{in} at the entrance of the vocal tract, because of the presence of p_{in}. To find the difference, we again use Bernoulli's law to obtain

$$U_{\text{in}}=\sqrt{\frac{2(p_0-p_{\text{in}})}{\rho}}A_g. \quad \text{(A20)}$$

By considering small-amplitude oscillation, and by noting that U_{in}, U_g, and A_g have both the time-averaged component and time-varying component, whereas p_{in} has only the time-varying component, we can linearize Eq. (A20) as follows:

$$U_{\text{in}}=U_g-\frac{p_{\text{in}}}{Z_g}, \quad \text{(A21)}$$

where Z_g is the glottal impedance defined by

$$Z_g=\frac{\sqrt{2p_0\rho}}{A_g}, \quad \text{(A22)}$$

and where $\overline{A_g}$ is the average area of A_g. The second term on the r.h.s. of Eq. (A21) implies that a reverse flow toward upstream is generated, which is proportional to p_{in}. The ratio of p_{in} to the flow is equal to Z_g.

To estimate the value of Z_g, we assumed the typical p_0 and $\overline{A_g}$ to be

$$p_0=10\ \text{cmH}_2\text{O}, \quad \overline{A_g}=0.5\times10^{-2}A_{\text{in}}, \quad \text{(A23)}$$

respectively.

From Eqs. (A16), (A18), and (A21), the volume velocity transfer function of the entire system including the vocal tract and the glottis becomes

$$\hat{T}_U\equiv\frac{U_{\text{out}}}{U_g}=\frac{T_U}{1+Z_{\text{in}}/Z_g}. \quad \text{(A24)}$$

Similarly, the pressure-to-velocity transfer function of the entire system becomes

$$\hat{T}_{p/U}\equiv\frac{p_{\text{out}}}{U_g}=\frac{T_{p/U}}{1+Z_{\text{in}}/Z_g}. \quad \text{(A25)}$$

In this paper, we calculated $\hat{T}_U$ to discuss the acoustic properties of the vocal tract, and used the time-domain representation of $\hat{T}_{p/U}$ for synthesis.

[1] B. Chernov and V. Maslov, ''Larynx—Double-sound generator,'' Proc. 11th Int. Conf. of Phonetic Science, Tallinn, Estonia, pp. 40–43 (1987).

[2] Q. H. Trân and D. Guillou, ''Original research and acoustical analysis in connection with the Xöömij style of biphonic singing,'' in *Musical Voices of Asia* (Heibonsha, Tokyo, 1980), pp. 162–173.

[3] T. Muraoka, K. Wagatsuma, and M. Horiuchi, ''Acoustic analysis of the Mongolian singing Xöömij,'' Proc. Fall Meet. Acoust. Soc. Jpn., pp. 385–386 (1983) (in Japanese).

[4] S. Adachi, S. Kinoshita, H. Tamagawa, and M. Yamada, ''MRI measurement of the vocal-tract shape while singing Xöömij and the synthesis based on the acoustic tube model,'' Tech. Rep. Musical Acoustics **MA96-10**, 9–16 (1996) (in Japanese).

[5] S. Adachi, S. Kinoshita, T. Komoike, H. Tamagawa, and M. Yamada, ''Study on sound production in Xöömij—Part 1: MRI measurement of the vocal-tract shape and the synthesis based on the acoustic tube model,''

Proc. Spring Meet. Acoust. Soc. Jpn., pp. 645–646 (1996) (in Japanese).
[6] T. Komoike, S. Kinoshita, M. Yamada, S. Adachi, and I. Nakayama, ''Study on sound production in Xöömij—Part 2: Perceptual experiment with synthesized sound,'' Proc. Spring Meet. Acoust. Soc. Jpn., pp. 647–648 (1996) (in Japanese).
[7] S. Adachi and M. Yamada, ''An acoustical study of sound production in biphonic singing, Xöömij,'' Proc. 1997 Japan-China Joint Meeting on Musical Acoustics, pp. 21–26 (1997).
[8] B. H. Story, I. R. Titze, and E. A. Hoffman, ''Vocal tract area functions from magnetic resonance imaging,'' J. Acoust. Soc. Am. **100**, 537–554 (1996).
[9] J. Dang, K. Honda, and H. Suzuki, ''Morphological and acoustical analysis of the nasal and the paranasal cavities,'' J. Acoust. Soc. Am. **96**, 2088–2100 (1994).
[10] R. Caussé, J. Kergomard, and X. Lurton, ''Input impedance of brass musical instruments—Comparison between experiments and numerical models,'' J. Acoust. Soc. Am. **75**, 241–254 (1984).
[11] M. M. Sondhi and J. Schroeter, ''A hybrid time-frequency domain articulatory speech synthesizer,'' IEEE Trans. Acoust., Speech, Signal Process. **ASSP-35**, 955–967 (1987).
[12] A. E. Rosenberg, ''Effect of glottal pulse shape on the quality of natural vowels,'' J. Acoust. Soc. Am. **49**, 583–590 (1971).
[13] The synthesized tones can be heard on the World Wide Web at http://www.hip.atr.co.jp/~adachi/Xoomij/Sound/.
[14] J. Dang and K. Honda, ''Acoustic characteristics of the piriform fossa in models and humans,'' J. Acoust. Soc. Am. **101**, 456–465 (1997).
[15] D. G. Childers and C. K. Lee, ''Vocal quality factors: Analysis, synthesis, and perception,'' J. Acoust. Soc. Am. **90**, 2394–2410 (1991).
[16] K. Ishizaka and J. L. Flanagan, ''Synthesis of voiced sounds from a two-mass model of the vocal cords,'' Bell Syst. Tech. J. **51**, 1233–1268 (1972).
[17] M. Yamada, ''Stream segregation in Mongolian traditional singing, Xöömij,'' Proc. Int. Sym. Musical Acoustics, Dourdan, pp. 540–545 (1995).
[18] J. L. Flanagan, *Speech Analysis, Synthesis and Perception*, 2nd ed. (Springer-Verlag, New York, 1972), Chap. 3, pp. 36–38.

Messa di voce: An investigation of the symmetry of crescendo and decrescendo in a singing exercise

Ingo R. Titze
National Center for Voice and Speech and Department of Speech Pathology and Audiology, The University of Iowa, Iowa City, Iowa 52242-1012

Russel Long
National Center for Voice and Speech and Wilber James Gould Voice Research Center, The Denver Center for the Performing Arts

George I. Shirley
National Center for Voice and Speech and School of Music, The University of Michigan

Elaine Stathopoulos
National Center for Voice and Speech and Department of Communication Disorders and Sciences, SUNY at Buffalo

Lorraine O. Ramig
National Center for Voice and Speech and Wilber James Gould Voice Research Center, The Denver Center for the Performing Arts

Linda M. Carroll
Teacher's College, Columbia University and Actors Studio, MFA Program, School of Dramatic Arts, The New School for Social Research

William D. Riley
Actors Studio, MFA Program, School of Dramatic Arts, The New School for Social Research

(Received 28 May 1998; revised 14 December 1998; accepted 7 January 1999)

A classical vocal exercise called ''messa di voce'' (Italian for ''placing the voice'') was used to study the symmetry of intensity increase and decrease in six trained singers. Ideally, the exercise is performed as a symmetric triangle, a linear increase in loudness, followed by a linear decrease. Given that some physiologic variables, like lung volume, undergo unidirectional change rather than a symmetric reversal, there is reason to believe that symmetries may not exist. It was found that highly trained singers who use large SPL ranges tend to abbreviate the decrescendo phase in comparison with the crescendo phase. In a few other cases, a plateau in SPL is reached, but an increase in loudness may still be perceived on the basis of a stronger vibrato or changes in timbre. [S0001-4966(99)04604-4]

PACS numbers: 43.75.Rs [WJS]

INTRODUCTION

Messa di voce (to put or place the voice) is a vocal exercise that dates to the camerata, a group of Italian composers and writers of the 16th century who gave birth to opera. The exercise is a crescendo followed by a decrescendo at a constant pitch and vowel. The claim is that if this exercise is performed smoothly and consistently, with many repetitions, the voice will achieve its proper ''placement.'' The Italian composer Gioacchino A. Rossini (1792–1868) gave this exercise high prominence by placing it first in a book of vocalizes entitled *Gorgheggi e Solfeggi* (1825). He considered the vocalizes to be fundamental to proper vocal development, reflecting the discipline imposed by the *bel canto* (beautiful singing) tradition. Rossini directed the singer to practice each exercise three times daily: the first time slowly and softly, the second time fast and soft, the third time fast and loud. The *messa di voce* exercise is one of the most difficult of all vocalizes to master. It is as if Rossini was saying ''Conquer this challenge successfully before you even think of attempting to do justice to the exercises that follow.'' He begins *messa di voce* at low C (C_3 or C_4 depending on gender) and extends it an octave and a half (to G_5 or G_6).

The Italian singing teacher Giuseppe Concone (1801–1861) also made it the first exercise in his Thirty Daily Exercises (Reprinted by Schirmer, 1894), a practice book found in many vocal studios today. Concone was a native of Turino, Italy, who made capital of his ability to impart vocal wisdom to those more gifted than he. His books of vocalizes remain popular today, their rigors never out of date.

Many classical singers use the *messa di voce* exercise to improve their vocal control. It requires multiple combinations of subglottal pressure and laryngeal muscle activity to keep fundamental frequency constant while gradually changing adduction and amplitude of vibration. Because an increase in amplitude of vibration raises F_0 (dynamic tension in the vocal folds increases), the laryngeal tensor muscles have to relax to compensate for this pitch rise. Thus because the exercise deliberately uses a gradual transition from *pianissimo* to *fortissimo* (and back), it challenges the singers'

ability to continuously reorganize intrinsic muscle activities while pitch, vowel, and timbre are attempted to be held constant. This ability is a hallmark of many accomplished classical singers. The *messa di voce* exercise has also been touted as an exercise to improve the smoothness of transition between the vocal registers. Miller (1986) states that ''*Messa di voce* is the classic device for achieving mastery of a wide range of dynamic contrast.'' Ideally, the entire physiologic range of sound pressure level (SPL) available at a given fundamental frequency (F_0) should be built into the exercise.

Given the value placed on this vocal exercise by singers, composers, and singing teachers, we deemed it appropriate to study some of its acoustic and physiologic characteristics. *Messa di voce* is well suited for laboratory study because it requires no accompaniment, is only on the order of 10 s long, is sung on a single vowel, and can be executed during various experimental conditions (e.g., with and without various sensors attached to the body).

Singers who are trained in Western classical styles are concerned about ''voice breaks'' in this exercise, sudden shifts from one voice quality to another as pitch or loudness is changed. For male singers, for example, the involuntary break from falsetto register (the boyish voice) to modal register (the more mature male voice) is usually an embarrassment because it suggests lack of control. The break often happens at high pitches, particularly when loudness is increased or decreased. For some, it brings back unpleasant memories of puberty, when the voice was somewhat unpredictable. For female singers, the break is not so catastrophic because it happens in the lower part of their pitch range, but it often distinguishes singers who can produce loud low notes (in chest voice) from those who cannot.

The purpose of this study was to begin to address the following questions: (1) Is the *messa di voce* executed as intended, that is, a symmetric increase and decrease of SPL?; (2) if not, can the SPL asymmetry be attributed to a corresponding asymmetry in subglottal pressure?; (3) do singers vary in their ability to avoid register breaks (abrupt transitions) in *messa di voce*?; and (4) for those who cannot avoid register breaks, are the breaks more frequent and severe in the decrescendo portion than in the crescendo portion? These questions were only partially answered, and only on a descriptive level. Detailed causal relationships await future studies, but the opportunity presented itself to have six singers in one location on two consecutive days. Recruitment of the same singers would otherwise have been more difficult because several had busy concert schedules. As a result of this accelerated time-frame of data collection, some respiratory calibration measures failed and less ambitious goals had to be set for analysis and interpretation of the data.

I. METHODS

The methods employed in this study have all been used previously (Rothenberg, 1973; Smitheran and Hixon, 1981; Watson *et al.*, 1989, 1990; Sundberg *et al.*, 1993; Stathopoulos and Sapienza, 1993; Thomasson and Sundberg, 1997). They involve placement of an airflow transducer over the mouth and nose, a pressure transducer in the oral cavity behind the lips, an electroglottograph on the neck, and two inductive coil movement transducers on the torso, one over the ribcage and one over the abdomen. With this combination of transducers, some respiratory and phonatory function can be inferred for the *messa di voce* exercise. More detail on the instrumentation is given below.

TABLE I. Profile of singers studied.

Subject	Age	Sex	Voice category	Experience
S1	25	F	Lyric Soprano	8 years
S2	39	F	Coloratura Soprano	22 years
S3	25	F	Lyric Soprano	7 years
B1	43	M	Lyric Baritone	24 years
T1	61	M	Lirico Spinto Tenor	40 years
T2	54	M	Lyric Tenor	20 years

A. Subjects

Three male and three female singers were used for this study. Table I shows a profile of their age, voice category, and experience (private lessons and concertizing). One tenor (T1) had been soloist for the Metropolitan Opera Company in New York for 11 years. The coloratura soprano and lyric baritone (S2 and B1) had sung in recitals for many years prior to becoming full-time teachers. The lyric sopranos (S1 and S3) were accomplished graduate students at the University of Colorado Music School with recital and opera workshop experience, and the tenor (T2) was an amateur soloist. The subjects were all volunteers in this study and completed the tasks in approximately 2–3 h. Much of the time was spent in respiratory equipment calibration for each individual singer.

B. Instrumentation

The experiment took place in an IAC recording booth (3.15 m wide×3.50 m long×2.59 m high) at the Wilbur James Gould Voice Research Center in Denver, Colorado. The subjects stood upright, with inductive coils (bands) surrounding their ribcage and abdomen, the electroglottograph attached to their neck, and (for some utterances) a flow mask placed over their mouth and nose. An experimenter provided the pitches with an electronic keyboard. A second experimenter stood behind the subject to assist in maintaining pressure between the flow mask on the facial skin to avoid air leakage (Fig. 1). Table II shows the group of signals that were recorded, the experimental condition (mask or no mask) for which the signals were analyzed, and the instrumentation used.

The sound pressure level (SPL) was determined in a continuous fashion from a microphone placed at a distance of 30 cm from the subject's lips. This signal was converted to dB SPL (*re*: 0.000 02 dyn/cm^2) using predetermined calibration levels from the B & K 2230 sound level meter. The EGG electrodes were held in place by a velcro collar (Fig. 1).

The wide-band oral airflow signal was detected with a circumferentially vented wire screen pneumotachograph mask and transducer (Rothenberg, 1973). This transducer was calibrated with a Gilmont 52274 shielded rotameter

FIG. 1. Photograph of subject (singer) assisted by one experimenter in keeping a tight seal on the face mask.

prior to collecting data from each subject. The acoustic peak-to-peak glottal flow was then estimated from the oral flow signal by low-pass filtering with a cutoff frequency of 1.5 times the fundamental. A glottal flow derivative was obtained numerically from this estimate, and the maximum flow declination rate (MFDR) was defined as the magnitude of the largest negative peak of this derivative flow waveform in each cycle.

Exhalation volume during each task was computed by integrating the flow signal; lung volume change was taken as the negative exhalation volume and normalized to each singer's maximum exhalation volume that was observed over all utterances. Thus for each singer, all lung volume changes ranged between 0 and 1. The integration procedure was verified by displacing 3 ls of air from a Collins volume calibrator through the mask system.

The intraoral air pressure (P_0) signal was sensed with a 5-cm-long polyethylene tube placed through the airflow mask. One end of the tube was placed between the participant's lips at a position approximately half-way between the corner of the mouth and mid-lip; the distal end of the tube was connected to an air pressure transducer (Glottal Enterprises MSIF-2). Prior to data collection, P_0 was calibrated in centimeters of water ($cm\,H_2O$) with a Dwyer U-tube manometer. The pressure and flow signals were amplified with a Glottal Enterprises MSIF-2 amplifier system.

During the tasks for which oral pressure was measured, each subject sang repetitions of the syllable /pæ/. This syllable was selected for estimating subglottal pressure (Smitheran and Hixon, 1981). Syllable rate and number of syllables varied to allow a natural and comfortable singing style. Subjects were required to achieve velopharyngeal closure (no nasalization) and to maintain a stop closure for at least 100 ms. Maintenance of velopharyngeal closure was monitored from the airflow waveform; airflow was required to be zero during the stop closure for each syllable.

Ribcage and abdomen expansion (and contraction) were monitored with a NonInvasive Monitoring Systems, Inc. (NIMS) Respigraph system. All maneuvers were performed in a standing position a minimum of three times. These included isovolume maneuvers performed at end expiratory level (EEL), vital capacity (VC), maximum rib cage capacity (RCC), and maximum abdominal capacity (ABC) maneuvers (Hoit and Hixon, 1986, 1987). The absolute values of the measures were not used, however, because of a nonrecoverable miscalibration in the data of two male subjects. Rather, ribcage, abdomen, and lung volume measures were normalized for each subject on a scale of 0 to 100% as mentioned before.

Subjects stabilized their quiet breathing before each utterance. End expiratory level (EEL) was identified as the mean minimum value for three cycles of tidal volume breathing before each utterance and used as a common reference point. Lung, rib cage, and abdominal volumes were normalized relative to each subjects' maxima.

All signals were recorded on a Sony PC-108M 8-channel DAT recorder. The data were digitized from the analog output of the tape recorder using a DATAQ DI-200 12-bit A/D board. EGG and oral flow were low-pass filtered at 3.5 kHz, and the remaining measurements were filtered at 300 Hz. These bandwidths were sufficient to capture the highest frequency of interest in the recorded signals. The data were then analyzed using Matlab on a Macintosh 8500.

C. Performance protocol

Each subject produced 27 tokens of the *messa di voce*, 3 pitches×3 mask conditions×3 repetitions each. The pitches were 220 Hz, 440 Hz, and 740 Hz for subject S1; 277 Hz, 622 Hz, and 830 Hz for subjects S2 and S3; 185, 311, and 349 Hz for B1; 220, 370, and 440 Hz for T1; 220, 294, and 370 Hz for T2. These pitch ranges of about 1.5 octaves were

TABLE II. Recording signals, experimental conditions, and instrumentation.

Signal	Condition for later analysis	Instrumentation
Sound pressure level	no mask, constant vowel	B & K 2230 sound level meter
Vocal fold contact area	no mask, constant vowel	Synchrovoice electroglottograph
Oral air flow (to infer acoustic glottal flow)	mask, constant vowel	Glottal Enterprises flow mask
Oral pressure (to infer subglottal pressure)	mask, repeated /æ/ syllables	Glottal Enterprises pressure transducer
Relative circumference of ribcage	no mask, constant vowel	NIMS respigraph system
Relative circumference of abdomen	no mask, constant vowel	NIMS respigraph system

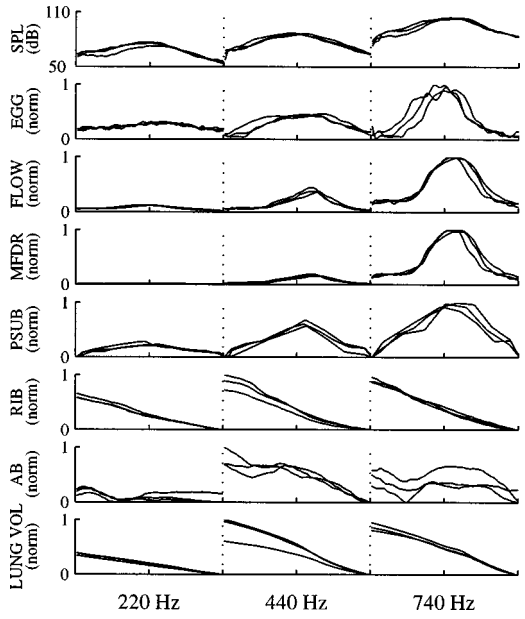

FIG. 2. Acoustic and aerodynamic traces for three tokens of the *messa di voce* exercise performed by subject S1 on three pitches.

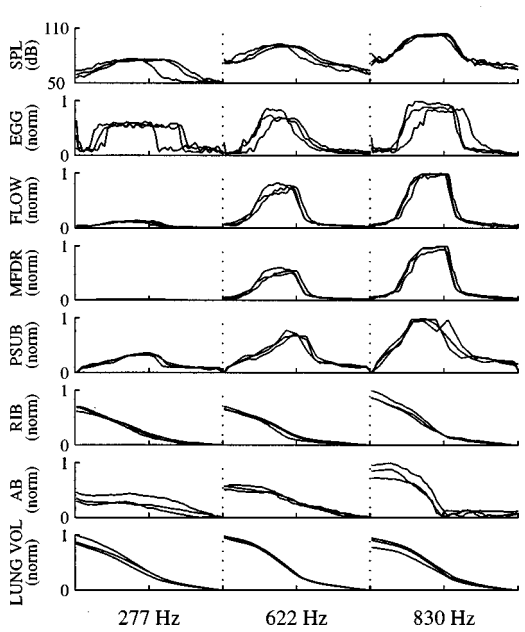

FIG. 3. Acoustic and aerodynamic traces for three tokens of the *messa di voce* exercise performed by subject S2 on three pitches.

judged to contain notes in the low, medium, and high parts of each of the female's vocal ranges and the medium to high parts of the male's ranges.

Prior to the three tokens that were designated as a ''take,'' the subjects practiced a few tokens. When they felt they were ready, the next three were considered ''the take.'' They had all warmed up their voices prior to entering the laboratory, of course.

Each token of the *messa di voce* was targeted to last about 10 s, 5 s for the crescendo and 5 s for the decrescendo. Not every subject felt comfortable with the 10 s duration exactly; hence, the data were time-normalized for ease of comparison. This time-normalization did not affect the symmetry or asymmetry of the exercise that we were testing. Also, no metronome or other pacing device was used, primarily because it would interfere with the audio signals and would create an unnatural way of producing the utterances.

II. RESULTS AND DISCUSSION

It was expected that there might be a large variability among the subjects due to age, gender, and experience, so we decided to display the results of each individual subject rather than as an ensemble average. Figures 2–7 show the performance in the subject order S1, S2, S3, B1, T1, and T2. There are three repetitions (tokens) of the *messa di voce* in each of three pitch columns, progressing from low pitch on the left to medium pitch in the middle to high pitch on the right of each figure. From top to bottom, we show the following signals: SPL at 30-cm distance, the electroglottograph (EGG) envelope, peak-to-peak glottal flow (FLOW), maximum flow declination rate (MFDR), subglottal pressure (PSUB), ribcage contraction (RIB), abdomen contraction (AB), and lung volume (LUNG VOL).

The signal amplitudes were normalized to the maximum value across all tokens for those signals that had no absolute magnitude calibration. This normalization highlighted the waveform symmetry, i.e., the relative increases and decreases over the crescendo and decrescendo phases.

A. Sound pressure level

Across all subjects, tokens, and pitches, SPL at 30 cm varied from a low of 50 dB (S2 on her low pitch in the decrescendo, Fig. 3) to a maximum of 103 dB (S1 and S2 on their high pitches in the loud portion, Figs. 2 and 3). This 53-dB dynamic range was never achieved by any subject on any single pitch, however. The largest single pitch SPL range was obtained by T1 (Fig. 6) who decreased from 100 dB to 55 dB on his middle pitch (a 45-dB change). Subjects S1 and S3 had the smallest SPL ranges, but showed the most con-

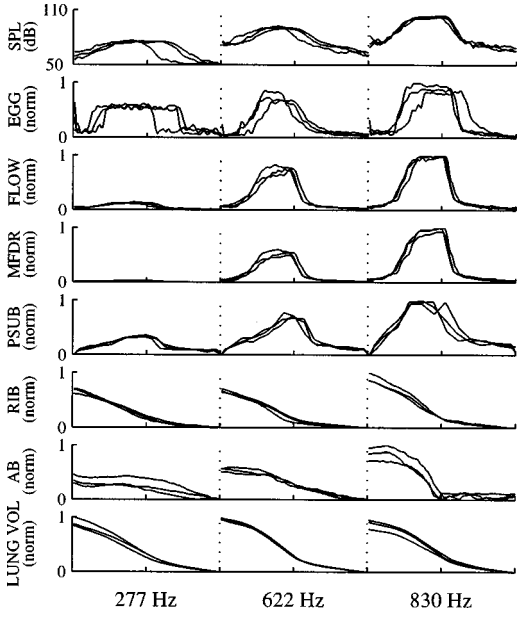

FIG. 4. Acoustic and aerodynamic traces for three tokens of the *messa di voce* exercise performed by subject S3 on three pitches.

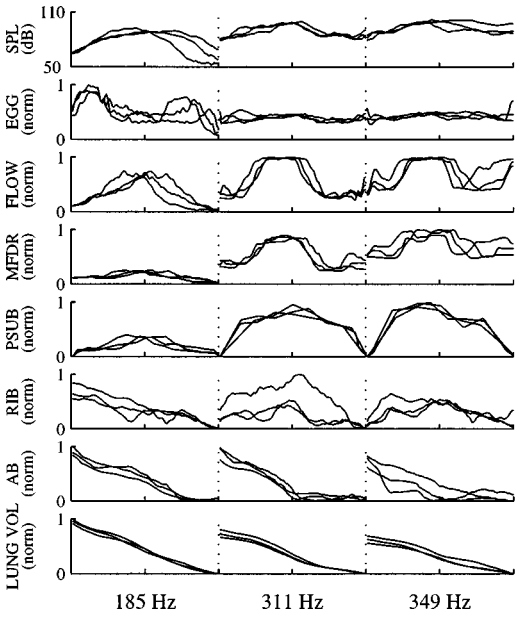

FIG. 5. Acoustic and aerodynamic traces for three tokens of the *messa di voce* exercise performed by subject B1 on three pitches.

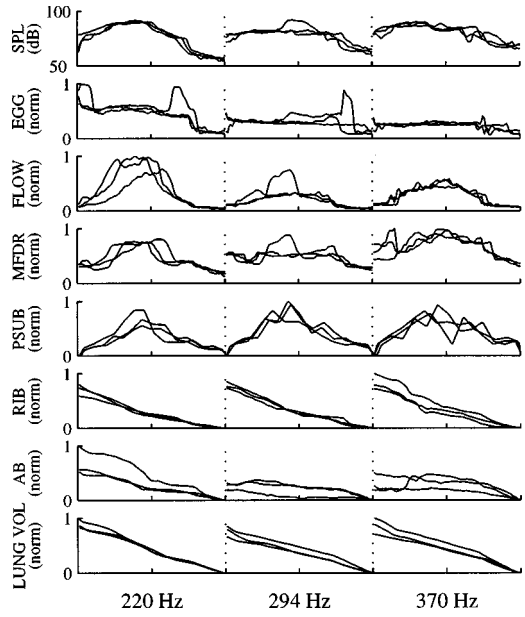

FIG. 7. Acoustic and aerodynamic traces for three tokens of the *messa di voce* exercise performed by subject T2 on three pitches.

sistent and symmetric variations over the entire set of exercises (Figs. 2 and 4). Subjects B1 and T2 (Figs. 5 and 7) had large SPL ranges on their low notes, but rather limited ranges on their middle and high notes.

Perhaps most interestingly, all *messa di voce* attempts with large SPL ranges on any given note showed some asymmetry, usually with a linear or *s*-shaped SPL rise and an exponential-like SPL fall. The expected (model) shape was triangular, i.e., an increasing ramp followed by a mirrored decreasing ramp. Deviations from this triangular model are best seen on the high note of S2 (Fig. 3) and on the middle note of T1 (Fig. 6). Symmetry did not appear to be of primary importance when large SPL ranges were attempted by these singers. It will be shown later that changes in spectrum

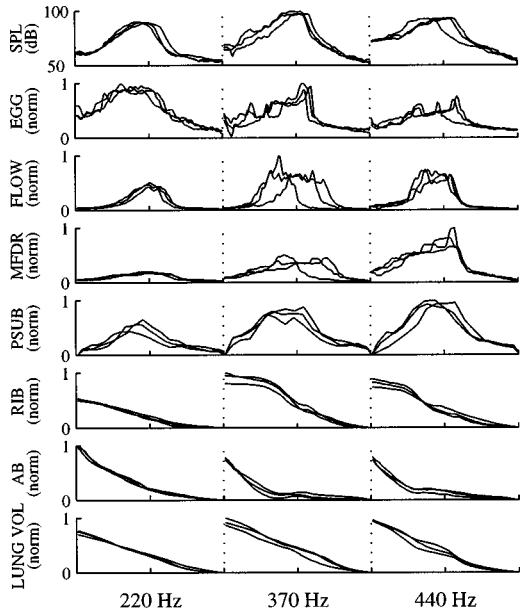

FIG. 6. Acoustic and aerodynamic traces for three tokens of the *messa di voce* exercise performed by subject T1 on three pitches.

and vibrato were used to create the perception of continued loudness change in the flat SPL region. For those singers who attempted smaller dynamic variations (S1 and S3 in Figs. 2 and 4, respectively), the peaks were only slightly rounded, suggesting that SPL changes reflected all the desired loudness changes.

B. Electroglottogram

The EGG signal was recorded primarily to assess stability of phonation. If a sudden register change were to occur, or if the larynx were to suddenly move up or down during the exercise, the EGG envelope should detect those changes. In general, we observed more fluctuations among the males than the females. Specifically, B1 (the baritone) had considerable token variability on the low note (Fig. 5), but much less on the middle and high note. The operatic tenor T1 had the most variable and asymmetric EGG waveform on the middle and high notes (Fig. 6), where his dynamic range was the largest (45 dB). We will discuss this variability later in a spectral context. Subject T2 (the amateur tenor) had one very problematic token with large fluctuations after voice onset and before voice offset (Fig. 7). These fluctuations were identified perceptually as chest-falsetto register breaks. The EGG waveform envelopes for sopranos S1 and S3 were basically smooth, but for S2 (the coloratura soprano), the signal shows a pronounced flat top (saturation) in the loud portion of all the tokens at all pitches (Fig. 3). This is also seen in other waveforms, suggesting that this subject was holding vibrational amplitude constant near the peak for a brief moment, a deliberate part of her technique.

C. Peak-to-peak FLOW and maximum flow declination rate

The peak-to-peak FLOW and maximum flow declination rates (MFDRs) were most symmetric and consistent across tokens for singers S1 and S3 on the low and middle

notes (Figs. 2 and 4). On the high note, S1 showed a more sudden rise and fall in FLOW and MFDR, while S3 skewed the FLOW deferentially for different tokens. Several singers complained about the difficulty of singing with the mask, especially at high notes when more jaw opening is needed than the mask can accommodate. Since the SPL trace, which was obtained without the mask, does not reflect this variable skewing, we suspect that this token variability is a mask artifact. Singer S2 executed the exercise more squarelike than ramplike (Fig. 3), with the major flow changes occurring over less than half of the length of the exercise. As mentioned above, S2 tended to reach a plateau near maximum loudness.

The male singers were all more variable in FLOW and MFDR than the females. B1 showed the flat-tops on FLOW that were characteristics of soprano S2 (compare Figs. 3 and 5 on the middle and high notes). The MFDRs of baritone B1 were too variable to show clear trends. Tenor T1 (Fig. 6) showed the greatest token variability on the middle note for FLOW and MFDR (where he achieved the largest dynamic range), but on the low and high note the productions were more consistent. Tenor T2 (Fig. 7) showed large token variability on the low and middle note, but basically had a ramplike pattern on the high note.

D. Subglottal pressure

Some problems should be noted at the outset with respect to the subglottal pressure curves. First, they are poorly sampled over the exercise. Generally, only 8–10 points were available because it sometimes takes more than one consonant–vowel syllable to establish one measurement of pressure (Smitheran and Hixon, 1981). Second, they are not from the same tokens as the remaining waveforms. The /pæ/ syllable repetition clearly compromised the ability of the singers to execute a smooth *messa di voce*, which led us to reject the repeated syllable utterances for analysis of the other waveforms. Thus only a loose correlation can be expected between subglottal pressure curves and other curves.

Nevertheless, the expected ramplike subglottal pressure (PSUB) patterns were produced by soprano S1 (Fig. 2), especially on the middle note. Soprano S2 ramped the pressure on the crescendo in a similar way, but relaxed it faster on the decrescendo (Fig. 3). Soprano S3 and baritone B1 (Figs. 4–5) showed a symmetrical rise and fall, but without a sharp peak at the top. Tenors T1 and T2 showed a triangular (ramplike) pattern as expected, but T2 was more variable than T1. Across all subjects, PSUB was one of the most symmetric wave shapes, with the exception of the asymmetry shown by S2.

E. Ribcage, abdomen, and lung volume displacements

Ribcage displacement (RIB) was a monotomically declining function for all subjects except B1. It generally mirrored the lung volume rather closely, as reported by Thomasson and Sundberg (1997) in a similar study that used complete songs as performance material. For subject B1 in our study, RIB showed paradoxical movement in the crescendo. The ribs expanded first (in the inspiratory direction) and then decreased (Fig. 5, middle and high notes). This initial expansion of the ribcage was accompanied by a faster decline (inward movement) of the abdomen to maintain a net lung volume decrease. Tenor T1 also had a tendency to delay ribcage movement, but did not actually expand the ribs. He did, however, compensate with abdominal movement the same way that B1 did. These paradoxical movements (or tendencies toward paradoxical movements) occurred only in the crescendo phase. Interpretations of these movements would have been much clearer if the actual lung volumes had been known, but as stated before, calibration failures prevented a full quantification of respiratory events.

In general, abdomen displacement was a little more variable for most subjects than ribcage displacement. This was also found by Thomasson and Sundberg (1997). Interestingly, the largest fluctuations in abdomen displacement occurred for singer S1 (Fig. 2), who was otherwise stereotypic across tokens on all other wave shapes. The abdomen moved in a paradoxical direction on the high note over part of the crescendo. Soprano S2, with her abbreviated decrescendo, showed a rapid abdominal movement, followed by a long period of zero displacement (Fig. 3, high note). Ribcage and lung volume changes for S2 had similar tendencies, but were more steadily declining. Soprano S3 had a reversal of abdomen movement on her low note (Fig. 4). At first, AB decreased a little, then it increased, and finally it decreased again. But lung volume remained linear in this process; so did ribcage displacement. Tenor T2 showed generally linear trends in all respiratory measures, but token variability was large, which may be a function of his limited training.

F. Spectral and vibrato effects

We return now to the two interesting ''flat-top'' cases, for which there were the largest overall SPL changes and the greatest asymmetry. Figure 8 shows a narrow-band spectrogram for one token of the high note (440 Hz) performed by subject T1. Superimposed on this spectrogram is the SPL curve. Note that there are three small stages of crescendo (registrations) for which successively more harmonic energy is recruited. The first stage has little energy above the third harmonic, the second stage has little energy above the sixth harmonic, and the final stage has significant energy above the tenth harmonic. The transitions between these stages agree with the fluctuations in the EGG waveform of the corresponding token in Fig. 6. In the final stage, where the SPL is nearly flat, the vibrato extent is increased. The combination of this vibrato increase and higher spectral content is likely to add to the perception of increased loudness.

The use of vibrato extent for vocal loudness is even more visible in Fig. 9, which represents one token of the high note of subject S2. Again, the illustration is a narrow-band spectrogram with the SPL curve superimposed. Note that a ''vibrato crescendo'' exists in the region where the SPL is relatively constant. Note also that this singer (a soprano) does not show the registration effect demonstrated by the tenor. Since both of these singers were the most experienced in their gender categories, the results suggest that they had perhaps acquired a skill not yet achieved by the others.

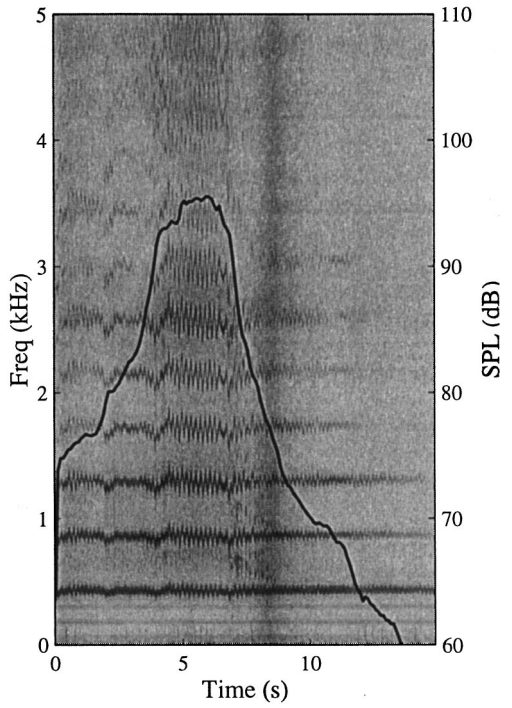

FIG. 8. Narrow-band spectrogram and overlaid SPL curve for one token of a *messa di voce* exercise performed by tenor T1 on the pitch A_4 (440 Hz).

III. CONCLUSIONS

We return now to the questions posed at the beginning of this paper. First, are the SPL increase and decrease symmetric in a *messa di voce* exercise? Our results have shown that SPL symmetry is a function of the SPL *range* in the exercise. Singers with a lower SPL range tend to have more symmetry, probably because they expend less of their lung volume in the exercise and can therefore control this lesser volume more evenly. On the other hand, those who maximize their SPL range tend to introduce considerable asymmetry. The observed asymmetry was characterized by a delayed rise in SPL, followed by an accelerated fall. This was demonstrated by the two most experienced singers, particularly on medium and high pitched notes. The SPL curve had a flat top during which spectral content and vibrato extent were increased, probably to boost the perception of loudness increase.

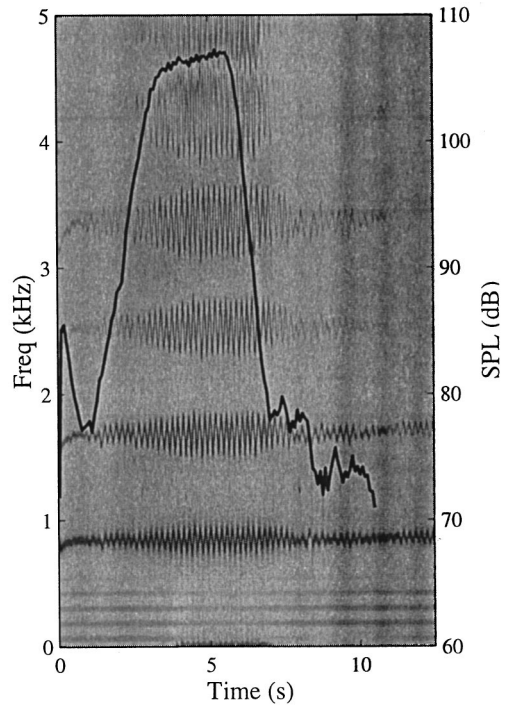

FIG. 9. Narrow-band spectrogram and overlaid SPL curve for one token of a *messa di voce* exercise performed by soprano S2 on a pitch A_5^b (830 Hz).

The asymmetries in SPL can best be attributed to subglottal pressure changes, although for experimental purposes the tokens did not match to see the exact correlation. The abbreviated decrescendo was generally accompanied by an early relaxation of subglottal pressure. Peak-to-peak glottal airflow and maximum flow declination rate generally followed the subglottal pressure pattern, which has been observed repeatedly before (Sundberg *et al.*, 1993; Stathopoulos and Sapienza, 1993). The SPL asymmetries cannot be attributed to nonuniform lung volume changes; these were generally quite linear throughout the exercise, even when SPL changes were asymmetric. However, substantial asymmetric variations were seen in abdomen and ribcage displacement across subjects, suggesting that some differences in respiratory strategy were used to control subglottal pressure. In particular, the baritone subject showed outward movement of the ribcage during the crescendo phase of the exercise while maintaining an increase in peak airflow and SPL. This was compensated for by a more rapid inward movement of the abdomen to maintain constant lung volume change.

The asymmetries observed did not seem to be associated with register breaks in any of the females. For the male singers, however, there seemed to be more laryngeal movement, judged by the variable EGG envelope. In particular, some register breaks occurred in both the crescendo and decrescendo portion of the exercise for the two tenors.

The asymmetry in the *messa di voce* was pitch dependent. Generally speaking, the higher pitches had more variability across tokens. The higher pitches also showed more cases of abbreviated decrescendos, suggesting that singers were anxious to get to the end of the exercise.

In summary, examination of the symmetry and controlling parameters among the varied classical voice types revealed that the singers used a variety of strategies to achieve a prescribed perceptual output. The singers did not share the same pedagogical approach to ''support'' (maintaining a controlled subglottal pressure), which may have influenced the varied patterns of ribcage and abdominal movement. Those subjects with more performing experience tended to have unique patterns among the measures tested, whereas those subjects still in formal training in the academic environment showed the more expected (stereotypic) behavior with less SPL variation. This indicates that optimization of the respiratory and vocal systems is a subject-specific process.

Future studies of *messa di voce* should include perceptual evaluation of the exercise. Does a perfect range in SPL really produce a perfect ramp in loudness? This could be

addressed with synthesis. Also, does perfect acoustic or perceptual symmetry reflect musical symmetry? It is conceivable that the abbreviated decrescendo observed in cases of high dynamic range may be musically more appropriate.

Future studies of *messa di voce* should also address the gradual recruitment of vocal fold tissue layers in vocal fold vibration (the mucosa, ligament, and muscle) as SPL is changing. These studies would be able to answer questions about voice register changes on a mechanistic level. An important question is: does the tension of a newly recruited tissue layer have to be equalized with the existing layers in vibration? If so, the difficulty of the exercise might be attributed to this need to balance ligament and muscle tension in the vocal folds. We are contemplating the use of simulation models of vocal fold vibration to answer questions of this nature.

ACKNOWLEDGMENTS

This work was supported by Grant No. P60-DC00976 from the National Institutes of Health. The authors thank Ronald C. Scherer and Christopher Dromey for assistance in data collection and analysis.

Concone, J. (**1894**). *Thirty Daily Exercises* (Schirmer, New York).
Hoit, J., and Hixon, T. (**1986**). ''Body type and speech breathing,'' J. Speech Hear. Res. **29**, 313–324.
Hoit, J., and Hixon, T. (**1987**). ''Age and speech breathing,'' J. Speech Hear. Res. **30**, 315–366.
Miller, R. (**1986**). *The Structure of Singing* (Schirmer, New York), p. 173.
Rossini, G. (**1825**). *Gorgheggi e Solfeggi* (Ricordi, Milan). Reprinted by Frangipani Press, Bloomington, Indiana (1986).
Rothenberg, M. (**1973**). ''A new inverse-filtering technique for deriving the glottal airflow waveform during voicing,'' J. Acoust. Soc. Am. **53**, 454–460.
Smitheran, J., and Hixon, T. (**1981**). ''A clinical method for estimating laryngeal airway resistance during vowel production,'' J. Speech Hear. Dis. **46**, 138–146.
Stathopoulos, E., and Sapienza, C. (**1993**). ''Respiratory and laryngeal measures of children during vocal intensity variation,'' J. Acoust. Soc. Am. **94**, 2531–2543.
Sundberg, J., Scherer, R., and Titze, I. (**1993**). ''Phonatory control in male singing. A study of the effects of subglottal pressure, fundamental frequency, and mode of phonation on the voice source,'' J. Voice **7**, 15–29.
Thomasson, M., and Sundberg, J. (**1997**). ''Consistency of phonatory breathing patterns in professional operatic singers,'' KTH Speech, Music and Hearing Quarterly Progress and Status Report **4**, 29–40.
Watson, P., Hixon, T., Stathopoulos, E., and Sullivan, D. (**1990**). ''Respiratory kinematics in female classical singers,'' J. Voice **4**, 120–128.
Watson, P., Hoit, J., Lansing, R., and Hixon, T. (**1989**). ''Abdominal muscle activity during classical singing,'' J. Voice **3**, 24–31.

A solution to diffraction biases in sonoelasticity: The acoustic impulse technique

Stefan Catheline, François Wu, and Mathias Fink
Laboratoire Ondes et Acoustique, E.S.P.C.I., Université Paris VII, U.M.R. 7587 C.N.R.S 1503, 10 rue Vauquelin 75231 Paris cedex 05, France

(Received 16 June 1998; accepted for publication 28 January 1999)

Several methods have been proposed to estimate the viscoelastic properties of soft biological tissues using forced low-frequency vibrations (10–500 Hz). Those methods are based on the measurement of phase velocity of the shear waves (~5 m/s). It is shown in this article that the measurements of velocity as well as attenuation are subjected to biases. These biases are related to reflected waves created at boundaries, to the nonnegligible size of the piston source which causes diffraction effects and to the influence of a low-frequency compressional wave. Indeed, a theoretical analysis of the field radiated by a point source explains how mechanical vibrations of a piston generate a shear wave with a longitudinal component and how this component can interfere with a low-frequency compressional wave. However, by using a low-frequency transient excitation, these biases can be avoided. Then the precise numerical values of elasticity and viscosity can be deduced. Experiments in phantoms and beef muscles are shown. Moreover, a relative hardness imaging of a phantom composed of two media with different elasticities is presented. [S0001-4966(99)00805-X]

PACS numbers: 43.80.Cs, 43.80.Ev [FD]

INTRODUCTION

The viscoelastic properties of soft biological tissues are not easily derived from the characteristics of the propagation of ultrasonic waves. Indeed, ultrasound behavior in biological tissues is similar to that in fluids, and conveys little or no information on the shear moduli of tissue. For the last ten years, many papers about viscoelastic properties of soft tissues have proposed low-frequency shear wave propagation as a vehicle for obtaining quantitative values of shear elasticity and viscosity or for making a relative stiffness imaging.[1,2] Elasticity and viscosity can be deduced from the measurement of the phase velocity and of the attenuation. By using surface Rayleigh wave, Kazakov and Klochkov calculated those parameters for human arms.[3]

Nevertheless, in bulk, not much has been done about quantitative measurements. One reason is that, whatever the method used to measure the displacements, i.e., quadrature phase technique,[4] MRI,[5] or pulsed Doppler technique,[6] shear waves are usually generated by forced monochromatic vibration (10–500 Hz). The consequence is that the amplitude and the phase of the monochromatic wave integrate various effects—discussed in this paper—and simple relations between velocity, attenuation, elasticity, and viscosity do not exist anymore. Another reason is that the shear waves in soft biological tissues are not very well known. The apparent shear wave velocity depends on frequency and does not fit the traditional theory of a plane wave propagating in a linear viscoelastic medium.[7] Thus to what extent can the classical theory be trusted? Lastly, it is interesting to learn how shear wave can be generated by a piston that vibrates perpendicularly to the surface and how a longitudinal component of displacement can be measured in the axis of the vibrator for the compressional wave and also for the shear wave. All of these issues will be addressed in the first part of this paper.

Section I presents an experiment in a phantom where shear waves are generated by sinusoidal vibrations of a piston. A careful analysis of the axial displacements reveals three different origins of biases on velocity and on attenuation measurements: the standing wave effects are due to interferences of waves reflected at boundaries (these exist as soon as monochromatic excitations are used in a confined medium), the diffraction effects caused by the appreciable size of the vibrator compared to the wavelength, and finally the interference effects between longitudinal components of a compressional and a shear wave. Indeed, in the exact calculus of the displacement field radiated by a point source, a longitudinal component of the shear wave appears and interferes with a low-frequency compressional wave. All of those effects will be discussed through various experiments.

Section II shows results of experiments in which a transient excitation of the piston is used. It avoids the biases described before and thus precise numerical values of shear elasticity and shear viscosity are calculated. Eventually, an image of slowness (velocity^{-1}) of the shear wave in a bilayered medium is made. This image allows separation of the hard part from the soft one.

I. BIASES ON PHASE VELOCITY AND ATTENUATION MEASUREMENTS

A. Experimental setup

When a motionless biological medium is illuminated by ultrasonic pulses, the acoustic speckle from the same zone of soft tissues remains the same as long as the scatters do not move. When LF (low-frequency) vibrations propagate inside the medium, they induce a LF motion of the scatters that can be detected and measured by correlating successive A-scans. Such a technique measures the displacements along the axis

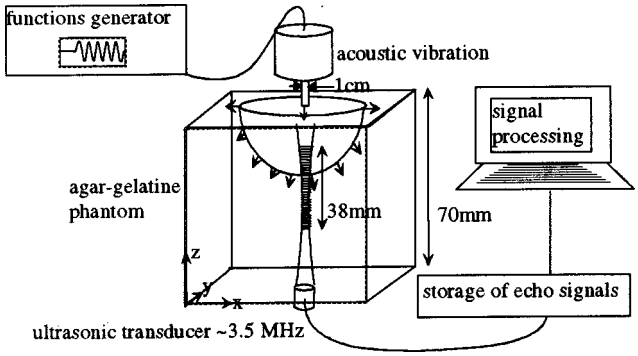

FIG. 1. Experimental setup: a 3.5-MHz transducer is illuminating tissues while LF vibration is applied by a circular piston ($a=0.5$ cm). Successive A-lines are recorded and analyzed for displacement measurement.

of the ultrasound beam. To first approximation, for small displacements inside the biological medium, the speckle motion is linearly related to the motion of the insonified medium.[8] This is the fundamental property that is exploited in the following experiment; Fig. 1.

We use a pulse echo system, with a pulse repetition frequency of 1300 Hz and a 3.5-MHz central frequency. The transducer has a 15 mm diameter and a focal depth of 40 mm. An agar-gelatin phantom, whose viscoelastic properties are roughly those of muscles,[9] is tested. Its dimensions are $10\times10\times7$ cm. It is a mixture of 3% agar and 6% gelatin. The agar powder ensures the medium to be scattering. On one side, a circular piston of 0.5 cm radius is set on the surface. The piston is built on a vibrator. The shape and the frequency of the LF vibrations are controlled with a function generator. On the opposite side of the phantom, the ultrasonic transducer is set so as to have a common axis with the vibrator. This insonified volume sketched in Fig. 1 is 38 mm deep. The A-lines are recorded in a 11-bit digitizer operating at 40 MHz. Each line is divided in 42 overlapping windows. Each window corresponds to a slice within the medium.

During the propagation of a 250-Hz sinus wave train generated by the vibrator, the axial displacements of those tissue slices are calculated with a cross-correlation technique between successive A-lines. This technique can measure displacements along the ultrasonic beam that are smaller than 1 μm for a tissue slice of typically 1 mm depth.[10] It shows good results for vibration frequencies ranging from 20 up to 300 Hz. We will see in the next paragraph that the tissue motion obtained with such an experimental setup can be temporally separated in four main zones. Only one of these zones can give a good value of velocity.

B. Tissue motion induced by a sinus wave train

Figure 2(a) presents a typical example of results that can be obtained with this technique. For each of the 42 slices, the axial displacement is plotted versus time. The LF vibration, started at time $t=35$ ms, is generated from the surface situated at 70 mm. Depth of 0 mm corresponds to the transducer position. The maximum amplitude is 13 μm. Four zones labeled (ABCD) are clearly apparent in Fig. 2(a): the first zone (A) shows null displacement from the motionless medium. In the second zone (B) the displacements are due to

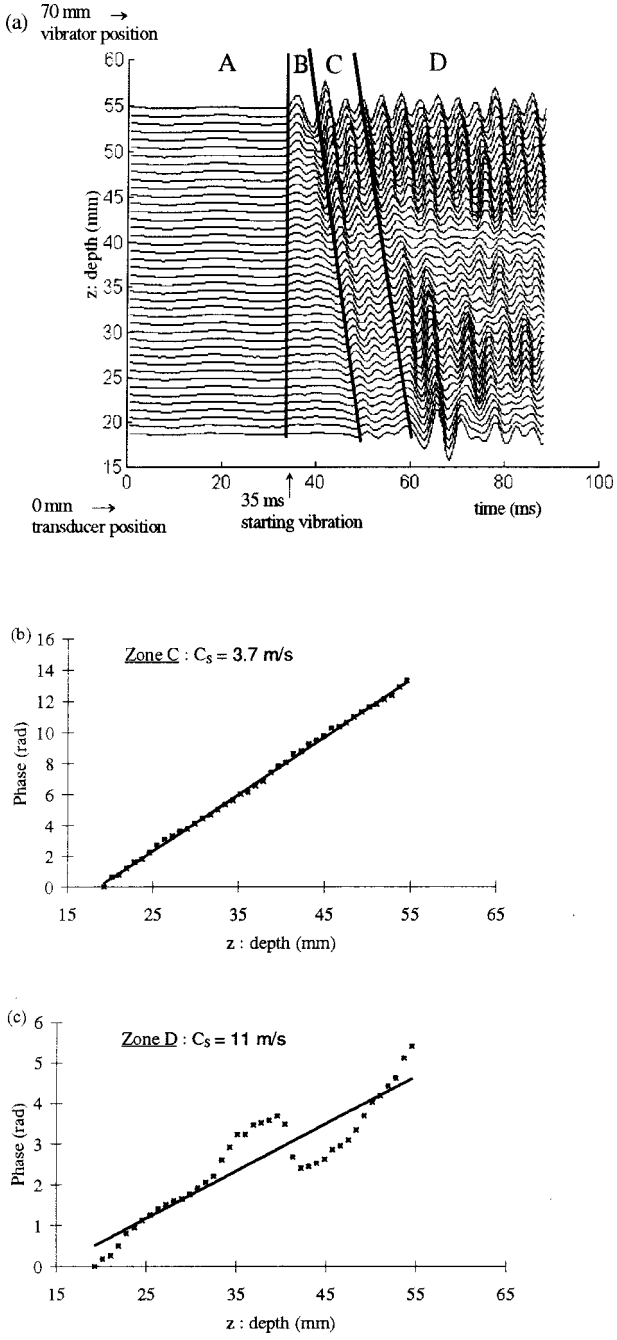

FIG. 2. (a) Axial displacements generated by a 250-Hz wave train. Each line represents the displacement of a tissue slice at one depth. Phase is calculated (b) from the transient zone (part C) and (c) from the monochromatic zone (part D). Velocity C_S is then deduced from the slope.

the propagation of a compressional wave. The third zone (C) contains displacements caused by a shear wave. Those statements will be discussed in Sec. I H. The transient modes of vibration (zones B and C) lead to the last zone (D) where monochromatic modes of vibration are setting up. Then, the displacements result from all the waves that are reflected at boundaries. The phases of those displacements are calculated for the last two zones. For the transient zone (C), the phase linearly varies with depth, as shown in Fig. 2(b), which is typical of a wave in an infinite medium. The phase velocity of the shear wave (3.7 m/s) is calculated from $V=\omega\cdot(\partial\varphi/\partial x)^{-1}$, where ω is the angular frequency and

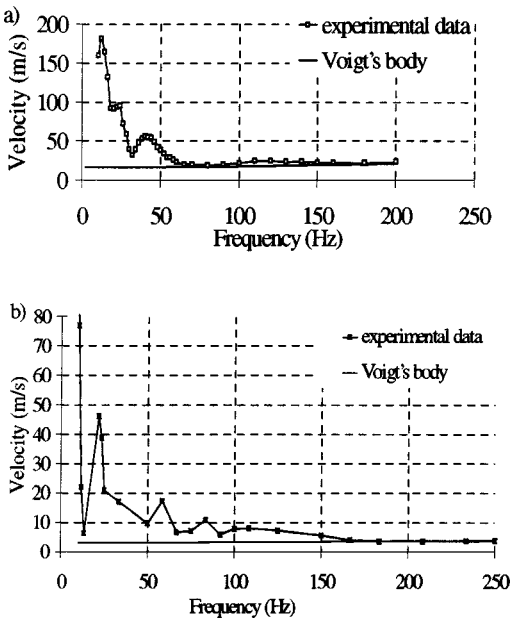

FIG. 3. Velocity of the shear wave in a beef muscle (a) and in a phantom (b) undergoing monochromatic vibrations compared with the theory of an infinite viscoelastic medium (Voigt's body).

$\partial\varphi/\partial x$ is the phase gradient. The same procedure is applied to the monochromatic zone (D). But the shear wave that propagates from the vibrator to the transducer interferes with waves reflected at boundaries. Thus the phase, Fig. 2(c), as well as the amplitude (that we will examine in the second part, Fig. 6), is strongly modified and a wrong value of phase velocity is obtained (11 m/s).

The numerical values of phase velocity of the shear wave are obtained here for a 250-Hz excitation frequency. By changing this frequency, dispersion curves are obtained (Figs. 3 and 4). In the following paragraphs, we will show a typical dispersion curve obtained in a beef muscle and in a phantom when monochromatic vibrations are used. We will try to understand the behavior of this curve that does not fit the traditional theory of viscoelastic medium. We will compare it to a dispersion curve obtained when transient vibrations are used. Precise analysis will show how those curves are affected by reflections at boundaries and by diffraction.

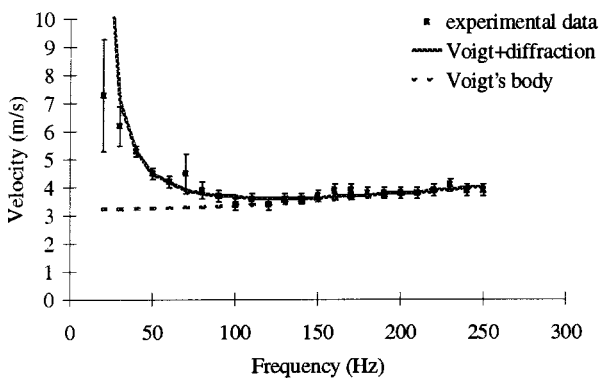

FIG. 4. Velocity of the low-frequency shear wave in an agar-gelatin phantom. Experimental data compared to velocity in a Voigt's body, Eq. (1), and to velocity in a Voigt's body modified by diffraction, Eq. (6).

C. Dispersion curves from monochromatic vibrations

Dispersion curves in a beef muscle and in a phantom are compared in this paragraph. The same experimental setup as shown in Fig. 1 is used. Monochromatic vibrations are applied. Thus the velocity measurements are obtained from monochromatic vibrations like the ones appearing in the zone D, Fig. 2(a). The vibration frequency ranges from 10 to 250 Hz. The radius of the vibrator is 1 cm in both media. The beef muscle is ''semi-membranosus.'' Its size is $8\times8\times6$ cm^3, the depth of the insonified volume ranges from 1 to 5 cm, and the beam is perpendicular to the muscle fibers. The exploration depth of the $10\times10\times7$ cm^3 phantom ranges from 3 to 7 cm. Experimental data, obtained at room temperature, are compared with the shear velocity C_S calculated from the classical theory of the viscoelastic medium (also called Voigt's body):[7]

$$C_S=\sqrt{\frac{2(\mu_1^2+\omega^2\mu_2^2)}{\rho(\mu_1+\sqrt{(\mu_1^2+\omega^2\mu_2^2)})}}. \tag{1}$$

In the literature, the value of the density is found to be $\rho=1100$ kg/m^3 in soft tissues.[11] The angular frequency ω is chosen experimentally and the Lamé coefficients μ_1 and μ_2, are determined in order to fit with the experimental behavior of the velocity as function of frequency.

The dispersion curves presented in Fig. 3 are similar to those found by Fujii *et al.*[12] or Kazakov and Klochkov.[3] Here are the typical deviations observed on velocity between the theoretical and the experimental data: Global velocity increases when frequency decreases, and local maxima are observed at 12, 25, 40 Hz in the beef and at 25, 55, 75 Hz in the phantom. Consequently, one may wonder if the global and local increase of the dispersive curve have a physical meaning, if they can be useful in determining viscoelastic parameters, or if they are only the effects of reflections at boundaries.

A way to get rid of reflections at boundaries is to work on the transient zone (C) of Fig. 2(a). In that case no reflection has yet disturbed the forward propagating wave.

D. Dispersion curve from transient vibrations

The experimental velocity as a function of frequency when transient vibrations are used in an agar-gelatin phantom is shown in Fig. 4. The velocity is calculated from the phase of the displacement of the transient zone (C). The error bars are deduced from the linear fits of these phases.

First, local maxima cannot be found anymore. We can conclude that they are created by reflections at boundaries; when boundary conditions are complicated, those maxima cannot lead to the determination of viscoelastic parameters. Second, the global increasing of phase velocity when frequency decreases still remains and it cannot be due to reflected waves. Fujii *et al.* suggested a modification of the shear wave nature[12] to explain the particular behavior of velocity at low frequency. We propose here another explanation based upon diffraction effects.

E. Diffraction effects on shear wave velocity measurements

Usually, the shear wave is generated from the surface with a monochromatic vibrating source, a circular piston whose diameter ranges usually from 10 to 70 mm. For a velocity of 3 m/s, the shear wavelength is 150 mm at 20 Hz and 10 mm at 300 Hz. The size of the piston is not negligible compared to the wavelength and the Fresnel zone (near field) can lie at a depth of 50 cm. Consequently, we suggest here a formulation of shear wave velocity that takes the diffraction effects into account.

As a first approximation we will develop a simple calculation for the axial displacement field of a circular source in an isotropic solid. Lhemery[13] showed that in a semi-infinite medium with free boundary conditions, the displacement in the far field is given by the well-known Rayleigh–Sommerfeld's solution. Results predicted by this model show good accuracy with exact numerical solution even in the near field. The exact calculation of the displacement vector is discussed later; see Eq. (7). It says that most of the radiated energy for low frequency is propagating through the medium as a shear wave. In Ref. 11, Oestrecher reached this conclusion by studying the mechanical impedance of biological tissues. Then the displacement component along the z axis can be calculated by assuming an acoustic potential $\Phi_z(z,t)$. According to Rayleigh–Sommerfeld's solution on the axis of the aperture,[14] this potential depends on V_n the amplitude velocity of vibration, a the radius of the aperture, z the depth along the aperture axis, and k the wave vector of a monochromatic shear wave. It is mathematically expressed as follows:

$$\Phi_z(z,t)=i\frac{V_n}{k}e^{i\omega t}[\exp(-ik\sqrt{z^2+a^2})-\exp(-ikz)]. \tag{2}$$

In Voigt's body;[11] k is defined as:

$$k=\sqrt{\frac{\rho\omega^2}{\mu_1+i\omega\mu_2}}. \tag{3}$$

Thus the particle velocity, the gradient of the acoustic potential, is given by:

$$V_z(z,t)=-V_n e^{i(\omega t-kz)}\left[\frac{z}{\sqrt{z^2+a^2}}\times\exp(-ik(\sqrt{z^2+a^2}-z)-1\right]. \tag{4}$$

It is now possible to write the particle velocity in the following form:

$$V_z(z,t)=V_0\exp(i(\omega t-kz+\varphi(z)), \tag{5}$$

where $\varphi(z)$ is the additive phase due to diffraction by the aperture. Eventually, the phase velocity that takes diffraction effects into account can be calculated from:

$$c^*=\frac{\omega}{\mathrm{Re}\left(k-\frac{\partial\varphi}{\partial z}\right)}.$$

The following expression is obtained:

$$c^*(\omega)=\frac{\omega}{\mathrm{Re}\left\{k+\frac{\partial}{\partial z}\left(\mathrm{atan}\left[\frac{\sin\left(kz\left(\sqrt{1+\frac{a^2}{z^2}}-1\right)\right)}{\cos\left(kz\left(\sqrt{1+\frac{a^2}{z^2}}-1\right)\right)-\sqrt{1+\frac{a^2}{z^2}}}\right]\right)\right\}}. \tag{6}$$

In the far field, if $z\gg a$, Eq. (6) gives the classical velocity of shear wave in an infinite medium. Otherwise, if $z\sim a$ and if frequency increases, the ''atan'' term becomes negligible compared to k; thus we find the classical velocity again. Finally Eq. (6) shows that the velocity increases when the frequency decreases or when the radius increases. This global behavior has been checked experimentally; see Fig. 4 and Fig. 5. The values used in Eq. (1) and Eq. (5) are $z=4$ cm, $a=5$ mm. The Lamé coefficients were: $\mu_1=10\,000$ Pa, $\mu_2=5$ Pa s. We obtain theoretical curves of Fig. 4.

The apparent phase velocity deduced from Eq. (6) fits the experimental data with good agreement when the frequency or the radius of the piston is changing. The deviation observed at 10 and 20 Hz is a consequence of the approximation that consists of ignoring the effect of the compressional wave. As we will see in the second part with the analytical solution of the field generated by a monochromatic point source in a semi infinite medium Eq. (8), the compressional wave cannot be neglected for a very low frequencies.

Figure 5 shows that the velocity depends on the radius of the piston: The apparent velocity increases with the size of the piston. For a 2 cm radius, the velocity is about 3.6 m/s, whereas for a 0.5 cm radius, it is only 3.3 m/s. This result is well predicted by Eq. (6).

We have only investigated the effects of reflected waves and diffraction on the shear wave velocity measurements. How about attenuation?

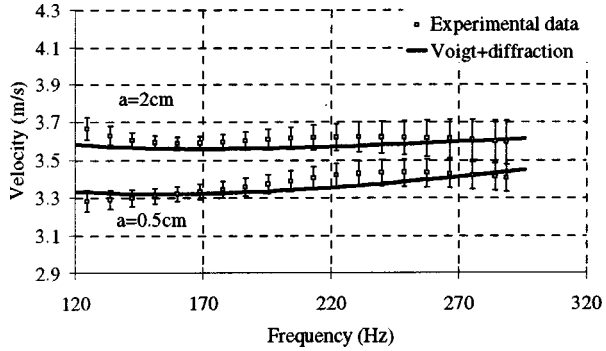

FIG. 5. The apparent shear wave velocity is modified by the size of the vibrator. Experimental and theoretical values [from Eq. (6)] are compared for a radius of 0.5 cm and 2 cm.

F. Attenuation measurements of the shear wave

Attenuation is calculated from the amplitude measurements of the shear wave, Fig. 2(a). Amplitudes in the monochromatic zone (D) result from interferences of reflected waves at boundaries and as a consequence it is difficult to predict the strong variations with depth represented in Fig. 6: no attenuation can be calculated. As a comparison, the amplitudes from the transient zone (C) and its exponential fit is also plotted. In that case, the exponential decrement does not fit the amplitude very well.

The deviations of the transient amplitude (zone C) from the exponential decrement cannot be attributed to diffraction effects because the size of the circular vibrator (0.5 cm) is small compared to the wavelength (1.5 cm). As a consequence, Fresnel's zone is too close to the vibrator (0.15 cm) to influence the amplitude measurement. In fact, another source of bias appears in this experiment. As we will see in the next paragraph, in isotropic homogeneous solids, a point force that is normally applied to the surface generates a longitudinal component of displacements in its axis. These displacements propagate as a compressional wave and as a shear wave. When monochromatic vibrations are used, those components interfere and the amplitude exhibits local maxima and minima.

G. Green's function in soft tissues

The propagation equation that takes boundary conditions into account admits Green's function as a solution. It describes the displacement field as function of space and time.

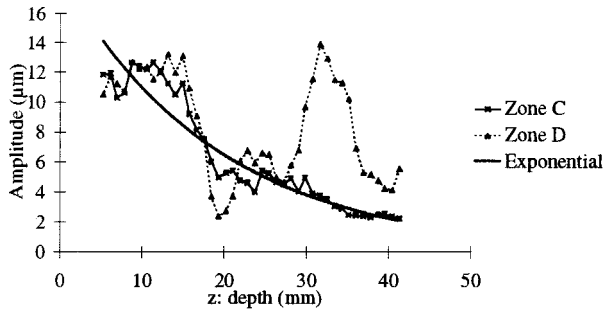

FIG. 6. The amplitude measurements are calculated from the displacements of Fig. 2(a). In the transient zone (C), the amplitude decrement is close to an exponential. The amplitude in the monochromatic zone (D) results from the interference of waves that reflect at boundaries.

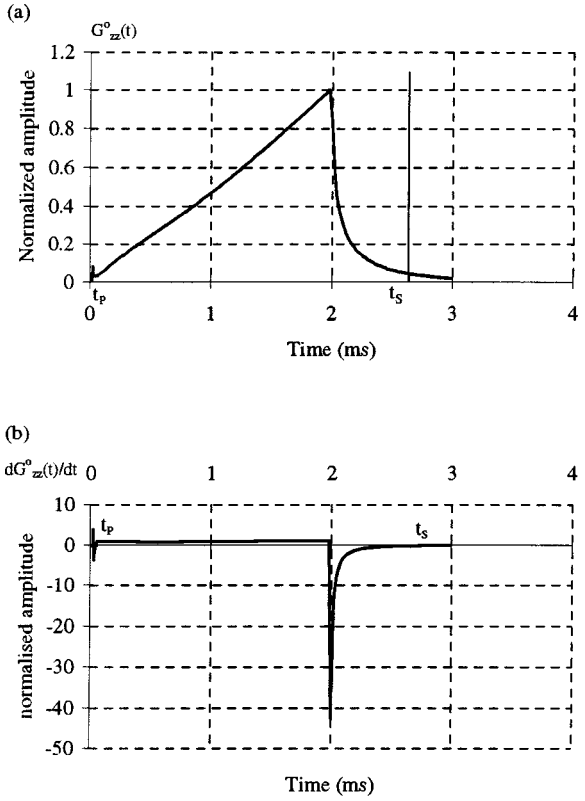

FIG. 7. Green's function (a) and its derivative (b) calculated in soft tissues at the epicenter, for a 2 cm depth and a 1-MHz sampling.

In an elastic solid, Green's function has been calculated by Gakenheimer and Miklowitz[15] for a Heaviside time dependence of a point force. Consequently, this solution is time differentiated in order to have Green's function for a delta excitation. In Appendix A, we present Green's function G^0_{ZZ}. It is the displacement field for a delta excitation in the axis of the punctual force. G^0_{ZZ} is the result of the contribution of a shear (S) and a compressional wave (P):

$$G^0_{ZZ}=G^S_{ZZ}+G^P_{ZZ}. \tag{7}$$

Green's function calculated here has not been adapted to our problem yet: indeed, in the experiments, the displacements are calculated from successive A-lines; what we measure is the particle velocity. Then, in order to compare the theoretical and experimental measurements, the time derivative of Green's function $(\partial G^0_{ZZ})/\partial t$ is calculated. Those functions of time $G^0_{ZZ}(t)$ and $[(\partial G^0_{ZZ})/\partial t](t)$ are plotted in Fig. 7. The overall shape of Green's function, Fig. 7(a), shows a Dirac δ at the arrival time t_P of the compressional wave, a linear increase between t_P and t_S (the arrival time of the shear wave) and a rapid decrease to zero at time t_S. On the time derivative, Fig. 7(b), the compressional wave appears as a δ' function at time t_P, the shear wave as a negative δ function, and a step function links these waves. In both representations, the amplitude of the shear wave dominates, which is a characteristic of soft biological medium; in metals, the amplitude of the axial displacement of the shear wave is negligible. Then, the displacement at a z_0 depth is obtained from the convolution between the time derivative of Green's function $(\partial G^0_{ZZ})/\partial t$ and the time excitation of the force, $F(t)$:

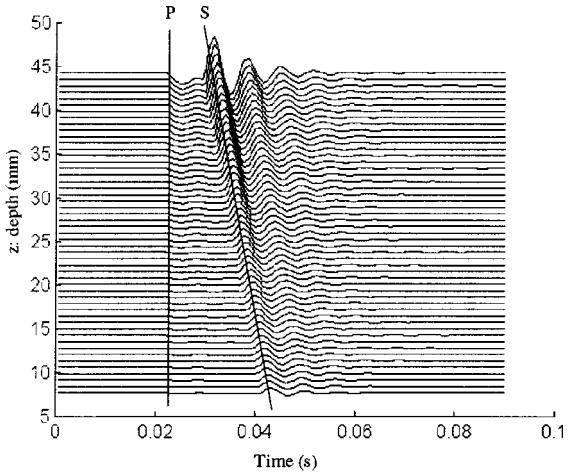

FIG. 8. Theoretical axial displacement of an elastic solid calculated from Green's function in the axis of the point force. The time dependence of the excitation is a 150-Hz damped sinusoid. Displacements due to the propagation of a compressional wave (*P*) and shear wave (*S*) are visible.

$$V_z(z_0,t)=\frac{\partial G^0_{ZZ}}{\partial t}\otimes F(t). \tag{8}$$

If the force excitation of the point source is a 150-Hz damped sinusoid, the theoretical displacement for a depth ranging from 7 to 44 mm is plotted in Fig. 8. (The theoretical axial displacement, Fig. 8, must be compared to the experimental one of Fig. 10 obtained in an agar-gelatin phantom.) In both cases, the axial particle velocity due to the propagation of a compressional wave (*P*) and shear wave (*S*) is clearly visible. The differences are first linked to the size of the medium: no back-propagating shear wave exists in the semi-infinite theoretical medium. Second, the theoretical medium is an elastic solid, thus no absorption and no dissipation occur in this ideal medium. Nevertheless, Green's function gives a good approximation of the behavior of soft tissues. In the next paragraph, a simplified formulation of Green's function explains what happens when very low and very high frequency of vibrations are applied.

H. Approximation of Green's function in soft tissues: Analytical solution of a monochromatic excitation

An approximation around arrival times of the compressional and the shear wave leads us to a simplified expression of Green's function (see Appendix B):

$$\frac{\partial G_{ZZ}}{\partial t}=\frac{C_P}{2\pi\mu z}\left\{\delta'(t-t_L)\frac{t}{\gamma^2}+[Y(t-t_P)-Y(t-t_S)]\times\frac{2}{\gamma^2 t_P}-2\frac{\delta(t-t_S)t}{\gamma t_S}\right\}. \tag{9}$$

Then, the particle velocity for monochromatic vibrations in an infinite elastic medium is obtained from the convolution of Eq. (9) with a sinusoid (see Appendix C):

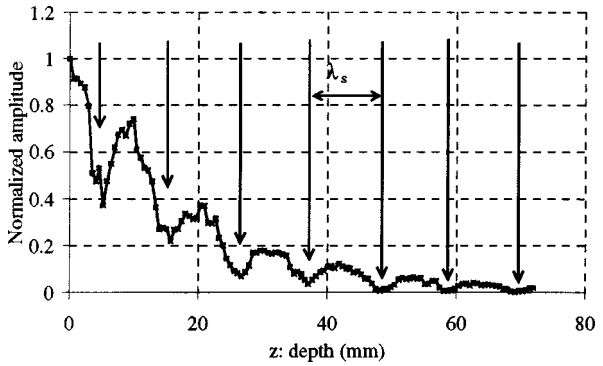

FIG. 9. Interference effect between *P* and *S* waves on amplitude along the vibrator axis when a circular piston is used. The radius of the piston is 1 cm. As a comparison, an exponential fit is also plotted.

$$s(t)=\frac{C_P}{2\pi\mu z^2\gamma^2}\left\{\omega t_P\cos\omega(t-t_P)-2\gamma\sin\omega(t-t_S)+\frac{2\gamma}{\omega t_S}[\cos\omega(t-t_S)-\cos\omega(t-t_P)]\right\}. \tag{10}$$

Three consequences clearly appear in Eq. (10):

(1) For high frequencies, the first term (the one multiplied by the angular frequency) dominates. Thus most of the energy propagates through the solid as a compressional wave.
(2) For very low frequencies, the last term (the one divided by the angular frequency) dominates. It represents a mixing of a shear wave and a compressional wave.
(3) Between those two frequencies, the middle term dominates: it is the shear wave.

In the frequency range of our experiments (250 Hz), even if the shear wave dominates, one can observe the consequences of the low-frequency term on amplitude. Indeed, local minima are observed when the terms ''$\cos\omega(t-t_P)$'' and ''$\cos\omega(t-t_S)$'' are in phase that is to say when

$$\omega(t-t_S)=\omega(t-t_P)+2n\Pi$$

or

$$Zn\approx n\lambda_S. \tag{11}$$

λ_S is the shear wavelength, n is an integer, and z_n are depths whose amplitudes have a local minimum. This condition tells us that local minima can be observed when the depths are one wavelength apart. This peculiar effect is due to the interference between the longitudinal component of a compressional and a shear wave.

I. Experimental verification

The same experimental setup as in Fig. 1 is used and the same axial displacements as in Fig. 2 are obtained. The radius of the circular piston is 10 mm and the frequency of the mechanical excitations is 250 Hz. The phantom is composed of 3% agar and 3% gelatin. Its dimensions are 10×10×9 cm. The amplitude of the displacements from the transient zone are shown in Fig. 9. (Two experiments were needed to get the amplitudes on 70 mm depth.) Local maxima and minima

are well visible on amplitude as function of depth along the axis of the vibrator. In this phantom, the velocity is 3 m/s and thus, for a 250-Hz frequency, the wavelength is estimated to be 1 cm. This is the distance that separates two consecutive minima. As far as the phase of the shear wave is concerned, it is also modified by the compressional wave but, for a point source with free boundary conditions (Dirichlet's boundary conditions), the shear wave dominates and its phase shows negligible interference effects. For example, in Fig. 2(b), one can hardly guess the inflection points on the phase plot: The amplitude is much more affected than the phase by the existence of the compressional wave at low frequency. Nevertheless, one may point out that those local minima on amplitude can be used to measure velocity since they arise one wavelength apart.

J. Summary and consequences

In this section, we have shown three different origins of bias on the measurement of velocity and attenuation of the shear wave in soft tissues. The first one is linked to the finite size of the medium: The waves that reflect from boundaries can strongly modify the velocity as well as the attenuation measurement. The second one is a consequence of the nonnegligible size of the piston. The influence of the diffraction on the velocity is shown when the frequency or the radius of the vibrator is changing. The third bias is due to the existence of a low-frequency compressional wave. The exact solution of the displacement field radiated by a point vibrator predicts the existence of an axial component for a shear and a compressional wave. Those components can interfere constructively or destructively and local extrema appear on amplitude. In the next section, we will describe a method that can avoid these biases. Then, the precise evaluation of the velocity and the attenuation leads us to the numerical value of shear elasticity and shear viscosity and also to the reconstruction of a bilayered phantom.

II. THE IMPULSE TECHNIQUE

A. Tissue motion induced by an impulse

The basic principle of the experiment presented in this section is still the one described in Fig. 1. The difference is that the excitation is no longer sinusoidal. It is replaced by a 2-ms pulsed excitation. Because of the mass of the piston, the real displacement is a damped sinusoid with a 150-Hz central frequency. The size of the source is still 0.5 cm since it is smaller than half a wavelength.

As is shown on the theoretical displacement, Fig. 8, only the shear and the compressional waves can be detected on the axis of a point source. The experimental displacements induced by a pulse excitation in an agar-gelatin phantom are represented in Fig. 10. At about 10 ms, the acoustic impulse is generated from the surface situated at a 60 mm depth by a point source. At $T=10\,\mathrm{ms}$, a first wave creates apparent simultaneous displacements at all depths: It is the compressional wave (*P*). A second wave propagates from the top to the bottom of the phantom at 2.7 ms^{-1}: It is the shear wave (*S*). A third wave is visible; when the shear wave reaches the opposite side of the phantom, it is reflected from the transducer back to the vibrator: It is the ''back'' shear wave (*BS*).

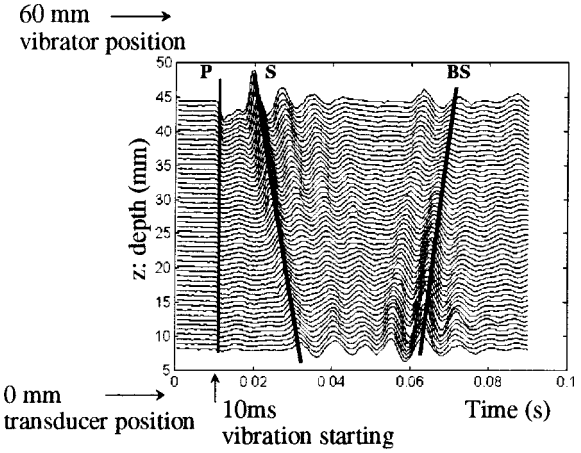

FIG. 10. Displacements in an agar-gelatin phantom. Each horizontal curve represents the displacements of a tissue slice as function of time at one depth along the ultrasonic beam.

Now, we can select the displacement only caused by the propagation of the shear wave front. The interferences with the back shear wave and with the compressional wave are avoided. Then, the velocity and the attenuation are calculated, respectively, from the phase, Fig. 11(a), and from the amplitude, Fig. 11(b), of the shear wave (*S*). By using the equation of velocity Eq. (1) and of attenuation, Eq. (12) obtained in viscoelastic medium,[7] Lamé coefficients are deduced: $\mu_1=7760\pm350$ Pa, $\mu_2=3.6\pm0.2$ Pa s:

$$\alpha_S=\sqrt{\frac{\rho\omega^2(\sqrt{\mu_1^2+\omega^2\mu_2^2}-\mu_1)}{2(\mu_1^2+\omega^2\mu_2^2)}}. \tag{12}$$

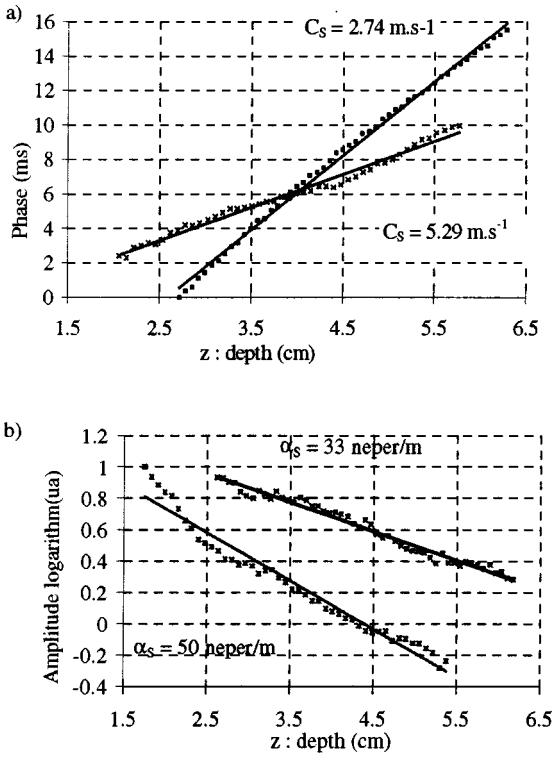

FIG. 11. Phase (a) and amplitude logarithm (b) of the shear wave (*S*) in an agar-gelatin phantom (squares) and in a beef muscle (crosses).

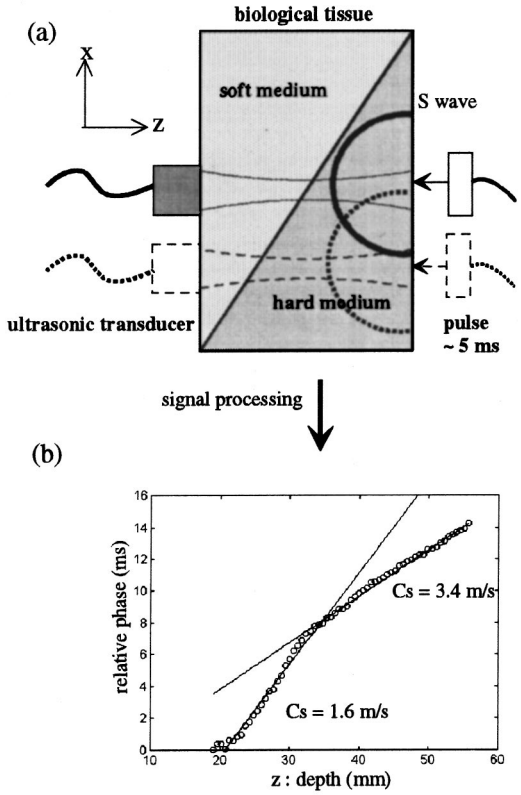

FIG. 12. (a) Experimental setup and (b) phase obtained in a phantom composed of two different media.

The same experiment is made in a beef muscle. The shear elasticity and shear viscosity are extracted from the experimental phase and amplitude measurements shown in Fig. 11(a) and (b): $\mu_1 = 21\,400 \pm 500$ Pa, $\mu_2 = 22.5 \pm 2.6$ Pa s.

Now, global quantitative measurement of shear elasticity and shear viscosity of soft tissues in bulk is possible. At the moment more studies are necessary to compare those values with classical measurements of elasticity and viscosity obtained with an INSTRON and a rheometer. But the order of magnitude of these results are in good agreement with the measurements of Parker.[9] The next step is to test this technique in inhomogeneous media. This is the topic of Sec. III.

B. Relative hardness imaging

The main goal of the acoustic impulse method is to realize an elasticity image of soft tissue. In this perspective, an agar-gelatin phantom was made. It was composed of two parts filling each side of the cube diagonal, Fig. 12(a). The first part (3% agar and 2% gelatin) was in contact with the transducer. The second part (3% agar and 6% gelatin) was in contact with the vibrator. The dimensions of the whole phantom were $8 \times 8 \times 7.5$ cm.

In first measurement of phase, Fig. 12(b) is obtained. Because of the different velocity of the shear wave in the two media, the phase shows two different sections. Velocity is calculated in the two different media from the inverse phase derivative. In order to avoid infinite value of local velocity, we scale the phase derivative in a 256 gray level image. It represents inverse velocity: slowness. Then, a 2-mm lateral displacement of the experimental setup along the *x*-axis is

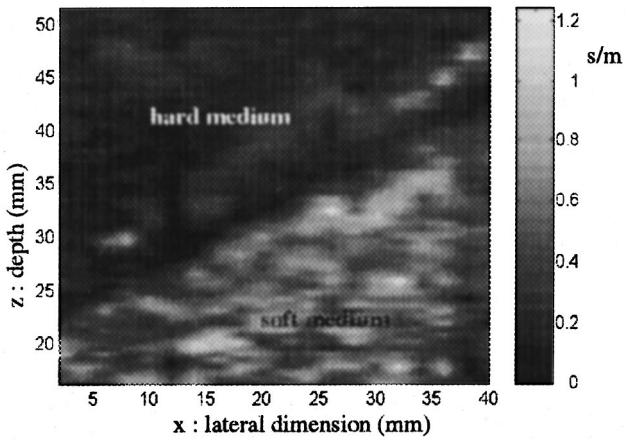

FIG. 13. Slowness image of a phantom composed of two media with different elasticities when the acoustic impulse technique is used.

applied [in the dashed line in Fig. 12(a)] and a second measurement of phase is obtained from another zone of the phantom. A second line of slowness is added to the image, and so on.

The image of Fig. 13 is made of 20 slowness lines. The two different parts are clearly defined: The bright part shows the zone where the velocity is the lowest, i.e., the soft medium, whereas the dark part shows the region where the velocity is the greatest: the hard medium. Further work is needed to determine the limits and the resolution of this method.

C. Elasticity order of magnitude

In the case in which viscosity is negligible compared to elasticity, that is to say up to 200 Hz or so, velocity is proportional to the square root of shear elasticity μ_1. In the first medium, the shear wave velocity is twice as small as the second one. Then, the second medium is about four times harder than the first medium. By comparison, the fibroadenoma tissue (a kind of fibrous tumor) is four times harder than the surrounding tissue. Hard nodules from breast cancer are thought to be up to seven times harder.[16]

III. CONCLUSION

The problem of wave generation in soft tissues has been investigated for a piston source. The displacement field along its axis is predicted by Green's functions in elastic solid. These mathematical solutions shows the propagation of first a low-frequency compressional wave and second of a shear wave. This shear wave is shown to have two important characteristics: It has a longitudinal component and it dominates for low frequency of vibrations. On the contrary, for high frequency, most of the energy of a piston propagates as a compressional wave in soft tissues. The viscoelastic parameters can be extracted from the propagation characteristics of this shear wave. But some biases can disturb the measurements. Thus in order to avoid: (1) the reflections at boundaries; (2) the diffraction effects of the piston; and (3) the interference effects that are caused by the existence of a low-frequency compressional wave; we have chosen to work with a pulsed point source. In this method, an acoustic im-

pulse is generated from the surface of the medium and the propagation characteristics of the pulse are measured. Signal processing based on the correlation of ultrasonic signals allows us to select the propagating shear wave and thus to separate it from both the compressional wave and from the reflected waves. Consequently, in opposition to sonoelasticity or elastography, this method is free from boundary conditions and thus numerical values of the viscoelastic parameters are found. Further works will compare this method to standard techniques. A preliminary image, based upon the local velocity measurement of the shear wave, shows the zones with different elasticity. In the future, information about both local velocity and local attenuation should lead to an absolute elasticity image.

APPENDIX A: GREEN'S FUNCTION FOR A PULSED TIME EXCITATION

Gakenheimer and Miklovitz[15] have calculated Green's function of a point source traveling on a surface of a semi-infinite elastic isotropic solid. We present here the solution corresponding to normal displacements induced by a motionless point source with a pulsed time dependence at the epicenter:

$$\begin{aligned} &G_{ZZ}^{0}=G_{ZZ}^{S}+G_{ZZ}^{P},\\ &G_{ZZ}^{S}=-\frac{C_P}{\pi\mu z^2}\frac{\partial}{\partial t}\left[Y(t-t_S)t\frac{k_2^S k_3^S}{k_5^S}\right],\\ &G_{ZZ}^{P}=\frac{C_P}{2\pi\mu z^2}\frac{\partial}{\partial t}\left[Y(t-t_P)t\frac{k_1^P k_3^P}{k_5^P}\right], \end{aligned} \tag{A1}$$

$$\begin{cases} k_1^S=\gamma^2\left(\dfrac{2t^2}{t_S^2}-1\right),\\ k_2^S=\gamma^2\left(\dfrac{t^2}{t_S^2}-1\right),\\ k_3^S=\sqrt{\gamma^2\left(\dfrac{t^2}{t_S^2}-1\right)+1},\\ k_4^S=\gamma\dfrac{t}{t_S},\\ k_5^S=k_1^{S2}-4k_2^S k_3^S k_4^S, \end{cases} \tag{A2}$$

$$\begin{cases} k_1^P=\left(\dfrac{2t^2}{t_P^2}-1\right)+\gamma^2,\\ k_2^P=\left(\dfrac{t^2}{t_P^2}-1\right),\\ k_3^P=\dfrac{t}{t_P},\\ k_4^P=\sqrt{\dfrac{t^2}{t_P^2}-1+\gamma^2},\\ k_5^P=k_1^{P2}-4k_2^P k_3^P k_4^P, \end{cases} \tag{A3}$$

where C_P is the compressional wave velocity, z is the depth along the axis of the point source, μ is the Lamé coefficient of shear elasticity, $Y(t-t_i)$ is the Heaviside function, t_S is the arrival time of the shear wave, t_P is the arrival time of the compressional wave, and $\gamma=C_P/C_S$.

APPENDIX B: APPROXIMATE EXPRESSION FOR GREEN'S FUNCTION

From Green's function obtained at the epicenter of a semi-infinite elastic solid for a pulsed time excitation, approximations of the normal displacements around the arrival time of the shear and the compressional wave are calculated here.

For $t\sim t_P$:

$$G_{ZZ}^{P}\approx\frac{C_P}{2\pi\mu z^2}\left[\frac{\delta(t-t_P)t}{\gamma^2}+\frac{Y(t-t_P)}{\gamma^2}\right]. \tag{B1}$$

For $t\sim t_S$:

$$G_{ZZ}^{S}\approx-\frac{C_P}{\pi\mu z^2}\left[\frac{2Y(t-t_S)t}{\gamma^2}\right]. \tag{B2}$$

For $t\gg t_S\gg t_P$ (far from the arrival time):

$$G_{ZZ}^{P}\approx\frac{C_P}{2\pi\mu z^2}\left[\frac{2Y(t-t_P)t}{\gamma^2 t_P}\right], \tag{B3}$$

$$G_{ZZ}^{S}\approx-\frac{C_P}{\pi\mu z^2}\left[\frac{Y(t-t_S)t}{\gamma^2 t_P}\right]. \tag{B4}$$

So the approximate expression is:

$$\begin{aligned} G_{ZZ}\approx\frac{C_P}{2\pi\mu z^2}\Bigg[&\frac{\delta(t-t_P)t}{\gamma^2}+[Y(t-t_P)-Y(t-t_S)]\frac{2t}{\gamma^2 t_P}\\ &-4\frac{Y(t-t_S}{\gamma^2}+\frac{Y(t-t_P)}{\gamma^2}\Bigg]. \end{aligned} \tag{B5}$$

As far as normal velocity of displacement is concerned, we finally obtain:

$$\begin{aligned} \frac{\partial G_{ZZ}}{\partial t}\approx\frac{C_P}{2\pi\mu z}\Bigg\{&\delta'(t-t_P)\frac{t}{\gamma^2}+[Y(t-t_P)-Y(t-t_S)]\\ &\times\frac{2}{\gamma^2 t_P}-4\frac{\delta(t-t_S)}{\gamma^2}+\frac{\delta(t-t_P)}{\gamma^2}\\ &+[\delta(t-t_P)-\delta(t-t_S)]\frac{2t}{\gamma^2 t_P}\Bigg\}. \end{aligned} \tag{B6}$$

APPENDIX C: CONVOLUTION OF GREEN'S APPROXIMATE FUNCTION WITH A SINUSOID

Let's consider S_{ZZ} as being the normal particle velocity at the epicenter of a semi-infinite elastic solid when sinus excitation of a point source is applied on the surface:

$$\begin{aligned} &S_{ZZ}=\frac{\partial G_{ZZ}}{\partial t}\otimes\sin(\omega t),\\ &S_{ZZ}=\frac{C_P}{2\pi\mu z}\Bigg\{\delta'(t-t_P)\frac{t}{\gamma^2}+[Y(t-t_P)-Y(t-t_S)]\\ &\quad\times\frac{2}{\gamma^2 t_P}-4\frac{\delta(t-t_S)}{\gamma^2}+\frac{\delta(t-t_P)}{\gamma^2}+[\delta(t-t_P)\\ &\quad-\delta(t-t_S)]\frac{2t}{\gamma^2 t_P}\Bigg\}\otimes\sin(\omega t). \end{aligned} \tag{C1}$$

Thus we must calculate the following terms:

$$\bullet[Y(t-t_P)-Y(t-t_S)]\otimes\sin(\omega t)=\int_{t_P}^{t_S}\sin\omega(t-\tau)d\tau,$$

$$[Y(t-t_P)-Y(t-t_S)]\otimes\sin(\omega t)$$
$$=\frac{-1}{\omega}[\cos\omega(t-t_S)-\cos\omega(t-t_P)],$$

$$\bullet\,\delta(t-t_S)t\otimes\sin(\omega t)=\int_{-\infty}^{+\infty}\delta(\tau)(\tau+t_S)\sin\omega(t-\tau-t_S)d\tau,$$

$$\delta(t-t_S)t\otimes\sin(\omega t)=t_S\sin\omega(t-t_S), \tag{C2}$$

$$\bullet\,\delta'(t-t_P)t\otimes\sin(\omega t)=\int_{-\infty}^{+\infty}\delta'(\tau)(\tau+t_P)$$
$$\times\sin\omega(t-\tau-t_P)d\tau,$$

$$\delta'(t-t_P)t\otimes\sin(\omega t)=-[\sin\omega(t-t_P)-\omega t_P\cos\omega(t-t_P)].$$

Then, the analytical solution can be written as:

$$s(t)=\frac{C_P}{2\pi\mu z^2\gamma^2}\left\{\omega t_P\cos\omega(t-t_P)-2\gamma\sin\omega(t-t_S)\right.$$
$$\left.+\frac{2\gamma}{\omega t_S}[\cos\omega(t-t_S)-\cos\omega(t-t_P)]\right\}. \tag{C3}$$

In this last expression, secondary order terms have been neglected.

[1] Y. Yamakoshi, J. Sato, and T. Sato, ''Ultrasonic imaging of internal vibration of soft tissue under forced vibration,'' IEEE Trans. Ultrason. Ferroelectr. Freq. Control **UFFC-37**, 45–53 (1990).

[2] F. Lee, J. P. Bronson, R. M. Lerner, K. J. Parker, S. R. Huang, and D. J. Roach, ''Sonoelasticity imaging results in *in vitro* specimens,'' Radiology **181**, 237–239 (1991).

[3] V. V. Kazakov and B. N. Klochkov, ''Low frequency mechanical properties of the soft tissue of the human arm,'' Biophysics. **34**, 742–747 (1989).

[4] V. Dutt, R. R. Kinnick, and J. F. Greanleaf, ''Acoustic shear wave displacement measurement using ultrasound,'' IEEE Ultrasonic Symposium **2**, 1185–1188 (1996).

[5] R. Muthupillari, D. J. Lomas, P. J. Rossman, J. F. Greenleaf, A. Manduca, and R. L. Ehman, ''Magnetic resonance elastography by direct visualization of propagating acoustic strain wave,'' Science **269**, 29 (1995).

[6] K. J. Parker and R. M. Lerner, ''Sonoelasticity of organs: Shear waves ring a bell,'' J. Ultrasound Med. **11**, 387–392 (1992).

[7] H. F. Pollard, *Sound Wave in Solid* (Pion Limited, London, 1977), p. 206.

[8] J. Ophir, I. Céspedes, H. Ponnekanti, Y. Yasdi, and X. Li, ''Elastography: A quantitative method for imaging the elasticity of biological tissues,'' Ultrason. Imaging **13**, 111–134 (1991).

[9] K. J. Parker, S. R. Huang, R. A. Musulin, and R. M. Lerner, ''Tissue response to mechanical vibrations for sonoelasticity imaging,'' Ultrasound Med. Biol. **16**, 241–246 (1990).

[10] W. F. Walker and G. E. Trahey, ''A fundamental limit on the performance of correlation based on phase correction and flow estimation technique,'' IEEE Trans. Ultrason. Ferroelectr. Freq. Control **UFFC-41** (1994).

[11] H. L. Oestrecher, ''Field and impedance of an oscillating sphere in a viscoelastic medium with an application to biophysics,'' J. Acoust. Soc. Am. **23**, (1951).

[12] K. Fujii, T. Sato, K. Kameyama, T. Inoue, K. Yokoyama, and K. Kobayashi, ''Imaging system of precise hardness distribution in soft tissue *in vivo* using forced vibration and ultrasonic detection,'' in *Acoustical Imaging* (Plenum, New York, 1995), Vol. 21.

[13] A. Lhemery, ''Un Modèle efficace pour Prédire le Champ Transitoire Rayonné dans un Milieu Elastique par les Transducteurs Ultrasonores,'' J. Phys. IV **4**, (1994).

[14] D. Royer and E. Dieulesaint, *Ondes Elastiques dans les Solides* (Masson, Paris, 1996), Tome 1, pp. 43–49.

[15] D. C. Gakenheimer and J. Miklowitz, ''Transient excitation of an elastic half-space by a point load traveling on the surface,'' J. Appl. Mech. **36**, 505 (1969).

[16] A. P. Sarvazyan, ''Shear acoustic properties of soft biological tissues in medical diagnotics,'' J. Acoust. Soc. Am. **93**, 2329 (1993).

Ultrasound-induced cell lysis and sonoporation enhanced by contrast agents

Mark Ward and Junru Wu
Department of Physics, University of Vermont, Burlington, Vermont 05405

Jen-Fu Chiu
Department of Biochemistry, University of Vermont, Burlington, Vermont 05405

(Received 19 August 1998; revised 9 September 1998; accepted 5 February 1999)

The enhancement of ultrasound-induced cell destruction, lysis, and sonoporation in low cell concentration suspensions (2×10^5/mL) by the presence of contrast agents (gas bubble to cell ratio=230) was demonstrated using cervical cancer cells (HeLa *S*3) suspensions containing micron-size denatured albumin microspheres filled with air (Albunex®) or octafluoropropane (Optison™). The suspensions were insonificated by 2-MHz continuous or tone burst ultrasound in near field. The spatial peak-pressure amplitude was 0.2 MPa. The enhancement of cell destruction due to Optison™ was shown to be much higher than that due to Albunex® for similar bubble concentration and ultrasound conditions. For tone burst exposures, significant lysis and sonoporation only occurred in the presence of a contrast agent. The majority of the bioeffects observed occured in the first 5 min of exposure. The relationship between the enhancement of bioeffects and duty cycle of tone burst ultrasound appears to indicate that both stable gas spheres of contrast agents and cavitation nuclei created by the disruption of the gas spheres play a significant role in causing the bioeffects. [S0001-4966(99)02205-5]

PACS numbers: 43.80.Gx, 43.35.Ei [FD]

INTRODUCTION

It is well known that a number of bioeffects can occur in a liquid when it is exposed to ultrasound. Typical examples include the acceleration or induction of chemical reactions, disruption of cells, and the degradation of DNA (Nyborg, 1996). These phenomena are related to the stimulated bubble activities that are commonly called acoustic cavitation. In a liquid, there are usually small dissolved air bubbles (called the nuclei for cavitation). These small bubbles, excited by ultrasound, may grow through coalescence or rectified diffusion. A bubble may oscillate vigorously or collapse adiabatically at a relatively high-pressure amplitude, producing internal gas pressure of hundreds to thousands of atmospheres and temperatures of thousands of degrees (°C) (Apfel, 1997). Consequently, shock waves and free radicals (H^+, O_2^-, and OH^-) may be produced. This type of cavitation has been called inertial cavitation. If viable cells exist in the liquid, cell-membrane damage (cell lysis) may occur (Miller *et al.*, 1996).

Interest in the bioeffects of ultrasound has been energized recently with the arrival of contrast agents for diagnostic ultrasound. These agents are often used to enhance echogenicity in diagnostic applications in cardiology (Goldberg, 1993), such as the evaluation of a cardiac condition, the visualization of blood flow, and the assessment of myocardial perfusion. Albunex® and Optison™ (formerly called FS069) are two commercially available ultrasound contrast agents (Mallinckrodt Medical, Inc., St. Louis, MO) approved for clinical use in the U. S. by the FDA. They are micron-size denatured albumin microspheres. The former are filled with air, and the latter contain octafluoropropane. The microbubble concentrations are $3-5\times10^8$/mL for Albunex® and $5-8\times10^8$/mL for Optison™. The mean diameter of the microbubbles is 2–5 μm for both (product specifications from Mallinckrodt Medical, Inc.). They both show maximum attenuation at a frequency between 2–3 MHz (Marsh *et al.*, 1997). Since the solubility of octafluoropropane in water is much lower than that of air, the effect of Optison™ is more persistent than that of Albunex®. It has been shown that the duration of contrast produced by Optison™ exceeds that of Albunex® significantly *in vivo* (>5 min vs <45 s). The ability of Optison™ to opacify the cardiac ventricular chambers is greater than Albunex®; the dose required to opacify the left ventricle is much smaller than that required by Albunex® (0.2 mL vs 15–20 mL) (Dittrich *et al.*, 1994, 1995; Brown *et al.*, 1996).

It has been found from *in vitro* studies that the presence of small amounts of Albunex® in whole blood can significantly reduce the acoustic pressure amplitude threshold for cavitation and hemolysis (Miller and Thomas, 1996; Brayman *et al.*, 1997). Miller *et al.* (1997) also found that at high cell concentration (5×10^9/mL) and low gas bubble to cell ratio (0.04), hemolysis increased with increasing contrast agent concentration and decreased with increasing cell concentration when 1.6 MPa, 10-μs, and 1% duty cycle 2.25-MHz pulses and Albunex® were applied. Enhancement of ultrasonically induced hemolysis by Optison™ was also compared to Albunex® (Miller and Gies, 1998), for pulsed exposure (2.4 MHz, 3.2 MPa pressure amplitude, 1% duty cycle and 10-μs pulses), greater hemolysis was observed using 50% Optison™ than 50% Albunex® after longer than 1 s exposure. It has also been found that by applying relatively low amplitude ultrasound, with spatial peak-pressure amplitude as low as 0.1 MPa, to Chinese hamster ovary cells in a

suspension that contains 10% Albunex® and has a gas bubble to cell ratio of 40, the membrane could become temporarily open to small and large molecules and then reseal (Bao *et al.*, 1997); the large molecules were then trapped in the cells. This phenomenon is called sonoporation. Sonoporation may be exploited to improve chemotherapy efficiency and gene transfection *in vivo* (Greenleaf, 1998).

The present study intends to examine the bioeffects, cell lysis, and sonoporation in particular, induced by low amplitude (0.2 MPa) 2-MHz ultrasound on suspensions of cervical cancer cells in the presence of contrast agents (Albunex® or Optison™). It is hypothesized that a high gas bubble (Optison™) to cell (cervical cancer cells) ratio (230) will result in significant amounts of cell destruction (complete disintegration of cells) in a low cell concentration suspension (2×10^5/mL) under exposure of low-amplitude ultrasound (0.2 MPa). It is further hypothesized that the amount of cells in a suspension of the same conditions which suffer partial lysis (partial lysis may be defined as a permanent violation of the cell-membrane integrity that does not cause the cell to disintegrate; it is still definable as a cell) and/or sonoporation will vary with parameters of the exposure, such as the total exposure time and the duty cycle of the ultrasound. Also, the use of Albunex® in place of Optison™ is expected to cause lower levels of the bioeffects under the same conditions.

I. EXPERIMENTAL METHODS

Cervical cancer cells (HeLa *S*3) were routinely cultured as a monolayer in 100-mm dishes in a solution of Dulbecco's Modified Eagle's minimal essential medium (DMEM) (GIBCO, Grand Island, New York) with 10% fetal bovine serum (FBS) (GIBCO, Grand Island, New York). When the cells reached approximately 70% confluency, they were harvested by trypsinization and resuspended at a concentration of 2×10^5 cells/mL. For exposures, 2-mL samples were aliquoted into six plastic culture tubes of 10 mm diameter and 75 mm length (Kimble, Owens-Illinois, Toledo, OH) and kept on ice; each tube had 4×10^5 cells. To two or three of the six test tubes, 240 μL Albunex® (Lot # 030897) or 140 μL of Optison™ (Lot # 114097) was added. Thus, the concentration of Albunex® (or Optison™) for samples in those tubes was equal to 12% (or 6.5%). This ensured that the bubble number concentration of the tubes filled with Albunex® was approximately the same as those of test tubes filled of Optison™. The ratio of gas bubbles to the cervical cancer cells was about 230. One at a time, the samples of the test tubes were placed in the exposure chamber, which consisted of a glass tank ($12\times12\times76$ cm) filled with water (no significant difference in all our results, which are to be presented, was found if the tank was filled with degassed or air-saturated water; data of the differences are not shown here) at room temperature. The sample tubes were attached at the top to a small dc motor, which rotated the sample at 200 rpm. This rotation ensured mixing of the sample throughout the exposure period, and eliminated the effect of cells and the microbubbles being pushed against the downstream wall by the sound waves. The test tubes were immersed in the water and aligned with the ultrasound beam. Samples in the test tubes were either exposed or sham-exposed (ultrasound turned off) one at a time for a period of time, and then returned to ice until all the exposures were completed and ready for analysis. The whole procedure was called a trial and lasted about one h or less. Several trials were performed under the same conditions but on different occasions.

After all samples were exposed in a trial, each sample was mixed and a small volume (50 μL) was placed in a hemocytometer chamber. This allowed the number of surviving cells in a known volume to be counted using a light microscope. Both sides of the hemocytometer were used, and the average was taken. Dead cells that were either completely disintegrated and not at all visible, or were obviously fragmented, were therefore not counted. Each trial's raw data were normalized to a sham-exposed sample to account for differences in preparation of each trial.

Two different transducers were used for this experiment. Both were driven by a Hewlett Packard 3314A function generator (Hewlett Packard, CA) and an ENI 2100L rf power amplifier (ENI, Rochester, NY). Transducer 1 was a device made in our laboratory, with a planar aperture diameter of 3.8 cm. It was operated in a continuous wave (cw) mode at a frequency of 2 MHz, one of its thickness modes. Transducer 2 was a Panametrics A 304 S planar transducer (2.5 cm diameter) (Panametrics, MA). It was operated in a tone burst mode, with a resonance frequency of 2 MHz. A small (the probe diameter is 0.2 mm) pvdf hydrophone was used to measure the ultrasound field at a plane which was parallel to the wavefront of the ultrasound and 10 cm from the front surface of the transducer. This was where the test tubes were installed. The positive peak pressure and negative peak pressure were found to be approximately equal for both transducers. The ultrasound fields of both transducers measured had typical near-field characteristics. The -6-dB beamwidths were 2.5 and 2 cm for transducer 1 and 2, respectively; they are both greater than the diameter of the test tubes. The spatial peak-pressure amplitude was determined to be 0.2 MPa *in situ* for both cases. The calibration of ultrasound amplitude was done using the beam scan and integration technique and the acoustic power measurement using the radiation force (Beissner, 1992). The attenuation of the test tubes was found by measuring the ultrasound amplitude with/without placing the test tube *in situ* and before the hydrophone. Figure 1 is an ultrasound pressure-amplitude distribution at the *in situ* plane for transducer 2.

To further investigate the cell lysis and sonoporation generated by ultrasound and contrast agents on HeLa *S*3 cells, another set of experiments was performed. The sample preparation was identical to the above described except that the cell suspension was supplemented with 10% fluorescein isothiocyanate–dextran (FITC-dextran) (10 mg/mL in phosphate buffered saline) (FD-500 S, Sigma Chemical Co., St. Louis, MO). These large fluorescent-labeled dextran molecules (average molecular weight 500 000) normally are unable to enter the cells. Samples were exposed to the 2-MHz tone burst ultrasound generated by transducer 2 for a period of time. After exposure, the samples were centrifuged and washed with fresh DMEM to remove the remaining fluorescent dextran, centrifuged again, and resuspended in 200 μL

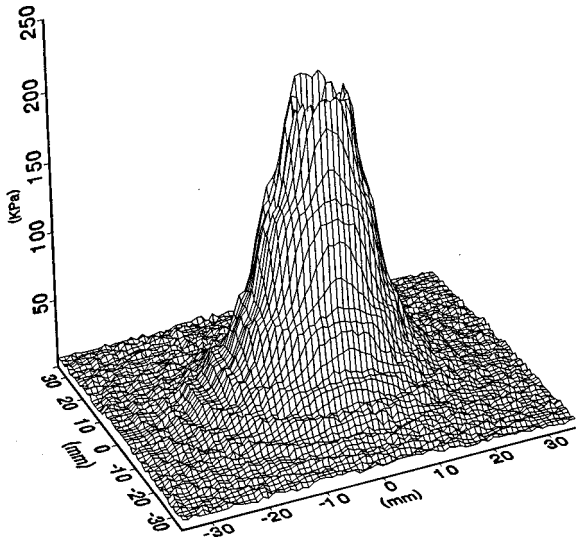

FIG. 1. Ultrasound amplitude distribution at a plane that is 10 cm from the transmitter and perpendicular to the ultrasound propagation.

of DMEM. At this time, an equal amount of trypan blue dye was added to each sample, bringing the total volume to 400 μL. The total number of cells, as well as cells that were stained with the trypan blue and cells that were fluorescent, was counted using a microscope (Nikon Optiphot-2) that could operate alternately in both normal and epifluorescent modes. When it was in epifluorescent mode, the wavelengths of the excitation and fluorescence were about 440 and 530 nm, respectively.

II. RESULTS

Figure 2 is a plot of the average relative number of surviving cells of seven independent trials of one sample taken per regimen counted by the hemocytometer vs sample test tube number (sample 1 to 6 corresponding to the horizontal axis from the left to the right in Fig. 2). Samples 1 and 6 were sham-exposed (No US) with Optison™ (W/OPT) added and sample 1 was used as a control. Samples 2 and 3 were exposed to the cw ultrasound for 10 min and had the addition of 0 (No OPT) and 140 μL Optison™ (W/OPT), respectively. Samples 4 and 5 were exposed to the tone burst ultrasound of 10-kHz repetition frequency and 10 % duty cycle (D. C.) for 10 min and had 0 and 140 μL Optison™, respectively. As expected, since samples 6 and 1 were both sham-exposed (rotated, but with the ultrasound off), they did not show any significant deviation from each other ($P=0.337$). Since the exposures were performed one at a time and in a sequential order from sample 1 to sample 6, this indicates that the effect of the time lapse (about 1 h) between sample 1 and sample 6 is not significant. Also, sham-exposed was a sample with 6.5 % Optison™ added, and the results (not shown) were very similar to those of samples 1 and 6. Significant reduction in cell number with respect to sample 1 was observed in sample 2 ($P=0.003$), sample 3 ($P<0.001$), sample 4 ($P=0.031$), and sample 5 ($P<0.001$). Comparing identical treatments with and without Optison™ added, it is seen that sample 3 is significantly less than sample 2 ($P=0.013$), and sample 5 is significantly less than sample 4 ($P<0.001$).

The second set of experiments was designed to evaluate the partial lysis (referred to simply as lysis henceforth) and sonoporation of the cells. The evidence of lysis or sonoporation was easily observable under microscopic studies. Only cells whose membranes were open when the trypan blue was added had their interiors stained. Similarly, only those cells whose membranes were open during the exposure, but closed at the time of washing, had FITC trapped inside. Since the trypan blue was added after the washing step, one would, in general, expect to end up with a sample containing some normal (unaffected) cells, some stained (lysed) cells, and some fluorescent (sonoporated) cells, with no cells both stained and fluorescent.

Figure 3 is a plot of the average percentage of stained (or fluorescent) cells of three trials versus sample number.

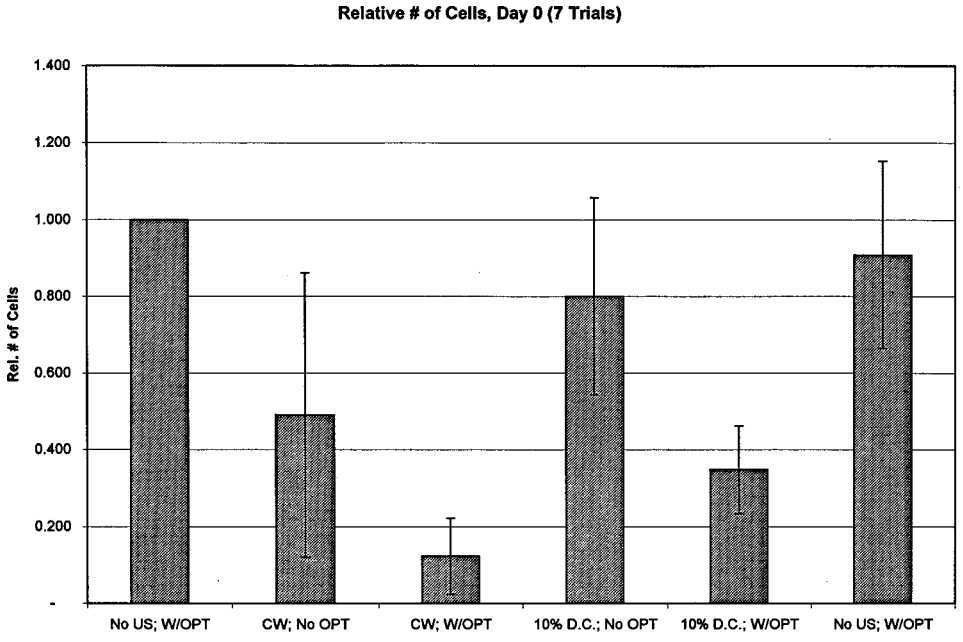

FIG. 2. Relative number of cells in each sample versus sample number. Samples were counted after all exposures were completed. All exposures or sham-exposures were 10 min. (1) Sham-exposed; (2) Continuous 2-MHz ultrasound, without Optison™; (3) Continuous 2-MHz ultrasound with 6.5% Optison™; (4) Tone burst (10% duty cycle) 2-MHz ultrasound, without Optison™; (5) Tone burst (10% duty cycle) 2-MHz ultrasound, with 6.5% Optison™; (6) Sham-exposed. The error bars represent one standard deviation from the mean of seven trials.

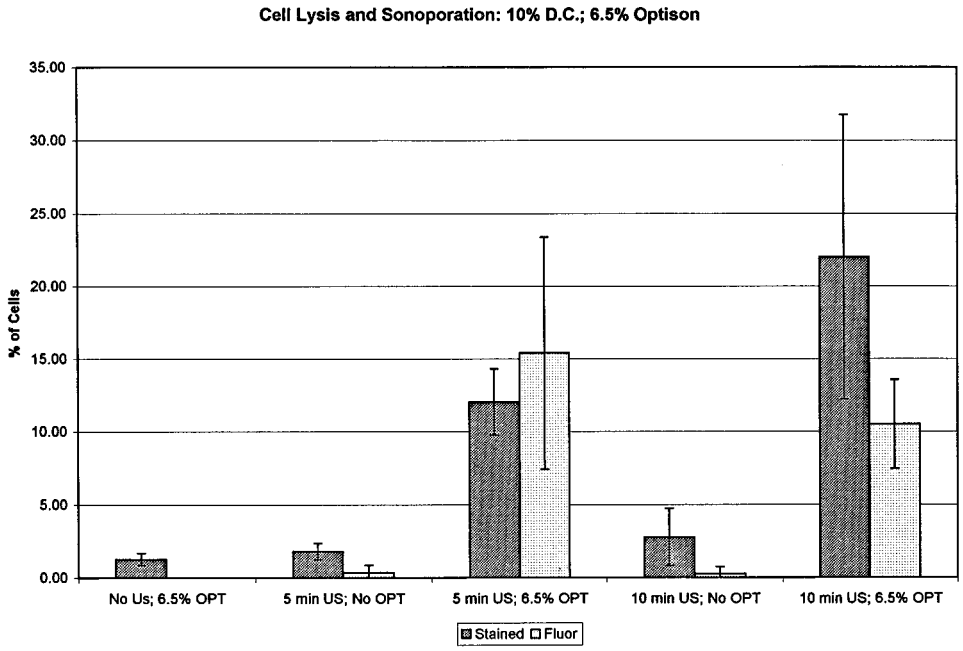

FIG. 3. Cell lysis is indicated by staining of cell interior with trypan blue dye. Fluorescent-labeled dextran trapped inside a cell indicates sonoporation. At least 100 total cells were counted in three separate trials. All samples were sham-exposed or exposed to 2-MHz ultrasound with a 10% duty cycle. (1) Sham-exposed for 5 min, with 6.5% Optison™; (2) Exposed for 5 min, without contrast agents; (3) Exposed for 5 min, with 6.5% Optison™; (4) Exposed for 10 min, without contrast agents; (5) Exposed for 10 min, with 6.5% Optison™. The error bars represent one standard deviation from the mean of three trials.

Sample 1 in Fig. 3, which was sham-exposed, had no fluorescent cells and very few (1.3%) stained cells. Samples 2 and 3 were exposed for 5 min of toneburst ultrasound of 10-kHz repetition frequency and 10 % duty cycle (D. C.), with and without the addition of 6.5 % Optison™, respectively. Likewise, samples 4 and 5 were exposed for 10 min, with and without 6.5 % Optison™. There were no observed cases of a cell that was both stained and fluorescent. Only sample 3 and sample 5 had significant percentages of fluorescent cells ($P=0.014$ and $P=0.002$). Those same samples also had the only significant percentages of stained cells ($P<0.001$ and $P=0.010$) larger than sample 1. The samples that did not have Optison™ added showed only insignificant amounts of staining or fluorescence. It may be noted that sample 5 does not have significantly higher percentages of lysis or sonoporation than sample 3 ($P=0.081$ and $P=0.188$, respectively).

Figure 4 is a similar plot, except 12% Albunex® was used to replace 6.5% Optison™. In this case, we include the result of a sample (sample 0) that was not exposed to ultrasound and had no Albunex® added. The result of sample 0 was similar to that of sample 1 (no ultrasound and with 12% Albunex® added). As in Fig. 3, only sample 3 and sample 5 had significant percentages of fluorescent cells ($P<0.001$ and $P=0.022$). Only sample 5 had a significant percentage of stained cells, relative to sample 1 ($P=0.039$). In comparing the data from Figs. 3 and 4, it is observed that for the treatment of sample 3, Optison™ results in significantly more lysis ($P=0.023$) and sonoporation ($P=0.041$) than Albunex®. For the treatment of sample 5, it is observed that

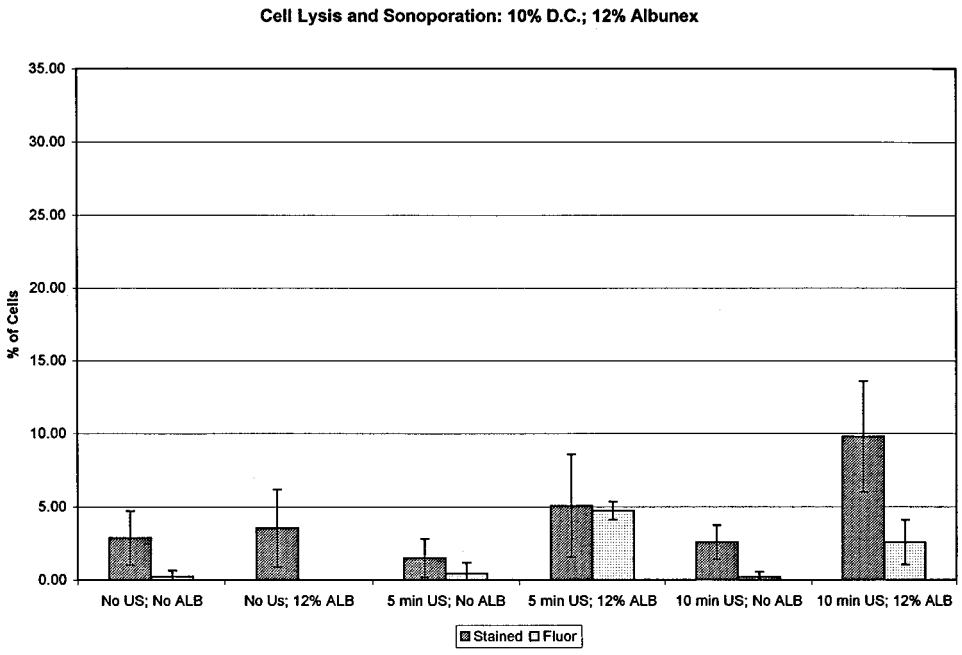

FIG. 4. There are 6 samples which are numbered from zero to six, respectively. All samples were sham-exposed or exposed to 2-MHz ultrasound with a 10% duty cycle. (1) Sham-exposed for 5 min, without contrast agents; (2) Sham-exposed for 5 min, with 12% Albunex®; (3) Exposed for 5 min, without contrast agents; (4) Exposed for 5 min, with 12% Albunex®; (4) Exposed for 10 min, without contrast agents; (5) Exposed for 10 minutes, with 12% Albunex®. The error bars represent one standard deviation from the mean of three trials.

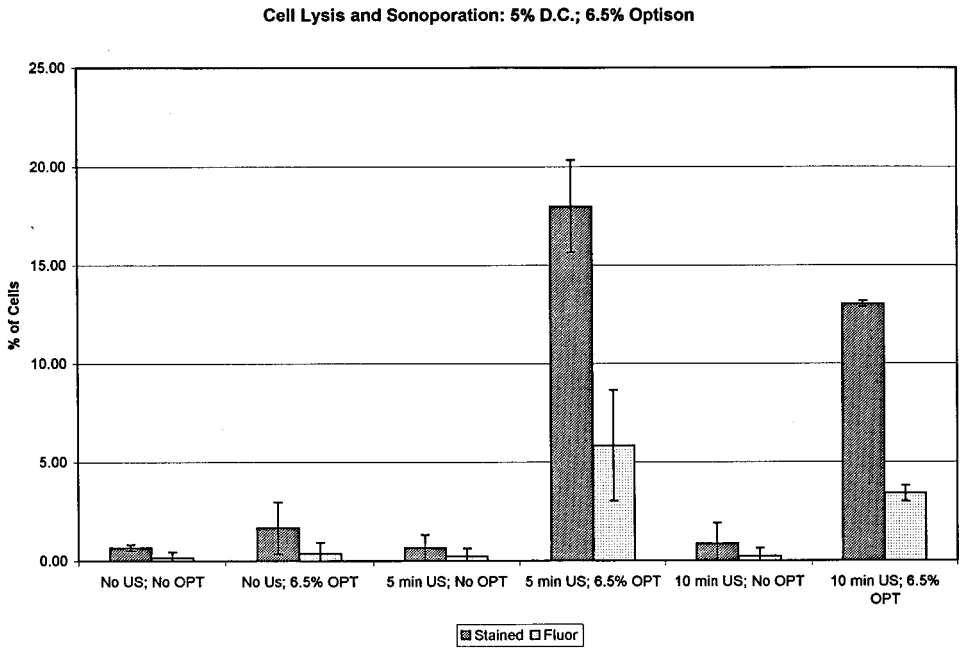

FIG. 5. Cell lysis is indicated by staining of cell interior with trypan blue dye. Fluorescent-labeled dextran trapped inside a cell indicates sonoporation. At least 100 total cells were counted in three separate trials. All samples were sham-exposed or exposed to 2-MHz ultrasound with a 5% duty cycle. (1) Sham-exposed for 5 min, with no Optison™; (2) Sham-exposed for 5 min, with 6.5% Optison™; (3) Exposed for 5 min, without contrast agents; (4) Exposed for 5 min, with 6.5% Optison™; (5) Exposed for 10 min, without contrast agents; (6) Exposed for 10 min, with 6.5% Optison™. The error bars represent one standard deviation from the mean of three trials.

Optison™ results in significantly more sonoporation ($P = 0.008$) than Albunex®, but the results for lysis are not quite significant ($P = 0.057$). (It is noted that ''significance'' is assigned using a somewhat arbitrary but commonly accepted cutoff of $P = 0.05$.)

Similar experiments were conducted using the same conditions as those in Fig. 3, except the ultrasound duty cycle was changed to either 5% or 15%. One might expect that the percentage of lysis or sonoporation would be somehow proportional to the duty cycle. The results are shown in Figs. 5 and 6, respectively. When comparing the percentage of lysis for a 5-min exposure (sample 3), both the 5% case and the 15% case show significantly higher levels ($P = 0.017$ and $P = 0.008$ respectively). For a 10-min exposure, the percentage of lysis from the 15% duty cycle is significantly different ($P = 0.037$) from the 10% duty cycle, but the 5% duty cycle is not significantly different. The percentages of sonoporation for the 5% and 15% duty cycle cases are not significantly different from the 10% case for either 5- or 10-min exposures.

III. DISCUSSION

Significant reduction in cell population is observed upon exposing HeLa *S*3 cells to 2 MHz ultrasound (both continuous wave and 10% duty cycle) in a rotating-tube exposure system. The level of reduction is significantly increased with the addition of 6.5% Optison™ (the ratio of gas bubbles to

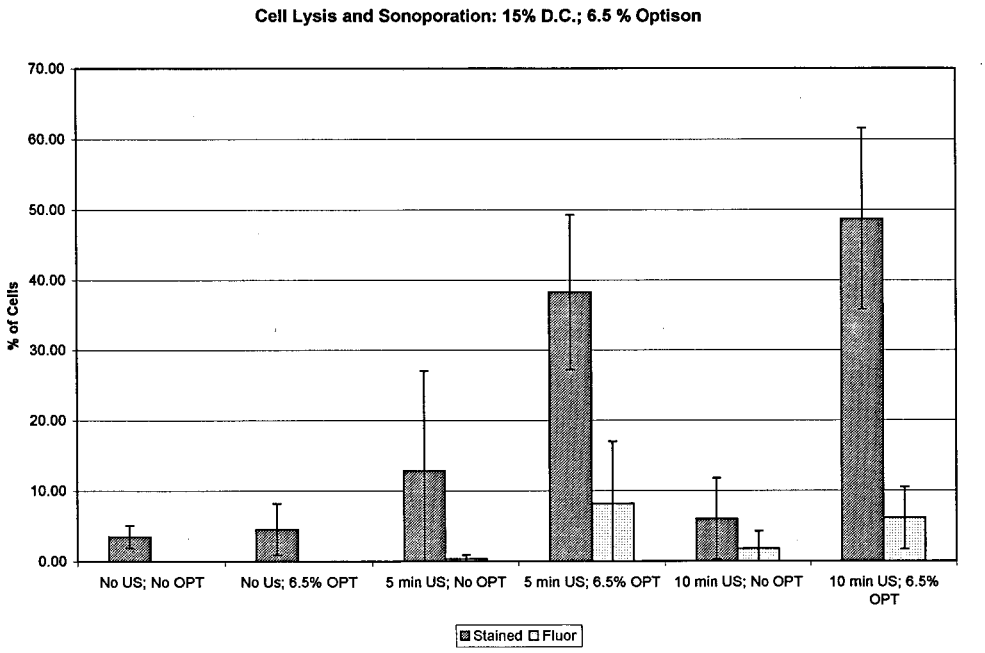

FIG. 6. Cell lysis is indicated by staining of cell interior with trypan blue dye. Fluorescent-labeled dextran trapped inside a cell indicates sonoporation. At least 100 total cells were counted in three separate trials. All samples were sham-exposed or exposed to 2-MHz ultrasound with a 15% duty cycle. (1) Sham-exposed for 5 min, with no Optison™; (2) Sham-exposed for 5 min, with 6.5% Optison™; (3) Exposed for 5 min, without contrast agents; (4) Exposed for 5 min, with 6.5% Optison™; (5) Exposed for 10 min, without contrast agents; (6) Exposed for 10 min, with 6.5% Optison™. The error bars represent one standard deviation from the mean of three trials.

cells is 230). A level of almost 90% reduction was observed in a samples exposed to continuous wave ultrasound with Optison™ present. Without Optison™ present, the 10% duty cycle exposure results in a relatively small effect (about 20% destruction), while with 6.5% Optison™, the effect is quite large (about 65% destruction). This implies that a threshold of ultrasound amplitude might be found at which there are no significant bioeffects unless a contrast agent is present.

The primary cause for cell death seen in Fig. 2 under the conditions used here is likely to be of a mechanical nature, resulting from shear stresses applied to the cell membranes; a similar conclusion was reached by Worthington *et al.* (1997). This was supported by the observation that the cell counts were performed shortly after exposure (order of ten minutes), before any slow biochemical processes (oncosis, apoptosis) had much opportunity to proceed, and the fact that large numbers of cells simply disappeared. Stresses to the membrane may stem from violent inertial cavitation, or microstreaming associated with intact gas bubbles (Gormley and Wu, 1998).

For 5- or 10-min exposures to 10% duty cycle ultrasound, cell lysis, and sonoporation, as indicated by trypan blue staining and trapping of large fluorescent-labeled dextran molecules, respectively, were significant when the cell suspension was supplemented with 6.5% Optison™. The percentage of lysis or sonoporation did not significantly increase when the exposure time was increased from 5 to 10 min. This suggests that after 5 min, the cavitation nuclei are no longer present in sufficient quantities to cause further bioeffects; prolonged exposure is essentially the same as having added no contrast agent. As previously demonstrated experimentally, contrast agents are unstable in an ultrasound field (Wu and Tong, 1998), therefore the effects observed here might be related to the contrast agent itself as well as free bubbles released from the unstable contrast agent and the shell remnants of the broken agent; they can play the role of cavitation nuclei. For low duty cycle-pulsed ultrasound, however, these nuclei may have time when they are not excited by the ultrasound to dissolve into the medium or otherwise disappear before the next pulse arrives. The general results seen in Fig. 4 are in agreement with this hypothesis in that the higher solubility of air (contained in the Albunex® microbubbles) compared with octafluoropropane (contained in the Optison™ microbubbles) would allow more nuclei to dissolve, resulting in less cavitation and consequently less lysis and sonoporation.

If this were true, then one would expect that a higher duty cycle (less ''off'' time) would allow fewer nuclei to escape, and therefore the incidence of lysis and sonoporation would increase. Results from 5- and 10-min exposures using 15% duty cycle did show significantly higher lysis than the 10% duty cycle case. However, there was not a significant difference in sonoporation observed. This may be explained if sonoporation of a cell in fact gives way to lysis with increased ultrasound exposure, a hypothesis not directly tested here.

Continuing the previous argument, a lower duty cycle (more off time) would allow more nuclei to escape, and evidence of lysis and sonoporation would be expected to decrease. Interestingly, a 5-min exposure to 5% duty cycle ultrasound showed a significantly higher percentage of lysis than the 10% duty cycle case. For 10-min exposures, there was no significant difference in lysis, nor were there significant differences in sonoporation for 5- or 10-min exposures (comparing 5% and 10% duty cycle exposures). The increase in lysis for the 5-min, 5% duty cycle case may further indicate that there are significant effects induced by both the stable contrast agents and the nuclei produced when an encapsulated bubble breaks apart. It is reasonable to suggest that a lower duty cycle (5%) will cause less disruption of the Optison™, allowing the cavitation due to stable gas spheres to persist. This reasoning is admittedly speculative, and was not specifically tested here.

The results of our experiments should be used with caution. First of all, the experiments were performed *in vitro*, which is quite different from *in vivo* situations related to diagnostic ultrasound. Second, the ultrasound applied in the experiments was also different from that used in diagnostic ultrasound; we used either cw or tone bursts that had a greater repetition frequency and duty cycle than those of diagnostic ultrasound relevant to ultrasound imaging applications. Recent investigation done by Killam *et al.* (1998) using *B*-mode ultrasound generated by a 5-MHz transducer on a Hewlett-Packard Sonos 1500 system produced no observed bioeffects in anesthetized rabbits in which Optison™ spheres were injected via their ear veins. Although 5 MHz is higher than 2 MHz, the probability to generate acoustic cavitation is lower; it still suggests that *in vivo* conditions may be quite different from those of *in vitro* experiments.

ACKNOWLEDGMENTS

The authors want to thank Dr. Wesley L. Nyborg and Dr. Gary H. Brandenburger for their useful comments, and Shigong Ye for his measurement of sound distributions. This work was partially supported by Mallinckrodt, Inc.

Apfel, R. E. (**1997**). ''Sonic effervescence: A tutorial on acoustic cavitation,'' J. Acoust. Soc. Am. **101**, 1227–1237.

Beissner, K. (**1992**). ''Radiation force and force balances,'' in *Ultrasonic Exposimetry*, edited by M. Ziskin and P. Lewin (CRC Press, Boca Raton, FL).

Bao, S., Thrall, B. D., and Miller, D. L. (**1997**). ''Transfection of a reporter plasmid into cultured cells by sonoporation *in vitro*,'' Ultrasound Med. Biol. **23**, 953–959.

Brayman, A. A., Strickler, P. L., Luan, H., Barned, S. L., Raeman, C. H., Cox, C., and Miller, M. W. (**1997**). ''Hemolysis of 40% hematocrit Albunex®-supplemented human erythrocytes by pulsed ultrasound frequency, acoustic pressure and pulse length dependence,'' Ultrasound Med. Biol. **23**, 1237–1250.

Brown, J., Alderman, J., Quedens-Case, C., and Taylor, K. J. W. (**1996**). ''Enhancement demonstration of neovascularity in a VX2 carcinoma by ultrasound contrast (FS069, MBI Inc.),'' J. Ultrasound Med. **15**, S18.

Dittrich, H. C., Bales, G. L., Hunt, R. M., McFerran, B. A., Leopold, G. R., and Greener, Y. (**1994**). ''Multiple organ tissue perfusion by intravenously (IV) administered novel ultrasound contrast agents in dogs,'' J. Ultrasound Med. **12**, S9.

Dittrich, H. C., Kuvelas, T., Dadd, K., Burns, D., Compton, H., Mizoguchi, A., and Widder, K. (**1995**). ''Safety and efficacy of the ultrasound contrast agent FS069 in normal human: results of a phase one trial,'' Circulation **92**, I464.

Goldberg, B. B. (**1993**). ''Ultrasound contrast agents,'' in *Advances in Ultrasound Techniques and Instrumentation*, edited by P. N. T. Wells (Churchill Livingstone, New York), pp. 35–45.

Gormley, G., and Wu, J. (**1998**). ''Acoustic streaming near Albunex® spheres,'' J. Acoust. Soc. Am. **104**, 3115–3118.

Greenleaf, J. F, Greenleaf, W. J., Kinnick, R., Sarkar, G., and Bolander, M. A. (pp. **1998**). *Enhancement of Ultrasound Mediated Transfection with Cavitation Micronuclei*, Proceedings, 16th International Congress on Acoustics and 135th Meeting Acoustical Society of America, Seattle, 1447–1448.

Killam, A. L., Greener, Y., McFerran, B. A., Maniquis, J., Bloom, A., Widder, K., and Dittrich, H. C. (**1998**). ''Lack of bioeffects of ultrasound energy after intravenous administration of FS069 in the anesthetized rabbit,'' J. Ultrasound Med. **17**, 349–356.

Marsh, J. N., Hall, C. S., Hughes, M. S., Mobley, J., Miller, J. G., and Branenburger, G. H. (**1997**). ''Broadband through-transmission signal loss measurements of Albunex® suspensions at concentrations approaching *in vivo* doses,'' J. Acoust. Soc. Am. **101**, 1155–1161.

Miller, D. L., and Thomas, R. M. (**1996**). ''Contrast-agent gas bodies enhance hemolysis induced by lithotripter shock waves and high-intensity focused ultrasound in whole blood,'' Ultrasound Med. Biol. **22**, 1089–1095.

Miller, D. L., Gies, R. A., and Chrisler, W. B. (**1997**). ''Ultrasonically induced hemolysis at high cell and gas body concentrations in a thin-disc exposure chamber,'' Ultrasound Med. Biol. **23**, 625–633.

Miller, D. L., and Gies, R. A. (**1998**). ''Enhancement of ultrasonically-induced hemolysis by perfluorocarbon-based compared to air-based echo-contrast agents,'' Ultrasound Med. Biol. **24**, 285–292.

Miller, M. W., Miller, D. L., and Brayman, A. A. (**1996**). ''A review of *in vitro* bioeffects of inertial ultrasonic cavitation from a mechanistic perspective,'' Ultrasound Med. Biol. **22**, 1131–1154.

Nyborg, W. L. (**1996**). ''Basic physics of low frequency therapeutic ultrasound,'' in *Ultrasound Argioplasty*, edited by R. J. Siegel (Kluwer Academic, Boston).

Worthington, A. E., Thompson, J, Rauth, A. M., and Hunt, J. W. (**1997**). ''Mechanism of ultrasound enhanced porphyrin cytotoxicity. Part I. A search for free radical effects,'' Ultrasound Med. Biol. **23**, 1095–1105.

Wu, J., and Tong, J. (**1998**). ''Experimental study of stability of contrast agents in an ultrasound field,'' Ultrasound Med. Biol. **24**, 257–265.

Acoustic flow perception in cf-bats: Properties of the available cues

Rolf Müller[a] and Hans-Ulrich Schnitzler
Animal Physiology, Zoological Institute, University of Tübingen, Morgenstelle 28, D-72076 Tübingen, Germany

(Received 8 September 1998; accepted for publication 26 January 1999)

Signal design in cf-bats is hypothesized to be commensurate with the evaluation of time-variant echo parameters, imposed by changes in the sound channel occurring as the bat flies by a target. Two such parameters, the proportional changes in Doppler frequency and sound pressure amplitude, are surveyed, employing a simplified acoustic model in order to assess their fitness for target localization given a translational movement within a plane. This is accomplished by considering the properties of the scalar fields given by the value of these putative sensory variables as a function of position in a plane. The considered criteria are: existence and extent of ambiguity areas (i.e., multiple solutions for target position), magnitude of the variables (relevant with regard to perceptual thresholds), as well as magnitude and orthogonality of the gradients (relevant to localization accuracy). It is concluded that these properties render the considered variables compatible with gross judgements of target position. This may be sufficient for behavioral contexts like obstacle avoidance, where adoption of suitable safety margins could compensate for the variance and bias associated with estimates of target location.
[S0001-4966(99)01105-4]

PACS numbers: 43.80.Ka [WA]

INTRODUCTION

Bat echolocation operates to a large extent as a mobile, airborne sonar system. The joint movement of emitter and receiver causes changes in the sound channel, which in turn are reflected in time-variant echo features. Assuming tractability of the inverse problem, these motion-related signal properties may be evaluated in order to characterize the position of a target relative to the observer. Such an egomotion-based analysis appears particularly straightforward in the case of stationary targets, e.g., obstacles, which do not contribute to the relative velocity between target and observer themselves. The study of obstacle avoidance performance constitutes a classical field of bat echolocation research (Griffin, 1958; Schnitzler and Henson, 1980). However, the underlying perceptual mechanisms have not received much scrutiny so far (a discussion in conjunction with ranging may be found in Simmons *et al.*, 1995). The majority of subsequent investigations have focused on a behavioral context of prey capture in midair in conjunction with a limited set of cues, mainly echo delay and interaural time or intensity differences. While these stimulus features doubtlessly constitute pivotal elements of auditory space percepts, they may be part of a more comprehensive set of cues, with the relative importance of elements being situation dependent.

A peculiar situation may be found in species of so-called cf-bats (e.g., the horseshoe bat *Rhinolophus ferrumequinum* or the mustached bat *Pteronotus parnellii*). Cf-bats are defined in terms of their sonar signal design, which accommodates within an individual pulse both, narrow- and wide-band portions. Short, wide-band, frequency modulated ''fm'' components flank a prolonged, narrow-band, constant frequency ''cf'' part with energy allocation to these components being task correlated (Tian and Schnitzler, 1997). Echolocation-based pursuit of a smooth trajectory through an obstacle arrangement—as cf-bats frequently do, i.e., in an aggregation of tree trunks—is most readily explained by some sort of configural information about the arrangement with respect to the current flight path (see Sec. II). Preliminary evidence (Denzinger and Schnitzler, 1998) supports the notion that during smooth passage through obstacle arrays the power spectral density (PSD) of the wide-band pulse portions is considerably lower than which might be delivered in different behavioral contexts, e.g., alighting on a perch (Tian and Schnitzler, 1997). Since the wide-band components may be regarded as the most likely substrate for the evaluation of timing cues and localization information based upon them, this finding may be referred to as a ''PSD paradox'' (Fig. 1). It needs to be clarified, however, that the attenuated wide-band portions' inadequacy for any purpose remains entirely conjectural. Only if evaluation of timing cues conveyed by the attenuated fm parts was indeed curtailed, postulating the involvement of additional cues would be inevitable.

With their comparatively long durations (up to 100 ms or more) and high duty cycles (up to 70%) the cf-segments of the echolocation pulses may lend themselves well to being substrates for monitoring time-variant, egomotion-related echo features. This report surveys two monaural parameters deemed as likely candidates for relevant sensory variables, namely the proportional changes in Doppler shift frequency and signal amplitude, in the context of a simplified 2-D obstacle avoidance task. Egomotion-induced time dependence of acoustic variables may be treated in gross analogy to the

[a]Present address: Department of Electrical Engineering, Yale University, New Haven, CT 06520-8284.

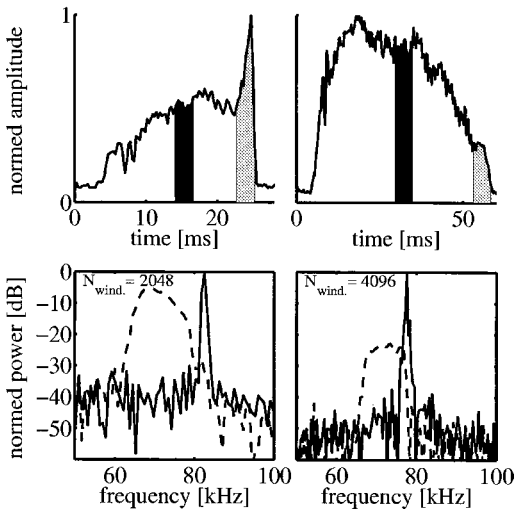

FIG. 1. Variable energy allocation to components in cf-fm echolocation pulses of the bat *Rhinolophus ferrumequinum*. The left two graphs depict a signal with a high power spectral density in the trailing fm portion; the right two graphs an example of a ''weak'' fm tail. The upper graphs show the respective signal envelopes, the lower graphs power spectral density estimates obtained for the windows marked by the corresponding filled areas in the envelopes. The solid lines are power spectral densities calculated for the cf portions (filled black in the upper graphs); the dashed lines are power spectral densities calculated for the fm portions (filled gray in the upper graphs).

visual flow field. This postulated analogy has already been addressed in previous work, which is briefly summarized below in Sec. I. The research reported here introduces the idea of hypothetical flow field usage in cf-bats involving the above putative sensory variables and focuses on assessing their suitability for the task under consideration. It does so by idealizing the acoustic properties of the scenes the animal may encounter. This approach is guided by the argument that usability of a set of cues in an idealized setting is a necessary (albeit not a sufficient) condition for viability as a hypothesis in a more realistic scenario.

I. PREVIOUS WORK ON ACOUSTIC FLOW FIELD PERCEPTION

The idea of resorting to egomotion-induced acoustic signal properties (acoustic flow) for obtaining configural information to be used for instance in control of motor behavior has been advocated and investigated by several researchers (Ashmead *et al.*, 1995; Jenison, 1997; Lee *et al.*, 1992; Rosenblum *et al.*, 1987; Schiff and Oldak, 1990). Most of these studies referred to the situation of human listeners. A notable exception is the work of Lee (1990, 1992), which addresses echolocation specifically and hence will be summarized briefly.

A. Acoustic flow and echolocation

The research by Lee *et al.* (1992) seeks to identify sensory variables in echolocation, which could subserve a braking control strategy based on incomplete configural knowledge. Braking control could employ the ratio of current distance and speed as a first order estimate of time-to-contact. Using these estimates parsimonious braking strategies can be implemented in order to achieve different motor goals (i.e., stopping short of stopping at or controlled collision with a target). For visual stimuli the image expansion rate may serve as a sensory variable providing time-to-contact estimates. Lee *et al.* (1992) showed that such estimates may be obtained from any sensory variable, which is a known power function of distance (time-to-contact $=\tau$-variables). With regard to auditory variables in echolocation he suggested use of the inverse proportional changes in a small angle subtended by two targets, in target bearing, echo delay and echo intensity.

In a general approach in contrast to attempting to meet the information requirements of a specific task, recovery of complete spatial information comprising position and velocity within a plane was demonstrated by Jenison (1997) using interaural time difference, intensity, and Doppler shift together with their derivatives with respect to time. Spatial dependence of intensity was modeled by spherical spreading loss and absorption, but did not take into account direction-dependent properties of the source or the receiver.

B. Experiments on usage of acoustic flow in humans

The idea of acoustic input being used for precise time-to-contact estimation in humans has been criticized on the basis of a ''division of labor'' between vision and audition, where the latter modality is seen as subserving primarily early warning and preparatory functions rather than conveying precise configural information (Guski, 1992). Without dismantling the general validity of ranking vision as the paramount spatial sense in humans, some experimental evidence demonstrating basic capabilities of listeners in estimating distance, time-of-passage or time-of-arrival from motion-related acoustic stimulus parameters has been provided (Rosenblum *et al.*, 1987; Schiff and Oldak, 1990; Ashmead *et al.*, 1995). With respect to the cues involved, the results of Rosenblum *et al.* (1987) are particularly informative in demonstrating that time-of-passage estimates can be based on interaural time difference, Doppler effect, or intensity change, when these sensory variables are presented in isolation.

II. INFORMATION REQUIRED FOR ECHOLOCATION-BASED OBSTACLE AVOIDANCE

One reason for the appeal of the visual flow field concept is that it allows for controlling motor behavior with incomplete information about the environment (τ-variables, see Sec. I A). Using closed loop control, obstacle avoidance is feasible with incomplete knowledge of target position, e.g., by making sure that no target falls short of a safety threshold for minimum bearing or time-to-contact. No claim is made here as to knowledge concerning the minimum amount of spatial information required for echolocation-based obstacle avoidance in cf-bats, but some preliminary arguments may be worth considering:

The decision window in time (or target range) open to the initiation of avoidance maneuvers is bounded by the earliest possible detection instant and the minimum reaction

time. Even at high duty cycles a significant portion of this window will be blanked out by gaps between signals. Hence, movement decisions have to be taken based on a small number of pulses. This constraint is more readily met by path planning based on configural knowledge than closed-loop control based on a single ''critical parameter,'' which cannot fully represent a two- or even three-dimensional configuration.

Strategies for generating trajectories, which reach a target by closed-loop control based on τ-variables, have been proposed by Lee *et al.* (1995). These strategies are based on a combination of the inverse proportional changes in bearing and range. The variables used in these τ-functions (range, bearing, and their derivatives) provide an overdetermined set of equations for the task considered and hence this approach can only be regarded as parsimonious in its coupling of perception and action but not in terms of the utilized spatial information. Depending on the sensory variables employed, the same holds true for echolocation-based braking: When devising a braking strategy in the case of a target with arbitrary, nonnegligible bearing, Lee *et al.* (1992) resorted to combining the τ-function in echo delay with bearing angle, again implying full knowledge of target position (assuming echo delay itself is retained).

In the absence of knowledge regarding the minimum spatial information required for obstacle avoidance based on echolocation sensing, considering the ability to perform a full recovery of target position from the measured variables appears an attractive default: Meeting a sufficient condition provides a satisfactory criterion for judging the suitability of a hypothetical set of cues. If the above constraints indeed precluded relying primarily on closed-loop control, it would even constitute a necessary condition. The same applies implicitly to the control strategies as envisioned by Lee *et al.* (1995).

Consequently, the work presented here adopts the usage of proportional changes (τ-variables) from the concept of visual flow, since this allows for elimination of (unknown) constants, but attempts to recover full spatial information within a plane. For this purpose target position will be specified by virtue of Cartesian coordinates (d,h), where the heading, h, is always aligned with the animal's velocity v. In this report only translational movements are considered. The orthogonal direction is referred to as the passing distance, d (see Fig. 2 for all geometrical definitions).

III. ASSESSMENT OF CUES

If the narrow-band segments of the cf-bats' pulses are considered in isolation, timing cues like monaural two-way transit time and interaural timing differences are unlikely candidates for stimulus features subserving target localization. The former is precluded by the narrow-band nature of the signal, the latter would require phase-coherent processing by the animal. The only apt binaural cue would be interaural intensity differences allowing for bearing estimates. Involvement of this cue in obstacle avoidance of the cf-bat *Rhinolophus ferrumequinum* has been demonstrated (Flieger and Schnitzler, 1973). The monaural cues provided by signal amplitude and Doppler frequency might be readily accessible as well; e.g., experimental evidence obtained in human listeners (Harris and Sergeant, 1971) showed minimum audible movement angles (angular speed 2.8°/s) measured under monaural conditions to be in general inferior to the binaural results but still indicative of usable motion-related information.

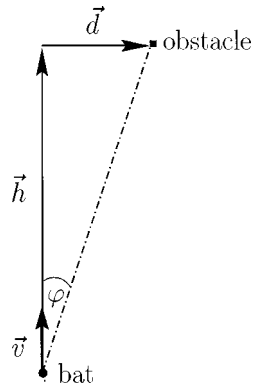

FIG. 2. Geometrical definitions for an obstacle avoidance task: obstacle position relative to the bat is specified by Cartesian coordinates: passing distance d and heading distance h; the animal's velocity **v** is aligned with the heading **h**. Bearing φ is the angle subtended by the heading and a radius vector between the positions of bat and target. All subsequent figures, which depict functions of position in the plane, make use of the same definition of coordinates and are aligned in the same manner as shown here.

A. Interaural intensity difference and proportional change in Doppler frequency

For cf-signals a narrow-band model of the Doppler effect suffices. Furthermore, in bats the assumption holds that the speed of the animal is small compared to the speed of sound ($v \ll c$). Thus the Doppler effect can be modeled as a frequency shift $f_d = 2 f_e (v/c) \cos\varphi$ (Skolnik, 1980), where f_e is the emitted frequency, v the speed, and φ the bearing. Using Cartesian coordinates (d,h) as shown in Fig. 2

$$f_d(d,h) = 2 f_e \frac{v}{c} \frac{h}{\sqrt{d^2+h^2}}. \tag{1}$$

Evidently, this Doppler model implies that the monaural cue Doppler shift constitutes merely another way of encoding the target's bearing, which may also be obtained by virtue of the binaural parameters time or intensity differences. However, using Doppler shift as a bearing cue appears less parsimonious, since it requires all other variables in Eq. (1) (v,c,f_e) to be known within the observation interval.

Considering derivatives with respect to time of φ, which itself could be encoded binaurally, and the monaurally accessible f_d as possible parameters of an acoustic flow field,

$$\dot{\varphi}(d,h) = \frac{v d}{d^2+h^2}, \tag{2}$$

$$\dot{f}_d(d,h) = -2 f_e \frac{v^2}{c} \frac{d^2}{(d^2+h^2)^{3/2}}, \tag{3}$$

it can be seen that $\dot{\varphi}(d,h)$ depends on the speed v and $\dot{f}_d(d,h)$ on its square. A biologically more appealing alternative to assuming a precise knowledge of speed is differentiation with respect to distance, which the animal may calibrate in its own motorical units (i.e., change per wing beat)

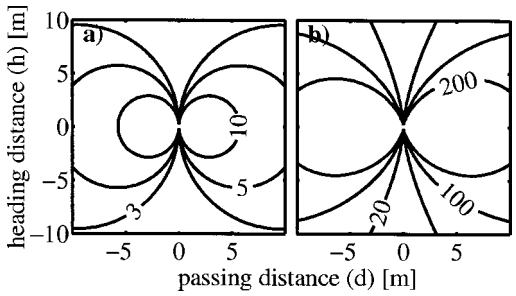

FIG. 3. (a) Partial derivative of bearing $\varphi(d,h)$ with respect to heading distance $\partial\varphi(d,h)/\partial h$[°/m] and (b) partial derivative of Doppler frequency $f_d(d,h)$ with respect to heading distance $\partial f_d(d,h)/\partial h$[Hz/m].

$$\frac{\partial\varphi}{\partial h} = -\frac{d}{d^2+h^2} = -\dot{\varphi}(d,h)/v, \tag{4}$$

$$\frac{\partial f_d}{\partial h} = 2\, f_e \frac{v}{c} \frac{d^2}{(d^2+h^2)^{3/2}} = -\dot{f}_d(d,h)/v$$

$$= 2\, f_e \frac{v}{c} \frac{d}{\sqrt{d^2+h^2}} \frac{\partial\varphi}{\partial h}. \tag{5}$$

In case of the bearing, differentiation with respect to distance constitutes a complete remedy to the explicit dependence on v [Eq. (4)]. This does not apply to the Doppler shift, however, where a first order dependence on v, c, and f_e is retained [Eq. (5)]. A cure may be found by resorting to the proportional change as a putative sensory variable Ψ:

$$\Psi(d,h) = \frac{\partial f_d}{\partial h} \Big/ f_d = \frac{d^2}{h(d^2+h^2)} [\mathrm{m}^{-1}]. \tag{6}$$

Although the emitted frequency f_e is among the canceled constants, the center frequency of the emission is still required in order to determine f_d from the received frequency without waiting until the instant of passage or at least until a lengthy stretch of Doppler history has been recorded. The beat frequency of interferences between pulse and echo would allow for an immediate estimation of f_d, but analysis of beats constitutes an ill-posed problem in the presence of more than two interfering signals (Müller and Schnitzler, submitted).

Isocontours of $\partial\varphi/\partial h$ in a plane define circles of radius $r = 1/2(\partial\varphi/\partial h)^{-1}$ and origin $(\pm r, 0)$ [Fig. 3(a)]; these circles constitute central cuts through the blur toroid described for visual flow by Whiteside and Samuel (1970). Alternatively, the isocontours can be regarded as Vieth–Müller circles known from stereogeometry, with ∂h corresponding to the stereo basis and $\partial\varphi$ to the vergence angle. The partial derivatives of bearing [Fig. 3(a)] and Doppler frequency [Fig. 3(b)] are fairly similar in the shape of the solutions obtained if the respective expressions in Eq. (4) and Eq. (5) are equated to some constant. Unfortunately, among the shared features is very little steepness in the region of small d and moderate h, where the point of operation for obstacle avoidance presumably has to be located. For scrutiny of the environment outside the context of obstacle avoidance, however, a cf-bat may look aside in order to combine maximum resolution by virtue of Doppler shifts [analogous to the broadside geometry of synthetic-aperture radar, e.g., Tomiyasu (1978)] with a favorable directionality gain.

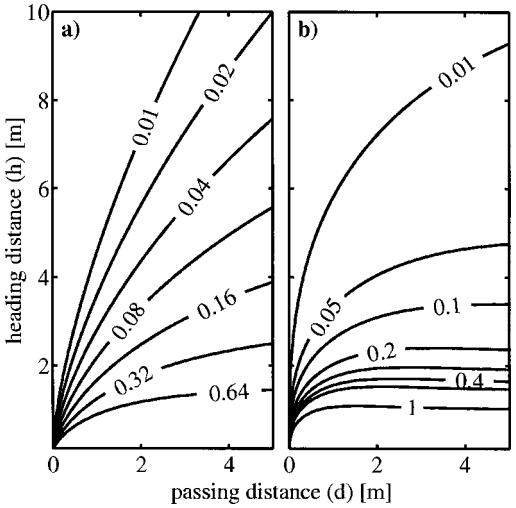

FIG. 4. Proportional change in Doppler frequency: (a) $\Psi(d,h)$[m^{-1}] (b) $|\mathrm{grad}\,\Psi(d,h)|$[$\mathrm{m}^{-2}$].

A measurement of $\Psi(d,h)$ (see Fig. 4) may be as readily interpreted as a curve in the d,h-plane as a value of $\partial\varphi/\partial h$. Thus considering the shape of the respective isocontours, both equally qualify as sensory variables. The efficiency of these variables in terms of accurate localization depends on how the magnitude of their gradients [see Fig. 4(b) for $|\mathrm{grad}\,\Psi\varphi(d,h)|$] relates to the respective perceptual thresholds. Large gradient magnitudes can be expected to favor accuracy, since a linear estimate of contour line spacing at point (d,h) associated with a given just-noticeable difference (jnd) in $\Psi(d,h)$ is provided by the ratio $\mathrm{jnd}/|\mathrm{grad}\,\Psi(d,h)|$. Currently, no psychoacoustical measurements in bats measuring sensitivity to changes in angle or proportional changes in frequency are available. Angular resolution was found to be 4.5° around the midline for *Rhinolophus ferrumequinum* (Airapetianz and Konstantinov, 1974), in the same species a frequency resolution of 30–60 Hz has been suggested (Schnitzler and Henson, 1980), which is consistent with measurements of critical ratios/critical bands (Long, 1980). The lowest thresholds for sinusoidal frequency modulation depth measured by Schuller (1979) in single neurons in the inferior colliculus of *Rhinolophus ferrumequinum* were ±10 Hz. Taking into account that applicability of these findings to the sensory tasks considered here is highly tentative, the results of comparing thresholds and gradients are necessarily inconclusive as to ranking the variables' suitability for the task under consideration.

Since both variables, $\partial\varphi/\partial h$ and Ψ provide only one equation each, determining a location within a plane would require including an additional equation in each case. $\partial\varphi/\partial h$ could for instance be combined with bearing itself (φ) yielding the following solutions

$$h = -\tan\varphi \Big/ \frac{\partial\varphi}{\partial h}(\tan^2\varphi + 1); \quad d = \pm h \tan\varphi. \tag{7}$$

Unlike $\partial\varphi/\partial h$, Ψ may not be combined with the parameter it was derived from (f_d), since this would reintroduce the explicit dependence on v. Combining Ψ with its derivative $\partial\Psi/\partial h$ suffices in order to solve for a position

$$h=\frac{3\Psi}{2\Psi^2-\partial\Psi/\partial h};$$
$$d=\pm h\Psi\sqrt{-\frac{3}{\Psi^2+\partial\Psi/\partial h}}\quad(d\neq 0\wedge h\neq 0). \tag{8}$$

However, resorting to these solutions hardly appears attractive, since higher order derivatives offer little robustness against noise and for targets straight ahead ($d=0\rightarrow\Psi=0$) no meaningful solution can be obtained. Therefore, it may be preferred to combine Ψ with a sensory variable not based upon the Doppler shift.

For subsequent analysis the monaural parameter $\Psi(d,h)$ will be chosen mainly in order to emphasize the potential role of monaural cues and assess their intrinsic information content. It is not intended to argue in favor of spatial percepts being sustained exclusively by monaural cues. A legitimate counter argument against monaural cues would be that solutions for positions will occur pairwise in the left and right hemifield. However, even with purely monaural sensing this simple ambiguity might be overcome readily by testing for the hypothesis that the true position is in one hemifield, e.g., by means of a tentative steering maneuver. This is not in contradiction to the arguments presented in Sec. II in favor of a steering approach to echolocation-based obstacle avoidance, since here we are concerned with a single-instant, binary hypothesis test only. Furthermore, Ψ has to offer two potential advantages over $\partial\varphi/\partial h$: It depends only on the direction of heading and not on the direction of gaze, therefore no additional correction is required should these two directions not coincide. When working on a mixture of several simultaneous echoes, meaningful estimation of angular changes requires determination of interaural intensity differences individually for signal components, which have to be resolved in the frequency domain. Hence, it may appear in some sense more parsimonious to resort to this frequency information directly for a position estimate based upon Ψ. When using the amplitude information (see Sec. III B), a strictly monaural approach in turn avoids dealing with an interaural correspondence problem.

B. Proportional change in sound pressure amplitude

In psychoacoustical experiments, Rosenblum *et al.* (1987) found monaural amplitude change the most effective acoustic variable to base a time of passage estimate on (the other variables tested were interaural intensity difference and Doppler shift) and Lee *et al.* (1992) considered a τ-variable of sound intensity a possible substrate for echolocation-based braking control. The work presented here tries to evaluate the factors contributing to the change in sound pressure amplitude with respect to their significance for localization within a plane.

1. Contributing acoustic properties

In order to assess the principal suitability of proportional change in sound pressure amplitude for localization or avoidance within a plane, the acoustic properties of the scene were simplified by assuming spherical radiation from point targets and propagation under the free field hypothesis. The highly directional nature of the echolocation system of *Rhinolophus* (Grinnell and Schnitzler, 1977) is accounted for by treating the bat as a point source with a superposed real-valued function of angle $0\leqslant\Phi(\varphi)\leqslant 1$, representing the joint directionality of emitter and receiver (see, e.g., Freedman, 1962). Invoking some elementary properties of wave propagation (Kinsler and Frey, 1962; Skolnik, 1980), the pressure amplitude measured by the animal in such a simplified scene would be

$$P(d,h,f)=\frac{\sqrt{2\rho_0 c I_0}\sigma}{4\pi(d^2+h^2)}m(f,d,h)\Phi(d,h), \tag{9}$$

where ρ_0 is the density of the medium, c the respective speed of sound, I_0 the intensity at some reference distance, σ the scattering coefficient, and $m(f,d,h)=10^{-\sqrt{d^2+h^2}\alpha(f)/10}$ the absorption term containing the absorption coefficient $\alpha(f)$ [dB/m]. Assuming that I_0 and σ are constant over small changes in heading (h) the derivative of P with respect to heading is

$$\frac{\partial P}{\partial h}=P\left[-\frac{2h}{d^2+h^2}-\frac{\ln(10)\alpha(f)h}{10\sqrt{d^2+h^2}}+\frac{\partial\Phi}{\partial h}\Big/\Phi\right]. \tag{10}$$

The unknown constants I_0 and σ cancel in the expression for the proportional change [Eq. (11)] leaving another putative sensory variable $\Theta(d,h)$, which is just a function of d,h. Apart from its variables, this function only contains some trivial constants ($\alpha(f)$,ln(10)/10) and the yet unresolved directionality $\Phi(d,h)$:

$$\Theta(d,h)=\frac{\partial P}{\partial h}\Big/P=-\frac{2h}{d^2+h^2}-\frac{\ln(10)\alpha(f)h}{10\sqrt{d^2+h^2}}+\frac{\partial\Phi}{\partial h}\Big/\Phi. \tag{11}$$

It seems noteworthy that, while the three terms accounting for geometrical attenuation, absorption, and influence of directionality respectively are linked multiplicatively in the expression for P [Eq. (9)], the aggregate proportional change Θ is the sum of the proportional changes in these three attenuation components [Eq. (11)]. The additive nature of these changes facilitates assessing the contributions of the three physical effects to the total proportional change in sound pressure experienced (Sec. III B 3).

As one possible next step toward improving the realism of the scene model employed it might be assumed that geometrical attenuation is some arbitrary power function of distance rather than r^2 as for spherical spreading of outgoing and received wave. The respective exponent would then propagate into the geometric attenuation term of Θ as an additional unknown. It appears not too far-fetched, however, to assume that a bat could calibrate for the spreading losses pertinent to the wave field it produces. As to the target's contribution to soundfield geometry, it would be required

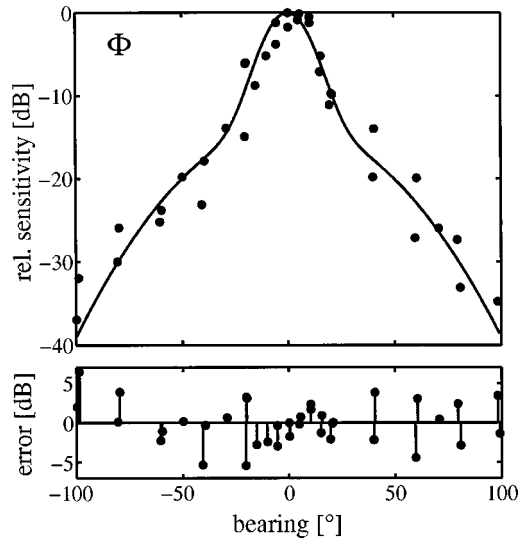

FIG. 5. Compound directionality data reproduced from Grinnell and Schnitzler (1977); a sum of two Gaussians [Eq. (12)] is fitted to the data. The lower graph shows the difference between the data and the fit.

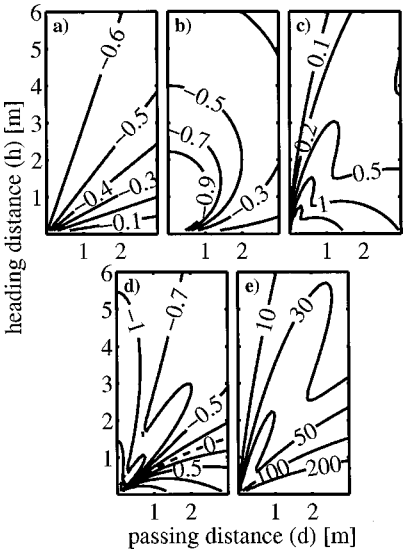

FIG. 6. Additive components in Θ: proportional changes in sound pressure [m^{-1}] due to (a) absorption (assuming a frequency of 80 kHz), (b) geometric attenuation, (c) ''sum-of-Gaussians'' directionality, (d) compound Θ [m^{-1}], (e) magnitude ratio of the gaze-dependent (directionality) and gaze-independent contributions (absorption and geometric attenuation) to Θ [%]; magnitude ratios >100% are possible, because gaze-dependent and -independent contributions differ in sign.

that the animal has some a *priori* knowledge about the approximate geometry of the targets to be encountered, i.e., cylinders when flying through tree trunks. If this is not the case, Θ cannot be used in the way suggested here and additional relationships would have to be introduced in order to cope with the unknown spreading losses.

2. Modeling of directionality

Data on the joint directionality of emitter and receiver in *Rhinolophus* are available from work by Grinnell and Schnitzler (1977). Receiver directionality was obtained by a behavioral paradigm measuring the noise-masking of Doppler compensation triggered by a sinusoidal fm signal from straight ahead. Reviewing the data of Grinnell and Schnitzler (1977), it was noted that the compound directionality data (emitter and receiver, reproduced in Fig. 5) appears to be in good agreement with the sum of two Gaussians:

$$\Phi(d,h)=Ae^{-\arctan^2(d/h)/2s_1^2}+(1-A)e^{-\arctan^2(d/h)/2s_2^2}. \tag{12}$$

The parameters used to fit the data provided by Grinnell and Schnitzler (1977) were: $A=0.794$, $s_1=0.195$, and $s_1=0.723$. Unfortunately, only two data points per measured bearing could be obtained from the work of Grinnell and Schnitzler (1977), precluding an estimate of the variance associated with these measurements. Therefore, no statistical measure for the goodness of fit is available and it would seem rather premature to speculate about an eventual physical meaning of this description. With these precautions in mind, the apparent change in steepness at ≈30° might be hypothesized to constitute a salient feature of data and fit alike. In order to assess the implications of this property for the geometrical interpretation of Θ, the results obtained with the ''sum-of-Gaussians'' model were compared to a more simplified version using just a single Gaussian. The contribution of a single Gaussian directionality with standard deviation s to $\Theta(d,h)$ is

$$\frac{\partial\Phi}{\partial h}\Big/\Phi=\frac{d\arctan(d/h)}{s^2(d^2+h^2)}. \tag{13}$$

For a sum-of-Gaussians directionality:

$$\frac{\partial\Phi}{\partial h}\Big/\Phi=\frac{d\arctan(d/h)}{(h^2+d^2)}\left[\frac{G_1}{s_1^2}+\frac{G_2}{s_2^2}\right]\Big/[G_1+G_2], \tag{14}$$

where G_1, G_2 are the two Gaussians [see Eq. (12)] and s_1, s_2 their respective standard deviations.

3. Shape of the solutions for a given Θ

Within a plane the solutions obtained by equating Eq. (11) to some constant constitute curves. To the animal only the total sound pressure formed by the contributions of absorption, geometric attenuation, and directionality and its derivative would be accessible. Nevertheless, in the paragraphs below these influences will be considered in isolation in order to yield a better understanding about how they might affect the perceptual salience of Θ.

a. The contribution of absorption to Θ. Equating the proportional change in absorption [the ratio of the derivative of absorption with respect to heading and absorption itself, i.e., the second right-hand term in Eq. (10)] to some value C defines a straight line through the origin with a slope of $[(\ln(10)\alpha(f)/10C)^2-1]^{-1/2}$ (Fig. 6). Maximum values in this component of Θ are found straight ahead, since the only geometrical variable absorption depends on is distance r and $\Delta r=\Delta h/\cos\varphi$. Since the proportional change in absorption [second right-hand term in Eq. (11)] can be rewritten as $\alpha(f)\ln(10)/10\cos\varphi$, the shape of its gradient is the same as for the change in bearing [Sec. III A, Fig. 3(a)] with isocontours forming circles to which the velocity vector is a tangent in the origin. This implies that, although the highest pressure

changes caused by absorption are found straight ahead, the contribution to accuracy within this region will be small.

b. The contribution of geometric attenuation to Θ. [First right-hand term in Eq. (10).] This is more favorable to straight ahead accuracy than absorption since isocontours for the magnitude of the gradient are circles with radius $\sqrt{2/C}$ (where C is the isocontour's value) centered on the current position of the animal and therefore do not put the forward direction at a disadvantage. A given value C for proportional change in geometric attenuation along heading also defines a circle, but unlike the one obtained for the gradient's magnitude it is located ahead of the animal with origin $(0,1/C)$ and radius $1/C$ (Fig. 6).

c. The contribution of directionality to Θ. Under the assumption that the ''sum-of-Gaussians'' fit to the data of Grinnell and Schnitzler (1977) mirrors a genuine feature of the directionality in combining a steep central region with peripherally more gentle slopes, the implications of this particular shape deserve some scrutiny. Since any signal parameters arising from the system's directionality will depend on the direction of gaze and not on the direction of heading, a possible biological design goal may be minimization of errors introduced by an uncompensated misalignment between these two directions. A complete remedy would be provided by an omnidirectional system. This would, however, preclude the usage of any amplitude cues generated by changes in a target's bearing along the flight path. A comparison between the sum-of-Gaussian fit and directionalities described by the narrower or the wider Gaussian from this sum in isolation shows that the behavior of the proportional changes in sound pressure caused by directionality are fairly similar at locations close to the midline for all three considered functions [Fig. 7(a), (c), (e)].

Hence, all three can be expected to display a similar robustness or susceptibility to small misalignments in the direction of gaze. The difference in the slope of the narrow and wide single Gaussian terms of the directionality model is reflected in isocontours of proportional sound pressure changes being displaced toward larger angles for the latter [Fig. 7(a), (c)]. This results in smaller gradient magnitudes throughout the entire plane [Fig. 7(b), (d)]. The isocontours of proportional pressure change for the sum-of-Gaussians [Fig. 7(e)] correspond to the composite nature of the directionality model: for small angles they are most similar to the narrow Gaussian, for large angles to the wide Gaussian. In between there is a transitional region where the greatest differences to both single Gaussians may be found (see Sec. III C for the implications of this transition). This results in gradient magnitudes being increased (about 7× at maximum) for the sum-of-Gaussian when compared to the wide Gaussian at bearings between ≈7° and ≈15°.

d. Sum of geometric attenuation, absorption, and directionality. The experienced proportional change in sound pressure Θ is composed additively from gaze-dependent (directionality) and gaze-independent contributions [geometric attenuation and absorption, see Eq. (11), Fig. 6]. The gaze dependence (directionality dependence) of the sum increases as a function of bearing [Fig. 6(e)]. Thus an evaluation of targets at small bearing angles may be carried out with sufficient accuracy without correcting for a misalignment in the directions of gaze and heading. For larger bearings such a correction will be mandatory.

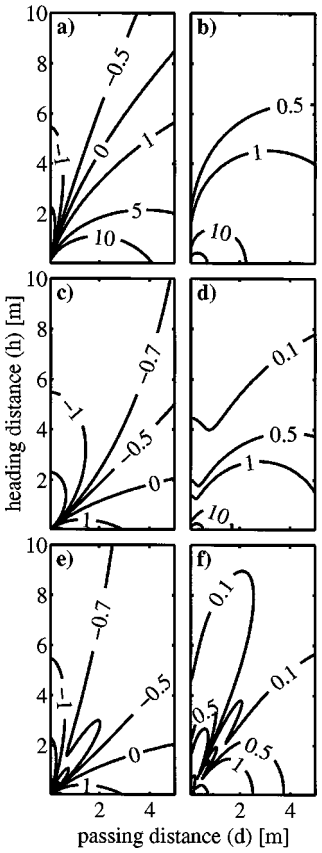

FIG. 7. Comparison of ''single Gaussian'' and ''sum-of-Gaussians'' directionalities: single Gaussian with standard deviation of the narrow Gaussian in the sum. (a) $\Theta(d,h)[\mathrm{m}^{-1}]$, (b) $|\mathrm{grad}\,\Theta(d,h)|[\mathrm{m}^{-2}]$; single Gaussian with standard deviation of the wider Gaussian in the sum, (c) $\Theta(d,h)[\mathrm{m}^{-1}]$, (d) $|\mathrm{grad}\,\Theta(d,h)|[\mathrm{m}^{-2}]$; sum-of-Gaussians, (e) $\Theta(d,h)[\mathrm{m}^{-1}]$, (f) $|\mathrm{grad}\,\Theta(d,h)|[\mathrm{m}^{-2}]$.

C. Reconstruction of target position

In assessing the principle suitability of a combination of $\Psi(d,h)$ and $\Theta(d,h)$ for a target position estimate, three criteria may be found useful: ambiguity, magnitude of the gradients of the two variables, and intersection angle of their isocontours (or, equivalently, angle subtended by the gradient vectors). Employing compound directionalities described by single Gaussians results in the inverse problem having two solutions for Ψ, Θ-pairs pertinent to certain positions (d,h) (see Fig. 8). The areas marred by these ambiguities do not extend centrally to some minimum bearing, the value of which depends on width of the Gaussian. Widening the Gaussian results in extending the area of unequivocal inversions [Fig. 8(a), (b)]. The distance between the two solutions can be extremely large on the fringe of the ''ambiguity area,'' so that one of the two could actually be rejected on the argument of a target at that position not being detectable. However, inside the ambiguity area a fairly wide range of distances between solutions is encountered, effectively prohibiting usage of such a simple strategy. The two-solution ambiguity area of the wide single Gaussian is shared by the

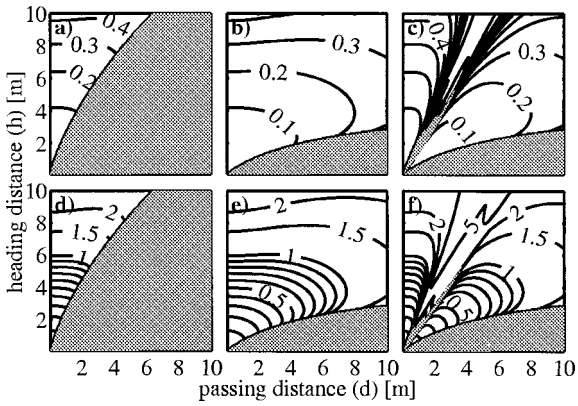

FIG. 8. Error in position estimate associated with misreading Ψ and Θ independently by 1% [(a),(b),(c)] or 5% [(d),(e),(f)]. Contour labels denote the maximum error in position estimate, which can result from this measuring accuracy, in meters. Gray patches mark areas where multiple solutions are found. (a) and (d): single Gaussian directionality with the larger standard deviation from the sum; (b) and (e): single Gaussian directionality with the smaller standard deviation from the sum; (c) and (f): sum-of-Gaussians.

sum-of-Gaussians directionality. Additionally, a small region is formed, where the inverse problem yields three solutions for the respective Ψ,Θ-combinations (Fig. 9). The small extent of this area, particularly in the direction of h, can be expected to render the ambiguities introduced a rather ephemeral nuisance during target passage.

The relevance of the gradients (Figs. 4, 7) to the spatial resolution conveyed by a single sensory variable has already been discussed (Sec. III A). In order to gauge the difference in position estimates associated with the jnd's for Ψ and Θ the angle between the gradients of the two variables has to be accounted for. A linear estimate of the distances between solutions found for over- or underestimating Ψ and Θ independently by the respective jnd can be obtained as the length of the diagonals of the parallelogram with heights $\mathrm{jnd}_\Psi/|\Psi|$, $\mathrm{jnd}_\Theta/|\Theta|$ and $\angle\{\Psi;\Theta\}$ being the angle between them. For small errors (e.g., 1% shown in Fig. 8) this linear estimate is in surprisingly good agreement with results obtained numerically, the latter being shown in Fig. 8. Thus if the animals' errors were likewise small, a linear approach could be employed in error estimation which in turn could be useful in computing safety margins. The accuracy with which an obstacle's location would have to be determined by the animal at a certain distance depends on a number of unknown factors, for instance safety margins adopted and maneuverability at hand in cases where an earlier estimate proves grossly wrong. Furthermore, for the results presented here (Fig. 8) to be a predictor of what an observer would experience, the assumption would have to be made that the notion of an approximately constant Weber fraction is applicable to the two putative sensory variables considered. Granted these uncertainties and assumptions, the errors in position estimate found for 1% and 5% both appear compatible with using these variables for a rough estimate of target location. Of course, the 1% results are far more convincing and hence it would be a strong argument for the feasibility of flow field perception based on these two putative sensory variables, if the respective Weber fractions were determined experimentally to fall within a few percent. The observation that errors are in general inversely proportional to distance is readily compatible with the requirements of obstacle avoidance, since the initial estimates of targets positions, which can be obtained already well ahead, as well as motion decisions based upon them, may be adjusted as more accurate information accumulates.

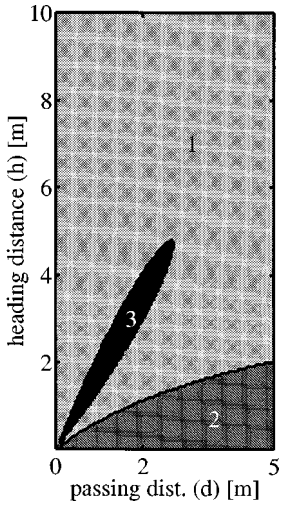

FIG. 9. Number of solutions associated with the $\Psi(d,h),\Theta(d,h)$ as a function of (d,h).

IV. CONCLUSIONS

Research on the suitability of constant frequency echoes for sustaining acoustic flow perception was motivated by circumstantial evidence suggesting the existence of a PSD paradox. Two monaural cues, the proportional changes in Doppler shift and sound pressure amplitude along heading, were tentatively chosen as possible sensory variables worth considering. Their potential importance within the mixture of cues likely to underlie echolocation-based spatial perception depends on the extent to which the PSD paradox imposes genuine perceptual restrictions. For judging the informational content of the hypothetic sensory variables, recovering target position in a plane was chosen as a default approach not to anticipate future insights into the most parsimonious informational basis for obstacle avoidance. Combining both variables (Ψ,Θ) results in two equations for d,h which do not contain any critical additional unknowns. Neither the amount of ambiguities nor the errors in position estimates associated with misreadings of the sensory variables are overtly prohibitive to basing obstacle localization upon those variables. Hence, suitability of the cues under consideration has been established in principle. This constitutes a necessary albeit not sufficient condition for these sensory variables actually being used by bats. In order to test the latter hypothesis experimental evidence obtained in bats actually performing the tasks under consideration is indispensable. As an intermediate step it would seem worthwhile to investigate how the perceptual skills found in the animals relate to the magnitudes of the sensory variables and their gradients, on which this study focused. In preparation for meaningful psychoacoustical experiments, some considerations may be helpful as to how the specifications required by acoustic flow perception relate to established facts about auditory function in

mammals in general and cf-bats in particular. Such an approach is taken in Müller and Schnitzler (submitted).

Airapetianz, E. S., and Konstantinov, A. I. (**1974**). *Echolocation in Nature* (Nauka, Leningrad). English translation: Joint Publications Research Service, Arlington, Virginia, No. 63328.

Ashmead, D. H., Davis, D. L., and Northington, A. (**1995**). ''Contribution of listeners' approaching motion to auditory distance perception,'' J. Exp. Psychol. **21**, 239–265.

Denzinger, A., and Schnitzler, H.-U. (**1998**). ''cf-fm Fledermäuse im Transferflug: wird das akustische Flußfeld genutzt?'' in *Visuelle Wahrnehmung: Beiträge zur 1. Tübinger Wahrnehmungskonferenz*, edited by H. H. Bülthoff, M. Fahle, K. R. Gegenfurtner, and H. A. Mallot (Knirsch, Kirchentellinsfurt), p. 84.

Flieger, E., and Schnitzler, H.-U. (**1973**). ''Ortungsleistungen der Fledermaus *Rhinolophus ferrumequinum* bei ein- und beidseitiger Ohrverstopfung.'' J. Comp. Physiol. **82**, 93–102.

Freedman, A. (**1962**). ''A mechanism of acoustic echo formation.'' Acustica **12**, 10–21.

Griffin, D. R. (**1958**). *Listening in the Dark* (Yale University Press, New Haven).

Grinnell, A. D., and Schnitzler, H.-U. (**1977**). ''Directional sensitivity of echolocation in the Horseshoe Bat *Rhinolophus ferrumequinum*. II. Behavioral directionality of hearing,'' J. Comp. Physiol. A **116**, 63–76.

Guski, R. (**1992**). ''Acoustic tau: an easy analogue to visual tau?'' Ecol. Psychol. **4**, 189–197.

Harris, J. D., and Sergeant, R. L. (**1971**). ''Monaural/binaural minimum audible angles for a moving sound source,'' J. Speech Hear. Res. **14**, 618–629.

Jenison, R. L. (**1997**). ''On acoustic information for motion,'' Ecol. Psychol. **9**, 131–151.

Kinsler, L. E., and Frey, A. R. (**1962**). *Fundamentals of Acoustics*, 2nd ed. (Wiley, New York).

Lee, D. N. (**1990**). ''Getting around with light or sound,'' in *The Perception and Control of Self-Motion*, edited by R. Warren and A. H. Wertheim (Erlbaum, Hillsdale, NJ).

Lee, D. N., Simmons, J. A., and Saillant, P. A. (**1995**). ''Steering by echolocation: a paradigm of ecological acoustics,'' J. Comp. Physiol. A **176**, 347–354.

Lee, D. N., van der Weel, F. R., Hitchcock, T., Matejowsky, E., and Pettigrew, J. D. (**1992**). ''Common principle of guidance by echolocation and vision,'' J. Comp. Physiol. A **171**, 563–571.

Long, G. R. (**1980**). ''Further studies of masking in the Greater Horseshoe bat, *Rhinolophus ferrumequinum*,'' in *Animal Sonar Systems*, edited by R. G. Busnel and J. F. Fish (Plenum, New York), pp. 929–932.

Müller, R., and Schnitzler, H.-U. (**submitted**). ''Acoustic flow as a basis for obstacle avoidance in cf-bats: Is extraction of flow parameters biologically plausible?'' J. Acoust. Soc. Am.

Rosenblum, L. D., Carello, C., and Pastore, R. E. (**1987**). ''Relative effectiveness of three stimulus variables for locating a moving sound source,'' Perception **16**, 175–186.

Schiff, W., and Oldak, R. (**1990**). ''Accuracy of judging time to arrival: effects of modality, trajectory and gender,'' J. Exp. Psychol. Hum. Percept. **16**, 303–316.

Schnitzler, H.-U., and Henson, O. W. J. (**1980**). ''Performance of airborne animal sonar systems: 1. Microchiroptera,'' in *Animal Sonar Systems*, edited by R. G. Busnel and J. F. Fish (Plenum, New York), pp. 109–181.

Schuller, G. (**1979**). ''Coding of small sinusoidal frequency and amplitude modulations in the inferior colliculus of 'CF-FM' bat *Rhinolophus ferrumequinum*,'' Exp. Brain. Res. **34**, 117–132.

Simmons, J. A., Ferragamo, M. J., Saillant, P. A., Haresign, T., Wotton, J. M., Dear, S. P., and Lee, D. N. (**1995**). ''Auditory dimensions of acoustic images in echolocation,'' in *Hearing by Bats*, edited by A. N. Popper and R. R. Fay (Springer-Verlag, New York), pp. 146–190.

Skolnik, M. E. (**1980**). *Introduction to Radar Systems*, 2nd ed. (McGraw-Hill, Kogakusha, Tokyo).

Tian, B., and Schnitzler, H.-U. (**1997**). ''Echolocation signals of the greater horseshoe bat (*Rhinolophus ferrumequinum*) in transfer flight and during landing,'' J. Acoust. Soc. Am. **101**, 2347–2364.

Tomiyasu, K. (**1978**). ''Tutorial review of synthetic-aperture radar (SAR) with applications to imaging of the ocean surface,'' Proc. IEEE **66**, 563.

Whiteside, T. C. D., and Samuel, G. D. (**1970**). ''Blur zone,'' Nature (London) **225**, 94–95.

Computer models for masked hearing experiments with beluga whales (*Delphinapterus leucas*)

Christine Erbe
Institute of Ocean Sciences, Acoustical Oceanography, 9860 W Saanich Rd., Sidney, British Columbia V8L 4B2, Canada

Andrew R. King
School of Earth Sciences, Macquarie University, Sydney, New South Wales 2109, Australia

Matthew Yedlin
University of British Columbia, Earth & Ocean Sciences, 2219 Main Mall, Vancouver, British Columbia V6T 1Z4, Canada

David M. Farmer
Institute of Ocean Sciences, Acoustical Oceanography, 9860 W Saanich Rd., Sidney, British Columbia V8L 4B2, Canada

(Received 24 July 1998; accepted for publication 28 January 1999)

Environmental assessments of manmade noise and its effects on marine mammals need to address the question of how noise interferes with animal vocalizations. Seeking the answer with animal experiments is very time consuming, costly, and often infeasible. This article examines the possibility of estimating results with software models. A matched filter, spectrogram cross-correlation, critical band cross-correlation, and a back-propagation neural network detected a beluga vocalization in three types of ocean noise. Performance was compared to masked hearing experiments with a beluga whale [C. Erbe and D. M. Farmer, Deep-Sea Res. II **45**, 1373–1388 (1998)]. The artificial neural network simulated the animal data most closely and raised confidence in its ability to predict the interference of a variety of noise sources with a variety of vocalizations. [S0001-4966(99)00905-4]

PACS numbers: 43.80.Lb, 43.80.Nd, 43.60.Lq [WA]

INTRODUCTION

Over the past couple of years, public awareness of human impact on nature has steadily increased. Living in the era of decreasing animal diversity, public concern about protecting species from becoming extinct has led to a rapid increase in environmental assessments of various human activities. History has shown that we often act too late, i.e., when a dying species cannot be saved anymore. Understanding, foresight, and preventative action is therefore of utmost importance.

Long considered as vast, hence invulnerable, our world's oceans have experienced extensive human abuse posing threats to all marine life. In particular, the protection of whales and dolphins has recently earned unprecedented public interest. Threats to marine mammals include accidental or intended takings (killings); entanglement in debris or fishing gear; habitat destruction; water contamination due to industrial pollution, oil spills, toxic chemicals, waste and sewage; changes in water temperature and salinity; physical alteration of habitat during offshore construction; overfishing of prey; and underwater noise exposure. Since the beginning of the industrial revolution, the world's oceans have become increasingly noisy. Ship traffic, oil and mineral exploration, and offshore construction all contribute to the noise pollution of marine-mammal habitat.

Noise can have a variety of effects on marine mammals such as behavioral disturbance, physiological damage to their auditory system as well as other organs and tissues, and masking. Marine mammals rely primarily on acoustics for communication and orientation. Manmade noise, however, has the potential of interfering with animal communication signals, odontocete (toothed whale) echolocation signals, environmental sounds animals might listen to for orientation, and predator and prey sounds. An understanding of the extent of masking is crucial for the writing of regulations for industrial underwater noise emission.

A few studies have examined masking with cetaceans (whales and dolphins) both psychophysiologically[1–7] and electrophysiologically.[8,9] Most of these looked at high-frequency signal discrimination; only three[1,4,7] provided masked hearing data at frequencies below 10 kHz, where most of the industrial noise spectra prevail. Masking has generally been studied with the signal being a pure tone and the masker being either a pure-tone or broad-band (white) and temporally consistent noise. These studies provided valuable information on the basic characteristics of the animal auditory filter, such as the relationship between the amplitude, frequency, and frequency bandwidth of signal and masker.

The study by Erbe and Farmer[7] was different in that it presented a ''holistic'' approach to masking where the masked signal was a complex animal vocalization and the masker was structured noise. Figure 1 shows power density spectrograms of the sounds used. The signal was a typical 2-s beluga vocalization consisting of six pulses with frequency components between 700 Hz and 8 kHz. Bubbler

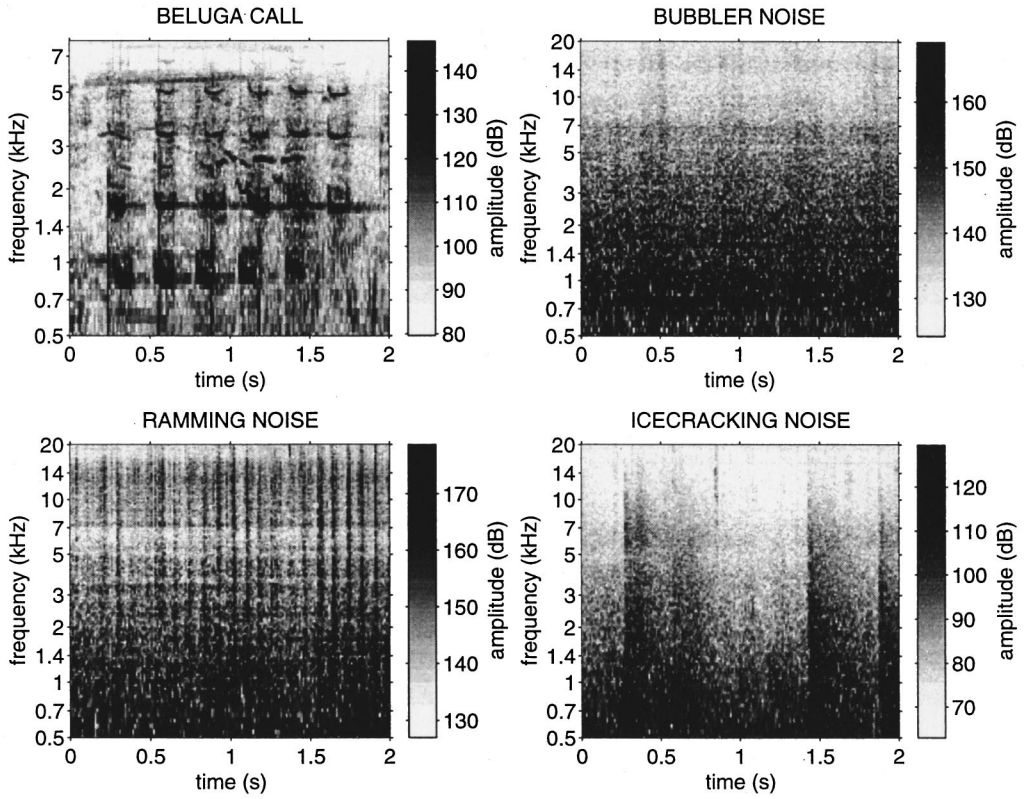

FIG. 1. Power density spectrogram of the beluga vocalization, an icebreaker's bubbler and propeller (ramming) noise, and natural ice-cracking noise in dB *re* 1(μPa^2/Hz)@1 m. A source level of 160 dB *re* 1 μPa@1 m was assumed for the beluga call. The source levels of the noises were, respectively, 194, 203, and 147 dB *re* 1 μPa@1 m.

noise emitted by the bubbler system of an icebreaker was temporally continuous and broadband, with most of the energy below 2 kHz. Propeller cavitation noise consisted of sharp broadband pulses occurring 11 times per s. It was also called ramming noise, because this sample was taken during the ice-ramming action of the icebreaker. Naturally occurring ice-cracking noise (ambient Arctic noise) exhibited broadband pulses at irregular intervals. The vocalization was mixed with 2-s samples of each of the three noises in various signal-to-noise ratios. Mixed sounds were played back to a beluga whale named Aurora, who indicated signal discrimination in a behavioral go/no-go paradigm. Aurora's response is replotted in Fig. 2. Bubbler noise exhibited the strongest interference with a detection threshold at a ''critical'' noise-to-signal ratio (nsr) of 15.4 dB (signal-to-noise ratio −15.4 dB). Propeller cavitation noise was second strongest in masking with a critical nsr of 18.0 dB. Natural ice-cracking noise was least masking, with an nsr of 29.0 dB.

As a means of assessing the degree of masking of a variety of industrial noises, animal experiments are inefficient because of the amount of time and cost involved. It would be preferable to have a fast, ground-truthed model simulating masked hearing experiments and thus predicting masking effects in cases where direct experiments with animals are infeasible. This article applies a variety of software tools, some of which are standard signal-processing methods, to the problem of detecting animal vocalizations in noise. Mellinger,[10] and Mellinger and Clark[11] used a matched filter, a hidden Markov model, and spectrogram image convolution to detect bowhead whale vocalizations in noise. The methods were compared with respect to their false alarm and miss rates. Spectrogram image convolution performed the best, having the smallest combined error rate. The hidden Markov model followed; matched filtering had the highest error rate. Potter *et al.*[12] designed an artificial neural network trained with back-propagation and tested it on the same bowhead data set. The neural net performed even better than spectrogram image convolution. Mellinger and Clark[13] tested

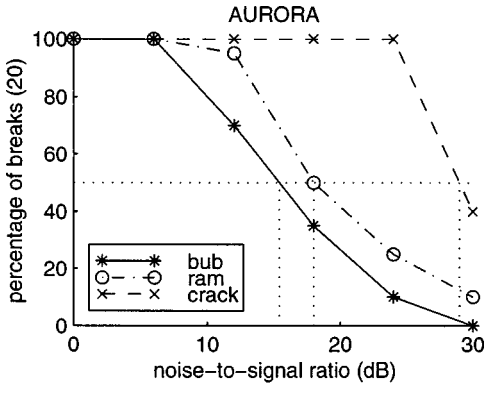

FIG. 2. Masked-hearing thresholds of the beluga whale, Aurora, in bubbler, ramming, and ice-cracking noise. The *x*-axis denotes the pressure noise-to-signal ratio in dB. Every mixture of the call with the three noises in the 6 nsr's shown was played exactly 20 times. The *y*-axis indicates how often Aurora heard the call in the noise, i.e., how often she broke away from the target. Defining the hearing threshold at 50% yields the following critical nsr's: 15.4 dB for bubbler system noise, 18.0 dB for ramming noise, and 29.0 dB for natural ice-cracking noise. [Reprinted from Ref. 7, Deep Sea Res. II **45**, 1383 ©1998, with permission from Elsevier Science.]

matched filtering and spectrogram image convolution on a few mysticete sounds from blue, fin, and minke whales. They found that matched filtering worked well if the signals to be detected were buried in white background noise. Spectrogram image convolution excelled if the interfering noise was structured, e.g., harmonic. In the case that the animal vocalization was a highly repetitive sequence of sounds occurring at regular intervals (a pulse train), a summed autocorrelation method proved useful. These previous studies compared the signal detection methods under the criterion of yielding the highest hit rate. In our study, the signal detectors are compared under the criterion ''How closely does the model's performance resemble that of the whale?'' Performance is judged in terms of the order and level of the maskers as determined by our earlier study.[7]

I. METHODS AND RESULTS

A. Matched filtering

In this section, we hypothesize that matched filtering can successfully model beluga masked-hearing experiments. For linear, time-invariant systems, a filter performs the convolution of an incoming time series $x[t]$ with its impulse response $h[t]$ to yield

$$y[t]=\sum_{k=-\infty}^{\infty} h[k]\cdot x[t-k]. \tag{1}$$

In problems of signal detection in noise, one wants to design a filter which—while convolving along the time series of input data—produces maximum output when there is complete overlap between the signal buried in noise and the desired pure signal. It can be shown that the optimal impulse response of such a filter has to be as long as the signal to be detected.[14] Furthermore, the filter coefficients have to be equal to the product of the inverted autocorrelation matrix of the noise and the time-reversed pure signal. For white noise, the autocorrelation matrix turns into the identity matrix, and the filter response equals the time inverse of the pure signal. As the filter coefficients are matched to the signal time series, one calls this filter a matched filter. The convolution of a time-reversed signal is equivalent to the cross correlation of the signal without time reversal. Therefore, matched filtering is equivalent to cross correlation of the input time series with the desired signal. We applied the matched filtering technique to ''near-white'' noises, as Fig. 3 indicates. The autocorrelation coefficients of the three noises (bubbler, ramming, and ice-cracking) and artificially created, Gaussian-distributed white noise are shown for comparison. In each case, a 2-s noise sample was correlated with a 3-s noise sample of the same type, and lags between 0 and 1 s were plotted. For zero lag, the coefficients were equal to 1. For all other lags, they oscillated around 0. In other words, the autocorrelation matrices of the noises were zero except for zero lag, i.e., the matrices were diagonal. The noises were, hence, white in the sense that they were uncorrelated with themselves.

In the discussion of our previous paper,[7] we put forward the idea that natural ice-cracking noise masked the least, because of its irregular temporal structure. The whale managed

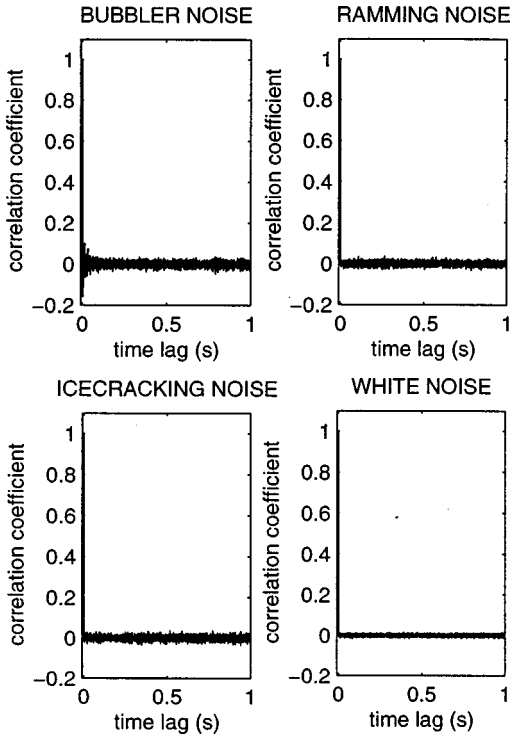

FIG. 3. Autocorrelation of the noise time series showing ''near-white'' behavior for the three Arctic noises.

to identify the vocalization in noise from short fractions which emerged through quieter gaps in the noise field. For the current analysis, we therefore assume that the whale can identify the vocalization if one of the six pulses in the call is audible. In order to calculate the impulse response $h[t]$ of the matched filter (simulating the whale's auditory filter), we cut each of the six 200-ms-long pulses, which we consider ''phonemes,'' out of the time series of the 2-s vocalization. We then computed the covariance matrix of the six phonemes and searched for its eigenvalues and eigenvectors. The eigenvector corresponding to the largest eigenvalue of the covariance matrix was the one correlating the best with each of the six phonemes. This eigenvector in a sense represented a ''mean'' phoneme and was therefore selected as the impulse response $h[t]$ of our matched filter. During the matched filtering process, the filter $h[t]$ then ''correlated along'' the time series of incoming sounds. These incoming sounds were mixed sounds $x[t]$, i.e., the point-by-point summation of the pressure time series of the vocalization $s[t]$ and each of the three noises $n[t]$

$$x[t]=s[t]+\alpha\cdot n[t], \tag{2}$$

where α determined the noise-to-signal ratio (nsr). The time series above had the same length $N=90\,112$ samples (sampling frequency 44 kHz, 2 s of sound). We did not vary the time offset between the signal and the noise; i.e., the signal always happened at the same time in the noise. This was the same during the animal experiments.[7] The cross-correlation coefficient at each time lag β as a function of the nsr could then be computed as Ref. 15

$$R_\beta(\alpha)=\frac{\Sigma_{t=1}^{M}h[t]x[t+\beta]}{\sqrt{\Sigma_{t=1}^{M}h^2[t]\cdot\Sigma_{t=1}^{M}x^2[t+\beta]}}. \tag{3}$$

The total number of lags β is $N-M+1$, with N denoting the length of the time series $x[t]$ and M being the number of samples in $h[t]$.

The normalization in Eq. (3) was chosen such that the filter's output would be 1 for perfect detection and 0 for no correlation. The behavior of the cross-correlation coefficients R_β as a function of α can be understood by looking at the limits $\alpha=0$ and $\alpha\to\infty$. With $x=s+\alpha\cdot n$,

$$\begin{aligned}R_\beta(\alpha)&=\frac{\Sigma h[t]x[t+\beta]}{\sqrt{\Sigma h^2[t]\cdot\Sigma x^2[t+\beta]}}=\frac{\Sigma h[t](s[t+\beta]+\alpha n[t+\beta])}{\sqrt{\Sigma h^2[t]\cdot\Sigma(s^2[t+\beta]+\alpha^2n^2[t+\beta]+2\alpha s[t+\beta]n[t+\beta])}}\\&=\frac{\Sigma h[t]s[t+\beta]+\alpha\Sigma h[t]n[t+\beta]}{\sqrt{\Sigma h^2[t]\cdot\Sigma s^2[t+\beta]+\alpha^2\Sigma h^2[t]\cdot\Sigma n^2[t+\beta]+2\alpha\Sigma h^2[t]\cdot\Sigma s[t+\beta]n[t+\beta]}}.\end{aligned} \tag{4}$$

For $\alpha=0$, the cross-correlation coefficients become

$$R_\beta(0)=\frac{\Sigma h[t]s[t+\beta]}{\sqrt{\Sigma h^2[t]\cdot\Sigma s^2[t+\beta]}}. \tag{5}$$

The value of the cross-correlation coefficient depends on how well the filter $h[t]$ matches the desired signal $s[t]$ over the length of the filter. At the lag of best overlap, the cross-correlation coefficient will be equal to 1, if the impulse response of the filter equals the time series of the desired signal: $h[t]=s[t]$. If the filter is not equal but only similar to the desired signal, as is the case in our model, the correlation coefficients will be slightly less than 1.

For $\alpha\to\infty$, we divide the numerator and denominator by α and let all the terms with α in the denominator go towards 0.

$$R_\beta(\alpha)=\frac{(1/\alpha)\Sigma h[t]s[t+\beta]+\Sigma h[t]n[t+\beta]}{\sqrt{(1/\alpha^2)\Sigma h^2[t]\cdot\Sigma s^2[t+\beta]+\Sigma h^2[t]\cdot\Sigma n^2[t+\beta]+(2/\alpha)\Sigma h^2[t]\cdot\Sigma s[t+\beta]n[t+\beta]}}, \tag{6}$$

$$\lim_{\alpha\to\infty}R_\beta(\alpha)=\frac{\Sigma h[t]n[t+\beta]}{\sqrt{\Sigma h^2[t]\cdot\Sigma n^2[t+\beta]}}. \tag{7}$$

Independent of the type of noise, all the plots of $R_\beta(\alpha)$ will always converge to the product of the filter's impulse response with the pure noise. In other words, if there is no signal in the noise, the output of the filter will not necessarily be 0 but slightly greater or smaller (negative) than 0. Thinking of the time series as vectors, $R_\beta(\alpha)$ converges to the cosine of the angle between the filter and the noise. Therefore, the more ''similar'' the filter and the noise are, the smaller the angle, the greater the cosine.

In matched filtering, as soon as the filter's output surpasses a preset threshold, the signal detection is deemed successful. Picking a threshold, however, is tricky. We first examined the fluctuation of the filter, when presented with pure noise. We therefore computed the cross correlation of the mean phoneme with each 2-s noise time series over all time lags β. This yielded a series of correlation coefficients R_β for each of the three noises. The standard deviations of the correlation coefficients were 0.033, 0.045, and 0.023 for bubbler, ramming, and ice-cracking noise, respectively. Given that we hypothesized the whale would detect the call in the noise if just one of the phonemes were audible, we looked for the maximum R over all lags β. A detection threshold should therefore be greater than the maximum correlation coefficient when pure noise is presented. For a comparison across methods, we picked a detection threshold at 0.5 in analogy to the whale experiment. The matched filter was normalized such that it would give an output close to 1 when the signal without added noise was presented, in analogy to a 100% signal-detection probability from Aurora when no or low noise was added, see Fig. 2. The matched filter was further chosen to give an output close to 0 in the case of pure noise, in analogy to a near-zero response probability of Aurora and because the animal was trained not to respond upon hearing pure noise.

Figure 4(a) shows the cross correlation of the mean phoneme with the call $s[t]$. The impulse response of the filter correlates well with the first four pulses in the call, and poorly with the last two. Figure 4(b) shows the results of the matched filtering. Taking thresholds at 0.5 yields the following critical nsr's: 1.6 dB for bubbler noise, 3.2 dB for ramming noise, and 10.0 dB for ice-cracking noise. The order of the noises is the same as with Aurora (Fig. 2); the relative distances of the thresholds are also similar. If one was to add an offset of 15.0 dB to the estimated thresholds of the matched filter, Aurora's results would be reproduced with a

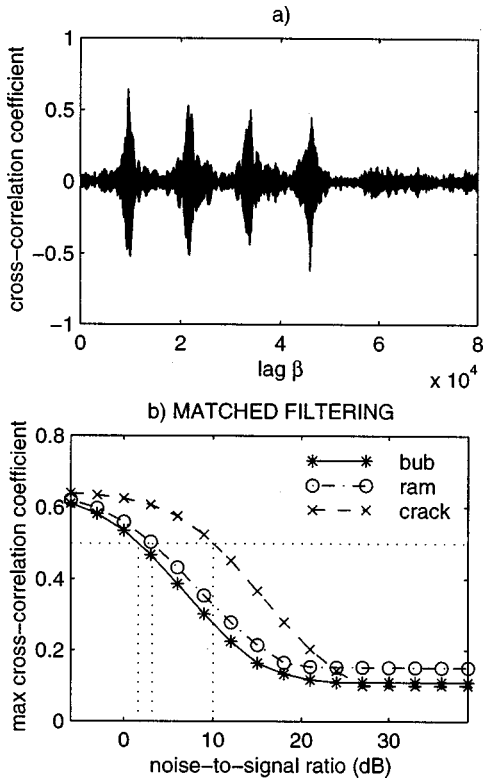

FIG. 4. (a) Cross correlation of the matched filter's impulse response with the time series of the beluga vocalization. The first four phonemes in the vocalization are detected well; the last two phonemes correlate poorly. (b) Matched filtering of the beluga vocalization buried in bubbler, ramming, and ice-cracking noise. The maximum cross-correlation coefficient over all lags β was plotted. Taking a threshold at 0.5, as in the whale experiment, classifies the noises in the same order as the whale did and with similar relative thresholds. The critical nsr's are 1.6 dB for bubbler noise, 3.2 dB for ramming noise, and 10.0 dB for ice-cracking noise.

maximum error of 13%, which we consider a good similarity. This offset of 15.0 dB was calculated such that the sum-squared-error between Aurora's critical nsr's and the modeled nsr's was minimized.

There are many different possible implementations of matched filters. Erbe[16] chose the full call $s[t]$ as the impulse response of the matched filter $h[t]$, rather than picking a mean phoneme. The order of the noises, however, was such that bubbler system noise exhibited the strongest interference, followed by ice-cracking noise, then ramming noise. In other words, the degree of masking for ice-cracking and ramming noise was reversed. Thresholds were also very close to each other, at 4.8 dB, varying only by 0.1 dB. Given that the mean phoneme impulse response presented in this paper worked better, a possible explanation could include that the animal indicated the call detection as soon as one phoneme was audible.

We also tried to take the exact time series of one 200-ms phoneme as $h[t]$, rather than calculating a mean phoneme. Each of the six phonemes in the beluga vocalization was taken as the impulse response of the filter one at a time. The particular phoneme chosen was cut out of the call $s[t]$ and correlated with mixtures of the shortened call and the three noises. The phoneme chosen as the filter was taken out of the time series of the call in order to avoid large autocorrelation values in the desired cross correlation. Also, in the wild, an animal could never have the exact time series of an incoming signal stored in its memory due to propagation effects and the inherent variability of time series of vocalizations. The results of this matched filtering method were that the order of the noises in the correlation coefficient plots varied depending on which phoneme was chosen as the filter. This was because each phoneme did not correlate equally well with the others.

Altogether, the matched filter presented in this article successfully modeled the relative degrees of masking of bubbler, ramming, and ice-cracking noise as measured with the trained beluga whale, Aurora. However, a generalization of these results to other vocalizations and noises needs to be treated with caution. This is for two reasons: First, the theory of a matched filter is based on white noise. A matched filter can therefore be expected to perform poorly in nonwhite, structured noise, as shown by Mellinger and Clark.[13] Spectrogram image convolution can be expected to work better for structured noise. Second, in the case of complex vocalizations (those having multiple frequencies which are not harmonics), two calls of the same type generally correlate poorly, which makes it difficult, if not impossible, to design the impulse response of a matched filter that will correlate well with the signals to be detected. From our experience, only constant frequency tones or single frequency whistles (with consistent time structure) correlate well in the time domain. We hypothesize that multifrequency (nonharmonic) vocalizations correlate poorly, because from utterance to utterance, only amplitude and frequency structure will be consistent, but not the phase. Sound propagation effects in the ocean further change the time series of animal vocalizations. Signal-detection methods based on spectrograms rather than time series might thus be more promising, because they no longer contain phase information.

B. Spectrogram cross correlation

In this section, we hypothesize that spectrogram cross correlation will model beluga masked hearing experiments better than matched filtering. In Mellinger and Clark's study[11] on automatic bowhead call detection in noise, spectrogram cross correlation (which they called spectrogram image convolution) had a higher call-detection rate than matched filtering and a hidden Markov model. Mellinger and Clark[13] showed that spectrogram cross correlation outperformed matched filtering, particularly if the interfering noise was nonwhite.

We want to compare spectrogram cross correlation to matched filtering under the criterion of how closely the thresholds and the order of noises resemble those of a beluga whale. The motivation for trying spectrogram cross correlation was twofold. First, the time series of two vocalizations or phonemes often correlate poorly because of varying phase. Phase information is lost in spectrograms. Spectrograms contain frequency, amplitude and time information which is consistent amongst calls of the same type. Therefore, spectrograms of calls or phonemes often correlate better than time series. Second, spectrogram representation is biologically more justified than time series representation: In the mammalian ear (of terrestrial as well as marine mammals),

the inner ear and auditory nerve serve simplistically as a series of tuned resonators or filters providing spectral information in real time to the brain.[17,18]

For each of the 2-s-long sounds (beluga vocalization, bubbler noise, ramming noise, ice-cracking noise, and mixtures of the call with the three noises), we computed a spectrogram by calculating the fast Fourier transform in blocks of 1024 data points, using Hamming windows with 50% overlap. We took the magnitude of the complex Fourier components. Negative frequencies and frequencies outside the call spectrum (>6 kHz) were discarded. With a sampling frequency of 44 kHz, the resulting spectrogram matrices were of size 139×175.

We constructed our kernel in a different way than Mellinger and Clark.[11] They actively placed positive numbers where there was energy in the spectrogram of the call and negative numbers on either side, and normalized the kernel such that the sum over all kernel values was 0. In order to construct our kernel, we selected the six call phonemes from the call spectrogram. Each phoneme spectrogram was of the size 139×11. Similar to our matched filter design, we computed the covariance matrix of the spectra of the six phonemes in the call and looked for the largest eigenvalue. The corresponding eigenvector was chosen as the kernel for spectrogram cross correlation after subtracting its mean.

Spectrogram cross correlations were then calculated according to

$$R_\beta(\alpha)=\frac{\Sigma_{t=1}^{11}\Sigma_{f=1}^{139}h[t,f]x[t+\beta,f]}{\sqrt{\Sigma_{t=1}^{11}\Sigma_{f=1}^{139}h^2[t,f]\cdot\Sigma_{t=1}^{11}\Sigma_{f=1}^{139}x^2[t+\beta,f]}}, \tag{8}$$

where $h[t,f]$ is the kernel and $x[t,f]$ is the spectrogram of the mixed sound. The time lag β had the size of one time sample in the spectrogram. Figure 5(a) shows the correlation of the kernel with the spectrogram of the vocalization. The first four phonemes are detected clearly; the last two phonemes correlate more poorly with the kernel.

Again, we hypothesize that the call can be detected if the correlation of the kernel with one phoneme in the call lies above a detection threshold. While correlating the kernel with the spectrograms of the mixed sounds, we therefore looked for the maximum $R_\beta(\alpha)$ over all lags β. The correlation curves $\max[R_\beta(\alpha)]$ for the three noises are shown in Fig. 5(b). The order of the noises was again the same as with the whale: bubbler noise was identified as the strongest masker, followed by ramming noise, then ice-cracking noise. For comparison, the detection threshold was taken at 0.5 yielding the following critical nsr's: 11.4 dB for bubbler noise, 13.8 dB for ramming noise, and 17.9 dB for ice-cracking noise. If the critical nsr's estimated by spectrogram cross correlation are shifted towards higher nsr's by an offset of 6.4 dB (taken to minimize the sum-squared-error), the critical nsr's of Aurora are reproduced with a maximum deviation of 16%.

Critical nsr's computed with spectrogram cross correlation depend on the number of Fourier components used during the fast Fourier transform. We tried spectrogram cross correlation with 512 instead of 1024 Fourier components. This gave the same correct order of noises, though with a maximum mismatch of 19% after shifting the critical nsr's such as to minimize the sum-squared-error between the modeled nsr's and Aurora's. In the case of 256 Fourier components the maximum mismatch was 27%; in the case of 2048, the maximum mismatch was 20%. The order of the noises was correct in all four cases. The best modeling results were achieved with 1024 Fourier components.

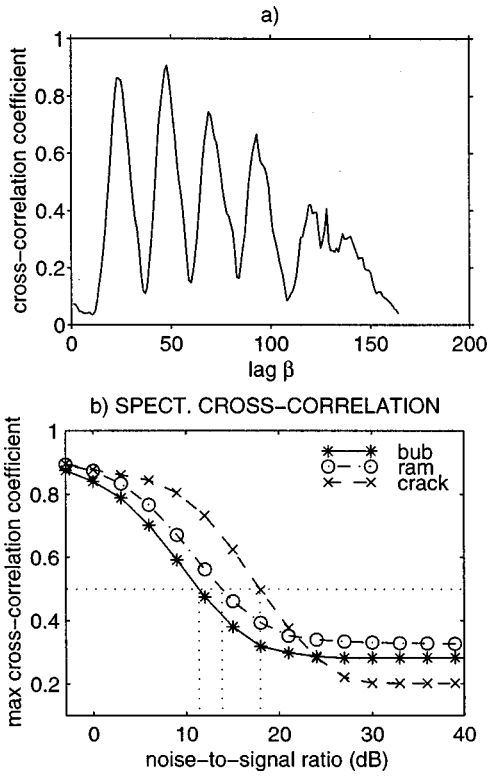

FIG. 5. (a) Cross correlation of the spectrogram kernel with the spectrogram of the beluga vocalization. Similar to the matched filter, the first four phonemes in the vocalization are detected well; the last two phonemes correlate poorly. (b) Spectrogram cross correlation of the beluga vocalization buried in bubbler, ramming, and natural ice-cracking noise. Plotted is the maximum cross-correlation coefficient over all lags β. With a threshold taken at 0.5, the critical nsr's are 11.4 dB for bubbler, 13.8 dB for ramming, and 17.9 dB for ice-cracking noise. The order of noises is correct.

Both matched filtering and spectrogram cross correlation managed to classify the three noises from strongest masking to least masking in the same order as the whale. Comparing critical nsr's, their relative distance is slightly closer to that of the whale in the case of matched filtering.

Erbe[16] chose the spectrogram of the entire vocalization as the kernel, which resulted in ice-cracking noise being identified as the strongest masker, followed by ramming noise, then bubbler noise. The order of the noises was exactly opposite to that of the whale, Aurora. This could mean that the detection of one phoneme is enough to recognize the vocalization and hence the correct modeling approach.

C. Critical band cross correlation

A quantity often measured in masked-hearing experiments is the critical ratio.[19] In the case that a pure tone is masked by a broadband white noise, the critical ratio is defined as the ratio of the intensity of the tone I_t divided by the

noise spectral density SI_n (intensity per Hz) at the level when the tone is just audible through the noise. The critical ratio is often expressed in decibels

$$\mathrm{CR} = 10 \cdot \log_{10} \frac{I_t}{SI_n}. \tag{9}$$

The mammalian auditory system can generally be represented as a series of overlapping bandpass filters.[18,19] The idea is that a listener trying to detect a signal in noise will ''choose'' an auditory filter with a center frequency close to that of the signal. Then, only the amount of noise coming through this filter will have an effect on masking the signal; noise at frequencies far away from the signal frequency will have no effect. Fletcher[20] hypothesized that at detection threshold, the intensity of the tone equaled the total intensity of the noise in the corresponding auditory filter (equal-power assumption)

$$I_t = SI_n \cdot \Delta f. \tag{10}$$

Substituting into CR yields

$$\mathrm{CR} = 10 \cdot \log_{10} \Delta f. \tag{11}$$

The critical ratio can therefore also be expressed in Hz as the approximated width of the auditory filter around the test tone

$$\Delta f = 10^{\mathrm{CR}/10}. \tag{12}$$

In 1940, Fletcher[20] did a masked-hearing experiment with human subjects, in which the signal was a pure tone and the masker was narrow-band white noise. Fletcher measured the intensity of the signal at detection threshold as a function of the noise bandwidth. For narrow-band noise (narrower than the bandwidth of the auditory filter), the signal-detection threshold increased with increasing noise bandwidth, i.e., increasing total noise power in the filter. Once the bandwidth of the noise reached the bandwidth of the auditory filter, the signal-detection threshold remained constant during further widening of the noise band. The noise bandwidth above which masking could not be increased was called the critical bandwidth. The critical bandwidth is thus the width of the auditory filter measured via Fletcher's band-widening technique; whereas the critical ratio is the filter width calculated from masked-hearing thresholds in broadband white noise.

Johnson[2] measured critical ratios for a bottlenose dolphin (*Tursiops truncatus*) for signal frequencies between 5 and 100 kHz and continuous broadband noise. In a double-logarithmic plot, a straight line could be fitted through the data points of CR as a function of frequency. This indicated that the dolphin auditory system may be modeled as a bank of constant *Q* filters. The quality factor *Q* of a bandpass filter is defined as the ratio of center frequency to filter width, measured at half-peak power. Constant *Q* implies an increase in filter width with center frequency. Au and Moore[5] also measured critical ratios of a bottlenose dolphin and obtained similar results to Johnson.[2] Johnson *et al.*[4] measured critical ratios between 40 Hz and 115 kHz in a beluga whale (*Delphinapterus leucas*). For frequencies less than 1 kHz, the critical ratio no longer increased with frequency, but appeared to become constant, indicating that a constant *Q* model only holds for frequencies above 1 kHz. A comparison across species further showed that the critical ratios of the beluga whale were about 3 dB smaller than those of the bottlenose dolphin. Au and Moore[5] also measured critical bandwidths for a bottlenose dolphin using Fletcher's band-widening technique. On average, the critical bands were 7.5 dB greater than the critical ratios, indicating that Fletcher's equal-power assumption might hold less well in the case of bottlenose dolphins. Larger critical bands mean that the signal power is less than the noise power at threshold.

Critical band analysis is based on simultaneous masking, i.e., when the signal and the masker happen at the same time. However, forward masking and backward masking exist, too, in which a time-limited masker precedes or follows the signal, respectively. For masking to occur, signal and masker must be less than a critical time interval apart. Vel'min and Dubrovskii,[21] Moore *et al.*,[22] and Au *et al.*[23] measured this interval with bottlenose dolphins for high-frequency echolocation signals. It was, on average, 300 μs. There are no data for critical time intervals at lower communication frequencies and no data for beluga whales. Vel'min and Dubrovskii[24] pointed out that dolphins might be equipped with two functionally (and possibly morphologically) independent auditory subsystems, one for communication and one for echolocation, in which case these critical intervals could not be applied to communication signals.

There are no data on critical bandwidths in beluga whales. For the current analysis, we therefore calculated the widths of the beluga auditory filters from Johnson's critical ratio data[4] using Eq. (12). For example, at 700 Hz (the lower limit of the call spectrum), the critical ratio is about 18 dB according to Johnson's experiment, yielding a filter bandwidth of 63 Hz. At 6 kHz (the upper limit of the call spectrum), the critical ratio is about 24 dB, yielding a bandwidth of 251 Hz. On average, for low frequencies, the filter width was about 6% of the center frequency. Or, in other words, the critical ratios were about 1/12th of an octave wide. Picking a center frequency f_0, the lower limit of the filter can be calculated as $f_l = 2^{-1/24} \cdot f_0$, the upper limit is $f_u = 2^{1/24} \cdot f_0$. Table I lists the center frequencies of the adjacent, i.e., nonoverlapping 12th-octave bands used in our study.

The computation of spectrogram cross correlation in the previous section involved linear frequency distribution and linear amplitudes. If cross correlation takes place in the mammalian brain, hypothetical spectrograms created by our ears are more likely logarithmic in frequency and amplitude. Therefore, we first computed power-density spectrograms of the beluga vocalization, the three noises, and all mixed sounds, using 1024 Fourier components and Hamming windows with 50% overlap. Power is the area underneath a power-density spectrum. Therefore, the total power passing through one frequency band could be calculated as the integral over the power density spectrum from f_l to f_u at each time in the power density spectrogram. We took $10 \cdot \log_{10}$ of the amplitudes to yield band levels in dB *re* 1 μPa. Furthermore, we adjusted the amplitudes relative to the beluga audiogram, which relates the amplitude of a pure tone at detection threshold (in the absence of noise) to the tone's frequency. According to the beluga audiogram, high frequen-

TABLE I. Center frequencies (Hz) of adjacent 12th-octave bands.

40	42	45	48	50	53	57	60	63	67
71	76	80	85	90	95	101	107	113	120
127	135	143	151	160	170	180	190	202	214
226	240	254	269	285	302	320	339	359	381
403	427	453	479	508	538	570	604	640	678
718	761	806	854	905	959	1 016	1 076	1 140	1 208
1 280	1 356	1 437	1 522	1 613	1 709	1 810	1 918	2 032	2 153
2 281	2 416	2 560	2 712	2 874	3 044	3 225	3 417	3 620	3 836
4 064	4 305	4 561	4 833	5 120	5 424	5 747	6 089	6 451	6 834
7 241	7 671	8 127	8 611	9 123	9 665	10 240	10 849	11 494	12 177
12 902	13 669	14 482	15 343	16 255	17 222	18 246	19 331	20 480	

cies were amplified. This audiogram was the mean of six published beluga audiograms[25,26,4] and the four frequencies measured by Erbe and Farmer.[7] Only the frequency bands between 700 Hz and 6 kHz, which occupy energy of the call, were chosen for this analysis. The kernel was again selected as the eigenvector of the largest eigenvalue of the covariance matrix of the call phonemes. We subtracted its mean.

Figure 6(a) shows the correlation of the kernel with the 12th-octave band spectrogram of the call. Compared to Fig. 5(a), the correlation peaks at the location of the six phonemes in the call are less sharp. The correlation maxima vary less from phoneme to phoneme than with the spectrogram cross-correlation method. Figure 6(b) shows the maximum cross-correlation coefficients of the kernel correlated with the band-averaged spectrograms of the mixed sounds. Although the curves change order with the nsr, nowhere does the order resemble that of the whale. The results are curious. The time resolution of the spectrograms used in the previous section and the band-averaged spectrograms used here was the same. The difference in correlation behavior therefore lies in the audiogram normalization, logarithmic amplitude, and band averaging. The failure of the critical band cross correlation compared to the spectrogram cross correlation (under the criterion of similarity to the whale's results) could indicate that a beluga whale's critical bands are narrower than the ones we calculated from Johnson's critical ratio data under the equal-power assumption: The spectrograms in the previous section contained 70 frequency samples, compared to 38 frequency bands used here.

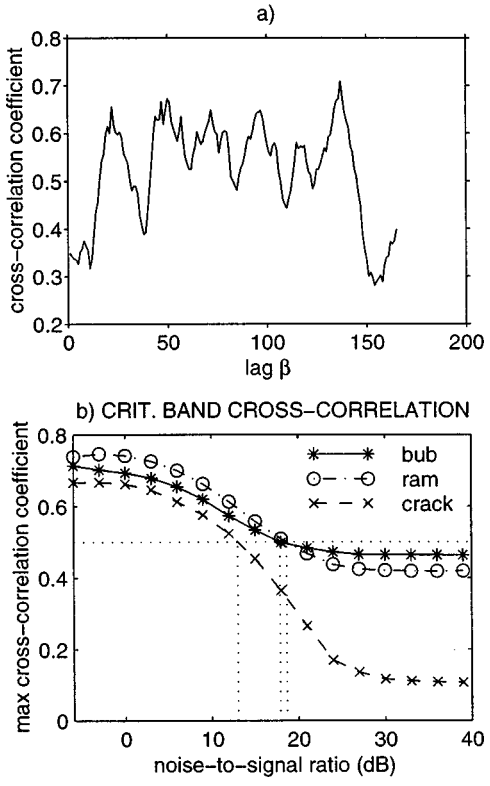

FIG. 6. (a) Critical band (CB) cross correlation of the kernel with the CB-averaged spectrogram of the beluga vocalization. The six phonemes are detected, though less sharply than in Fig. 5(a). (b) Critical band cross correlation of the beluga vocalization in bubbler system noise, ramming noise, and natural ice-cracking noise using a time resolution of 23 ms. Taking a threshold at 0.5, this method could not reproduce the correct order of noises.

A different interpretation of Fig. 6(b) would involve picking a different threshold. The animal might pick a different threshold for each noise depending on how large the cross-correlation coefficients of the correlation of the pure noises with the kernel are. The cross correlations for infinite nsr in Fig. 6(b) are fairly large, particularly for bubbler and ramming noise. The difference between the maximum cross-correlation coefficient at low noise levels (when the call is easily detectable) and at high noise levels (when the call is undetectable) is largest for ice-cracking noise, then ramming, then bubbler noise. One possible interpretation of this is that it would be ''easier'' for the animal to detect the call in the ice-cracking noise than in the other two noises, in the sense that there is a larger range over which the animal can set a threshold in order to indicate call detection with confidence. This interpretation would put the three noises back into the correct order.

It is obvious that spectrogram cross-correlation methods depend on the frequency and time resolution of the spectrograms, i.e., the number of Fourier components used in the Fourier transform. Limited by the fixed sampling rate, there is a tradeoff between the frequency and time resolution in spectrograms. The sampling frequency was $f_s = 44\,\mathrm{kHz}$ for our recordings. With $n_{\mathrm{fft}} = 1024$ Fourier components, the spectrograms used in the previous section had a frequency resolution of $\Delta f = f_s / n_{\mathrm{fft}} = 43\,\mathrm{Hz}$. Frequency samples were averaged into 38 12th-octave bands in the current section. The time resolution was $\Delta t = 1/\Delta f = 23\,\mathrm{ms}$ in both sections. This was considerably wider than the critical time interval for dolphin echolocation. In order to test the effect of decreasing the time interval, critical band cross correlation was tried with $n_{\mathrm{fft}} = 512$ and 256. This decreased the frequency

resolution to 86 and 172 Hz, respectively. The time resolution doubled to $\Delta t = 12$ and 6 ms. A further increase in time resolution would result in fewer frequency samples than 38 bands. Taking thresholds at 50% still classified the noises in the wrong order to the whale. However, using the difference between starting and end point for each curve showed that ice-cracking noise correlations had the largest variation, followed by ramming, then bubbler, noise. This could be interpreted in terms of the whale's facility to set a threshold with confidence, yielding a ''better'' call detection in ice-cracking noise. This would give the same order of noises as with the whale.

D. Artificial neural network

Artificial neural networks (ANN) have successfully been applied to automatic detection of human speech signals.[27] Potter *et al.*[12] used an artificial neural network to detect calls of the bowhead whale in noisy Arctic recordings. Their neural network outperformed a matched filter, a hidden Markov model, and spectrogram cross correlation. We hypothesize that a neural network can also outperform our previous methods when judged under the criterion of closeness to the whale's response. Our hypothesis is based on two facts. First, the previously employed correlation techniques were linear filters. The mammalian auditory system, however, is highly nonlinear.[18,19] The neural network designed in this section is nonlinear. Second, the impulse responses (kernels) of the filters in the previous sections were chosen as eigenvectors of the covariance matrix of call phonemes. This might not be the best approach to the whale's filter. In neural network analysis, a ''kernel'' does not need to be chosen by the operator *a priori*. Rather, the network learns to recognize features from a set of training data. This process is biologically more justified than picking a present kernel.

An ANN can be regarded as a very simple model of the biological neural system, the brain. Both networks are complex, massively parallel information-processing systems which learn from experience and store their knowledge. The major types of ANNs, their history, and applications are described by Haykin.[28] For our ANN design, we chose a fully connected two-layer network trained with back propagation.[29] During the training phase, the ANN was repeatedly presented with a training matrix of noisy beluga calls and pure noise. The network's weights and biases were adjusted from iteration to iteration such that the sum-squared-error (between the desired and actual output) of the network was minimized. We found two modifications to the back-propagation learning rule useful. The inclusion of momentum[30] avoided getting stuck in a high local minimum of the ANNs error performance surface; an adaptive learning rate helped to speed convergence. During the generalization phase, weights and biases were kept constant, and the ANN was presented with the mixed sounds played to the beluga whale. Its call detection performance could then be compared to the methods of the previous sections.

We tested different numbers of neurons in the hidden layer. From our experience, the fewer neurons, the faster the computation of one epoch; the more neurons, the faster the convergence of the neural network (in fewer epochs) to its preset minimum error. Rather than picking the number of hidden-layer neurons corresponding to the minimal computation time, we chose the minimum number of neurons required for the network to converge to its desired minimum error, at the expense of a larger computation time. The reason was that the performance of the neural network during generalization seemed more stable with fewer neurons, i.e., less dependent on the initial conditions. The desired sum-squared-error was set to 0.001. Our ANN had three neurons in the hidden layer and one output neuron. Initial weights and biases were chosen randomly.

We tried both sigmoid and hyperbolic tangent transfer functions and did not find major performance differences. We eventually settled on sigmoid functions, because they have the convenient advantage that their output lies between 0 and 1, where one can interpret 0 as ''no recognition'' and 1 as ''full recognition'' of a particular input pattern. The second argument for choosing sigmoid transfer functions was their biological motivation. They have been said to simulate the refractory phase of real neurons.[31]

The idea was to train our ANN to detect beluga call features in spectrograms of mixed sounds. For the training matrix, we needed a large number of noisy versions of the beluga vocalization. In order to create the training matrix, we first computed the spectrogram of the beluga vocalization using 512 Fourier components and Hamming windows with 50% overlap. This resulted in 89 856 amplitude data, which would require the same amount of neurons in the input layer. ANNs with too many neurons generalize poorly, and computation time increases rapidly with the number of neurons. Finally, ANN analysis which is based on matrix multiplications easily exceeded the computer's virtual memory. Therefore, dramatic data reduction and compression prior to neural network computation was essential. For data reduction, we discarded the first and last 200 ms of the spectrogram before call onset and behind the last phoneme. Furthermore, we limited the frequency band to between 700 Hz and 6 kHz. This way, only the exact time and frequency range occupied by the call was selected. For data compression, we averaged the call spectrogram into a square grid of 20 time steps and 20 frequencies. Modeling the beluga auditory system as a bank of constant Q filters, Table I gave about 38 bandwidths between 700 Hz and 6 kHz. We thus chose a filter array half as fine. Along the time axis, each of the 20 boxes was 82-ms long, which was very much coarser than the critical interval of 300 μs reported for bottlenose dolphins in the case of echolocation.

A training matrix for the neural network was then created by adding noise to the call, not in the time series but in the averaged spectrogram (subscript s for spectrogram domain). We deliberately did not include any of the three test noises in the training matrix in order to prevent the ANN from deriving a cue from the particular noise characteristics rather than call features. In order to evenly span the input space, we added noise matrices that were orthogonal to each other. In particular, we chose doubly periodic background noise, where the amplitude varied both with frequency and time. Altogether, 800 noise matrices of the form

$$n_s[t,f]=\sin\left(\frac{2\pi\omega_t t}{T}+\phi_t\right)\cdot\sin\left(\frac{2\pi\omega_f f}{F}+\phi_f\right)+0.1$$
$$\cdot\,\mathrm{rand}(t,f), \tag{13}$$

were computed with $T=20$ and $F=20$. This equation describes a two-dimensional sine wave overlapped by random values. The angular frequencies ω_t and ω_f were taken from the set [0,1/2,1,...,6] with equal numbers of each combination. The frequencies were less than half the grid size, because some networks had difficulty converging if higher frequencies were included. This was in analogy to visual discrimination of training matrices. When n_s matrices were plotted with colors representing amplitude, the human eye could easily detect the call in low-frequency, but not high-frequency, noise. The phases ϕ_t and ϕ_f were chosen randomly between 0 and π. Random white noise was added with values between 0 and 0.1. We created another 50 noise matrices of entirely random values.

The root-mean-square (rms) amplitudes of the call and the 850 noises were calculated in the spectrogram domain. The spectrograms were divided by their rms amplitude in order to normalize the sounds. Sounds were then mixed according to

$$x_s[t,f]=s_s[t,f]+\alpha_s\cdot n_s[t,f], \tag{14}$$

with α_s varying between 0 and 1. The same recording of the vocalization was chosen every time. All the 20×20 matrices of mixed sounds were reshaped into 400-element-long column vectors by placing the 2nd column of 20 frequency values underneath the 1st column, following with the 3rd column and so forth. We put the 850 column vectors of the mixed spectrograms and the 850 column vectors of the pure-noise matrices together into a training matrix of the size 400×1700. The desired output was set to 1 for the first 850 training vectors representing noisy versions of the call spectrogram. The desired output was set to 0 for the last 850 training vectors representing pure noise. Given that the nsr of the training vectors was low, an output of 1 would thus indicate successful call detection, while an output of 0 would indicate call absence.

With the training matrix and desired output thus chosen, we trained the ANN with back propagation until the sum-squared-error was less than 0.001. This required about 1000 iterations, i.e., repeated presentations of the training matrix. After completed convergence, we held the weights and biases constant. In order to check for a proper generalization of the ANN, we presented the network with the averaged and reshaped spectrogram matrices of the beluga vocalization and bubbler, ramming, and ice-cracking noise. The output was 1 for the call and 0 for the three noises, as desired.

The network was then presented with the averaged and reshaped spectrogram matrices of the original mixtures of the call with the three noises in (time series) nsr's of 0, 3,...,30 dB. The ANN was trained ten times with varying (random) initial conditions (weights and biases). Figure 7 shows the network's mean output at each nsr. Taking the thresholds at 50% yielded the following critical nsr's: 1.6 dB for bubbler noise, 4.7 dB for ramming noise, and 14.0 dB for ice-cracking noise. The standard deviations were 0.9 dB for bubbler and ramming noise, and 1.4 dB for ice-cracking noise. Therefore, not only the order of the noises from strongest to weakest masking was the same as for the whale, but also the relative degrees of masking were similar. Subtracting the net's thresholds from Aurora's yielded an offset of 13.8 dB for bubbler, 13.2 dB for ramming, and 15 dB for ice-cracking noise. Thus, shifting the net's thresholds an average of 14.0 dB to higher nsr's gave Aurora's results with a maximum error of 6%.

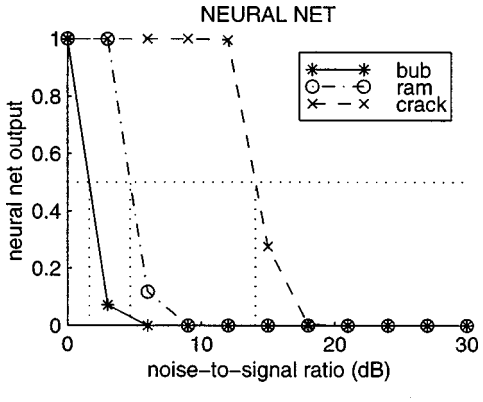

FIG. 7. Mean masked-detection thresholds of the neural network in bubbler, ramming, and ice-cracking noise after running the ANN ten times with different initial conditions. Taking the threshold at 0.5 yielded the following critical nsr's. 1.6 dB for bubbler, 4.7 dB for ramming, and 14.0 dB for natural ice-cracking noise. With an offset of 14.0 dB, the network modeled Aurora's thresholds within 6%.

This ''calibration'' of the neural network to Aurora's performance was necessary because the neural net did not get any species or individual-specific input data. We tried a normalization of training and generalization sounds with respect to the beluga audiogram. However, as the vocalization used was limited to between 700 Hz and 6 kHz, where the audiogram was basically linear, this normalization did not affect the neural network's performance. For more broadband sounds, though, audiogram normalization might become important and a good means of including biological background data in the computer modeling.

II. DISCUSSION

The purpose of this study was to develop an automatic and objective detector for beluga vocalizations in noise. Rather than designing the detector such that it would find the quietest calls with the smallest possible false alarm and miss rates, the detector was supposed to detect beluga calls with the same probability as a beluga whale, in particular the beluga whale trained and used for masked-hearing experiments by Erbe and Farmer.[7] A detector that models beluga masked-hearing experiments could then be used efficiently for environmental assessments of manmade noise with respect to masking of animal vocalization signals. A reliable model is particularly desirable in cases where direct experiments with trained animals are impractical.

We presented a variety of software algorithms which are commonly used for signal detection in noise. Their performance was compared to the masked-hearing experiments with the beluga whale Aurora.[7] In the first section, a matched

filter correlated the time series of a mean call phoneme with the time series of mixed sounds containing both call and noise. Signal detection was deemed successful when the filter's output surpassed a threshold of 0.5. The matched filter classified the three noises in the same order as the beluga whale: bubbler system noise was identified as the strongest masker, followed by propeller cavitation, then natural ice-cracking noise. The relative distances between the critical noise-to-signal ratios (nsr), at which the call was just detectable in the three noises, were similar to those of the whale with a maximum deviation of 13%. We considered this a good similarity and hence accepted our hypothesis that a matched filter could successfully model the whale's results.

In the second section, a mean phoneme spectrogram was correlated with spectrograms of mixed sounds containing both call and noise. Taking a detection threshold at 0.5, the noises were again classified in the correct order. Relative distances between critical nsr's, however, had a maximum deviation of 16%, slightly higher than for the matched filter. Mellinger and Clark[11] found that spectrogram cross correlation outperformed matched filtering, if compared under the criterion of the smallest miss and false-alarm rates. In our analysis, matched filtering slightly outperformed spectrogram cross correlation under the criterion of closeness to the whale's response. We therefore had to reject our hypothesis that spectrogram correlation could outperform matched filtering.

In the third section, we modified the spectrogram correlator to include some basic bioacoustic information about the beluga auditory system, such as the width of the animal's auditory filter and the animal's audiogram. Taking the threshold at 0.5 again led to the wrong order of noises. We suggested the possible explanation that the critical bands of the beluga whale were narrower than the ones we calculated from critical ratio data. If so, Fletcher's equal-power assumption,[20] which works reasonably well in humans,[19] would not be valid for beluga whales. We further offered a different interpretation of the critical band correlation results involving different thresholds for the three noises. This would put the noises into the correct order again. If this same argument were applied to the spectrogram cross correlation and matched filtering section, however, these two methods would not be able to classify the noises in the correct order. It would, at this stage, clearly be useful to collect more masked-hearing data from the animal to corroborate one or the other method of picking a detection threshold.

In the fourth section, we hypothesized that an artificial neural network trained with back propagation to detect call features in noise would outperform the previous methods. Potter *et al.*[12] found that this type of neural network had the smallest error rate when compared to spectrogram cross correlation and matched filtering. The neural network we designed outperformed our spectrogram correlator and matched filter under the criterion of closeness to the whale's response, leading us to accept our hypothesis. The noises were classified in the correct order with a maximum deviation of the relative distances between critical nsr's of 6%. The threshold was taken at 0.5 again. The alternative interpretation offered for the critical band cross correlation cannot be applied to the neural network, because the signal-only and noise-only outputs were the same for the three noises.

In summary, the neural network modeled the whale's performance the best. It thus raised confidence in its ability to predict the degree of masking of other types of noise. At this stage, it would be advisable to let the ANN perform on further noises and subsequently return to the aquarium to test the same sounds on the beluga whale. We also suggest inclusion of further vocalizations of different time and frequency structure. This would allow conclusions about the interference of manmade noise with beluga communication sounds in general. Furthermore, it would be desirable to train beluga whales of different age and sex in order to average out individual differences. Ultimately, we would like to apply an integrated tool of animal experiments and subsequent computer modeling to a variety of marine mammal species.

ACKNOWLEDGMENTS

We wish to express our thanks to Kurt Fristrup and two anonymous reviewers for many constructive suggestions. This work was supported by the Canadian Coast Guard, Central and Arctic Region, under supervision of Patrice St-Pierre.

[1] V. I. Burdin, V. I. Markov, A. M. Reznik, V. M. Skornyakov, and A. G. Chupakov, ''Ability of *Tursiops truncatus* Ponticus Barabasch to distinguish a useful signal against a noise background,'' in *Morphology and Ecology of Marine Mammals*, edited by K. K. Chapskii and V. E. Sokolov (Wiley, New York, 1973), pp. 162–168.

[2] C. S. Johnson, ''Masked tonal thresholds in the bottlenosed porpoise,'' J. Acoust. Soc. Am. **44**, 965–967 (1968).

[3] C. S. Johnson, ''Auditory masking of one pure tone by another in the bottlenose porpoise,'' J. Acoust. Soc. Am. **49**, 1317–1318 (1971).

[4] C. S. Johnson, M. W. McManus, and D. Skaar, ''Masked tonal hearing thresholds in the beluga whale,'' J. Acoust. Soc. Am. **85**, 2651–2654 (1989).

[5] W. W. L. Au and P. W. B. Moore, ''Critical ratio and critical bandwidth for the Atlantic bottlenose dolphin,'' J. Acoust. Soc. Am. **88**, 1635–1638 (1990).

[6] J. A. Thomas, J. L. Pawloski, and W. W. L. Au, ''Masked hearing abilities in a false killer whale (*Pseudorca crassidens*),'' in *Sensory Abilities of Cetaceans—Laboratory and Field Evidence*, edited by J. A. Thomas and R. A. Kastelein (Plenum, New York, 1990), pp. 395–404.

[7] C. Erbe and D. M. Farmer, ''Masked hearing thresholds of a beluga whale (*Delphinapterus leucas*) in icebreaker noise,'' Deep Sea Res. II **45**, 1373–1388 (1998).

[8] A. Supin and V. Popov, ''Frequency-selectivity of the auditory system in the bottlenose dolphin, *Tursiops truncatus*,'' in *Sensory Abilities of Cetaceans—Laboratory and Field Evidence*, edited by J. A. Thomas and R. A. Kastelein (Plenum, New York, 1990), pp. 385–393.

[9] A. Y. Supin, V. V. Popov, and V. O. Klishin, ''ABR frequency tuning curves in dolphins,'' J. Comp. Physiol. A **173**(5), 749–656 (1993).

[10] D. K. Mellinger, ''Handling time variability in bioacoustic transient detection,'' in *Oceans '93, Engineering in Harmony with the Ocean, Proceedings IEEE*, Vol. III, pp. 116–121 (1993).

[11] D. K. Mellinger and C. W. Clark, ''A method for filtering bioacoustic transients by spectrogram image convolution,'' in *Oceans '93, Engineering in Harmony with the Ocean, Proceedings IEEE*, Vol. III, pp. 122–127 (1993).

[12] J. R. Potter, D. K. Mellinger, and C. W. Clark, ''Marine mammal call discrimination using artificial neural networks,'' J. Acoust. Soc. Am. **96**, 1255–1262 (1994).

[13] D. K. Mellinger and C. W. Clark, ''Methods for automatic detection of mysticete sounds,'' Mar. Fresh. Behav. Physiol. **29**, 163–181 (1997).

[14] J. H. Karl, *An Introduction to Digital Signal Processing* (Academic, San Diego, 1989).

[15] E. C. Ifeachor and B. W. Jervis, *Digital Signal Processing: A Practical*

Approach (Addison-Wesley, Wokingham, England, 1993).
[16] C. Erbe, ''The masking of beluga whale (*Delphinapterus leucas*) vocalizations by icebreaker noise,'' Ph.D. thesis, University of British Columbia, Canada (1997).
[17] G. von Békésy, *Experiments in Hearing* (McGraw-Hill, New York, 1960).
[18] J. O. Pickles, *An Introduction to the Physiology of Hearing* (Academic, San Diego, 1988).
[19] B. C. J. Moore, *An Introduction to the Psychology of Hearing* (Academic, San Diego, 1997), 4th ed.
[20] H. Fletcher, ''Auditory patterns,'' Rev. Mod. Phys. **12**(1), 47–65 (1940).
[21] V. A. Vel'min and N. A. Dubrovskii, ''The critical interval of active hearing in dolphins,'' Sov. Phys. Acoust. **22**(4), 351–352 (1976).
[22] P. W. B. Moore, R. W. Hall, W. A. Friedl, and P. E. Nachtigall, ''The critical interval in dolphin echolocation: what is it?'' J. Acoust. Soc. Am. **76**, 314–317 (1984).
[23] W. W. L. Au, P. W. B. Moore, and D. A. Pawloski, ''Detection of complex echoes in noise by an echolocating dolphin,'' J. Acoust. Soc. Am. **83**, 662–668 (1988).
[24] V. A. Vel'min and N. A. Dubrovskii, ''Auditory analysis of pulse tones by dolphins,'' Dokl. Akad. Nauk SSSR **225**, 470–473 (1975).
[25] M. J. White, Jr., J. Norris, D. Ljungblad, K. Baron, and G. di Sciara, ''Auditory thresholds of two beluga whales (*Delphinapterus leucas*),'' Report by Hubbs/Sea World Research Institute for Naval Ocean System Center, Report 78–109 (San Diego, CA, 1978).
[26] F. T. Awbrey, J. A. Thomas, and R. A. Kastelein, ''Low-frequency underwater hearing sensitivity in belugas (*Delphinapterus leucas*),'' J. Acoust. Soc. Am. **84**, 2273–2275 (1988).
[27] D. P. Morgan and C. L. Scofield, *Neural Networks and Speech Processing* (Kluwer Academic, Boston, 1991).
[28] S. Haykin, *Neural Networks: A Comprehensive Foundation* (Macmillan College Publishing, New York, 1994).
[29] D. E. Rumelhart, G. E. Hinton, and R. J. Williams, ''Learning internal representations by error propagation,'' in *Parallel Distributed Processing*, edited by D. E. Rumelhart and J. L. McClelland (MIT Press, Cambridge, MA, 1986), pp. 318–362.
[30] D. E. Rumelhart, G. E. Hinton, and R. J. Williams, ''Learning representations by back-propagating errors,'' Nature (London) **323**, 533–536 (1986).
[31] F. J. Pineda, ''Generalization of backpropagation to recurrent and higher order neural networks,'' in *Neural Information Processing Systems*, edited by D. Z. Anderson (American Institute of Physics, New York, 1988), pp. 602–611.

LETTERS TO THE EDITOR

This Letters section is for publishing (a) brief acoustical research or applied acoustical reports, (b) comments on articles or letters previously published in this Journal, and (c) a reply by the article author to criticism by the Letter author in (b). Extensive reports should be submitted as articles, not in a letter series. Letters are peer-reviewed on the same basis as articles, but usually require less review time before acceptance. Letters cannot exceed four printed pages (approximately 3000–4000 words) including figures, tables, references, and a required abstract of about 100 words.

Comments on "Acoustic wave propagation through porous media revisited" [J. Acoust. Soc. Am. 100, 2949–2959 (1996)]

D. M. J. Smeulders[a] and S. Sorek[b]
Delft University of Technology, P.O. Box 5028, 2600 GA, The Netherlands

M. E. H. van Dongen
Eindhoven University of Technology, P.O. Box 513, 5600 MB, The Netherlands

(Received 15 May 1997; accepted for publication 22 June 1998)

In a 1996 paper by T. W. Geerits, published in this *Journal*, it was claimed that a new theory for acoustic wave propagation in porous media was derived. It will be shown that this claim is not justified. Correct application of the averaging procedures and correct interpretation of the dissipation leads to a one-to-one agreement with the Biot theory, which was published in this *Journal* in 1956 [M. A. Biot, J. Acoust. Soc. Am. **28**, 168–178, 179–191 (1956)]. © *1999 Acoustical Society of America.* [S0001-4966(98)00210-0]

PACS numbers: 43.20.Gp [DEC]

I. MACROSCOPIC EQUATIONS

We will compare the momentum equations and the stress–strain relations by Geerits (1996) (referred to by ''G'' in the following) and Biot (1956) (referred to by ''B'' in the following) for the case of isotropic porous media in absence of body forces and dissipation. The fluid momentum equation (G45) then becomes

$$\frac{\partial}{\partial x_i}\langle\sigma\rangle = m^{ff}\langle\dot{v}_i^f\rangle + m^{fs}\langle\dot{v}_i^s\rangle, \tag{1}$$

where σ is the microscopic fluid traction, and $\mathbf{v}^f$ and $\mathbf{v}^s$ are the microscopic velocities of the fluid and the solid, respectively. The averaging $\langle\cdots\rangle$ of the microscopic quantities takes place over the bulk volume V_b, consisting of pore space and solid grains. The parameters m^{ff} and m^{fs} are specific masses. We have substituted the identities for isotropic media $m_{ij}^{ff} = m^{ff}\delta_{ij}$ and $m_{ij}^{fs} = m^{fs}\delta_{ij}$ into the original equation (G45) to obtain (1). The dot over a variable denotes the time derivative of that variable.

In the Biot paper, macroscopic fluid and solid displacements **U** and **u** are defined. They are intrinsic variables, which means that the averaging has taken place over the fluid space ϕV_b and the solid space $(1-\phi)V_b$, respectively, where ϕ is the porosity. Thus (1) becomes in its linearized form:

$$\frac{\partial}{\partial x_i}\langle\sigma\rangle = \phi m^{ff}\ddot{U}_i + (1-\phi)m^{fs}\ddot{u}_i. \tag{2}$$

The corresponding relation in the Biot paper is given by (B3.21):

$$\frac{\partial s}{\partial x_i} = \rho_{22}\ddot{U}_i + \rho_{12}\ddot{u}_i, \tag{3}$$

where the scalar s represents the forces per unit bulk area acting on the fluid part of each face of a unit cube of porous material. Therefore, $s = \langle\sigma\rangle$. Furthermore, denoting the fluid density by ρ_f, Biot defines $\rho_{22} = \phi\rho_f - \rho_{12}$, where ρ_{12} is the mass coupling parameter. From (2) and (3) it can easily be seen that

$$m^{ff} = \frac{\rho_{22}}{\phi}, \quad m^{fs} = \frac{\rho_{12}}{(1-\phi)}. \tag{4}$$

In a similar way the solid momentum equation (G47) in the paper by Geerits can be compared with its Biot equivalent (B3.21), and it follows that for the specific masses m^{ss} and m^{sf} it can be written that

$$m^{ss} = \frac{\rho_{11}}{(1-\phi)}, \quad m^{sf} = \frac{\rho_{12}}{\phi}, \tag{5}$$

where, denoting the solid density by ρ_s, Biot defines $\rho_{11} = (1-\phi)\rho_s - \rho_{12}$. We immediately notice that m^{fs} and m^{sf} are not identical as is stated by Geerits in his symmetry relations (G64). Essentially, this is due to the fact that the velocities are averaged over the bulk volume instead of over the intrinsic volume. This averaging also gives rise to misleading results in the expression for the kinetic energy (G75). We will evaluate this expression for the case of a porous medium consisting of an ensemble of parallel tubes. We will assume that the porous medium is rigid, i.e., $v_i^s = 0$:

$$E_{\text{kin}} = \tfrac{1}{2}m^{ff}\langle v_i^f\rangle\langle v_i^f\rangle, \tag{6}$$

[a]Electronic mail: d.m.j.smeulders@ta.tudelft.nl
[b]On leave from Ben-Gurion University, Beer-sheva, Israel.

where $m^{ff}=\rho_f-m^{sf}$. This means that the kinetic energy is given by $\frac{1}{2}\rho_f(\phi\dot{U})^2$, where $\dot{U}$ is the uniform fluid velocity in the direction of the tubes. Obviously, the correct expression is given by $\frac{1}{2}\phi\rho_f\dot{U}^2$, as becomes clear from Biot's equation (B3.2).

For the stress–strain relations, we follow the same procedure. Omitting the source density, (G46) becomes

$$\frac{\partial}{\partial x_i}\langle v_i^f\rangle = k^{ff}\langle\dot{\sigma}\rangle + \frac{1}{3}k^{fs}\langle\dot{\sigma}_{kk}^s\rangle, \tag{7}$$

where σ_{ij}^s is the microscopic solid stress tensor, and k^{ff} and k^{fs} are scalar compressibilities.

In the Biot paper, the stress–stain relations (B2.12) are written as

$$\begin{aligned}\tau_{ij} &= 2Ge_{ij}+Ae_{kk}\delta_{ij}+Q\epsilon_{kk}\delta_{ij},\\ s &= Qe_{kk}+R\epsilon_{kk},\end{aligned} \tag{8}$$

where

$$e_{ij}=\frac{1}{2}\left(\frac{\partial u_i}{\partial x_j}+\frac{\partial u_j}{\partial x_i}\right), \quad \epsilon_{ij}=\frac{1}{2}\left(\frac{\partial U_i}{\partial x_j}+\frac{\partial U_j}{\partial x_i}\right). \tag{9}$$

The tensor τ_{ij} represents the forces per unit bulk area acting on the solid parts of each face of a unit cube of porous material. Furthermore A, Q, and R are generalized elastic constants which can be related to such measurable quantities as the fluid bulk modulus K_f, the matrix shear modulus G, and to K_b and K_s, which are the bulk moduli of the porous frame and individual grains respectively. From (8) it can be derived that

$$\dot{\epsilon}_{kk}=\frac{D}{DR-Q^2}\,\dot{s}-\frac{1}{3}\,\frac{Q}{DR-Q^2}\,\dot{\tau}_{kk}, \tag{10}$$

where $3D=2G+3A$. Relation (10) can now be compared with (7), where we notice that the LHS of (7) equals $\phi\dot{\epsilon}_{kk}$, that $\langle\dot{\sigma}\rangle=\dot{s}$, and that $\dot{\tau}_{kk}=\langle\dot{\sigma}_{kk}^s\rangle$. It then follows that

$$k^{ff}=\frac{D\phi}{DR-Q^2}, \quad k^{fs}=\frac{-Q\phi}{DR-Q^2}. \tag{11}$$

In a similar way, the solid equation (G48) can be compared with its Biot equivalent (B2.12). Then it is found that $k^{sf}=-Q(1-\phi)/(DR-Q^2)$. This means that also the compressibility parameters introduced by Geerits can directly be expressed in terms of Biot parameters. Moreover, the symmetry relation (G65) $k^{fs}=k^{sf}$ does not hold.

II. DISSIPATION

In order to describe dissipation, Geerits introduces on the macroscale the parameters R^{fs} and R^{sf}. These parameters represent the so-called ''losses of the interface type,'' also referred to as ''inertial losses,'' or ''losses due to tortuosity.'' This is not a realistic concept. The correct concept is based on viscosity, and was introduced by Biot (1956), who defined a frequency-dependent friction factor $b(\omega)$. At low frequencies, $b(\omega)=b_0=\eta\phi^2/k_0$, where η is the fluid viscosity, and k_0 is the permeability. At higher frequencies, when the viscous skin depth $\delta=\sqrt{2\eta/\omega\rho_f}$ decreases, inertia will become dominant over viscosity. However, inertia has nothing to do with the damping of the waves. At all frequencies, all damping is exclusively caused by viscosity. This can elegantly be illustrated for plane wave propagation in a rigid tortuous porous medium filled with a viscous compressible fluid. For propagation in the z direction, an $\exp i(\omega t-kz)$ dependence for the relevant variables is introduced, where $k=\omega/c$ is the wave number and c is the wave velocity. The momentum equation for the fluid is now given by (Johnson and Plona, 1982):

$$i\omega\rho_f\left[\alpha_\infty-\frac{ib(\omega)}{\omega\phi\rho_f}\right]\hat{w}=ik\hat{p}. \tag{12}$$

Here, α_∞ denotes the tortuosity. It is a purely geometrical quantity, independent of fluid or solid densities, and its value is always greater than or equal to unity. The fluid velocity and pressure are denoted by $\hat{w}$ and $\hat{p}$, respectively. Combination of (12) with the mass conservation law yields the dispersion relation:

$$k=\frac{\omega}{c_f}\sqrt{\alpha_\infty-\frac{ib(\omega)}{\phi\rho_f\omega}}, \tag{13}$$

where c_f is the speed of sound in the fluid. The damping factor d is defined as $-\mathrm{Im}(k)$. This means that if viscosity is neglected, i.e., $b(\omega)=0$, the waves will not be damped and propagate with a characteristic wave speed $c_{\mathrm{ref}}=c_f/\sqrt{\alpha_\infty}$. If on the other hand tortuosity is neglected, i.e., $\alpha_\infty=1$, the damping of the waves definitely does not disappear. In this case (13) describes the wave propagation and damping in a fluid cylinder with fixed walls. We therefore conclude that damping is a viscosity-based mechanism, and not a tortuosity-based mechanism. This also means that for the parameters R^{sf} and R^{fs} in the paper by Geerits, it can simply be written that

$$R^{sf}=b(\omega)/\phi, \quad R^{fs}=b(\omega)/(1-\phi). \tag{14}$$

Also in this case, the symmetry $R^{sf}=R^{fs}$ claimed by Geerits does not hold. Moreover, we notice that the dissipation parameters can simply be written in terms of Biot parameters. Detailed expressions for the friction factor $b(\omega)$ were given by Johnson *et al.* (1987) and Smeulders *et al.* (1992).

III. CONCLUSIONS

We have shown that the mass and compressibility parameters introduced by Geerits can directly be expressed in terms of existing Biot parameters. The averaging procedures used by Geerits give rise to misleading symmetry relations. The newly introduced dissipation parameters describe in fact a viscous mechanism, discussed previously by, among others, Biot (1956), Auriault *et al.* (1985), and Johnson *et al.* (1987).

Auriault, J. L., Borne, L., and Chambon, R. (**1985**). ''Dynamics of porous saturated media, checking of the generalized low of Darcy,'' J. Acoust. Soc. Am. **77**, 1641–1650.

Biot, M. A. (**1956**). ''Theory of propagation of elastic waves in a fluid-saturated solid. I. Low frequency range,'' J. Acoust. Soc. Am. **28**, 168–178 and ''II. Higher frequency range,'' J. Acoust. Soc. Am. **28**, 179–191.

Geerits, T. W. (**1996**). ''Acoustic wave propagation through porous media revisited,'' J. Acoust. Soc. Am. **100**, 2949–2959.

Johnson, D. L., and Plona, T. J. (**1982**). ''Acoustic slow waves and the consolidation transition,'' J. Acoust. Soc. Am. **72**, 556–565.

Johnson, D. L., Koplik, J., and Dashen, R. (**1987**). ''Theory of dynamic permeability and tortuosity in fluid-saturated porous media,'' J. Fluid Mech. **176**, 379–402.

Smeulders, D. M. J., Eggels, R. L. G. M., and van Dongen, M. E. H. (**1992**). ''Dynamic permeability: reformulation of theory and new experimental and numerical data,'' J. Fluid Mech. **245**, 211–227.

Elastic waves in monoclinic incompressible materials and reflection from an interface

Dimitrios A. Sotiropoulos
Department of Engineering Sciences, Technical University of Crete, Chania 73100, Greece

Sudhakar Nair
Department of Mechanical, Materials and Aerospace Engineering, Illinois Institute of Technology, Chicago, Illinois 60616

(Received 6 February 1998; revised 15 January 1999; accepted 19 January 1999)

The reflection of plane elastic waves from a free surface of monoclinic incompressible materials is examined under plane strain conditions in a plane of material symmetry. It is found that this problem can be equivalently treated by elastic wave reflection in orthotropic incompressible materials if the material constants of the monoclinic material are properly related to those of the orthotropic material. Thus the range of existence of the two (one homogeneous and the other homogeneous or inhomogeneous) reflected waves in a monoclinic material, including points corresponding to zero amplitude reflected waves, can be obtained from that given in a previous paper [Nair and Sotiropoulos, J. Acoust. Soc. Am. **102**, 102–109 (1997)] where an orthotropic material was treated.
 [S0001-4966(99)03304-4]

PACS numbers: 43.20.Fn [ANN]

INTRODUCTION

The reflection of elastic waves from a free surface of anisotropic incompressible materials has applications in the areas of ultrasonic nondestructive evaluation of rubberlike materials, including some biological tissues, and of design of surface reinforcements, among other areas. In the present letter, the anisotropy considered is that of a monoclinic material and plane strain conditions prevail in the plane of material symmetry in which propagation occurs. In a recent paper, Nair and Sotiropoulos (1997) treated the same problem but for an orthotropic material, where references to relevant literature are cited. For an example of the plane strain approximation in an experiment the reader may consult Hirao *et al.* (1981).

The range of existence of the two (one homogeneous and the other homogeneous or inhomogeneous) reflected waves in terms of the angle of incidence of a homogeneous wave, the orientation of the free surface, and the material constants is obtained in the present paper by establishing that the monoclinic material can be equivalently treated by the orthotropic material if their elastic constants are properly related. This includes points in the range of existence corresponding to zero amplitude reflected waves. For these points, it is necessary to prove that the components of traction on the free surface for the monoclinic material become identical to those of the orthotropic material once the equivalent material constants are used. This equivalency, in so far as reflection of elastic waves is concerned, could also be established by a transformation of the elastic constants matrix of the monoclinic material, a process which would have undoubtedly been algebraically cumbersome.

EQUIVALENCY OF MONOCLINIC AND ORTHOTROPIC INCOMPRESSIBLE MATERIALS IN PLANE STRAIN MOTION

A monoclinic incompressible material occupying the region $-\infty<\bar{x}_1, \bar{x}_3<\infty$, $0<\bar{x}_2<\infty$ is considered. The linear stress–strain relations are expressed, with respect to a x_1, x_2, $x_3=\bar{x}_3$ rectangular coordinate system with the x_1-axis at an angle ϕ to $\bar{x}_1$, as

$$\sigma_i=\begin{cases} C_{ij}\gamma_j-p, & i=1,2,3 \\ C_{ij}\gamma_j, & i=4,5,6. \end{cases} \tag{1}$$

where σ_i and γ_i are defined as

$$\begin{aligned} &\{\sigma_i\}=[\sigma_{11}\ \ \sigma_{22}\ \ \sigma_{33}\ \ \sigma_{23}\ \ \sigma_{31}\ \ \sigma_{12}]^T, \\ &\{\gamma_i\}=[\epsilon_{11}\ \ \epsilon_{22}\ \ \epsilon_{33}\ \ 2\epsilon_{23}\ \ 2\epsilon_{31}\ \ 2\epsilon_{12}]^T, \\ &\epsilon_{ij}=(u_{i,j}+u_{j,i})/2, \quad i,j=1,2,3; \end{aligned} \tag{2}$$

with σ_{ij} being the stress components, ϵ_{ij} the strain components, and u_i the displacement components with the comma denoting differentiation with respect to spatial coordinates. In Eq. (1) repeated indices imply summation, p is the hydrostatic pressure, and C_{ij} are the elastic constants given as

$$\begin{bmatrix} C_{11} & C_{12} & C_{13} & 0 & 0 & C_{16} \\ C_{12} & C_{22} & C_{23} & 0 & 0 & C_{26} \\ C_{13} & C_{23} & C_{33} & 0 & 0 & C_{36} \\ 0 & 0 & 0 & C_{44} & C_{45} & 0 \\ 0 & 0 & 0 & C_{45} & C_{55} & 0 \\ C_{16} & C_{26} & C_{36} & 0 & 0 & C_{66} \end{bmatrix} \tag{3}$$

of which, because of incompressibility, only nine are independent.

Under plane strain in the x_1-x_2 plane of material symmetry, the equations of motion, assuming small displacements and no body force, are

$$\sigma_{ji,j}=\rho\ddot{u}_i, \quad i,j=1,2, \tag{4}$$

where ρ is the mass density of the material and the dot denotes differentiation with respect to time. The incompressibility condition,

$$u_{1,1}+u_{2,2}=0, \tag{5}$$

can be satisfied by introducing the displacement potential ψ as

$$u_1=\psi_{,2}, \quad u_2=-\psi_{,1}. \tag{6}$$

With these, Eqs. (4), upon elimination of p, yield

$$\alpha[\Delta^2\psi+4\beta\psi_{,1122}+2\gamma(\psi_{,2212}-\psi_{,1112})]=\Delta\ddot{\psi}, \tag{7}$$

where Δ is the two-dimensional Laplace operator and

$$\alpha=C_{66}/\rho, \quad 4\beta=(C_{11}+C_{22}-2C_{12}-4C_{66})/C_{66}, \quad \gamma=(C_{16}-C_{26})/C_{66}. \tag{8}$$

It is noted that for orthotropic materials $\gamma=0$. Equation (7) can be transformed to an equation equivalent to the governing equation of orthotropic materials (which involves only two material constants). This is done by first introducing a new coordinate system (x_1',x_2') where the x_1'-axis makes an angle ϕ^* with the x_1-axis. Then, if ϕ^* is chosen such that

$$\tan 4\phi^*=\gamma/\beta, \tag{9}$$

Eq. (7), with respect to the x_1', x_2' system, becomes

$$\alpha'[\Delta^2\psi+4\beta'\psi_{,1122}]=\Delta\ddot{\psi}, \tag{10}$$

in which

$$\alpha'=\alpha(2+\beta-\sqrt{\beta^2+\gamma^2})/2, \quad \beta'=\alpha\sqrt{\beta^2+\gamma^2}/\alpha', \tag{11}$$

and the Laplace operator, Δ, is now in terms of x_1' and x_2'.

It is noted that this reduction of constants is a consequence of the plane strain assumption in the context of incompressibility. Equation (10), with $\alpha'=\alpha$, $\beta'=\beta$, ($\gamma=0$), was investigated with reference to the range of existence of reflected plane elastic waves in orthotropic incompressible materials by Nair and Sotiropoulos (1997). The range of existence was found by using the reflection law and the slowness surface in terms of the angle of incidence of a homogeneous wave, the orientation of the free surface, and the material constant, α/β. The critical orientation beyond which there exist two homogeneous reflected waves was subsequently derived. To determine the amplitudes of the reflected waves it is necessary to use explicitly the free surface conditions on stresses as it was done to determine the exclusion points, that is, points in the range of existence corresponding to a zero amplitude reflected homogeneous (when there exist two homogeneous reflected waves) or inhomogeneous (surface) wave. Thus to establish the full equivalency between incompressible monoclinic and orthotropic materials in so far as the reflection of plane waves is concerned, it must also be shown that the traction components on the free surface are identical under Eq. (11) for the two materials.

For time harmonic plane elastic waves ψ is written as

$$\psi=Ae^{-i\omega t}e^{i\omega(x_1\cos\theta+x_2\sin\theta)/v}, \tag{12}$$

where A is the potential amplitude taken to be small in accordance with the linearity assumption. Here, ω is the circular frequency, θ is the angle of the propagation direction from the x_1-axis, and v is the phase speed.

Substitution of Eq. (12) in the equation of motion (7) yields

$$v^2=\alpha(1+\beta\sin^2 2\theta-\gamma\sin 2\theta\cos 2\theta), \tag{13}$$

as the propagation condition, i.e., the condition that the phase speed, material constants, and direction of propagation must satisfy. However, in accordance with the discussion above, Eq. (13) may equivalently be written as

$$v^2=\alpha'(1+\beta'\sin^2 2\theta'), \quad \theta'=\theta-\phi^*, \tag{14}$$

with α', β' given by Eq. (11) and ϕ^* by Eq. (9). In Eq. (14), θ' represents the angle that the propagation direction makes with the x_1'-axis, the direction of minimum speed. Then, using v as given by Eq. (13) and solving for p from Eqs. (4) in terms of ψ, the stress components in the (x_1,x_2) system are expressed as

$$\begin{aligned}
\sigma_{11}&=\frac{\alpha\omega^2}{v^2}\left[-(1+\beta)\sin 2\theta+\frac{1}{2}\beta\sin 4\theta+\frac{1}{2}\gamma(\cos 2\theta-\cos 4\theta)\right]\psi,\\
\sigma_{12}&=\frac{\alpha\omega^2}{v^2}\left[\cos 2\theta-\frac{1}{2}\gamma\sin 2\theta\right]\psi,\\
\sigma_{22}&=\frac{\alpha\omega^2}{v^2}\left[(1+\beta)\sin 2\theta+\frac{1}{2}\beta\sin 4\theta-\frac{1}{2}\gamma(\cos 2\theta+\cos 4\theta)\right]\psi.
\end{aligned} \tag{15}$$

In the $(\overline{x_1},\overline{x_2})$ system these yield

$$\begin{aligned}
\overline{\sigma}_{12}&=\frac{\alpha'\omega^2}{v^2}[\cos 2\theta'\cos 2\phi'-(1+\beta')\sin 2\theta'\sin 2\phi']\psi,\\
\overline{\sigma}_{22}&=\frac{\alpha'\omega^2}{v^2}[\sin 2(\theta'+\phi')+\beta'\sin 2\theta'(\cos 2\theta'+\cos 2\phi')]\psi,
\end{aligned} \tag{16}$$

where $\phi'=\phi+\phi^*$. Setting $\phi^*=0$ and $\alpha'=\alpha$, $\beta'=\beta$ these stresses become identical to those associated with the free surface of an orthotropic material, which were derived in a recent paper by Nair and Sotiropoulos (1997).

Therefore, it has now been established that the reflection of plane elastic waves in a monoclinic incompressible material under plane strain in the plane of material symmetry in which the propagation occurs can be equivalently treated by the reflection in an orthotropic incompressible material if their material constants are related by Eq. (11). Hence, the range of existence of the two (one homogeneous and the other homogeneous or inhomogeneous) reflected waves in terms of the angle of incidence of a homogeneous wave, the orientation of the free surface, and the material constants, is given by Nair and Sotiropoulos (1996) where that of the orthotropic material was obtained. This includes points in the range of existence corresponding to only one reflected (ho-

mogeneous) wave, the other having zero amplitude. The critical orientation beyond which there exist two homogeneous reflected waves can also be readily obtained from that of the orthotropic material which is given in explicit form in the cited reference.

Nair, S., and Sotiropoulos, D. A. (**1997**). ''Elastic waves in orthotropic incompressible materials and reflection from an interface,'' J. Acoust. Soc. Am. **102**, 102–109.

Hirao, M., Fukuoka, H., and Hori, K. (**1981**). ''Acoustoelastic effect of Rayleigh surface wave in isotropic material,'' J. Appl. Mech. **48**, 119–124.

Abstract exercises in cochlear modeling: Reply to "What should be the goals of cochlear modeling?" [J. Acoust. Soc. Am. 102, 3054 (1997)]

Egbert de Boer[a)]
Rm. D2-226, Academic Medical Center, Meibergdreef 9, 1105 AZ, Amsterdam, The Netherlands

(Received 27 April 1998; revised 20 November 1998; accepted 14 January 1999)

[S0001-4966(99)04004-7]

PACS numbers: 43.64.Kc, 43.64.Bt [RDF]

In this note the use and value of studying a cochlear model that contains ''nonrealizable'' components is defended.

Consider a linear *nonclassical* model of the cochlea (de Boer, 1997a), and assume that it is built up exclusively from ''physically realizable'' elements and that it is (zero-point) stable. In the response of the model all mechanical elements and the fluid execute movements whereby no physical law is violated. A more or less abstract parameter, the ''effective basilar-membrane impedance,'' can be derived from the solution. In a nonclassical model this impedance may turn out to be noncausal (a trivial example involving a delay line is mentioned in the cited paper). Next, a classical model (the second model) is constructed with the same impedance. If the retrieved impedance is noncausal, the elements of the second model cannot be constructed only from ''realizable'' elements. In this respect Richard Chadwick (Chadwick, 1997) is completely right: the second model is ''nonrealizable.'' However, the response of that classical model is identical to that of the original model, and *will not violate any physical law* (de Boer, 1997a). This applies, specifically, to all aspects of fluid movement. Therefore, with respect to the physics of the fluid, the second model is no less ''realizable'' than the original one. In addition, both models are stable. And this applies to every frequency, so that *scaling of frequency to place in the second model is not different from that in the first one*. The study of the second model (a classical model) may be called an ''abstract exercise'' because it involves a nonrealizable component. In the cited case the abstract exercise has been quite useful, and has, for instance, led to new notions about minimum phase (de Boer, 1997b).

I personally believe strongly in the value of abstract exercises in cochlear modeling. Stronger, I think that deeper insight can only be obtained in this way, and not by first trying out one, and next another model *ad infinitum* (do I stick out my neck far enough?). I can refer to other examples of abstract exercises that have increased insight or understanding. An example is formed by a ''locally active model'' as introduced by Kim *et al.* (1980). In this case the basilar-membrane impedance by itself cannot be constructed from realizable elements because it has (locally) a negative real part. However, this type of impedance results quite logically when some type of ''active'' transducer is included in the model. Examples of realizable locally active models are abundant in the literature (some are listed in de Boer, 1996). I like to stress that such a model as a whole is stable, causal, and well-behaved in every respect (at least, it should be). Another example is in Kanis and de Boer (1997) where the mechanism of (self-)suppression was switched off while that of combination-tone generation remained on. A procedure like this would be absolutely impossible in the ''real'' world but it was useful in unraveling the mechanism of combination-tone generation.

In conclusion, I think that exploring systems containing ''unrealizable'' elements is fruitful in many cases, and taking them apart to study their components is equally fruitful. The only proviso should be that the system, *considered in its entirety*, should be stable and noncausal.

[a)]Electronic mail: e.deboer@amc.uva.nl

Chadwick, R. S. (**1997**). ''What should be the goals of cochlear modeling?,'' J. Acoust. Soc. Am. **102**, 3054.

de Boer, E. (**1996**). ''Mechanics of the cochlea: Modeling efforts,'' in *The Cochlea*, edited by P. Dallos, A. N. Popper, and R. R. Fay (Springer-Verlag, New York), pp. 258–317.

de Boer, E. (**1997a**). ''Classical and nonclassical models of the cochlea,'' J. Acoust. Soc. Am. **101**, 2148–2150.

de Boer, E. (**1997b**). ''Cochlear models and minimum phase,'' J. Acoust. Soc. Am. **102**, 3810–3813.

Kanis, L. J., and de Boer, E. (**1997**). ''Frequency dependence of acoustic distortion products in a locally active model of the cochlea,'' J. Acoust. Soc. Am. **101**, 1527–1531.

Kim, D. O., Neely, S. T., Molnar, C. E., and Matthews, J. W. (**1980**). ''An active cochlear model with negative damping in the partition: Comparison with Rhode's ante- and post-mortem observations,'' in *Psychophysical, Physiological and Behavioral Studies in Hearing*, edited by G. v.d. Brink and F. A. Bilsen (Delft U. P., Delft), pp. 7–14.

 0001-4966/99/105(5)/2984/1/$15.00

On solution techniques for cochlear models: Reply to "Comments on 'A method for forward and inverse solutions of a three-dimensional model of the cochlea'" [J. Acoust. Soc. Am. 103, 3729 (1998)]

Egbert de Boer[a)]
Room D2-226, Academic Medical Center, University of Amsterdam, Meibergdreef 9, 1105 AZ, Amsterdam, The Netherlands

(Received 27 April 1998; revised 20 November 1998; accepted 14 January 1999)

This note explains steps in the solution of a three-dimensional model that have been criticized. The emphasis is on ''separation'' of variables in the Laplace equation. © *1999 Acoustical Society of America.* [S0001-4966(99)04104-1]

PACS numbers: 43.64.Kc, 43.64.Bt [RDF]

Let me try to straighten out some of the problems described by Duifhuis in his comment on my Letter entitled ''A method for forward and inverse solutions of a three-dimensional model'' (de Boer, 1998). I will treat the various subjects in the sequence from general to special.

I. LINEARITY

Every analysis is valid within its own restrictions. I want to stress that the domain of applicability of linear analysis for the cochlea is far larger than is usually envisaged. When the model considered is nonlinear, and the nonlinear elements are embedded in it in a well-prescribed way, the response of the model can be analyzed as if it were linear. The proviso is that ''response'' must be taken to mean either ''averaged transfer function'' or ''input–output cross-correlation function'' for a *wide-band noise stimulus*. This statement is proved in de Boer (1997). In my letter a reference to this paper is included (Introduction, second paragraph). One of the conditions mentioned in that paper is that the model is tacitly assumed to be zero-point stable. This implies that the analysis does not encompass spontaneous oscillations. Another approach to nonlinear systems by way of linear concepts is via the Wiener–Volterra series expansion. The latest example in cochlear mechanics is Recio *et al.* (1997).

II. SHOULD k IN $Q(k)$ BE REAL OR COMPLEX?

In my original analysis (de Boer, 1981) the model equation is formulated so that it contains an integral over a *real* variable k, the wave number. Separability of the Laplace equation is used; this is a property of the *coordinate system* used. The Cartesian system is one of the (11) coordinate systems that allow separation of variables (Morse and Feshbach, 1953, section 5.1, pp. 494–523). Let me highlight some steps in the derivation. In the initial conception the length of the model is infinite. The model has to have the same dimensions (height h, width b) and the partition has to have the same vibration pattern of the basilar membrane (BM) over the entire length. Then, the Laplace equation is separable in x (the longitudinal direction), y (the radial direction) and z (the vertical direction). A *partial solution* can be written as a product of three functions, each dependent on only one variable, x, y, or z:

$$p(x,y,z)=u(x)v(y)w(z). \tag{1}$$

The solution function $u(x)$ in the x dimension has a free parameter k that can be interpreted as a ''wave number.'' The solution function $v(y)$ in the y direction is determined by a kind of ''quantum number,'' n, that can have all possible integral values. Finally, the solution function $w(z)$ in the z dimension contains a parameter m that is a unique function of k and n.

It is stressed that *this separation is valid only for a single partial solution*, with *one* value of k, n, and m. The complete solution for the pressure follows from summation over n and integration over k. Up to this point, the integration path is entirely free. The solution function $u(x)$ in the x direction is of the form $\exp(-ikx)$. The functions $\exp(-ikx)$ with real k form a ''complete'' set, meaning that they can approximate a given (well-behaved) function arbitrarily well (via the Fourier transform). This means that it is sufficient *to carry out the integration in the model equation over real k*. After integration over k and summation over n the fluid wave can be matched to the BM impedance. In the formulation of the BM boundary condition, the function $Q(k)$ is defined in terms of a sum over n [see Eq. (27) in de Boer, 1981]. It follows that for forward and inverse solutions only values of the function $Q(k)$ *with k real* are relevant.

In an earlier paper (de Boer, 1980) I have used a similar technique to solve a cylindrical model. An infinitely long cylindrical structure also leads to separability of the Laplace equation. In that case, too, the solution function in the x-domain is $\exp(-ikx)$ so that $Q(k)$ for that model is again a function of *real k*. In both cases the model equation contains the function $Q(k)$, but only with real values of k.

A function $Q(k)$ with k *complex* serves other purposes. It can, for instance, be used in the formulation of the response of a model with a homogeneous BM impedance. Most often it appears in the context of the LG[1] (often called WKB[2]) approximation. The complex values of k are the

[a)]Electronic mail: e.deboer@amc.uva.nl

roots of the ''eikonal equation'' [see, for instance, Eq. (6) in de Boer and Viergever, 1982]. When used in cochlear mechanics, the LG approximation implies the assumption that only *uni-directional* waves exist in the model. My analysis does not use the LG approximation, because it has been my aim to have a model that supports forward and retrograde waves equally well.

III. FOURIER TRANSFORMS

Duifhuis' argument about separability and Fourier transforms is based on the idea that $Q(k)$ arises simply as the Fourier transform of the distribution of the pressure over x. This is not true. The distribution of the vertical velocity is involved too. This is so because (apart from a factor) $Q(k)$ is the impedance of the oscillating fluid column when in the x-direction a wave with wave number k is propagating. To find this impedance, we have to summate Eq. (1) over n, putting in coefficients chosen such that the boundary condition over the coordinate y is satisfied. Then, we have to take the derivative with respect to z to find the BM velocity, etc., etc. I repeat that separability is only valid for one partial solution. The actual pressure solution is defined as an integral and a sum over functions which depend on all three variables, x, y, and z.

IV. BOUNDARY CONDITIONS

Boundary conditions at the two end points of the model (the ''stapes'' and the ''helicotrema'') constitute a bigger problem than is revealed in Duifhuis' comment. The problem mentioned (a nonuniform fluid velocity distribution) also appears at the stapes location. The ''stapes velocity'' is prescribed at the plane of the BM, $z=0$, and there is no guarantee that the velocity is the same at all values of z. However, it can be shown that errors due to the use of the boundary condition at the plane $z=0$ do not propagate further than over a distance that is comparable to the height h. How to cope with this problem in a time-domain solution is outside the scope of my letter.

V. SYMMETRY

I specifically assume the model to be symmetric in the z direction. The extrapolation of $Q(k)$ to asymmetric models is straightforward. Effects of asymmetry in three-dimensional models can also be studied with the more general analysis method of Mammano and Nobili (1993).

VI. UNDERSTANDING COCHLEAR MECHANICS

My letter does not claim to help understanding cochlear mechanics; it only provides a technique to study it more easily (see the section ''Application notes'').

[1]Abbreviation of Liouville-Green.
[2]Abbreviation of Wentzel-Kramers-Brillouin.

de Boer, E. (**1980**). ''A cylindrical cochlea model—The bridge between two and three dimensions,'' Hearing Res. **3**, 109–131.

de Boer, E. (**1981**). ''Short waves in three-dimensional cochlea models: Solution for a 'block' model,'' Hearing Res. **4**, 53–77.

de Boer, E. (**1997**). ''Connecting frequency selectivity and nonlinearity for models of the cochlea,'' Aud. Neurosci. **3**, 377–388.

de Boer, E. (**1998**). ''A method for forward and inverse solutions of a three-dimensional model of the cochlea,'' J. Acoust. Soc. Am. **103**, 3725–3728 (1998).

de Boer, E., and Viergever, M. A. (**1982**). ''Validity of the Liouville-Green (or WKB) method for cochlear mechanics,'' Hearing Res. **8**, 131–155.

Duifhuis, H. (**1998**). ''Comments on 'A method for forward and inverse solutions of a three-dimensional model of the cochlea' '' [J. Acoust. Soc. Am. **103**, 3725 (1998)], J. Acoust. Soc. Am. **103**, 3729.

Mammano, F., and Nobili, R. (**1993**). ''Biophysics of the cochlea: Linear approximation,'' J. Acoust. Soc. Am. **93**, 3320–3332.

Morse, P. M, and Feshbach, H. (**1953**). *Methods of Theoretical Physics* (McGraw-Hill, New York).

Recio, A., Narayan, S. S., and Ruggero, M. A. (**1997**). ''Wiener–Kernel analysis of basilar-membrane responses to white noise,'' in *Diversity in Auditory Mechanisms*, edited by E. R. Lewis, G. R. Long, R. F. Lyon, P. M. Narins, C. R. Steele, and E. E. Hecht-Poinar (World Scientific, Singapore), pp. 325–331.

Discrimination of amplitude-modulation phase spectrum

Christian Lorenzi
Laboratoire de Psychologie Expérimentale, UMR CNRS 8581, Institut de Psychologie, Université René Descartes Paris V, 28, Rue Serpente, 75006 Paris, France

Frédéric Berthommier
Institut de la Communication Parlée, UPRESA CNRS 5009, INPG, 46, avenue Félix Viallet, 38031 Grenoble Cédex, France

Laurent Demany
Laboratoire de Neurophysiologie, UMR CNRS 5543, Université Bordeaux 2, 146 rue Léo Saignat, F-33076 Bordeaux Cédex, France

(Received 8 December 1997; revised 15 February 1999; accepted 17 February 1999)

Listeners were asked to discriminate between two amplitude-modulation functions imposed on white noise and consisting of the sum of two sinusoids. The frequency ratio of the sinusoids constituting each function was 2 or 3. In one function, the sinusoids had a constant relative phase. In the other function, their phase relation was continuously and cyclically changing, at a slow rate. For all listeners, the two functions with a frequency ratio of 2 were easily discriminated. However, discrimination was impossible when the frequency ratio was 3. Simulations were performed using an envelope-detector model and various decision statistics. The max/min statistic predicted discrimination above chance level when the frequency ratio was 3. It seems, therefore, that listeners are unable to use this statistic. In contrast, the crest factor and skewness of the envelope accounted well for the discrimination data. © *1999 Acoustical Society of America.* [S0001-4966(99)05303-5]

PACS numbers: 43.66.Mk, 43.66.Nm, 43.66.Ba [DWG]

INTRODUCTION

In a recent study, Strickland and Viemeister (1996) measured thresholds for the detection of a sinusoidal amplitude modulation (AM) in the presence of another sinusoidal AM, acting as a masker. The two sinusoidal AMs had different frequencies forming a ratio f_2/f_1 of 2 or 3, and thresholds were measured as a function of the relative phase of the masker and signal. The two AM components were imposed on a white-noise carrier, so that the long-term spectra of all stimuli were flat. The authors showed that detection thresholds depend upon the phase of the masker modulation for $f_2/f_1=2$, but not for $f_2/f_1=3$. They attempted to account for their findings using a linear envelope-detector model and the following envelope statistics: the variance of the envelope; the fluctuations of the envelope power (i.e., the fourth central moment of the envelope); the envelope maximum scaled by the rms power or ''crest factor;'' the ratio formed by the maximum and minimum of the envelope or ''max/min.'' The phase effects could be accounted for by the max/min statistic. Using the crest factor and the fourth central moment of the envelope, the existence of phase effects was also predicted, but the corresponding effects were not consistent with those actually observed.

For $f_2/f_1=3$, the absence of a phase effect on the signal threshold did not imply that the phase of the signal has no audible effect when the signal is above threshold. Indeed, the relative phase of two sinusoids with a frequency ratio of 3 has a large effect on the shape of their sum when their amplitudes are similar. In the first part of this study, the auditory system's sensitivity to changes in the relative phase of two simultaneous AMs forming a frequency ratio of 2 or 3 was assessed for AM components which, in most conditions, were both clearly detectable. We then looked for an envelope statistic accounting successfully for the overall results.

I. PSYCHOPHYSICAL EXPERIMENT ON AM PHASE DISCRIMINATION

A. Method

Two sinusoidal AMs were simultaneously imposed on a noise carrier. On each trial, the listener was presented with two observation intervals, a ''standard'' interval and a ''target'' interval, randomly ordered. The listener's task was to determine if the target interval was the first or the second. In the standard interval, the amplitude envelope of the noise carrier was of the form

$$E(t)=1+m_1\sin(2\pi f_1 t+\phi_1)+0.5\sin(2\pi f_2 t+\phi_2),$$
$$(f_2/f_1=2 \text{ or } 3; \quad m_1\leqslant 0.5), \tag{1}$$

where t is time, m_1 and f_1, respectively, represent the depth and frequency of the first modulation, f_2 represents the frequency of the second modulation, and ϕ_1 and ϕ_2 represent the starting phases of each modulation, randomized on each trial. The frequencies f_1 and f_2 were [100 Hz, 200 Hz], [150 Hz, 300 Hz], or [100 Hz, 300 Hz]. m_1 ranged from 0 to 0.5.

In the target interval, f_2 was increased by a small amount Δf of 0.5 Hz, 1 Hz, or 2 Hz, which was too small to be detected as a change in envelope rate. The equation of the target envelope was then

$$E(t)=1+m_1\sin(2\pi f_1 t+\phi_3)$$
$$+0.5\sin[2\pi(f_2+\Delta f)t+\phi_4], \tag{2}$$

where ϕ_3 and ϕ_4 represent the starting phases of each modulation, randomized on each trial like ϕ_1 and ϕ_2 in Eq. (1).

 0001-4966/99/105(5)/2987/4/$15.00

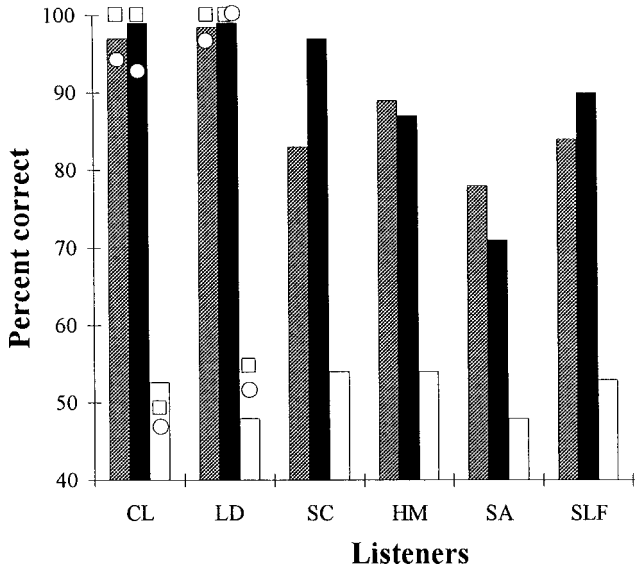

FIG. 1. Results of the psychophysical experiment for $m_1 = 0.50$. The vertical bars show the individual data obtained for $\Delta f = 1$ Hz. Gray bars: $f_1 = 100$ Hz, $f_2 = 200$ Hz; black bars: $f_1 = 150$ Hz, $f_2 = 300$ Hz, unfilled bars: $f_1 = 100$ Hz, $f_2 = 300$ Hz. The unfilled symbols show the data obtained for $\Delta f = 0.5$ Hz (circles) and $\Delta f = 2$ Hz (squares).

The target envelope could be described as the sum of two sinusoids identical in every respect to those forming the standard envelope, but no longer phase locked: in the target envelope, the relative phase of two sinusoids at f_1 and f_2 Hz was continuously and cyclically changing, with a periodicity of $1/\Delta f$ s (i.e., 2, 1, or 0.5 s). In consequence of this phase rotation, the target could logically be discriminated from the standard as soon as *any* phase relation of the two sinusoids was discriminable from *any* other phase relation.

The carrier was a white noise presented at 60 dB SPL. Each stimulus had a total duration of 4 s. A silent pause of 500 ms separated the two stimuli of each trial. After each trial, feedback concerning response accuracy was provided visually. Trials were organized in blocks of 100 during which m_1, f_1, f_2, and Δf were fixed. The stimuli were generated with a sampling rate of 20 kHz, low-pass filtered at 8.0 kHz, and presented binaurally via headphones (Stax Lambda Pro) in a soundproof booth.

B. Results

Six listeners participated in the experiment. The results obtained with $m_1 = 0.5$ are shown in Fig. 1. Each of the six listeners was tested for at least 300 trials with $\Delta f = 1$ Hz. The corresponding data are displayed by gray bars for [$f_1 = 100$ Hz, $f_2 = 200$ Hz], black bars for [$f_1 = 150$ Hz, $f_2 = 300$ Hz], and unfilled bars for [$f_1 = 100$ Hz, $f_2 = 300$ Hz]. When f_2/f_1 was equal to 2, the percentage of correct responses (P_c) always exceeded 70%. The performance of two listeners, CL and LD, was nearly perfect. For this frequency ratio, the listeners reported that they identified the target stimulus by detecting in it a cyclically emerging-then-vanishing ''buzz'' or ''rattle'' sound. By contrast, when f_2/f_1 was equal to 3, P_c never exceeded significantly the 50%-chance level. Similar results were obtained when Δf was set at 0.5 or 2 Hz instead of 1 Hz for listeners CL and LD (see the unfilled circles and squares in Fig. 1).

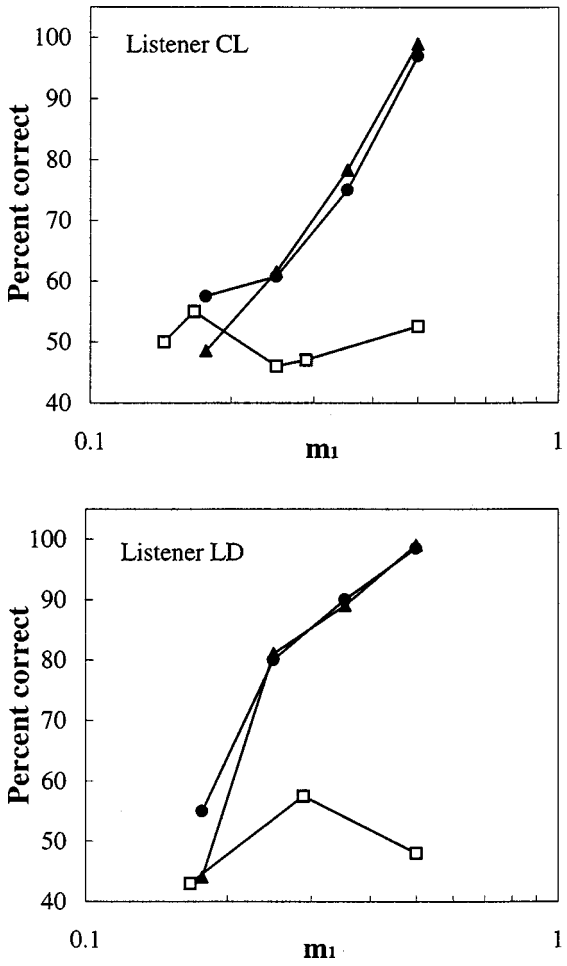

FIG. 2. Psychometric functions measured in listeners CL and LD. $\Delta f = 1$ Hz. Circles: $f_1 = 100$ Hz, $f_2 = 200$ Hz; triangles: $f_1 = 150$ Hz, $f_2 = 300$ Hz; squares: $f_1 = 100$ Hz, $f_2 = 300$ Hz.

The effect of m_1 on performance was investigated in listeners CL and LD for Δf fixed at 1 Hz. Figure 2 shows the obtained psychometric functions. Each data point is based on at least 100 trials (up to 500). The two listeners behaved similarly. For $f_2/f_1 = 3$ (open squares), P_c did not exceed chance. For $f_2/f_1 = 2$ (closed circles and triangles), the results were essentially independent of f_1 and f_2: for each listener, the chance level was exceeded significantly ($P < 0.001$, binomial test) as soon as m_1 reached 0.25.

II. MODELING AM PHASE DISCRIMINATION

We shall attempt here to account for our psychophysical results on the basis of the linear envelope-detector model used by Strickland and Viemeister (1996).

A. Description of the model

We implemented a computational version of this model consisting of four successive processing stages: (1) a predetection bandpass filter (1st-order Butterworth) of 2-kHz bandwidth, centered at 5 kHz; (2) a half-wave rectifier; (3) a low-pass filter (1st-order Butterworth) with a 3-dB cutoff frequency f_c ranging between 66 and 250 Hz; (4) a decision

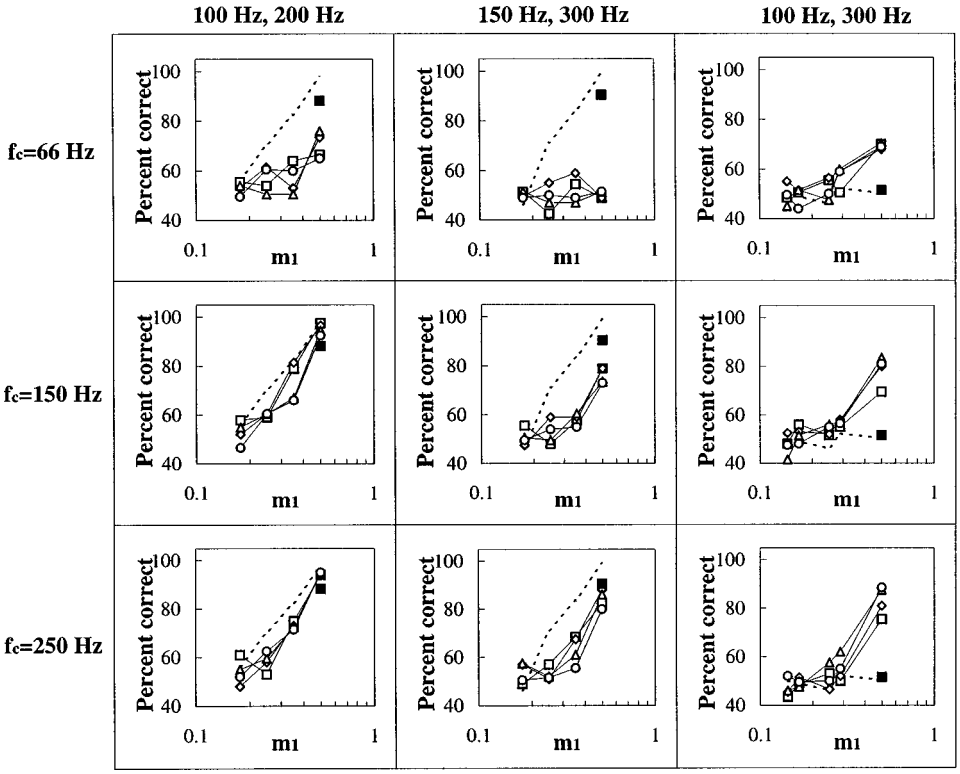

FIG. 3. Percent-correct performance predicted by the envelope-detector model with max/min as the envelope statistic. $\Delta f = 1$ Hz. f_c is set to 66 Hz (top panels), 150 Hz (middle panels), or 250 Hz (bottom panels). Δt is set to 12.5 ms (squares), 25 ms (diamonds), 50 ms (triangles), or 100 ms (circles). The dashed lines show the average psychometric functions measured in listeners CL and LD. The filled squares show the average data obtained from the six listeners for $m_1 = 0.5$.

device generating a statistic from the output of the low-pass filter.

In the model, the output of the low-pass filter represents the *internal* envelope $[e(t)]$ of the stimuli. We considered five statistics of $e(t)$: (1) the standard deviation (σ), that is the second central moment (Viemeister, 1979); (2) the skewness, corresponding to the third central moment; (3) the kurtosis, corresponding to the fourth central moment; (4) max/min, i.e., the ratio of the maximum to the minimum of $e(t)$ (Forrest and Green, 1987); (5) the ''crest factor,'' corresponding to the ratio of the maximum of $e(t)$ to its rms power (Hartmann and Pumplin, 1988).

In previous studies on AM detection and discrimination, each envelope statistic was computed over the whole observation interval. This approach assumed that listeners extract a ''global feature'' over the entire stimulus. In the present study, however, the stimuli were much longer (4 s); they were so long that it seemed *a priori* unreasonable to make the same assumption. Moreover, listeners reported identifying the target stimulus by detecting in it a *cyclically* emerging and vanishing ''buzz-like'' sound. Instead of computing a global statistic, listeners certainly extracted ''local features'' based on shorter time intervals. This hypothesis was implemented in the present model by calculating the envelope statistics within adjacent rectangular windows of a short duration Δt. The final decision statistic corresponded to the standard deviation of the values calculated within the successive temporal windows.

For a given envelope statistic, Strickland and Viemeister (1996) set f_c so that the detection thresholds for sinusoidal AM approximated the form of the average temporal modulation transfer function of their listeners. They set f_c to 70 Hz for simulations using σ, 150 Hz for simulations using max/min and the crest factor, and 250 Hz for simulations using the kurtosis. In the present study, we tested four values of f_c: 66, 150 and 250. For each f_c and each envelope statistic, four values of Δt were tested: 12.5, 25, 50, and 100 ms.

The simulations were performed using the stimuli and the two-interval, two-alternative forced-choice procedure described in Sec. I. On a given trial, a correct response was obtained if the standard deviation of the calculated statistics was larger for the target stimulus than for the standard stimulus. In each condition, 200 trials were used to estimate the percentage of correct responses. Psychometric functions equivalent to those measured in listeners were obtained for the three frequency pairs (f_1, f_2).

B. Results

P_c simulated using the σ, and kurtosis statistics were at chance values in all conditions. P_c values predicted using the max/min statistic for $\Delta f = 1$ Hz are presented in Fig. 3. For comparison, the average psychometric functions measured in listeners CL and LD, and the average performance of the six listeners for $m_1 = 0.5$, are plotted along with the simulated data. Increasing f_c generally increased the simulated discrimination performance. For $f_2/f_1 = 2$ and $m_1 = 0.5$, P_c predicted with an f_c of 250 Hz and a Δt of 25 or 50 ms was close to the average performance of all listeners. However, for $f_2/f_1 = 2$ and $m_1 < 0.5$, the predicted P_c was always below the performance levels measured in listeners CL and LD. For $f_2/f_1 = 3$ and $m_1 < 0.5$, the predicted P_c was always close to the chance level, as found for listeners CL and LD. However, for $f_2/f_1 = 3$ and $m_1 = 0.5$, the predicted P_c was always above chance, and exceeded 80% when f_c and Δt were greater than 66 Hz and 12.5 ms, respectively. In com-

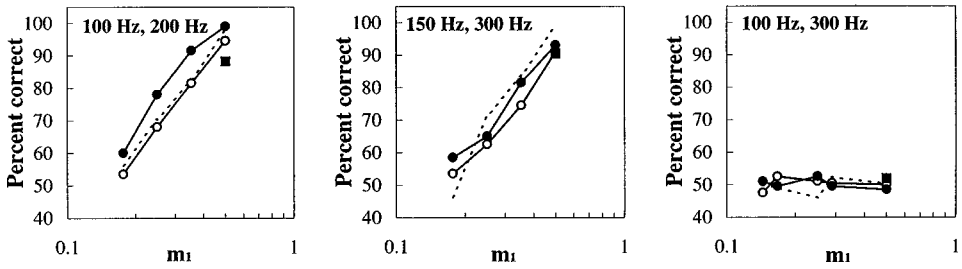

FIG. 4. Psychometric functions predicted by the envelope-detector model with the skewness (filled circles) and the crest factor (unfilled circles) statistics, for $\Delta f = 1$ Hz. Model parameters: $f_c = 150$ Hz, $\Delta t = 50$ ms. The dashed lines show the average psychometric functions measured in listeners CL and LD. The filled squares show the average data obtained from the six listeners for $m_1 = 0.5$.

parison the average performance for all listeners was at chance level.

The crest factor and the skewness statistics predicted the psychophysical data relatively well only when f_c and Δt were 150 Hz and 50 ms, respectively. Figure 4 shows the psychometric functions predicted using these statistics with $\Delta f = 1$ Hz, $f_c = 150$ Hz, and $\Delta t = 50$ ms. For $f_2/f_1 = 3$, P_c predicted by the crest factor (unfilled circles) and skewness (filled circles) statistics never exceeded the chance level. For $f_2/f_1 = 2$, both statistics generally accounted for the psychophysical data. The discrimination performance predicted by the skewness was greater than that measured in listeners CL and LD when f_1 and f_2 were 100 and 200 Hz, respectively, and matched relatively well the psychophysical data when f_1 and f_2 were 150 and 300 Hz. The discrimination performance predicted by the crest factor matched the average data for listeners CL and LD when f_1 and f_2 were 100 and 200 Hz, but was somewhat lower than that observed psychophysically when f_1 and f_2 were 150 and 300 Hz.

P_c was finally simulated for a phase rotation rate of π rad/s ($\Delta f = 0.5$ Hz) and 4π rad/s ($\Delta f = 2$ Hz) (not shown here). Again, when f_c is 150 Hz and Δt is 50 ms, the crest factor and skewness statistics account rather well for the average discrimination performance of listeners CL and LD measured with frequency ratios f_2/f_1 of 2 and 3. In contrast, the max/min statistic still predicts that P_c should exceed the chance level for $f_2/f_1 = 3$ and $m_1 = 0.5$.

III. GENERAL DISCUSSION

In our psychophysical experiment, listeners were asked to detect changes in the phase spectrum of temporal envelopes. The task appeared to be easy in some conditions, but surprisingly difficult—and even impossible—in other conditions. Our results tally with the masking data of Strickland and Viemeister (1996). However, our modeling study questions a conclusion drawn by these authors.

Strickland and Viemeister successfully predicted their masking data with an envelope-detector model which assumed that listeners base their decision on the envelope max/min ratio; other envelope statistics were markedly less successful. In our study, by contrast, the max/min statistic did not predict listeners' performance when the frequency ratio of the two AM components constituting the temporal envelope was 2, except when the two AM components were of equal amplitude. Moreover, the max/min statistic predicted a sensitivity to phase changes when the frequency ratio was 3; that is, when phase changes were inaudible for all listeners. This result clearly argues against the idea that listeners can compute the max/min statistic. Therefore, it is still not clear which metric can predict phase effects when they are measured with a masking paradigm as in Strickland and Viemeister's experiment.

In their modeling study, Strickland and Viemeister computed each envelope statistic over the whole stimulus. In contrast, we calculated each envelope statistic within adjacent temporal windows of a short duration, the final decision statistic corresponding to the standard deviation of the values calculated within the successive windows. One may therefore argue that the differences in simulation results between these two studies originate from a difference in modeling assumptions. However, Strickland and Viemeister (and Bacon and Grantham, 1989) also assumed that listeners are able to make decisions over short intervals (<100 ms) in order to predict the ''negative masking'' effect (the improved detectability of a high-frequency AM signal when it is added to a low-frequency AM masker). Let us note, in addition, that the discrepancy regarding max/min predictions cannot be explained in terms of differences in range of variation of this statistic.

Unlike max/min, the crest factor and the skewness statistics could be used to predict the present psychophysical data relatively well. Further work is therefore required to differentiate between these two statistics. Our predictions were based on the assumption that, in the auditory system, the temporal envelope of sound stimuli is smoothed by a single low-pass filter. An alternative hypothesis is that temporal envelopes are analyzed by a bank of bandpass ''modulation filters'' (e.g., Dau *et al.*, 1997). It remains to be determined if the properties of these filters could explain the perceptua phenomena reported here.

ACKNOWLEDGMENTS

We thank Mike A. Akeroyd and Brian C. J. Moore for comments on this manuscript, and Elizabeth A. Strickland for helpful discussions.

Bacon, S. P., and Grantham, D. W. (**1989**). ''Modulation masking patterns: Effects of modulation frequency, depth and phase,'' J. Acoust. Soc. Am. **85**, 2575–2580.

Dau, T., Kollmeier, B., and Kohlrausch, A. (**1997**). ''Modeling auditory processing of amplitude modulation. II. Spectral and temporal integration,'' J. Acoust. Soc. Am. **102**, 2906–2919.

Forrest, T. G., and Green, D. M. (**1987**). ''Detection of partially filled gaps in noise and the temporal modulation transfer function,'' J. Acoust. Soc. Am. **82**, 1933–1943.

Hartmann, W. M., and Pumplin, J. (**1988**). ''Noise power fluctuations and the masking of sine signals,'' J. Acoust. Soc. Am. **83**, 2277–2289.

Strickland, E. A., and Viemeister, N. F. (**1996**). ''Cues for discrimination of envelopes,'' J. Acoust. Soc. Am. **99**, 3638–3646.

Viemeister, N. F. (**1979**). ''Temporal modulation transfer functions based upon modulation thresholds,'' J. Acoust. Soc. Am. **66**, 1364–1380.

Erratum: "Simplified models of transient elastic waves in finite axisymmetric layered media" [J. Acoust. Soc. Am. 104, 3369–3384 (1998)]

Michael El-Raheb
The Dow Chemical Company, Midland, Michigan 48674

(Received 4 February 1999; accepted for publication 18 February 1999)

[S0001-4966(99)04305-2]

PACS numbers: 43.20.Jr, 43.40.Dx [CBB]

The definition of ∇_n^2 in Eq. (1c) should be

$$\nabla_n^2=\frac{\partial^2}{\partial r^2}+\frac{1}{r}\frac{\partial}{\partial r}-\frac{n^2}{r^2}\,. \tag{1c}$$

The factor $G_b h^2/h_b$ in Eqs. (4), (5a), and (5b) should be $G_b h^2/4h_b$. In Appendix A, Eq. (A8) should be

$$\tau_K(z)=-\frac{h}{2}\,k_z G_b\Big[\Psi_{i+k-2}\sin k_z z+(\Psi_{i+k-1}+\Psi_{i+k-2}\cos k_z h_b)\,\frac{\cos k_z z}{\sin k_z h_b}\Big], \tag{A8}$$

while Eq. (A9) should read

$$\overline{M}_r=-(\tau_1(h_b)+\tau_2(0))\,\frac{h}{2}=\left(\frac{h}{2}\right)^2\frac{1}{h_b}\,\frac{k_z h_b}{\sin k_z h_b}\,G_b[2\Psi_i\cos k_z h_b+\Psi_{i+1}+\Psi_{i-1}], \tag{A9}$$

which changes Eq. (A10) to

$$\overline{M}_r=\left(\frac{h}{2}\right)^2 G_b[2\Psi_i+\Psi_{i+1}+\Psi_{i-1}]/h_b\,. \tag{A10}$$

 0001-4966/99/105(5)/2991/1/$15.00